Jun-ichiro Ishibashi
Kyoko Okino
Michinari Sunamura
Editors




Subseafloor Biosphere Linked to Hydrothermal Systems

TAIGA Concept

Springer Open

Subseafloor Biosphere Linked to Hydrothermal Systems

Jun-ichiro Ishibashi • Kyoko Okino
Michinari Sunamura
Editors

Subseafloor Biosphere Linked to Hydrothermal Systems

TAIGA Concept

Springer Open

Editors
Jun-ichiro Ishibashi
Department of Earth and Planetary Science, Faculty of Sciences
Kyushu University
Fukuoka, Japan

Kyoko Okino
Atmosphere and Ocean Research Institute
The University of Tokyo
Kashiwa, Chiba, Japan

Michinari Sunamura
Department of Earth and Planetary Science
Graduate School of Science
The University of Tokyo
Tokyo, Japan

ISBN 978-4-431-54864-5 ISBN 978-4-431-54865-2 (eBook)
DOI 10.1007/978-4-431-54865-2
Springer Tokyo Heidelberg New York Dordrecht London

Library of Congress Control Number: 2014948334

Printed on acid-free paper

Springer is part of Springer Science+Business Media (www.springer.com)

Preface

This e-book is a collection of scientific results of studies obtained during the TAIGA project between 2008 and 2012. The TAIGA project was planned and organized to elucidate interactions between the lithosphere, hydrosphere, and biosphere through the fluid advection system beneath the seafloor through many cruises, modeling, and laboratory experiments. This interdisciplinary project was funded by MEXT (Ministry of Education, Culture, Sports, Science and Technology in Japan) from FY 2008 to FY 2012, as a project of a "Grant-in-Aid for Scientific Research on Innovative Areas". The program name "TAIGA" represents a dynamic fluid advection system beneath the seafloor (In Japanese, *taiga* refers to "a great river"), as introduced in Chap. 1.

Multidisciplinary scientists from universities and institutes and many students worked together synergically for this program. Five research projects (A01–A05) were organized to attain major goals under the framework of the TAIGA program, as follows. A01: Diversity of TAIGA controlled by various geologic and geophysical structures; A02: Biogeochemical impact of TAIGA flux on the deep-sea environment; A03: Evolution of TAIGA—constraints from geochronology and molecular genetics; A04: Clarification of in situ physical, chemical, and biological interactive processes in TAIGAs; and A05: Laboratory experiments to elucidate chemical and biological interactions in TAIGA. However, many individual specific studies were conducted by members across teams and disciplines, as will be obvious in the contents of this book.

Several research cruises, dive expeditions, and drilling operations were conducted during the TAIGA project. To conduct these ocean field studies efficiently, three integrated study sites were selected, namely, the Central Indian Ridge, the Southern Mariana Trough, and the Okinawa Trough. Each of them represents different types of TAIGAs, as introduced in Chap. 1. Shallow seafloor drilling expeditions employing a Benthic Multicoring System (BMS) were conducted twice as hosted by the TAIGA project, once in August 2010 in the Southern Mariana Trough, and the other in July 2011 in the Okinawa Trough. Deep seafloor drilling during the Integrated Ocean Drilling Program (IODP) Expedition 331 was conducted in the Okinawa Trough in September 2010, in which several TAIGA project members participated. More than 30 submersible dive expeditions and surface ship research cruises were conducted under the framework of Japan Agency for Marine–Earth Science and Technology (JAMSTEC) deep-sea investigations and of the Atmosphere Ocean Research Institute, The University of Tokyo. These cruises were executed by research proposals submitted by TAIGA project members.

This e-book consists of 51 chapters, which have been contributed by TAIGA project members as individual parts and critically reviewed by external reviewers or TAIGA project members. Part I compiles interdisciplinary studies, including summary articles for each research program. Parts II, III, and IV compile studies related to the three integrated study sites, the Central Indian Ridge, the Southern Mariana Trough, and the Okinawa Trough. Some of the chapters include review sections to overview the project results together with a summary of the background information and previous studies of the target site or the specialized field, for the benefit of readers. Appendices in three parts compile rather short reports which omit full discussion in order to give additional data or results.

This volume is being published as "an open access e-book," which is a new style of publication for scientific articles. We hope that this e-book is well accepted among the scientific community as a whole, since it is the first publication covering wide ranges of research topics both on the arc–backarc systems such as the western Pacific and on the mid-ocean ridge system such as the Indian Ocean. We would like to urge readers to inform their colleagues of this publication by quoting it as follows:

Subseafloor Biosphere Linked to Hydrothermal Systems: TAIGA Concept
http://link.springer.com/978-4-431-54865-2

Tokyo, Japan — Tetsuro Urabe
Fukuoka, Japan — Jun-ichiro Ishibashi
March 2014

Editorial Board

The editorial board was organized from the principal members of the TAIGA project to handle editing work of the chapters. Members are listed below.

Acknowledgments

We would like to express our appreciation to the Ministry of Education, Culture, Sports, Science and Technology of Japan for funding this project from FY 2008 to FY 2012 (#20109001–20109006), as a project of a Grant-in-Aid for Scientific Research on Innovative Areas. Additional funding in FY 2013 supported editing work and publication of this e-book. We especially thank the crew, submersible teams, drilling operators, and onboard scientists of all of the research cruises related to the project.

Ken Kimlicka and Taeko Sato at Springer Japan provided efficient assistance during all stages of the process of editing. Photographs on the cover were kindly provided by JAMSTEC. Harumi Fujita supported the handling, reviewing, and editing of the manuscripts.

We sincerely appreciate the external reviewers (listed below) who substantially improved the accuracy of the contents and clarity of the presentations.

List of External Reviewers

Wolfgang Bach
Department of Geosciences, University of Bremen

Stace E. Beaulieu
Woods Hole Oceanographic Institution

Hitoshi Chiba
Graduate School of Natural Science and Technology, Okayama University

Jon Copley
Ocean and Earth Science, University of Southampton

Cornel E. J. de Ronde
GNS Science

Jérôme Dyment
Institut de Physique du Globe de Paris, CNRS

Rob L. Evance
Woods Hole Oceanographic Institution

Toshiya Fujiwara
Institute for Research on Earth Evolution, JAMSTEC

Toshitaka Gamo
Atmosphere and Ocean Research Institute, The University of Tokyo

Yumiko Harigane
Geological Survey of Japan, AIST

Steven P. Hollis
Earth Science and Resource Engineering, CSIRO

Hironobu Hyodo
Research Institute of Natural Sciences, Okayama University of Science

Osamu Ishizuka
Geological Survey of Japan, AIST

Takashi Itoh
College of Education, Ibaraki University

Hiroyuki Kimura
Graduate School of Science, Shizuoka University

Tsuyoshi Komiya
Graduate School of Arts and Sciences, The University of Tokyo

Kaoru Kubokawa
Misaki Marine Biological Station, The University of Tokyo

Jun-ichi Miyazaki
Graduate School of Education, Yamanashi University

Takashi Naganuma
Graduate School of Biosphere Science, Hiroshima University

Masao Nakanishi
Graduate School of Science, Chiba University

Kenji Nanba
Faculty of Symbiotic Systems Science, Fukushima University

Kiyotaka Ninagawa
Faculty of Science, Okayama University of Science

Jun Nishikawa
Atmosphere and Ocean Research Institute, The University of Tokyo

Azusa Nishizawa
Hydrographic and Oceanographic Department of Japan

Yoshifumi Nogi
National Institute of Polar Research

Tatsuo Nozaki
Institute for Research on Earth Evolution, JAMSTEC

Yasuhiko Ohara
Hydrographic and Oceanographic Department of Japan

Soichi Omori
The Open University of Japan

Takenori Sasaki
The University Museum, The University of Tokyo

Takazo Shibuya
Precambrian Ecosystem Laboratory, JAMSTEC

Motohiro Shimanaga
Center for Marine Environment Studies, Kumamoto University

Robert Stern
Department of Geosciences, The University of Texas at Dallas

Saiko Sugisaki
Graduate School of Science, the University of Tokyo

Narumi Takahashi
Institute for Research on Earth Evolution, JAMSTEC

Yoshinori Takano
Institute of Biogeoscience, JAMSTEC

Fernando Tornos
Centro de Astrobiología, CSIC-INTA

Yuichiro Ueno
Earth–Life Science Institute, Tokyo Institute of Technology

Susumu Umino
Faculty of Natural System, Kanazawa University

Tomoo Watsuji
Institute of Biogeoscience, JAMSTEC

Toshitsugu Yamazaki
Atmosphere and Ocean Research Institute, The University of Tokyo

Fumitaka Yanagisawa
Faculty of Science, Yamagata University

Contents

Part VI Appendix II: Drilling Reports

Part VII Appendix III: Data Reports

Part I

Interdisciplinary Studies

Introduction of TAIGA Concept

1

Tetsuro Urabe, Jun-ichiro Ishibashi, Michinari Sunamura, Kyoko Okino, Ken Takai, and Katsuhiko Suzuki

Abstract

After the discovery of seafloor hydrothermal venting, it became evident that the subseafloor fluid advection system plays an extremely important role in the Earth's element cycle. We designate these fluid advections as sub-seafloor TAIGAs (which stand for **T**rans-crustal **A**dvection and **I**n-situ biogeochemical processes of **G**lobal sub-seafloor Aquifers. In Japanese, "taiga" refers to "a great river"). This concept emphasizes dynamic signature of subseafloor hydrosphere, especially for a hydrothermal fluid circulation system that might support subseafloor microbial ecosystem. However, the link between the fluid advection and microbial activity has never been clearly demonstrated. We therefore hypothesized four types of sub-seafloor TAIGAs; hydrogen, methane, sulfur, and iron to investigate the relation. Each type of TAIGA is characterized by the most dominant reducing substance available for chemosynthesis. Our trans-disciplinary research between 2008 and 2012 indicates that the hypothesis is valid and the microbial activity within the flow of TAIGAs has strong linkage to chemical characteristics of each TAIGA; that is, the subseafloor TAIGA supplies four different kinds of electron donor for respective chemolithoautotroph ecosystem which is suitable for particular electron donor. It is also shown that the composition of dissolved chemical species in the subseafloor TAIGAs are substantially affected by the geological background of their flow path such as volcanism, surrounding host rocks and tectonic settings. Our research clearly indicates that the chemosynthetic sub-seafloor biosphere is controlled and supported by Earth's endogenous flux of heat and mass beneath the seafloor.

Keywords

Arc-backarc system • Chemosynthesis • Global heat and mass flux • Hydrothermal activity • Mid-ocean ridge • Oceanic crust • Subseafloor biosphere

T. Urabe (✉) • M. Sunamura
Department of Earth and Planetary Science, Graduate School of Science, The University of Tokyo, Tokyo 113-0033, Japan
e-mail: urabe@eps.s.u-tokyo.ac.jp

J.-i. Ishibashi
Department of Earth and Planetary Sciences, Faculty of Sciences, Kyushu University, Fukuoka 812-8581, Japan

K. Okino
Atmosphere and Ocean Research Institute, The University of Tokyo, Kashiwa, Chiba 277-8564, Japan

K. Takai
Department of Subsurface Geobiological Analysis and Research (D-SUGAR) and Research and Development (R&D) Center for Submarine Resources, Japan Agency for Marine-Earth Science and Technology (JAMSTEC), Yokosuka, Kanagawa 237-0061, Japan

K. Suzuki
Institute for Research on Earth Evolution (IFREE) and Precambrian Ecosystem Laboratory (PEL), Japan Agency for Marine-Earth Science and Technology (JAMSTEC), Yokosuka, Kanagawa 237-0061, Japan

J.-i. Ishibashi et al. (eds.), *Subseafloor Biosphere Linked to Hydrothermal Systems: TAIGA Concept*,
DOI 10.1007/978-4-431-54865-2_1,

1.1 Subseafloor Biosphere and Hydrosphere

The finding of unique macrobenthos community around deep-sea hydrothermal vent sites in the late 1970s attracted a lot of attention among various scientists. The high biomass density indicates that the hydrothermal site is one of the most dynamic and productive ecosystems on the earth (Childress and Fisher 1992; Fisher et al. 2007). The ecosystem is believed to be sustained by primary production of chemolithoautotrophic microbes, partly symbiotic, which produce organic compounds through chemosynthesis using chemical energy of inorganic materials dissolved in hydrothermal fluids. The high primary production based on these reactions demolishes the traditional idea that all organisms living on the earth depend solely on the photosynthesis using sunlight. In the sulfide chimney structure of the vents, various chemolithoautotrophic microbes were found both under various redox and thermal conditions (Deming and Baross 1993; Takai and Horikoshi 1999; Kelley et al. 2002). These findings suggest that the microbial ecosystem would be developed extensively beneath the seafloor, if there exists sufficient permeability within the oceanic crusts.

Such a hypothesis is supported by an observation that significant amount of water may exist within the oceanic crust (e.g., Johnson et al. 2006). The compilation of the measured porosity of the oceanic crust indicates that the values are up to 34 % in the young oceanic crust and higher than 10 % even in altered crust older than 10 Ma (Johnson and Pruis 2003). The total mass of water below the seafloor was estimated to be 26×10^{18} kg, which corresponds to ~2 % of that of the entire mass of seawater. This size is much larger than that of continental groundwater, and comparable to that of ice on the polar regions (Mottl et al. 2007).

As a first-order approximation, the type of fluid advection system could be estimated by the thermal regime of the seafloor. According to the thermal model calculations (e.g., Stein and Stein 1992), heat discharge through the seafloor is classified into three categories; high-temperature hydrothermal fluid advection at the axial region of mid-oceanic ridge, low-temperature hydrothermal fluid circulation at the ridge flank region where there is impermeable sediment cover, and conductive cooling through the surface of the oceanic crust. At the ridge axis whose crustal age is younger than 1 Ma, the axial magma chamber is the most important heat source to drive high-temperature fluid circulation. Global heat flux through the ridge axes is estimated as $(1.5–2.8) \times 10^{12}$ W from crust formation rate along all the ridge axes on the earth (Mottl 2003). And this heat flux corresponds to water mass flux of $(3.1–5.9) \times 10^{16}$ g/year, assuming the temperature of the hydrothermal fluid is 350 °C (Mottl 2003). On the other hand, the heat generated from cooling of the lithosphere is dominant at the ridge flank regions. Heat flux at the ridge flank region is as large as $(5.1–9.1) \times 10^{12}$ W, considering the temperature of the oceanic crust to be 10–40 °C (Johnson and Pruis 2003). Because the heat in the ridge flank is transported by low temperature fluid (5–20 °C), estimated water mass flux should be as large as $(0.2–2.0) \times 10^{19}$ g/year (Mottl 2003). This estimation leads to a conclusion that mass flux of the ridge flank region is much larger than that of the ridge axis region, and comparable to the total water flux of terrestrial rivers ($=3.74 \times 10^{19}$ g/year). Such advective flow in the ridge flank region was confirmed at seamounts located in the eastern flank of the Juan de Fuca ridge where low temperature fluid advection has been observed by submersible dives and ODP/IODP drillings (Fisher et al. 2003).

Estimation of global geochemical flux transported through the seafloor is a more difficult problem and was tackled with two different approaches (e.g., Alt 2003). One approach is a calculation by multiplying the chemical composition of the venting fluids and the estimated water mass flux (e.g., Elderfield and Schultz 1996). The major source of uncertainty in this approach comes from the fact that the contribution of the mass flux by the low temperature hydrothermal fluid at the ridge flank could not be taken into account. The limited information on the chemistry of circulating fluid in the ridge flank region revealed that the low temperature hydrothermal fluid showed different chemistry from that of the high temperature fluid from the axial area (Mottl et al. 1998). For example, the low temperature fluid acts as sink for alkali elements (Na, K, and Li) and some nutrients (NO_3, PO_4) in addition to Mg and SO_4 ions. Besides, the data on minor components are missing especially for the low temperature fluids.

The other approach is a calculation based on geochemical budget during alteration process of the oceanic crust (e.g., Bach et al. 2003). The difference in chemical composition between the fresh and altered oceanic crusts was integrated to estimate net elemental supply to and removal from the oceanic crust by the advective fluids. Although estimated fluxes from these two approaches still show large discrepancy, these efforts shed light on global geochemical flux by advective flow beneath the seafloor. It is suggested that the hydrothermal flux is comparable for several major and minor elements to that of river run off on the continent (Wheat and Mottl 2004). In addition, the hydrothermal fluid circulation within the oceanic crust, including low-temperature fluid advection and the rock alteration were considered to affect on the whole-earth-mantle dynamics by regulating the cool process of the Earth.

There is no doubt that the subseafloor fluid advection plays an extremely large role in the Earth's element cycle especially for fluid-mobile elements. However, it is not clear whether the fluid is also responsible or not for the existence

of so-called deep biosphere through lithochemoautotrophic metabolism. So we would like to further investigate this possibility.

1.2 Hydrothermal Systems as a Window of Sub-seafloor TAIGAs

We propose to designate these hydrothermal fluid advections as sub-seafloor TAIGAs (which stand for **T**rans-crustal **A**dvection and **I**n-situ biogeochemical processes of **G**lobal sub-seafloor Aquifers. In Japanese, "taiga" refers to "a great river"). This name emphasizes dynamic signature of subseafloor hydrosphere. Fluid chemistry of the advective flow would be controlled by the similar processes to rivers on land, which may change their chemistry gradually along the pathway. Sub-seafloor TAIGAs have a wide range of inputs and outputs including exchange components with the earth's crust through hydrothermal alteration, dissolution and precipitation of materials en route, and interactions with biosphere in their watershed areas.

Although wide variety of driving forces have been proposed for fluid advections beneath the seafloor, such as, tectonic compaction, hydraulic head, and decomposition of hydrate (Ge et al. 2003), thermally-generated density contrasts driven by a heat source such as magma chamber along the mid-ocean ridges undoubtedly induces the most dynamic fluid advection. As magma intrusion causes high temperature environment, seawater becomes more reactive with the surrounding rocks such as mid-ocean ridge basalt (MORB). Besides, degassing of CH_4, CO_2, CO, and H_2 from the magma would significantly increase the geochemical flux of several chemical species and be transported by hydrothermal fluid circulation, which fuels ecosystems in active sub-seafloor TAIGAs. Moreover, the high-temperature hydrothermal fluid vented at "river mouth" mixes with the ambient seawater as it rises, to form hydrothermal plumes, which could host another regime of chemolithoautotrophic microbes.

Apart from the axial region of the mid-oocean ridges, diversity in fluid chemistry has been recognized in association with the findings of seafloor hydrothermal systems in various tectonic settings (e.g. Gamo et al. 2006; Seyfried et al. 2004). Fluid chemistry is basically controlled by hydrothermal interactions with surrounding rocks, which means the chemical signature of the rocks is an important factor for the diversity. Difference in elemental concentrations would be more obvious in minor species such as B, Cs, As, Sb and other fluid-soluble (or fluid-mobile) incompatible elements, which are difficult to be fixed into alteration minerals during high-temperature fluid-rock interactions. Fluid chemistry is affected also by various materials encountered during the fluid circulation, such as magmatic volatiles from the heat source magma and/or organic matter accumulated in sediment around the hydrothermal system. They supply chemical species which control pH of the fluid by dissolution (such as CO_2, SO_2, HCl, H_2S) or oxic-reductive state (such as H_2S, H_2) when dissolved in the fluid. Moreover, some of these species are also important energy source for microbiological metabolism, as will be discussed later.

It should be pointed out that the estimation of geochemical flux does not consider contributions and diversity of the hydrothermal systems in the arc-backarc setting. Baker et al. (2008) estimated that submarine volcanoes in intraoceanic arcs could supply a hydrothermal discharge equal to ~10 % of that from the global mid-ocean ridge, based on combining the statics from their studies on Tonga-Kermadec Arc and Mariana Arc. They also emphasized the geochemical impact may be even more significant, since many chemical species are often more highly concentrated in arc fluids than in mid-ocean ridges fluids. Variations of chemical species in hydrothermal fluids may directly affect microbial metabolism and subsequent vent macrofauna. A major re-examination for estimation for geochemical flux is required.

1.3 Diversity of Subseafloor TAIGAs

In order to understand linkage between the microbial activity and chemical characteristics of hydrothermal and advective flows, we propose four types of sub-seafloor TAIGAs. Each type of TAIGA is characterized by the most dominant reducing substance available for different chemosyntheses.

For example, if we focus on elemental cycles of carbon, variety of carbon fixation processes and, on the other hand, processes converting organic carbon to inorganic carbon (mineralization) have been recognized to occur within active hydrothermal systems. There are two important mechanisms to fix carbon to organic species; primary biomass production by microbial chemosynthesis and a non-biological process (Fischer–Tropsch-type reaction). The latter reaction, which synthesizes hydrocarbons and other organic matter from CO_2 and H_2, is known to occur under the high-temperature hydrothermal conditions that result from processes such as serpentinization of olivine, based on experimental studies (e.g., McCollom and Seewald 2001).

The known metabolic reactions used by chemosynthetic microbes are listed in Table 1.1. The metabolism of microorganisms in the subseafloor biosphere can be expressed as a reaction between a reducing substance (electron donor) and an oxidant (electron acceptor) (McCollom and Shock 1997). To categorize wide ranges of the chemosynthetic metabolic reactions, we take notice of major reducing substances (electron donors); that is, hydrogen, methane, sulfur, and iron as the primary reducing substances that serve as energy source. Within each type of TAIGAs, chemolithoautotrophic

Table 1.1 Known redox reactions associated with chemolithoautotrophic microbes in a deep-sea hydrothermal vent environment (modified after Fisher et al. 2007)

Reductant	Oxydant	Chemical reaction
Hydrogen	Oxygen	$2H_2 + O_2 \rightarrow 2H_2O$
Hydrogen	Ferric compounds	$H_2 + 2Fe^{3+} \rightarrow 2Fe^{2+} + 2H^+$
Hydrogen	Sulfate	$4H_2 + SO_4^{2-} + 2H^+ \rightarrow H_2S + 4H_2O$
Hydrogen	Carbon dioxyde	$4H_2 + CO_2 \rightarrow CH_4 + 2H_2O$
Hydrogen	Native sulfur	$H_2 + S^0 \rightarrow H_2S$
Hydrogen	Nitrate	$5H_2 + 2NO_3^- + 2H^+ \rightarrow N_2 + 6H_2O$
Methane	Oxygen	$CH_4 + 2O_2 \rightarrow CO_2 + 2H_2O$
Methane	Sulfate	$CH_4 + SO_4^{2-} \rightarrow HCO_3^- + HS^- + H_2O$
Sulfide	Oxygen	$HS^- + 2O_2 \rightarrow SO_4^{2-} + H^+$
Native sulfur	Oxygen	$2S^0 + 2H_2O + 3O_2 \rightarrow 2SO_4^{2-} + 4H^+$
Thiosulfate	Oxygen	$S_2O_3^{2-} + 2O_2 + H_2O \rightarrow 2SO_4^{2-} + 2H^+$
Sulfide	Nitrate	$10HS^- + 4H^+ + 14NO_3^- \rightarrow 10SO_4^{2-} + 7\,N_2 + 2H_2O$
Native sulfur	Nitrate	$5S^0 + 2H_2O + 6NO_3^- \rightarrow 5SO_4^{2-} + 4H^+ + 3\,N_2$
Thiosulfate	Nitrate	$5S_2O_3^{2-} + 8NO_3^- + H_2O \rightarrow 10SO_4^{2-} + 2H^+ + 4\,N_2$
Ferrous compounds	Oxygen	$4Fe^{2+} + O_2 + 4H^+ \rightarrow 4Fe^{3+} + 2H_2O$
Ferrous compounds	Nitrate	$10Fe^{2+} + 2NO_3^- + 12H^+ \rightarrow N_2 + 10Fe^{3+} + 6H_2O$
Nitrite	Oxygen	$2NO_2^- + O_2 \rightarrow 2NO_3^-$
Ammonia	Oxygen	$2NH_3 + 3O_2 \rightarrow 2NO_2^- + 2H^+ + 2H_2O$

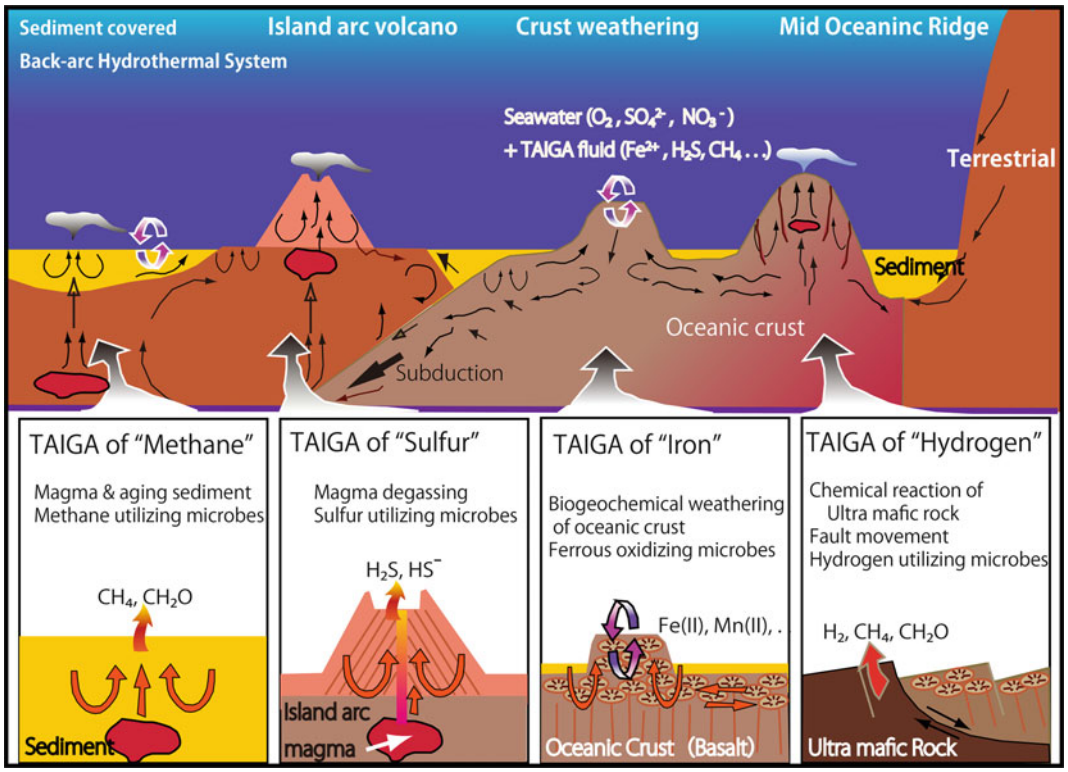

Fig. 1.1 Schematic model of four types of subseafloor fluid advection system (TAIGA). Fluid chemistry reflects tectonic and magmatic activities of the seafloor and controls chemosynthesis of subseafloor biosphere

metabolism is represented by an activity of following microorganisms; hydrogen oxidizers including methanogens, methan oxidizers such as methanotrophs, sulfur oxidizers, and, iron and manganese oxidizers.

As terrestrial rivers supply nutrients and essential elements to the ecosystem developed along the watershed areas, subseafloor TAIGAs supply electron donors for chemolithoautotroph ecosystems in active hydrothermal systems. Flow pathways and dissolved chemical species of the subseafloor TAIGAs are strongly affected by the geological background such as surrounding host rocks and tectonic settings (Fig. 1.1). In the following paragraphs, expected

linkage among the microbial activity, fluid chemistry, and geological background of hydrothermal systems in each type of TAIGA is outlined.

1.3.1 TAIGA of Hydrogen

In 2004, hydrogen-based methanogenic-microbial ecosystem is proposed beneath the seafloor of the active hydrothermal field in the Central Indian Ridge by Takai et al. (2004a). They called this ecosystem the hyperthermophilic SLiME or "HyperSLiME", after the name of SLiME (subsurface lithoautotrophic microbial ecosystem), which had been proposed by Stevens and McKinley (1995) for bacteria found in a deep well in flood basalt sequences in Columbia River valley. Takai et al. (2004b) strongly suggested that the hydrogenotrophic methanogenesis reaction was actively taking place based on the evidence of high concentration of H_2 in the hydrothermal fluid and rich in $\delta^{13}C$-depleted CH_4 that is interpreted as results of the microbial consumption and/or the methanogenic archaeal production. The CH_4 generated by methanogens becomes to be an important electron donor for the methane oxidizers at the seafloor.

Similar microbiological and geochemical evidence for hydrogen oxidation have also been found at the Mariner Field of the Lau Basin (Takai et al. 2008a), Suiyo Seamount of the Izu-Bonin arc (Toki et al. 2008), Logatchev Field of Mid Atlantic Ridge (Petersen et al. 2011), and other locations (Takai et al. 2005), and it is believed that this phenomenon can be seen in a broad range of hydrothermal vents (Takai et al. 2004a). The key point of this TAIGA is the high concentration of H_2 which is the most reductive substance on the Earth and the ultimate electron donor. These lines of evidence strongly suggest that this metabolism may occur even in the Earth's lower crust where the redox state is lower than that of the upper crust, and this biogeochemical processes also affects microbial ecosystems such as methanotrophy which may exist in shallower environment of higher redox states. It is also pointed out that the hydrogen oxidizing hyperthermophiles occupy the deep-rooted position on the evolutionary tree that is close to the common ancestor of all life forms (Takai et al. 2008b). Therefore, this metabolism may be the oldest on the Earth and also occupy the most fundamental position in the present-day chemolithoautotrophic communities.

The most notable source of H_2 in hydrothermal fluid is serpentinization reaction in ultramafic rocks during the hydrothermal alteration (Charlou et al. 2002; Nakamura et al. 2009). TAIGA of hydrogen is expected to occur in a tectonic setting of slow or ultra-slow spreading ridge where outcrop of ultramafic rocks is often observed. Exhumation of ultramafic rocks is closely related to the block movements along faults and the fluid circulation in TAIGA of hydrogen is caused by heat mined from lower crust/upper mantle along the faults. Besides, mechanochemical production of H_2 associated with fault movement has been proposed (e.g., Hirose et al. 2011). In other words, it is indicated from experiments that physically broken mineral surfaces react with H_2O to generate H_2. Another important source of H_2 is thermal decomposition of organic matter during fluid-sediment interaction (Kawagucci et al. 2013). Such interaction is expected to occur in a hydrothermal system which is hosted within thickly accumulated sediment. However, the extent of H_2 enrichment in sediment-associated systems is not so significant compared with that in ultramafic rock-hosted system.

1.3.2 TAIGA of Methane

Hydrothermal fluids of sediment-associated systems are often characterized by enrichment in CH_4. Concentration of CH_4 in a sediment-associated hydrothermal system is basically two or three orders higher than that of sediment-starved hydrothermal system. In TAIGA of methane, abundant CH_4 is considered as derived from decomposition of organic matter contained in the sediments, and involved into the hydrothermal fluid by various processes. Thermal degradation of organic matter has been considered as an important process to produce abundant CH_4 (e.g., Cruse and Seewald 2006), while Kawagucci et al. (2013) recently demonstrated microbial methanogenesis within the fluid recharge region could supply abundant CH_4. In either case, other organic matter-derived species such as NH_4^+ and HCO_3^- can be abundantly involved into the hydrothermal fluid. These dissolved species would control pH of the fluid and may have high buffer potential in the low temperature condition during the mixing of the hydrothermal fluid and ambient seawater (Tivey et al. 1999).

CH_4 is strong-reductive species, which can be utilized as energy source of electron donor for metabolic reactions. Aerobic and anaerobic methanotroph based-microbial ecosystem has been found in the Okinawa Trough, both as the symbiotic bacteria of Bathymodiolus and ANME-2 archaea which oxidizes CH_4 anaerobically in collaboration with δ-proteobacteria (Nakagawa et al. 2005).

1.3.3 TAIGA of Sulfur

Magmatic volatiles including H_2O, CO_2, and SO_2 are degassed from arc magma during its cooling process. It is known that SO_2 reacts with water, causing a disproportionation reaction where SO_2 dissociates into H_2S and SO_4 at around 400 °C (Hedenquist 1995). Then, involvement of

magma-derived H_2S volatiles into the hydrothermal fluid would act as an important source of reductive sulfur species. Supply of these magmatic volatiles into hydrothermal fluid is common for all the hydrothermal systems related to magma intrusion. However extent of their influence would be different according to the tectonic settings. While the magma in the mid-oceanic ridge is often depleted in the volatile species, magma in the arc-backarc setting is usually enriched in the volatile species reflecting involvement of subducted materials during magma generation process. Moreover, redox state of silicic magma and mafic magma is controlled by different buffer systems, which would affect redox state of the volatile species composition.

In addition to H_2S, various sulfur species with different redox states are known to occur in hydrothermal environment. There exists a diverse range of autotrophic microorganisms that can use these compounds for their metabolism. TAIGA of sulfur is expected to occur extensively in wide range of hydrothermal systems, which are hosted by felsic to mafic magmatism and devoid of organic matter-rich sediment. In such environment, other important reduced species, H_2 and CH_4 are not expected to be abundant in the hydrothermal fluid.

1.3.4 TAIGA of Iron

Furnes et al. (2001) proposed that microorganisms are the primary cause of the seafloor weathering of oceanic crusts as they dissolve the volcanic glass, produce hydrated shells, and form biofilms. Little is known about the nature of the microorganisms which cause this alteration, however there are cases where the iron oxidizing bacteria *Gallionella* has been found (Thorseth et al. 1995). In aged seafloor basalts, elevated cell density and highly diverse microbial community has been found (e.g. Santelli et al. 2008).

Aerobic oxidation of ferrous iron in the oceanic crust could be one of important energy sources for the microbial ecosystem if it becomes accessible for use. Since iron is the fourth most plentiful element on the Earth, the subseafloor biosphere supported by TAIGA of iron could be extensive if iron works for electron donor for the microbial ecosystem. Bach and Edwards (2003) estimated available energy from reduced iron species in the oceanic crust and proposed that microbial activity which depends on alteration (weathering) of basalt can exist within the pore spaces of the oceanic crust of the age younger than 10 Ma, although their activity is difficult to detect.

Distal part of an active hydrothermal system hosted by basaltic lava could provide a good test field to study the TAIGA of iron, because low temperature acidic hydrothermal fluids may extract ferrous ion from basalt and supply it in an accessible form to the microbial ecosystems.

1.4 Interdisciplinary Studies During TAIGA Project

Three integrated study areas were established to investigate the representative fields for the four types of TAIGAs. The first target area is the Central Indian Ridge for the "TAIGA of hydrogen". This is because the Rodrigues Triple Junction at the southern Central Indian Ridge is the place where the first hydrogen-based chemoautotrophic microorganisms were reported (Takai et al. 2004a). We located another "TAIGA of hydrogen" near there during the project. The second target area is the South Mariana Trough. In this region, four active hydrothermal fields had been located (Kakegawa et al. 2008), and they are expected to represent "TAIGA of sulfur", as geophysical studies revealed excess magmatic supply in this region. Moreover, low temperature hydrothermal activities are expected to represent "TAIGA of iron" since abundant fresh basalt lava flow and strongly acidic hydrothermal fluids have been observed in this region. The third target area is Okinawa Trough. In this region, more than five active hydrothermal fields had been located in sedimented backarc rift. These hydrothermal activities are expected to represent "TAIGA of methane". They are found in caldera-like volcanic depressions or volcanic knolls related to arc/backarc volcanic activity which is covered with thick terrigenous and/or volcanic sediments. These sediments include substantial amount of organic material which were derived from Asian continent. Integrated Ocean Drilling Program (IODP) Expedition 331 drilled this target to investigate the deep structure of the hydrothermal system in 2010. Besides, shallow coring expedition was performed using Benthic Multicoring System (BMS) on-board the R/V Hakurei-Maru No. 2.

As a matter of course, these three targets never be able to represent entire variety of hydrothermal activities and the associated chemical signature found on global deepsea floor. However, the integrated research on these characteristic examples will provide us not only the biogeochemical nature of the venting fluids but also entire image of the hydrothermal systems that produce the fluids as the consequence of interaction between the solid and fluid earth. The combination of the results on the elementary steps of microbial metabolism, geochemical cycles, and tectonic framework of the advection will enhance our understanding and allow us to make overall estimation of the deep biosphere.

Therefore, we conducted a variety of physical, chemical and (micro)biological approaches were taken on these four TAIGAs to examine the wholistic views of these regions. Fundamental micro-scales of interaction processes between solid (rocks and minerals), fluid (water, solutes and gas) and

life (microbial communities) were clarified by in situ, onboard and onshore observations, analyses and experiments. A link between the geophysical and geochemical structure around vent sites and the hydrothermal ecosystem were studied by surface mapping, OBS/OBEMs deployment experiments, and petrochemical studies of collected rocks and ores. Biogeochemical impacts of TAIGA discharge to the surrounding marine environments were revealed by comprehensive investigation of geophysical, geochemical, and microbiological phenomena in hydrothermal plumes. In addition to these field studies, experimental studies aimed to reproduce chemical and microbiological process in the TAIGA steps using high-pressure and high-temperature experimental apparatus were conducted. Furthermore, two different methodologies were developed with a view to estimate ages of hydrothermal events and phenomena; application of geochronological techniques to hydrothermal minerals and systematic analysis of phylogenetic relationships among animal species in hydrothermal vent fields.

As a conclusion, we would like to point out that our "TAIGA hypothesis" was proven to be valid which you will see in this book. It is also shown that the chemosynthetic metabolism based on sulfur species is always important even within the TAIGA of hydrogen or the TAIGA of methane. In fact, it is known that the most active microbial communities at high-temperature hydrothermal vents, regardless of the tectonic location, are bacteria which oxidize and reduce various sulfur species (Nakagawa et al. 2006; Takai et al. 2008a and the references therein).

In this e-book, readers will find wide variety of results from these interdisciplinary studies. The main reason why we choose this publication form is to provide the readers with comprehensive views of these target regions: Wide ranges of topics both on the arc-backarc systems in western Pacific and on mid-ocean ridge system of the Indian Ocean were covered, which are compared with each other based on the idea of four types of TAIGAs. We believe this e-book provide a good base for discussion on linkage between the subseafloor biosphere and hydrosphere with global perspective.

Acknowledgements We would like to express our appreciation to Ministry of Education, Culture, Sports, Science and Technology in Japan for funding this project from FY2008 to FY2012 (#20109001-20109006), as a project of Grant-in-Aid for Scientific Research on Innovative Areas.

References

Alt JC (2003) Hydrothermal fluxes at mid-ocean ridges and on ridge flanks. C R Geosci 335:853–864

Bach W, Edwards KJ (2003) Iron and sulfide oxidation within the basaltic ocean crust: implications for chemolithoautotrophic primary biomass production. Geochim Cosmochim Acta 67:3871–3887

Bach W, Peuker-Ehrenbrink B, Hart SR, Blusztajn JS (2003) Geochemistry of hydrothermally altered oceanic crust: DSDP/ODP Hole 504B – implications for seawater- crust exchange budgets and Sr- and Pb-isotopic evolution of the mantle. Geochem Geophys Geosyst 4:8904

Baker ET, Embley RW, Walker SL, Resing JA, Lupton JE, Nakamura K-I, de Ronde CEJ, Massoth GJ (2008) Hydrothermal activity and volcano distribution along the Mariana arc. J Geophys Res 113: B08S09

Charlou JL, Donval JP, Fouquet Y, Jean-Baptiste P, Holm N (2002) Geochemistry of high H_2 and CH_4 vent fluids issuing from ultramafic rocks at the rainbow hydrothermal field (36°14′N, MAR). Chem Geol 191:345–359

Childress JJ, Fisher CR (1992) The biology of hydrothermal vent animals; physiology, biochemistry and autotrophic symbioses. Oceanogr Mar Biol 30:337–441

Cruse AM, Seewald JS (2006) Geochemistry of low-molecular weight hydrocarbons in hydrothermal fluids from Middle Valley, northern Juan de Fuca Ridge. Geochim Cosmochim Acta 70:2073–2092

Deming JW, Baross JA (1993) Deep-sea smokers: windows to a subsurface biosphere? Geochim Cosmochim Acta 57:3219–3230

Elderfield H, Schultz A (1996) Mid-ocean ridge hydrothermal fluxes and the chemical composition of the ocean. Ann Rev Earth Planet Sci 24:191–224

Fisher AT, Davis EE, Hutnak M, Spiess V, Zuhlsdorff L, Cherkaoul A, Christiansen L, Edwards K, Macdonald R, Villinger H, Mottl MJ, Wheat CG, Becker K (2003) Hydrothermal recharge and discharge across 50 km guided by seamounts on a young ridge flank. Nature 421:618–621

Fisher CR, Takai K, Le Bris N (2007) Hydrothermal vent ecosystems. Oceanography 20:14–25

Furnes H, Staudigel H, Thorseth IH, Torsvik T, Muehlenbachs K, Tumyr O (2001) Bioalteration of basaltic glass in the oceanic crust. Geochem Geophys Geosyst 2:2000GC000150

Gamo T, Ishibashi J, Tsunogai U, Okamura K, Chiba H (2006) Unique geochemistry of submarine hydrothermal fluids from arc-backarc settings of the western Pacific. In: Christie DM, Fisher CR, Lee S-M, Givens S (eds) Back-arc spreading systems: geological, biological, chemical, and physical interactions. AGU monograph series, vol 166, American Geophysical Union, Washington, DC, pp 147–161

Ge S, Bekins B, Bredehoeft J, Brown K, Davis EE, Gorelick SM, Henry P, Kooi H, Moench AF, Ruppel C, Sauter M, Screaton E, Swart PK, Tokunaga T, Voss CI, Whitaker F (2003) Fluid flow in sub-seafloor processes and future ocean drilling. Eos Trans Am Geophys Union 84:145–152

Hedenquist JW (1995) The ascent of magmatic fluid: discharge versus mineralization. in Magmas. In: Thompson JFH (ed) Fluids, and ore deposits, Mineralogical Association of Canada, Short Course, vol 23, Mineralogical Association of Canada, Nepean, Ontario, Canada, pp 263–290

Hirose T, Kawagucci S, Suzuki K (2011) Mechanoradical H_2 generation during simulated faulting: implications for an earthquake-driven subsurface biosphere. Geophys Res Lett 38, L17303

Johnson HP, Pruis MJ (2003) Flux of fluid and heat from the oceanic crustal reservoir. Earth Planet Sci Lett 216:565–574

Johnson HP, Baros JA, Bjorklund TA (2006) On sampling the upper crustal reservoir of the NE Pacific Ocean. Geofluids 6:251–271

Kakegawa T, Utsumi M, Marumo K (2008) Geochemistry of sulfide chimneys and basement pillow lavas at the Southern Mariana Trough (12.55°N–12.58°N). Resour Geol 58:249–266

Kawagucci S, Ueno Y, Takai K, Toki T, Ito M, Inoue K, Makabe A, Yoshida N, Muramatsu Y, Takahata N, Sano Y, Narita T, Teranishi G, Obata H, Nakagawa S, Nunoura T, Gamo T (2013) Geochemical origin of hydrothermal fluid methane in sediment-associated fields and its relevance to the geographical distribution of whole hydrothermal circulation. Chem Geol 339:213–225

Kelley DS, Baross JA, Delaney JR (2002) Volcanoes, fluids, and life at mid-ocean ridge spreading centers. Ann Rev Earth Planet Sci 30: 385–491

McCollom TM, Seewald JS (2001) A reassessment of the potential for reduction of dissolved CO_2 to hydrocarbons during serpentinization of olivine. Geochim Cosmochim Acta 65:3769–3778

McCollom TM, Shock EL (1997) Geochemical constraints on chemolithoautotrophic metabolism by microorganisms in seafloor hydrothermal systems. Geochimica et Cosmochimica Acta 61: 4375–4391

Mottl ML (2003) Partitioning of energy and mass fluxes between mid-ocean ridge axes and flanks at high and low temperature. In: Halbach PE (ed) Energy and mass transfer in marine hydrothermal systems. Dahlem University Press, Berlin, pp 271–286

Mottl MJ, Wheat CG, Baker E, Becker N, Davis E, Feely R, Grehan A, Kadko D, Lilley M, Massoth G, Moyer C, Sansone F (1998) Warm springs discovered on 3.5 Ma oceanic crust, eastern flank of the Juan de Fuca Ridge. Geology 26:51–54

Mottl MJ, Glazer BT, Kaiser RI, Meech KJ (2007) Water and astrobiology. Chemie der Erde 67:253–282

Nakagawa S, Takai K, Inagaki F, Chiba H, Ishibashi J-I, Kataoka S, Hirayama H, Nunoura T, Horikoshi K, Sako Y (2005) Variability in microbial community and venting chemistry in a sediment-hosted backarc hydrothermal system: impacts of subseafloor phase-separation. FEMS Microbiol Ecol 54:141–155

Nakagawa T, Takai K, Suzuki Y, Hirayama H, Konno U, Tsunogai U, Horikoshi K (2006) Geomicrobiological exploration and characterization of a novel deep-sea hydrothermal system at the TOTO caldera in the Mariana Volcanic Arc. Environ Microbiol 8:37–49

Nakamura K, Morishita T, Bach W, Klein F, Hara K, Okino K, Takai K, Kumagai H (2009) Serpentinized troctolites exposed near the Kairei hydrothermal field Central Indian Ridge: insights into the origin of the Kairei hydrothermal fluid supporting a unique microbial ecosystem. Earth Planet Sci Lett 280:128–136

Petersen JM, Zielinski FU, Pape T, Seifert R, Moraru C, Amann R, Hourdez S, Girguis PR, Wankel SD, Barbe V, Pelletier E, Fink D, Borowski C, Bach W, Dubilier N (2011) Hydrogen is an energy source for hydrothermal vent symbioses. Nature 476:176–180

Santelli CM, Orcutt BN, Banning E, Bach W, Moyer GL, Sogin ML, Staudigel H, Edwards KJ (2008) Abundance and diversity of microbial life in ocean crust. Nature 453:653–656

Seyfried Jr WE, Foustoukos DI, Allen DE (2004) Ultramafic-hosted hydrothermal systems at mid-ocean ridges: chemical and physical controls on pH, redox and carbon reduction reactions. In: German C, Lin J (eds) Mid-ocean ridges: hydrothermal interactions between the lithosphere and oceans, American Geophysical Union Geophysical Monograph Series, vol. 148, American Geophysical Union, Washington, DC, pp 267–284

Stein CA, Stein S (1992) A model for the global variation in oceanic depth and heat flow with lithospheric age. Nature 359:123–137

Stevens TO, McKinley JP (1995) Lithoautotrophic microbial ecosystems in deep basalt aquifers. Science 270:450–454

Takai K, Horikoshi K (1999) Genetic diversity of Archaea in deep-sea hydrothermal vent environments. Genetics 152:1285–1297

Takai K, Gamo T, Tsunogai U, Nakayama N, Hirayama H, Nealson K, Horikoshi K (2004a) Geochemical and microbiological evidence for a hydrogen-based, hyperthermophilic subsurface lithoautotrophic microbial ecosystem (HyperSLiME) beneath as active deep-sea hydrothermal field. Extremophiles 8:269–282

Takai K, Nealson KH, Horikoshi K (2004b) *Methanotorris formicicus* sp. nov., a novel extremely thermophilic, methane-producing archaeon isolated from a black smoker chimney in the Central Indian Ridge. Int J Syst Evol Microbiol 54:1095–1100

Takai K, Hirayama H, Nakagawa T, Suzuki Y, Nealson KH, Horikoshi K (2005) *Lebetimonas acidiphila* gen. nov., sp. nov., a novel thermophilic, acidophilic, hydrogen-oxidizing chemolithoautotroph within the 'Epsilonproteobacteria', isolated from a deep-sea hydrothermal fumarole in the Mariana Arc. Int J Syst Evol Microbiol 55:183–189

Takai K, Nunoura T, Ishibashi J, Lupton J, Suzuki R, Hamasaki H, Ueno Y, Kawagucci S, Gamo T, Suzuki Y, Hirayama H, Horikoshi K (2008a) Variability in the microbial communities and hydrothermal fluid chemistry at the newly discovered Mariner hydrothermal field, southern Lau Basin. J Geophys Res 113, G02031

Takai K, Nakamura K, Toki T, Tsunogai U, Miyazaki M, Miyazaki J, Hirayama H, Nakagawa S, Nunoura T, Horikoshi K (2008b) Cell proliferation at 122 °C and isotopically heavy CH_4 production by a hyperthermophilic methanogen under high-pressure cultivation. Proc Natl Acad Sci USA 105:10949–10954

Thorseth IH, Torsvik T, Furnes H, Muehlenbachs K (1995) Microbes play an inportant role in the alteration of oceanic crust. Chem Geol 126:137–146

Tivey MK, Stakes DS, Cook TL, Hannington MD, Petersen S (1999) A model for growth of steep-sided vent structures on the endeavour segment of the Juan de Fuca Ridge: results of a petrologic and geochemical study. J Geophys Res 104:22859–22883

Toki T, Tsunogai U, Ishibashi J, Utsumi M, Gamo T (2008) Methane enrichment in low-temperature hydrothermal fluids from the Suiyo Seamount in the Izu-Bonin Arc of the western Pacific Ocean. J Geophys Res 113:B08S13

Wheat CG, Mottl MJ (2004) Geochemical fluxes through ridge flanks. In: Davis EE, Elderfield H (eds) Hydrolgeology of the oceanic lithosphere. Cambridge University Press, Cambridge, pp 627–658

Geochemical Constraints on Potential Biomass Sustained by Subseafloor Water–Rock Interactions

2

Kentaro Nakamura and Ken Takai

Abstract

Since the first discovery of macrofaunal and microbial communities endemic to hydrothermal vents, chemolithoautotrophic microorganisms at and beneath the seafloor have attracted the interest of many researchers. This type of microorganism is known to obtain energy from inorganic substances (e.g., reduced sulfur compounds, molecular hydrogen, and methane) derived from subsurface physical and chemical processes, such as water–rock interactions. As the primary producers, they sustain chemosynthetic ecosystems, which are fundamentally different from terrestrial and shallow marine ecosystems that are sustained by photosynthetic primary production. It is possible that the chemosynthetic ecosystems at and beneath the seafloor are vast and metabolically active, playing an important role in the global geochemical cycles of many bio-essential elements. However, even today, the spatial and temporal distributions of the unseen chemosynthetic biosphere are largely uncertain. Here, we present geochemical constraints on the estimate of the potential biomass in seafloor and subseafloor chemosynthetic ecosystems sustained by high-temperature deep-sea hydrothermal activities and low-temperature alteration/weathering of oceanic crust. The calculations are based on the fluxes of metabolic energy sources (S, H_2, Fe, and CH_4), the chemical energy yields for metabolic reactions, and the maintenance energy requirements. The results show that for deep-sea hydrothermal vent ecosystems, most bioavailable energy yields (86 %) are due to oxidation reactions of S. In contrast, for subseafloor oceanic crust ecosystems, oxidation reactions of Fe and S generally yield the same amounts of bioavailable energy (59 % and 41 %, respectively). The estimated biomass potential in the subseafloor oceanic crust ecosystems (0.14 Pg C) is one order of magnitude higher than that in global deep-sea hydrothermal vent ecosystems (0.0074 Pg C), most likely reflecting the greater flux of

The online version of this chapter (doi:10.1007/978-4-431-54865-2_2) contains supplementary material, which is available to authorized users.

K. Nakamura (✉)
Precambrian Ecosystem Laboratory (PEL), Japan Agency for Marine-Earth Science and Technology (JAMSTEC), 2-15 Natsushima, Yokosuka, Kanagawa 237-0061, Japan

Submarine Hydrothermal System Research Group, Japan Agency for Marine-Earth Science and Technology (JAMSTEC), 2-15 Natsushima, Yokosuka, Kanagawa 237-0061, Japan

Present address: Department of Systems Innovation, School of Engineering, The University of Tokyo, 7-3-1 Hongo, Bunkyo-ku, Tokyo 113-8656, Japan
e-mail: kentaron@sys.t.u-tokyo.ac.jp

K. Takai
Precambrian Ecosystem Laboratory (PEL), Japan Agency for Marine-Earth Science and Technology (JAMSTEC), 2-15 Natsushima, Yokosuka, Kanagawa 237-0061, Japan

Submarine Hydrothermal System Research Group, Japan Agency for Marine-Earth Science and Technology (JAMSTEC), 2-15 Natsushima, Yokosuka, Kanagawa 237-0061, Japan

Subsurface Geobiology Advanced Research (SUGAR) Project, Japan Agency for Marine-Earth Science and Technology (JAMSTEC), 2-15 Natushima, Yokosuka, Kanagawa 237-0061, Japan

J.-i. Ishibashi et al. (eds.), *Subseafloor Biosphere Linked to Hydrothermal Systems: TAIGA Concept*,
DOI 10.1007/978-4-431-54865-2_2,

low-temperature fluids circulating within the oceanic crust than that of high-temperature focused fluids venting at ridge axes. The overall biomass potential of the chemosynthetic ecosystems, estimated to be 0.15 Pg C, corresponds to only 0.02 % of the Earth's total living biomass. This estimate suggests that chemosynthetic ecosystems comprise a rare biomass fraction of the modern Earth's biosphere, probably reflecting a significantly smaller energy flux from Earth's interior compared with that from the sun.

Keywords
Biomass potential • Chemosynthetic ecosystems • Hydrothermal activity • Low-temperature alteration/weathering • Oceanic crust

2.1 Introduction

It was long believed that essentially all life forms on Earth were sustained by the primary production of photosynthetic organisms and substantially relied on energy supplied from the sun. In the past century, the ubiquitous presence of lithoautotrophic microorganisms on the Earth has been gradually recognized (Dworkin 2012). However, these organisms were not considered important on the global scale because they were thought to represent only a small fraction of the microbial community in most environments, and most of these organisms consume inorganic compounds produced by the degradation of biologically derived organic matter. In the late 1970s, when deep-sea hydrothermal activities first began to be explored, it became apparent that the biological communities present in the dark seafloor environments were dense in biomass and diverse in species (Corliss et al. 1979; Spiess et al. 1980). It was suggested that these organisms must rely on a different source of energy. Furthermore, in the past decade the existence of potentially vast and metabolically active microbial populations within the oceanic crust was also suggested by several studies (Bach and Edwards 2003; Cowen et al. 2003; Lever et al. 2013). In contrast to most of the surface biological communities, in which the food chains start with the primary production of photosynthetic organisms, the newly discovered deep-sea ecosystems are likely dependent on the primary production of symbiotic and free-living chemolithoautotrophic microorganisms that obtain energy from the oxidation of inorganic compounds (e.g., H_2S, CO_2, H_2, and CH_4) essentially provided by the subseafloor water–rock interactions. It is now hypothesized that such deep, dark ecosystems (often described as chemosynthetic communities) comprise a considerably widespread biosphere associated with the global deep-sea hydrothermal systems and perhaps an even more vast biosphere in the subseafloor igneous oceanic crust (Edwards et al. 2005; Schrenk et al. 2010; Orcutt et al. 2011).

In the past several decades, the deep-sea chemosynthetic communities at and beneath the seafloor have been extensively studied along the following three general directions of scientific interest. The first is that most of the microbial components of the deep-sea chemosynthetic communities are extremophiles that have important physiological and biochemical functions and biomaterials for understanding the limits of life and biological activities on this planet (Takai 2011). The second interest is that such microbes represent models most likely to elucidate the origin and early evolution of life on Earth and to predict possible extraterrestrial organisms and the habitability of other planets and moons (Jannasch and Mottl 1985; Nealson et al. 2005; Takai et al. 2006). The third interest is related to the estimation and quantification of how the metabolisms and functions of the deep-sea chemosynthetic communities impact the global biogeochemical cycles of C, Fe, S, and other bio-essential elements (Edwards et al. 2005; Schrenk et al. 2010; Kallmeyer et al. 2012). Despite an increasing number of studies that have been published regarding the first and second interests (Horikoshi and Tsujii 1999; McCollom 1999; Varnes et al. 2003; Hoehler 2004; Gerday and Glansdorff 2007; Takai 2011), much less is known about the third (i.e., the abundance and distribution of deep-sea and deep subseafloor chemosynthetic ecosystems and their impact on the global biogeochemical cycles of the bio-essential elements). Several authors have estimated the potential production rate of biomass by the chemosynthetic ecosystems (McCollom and Shock 1997; Bach and Edwards 2003). However, the biomass production rate cannot be used directly for the estimation of biomass. Thus, we cannot so far interpret the abundance and distribution of the deep, dark ecosystems and their role as reservoirs of the bio-essential elements. Here, we present the first theoretical estimation of the potential biomass that could be sustained by high-temperature deep-sea hydrothermal vent activity and low-temperature oceanic crust alteration/weathering.

2.2 Method to Estimate the Potential Biomass Sustained by Chemosynthetic Primary Production

In this study, we attempt to estimate the potential biomass that could be sustained by the chemosynthetic energy sources derived from high-temperature deep-sea hydrothermal activity and low-temperature oceanic crust alteration/weathering. The biomass potential of chemosynthetic communities can be calculated based on the flux of chemosynthetic energy sources, bioavailable energy yields, and maintenance energy requirements as follows:

$$BM = F_{ces}\ BE\ ME^{-1} \tag{2.1}$$

where BM is the potential biomass that could be sustained by chemosynthetic energy sources derived from high-temperature deep-sea hydrothermal activity and low-temperature oceanic crust alteration/weathering, F_{ces} is the overall flux of the chemosynthetic energy sources, BE is the bioavailable energy yield from a chemosynthetic metabolic reaction per unit of energy source, and ME is the species-independent maintenance energy requirement.

The bioavailable energy yield, BE, was determined by calculating the Gibbs free-energy change in each of the metabolic reactions following the method developed by McCollom and Shock (1997), Shock and Holland (2004), and McCollom (2007). The predominant chemolithotrophic energy metabolisms examined in this study are listed in Table 2.1. The overall Gibbs free energy of a reaction can be calculated using the following equation:

$$BE = \Delta G_r = \Delta G_r^{\circ} + RT\,lnQ \tag{2.2}$$

where ΔG_r is the Gibbs free energy of the reaction, ΔG_r° is the standard-state Gibbs free energy of the reaction, R is the universal gas constant, T is the temperature in Kelvin, and Q is the activity quotient of the compounds involved in the reaction. The Q term takes into account the contribution of the fluid composition to the Gibbs energy of each reaction.

Maintenance energy, ME, is defined as the minimum rate of energy intake to maintain molecular and cellular integrities and functions, which is expressed as the energy flux required to maintain a certain amount of biomass over a certain unit of time. In this study, the maintenance energy requirement is calculated using the following equation, according to Harder (1997):

$$ME = A \cdot e^{-Ea/RT} \tag{2.3}$$

where Ea is the activation energy of 69.4 kJ/mol, R is the universal gas constant, T is the temperature in Kelvin, and A is an empirically derived constant. The constant values of A, as determined in chemostat experiments, for aerobic and anaerobic microorganisms are 8.13×10^{12} and 4.99×10^{12} kJ/g dry weight/day, respectively (Tijhuis et al. 1993; Harder 1997). However, it is known that this value is likely 3–6 orders of magnitude lower for the maintenance and survival of microorganisms in natural systems. Price and Sowers (2004) noted that the reported energy flux requirements were classified roughly into three categories, with values of 'growth' exceeding those of 'maintenance' by approximately three orders of magnitude and exceeding those of 'survival' by 5–6 orders of magnitude. In this study, following Hoehler (2004), we performed the calculation using values for the maintenance energy factor, A, of 8.13×10^9 and 4.99×10^9 kJ/g dry weight/day for aerobic and anaerobic reactions, respectively. These values correspond to the 'maintenance' state described by Price and Sowers (2004). The 'maintenance' state values used here are likely appropriate for the estimation of steady-state biomass potential without growth or reduction.

2.2.1 Deep-Sea Hydrothermal Vent Communities

To estimate the biomass potential of deep-sea hydrothermal vent communities, as part of the chemosynthetic ecosystems

Table 2.1 Metabolic reactions for chemolithoautotrophy considered in this study

Energy metabolism	Overall chemical reaction
Aerobic reactions	
1. Aerobic methanotrophy	$CH_4 + 2O_2 = CO_2 + 2H_2O$
2. Hydrogenotrophic O_2-reduction	$H_2 + 1/2O_2 = H_2O$
3. Thiotrophic (H_2S-oxidizing) O_2-reduction	$H_2S + 2O_2 = SO_4^{2-} + 2H^+$
4. Fe(II)-oxidizing O_2-reduction	$Fe^{2+} + 1/4O_2 + H^+ = Fe^{3+} + 1/2H_2O$
Anaerobic reactions	
5. Hydrogenotrophic methanogenesis	$H_2 + 1/4CO_2 = 1/4CH_4 + 1/2H_2O$
6. Hydrogenotrophic SO_4-reduction	$H_2 + 1/4SO_4^{2-} + 1/2H^+ = 1/4H_2S + H_2O$
7. Hydrogenotrophic Fe(III)-reduction	$H_2 + 2Fe^{3+} = 2Fe^{2+} + 2H^+$
8. Anoxic methanotrophy with SO_4-reduction	$CH_4 + SO_4^{2-} = HCO_3^- + HS^- + H_2O$

at and beneath the seafloor, Eq. (2.1) is converted to the following relation:

$$BM_{hydro} = F_{hydro} BE_{hydro} ME^{-1} \quad (2.4)$$

where BM_{hydro} is the potential biomass (g dry weight) that could be theoretically sustained by the total deep-sea hydrothermal fluid inputs, such as high-temperature vents; F_{hydro} is the overall flux of deep-sea hydrothermal fluid flows (kg hydrothermal fluid/year); BE_{hydro} is the sum of the predominant chemosynthetic metabolic energy yields from 1 kg of end-member hydrothermal fluid (kJ/kg hydrothermal fluid); and ME is the maintenance energy requirement, that is, the energy supply required to sustain a certain amount of biomass per unit of time (kJ/g dry weight/year).

As originally proposed by McCollom and Shock (1997), the bioavailable energy yield, BE_{hydro}, represents the amount of chemical energy potentially available from the metabolisms of chemolithotrophic microorganisms during the mixing of hydrothermal vent fluid with seawater. A source of chemical energy is a basic requirement for all organisms, and, in the case of chemolithotrophs in deep-sea hydrothermal vent environments, the energy sources arise from the chemical disequilibria that develop during the mixing of hydrothermal fluids with seawater. In this study, for the sake of convenience the average values of BE_{hydro} in four hypothetical mixing waters with temperature ranges of <25 °C, 25–45 °C, 45–80 °C, and 80–125 °C are calculated. These temperature ranges represent chemolithotrophic metabolisms of psychrophilic, mesophilic, thermophilic and hyperthermophilic microbial components, respectively. The mixing calculations were performed using the computer program EQ3/6, Version 8.0 (Wolery and Jarek 2003). The thermodynamic database necessary for the EQ3/6 operations and the values of the standard Gibbs energy for the chemolithotrophic metabolic reactions were generated using the SUPCRT92 code and database (Johnson et al. 1992). The SUPCRT92 database used here is the thermodynamic dataset for aqueous species and complexes from Shock and Helgeson (1988), Shock and Helgeson (1990), and Shock et al. (1997), with recent upgrades of the slop98.dat database (see Wolery and Jove-Colon 2004) and the OBIGT.dat database (see also http://www.predcent.org/).

2.2.2 Subseafloor Basaltic Oceanic Crust Communities

To estimate the biomass potential of the chemosynthetic communities in subseafloor basaltic aquifers within the oceanic crust, Eq. (2.1) is converted to the following relation:

$$BM_{awoc} = F_{awoc} BE_{awoc} ME^{-1} \quad (2.5)$$

where BM_{awoc} is the potential biomass (g dry weight) that could be theoretically sustained by low-temperature alteration/weathering of oceanic crust in the subseafloor basaltic aquifer, F_{awoc} is the overall flux of reduced iron and sulfur in the basaltic ocean crust supplied during the low-temperature alteration/weathering of oceanic crust, BE_{awoc} is the chemosynthetic metabolic energy yields of reduced iron- and sulfur-oxidation reactions in the subseafloor basaltic aquifer within the oceanic crust (kJ/mol S, Fe), and ME is the maintenance energy requirement described above (kJ/g dry weight/year).

The calculation of BE_{awoc} for the subseafloor basaltic oceanic crust communities generally follows the method described by Bach and Edwards (2003), which is in turn based on McCollom and Shock's model described above. The chemolithotrophic energy metabolisms examined in the calculation are Fe(II)- and H_2S-oxidation reactions (reactions 4 and 7 in Table 2.1). BE_{awoc} is calculated using the same equation used in the calculation for the deep-sea hydrothermal vent communities. Following Bach and Edwards (2003), the temperature and pressure conditions of the ridge flank aquifer are set at 10 °C and 250 bar, respectively. The activity quotient of the reactants and reaction products is also calculated based on the compositional data used in Bach and Edwards (2003) (see table 3 in Bach and Edwards 2003).

2.3 Potential Biomass Sustained by High-Temperature Deep-Sea Hydrothermal Systems

2.3.1 Geochemical Characteristics of Deep-Sea Hydrothermal Fluids

It is known that the variation in composition of the chemolithotrophic energy metabolisms of deep-sea hydrothermal vent microbial communities is highly affected by the chemical compositions of hydrothermal fluids (Nakamura and Takai 2014). In this study, therefore, we used the extensive dataset for the chemical compositions of 89 high-temperature end-member hydrothermal fluids compiled by Nakamura and Takai (2014) (Suppl. Table 2.1) to identify the variation of the chemical composition of deep-sea hydrothermal vent fluids. The dataset covers the sediment-starved mid-ocean ridge hydrothermal systems (MOR) in the Pacific, Atlantic, and Indian Oceans; the sediment-starved arc-backarc hydrothermal systems (ABA) in the western Pacific region; and the sediment-associated hydrothermal systems (SED) in the eastern Pacific and the Okinawa Trough (Fig. 2.1). These hydrothermal systems are further classified into basalt-hosted MOR systems (MOR-B), ultramafic rock-associated MOR systems (MOR-U), mafic rock-hosted ABA systems (ABA-M), felsic rock-hosted ABA systems (ABA-F), sediment-associated

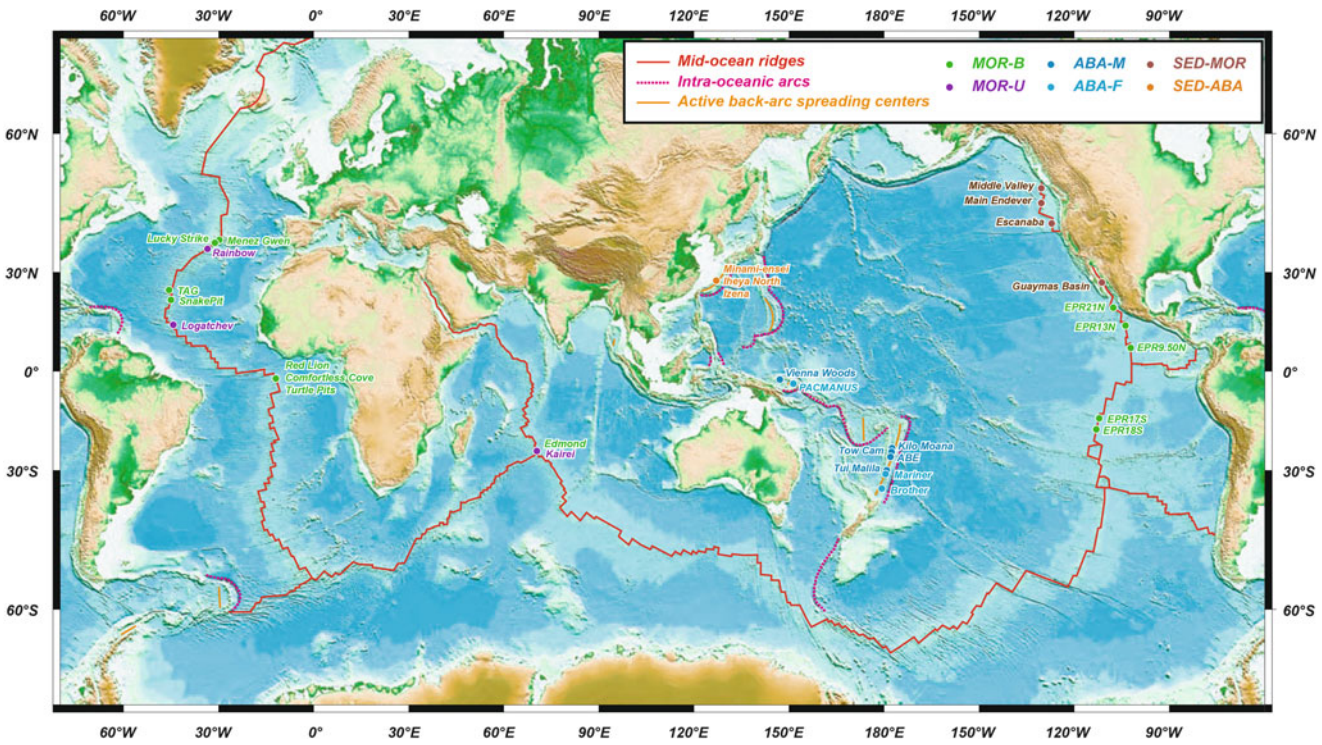

Fig. 2.1 Index map showing the locations of the active hydrothermal vent sites used in this study with the mid-ocean ridges, intra-oceanic arcs, and active back-arc spreading centers. Abbreviations: MOR-B basalt-hosted system in mid-ocean ridge settings, MOR-U ultramafic rock-hosted system in mid-ocean ridge settings, ABA-M mafic rock-hosted system in arc-backarc settings, ABA-F felsic rock-hosted system in arc-backarc settings, SED-MOR sediment-associated system in mid-ocean ridge settings, SED-ABA sediment-associated system in arc-backarc settings

MOR systems (SED-MOR), and sediment-associated ABA systems (SED-ABA).

The compiled data are plotted on diagrams of H_2, H_2S, and CH_4 concentrations against the Cl concentration (Fig. 2.2). These plots show negative correlations between these gas-component concentrations and the Cl content, with the exception of the H_2-enriched MOR-U samples and CH_4-enriched SED samples (described below). This pattern is attributed to the phase separation and phase partitioning of hydrothermal fluids (German and Von Damm 2004). It is known that phase separation tends to generate both Cl-depleted/volatile-enriched vapor and Cl-enriched/volatile-depleted brine under subcritical or supercritical temperature and pressure conditions (Butterfield et al. 2003; Foustoukos et al. 2007). In contrast to the gas-components, the correlations between the Fe and Cl concentrations are not so clear, while some vapor-rich samples exhibit positive correlations with Cl (Fig. 2.3a). Instead, the Fe concentrations correlate well with the pH of the hydrothermal fluids (Fig. 2.3b).

Some highly Cl-depleted hydrothermal fluids (<100 mmol/kg) exhibit considerably high concentrations of H_2, H_2S, and CH_4 (Fig. 2.2). It has been revealed that such extremely gas-enriched fluid emissions are very temporary, limited to a period of several weeks to months after a volcanic and/or seismic event (Lilley et al. 2003). Thus, the extremely gas-enriched fluid emissions are exceptional and cannot be regarded as steady-state activities. Therefore, the chemical data of hydrothermal fluids with Cl concentrations of <100 mmol/kg are excluded from the estimation of potential biomass in this study.

The H_2 concentrations of most of the hydrothermal fluids, except for the extremely gas-enriched entities, range from ~0.01 to ~1 mmol/kg (Fig. 2.2a). Significant H_2 enrichment (>1 mmol/kg) is, however, identified in all the ultramafic rock-associated MOR-U fluids (Fig. 2.2a). It has been documented that the serpentinization reaction in ultramafic rocks during hydrothermal alteration provides significant amounts of H_2 to the hydrothermal fluids (Charlou et al. 2002; McCollom and Bach 2009; Nakamura et al. 2009). Our compilation apparently confirmed the significant H_2 enrichment in the MOR-U fluids among all types of hydrothermal fluids. In addition to the MOR-U fluids, a number of the sediment-associated SED-MOR and SED-ABA fluids also exhibit abundant dissolved H_2 (Fig. 2.2a). This can be attributed to the thermal decomposition of organic matter included in sediments under a specific hydrogeologic structure (e.g., dominant high-temperature interactions between hydrothermal fluids and sediments in the discharging stages following the subseafloor water–rock hydrothermal reactions) (Kawagucci et al. 2013). It is noteworthy that

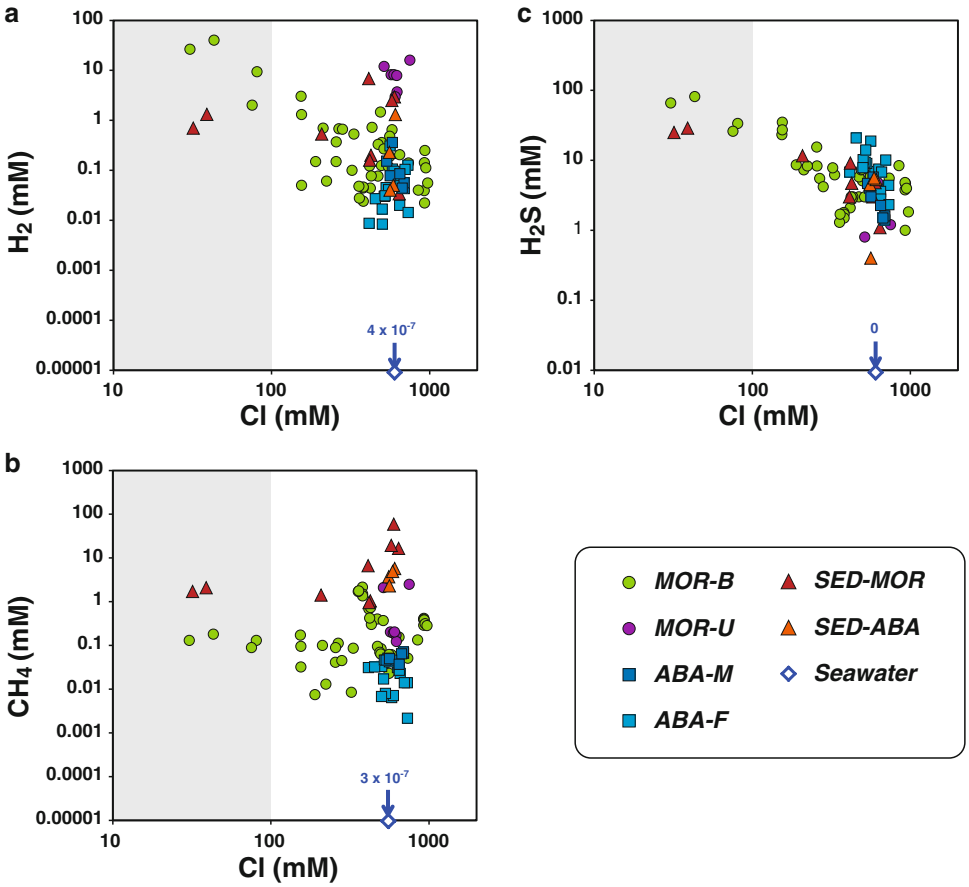

Fig. 2.2 (**a**) H_2, (**b**) CH_4, and (**c**) H_2S versus Cl plots for hydrothermal vent fluids venting in the mid-ocean ridge and arc-backarc settings. *Gray areas* represent the extremely vapor-rich hydrothermal fluids with <100 mmol/kg of Cl concentration, which are excluded from the estimation of biomass potential in this study. Abbreviations: *MOR-B* basalt-hosted system in mid-ocean ridge settings, *MOR-U* ultramafic rock-hosted system in mid-ocean ridge settings, *ABA-M* mafic rock-hosted system in arc-backarc settings, *ABA-F* felsic rock-hosted system in arc-backarc settings, *SED-MOR* sediment-associated system in mid-ocean ridge settings, *SED-ABA* sediment-associated system in arc-backarc settings

the extent of H_2 enrichment in the SED fluids is considerably lower than that in MOR-U fluids (Fig. 2.2a).

The CH_4 concentrations in most deep-sea hydrothermal fluids vary from ~0.001 to ~1 mmol/kg (Fig. 2.2b). Notable enrichment of dissolved CH_4 in the hydrothermal fluids is identified in all the SED fluids (Fig. 2.2b). The CH_4 enrichment can be attributed to the thermal decomposition of organic matter in sediments in higher temperature (>~120 °C) regions (reaction and/or discharge zones) and/or to microbial methanogenesis in relatively lower temperature (<~120 °C) regions (e.g., recharge zone) (Lilley et al. 1993; Kawagucci et al. 2011, 2013). Some of the MOR-U fluids also have significantly high CH_4 concentrations, most likely due to the chemical reduction of CO_2 (abiotic methanogenesis) under the highly reduced (H_2-rich) hydrothermal conditions (Charlou et al. 2002). Our compilation shows that CH_4 enrichment in the MOR-U fluids is much less than that in the SED fluids (Fig. 2.2b, Suppl. Table 2.1).

In contrast to the H_2 and CH_4 concentrations, the H_2S levels are constantly high (>~1 mmol/kg), and their variation is noticeably small (ranging from ~1 to ~10 mmol/kg) in any type of deep-sea hydrothermal fluid (Fig. 2.2c). Therefore, in deep-sea hydrothermal fluids without H_2 and CH_4 enrichment, H_2S is the most abundant reductive gas species available for the chemolithotrophic metabolisms of microbial communities. Additionally, the Fe concentrations vary from ~0.01 to ~10 mmol/kg; these values are correlated with the pH of the hydrothermal fluids (Fig. 2.3b). The felsic rock-hosted ABA-F fluids tend to have high Fe concentrations and low pH values (Fig. 2.3b), probably due to volatile input from magmas. On the other hand, sediment-associated SED fluids generally exhibit relatively low Fe concentrations and high pH values (Fig. 2.3b), probably reflecting the presence of organic matter serving as the NH_3/NH_4^+ buffer (German and Von Damm 2004).

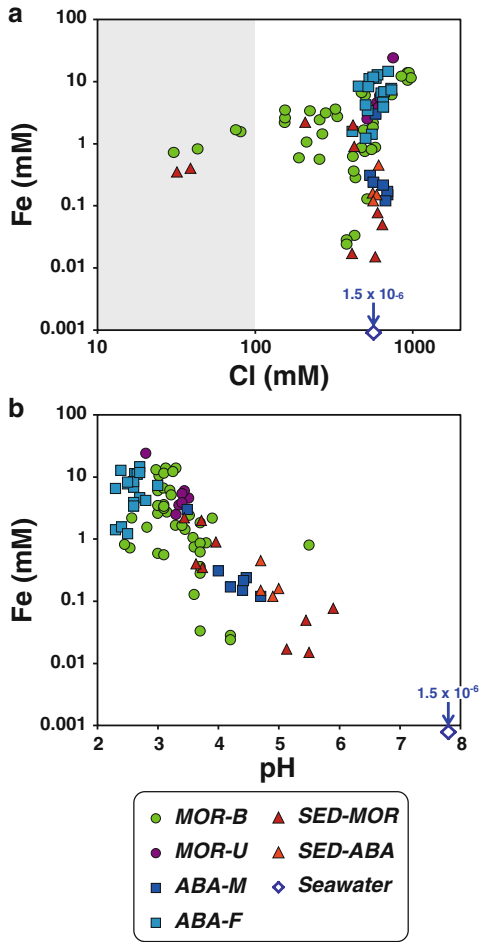

Fig. 2.3 Fe versus (**a**) Cl and (**b**) pH plots for hydrothermal vent fluids venting in the mid-ocean ridge and arc-backarc settings. *Gray areas* represent the extremely vapor-rich hydrothermal fluids with <100 mmol/kg of Cl concentration. Abbreviations: *MOR-B* basalt-hosted system in mid-ocean ridge settings, *MOR-U* ultramafic rock-hosted system in mid-ocean ridge settings, *ABA-M* mafic rock-hosted system in arc-backarc settings, *ABA-F* felsic rock-hosted system in arc-backarc settings, *SED-MOR* sediment-associated system in mid-ocean ridge settings, *SED-ABA* sediment-associated system in arc-backarc settings

2.3.2 Bioavailable Energy Yield from Deep-Sea Hydrothermal Fluids

To address the effect of hydrothermal fluid chemistry on the biomass potential of deep-sea hydrothermal vent ecosystems, the bioavailable energy yields of various chemolithotrophic metabolisms are determined. In this study, as listed in Table 2.1, we consider potentially predominant aerobic and anaerobic chemolithotrophic energy metabolisms driven by H_2, H_2S, Fe^{2+} and CH_4. Note that these elements derived from hydrothermal fluids are not entirely consumed by biological activities. Indeed, it is generally considered that significant parts of the Fe^{2+} and H_2S in hydrothermal fluids are oxidized abiotically. In our calculation, however, we assume that all these elements are used for chemolithoautotrophic metabolism to estimate the upper limit of biomass that could be sustained by deep-sea hydrothermal activities (the biomass potential).

Figure 2.4 shows the metabolic energy yields maximally obtained from 1 kg of hydrothermal fluids for each of the hydrothermal systems MOR-B, MOR-U, ABA-M, ABA-F, SED-MOR, and SED-ABA. It should be noted here that the bioavailable energy yields were calculated based on an assumption that each of the aerobic and anaerobic reactions could use all the O_2 and H_2/SO_4 in the mixed fluids. For the reason, the energy yield from each of the reactions represents the maximum energy for the reaction available from the mixing fluids, and thus the sum of the energy available from all of the metabolic reactions are larger than the actual potential energy yields from the mixing fluids. In Fig. 2.4, for the aerobic energy metabolisms the bioavailable energy yield at <25 °C is larger by far than the yields of the higher temperature conditions. The anaerobic energy metabolisms become more favorable at higher temperatures, although the bioavailable energy yields by the anaerobic metabolisms at all temperature ranges are significantly lower than those of aerobic metabolisms at <25 °C. Consequently, it is suggested that aerobic chemolithotrophs in lower temperature conditions (mostly psychrophilic) are mainly responsible for the primary production of the associated microbial and macrofaunal communities in the global deep-sea hydrothermal vent environments.

In the MOR-B, ABA-M, and ABA-F systems, aerobic thiotrophy at low-temperature conditions (<25 °C) is by far the most energetically favorable compared with the other aerobic and anaerobic metabolisms at any temperature condition (Fig. 2.4). In the H_2-enriched MOR-U system, aerobic hydrogenotrophic metabolisms can produce much greater energy for biomass production than aerobic thiotrophic metabolisms (Fig. 2.4). This type of hydrothermal system is also characterized by significant energy yields from anaerobic hydrogenotrophic chemolithotrophs (e.g., methanogens and sulfate-reducers) under high-temperature conditions (Fig. 2.4). Similarly, the CH_4-enriched SED-MOR and SED-ABA systems have significant potential to yield energy for aerobic methanotrophs at lower temperatures and for anaerobic methanotrophic sulfate-reducers at higher temperatures (Fig. 2.4). The aerobic Fe(II)-oxidation reaction yields the second-highest metabolic energy in ABA-F systems and some hydrothermal vents in MOR-B systems, although the aerobic thiotrophy produces much higher energy than the aerobic Fe(II)-oxidation (Fig. 2.4). However, very little energy is available from anaerobic Fe(III)-reduction at any temperature condition in any type of hydrothermal system due to the extremely low concentration of ferric iron both in seawater and hydrothermal fluids.

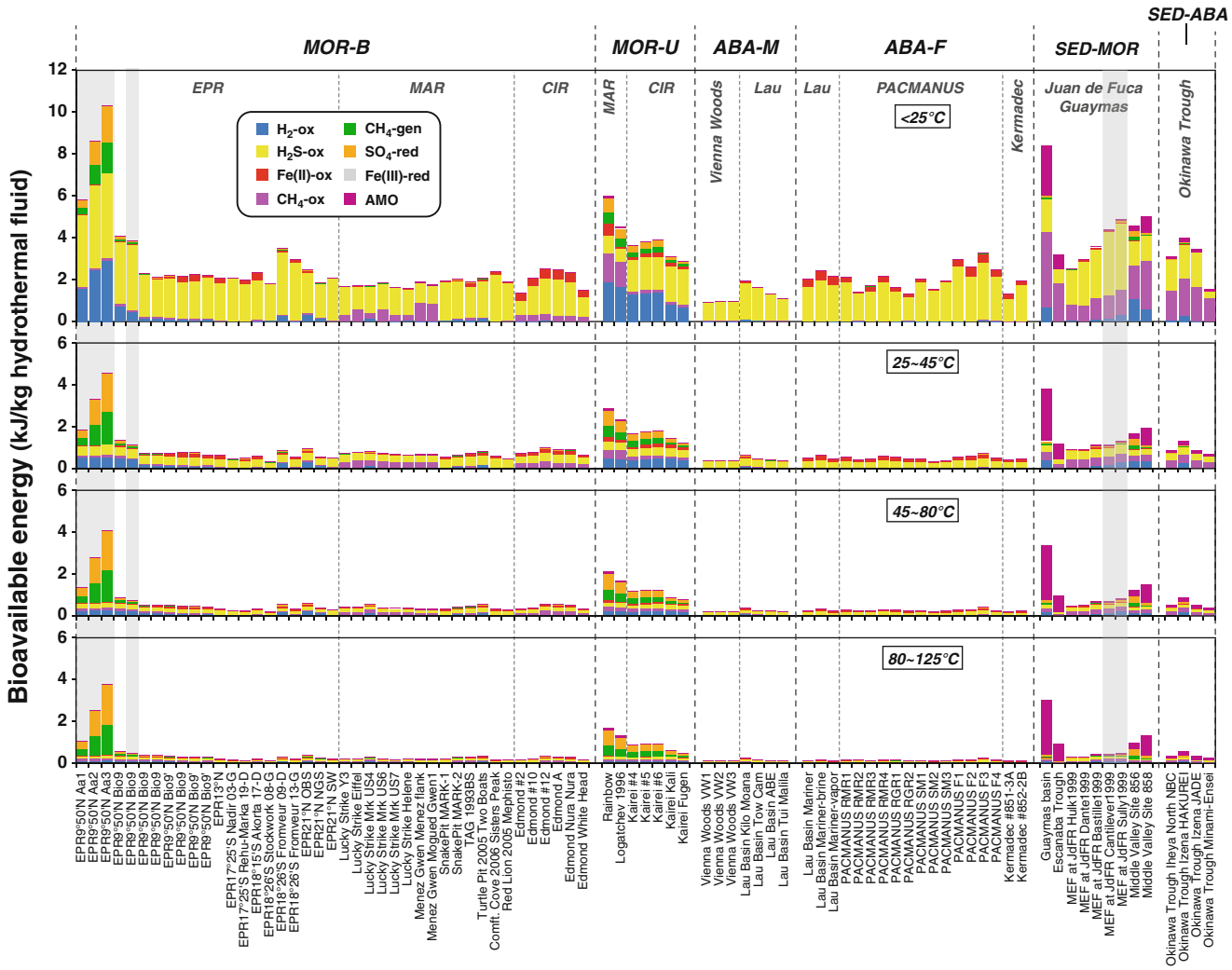

Fig. 2.4 Bar chart showing metabolic energies (kJ/kg hydrothermal fluid) available from the six aerobic and anaerobic reactions (Table 2.1) in 89 hydrothermal vent sites at temperature ranges of <25, 25–45, 45–80, and 80–125 °C in the MOR-B, MOR-U, ABA-M, ABA-F, SED-MOR, and SED-ABA systems. *Shaded vent sites* are excluded from the estimation of biomass potential in this study because of their unusual chemical compositions (<100 mmol/kg of Cl). See text for more details. Abbreviations: *MOR-B* basalt-hosted system in mid-ocean ridge settings, *MOR-U* ultramafic rock-hosted system in mid-ocean ridge settings, *ABA-M* mafic rock-hosted system in arc-backarc settings, *ABA-F* felsic rock-hosted system in arc-backarc settings, *SED-MOR* sediment-associated system in mid-ocean ridge settings, *SED-ABA* sediment-associated system in arc-backarc settings, *ABA* arc-backarc hydrothermal system, *SED* sediment-associated hydrothermal system, *H_2S-ox* aerobic H_2S-oxidation, *H_2-ox* aerobic H_2-oxidation, *CH_4-ox* aerobic CH_4-oxidation, *SO_4-re* anaerobic SO_4-reduction, *AMO* anaerobic CH_4-oxidation

Figure 2.5 shows the average values of bioavailable energy yields from each of the energy metabolisms in the MOR-B, MOR-U, ABA, and SED systems. Because there are essentially no differences in the bioavailable energy yields between the ABA-M and ABA-F systems or between the SED-MOR and SED-ABA systems (Fig. 2.4), we use the average value of the ABA and SED systems for the estimation of potential biomass described below. In the MOR-B and ABA systems, the aerobic thiotrophy at <25 °C is by far the most energetically favorable, whereas the contribution of the other energy metabolisms is essentially negligible (Fig. 2.5). In contrast, in the MOR-U system, the aerobic hydrogen-oxidation at <25 °C is the most energetically favorable. This is due to the high concentrations of H_2 and relatively low concentrations of H_2S in the MOR-U fluids. Additionally, at high-temperature conditions anaerobic hydrogenotrophic energy metabolisms yield more energy than aerobic hydrogen-oxidation (Fig. 2.5). In the SED system, the aerobic methanotrophic energy production is comparable to thiotrophic production at low temperatures (<25 °C), whereas anaerobic methanotrophy is the most energetically favorable at high temperatures (>45 °C), reflecting the high concentration of CH_4 in the hydrothermal fluids (Fig. 2.5).

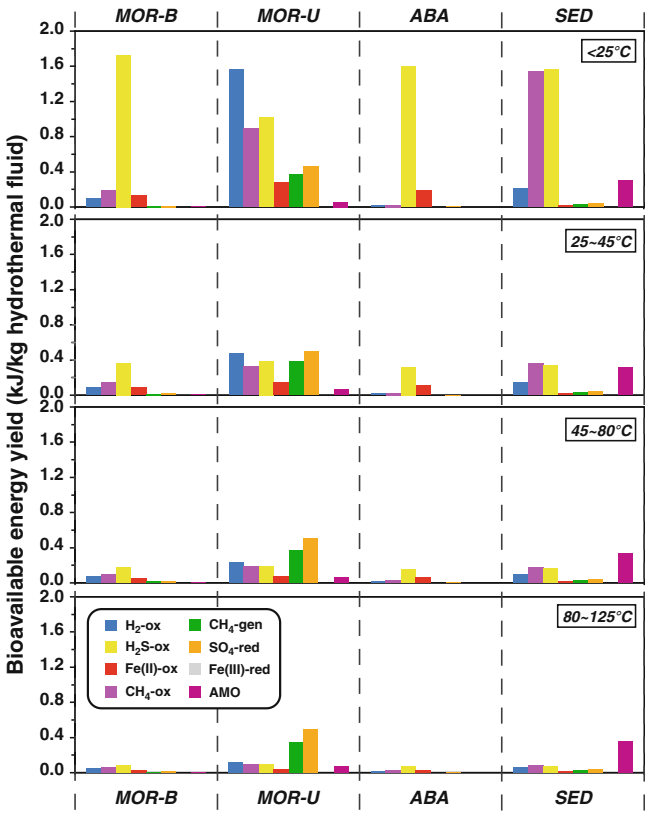

Fig. 2.5 *Bar chart* showing averaged metabolic energies (kJ/kg hydrothermal fluid) available from the six aerobic and anaerobic reactions (Table 2.1) at temperature ranges of <25, 25–45, 45–80, and 80–125 °C in the MOR-B, MOR-U, ABA, and SED systems. Abbreviations: *MOR-B* basalt-hosted system in mid-ocean ridge settings, *MOR-U* ultramafic rock-hosted system in mid-ocean ridge settings, *ABA* arc-backarc hydrothermal system, *SED* sediment-associated hydrothermal system, *H_2S-ox* aerobic H_2S-oxidation, *H_2-ox* aerobic H_2-oxidation, *CH_4-ox* aerobic CH_4-oxidation, *SO_4-re* anaerobic SO_4-reduction, *AMO* anaerobic CH_4-oxidation

2.3.3 Fluxes of Deep-Sea Hydrothermal Fluids

The total amount of high-temperature hydrothermal fluid flux from the MOR system into the ocean has been estimated as 5.6×10^{15} g/year, based on the production rate of oceanic crust (Elderfield and Schults 1996; Mottl 2003). This calculation is based on the assumption that 10 % of the hydrothermal budget results from high-temperature focused flows and that 90 % results from lower-temperature fluid flows. This assumption has recently been supported by the geochemical evidence from hydrothermally altered oceanic crust by Nielsen et al. (2006). Indeed, at least two types of alteration (high-temperature (>250 °C) with a low water/rock ratio and low-temperature (<150 °C) with a high water/rock ratio) have long been recognized in oceanic crust, in both on-axis and off-axis regions of mid-ocean ridges (Fig. 2.6) (Alt et al. 1986, 1996a, b; Nakamura et al. 2007). In this study, therefore, we adopt this value as the total high-temperature hydrothermal fluid flux from the MOR system.

Based on the chemical characteristics of hydrothermal fluids and the bioavailable energy yields described in the previous sections, the MOR system is further divided into the following three types: (1) the ultramafic rock-associated H_2-rich MOR-U system, (2) the sediment-associated CH_4-rich SED-MOR system, and (3) the relatively H_2S-rich MOR-B system. To estimate the fluxes of the H_2-enriched, CH_4-enriched, and H_2S-enriched fluids separately, we attempted to allocate the total amount of MOR hydrothermal fluid flux into the three hydrothermal systems as follows.

In the mid-ocean ridges explored so far, the presence of ultramafic rocks is mostly recognized at slow and ultra-slow spreading ridges (Cannat et al. 2006; Escartin et al. 2008). Recent geophysical surveys have predicted that ultra-slow and slow spreading ridges occupy 20 % and 40 % of the mid-ocean ridge extent, respectively (Cannat et al. 2006; Schwartz et al. 2005). In addition, extensive chemical surveys of hydrothermal plumes have suggested that the general incidence ratio of hydrothermal activities along the mid-ocean ridge is linearly correlated with the spreading rate (Baker and German 2004; Baker et al. 2004). According to the results of Baker et al. (2004), the incidence ratios of hydrothermal plumes (activities) can be estimated as 0.08, 0.25, and 0.67 at the ultra-slow, slow, and moderate to fast spreading ridges, respectively. Given that the hydrothermal fluid fluxes are correlated with the plume incidence, as well as the ridge lengths, we can break down the total MOR hydrothermal flux (5.6×10^{15} g/year) into 2.4×10^{14} g/year, 1.5×10^{15} g/year, and 3.9×10^{15} g/year at the ultra-slow, slow, and moderate to fast spreading ridges, respectively.

Cannat et al. (2006) reported that, based on the geophysical surveys at the ultra-slow spreading ridge of the Southwest Indian Ridge, 59 % of the seafloor is a typical type covered with basaltic lava flows, whereas 37 % is smooth and 4 % is corrugated. The smooth seafloor is composed mostly of ultramafic rocks, whereas the corrugated seafloor consists of basaltic lavas on one side and ultramafic/gabbroic rocks on the other side (Cannat et al. 2006). If we assume here that (1) all of the ultra-slow spreading ridges have 37 % smooth seafloor and 4 % corrugated seafloor, as is the case for the Southwest Indian Ridge, and (2) all of the smooth-seafloor regions and half of the corrugated-seafloor regions have a potential to generate H_2-rich hydrothermal fluids, we can estimate that 39 % of ultra-slow spreading ridges can host the H_2-rich hydrothermal system.

In the slow spreading Mid-Atlantic Ridge, Escartin et al. (2008) showed that 50 % of the ridge axis regions were symmetric, and the rest were asymmetric. Based on seafloor morphology, the symmetric and asymmetric ridges can be

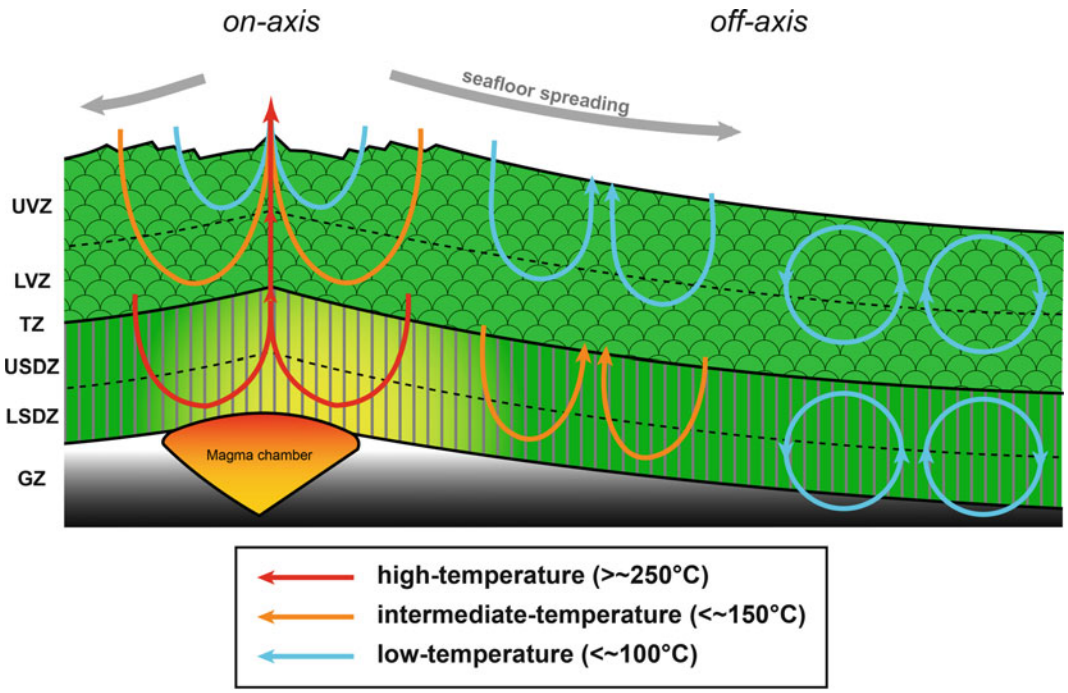

Fig. 2.6 Schematic illustration showing hydrothermal circulation within oceanic crust in on- and off-axis regions (modified from Nakamura et al. 2007). The red, orange, and blue arrows represent high- (>~250 °C), intermediate- (<~150 °C), and low-temperature (<~100 °C) fluid flows, respectively. Abbreviations: UVZ upper volcanic zone, LVZ lower volcanic zone, TZ transition zone, USDZ upper sheeted dike zone, LSDZ lower sheeted dike zone, GZ gabbro zone

comparable to the typical volcanic seafloor and corrugated seafloor described by Cannat et al. (2006), respectively. Thus, the seafloor at the symmetric ridge regions can be regarded as composed mostly of basaltic lava flows, whereas the asymmetric regions consist of basaltic lavas on one side and ultramafic/gabbroic rocks on the other side. As is the case for the ultra-slow spreading ridges, therefore, we can estimate that 25 % of slow spreading ridges can host the hydrothermal systems producing H_2-enriched hydrothermal fluids.

There are also sediment-associated ridges, which are geographically located in close proximity to continents (Fig. 2.1). In this study, the Juan de Fuca Ridge, the Gorda Ridge, and the Gulf of California in the northeast Pacific Ocean and the Red Sea are defined as the sediment-associated ridges. The spreading rate of the ridges is variable: moderate to fast in the northeast Pacific Ocean but slow in the Red Sea. The total lengths of the ridges in the northeast Pacific Ocean and the Red Sea are evaluated to be each ~2,000 km, which corresponds to 8.3 % each of the total lengths of the moderate to fast spreading ridges and the slow spreading ridges.

Based on the estimations described above, the hydrothermal fluid fluxes from the H_2-rich MOR-U system, the CH_4-rich SED-MOR system, and the H_2S-rich MOR-B system can be estimated to be 4.6×10^{14}, 4.4×10^{14}, and 4.7×10^{15} g/year, respectively. It should be noted here that, in the slow and ultra-slow spreading ridges composed both of typical basaltic seafloor and corrugated/smooth seafloor with ultramafic rocks, hydrothermal fluid flux is likely to be lower in the corrugated/smooth seafloor regions compared with the typical seafloor region. This is because corrugated/smooth seafloor is considered to be formed by tectonic (amagmatic) processes rather than magmatic processes, resulting in a lack of heat source in the corrugated/smooth seafloor regions. However, we still do not know much about the difference of hydrothermal fluxes between magmatic and amagmatic regions of the slow and ultra-slow spreading ridges. In our model calculation, therefore, we simply applied the plume incidence ratios for slow and ultra-slow spreading ridges (Baker et al. 2004), which is an average value with both magmatic and amagmatic regions. For this reason, the estimated flux of the MOR-U fluids can be regarded as the maximum value.

In contrast to the case of the MOR hydrothermal systems described above, there has been no previous estimation of the total hydrothermal fluid flux from the ABA systems. Thus, we attempt to estimate the hydrothermal flux from the ABA systems in a similar manner to the estimation of the MOR hydrothermal fluid flux. Following the method used to calculate the MOR hydrothermal fluid flux, the flux from the ABA systems was estimated from the global crustal (magma) production rate in arc-backarc settings. For arc settings, we focus only on submarine hydrothermal

activities, not on subaerial hydrothermal activities. Thus, only the intra-oceanic arcs, totaling approximately 17,000 km (nearly 40 % of the subduction margins of the Earth) (Leat and Larter 2003), are considered, although not all intra-oceanic arc volcanism is submarine. The magma (crust)-addition rate in the western Pacific island arcs (a typical intra-oceanic arc) was estimated to be 30–95 km^3/km/Myr (Dimalanta et al. 2002). If we assume that all intra-oceanic arcs have the same magma-addition rate, the crustal production rate of these arcs is estimated to be 0.51–1.6 km^3/year. For simplicity, we use an average value of 1.1 km^3/year, which corresponds to 5.5 % of the oceanic crustal production rate at mid-ocean ridges.

It is also known that most of the intra-oceanic arcs accompany back-arc spreading or rifts, except for the Solomon and Aleutian arcs (Gerya 2011). Among these arcs, the Okinawa Trough (~1,000 km) (Hirata et al. 1991), the Mariana Trough (~1,300 km) (Hawkins and Melchior 1985), the Manus Basin (~120 km) (Reeves et al. 2011), the North Fiji Basin (~800 km) (Tanahashi et al. 1994), the Lau Basin (~2,000 km) (Parson and Wright 1996), the East Scotia Basin (~500 km) (Rogers et al. 2012), the Bransfield Basin (~300 km) (Janik 1997), the Andaman Basin (~80 km) (Rao et al. 1996), and the Marsili Basin (~70 km) (Ventura et al. 2013) are known to be currently active (Fig. 2.1). Thus, we assume here that all these currently active back-arc spreading centers (total length of ~6,200 km) have an average crustal thickness of 6 km and an average spreading rate of 5 cm/year (both values are the same as the mid-ocean ridge average), although their spreading rates and crustal thicknesses are known to be variable (slow to fast spreading and crustal thicknesses of a few km to >10 km). Consequently, the crustal production rate of the back-arc spreading is estimated to be 2.1 km^3/year, corresponding to 10 % of the oceanic crustal production rate.

It is also important to note that no active H_2-enriched hydrothermal system associated with ultramafic rocks have ever been discovered in arc-backarc settings. However, the SED hydrothermal system characterized by CH_4-enriched fluids is known in the Okinawa Trough (Kawagucci et al. 2011), which has ~1,000 km each of arc and back-arc systems. Taking into account the total crustal production rate and the fraction of the sediment-associated region, the hydrothermal fluid fluxes from the sediment-associated SED-ABA system and the rest of the ABA system are estimated to be 1.1×10^{14} and 7.8×10^{14} g/year, respectively.

A summary of the estimated hydrothermal fluid fluxes from the global MOR and ABA systems is shown in Fig. 2.7. It is evident that the largest hydrothermal fluid flux (72.4 %) is provided by the MOR-B system. In contrast, the mass contributions of the ABA (12.0 %), MOR-U (7.1 %), and SED (8.5 %) systems are quite limited.

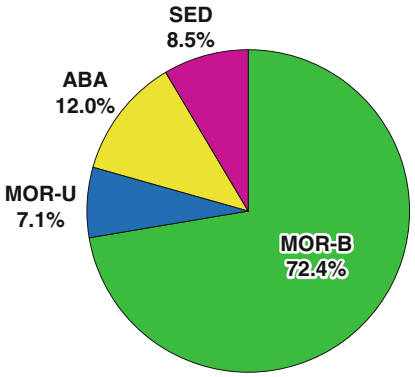

Fig. 2.7 Hydrothermal fluid fluxes from MOR-B, MOR-U, ABA, and SED systems. Abbreviations: MOR-B basalt-hosted system in mid-ocean ridge settings, MOR-U ultramafic rock-hosted system in mid-ocean ridge settings, ABA arc-backarc hydrothermal system, SED sediment-associated hydrothermal system

2.3.4 Biomass Potential in Deep-Sea Hydrothermal Vent Ecosystems

In the above sections, we described the estimates of the hydrothermal fluid fluxes and the bioavailable energy yields of various chemolithotrophic metabolisms in different types or settings of deep-sea hydrothermal systems. Here, using Eq. (2.4), we approach an estimate of the biomass potential sustained by deep-sea hydrothermal fluid inputs from the MOR-B, MOR-U, ABA, and SED systems. As mentioned above, the total amounts of energy available from all the metabolic reactions are larger than the actual potential energy yields from the mixing fluids because of the assumption that each of the aerobic and anaerobic reactions can use all the O_2 and H_2/SO_4 in the mixed fluids, respectively. Therefore, to provide the maximum estimate of biomass in these deep-sea hydrothermal vent ecosystems, the most energetically favored metabolisms under the aerobic and anaerobic conditions (using O_2 and H_2/SO_4, respectively) are chosen.

The only exception is the SED system, where the psychrophilic aerobic thiotrophy and methanotrophy can produce nearly the same bioavailable energy yield (Fig. 2.5). For hydrothermal vent sites, the most energetically favored aerobic metabolism is psychrophilic aerobic thiotrophy at some sites and psychrophilic aerobic methanotrophy at other sites, although hyperthermophilic anoxic methanotrophy with SO_4-reduction is the most energetically favorable anaerobic metabolism at all sites (Fig. 2.4). Indeed, biological investigations of the hydrothermal vents of the SED system have revealed the presence of significant amounts of aerobic methanotrophs (Watsuji et al. 2010; Lesniewski et al. 2012). For this reason, in the estimation we use methane-oxidation reactions as the most energetically favored metabolisms for the SED system. In this case, methane in the mixing fluid is competitively used for both aerobic and anaerobic methanotrophy, resulting in

lower total amounts of energy obtained from the mixing fluid. However, the assumption's influence on the estimation of biomass is thought to be limited for the following reasons: (1) the effect of anaerobic methanotrophy on total bioavailable energy yield is relatively minor, and (2) a shortage of aerobic methanotrophy can be supplemented with aerobic thiotrophy. Therefore, for the sake of convenience, we separately estimated the maximum amounts of energy available from aerobic and anaerobic methane-oxidation reactions based on the assumption that each reaction can use all the CH_4 in the mixing fluid. Finally, the sum of the estimated values is used as the potential bioavailable energy yield of the SED system.

Consequently, the most energy-yielding metabolisms for the biomass development are assumed to be psychrophilic aerobic thiotrophy and hyperthermophilic hydrogenotrophic sulfate reduction in the MOR-B and ABA systems, psychrophilic aerobic hydrogenotrophy and hyperthermophilic hydrogenotrophic sulfate-reduction in the MOR-U system, and psychrophilic aerobic methanotrophy and hyperthermophilic methanotrophic sulfate-reduction in the SED system.

The calculated biomass potential is shown in Fig. 2.8. The result indicates that almost all the biomass estimated is sustained by aerobic psychrophilic chemolithotrophic production, and the contributions of anaerobic hyperthermophilic chemolithotrophs are essentially negligible (Fig. 2.8a). This is attributed to the lower abundances of H_2- and CH_4-rich hydrothermal systems (MOR-U and SED), lower energy yields of high-temperature anaerobic reactions per a given amount of hydrothermal fluids, and a higher maintenance cost at higher temperatures as shown in Eq. (2.3).

The biomass potentials in the MOR-B, MOR-U, ABA, and SED hydrothermal systems are calculated to be 5.5×10^{12} g C, 4.9×10^{11} g C, 8.4×10^{11} g C and 5.9×10^{11} g C, respectively. It is clear that most of the overall biomass is sustained by the MOR-B system (Fig. 2.8b), reflecting the largest hydrothermal fluid flux from the MOR-B system among all the systems (Fig. 2.7). The biomass potentials sustained by each energy metabolism are calculated to be 6.4×10^{12} g C for aerobic thiotrophy, 4.9×10^{11} g C for aerobic hydrogenotrophy, 5.9×10^{11} g C for aerobic methanotrophy, 3.4×10^{8} g C for hydrogenotrophic sulfate reduction, and 2.9×10^{8} g C for anaerobic methanotrophic sulfate reduction. As shown in Fig. 2.8c, more than 85 % of the overall estimated biomass for the global deep-sea hydrothermal vent ecosystems is sustained by aerobic thiotrophic populations. This result clearly indicates the significance of inorganic reduced-sulfur compounds entrained from hydrothermal fluid emissions for biomass production in the global deep-sea hydrothermal vent ecosystems of the modern Earth. The biomass potentials sustained by the aerobic oxidations of H_2 and CH_4 in the hydrothermal fluids are one order of magnitude lower than that sustained by the hydrothermal sources of reduced-sulfur compounds. In contrast, the impact of anaerobic (hyper)thermophilic chemolithotrophs on the biomass potential of global deep-sea hydrothermal vent ecosystems are essentially negligible on the modern Earth.

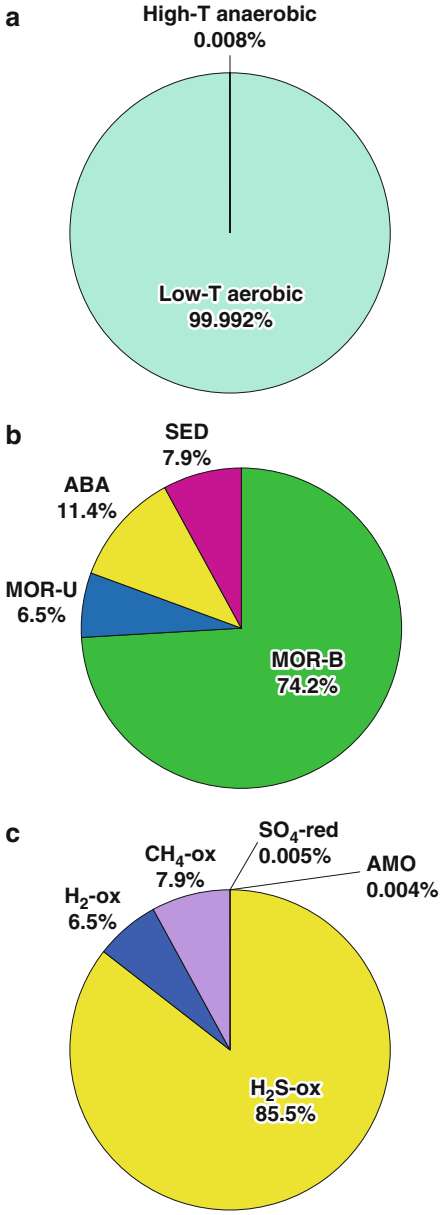

Fig. 2.8 Relative amounts of potential biomass sustained by (**a**) low-temperature aerobic reactions and high-temperature anaerobic reactions, (**b**) MOR-B, MOR-U, ABA, and SED systems, and (**c**) H_2S-ox, H_2-ox, CH_4-ox, SO_4-red, and AMO reactions. Abbreviations: MOR-B basalt-hosted system in mid-ocean ridge settings, MOR-U ultramafic rock-hosted system in mid-ocean ridge settings, ABA arc-backarc hydrothermal system, SED sediment-associated hydrothermal system, H_2S-ox aerobic H_2S-oxidation, H_2-ox aerobic H_2-oxidation, CH_4-ox aerobic CH_4-oxidation, SO_4-red anaerobic SO_4-reduction, AMO anaerobic CH_4-oxidation

2.4 Potential Biomass Sustained by Low-Temperature Alteration/Weathering of Oceanic Crust

In addition to the high-temperature hydrothermal systems at the mid-ocean ridge axis, we now know that low-temperature water–rock interactions (low-temperature alterations including so-called ocean floor weathering) occur in both on-axis and off-axis regions (Fig. 2.6) (e.g., Alt et al. 1986, 1996a, b; Mottl and Wheat 1994; Nakamura et al. 2007). It is considered that the low-temperature fluid-flows and water–rock interactions play pivotal roles in heat and chemical exchanges between the ocean and oceanic crust (Wheat and Mottl 2000). Even at the mid-ocean ridge axis, most of the hydrothermal budget (~90 %) is driven by low-temperature fluid circulation (Elderfield and Schults 1996; Nielsen et al. 2006). Furthermore, most of the global hydrothermal budget is likely led by the low-temperature fluid flows on the mid-ocean ridge flanks, where approximately 2–3 times greater heat loss occurs than on the axis (Stein et al. 1995; Elderfield and Schults 1996). This estimation leads us to consider that there may be a spatially enormous, previously unseen biosphere in the ridge-flank regions. However, to date, exploration of the potentially habitable igneous ocean crust, mostly at the mid-ocean ridge flanks, remains insufficient (Edwards et al. 2012; Lever et al. 2013).

The igneous ocean crust is known to harbor the largest aquifer system on Earth, potentially representing approximately 2 % of the ocean's fluid volume (Johnson and Priuis 2003). It has been noted that the oceanic crust aquifer is hydrothermally driven (Sclater et al. 1980; Stein and Stein 1994) and that fluids are exchanged with the overlying oceans on the order of every 100,000 years (Elderfield and Schults 1996). Surprisingly, the estimated fluid flux from the oceanic crust to the deep ocean is roughly equivalent to the global annual flux of riverine inputs to the oceans (Elderfield and Schults 1996). In contrast to the high-temperature on-axis hydrothermal systems, however, both the chemical composition and the physical properties of the low-temperature crustal fluids are largely uncertain because of difficulty in accessing the low-temperature fluid-flow systems within the oceanic crust. Therefore, it is quite difficult to estimate the flux of chemosynthetic energy sources derived by the low-temperature fluid flows based on the direct investigation of the fluids.

In addition to the chemistry of the low-temperature crustal fluids, the petrological and geochemical properties of altered oceanic crust (the other product of water–rock interactions in the on- and off-axis regions of the mid-ocean ridge) can provide important insights into the chemical exchange processes during the low-temperature water–rock interactions (e.g., Alt et al. 1996a, b; Staudigel et al. 1996; Teagle et al. 1996; Nakamura et al. 2007). Indeed, Bach and Edwards (2003) estimated the bioavailable energy yield by low-temperature water–rock interactions at the ridge-flank regions based on geochemical data for altered oceanic crust. Following the method proposed by Bach and Edwards (2003), we can estimate the bioavailable energy yield and fluxes of the energy sources from the low-temperature alteration of oceanic crust. This estimate, in turn, leads to the estimation of the biomass potential sustained by the low-temperature water–rock interactions within the oceanic crust.

2.4.1 Processes and Fluxes of Elemental Exchange Between Seawater and Oceanic Crust During Low-Temperature Alteration/Weathering

The uppermost 200–500 m of basaltic ocean crust is known to be characterized by a high permeability that facilitates the circulation of large quantities of seawater (Fisher 1998; Fisher and Becker 2000). Within the oceanic crust aquifer, basaltic rocks react with oxygenated deep-sea water to form secondary minerals, replacing primary phases (e.g., glass, olivine, and metal sulfides) and/or filling fractures and void spaces (Alt et al. 1996a, b; Teagle et al. 1996; Talbi and Honnorez 2003). This process changes the composition of both the seawater and the oceanic crust (Hart and Staudigel 1986; Alt et al. 1996a, b; Staudigel et al. 1996; Elderfield et al. 1999; Nakamura et al. 2007). During the low-temperature alteration/weathering of oceanic crust, chemical energy for lithoautotrophy can arise from the redox reactions between the reduced basaltic rocks and relatively oxidized seawater. In this environment, reduced forms of elements (e.g., ferrous iron, sulfide sulfur, and divalent manganese) in the rocks are out of equilibrium with oxidants, such as O_2 and NO_3, in the seawater because low-temperature water–rock reactions are kinetically sluggish. This provides an opportunity for microorganisms to catalyze the reactions and to exploit the components for metabolism and growth (Bach and Edwards 2003).

Because of the significantly higher abundances of Fe and S than Mn and other reduced forms of metals in basalt, the oxidations of Fe and S become the most abundant energy sources for chemolithotrophic metabolism (Bach and Edwards 2003). Another potential energy source is H_2, which is generated via hydrolysis by Fe in basaltic glass or Fe-rich minerals (Bach and Edwards 2003). It has been suggested that a portion of ridge-flank aquifer in the SED system could host sulfate reducers (Lever et al. 2013).

However, under the entirely oxidizing conditions with the high seawater/rock ratio expected for the oceanic crust aquifer (Alt et al. 1996a, b; Teagle et al. 1996), the occurrence of hydrolysis by Fe seems to be limited during low-temperature alteration/weathering. Moreover, it is unlikely that such highly oxidized aquifer systems provide widespread habitats for anaerobic chemolithotrophs (e.g., methanogens and sulfate reducers). Indeed, the incidence of low-temperature H_2-based microbial communities in the terrestrial subsurface basaltic aquifers is highly controversial (Stevens and McKinley 1995, 2000, 2001; Anderson et al. 1998, 2001). In the present contribution, therefore, we adopt only the aerobic oxidation of Fe and S during the low-temperature water–rock interactions within the oceanic crust. Additionally, as noted in the previous section of hydrothermal vent ecosystems, not all the Fe and S is used for biological activities. More likely, it is possible that most of the Fe and S in basaltic ocean crust is oxidized abiotically. In our calculation, however, we assume that all these elements are used for chemolithoautotrophic metabolism (aerobic oxidation of Fe and S) to estimate the biomass potential (i.e., the upper limit of biomass) of the deep subsurface biosphere in igneous ocean crust.

2.4.1.1 Iron

Here, we estimate the degree, extent, and timing of Fe-oxidation during low-temperature alteration/weathering of basaltic ocean crust based on the geochemical data from DSDP, ODP, and IODP, which were compiled by Bach and Edwards (2003) (Suppl. Table 2.2). The oxidation state (Fe(III)/ΣFe) of fresh basaltic ocean crust is known to be 0.15 ± 0.05 (Christie et al. 1986; Bach and Erzinger 1995). In this study, therefore, the original Fe(III) content of the fresh oceanic crust is estimated based on the total Fe content and the oxidation state. Then, using the estimated original Fe (III) and the observed Fe(III) contents, we calculate the amounts of Fe(II) oxidized to Fe(III) during low-temperature alteration/weathering.

Figure 2.9a shows a change in the amounts of Fe(II) that oxidized to Fe(III) in basalt with crust age. The figure clearly indicates that the Fe(II) in basaltic ocean crust is gradually oxidized to Fe(III) during low-temperature alteration/weathering in off-axis regions. The oxidation of Fe is continuous but wanes with a time-dependent logarithm (Fig. 2.9a). This is consistent with geophysical (Stein and Stein 1994; Fisher and Becker 2000; Jarrard 2003) and geochemical (Hart and Staudigel 1986; Peterson et al. 1986; Booij et al. 1995) lines of evidence suggesting that vigorous seawater circulation and oxidative alteration take place especially in young crust. Although the timing for the termination of the circulation and alteration is still uncertain, a simple model of age-dependent oxidative alteration was employed in this study, based on the change in geophysical parameters sensitive to crustal hydration (Jarrard 2003).

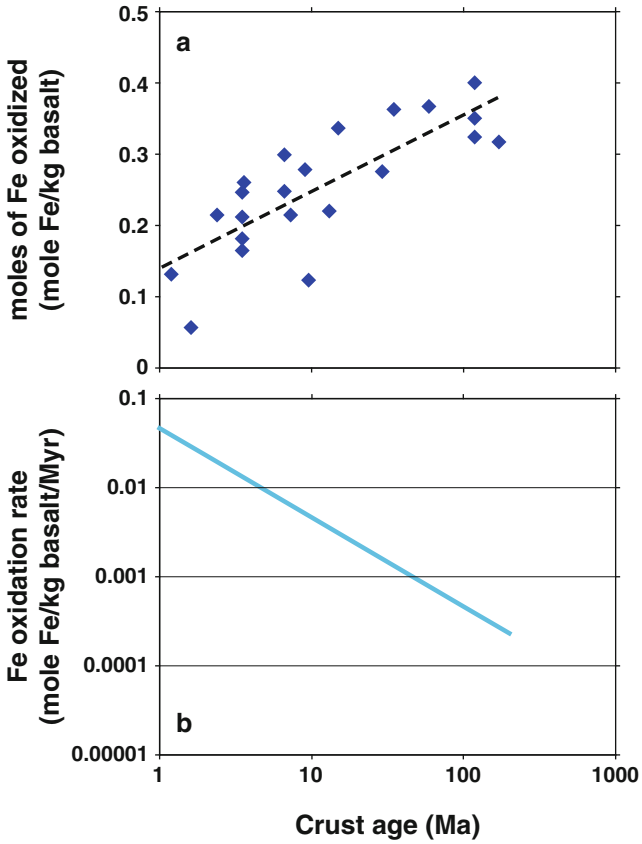

Fig. 2.9 Changes in (**a**) the amounts of Fe (II) oxidized to Fe (III) and (**b**) the Fe-oxidation rate of basaltic ocean crust with crust age

Based on the relationship of the Fe-oxidation with crust age in oceanic crust (Fig. 2.9a) and the average age of subducted oceanic crust (60 Ma) (Schubert et al. 2001), we can estimate the average amounts of Fe(II) oxidized to Fe(III) in oceanic crust during low-temperature alteration/weathering to be 0.33 mol Fe/kg basalt. The Fe-oxidation budget can be converted to a steady-state oxidation rate of Fe by multiplying by the annual mass of basaltic ocean crust produced. Following the assumptions provided by Bach and Edwards (2003) (a seafloor production rate of 3.0 km^2/year, a depth extent of oxidation of 500 m, an upper crustal porosity of 0.10, and a basalt density of 2,950 kg/m^3), the annual production mass of the altered oceanic crust is estimated to be 4.0×10^{12} kg/year. With the estimated Fe-oxidation budget (0.33 mol Fe/kg basalt) and the annual production rate of altered oceanic crust (4.0×10^{12} kg/year), we calculated global upper ocean-crust oxidation rates of 1.3×10^{12} mol Fe/year. In addition to the steady-state oxidation rate, we also calculate the specific Fe-oxidation rate at the each age of oceanic crust (Fig. 2.9b) by differentiating the curve of the Fe-oxidation progress with crust age (Fig. 2.9a).

The result clearly shows that a much higher Fe-oxidation rate occurs in younger oceanic crust (Fig. 2.9b).

2.4.1.2 Sulfur

Even today, data for S concentrations in altered oceanic crust are quite scarce. In this study, we use S-concentration data from DSDP, ODP, and IODP. These data were compiled by Bach and Edwards (2003) and more recently provided by Miller and Kelley (2004), Rouxel et al. (2008), and Alt and Shanks (2011) (Suppl. Table 2.2). It is known that the speciation of S in basaltic magma is dominated by sulfide. Because sulfide has a strong affinity for FeO in the melt, the solubility of S is essentially controlled by the concentration of Fe (Mathez 1976; Wallace and Carmichael 1992). Thus, we can estimate the primary S concentration in basaltic ocean crust using the following empirical relationship between total Fe and S concentrations for sulfide-saturated basaltic magma (Mathez 1979):

$$\mathrm{S}\ [\mathrm{wt}\%] = 0.023\ \mathrm{Fe}\ [\mathrm{wt}\%] - 0.059 \qquad (2.6)$$

During low-temperature alteration/weathering of basaltic ocean crust, the sulfide in the basalt is oxidized to sulfate. Because of the high solubility of sulfate in seawater, the oxidized S during the alteration/weathering is leached from the basalt, resulting in a decrease of total sulfur content. Thus, the differences between the calculated initial S concentrations and the observed S concentrations in altered oceanic crust can be regarded as the amounts of S oxidized during alteration/weathering. Figure 2.10a shows that the amount of oxidized S in oceanic crust changes with the age of oceanic crust, although the extent of S-oxidation in oceanic crust is much more variable compared with that of Fe-oxidation (Fig. 2.9a).

The compiled DSDP, ODP, and IODP data generally show a correlation between the amounts of oxidized S and the logarithmic age of oceanic crust (Fig. 2.10a). Thus, we also employ a simple model of age-dependent oxidative alteration, as in the case for the Fe-oxidation described above. In this model, the S-oxidation rate decreases in proportion to the logarithmic age of oceanic crust. Following the same method used in the calculation of the Fe-oxidation budget, we can estimate the average amounts of oxidized S during low-temperature alteration/weathering of oceanic crust to be 0.02 mol S/kg basalt. The S-oxidation budget can be converted to a steady-state oxidation rate of 8.1×10^{10} mol S/year by multiplying by the mass of the annual production of altered oceanic crust. We can also calculate the specific S-oxidation rate at each age of oceanic crust, showing that a much higher S-oxidation rate is achieved in younger oceanic crust (Fig. 2.10b), as in the case for Fe-oxidation.

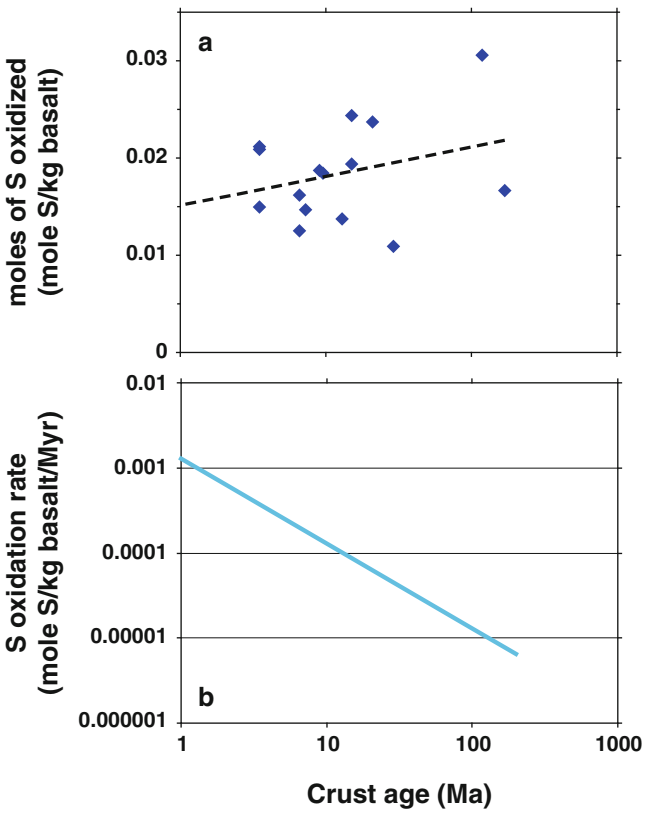

Fig. 2.10 Changes in (**a**) the amounts of reduced sulfur oxidized to sulfate and (**b**) the sulfur-oxidation rate of basaltic ocean crust with crust age

2.4.2 Bioavailable Energy Yield from Low-Temperature Alteration/Weathering of Oceanic Crust

Following Bach and Edwards (2003), the metabolic energy yields for Fe- and S-oxidation reactions in the low-temperature basalt aquifer are calculated to be 66.2 kJ/mol Fe and 751 kJ/mol S, respectively. Then, using the metabolic energy yields and the Fe- and S-oxidation rates (1.3×10^{12} mol Fe/year and 8.1×10^{10} mol S/year, respectively) estimated in the previous section, the amounts of energy for chemolithotrophic Fe- and S-oxidizing metabolisms during low-temperature alteration/weathering of basaltic ocean crust are estimated to be 8.8×10^{13} kJ/year and 6.1×10^{13} kJ/year, respectively. In this case, the requisite amounts of oxygen for the Fe- and S-oxidation reactions (3.3×10^{11} mol O_2/year and 1.6×10^{11} mol O_2/year, respectively) are much smaller than the supply rate (1.4×10^{12} mol O_2/year) calculated from the fluid flux though oceanic crust. It is noteworthy that, although the S-oxidation rate (0.81×10^{11} mol S/year) is one order of magnitude lower than the Fe-oxidation rate (1.3×10^{12} mol Fe/year), the energy yield of the S-oxidizing metabolisms is comparable to that of the Fe-oxidizing metabolisms. This

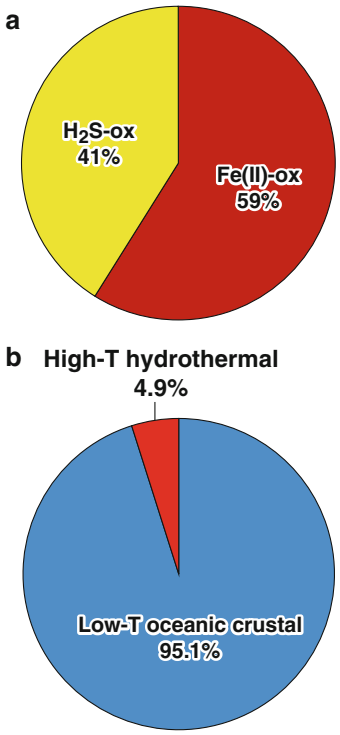

Fig. 2.11 Relative amounts of potential biomass sustained by (**a**) Fe(II)- and H_2S-oxidation reactions and (**b**) high-temperature hydrothermal activity and low-temperature oceanic crust alteration/weathering

reflects a much higher energy yield per mole of electron acceptor from the S-oxidation reaction than the Fe-oxidation reaction. This suggests that for both the high-temperature hydrothermal systems and the low-temperature oceanic crust aquifer systems, the reduced form of S is an important energy source for chemosynthetic ecosystems on the modern Earth, while the Fe-oxidation reaction is the most energetically favorable in the basaltic ocean crust aquifer.

2.4.3 Biomass Potential in Oceanic Crust Ecosystems

Based on Eq. (2.5), we calculated the biomass potential sustained by the low-temperature alteration/weathering using the estimated values of the bioavailable energy yields, the rates of Fe- and S-oxidations, and the maintenance energy requirement. The potential biomass sustained by the Fe- and S-oxidation reactions is calculated to be 8.5×10^{13} g C and 5.9×10^{13} g C, respectively. The results show that nearly the same population sizes can be fostered by the Fe- and S-oxidizing energy metabolisms during the low-temperature alteration/weathering of basaltic ocean crust (Fig. 2.11a). This implies that both the aerobic Fe-oxidizers and the aerobic S-oxidizers play important biogeochemical and ecological roles in the subseafloor crust ecosystems. Moreover, it is interesting that the overall biomass potential in the oceanic crust ecosystems (1.4×10^{14} g C) is one order of magnitude higher than that in the high-temperature hydrothermal vent ecosystems (0.74×10^{13} g C) (Fig. 2.11b). The difference in overall biomass potentials is likely dependent on the difference in hydrothermal heat fluxes between the low-temperature on- and off-axis flows (~9 TW) and the high-temperature axial flow (~0.3 TW) (Elderfield and Schults 1996). Note here that the biomass potential estimation of the oceanic crust ecosystems is completely independent of the heat flux data.

In addition to the amount of biomass in the oceanic crust, we can also calculate the cell abundances (6.1×10^{27} cells for aerobic Fe-oxidizers and 4.2×10^{27} cells for aerobic S-oxidizers) and the possible average cell densities in the hypothetically habitable spaces (6.7×10^{4} cells/cm^3 for aerobic Fe-oxidizers and 4.7×10^{4} cells/cm^3 for aerobic S-oxidizers) using a carbon content value of 14 fg C/cell (Kallmeyer et al. 2012) together with average values of density, porosity, and age of oceanic crust. The estimated total cell abundance in igneous oceanic crust (1.0×10^{28} cells) is much lower than the recently estimated global subseafloor sedimentary microbial abundance (2.9×10^{29} cells) (Kallmeyer et al. 2012). The average cell density in oceanic crust (~1.1×10^{5} cells/cm^3) is comparable to that in subseafloor sedimentary habitats in the mid-ocean gyres (Fig. 2.12) (Kallmeyer et al. 2012). It is worth noting that the cell density in oceanic crust is much higher in younger oceanic crust (e.g., <1 Ma) than in older oceanic crust (e.g., >100 Ma) (Fig. 2.12) because of the difference in Fe- and S-oxidation rate with crustal age. This leads us to propose that the exploration and investigation of deep subseafloor oceanic crustal microbial communities should be performed in the young oceanic crust.

2.5 Microbial Biomass Potentials Associated with Fluid Flows in Ocean and Oceanic Crust and the Impact on Global Geochemical Cycles on the Modern Earth

In the present contribution, we estimate the biomass potentials of ecosystems associated with the global high-temperature hydrothermal and low-temperature crustal fluid flow systems in the deep ocean and oceanic crust (0.0074 and 0.14 Pg C, respectively). The results lead to a grand total of 0.15 Pg C, which represents the overall biomass potential of the deep-sea and deep-subseafloor biospheres sustained by inorganic compounds provided by subseafloor water–rock interactions. The estimated biomass potential comprises no more than 0.02 % of the total living biomass on modern Earth (Fig. 2.13a) (Kallmeyer et al. 2012). It should be

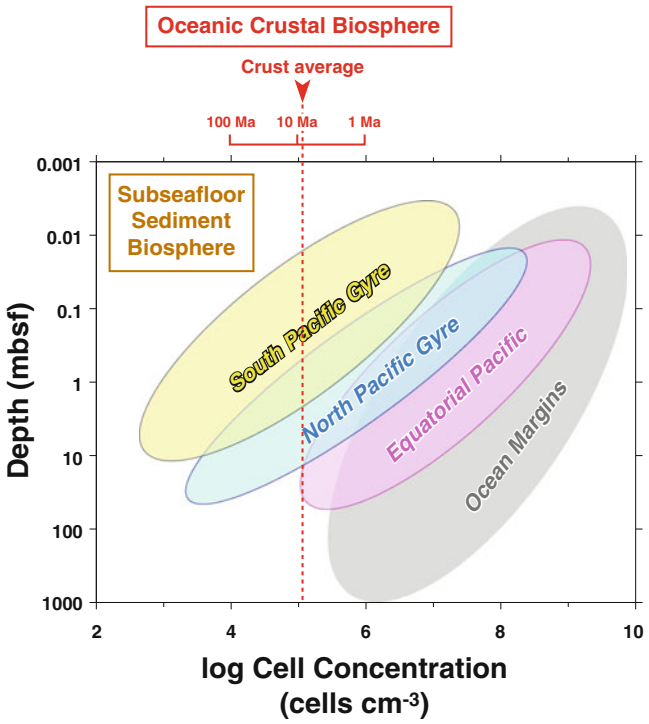

Fig. 2.12 Comparison of cell concentrations in the subseafloor sediment biosphere with that in the oceanic crust biosphere (modified from Kallmeyer et al. 2012). The maximum estimate of cell concentrations of the oceanic crust biosphere is generally comparable to the subseafloor sediment in the North and South Pacific Gyres. Note that the cell concentration of the oceanic crust biosphere is the maximum estimate, whereas that of subseafloor sediment biosphere is the actual observed value

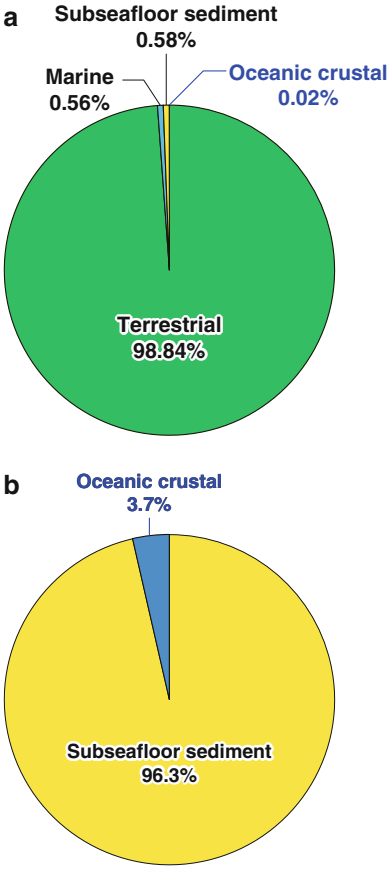

Fig. 2.13 Comparisons of the estimated potential biomass of the oceanic crust biosphere (including the high-temperature hydrothermal vent biosphere and the lowtemperatur oceanic crust biosphere) with the amounts of biomass in (**a**) terrestrial, marine, and subseafloor sediment biospheres and (**b**) subseafloor sediment biosphere

noted that because our biomass potential estimations are the maximum estimation, the real biomass abundances are likely to be significantly lower than the estimated values.

In addition to the subseafloor crustal ecosystems, subseafloor sedimentary ecosystems have attracted much attention (Whitman et al. 1998). The latest estimation has revealed that the subseafloor sedimentary biomass of microorganisms may represent 0.6 % of the Earth's total biomass (Fig. 2.13a) (Kallmeyer et al. 2012). It should be noted here that the subseafloor sedimentary biomass would be substantially sustained by the solar energy input through organic carbon sources derived from terrestrial and shallow marine phototrophic production, as suggested by a general trend of decreasing cell abundance in subseafloor sediments with increasing depth (Parkes et al. 1994; Kallmeyer et al. 2012). Even compared with the subseafloor sedimentary biomass, the estimated biomass potential of the chemosynthetic ecosystems sustained by the subseafloor high-temperature and low-temperature water–rock interactions is quite small, only 3.7 % of the sedimentary biomass (Fig. 2.13b). It is, therefore, very likely that most of the Earth's total biomass, including the subseafloor sediment biosphere, is sustained by solar energy via photosynthetic primary production in the terrestrial and ocean surface biospheres. This is consistent with the large difference in energy mass balance on the modern Earth between the whole solar energy flux (174,260 TW) (Smil 2008) and the oceanic heat flux (~9 TW) (Elderfield and Schults 1996).

The present study shows that the potential biomass of the deep-sea and deep subseafloor ecosystems sustained by the inorganic substrates provided by crust-seawater interactions is a tiny fraction of the global biomass on the modern Earth. This suggests that there are no large chemosynthetic communities in the deep-sea and deep subseafloor crust region that might comprise an unseen majority of the modern Earth's biosphere. It should be noted, however, that the very small biomasses of the deep-sea and deep subseafloor ecosystems do not mean they have insignificant functions and roles in the global biogeochemical cycles of C, Fe, S, and other bio-essential elements throughout the long history of the co-evolution of the Earth and life. The present contribution invites future quantitative investigations into the global biogeochemical cycles.

Moreover, our estimate of biomass potentials and compositional patterns in different geological settings of deep-sea hydrothermal systems and chemolithotrophic energy metabolisms suggests potentially strong interrelationships among the geological settings, the physical-chemical conditions of hydrothermal fluids (and seawater), and the dominant energy metabolisms for the biomass potential in the global deep-sea hydrothermal and ridge-flank aquifer environments. These interrelationships will provide key insights into the evolutionary implications of the energy mass balance and biomass production in the origin and evolution of life on Earth as well as future exploration of extraterrestrial life on other planets and moons.

Acknowledgments We would like to thank the two anonymous reviewers for their comments and suggestions, which helped to improve the manuscript. This research was financially supported by the Ministry of Education, Culture, Science, and Technology (MEXT) of Japan, through a special coordination fund (Project TAIGA: Transcrustal Advection and In situ biogeochemical processes of Global subseafloor Aquifer).

References

Alt JC, Shanks WC (2011) Microbial sulfate reduction and sulfur budget for a complete section of altered oceanic basalts, IODP Hole 1256D (eastern Pacific). Earth Planet Sci Lett 310:73–83

Alt JC, Honnorez J, Laverne C, Emmermann R (1986) Hydrothermal alteration of a 1 km section through the upper oceanic crust, DSDP Hole 504B: mineralogy, chemistry and evolution of seawater–basalt interactions. J Geophys Res 91:10309–10335

Alt JC, Laverne C, Vanko DA, Tartarotti P, Teagle DAH, Bach W, Zuleger E, Erzinger J, Honnorez J, Pezard PA, Becker K, Salisbury MH, Wilkens RH (1996a) Hydrothermal alteration of a section of upper oceanic crust in the eastern equatorial Pacific: a synthesis of results from Site 504 (DSDP Legs 69, 70 and 83, and ODP Legs 111, 137, 140 and 148). Proc ODP Sci Results 148:417–434

Alt JC, Teagle DAH, Laverne C, Vanko D, Bach W, Honnorez J, Becker K (1996b) Ridge flank alteration of upper oceanic crust in the eastern Pacific: a synthesis of results for volcanic rocks of Holes 504B and 896A. Proc ODP Sci Results 148:435–450

Anderson RT, Chapelle FH, Lovley DR (1998) Evidence against hydrogen-based microbial ecosystems in basalt aquifers. Science 281:976–977

Anderson RT, Chapelle FH, Lovley DR (2001) Comment on "Abiotic controls on H_2 production from basalt-water reactions and implications for aquifer biogeochemistry". Environ Sci Technol 35:1556–1557

Bach W, Edwards KJ (2003) Iron and sulfide oxidation within the basaltic ocean crust: extent, processes, timing, and implications for chemolithoautotrophic primary biomass production. Geochim Cosmochim Acta 67:3871–3887

Bach W, Erzinger J (1995) Volatile components in basalts and basaltic glasses from the EPR at 9°30′N. Proc ODP Sci Results 142:23–29

Baker ET, German CR (2004) On the global distribution of hydrothermal vent fields. In: German C, Lin J, Parson L (eds) Mid-ocean ridges: hydrothermal interactions between the lithosphere and oceans. Geophysics Monograph, vol 148. AGU, Washington, D. C., pp 245–266

Baker ET, Edmonds HN, Michael PJ, Bach W, Dick HJB, Snow JE, Walker SL, Banerjee NR, Langmuir CH (2004) Hydrothermal venting in magma deserts: the ultraslow-spreading Gakkel and South West Indian Ridges. Geochem Geophys Geosyst 5:Q08002 doi:10.1029/2004GC000712

Booij E, Gallahan WE, Staudigel H (1995) Ion-exchange experiments and Rb/Sr dating on celadonites from the Troodos ophiolite. Cyprus Chem Geol 126:155–167

Butterfield DA, Seyfried Jr WE, Lilley MD (2003) Composition and evolution of hydrothermal fluids. In: Halbach PE, Tunnicliffe V, Hein JR (eds) Energy and mass transfer in marine hydrothermal systems. Dahlem University Press, Berlin, pp 123–161

Cannat M, Sauter D, Mendel V, Ruellan E, Okino K, Escartin J, Combier V, Baala M (2006) Modes of seafloor generation at a melt-poor ultraslow-spreading ridge. Geology 34:605–608

Charlou JL, Donval JP, Fouquet Y, Jean-Baptiste P, Holm N (2002) Geochemistry of high H_2 and CH_4 vent fluids issuing from ultramafic rocks at the Rainbow hydrothermal field (36°14′N, MAR). Chem Geol 191:345–359

Christie DM, Carmichael ISE, Langmuir CH (1986) Oxidation states of mid-ocean ridge basalt glasses. Earth Planet Sci Lett 79:397–411

Corliss JB, Dymond J, Gordon LI, Edmond JM, Von Herzen RP, Ballard RD, Green K, Williams D, Bainbridge A, Crane K, van Andel TH (1979) Submarine thermal springs on the Galapagos Rift. Science 203:1073–1083

Cowen JP, Giovannoni SJ, Kenig F, Johnson HP, Butterfield D, Rappe MS, Hutnak M, Lam P (2003) Fluids from aging oceanic crust that support microbial life. Science 299:120–123

Dimalanta C, Taira A, Yumul GP, Tokuyama H, Mochizuki K (2002) New rates of western Pacific island arc magmatism from seismic and gravity data, Earth Planet. Sci Lett 202:105–115

Dworkin M (2012) Sergei Winogradsky: a founder of modern microbiology and the first microbial ecologist. FEMS Microbiol Rev 36:364–379

Edwards KJ, Bach W, McCollom TM (2005) Geomicrobiology in oceanography: micrrobe-mineral interactions at and below the seafloor. Trends Microbiol 13:449–456

Edwards KJ, Fisher AT, Wheat CG (2012) The deep subsurface biosphere in igneous ocean crust: frontier habitats for microbiological exploration. Front Microbiol 3. doi:10.3389/fmicb.2012.00008

Elderfield H, Schults A (1996) Mid-ocean ridge hydrothermal fluxes and the chemical composition of the ocean. Ann Rev Earth Planet Sci 24:191–224

Elderfield H, Wheat CG, Mottl MJ, Monnin C, Spiro B (1999) Fluid and geochemical transport through oceanic crust: a transect across the eastern flank of the Juan de Fuca Ridge. Earth Planet Sci Lett 172:151–165

Escartin J, Smith DK, Cann J, Schouten H, Langmuir CH, Escrig S (2008) Central role of detachment faults in accretion of slow-spreading oceanic lithosphere. Nature 455:790–795

Fisher AT (1998) Permeability within basaltic oceanic crust. Rev Geophys 36:143–182

Fisher AT, Becker K (2000) Channelized fluid flow in oceanic crust reconciles heat-flow and permeability data. Nature 403:71–74

Foustoukos DI, And WE, Seyfried J (2007) Fluid phase separation processes in submarine hydrothermal systems. Rev Mineral Geochem 65:213–239

Gerday C, Glansdorff N (eds) (2007) Physiology and biochemistry of extremophiles. ASM Press, Washington, D.C

German CR, Von Damm KL (2004) Hydrothermal processes. In: Turekian KK, Holland HD (eds) The oceans and marine

geochemistry, treatise on geochemistry, vol 6. Elsevier, New York, pp 181–222
Gerya TV (2011) Intra-oceanic Subduction Zones. In: Brown D, Ryan PD (eds) Arc-Continent Collistion. Springer, Berlin, pp 23–51
Harder J (1997) Species-independent maintenance energy and natural population sizes. FEMS Microbiol Ecol 23:39–44
Hart SR, Staudigel H (1986) Ocean crust vein mineral deposition: Rb/Sr ages, U-Th-Pb geochemistry, and duration of circulation at DSDP Sites 261, 462, and 516. Geochim Cosmochim Acta 50:2751–2761
Hawkins JW, Melchior JT (1985) Petrology of Mariana Trough and Lau Basin basalts. J Geophys Res 90:11431–11468
Hirata N, Kinoshita H, Katao H, Baba H, Kaiho Y, Koresawa S, Ono Y, Hayashi K (1991) Report on DELP 1988 cruise in the Okinawa Trough part 3. Crustal structure of the southern Okinawa Trough. Bull ERI Univ Tokyo 66:37–70
Hoehler TM (2004) Biological energy requirements as quantitative boundary conditions for life in the subsurface. Geobiology 2:205–215
Horikoshi K, Tsujii K (eds) (1999) Extremophiles in deep-sea environments. Springer, Berlin
Janik T (1997) Seismic crustal structure of the Baransfield Strait. West Antarctica Polish Polar Res 18:171–225
Jannasch HW, Mottl MJ (1985) Geomicrobiology of deep-sea hydrothermal vents. Science 229:717–725
Jarrard RD (2003) Subduction fluxes of water, carbon dioxide, chlorine, and potassium. Geochem Geophys Geosyst 4:8905. doi:10.1029/2002GC000392
Johnson HP, Priuis MJ (2003) Fluxes of fluid and heat from the oceanic crustal resevoir. Earth Planet Sci Lett 216:565–574
Johnson JW, Oelkers EH, Helgeson HC (1992) SUPCRT92: a software package for calculating the standard molal thermodynamic properties of minerals, gases, aqueous species, and reactions for 1 to 5000 bar and 0 to 1000°C. Comput Geosci 18:899–947
Kallmeyer J, Pockalny R, Adhikari RR, Smith DC, D'Hondt S (2012) Global distribution of microbial abundance and biomass in subseafloor sediment. Proc Natl Acad Sci U S A 109:16213–16216
Kawagucci S, Chiba H, Ishibashi J, Yamanaka T, Toki T, Muramatsu Y, Ueno Y, Makabe A, Inoue K, Yoshida N, Nakagawa S, Nunoura T, Takai K, Takahata N, Sano Y, Narita T, Teranishi G, Obata H, Gamo T (2011) Hydrothermal fluid geochemistry at the Iheya North field in the mid-Okinawa Trough: implication for origin of methane in subseafloor fluid circulation systems. Geochem J 45:109–124
Kawagucci S, Ueno Y, Takai K, Toki T, Ito M, Inoue K, Makabe A, Yoshida N, Muramatsu Y, Takahata N, Sano Y, Narita T, Teranishi G, Obata H, Nakagawa S, Nunoura T, Gamo T (2013) Geochemical origin of hydrothermal fluid methane in sediment-associated fields and its relevance to the geographical distribution of whole hydrothermal circulation. Chem Geol 339:213–225
Leat PT, Larter RD (2003) Intra-oceanic subduction systems: introduction. In: Larter RD, Leat PT (eds) Intra-oceanic subduction systems: tectonic and magmatic processes. Geol Soc London, Spec. Publ., vol 219, pp 1–17
Lesniewski RA, Jain S, Anantharaman K, Schloss PD, Dick GJ (2012) The metatranscriptome of a deep-sea hydrothermal plume is dominated by water column methanotrophs and lithotrophs. ISME J 6:2257–2268
Lever MA, Rouxel O, Alt JC, Shimizu N, Ono S, Coggon RM, Shanks WC, Lapham L, Elvert M, Prieto-Mollar X, Hinrichs K-U, Inagaki F, Teske A (2013) Evidence for microbial carbon and sulfur cycling in deeply buried ridge flank basalt. Science 339:1305–1308
Lilley MD, Butterfield DA, Olson EJ, Lupton JE, Macko SA, McDuff RE (1993) Anomalous CH_4 and NH_4^+ concentrations at an unsedimented mid-ocean-ridge hydrothermal system. Nature 364:45–47
Lilley MD, Butterfield DA, Lupton JE, Olson EJ (2003) Magmatic events can produce rapid changes in hydrothermal vent chemistry. Nature 422:878–881
Mathez EA (1976) Sulfur solubility and magmatic sulfides in submarine basalt glass. J Geophys Res 81:4269–4276
Mathez EA (1979) Sulfide relations in Hole 418A flows and sulfur contents of glasses. Int Repts DSDP 51–53:1069–1085
McCollom TM (1999) Methanogenesis as a potential source of chemical energy for primary biomass production by autotrophic organisms in hydrothermal systems on Europa. J Geophys Res 104:30729–30742
McCollom TM (2007) Geochemical constraints on sources of metabolic energy for chemolithoautotrophy in ultramagic-hosted deep-sea hydrothermal systems. Astrobiology 7:933–950
McCollom TM, Bach W (2009) Thermodynamic constraints on hydrogen generation during serpentinization of ultramafic rocks. Geochim Cosmochim Acta 73:856–875
McCollom TM, Shock EL (1997) Geochemical constraints on chemolithoautotrophic metabolism by microorganisms in deep-sea hydrothermal systems. Geochim Cosmochim Acta 61:4375–4391
Miller DJ, Kelley J (2004) Low-temperature alteration of basalt over time: a synthesis of results from Ocean Drilling Program Leg 187. Proc ODP Sci Results 187:1–29
Mottl MJ (2003) Partitioning of energy and mass fluxes between mid-Ocean ridge axes and flanks at high and low temperature. In: Halbach P, Tunnicliffe V, Hein J (eds) Energy and mass transfer in marine hydrothermal systems. Dahlem University Press, Berlin, pp 271–286
Mottl MJ, Wheat CG (1994) Hydrothermal circulation through mid-ocean ridge flanks: Fluxes of heat and magnesium. Geochim Cosmochim Acta 58:2225–2237
Nakamura K, Takai K (2014) Theoretical constraints of physical and chemical properties of hydrothermal fluids on variations in chemolithotrophic microbial communities in seafloor hydrothermal systems. Progress Earth Planet Sci 1. doi: 10.1186/2197-4284-1-5
Nakamura K, Kato Y, Tamaki K, Ishii T (2007) Geochemistry of hydrothermally altered basaltic rocks from the Southwest Indian Ridge near the Rodriguez Triple Junction. Mar Geol 239:125–141
Nakamura K, Morishita T, Bach W, Klein F, Hara K, Okino K, Takai K, Kumagai H (2009) Serpentinized troctolites exposed near the Kairei Hydrothermal Field, Central Indian Ridge: insights into the origin of the Kairei hydrothermal fluid supporting a unique microbial ecosystem. Earth Planet Sci Lett 280:128–136
Nealson KH, Inagaki F, Takai K (2005) Hydrogen-drien subsurface lithoautotrophic microbial ecosystems (SLiMEs): do they exist and why should we care? Trends Microbiol 13:405–410
Nielsen SG, Rehkamper M, Teagle DAH, Butterfield DA, Alt JC, Halliday AN (2006) Hydrothermal fluid fluxes calculated from the isotopic mass balance of thallium in the ocean crust. Earth Planet Sci Lett 251:120–133
Orcutt BN, Sylvan JB, Knab NJ, Edwards KJ (2011) Mibrobial ecology of the dark ocean above, at, and below the seafloor. Microbiol Mol Biol Rev 75:361–422
Parkes RJ, Cragg BA, Bale SJ, Getliff JM, Goodman K, Rochelle PA, Fry JC, Weightman AJ, Harvey SM (1994) Deep bacterial biosphere in Pacific-Ocean sediments. Nature 371:410–413
Parson LM, Wright IC (1996) The Lau-Havre-Taupo back-arc basin: a southward-propagating, multi-stage evolution from rifting to spreading. Tectonophysics 263:1–22
Peterson C, Duncan R, Scheidegger KF (1986) Sequence and longevity of basalt alteration at Deep Sea Drilling Project Site 597. Int Repts DSDP 92:505–515
Price B, Sowers T (2004) Temperature dependence of metabolic rates for microbial growth, maintenance, and survival. Proc Natl Acad Sci U S A 101:4631–4636

Rao PS, Kamesh Raju KA, Ramprasad T, Nagender Nath B, Ramalingeswara Rao B, Rao ChM, Nair RR (1996) Evidence for hydrothermal activity in the Andaman Backarc Basin. Curr Sci 70:379–385

Reeves EP, Seewald JS, Saccocia P, Bach W, Craddock PR, Shanks WC, Sylva SP, Walsh E, Pichler T, Rosner M (2011) Geochemistry of hydrothermal fluids from the PACMANUS, Northeast Pual and Vienna Woods hydrothermal fields, Manus Basin. Papua New Guinea Geochim Cosmochim Acta 75:1088–1123

Rogers AD, Tyler PA, Connelly DP, Copley JT, James R, Larter RD, Linse K, Mills RA, Garabato AN, Pancost RD, Pearce DA, Polunin NVC, German CR, Shank T, Boersch-Supan PH, Alker BJ, Aquilina A, Bennett SA, Clarke A, Dinley RJJ, Graham AGC, Green DRH, Hawkes JA, Hepburn L, Hilario A, Huvenne VAI, Marsh L, Ramirez-Llodra E, Reid WDK, Roterman CN, Sweeting CJ, Thatje S, Zwirglmaier K (2012) The discovery of new deep-sea hydrothermal vent communities in the Southern Ocean and implications for biogeography. PLoS Biol 10:e1001234. doi:10.1371/journal.pbio.1001234

Rouxel O, Ono S, Alt J, Rumble D, Ludden J (2008) Sulfur isotope evidence for microbial sulfate reduction in altered oceanic basalts at ODP Site 801. Earth Planet Sci Lett 268:110–123

Schrenk MO, Huber JA, Edwards KJ (2010) Microbial provinces in the subseafloor. Ann Rev Mar Sci 2:279–304

Schubert G, Turcotte DL, Olson P (2001) Mantle convection in the Earth and Planets. Cambridge University Press, Cambridge

Schwartz JJ, John BE, Cheadle MJ, Miranda EA, Grimes CB, Wooden JL, Dick HJB (2005) Dating the growth of oceanic crust at a slow-spreading ridge. Science 310:654–657

Sclater JG, Jaupart C, Galson D (1980) The heat flow through oceanic and continental crust and the heat loss of the Earth. Rev Geophys Space Phys 18:269–311

Shock EL, Helgeson HC (1988) Calculation of the thermodynamic and transport properties of aqueous species at high pressures and temperatures: correlation algorithms for ionic species and equation of state predictions to 5 kb and 1000°C. Geochim Cosmochim Acta 52:2009–2036

Shock EL, Helgeson HC (1990) Calculation of the thermodynamic and transport properties of aqueous species at high pressures and temperatures: standard partial molal properties of organic species. Geochim Cosmochim Acta 54:915–945

Shock EL, Holland ME (2004) Geochemical energy sources that support the subsurface biosphere. In: Wilcock WSD, DeLong EF, Kelley DS, Baross JA, Cary SC (eds) The subseafloor biosphere at mid-ocean ridges. Geophysics Monograph Series, vol 144. AGU, Washington, D.C., pp 153–165

Shock EL, Sassani DC, Willis M, Sverjensky DA (1997) Inorganic species in geologic fluids: correlations among standard molal thermodynamic properties of aqueous ions and hydroxide complexes. Geochim Cosmochim Acta 61:907–950

Smil V (2008) Energy in nature and society: general energetics of complex systems. MIT, Cambridge

Spiess FN, MacDonald KC, Atwater T, Ballard R, Carranza A, Cordoba D, Cox C, Diaz Garcia VM, Francheteau J, Guerrero J, Hawkins J, Haymon R, Hessler R, Juteau T, Kastner M, Larson R, Luyendyk B, Macdougall JD, Miller S, Normark W, Orcutt J, Rangin C (1980) East Pacific Rise: hot springs and geophysical experiments. Science 207:1421–1433

Staudigel H, Plank T, White B, Schmincke J-U (1996) Geochemical fluxes during seafloor alteration of the basaltic upper oceanic Crust: DSDP sites 417 and 418. In: Bebout GE, Scholl DW, Kirby SH, Platt JP (eds) Subduction top to bottom. Geophysics Monograph Series, vol 96. American Geophysical Union, Washington, D.C., pp 19–38

Stein CA, Stein S (1994) Constraints on hydrothermal heat flux through the oceanic lithosphere from global heat flow. J Geophys Res 99:3081–3095

Stein CA, Stein S, Pelayo AM (1995) Heat flow and hydrothermal circulation. In: Humphris S, Mullineaux L, Zierenberg R, Thomson R (eds) Seafloor hydrothermal systems, physical, chemical, biological, and geological interactions. Geophysics Monograph Series, vol 91. American Geophysical Union, Washington, D.C., pp 425–445

Stevens TO, McKinley JP (1995) Lithoautotrophic microbial ecosystems in deep basalt aquifers. Science 270:450–454

Stevens TO, McKinley JP (2000) Abiotic controls on H_2 production from basalt-water reactions and implications for aquifer biogeochemistry. Environ Sci Technol 34:826–831

Stevens TO, McKinley JP (2001) Response to comment on "Abiotic controls on H_2 production from basalt-water reactions and implications for aquifer biogeochemistry". Environ Sci Technol 35:1558–1559

Takai K (2011) Limits of life and biosphere: lesson from detection of microorganisms in deep-sea and deep subsurface in the Earth. In: Gargaud M, Lopez-Garcia P, Martin H (eds) Origins and evolution of life: an astrobiological perspective. Cambridge Univeristy Press, Cambridge, pp 469–486

Takai K, Nakamura K, Suzuki K, Inagaki F, Nealson KH, Kumagai H (2006) Ultramafics-Hydrothermalism-Hydrogenesis-HyperSLiME (UltraH^3) linkage: a key insight into early microbial ecosystem in the Archean deep-sea hydrothermal systems. Paleontol Res 10:269–282

Talbi EH, Honnorez J (2003) Low-temperature alteration of mesozoic oceanic crust, Ocean Drilling Program Leg 185. Geochem Geophys Geosyst 4:8906. doi:10.1029/2002GC000405

Tanahashi M, Kisimoto K, Joshima M, Jarvis P, Iwabuchi Y, Ruellan E, Auzende JM (1994) 800-km-long N-S spreading system of the North Fiji Basin. Mar Geol 116:5–24

Teagle DAH, Alt JC, Bach W, Halliday AN, Erzinger J (1996) Alteration of upper oceanic crust in a ridge-flank hydrothermal upflow zone: mineral, chemical, and isotopic constraints from Hole 896A. Proc ODP Sci Results 148:119–150

Tijhuis L, van Loosdrecht MCM, Heijnen JJ (1993) A thermodynamically based correlation for maintenance Gibbs energy requirements in aerobic and anaerobic chemotrophic growth. Arch Microbiol 42:509–512

Varnes ES, Jakosky BM, McCollom TM (2003) Biological potential of Martian hydrothermal systems. Astrobiology 3:407–414

Ventura G, Milano G, Passaro S, Sprovieri M (2013) The Marsili Ridge (Southern Tyrrhenian Sea, Italy): an island-arc volcanic complex emplaced on a 'relict' back-arc basin. Earth Sci Rev 116:85–94

Wallace P, Carmichael ISE (1992) Sulfur in basaltic magmas. Geochim Cosmochim Acta 56:1863–1874

Watsuji T, Nakagawa S, Tsuchida S, Toki T, Hirota A, Tsunogai U, Takai K (2010) Diversity and function of epibiotic microbial communities on the galatheid crab, *Shinkaia crosnieri*. Microbes Environ 25:288–294

Wheat CG, Mottl MJ (2000) Composition of pore and spring waters from Baby Bare: global implications of geochemical fluxes from a ridge flank hydrothermal system. Geochim Cosmochim Acta 64:629–642

Whitman WB, Coleman DC, Wiebe WJ (1998) Prokaryotes: the unseen majority. Proc Natl Acad Sci U S A 95:6578–6583

Wolery TW, Jarek RL (2003) Software user's manual EQ 3/6 (version 8.0). Sandia National Laboratories, Albuquerque

Wolery TJ, Jove-Colon CF (2004) Qualification of thermodynamic data for geochemical modeling of mineral–water interactions in dilute systems. U.S. Dept. of Energy Report, ANL-WIS-GS-000003 REV00. Bechtel SAIC Company, LLC, Las Vegas

Microbial Cell Densities, Community Structures, and Growth in the Hydrothermal Plumes of Subduction Hydrothermal Systems

3

Michinari Sunamura and Katsunori Yanagawa

Abstract

In this report, we compile a study of microbial populations in deep-sea hydrothermal plumes with providing some new data set, and discuss the relationships with geological settings and the type of the hydrothermal system, e.g. ridge or subduction, in the context of the hypothesis "four TAIGAs" (Urabe et al. Chap. 1). Deep-sea hydrothermal plumes represent one of the best habitats for chemolithotrophic microbes to drive primary production in hydrothermal systems. Microbial cell densities in hydrothermal plumes are up to several times more elevated than in the general abyssal seawater. Putative sulfur utilizers, e.g. SUP05 and *Alcanivorax* in *gammaproteobacteria*, SAR324 in *deltaproteobacteria*, and several *epsilonproteobacteria*, are the dominant microbes that are detected from most of hydrothermal plumes. The microbial community compositions in the plume of an arc-backarc system are different from those of a mid-oceanic ridge hydrothermal system. This is because the cell densities and community composition of the putative sulfur oxidizers may be regulated by reduced sulfur species due to the pH and Eh conditions of the subseafloor and surrounding seawater. Aerobic methanotrophs are found in hydrothermal plumes which contain high concentrations of molecular hydrogen and methane. Quantitative microbial cell analysis by catalyzed reporter deposition based fluorescent in situ hybridization (CARD-FISH) show that the SUP05 populations are 60–100 % responsible for increased microbial cell densities in the hydrothermal plumes of arc-backarc fields. The contribution of the SUP05 cell densities in the plume microbial community is closely connected with the chemical energy from hydrothermal fluids in various types of TAIGA.

Keywords

Deep-sea hydrothermal plume • Fluorescence in situ hybridization (FISH) • Quantitative microbial community analysis • SUP05 (*Thioglobus*)

3.1 Introduction to Hydrothermal Plumes and the TAIGA Concept

Deep-sea hydrothermal plumes have been found in hydrothermal fields located in mid-oceanic ridges, subduction zones, and hotspot submarine volcanoes all over the world. Hot hydrothermal fluids emanated from hydrothermal vents are less dense than general abyssal seawater, therefore the fluids rise into the deep sea, mix with surrounding seawater, and form a deep-sea hydrothermal plume. The first, rising stage of hydrothermal plume evolution is termed the

M. Sunamura (✉)
Department of Earth and Planetary Science, University of Tokyo, 7-3-1 Hongo, Bunkyo-ku, Tokyo 113-0033, Japan
e-mail: sunamura@eps.s.u-tokyo.ac.jp

K. Yanagawa
Department of Earth and Planetary Science, University of Tokyo, 7-3-1 Hongo, Bunkyo-ku, Tokyo 113-0033, Japan

Subsurface Geobiology Advanced Research (SUGAR) Project, Japan Agency for Marine-Earth Science and Technology (JAMSTEC), Yokosuka 237-0061, Japan

J.-i. Ishibashi et al. (eds.), *Subseafloor Biosphere Linked to Hydrothermal Systems: TAIGA Concept*,
DOI 10.1007/978-4-431-54865-2_3,

buoyant plume. The buoyant plume undergoes substantial dilution with surrounding seawater due to accompanying turbulence. The mixing causes progressive dilution, and then the plume becomes less buoyant among stratified abyssal seawater and evetually reaches some finite maximum height above the seafloor to spread out laterally. This later stage is termed the nonbuoyant plume (or the neutrally buoyant plume) (German and Von Damm 2003).

The hydrothermal fluids are hot and contain many chemical species originated from magma and subseafloor rocks. Therefore the hydrothermal plume, which is formed by the spouting hydrothermal fluid, acts as an important and major interface between the oceanic lithosphere and seawater, and is important for exchanging heat flux and for the reaction between hydrothermal fluid-derived reduced chemicals and oxidants from the surface of the earth. A hydrothermal plume contains both reduced chemicals from hydrothermal fluids and oxidants from seawater, thus a hydrothermal plume is one of the most important habitats for chemolithotrophic microbes in deep-sea hydrothermal systems. According to the TAIGA concept (see Urabe et al. Chap. 1), the chemical components of the hydrothermal fluid and plume are regulated by the geological background, and the hydrothermal systems can be categorized into four groups: (1) sulfur TAIGA with reduced sulfur from magma, (2) methane TAIGA with high methane and ammonium from the sediments around the channels of hydrothermal fluid circulation beneath the seafloor, (3) hydrogen TAIGA with molecular hydrogen (H_2) from serpentinization or the breaking of rocks due to fault activity, and (4) iron TAIGA with Fe^{2+} leached from fresh basalt by acidic hydrothermal fluids. The chemical compositions of the four types of TAIGA control and restrict the microbial community and their functions. In addition, hydrothermal systems are often categorized according to their tectonic background; mid oceanic ridge (MOR) systems, arc-backarc systems, and hot spot systems.

3.2 Microbial Communities in Hydrothermal Plumes

Chemical signals derived from hydrothermal fluids are widely used to detect hydrothermal plumes as anomalies from the general abyssal seawater. These chemical signals include turbidity, oxidation-reduction potential, ^3He, manganese, iron, methane, and molecular hydrogen. Microbial cell densities in a plume are also elevated up to several dozens times higher than those of the general abyssal seawater (Cowen et al. 1986; Naganuma et al. 1989; Winn et al. 1986). This indicates that the microbial community in the plume interacts strongly with the hydrothermal fluid chemicals in the plume. Indeed, the activities of methane oxidation (DeAngelis et al. 1991, 1993; Tsunogai et al. 2000), ammonium oxidation (Lam et al. 2004, 2008), and iron and manganese oxidation (Cowen et al. 1986) have been detected in the plume. Analysis of microbial community structures (Dick and Tebo 2010; Dick et al. 2013; Sunamura et al. 2004) and metagenome/transcriptome (Anantharamana et al. 2013; Dick et al. 2013; Lesniewski et al. 2012) also has shown sulfur oxidation, ammonium oxidation, aerobic methane oxidation, hydrogen oxidation, and heterotrophic activity in the plumes.

Microbial community structures based on SSU rRNA genes in the plumes have been studied in MOR hydrothermal systems including, for example, Guaymas Basin (Dick and Tebo 2010), Juan de Fuca Ridge (Lam et al. 2008) at the East Pacific Rise (EPR), Mid Cayman (German et al. 2010) at the Mid Cayman Rise, and Kairei Field (Noguchi et al. Chap. 15) at the Central Indian Oceanic Ridge (CIR). These hydrothermal fields are categorized into methane, sulfur, and hydrogen TAIGA fields. In contrast, there has been little study related to microbial communities in arc/backarc hydrothermal systems in subduction region. Only a hydrothermal plume at the Suiyo Seamount (Sunamura et al. 2004) located on the Izu-Ogasawara Arc has been studied. Figure 3.1 shows the microbial community structures in the plume of arc/backarc hydrothermal system, which we collected and analyzed as a representative of methane and sulfur TAIGA. The key microbial lineages in hydrothermal plumes are selected based on a review paper of microbial studies in hydrothermal plumes and anoxic seawater (Dick et al. 2013).

In these key microbial linages, the SUP05 phylotype is recognized as the most abundant and universal species in deep-sea hydrothermal plumes of all over the world. The SUP05 phylotype in these plumes was first documented in the Suiyo Seamount hydrothermal plume (Sunamura et al. 2004), and the SUP05 phylotype has been found to be dominant in many anoxic seawater sites (Lavik et al. 2009; Walsh et al. 2009) all over the world. SUP05 is known to be a close relative to symbionts of hydrothermal chemosynthetic mytilids and vesicomyids (Duperron et al. 2005; Fujiwara et al. 2000). These can grow chemolithoautotrophically with sulfur (Marshall and Morris 2012; Walsh et al. 2009) or H_2 (Anantharamana et al. 2013; Petersen et al. 2011) as an electron donor, and oxygen or nitrate as an electron acceptor. The representative isolate of SUP05 grow with thiosulfate, which is accumulated as native sulfur vesicles in a cell and, in addition to sulfur compounds, it can grow heterotrophically (Marshall and Morris 2012). This wide variation of energy and carbon metabolism may sustain SUP05 as the primary key species in hydrothermal plume microbial communities. We also found abundant *Alcanivorax*, SAR324, and several epsilon proteobacterial phylotypes in the plume microbial community. The lineages

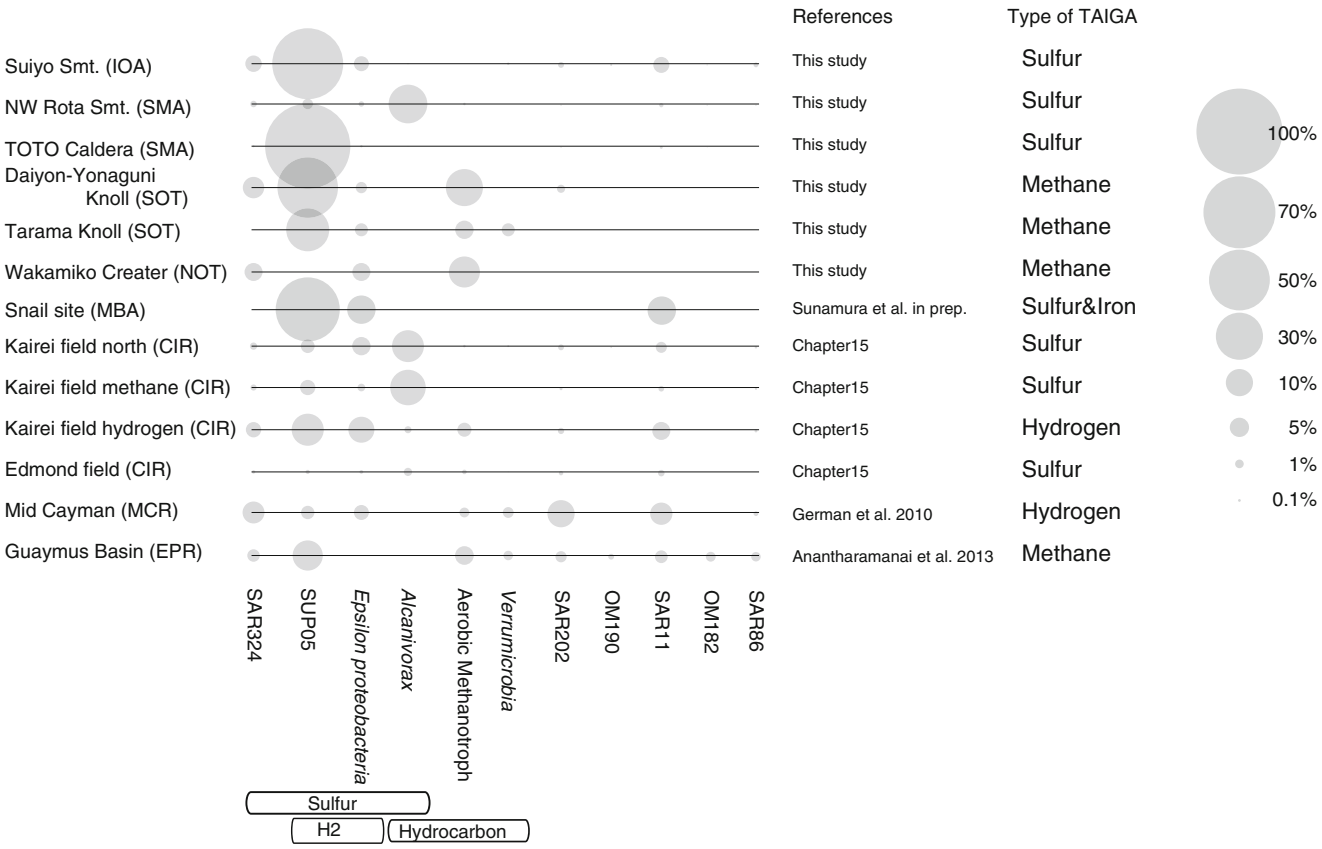

Fig. 3.1 Abundance of key microbial community populations in plumes. The 16S rRNA gene sequences were obtained by cloning/Sanger sequencing for the Daiyon-Yonaguni Knoll, Tarama Knoll, and Wakamiko Creater samples, and by 454 pyrosequencing for the Suiyo Seamount, NW Rota Seamount, TOTO Caldera and CIR samples for this study and Noguchi et al. in Chap. 15. The sequences of Mid Cayman and Guaymus Basin were downloaded from DDBJ or VAMPS. The abbreviated names for hydrothermal zones are as follows: Izu-Ogasawara Arc (IOA), Southern Mariana Arc (SMA), Southern Mariana Trough Backarc (MBA), Southern Okinawa Trough (SOT), Northern Okinawa Trough (NOT), Central Indian Ridge (CIR), Mid Cayman Rise (MCR), and East Pacific Rise (EPR)

of these microbes have sulfur-metabolism genes for dissimilar sulfur oxidation (Lai et al. 2012; Nakagawa et al. 2007; Swan et al. 2011) for *Alcanivorax*, *epsilon proteobacteria*, and SAR324, respectively. The abundance of potential sulfur oxidizers in the plume is in the good agreement with the result of thermodynamic calculation, which is that sulfur oxidation was the most effective energy source in the mixing zone of deep-sea hydrothermal fluids and general abyssal seawater based on the chemical composition of EPR hydrothermal fluids (McCollom and Shock 1997). On the other hand, 16S rRNA genes of SUP05 lineage was not detected from hydrothermal plume samples in Wakamiko Crater field. In this field, hydrothermal plume shows low pH (6.3–6.8) due to entrainment of volcanic fumaroles in the crater seawater (Yamanaka et al. 2013). The relatively low SUP05 populations was also notable for NW Rota Seamount hydrothermal plume, where very low pH caused by acid sulfate hydrothermal fluid (Resing et al. 2007). In such low pH condition, dominant reduced sulfur species are not HS^- but H_2S and native sulfur species, and thiosulfate is not stable. In addition, the growth zone of SUP05 lineage is restricted to early stage of hydrothermal plume (see next section), therefore it is essential to import substrates quickly into a cell. Lack of availability of substrates could be responsible for absence of SUP05 in hydrothermal plume. To know the difference in the SUP05 populations between the ridge and arc-backarc hydrothermal systems, further studies such as recycling of SUP05 cells within the plume, activities of dissolved sulfur chemicals, and toxicity of hydrothermal fluid chemicals are needed. Close relatives of SUP05 are able to utilize H2S, HS-, native sulfur, and thiosulfate for growth (Marshall and Morris 2012; Walsh et al. 2009). We proposed here that uptake of the substrate into a cell may be regulated by the stability and states of the sulfur species which caused by pH and Eh.

Figure 3.1 clearly shows that the aerobic methanotrophic lineages are found only in hydrothermal systems where abundant methane and H_2 are available (TAIGA of methane and H_2). The results indicate that aerobic methanotrophic

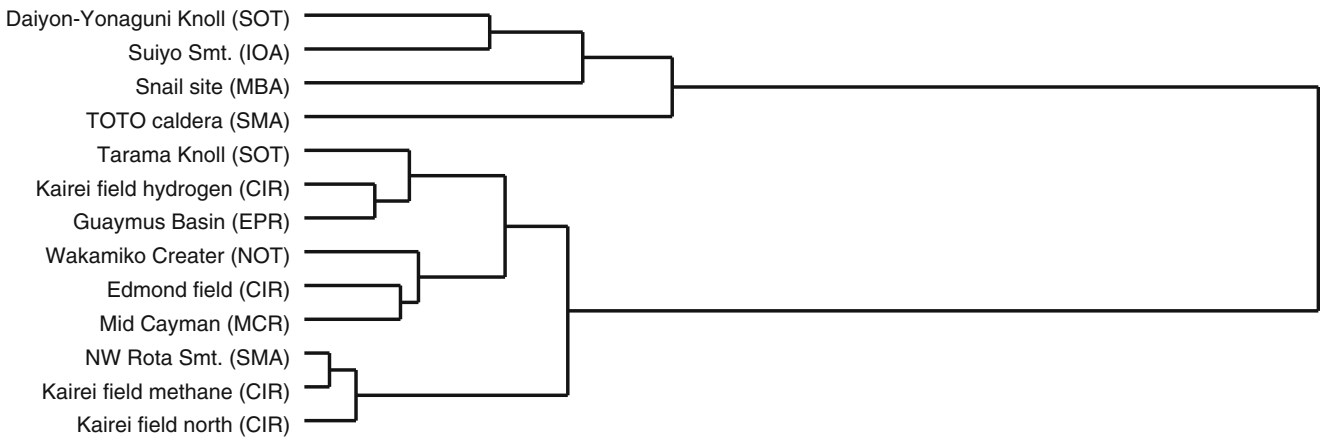

Fig. 3.2 Dendrogram of key microbial communities in the hydrothermal plumes. The dendrogram was calculated based on the Ward distance method (Ward 1963) using the proportions of key microbial lineages that are shown in Fig. 3.1

populations are restricted by high concentrations of methane in hydrothermal fluid as predicted by the TAIGA hypothesis.

Cluster analysis based on the key species populations indicated that the community structures were separated into two groups (Fig. 3.2). The grouping seems to depend on the SUP05 population which is able to use reduced sulfur compounds (Lesniewski et al. 2012; Marshall and Morris 2012) and H_2 (Anantharamana et al. 2013; Petersen et al. 2011) as the energy source for chemolithotrophic growth. The first group consists of the plumes of arc-backarc hydrothermal systems with high microbial cell density anomalies. This group contains high SUP05 populations of greater than 50 %. The second group includes the other hydrothermal plumes and could be categorized into three sub-groups. The sub-groups appear to be unrelated to the geological settings of the hydrothermal systems (i.e. ridge or subduction) or to the chemical composition of the original hydrothermal fluids (categories of TAIGA). Analysis of the microbial community structure indicated that the SUP05 lineage was the most important for understanding microbial ecology in the deep-sea hydrothermal plumes.

3.3 Growth Zone of SUP05

To understand the sulfur and carbon cycles in a hydrothermal field, it is essential to determine the origin and the growth zone of plume-specific microbial communities. Detection and cultivation of hyperthermophiles in an event plume (Summit and Baross 1998) indicates that subseafloor and high temperature hydrothermal fluids are one of the origin of the plume microbes. The SUP05 phylotypes have been detected in the low temperature diffuse hydrothermal flows at a level of more than 99 %(Sunamura et al. 2004), indicating that diffuse flow venting is one of the origins. Quantitative comparison between microbial cell densities and methane concentration among high temperature hydrothermal fluids, low temperature diffuse flows, and hydrothermal plume waters indicated that in situ growth in the plume is most important in the case study of the Suiyo Seamount hydrothermal field (Sunamura et al. 2009) (Fig. 3.3) where SUP05 phylotype dominate microbial communities in the plume (Sunamura et al. 2004). To understand the plume-microbiological impact on deep sea, we need to narrow a more detailed growth zone in the plume.

3.4 Changes in the Microbial Community During the "Chemical Evolution" of a Plume

Biogeochemical studies of chemical composition of substrates (Malahoff et al. 2006; Resing et al. 2009) and the stable isotope analysis of methane carbon (Tsunogai et al. 2000) in plumes have suggested that the chemical features of a plume change with the dilution process and distance from the vent. This is referred to as the "chemical evolution of plume". Several previous studies could not find any positive and clear correlation between the total cell density and the physicochemical parameters in the plume. Moreover the changes occurring in the microbial community during the chemical evolution of plume are still unclear. Figure 3.4 shows the relationship between cell densities that are higher than the background (cell density anomalies) and bacteria and SUP05 cell densities determined by the (CARD-)FISH method in various hydrothermal plumes. Good linear correlation between the cell density anomalies and the SUP05 cell densities (Fig. 3.4) indicates that very little "microbial community evolution" occurred during the chemical evolution of the non-buoyant plume.

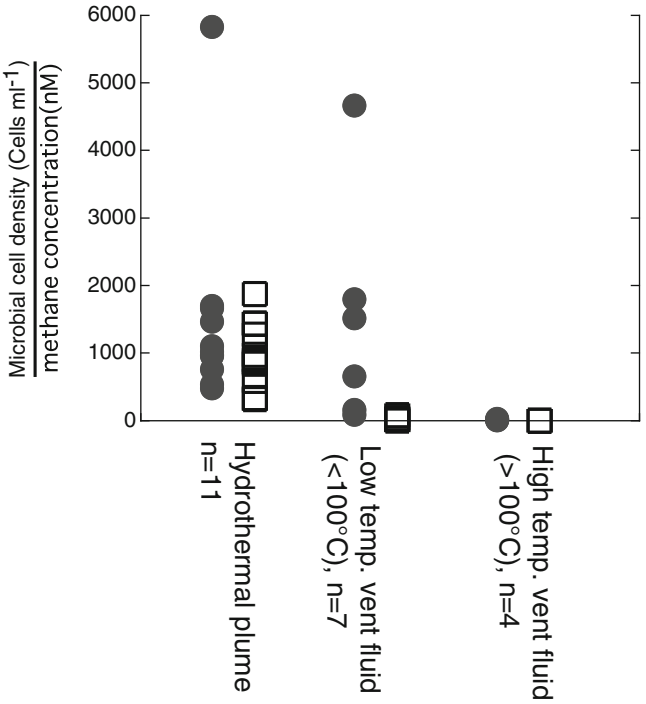

Fig. 3.3 Variation in ratios of microbial density and hydrothermal chemicals among hydrothermal plumes, low temperature hydrothermal fluids, and high temperature hydrothermal fluids. This figure is cited from Sunamura et al. (2009). *Filled circle*: Increased in total cell density divided by methane concentration in hydrothermal samples *open square*: SUP05(typical thiotrophic phylotype in the Suiyo Seamount hydrothermal plume) cell density divided by methane concentration in hydrothermal samples

3.5 Contribution of a Specific Microbial Community for Total Plume Microbial Ecosystem

The values of the correlation slope between the microbial cell anomalies and the specific cell densities determined by FISH microscopic counts show the ratios of specific microbial species contributions in the plume microbial communities (Fig. 3.4). Based on these values, bacterial cells are responsible for almost all of the increase in microbial population in the plume and therefore the archaeal contribution is much smaller than that of bacteria. Moreover, SUP05 cells contribute from 60 to 98 % of the anomaly biomass in the plume (Fig. 3.4). Microbial population in the plume is regulated by input and removal; the inputs are in situ chemolithotrophic growth, in situ heterotrophic growth, immigration from vent fluids, and the removals are infection by virus, predation, and sedimentation. Because the contributions of specific microbial populations in the plume as estimated above do not consider removal, the contribution values may be overestimated. Our preliminary result in the southern Mariana plume showed the high correlation coefficient between microbial cell densities and manganese concentration. This indicates that the removal of microbial cells is small compared to the increase in microbial cells. We compared the contribution of SUP05 in the total microbial cell anomaly in the plume with the physical and chemical characteristics of the venting hydrothermal fluid which formed the hydrothermal plume. Within the parameters, we found a close correlation between the SUP05 contribution in the total microbial cell anomaly in the plume and the proportion of sulfur oxidation thermodynamic energy in the expected total thermodynamic energy from mixing of each hydrothermal fluid and abyssal seawater (Fig. 3.5). The positive correlation ($r^2 = 0.96$) suggests that chemical composition of hydrothermal fluids regulates the SUP05 cell density ratios in microbial community, an idea which is proposed in the TAIGA hypothesis. The hydrothermal plume covers and expands from just after hydrothermal fluid spouting out into the seawater to non-buoyant hydrothermal plume. The widespread area and the length of the reaction time in the hydrothermal plume allows most of chemical energy to be used for microbial activity and growth. This idea would explain our conclusion that the composition of hydrothermal fluid chemicals regulates the microbial community structure in the plume. The SUP05 phylotype is known to possess various types of metabolism for growth energy, e.g. sulfur oxidation (Marshall and Morris 2012; Walsh et al. 2009), hydrogen oxidation (Anantharamana et al. 2013; Petersen et al. 2011), and heterotrophy

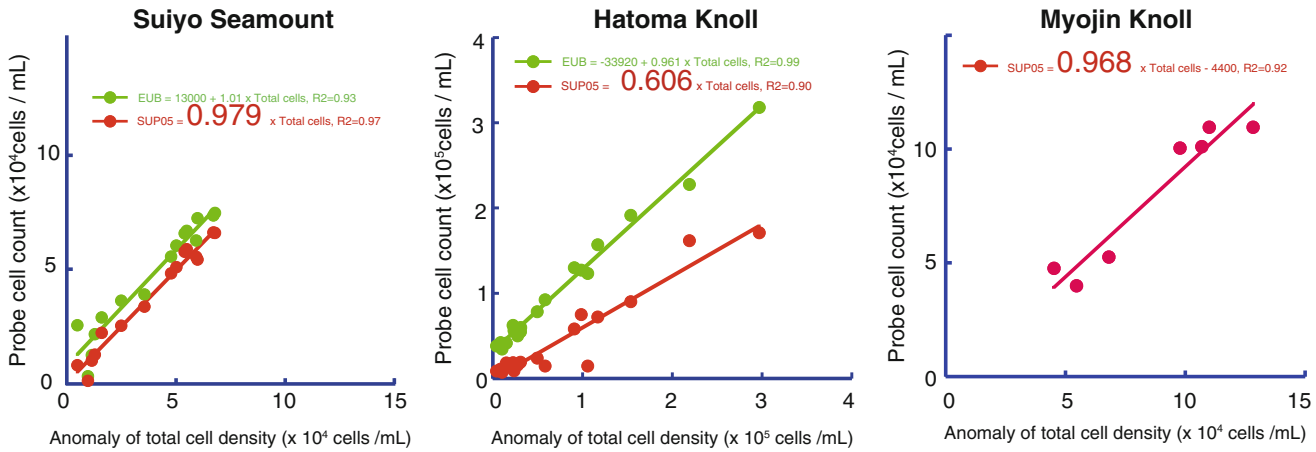

Fig. 3.4 Relationships between the specific microbial cell population and the total cell population anomaly in three plumes, the Suiyo seamount (data from Sunamura et al. 2004), the Myojin Knoll (this study), and the Haoma Knoll (this study). The total cell density anomalies were estimated by comparison with general abyssal seawater. Red indicates SUP05 cells as determined by a mixture of SUP05-187, 988, and 1245 probes, and green indicates bacterial cells as determined by a mixture of EUB338 I-III probes

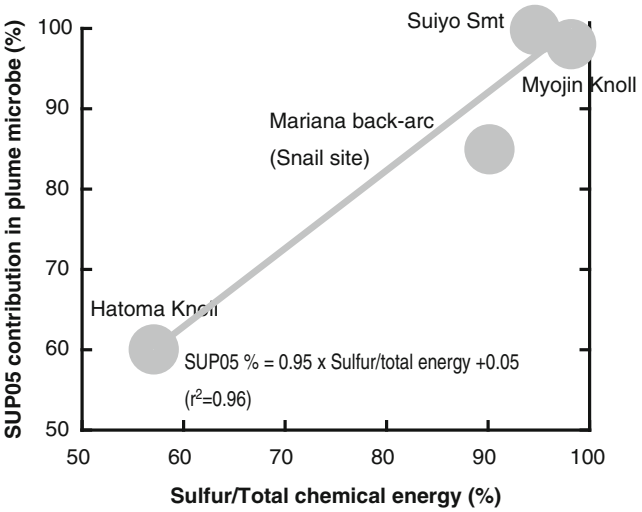

Fig. 3.5 Relationshop between the SUP05 proportions and the potential chemical energy in plumes of various hydrothermal fields. The SUP05 proportions were determined based on the relationship between SUP05 cell densities and microbial cell density anomalies in the plume from Fig. 3.4 and Sunamura et al., to be submitted. The potential chemical energy is the proportion of potential thermodynamical energy from sulfur oxidation in the total reduced chemical oxidation, which includes methane, reduced sulfur species, dihydrogen (H_2), ammonium, iron, and manganese calculated from the end-member chemical concentrations in hydrothermal fluids (Toki et al. Chap. 24, Kawagucci Chap. 35). Thermodynamic calculations were based on (Edwards et al. 2005)

(Marshall and Morris 2012). To understand the regulation mechanism of the plume microbial community, we will need to determine the status of sulfur chemical species, gas species, and metal species during plume evolution in the future.

3.6 Conclusion and Future Perspectives

In this chapter, we compiled our qualitative and quantitative data regarding the plume microbial community of various hydrothermal fields and compare their characteristics inthe context of four TAIGA. We conclude that (1) bacteria is the major player in the hydrothermal plume, (2) SUP05 is the most important key species in the plume microbial community, (3) the SUP05 population represents the arc-backarc and ridge plume communities, and it is regulated by the chemical composition of the hydrothermal fluid, (4) the SUP05 major growth area is restricted to the plumes, not below the seafloor, and (5) methanotrophs are a microbial signature of hydrogen and methane TAIGA. To understand the biogeochemical impacts of plume microbes on the deep ocean, in the future we will need to determine the microbial production rate and in situ microbial activities through in situ incubation, transcriptomics, and more dense sampling.

3.7 Materials and Methods

3.7.1 Samples Used in This Study

The hydrothermal plume samples used in this study were collected at the Okinawa Trough (4 sites: Hatoma Knoll in cruise KT05-26, Daiyon-Yonaguni Knoll in KT09-26, Tarama Knoll in NT08-11, and Wakamiko Creater in KT09-29) (see Ishibashi et al. Chap. 29; Yamanaka et al. Chap. 49), and the Izu-Mariana Arc (4sites: Suiyo Seamount in cruise KH11-05, Myojin Caldera in NT06-21, TOTO Caldera in KR08-05, NW Rota Seamount in NT10-13) using a Niskin bottle water sampler with CTD-CMS or

ROV Hyper dolphin 3 K. Hydrothermal fluids in the subduction system are rich in sulfides. The hydrothermal fluids in the Okinawa Trough are characterized by a rich methane content. Those in the Ogasawara Arc are characterized by poor content of other reduced chemicals and those of the Mariana Trough, are characterized by a rich iron contents. Microbial cells in the plume samples were filtered and concentrated on 0.22 μm pore sized membrane filters (Type GV, Millipore) for DNA analysis. Other water samples were fixed with neutralized formalin (final concentration: 3.5 %) and microbial cells were filtered on 0.2 μm pore-sized polycarbonate membrane filters (Nuclepore filter, Whatman) on board. These samples were stored at −80 °C prior to analysis.

3.7.2 Analytical Methods

Microbial DNA on the filter samples was extracted using an Ultra Clean Soil DNA Extraction Kit (MOBio) according to manufacturer's instructions. To determine the 16S rRNA gene sequences in the samples, we used cloning/Sanger sequencing method or Roche-454 sequencer with a DNA tag for each sample. For the cloning/Sanger method, the 16S rRNA genes were amplified by PCR method with a 27F-1492R primer set (Reysenbach et al. 2000) using Takara ex taq DNA polymerase (Takara bio) and then the amplified 16S rRNA gene sequences were determined by ABI3100 sequencers after cloning using a TA Cloning Kit (Invitrogen). For the Roch-454 sequencer, the 16S rRNA genes were amplified by a 530F-907R primer set (Nunoura et al. 2012) with adaptor and tags by PCR using LA taq DNA polymerase (Takara bio) and the sequences of the amplicons were determined by Roche 454 sequencers. Sequences were analyzed on the Mothur software package (Schloss et al. 2009) using Silva v.1.02. The SUP05 phylotype and bacterial cells were quantified by direct counting under fluorescent microscopy (BX51, Olympus) with CARD-FISH staining of the cells using Cy3-tyramide (Yanagawa and Sunamura in Chap. 6) (Hirayama et al. 2007; Pernthaler et al. 2002) by SUP05 mix probe for the SUP05 phylotype and EUB338 I-III probe for the bacterial cells (Daims et al. 1999; Stahl and Amann 1991). For determination of the SUP05 phylotype, we used a SUP05 mix DNA probe, which is a mixture of newly designed SUP05-988 (5′-AAGTTCCGTGTATGTCAAGA-3′) and SUP05-1245 (5′-GCTTAGCAACCCTTTGTCC-3′) probes, in addition to a SUP05-187 probe (Sunamura et al. 2004).

Acknowledgements This work was funded by the Ministry of Education, Culture, Science and Technology (MEXT), Japan, through the Grant-in-Aid for Scientific Research: Project TAIGA (New Scientific Research on Innovative Areas, 20109003) and the Archaean Park Project (International Research Project on Interaction between Sub-Vent Biosphere and Geo-Environments). Thanks are due to the crews of the R/V *Tansei-maru*, and the R/V *Natsushima* and the operation teams of *HyperDolphin* during the KT05-16, KT09-26, NT06-21, NT10-13 cruises. We also thank the on board science parties from all of the cruises and the members of project TAIGA for the sample collection opportunities and for helpful discussions.

References

Anantharamana K, Breierb JA, Sheika CS, Dick GJ (2013) Evidence for hydrogen oxidation and metabolic plasticity in widespread deep-sea sulfur-oxidizing bacteria. Proc Natl Acad Sci U S A 110:330–335

Cowen JP, Massoth GJ, Baker ET (1986) Bacterial scavenging of Mn and Fe in a mid-field to far-field hydrothermal particle plume. Nature 322:169–171

Daims H, Bruhl A, Amann R, Schleifer K-H, Wagner M (1999) The domain-specific probe EUB338 is insufficient for the detection of all Bacteria: development and evaluation of a more comprehensive probe set. Syst Appl Microbiol 22:434–440

DeAngelis MA, Baross JA, Lilley MD (1991) Enhanced microbial methane oxidation in water from a deep-sea hydrothermal vent field at simulated in situ hydrostatic pressures. Limnol Oceanogr 36(3):565–570

DeAngelis MA, Lilley MD, Olsen EJ, Baross JA (1993) Methane oxidation in deep-sea hydrothermal plumes of the endeavour segment of the Juan de Fuca Ridge. Deep Sea Res I 40(6):1169–1186

Dick GJ, Tebo BM (2010) Microbial diversity and biogeochemistry of the Guaymas Basin deep-sea hydrothermal plume. Environ Microbiol 12(5):1334–1347

Dick GJ, Anantharaman K, Baker BJ, Li M, Reed DC, Sheik CS (2013) The microbiology of deep-sea hydrothermal vent plumes: ecological and biogeographic linkages to seafloor and water column habitats. Front Microbiol 4:124. doi:10.3389/fmicb.2013.00124

Duperron S, Nadalig T, Caprais JC, Sibuet M, Fiala-Medioni A, Amann R, Dubilier N (2005) Dual symbiosis in a *Bathymodiolus* sp mussel from a methane seep on the gabon continental margin (southeast Atlantic): 16S rRNA phylogeny and distribution of the symbionts in gills. Appl Environ Microbiol 71(4):1694–1700

Edwards KJ, Bach W, McCollom TM (2005) Geomicrobiology in oceanography: microbe–mineral interactions at and below the seafloor. Trend Microb 13:449–456

Fujiwara Y, Takai K, Uematsu K, Tsuchida S, Hunt JC, Hashimoto J (2000) Phylogenetic characterization of endosymbionts in three hydrothermal vent mussels: influence on host distributions. Mar Ecol Prog Ser 208:147–155

German CR, Von Damm KL (2003) Hydrothermal processes. In: The Oceans and Marine Geochemistry, 1st Edition, H. Elderfield (ed), Treatise on geochemistry, vol 6, Elsevier (Pergamon), Oxford, UK, 625 pp

German CR, Bowen A, Coleman ML, Honig DL, Huber JA, Jakuba MV, Kinsey JC, Kurz MD, Leroy S, McDermott JM, Lépinay BMD, Nakamura K, Seewald JS, Smith JL, Sylva SP, Dover CLV, Whitcomb LL, Yoerger DR (2010) Diverse styles of submarine venting on the ultraslow spreading Mid-Cayman Rise. Proc Natl Acad Sci U S A 107(32):14020–14025

Hirayama H, Sunamura M, Takai K, Nunoura T, Noguchi T, Oida H, Furushima Y, Yamamoto H, Oomori T, Horikoshi K (2007) Culture-dependent and -independent characterization of microbial

communities associated with a shallow submarine hydrothermal system occurring within a coral reef off Taketomi Island, Japan. Appl Environ Microbiol 73:7642–7656

Lai Q, Li W, Shao Z (2012) Complete genome sequence of *Alcanivorax dieselolei* type strain B5. J Bacteriol 194:6674

Lam P, Cowen JP, Jones RD (2004) Autotrophic ammonia oxidation in a deep-sea hydrothermal plume. FEMS Microbiol Ecol 47 (2):191–206

Lam P, Cowen JP, Popp BN, Jones RD (2008) Microbial ammonia oxidation and enhanced nitrogen cycling in the endeavour hydrothermal plume. Geochim Cosmochim Acta 72(9):2268–2286

Lavik G, Stuhrmann T, Bruchert V, Van der Plas A, Mohrholz V, Lam P, Mussmann M, Fuchs BM, Amann R, Lass U, Kuypers MMM (2009) Detoxification of sulphidic African shelf waters by blooming chemolithotrophs. Nature 457(7229):581–586

Lesniewski RA, Jain S, Anantharaman K, Schloss PD, Dick GJ (2012) The metatranscriptome of a deep-sea hydrothermal plume is dominated by water column methanotrophs and lithotrophs. ISME J 6:2257–2268

Malahoff A, Kolotyrkina IY, Midson BP, Massoth GJ (2006) A decade of exploring a submarine intraplate volcano: hydrothermal manganese and iron at Lo?'ihi volcano, Hawai'i. Geochem Geophys Geosys 7:Q06002

Marshall KT, Morris RM (2012) Isolation of an aerobic sulfur oxidizer from the SUP05/Arctic96BD-19 clade. ISME J 7:452–455

McCollom TM, Shock EL (1997) Geochemical constraints on chemolithoautotrophic metabolism by microorganisms in seafloor hydrothermal systems. Geochim Cosmochim Acta 61:4375–4391

Naganuma T, Otsuki A, Seki H (1989) Abundance and growth-rate of bacterioplankton community in hydrothermal vent plumes of the North Fiji Basin. Deep Sea Res A 36(9):1379–1390

Nakagawa S, Takaki Y, Shimamura S, Reysenbach A-L, Takai K, Horikoshi K (2007) Deep-sea vent -proteobacterial genomes provide insights into emergence of pathogens. Proc Natl Acad Sci U S A 104:12146–12150

Nunoura T, Takaki Y, Kazama H, Hirai M, Ashi J, Imachi H, Takai K (2012) Microbial diversity in deep-sea methane seep sediments presented by SSU rRNA gene tag sequencing. Microbs Environ 27(4):382–390

Pernthaler A, Pernthaler J, Amann R (2002) Fluorescence in situ hybridization and catalyzed reporter deposition for the identification of marine bacteria. Appl Environ Microbiol 68(6):3094–3101

Petersen JM, Zielinski FU, Pape T, Seifert R, Moraru C, Amann R, Hourdez S, Girguis PR, Wankel SD, Barbe V, Pelletier E, Fink D, Borowski C, Bach W, Dubilier N (2011) Hydrogen is an energy source for hydrothermal vent symbioses. Nature 476:176–180

Resing JA, Lebon G, Baker ET, Lupton JE, Embley RW, Massoth GJ, Chadwick WW, De Ronde CEJ (2007) Venting of acid-sulfate fluids in a high-sulfidation setting at NW rota-1 submarine volcano on the Mariana arc. Econ Geol 102(6):1047–1061

Resing JA, Baker ET, Lupton JE, Walker SL, Butterfield DA, Massoth GJ, Nakamura K (2009) Chemistry of hydrothermal plumes above submarine volcanoes of the Mariana arc. Geochem Geophys Geosyst 10:Q02009

Reysenbach A-L, Longnecker K, Kirshtein J (2000) Novel Bacterial and Archaeal lineages from an in situ growth chamber deployed at a Mid Atlantic Ridge hydrothermal vent. Appl Environ Microbiol 66 (9):3798–3806

Schloss PD, Westcott SL, Ryabin T, Hall JR, Hartmann M, Hollister EB, Lesniewski RA, Oakley BB, Parks DH, Robinson CJ, Sahl JW, Stres B, Thallinger GG, Van Horn DJ, Weber CF (2009) Introducing mothur: open-source, platform-independent, community-supported software for describing and comparing microbial communities. Appl Environ Microbiol 75(23):7537–7541

Stahl DA, Amann R (1991) Development and application of nucleic acid probes. In: Stackebrandt E, Goodfellow M (eds) Nucleic acid techniques in bacterial systematics. Wiley, Chichester, pp 205–248

Summit M, Baross JA (1998) Thermophilic subseafloor microorganisms from the 1996 north Gorda Ridge eruption. Deep Sea Res Part II Top Stud Oceanogr 45(12):2751–2766

Sunamura M, Higashi Y, Miyako C, Ishibashi J, Maruyama A (2004) Two Bacteria phylotypes are predominant in the Suiyo Seamount hydrothermal plume. Appl Environ Microbiol 70 (2):1190–1198

Sunamura M, Noguchi T, Yamamoto H, Okamura K (2009) Environmental and ecological impact on deep-sea environment from deep-sea hydrothermal system (in Japanese with English abstruct). Chigaku Zasshi 118(6):1160–1173

Swan BK, Martinez-Garcia M, Preston CM, Sczyrba A, Woyke T, Lamy D, Reinthaler T, Poulton NJ, Masland EDP, Gomez ML, Sieracki ME, DeLong EF, Herndl GJ, Stepanauskas R (2011) Potential for chemolithoautotrophy among ubiquitous bacteria lineages in the dark ocean. Science 333:1296–1300

Tsunogai U, Yoshida N, Ishibashi J-I, Gamo T (2000) Carbon isotopic distribution of methane in deep-sea hydrothermal plume, Myojin Knoll Caldera, Izu-Bonin arc: implications for microbial methane oxidation in the oceans and applications to heat flux estimation. Geochim Cosmochim Acta 64:2439–2452

Walsh DA, Zaikova E, Howes CG, Song YC, Wright JJ, Tringe SG, Tortell PD, Hallam SJ (2009) Metagenome of a versatile chemolithoautotroph from expanding oceanic dead zones. Science 326:578–582

Ward JH (1963) Hierarchical grouping to optimize an objective function. J Am Stat Assoc 58:236–244

Winn CD, Karl DM, Massoth GJ (1986) Microorganisms in deep-sea hydrothermal plumes. Nature 320:744–746

Yamanaka T, Maeto K, Akashi H, Ishibashi J, Miyoshi Y, Okamura K, Noguchi T, Kuwahara Y, Toki T, Tsunogai U, Ura T, Nakatani T, Maki T, Kubokawa K, Chiba H (2013) Shallow submarine hydrothermal activity with significant contribution of magmatic water producing talc chimneys in the Wakamiko Crater of Kagoshima Bay, southern Kyushu. Jpn J Volcanol Geotherm Res 258:74–84. doi:10.1016/j.jvolgeores.2013.04.007

Systematics of Distributions of Various Elements Between Ferromanganese Oxides and Seawater from Natural Observation, Thermodynamics, and Structures

4

Yoshio Takahashi, Daisuke Ariga, Qiaohui Fan, and Teruhiko Kashiwabara

Abstract

Metal oxides including iron oxides, manganese oxides, and ferromanganese oxides have been frequently found at seafloor as a result of the release of dissolved iron and manganese from various sources including hydrothermal activities. These precipitates can adsorb or incorporate various elements, which can affect the behavior of the elements in marine environment. In addition, these precipitates can be resources of rare metals due to their high abundances in ferromanganese oxides. In this review, our aims are (i) to summarize distribution of various trace elements between ferromanganese oxides and seawater, (ii) to understand the distributions based on thermodynamic parameters, and (iii) to show the relationship between the distribution and structural information of the species adsorbed onto the ferromanganese oxides. For this purpose, our original data of chromate adsorption on ferrihydrite was also included. These attempts enable us to obtain systematic explanation of the solid-water distributions of various elements in marine environment, which in turn gives us clearer view on (i) the mechanism of isotopic fractionation during adsorption which is linked to the understanding of paleoenvironment based on the isotope geochemistry and (ii) prediction of abundances of various elements in the ferromanganese oxides that are important from the viewpoint of exploration of marine resources.

Keywords

Ferromanganese oxide • Adsorption • Surface complex • Systematics • EXAFS

Y. Takahashi (✉)
Department of Earth and Planetary Science, Graduate School of Science, The University of Tokyo, 7-3-1 Hongo, Bukyo-ku, Tokyo 113-0033, Japan

Department of Earth and Planetary Systems Science, Graduate School of Science, Hiroshima University, 1-3-1 Kagamiyama, Higashi-Hiroshima, Hiroshima 739-8526, Japan

Institute for Research on Earth Evolution(IFREE)/Submarine Resources Research Project (SRRP), Japan Agency for Marine-Earth Science and Technology (JAMSTEC), 2-15 Natsushimacho, Yokosuka, Kanagawa 237-0061, Japan
e-mail: ytakaha@eps.s.u-tokyo.ac.jp

D. Ariga • Q. Fan
Department of Earth and Planetary Systems Science, Graduate School of Science, Hiroshima University, 1-3-1 Kagamiyama, Higashi-Hiroshima, Hiroshima 739-8526, Japan

T. Kashiwabara
Institute for Research on Earth Evolution(IFREE)/Submarine Resources Research Project (SRRP), Japan Agency for Marine-Earth Science and Technology (JAMSTEC), 2-15 Natsushimacho, Yokosuka, Kanagawa 237-0061, Japan

J.-i. Ishibashi et al. (eds.), *Subseafloor Biosphere Linked to Hydrothermal Systems: TAIGA Concept*,
DOI 10.1007/978-4-431-54865-2_4,

4.1 Introduction

In natural waters, precipitation-dissolution process is primarily controlling the dissolved concentrations of various elements, especially for major elements at earth's surface such as calcium and iron. It is often the case, however, that concentrations of trace elements in seawater are controlled by the adsorption-desorption reactions between water and various solid phases such as particulate matters, chemical deposits, and sediments present in marine environment (Langmuir 1997). In particular, adsorption mechanism and local structure of ions adsorbed on the solid phases are closely related to their concentrations in the aqueous phase. Moreover, it has been recently revealed that isotopic ratios of trace elements in seawater were also affected by the adsorption-desorption reactions (Lyons et al. 2009; Kashiwabara et al. 2011). Among various phases, iron and manganese oxides play an important role on controlling concentrations and isotopic ratios of trace elements in seawater.

In marine environment, metal ions are supplied mainly from fluvial source, hydrothermal fluid at seafloor vent, and dissolution of airborne particles at seawater surface. Among them, it has been indicated that the amounts of iron and manganese supplied from hydrothermal activities to ocean are larger than those from fluvial components as a total budget (Elderfield and Schultz 1996). Although it has been shown that manganese can be transported for long distance from hydrothermal vents, it has been revealed recently that iron can also travel relatively for long distance (Sander and Koschinsky 2011). Hence, ferromanganese oxides can be considered as chemical deposit that can be more or less produced related to the hydrothermal activities in marine environment. This book collected various scientific contributions related to hydrothermal activities at seafloor. From this aspect, ferromanganese oxide is important as one of consequences produced by such hydrothermal activities, which in turn can affect abundances and isotopic ratios of various trace elements in marine system.

To evaluate the effect of adsorption reactions on ferromanganese oxides, systematic understanding of adsorption of various trace elements is needed. The degree of adsorption reaction can be apparently designated by the adsorption distribution coefficient (= K_d) for an ion M as

$$K_d = [M_{ads}] / [M_{dis}], \quad (4.1)$$

where $[M_{ads}]$ and $[M_{dis}]$ are concentrations of adsorbed M in the solid phase and dissolved M in the aqueous phase, respectively. This manuscript aims to describe what is known for the adsorption reactions of trace elements with iron and manganese oxides to understand the effect on their concentrations and isotopic abundances in marine environment. In addition to the adsorption reaction, which is confined to the reaction at the solid-water interface in a narrow sense, incorporation into the iron and manganese oxides can be also important. The process can be called as coprecipitation that can be regulated by the size of the trace element to a larger degree than the adsorption reaction, since the coprecipitation incorporates the trace elements within the three dimensional structure of the precipitates (e.g., Cornell and Schwertmann 2003). However, we focus in this manuscript on the adsorption reaction which can be regarded as an elemental process even for the coprecipitation.

4.2 General Tendency for Cations

To discuss the affinity of trace elements for ferromanganese oxides, distribution ratios of trace elements in hydrogenetic ferromanganese oxides normalized by their concentrations in seawater are shown in Fig. 4.1 modified from Hein et al. (2000, 2003). The ratios for the hydrogenetic type can be important to discuss the solid-water distributions of various elements, since this type incorporates trace elements directly from those dissolved in seawater. This order of enrichment reflected in Fig. 4.1 can be explained by several factors such as

1. The ratio was generally higher for cations than those for anions. This fact is possibly caused by the fact that surface of the solid phase is negatively charged due to the dissociation of hydroxyl group at the surface of ferromanganese oxides, or in particular for manganese oxide (Langmuir 1997).
2. Cobalt is highly enriched due to the oxidation of its reductive form of Co(II) into its oxic species, Co(III) (Takahashi et al. 2007). Since Co(III) species is less soluble than Co(II) species, the enrichment of Co can be marked compared with other elements. Such oxidation is important reactions during the incorporation of trace elements into ferromanganese oxides due to the strong oxidation potential of manganese oxides. Similarly, the enrichment of Ce is much larger than those of other trivalent rare earth elements (REEs). This is also caused by the oxidation of Ce(III) into Ce(IV) by the oxidation potential of the manganese oxides, as shown by the large positive Ce anomalies in the hydrogenetic ferromanganese oxides (Takahashi et al. 2000; Takahashi et al. 2007). It is possible that oxidation of Tl(I) into Tl(III) can be also important for the enrichment of thallium into ferromanganese oxides (Peacock and Moon 2012).
3. If the oxidation reaction results in the increase of the solubility for an element, the degree of the enrichment can be lower such as for selenium and chromium by the oxidation of Se(IV) and Cr(III) into more soluble Se(VI) and Cr(VI). Hexavalent U, uranyl ion, forms anionic carbonate species in seawater (e.g., $UO_2(CO_3)_3^{4-}$) which inhibits interaction of uranyl ions with

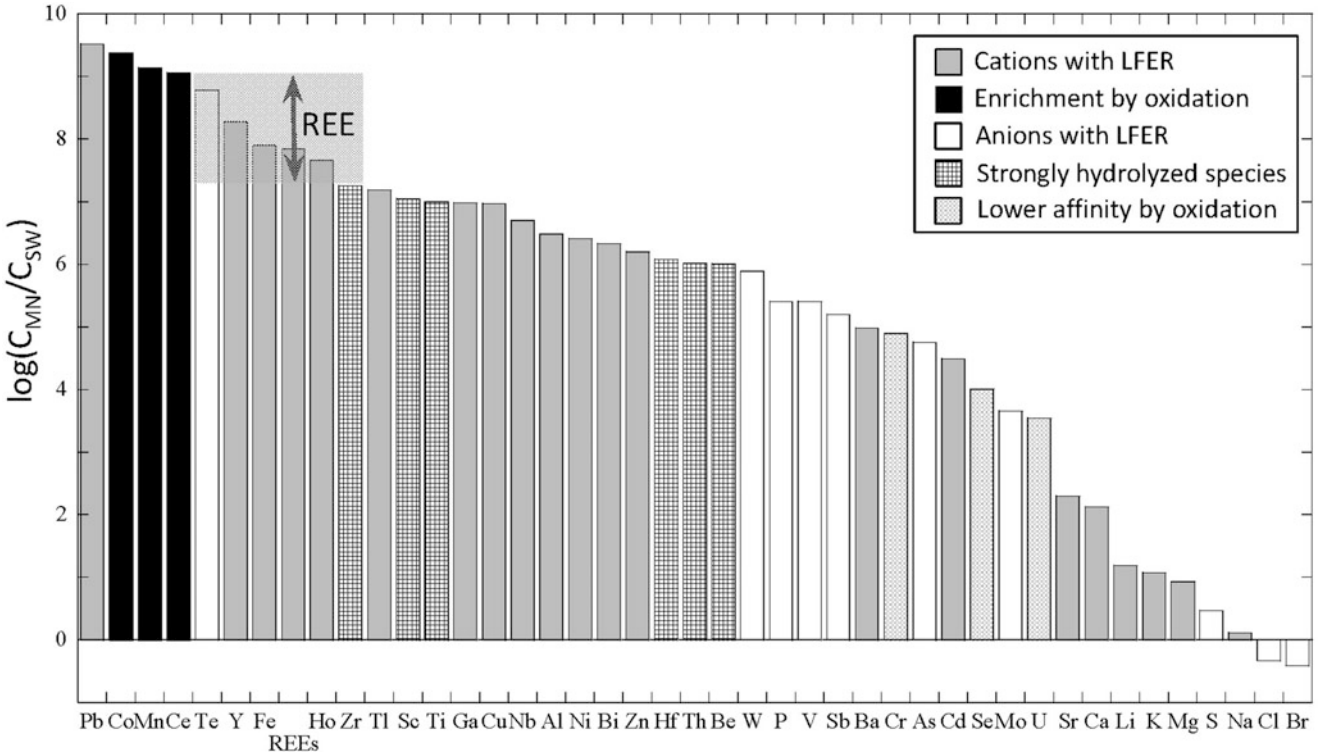

Fig. 4.1 Concentrations of various elements in hydrogenetic ferromanganese oxides (=C_{MN}) normalized by those in seawater (=C_{SW}) modified from Hein et al. (2000, 2003). Characteristic of incorporation of each element into hydrogenetic ferromanganese oxides is also indicated. *LFER* linear free energy relationship

ferromanganese oxides. Reduced form, U(IV), is highly insoluble, but U(IV) is readily oxidized in the presence of manganese oxides, which results in the lower abundance of U in ferromanganese oxides.

As indicated in (4.1), enrichment of cations is generally lager than that of anions (Fig. 4.1) and the cations (M^{z+}) are mainly bound to dissociated hydroxyl group at the surface of ferromanganese oxides ($\equiv$ S - O^-) formulated by the reaction below:

$$\equiv \text{S-O}^- + \text{M}^{z+} <=> \equiv \text{S-O-M}^{(z-1)+} \qquad (4.2)$$

The reaction can be written by adsorption distribution coefficient K_d:

$$K_d = \left[\equiv \text{S-O-M}^{(z-1)+}\right]/([\text{M}^{z+}][\equiv \text{S-O}^-]) \qquad (4.3)$$

In particular, surface of manganese oxide is negatively charged, which leads to the preferential adsorption of cations.

Based on the relationship above, we can suggest relationships due to the analogous reaction of hydroxide formation of M^{z+}:

$$\text{HO}^- + \text{M}^{z+} <=> \text{H-O-M}^{(z-1)+} \qquad (4.4)$$

the stability of which is expressed by the stability constant of β_{OH} (Langmuir 1997),

$$\beta_{OH} = \left[\text{MOH}^{(z-1)+}\right]_{eq}/\left([\text{M}^{z+}]_{eq}[\text{OH}^-]_{eq}\right). \qquad (4.5)$$

In this case, it is expected that $\log K_d$ has a linear relationship against $\log\beta_{OH}$ as

$$\log K_d = a \log\beta_{OH} + b, \qquad (4.6)$$

where a and b are constants. Actually, K_d estimated by the solid-water distribution between ferromanganese oxides and seawater seems to be proportional to $\log\beta_{OH}$ as suggested by Li (1981, 1982) for cations (Fig. 4.2). This relationship is called as Linear Free Energy Relationship (LFER). As a result, the cation with larger stability constant with hydroxide is generally enriched into ferromanganese oxides. The ions with exceptionally different behavior is found in Fig. 4.2 for Co, Ce, Ba, and U, which can be interpreted by following reasons: (i) Co and Ce for the factor (4.2) as written above; (ii) Ba for the formation of insoluble sulfate (=barite) in the marine environment; (iii) UO_2^{2+} for its high stability of $UO_2(CO_3)_3^{4-}$ as dissolved species as indicated before.

To examine more clearly the LFER for cations, intrinsic surface complexation constant (= K_{int-2}: one of two intrinsic surface complexation constants, $K_{int\text{-}1}$and $K_{int\text{-}2}$, without electrostatic effect) experimentally obtained for ferrihydrite is discussed here due to the availability of a large amount of the data in Dzombak and Morel (1990), by which the

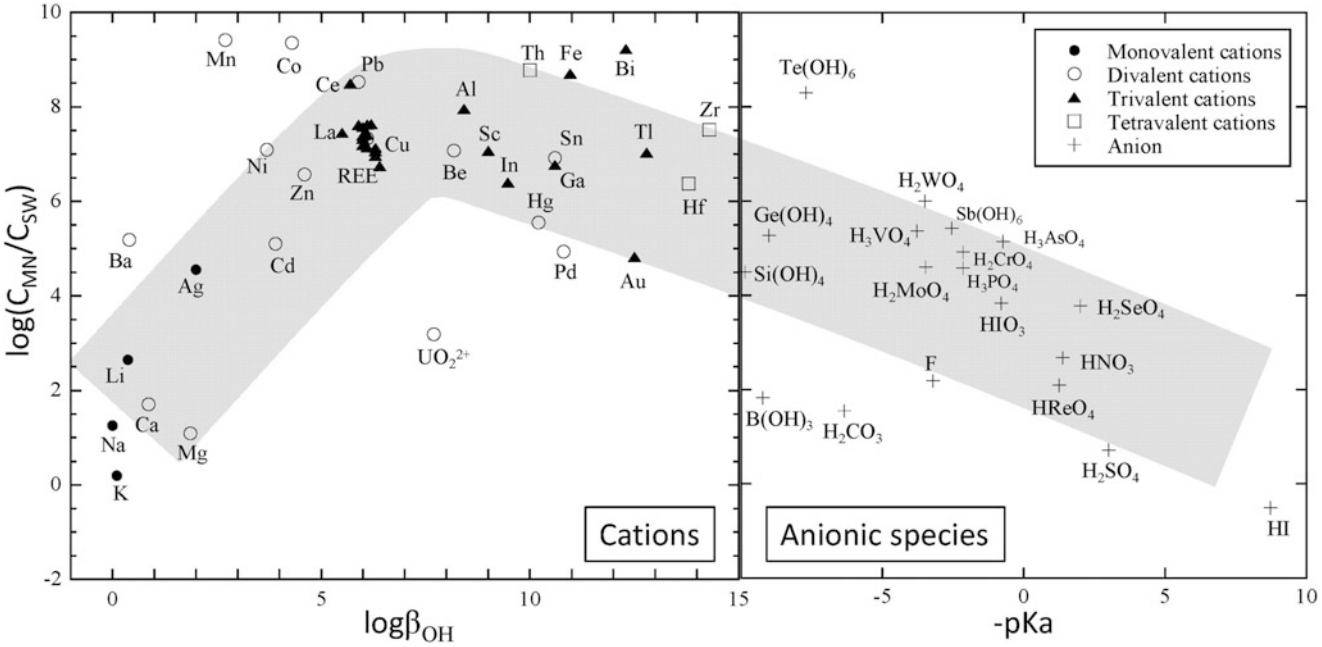

Fig. 4.2 Comparison of $\log(C_{MN}/C_{SW})$ to $\log\beta_{OH}$ for cations and –pKa of conjugate acids for anionic species

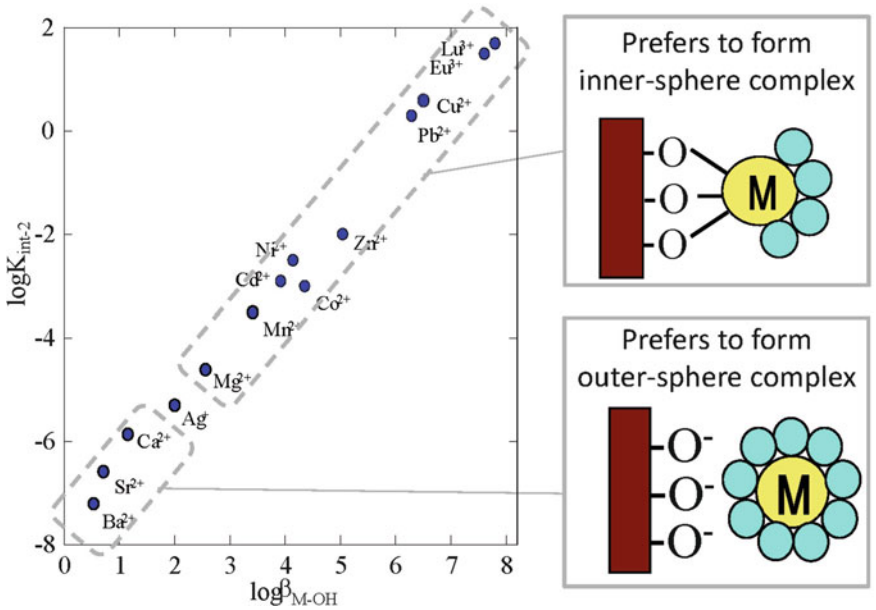

Fig. 4.3 The relationship between $\log K_{int\text{-}2}$ obtained by surface complex modeling for ferrihydrite (Dzombak and Morel 1990) and $\log\beta_{OH}$ for various cations, which is related to the preference to form either inner- or outer-sphere complex on ferrihydrite

relationship in Fig. 4.3 is depicted. The results again showed that the cation with larger $\log\beta_{OH}$ can have higher affinity for ferrihydrite. This tendency can explain high enrichment of Pb^{2+} and rare earth elements (REE) onto natural ferromanganese oxides. For hard cations (alkaline metal ions, alkaline earth metal ions, and rare earth ions), the systematics observed can be related to "ion potential" expressed by z/r, where z and r are charge and ionic radius of the ion. The higher the ion potential is, the larger the enrichment of the cation was observed. It has been previously suggested that enrichment of Pb is caused by the oxidation of Pb^{2+} into Pb^{4+}, but it is not likely based on the spectroscopic analyses (Takahashi et al. 2007). The high affinity for ferromanganese oxides coupled with high covalent characteristic of Pb^{2+} should be responsible for the large enrichment of Pb into the ferromanganese oxides.

Enrichment of Cu^{2+} in the natural ferromanganese nodules is not as large as that expected from $\log\beta_{OH}$ and $\log K_d$ values. This can be explained by preferential formation of organic complex for Cu^{2+} dissolved in seawater. The enrichment of Cu^{2+} for diagenetic ferromanganese nodule within sediment is generally larger than that in the

hydrogenetic ferromanganese nodule or crust growing at the surface of sediment or basement rock (Verlaan et al. 2004). The former type grows faster than hydrogenetic one by high flux of dissolved Mn^{2+} in the porewater in the sediment provided by the upward diffusion of dissolved Mn^{2+} in the sediment following the reduction of MnO_2 to Mn^{2+} (Dymond et al. 1984). The oxidation reaction by MnO_2 is accompanied with oxic degradation of organic matter in the deeper layer. On the other hand, the latter type (= hydrogenetic type) is formed by the direct precipitation of ferromanganese oxides in the water column. Thus, the preferential complexation of Cu^{2+} with organic matter and its degradation within the sediment is related to the large enrichment of Cu^{2+} in diagenetic ferromanganese oxides (Verlaan et al. 2004), but not the case for the hydrogenetic ferromanganese oxides expressed in Fig. 4.1.

Preferential formation of stable hydrolyzed species in the aqueous phase or even hydroxide precipitate can be a reason for the lower enrichment of high field strength elements such as Al^{3+}, Sc^{3+}, In^{3+}, Th^{4+}, Ga^{3+}, Fe^{3+}, Zr^{4+}, and Hf^{4+}. The $\log\beta_{OH}$ values for these ions are very large, but the degree of their enrichment is lower than the linear line expected from other cations in Fig. 4.2.

4.3 General Tendency for Anions

Similarly, anions can be attracted to the positively-charged surface of ferromanganese oxides ($\equiv$ S-OH_2^+) as shown by the following reaction including the anion written as L^{y-}:

$$\equiv \text{S-OH}_2^+ + \text{L}^{y-} <=> \equiv \text{S-L}^{(y-1)-} + \text{H}_2\text{O} \qquad (4.7)$$

with K_d as below:

$$K_d = \left[\equiv \text{S-L}^{(y-1)-}\right] / ([\equiv \text{S-OH}_2^+][\text{L}^{y-}]) \qquad (4.8)$$

For this reaction, we can expect another LFER based on the proton dissociation reaction known for many anions:

$$\text{H}^+ + \text{L}^{y-} <=> \text{HL}^{(y-1)-} \qquad (4.9)$$

In this case, we consider proton dissociation constant K_a (Langmuir 1997), by which we can write the equilibrium constant of the reaction above as $1/K_a$. Thus, LFER relationship for anions can be written as

$$\log K_d = a \log(1/K_a) + b = a\,pK_a + b \qquad (4.10)$$

This relationship was also suggested by Li (1981, 1982) as shown in right side of Fig. 4.2, where it is evident that the distribution ratio to ferromanganese oxide normalized to that in seawater is correlated to pKa_1 of the conjugate acids of the anions such as H_2SO_4 (conjugate acid) to HSO_4^- (anion) or HSO_4^- (conjugate acid) to SO_4^{2-} (anion). Equilibrium constant of the latter reaction between HSO_4^- and SO_4^{2-} is expressed by pKa_2, second proton dissociation constant of diprotic or triprotic acid. Similarly to Fig. 4.3, the comparison of pKa_2 value to $\log K_{int-2}$ defined in surface complexation model (Dzombak and Morel 1990) was also depicted for divalent oxyanions such as SO_4^{2-}, SeO_4^{2-}, MoO_4^{2-}, WO_4^{2-}, CrO_4^{2-}, SO_3^{2-}, SeO_3^{2-}, and SiO_3^{2-} (Fig. 4.4). In this figure, we can also see the clear correlation, showing that weaker acid that has higher affinity for proton (or larger pKa) can be more strongly adsorbed onto the surface of ferrihydrite.

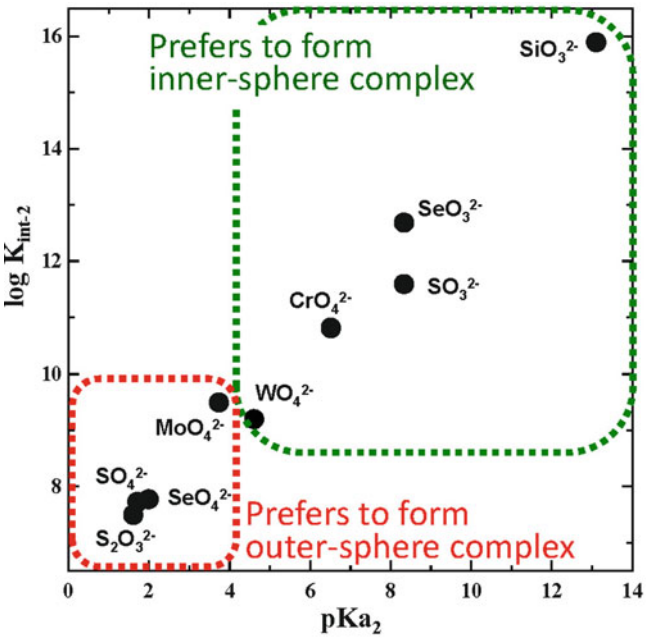

Fig. 4.4 The relationship between $\log K_{int-2}$ obtained by surface complex modeling for ferrihydrite (Dzombak and Morel 1990) and pKa_2 for conjugate acids of for various divalent oxyanions, which is related to the preference to form either inner- or outer-sphere complex on ferrihydrite

4.4 Relationship Between Distribution of Trace Elements and Their Local Structures at the Solid–Water Interface

The LFER suggests that the difference of distribution ratios of trace elements to ferromanganese oxides is primarily decided by the chemical affinity of each ion to the solid surface. If the affinity of one cation is larger for hydroxide ion (= larger β_{OH}) than the other cation, the ion also has a larger affinity to the proton-dissociated site on the solid phase. Similarly, if one conjugate acid (e.g., oxyacid like arsenate) has a larger affinity to proton (= larger pK_a) than the other, adsorption of the anion on the solid surface is relatively more stable in terms of the replacement of

hydroxyl groups attached to Fe^{3+} or Mn^{4+} by the anionic species. These species, including both cations and anions, which form direct bonding to the solid surface can be called as inner-sphere complex (Fig. 4.3). On the other hand, there are other species that can be retained on the solid surface without specific chemical bonding to the surface. In this case, the ion is electrostatically attracted to the surface without formation of chemical bonding (Fig. 4.3). The reaction can be called as ion-exchange reaction, where the species is known as outer-sphere complex.

For cations, for example, the difference of the affinity is also consistent with the local structure of cations adsorbed on the solid-water interface (Fig. 4.3). Based on the surface complex modeling on ferrihydrite or goethite, $Sr^{2+}$and Ca^{2+} mainly form outer-sphere complex to the surface (e.g., Cowan et al. 1991; Rahnemaie et al. 2006). On the other hand, Mg^{2+} having larger K_d value (Fig. 4.3) forms inner-sphere complex to goethite or ferrihydrite (e.g., Cowan et al. 1991; Rahnemaie et al. 2006). The difference of the structure, either outer-sphere or inner-sphere complexation, is directly linked to the stability of the surface complex: the K_d value of the ions forming outer-sphere complex is smaller than that forming inner-sphere complex.

The actual species of the surface complexes must be studied by any spectroscopic methods. Among various spectroscopic methods, extended X-ray absorption fine structure (EXAFS) is a unique technique (Bunker 2010), since (i) the method can be applied to almost all elements, (ii) the method is highly selective to the element without severe interference of other elements, (iii) the method is very sensitive that can be applied to trace elements at the solid-water interface, and (iv) the method is applicable in the presence of water in the system without necessity of drying upon the measurement. The EXAFS can give distance (R) of center atom to the neighboring atoms with coordination number (CN) of the neighboring atom. In the adsorption system, EXAFS can reveal the type of the surface complex based on the R with CN for first and second neighboring atoms, as exemplified by La^{3+} adsorbed on ferrihydrite (Fig. 4.5; Nakada et al. 2013). If the populations of inner- and outer- sphere complexes are rather similar, it is sometimes difficult to determine the CN of the second neighboring atom, or Fe in this case. More importantly, however, the presence of the peak of the second neighboring atom (e.g., La-Fe in Fig. 4.5) is important, which can be strong evidence of the formation of inner-sphere complex, or more precisely the dominance of the inner-sphere complex for the ion.

Taking account of the background of the EXAFS spectroscopy, let us consider the structure, whether inner- or outer-sphere complex are important for the cations and anions related to Figs. 4.3 and 4.4. As for cations, Sr^{2+} forms outer-sphere complex on ferrihydrite (Langley et al. 2009). Although spectroscopic information on the

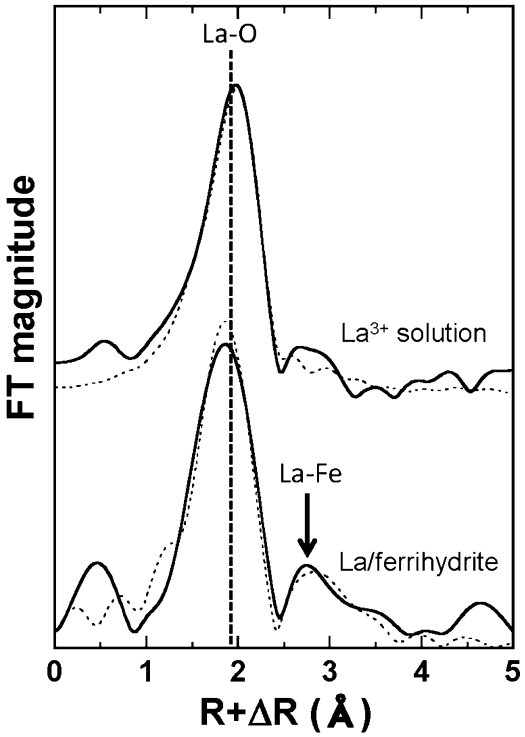

Fig. 4.5 Lanthanum K-edge EXAFS in R-space as an example of spectrum for cations adsorbed on ferrihydrite

surface complexes of Ca^{2+}, Ag^{+}, and Mg^{2+} is not available, inner-sphere complex on ferrihydrite has been observed for Cd^{2+}adsorbed on iron oxides (e.g., Spadini et al. 1994). These facts both from modeling and spectroscopic results illustrate that the chemical affinity expressed by $\log\beta_{OH}$ decides whether the ion forms inner- or outer-sphere complex on ferrihydrite. In this discussion, it must be noted that all ions more or less form both inner- and outer-sphere complexes on the solid phase. However, the ratio of the inner- to outer- sphere complexes on certain solid phase can follow the order shown in Fig. 4.3.

Similar tendency has been suggested for oxyanions based on the structure of surface complexes of oxyanions on ferrihydrite recently revealed by Harada and Takahashi (2008) and Kashiwabara et al. (2011, 2013). Harada and Takahashi (2008) studied adsorbed species of selenate, selenite, tellurite, and tellurate on ferrihydrite. They concluded that selenate forms outer-sphere complex on ferrihydrite, whereas selenite, tellurite, and tellurate form inner-sphere complex based on the EXAFS analyses. Kashiwabara et al. (2011, 2013) showed that molybdate and tungstate form outer- and inner-sphere complexes on ferrihydrite, respectively. In Fig. 4.4, it is also evident that the affinity to the solid surface ($\log K_{int\text{-}2}$) is larger for those ions forming inner-sphere complex (selenite, tellurite, and tellurate) than that taking outer-sphere complex (selenate and molybdate). However, the tendency is somewhat opposite between molybdate and tungstate. Hence, more details

for oxyanions will be given below including additional spectroscopic data of chromate adsorption on ferrihydrite, since chromium is a congener of molybdenum and tungsten.

4.5 Adsorption of Chromate: Additional Spectroscopic Data

To obtain more structural information on the adsorption of divalent oxyanions on ferrihydrite, EXAFS spectrum of chromate was also obtained in this study. As seen in Fig. 4.4, information of chromate can be important, since the ion is located between tungstate and selenate discussed above in terms of the pKa_2 value. For this purpose, chromium K-edge (5.989 keV) EXAFS was mainly measured at beamline BL-12C of KEK Photon Factory (Tsukuba, Japan) with a Si(111) double–crystal monochromator and two mirrors. The measurement was carried out at room temperature under ambient conditions. The XAFS spectra of the reference compounds were collected in transmission mode, whereas those of the experimental samples were obtained in the fluorescence mode. In the latter mode, the sample was positioned at 45° with respect to the incident, while a 19–element germanium semiconductor detector (Canberra, USA) placed at 90° to the incident beam. Multiple scans were taken for low Cr concentration samples to obtain sufficiently high signal/noise ratio for EXAFS simulations. Repeated scan gave identical spectra, which assures the minimal alteration of the sample by the incident X-ray.

As for the sample of chromate adsorbed on ferrihydrite, adsorption experiments were carried out using 20 mg of ferrihydrite and 10 mL chromate solution. Adsorption envelops under different ionic strengths were obtained at various pH at an initial chromate concentration of ca. 300 μM. Ionic strength was adjusted to 0.010 M or 0.70 M by $NaNO_3$ at each pH. The pH was adjusted by a 0.10 M NaOH or 0.10 M HNO_3 solution to desired values. After 24 h of equilibration at 25 °C, samples were filtered using 0.20 μm membrane filter. The filtrates were diluted adequately, and concentrations of chromate were measured by ICP-MS to obtain the amount of chromate adsorbed on ferrihydrite.

The adsorption envelopes for chromate on ferrihydrite are shown in Fig. 4.6. The result shows that the adsorption of chromate depends on pH, where the maximum chromate adsorption was found at pH 5. The pH dependence of adsorption of oxyanions is often related to the charges loaded on the solid phase and proton dissociation behavior of oxyacids. As for ferrihydrite employed as solid phase in this study, negative charges increase with the increase in pH (Langmuir 1997), where the adsorption amount of anion monotonously decreases if the form of the anion does not change. The maximum adsorption at pH 5 reflects the influence of acid dissociation behavior of chromic acid:

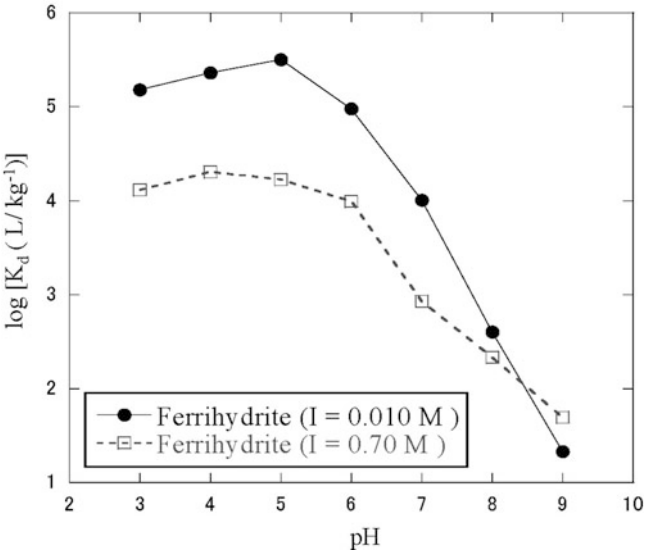

Fig. 4.6 Adsorption envelopes for chromate on ferrihydrite at I = 0.010 and 0.70 M

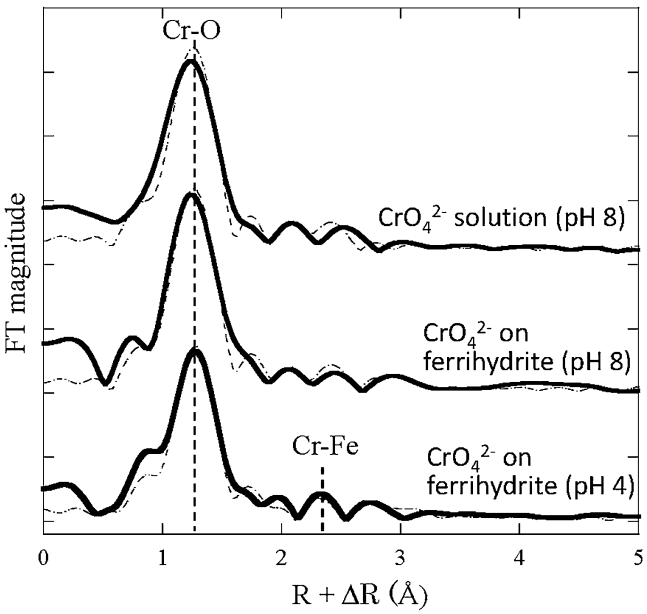

Fig. 4.7 Chromium K-edge EXAFS in R space for chromate solution and chromate adsorbed on ferrihydrite

the increase of K_d up to pH 5 was caused by its larger pKa_2 value for second dissociation ($pKa_2 = 6.51$). As the concentration of ionic strength ($NaNO_3$) increased from 0.010 to 0.70 M, the chromate adsorption on ferrihydrite obviously decreased (Fig. 4.6). The decrease of K_d by the increase of ionic strength suggests the formation of outer-sphere complex for chromate adsorbed on ferrihydrite (Hayes et al. 1988).

Figure 4.7 shows Cr K–edge EXAFS spectra, or their radial structural functions (RSF: phase shift not corrected)

Table 4.1 Structural parameters of chromate adsorbed on ferrihydrite and solution obtained by curve fitting of EXAFS spectra

Sample	Shell	CN	R (Å)	ΔE^o (eV)	σ^2	R factor (%)
Cr (VI)-solution (pH 8)	Cr-O	3.5	1.66	−2.56	0.003[a]	3.80
Ferrihydrite (pH 4)	Cr-O	3.3	1.66	1.63	0.003[a]	3.56
	Cr-Fe	0.40	3.33		0.002[a]	
Ferrihydrite (pH 8)	Cr-O	3.3	1.66	−2.38	0.003[a]	3.85

[a]Fixed value in the fitting process

for the chromate solution and chromate adsorbed on ferrihydrite. The adsorption samples on ferrihydrite at pH 4 and 8 were measured, where we found that all the spectra in Fig. 4.7 were almost the same. However, spectra of solution and adsorbed sample were slightly different. Although the position of the first shell (R = ca. 1.6 Å) are similar between solution and adsorption samples, a second shell at R = 2.8 Å was observed at pH 4. However, the peak is not evident at pH 8 and for chromate solution (Fig. 4.7).

The CN, interatomic distances (R), and Debye–Waller factors (σ^2) obtained from the curve–fitting analysis are summarized in Table 4.1. The parameters obtained for the sample at pH 8 was almost identical to those of the solution sample (Table 4.1). Although the spectrum for the adsorption sample at pH 4 was fitted well with Cr–Fe assigned as the second shell, the CN value was very small (ca. 0.4). These facts suggested that chromate is adsorbed on ferrihydrite mainly as outer–sphere complex with contribution of a small amount of inner–sphere complex at lower pH. This EXAFS data are consistent with what was estimated by the dependence of K_d on ionic strength.

4.6 Two pKa Model

The previous section has shown that chromate is adsorbed on ferrihydrite mainly as outer–sphere complex. In our previous studies, it was found that molybdate and tungstate are adsorbed on ferrihydrite as outer–sphere and inner–sphere complexes, respectively (Kashiwabara et al. 2011, 2013). In spite of possible similar chemical characteristics as congeners, chromate, molybdate, and tungstate are adsorbed on ferrihydrite by different attachment modes (i.e., inner– or outer– sphere). The attachment mode in turn is closely related to the solid–water distribution of the oxyanions as seen from the adsorption of chromate, molybdate, and tungstate (Figs. 4.1 and 4.4): tungstate which forms inner–sphere complex is largely distributed to the solid phase, but chromate and molybdate forming outer–sphere complexes are soluble due to the smaller affinity to the solid phase.

As suggested in Sect. 4.4, LFER has been utilized, in which equilibrium constant such as $\log K_d$ is proportional to that of pK_a of conjugate acids of oxyanions such as $HMoO_4^-$ for molybdate (MO_4^{2-}). In this context, Dzombak and Morel (1990) showed that the logarithm of intrinsic surface complex constant $K_{int\text{-}2}$ is linearly correlated with that of pKa_2 of such oxyacids (Fig. 4.4). The acid with low pK_a (= strong acid) prefers to release proton due to the high stability of hydration of the conjugate oxyanions, which results in the formation of outer–sphere complex as indicated above and vice versa. Hence, we compared pK_{a1} and pK_{a2} for various acids of divalent oxyanions such as Group A (SeO_4^{2-}, SO_4^{2-}, CrO_4^{2-}, MoO_4^{2-}) and Group B (WO_4^{2-}, TeO_3^{2-}, SeO_3^{2-}, $TeO_2(OH)_4^{2-}$, in Fig. 4.4. The former group prefers to form outer–sphere complex on ferrihydrite (Bigham et al. 1990; Harada and Takahashi 2008; Kashiwabara et al. 2011), while the latter inner–sphere complex (Harada and Takahashi 2008; Waychunas et al. 1993; Pokrovski et al. 2003; Kashiwabara et al. 2013).

As shown in Fig. 4.8, pK_{a2} rather than pK_{a1} value is correlated with the preference of inner–sphere complex. In the case of pK_{a1}, pK_{a1} values of conjugate acids of TeO_3^{2-} and SeO_3^{2-} are relatively low, but these anions mainly form inner–sphere complexes to ferrihydrite. On the other hand, pK_{a2} value can predict the formation of inner–sphere complex: oxyanions with pK_{a2} larger than WO_4^{2-} prefer to form inner–sphere complex (Fig. 4.4). However, the chromate which forms outer–sphere complex with larger pK_{a2} is exceptional in this relationship. Instead of pK_{a1} or pK_{a2}, we here propose that the average of pKa_1 and $pK_{a2}\left(= p\overline{K}_a = pK_{a1} + pK_{a2}\right)/2)$ can be more useful to predict the inner–sphere and outer–sphere complexation: conjugate anions of oxyacids having $p\overline{K}_a$ larger than H_2WO_4 prefer to form inner–sphere complex on ferrihydrite.

Inclusion of both pK_{a1} and pK_{a2} for this criterion is reasonable considering the structure of surface complexes. If these oxyanions such as chromate, molybdate, and tungstate form inner–sphere complexes, it is most likely that they form bidentate complex to the ferrihydrite surfaces via. two oxygens from the center atom as shown for molybdate and tungstate. The better correlation between the outer–/inner–sphere complex and $p\overline{K}_a$ rather than pK_{a1} and pK_{a2} means that both of two –OH groups of the oxyanion are responsible for the stability of its surface complex to the ferrihydrite surface. This fact is consistent with the structural data that they form bidentate surface complex to ferrihydrite: these divalent oxyanions are bound to the ferrihydrite surface via. two oxygens, if they form inner-sphere complex (e.g.,

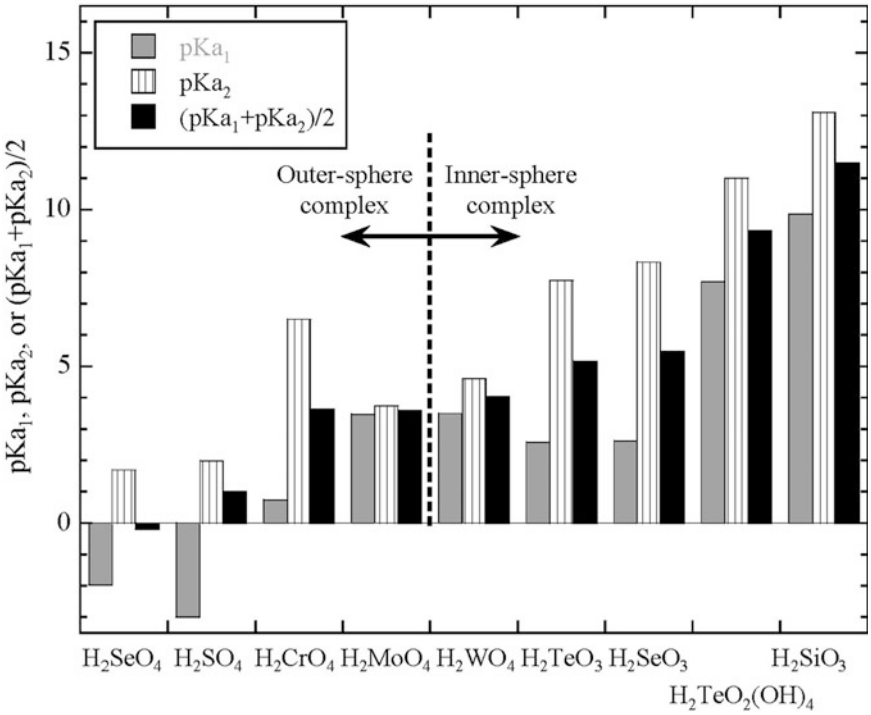

Fig. 4.8 The pKa values and attachment modes on ferrihydrite of various oxyanions

Kashiwabara et al. 2011; Kashiwabara et al. 2013). Thus, the chemical effect of both proton dissociation groups must be taken into account to evaluate the stability of the surface complex reflected in pKa_1 and pKa_2. Hence, $p\overline{K}_a = (pK_{a\,1} + pK_{a\,2})/2$ is shown to be useful to predict attachment mode of oxyanions to ferrihydrite.

4.7 Conclusions and Implications

In this review, it was clear that attachment mode of the surface complex is closely related to the solid-water distribution or the degree of enrichment to ferromanganese oxides for various elements. Moreover, attachment mode of the surface complex governs the isotopic fractionation of trace elements during the adsorption on solid phases indicated in Sect. 4.1. It has been indicated that adsorption reaction with outer-sphere complexations does not induce isotopic fractionation, possibly because the local structure of the element does not change by the adsorption reaction. However, formation of inner-sphere complex during adsorption can cause isotopic fractionation. For example, it has been indicated that molybdenum isotope can be fractionated by its adsorption on manganese oxides by the inner-sphere complexation, but not on ferrihydrite adsorbing molybdate ion as outer-sphere complex of hydrated ion (Kashiwabara et al. 2011). Similarly, adsorption of chromate does not cause large isotopic fractionation due to the outer-sphere complexation for the adsorption.

On the other hand, the adsorption structure can be systematically interpreted by the pKa value of conjugate acid and $\log\beta_{OH}$ for anions and cations, respectively. Hence, such systematic understanding of the adsorption reaction in terms of pKa and $\log\beta_{OH}$ enables us to predict the distribution and isotopic fractionation of various elements. Considering that the distribution and isotopic fractionation are very important for the understanding the behavior in marine environment, enrichment mechanism, and development of isotopic ratio as paleoenvironmental tool for various elements, systematic interpretation described in this study is useful in various geochemical aspects.

Acknowledgements This research was supported by a grant-in-aid for scientific research from the Ministry of Education, Science, Sports, and Culture of Japan including "TAIGA" project accepted as a Scientific Research on Innovative Areas. This work has been performed with the approval of JASRI (Proposal No. 2013A1177) and KEK (Proposal No. 2009G585 and 2011G635).

References

Bigham JM, Schwertmann U, Carlson L, Murad E (1990) A poorly crystallized oxyhydroxy sulfate of iron formed by bacterial oxidation of Fe(II) in acid mine waters. Geochim Cosmochim Acta 54:2743–2758

Bunker G (2010) Introduction to XAFS: a practical guide to X-ray absorption 0fine structure spectroscopy. Cambridge University Press, London

Cornell RM, Schwertmann U (2003) The iron oxides. Wiley-VCH, Weinheim

Cowan CE, Zachara JM, Resch CT (1991) Cadmium adsorption on iron-oxides in the presence of alkaline-earth elements. Environ Sci Technol 25:437–446. doi:10.1021/es00015a009

Dymond J, Lyle M, Finey B, Piper DZ, Murphy K, Conard R, Pisias N (1984) Ferromanganese nodules from MANOP Sites H, S, and R—control of mineralogical and chemical composition by multiple accretionary processes. Geochim Cosmochim Acta 48:931–949

Dzombak DA, Morel FMM (1990) Surface complexation modeling: hydrous ferric oxide. Wiley, New York, p 393

Elderfield H, Schultz A (1996) Mid-ocean ridge hydrothermal fluxes and the chemical composition of the ocean. Ann Rev Earth Planet Sci 24:191–224. doi:10.1146/annurev.earth.24.1.191

Harada T, Takahashi Y (2008) Origin of the difference in the distribution behavior of tellurium and selenium in a soil–water system. Geochim Cosmochim Acta 72:1281–1294

Hayes KF, Papelis C, Leckie LO (1988) Modeling ionic strength effects on anion adsorption at hydrous oxides/solution interfaces. J Colloid Interface Sci 125:717–726

Hein JR, Koschinsky A, Bau M, Manheim FT, Kang J-K, Roberts L (2000) Cobalt-rich ferromanganese crusts in the Pacific. In: Cronan DS (ed) Handbook of marine mineral deposits. CRC, Boca Raton, pp 239–279

Hein JR, Koschinsky A, Halliday AN (2003) Global occurrence of tellurium-rich ferromanganese crusts and a model for the enrichment of tellurium. Geochim Cosmochim Acta 67:1117–1127

Kashiwabara T, Takahashi Y, Tanimizu M, Usui A (2011) Molecular scale mechanisms of distribution and isotopic fractionation of molybdenum between seawater and ferromanganese oxides. Geochim Cosmochim Acta 75:5762–5784

Kashiwabara T, Takahashi Y, Matthew AM, Uruga T, Tanida H, Terada Y, Usui A (2013) Tungsten species in natural ferromanganese oxides related to its different behavior in oxic ocean from molybdenum. Geochim Cosmochim Acta 75:5762–5784

Langley S, Gault AG, Ibrahim A, Takahashi Y, Renaud R, Fortin D, Clark ID, Ferris FG (2009) Sorption of strontium onto bacteriogenic iron oxides. Environ Sci Technol 43:1008–1014. doi:10.1021/es802027f

Langmuir D (1997) Aqueous environmental geochemistry. Prentice Hall, Upple Saddle River

Li Y-H (1981) Ultimate removal mechanisms of elements from the ocean. Geochim Cosmochim Acta 45:1659–1664

Li Y-H (1982) Ultimate removal mechanisms of elements from the ocean (reply to a comment by M. Whitfield and D. R. Turner). Geochim Cosmochim Acta 46:1993–1995

Lyons TW, Anbar AD, Severmann S, Scott C, Gill BC (2009) Tracking Euxinia in the ancient ocean: a multiproxy perspective and proterozoic case study. Annu Rev Earth Planet Sci 37:507–534

Nakada R, Tanimizu M, Takahashi Y (2013) Difference in the stable isotopic fractionations of Ce, Nd, and Sm during adsorption on iron and manganese oxides and its interpretation based on their local structures. Geochim Cosmochim Acta 121:105–119

Peacock CL, Moon EM (2012) Oxidative scavenging of thallium by birnessite: explanation for thallium enrichment and stable isotope fractionation in marine ferromanganese precipitates. Geochim Cosmochim Acta 84:297–313

Pokrovski GS, Schott J, Farges F, Hazemann JL (2003) Iron (III)–silica interactions in aqueous solution: insights from X-ray absorption fine structure spectroscopy. Geochim Cosmochim Acta 67:3559–3573

Rahnemaie R, Hiemstra T, van Riemsdijk WH (2006) Inner- and outer-sphere complexation of ions at the goethite-solution interface J Colloid Interface Sci 297:379–388

Sander SG, Koschinsky A (2011) Metal flux from hydrothermal vents increased by organic complexation. Nat Geosci 4:145–150

Spadini L, Manceau A, Schindler PW, Charlet L (1994) Structure and stability of Cd2+ surface complexes on ferric oxides: 1. Results from EXAFS spectroscopy. J Colloid Interface Sci 168:73–86

Takahashi Y, Shimizu H, Usui A, Kagi H, Nomura M (2000) Direct observation of tetravalent Cerium in ferromanganese nodules and crusts by X-ray absorption near-edge structure (XANES). Geochim Cosmochim Acta 64:2929–2935

Takahashi Y, Manceau A, Geoffroy N, Marcus MA, Usui A (2007) Chemical and structural control of the partitioning of Co, Ce, and Pb in marine ferromanganese oxides. Geochim Cosmochim Acta 71:984–1008

Verlaan PA, Cronan DS, Morgan CL (2004) A comparative analysis of compositional variations in and between marine ferromanganese nodules and crusts in the South Pacific and their environmental controls. Prog Oceanogr 63:125–158

Waychunas GA, Rea BA, Fuller CC, Davis JA (1993) Surface–chemistry of ferrihydrite: Part 1. EXAFS studies of the geometry of coprecipitated and adsorbed arsenate. Geochim Cosmochim Acta 57:2251–2269

5 Evaluating Hydrothermal System Evolution Using Geochronological Dating and Biological Diversity Analyses

Hidenori Kumagai, Hiromi Watanabe, Takuya Yahagi, Shigeaki Kojima, Shun'ichi Nakai, Shin Toyoda, and Jun-ichiro Ishibashi

Abstract

To elucidate the evolution of hydrothermal activities, we conducted an interdisciplinary study including geochemistry and biology to develop a method of obtaining reliable age information. As geochemical dating techniques, two methods applicable for hydrothermal ore minerals were developed and improved: electron spin resonance method and uranium–thorium disequilibrium method. Cross checks between the two methods generally showed good agreement for the range of hundreds to thousands of years. As biological analysis, the biodiversity among faunal communities in the targeted areas was analyzed at the species and DNA levels. Species and genetic diversity of the local fauna were not always correlated to geochemical dating, either in the southern Mariana Trough region or in the Okinawa Trough region. Although the results are not simple, comparison of age information obtained from analyses of these two disciplines potentially provides important constraints for discussion of the history and evolution of hydrothermal activities.

Keywords

Biodiversity • ESR • Geochronology • Life-span of hydrothermal activity • Mitochondrial mismatch analysis • U-Th disequilibrium

H. Kumagai (✉)
Submarine Resources Research Project, JAMSTEC, Yokosuka, Japan

Institute for Research on Earth Evolution, JAMSTEC, Yokosuka, Japan

Present address: R&D Center for Submarine Resources, JAMSTEC, Yokosuka, Japan
e-mail: kumagai@jamstec.go.jp

H. Watanabe
Department of Marine Biodiversity Research, JAMSTEC, Yokosuka, Japan

Institute of Biogeosciences, JAMSTEC, Yokosuka, Japan

T. Yahagi
Graduate School of Frontier Sciences, The University of Tokyo, Kashiwa, Japan

Atmosphere and Ocean Research Institute, The University of Tokyo, Kashiwa, Japan

S. Kojima
Atmosphere and Ocean Research Institute, The University of Tokyo, Kashiwa, Japan

Graduate School of Frontier Sciences, The University of Tokyo, Kashiwa, Japan

S. Nakai
Earthquake Research Institute, The University of Tokyo, Tokyo, Japan

S. Toyoda
Okayama University of Science, Okayama, Japan

J.-i. Ishibashi
Submarine Resources Research Project, JAMSTEC, Yokosuka, Japan

Faculty of Sciences, Kyushu University, Fukuoka, Japan

J.-i. Ishibashi et al. (eds.), *Subseafloor Biosphere Linked to Hydrothermal Systems: TAIGA Concept*,
DOI 10.1007/978-4-431-54865-2_5,

5.1 Introduction

Deep-sea hydrothermal systems have strongly attracted broad interest from science since their discovery in the late 1970s (e.g. Hessler and Kaharl 1995). The time scale for hydrothermal activity is an important factor to estimate the extent of hydrothermal deposits and the evolutionary process of chemosynthesis-based communities in submarine hydrothermal systems. The chemical flux from hydrothermal systems constrains the supply of substances fostering chemosynthesis-based communities. Therefore, flux intensities affect the biogeochemical reactions and the biological diversities in vent areas. The geochemical diversity observed in vent fluids can be elucidated as a result from scavenging process of the infiltrated seawater, frequently forming impressive chimney structures on the seafloor (e.g. Tivey 1995). Such infiltrated seawater, passing through the subseafloor environment, contains complex biogeochemical ingredients extracted from host formations up to the wider regional scale (e.g. Tsuji et al. 2012). The circulation of hydrothermal systems between seawater and the subseafloor environment has played an important role in the geochemical evolution of the earth. It has provided volatiles and metals that have sustained unique communities and ecosystems in hydrothermal areas from the beginning of Earth's ecosystems (e.g. Rasmussen 2000).

The dating of divergence events and the evolutionary timescale from phylogenetic analysis remains difficult because the molecular clock to estimate a rate of molecular evolution can vary markedly over time and among species. Although a common calibration method of molecular clock is an examination of the fossil record (e.g. Cruzan and Templeton 2000; Smith et al. 2006; Weir and Schluter 2008), fossil evidence of hydrothermal vent communities is rare because of the destruction of vent fauna by hydrothermal activity itself. Other methods of calibrating the molecular clock in gene sequences of hydrothermal vent fauna might be geochronological dating techniques of hydrothermal ore minerals and geological events.

A few studies have been conducted to constrain the lifetime of activity at hydrothermal sites (e.g. Jamieson et al. 2013, and references therein). Such a small amount of constraint is partly attributable to the limited availabilities of numerical dating methods applied to the hydrothermal deposits at inactive sites directly: a gap of 10^2–10^3 years (Jamieson et al. 2013). One early trial of geochronology is reported by Lalou et al. (1985). They applied ^{210}Pb–Pb and ^{230}Th–^{234}U disequilibrium method to sulfide deposits collected on and near the ridge axis. The determined ages were as high as 2,100 years. Another trial is on TAG-site, which develops slightly off the MAR-axis in 26°45′N (Rona 1984). You and Bickle (1998) reported precipitated age variation within the hydrothermally formed "mound" at the TAG-site, which exceeds 10 ka for core samples obtained in ODP Leg158. Some efforts to generalize these results for ordinary hydrothermal systems have been undertaken for the following reasons: (1) unusually large size of mounds within present-day hydrothermal mounds and (2) the slow spreading environment in which TAG is formed. The former point implies that the duration of the hydrothermalism beneath TAG is unusually long-lived or vigorous or both. Consequently, coupling of methodological challenges to produce reliable age information was conducted for the TAIGA project (Urabe et al. Chap. 1).

Here, the expected life cycle of hydrothermal system ranges from approximately a few years to a few tens of thousands of years. Such a range demands some composite dating protocol for ore minerals. Therefore, we first developed and improved two radiometric dating methods for application to hydrothermal deposits consisting mainly of sulfides and sulfates. Once we achieved such a method, we were able to couple them with ecological analyses to develop a comprehensive analytical protocol to obtain reliable age and duration information related to hydrothermal systems in much broader spectra of hydrothermal activities. For a much longer time range, $>10^5$ years, K–Ar/Ar–Ar methods are applicable. Consequently, in all, the investigated time-span ranged from a few years to a few millions years (Fig. 5.1). The methods developed in our project were applied to two Intensive Survey Sites (ISSs) of the entire "TAIGA" project, of which the results are also reported in this volume (Fujiwara et al. Chap. 34; Ishibashi et al. Chap. 23).

To conduct these studies, the following difficulties to be solved were recognized at the beginning of our project. The first is raised from the phylogeographic aspect. A dearth of precise information related to the molecular evolutionary rates (mutation rate) in genes might cause a discrepancy of interspecies or intraspecies phylogeography. Dispersal and transition events of vent fauna in hydrothermal system are affected strongly by many environmental constraints such as water depths, temperatures, deep-sea currents, and geochemical conditions. Not only calibration methods for such uncertainty but also investigations of life cycles for the vent endemic species must be conducted to produce better phylogeographic information. The latter must be pursued from a geochronological perspective. To obtain reliable numerical ages, a closed system is normally required. However, it is apparently easily disturbed for the samples of ore minerals in the vicinity of the hydrothermal vents. Near active vents, a non-steady and sometimes intermittent supply of vent fluid might occasionally replace the ore minerals once they have been formed. Further abrupt heating influenced by higher temperature fluids might break its closed system, causing a loss of accumulated daughter nuclei or erasure of radiation-related signals used in radiometric dating. These concerns are discussed in later sections.

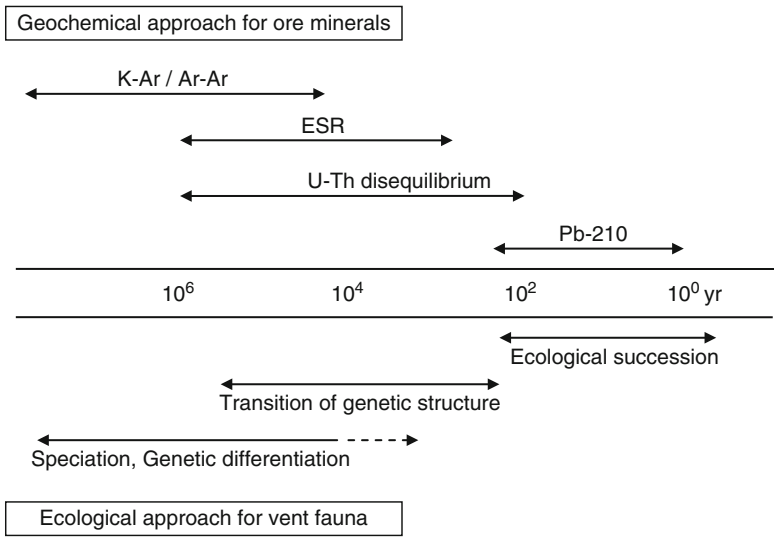

Fig. 5.1 Targeted age ranges of respective dating methods

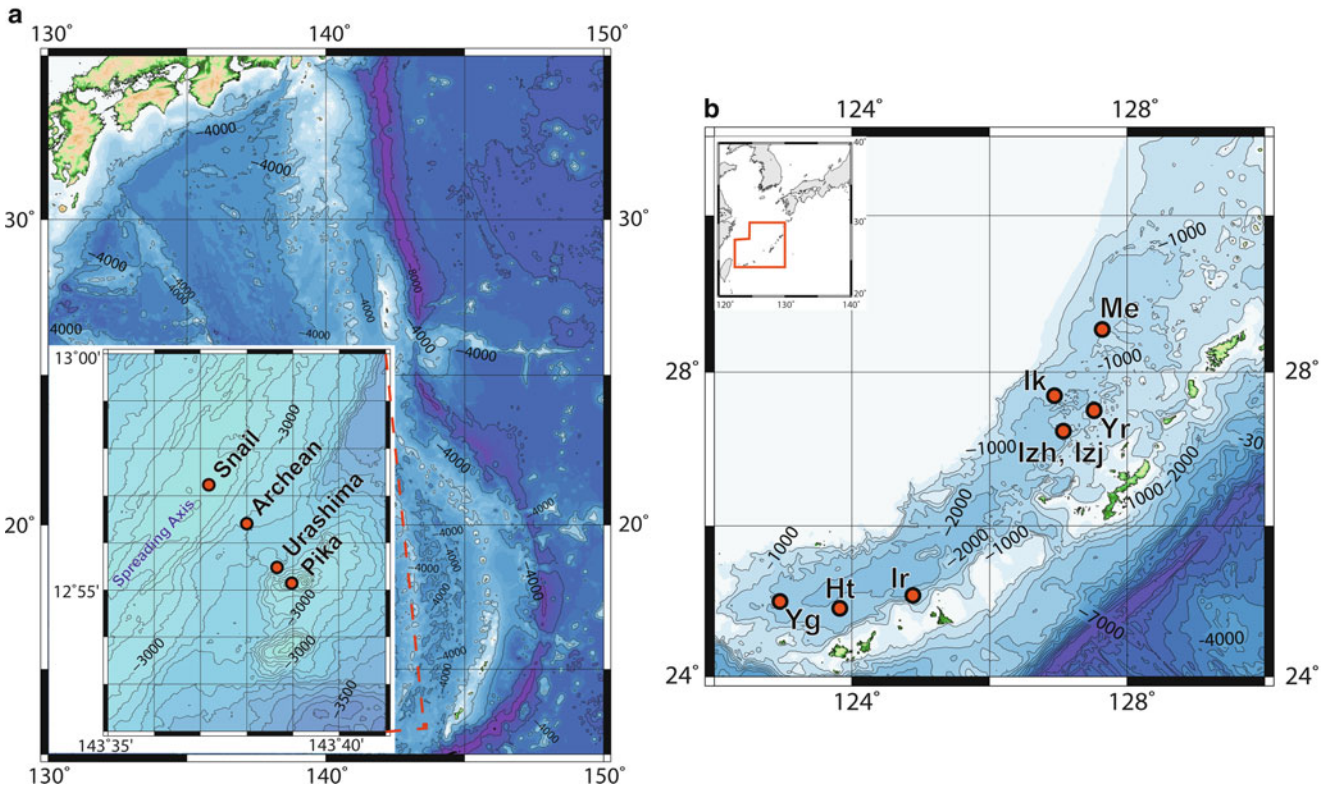

Fig. 5.2 Topographic maps of the studied area according to the global dataset of topography model, ETOPO1 (Amante and Eakins 2009). (**a**) Southern Mariana Trough. Studied hydrothermal sites and current spreading axis are shown in the inset, with the magnified area shown in red box on main panel. This local topography was obtained by R/V Yokosuka of JAMSTEC, at YK09-08 Cruise. Detailed descriptions are from a report by Seama et al. (Chap. 17). (**b**) Okinawa Trough. Studied hydrothermal sites are shown as follows: Yg, Daiyon-Yonaguni Knoll; Ht, Hatoma Knoll; Ir, Irabu Knoll; Izh, Hakurei-site in Izena Hole; Izj, JADE-site in Izena Hole; Ik, Iheya North Knoll; Yr, Yoron Hole; Me, Minami-Ensei Knoll. Detailed descriptions were given by Ishibashi et al. (Chap. 29)

The targeted areas for this study were two of three focused areas of the TAIGA-project: the Southern Mariana Trough and Okinawa Trough (Fig. 5.2). In these areas, very active hydrothermal activities have been located (Seama et al. Chap. 17; Ishibashi et al. Chap. 29). The third focused area of TAIGA-project, hydrothermal fields in the central Indian Ocean, is unsuitable for this study because only two active sites have been recognized at the beginning of the project (Nakamura et al. Chap. 12).

5.2 Development of Dating Methods

5.2.1 Geochemical Approach for Ore Minerals

In our project, two geochronological methods to be applied to the hydrothermal ore minerals consisted mainly of sulfides and sulfates were newly developed: (1) electron spin resonance dating (ESR dating) was applied mainly to barite ($BaSO_4$) (Fujiwara et al. Chap. 34; Toyoda et al. 2012), and (2) uranium–thorium disequilibrium dating (U–Th dating) was applied to hydrothermal sulfide minerals consisting mainly of pyrite and sphalerite (Ishibashi et al. Chap. 23; Takamasa et al. 2013). Both methods applied to the samples from the southern Mariana Trough generally showed good agreement in their ages (Fig. 5.3). This issue is discussed in a later section in detail.

Here the ESR-dating is based on the accumulation of unpaired electron in the sample specimen induced by irradiation of high-energy particles and exposure to electromagnetic waves. Such irradiation mainly results from gamma-ray radiation resulting from the strong attenuation for charged particles in seawater. Consequently, the estimation of annual irradiation rate from ore deposits themselves is crucially important to calculate the irradiation age. Where the external radiation was effectively shielded by seawater, an approximation incorporating the internal radiation generated in and around ore precipitates is expected to be sufficient. In addition, ^{226}Ra in barite of a black smoker is unsupported (decaying) because ^{230}Th is negligible in black smokers as a result of its valence and charges, which considerably simplifies the determination of the ages of the target minerals. Here, Ba serves as a proximal stable isotope for Ra that has no stable isotopes of its own. In fact, ^{226}Ra/Ba in chimney deposits will decrease as a result of radioactive decay of ^{226}Ra after their formation. Within sulfate minerals, barite was chosen as the target mineral because the obtained signals are clear. To estimate the in-situ dose-rate in a deep-sea environment, we calibrated yields of the ESR signals in a known/measured dose-rate as reported by Toyoda et al. (2012). Such a dose rate includes α-radiation using an Al_2O_3-target. The target tube was deployed near an active vent site in the Mariana Trough and was left for 29 days. Subsequently, it was retrieved for calibration. Details were reported by Toyoda et al. (2012).

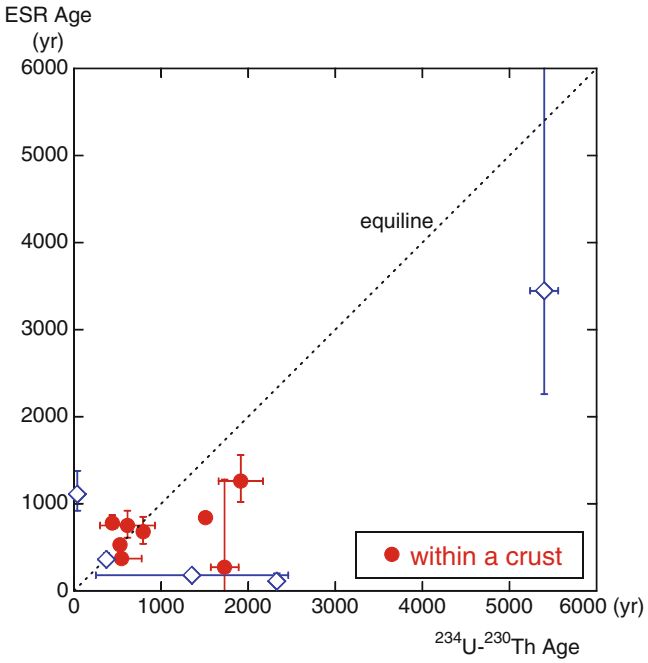

Fig. 5.3 An age comparison obtained using two geochemical methods: U–Th disequilibrium and ESR. Samples used were collected in the Southern Mariana Trough. Aliquots taken from a single crust to check reproducibility of the methods are shown in *red circles* (Takamasa et al. 2013). Other U–Th data, shown as open diamonds, were taken from a report by Ishibashi et al. (Chap. 23), compared to unpublished ESR data (Fujiwara et al. Pers. Comm.). Here in the case in which the ages obtained from both methods mutually agree, such data are shown on the "equiline"

The obtained ESR ages from the TAIGA project have also been reported in this volume (Ishibashi et al. Chap. 23; Fujiwara et al. Chap. 34). The determined ages for the samples from the southern Mariana Trough were 1.5×10^2–5.3×10^3 years; those from the Okinawa Trough were 4.0–1.6×10^4 years.

The second one is the U–Th dating, which uses the deviation of radioactivity from the radioactive equilibrium. A well known characteristic of the radioactive decay series under secular equilibria is that the specific radioactivities of parent and daughter elements are equivalent. Before reaching this state, i.e. under transient equilibrium, the radioactivity of the daughter element is markedly less than that of the parent nuclei. During our project, a ^{234}U–^{230}Th system was adopted; respective half-lives ^{230}Th and ^{234}U are 7.6×10^4 years and 2.5×10^5 years. Here, thorium is less soluble in hydrothermal fluids and is not precipitated in hydrothermal minerals, although uranium is precipitated in these minerals. Therefore, ^{230}Th in the mineral simply accumulates from ^{234}U over time, which provides a criterion of the evaluation of data quality. In general, the direct determination is based on the radioactivity measurement, but the radioactivity of the targeted nuclei of the focused system is low because the half life of ^{238}U, their ultimate parent, is much longer, $>4.5 \times 10^9$ years. Consequently, direct measurements of the abundances of ^{234}U and ^{230}Th were applied in our TAIGA project, which required development of the precise quantification on trace amounts of both ^{230}Th and of ^{234}U. Because of the half-lives of our targeted parent–daughter pair, our method can be used to calculate the ages of minerals as young as 50 years when a

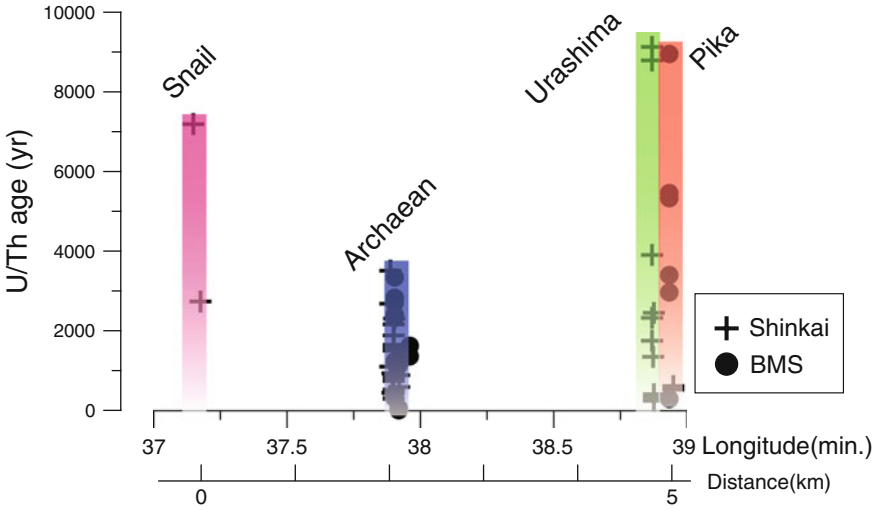

Fig. 5.4 Compiled geochemical ages obtained in Southern Mariana Trough. Original data were reported by Ishibashi et al. (Chap. 23). The Snail site is on the current ridge axis. The distance from the ridge axis is shown as an alternative horizontal-axis in kilometer units

sample contains sufficient uranium but little thorium. However, the upper limit of the range of this dating method is limited to 4.0×10^5 years, which is around eight times the half life of the daughter: ^{230}Th.

Detailed protocols of U–Th dating were reported by Takamasa et al. (2013). We analyzed uranium and thorium isotope ratios in mineral specimens using a Multicollector-ICP-MS (IsoProbe; GV Instruments Ltd.). The powdered and sieved ore samples were separated electromagnetically using an isodynamic separator to concentrate pyrite and other sulfide minerals. Two mesh ranges were adopted for this study: 100–250 and 250–500 μm (see also Fujiwara et al. Chap. 34). Then, the chemically leached specimens were rinsed, dried, and decomposed using nitric acid. Before the ICP-MS measurements, uranium and thorium were separated from sample solutions under two steps of column chromatography. During this process, barium (Ba) and lead (Pb) were also separated carefully to suppress their interference of signals from targeted isotopes: ^{234}U or ^{230}Th.

We determined the ages of hydrothermal deposits samples, with each sample collected by submersible or as a drilled core from the southern Mariana Trough and Okinawa Trough. In the southern Mariana Trough, samples were collected from four sites on and near ridge axis: Snail, Archean, Urashima and Pika sites. The determined U–Th ages were < ca. 7,200 years, ca. 3,500 years, ca. 9,100 years and ca. 9,000 years, respectively (Fig. 5.4). These ranges are shorter than that of the TAG mound (You and Bickle 1998). Here the samples from the Snail site contain low uranium, which raises a concern about a significant loss of uranium from the ore minerals occurring after their formation. Aside from one exceptionally old sample from the Snail site, samples from the Archean site show younger ages than those from the Urashima or Pika sites. This result suggests that the oldest ages from each site are apparently correlated with the distance from the spreading axis in Mariana Trough, at least in off-axis activity (Fig. 5.4). The ESR ages were consistent with the U–Th ages (Takamasa et al. 2013).

In the Okinawa Trough, it is difficult to find such a simple relation with a geographical position of the vent area, e.g. with distance from the spreading axis. The Okinawa Trough is still in the early rifting stage before the normal seafloor/backarc spreading (Ishibashi et al. Chap. 29 and references therein). Therefore, no clear spreading center is apparent yet. The respective ranges of the determined ages of vent deposits are up to 11, 18, 144, 97, and 12 ka for Daiyon-Yonaguni Knoll, Hatoma Knoll, Hakurei-site of Izena-Hole, Iheya North Knoll, and Yoron-Hole (Fujiwara et al. Chap. 34). All ranges include one or two extremely old values, as discussed later. The longest duration of hydrothermal activity was estimated for Hakurei-site of Izena Hole, 16,000 years, even excluding one extreme value. The Izena Hole is a tectonically formed seafloor depression. It might be influenced by rather long activity of the Hakurei-site in the same order of magnitude as that of the TAG mound reported by You and Bickle (1998).

5.2.2 Comparison between ESR and U–Th ages

The selected age pairs determined using ESR and U-Th methods for samples from active hydrothermal fields of Southern Mariana Trough are presented in Fig. 5.3. The U-Th ages were obtained from sulfide minerals that had been sieved and magnetically separated (mostly pyrite and sphalerite). The ESR ages were from barite that had been concentrated from sulfide-rich breccia. Some sulfide samples, from the Archean site, are also analyzed using the ESR method for cross-checking. The ages obtained using the two methods mostly show a correlation in the

diagram. Both ages are well matched down to the order of hundreds of years (~10^2 years). This time range is well within the range of the vent complex consisting of several feed paths in the particular field. Although the reason causing the discrepancy remains unclear, the ESR ages tend to be lower than U–Th ages in the case of Southern Mariana sulfides (Fig. 5.3). This phenomenon might be the result of the robustness of a closed-system of each method. Here ESR signals might be reset by thermal disturbances, whereas U–Th ages might be disturbed by the dissolution or the adsorption of targeted isotopes.

To interpret the obtained ages, special caution for extremely old U–Th ages should be discussed. One remarkable case is that of a sample from the Snail site in the southern Mariana Trough. The old U–Th age was obtained from only one very-low-U sample, <50 ppb of ^{238}U at the site (Ishibashi et al. Chap. 23). This low U concentration suggests a loss of uranium after their precipitation, which is apparently consistent with much younger ESR ages determined at the site up to 110 years. It might be result of acidic fluid recurrence to minerals once precipitated, where oxidized uranium becomes soluble again. In the Okinawa Trough, more than five samples also contain such low uranium. However, extreme U–Th ages remain for all sites (Fig. 5.5). Another possibility is sediment contamination during and after formation of the analyzed deposits. For further comparison with ecological information, extreme ages of all the sites should be treated carefully. Therefore, in the Okinawa Trough, age ranges are up to the 16,000 year, as shown in colored bars in Fig. 5.5.

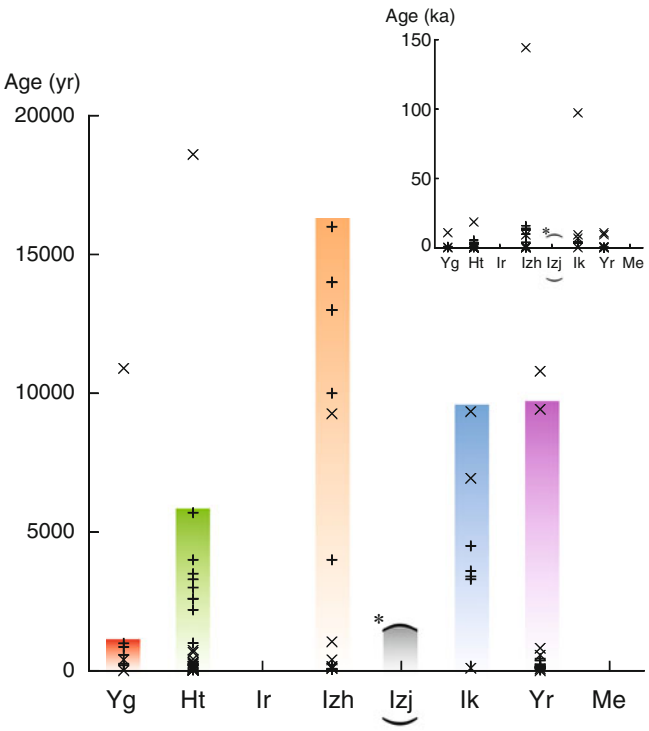

Fig. 5.5 Geochemical age range determined from the sulfide and sulfate deposits in Okinawa Trough. Active sites are shown from approximately SW to NE. The left-hand side is the southwestern end. Here, all obtained ages including extremely old two values are shown in the *inset*. Colored bars represent reliable age ranges for respective sites. The localities are denoted as described for Fig. 5.2b. Age data of JADE site in Izena Hole were not obtained in this study. Consequently, the data range is in parenthesis and denoted by a "*" symbol (Zeng et al. 2009)

5.2.3 Ecological Analyses of Vent Fauna

The estimation for evolutionary processes of hydrothermal activities has been done using three biological features: (1) species diversity of vent fauna, (2) genetic diversity of a population, and (3) speciation events (Fig. 5.1). The species diversity fluctuates in the change of habitat conditions. In the case of hydrothermal systems, drastic ecological succession starts from a newly created vent site or a sterilized site after volcanic eruption (Govenar 2010; and references therein). The first majority of inhabitants at this primary stage includes thermophilic prokaryotes (Lutz et al. 1994; Shank et al. 1998). Planktonic larvae or adults of vent-specific faunal species migrate from other vent areas, settle on a suitable niche, and gradually make a large and complex-structured faunal aggregation with high diversity of species. Therefore, high species diversity was only observable in continuous vent fields. Species diversity of vents conveys the short-scale fluctuation of vent activity.

Once an organism settles in a suitable environment of the vent field, the demographic expansion of the fauna begins. The genetic diversity of a population should be correlated positively with its effective population size (number of individuals involved in reproduction), and it is regarded as tracer of past demographic expansion of a population (Rogers and Harpending 1992). Therefore, the genetic diversity of a population can be an estimator of the past population expansion after settlement of vent species, or formation of a vent environment that is suitable for the species. The temporal change of genetic variation can be examined using a molecular clock hypothesis, which has been used to estimate divergence times. The molecular clock hypothesis states that DNA and protein sequences evolve at a mutation rate, which is constant over time and among populations. For example, the partial sequence of mitochondrial cytochrome oxidase c subunit I (COI) gene, which is commonly used as a barcode of species, has been investigated. Reportedly 1.4 % sequence divergence per 10^6 years occurred on the gene sequence of snapping shrimp (Knowlton and Weigt 1998). However, the rates of accumulation of genetic variation are not the same among

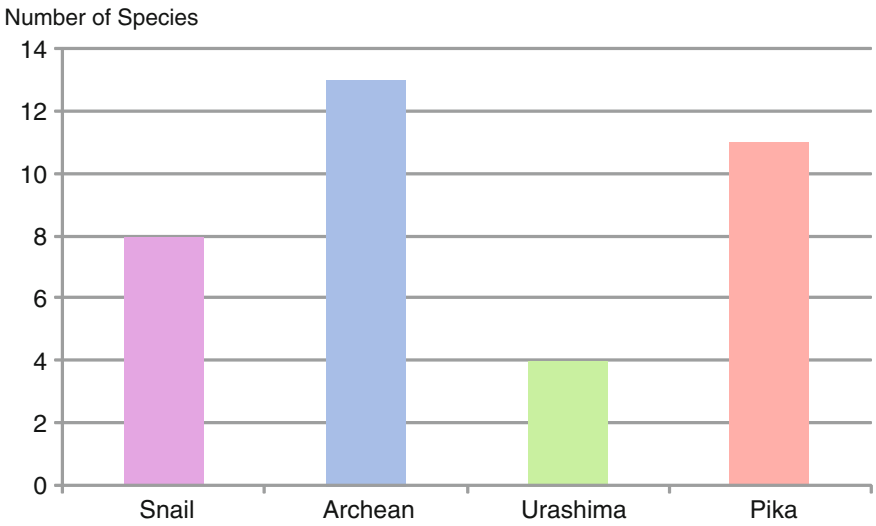

Fig. 5.6 Number of species collected at active hydrothermal sites in the southern Mariana Trough

species (e.g. large animals have lower genetic diversity than small ones; Beebee and Rowe 2008), and the dating of vent activity with genetic diversity can only provide relative ages for many species.

The expanded population might be divided into two or more subpopulations either sympatrically or allopatrically. Without gene exchange or connectivity among the subpopulations, genetic differentiation accumulates and eventually causes speciation, which is an irreversible event. With calibration of the molecular clock, speciation ages of some vent animals have been estimated in million year order with geologic events (Shank et al. 1999; Johnson et al. 2006, 2010). Estimation of the speciation date of vent species provides the longest scale.

To investigate the relation between biodiversity described above and hydrothermal activity, we examine the dataset of species diversity as well as genetic diversity based on partial COI sequences of vent species in the southern Mariana Trough and the Okinawa Trough.

In the Southern Mariana Trough, six active hydrothermal sites have been found in all. Four sites, located linearly across the spreading axis, were specifically examined in this study. In these four sites, the fauna associated with the Archean sites accounted for the largest number of species (Fig. 5.6), which implies that the present vent-related community of the Archean site has a longer history than those of other three sites, even though the number of species was almost half of those in the Central Mariana Trough (see Kojima and Watanabe Chap. 26). In addition, the evenness or relative abundance is important to assess the biodiversity and community structure. Nevertheless, no quantitative analysis has been reported in this area. The Archean site develops at the greatest water depth (2,990 m) among the four Southern Mariana sites between the current spreading axis and an off-axis seamount. The biodiversity of the particular vent field might depend partly on the water depth developed, although differences in sampling efforts or temporal changes might also affect the results. Comparison of genetic diversity as a mismatch distribution (Fig. 5.7), which describes mismatches among paired sequences in a population consisting of a single species, shows the difference of relative ages of population expansion. *Alviniconcha* gastropods and *Neoverruca* barnacles clearly show the greater genetic diversity with greater distances from the ridge axis (Fig. 5.7a, c). However, *Chorocaris* shrimps showed two peaks in their mismatch distribution (Fig. 5.7b) reflecting their complex history in the southern Mariana Trough vent fields, such as population subdivision and re-connection. Using a molecular marker with higher resolution capability than the COI gene, such events were also shown to have occurred for *Alviniconcha* gastropods in the Mariana Trough (Hidaka et al. Chap. 27). This evidence might show some events such as decrease of hydrothermal activity in the Mariana Trough about 1 Ma: details are presented by Hidaka et al. (Chap. 27).

In the Okinawa Trough, a comprehensive investigation of vent fauna with quantitative sampling and geochemical measurements was conducted as a part of TAIGA project. The faunal list in the vent fields in the Okinawa Trough was updated (Watanabe et al. Chap. 40). The number of species recorded is the highest in vent fauna in the Minami Ensei Knoll, although it is low in the Yoron Hole and Irabu Knoll (10 and 14, respectively; Fig. 5.8). These two sites were discovered recently (Fukuba et al.; Chaps. 47 and 48). Additional surveys should be conducted to confirm this result. Otherwise, they were actually newly established hydrothermal activities. The fauna might be represented by rapidly colonized species. Indeed, one representative of these fauna, *Shinkaicaris leurokolos*, shows high genetic diversity in all examined vent fields,

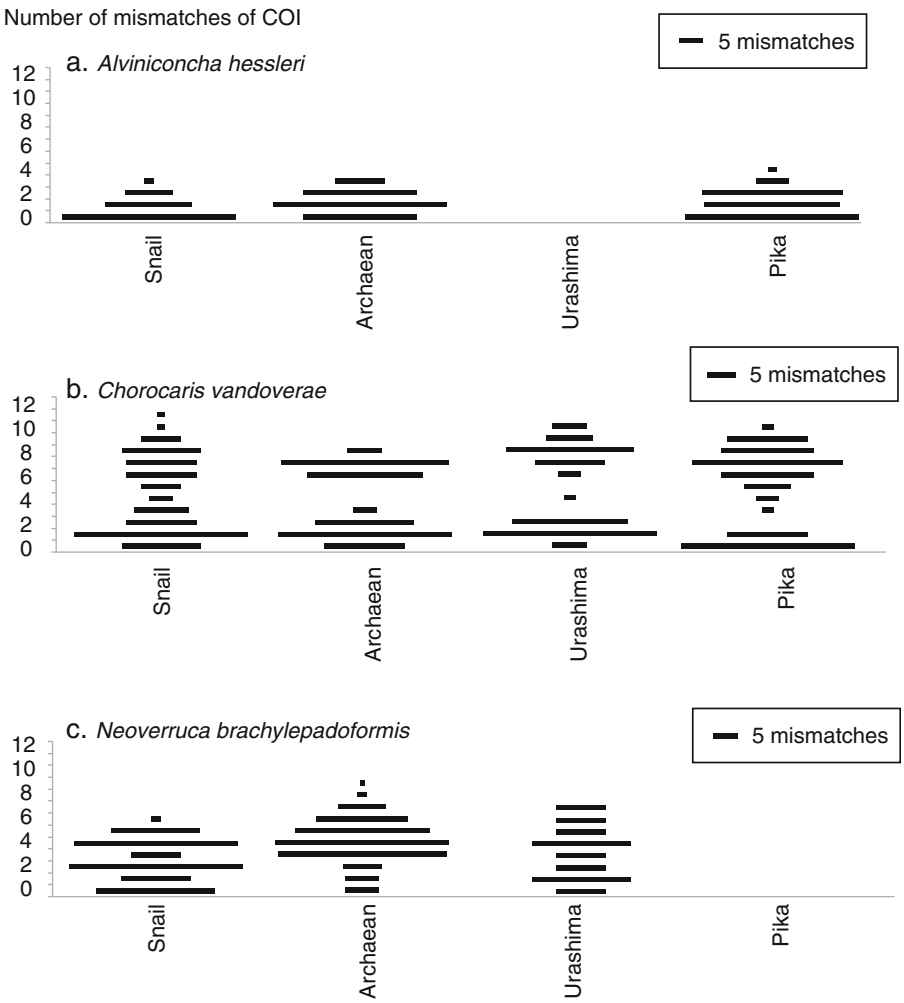

Fig. 5.7 Genetic divergence of COI gene indicated as mismatches in base sequences among three vent endemic species in the Southern Mariana Trough. *Scale bars* are shown as five mismatches of partial COI sequences

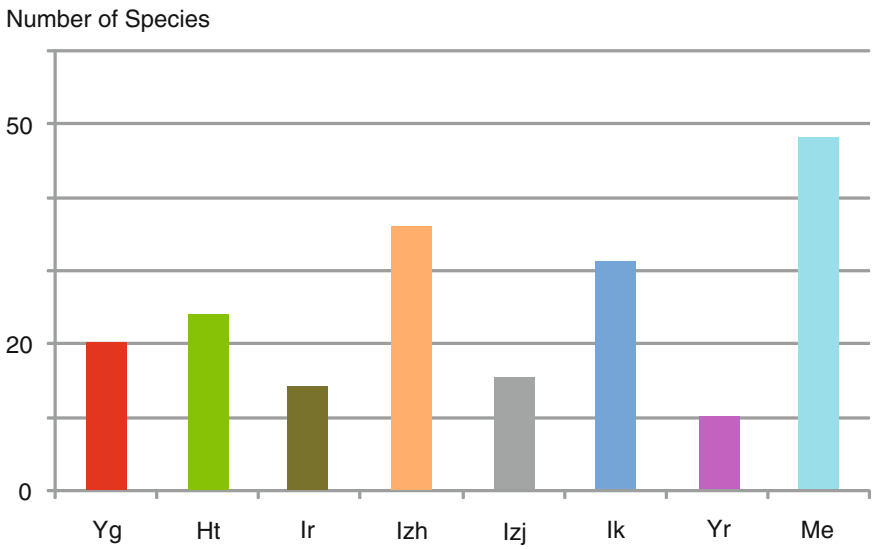

Fig. 5.8 Numbers of species collected at active hydrothermal sites in Okinawa Trough. Localities are denoted as described for Fig. 5.2b

implying high fecundity in a short period because genetic diversity is generated only in embryonic production and because life-history strategies strongly affect genetic diversity (Fig. 5.9). This aspect will be discussed in the next section through comparison with geochemical dating results.

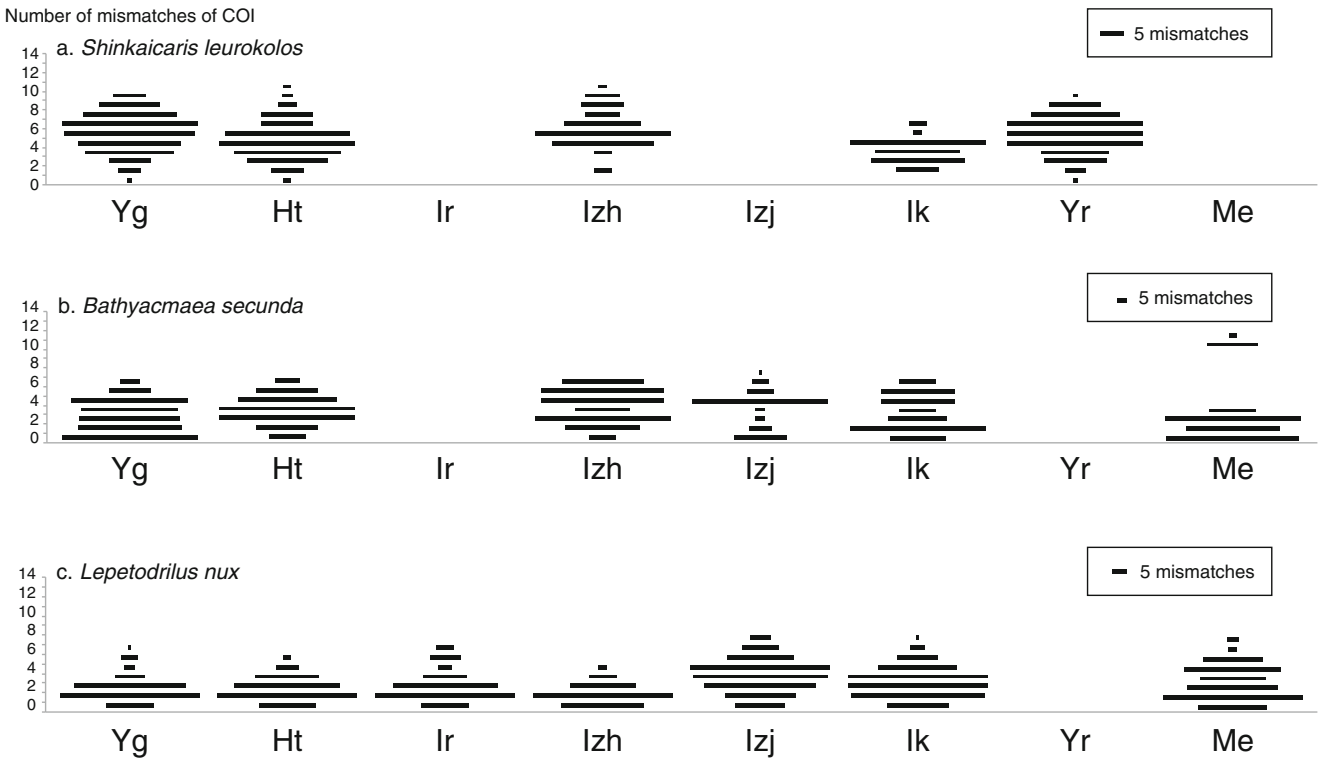

Fig. 5.9 Genetic divergence of COI gene indicated as mismatches in base sequences among three vent endemic species of the Okinawa Trough. (**a**) *Shinkaicaris leurokolos*, (**b**) *Bathyacmaea secunda*, (**c**) *Lepetodrilus nux*. Localities are shown as in Fig. 5.2b. *Scale bars* are shown as five mismatches of partial COI sequences

5.3 Comparisons Between Ecological and Geochemical Age Information

As a challenge to estimate the evolution history of hydrothermal system in the aspect of the relations between geochemical environment and ecological responses, a comparative analysis of the chronological information obtained both from geochemical dating and from ecological analyses was conducted.

Results obtained from two different approaches were not simply comparable even under a simple geographical setting in the southern Mariana Trough. From the geochemical data, the ages of the hydrothermal sites composed of multiple vents were fairly correlated with the distance from the present day's spreading center where the seafloor is newly formed, which implies that the durations of the faunal communities could be longer in the distant vent field from the spreading axis. However, that inference is not fully supported by the ecological approach. The vent endemic communities might be severely damaged or exterminated if the older vent field experienced later eruption or seafloor renewal by lava flows. Such is not the case of an observed reversal in the numbers of species between Archean and Urashima/Pika sites because such seafloor renewal is not implied at the Urashima/Pika site, but it is at the Archean site, as indicated by high magnetization (Fujii et al. 2013). Another complexity is apparent from the genetic diversity at the Snail site: it is as large as those at the other three sites (Fig. 5.7b, c). This point is partly supported by the rather old age, up to 7.2 ka, at the Snail site, although only one exceptional datum shows such an old age. In contrast, a phylogeographical approach suggests a 0.2–1.0 Ma history for populations in the area (Hidaka et al. Chap. 27). This discrepancy has yet to be investigated.

Furthermore, a complicated situation was observed in the Okinawa Trough. *Bathyacmaea secunda* as a vent endemic species showed greater genetic diversity at the Hakurei site in the Izena Hole, which was indicated as the number of mismatches of the COI sequences (Fig. 5.9b). It is apparently consistent with the longer life of the vents at the Hakurei site estimated as exceeding 16 ka from geochemical data. However, genetic diversities of the *Shinkaicaris* at Daiyon-Yonaguni Knoll were as great as those at Yoron Hole, although their ranges of geochronological ages were different. They were also considerably younger than results show for the Hakurei-site (Figs. 5.5 and 5.9a). This point might be explained by the high-larval dispersal potentials of the species, resulting in a higher rate of gene flow among local populations. In terms

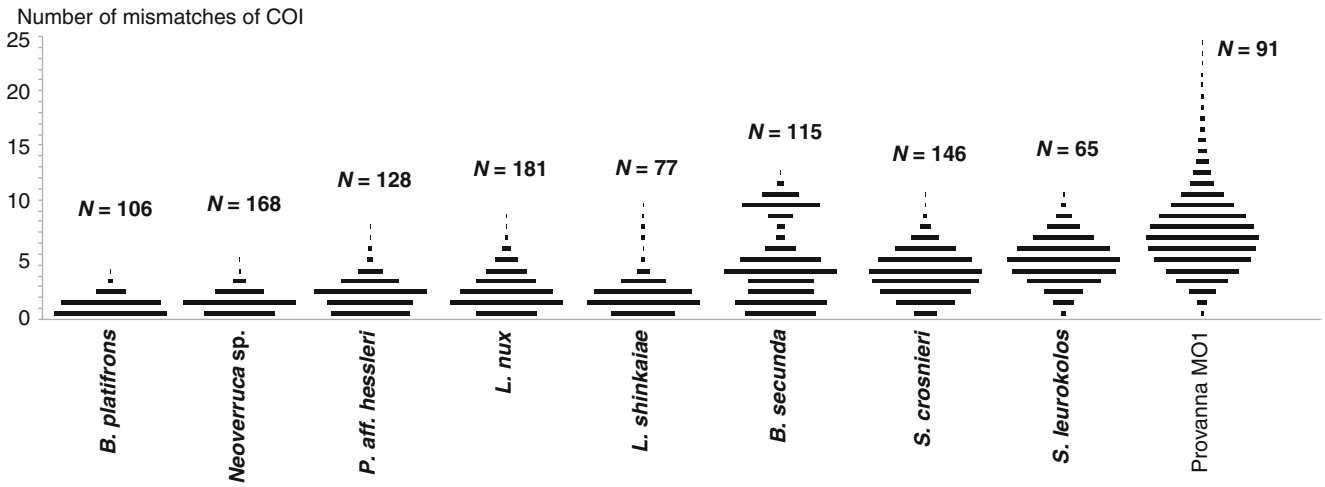

Fig. 5.10 Genetic mismatch diagram of COI gene sequences for typical faunal species in Okinawa Trough. This diagram shows entire variations for each species counted in the Okinawa Trough; the analyzed number of individuals is shown as *N*

of the inter-species comparison, the trend in genetic diversities of local populations of two limpets *Bathyacmaea secunda* and *Lepetodrilus nux* differed. Higher genetic diversity was observed in the southern populations in *Bathyacmaea secunda*, but lower genetic diversity was observed in the same ranges of populations in *Lepetodrilus nux* (Fig. 5.9b, c). Ecological features of vent faunas are necessary for more precise estimation of biological and geological histories of vent fields.

The trends of diversity are also different among species, even for similar animals inhabiting areas that are close to each other (Fig. 5.10). This result indicates that the genetic diversities of the species positioned on the right-hand side develop quickly. However, those of species on the left-hand side develop slowly. In other words, the variety of genetic diversity means that we have a series of scales with several ranges of resolution. Among the analyzed species shown in Fig. 5.9, *Shinkaicaris leurokolos* is the species for which the quickest genetic substitution is expected: all analyzed sites showed uniformly high diversities. However, such diversity has not developed among the slowest species: *Lepetodrilus nux*. Among these three, the intermediate, *Bathyacmaea secunda*, might adequately reflect the ages of the hydrothermal vent sites, which is apparently consistent with geochronological results, even including extremely old ages (Fig. 5.5). According to the genetic diversities of *Shinkaicaris leurokolos* and *Bathyacmaea secunda,* the estimated ages of populations are on the order of 10^4 years, which corresponds well to the ranges inferred using a geochronological approach.

Ecological information will help to interpret these results of phylogeographic analyses and will be useful to estimate the ages of hydrothermal vent sites in the Okinawa Trough. Even for the same vent sites, inhabitants show various levels of genetic diversity, which are expected to correspond to their ecological characteristics. Consequently, ecological information of respective species on their life-history strategies, including reproduction and larval dispersal ability, are necessary to interpret genetic diversity of faunal populations and for application to estimate the history of hydrothermal activity.

5.4 Conclusions

The duration of present-day hydrothermal activities estimated from geochemical dating of ore minerals has approximately up to a few tens of thousands of years as reliable maxima in the Okinawa Trough and in the Southern Mariana Trough as back-arc tectonic settings. This duration is apparently in the same order of magnitude of duration as the TAG mound activity under the slow spreading condition of Mid-Atlantic Ridges. The results of ecological analyses presented herein showed various genetic structures among species, although they inhabit the same vent fields. Whereas populations of some species simply increase their genetic diversity along with the duration of hydrothermal activity, those of others show no such relation. Consequently, we can expect to select adequate species for dating the activities based on the genetic population structure of vent-endemic species. Correspondence to results obtained using geochemical dating will offer a useful evaluation criterion for the selection of the adequate species.

Acknowledgements All maps were tabulated using GMT software, a free mapping tool (Wessel and Smith 1998). This study was supported by the "TAIGA project," which was funded by a Grant-in-Aid for Scientific Research on Innovative Areas (KAKENHI, No. 20109004) from the Ministry of Education, Culture, Sports, Science and

Technology (MEXT), Japan. The final stage of this study was also supported by Submarine Resources Research Project, JAMSTEC. Constructive comments by three reviewers, Prof. H. Hyodo of Okayama Univ. Sci. and Drs. K. Sato and H. Yamamoto of JAMSTEC, greatly improved this article.

References

Amante C, Eakins BW (2009) ETOPO1 1 arc-minute global relief model: procedures, data sources and analysis. NOAA Technical Memorandum NESDIS NGDC-24, National Geophysical Data Center, Boulder, Colorado, p 19

Beebee T, Rowe G (2008) An introduction to molecular ecology. Oxford University Press, Oxford, p 400

Cruzan MB, Templeton AR (2000) Paleoecology and coalescence: phylogeographic analysis of hypotheses from the fossil record. Trend Ecol Evol 15:491–496

Fujii M, Okino K, Honsho C, Dyment J, Florent S, Mochizuki N (2013) Developing near-bottom magnetic measurements using a 3D forward modeling technique: application to hydrothermal vent fields. In: Proceedings of international symposium on underwater technology 2013, presented in international symposium on underwater technology 2013, March 2013, Tokyo, Japan

Govenar B (2010) Shaping vent and seep communities: Habitat provision and modification by foundation species. In: Kiel S (ed) The vent and seep biota: aspects from microbes to ecosystems. Springer, New York, pp 403–432

Hessler RR, Kaharl VA (1995) The deep-sea hydrothermal vent community: an overview. In: Humphris SE et al (eds) Seafloor hydrothermal systems. Geophysics Monograph Series, vol 91. American Geophysical Union, Washington, D.C., pp 72–84

Jamieson JW, Hannington MD, Clague DA, Kelley DS, Delaney JR, Holden JF, Tivey MK, Kimpe LE (2013) Sulfide geochronology along the endeavour segment of the Juan de Fuca ridge. Geochem Geophys Geosyst 14(7):2084–2099. doi:10.1002/ggge.20133

Johnson SB, Young CR, Jones WJ, Warén A, Vrijenhoek RC (2006) Migration, isolation, and speciation of hydrothermal vent limpets (Gastropoda; Lepetodrillidae) across the Blanco Transform fault. Biol Bull 210:140–157

Johnson SB, Warén A, Lee RW, Kano Y, Kaim A, Davis A, Strong EE, Vrijenhoek RC (2010) Rubyspira, new genus and two new species of bone-eating deep-sea snails with ancient habits. Biol Bull 219:166–177

Knowlton N, Weigt LA (1998) New dates and new rates for divergence across the Isthmus of Panama. Proc R Soc Lond Ser B Biol Sci 265:2257–2263

Lalou C, Brichet E, Hekinian R (1985) Age dating of sulfide deposits from axial and off-axial structures on the East Pacific Rise near 12°50′N. Earth Planet Sci Lett 75(1):59–71

Lutz RA, Shank TM, Fornari DJ, Haymon RM, Lilley MD, Von Damm KL, Desbruyeres D (1994) Rapid growth at deep-sea vents. Nature 371:663–664

Rasmussen B (2000) Filamentous microfossils in a 3,235-million-year-old volcanogenic massive sulphide deposit. Nature 405:676–679

Rogers AR, Harpending H (1992) Population growth makes waves in the distribution of pairwise genetic differences. Mol Biol Evol 9:552–569

Rona PA (1984) Hydrothermal mineralization at seafloor spreading centers. Earth Sci Rev 20(1):1–104

Shank TM, Fornari DJ, Von Damm KL, Lilley MD, Haymon RM, Lutz RA (1998) Temporal and spatial patterns of biological community development at nascent deep-sea hydrothermal vents (9°50′N, East Pacific Rise). Deep Sea Res II 45:465–515

Shank TM, Black MB, Halanych KM, Lutz RA, Vrijenhoek RC (1999) Miocene radiation of deep-sea hydrothermal vent shrimp (Caridea: Bresiliidae): evidence from mitochondrial cytochrome oxidase subunit I. Mol Phylogenet Evol 13:244–254

Smith AB, Pisani D, Mackenzie-Dodds JA, Stockley B, Webster BL, Littlewood DTJ (2006) Testing the molecular clock: molecular and paleontological estimates of divergence times in the Echinoidea (Echinodermata). Mol Biol Evol 23(10):1832–1851

Takamasa A, Nakai S, Sato F, Toyoda S, Banerjee D, Ishibashi J (2013) U–Th radioactive disequilibrium and ESR dating of a barite-containing sulfide crust from South Mariana Trough. Quat Geochronol 15:38–46. doi:10.1016/j.quageo.2012.12.002

Tivey MK (1995) Modeling chimney growth and associated fluid flow at seafloor hydrothermal vent site. In: Humphris SE et al (eds) Seafloor hydrothermal systems. Geophysics Monograph Series, vol 91. American Geophysical Union, Washington, D.C., pp 158–177

Toyoda S, Sato F, Nishido H, Kayama M, Ishibashi J (2012) The alpha effectiveness of the dating ESR signal in barite. Radiat Meas 47:900–902

Tsuji T, Takai K, Oiwane H, Nakamura Y, Masaki Y, Kumagai H, Kinoshita M, Yamamoto F, Okano T, Kuramoto Si (2012) Hydrothermal fluid flow system around the Iheya North Knoll in the mid-Okinawa trough based on seismic reflection data. J Volcanol Geotherm Res 213–214:41–50

Weir JT, Schluter E (2008) Calibrating the avian molecular clock. Mol Ecol 17:2321–2328

Wessel P, Smith WH (1998) New, improved version of the generic mapping tools released. EOS Trans Am Geophys Union 79:579

You CF, Bickle MJ (1998) Evolution of an active sea-floor massive sulphide deposit. Nature 394:668–671

Zeng Z, Yu S, Yin X, Wang X, Zhang G, Wang X, Chen D (2009) Element enrichment and U-series isotopic characteristics of the hydrothermal sulfides at Jade site in the Okinawa Trough. Sci China Ser D Earth Sci 52(7):913–924

Quantification of Microbial Communities in Hydrothermal Vent Habitats of the Southern Mariana Trough and the Mid-Okinawa Trough

6

Katsunori Yanagawa, Jun-ichiro Ishibashi, Takao Arai, Tetsuro Urabe, and Michinari Sunamura

Abstract

The structure of microbial populations near chemosynthetic faunal communities of two geographically and geologically distinct deep-sea hydrothermal vent fields were quantitatively evaluated using catalyzed reporter deposition-fluorescence in situ hybridization (CARD-FISH). The hydrothermal vent of the Southern Mariana Trough (SMT) was dominated by colonization of gastropods in the low-temperature diffuse hydrothermal fluid, whereas macrofauna in mixing zones of the Mid-Okinawa Trough (MOT) consisted of polychaetes, galatheid crabs, and bivalves. A quantitative comparison revealed that the microbial community of the SMT hydrothermal vent field is significantly different from that of the MOT and is strongly influenced by mixing conditions between reduced hydrothermal fluid and oxygenated seawater. In particular, a high proportion of *Epsilonproteobacteria* was found in the SMT hydrothermal fluid, which is composed of approximately 88 % seawater. In contrast, sulfur oxidizers in *Gammaproteobacteria* were most abundant near vent fauna habitats in the MOT. Our results suggest that the SMT hydrothermal environment is distinct from that of the MOT and affects the community structure of macrofauna and microbial flora.

Keywords

Deep-sea hydrothermal vent • Fluorescence in situ hybridization (FISH) • Hydrothermal mixing zone • Quantitative microbial community analysis

6.1 Introduction

In a deep-sea hydrothermal environment, mixing between hot, reduced hydrothermal vent fluids and cold, oxygenated ambient seawater forms a steep physical and chemical gradient. Vent-derived electron donors and seawater-derived electron acceptors are a source of energy for chemolithotrophic growth of prokaryotes, both of free-living and symbiotic forms. Consequently, these microorganisms play a fundamental role in sustaining primary production in hydrothermal ecosystems, supporting the growth of heterotrophic microbial flora and fauna, and maintaining the diversity and population density, thus creating an oasis for life in the deep-sea "desert" (Corliss et al. 1979; Karl 1995).

The geochemical profiles of hydrothermal fluids fluctuate temporally and spatially, due to the complex inorganic

K. Yanagawa (✉)
Department of Earth and Planetary Science, University of Tokyo, 7-3-1 Hongo, Bunkyo-ku, Tokyo 113-0033, Japan

Subsurface Geobiology Advanced Research (SUGAR) Project, Japan Agency for Marine-Earth Science and Technology (JAMSTEC), Yokosuka 237-0061, Japan
e-mail: kyanagawa@jamstec.go.jp

J.-i. Ishibashi
Department of Earth and Planetary Sciences, Faculty of Science, Kyushu University, Higashi-ku, Fukuoka 812-8581, Japan

T. Arai
Department of Applied Biological Science, Tokyo University of Science, 2641 Yamazaki, Noda, Chiba 278-851, Japan

T. Urabe • M. Sunamura
Department of Earth and Planetary Science, University of Tokyo, 7-3-1 Hongo, Bunkyo-ku, Tokyo 113-0033, Japan

J.-i. Ishibashi et al. (eds.), *Subseafloor Biosphere Linked to Hydrothermal Systems: TAIGA Concept*,
DOI 10.1007/978-4-431-54865-2_6,

Table 6.1 CARD-FISH probes used in this study

Probe	Specificity	Sequence (5′–3′)[a]	Target site[b]	FA (%, vol/vol)[c]	NaCl (mM)[d]	References
EUB338 I	*Bacteria*	GCTGCCTCCCGTAGGAGT	16S, (338–355)	55	3	Amann et al. (1995)
EUB338 II	*Planctomycetales*	GCAGCCACCCGTAGGTGT	16S, (338–355)	55	3	Daims et al. (1999)
EUB338 III	*Verrucomicrobiales*	GCTGCCACCCGTAGGTGT	16S, (338–355)	55	3	Daims et al. (1999)
ARCH915	*Archaea*	GTGCTCCCCCGCCAATTCCT	16S, (915–934)	60	0	Amann et al. (1995)
ALF968	*Alphaproteobacteria*	GGTAAGGTTCTGCGCGTT	16S, (968–985)	30	3	Neef (1997)
BET42a	*Betaproteobacteria*	GCCTTCCCACTTCGTTT	23S, (1027–1043)	55	3	Manz et al. (1992)
GAM42a	*Gammaproteobacteria*	GCCTTCCCACATCGTTT	23S, (1027–1043)	55	3	Manz et al. (1992)
DEL495	*Deltaproteobacteria*	ARTTAGCCGGYGCTTCCT	16S, (495–512)	55	3	Loy et al. (2002)
EP402	*Epsilonproteobacteria*	GAAAKGYGTCATCCTCCACG	16S, (402–423)	35	42	Takai et al. (2004)
CF319a	*Cytophaga-Flavobacterium*	TGGTCCGTRTCTCAGTAC	16S, (319–336)	55	3	Manz et al. (1996)
SUP05-187	SUP05	GGGCTCCTTTTCTCCATA	16S, (787–205)	55	3	Sunamura et al. (2004)

[a]M = A or C, R = G or A, Y = C or T, W = A or T, K = G or T
[b]Position in the 16S or 23S rRNA of *E. coli*
[c]Formamide concentrations in the hybridization buffer
[d]NaCl concentrations in the wash buffer

reactions in the fluid conduit (Le Bris et al. 2006; Rogers et al. 2007; Zielinski et al. 2011). The fluctuation of geochemical composition in hydrothermal mixing zones may have a significant impact on the rate of microbial growth and metabolic activity, biogeochemical reactions, and the dominant microbial population. In particular, reduced compounds such as H_2, CH_4, HS^-, and Fe^{2+} are not only essential energy sources for chemolithotrophs but also factors that control the composition and density of the microbial community. Previous studies have investigated habitat components, for example, the boundary zone (interface) between hydrothermal fluid and ambient seawater, including low-temperature diffusive flow (Holden et al. 1998; Huber et al. 2002, 2003; Perner et al. 2007), chimney structures (Schrenk et al. 2003; Takai et al. 2001), and hydrothermal sediments (Nunoura et al. 2010; Teske et al. 2002; Yanagawa et al. 2013). These studies demonstrated the prevalence of *Gammaproteobacteria*, *Deltaproteobacteria, Epsilonproteobacteria*, *Bacteroidetes*, *Firmicutes,* and various candidate divisions in the hydrothermal system. Due to fluctuations in the environmental conditions, microbial communities in hydrothermally influenced regions exhibit variability on various spatial and temporal scales, including large-scale intra- and inter-field variability (Flores et al. 2012; Huber et al. 2010; Nunoura and Takai 2009), short-term temporal and spatial variability (Perner et al. 2009, 2013), and spatial variability on a small scale of a few centimeters to meters (Nakagawa et al. 2005; Takai et al. 2004). However, most studies focused on the variability of specific microbial populations in the zone adjacent to hydrothermal vents. To better understand microbial population dynamics and their relation to hydrothermal environments in terms of chemistry and temperature, a quantitative approach to whole microbial members is necessary.

Despite the data accumulation of microbial diversity based on 16S rRNA sequencing, relatively few studies have conducted a quantitative analysis of microbial community composition in hydrothermal mixing zones. Fluorescence in situ hybridization (FISH) is one of the most reliable methods for quantifying microbial populations and can provide important information regarding the spatial distribution, diversity, abundance, and composition of microbial communities in the environment. Here, we describe the microbial composition of regions where reduced hydrothermal fluid and oxygenated seawater mix using catalyzed reporter deposition FISH (CARD-FISH). The hydrothermal fluid samples were collected around the Southern Mariana Trough (SMT) and the Mid-Okinawa Trough (MOT) in the western Pacific, two geographically and geologically distinct hydrothermal vents. The zonation of hydrothermal vent fauna (gastropods, polychaetes, galatheid crabs, and mussels) was used as a potential environmental indicator of physical and chemical gradients formed by the mixing of reduced hydrothermal fluid and oxygenated seawater. CARD-FISH, using nine oligonucleotide probes, identified several major phylogenetic groups including *Bacteria, Archaea, Alphaproteobacteria*, *Betaproteobacteria*, *Gammaproteobacteria*, *Deltaproteobacteria, Epsilonproteobacteria*, the *Cytophaga-Flavobacterium* cluster, and the SUP05 group of gammaproteobacterial sulfur oxidizers (Table 6.1) as components of the microbial community

associated with hydrothermal fluids and nearby vent fauna. These results increase our understanding of meso-scale (tens of centimeters to meters) spatial variation in microbial populations and long-term (year-scale) microbial dynamics.

6.2 Materials and Methods

6.2.1 Sampling Sites and Sample Collection

The hydrothermally influenced fluids were collected around the shimmering water that emerged through the gastropod patches (Snail site: 12°57.190′N, 143°37.165′E, water depth: 2,850 m) at the center of the spreading back-arc basin of the SMT (for a detailed description, see Toki et al. Chap. 45), and around the hydrothermal mixing zones within the large sulfide mound (North Big Chimney: 27°47.451′N, 126°53.805′E, water depth: 982 m) in the Iheya North Knoll hydrothermal field of the MOT (see Kawagucci Chap. 30). From the SMT hydrothermal field, 11 different shimmering fluids and 2 ambient seawater samples were collected during the YK03-09 cruise (14 Oct to 14 Nov 2003) and the YK05-09 cruise (24 Jul to 10 Aug 2005) of the R/V *Yokosuka* using the manned submersible *Shinkai 6500* and during the TN167A cruise (15–27 Mar 2004) of the R/V *Thomas G. Thompson* using the remotely operated vehicle (ROV) *ROPOS* (Table 6.2). The Snail site is located on a mound of pillow lava, and low-temperature diffuse fluids emanate from hydrothermal vents and are densely inhabited with the gastropod *Alviniconcha hessleri* around Marker #21 and Marker #24. A low-temperature hydrothermal vent site is also located to the south of the Snail site, where a microbial mat-like structure was observed in the vicinity of Marker #78. From the MOT, 3 hydrothermal fluids and 2 seawater samples were obtained during the NT05-03 cruise (14–20 Apr 2003) of the R/V *Natsushima* using the ROV *Hyper-Dolphin* (Table 6.2). Hydrothermal vents are surrounded by habitat zones of polychaetes, galatheid crabs (*Shinkaia crosnieri*), and bivalves (genus *Bathymodiolus*), in order of increasing distance from the vent, which may be due to the optimal hydrothermal mixing required to support the growth of these species.

The hydrothermal fluid samples were taken from each SMT and MOT sampling area using a bag sampling system, a rotary clean seawater sampling system (Kato et al. 2009), and a Niskin bottle (Table 6.2). The collected samples were immediately fixed for 6 h with 3.7 % neutralized formalin and stored at −80 °C for analysis onshore.

6.2.2 Chemical Characteristics of Hydrothermal Fluids

The onboard analyses, including potentiometric techniques, colorimetric methods, titration, and liquid chromatography were performed as described by Gieskes et al. (1991). The pH at room temperature was determined using a pH meter with a combined glass electrode (IWAKI, IW055-BNC). The pH meter was calibrated daily using JSCS buffer solutions (pH = 6.865 and 4.010). Alkalinity was determined by titration with hydrochloric acid. The endpoint was calculated by Gran plot, using a pH meter (Corning, M-250) as a potentiometer. The calibration was verified by analyzing IAPSO standard seawater (with a known alkalinity of 2.45 mM), and the analytical precision was estimated to be within 3 %. The concentrations of dissolved silica, ammonium ions, and hydrogen sulfide were measured with a colorimeter by classical methods (Hach, DR2010) using molybdenum blue, indo-phenol and methylene blue, respectively. The analytical precision was generally estimated to be within 3 % for the seawater analysis.

The nitrate concentration was determined onboard using a liquid chromatograph (Shimadzu, LC10AI) with a UV detector ($\lambda = 220$ nm, Shimadzu, SPD10AVP) following a modified protocol (Maruo et al. 2006). To eliminate interference from major anions such as Cl^- and SO_4^{2-}, a high-capacity anion exchange column (Tosoh, TSK gel-SAX, 4.6 × 50 mm) was used with a 1 M sodium chloride eluent at a flow rate of 0.8 ml/min. Chloride concentration was determined by Mohr's method, using silver nitrate solution as the titrant and chromate solution as the indicator. Sulfate concentration was determined in the onshore laboratory using an ion chromatograph (Dionex DX-100) after diluting the samples to a ratio of 1:300. The concentrations of major and minor cations (Na, K, Ca, Mg, Sr, B, Mn, and Fe) were determined in the onshore laboratory using a flame spectrophotometer (Shimadzu AA-680) and inductively coupled plasma atomic emission spectrometry (ICP-AES; Seiko, SPS 1200AR) after diluting the samples adequately. The precision of these instrumental analyses was estimated to be within 5 % based on repeated analysis of a working standard.

All of the geochemical data from the SMT hydrothermal field are shown by Toki et al. (Chap. 45).

6.2.3 Catalyzed Reporter Deposition-Fluorescence In Situ Hybridization

The fixed samples were thawed and filtered through 0.2-μm-pore-size polycarbonate filters to isolate microbial cells.

Table 6.2 General description and CARD-FISH-based microbial community composition of the samples used in this study

Cluster[a]	Field	Site	Dive	Sample number[b]	Sampling location	Date	Temp. (°C)	Mg (mM)	Seawater content[d] (%)	Total cell count (cells/ml)	CARD-FISH-positive cells (% of total cell count)								
											EUB338	ARCH915	ALF968	BET42a	GAM42a	DEL495	EP402	CF319a	SUP05
Low-temperature shimmering	SMT	Mk#21	D792	RC2	Gastropods	2003.10.29	~79	45.3	89.0	7.8×10^4	45.7	8.0	0.4	5.0	9.8	1.8	8.1	0.1	nd
	SMT	Mk#24	D902	RC1	Gastropods	2005.7.28	39.3	46.1	90.6	1.9×10^5	51.5	0.0	2.5	15.3	10.2	5.9	12.1	3.0	nd
	SMT	Mk#24'	R773	RC5	Gastropods	2004.3.20	41	44.2	86.8	3.0×10^5	51.2	0.3	0.0	13.7	8.4	0.7	11.4	0.0	nd
	SMT	Mk#21	R780	RC1	Gastropods	2004.3.26	50.1	43.9	86.2	1.8×10^5	54.7	1.8	3.9	14.6	22.9	4.3	10.8	1.8	nd
	SMT	Mk#78	R775	RC3	Microbial mat	2004.3.22	23.3	41.1	80.7	1.2×10^5	51.3	26.3	0.0	8.6	24.0	0.0	4.2	0.0	nd
	SMT	Mk#78	R775	RC4	Microbial mat	2004.3.22	58.1	48.2	94.7	1.5×10^5	45.1	12.4	0.0	13.2	16.1	8.2	0.0	0.0	nd
	SMT	Mk#21	R780	RC6	Gastropods	2004.3.26	50.9	44	86.4	2.2×10^5	64.1	2.5	3.8	12.7	26.3	12.7	12.4	1.7	nd
	SMT	Mk#24'	R773	RC4	Gastropods	2004.3.20	48.7	45.3	89.0	1.7×10^5	58.1	10.3	0.9	11.6	20.1	4.0	20.3	0.1	nd
	SMT	Mk#24	D789	RC2	Gastropods	2003.10.26	~110	40.7	80.0	5.2×10^4	62.1	15.7	17.5	7.1	21.8	1.5	2.7	3.8	nd
Collected in 2005	SMT	Mk#24	D904	RC3	Gastropods	2005.8.2	74.5	44.4	87.2	1.3×10^5	65.1	10.7	5.0	46.2	7.8	2.6	1.5	0.7	nd
	SMT	Mk#24	D904	RC5	Gastropods	2005.8.2	111.4	39.3	77.2	6.4×10^4	46.3	1.0	1.6	32.3	0.8	2.0	4.3	1.3	nd
Seawater-dominant	SMT	Mk#24	D789	N1	Ambient seawater	2003.10.26	3	50.9	100	2.5×10^4	45.6	10.9	0.9	1.0	0.7	10.5	1.6	0.8	nd
	SMT	Mk#78	R775	N	Ambient seawater	2004.3.22	1.4	49.1	96.5	1.8×10^4	31.5	5.3	0.4	0.0	0.0	6.2	0.6	0.1	nd
	MOT	NBC	D392	B2	Polychaetes	2005.4.15	8	48.7	92.5	9.3×10^4	56.9	27.2	0.2	0.0	0.3	1.1	2.4	0.8	21.7
	MOT	NBC	D392	N	10 m above the vent	2005.4.15	nd[c]	49.2	93.3	1.0×10^5	54.2	27.4	0.0	0.0	0.2	0.1	0.1	0.0	13.5
	MOT	NBC	D393	B3	Bivalves	2005.4.16	5	48.8	92.7	1.2×10^5	57.0	nd	0.5	0.0	0.5	4.9	3.1	2.0	24.9
	MOT	NBC	D394	B2	Galatheids	2005.4.17	nd	49.3	93.5	1.9×10^5	60.3	nd	0.6	0.0	1.2	8.5	4.9	1.7	20.5
	MOT	NBC	D393	N	1 m above the vent	2005.4.16	nd	44.5	84.5	1.4×10^5	65.0	nd	0.3	0.0	0.0	0.6	0.2	1.2	18.7

[a]Clusters are defined in Fig. 6.3

[b]The hydrothermal fluid samples were taken using a bag sampling system (B), a rotary clean seawater sampling system (RC), and a Niskin bottle (N)

[c]Not determined

[d]Seawater content (%) = $[Mg]/[Mg]_{background} \times 100$. $[Mg]_{background}$ in the SMT and MOT were estimated to be 50.9 mM (Toki et al. Chap. 45) and 52.7 mM (Nakagawa et al. 2005), respectively

CARD-FISH was performed according to a previously published protocol (Pernthaler et al. 2002) with slight modifications, as described below. Microbial cells on polycarbonate filters were permeabilized with lysozyme (10 mg/ml in 0.05 M EDTA and 0.1 M Tris–HCl buffer [pH 7.5]) for 70 min at 37 °C. The filters were then treated with 1 % H_2O_2 in methanol for 30 min at room temperature to deactivate the endogenous peroxidase. The microbial cells were then hybridized for 3 h at 35 °C in hybridization buffer containing a horseradish peroxidase (HRP)-labeled oligonucleotide probe (final concentration: 5 pmol/μl). The filter was then incubated in a washing buffer for 10 min at 37 °C. The oligonucleotide probes, formamide concentrations in the hybridization buffer, and salt concentrations in the washing buffer are listed in Table 6.1. The filters were further washed with 0.05 % TritonX-100 in 1× PBS (145 mM NaCl, 1.4 mM NaH_2PO_4, 8 mM Na_2HPO_4 [pH 7.4]) for 15 min at room temperature and then incubated in a 1:50 Cy3-labeled tyramide solution (TSA direct; PerkinElmer) for 10 min at 37 °C in the dark. The filter was then washed with 0.05 % TritonX-100 in 1× PBS and dehydrated with ethanol. The microbial cells on each filter were stained with 1 μg/ml of 4′,6-diamidino-2-phenylindole (DAPI). A ProLong Antifade Kit (Molecular Probes) was used to prevent photobleaching. To estimate the cell density, more than 1,000 cells in at least 25 microscopic fields were counted for each filter.

6.2.4 Cluster Analysis of Microbial Community Composition by CARD-FISH

A comparison of the microbial community structures was performed by cluster analysis using the web-based program Black Box (http://aoki2.si.gunma-u.ac.jp/index.html). A clustering algorithm based on the Ward method (Ward 1963) was applied to the bacterial community composition as determined by CARD-FISH using the oligonucleotide probes EUB338 I-III, ALF968, BET42a, GAM42a, DEL495, EP402, and CF319a. To reflect differences in the quantitative compositions of the microbial communities, none of the parameters were normalized.

6.3 Results and Discussion

6.3.1 Quantitative Assessment of Microbial Community Composition by CARD-FISH

The chemical composition of the hydrothermal fluid was strongly affected by the degree of dilution in the ambient seawater. Estimates based on Mg concentrations suggest that the fluid samples contained a large amount of seawater, ranging from 77.2 to 94.7 % (Table 6.2). However, the microbial community composition of the hydrothermally influenced samples was significantly different from that of the ambient seawater. The CARD-FISH with specific oligonucleotide probes determined taxonomic composition and population size of prokaryotes inhabiting the hydrothermal vent environment. Up to 65.1 % of the total cell count by DAPI staining hybridized with the bacteria-specific probes EUB338 I-III, while up to 27.4 % of the total cell count hybridized with the archaea-specific probe ARCH915 (Table 6.2 and Fig. 6.1). Approximately one-half to one-third of the total cell count did not hybridize to either the bacteria- or archaea-specific probes and had smaller cell size than the other cells. Members of the *Gammaproteobacteria* were abundant in most of the samples from the SMT, accounting for more than half of the bacterial cells (~26.3 % of the total cell count). In contrast, the most abundant group in the fluid samples collected at the SMT in 2005 (D904RC3 and RC5) was *Betaproteobacteria*, which represented approximately 75 % of the bacterial cell counts. Members of the *Epsilonproteobacteria* also constituted a significant fraction of the microbial cells in the SMT hydrothermal fluids, representing up to 20.3 % of the total cell count. The *Epsilonproteobacteria* are widely distributed in deep-sea hydrothermal environments that are microaerophilic or anaerobic. The *Epsilonproteobacteria* include various chemolithoautotrophs that are capable of using hydrogen and sulfide as electron donors, and oxygen, nitrate, and elemental sulfur as electron acceptors (Campbell et al. 2006). At the SMT hydrothermal field, the *Epsilonproteobacteria* dominantly inhabited zones where the seawater content was between 86.2 and 90.6 % (Fig. 6.2). Our findings suggest that these bacterial groups are not randomly distributed in the hydrothermal environments but have a preference for a specific ecological niche. The ALF968- and DEL495-positive cells were abundant in the D789RC2 and D780RC6 samples, respectively. However, relatively few of these cells were detected in the other samples. CF319a-positive cells had a very low detectability, accounting for less than 3.8 % of most samples. In the samples from the MOT, most oligonucleotide probes identified very few cells, with the exception of SUP05-187. The SUP05 group of sulfur oxidizers in *Gammaproteobacteria* was most abundant near vent fauna habitats in the MOT, as previously shown in the hydrothermal plume at the Suiyo Seamount (Sunamura et al. 2004). Sulfur oxidation would be one of the most feasible reactions in the hydrothermal environment of the MOT.

6.3.2 Spatial and Temporal Variations in the Composition of the Bacterial Community

While the 18 samples have different profiles in bacterial components, cluster analysis revealed that the bacterial

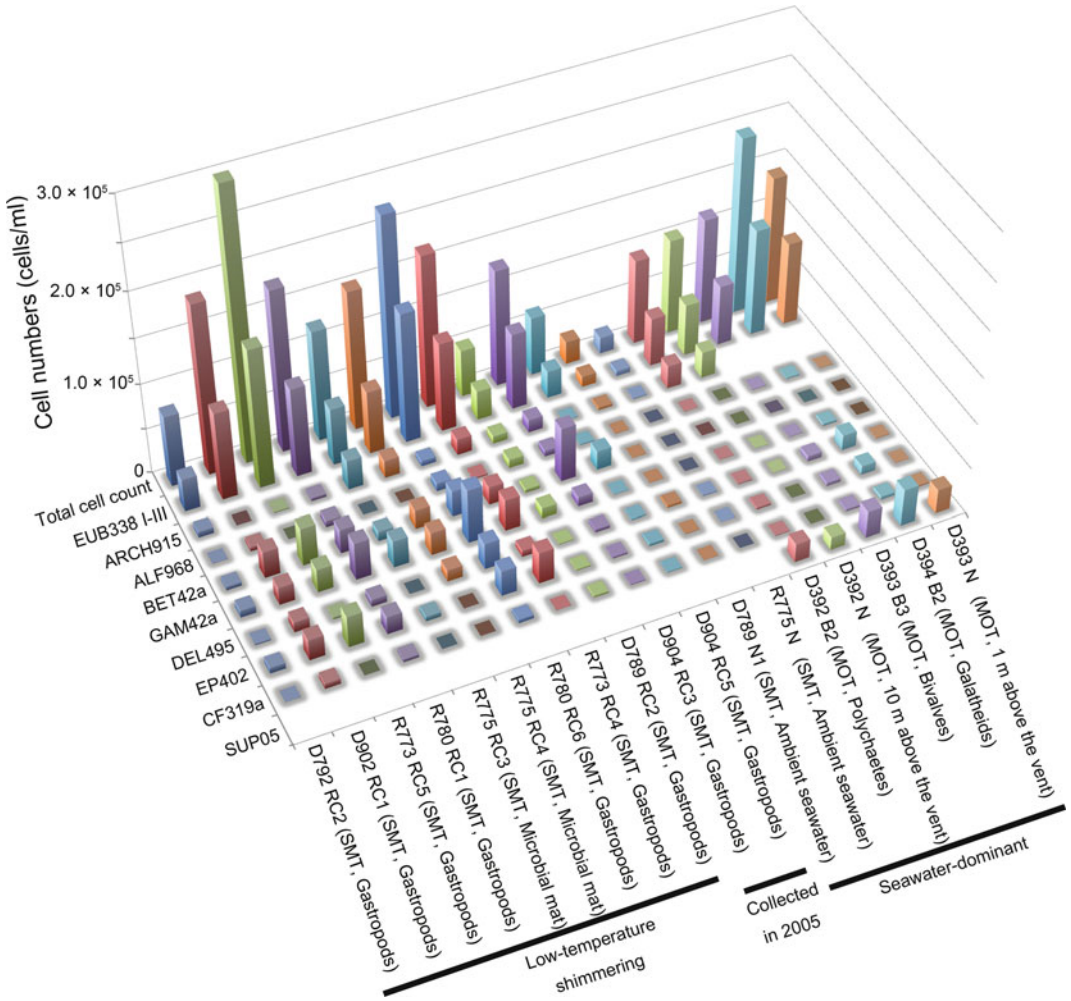

Fig. 6.1 Microbial community composition determined by CARD-FISH analysis

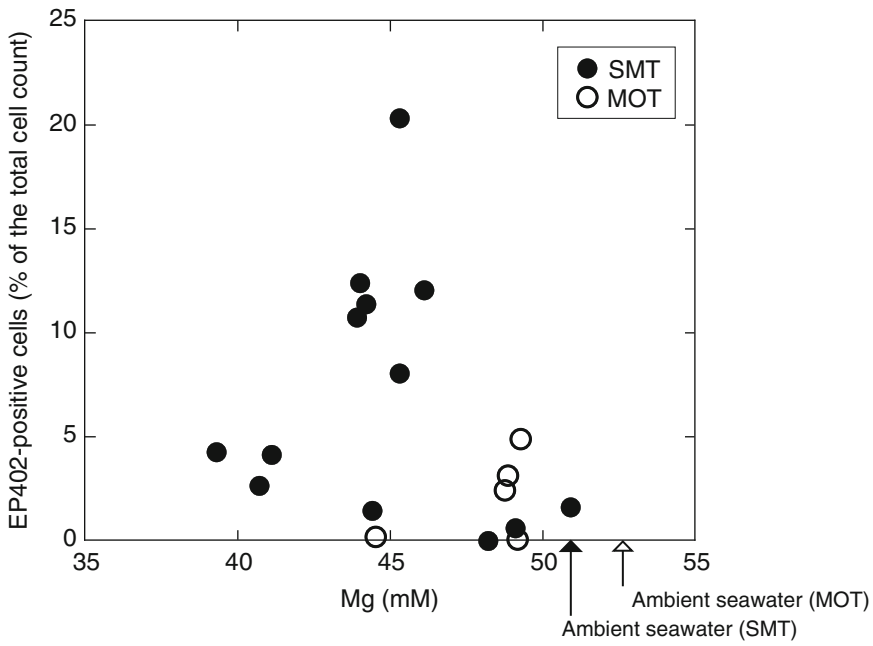

Fig. 6.2 The relative abundance of *Epsilonproteobacteria* in the mixed hydrothermal fluid and ambient seawater samples. The number of *Epsilonproteobacteria* cells was determined by CARD-FISH using the EP402 probe. *Solid circles*, hydrothermal fluid samples from the Southern Mariana Trough (SMT); *open circles*, hydrothermal fluid samples from the Iheya North Knoll hydrothermal field of the Mid-Okinawa Trough (MOT)

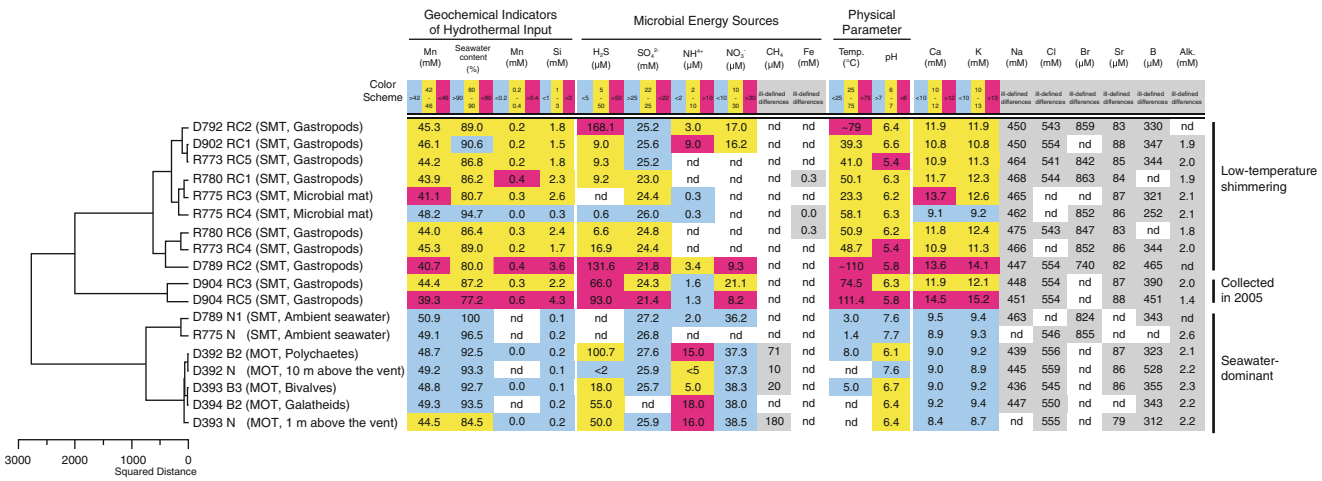

Fig. 6.3 Cluster analysis of the 18 bacterial communities and their environmental parameters in the deep-sea hydrothermal fluid and ambient seawater samples. The squared distance was calculated using the cell numbers as determined by CARD-FISH. The physical and chemical compositions of the hydrothermal fluids are color-coded to represent the degree of hydrothermal input in descending order from *red* to *yellow* to *blue*. *Gray* indicates samples that did not exhibit significant differences

communities in the hydrothermal mixing zone formed a separate cluster from those in ambient seawater (Fig. 6.3). The chemical characteristics of the clusters suggest the following three distinguishable habitats conditions: (i) the seawater-dominant fluids composed of ambient seawater with a small portion of hydrothermal fluids, (ii) low-temperature shimmering, and (iii) the fluid samples collected at the SMT in 2005.

6.3.2.1 Seawater-Dominant Fluids

This cluster consisted of the ambient seawater samples and highly diluted hydrothermal fluids (Fig. 6.3). The average temperature during the sampling period ranged from 1.4 to 8.0 °C, and the Mg concentration ranged from 44.5 to 50.9 mM, corresponding to seawater proportions ranging from 84.5 to 100 %. Total cell densities ranged from 1.8 to 19 × 10^4 cells/ml (Table 6.2). CARD-FISH-positive cells for the probes of ALF968-, BET42a-, GAM42a-, DEL495-, EP402-, and CF319a were low in these samples (Table 6.2 and Fig. 6.1), possibly caused by the low expression of their ribosomal RNA or the dominance of other unidentified microbes.

6.3.2.2 Low-Temperature Shimmering

This cluster was composed of the samples from the SMT hydrothermal mixing zone (Fig. 6.3). The average temperature during the sampling period ranged from 23.3 to 110 °C, and the Mg concentration ranged from 40.7 to 48.2 mM, corresponding to seawater proportions ranging from 80 to 94.7 %. Total cell densities ranged from 5.2 to 30 × 10^4 cells/ml (Table 6.2). Though these shimmering fluid samples contained a substantial amount of seawater, the microbial community compositions in this cluster were notably different from the background seawater samples. The microbial communities were mainly composed of BET42a-, GAM42a-, DEL495-, and EP402-positive cells (Table 6.2 and Fig. 6.1). A particularly high abundance of EP402-positive cells was detected in the sample of R773 RC4, comprising 20.3 % of the total cell count. However, EP402-positive cells accounted for less than 5 % of the total cell count in 12 of the 18 hydrothermal fluid samples (Fig. 6.2). The abundance of *Epsilonproteobacteria* in hydrothermal systems reported in previous studies is similar to the results found in this study (Nakagawa et al. 2006; Perner et al. 2007).

The microbial cell numbers were consistently high in the fluid samples from this cluster. Indeed, the total cell number in R773RC5 was 15-fold higher than in the ambient seawater samples (D789N1 and R775N). Furthermore, the microbial cells in the hydrothermal fluid samples were highly morphologically diverse, including rods, cocci, and filaments. A number of EP402-positive cells contained long filaments that were 3 μm wide and >100 μm in length. In contrast, the microbial cells isolated from the ambient seawater samples were mainly small cocci. Because the filamentous EP402-positive cells exceeded the other cells in size, their biogeochemical impact on the hydrothermal ecosystem would be larger compared to an equal number of smaller cells. Future characterization of these filamentous populations is needed to address this issue.

The microbial community composition in this cluster most likely reflects the difference in fluid chemistry. The emanating hydrothermal fluids are mixed with and cooled by ambient seawater. The low-temperature shimmering is enriched with reduced inorganic compounds (electron donors) from hydrothermal fluid and oxidants (electron acceptors) derived from ambient seawater. Therefore, a physicochemical gradient produced from oxic/anoxic

conditions and high/low temperatures around the hydrothermal vent may produce various habitat conditions to induce a phylogenetically, functionally, and morphologically diverse microbial community. The high proportion of *Epsilonproteobacteria* inhabiting oxygenated and low- to medium-temperature environments has been reported in previous studies (Huber et al. 2003; Nakagawa et al. 2005).

6.3.2.3 The Fluid Samples Collected at the SMT in 2005

The samples collected during the YK05-09 cruise in 2005 clustered separately from the other SMT samples (Fig. 6.3). The average temperature during the sampling period ranged from 74.5 to 111.4 °C, and the Mg concentration ranged from 39.3 to 44.4 mM, corresponding to seawater proportions ranging from 77.2 to 87.2 % (Table 6.2). Total cell densities ranged from 6.4 to 13 $\times$ 10^4 cells/ml (Table 6.2). This cluster was dominated by *Betaproteobacteria*, which accounted for ~46.2 % of the total cell count (Table 6.2 and Fig. 6.1). The dominance of *Betaproteobacteria* in habitats adjacent to gastropod aggregates may be supported by organic compounds excreted from gastropods, because heterotrophy is a dominant lifestyle in *Betaproteobacteria*. A similar temporal change in microbial community composition was previously observed in samples collected from the SMT borehole (Kato et al. 2009). This change may be due to long-term (year-scale) temporal fluctuation in the microbial community caused by a change in environmental factors.

6.3.3 Hydrothermal Habitats for Microbial and Macrofaunal Communities

Total cell densities ranged from 5.1 to 30 $\times$ 10^4 cells/ml in the hydrothermal fluid samples to 1.8 to 4.2 $\times$ 10^4 cells/ml in the ambient seawater samples (Table 6.2). Hence, the microbial cell abundance at the SMT was two- to ten-fold higher than in ambient seawater. In contrast, the total cell number in the hydrothermal fluid in the MOT was only twice that in the seawater samples. These data clearly indicate that the microbial community relies on hydrothermal energy input to the deep-sea where energy sources are typically scarce, and they reveal the regional variation and temporal fluctuation.

The stability of the hydrothermal activity is a primary factor to sustain the microbial and macrofaunal communities. The hydrothermal vents in the SMT are estimated to be stable over several years with regard to temperature and geochemical composition (Toki et al. Chap. 45). In contrast, the high-temperature venting activity in the MOT may create fluctuating habitats for both microorganisms and macrofauna due to vigorous mixing conditions.

6.4 Conclusions

In this study, we used a CARD-FISH-based quantitative approach to demonstrate that the microbial community composition of the SMT hydrothermal field is distinct from that of the MOT hydrothermal field. The SMT mixing zone harbored phylogenetically and morphologically diverse and abundant microbial populations compared to seawater-dominant samples. Although it was not possible to obtain data on the metabolism of microbial species detected by CARD-FISH (i.e., whether they were chemolitho-, mixo- or heterotrophic), the microbial community may include heterotrophs such as *Alphaproteobacteria*, *Betaproteobacteria,* and *Cytophaga-Flavobacterium* clusters. This finding may indicate that hydrothermal fluid components have an indirect impact on heterotrophic microbial populations. If so, future investigations should focus on the food web within the macrofaunal community. Our quantitative data will help predict the contribution of microbes to biogeochemical processes in deep-sea hydrothermal environments. Further research is needed to gain a better understanding of the functional role and biogeochemical impact of hydrothermal vent microorganisms.

Acknowledgements We are deeply grateful to the crews of the R/V *Thomas G. Thompson,* the R/V *Yokosuka*, and the R/V *Natsushima* and the operation teams of the ROV *ROPOS*, *Shinkai 6500,* and *HyperDolphin* during the YK03-09, YK05-09, TN167A, and NT05-03 cruises. We also thank the shipboard science parties for the cruises and the members of the project TAIGA and Archaean Park for providing us with valuable samples and for helpful discussions. This work was supported in part by the Grant-in-Aid for Scientific Research: Project TAIGA (New Scientific Research on Innovative Areas, 20109003) and the Archaean Park Project (International Research Project on Interaction between Sub-Vent Biosphere and Geo-Environments).

References

Amann RI, Ludwig W, Schleifer KH (1995) Phylogenetic identification and in situ detection of individual microbial cells without cultivation. Microbiol Rev 59(1):143–169

Campbell BJ, Engel AS, Porter ML, Takai K (2006) The versatile ε-proteobacteria: key players in sulphidic habitats. Nat Rev Microbiol 4(6):458–468

Corliss JB et al (1979) Submarine thermal springs on the Galápagos Rift. Science 203(4385):1073–1083

Daims H, Brühl A, Amann R, Schleifer K-H, Wagner M (1999) The domain-specific probe EUB338 is insufficient for the detection of all bacteria: development and evaluation of a more comprehensive probe set. Syst Appl Microbiol 22(3):434–444

Flores GE, Shakya M, Meneghin J, Yang ZK, Seewald JS, Geoff Wheat C, Podar M, Reysenbach AL (2012) Inter-field variability in the microbial communities of hydrothermal vent deposits from a back-arc basin. Geobiology 10(4):333–346

Gieskes JM, Gamo T, Brumsack H (1991) Chemical methods for interstitial water analysis aboard Joides Resolution. Ocean Drilling Program Technical Note 15

Holden JF, Summit M, Baross JA (1998) Thermophilic and hyperthermophilic microorganisms in 3–30 °C hydrothermal fluids following a deep-sea volcanic eruption. FEMS Microbiol Ecol 25 (1):33–41

Huber JA, Butterfield DA, Baross JA (2002) Temporal changes in archaeal diversity and chemistry in a mid-ocean ridge subseafloor habitat. Appl Environ Microbiol 68(4):1585–1594

Huber JA, Butterfield DA, Baross JA (2003) Bacterial diversity in a subseafloor habitat following a deep-sea volcanic eruption. FEMS Microbiol Ecol 43(3):393–409

Huber JA, Cantin HV, Huse SM, Mark Welch DB, Sogin ML, Butterfield DA (2010) Isolated communities of *Epsilonproteobacteria* in hydrothermal vent fluids of the Mariana Arc seamounts. FEMS Microbiol Ecol 73(3):538–549

Karl DM (1995) Ecology of free-living, hydrothermal vent microbial communities. In: Karl DM (ed) The microbiology of deep-sea hydrothermal vents. CRC, Boca Raton, pp 35–124

Kato S et al (2009) Abundance of *Zetaproteobacteria* within crustal fluids in back-arc hydrothermal fields of the Southern Mariana Trough. Environ Microbiol 11(12):3210–3222

Le Bris N, Govenar B, Le Gall C, Fisher CR (2006) Variability of physico-chemical conditions in 9°50′N EPR diffuse flow vent habitats. Mar Chem 98(2–4):167–182

Loy A, Lehner A, Lee N, Adamczyk J, Meier H, Ernst J, Schleifer K-H, Wagner M (2002) Oligonucleotide microarray for 16S rRNA gene-based detection of all recognized lineages of sulfate-reducing prokaryotes in the environment. Appl Environ Microbiol 68 (10):5064–5081

Manz W, Amann R, Ludwig W, Wagner M, Schleifer K-H (1992) Phylogenetic oligodeoxynucleotide probes for the major subclasses of proteobacteria: problems and solutions. Syst Appl Microbiol 15 (4):593–600

Manz W, Amann R, Ludwig W, Vancanneyt M, Schleifer K-H (1996) Application of a suite of 16S rRNA-specific oligonucleotide probes designed to investigate bacteria of the phylum cytophaga-flavobacter-bacteroides in the natural environment. Microbiology 142(5):1097–1106

Maruo M, Doi T, Obata H (2006) Anion chromatographic determination of submicromolar nitrate in seawater with a high-capacity anion exchanger and lithium chloride eluent on shipboard. Anal Sci 22:1175–1178

Nakagawa S, Takai K, Inagaki F, Chiba H, Ishibashi J, Kataoka S, Hirayama H, Nunoura T, Horikoshi K, Sako Y (2005) Variability in microbial community and venting chemistry in a sediment-hosted backarc hydrothermal system: impacts of subseafloor phase-separation. FEMS Microbiol Ecol 54(1):141–155

Nakagawa T, Takai K, Suzuki Y, Hirayama H, Konno U, Tsunogai U, Horikoshi K (2006) Geomicrobiological exploration and characterization of a novel deep-sea hydrothermal system at the TOTO caldera in the Mariana Volcanic Arc. Environ Microbiol 8 (1):37–49

Neef A (1997) Anwendung der in situ Einzelzell-Identifizierung von Bakterien zur Populationsanalyse in komplexen mikrobiellen Biozönosen. Doctoral thesis (Technische Universität München)

Nunoura T, Takai K (2009) Comparison of microbial communities associated with phase-separation-induced hydrothermal fluids at the Yonaguni Knoll IV hydrothermal field, the Southern Okinawa Trough. FEMS Microbiol Ecol 67(3):351–370

Nunoura T et al (2010) Archaeal diversity and distribution along thermal and geochemical gradients in hydrothermal sediments at the Yonaguni Knoll IV hydrothermal field in the southern Okinawa Trough. Appl Environ Microbiol 76(4):1198–1211

Perner M, Seifert R, Weber S, Koschinsky A, Schmidt K, Strauss H, Peters M, Haase K, Imhoff JF (2007) Microbial CO_2 fixation and sulfur cycling associated with low-temperature emissions at the Lilliput hydrothermal field, southern Mid-Atlantic Ridge (9°S). Environ Microbiol 9(5):1186–1201

Perner M, Bach W, Hentscher M, Koschinsky A, Garbe-Schönberg D, Streit WR, Strauss H (2009) Short-term microbial and physico-chemical variability in low-temperature hydrothermal fluids near 5°S on the Mid-Atlantic Ridge. Environ Microbiol 11(10):2526–2541

Perner M, Gonnella G, Hourdez S, Böhnke S, Kurtz S, Girguis P (2013) In situ chemistry and microbial community compositions in five deep-sea hydrothermal fluid samples from Irina II in the Logatchev field. Environ Microbiol 15(5):1551–1560

Pernthaler A, Pernthaler J, Amann R (2002) Fluorescence in situ hybridization and catalyzed reporter deposition for the identification of marine bacteria. Appl Environ Microbiol 68(6):3094–3101

Rogers KL, Amend JP, Gurrieri S (2007) Temporal changes in fluid chemistry and energy profiles in the vulcano island hydrothermal system. Astrobiology 7(6):905–932

Schrenk MO, Kelley DS, Delaney JR, Baross JA (2003) Incidence and diversity of microorganisms within the walls of an active deep-sea sulfide chimney. Appl Environ Microbiol 69(6):3580–3592

Sunamura M, Higashi Y, Miyako C, Ishibashi J, Maruyama A (2004) Two bacteria phylotypes are predominant in the Suiyo Seamount hydrothermal plume. Appl Environ Microbiol 70(2):1190–1198

Takai K, Komatsu T, Inagaki F, Horikoshi K (2001) Distribution of archaea in a black smoker chimney structure. Appl Environ Microbiol 67(8):3618–3629

Takai K, Oida H, Suzuki Y, Hirayama H, Nakagawa S, Nunoura T, Inagaki F, Nealson KH, Horikoshi K (2004) Spatial distribution of marine crenarchaeota group I in the vicinity of deep-sea hydrothermal systems. Appl Environ Microbiol 70(4):2404–2413

Teske A, Hinrichs K-U, Edgcomb V, de Vera Gomez A, Kysela D, Sylva SP, Sogin ML, Jannasch HW (2002) Microbial diversity of hydrothermal sediments in the Guaymas Basin: evidence for anaerobic methanotrophic communities. Appl Environ Microbiol 68 (4):1994–2007

Ward JH (1963) Hierarchical grouping to optimize an objective function. J Am Stat Assoc 58(301):236–244

Yanagawa K et al (2013) Metabolically active microbial communities in marine sediment under high-CO_2 and low-pH extremes. ISME J 7:555–567

Zielinski FU, Gennerich H-H, Borowski C, Wenzhöfer F, Dubilier N (2011) In situ measurements of hydrogen sulfide, oxygen, and temperature in diffuse fluids of an ultramafic-hosted hydrothermal vent field (Logatchev, 14°45′N, Mid-Atlantic Ridge): implications for chemosymbiotic bathymodiolin mussels. G Cubed 12(9):Q0AE04

Development of Hydrothermal and Frictional Experimental Systems to Simulate Sub-seafloor Water–Rock–Microbe Interactions

7

Katsuhiko Suzuki, Shingo Kato, Takazo Shibuya, Takehiro Hirose, Shigshi Fuchida, V.J Rejish Kumar, Motoko Yoshizaki, Yuka Masaki, Kentaro Nakamura, Kensei Kobayashi, Harue Masuda, Akihiko Yamagishi, and Tetsuro Urabe

Abstract

Since the discovery in 1977 of deep-sea hydrothermal vents, they have been shown to host unique but diverse biological communities, despite the dark, barren ocean-floor settings in which they exist. Recent research has indicated that the production by fault systems of abundant reducing agents such as hydrogen possibly sustains the microbial communities in these chemoautotrophic ecosystems. High-pressure and high-temperature hydrothermal experiments, and friction experiments, have resulted in the development of important new experimental apparatuses. A batch-type (closed) experimental system that creates

K. Suzuki (✉)
Institute for Research on Earth Evolution (IFREE), Japan Agency for Marine-Earth Science and Technology (JAMSTEC), 2-15 Natsushima, Yokosuka 237-0061, Japan

Precambrian Ecosystem Laboratory, Japan Agency for Marine-Earth Science and Technology (JAMSTEC), 2-15 Natsushima, Yokosuka 237-0061, Japan

Seafloor Resources Research Project (SRRP), Japan Agency for Marine-Earth Science and Technology (JAMSTEC), 2-15 Natsushima, Yokosuka 237-0061, Japan
e-mail: katz@jamstec.go.jp

S. Kato
Japan Collection of Microorganisms, RIKEN BioResource Center, 3-1-1 Koyadai, Tsukuba, Ibaraki 305-0074, Japan

Department of Molecular Biology, Tokyo University of Pharmacy and Life Science, 1432-1 Horinouchi, Hachioji, Tokyo 192-0392, Japan

T. Shibuya
Precambrian Ecosystem Laboratory, Japan Agency for Marine-Earth Science and Technology (JAMSTEC), 2-15 Natsushima, Yokosuka 237-0061, Japan

Seafloor Resources Research Project (SRRP), Japan Agency for Marine-Earth Science and Technology (JAMSTEC), 2-15 Natsushima, Yokosuka 237-0061, Japan

T. Hirose
Kochi Institute for Core Sample Research, Japan Agency for Marine-Earth Science and Technology (JAMSTEC), 200 Monobe-otsu, Nankoku, Kochi 783-8502, Japan

S. Fuchida • H. Masuda
Department of Geosciences, Osaka City University, 3-3-138, Sugimoto Sumiyoshi-ku, Osaka 558-8585, Japan

V.J Rejish Kumar • A. Yamagishi
Department of Molecular Biology, Tokyo University of Pharmacy and Life Science, 1432-1 Horinouchi, Hachioji, Tokyo 192-0392, Japan

M. Yoshizaki
Precambrian Ecosystem Laboratory, Japan Agency for Marine-Earth Science and Technology (JAMSTEC), 2-15 Natsushima, Yokosuka 237-0061, Japan

Department of Earth and Planetary Sciences, Tokyo Institute of Technology, 2-12-1 Ookayama, Meguro-ku, Tokyo 152-8551, Japan

Y. Masaki
Institute for Research on Earth Evolution (IFREE), Japan Agency for Marine-Earth Science and Technology (JAMSTEC), 2-15 Natsushima, Yokosuka 237-0061, Japan

Seafloor Resources Research Project (SRRP), Japan Agency for Marine-Earth Science and Technology (JAMSTEC), 2-15 Natsushima, Yokosuka 237-0061, Japan

K. Kobayashi
Graduate School of Engineering, Yokohama National University, 79-5 Tokiwadai, Hodogaya-ku, Yokohama, Kanagawa 240-8501, Japan

T. Urabe
Department of Earth and Planetary Science, The University of Tokyo, 7-3-1 Hongo, Bunkyo-ku, Tokyo 113-0033, Japan

K. Nakamura
Department of Systems Innovation, The University of Tokyo, 7-3-1 Hongo, Bunkyo-ku, Tokyo 113-8656, Japan

J.-i. Ishibashi et al. (eds.), *Subseafloor Biosphere Linked to Hydrothermal Systems: TAIGA Concept*,
DOI 10.1007/978-4-431-54865-2_7,

equilibrium conditions has contributed greatly to our understanding of sub-seafloor hydrothermal reactions. Flow-type experimental systems have allowed investigation of natural systems under non-equilibrium conditions. Friction experiments have recently been developed to better understand generation of the hydrogen that makes fault systems habitable by primary producers. These experiments suggest that microbial ecosystems sustained by chemical energy derived from fault systems might be widely distributed within oceanic crust. Moreover, flow-type systems that can be used to simulate natural hydrothermal environments that include crustal aquifers might provide insights into the ecological significance of microorganisms and their global contribution to biogeochemical cycles in the ocean and crust.

Here we describe hydrothermal and friction experiment systems that we developed during our Trans-crustal Advection and In-situ biogeochemical processes of Global subseafloor Aquifer (TAIGA) project, and consider the application of some of them to explore the interactions among rocks, fluids, and microbes. For this purpose, our original data obtained in the experiment of interaction between basalt and water in the flow-type system was also included.

Keywords
Friction experiment • Hydrothermal experiment

7.1 Introduction

Hydrothermal experiments using a gun barrel were first undertaken in the 1850s. These experiments determined the solubilities of minerals and investigated their growth mechanisms. Since then, researchers on ore genesis have used experimental apparatuses to investigate the alteration of wall rocks and its relation with hydrothermal gold mineralization.

Hydrothermal interactions between seawater and the lithosphere strongly influence the chemistry of the oceans and control heat exchange between the lithosphere and hydrosphere (Alt 1995). The discovery of deep-sea hydrothermal vents at the Galapagos Spreading Center in 1977 (Corliss et al. 1979; Spiess et al. 1980) inspired much interest in deep-sea hydrothermal systems from scientists in various fields. Gold proposed that microbial ecosystems are widely distributed in sub-seafloor aquifers (Gold 1992). The existence of sub-seafloor ecosystems has been verified by biochemical analyses of samples collected during deep ocean-floor drilling (Cowen et al. 2003; Kimura et al. 2003; Higashi et al. 2004; Nakagawa et al. 2004; Hara et al. 2005; Huber et al. 2006). These studies have shown that hydrothermal vents and deep sea low-temperature springs host diverse biological communities that are sustained by the production of reducing agents such as hydrogen, methane, sulfur, and iron (the TAIGA systems; see Chap. 1), despite the dark, barren ocean-floor settings in which they live (Kelley et al. 2005; Nealson et al. 2005; Takai et al. 2006). These chemoautotrophs obtain energy from the chemical potential between reducing agents in hydrothermal/spring solutions and oxidizing seawater.

Although various types of hydrothermal fluids with different chemistries issue from the ocean floor (Kelley et al. 2005), such fluids in abyssal hydrothermal systems have been proposed as nurturers of the earliest microbial ecosystems. The Rainbow and Kairei fields on the Central Indian Ridge are extremely enriched in H_2 (Takai et al. 2004; Gallant and Von Damm 2006; Kumagai et al. 2008) and host a phylogenetically primitive ecosystem (Yanagawa and Kojima 1985; Russell and Hall 1997). However, because opportunities for investigative cruises have been limited, laboratory experiments have been used effectively to considerably increase our knowledge of the chemistry of hydrothermal vents. An advantage of an experimental approach is that it allows examination of the processes and interactions among hydrothermal solutions, rocks, fault systems, organic matter, and microbial communities by simulating the hydrothermal conditions beneath the seafloor. However, simulating the physical and chemical conditions of seafloor hydrothermal systems in the laboratory is challenging (Seewald 1994; Seyfried et al. 1998). Hydrothermal experiments must be designed to withstand high fluid pressures (up to 50 MPa) and permit temporal monitoring of changes in the composition of fluids coexisting with complex mineral assemblages over a wide range of reaction temperatures. Closed batch-type experimental systems have been used to simulate hydrothermal conditions for several decades (Thornton and Seyfried 1987; Seyfried and Ding 1993), and flow-through systems have more recently been designed to study this environment (Normand et al. 2002).

In 2008, we commence the multi-disciplinary TAIGA (Trans-crustal Advection and In-situ biogeochemical

processes of Global sub-seafloor Aquifer) project, which focuses on interactions among the lithosphere, hydrosphere, and biosphere by examining fluid circulation systems beneath the seafloor. TAIGA is a multi-disciplinary project that uses geophysics (to investigate crustal structure), petrology, geochemistry, microbiology, and laboratory experiments. During the TAIGA project, we developed various experimental systems. In this review, we discuss those apparatuses and others used in hydrothermal and friction experiments, and consider the application of some of them to reveal mechanisms of interaction among rocks, fluids, and microbes. Hydrothermal and frictional experimentation is very much dependent on the development of new experimental apparatuses and techniques, which have been used to achieve successful simulations of various sub-surface conditions in hydrothermal and fault systems. We first describe the two types of apparatus that have been used in hydrothermal experiments (closed batch-type and flow-through devices) and then describe the frictional experiment (simulated fault) system.

7.2 Hydrothermal Experimental Apparatus

7.2.1 Batch-Type Systems

The first known hydrothermal experiment was conducted using a gun barrel (Sénarmont 1851). Typical modern hydrothermal apparatuses are the cold-seal type developed by Tuttle (1948, 1949) and an apparatus developed by Morey and Ingerson (1937) and Morey (1942). Tuttle's cold-seal autoclave had a small reaction cell (less than a few tens of milliliters) with a seal outside the furnace (cold seal), and it could be used at temperatures up to 1,200 °C and pressures of 100–200 MPa. The autoclave designed by Morey and co-workers had a larger cell (more than 250 mL), with metal packing and a Bridgeman seal (Bridgeman 1949), and it could be used at temperatures above 400 °C. An autoclave with an even larger volume (up to 1,000 mL) and a flat flange seal designed by Barnes (1963, 1971) was equipped with a rocking system to promote the rock–water reaction and used the first, simple in situ sampling system. This system was frequently used for experiments on alteration of rocks during investigations of ore genesis.

7.2.1.1 Dickson-Type Autoclave

Dickson et al. (1963) designed the autoclave that is most commonly used today, and significant progress has been made in hydrothermal experiments using it. The Dickson-type autoclave is made of Inconel alloy, which is corrosion resistant and retains adequate strength at elevated temperatures and pressures. We used a Dickson-type autoclave in our TAIGA project at the Japan Agency for Marine-Earth Science and Technology (JAMSTEC) to reproduce hydrothermal conditions of up to 600 °C and 60 MPa. One of the characteristics of the Dickson-type apparatus is that it has a flexible reaction cell in the metal autoclave (Fig. 7.1) that allows in situ sampling of reacted solutions without a significant decrease in the pressure within the cell. Though the flexible cell gradually shrinks when sample solution is removed, a pump provides a small continuous flow of pressurized water within the autoclave to maintain the pressure and temperature. Another advantage of the Dickson-type apparatus is that the metal autoclave is isolated from corrosive high-salinity reaction water. These features have allowed researchers to make considerable progress in understanding deep-sea hydrothermal systems (e.g., Berndt et al. 1996; Seyfried et al. 1998, 2007; McCollom and Seewald 2001, 2003a, b, 2007; Yoshizaki et al. 2009; Shibuya et al. 2013). Because the reaction cell of the initial system was made of Teflon (Dickson et al. 1963), the experiment could only be performed at temperatures of less than 285 °C, too cold to reproduce high-temperature hydrothermal reactions. A thin gold bag was later used for the reaction cell (Rytuba et al. 1978), but it was difficult to seal the sample and solution in the bag without creating a pin hole. The use of a Ti head on the gold bag markedly improved the Dickson-type hydrothermal experimental system (Seyfried et al. 1979; Seyfried 1987) (Fig. 7.2). Because titanium oxide is resistant to corrosion by seawater, the surface of the Ti head is deliberately oxidized before experimental use to avoid production of abundant H_2 by the reaction of Ti metal with seawater. Fluid samples can be extracted from the reaction cell through a gold-lined tube at any time during an experiment. The gold tube is inserted into a stainless steel or Inconel tube, and both ends of the gold tube are then expanded by heating with a torch such that they cover the ends of the stainless steel or Inconel tube (Fig. 7.3). To eliminate organic matter that will react with hydrogen to produce methane, all of the materials that will come into contact with the reaction fluid during the experiment are baked in a muffle furnace at 500 °C for 3 h before use.

We used a batch-type system at JAMSTEC to reproduce a komatiite hydrothermal system. We first synthesized komatiite in a redox-controlled furnace (e.g., Yoshizaki et al. 2009) and then pulverized the komatiite before placing it in our experimental apparatus. Abundant hydrogen was produced by the reaction of the komatiite with artificial seawater at 350 °C and 50 MPa (Yoshizaki et al. 2009). We also conducted water–rock reaction experiments in the presence of CO_2 in a Dickson-type system (Shibuya et al. 2013). The reaction solution was a mixture of $NaHCO_3$, NaCl, 36 % HCl, and pure water. To avoid degassing of CO_2 by reaction of $NaHCO_3$ and HCl before the reaction cell was sealed, the $NaHCO_3$ and HCl were separately

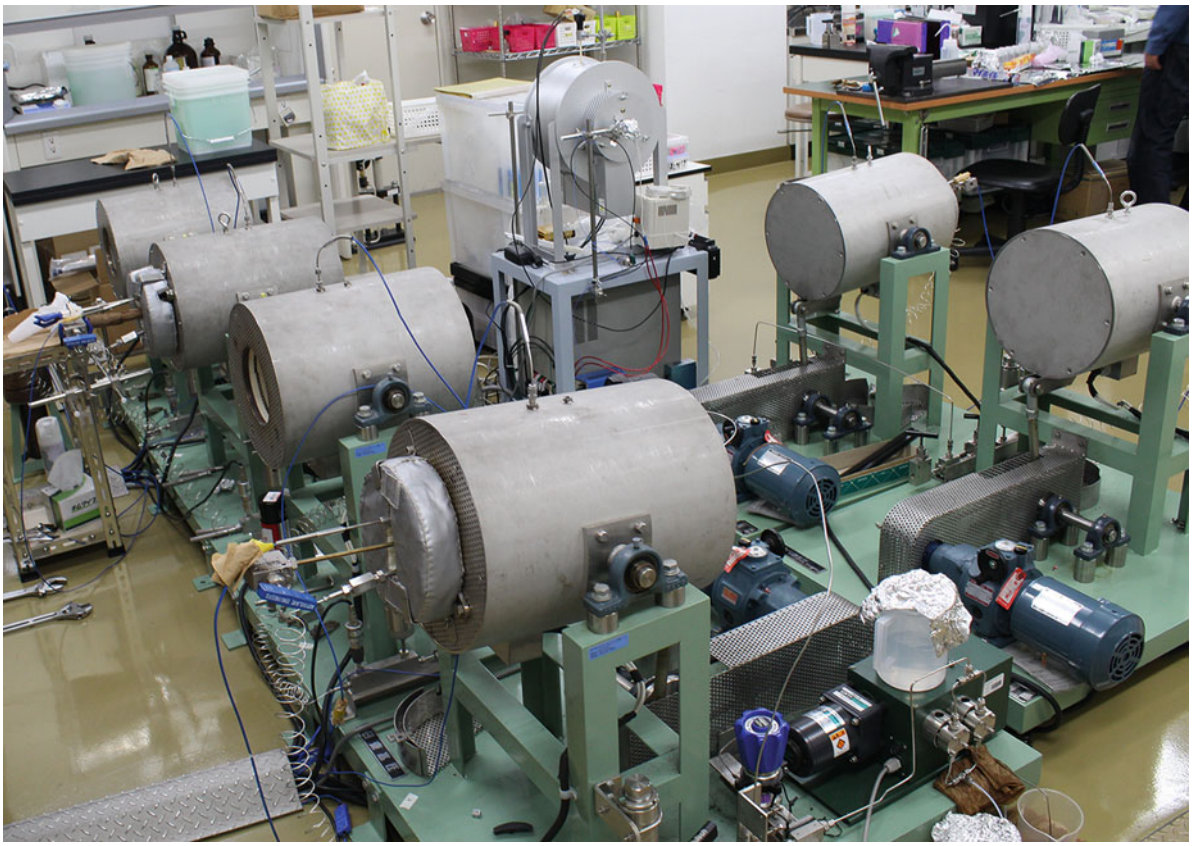

Fig. 7.1 Photo of Dickson-type autoclaves at JAMSTEC

loaded into the bottom and top, respectively, of the reaction cell in addition to the basalt powder and NaCl solution being loaded into the bottom. After the reaction cell was sealed, it was shaken to dissolve and completely mix these reagents.

7.2.1.2 Batch Experiments to Investigate Amino Acid Reactions During Interactions of Sediments and Hydrothermal Solutions

To investigate the reactions of amino acids under deep-sea hydrothermal conditions, we designed two batch-type autoclave reactors at Osaka City University. The first type used a Teflon jar as the reaction vessel (25 mL) within a stainless steel autoclave. A Teflon reaction vessel was chosen for ease of handling and because it would not react with the reaction fluids, but this choice limited the maximum reaction temperature to 200 °C. The system was not equipped with an in situ sampling system; reacted samples were collected after the experiment.

The second batch-type autoclave used a titanium reaction vessel and lid (volume 160 mL) with an in situ sampling system (Fig. 7.4) that allowed sampling of the solution during the experiment. After a sample was placed in the vessel, argon gas was flushed through the system to prevent oxidation, and the vessel was tightly closed and heated by a mantle heater to a maximum temperature of 300 °C. Gold mesh in the head of the sampling valve was used to prevent contamination of the collected liquid phase by solids. The temperature of the reactor was controlled and monitored with a thermocontroller. Solutions were collected from the reactor at predetermined time intervals without reducing the temperature of the reactor vessel.

Reactors such as those described above provide a means to observe dissolution of organic and inorganic matter from rocks and sediments under various hydrothermal conditions. These experimental systems have been used to observe the behavior and dissolution processes of amino acids during reactions between NaCl solutions and natural seafloor sediments (Ito et al. 2006, 2009). Ito and co-workers reported that amino acids were rapidly released from the sediments and were then gradually decomposed in hydrothermal solution at temperatures above 150 °C. Reactors such as these enable observation under hydrothermal conditions of the kinetic behavior and the stability of organic matter such as amino acids, peptides, and proteins. For example, comparison of the effect of heating of six amino acids (Glycine, Serine, Glutamate, Lysine, Cysteine, and Proline) under acidic and alkaline hydrothermal conditions at 150 °C for 3–168 h indicated that amino acids are

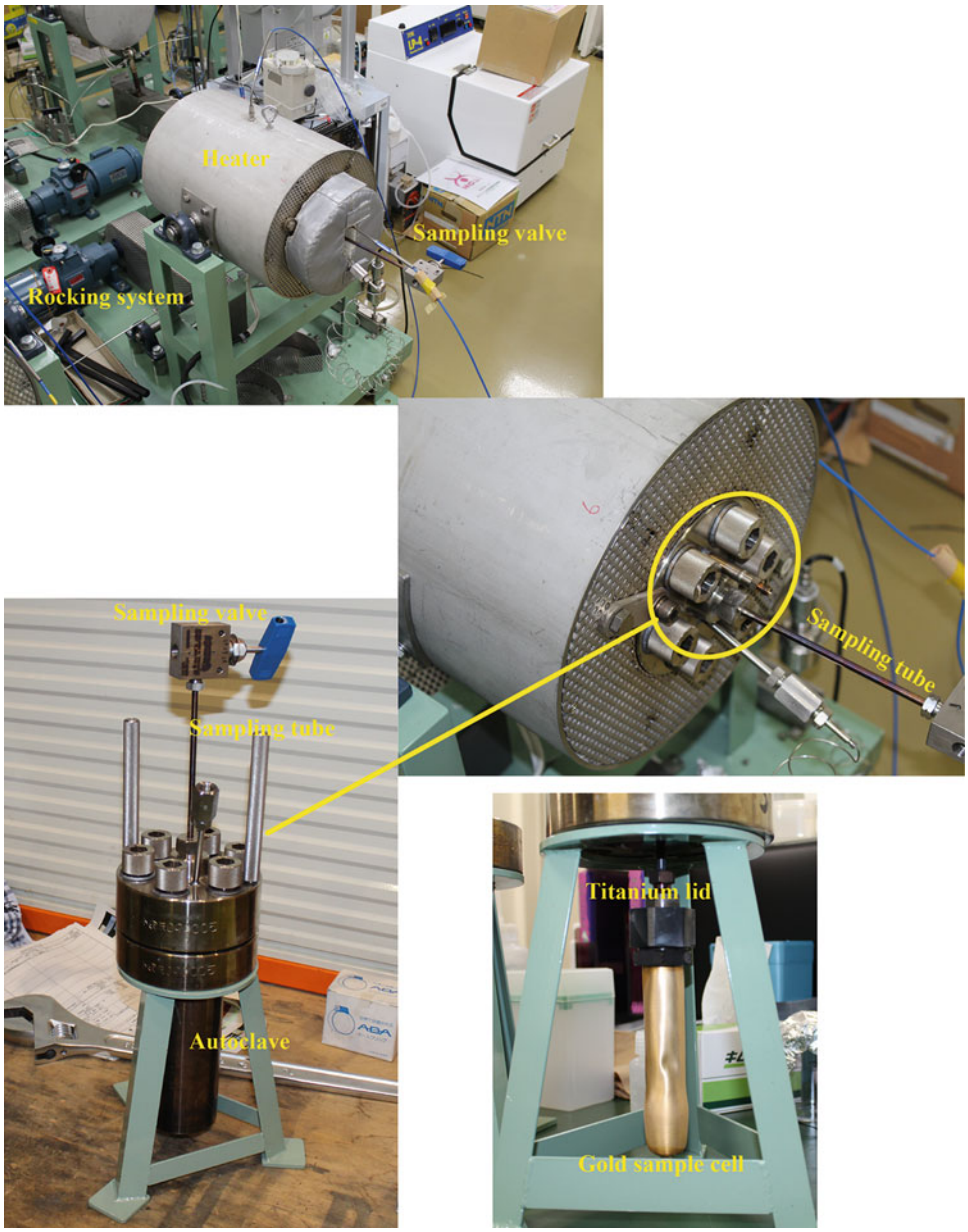

Fig. 7.2 Photos of Dickson-type hydrothermal system showing detail views of gold sample cell with Ti lid

kinetically less stable under acidic conditions than under alkaline conditions (Ito et al. 2006, 2009).

7.2.2 Flow-Type Systems

The advantage of flow-type systems over batch-type systems is that they better simulate the water–rock interactions of natural hydrothermal systems. In batch-type systems, the chemical composition and pH of the reaction solution change with time, whereas flow-type systems allow these parameters to remain constant during an experiment.

A flow-type system was first designed in the 1950s, as described by Williams-Jones et al. (1994). A simple, single-path flow-type apparatus for measuring the solubility of various minerals was designed for use in experiments on the alteration of minerals during hydrothermal ore genesis (Morey and Hesselgesser 1951; Morey and Chen 1955; Morey and Fournier 1961). Other researchers have used this single-path system to measure the solubility of magnetite, NiO, and UO_2 (Seweeton and Baes 1970; Tremaine and Leblanc 1980; Tremaine et al. 1981), to determine the mobility of uranium in felsic volcanic rocks (Zielinski 1979), and to analyze serpentinization (Barnes et al. 1972). A circulation path flow-type experimental system, which was first designed by Barnes et al. (1983), has been used in kinetic studies of mineral–water interactions (Charles and Bayhurst 1983; Barnes and Gould 1992).

Fig. 7.3 Photo of sampling tube with gold liner

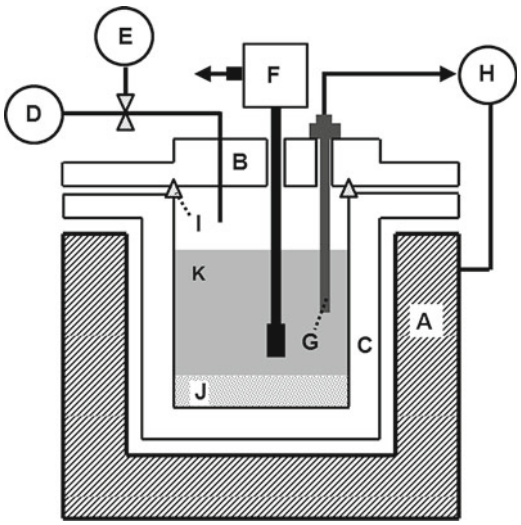

A: Mantle heater, B: Lid, C: Reaction vessel,
D: Argon gas cylinder, E: Pressure gauge,
F: Sampling valve, G: thermocouple,
H: Controller and Recorder, I: Gascket (teflon or aluminum), J: Solid sample, K: Liquid sample

Fig. 7.4 Schematic diagram of apparatus used for batch experiment to examine amino acid reactions during interaction between sediments and hydrothermal solutions

The technical difficulties associated with the various flow-type experimental apparatuses are generally greater than those of batch-type apparatuses. With flow-type apparatuses it is difficult to precisely control the temperature, pressure, and flow rate of the reaction solution. Redox reaction conditions cannot be controlled or measured, and obtaining material to construct the experimental apparatus is problematic. The flow tubes in various components of flow-type systems are commonly made of stainless steel alloys (e.g., Hastelloy or Inconel) because of their resistance to corrosion, ease of handling, and low cost. We built a flow-type system with stainless steel flow tubes (described later). When artificial seawater was used in that system, it caused severe corrosion of the flow tubes and pressure gauges. If high-salinity solutions such as seawater are to be reacted in flow-type systems, the corrosion problem must be addressed. One solution to this problem is to use titanium steel for all parts of the apparatus that will be in contact with high-salinity reaction solutions. However, the low heat resistance of Ti steel is a disadvantage in this case. If reaction temperatures and pressures lower than 100 °C and 35 MPa are required, the use of tubes made of polyether-etherketone (PEEK) resin may be possible, but an ideal solution for this problem is yet to be identified. The problem of corrosion was also encountered in hydrothermal experiments using artificial seawater in the reactor system for a microbial study (see Sect. 7.2). The concentrations of chemical components such as Fe, Ni, and Cr in SUS 316 stainless steel or Hastelloy alloy C-276 reactors increased considerably during these experiments, implying corrosion of the reactor vessels by seawater under conditions of 400 °C and 40 MPa. Further modifications, such as gold plating of the walls of the reaction vessel, are needed to reproduce the environments experienced by microbial ecosystems in deep-sea hydrothermal systems.

7.2.2.1 Flow-Type Experimental System for Simulation of Water–Rock Interactions

A flow-type experimental system (Fig. 7.5) has been installed at JAMSTEC to investigate water–rock interactions. We used the twofold (outer and inner) reaction tube of this system (Fig. 7.6) for our experiment. In this system, reaction solution is transferred from a 10 L plastic storage bottle into the inner tube of the reaction zone (red line on Fig. 7.5), which is made of Ti to prevent corrosion due to reaction with the solution. The outer tube surrounding the reaction tube is filled with pure water pressurized by a pump used for High Performance Liquid Chromatography (HPLC). The pressures within the outer and inner (reaction) tubes can be increased up to 100 MPa and are manually balanced by using two back-pressure valves. The solid rock sample is placed in the center tube and the reaction solution is introduced at a maximum temperature of 500 °C and reacted with the rock sample and the cooled in a cold bath. The reacted solution is extracted via the sampling tube connected to the back pressure valve. A gas-tight syringe is used to sample the gases (H_2, CO_2, CH_4, and C_2H_6) in the reacted solution for analysis using gas chromatography. The reacted solution is also analyzed by inductively coupled plasma atomic emission spectrometry (ICP-AES) and ion chromatography for dissolved elements including Na, K, Ca, and Cl. Because the sensors of the pressure gauges

Fig. 7.5 Photos of flow-type experimental system developed at JAMSTEC for simulation of water–rock interactions

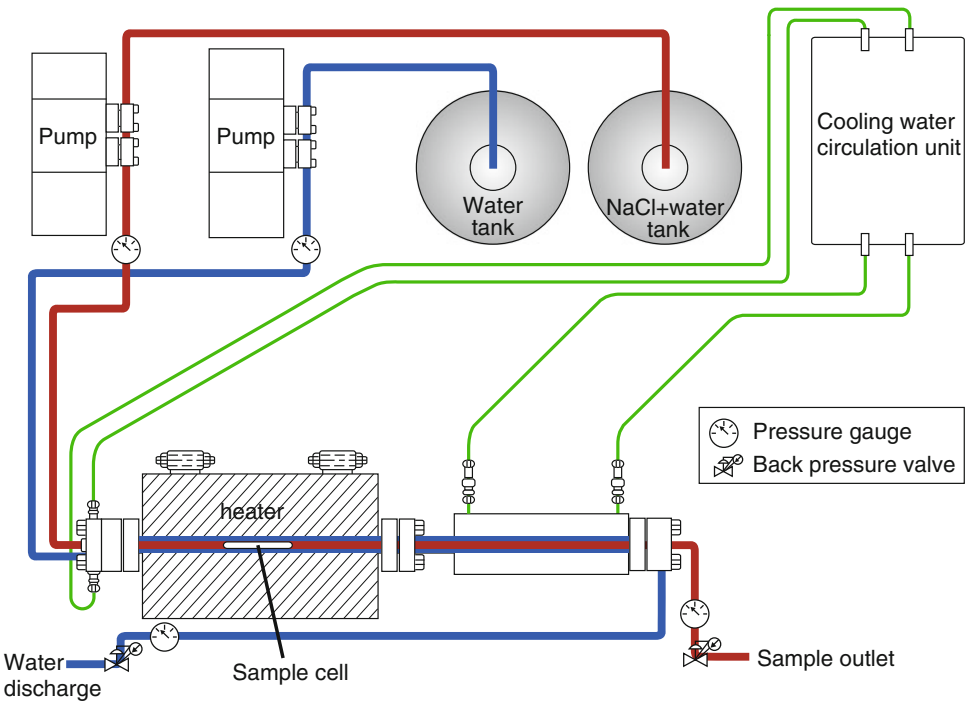

Fig. 7.6 Schematic diagram of flow-type experimental system at JAMSTEC used for simulations of water–rock interactions

used are commonly made of easily corroded stainless steel containing Cu, we covered the pressure sensor with a thin corrosion-resistant plate to isolate it from the reaction solution.

7.2.2.2 Flow-Type Experimental System for Simulation of Microbial Ecosystems in a Deep-Sea Hydrothermal Vent System

Our current understanding of the ecology of hydrothermal vent systems is severely limited by the difficulty of obtaining adequate quantities of samples at appropriate spatial and temporal intervals. Microbial consortia consisting mainly of Bacteria and Archaea have been found in hydrothermal deposits (such as black smoker chimneys) and close to hydrothermal systems, for example, in areas where plumes of hot hydrothermal waters mix with cold ambient seawater, and in the mixing zone below the seafloor. Both culture-dependent and culture-independent approaches have provided inventories of microbial diversity at various deep-sea vent fields in different geological settings (e.g., Takai et al. 2001; Reysenbach and Shock 2002; Nercessian et al. 2003; Schrenk et al. 2003; Hara et al. 2005; Nakagawa et al. 2005; Kato et al. 2009a, b, c, 2013a, b). However, these studies have provided only snapshots of dynamic microbial communities. Reproduction in the laboratory of both hydrothermal systems and their microbial communities will help us to explore the growth and metabolism of deep-sea vent microbes and to understand their role in biogeochemical processes in seafloor vent systems. Furthermore, such hydrothermal reactor systems can be used to study past hydrothermal processes, perhaps even those in extraterrestrial environments. For example, Shibuya et al. (2010) hypothesized that hydrothermal fluids in Archaean hydrothermal systems were highly alkaline. Flow-type experimental systems have a considerable advantage over batch-type systems where cultivation of microbes is required; hypotheses such as that of Shibuya et al. (2010) can be experimentally examined by simulation in a flow-type system. The fluids and precipitants so generated will provide valuable information on the Archaean ocean.

Although batch-type systems have been used to investigate interactions among microbial ecosystems, minerals, and hydrothermal solutions, flow-through devices have also been designed to study these interactions (Normand et al. 2002). Kato et al. (2013a) reported a flow-type hydrothermal reactor system that can simulate microbial and chemical processes in a deep-sea hydrothermal system. Although the reactor system has not yet been used to reproduce a microbial ecosystem, they successfully investigated the dissolution of major elements (Si, Na, Al, K, Fe, and P) from basaltic rocks at high temperature (340 °C) and pressure (40 MPa) under conditions of ultrapure water flow (Kato et al. 2013a). Their study was the first to demonstrate dissolution of phosphorus (a major element that is essential for life) from basaltic rocks in a flow-type hydrothermal experiment, thus providing important insights into the sustainability of microbial ecosystems in deep-sea hydrothermal systems.

Previous hydrothermal experiments (both batch- and flow-type experiments) have considered dissolution of the major elements in rocks, but not the minor elements that potentially affect the growth of microbes. Our hydrothermal experiment (described below) provides direct evidence for dissolution of As, Ni, Zn, Rb, V, and Li from basaltic rocks at high temperature (340 °C) and pressure (40 MPa).

The hydrothermal reactor system we used has been described in detail by Kato et al. (2013a). In brief, the reactor system consists of a preheating bath (100 mL), a water–rock reaction bath (390 mL), and a cooling bath (5 L) (Fig. 7.7). It is a flow-through system operated by a double-plunger HPLC pump. The preheating and reaction baths are equipped with heaters that can heat them to 300 °C and 500 °C, respectively. Fluid pressure inside the reactor system can reach 50 MPa and is maintained by a back-pressure regulator. Temperatures in the preheating and the reaction baths, and pressure inside the reactor system, are continuously monitored by a computer connected to the system. The reaction bath and connected lines are made of Hastelloy alloy C-276. Other components of the system are made of SUS316 stainless steel. Cool water pumped into the cooling bath simulates the mixing of hydrothermal fluids with cool seawater. The temperature in the cooling bath is maintained at 5 °C by a cooling water jacket.

Kato et al. (2013a) reported the dissolution of major elements from basaltic rocks under the following conditions: fluid pressure of 40 MPa, preheating bath at 250 °C, reaction bath at 340 °C, and water flow of 6 mL/h. The reactor system was operated for 1,271 h using basalt samples and ultrapure water, and for 1,920 h without basalts (blank test). Fluid samples were collected intermittently from the cooling bath, and then analyzed by multi-channel ICP-AES (SPS5500; SII NanoTechnology, Chiba, Japan). The original concentrations of minor elements in the basalts (also determined by the ICP-AES) were V, 411 ppm; Rb, 130 ppm; Zn, 91.3 ppm; Ni, 11.1 ppm; and Li, 7.33 ppm.

The changes of concentrations of As, Ni, Zn, Rb, V, and Li in the collected samples that are the same ones as those reported by Kato et al. (2013a) during the experiment are shown (Fig. 7.8). The final concentrations of these elements are clearly higher than those of the blank test, indicating that they were dissolved from the basaltic rocks during the experiment. These elements, if dissolved from basaltic rocks in deep-sea hydrothermal systems, might support the growth of microbes living there. Arsenic is used by microbes in the form of organoarsenicals, which are involved in microbial cellular functions, or as an electron acceptor

during anaerobic respiration (Stolz et al. 2006). Nickel and Zn are necessary for enzymes to function as cofactors (Morel and Price 2003). Vanadium is used by some microbes as a cofactor for nitrogen-fixation enzymes (nitrogenase) (Robson et al. 1986). Lithium and Rb are probably not essential for life, and their effect on microbial growth is unclear.

7.2.2.3 Supercritical Water Flow-Type System to Simulate Amino Acid Reactions

To examine the possible reactions of amino acids in simulated hydrothermal systems, we constructed a supercritical water-flow reactor (SCWFR) at Yokohama National University (Fig. 7.9). The SCWFR is equipped with an infrared (IR) gold image furnace. The temperature of fluid in the reaction tube is monitored with thermocouples. We examined the polymerization of glycine and the stability of some amino acids under high temperature conditions up to and above the critical temperature for water.

The sample solution was pumped into the reaction tube with an HPLC pump. The fluid pressure was kept at 25 MPa by a back-pressure regulator. Without preheating, the fluid was rapidly heated (within a few seconds) to 400 °C by an IR gold image furnace. The furnace was equipped with four 26.5 cm quartz–tungsten lamps within a gold-plated body, and radiated heat uniformly into the reaction tube. The reaction tube was made of Hastelloy alloy C-276, and connectors in the high-temperature area of the system were

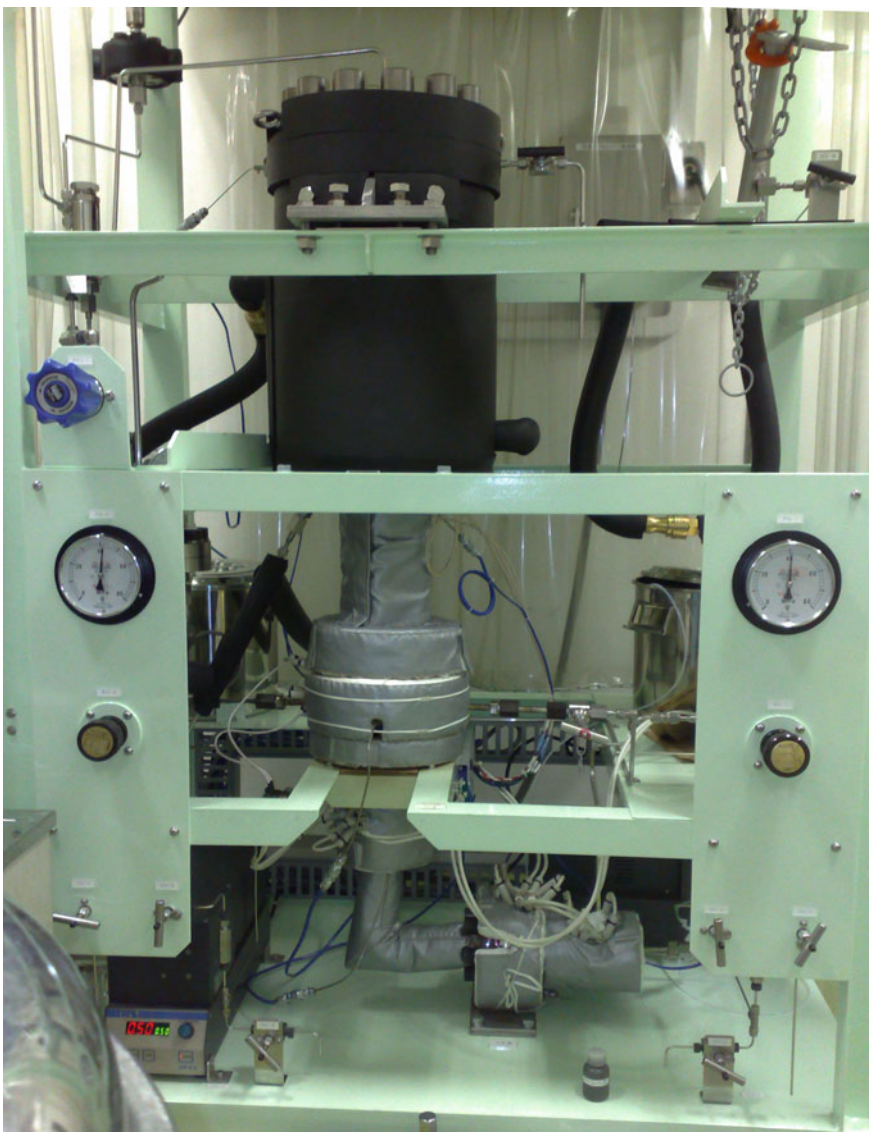

Fig. 7.7 Photo and schematic diagram of flow-type hydrothermal reactor system described previously (Kato et al. 2013a)

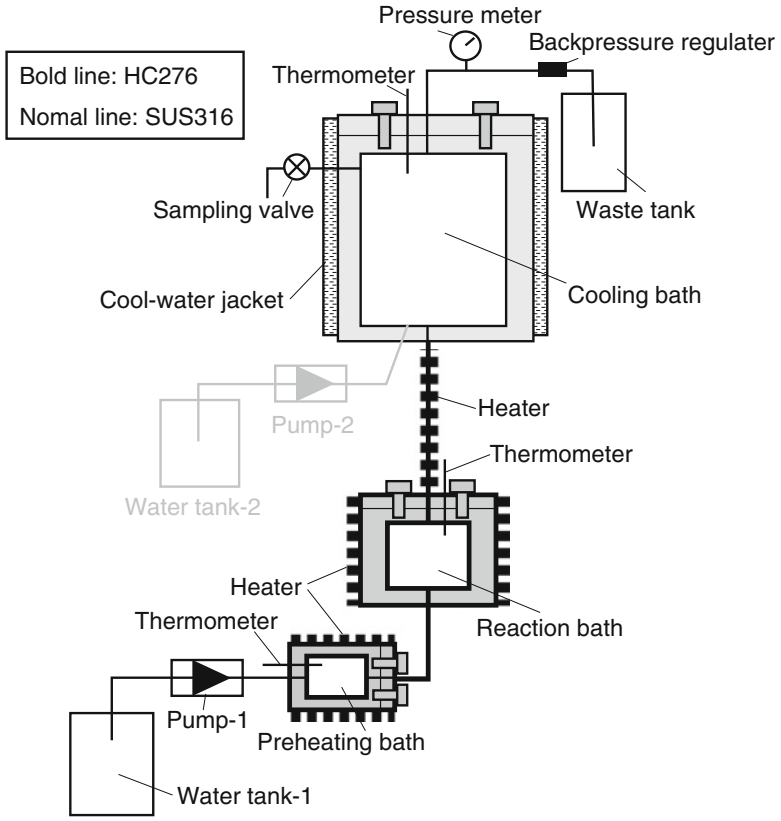

Fig. 7.7 (continued)

made of Inconel (INC-200-3). Temperatures both inside and outside the reaction tube were monitored with thermocouples. The thermocouple used to monitor fluid temperature was sheathed with Inconel.

The reactor was used to examine the formation of organic aggregates from a solution of complex organic compounds that were abiotically synthesized from a simulated primitive earth atmosphere by irradiation with high-energy protons (Kurihara et al. 2012). Under hydrothermal conditions, the structure of some of the resultant organic compounds changed, forming organic aggregates. The formation of organic aggregates such as these might have been an important step in the chemical evolution that led to the development of life on Earth. The reactor system was also used below the critical temperature of water. We tested the stability and reaction of several amino acids at 200–250 °C (Chandru et al. 2013). The resultant data showed that the survivabilities of individual amino acids in the simulators differed. We found that the stability of the amino acids was constrained by heating time, exposure time to cold quenching, and the presence and amounts of metal ions and silica (e.g., Chandru et al. 2013).

7.3 High-Velocity Friction Apparatus for Simulation of Faulting in an Earthquake-Driven Subsurface Biosphere

To simulate faulting, which would generate hydrogen to sustain methanogenesis, we modified a rotary-shear, high-speed friction testing apparatus at JAMSTEC to measure the physical properties of faults (Shimamoto and Tsutsumi 1994; Hirose and Shimamoto 2005). High-speed slip on a fault under normal stress is simulated in this apparatus by placing a pair of solid (or hollow) cylindrical specimens end to end and applying an axial load. Then, one specimen is kept stationary and the other rotated at high speed (Fig. 7.10). To measure the concentration of the hydrogen generated, the experiment was conducted in a pressure vessel attached to a gas chromatograph (Fig. 7.11, Hirose et al. 2011, 2012). Samples for stable isotope analysis were removed via a septum mounted on the vessel by means of a gas-tight syringe and stored in a helium-filled glass vial for later analysis by continuous-flow isotope ratio mass

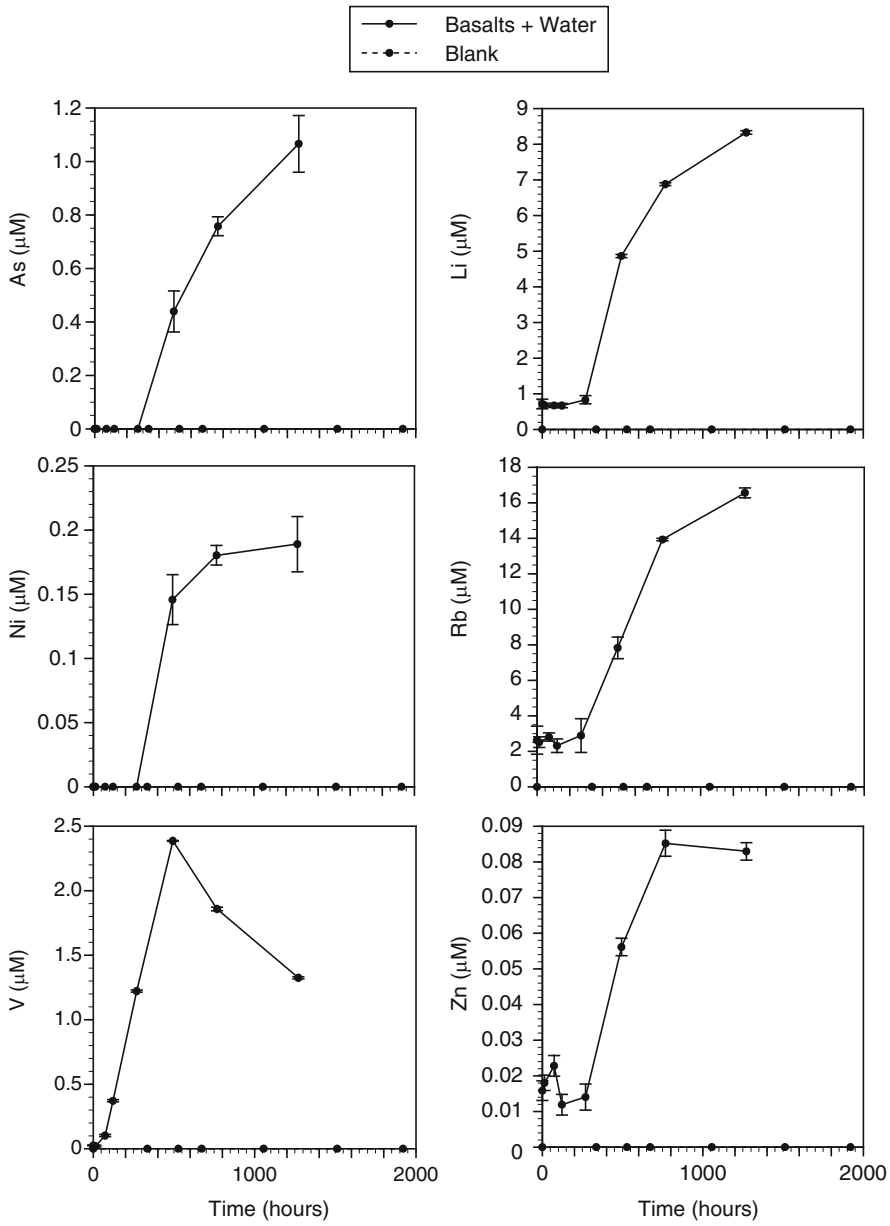

Fig. 7.8 Changes of concentrations of As, Ni, Zn, Rb, V, and Li in samples taken during experiments conducted using the reactor shown in Fig. 7.7

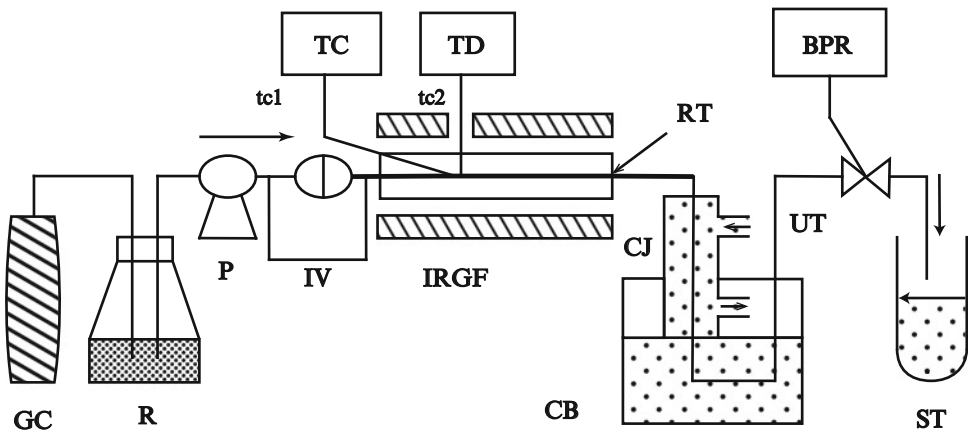

Fig. 7.9 Schematic diagram of Supercritical Water Flow Reactor (SCWFR) developed at National Yokohama University (Islam et al. 2003). *GC* gas cylinder, *R*, reservoir, *P* HPLC pump, *IV* injection valve, *IRGF* infrared gold image furnace, *RT* reaction tube, *TC* temperature controller, *TD* temperature display, *tc1* and *tc2* thermocouples, *CB* cold bath (0 °C), *CJ* cooling jacket, *UT* outlet tube, *BPR* back pressure regulator, *ST* sampling tube

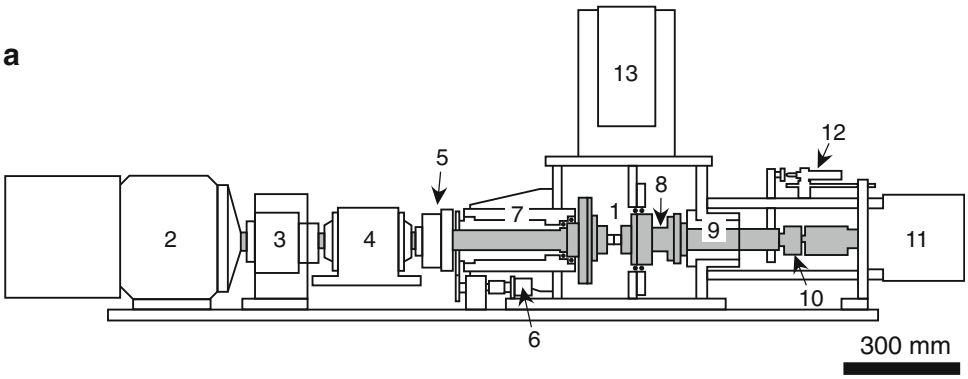

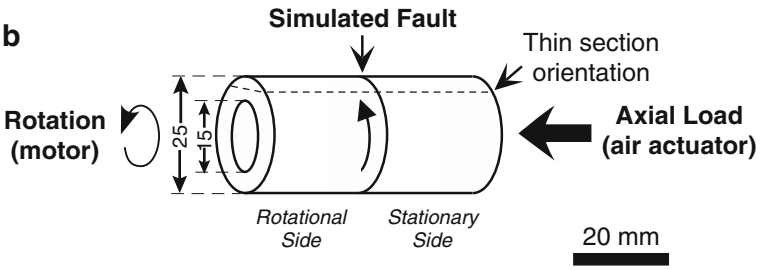

Fig. 7.10 Schematic diagrams of the rotary-shear, high-speed friction testing apparatus (Shimamoto and Tsutsumi 1994)

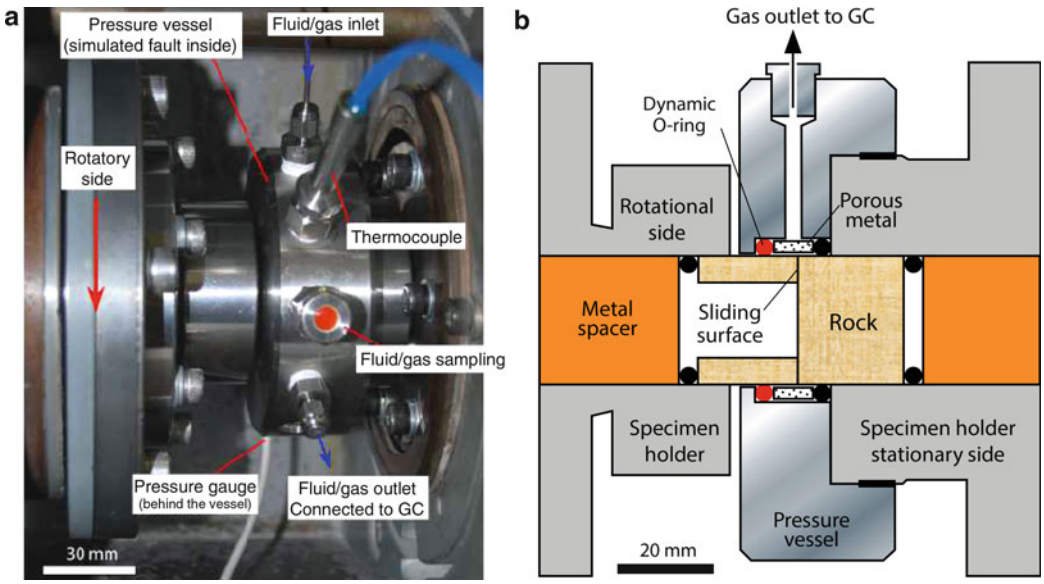

Fig. 7.11 Photo and schematic diagram of pressure vessel equipped with the friction experiment system (Hirose et al. 2011)

spectrometry (Kawagucci et al. 2010). The pressure vessel was filled with air at a room humidity of ~45 % for most of the experiments, but for some experimental runs air was replaced with argon gas to replicate the nominally anoxic conditions under which earthquakes normally occur.

For our experiments, we used typical rock types of the Earth's crust, such as basalt, dunite, granite, marble, and sandstone. The sliding surfaces of the specimens were first ground and roughened with 100 grit SiC powder. They were then either dried in an oven at 100 °C for at least two weeks, or saturated with distilled water in a vacuum chamber. Sliding was at a constant velocity of 1.6 m/s under a normal stress of 0.5–2.5 MPa for a total displacement of 10 m. The H_2 released was measured by a vessel-mounted gas chromatograph with a thermal conductivity detector. The H_2O used to wet the specimens and the H_2 released from the wet-basalt specimen were also sampled for stable isotope analyses. We found that abundant H_2 was produced during the friction experiments and that the amounts of H_2 produced were proportional to the frictional work done (Hirose et al. 2011, 2012).

Friction at a dynamic O-ring seal (Teflon-containing O-ring: Product No. TOMBO No.2670-FA-F) used in the reaction vessel to confine the released gas during rapid sliding (Fig. 7.11, Hirose et al. 2011) contributed to the measured shear traction. Therefore, to determine accurately the frictional work acting on the fault, the mechanical data must be corrected. To evaluate the friction at the contact between the O-ring and the outer surface of the rock, we opened a 1-mm-wide space between the rotational and stationary specimens and then measured the shear traction due to O-ring friction only. This experiment was conducted for all of the rock types we used under the same conditions as the primary experiments, except that no normal load was applied. We found that frictional behavior was independent of rock type. For an applied normal stress of 1 MPa, O-ring friction contributed ~18 % to the initial peak and <8 % to the steady-state measured shear traction. To account for this contribution, we simply subtracted the shear traction determined in the supplementary experiments from the raw traction data for each experiment.

Hydrogen was also released from the O-ring as a result of abrasive wear and frictional heat during sliding. We measured the concentration of H_2 gas generated only from the O-ring in all blank experiments by again opening a 1-mm-wide space between the rotational and stationary specimens and then measuring the H_2 gas generated. The H_2 gas concentration from the O-ring varied from 50 to 195 ppm, depending on the initial surface roughness of the outer surfaces of the specimens and on their outer diameter. Thus, we determined the amount of H_2 generated by faulting alone by simply subtracting 150 ppm from the raw data from each experiment (Hirose et al. 2011). The O-ring contribution of 150 ppm corresponds to between 4 % and 35 % of the measured H_2 during the experiments described by Hirose et al. (2011). The H_2 generated from the O-ring might be a function of shear displacement. However, because we used a displacement of 10 m in all experiments, this was not an important issue.

Acknowledgments We thank Mamiko Umetsu and Sayuri Kubo for drawing some figures. The comments by Yoshinori Takano and Fumitaka Yanagisawa considerably improved our manuscript. This study was supported by MEXT, Grant-in-Aid for Scientific Research on Innovative Areas "Project TAIGA: Trans-crustal Advection and In-situ biogeochemical process of Global sub-seafloor Aquifer". Authors wish to thank Prof. Urabe and members of Project TAIGA for their collaboration and discussion.

References

Alt JC (1995) Sulfur isotopic profile through the oceanic crust: sulfur mobility and seawater-crustal sulfur exchange during hydrothermal alteration. Geology 23:585–588

Barnes HL (1963) Ore solution chemistry. I. Experimental determination of mineral solubilities. Econ Geol 58:1054–1060

Barnes HL (1971) Investigation in hydrothermal sulfide systems. In: Ulmer GC (ed) Research Techniques for High Pressure and High Temperature. Springer-Verlag, Berlin Heidelberg, pp 317–335

Barnes HL, Gould WW (1992) Hydrothermal replacement of carbonates by sulfides. Paper presented at 7th international symposium on water–rock interaction Balkema, Utah, 13–18 July 1992

Barnes I, Rapp JB, O'Neill JR, Sheppard RA, Gude AJ (1972) Metamorphic assemblages and the direction of flow of metamorphic fluids in four instances of serpentinization. Contrib Mineral Petrol 35:263–276

Barnes HL, Downs WF, Rimstidt JD (1983) Experimental determination of rates of hydrothermal reactions. Paper presented at the 1st international symposium on hydrothermal reactions, Tokyo Institute of Technology, Tokyo

Berndt ME, Allen DE, Seyfried WE (1996) Reduction of CO_2 during serpentinization of olivine at 300°C and 500 bar. Geology 24:351–354

Bridgeman PW (1949) The physics of high pressure. Bell and Sons, London, 445 pp

Chandru K, Imai E, Kaneko T, Obayashi Y, Kobayashi K (2013) Survivability and Abiotic Reactions of Selected Amino Acids in Different Hydrothermal System Simulators. Origins Life Evol Biospheres 43:99–108. doi:10.1007/s11084-013-9330-9

Charles RW, Bayhurst GK (1983) Rock-fluid interactions in a temperature gradient: biotite granodiorite + H_2O. J Volcanol Geotherm Res 15:137–166. doi:10.1016/0377-0273(83)90098-7

Corliss JB, Dymond J, Gordon LI, Edmond JM, Herzen RPV, Ballard RD, Green K, Williams D, Bainbridge A, Crane K, Vanandel TH (1979) Submarine thermal springs on the Galapagos Rift. Science 203:1073–1083. doi:10.1126/science.203.4385.1073

Cowen JP, Giovannoni SJ, Kenig F, Johnson HP, Butterfield D, Rappe MS, Hutnak M, Lam P (2003) Fluids from aging ocean crust that support microbial life. Science 299:120–123. doi:10.1126/science.1075653

Dickson FW, Blount CW, Tunell G (1963) Use of hydrothermal solution equipment to determine the solubility of anhydrite in water from 100°C to 275°C and from 1 bar to 1000 bars. Am J Sci 261:61–78

Gallant RM, Von Damm KL (2006) Geochemical controls on hydrothermal fluids from the Kairei and Edmond Vent Fields, 23°–25° S, Central Indian Ridge. Geochem Geophys Geosyst 7. doi:10.1029/2005gc001067

Gold T (1992) The deep, hot biosphere. Proc Natl Acad Sci U S A 89:6045–6049

Hara K, Kakegawa T, Yamashiro K, Maruyama A, Ishibashi JI, Marumo K, Urabe T, Yamagishi A (2005) Analysis of the archaeal sub-seafloor community at Suiyo Seamount on the Izu-Bonin Arc. Space Life Sci Closed Ecol Syst Earth Space Appl 35:1634–1642. doi:10.1016/j.asr.2005.04.111

Higashi Y, Sunamura M, Kitamura K, Nakamura K, Kurusu Y, Ishibashi J, Urabe T, Maruyama A (2004) Microbial diversity in hydrothermal surface to subsurface environments of Suiyo Seamount, Izu-Bonin Arc, using a catheter-type in situ growth chamber. Fems Microbiol Ecol 47:327–336. doi:10.1016/s0168-6496(04)00004-2

Hirose T, Shimamoto T (2005) Growth of molten zone as a mechanism of slip weakening of simulated faults in gabbro during frictional melting. J Geophys Res Solid Earth 110. doi:10.1029/2004jb003207

Hirose T, Kawagucci S, Suzuki K (2011) Mechanoradical H_2 generation during simulated faulting: implications for an earthquake-driven subsurface biosphere. Geophys Res Lett 38. doi:10.1029/2011gl048850

Hirose T, Kawagucci S, Suzuki K (2012) Correction to "Mechanoradical H_2 generation during simulated faulting: Implications for an earthquake-driven subsurface biosphere". Geophys Res Lett 39:L23304. doi:10.1029/2012GL054539

Huber AB, Kania A, Tran TS, Gu CH, Garcia ND, Lieberam I, Johnson D, Jessel TM, Ginty DD, Kolodkin AL (2006) Distinct roles for secreted semaphorin signaling in spinal motor axon guidance. Neuron 49:319. doi:10.1016/j.neuron.2006.01.002

Islam Md. N, Kaneko T, Kobayashi K (2003) Reaction of amino acids in a supercritical water-flow reactor simulating submarine hydrothermal systems. Bull Chem Soc Jpn 76:1171–1178

Ito M, Gupta LP, Masuda H, Kawahata H (2006) Thermal stability of amino acids in seafloor sediment in aqueous solution at high temperature. Org Geochem 37:177–188. doi:10.1016/j.orggeochem.2005.09.004

Ito M, Yamaoka K, Masuda H, Kawahata H, Gupta LP (2009) Thermal stability of amino acids in biogenic sediments and aqueous solutions at seafloor hydrothermal temperatures. Geochem J 43:331–341

Kato S, Kobayashi C, Kakegawa T, Yamagishi A (2009a) Microbial communities in iron-silica-rich microbial mats at deep-sea hydrothermal fields of the Southern Mariana Trough. Environ Microbiol 11:2094–2111. doi:10.1111/j.1462-2920.2009.01930.x

Kato S, Hara K, Kasai H, Teramura T, Sunamura M, Ishibashi J-I, Kakegawa T, Yamanaka T, Kimura H, Marumo K, Urabe T, Yamagishi A (2009b) Spatial distribution, diversity and composition of bacterial communities in sub-seafloor fluids at a deep-sea hydrothermal field of the Suiyo Seamount. Deep Sea Res Part I Oceanogr Res Papers 56:1844–1855. doi:10.1016/j.dsr.2009.05.004

Kato S, Yanagawa K, Sunamura M, Takano Y, Ishibashi J-I, Kakegawa T, Utsumi M, Yamanaka T, Toki T, Noguchi T, Kobayashi K, Moroi A, Kimura H, Kawarabayasi Y, Marumo K, Urabe T, Yamagishi A (2009c) Abundance of Zetaproteobacteria within crustal fluids in back-arc hydrothermal fields of the Southern Mariana Trough. Environ Microbiol 11:3210–3222. doi:10.1111/j.1462-2920.2009.02031.x

Kato S, Shibuya T, Nakamura K, Suzuki K, Rejishkumar VJ, Yamagishi A (2013a) Elemental dissolution of basalts with ultrapure water at 340°C and 40 MPa in a newly developed flow-type hydrothermal apparatus. Geochem J 47:89–92

Kato S, Nakawake M, Kita J, Yamanaka T, Utsumi M, Okamura K, Ishibashi J-I, Ohkuma M, Yamagishi A (2013b) Characteristics of microbial communities in crustal fluids in a deep-sea hydrothermal field of the Suiyo seamount. Front Microbiol 4:85. doi:10.3389/fmicb.2013.00085

Kawagucci S, Toki T, Ishibashi J, Takai K, Ito M, Oomori T, Gamo T (2010) Isotopic variation of molecular hydrogen in 20–375°C hydrothermal fluids as detected by a new analytical method. J Geophys Res 115, G03021. doi:10.1029/2009JG001203

Kelley DS, Karson JA, Fruh-Green GL, Yoerger DR, Shank TM, Butterfield DA, Hayes JM, Schrenk MO, Olson EJ, Proskurowski G, Jakuba M, Bradley A, Larson B, Ludwig K, Glickson D, Buckman K, Bradley AS, Brazelton WJ, Roe K, Elend MJ, Delacour A, Bernasconi SM, Lilley MD, Baross JA, Summons RT, Sylva SP (2005) A serpentinite-hosted ecosystem: the lost city hydrothermal field. Science 307:1428–1434. doi:10.1126/science.1102556

Kimura H, Asada R, Masta A, Naganuma T (2003) Distribution of microorganisms in the subsurface of the manus basin hydrothermal vent field in Papua new guinea. Appl Environ Microbiol 69:644–648. doi:10.1128/aem.69.1.644-648.2003

Kumagai H, Nakamura K, Toki T, Morishita T, Okino K, Ishibashi JI, Tsunogai U, Kawagucci S, Gamo T, Shibuya T, Sawaguchi T, Neo N, Joshima M, Sato T, Takai K (2008) Geological background of the Kairei and Edmond hydrothermal fields along the Central Indian Ridge: implications of their vent fluids' distinct chemistry. Geofluids 8:239–251. doi:10.1111/j.1468-8123.2008.00223.x

Kurihara H, Yabuta H, Kaneko T, Obayashi Y, Takano Y, Kobayashi K (2012) Characterization of organic aggregates formed by heating products of simulated Primitive Earth atmosphere experiments. Chem Lett 41:441–443. doi:10.1246/cl.2012.441

McCollom TM, Seewald JS (2001) A reassessment of the potential for reduction of dissolved CO_2 to hydrocarbons during serpentinization of olivine. Geochim Cosmochim Acta 65:3769–3778. doi:10.1016/s0016-7037(01)00655-x

McCollom TM, Seewald JS (2003a) Experimental constraints on the hydrothermal reactivity of organic acids and acid anions: I. Formic acid and formate. Geochim Cosmochim Acta 67:3625–3644. doi:10.1016/s0016-7037(03)00136-4

McCollom TM, Seewald JS (2003b) Experimental study of the hydrothermal reactivity of organic acids and acid anions: II. Acetic acid, acetate, and valeric acid. Geochim Cosmochim Acta 67:3645–3664. doi:10.1016/s0016-7037(03)00135-2

McCollom TM, Seewald JS (2007) Abiotic synthesis of organic compounds in deep-sea hydrothermal environments. Chem Rev 107:382–401. doi:10.1021/cr0503660

Morel FMM, Price NM (2003) The biogeochemical cycles of trace metals in the oceans. Science 300:944–947. doi:10.1126/science.1083545

Morey GW (1942) Solubility of solids in water vapor. Proc Am Soc Testing Mater 42:980–988

Morey GW, Chen WT (1955) The action of hot water on some feldspars. Am Mineral 40:996–1000

Morey GW, Fournier RO (1961) The decomposition of microcline, albite, and nepheline in hot water. Am Mineral 46:688–699

Morey GW, Hesselgesser JM (1951) The solubility of some minerals in superheated steam at higher pressures. Econ Geol 46:821–835

Morey GW, Ingerson E (1937) The pneumatolytic and hydrothermal alteration and synthesis of silicates. Econ Geol 32:607–761

Nakagawa T, Ishibashi JI, Maruyama A, Yamanaka T, Morimoto Y, Kimura H, Urabe T, Fukui M (2004) Analysis of dissimilatory sulfite reductase and 16S rRNA gene fragments from deep-sea hydrothermal sites of the Suiyo Seamount, Izu-Bonin Arc, Western Pacific. Appl Environ Microbiol 70:393–403. doi:10.1128/aem.70.1.393-403.2004

Nakagawa S, Inagaki F, Takai K, Horikoshi K, Sako Y (2005) *Thioreductor micantisoli* gen. nov., sp nov., a novel mesophilic, sulfur-reducing chemolithoautotroph within the epsilon-Proteobacteria isolated from hydrothermal sediments in the Mid-Okinawa Trough. Int J Syst Evol Microbiol 55:599–605. doi:10.1099/ijs.0.63351-0

Nealson KH, Inagaki F, Takai K (2005) Hydrogen-driven subsurface lithoautotrophic microbial ecosystems (SLiMEs): do they exist and why should we care? Trends Microbiol 13:405–410. doi:10.1016/j.tim.2005.07.010

Nercessian O, Reysenbach AL, Prieur D, Jeanthon C (2003) Archaeal diversity associated with in situ samplers deployed on hydrothermal vents on the East Pacific Rise (13°N). Environ Microbiol 5:492–502. doi:10.1046/j.1462-2920.2003.00437.x

Normand C, Williams-Jones AE, Martin RF, Vali H (2002) Hydrothermal alteration of olivine in a flow-through autoclave: nucleation and growth of serpentine phases. Am Mineral 87:1699–1709

Reysenbach AL, Shock E (2002) Merging genomes with geochemistry in hydrothermal ecosystems. Science 296:1077–1082. doi:10.1126/science.1072483

Robson RL, Eady RR, Richardson TH, Miller RW, Hawkins M, Postgate JR (1986) The alternative nitrogenase of Azotobacter-Chroococcum is a vanadium enzyme. Nature 322:388–390. doi:10.1038/322388a0

Russell MJ, Hall AJ (1997) The emergence of life from iron monosulphide bubbles at a submarine hydrothermal redox and pH front. J Geol Soc 154:377–402. doi:10.1144/gsjgs.154.3.0377

Rytuba JJ, Potter JM, Dickson FW, Radtke AS (1978) Experimental alteration of rhyolite glass at 300 ºC: Implication for silicate mineral zoning in modermitt mercury deposit, Nevada. Trans Am Geophys Union 59:1221

Schrenk MO, Kelley DS, Delaney JR, Baross JA (2003) Incidence and diversity of microorganisms within the walls of an active deep-sea sulfide chimney. Appl Environ Microbiol 69:3580–3592. doi:10.1128/aem.69.6.3580-3592.2003

Seewald JS (1994) Evidence for metastable equilibrium between hydrocarbons under hydrothermal conditions. Nature 370:285–287. doi:10.1038/370285a0

Sénarmont HD (1851) Expérience sur la formation des minéraux par voie humide dans les gîtes métallifères concrétionnés. Annales de Chimie et Physique, Troisième Séries 129–175

Seweeton FH, Baes CF Jr (1970) The solubility of magnetite and hydrolysis of ferrous ion in aqueous solutions at elevated temperatures. J Chem Thermodyn 2:479–500

Seyfried WE Jr (1987) Experimental and theoretical constraints on hydrothermal alteration processes at midocean ridges. Annu Rev Earth Planet Sci 15:317–335. doi:10.1146/annurev.ea.15.050187.001533

Seyfried WE Jr, Ding K (1993) The effect of redox on the relative solubilities of copper and iron in Cl-bearing aqueous fluids at elevated-temperatures and pressures: an exprimental study with application to subseafloor hydrothermal systems. Geochim Cosmochim Acta 57:1905–1917. doi:10.1016/0016-7037(93)90083-9

Seyfried WE Jr, Gordon PC, Dickson FW (1979) New reaction cell for hydrothermal solution equipment. Am Mineral 64:646–649

Seyfried WE Jr, Chen X, Chan LH (1998) Trace element mobility and lithium isotope exchange during hydrothermal alteration of seafloor weathered basalt: An experimental study at 350°C, 500 bars. Geochim Cosmochim Acta 62:949–960. doi:10.1016/s0016-7037(98)00045-3

Seyfried WE Jr, Foustoukos DI, Fu Q (2007) Redox evolution and mass transfer during serpentinization: an experimental and theoretical study at 200°C, 500 bar with implications for ultramafic-hosted hydrothermal systems at Mid-Ocean Ridges. Geochim Cosmochim Acta 71:3872–3886. doi:10.1016/j.gca.2007.05.015

Shibuya T, Komiya T, Nakamura K, Takai K, Maruyama S (2010) Highly alkaline, high-temperature hydrothermal fluid generated by Archean CO_2-rich seawater. Geochim Cosmochim Acta 74:A951

Shibuya T, Yoshizaki M, Masaki Y, Suzuki K, Takai K, Russell MJ (2013) Reactions between basalt and CO_2 -rich seawater at 250 and 350°C, 500 bars: Implications for the CO_2 sequestration into the modern oceanic crust and the composition of hydrothermal vent fluid in the CO_2 -rich early ocean. Chem Geol 359:1–9. doi:10.1016/j.chemgeo.2013.08.044

Shimamoto T, Tsutsumi A (1994) A new rotary-shear high-velocity frictional testing machine: its basic design and scope of research (in Japanese with English abstract). Struct Geol 39:65–78

Spiess FN, Macdonald KC, Atwater T, Ballard R, Carranza A, Cordoba D, Cox C, Diazgarcia VM, Francheteau J, Guerrero J, Hawkins J, Haymon R, Hessler R, Juteau T, Kastner M, Larson R, Luyendyk B, Macdougall JD, Miller S, Normark W, Orcutt J, Rangin C (1980) East Pacific rise: hot springs and geophysical experiments. Science 207:1421–1433. doi:10.1126/science.207.4438.1421

Stolz JF, Basu P, Santini JM, Oremland RS (2006) Arsenic and selenium in microbial metabolism. Annu Rev Microbiol 60:107–130. doi:10.1146/annurev.micro.60.080805.142053

Takai K, Komatsu T, Inagaki F, Horikoshi K (2001) Distribution of archaea in a black smoker chimney structure. Appl Environ Microbiol 67:3618–3629. doi:10.1128/aem.67.8.3618-3629.2001

Takai K, Gamo T, Tsunogai U, Nakayama N, Hirayama H, Nealson KH, Horikoshi K (2004) Geochemical and microbiological evidence for a hydrogen-based, hyperthermophilic subsurface lithoautotrophic microbial ecosystem (HyperSLiME) beneath an active deep-sea hydrothermal field. Extremophiles 8:269–282. doi:10.1007/s00792-004-0386-3

Takai K, Nakamura K, Suzuki K, Inagaki F, Nealson KH, Kumagai H (2006) Ultramafics-Hydrothermalism-Hydrogenesis-HyperSLiME (UltraH^3) linkage: a key insight into early microbial ecosystem in the Archean deep-sea hydrothermal systems. Paleontol Res 10:269–282

Thornton EC, Seyfried WE (1987) Reactivity of organic-rich sediment in seawater at 350°C, 500 bars: Experimental and theoretical constraints and implications for the Guaymas Basin hydrothermal system. Geochim Cosmochim Acta 51:1997–2010. doi:10.1016/0016-7037(87)90188-8

Tremaine PR, Leblanc JC (1980) The solubility of nickel oxide and hydrolysis of Ni^{2+} in water to 573 K. J Chem Thermodyn 12:521–538. doi:10.1016/0021-9614(80)90182-2

Tremaine PR, Chen JD, Wallace GJ, Boivin WA (1981) Solubility of uranium (IV) oxide in alkaline aqueous solutions to 300°C. J Solut Chem 10:221–230. doi:10.1007/bf00653099

Tuttle OF (1948) A new hydrothermal quenching apparatus. Am J Sci 246:628–635

Tuttle OF (1949) Two pressure vessels for silicate-water studies. Geol Soc Am Bull 60:1727–1729

Williams-Jones AE, Wood SA, Mountain BW, Gammons CH (eds) (1994) Experimental water-rock interaction: Applications to ore-forming hydrothermal systems. St. John's, Newfoundland, pp 131–160

Yanagawa H, Kojima K (1985) Thermophilic microspheres of peptide-like polymers and silicates formed at 250°C. J Biochem 97:1521–1524

Yoshizaki M, Shibuya T, Suzuki K, Shimizu K, Nakamura K, Takai K, Omori S, Maruyama S (2009) H_2 generation by experimental hydrothermal alteration of komatiitic glass at 300°C and 500 bars: a preliminary result from on-going experiment. Geochemical Journal 43:E17–E22

Zielinski RA (1979) Uranium mobility during interaction of rhyolitic obsidian, perlite, and felite with alkaline carbonate solution: T = 120°C, P = 210 kg/cm^2. Chem Geol 27:47–63

8 Experimental Hydrogen Production in Hydrothermal and Fault Systems: Significance for Habitability of Subseafloor H_2 Chemoautotroph Microbial Ecosystems

Katsuhiko Suzuki, Takazo Shibuya, Motoko Yoshizaki, and Takehiro Hirose

Abstract

Hydrogen generated in hydrothermal and fault systems has recently received considerable attention as a potential energy source for hydrogen-based microbial activity such as methanogenesis. Laboratory experiments that have reproduced conditions for the serpentinization of ultramafic rocks such as peridotite and komatiite have clarified the chemical and petrological processes of H_2 production. In a frictional experimental study, we recently showed that abundant H_2 can also be generated in a simulated fault system. This result suggests that microbial ecosystems might exist in subseafloor fault systems. Here we review the experimental constraints on hydrogen production in hydrothermal and fault systems.

Keywords

Friction experiment • Hydrogen generation • Hydrothermal experiment • Simulated fault system • Ultramafic rocks

8.1 Introduction

The discovery of chemolithoautotrophic microbial ecosystems in the modern ocean has suggested that hydrothermal fluids enriched in H_2 fuel H_2-driven primary producers such as hyperthermophilic hydrogenotrophic methanogens (Cannat et al. 1997; Takai et al. 2004; Kelley et al. 2005) . Moreover, multidisciplinary studies have indicated that an H_2-driven chemolithoautotrophic ecosystem may have supported the earliest life on Earth (Russell and Hall 1997; Sleep et al. 2004; Kelley et al. 2005; Canfield et al. 2006; Takai et al. 2006). H_2-rich hydrothermal fluids are generated by the serpentinization of Mg- and Fe-rich ultramafic rocks, which are igneous and meta-igneous

K. Suzuki (✉)
Institute for Research on Earth Evolution (IFREE), Japan Agency for Marine-Earth Science and Technology (JAMSTEC), 2-15 Natsushima, Yokosuka 237-0061, Japan

Precambrian Ecosystem Laboratory, Japan Agency for Marine-Earth Science and Technology (JAMSTEC), 2-15 Natsushima, Yokosuka 237-0061, Japan

Seafloor Resources Research Project (SRRP), Japan Agency for Marine-Earth Science and Technology (JAMSTEC), 2-15 Natsushima, Yokosuka 237-0061, Japan
e-mail: katz@jamstec.go.jp

T. Shibuya
Precambrian Ecosystem Laboratory, Japan Agency for Marine-Earth Science and Technology (JAMSTEC), 2-15 Natsushima, Yokosuka 237-0061, Japan

Seafloor Resources Research Project (SRRP), Japan Agency for Marine-Earth Science and Technology (JAMSTEC), 2-15 Natsushima, Yokosuka 237-0061, Japan

M. Yoshizaki
Precambrian Ecosystem Laboratory, Japan Agency for Marine-Earth Science and Technology (JAMSTEC), 2-15 Natsushima, Yokosuka 237-0061, Japan

Department of Earth and Planetary Sciences, Tokyo Institute of Technology, 2-12-1 Ookayama, Meguro-ku, Tokyo 152-8551, Japan

T. Hirose
Kochi Institute for Core Sample Research, Japan Agency for Marine-Earth Science and Technology (JAMSTEC), 200 Monobe-otsu, Nankoku, Kochi 783-8502, Japan

J.-i. Ishibashi et al. (eds.), *Subseafloor Biosphere Linked to Hydrothermal Systems: TAIGA Concept*,
DOI 10.1007/978-4-431-54865-2_8,

rocks consisting mainly (>90 %) of mafic minerals with high magnesium and iron contents. These rocks have a very low silica content (<45 %), MgO generally more than 18 %, high FeO, and low potassium. The Earth's mantle is composed of ultramafic rocks. The production of hydrogen by the serpentinization of ultramafic rocks is a central tenet of the hypothesis that life first emerged on Earth in an H_2-rich hydrothermal environment (Russell et al. 2010).

In the modern ocean, the basement rocks of the oceanic crust are generally composed of mid-ocean ridge basalt (MORB). Along slow-spreading ridges such as the North Atlantic Ridge and the Southwest Indian Ridge, volcanic activity is low and severely serpentinized peridotites (peridotite: ultramafic rocks composed of olivine and pyroxene) are exposed along transform faults (e.g., Miyashiro et al. 1969; Aumento and Loubat 1971; Cannat 1993). Hydrogen-enriched hydrothermal fluids are common in such peridotite-dominated slow-spreading ridge settings (Kelley et al. 2001; Früh-Green et al. 2004). Since the first discovery of natural peridotite-hosted hydrothermal vents with abundant H_2 at Logachev field on the Mid-Atlantic Ridge in 1995 (Krasnov et al. 1995), other peridotite-hosted and -associated hydrothermal vents have been found, namely, the Rainbow, Nibelungen, Lost City, and Achaze fields on the Mid-Atlantic Ridge (Charlou et al. 1998, 2002, 2008; Douville et al. 2002; Kelley et al. 2005; Melchert et al. 2008) and the Kairei field on the Central Indian Ridge (Van Dover et al. 2001). A pronounced feature of peridotite-hosted systems is the presence of hydrothermal solutions enriched not only in H_2 but also in CH_4 and other hydrocarbons (Charlou et al. 2002). Measured H_2 concentrations in these fluids range from 2.5 to 16 mmol/kg, with the highest concentrations reported at steady-state, unsedimented mid-ocean ridge hydrothermal vents. The generated H_2 supports ecosystems, including hyperthermophilic subsurface lithoautotrophic ecosystems (HyperSLiME) (Takai et al. 2004; Nealson et al. 2005), in which methanogens utilize H_2 and CO_2 and produce methane as a metabolic product.

Several petrographical (Cressey 1979) and theoretical (Wetzel and Shock 2000; Sleep et al. 2004) studies have examined the H_2-generating geochemical and mineralogical reactions associated with the serpentinization of ocean-floor ultramafic rocks, and experimental investigations (Berndt et al. 1996; Allen and Seyfried 2003; Seyfried et al. 2007) have significantly increased our understanding of the mechanisms of H_2 production during serpentinization. In the present paper, we focus on these experimental results, because it is generally difficult to directly observe chemical processes in subseafloor environments. Thermodynamic modeling of seawater–peridotite reactions is also an important tool, both for understanding the experimental results and for inferring the natural serpentinization processes (Klein et al. 2009; McCollom and Bach 2009). McCollom and Bach (2009) examined the effect of temperature on the mineral assemblage and fluid composition produced by serpentinization of harzburgite (a peridotite consisting mainly of olivine and orthopyroxene) (Fig. 8.1). They reported that at temperatures below 315 °C, the serpentinized rock was composed of typical serpentinite minerals, such as serpentine, brucite, magnetite, and minor secondary clinopyroxene. With increasing temperature, the amount of magnetite increased, and consequently, the concentration of H_2 generated by serpentinization also increased with temperature up to ~360 mmol/kg. Above 315 °C, however, olivine became stable and coexisted in equilibrium with other secondary minerals and fluid, and above 390 °C it remained almost completely unaltered. Therefore, the amount of Fe converted to magnetite decreased as the temperature increased above 315 °C, with the result that the H_2 concentration in the fluid was lower at these higher temperatures. Contrary to expectation, theoretical modeling of these water–rock interactions does not always produce results that are quantitatively consistent with the experimental results. Therefore, further investigation is needed to

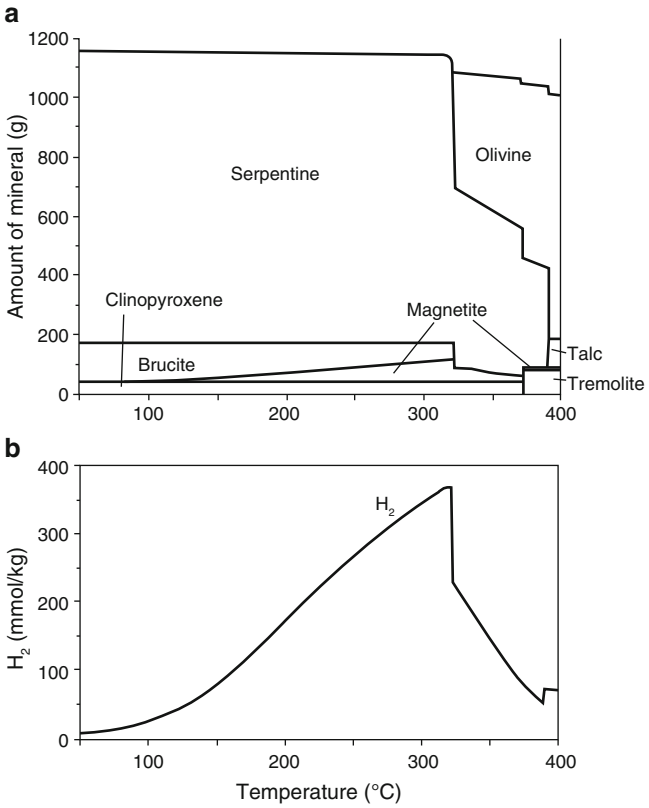

Fig. 8.1 Predicted alteration mineralogy and fluid composition during hydrothermal alteration of harzburgite over a range of temperatures at a 1:1 water:rock ratio, modified from McCollom and Bach (2009). (**a**) Equilibrium mineral composition: amount of each mineral per kilogram of harzburgite reacted. (**b**) H_2 concentration in the fluid

clarify the reasons for the discrepancy between theoretical and experimental results.

Another extreme environment where H_2 may be abundant is found in natural fault systems. Wakita et al. (1980) first reported high concentrations of H_2 (up to 3 % v/v) in soil gas from sites in the Yamasaki fault zone, southwestern Japan, and Wiersberg and Erzinger (2008) reported high concentrations of H_2 in drilling cores obtained near micro-earthquake hypocenters along the San Andreas fault in California. These observations led to the hypothesis that methanogenic ecosystems might also be found in deep fault systems below the seafloor. To examine whether fault-driven H_2 generation can produce enough H_2 to maintain a chemolithoautotrophic microbial ecosystem, we conducted high-velocity sliding experiments using velocities and displacements typical of natural earthquakes (Hirose et al. 2011, 2012).

Thus, both hydrothermal and frictional experimental systems can be effectively used to elucidate physicochemical processes in natural systems. In this chapter, we review experiments, performed both as part of Project TAIGA (Trans-crustal Advection and In-situ bio-geochemical processes of Global sub-seafloor Aquifer) and by other groups, examining the generation of hydrogen by water/rock interactions at high temperature and pressure, including both reactions between water and komatiite, an Archean volcanic ultramafic rock, and those in frictional fault systems.

8.2 Constraints on H_2 Production During Experimental Hydrothermal Alteration of Ultramafic Rocks

Peridotite exposed on slow-spreading ridge systems is often severely serpentinized as a result of hydration due to long-term reaction with seawater (Ildefonse et al. 2007; Morishita et al. 2009; Nakamura et al. 2009). Isotopic investigations have shown that such serpentinized peridotites, similar to altered MORB, are the products of high-temperature and -pressure reactions between peridotite and seawater (Wenner and Taylor 1971, 1973; Sakai and Tsutsumi 1978). Hydrothermal alteration of peridotite was studied experimentally (Seyfried and Dibble 1980; Hajash and Chandler 1981; Janecky and Seyfried 1986) even before the discovery of natural peridotite-hosted hydrothermal vents at Logachev field (Krasnov et al. 1995). Reactions between peridotite and seawater under high temperature and pressure have also been examined in batch-type experiments (see Chap. 7). Under high temperature and pressure, the oxidation of ferrous ion [Fe(II)] in primary minerals such as olivine and pyroxene to Fe(III) in secondary minerals such as magnetite reduces water and releases H_2 gas:

$$2(\mathrm{FeO})_{\mathrm{mineral}} + \mathrm{H_2O} \rightarrow (\mathrm{Fe_2O_3})_{\mathrm{mineral}} + \mathrm{H_2} \qquad (8.1)$$

where $(\mathrm{FeO})_{\mathrm{rock}}$ denotes the ferrous constituent of a primary silicate mineral such as olivine and $(\mathrm{Fe_2O_3})_{\mathrm{rock}}$ denotes the ferric constituent of an secondary alteration mineral such as magnetite. The serpentinization of olivine (Fo_{90}) generates H_2 as follows:

$$\underset{\text{Olivine (Fo}_{90}\text{)}}{\mathrm{Mg_{1.8}Fe_{0.2}SiO_4}} + 1.37\mathrm{H_2O} \rightarrow \underset{\text{Serpentine}}{0.5\mathrm{Mg_3Si_2O_5(OH)_4}} + \underset{\text{Brucite}}{0.3\mathrm{Mg(OH)_2}} + \underset{\text{Magnetite}}{0.067\mathrm{Fe_3O_4}} + 0.067\mathrm{H_2} \qquad (8.2)$$

In this reaction, olivine supplies Fe(II), and hydrogen and magnetite, which contains Fe(II) and Fe(III) in equal amounts, are produced. Note that Eq. (8.2) is a simplified formula provided to illustrate the generation of H_2 by serpentinization; in natural systems, the produced serpentine and brucite commonly contain Fe as well.

Janeckey and Seyfried (1986) experimentally investigated the serpentinization of harzburgite at 300 °C and 50 MPa, but they did not measure hydrogen continuously during their experiment. Instead, they collected samples for hydrogen measurement only twice, after 10 months and 2 years. In both samples, they found high concentrations of H_2 (0.1 and 0.33 mmol/kg), but because they did not measure H_2 in other fluid samples collected during the experiment, the H_2 generation reaction cannot be unambiguously interpreted. Using a similar experimental apparatus, McCollom and Seewald (2001) assessed the potential of olivine serpentinization to reduce CO_2 and produce hydrocarbons. In their experiments, they reacted powdered olivine with a 0.5 M NaCl solution at 300 °C and 35 MPa and obtained abundant H_2 (concentration > 70 mmol/kg, Fig. 8.2) after 700 h.

Allen and Seyfried (2003) reacted olivine, orthopyroxene, and clinopyroxene, the major constituent minerals in peridotite, with a NaCl–$MgCl_2$ solution at 400 °C and 50 MPa to assess the potential of these minerals to produce H_2. They used olivine (Fo_{89}), orthopyroxene (En_{85}), and clinopyroxene (Di_{89}) both individually and in combination to constrain the chemical processes of ultramafic-hosted hydrothermal systems in mid-ocean ridges. The olivine alteration rate was slow, as indicated by the absence of hydrous alteration products, whereas reactions including pyroxenes were rapid, resulting in significant increases in dissolved H_2 as well as in Ca, SiO_2, and Fe (Fig. 8.3), and in the formation of SiO_2-rich secondary minerals such as talc, tremolite, and magnetite (Fig. 8.3; McCollom and Bach 2009). High pH and low Fe

concentrations are theoretically predicted under the assumption of full equilibrium at 400 °C and 50 MPa in the MgO-CaO-FeO-Fe_2O_3-SiO_2-Na_2O-H_2O-HCl system (Allen and Seyfried 2003). In their laboratory experiments, however, Allen and Seyfried (2003) reported that when the initial olivine:pyroxene ratio was 3:1 (the typical mineral composition of abyssal peridotite), pH remained low and Fe concentrations remained high. Moreover, the pH also remained relatively low in their experiments that included orthopyroxene and clinopyroxene, a result that may have been caused by talc–fluid and talc–tremolite–fluid equilibria, respectively.

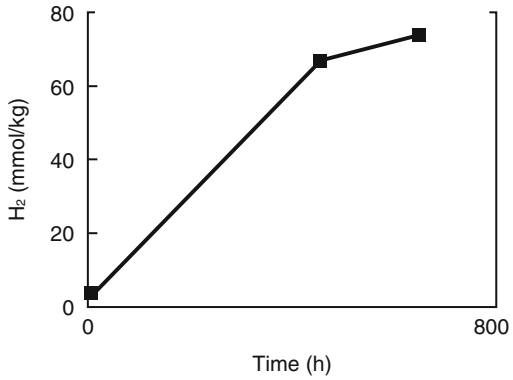

Fig. 8.2 Measured concentrations of dissolved H_2 during a hydrothermal reaction in the presence of olivine at 300 °C and 35 MPa as a function of reaction time. Modified from McCollom and Seewald (2001)

Allen and Seyfried (2003) suggested that the reactions occurring in ultramafic rock-hosted hydrothermal systems such as the Rainbow system on the Mid-Atlantic Ridge may be very similar to those observed in these experiments, because of the similarity of the experimental conditions to the temperature and chemistry conditions of the vent fluid, in which concentrations of SiO_2, Ca, H_2, and Fe are relatively high (Charlou et al. 1998, 2002). In fact, Fe concentrations in the Rainbow system, which are the highest of any vent system yet discovered, imply a relatively low pH in the subseafloor reaction zone. The findings of Allen and Seyfried (2003) are very important because the experimental results together with the observed Rainbow fluid chemistry suggest that pyroxene dissolution is the dominant reaction in the Rainbow hydrothermal system, even though abundant olivine is present in the reaction zone. To better constrain the temporal evolution of the hydrothermal alteration of ultramafic rocks in subseafloor reaction zones, experimental data

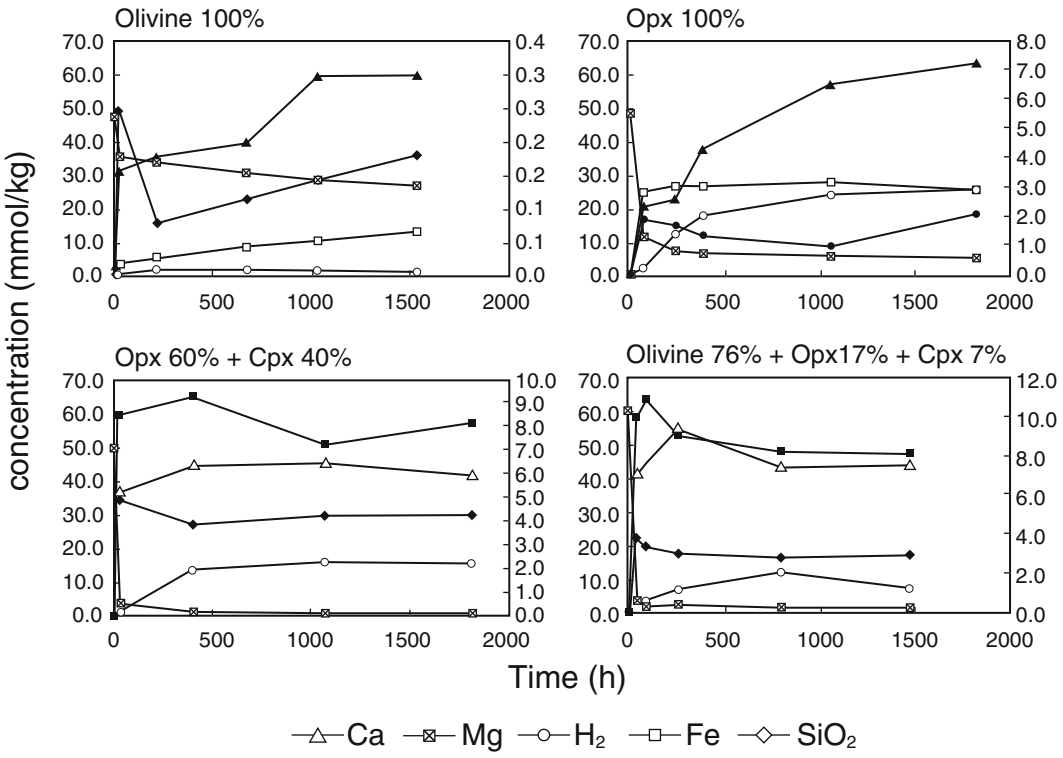

Fig. 8.3 Changes in the dissolved concentrations of selected species with time during four experiments, modified from Allen and Seyfried (2003). All experiments were performed at 400 °C, 50 MPa and with mineral:fluid ratios from 2 to 4. Values on the left vertical axis apply to species represented by *open symbols* and to Mg, and those on the right axis apply to species represented by *closed symbols*. *Cpx* clinopyroxene, *Opx* orthopyroxene

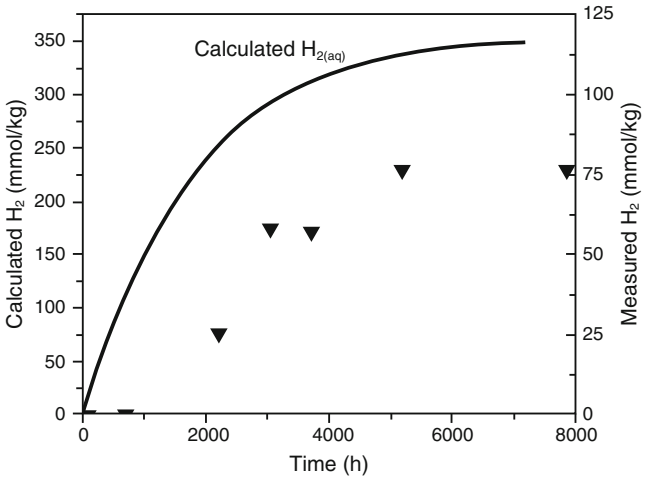

Fig. 8.4 Calculated (*line*) and measured (*inverted triangles*) time-series changes in dissolved hydrogen in fluid coexisting with lherzolite and alteration products (Seyfried et al. 2007). The difference between measured and predicted dissolved H_2 concentrations may reflect (in part) the lack of thermodynamic data for Fe-rich alteration minerals in the database used for the theoretical model

obtained under various conditions should be compared with thermodynamic simulation results.

The experiments just described were conducted at high temperatures (300 °C or higher), but actual reaction zone temperatures in ultramafic rocks are likely to be variable. For example, in the Lost City hydrothermal field on the Mid-Atlantic Ridge, H_2 is abundant, the pH is high, and the reactions occur at moderately low temperature. When Seyfried et al. (2007) experimentally constrained hydrogen production at the low temperature of 200 °C and 50 MPa, they found that changes in the concentrations of Ca, Mg, and Si in the reacted fluid agreed quantitatively with those predicted theoretically by a reaction pathway model of seawater–lherzolite interaction (fluid:rock mass ratio, 1:1) at 200 °C and 50 MPa. However, the time variations of pH, dissolved chloride, and H_2 monitored during their experiment did not agree with the theoretically predicted results (Fig. 8.4). Dissolved H_2 increased in a series of abrupt steps, and reached a maximum concentration that was only about 20 % of the theoretically predicted concentration. Interestingly, serpentine, the most abundant alteration mineral, contained both ferric and ferrous iron, and magnetite was present only in trace amounts. They therefore inferred that the low rate of H_2 generation, which was lower than that estimated on the basis of predicted serpentinization rates, was due to the production of diverse Fe-bearing alteration minerals.

In a recent experiment, Mayhew et al. (2013) reacted ultramafic and mafic rocks such as peridotite and minerals such as pyroxene, olivine, and magnetite with an anoxic fluid at 55 °C and 100 °C, temperatures that are habitable for (hyper)thermophilic microbes. Their synchrotron-based X-ray analysis results showed that the amount of H_2 produced was strongly dependent on whether spinel phases such as magnetite were present, and they observed Fe(III)-oxide products on the surface of the spinels. They proposed, therefore, that Fe(II) and water adsorbed on the surface of spinels reacted together under kinetic control to produce H_2 at low temperatures.

8.3 Experimental H_2 Generation During Komatiite Alteration: Simulation of an Archean Hydrothermal System

The experiments described in Sect. 8.2 showed by simulating peridotite–seawater systems that abundant H_2 is generated in a modern slow-spreading ridge by the serpentinization of peridotite. Sufficiently high concentrations of H_2 occur in the vent fluids of these systems to sustain an ecosystem based on H_2-driven chemolithoautotrophic primary producers such as methanogens. Moreover, an H_2-driven ecosystem is the most probable candidate habitat for the earliest life on Earth (Russell and Hall 1997; Sleep et al. 2004; Kelley et al. 2005; Takai et al. 2006; Canfield et al. 2006). On this basis, it has been hypothesized that hydrothermal fluids with H_2, sufficiently abundant to sustain methanogens, existed in the early Earth (Takai et al. 2006).

In contrast to the modern ocean, in the Hadean and early Archean ocean, peridotite was probably scarce beneath the crust of the ocean floor, because at that time the oceanic crust may have been two to three times the thickness of the modern oceanic crust (Ohta et al. 1996; Moores 2002; Takai et al. 2006). In this tectonic setting, komatiite, a distinctive ultramafic volcanic rock, was most likely the main component of ultramafic rocks on the floor of Hadean and Archean oceans. In fact, komatiite is common in Archean greenstone belts, whereas it is less common in Proterozoic successions and quite rare in Phanerozoic strata (Condie 2005). We therefore hypothesized that komatiite was the dominant ultramafic rock in the early history of the Earth (Yoshizaki et al. 2009) and that the interaction of komatiite with fluid at high temperature produced abundant H_2. To test this hypothesis, we examined whether we could reproduce a hydrothermal environment habitable for early life by experimentally reacting komatiite with water.

Modern komatiite in exposed Archean rocks has already been severely altered, so komatiite in its present form could not be used for our experiments. Therefore, we synthesized komatiite glass by dehydrating and remelting serpentinized komatiite collected from the Komati Formation, Barberton Greenstone Belt, South Africa, and then reacted the synthesized komatiitic glass with an NaCl solution at 300 °C and 50 MPa (Yoshizaki et al. 2009).

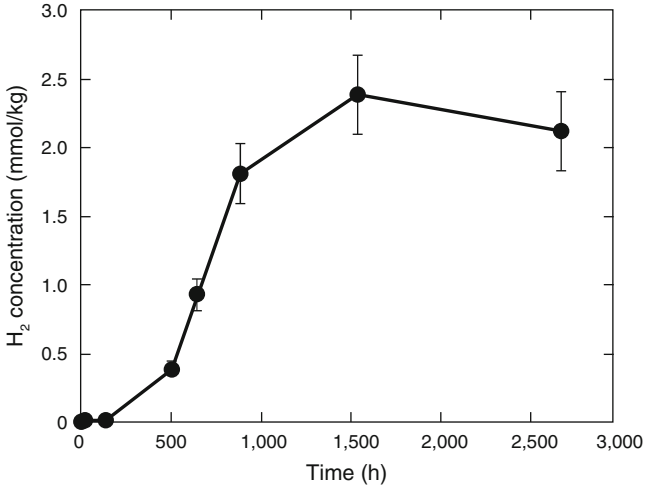

Fig. 8.5 Changes in the dissolved H_2 concentration with time during a komatiitic glass–water reaction experiment (Yoshizaki et al. 2009). The experiment was performed at 300 °C and 50 MPa with an initial water: rock ratio of 4:1

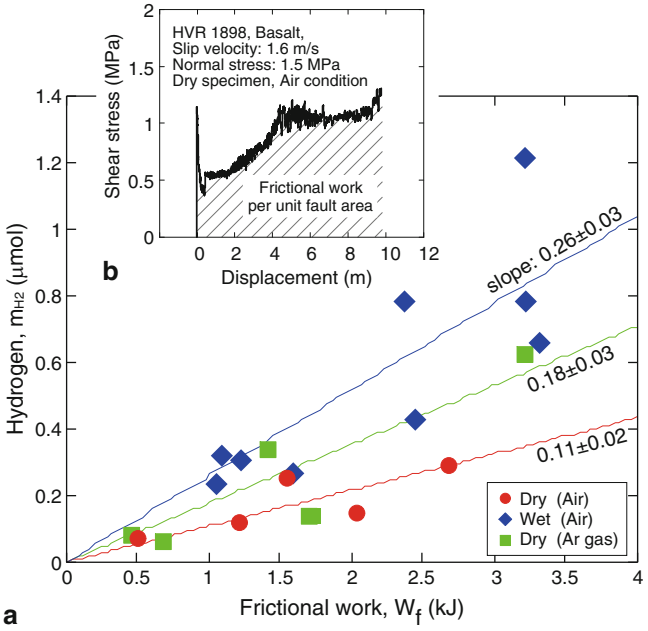

Fig. 8.6 (**a**) Hydrogen generation (μmol) as a function of frictional work (kJ) during high-velocity friction experiments with dry and wet basalt specimens at a slip velocity of 1.6 m/s and a displacement of 10 m under an air or argon gas atmosphere (Hirose et al. 2011). The amount of hydrogen generated tended to increase linearly with frictional work (correlation coefficient of 0.814, 0.899, and 0.777 for wet-air, dry-Ar gas, and dry-air conditions, respectively). (**b**) A typical shear stress versus displacement curve obtained during a friction experiment. Frictional work was calculated by integrating shear stress over the displacement (area under the shear stress versus displacement curve) and then multiplying the result by the fault surface area

The concentration of produced H_2 reached 2.4 mmol/kg after 1500 h (Fig. 8.5) (Yoshizaki et al. 2009). This concentration is comparable to concentrations obtained by hydration of peridotitic rocks (see Sect. 8.2). These results suggest that hydrothermal alteration of komatiite in the Hadean and early Archean may have provided sufficient H_2 to fuel microbial ecosystems in the vicinity of hydrothermal vents.

8.4 Mechanoradical H_2 Generation During Simulated Faulting

As we have described, hydrothermal alteration of peridotites and komatiites can produce abundant H_2 in subseafloor settings. Other potential sites of H_2 generation are active fault systems. Earthquake or fault-related H_2 generation was first found by gas monitoring along the active Yamasaki fault, southwestern Japan (Wakita et al. 1980), and more recently H_2 generation has been inferred from drill cores obtained near microearthquake hypocenters along the San Andreas fault in California (Wiersberg and Erzinger 2008). Kita et al. (1982) suggested that H_2 may be generated in fault systems by the following reaction, expressed in terms of mechanoradicals on fresh surfaces of silicate minerals and water molecules:

$$2(\equiv \mathrm{Si})^{\cdot} + 2\mathrm{H_2O} \rightarrow 2(\equiv \mathrm{SiOH}) + \mathrm{H_2} \qquad (8.3)$$

Experiments in which a ball mill was used to crush rocks had previously reproduced possible mechanoradical reactions during faulting (Kita et al. 1982; Kameda et al. 2004), but no quantitative investigations of the generation of H_2 in an active fault system have been carried out. To examine whether a natural fault system can produce enough H_2 to sustain a microbial methanogen-based ecosystem, we performed high-velocity sliding experiments that reproduced slip velocities and displacements typical of natural earthquakes and then quantitatively estimated the concentrations of H_2 produced (Hirose et al. 2011). To collect the generated gas samples, we placed a reaction cell around the rock specimen in a high-velocity frictional experiment system (see Chap. 7 in this volume). The results showed that H_2 generation increases with frictional work (i.e., earthquake magnitude) (Fig. 8.6). Therefore, the earthquake-derived H_2 flux in nature can be estimated by establishing the correlation between H_2 production and earthquake magnitude (Hirose et al. 2011, 2012). Moreover, an H_2 fluid concentration higher than 1.1 mmol/kg can be achieved in a fault zone after even a small-magnitude earthquake (Hirose et al. 2011, 2012). This concentration of H_2 is potentially high enough to sustain a methanogen-based ecosystem, we can expect to find diverse microbial ecosystems in deep fault systems. Thus, such fault systems may also have provided habitable zones for early life on Earth.

8.5 Concluding Remarks and Future Perspectives

In modern oceans, H_2-rich hydrothermal fluids (i.e., H_2 concentrations from a few to a few tens mmol/kg) have been observed in ultramafic rock-hosted systems. Such concentrations are sufficiently high to sustain H_2-based lithoautotrophic microbial ecosystems, including phylogenetically ancient microbes (Takai et al. 2006). In this regard, the experiments simulating H_2 generation described here have improved our understanding of not only geochemical and biological interactions driven by serpentinization in modern oceans but also the potential habitability of Hadean/Archean komatiite hydrothermal systems, in which life might have originated. Additionally, the results of friction experiments suggest the intriguing idea that H_2 generated in a fault system might also sustain lithoautotrophic microbial ecosystems. Such fault system ecosystems may also have existed on the early Earth. To verify the fault zone model, we anticipate the results of microbial investigations of fault systems performed using fresh drill cores. It should be emphasized, however, that there are certain basic difficulties associated with the described hydrothermal experiments. For example, as described in Sect. 8.2, some results from experimental hydrothermal reactions conflict with both natural observations and theoretical calculations. The discrepancies may reflect mainly inappropriate initial experimental conditions or inaccurate thermodynamic data. Thus, future experiments must correct these problems.

Acknowledgments We thank Mamiko Umetsu for drawing some of the figures. Comments by Prof. Fumitaka Yanagisawa considerably improved our manuscript. This study was supported by a Grant-in-Aid for Scientific Research on Innovative Areas (no. 20109006) to "Project TAIGA: Trans-crustal Advection and In-situ bio-geochemical processes of Global sub-seafloor Aquifer" from the Ministry of Education, Culture, Sports, Science and Technology (MEXT) of Japan. We also thank Prof. Urabe and members of Project TAIGA for their collaboration and useful discussions.

References

Allen DE, Seyfried WE (2003) Compositional controls on vent fluids from ultramatic-hosted hydrothermal systems at mid-ocean ridges: an experimental study at 400 °C, 500 bars. Geochim Cosmochim Acta 67:1531–1542. doi:10.1016/s0016-7037(02)01173-0

Aumento F, Loubat H (1971) The Mid-Atlantic Ridge near 45°N, serpentinized ultramafic intrusions. Can J Earth Sci 8:631–663

Berndt ME, Allen DE, Seyfried WE (1996) Reduction of CO_2 during serpentinization of olivine at 300 °C and 500 bar. Geology 24:351–354

Canfield DE, Rosing MT, Bjerrum C (2006) Early anaerobic metabolisms. Philos Trans R Soc B Biol Sci 361:1819–1834

Cannat M (1993) Emplacement of mantle rocks in the seafloor at mid-ocean ridges. J Geophys Res 98:4163–4172

Cannat M, Lagabrielle Y, Bougault H, Casey J, de Coutures N, Dmitriev L, Fouquet Y (1997) Ultramafic and gabbroic exposures at the Mid-Atlantic Ridge: geological mapping in the 15°N region. Tectonophysics 279:193–213

Charlou JL, Fouquet Y, Bougault H, Donval JP, Etoubleau J, Jean-Baptiste P, Dapoigny A, Appriou P, Rona PA (1998) Intense CH_4 plumes generated by serpentinization of ultramafic rocks at the intersection of the 15°20′N fracture zone and the Mid-Atlantic Ridge. Geochim Cosmochim Acta 62:2323–2333. doi:10.1016/S0016-7037(98)00138-0

Charlou JL, Donval JP, Fouquet Y, Jean-Baptiste P, Holm N (2002) Geochemistry of high H_2 and CH_4 vent fluids issuing from ultramafic rocks at the Rainbow hydrothermal field (36°14′M, MAR). Chem Geol 191:345–359

Charlou JL, Donval JP, Konn C, Birot D, Sudarikov S, Jean-Baptiste P, Fouquet Y; Scientific Party of the Serpentine Cruise (2008) High hydrogen and abiotic hydrocarbons from new ultramafic hydrothermal sites between 12°N and 15°N on the Mid Atlantic Ridge-Results of the SERPENTINE cruise, EOS Transactions, AGU, Fall Meeting Supplement, Abstract, *88*, T51F-04

Condie KC (2005) Earth as an evolving planetary system. Elsevier, Burlington

Cressey BA (1979) Electron microscopy of serpentinite textures. Can Mineral 17:741–756

Douville E, Charlou JL, Oelkers EH, Bienvenu P, Jove Colon CF, Fouquet DJPY, Prieur D, Appriou P (2002) The rainbow vent fluids (36°14′M, MAR): the influence of ultramafic rocks and phase separation on trace metal content in Mid-Atlantic Ridge hydrothermal fluids. Chem Geol 184:37–48

Früh-Green GL, James AD, Plas A, Kelley DS, Geobety B (2004) Serpentinization of oceanic peridotites: implications for geochemical cycles and biological activity. Subseafloor Biosphere Mid Ocean Ridges 144:119–136

Hajash A, Chandler GW (1981) An experimental investigation of high-temperature interactions between seawater and rhyolite, andesite, basalt and peridotite. Contrib Mineral Petrol 78:240–254

Hirose T, Kawagucci S, Suzuki K (2011) Mechanoradical H_2 generation during simulated faulting: Implications for an earthquake-driven subsurface biosphere. Geophys Res Lett 38. doi:10.1029/2011gl048850

Hirose T, Kawagucci S, Suzuki K (2012) Correction to "Mechanoradical H_2 generation during simulated faulting: implications for an earthquake-driven subsurface biosphere". Geophys Res Lett 39:L23304 doi:10.1029/2012GL054539

Ildefonse B, Blackman DK, John BE, Ohara Y, Miller DJ, MacLeod CJ (2007) Oceanic core complexes and crustal accretion at slow-spreading ridges. Geology 35:623–626. doi:10.1130/G23531A.1

Janeckey DR, Seyfried WE Jr (1986) Hydrothermal serpentinization of peridotite within the oceanic crust: experimental investigations of mineralogy and major element chemistry. Geochim Cosmochim Acta 50:1357–1378

Janecky DR, Seyfried WE (1986) Hydrothermal serpentinization of peridotite within the oceanic-crust: experimental investigations of mireralogy and major element chemistry. Geochim Cosmochim Acta 50:1357–1378. doi:10.1016/0016-7037(86)90311-x

Kameda J, Saruwatari K, Tanaka H, Tsunomori F (2004) Mechanisms of hydrogen generation during the mechanochemical treatment of biotite within D_2O media. Earth Planets Space 56:1241–1245

Kelley DS, Karson JA, Blackman DK, Fruh-Green GL, Butterfield DA, Lilley MD, Olson EJ, Schrenk MO, Roe KK, Lebon GT, Rivizzigno

P, Party ATS (2001) An off-axis hydrothermal vent field near the Mid-Atlantic Ridge at 30 degrees N. Nature 412:145–149. doi:10.1038/35084000

Kelley DS, Karson JA, Fruh-Green GL, Yoerger DR, Shank TM, Butterfield DA, Hayes JM, Schrenk MO, Olson EJ, Proskurowski G, Jakuba M, Bradley A, Larson B, Ludwig K, Glickson D, Buckman K, Bradley AS, Brazelton WJ, Roe K, Elend MJ, Delacour A, Bernasconi SM, Lilley MD, Baross JA, Summons RT, Sylva SP (2005) A serpentinite-hosted ecosystem: the lost city hydrothermal field. Science 307:1428–1434. doi:10.1126/science.1102556

Kita I, Matsuo S, Wakita H (1982) H_2 Generation by reaction between H_2O and crushed rock: an experimental study on H_2 degassing from the active fault zone. J Geophys Res 87:789–795. doi:10.1029/JB087iB13p10789

Klein F, Bach W, Joens N, McCollom T, Moskowitz B, Berquo T (2009) Iron partitioning and hydrogen generation during serpentinization of abyssal peridotites from 15 degrees N on the Mid-Atlantic Ridge. Geochim Cosmochim Acta 73:6868–6893. doi:10.1016/j.gca.2009.08.021

Krasnov SG, Cherkashev GA, Stepanova TV, Batuyev BN, Krotov AG, Malin BV, Maslob MN, Markov VF, Poroshina IM, Samovarov MS, Ashadze AM, Lazareva LI, Ermolayev IK (eds) (1995) Detailed geological studies of hydrothermal fields in the North Atlantic. Geological Society of London, Special Publication, pp 43–64

Mayhew LE, Ellison1 ET, McCollom TM, Trainor TP, Templeton AS (2013) Hydrogen generation from low-temperature water.rock reactions. Nat Geosci 6:478–484. doi:10.1038/NGEO1825.

McCollom TM, Bach W (2009) Thermodynamic constraints on hydrogen generation during serpentinization of ultramafic rocks. Geochim Cosmochim Acta 73:856–875. doi:10.1016/j.gca.2008.10.032

McCollom TM, Seewald JS (2001) A reassessment of the potential for reduction of dissolved CO_2 to hydrocarbons during serpentinization of olivine. Geochim Cosmochim Acta 65:3769–3778. doi:10.1016/s0016-7037(01)00655-x

Melchert B, Devey CW, German CR, Lackschewitz KS, Seifert R, Walter M, Mertens C, Yoerger DR, Baker ET, Paulick H, Nakamura K (2008) First evidence for high-temperature offaxis venting of deep crustal/mantle heat: the Nibelungen hydrothermal field, southern Mid-Atlantic Ridge. Earth Planet Sci Lett 275:61–69

Miyashiro A, Shido F, Ewing M (1969) Composition and origin of serpentinites from the Mid-Atlantic Ridge near 24° and 30° North Latitude. Contrib Mineral Petrol 23:117–127

Moores EM (2002) Pre-1 Ga (pre-Rodinian) ophiolites: their tectonic and environmental implications. Geol Soc Am Bull 114:80–95. doi:10.1130/0016-7606(2002)114<0080:pgprot>2.0.co;2.

Morishita T, Hara K, Nakamura K, Sawaguchi T, Tamura A, Arai S, Okino K, Takai K, Kumagai H (2009) Igneous, alteration and exhumation processes recorded in abyssal peridotites and related fault rocks from an oceanic core complex along the Central Indian Ridge. J Petrol 50. doi:10.1093/petrology/egp025

Nakamura K, Morishita T, Bach W, Klein F, Hara K, Okino K, Takai K, Kumagai H (2009) Serpentinized troctolites exposed near the Kairei Hydrothermal Field, Central Indian Ridge: Insights into the origin of the Kairei hydrothermal fluid supporting a unique microbial ecosystem. Earth Planet Sci Lett 280:128–136. doi:10.1016/j.epsl.2009.01.024

Nealson KH, Inagaki F, Takai K (2005) Hydrogen-driven subsurface lithoautotrophic microbial ecosystems (SLiMEs): do they exist and why should we care? Trends Microbiol 13:405–410. doi:10.1016/j.tim.2005.07.010

Ohta H, Maruyama S, Takahashi E, Watanabe Y, Kato Y (1996) Field occurrence, geochemistry and petrogenesis of the Archean mid-oceanic ridge basalts (AMORBs) of the Cleaverville area, Pilbara craton, western Australia. Lithos 37:199–221. doi:10.1016/0024-4937(95)00037-2

Russell MJ, Hall AJ (1997) The emergence of life from iron monosulphide bubbles at a submarine hydrothermal redox and pH front. J Geol Soc 154:377–402. doi:10.1144/gsjgs.154.3.0377

Russell MJ, Hall AJ, Martin W (2010) Serpentinization as a source of energy at the origin of life. Geobiology 8:355–371. doi:10.1111/j.1472-4669.2010.00249.x

Sakai H, Tsutsumi M (1978) D/H fractionation factors between serpentine and water at 100 °C to 500 °C and 2000 bars water pressure, and the D/H ratios of natural serpentines. Econ Geol 40:231–242

Seyfried WE Jr, Dibble WE Jr (1980) Seawater-peridotite interaction at 300 °C and 500 bars: implications for the origin of oceanic serpentinites. Geochim Cosmochim Acta 44:309–321

Seyfried WE Jr, Foustoukos DI, Fu Q (2007) Redox evolution and mass transfer during serpentinization: an experimental and theoretical study at 200 °C, 500 bar with implications for ultramafic-hosted hydrothermal systems at Mid-Ocean Ridges. Geochim Cosmochim Acta 71:3872–3886. doi:10.1016/j.gca.2007.05.015

Sleep NH, Meibom A, Fridriksson T, Coleman RG, Bird DK (2004), H_2-rich fluids from serpentinization: geochemical and biotic implications. Proc Natl Acad Sci U S A 101:12818–12823

Takai K, Gamo T, Tsunogai U, Nakayama N, Hirayama H, Nealson KH, Horikoshi K (2004) Geochemical and microbiological evidence for a hydrogen-based, hyperthermophilic subsurface lithoautotrophic microbial ecosystem (HyperSLiME) beneath an active deep-sea hydrothermal field. Extremophiles 8:269–282. doi:10.1007/s00792-004-0386-3

Takai K, Nakamura K, Suzuki K, Inagaki F, Nealson KH, Kumagai H (2006) Ultramafics-Hydrothermalism-Hydrogenesis-HyperSLiME (UltraH^3) linkage: a key insight into early microbial ecosystem in the Archean deep-sea hydrothermal systems. Paleontologic Res 10:269–282

Van Dover CL, Humphris SE, Fornari D, Cavanaugh CM, Collier R, Goffredi SK, Hashimoto J, Lilley MD, Reysenbach AL, Shank TM, Von Damm KL, Banta A, Gallant RM, Gotz D, Green D, Hall J, Harmer TL, Hurtado LA, Johnson P, McKiness ZP, Meredith C, Olson E, Pan IL, Turnipseed M, Won Y, Young CR, Vrijenhoek RC (2001) Biogeography and ecological setting of Indian Ocean hydrothermal vents. Science 294:818–823. doi:10.1126/science.1064574

Wakita H, Nakamura Y, Kita I, Fujii N, Notsu K (1980) Hydrogen release: new indicator of fault activity. Science 210:188–190. doi:10.1126/science.210.4466.188

Wenner DB, Taylor HP (1971) Temperatures of serpentinization of ultramafic rocks, based on $^{16}O/^{18}O$ fractionation between coexisting serpentine and magnetite. Contrib Mineral Petrol 32:165–185

Wenner DB, Taylor HP (1973) Oxygen and hydrogen isotope studies of the serpentinization of ultramafic rocks in oceanic environments and continental ophiolite complexes. Am J Sci 273:207–239

Wetzel LR, Shock EL (2000) Distinguishing ultramafic- from basalt-hosted submarine hydrothermal systems by comparing calculated vent fluid compositions. J Geophys Res Solid Earth 105:8319–8340. doi:10.1029/1999JB900382

Wiersberg T, Erzinger J (2008) On the origin and spatial distribution of gas at seismogenic depths of the San Andreas Fault from drill mud gas analysis. Appl Geochem 23:1675–1690. doi:10.1016/j.apgeochem.2008.01.012

Yoshizaki M, Shibuya T, Suzuki K, Shimizu K, Nakamura K, Takai K, Omori S, Maruyama S (2009) H_2 generation by experimental hydrothermal alteration of komatiitic glass at 300 °C and 500 bars: a preliminary result from on-going experiment. Geochem J 43: E17–E22

Experimental Assessment of Microbial Effects on Chemical Interactions Between Seafloor Massive Sulfides and Seawater at 4 °C

9

Shingo Kato, Katsuhiko Suzuki, Takazo Shibuya, Jun-ichiro Ishibashi, Moriya Ohkuma, and Akihiko Yamagishi

Abstract

To assess the effects of microbes on the exchange of Cu, Zn, and P between seafloor massive sulfide (SMS) deposits and seawater, we monitored the variation of the concentrations of Cu, Zn, and P in the artificial seawater of reaction systems that did or did not also include slabs and microbes originating from an SMS sample at 4 °C for 71 days. Dissolution of Cu and Zn from the slabs was observed when microbes were present or absent. Zinc from the slabs dissolved 1.4–2.3 fold more rapidly when microbes were present. In the presence of slabs and microbes, the rate of removal of P from the artificial seawater was the sum of the individual removal rates associated with the slabs and microbes. Six bacterial phylotypes including *Halomonas* and *Marinobacter* were present at the end of the experiment as shown by PCR-based analysis targeting 16S rRNA genes. These bacteria probably contribute to the release of Zn from the SMS slab and removal of P from the artificial seawater. Our results provide further insights into the role(s) of microbes on the geochemical interactions between SMS deposits and seawater.

Keywords

Bacteria • Batch experiment • Elemental cycle • Microbial dissolution • Seafloor massive sulfides

The online version of this chapter (doi:10.1007/978-4-431-54865-2_9) contains supplementary material, which is available to authorized users.

S. Kato
Japan Collection of Microorganisms, RIKEN BioResource Center, 3-1-1 Koyadai, Tsukuba, Ibaraki 305-0074, Japan

Department of Molecular Biology, Tokyo University of Pharmacy and Life Science, 1432-1 Horinouchi, Hachioji, Tokyo 192-0392, Japan

K. Suzuki
Institute for Research on Earth Evolution (IFREE), Japan Agency for Marine-Earth Science and Technology (JAMSTEC), 2-15 Natsushima, Yokosuka, Kanagawa 237-0061, Japan

Submarine Resources Research Project (SRRP) and Precambrian Ecosystem Laboratory (PEL), Japan Agency for Marine-Earth Science and Technology (JAMSTEC), 2-15 Natsushima, Yokosuka, Kanagawa 237-0061, Japan

T. Shibuya
Submarine Resources Research Project (SRRP) and Precambrian Ecosystem Laboratory (PEL), Japan Agency for Marine-Earth Science and Technology (JAMSTEC), 2-15 Natsushima, Yokosuka, Kanagawa 237-0061, Japan

J.-i. Ishibashi
Department of Earth and Planetary Sciences, Faculty of Science, Kyushu University, Hakozaki, Higashi-ku, Fukuoka 812-8581, Japan

M. Ohkuma
Japan Collection of Microorganisms, RIKEN BioResource Center, 3-1-1 Koyadai, Tsukuba, Ibaraki 305-0074, Japan

A. Yamagishi (✉)
Department of Molecular Biology, Tokyo University of Pharmacy and Life Science, 1432-1 Horinouchi, Hachioji, Tokyo 192-0392, Japan
e-mail: yamagish@toyaku.ac.jp

J.-i. Ishibashi et al. (eds.), *Subseafloor Biosphere Linked to Hydrothermal Systems: TAIGA Concept*,
DOI 10.1007/978-4-431-54865-2_9,

9.1 Introduction

Seafloor massive sulfide (SMS) deposits occur at and around the plate boundaries, e.g., mid-ocean ridges, back-arc basins and volcanic arcs (Hannington et al. 2011). These SMS deposits consist of relatively insoluble sulfide minerals, e.g., pyrite (FeS_2), chalcopyrite ($CuFeS_2$), sphalerite (ZnS), and galena (PbS), and also contain trace elements such as Au, Ag, Co and in some cases, Ni (Herzig and Hannington 1995). The hydrothermally active and inactive vents of chimney- and mound-shaped SMS deposits are microbe-rich environments, with microbial densities of up to 10^{10} cells (g sulfide)$^{-1}$ (Kato et al. 2010; Schrenk et al. 2003; Suzuki et al. 2004; Takai and Horikoshi 1999), which are densities comparable with those in soils and animal bowels (Whitman et al. 1998). Dissolved H_2, H_2S, CH_4 and Fe^{2+} supplied from hydrothermal fluids in the active sulfide vents serve as energy sources for the microbial communities. Conversely, microbial communities in inactive sulfide vents apparently use metal sulfides as energy sources (Edwards et al. 2003a). An in situ examination of SMS ores with time suggested that sulfide minerals on the seafloor are highly weathered by microbes (Edwards et al. 2003b). However, a quantitative assessment of the elements released from or adsorbed by SMS deposits mediated by microbes had not been done prior to this report.

Considering the high levels of heavy metals in the SMS deposits and the ubiquity of these deposits on the seafloor (Hannington et al. 2011; Herzig and Hannington 1995), an experimental study of the change with time of the SMS components via microbial activity is important to understand how such events impact the oceanic biogeochemical cycles. The concentrations of certain heavy metals, e.g., Fe, Zn, Mn, Cu and Ni, which are essential for oceanic microbial viability, are extremely small (<0.1 μM) in the ocean (Morel and Price 2003; Sohrin and Bruland 2011). The exchange of these heavy metals between seawater and SMS deposits is potentially needed for the maintenance of important oceanic microbial ecosystems.

Here, we report the effects of microbes on the exchanges of elements between SMS samples and seawater by simulating the environmental conditions of deep seafloor (i.e., low temperature, weakly alkaline pH and a small amount of organic carbon). The goals of this study were (i) to measure the kinetics of the dissolution of certain metals and P from a recovered SMS sample and (ii) to assess if and how microbial communities affect the kinetics.

9.2 Materials and Methods

9.2.1 Sample Collection

A portion of massive sulfide ore (sample ID, D903-R1) was collected from a hydrothermal vent field, called the Archaean site (12°56.35′N, 143°38.0′E; depth, 3,076 m), in the Southern Mariana Trough during the YK05-09 cruise (July to August 2005) by the manned submersible *Shinkai 6500* (JAMSTEC, Japan) of the R/V *Yokosuka* (JAMSTEC, Japan). A bathymetric map of the vent field is shown in a previous report (Kato et al. 2010) and also in Seama et al. (Chap. 17). The SMS sample (Suppl. 9.1a) was washed with filter-sterilized seawater and crushed into fist-sized, subsurface, non-oxidized samples, using an autoclave-sterilized hammer and chisel in a clean box on board. Some of the samples were stored at −80 °C in DNA/RNA-free plastic tubes for DNA extraction and the others were stored at 4 °C for inoculation and mineralogical studies.

9.2.2 Experimental Medium

The artificial seawater (ASW) was a modification of that described in the previous report (Jannasch et al. 1996) and contained 20.0 g NaCl; 3.0 g $MgCl_2{\cdot}6H_2O$; 6.0 g $MgSO_4{\cdot}7H_2O$; 1.0 g $(NH_4)_2SO_4$; 0.2 g $NaHCO_3$; 0.3 g $CaCl_2{\cdot}2H_2O$; 0.5 g KCl; 0.015 g KH_2PO_4, 1 mL of vitamin solution (DSMZ medium 141; http://www.dsmz.de) and 1 mL of marine trace element solution (DSMZ medium 511), in 1 L of distilled water. The pH value of the ASW was 7.3 before autoclaving and 8.1 afterwards. To simulate the low concentrations of organic compounds found in deep seawater, Bacto yeast extract (BD Difco, NJ, USA) was added from an autoclaved stock solution to render the concentration to be 10 mg (corresponding to 3.3 mg of carbon) L^{-1} in the final medium as described previously (Jannasch et al. 1996).

9.2.3 Batch Experiments

A sample of the interior of the SMS was cut into small slabs (10 × 10 × 1 mm; Suppl. 9.1b) using a low speed diamond saw (Struers Minitor, Westlake, OH, USA). Each slab weighed 0.35 ± 0.05 g. The relative surface area of each slab was 5.72 ± 0.01 m^2 g^{-1}, as determined by the BET-N_2 method (Seishin Enterprise Co., Ltd., Tokyo, Japan). The slabs were cleaned and sterilized by soaking them in ethanol

and acetone for 2 h each according to Edwards et al. (2000) and then dried by flushing with N_2 gas at room temperature.

Sterile 250-mL glass culture flasks, each containing 100 mL of ASW and capped with sponge plugs, were used to contain the incubations. Each flask contained one of the following systems: ASW with slabs and an inoculum; ASW with only slabs; ASW with only an inoculum; only ASW. The contents of all systems were prepared in duplicate, except for the system of only ASW. The inoculum was prepared from a slurry of the mostly oxidized surface of the SMS sample. The cell density of the slurry was $3.62 \pm 0.65 \times 10^7$ cells mL^{-1} (corresponding to $2.22 \pm 0.38 \times 10^6$ cells (g sulfide)$^{-1}$) determined by fluorescence microscopy (Kato et al. 2009a). The systems containing slabs and an inoculum are denoted as MC1 and MC2; those with only slabs as C1 and C2; those with only an inoculum as M1 and M2; and the negative control, without slabs and an inoculum as N (i.e., blank test), respectively. MC1, MC2, C1 and C2 each contained 10 slabs. One milliliter of the slurry was added into each of MC1, MC2, M1 and M2. These reaction systems were incubated in a cold room at 4 °C.

An aliquot of 3 mL (1 mL for direct cell counting and 2 mL for chemical analyses) was removed from each culture with a sterile disposable syringe at 4, 42, 140, 332, 782, and 1698 h after the start of the experiment. Before sampling, each medium was gently withdrawn and returned by action of a sterile disposable syringe three times. To determine the number of cells, each sample was filtered through a black polycarbonate filter (pore size, 0.2 μm; diameter, 13 mm; Advantec, Tokyo, Japan). Each filter was washed twice with ultra-pure water, and then was dried in a sterilized Petri dish and stored at −20 °C. For the chemical analyses, each sample was filtered through a polycarbonate filter (pore size, 0.2 μm; diameter, 25 mm; Advantec, Tokyo, Japan), and the filtrates were individually stored in an acid-cleaned 2-mL polypropylene tube. Approximately 300 μL of each filtrate was used for the pH measurement.

At the end of the incubations, a 60 mL aliquots of each solution was filtered through a polycarbonate filter (pore size, 0.2 μm; diameter, 13 mm; Advantec, Tokyo, Japan). The filters were stored at −80 °C prior to DNA analysis. To remove the microbes that were loosely attached to the slabs, the slabs were gently swished in sterilized Petri dishes containing 30 mL of ultra-pure water with tweezers. The water was replaced three times. Five slabs from each experiment were stored at −80 °C for DNA analysis, and the other five slabs were fixed with 3.7 % (w/v) formalin at 4 °C over night and then stored in a 1:1 ethanol/phosphate-buffered saline mixture at −20 °C until microscopy was performed.

9.2.4 Chemical Analysis

To determine the chemical composition of the retrieved SMS sample, 0.1 g of the slabs was pulverized and decomposed in HNO_3-HF-$HClO_4$ solution at 90 °C. The solution was evaporated at 90 °C. The residue was dried at 140 °C and then dissolved in 1.25 mL HCl-HNO_3 solution at 90 °C. The concentration of each element was determined by multi-channel inductively coupled plasma-optical emission spectrometry (ICP-OES) (SPS5500; SII NanoTechnology, Chiba, Japan). The chemical composition of the sample was 42.9 wt% Fe (weight per total weight); 694 ppm Zn; 594 ppm Al; 114 ppm Co; 106 ppm Cu; 97.4 ppm Mg; 72.9 ppm Ba; 46.0 ppm Ca; 32.4 ppm Cd; 30.0 ppm Ni; 23 ppm Na; 9.3 ppm V; 6.90 ppm Rb; 6.80 ppm Sr; 4.0 ppm Mn. We assumed that the remaining solid, which could not be quantified, was sulfur. The uncertainties for the ICP-OES analysis were within ±5 % for Al, Ba, Ca, Cd, Cu, Fe, Mg, Rb, Sr and Zn, and approximately ±10 % for Co, Mn, Na, Ni and V. The detection limit for the aforementioned elements was <10 ppb. Ikehata et al. (Chap. 22) characterized the mineral content of a bulk sample of this SMS of D903-R1, and showed that it was primarily composed of cryptocrystalline pyrite and marcasite with lesser amounts of sphalerite, chalcopyrite, and barite.

The pH of each system was measured with a TWIN pH meter (HORIBA, Kyoto, Japan). Concentrations of Cu, Zn and P in the ASW samples with time were measured using the ICP-OES system as described above. The detection limits were 2.25 nmol L^{-1} for Cu, 239 nmol L^{-1} for P, and 5.54 nmol L^{-1} for Zn. The uncertainty for the P measurement was ±5 % and that for the Cu and Zn measurement was approximately ±10 %. We also assessed the concentrations of the other elements that had been detected in the SMS sample; however, no clear temporal trends were observed because of their low concentrations (data not shown). The concentration of each element was corrected for the decrease in the sample volume and the loss of element mass during the sampling using the following equation (Eq. 4 in Wu et al. 2007):

$$C'j,i = \frac{Cj,i[V_0 - (j-1)Vs] + \sum_{h=1}^{j-1} Ch,iVs}{V_0} \quad (9.1)$$

where $C'_{j,i}$ is the corrected concentration of element i in the jth sample (j = 1,2...,7), and $C_{j,i}$ is the measured concentration. V_0 is the initial volume (0.1 L), V_s is the sample volume (0.003 L), and the term $\sum_{h=1}^{j-1} Ch,iVs$ accounts for the total mass of element i extracted during the samplings.

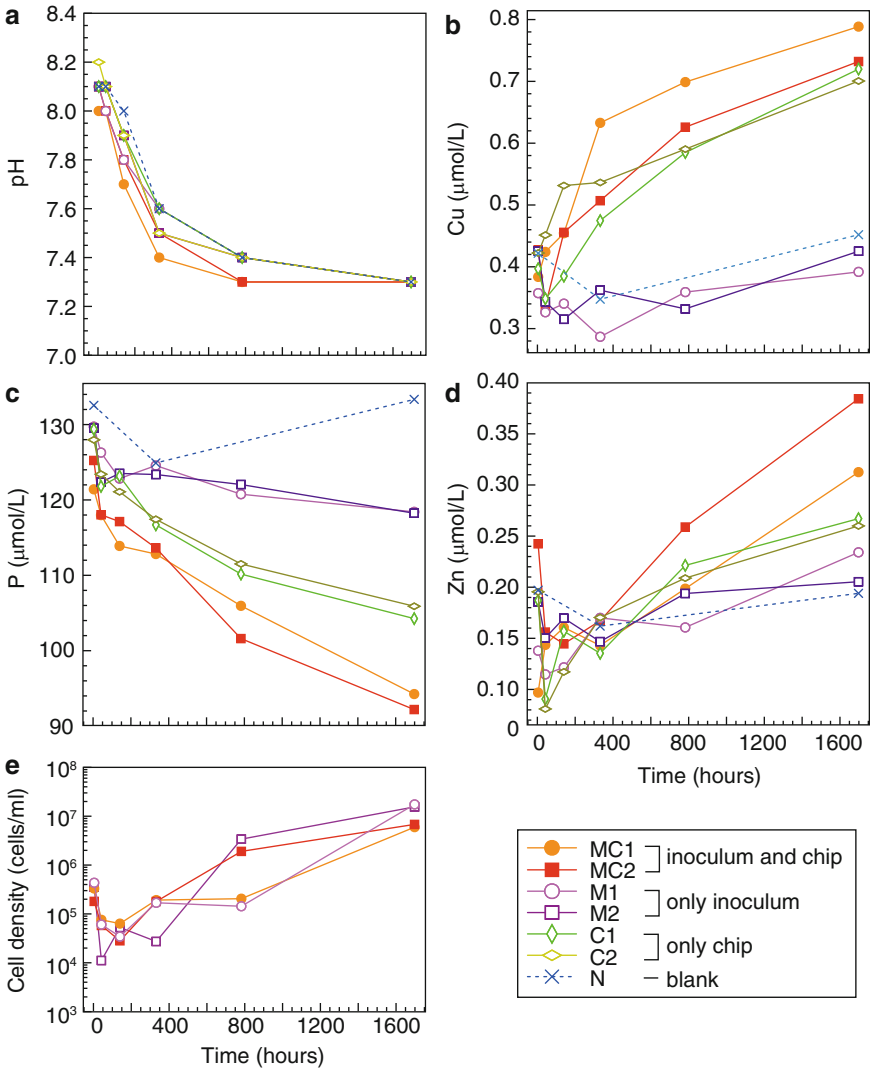

Fig. 9.1 Changes in cell density, pH, the concentrations of Cu, P and Zn during the course of the experiments. (**a**) pH values. Concentrations of (**b**) Cu, (**c**) P, and (**d**) Zn. (**e**) Cell density. Symbol for the systems are shown in the *box* at the lower right of the figure (see text for details)

The rate constant (dC'/dt) of dissolution for each element was calculated for the 332–1,698 h period (Suppl. 9.2), a time when the pH values of the ASW were between 7.3 and 7.5 (Fig. 9.1a and Suppl. 9.3). The release or removal rate (R) of each element to or from the ASW, respectively, was calculated using the corresponding rate constant (dC'/dt), the initial fluid volume (V_0, 0.1 L), the relative surface area (A, 5.72 $m^2\ g^{-1}$), the total mass of the slabs in each system (m, 3.11–3.33 g), and Eq. 5 in Wu et al. (2007):

$$R = \frac{dC'i}{dt}\frac{V_0}{Am}, \tag{9.2}$$

The values for R are listed in Table 9.1.

9.2.5 16S rRNA Gene Clone Library Construction and Phylogenetic Analysis

The 16S rRNA gene analysis was performed as described (Kato et al. 2009a, b). Partial 16S rRNA genes in extracted genomic DNA were amplified by PCR with the prokaryote-universal primer set, Uni515F and Uni1406R (Kato et al. 2009a). The PCR products were cloned and the nucleotide sequences of randomly selected clones were determined. Nucleotide sequences were aligned using ClustalW 2.0.12 (Larkin et al. 2007). Sequences with at least 97 % similarity according to DOTUR (Schloss and Handelsman 2005) were treated as the same phylotype. Maximum-likelihood (ML) trees were constructed using PHYML (Guindon and Gascuel 2003). Bootstrap values were calculated using 100 replicates.

Table 9.1 Rates of dissolution of Cu and Z from the SMS slabs and of removal of P from the ASW of the samples containing both microbes and slabs (MC1, 2) microbes, and only slabs (C1, 2)

	Dissolution rate (mol m^{-2} s^{-1})		
Sample ID	Cu	P	Zn
MC1	2.4.E-16	−2.0.E-14	1.9.E-16
MC2	1.7.E-16	−2.2.E-14	2.3.E-16
C1	2.5.E-16	−1.3.E-14	1.3.E-16
C2	1.9.E-16	−1.3.E-14	1.0.E-16

9.2.6 Fluorescence Microscopy

Microbes on the filters and slabs were stained with SYBR Green I. Microscope images were recorded using a fluorescence microscope BX60 (Olympus, Tokyo, Japan) and a cooled CCD camera (Penguin 600CL, Pixera, San Jose, CA, USA). At least 30 fields of the images of each filter and slab were used for cell counting.

9.2.7 Accession Numbers

Sequence data were submitted to the DDBJ database under the accession numbers AB600466 to AB600509 for the 16S rRNA genes recovered from the inoculum, and AB600510 to AB600530 for the 16S rRNA genes recovered at the end of the experiment.

9.3 Results and Discussion

9.3.1 Concentrations and Release/Removal Rates of Elements to/from the ASW Samples

The initial pH values of the incubations were between 8.2 and 8.0. They decreased to 7.6–7.4 by 332 h and finally to 7.3 (Fig. 9.1a) after 1,698 h. The pH drop may have resulted from dissolution of CO_2 from the air because the drop was observed in all samples including N. The change in the concentrations of each element differed during the 4–332-h and 332–1,698-h periods; Fig. 9.1b–d, see also Suppl. 9.3). A dC'/dt value for each element was calculated for the 332–1,698-h period when the pH of the systems remained between 7.3 and 7.5 (Fig. 9.1a). Results of the calculation are shown in Suppl. 9.2.

Leaching of Cu and Zn, which were relatively abundant in the slabs (see above), was observed in the presence and absence of the microbes (Fig. 9.1b, d). In particular, R for Zn dissolution was greater (1.4–2.3 folds) when microbes were present (Table 9.1). The dC'/dt values for Zn were similar for each pair of duplicated samples, i.e., MC1 and MC2, and C1 and C2 (Fig. 9.1d and Suppl. 9.2). In contrast, no differences for the R values of Cu associated with the MC1 and MC2, and C1 and C2 samples were observed.

When SMS slabs were present in a reaction system, P was removed even if microbes were not (Fig. 9.1c). P was also removed in the presence of microbes when slabs were absent (Fig. 9.1c). The dC'/dt absolute values for P were greater when only slabs were present (C1 and C2) than when only microbes were present (M1 and M2; Fig. 9.1c, Suppl. 9.2), indicating that the rate of precipitation or adsorption of P onto the sulfide slabs was faster than the rate of uptake by the microbes. dC'/dt for P in the systems that included slabs and microbes (MC1 and MC2) were corresponding to the sums of the values for M1 or M2 and C1 or C2 (Suppl. 9.2).

9.3.2 Microbial Communities

The temporal changes in cell densities are shown in Fig. 9.1e, with decreases seen in the MC1, MC2, M1 and M2 systems to 10^4–10^5 cells mL^{-1} at 140 h and increases up to 10^6–10^7 cells mL^{-1} by 1,698 h. The cell densities in the C1, C2 and N systems could not be reliably counted by microscopy ($<10^3$ cells mL^{-1}). Cell colonies were observed on the MC1 and MC2 slabs at the end of the experiment (6.92 ± 4.55 and $5.76 \pm 3.28 \times 10^5$ cells cm^{-2}, respectively; Suppl. 9.4).

16S rRNA gene clone libraries were constructed from the genomic DNA extracted from the ASW samples and SMS slabs at the end of the experiment. The Inoc library is that from microbes in the original inoculum. The MC1lq, MC2lq, M1lq and M2lq libraries are from microbes in the MC1, MC2, M1 and M2 ASW samples, respectively. The MC1cp and MC2cp libraries are from microbes on the MC1 and MC2 slabs, respectively. The total numbers of the analyzed clones are 91, 45, 46, 47, 48, 20 and 20 for Inoc, MC1lq, MC1cp, MC2cp, MC2lq, M1lq and M2lq, respectively. 16S rRNA genes were not detected by PCR from the ASW samples and slabs from the C1 and C2 systems or from the ASW of the N system.

The clones in the Inoc library were affiliated with the following taxonomic groups (Fig. 9.2 and Suppl. 9.5): *Actinobacteria* (5.4 % of the total number of clones), *Bacteroidetes* (2.2 %), *Chloroflexi* (1.1 %), *Planctomycetes* (6.5 %), *Alphaproteobacteria* (16.3 %), *Deltaproteobacteria* (2.2 %), *Gammaproteobacteria* (63.0 %), *Zetaproteobacteria* (1.1 %), *Verrucomicrobia* (1.1 %) and *Euryarchaeota* (1.1 %). Many of the phylotypes in the Inoc library are similar to uncultured environmental clones recovered from the sulfide chimneys of the inactive vents (Kato et al. 2010), from the oceanic basaltic rocks (Santelli et al. 2008) and marine sediments but are distantly related to known species with <95 % of 16S rRNA gene similarity. Phylotypes (the

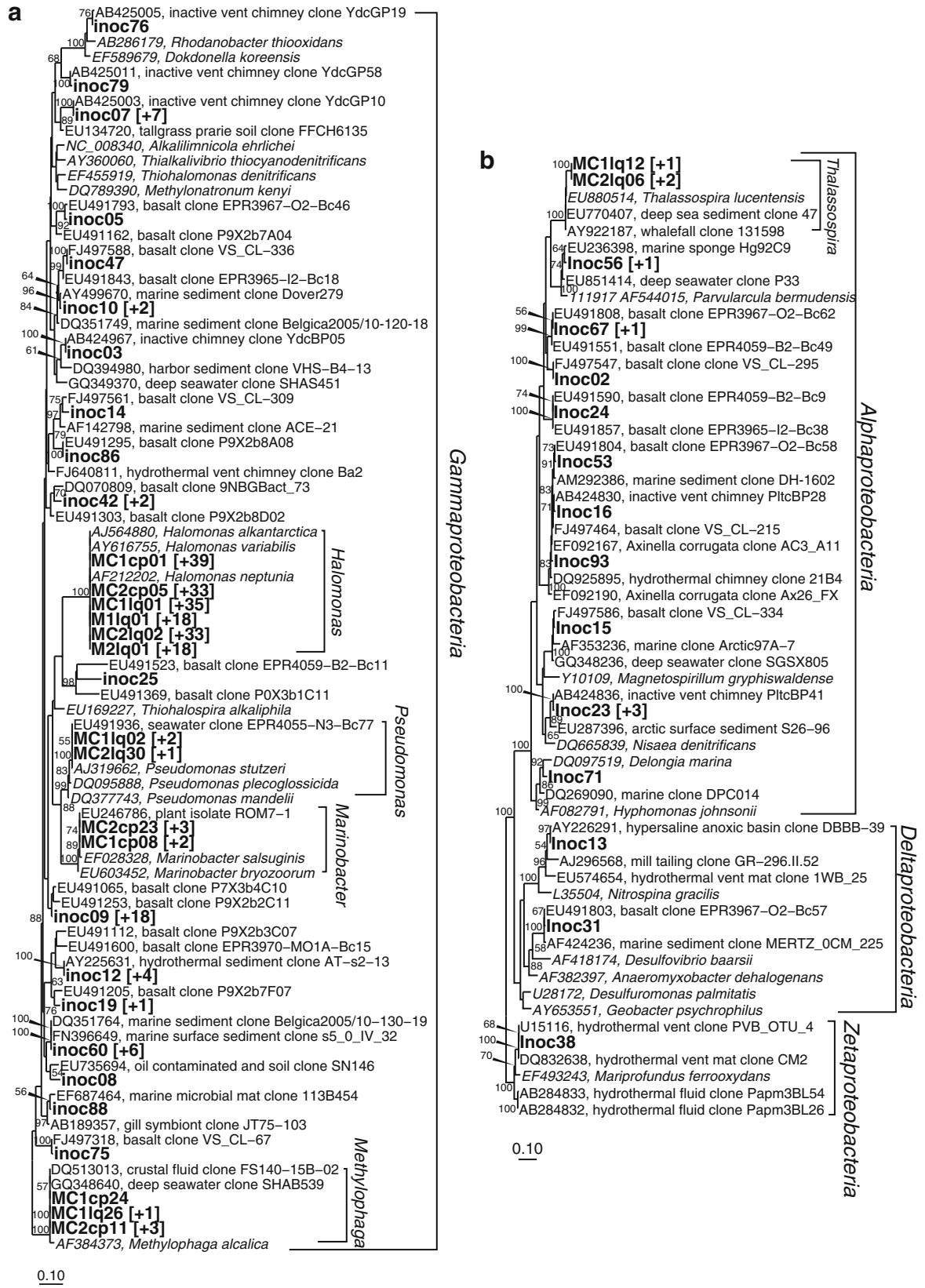

Fig. 9.2 Phylogenetic trees for *Proteobacteria*. The ML trees for (**a**) *Gammaproteobacteria* and (**b**) *Deltaproteobacteria*, *Alphaproteobacteria* and *Zetaproteobacteria* were inferred using 753 and 752 homologous positions in the alignment dataset, respectively. *Mariprofundus ferrooxydans* (EF493243) or *Halomonas aquamarina* (AJ306888) were used as the out groups for each tree (data not shown). Bootstrap values (>50 %) based on 100 replicates are shown at the branch points. The *scale bar* represents 0.1 nucleotide substitutions per sequence position. The clone numbers are shown in *bold type*. The numbers that follow in *brackets* indicate the number of detected clones

Table 9.2 Number of PCR clones detected in the ASW samples and slabs at the end of the experiments

	Sample ID					
	MC1cp	MC1lq	MC2cp	MC2lq	M1lq	M2lq
Bacteroidetes						
Sphingobacteria						
Algoriphagus	1 (2.2)	3 (6.5)	5 (10.6)	9 (18.8)	1 (5.0)	1 (5.0)
Proteobacteria						
Alphaproteobacteria						
Thalassospira		2 (4.3)		3 (6.3)		
Gammaproteobacteria						
Halomonas	40 (88.9)	36 (78.3)	34 (72.3)	34 (70.8)	18 (90.0)	17 (85.0)
Marinobacter	2 (4.4)	2 (4.3)	3 (6.4)	1 (2.1)		
Methylophaga	1 (2.2)	2 (4.3)	4 (8.5)			2 (10.0)
Pseudomonas	1 (2.2)	1 (2.2)	1 (2.1)	1 (2.1)	1 (5.0)	
Total	45 (100)	46 (100)	47 (100)	48 (100)	20 (100)	20 (100)

Numbers in parentheses are the percentage of the clones in each taxon

representative clones: inoc38 and 51) related to *Mariprofundus ferrooxydans* (95 % similarity) of *Zetaproteobacteria* and *Ferrimicrobium acidiphilum* (89 % similarity) of *Actinobacteria*, which are iron-oxidizing bacteria, were also detected in the Inoc library. In contrast to the great diversity of the microbial community in the original inoculum, only six phylotypes were detected at the end of the experiment (Table 9.2). These phylotypes were completely different from those in the Inoc library (Fig. 9.2 and Suppl. 9.5), probably because the original phylotypes had been out-competed during the incubation periods.

9.3.3 Microbial Effects on Chemical Interaction on Sulfide Deposits

The bacterial species, e.g., *Halomonas* and *Marinobacter*, found at the end of the experiment should be minor constituents of the microbial community of the in situ SMS deposits because they were not detected in the original inoculum. The species present at the end of the experiment were probably selected by the experimental conditions. These species may have influenced the release of Zn and removal of P. Remarkably, these species have been detected in SMS samples in various deep-sea fields (Edwards et al. 2003b; Kaye et al. 2010; Rogers et al. 2003), suggesting that they may play a role in the release of Zn and removal of P in situ.

Our results suggest that microbial action accelerated Zn dissolution from the SMS slabs. Iron-oxidizing bacteria convert Fe^{2+} to Fe^{3+}, such that Fe^{3+} can then react with sphalerite (ZnS) as oxidants to release Zn^{2+} (Fowler and Crundwell 1999) as follows:

$$4Fe^{2+} + O_2 + 4H^+ \rightarrow 4Fe^{3+} + 2H_2O \quad (9.3)$$

$$ZnS + 2Fe^{3+} \rightarrow Zn^{2+} + 2Fe^{2+} + S \quad (9.4)$$

In fact, the SMS samples contain sphalerite (Ikehata et al. Chap. 22). The genus *Marinobacter* includes an iron-oxidizing bacterium that has been isolated from an SMS sample (Edwards et al. 2003c). In addition, local acidification on the sulfide slabs by microbes might also have accelerated the dissolution of Zn in our systems, similar to that of silicate dissolution by *Arthrobacter* sp. (Liermann et al. 2000). The genus *Halomonas* includes acid-producing bacteria (Sanchez-Porro et al. 2010). Our 16S rRNA gene analysis indicates that the *Marinobacter* sp. and *Halomonas* sp. were attached to the slabs. Thus, the activity of these species likely contributed to the acceleration of the Zn dissolution from the sulfide slabs. In contrast to the dissolution of Zn, we did not observe a significantly accelerated Cu dissolution from the slabs.

P was removed from the ASW when microbes and/or slabs were present. Microbes use P as a nutrient. An increase in cell numbers with time was observed in the systems to which the inoculum had been added (Fig. 9.1e). Other reports have suggested that P is removed from seawater by adsorption onto the solid surfaces of sediments and rocks (Berner 1973; Wheat et al. 1996), which is consistent with our observation that P is removed from the systems containing only slabs (Fig. 9.1c). Notably, P was removed from the ASW more rapidly when only slabs were present, than when only microbes were present (Fig. 9.1c); however, rate of P removal from seawater on actual environments by SMS deposits and by microbes in situ should fluctuate according to the in situ physicochemical conditions and the degree of microbial activity.

9.3.4 Conclusion and Perspective

In the present study, we conducted batch experiments with and without the SMS samples and microbes at 4 °C and monitored certain chemical and microbial changes in the

reaction systems for 71 days. The dissolution rate of Zn from the SMS slabs was faster when microbes were present than in the absence of microbes, suggesting that the microbes accelerated Zn dissolution. Removal of P from the ASW was observed when microbes were present or absent and slabs were present. Our results should lead to a better understanding of the roles played by SMS deposits with microbes in the oceanic biogeochemical cycles.

Between 1 and 90 million-tons of the SMS deposits are estimated to be present in each hydrothermal field (Herzig and Hannington 1995). Given that the total amount of SMS deposits on the seafloor and their relative surface areas are approximately 100 million-tons and 6 $m^2\ g^{-1}$, respectively, the flux of P adsorbed onto SMS deposits can be calculated as 4×10^8 mol $year^{-1}$ with the use of the averaged *R* value from Table 9.1 for the MC systems. This value is approximately one-hundredth of the input of P yearly into the oceans from rivers (3×10^{10} mol $year^{-1}$) (Elderfield and Schultz 1996), which suggests that adsorption of P by SMS deposits with microbes helps control the levels of oceanic P. Similar calculations suggest that the yearly release of Zn from the SMS deposits (approx. $\sim 2 \times 10^6$ mol $year^{-1}$) should be much smaller than that from rivers (approx. $\sim 10^{10}$ mol $year^{-1}$) (Elderfield and Schultz 1996). Our estimates are rough approximations because the total amount of SMS deposits are probably underestimated and the necessary in situ microbial and physicochemical information has not been adequately delineated. Additional investigations are needed to more accurately calculate the fluxes of elements associated with SMS deposits.

Acknowledgements We thank Dr. Kenji Shimizu (IFREE, JAMSTEC) for preparing the SMS slabs. We thank the crew of the R/V *Yokosuka* and the operation team of *Shinkai 6500* for their cooperation in sample collection. We are also grateful to the scientists of the YK05-09 cruise and to the members of Project TAIGA (Trans-crustal Advection and In-situ biogeochemical processes of Global sub-seafloor Aquifer) for providing valuable samples and for helpful discussions. Furthermore, we are grateful to two anonymous reviewers for valuable comments and suggestions. This research was funded by the Ministry of Education, Culture, Science and Technology (MEXT), Japan, through a Grant-in-Aid for Scientific Research on Innovative Areas (Project TAIGA, #20109006) and partly by the RIKEN Special Postdoctoral Researchers Program.

References

Berner RA (1973) Phosphate removal from sea water by adsorption on volcanogenic ferric oxides. Earth Planet Sci Lett 18(1):77–86

Edwards KJ, Bond PL, Banfield JF (2000) Characteristics of attachment and growth of thiobacillus caldus on sulphide minerals: a chemotactic response to sulphur minerals? Environ Microbiol 2 (3):324–332

Edwards KJ, Bach W, Rogers DR (2003a) Geomicrobiology of the ocean crust: a role for chemoautotrophic fe-bacteria. Biol Bull 204 (2):180–185

Edwards KJ, McCollom TM, Konishi H, Buseck PR (2003b) Seafloor bioalteration of sulfide minerals: results from in situ incubation studies. Geochim Cosmochim Acta 67(15):2843–2856

Edwards KJ, Rogers DR, Wirsen CO, McCollom TM (2003c) Isolation and characterization of novel psychrophilic, neutrophilic, Fe-oxidizing, chemolithoautotrophic α- and γ-proteobacteria from the deep sea. Appl Environ Microbiol 69(5):2906–2913

Elderfield H, Schultz A (1996) Mid-ocean ridge hydrothermal fluxes and the chemical composition of the ocean. Annu Rev Earth Planet Sci 24(1):191–224. doi:10.1146/annurev.earth.24.1.191

Fowler TA, Crundwell FK (1999) Leaching of zinc sulfide by thiobacillus ferrooxidans: bacterial oxidation of the sulfur product layer increases the rate of zinc sulfide dissolution at high concentrations of ferrous ions. Appl Environ Microbiol 65(12):5285–5292

Guindon S, Gascuel O (2003) A simple, fast, and accurate algorithm to estimate large phylogenies by maximum likelihood. Syst Biol 52(5):696–704

Hannington M, Jamieson J, Monecke T, Petersen S, Beaulieu S (2011) The abundance of seafloor massive sulfide deposits. Geology 39(12):1155–1158. doi:10.1130/g32468.1

Herzig PM, Hannington MD (1995) Polymetallic massive sulfides at the modern seafloor a review. Ore Geol Rev 10(2):95–115

Jannasch HW, Wirsen CO, Doherty KW (1996) A pressurized chemostat for the study of marine barophilic and oligotrophic bacteria. Appl Environ Microbiol 62(5):1593–1596

Kato S, Kobayashi C, Kakegawa T, Yamagishi A (2009a) Microbial communities in iron-silica-rich microbial mats at deep-sea hydrothermal fields of the Southern Mariana Trough. Environ Microbiol 11(8):2094–2111

Kato S, Yanagawa K, Sunamura M, Takano Y, Ishibashi J, Kakegawa T, Utsumi M, Yamanaka T, Toki T, Noguchi T, Kobayashi K, Moroi A, Kimura H, Kawarabayasi Y, Marumo K, Urabe T, Yamagishi A (2009b) Abundance of *Zetaproteobacteria* within crustal fluids in back-arc hydrothermal fields of the Southern Mariana Trough. Environ Microbiol 11(12):3210–3222

Kato S, Takano Y, Kakegawa T, Oba H, Inoue K, Kobayashi C, Utsumi M, Marumo K, Kobayashi K, Ito Y, Ishibashi J, Yamagishi A (2010) Biogeography and biodiversity in sulfide structures of active and inactive vents at deep-sea hydrothermal fields of the Southern Mariana Trough. Appl Environ Microbiol 76(9):2968–2979. doi:10.1128/aem.00478-10

Kaye JZ, Sylvan JB, Edwards KJ, Baross JA (2010) *Halomonas* and *Marinobacter* ecotypes from hydrothermal vent, subseafloor, and deep-sea environments. FEMS Microbiol Ecol 75(1):123–133. doi:10.1111/j.1574-6941.2010.00984.x

Larkin MA, Blackshields G, Brown NP, Chenna R, McGettigan PA, McWilliam H, Valentin F, Wallace IM, Wilm A, Lopez R, Thompson JD, Gibson TJ, Higgins DG (2007) Clustal W and Clustal X version 2.0. Bioinformatics 23(21):2947–2948. doi:10.1093/bioinformatics/btm404

Liermann LJ, Barnes AS, Kalinowski BE, Zhou X, Brantley SL (2000) Microenvironments of pH in biofilms grown on dissolving silicate surfaces. Chem Geol 171(1–2):1–16

Morel FMM, Price NM (2003) The biogeochemical cycles of trace metals in the oceans. Science 300(5621):944–947. doi:10.1126/science.1083545

Rogers DR, Santelli CM, Edwards KJ (2003) Geomicrobiology of deep-sea deposits: Estimating community diversity from low-temperature seafloor rocks and minerals. Geobiology 1 (2):109–117. doi:10.1046/j.1472-4669.2003.00009.x

Sanchez-Porro C, Kaur B, Mann H, Ventosa A (2010) *Halomonas titanicae* sp. nov., a halophilic bacterium isolated from the RMS Titanic. Int J Syst Evol Microbiol 60(12):2768–2774. doi:10.1099/ijs.0.020628-0

Santelli CM, Orcutt BN, Banning E, Bach W, Moyer CL, Sogin ML, Staudigel H, Edwards KJ (2008) Abundance and diversity of microbial life in ocean crust. Nature 453(7195):653–656

Schloss PD, Handelsman J (2005) Introducing DOTUR, a computer program for defining operational taxonomic units and estimating species richness. Appl Environ Microbiol 71(3):1501–1506

Schrenk MO, Kelley DS, Delaney JR, Baross JA (2003) Incidence and diversity of microorganisms within the walls of an active deep-sea sulfide chimney. Appl Environ Microbiol 69(6):3580–3592

Sohrin Y, Bruland KW (2011) Global status of trace elements in the ocean. TrAC Trends Anal Chem 30(8):1291–1307

Suzuki Y, Inagaki F, Takai K, Nealson KH, Horikoshi K (2004) Microbial diversity in inactive chimney structures from deep-sea hydrothermal systems. Microb Ecol 47(2):186–196

Takai K, Horikoshi K (1999) Genetic diversity of archaea in deep-sea hydrothermal vent environments. Genetics 152 (4):1285–1297

Wheat CG, Feely RA, Mottl MJ (1996) Phosphate removal by oceanic hydrothermal processes: an update of the phosphorus budget in the oceans. Geochim Cosmochim Acta 60(19):3593–3608

Whitman WB, Coleman DC, Wiebe WJ (1998) Prokaryotes: the unseen majority. Proc Natl Acad Sci U S A 95:6578–6583

Wu L, Jacobson AD, Chen H-C, Hausner M (2007) Characterization of elemental release during microbe-basalt interactions at T = 28 °C. Geochim Cosmochim Acta 71(9):2224–2239

10 A Compilation of the Stable Isotopic Compositions of Carbon, Nitrogen, and Sulfur in Soft Body Parts of Animals Collected from Deep-Sea Hydrothermal Vent and Methane Seep Fields: Variations in Energy Source and Importance of Subsurface Microbial Processes in the Sediment-Hosted Systems

Toshiro Yamanaka, Sho Shimamura, Hiromi Nagashio, Shosei Yamagami, Yuji Onishi, Ayumi Hyodo, Mami Mampuku, and Chitoshi Mizota

Abstract

The stable isotopic signatures of biophilic elements, such as carbon, nitrogen, and sulfur, exhibited in animal soft body parts are excellent indicators for evaluating the pathways of energy and food sources. Thioautotrophic and methanotrophic nutrition prevailed in deep-sea hydrothermal vent and methane seep areas results in sulfide-sulfur and methane-carbon isotopic ratios. In this study, we reevaluated the carbon, nitrogen, and sulfur isotope compositions of animals taken from deep-sea hydrothermal vents and methane seep areas in order to understand the detailed pathways of energy and food sources for the habitants. The results showed that most animals collected from sediment-starved hydrothermal areas rely on thioautotrophic nutrition, using hydrogen sulfide dissolved in venting fluids as the sole primary energy source. On the other hand, animals from sediment-covered hydrothermal vent and cold seep fields show some variations in energy sources, of both hydrothermal and microbial origins. Sediment-covered areas tend to be enriched in biomass and diversity relative to sediment-starved areas. The results suggest that fluid discharged through sediments to the seafloor are strongly affected by subsurface microbial processes and result in increased biomass and diversity of the seafloor animal community.

The online version of this chapter (doi:10.1007/978-4-431-54865-2_10) contains supplementary material, which is available to authorized users.

T. Yamanaka (✉) • S. Shimamura • H. Nagashio
S. Yamagami • Y. Onishi
Graduate School of Natural Science and Technology, Okayama University, 1-1, Naka 3-chome, Kita-ku, Okayama 700-8530, Japan
e-mail: toshiroy@cc.okayama-u.ac.jp

A. Hyodo
Faculty of Science, Kyushu University, 6-10-1, Hakozaki, Higashi-ku, Fukuoka 812-8581, Japan

M. Mampuku
Graduate School of Social and Cultural Studies, Kyushu University, 4-2-1, Ropponmatsu, Chuo-ku, Fukuoka 810-8560, Japan

C. Mizota
Faculty of Agriculture, Iwate University, 3-18-8 Ueda, Morioka, Iwate 020-8550, Japan

J.-i. Ishibashi et al. (eds.), *Subseafloor Biosphere Linked to Hydrothermal Systems: TAIGA Concept*,
DOI 10.1007/978-4-431-54865-2_10,

Keywords
Chemosynthesis-based animals • Food ecology • Hydrothermal vent community • Methane seep community • Stable isotopes

10.1 Introduction

Since the first discovery of hydrothermal vent communities in 1977, the stable isotopic signatures of chemosynthesis-based animal species have been used to evaluate the isolation of vent communities from the usual marine food web systems that are supported by photoautotrophic primary production (e.g., Nelson and Fisher 1995; Mizota and Yamanaka 2003). Average carbon isotopic composition of marine photoautotrophic products produced by phytoplankton have been documented at $\delta^{13}C = \sim -22$ ‰, although they show a wide range ($\delta^{13}C = -16$ to -28 ‰), reflecting a variety of carbon fixation pathways together with physico-chemical conditions (e.g., Rees et al. 1978). The sulfur isotopic compositions of common marine animals, supported by the same photoautotrophic production, reflect the signature of sulfates dissolved in seawater, which is uniform throughout the oceans ($\delta^{34}S = +21$ ‰) (Rees et al. 1978) and the sole nutrient source of sulfur for primary producers. On the other hand, it is reported that the carbon isotopic ratios of thioautotrophic microbes that use the Calvin cycle involving RuBisCO (ribulose 1,5-bisphosphate carboxylase/oxygenase) for carbon fixation have a relatively narrow range of $\delta^{13}C$ values, namely -35 ± 5 ‰, and it is known that other types of thioautotrophic microbes have significantly higher $\delta^{13}C$ values (≥ -20 ‰) (e.g., Nelson and Fisher 1995; Markert et al. 2007). Furthermore, sulfur isotopic ratios of thioautotrophic microbes reflect sulfide nutrition with a limited kinetic isotope effect (~ -5 ‰) through the cell membrane (Fry et al. 1983). In natural environments, $\delta^{34}S$ values of sulfides, which are mainly derived from volcanism and bacterial sulfate reduction, are clearly lower than those of sulfate-sulfur dissolved in seawater (e.g., Thode 1988; Canfield 2001). In the case of methanotrophic microbes, which are another important primary producer in the seep food web, carbon isotopic ratios reflect methane nutrition, while sulfur isotopic ratios reflect seawater sulfate-sulfur, similar to photoautotrophs. Some of the methane derived from pyrolysis of organic matter have carbon isotopic ratios similar to those of photoautotrophic products. Nevertheless, microbial methane, which prevails in anoxic sediments, has significantly lower $\delta^{13}C$ values (≤ -45 ‰), whereas abiotic methane has distinguishably high $\delta^{13}C$ values (> -20 ‰) (e.g., Schoell 1988).

However, the nitrogen sources for chemosynthesis-based animals are not well understood (Kennicutt et al. 1992; Fisher et al. 1994). Previously reported $\delta^{15}N$ values for soft tissues from thiotrophic and methanotrophic animals range from -20 to $+7$ ‰ (e.g., Nelson and Fisher 1995; Mizota and Yamanaka 2003). Such negative $\delta^{15}N$ values of marine animal soft tissues have been reported only in communities consisting of chemosynthesis-based animals (e.g., Saino and Ohta 1989; Fiala-Médioni et al. 1993; Mizota and Yamanaka 2003) and cyanobacteria, which have the ability to fix dinitrogen (-3 to $+0$ ‰) (Minagawa and Wada 1984; Carpenter et al. 1997). The nitrogen nutrition of symbiotic bacteria is not well understood.

Stable isotopic signatures are quite useful indicators for distinguishing chemosynthesis-based animals from the phototrophic food web. Their isotopic signatures can possibly be used to identify the energy source for chemosynthesis. Mizota and Yamanaka (2003) reviewed the carbon, nitrogen, and sulfur isotopic compositions of chemosynthesis-based animals and the associated methane and sulfide data published prior to 2003, and discussed the flow of chemical energy from emitting fluids to the animal community. In the review, the importance of environmental isotopic data sets of sulfide-, methane-, and nitrogen-issuing species, was emphasized. Nevertheless, environmental isotopic data sets have not been fully integrated. Some animal clusters have been found far from vents where significant concentrations of sulfide and methane have been detected. Furthermore, $\delta^{15}N$ values of nitrate, nitrite, and ammonium from the environment have not been reported. Most reported geochemical data from hydrothermal and seep fields are derived from venting fluids and visible seepages. This implies that the reported values are almost comparable to the end-member (i.e., deep-seated source) values. Therefore, it is difficult to directly compare the isotopic data to the soft body parts of animals, especially in sediment-hosted systems (i.e., methane seeps and sediment-covered hydrothermal fields), where emitting fluids penetrate through thick clastic sediments and are subsequently subjected to subsurface microbial transformation. An obvious example is methane seep communities dominated by thiotrophic animals, which use microbial hydrogen sulfide derived from sulfate reduction with methane as an electron donor (e.g., Mizota and Yamanaka 2003).

In addition, reduced chemical species, such as hydrogen sulfide and methane discharged from the seafloor, are incorporated by chemosynthetic and methanotrophic microbes, and the resulting microbial products have been considered to support not only vent- and seep-endemic animal communities but also common benthic and epibenthic animals. In the case of hydrothermal systems, discharge of these chemicals mainly originates from venting chimneys. In fact, at hydrothermal fields lacking sediment cover,

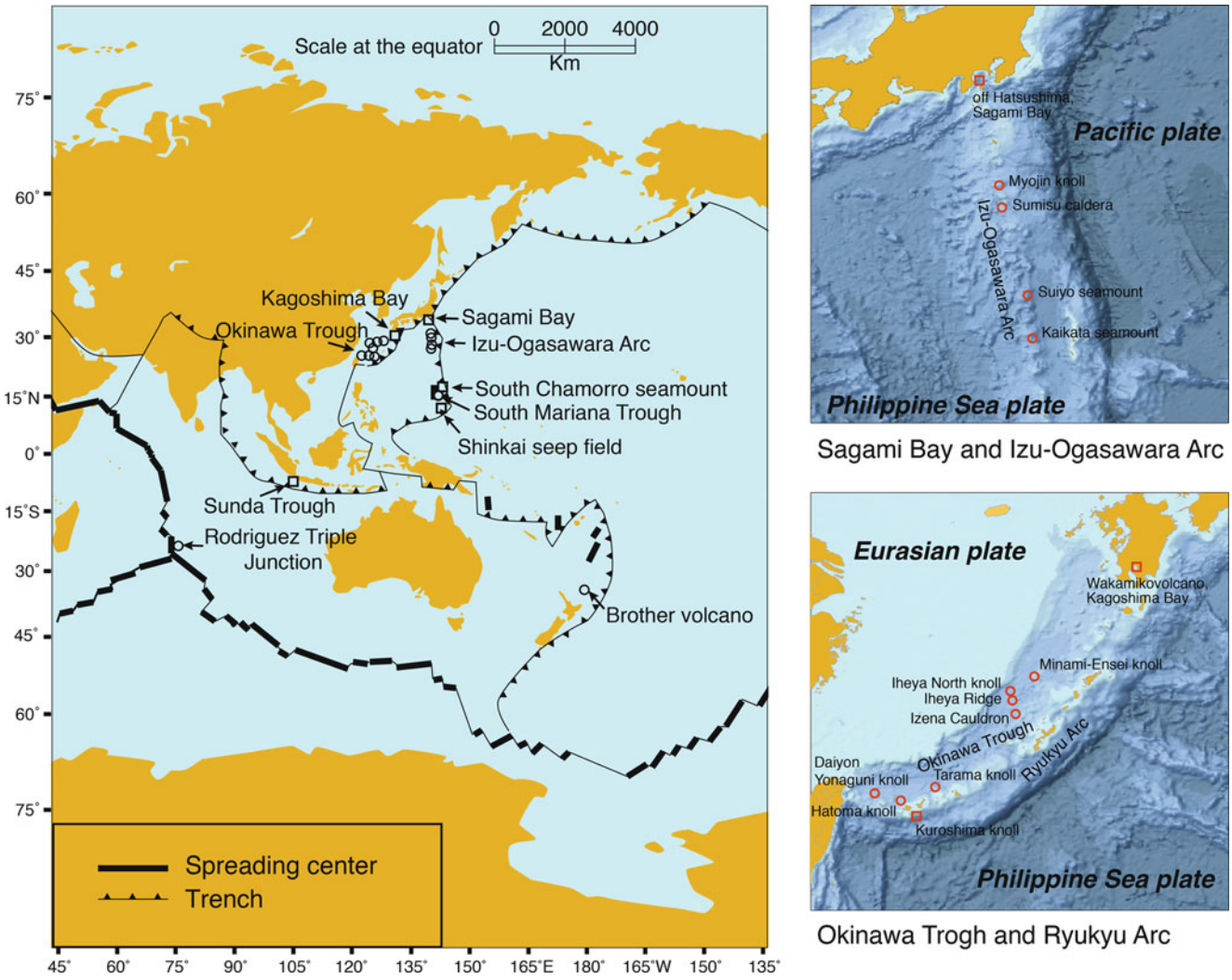

Fig. 10.1 Maps showing the sample locations of this study. *Open circles* indicate hydrothermal fields. *Open squares* indicate methane seep fields. The Wakamiko site in Kagoshima Bay and the Shinkai seep field of Southern Mariana are categorized as methane seeps

hydrothermal discharge is mostly confined to venting chimneys and underlying hydrothermal mounds. Hydrothermal fields covered by thick clastic sediments have a few additional pathways for hydrothermal fluid discharge, e.g., diffusion into aquifers in overlying sediments. The fluids diffused within the sediments provide reduced chemical species and other nutrients to subsurface microbes. Some of the microbes may be grazed upon, thereby supporting benthic animals, and the others may generate reduced chemical species once more. Such secondary chemicals are also thought to support chemosynthesis-based animals that inhabit hydrothermal field and methane seep communities mentioned above.

Since 2003, reconnaissance surveying and sampling of chemosynthesis-based animals using submersibles from Japan and other countries is ongoing, and the following isotopic analyses have been made. In this Chapter, we have compiled the latest isotopic data from soft tissues of diverse animals and environments located near hydrothermal vents and methane seeps of the extensive areas indicated in Fig. 10.1. We discuss the variations in energy and food sources of the environments from the view point of "TAIGA" (subseafloor fluid flow system, Urabe, Chap. 1), together with the importance of sub-seafloor microbial processes.

10.2 Materials and Methods

10.2.1 Geological Background of the Sample Materials

10.2.1.1 Okinawa Trough

The Okinawa Trough (Fig. 10.1) is a typical back-arc rifting basin between the east margin of the East China Sea and the Ryukyu Islands (e.g., Letouzey and Kimura 1986). The trough is filled with thick clastic sediments derived from surrounding

continents and islands, together with volcaniclastic sediments associated with arc and back-arc volcanism in this area (Tsugaru et al. 1991; Ishibashi et al. Chap. 29). Vigorous hydrothermal activities associated with volcanism have been observed in the trough, and the chemistry of emitting fluids has been characterized by high volatiles (i.e., CO_2 and methane) and ammonium concentrations, suggesting the significant interaction of magma with sedimentary organic matter (e.g., Ishibashi and Urabe 1995; Kawagucci, Chap. 35). Therefore, many of the hydrothermal activities in the Okinawa Trough are interpreted as a typical sediment-hosted system. Chemosynthesis-based animal communities have been found around the hydrothermal venting area, and they have been characterized by the presence of dense *Bathymodiolus* mussels, vestimentiferan tubeworms, and galatheid crab communities (e.g., Fujikura et al. 2012; Watanabe and Kojima, Chap. 40).

Animal samples were obtained from the following hydrothermal fields: Minami-Ensei knoll, Izena Hole, Iheya Ridge, Iheya North knoll, Tarama knoll, Daiyon-Yonaguni knoll, and Hatoma knoll (Fig. 10.1).

10.2.1.2 Izu-Ogasawara Arc

The Izu-Ogasawara Islands (Fig. 10.1) are a volcanic arc associated with subduction of the Pacific Plate beneath the Philippine Plate. Deep-sea hydrothermal activities have been identified in the calderas and craters of the submerged volcanoes (e.g., Glasby et al. 2000). The hydrothermal areas lack clastic sediments except for a small amount of volcaniclastic sediment that fills in the craters and calderas (e.g., Iizasa 1993; Takano et al. 2004). Relative to the fluids emitting from the Okinawa Trough, the resulting chemistry of the hydrothermal fluids is characterized by significantly lower methane and ammonium concentrations, i.e., a sediment-starved system (e.g., Ishibashi and Toki 2012). Chemosynthesis-based animal communities have been found around the fluid venting areas and have been characterized by occurrence of dense *Bathymodiolus* mussels (e.g., Fujikura et al. 2012).

Animal samples were collected from the following hydrothermal fields: Myojin Knoll, Sumisu caldera, Suiyo seamount, and Kaikata seamount (Fig. 10.1).

10.2.1.3 Additional Hydrothermal Fields

Animal samples were also collected from the following hydrothermal fields and used for isotopic analyses: three sites at the southern most portion of the Mariana back-arc spreading center in the South Mariana Trough (the Snail, Archaean, and Yamanaka sites), Brothers Volcano in the Kermadec Arc (New Zealand), and Hakuho Knoll at the Rodriguez Triple Junction (Central Indian Ridge) (Fig. 10.1). The lack of clastic sediments in the hydrothermal fields reflects ammonium concentrations < 20 μM/kg (Kato et al. 2009; de Ronde et al. 2011; Gamo et al. 2001), due to minimal contribution of sedimentary organic matter to the hydrothermal fluids. Bio-diversity of the animal communities observed at the Snail and Yamanaka sites in the South Mariana Trough was very low (Kojima and Watanabe, Chap. 26). Dense *Alviniconcha* snails (Wheat et al. 2003), crabs (*Gandalfus* sp.) and sea anemones (*Marianactis* sp.) have been identified. High bio-diversity, including dense long-necked barnacles (*Volcanolepas osheai*), shrimp (*Alvinocaris* sp.), and vestimentiferan tubeworms (*Lamellibrachia* sp.), has been observed in the animal community at the Brother Volcano site (Kermadec Arc), while many types of animals, such as *Rimicaris* shrimp, *Bathimodiolus* mussels, *Alviniconcha* snails (de Ronde et al. 2011), and Brachyuran crabs, have been observed at the Kairei hydothermal field on Hakuho Knoll (Central Indian Ridge) (Hashimoto et al. 2001; Watanabe and Beedessee, Chap. 16).

10.2.1.4 Sagami and Kagoshima Bays and Kuroshima Knoll

Sagami and Kagoshima Bays and Kuroshima Knoll (Fig. 10.1) are areas with significantly high methane flux from the seafloor (Masuzawa et al. 1992; Yamanaka et al. 2013). Sagami Bay and Kuroshima Knoll are located on the fore-arc regions, which are related to subduction of the Philippine Plate, where compression stress associated with subduction is a possible driving force for methane seepage. In Kagoshima Bay, methane rich gas is emitted from fumaroles, together with volcanic gas associated with the volcanic activity of the Wakamiko volcano. Sedimentary organic matter has been considered a primary source for methane as a result of microbial metabolism or pyrolysis. Chemosynthesis-based animal communities have been found around the seepages and have been characterized by the occurrence of dense *Bathymodiolus* mussel, *Calyptogena* clam, and vestimentiferan tubeworm communities (e.g., Fujikura et al. 2012).

10.2.1.5 Additional Methane Seep Fields

Methane seepages from the seafloor have been reported from South Chamorro Seamount (Northern Mariana Fore-arc) (Yamanaka et al. 2003b), Shinkai Seep Field (Southern Mariana Fore-arc) (Ohara et al. 2012), and the western edge of Sunda Trough (off southwest Java) (Okutani and Soh 2005) (Fig. 10.1), and characteristic animal communities have also been reported around the seepages. *Calyptogena* clams have been observed at all of these sites, while *Bathymodiolus* mussels are primarily observed on the South Chamorro Seamount. The South Chamorro Seamount is a large serpentine mud volcano, while the Shinkai Seep Field is an outcrop of serpentinized peridotite (Ohara et al. 2012). This suggests that methane emitting from these sites

may be an abiotic product of the reaction between carbon dioxide and dihydrogen, which are expected to occur during serpentinization (Berndt et al. 1996). Serpentinization of the seafloor may be the cause of hydrothermal activity at sites such as the Rainbow and Lost City hydrothermal fields (Kelley et al. 2005). A detailed geochemical study has recently been conducted on the Shinkai Seep Field (Ohara et al. 2012). Therefore, in this study we have categorized this system as a methane seep.

Methane seepage at the Sunda Trough is located in a fore-arc basin covered with thick clastic sediments, suggesting that the tectonic background is comparable with the cold seepages of Sagami Bay. This means that the primary source of methane is expected to be organic matter of sedimentary origin.

10.2.2 Animal, Sediment, and Fluid Sampling Procedures

The animal samples used in this study are listed in Table 10.1. In addition to common marine benthic animals, such as sponges, sea cucumbers, starfishes, and fishes, well known chemosynthesis-based animals, including three bivalves (*Calyptogena*, *Bathymodiolus*, *Acharax*), two shrimps (*Alvinocaris*, *Limicaris*), two tubeworms (*Lamellibrachia*, *Alaysia*), one gastropoda (*Alviniconcha*), one galatheid crab (*Shinkaia*), among others, were analyzed for the carbon, nitrogen, and sulfur isotopic ratios in their soft tissues.

The sampling areas of the animals used in this study are also indicated in Table 10.1. The deep-sea hydrothermal fields of Okinawa Trough, Izu-Ogasawara Arc, Mariana Trough in the North Pacific Ocean, Kermadec Arc in the South Pacific Ocean, and Rodriguez Triple Junction in the Indian Ocean, and the methane seeps (cold seeps) of Kagoshima and Sagami Bays, Ryukyu and Mariana fore-arcs in the Pacific Ocean, and Sunda Trough in the Indian Ocean, were subjected to sample collection using submersibles (ROVs/HyperDolphin and Kaiko, DSV/Shinkai 6500 belonging to JAMSTEC and RV/Ropos belonging to Canadian Scientific Submersible Facility).

During the dive studies, animal samples were collected with a suction sampler or manipulator equipped with the submersible. Fluid and sediments used for geochemical characterization were collected using all-titanium ALVIN-type fluid samplers (Von Damm et al. 1985), gas-tight WHATS fluid samplers (Tsunogai et al. 2003), multi-cylinder type ROCS fluid samplers (Yamanaka et al. 2013), and NISKIN bottles equipped with the submersibles. The fluid and sediment samples were collected as close as possible to the animal habitat in order to evaluate the relationship between the animal soft bodies and the energy sources for the chemosynthesis-based animal communities, using isotopic signatures.

10.2.3 Analytical Procedures

Soft tissues of bivalve and gastropoda samples were dissected into gill, foot, mantle, adductor and viscera sections, and subjected to isotopic analyses. For vestimentiferan tubeworm samples, the soft body parts were dissected into gill, vestimentifera, and trophosome sections, and the trophosome sections were used for the analyses. Muscle samples were separated from the crustacean species. Other animals, such as limpets, sponges, polychaetes, etc., were used as whole-body samples due to small size or complex anatomy. The tissues dissected for analyses were treated with 1 M hydrochloric acid to remove carbonates, then freeze-dried prior to grinding. Preparation for sulfur isotopic measurements in the soft tissues was described previously (Mizota et al. 1999; Yamanaka et al. 2000a, b). Briefly, to remove excess seawater sulfate, the dissected soft tissues were dialyzed repeatedly in cellulose bags against 1 M lithium chloride solution at 5 °C. Dialyzed samples were then freeze-dried and pulverized. Samples of large size ($\geq$1 g dry weight) were placed in a Parr bomb 1108 Oxygen Combustion Vessel (a stainless steel vessel filled with oxygen gas under high-pressure (30 kg/cm^2) and a few milliliters of distilled water). After combustion, the dried samples were completely converted into gas, and all sulfur compounds were trapped as sulfates in the distilled water within the vessel. The resulting sulfates were precipitated as $BaSO_4$. The dried soft tissue samples were measured for carbon, nitrogen, and sulfur isotopic ratios using an EA/irMS (IsoPrime coupled with Euro Vector EA3000, GV Instruments, UK, and Delta Plus coupled with CE Instrument NA2500, Thermo Quest, USA). Small-sized samples for sulfur isotope analysis were wrapped within tin capsules and directly subjected to EA/irMS.

Sulfide-sulfur were recovered from the substrate sediments by treatment with warm ($\leq$80 °C) 30 % hydrogen peroxide solution to generate sulfates, which were finally converted into $BaSO_4$. Dissolved sulfide in the hydrothermal fluids was fixed on board in order to precipitate zinc sulfide, and then it was converted to sulfate for recovery as $BaSO_4$ precipitate. The $BaSO_4$ precipitate was converted into SO_2 gas, as described by Yanagisawa and Sakai (Yanagisawa and Sakai 1983).

The concentration and carbon isotope composition of the dissolved methane in the water samples were determined following the methods of Tsunogai et al. (2000), using an isotope-ratio-monitoring-GC/MS (MAT 252, Thermo Quest, USA). The methane content in the samples was calculated by comparing the $^{44}CO_2$ output with that of a working standard gas containing *c*. 500 ppm methane in nitrogen.

All of the isotopic values were expressed using δ notation as a per mill deviation (‰) from international reference materials (VPDB for $\delta^{13}C$, CDT for $\delta^{34}S$ and atmospheric N_2 for $\delta^{15}N$, respectively). Analytical errors associated with the overall process of these determinations were 0.2, 0.3, and 0.3‰, respectively.

Table 10.1 Animal samples discussed in this paper

							Organism				Sampling Info			
Type	Area	Field	Site (marks in figures)	Longitude	Latitude	Depth (m)	Category	Genus (Order or Family)	Species	Food ecology[a]	Submarsible type	Dive #	Year/ Month	Note
Hydrothermal system	Okinawa Trough	Minami-Ensei knoll	(MEn)	127°38.392′E	28°23.476′N	701–709	Sea sponge	(Demospongiae)	?	Heterotroph (F)	HyperDolphin	1327, 1328	2011/9	
		Izena Hole	JADE (IzJ)	127°04.884′E	27°16.296′N	1,305	Crab	*Shinkaia*	*crosnieri*	Heterotroph and ectosymbiosis	HyperDolphin	1184	2010/9	
				127°04.500′E	27°15.936′N	1,536	Crab	*Paralomis*	*verrilli*	Heterotroph (C)	HyperDolphin	1193	2010/9	
				127°04.500′E	27°15.936′N	1,536	Crab	*Paralomis*	?	Heterotroph (C)	HyperDolphin	1193	2010/9	
				127°04.884′E	27°16.296′N	1,305	Shrimp	*Alvinocaris*	*longirostris*	Heterotroph and ectosymbiosis	HyperDolphin	1184	2010/9	
				127°04.877′E	27°16.299′N	1,536	Shrimp	*Opaepele*	*loihi*	Heterotroph and exosymbiosis	HyperDolphin	1192	2010/9	
				127°04.494′E	27°15.942′N	1,520	Bivalve	*Bathymodiolus*	*platifrons*	Endosymbiosis (M)	HyperDolphin	1188	2010/9	
				127°04.877′E, 127°04.500′E	27°16.299′N, 27°15.936′N	1,536	Gastropoda	*Provanna*	?	Heterotroph (G)	HyperDolphin	1192, 1193	2010/9	
				127°04.884′E	27°16.296′N	1,300–1,535	Limpet	*Lepetodrilus*	*nux*	Heterotroph (G)	HyperDolphin	1184, 1192, 1193	2010/9	
				127°04.877′E, 127°04.500′E	27°16.299′N, 27°15.936′N	1,536	Limpet	*Bathyacmaea*	*secunda*	Heterotroph (G)	HyperDolphin	1192, 1193	2010/9	
				127°04.878′E	27°16.302′N	1,306	Fish	(Zoarcidae)	?	Heterotroph (C)	HyperDolphin	1192	2010/9	
				127°04.500′E	27°15.936′N	1,536	Starfish	(Goniasteridae)	?	Heterotroph (D)	HyperDolphin	1193	2010/9	
				127°04.500′E	27°15.936′N	1,536	Starfish	(Asteroidea)	?	Heterotroph (D)	HyperDolphin	1193	2010/9	
				127°04.884′E	27°16.296′N	1,305	Sea sponge	(Demospongiae)	?	Heterotroph (F)	HyperDolphin	1184	2010/9	
				127°04.500′E	27°15.936′N	1,536	Sea sponge	(Hexachtinellida)	?	Heterotroph (F)	HyperDolphin	1193	2010/9	
				127°04.500′E	27°15.936′N	1,536	Sea sponge	(Demospongiae)	?	Heterotroph (F)	HyperDolphin	1193	2010/9	
				127°04.494′E	27°15.942′N	1,520	Polychaeta	*Branchipolynoe*	*pettiboneae*	Heterotroph (P)	HyperDolphin	1188	2010/9	Parasite on *Bathymodiolus* mussels
				127°04.799′E	27°16.226′N	1,335	Polychaeta	*Paradialychone*	?	Endosymbiosis (T)	HyperDolphin	1193	2010/9	
			Hakurei (IzH)	127°04.134′E, 127°04.141′E	27°14.940′N, 27°14.944′N	1,593	Crab	*Shinkaia*	*crosnieri*	Heterotroph and ectosymbiosis	HyperDolphin	1191, 1311	2010/9, 2011/8	
				127°04.089′E	27°14.815′N	1,617	Bivalve	*Bathymodiolus*	*japonicus*	Endosymbiosis (M)	HyperDolphin	1329	2011/10	
		Ihaya Ridge	(IhR)	126°58.188′E	27°33.018′N	1,399	Crab	*Shinkaia*	*crosnieri*	Heterotroph and ectosymbiosis	HyperDolphin	1183	2010/9	
				126°58.188′E	27°33.018′N	1,399	Shrimp	*Alvinocaris*	*longirostris*	Heterotroph and ectosymbiosis	HyperDolphin	1183	2010/9	
				126°58.188′E	27°33.018′N	1,399	Bivalve	*Calyptogena*	*okutanii*	Endosymbiosis (T)	HyperDolphin	1183	2010/9	

			126°58.188′E	27°33.018′N	1,399	Bivalve	*Acharax*	?	Endosymbiosis (T)	HyperDolphin	1183	2010/9	
			126°58.188′E	27°33.018′N	1,399	Tube worm	*Alaysia*	?	Endosymbiosis (T)	HyperDolphin	1183	2010/9	
	Iheya North Knoll	(IhN)	127°04.494′E	27°15.942′N	1,520	Crab	*Shinkaia*	*crosnieri*	Heterotroph and ectosymbiosis	HyperDolphin	1188	2010/9	
			127°04.494′E	27°15.942′N	1,520	Bivalve	*Calyptogena*	*soyoae*	Endosymbiosis (T)	HyperDolphin	1188	2010/9	
			127°04.494′E	27°15.942′N	1,520	Bivalve	*Bathymodiolus*	*platifrons*	Endosymbiosis (M)	HyperDolphin	1188	2010/9	
			126°53.993′E	27°47.286′N	993	Tube worm	*Lamellibrachia*	?	Endosymbiosis (T)	HyperDolphin	222	2003/9	
			126°53.993′E	27°47.286′N	993	Barnacle	*Ashinkailepas*	*seepiophilia*	heterotroph (F)	HyperDolphin	222	2003/9	
	Tarama knoll	(Tr)	124°32.165′E	25°05.469′N	1,732	Shrimp	*Alvinocaris?*	?	Heterotroph and ectosymbiosis	HyperDolphin	1322	2011/9	Found in the gut of *Liparis*
			124°32.349′E	25°05.576′N	1,556	Fish	*Liparis*	?	Heterotroph (C)	HyperDolphin	1034	2009/7	
			124°32.165′E	25°05.469′N	1,732	Fish	*Liparis*	?	Heterotroph (C)	HyperDolphin	1322	2011/9	
			124°32.310′E	25°05.554′N	1,588	Starfish	(Asteroidea)	?	Heterotroph (D)	HyperDolphin	1034	2009/7	Preyed on sponge
			124°32.310′E	25°05.554′N	1,588	Sea sponge	(Hexachtinellida)	?	Heterotroph (F)	HyperDolphin	1034	2009/7	
			124°32.136′E	25°05.326′N	1,850	Soft coral	(Alcyonacea)	?	Heterotroph (F)	HyperDolphin	1108	2010/4	
			124°32.124′E	25°05.303′N	1,862	Sea cucumber	*Enypniaster*	*eximia*	Heterotroph (D)	HyperDolphin	1108	2010/4	
			124°32.364′E	25°05.631′N	1,500	Octopus	*Benthoctopus*	?	Heterotroph (C)	HyperDolphin	1033	2009/7	
	Daiyon-Yonaguni knoll	(Yo)	122°41.999′E	24°50.931′N	1,336	Crab	*Shinkaia*	*crosnieri*	Heterotroph and ectosymbiosis	Shinkai2000	1273	2001/5	
			122°41.999′E	24°50.931′N	1,336	Bivalve	*Bathymodiolus*	*platifrons*	Endosymbiosis (M)	Shinkai2000	1273	2001/5	
	Hatoma knoll	(Ht)	123°50.369′E	24°51.451′N	1,523	Crab	*Shinkaia*	*crosnieri*	Heterotroph and ectosymbiosis	Shinkai2000	1352	2002/5	
			123°50.369′E	24°51.451′N	1,523	Shrimp	*Alvinocaris*	*longirostris*	Heterotroph and ectosymbiosis	Shinkai2000	1352	2002/5	
			123°50.369′E	24°51.451′N	1,523	Shrimp	*Lebbeus*	*washingtonianus*	Heterotroph (D)	Shinkai2000	1352	2001/5	
			123°50.369′E	24°51.451′N	1,523	Crab	*Munidopsis*	*ryukyuensis*	Heterotroph (D)	Shinkai2000	1352	2002/5	
			123°50.365′E	24°51.558′N	1,484	Crab	*Paralomis*	?	Heterotroph (C)	Shinkai2000	1361	2002/6	
			123°50.369′E	24°51.451′N	1,523	bivalve	*Bathymodiolus*	*platifrons*	Endosymbiosis (M)	Shinkai2000	1270	2001/5	
Izu-Ogasawara arc	Myojin knoll	(My)	139°52′E	32°06′N	1,274	Crab	*Gandalfus*	*yunohana*	Heterotroph (D)	HyperDolphin	185	2003/6	
			139°52.081′E	32°06.278′N	1,303	Bivalve	*Bathymodiolus*	*septemdierim*	Endosymbiosis (T)	HyperDolphin	1284	2011/6	

(*continued*)

Table 10.1 (continued)

Type	Area	Field	Site (marks in figures)	Longitude	Latitude	Depth (m)	Organism				Sampling Info			Note
							Category	Genus (Order or Family)	Species	Food ecology[a]	Submarsible type	Dive #	Year/ Month	
		Sumisu caldera	(Sm)	140°04.258′E	31°28.179′N	686	Bivalve	*Bathymodiolus*	*septemdierim*	Endosymbiosis (T)	HyperDolphin	84	2002/3	
				140°04.258′E	31°28.179′N	686	Sea sponge	*Characella*	?	Endosymbiosis (T)	HyperDolphin	84	2002/3	Provided from Dr. Lindsay
				140°04.258′E	31°28.179′N	686	Tube worm	*Lamellibrachia*	?	Endosymbiosis (T)	HyperDolphin	84	2002/3	
		Suiyo Seamount	(Sy)	140°38.668′E	28°34.268′N	1,381	Bivalve	*Bathymodiolus*	*septemdierim*	Endosymbiosis (T)	HyperDolphin	1285	2011/6	
		Kaikata Seamount	(Kt)	141°04.3′E	26°42.5′N	508	Crab	*Gandalfus*	*yunohana*	Heterotroph (D)	HyperDolphin	186	2003/6	Provided from Dr. Tsuchida
				141°04.250′E	26°42.500′N	448	Crab	*Leptodius*	*exaratus*	Heterotroph (D)	Shinkai2000	1234	2000/11	Provided from Dr. Tsuchida
				141°04.250′E	26°42.500′N	448	Fish	*Symphurus*	*orientalis*	Heterotroph (C)	Shinkai2000	1234	2000/11	Provided from Dr. Tsuchida
	South Mariana Trough	Mariana backarc spreading center	Snail site (Sn)	143°37.195′E	12°57.167′N	2,860	Crab	*Gandalfus*	*yunohana*	Heterotroph (D)	Shinkai6500	793	2003/10	
				143°37.167′E	12°57.185′N	2,861	Gastropoda	*Alviniconca*	*hessri*	Endosymbiosis (T)	ROPOS	776	2004/3	
			Archaean site (Ar)	143°37.901′E	12°56.370′E	2,990	Gastropoda	*Phymorhynchus*	?	Heterotroph (D)	ROPOS	781	2004/3	
			Yamanaka site (Ym)	143°36.789′E	12°56.660′N	2,827	Bernacle	*Neoverruca*	*brachylepadoformis*	Heterotroph (F)	ROPOS	779	2004/3	
				143°36.796′E	12°53.638′N	2,828	Sea anemone	*Marianactis*	?	Heterotroph (D)	*ditto*	774	2004/3	
	Kermadec Arc	Brothers Volcano	Lower Cone site (Br)	179°04.302′E	34°52.722′S	1,336	Tube worm	*Lamellibrachia*	sp.1	Endosymbiosis (T)	Shinkai6500	854	2004/11	
				179°04.302′E	34°52.722′S	1,336	Tube worm	*Lamellibrachia*	sp.2	Endosymbiosis (T)	*ditto*	854	2004/11	
				179°04.302′E	34°52.722′S	1,336	Barnacle	*Vulcanolepas*	*osheai*	Heterotroph (F)	*ditto*	854	2004/11	
	Rodriguez Triple Junction, Central Indian Ridge	Hakuho Knoll	Kaiko field (RtK)	70°02.40′E	25°19.16′S	2,432, 2,442	Bivalve	*Bathymodiolus*	*marisindicus*	Endosymbiosis (T)	Kaiko	168, 169	2000/8	
Methane seep	Ryukyu arc	Kuroshima knoll	(Kr)	124°11.547′E, 124°11.535′E	24°07.798′N, 24°07.805′N	638, 624	Bivalve	*Bathymodiolus*	*hirtus*	Endosymbiosis (M)	Shinkai2000	1355, 1364	2002/5, 6	
(cold seep)				124°11.547′E, 124°11.535′E	24°07.798′N, 24°07.805′N	638, 624	Bivalve	*Bathymodiolus*	*securiformis*	Endosymbiosis (M)	Shinkai2000	1355, 1364	2002/5, 6	
				124°11.547′E, 124°11.535′E	24°07.798′N, 24°07.805′N	638, 624	Bivalve	*Calyptogena*	*kawamurai*	Endosymbiosis (T)	Shinkai2000	1355, 1364	2002/5, 6	
	Kyushu Island	Kagoshima Bay	Wakamiko (KgW)	130°48.052′E	31°39.742′N	102	Tube worm	*Lamellibrachia*	*satsuma*	Endosymbiosis (T)	HyperDolphin	686	2007/6	
	Sagami Trough	off Hatsushima	(SbH)	139°13.396′E	35°00.926′N	928	Shrimp	*Alvinocaris*	*longirostris*	Heterotroph and ectosymbiosis	HyperDolphin	1293	2011/6	
	(Sagami Bay)			139°13.380′E	35°00.940′N	910	Bivalve	*Bathymodiolus*	*platifrons*	Endosymbiosis (M)	HyperDolphin	1291	2011/6	

			139°13.494′E, 139°13.380′E	35°00.222′N, 35°00.940′N	1,180, 910	Bivalve	*Bathymodiolus*	*japonicus*	Endosymbiosis (M)	HyperDolphin	524, 1291	2006/3, 2011/6	
			139°13.322′E	35°00.955′N	855	Bivalve	*Calyptogena*	*okutanii*	Endosymbiosis (T)	HyperDolphin	1291	2011/6	
			139°13.322′E	35°00.955′N	855	Bivalve	*Calyptogena*	*soyoae*	Endosymbiosis (T)	HyperDolphin	1291	2011/6	
			139°13.482′E	35°00.222′N	1,172	Bivalve	*Acharax*	*johnsoni*	Endosymbiosis (T)	HyperDolphin	528	2006/3	
			139°13.482′E	35°00.222′N	1,172	Bivalve	(Thyasiridae)	?	Endosymbiosis (T)	HyperDolphin	528	2006/3	
			139°13.482′E	35°00.222′N	1,172	Bivalve	*Conchocela*	*bisecta*	Endosymbiosis (T)	HyperDolphin	528	2006/3	
			139°13.458′E	35°00.168′N	1,173	Gastropoda	*Provanna*	*glabra*	Heterotroph (C)	HyperDolphin	525	2006/3	
			139°13.458′E, 139°13.482′E	35°00.168′N, 35°00.222′N	1,173, 1,172	Gastropoda	*Margarites*	*shinkai*	Heterotroph (D)	HyperDolphin	525, 528	2006/3	
			139°13.494′E	35°00.222′N	1,180	Gastropoda	*Phymorhynchus*	*buccinoides*	Heterotroph (D)	HyperDolphin	524	2006/3	
			139°13.458′E	35°00.168′N	1,173	Gastropoda	*Bathyacmaea*	*nipponica*	Heterotroph (D)	HyperDolphin	525	2006/3	
			139°13.494′E	35°00.222′N	1,180	Gastropoda	*Oenopota*	*sagamiana*	Heterotroph (D)	HyperDolphin	524	2006/3	
			139°13.458′E	35°00.168′N	1,173	Starfish	*Ophiuroidea*	?	Heterotroph (D)	HyperDolphin	525	2006/3	
			139°13.560′E	35°00.054′N	1,184	Sea anemone	*Actiniaria*	?	Heterotroph (D)	HyperDolphin	524	2006/3	
			139°13.482′E	35°00.222′N	1,172	Tube worm	*Lamellibrachia*	?	Endosymbiosis (T)	HyperDolphin	528	2006/3	
			139°13.482′E	35°00.222′N	1,172	Tube worm	*Alaysia*	?	Endosymbiosis (T)	HyperDolphin	528	2006/3	
			139°13.458′E	35°00.168′N	1,173	Polychaeta	*Nicomache*	*ohtai*	Heterotroph (D)	HyperDolphin	525	2006/3	
	Northern Mariana arc	South Chamorro seamount (SCh)	146°00.210′E	13°46.999′N	2,900	Bivalve	*Bathymodiolus*	?	Endosymbiosis (D)	Kaiko	165	2000/6	
	Southern Mariana arc	Shinkai (SmS) Seep Field	143°02.94′E	11°39.09′N	5,620	Bivalve	*Calyptogena*	*mariana*	Endosymbiosis (T)	Shinkai6500	1234	2010/9	Provided from Dr. Ohara
	Sunda Trough	off southwest corner of Java (Jv)	105°47.202′E, 105°46.998′E	7°24.600′S, 7°24.600′S	2,390, 2,100	Bivalve	*Calyptogena*	*garuda*	Endosymbiosis (T)	Shinkai6500	716, 727	2002/10	Provided from Dr. Soh

[a]Reported food ecology in previous literature: heterotroph (C): Carniver, Scavenger and/or Grazer, (D): Detritus and sediment feeder, (F): Filter feeder, (G): Grazer, (P) Parasite, ectosymbiosis (T) and endosymbiosis (T): harboring only thioautotrophic endosymbiont, endosymbiosis (M): harboring only methanotrophic endosymbiont, endosymbiosis (d): harboring both thiotrophic and methanotrophic endosymbionts

10.3 Analytical Results for Isotopic Composition

10.3.1 Isotopic Compositions of Animal Samples from Hydrothermal Fields

The analytical results for the isotopic compositions of animal soft body parts and issuing fluids are summarized in Tables 10.2 and 10.3. Diagrams of the relationships among nitrogen and sulfur isotopic ratios vs. carbon isotopic ratios are shown in Figs. 10.2 and 10.3. Abbreviations in the figures indicate the locations of the samples (red-colored abbreviations indicate sediment-starved hydrothermal fields, see Table 10.1), and the asterisks to the right of the abbreviations indicate the species that harbor methanotrophic endosymbionts. The diagrams also indicate the approximate ranges of common marine organisms that rely on phototrophic products (insert enclosed by green dotted box). The $\delta^{13}C$ vs. $\delta^{15}N$ plot in Fig. 10.2 shows that many animals, especially crustacean species, were among the range of common marine organisms, while the $\delta^{13}C$ vs. $\delta^{34}S$ plot (Fig. 10.3) indicates that most samples had lower $\delta^{34}S$ values ($<$ +15 ‰), relative to the common marine organisms. *Calyptogena* clams, indicated by open circles, had a typical thioautotrophic range of $\delta^{13}C = -35 \pm 5$ ‰ and $\delta^{34}S \ll +15$ ‰, while *Bathymodiolus* mussels, which harbor thioautotrophic and/or methanotrophic endosymbionts in their gill tissues, showed wider $\delta^{13}C$ values ranging from −50 to −25 ‰ and significantly low $\delta^{15}N$ values (<0 ‰, Fig. 10.2). Nearly all methanotrophic mussels had high $\delta^{34}S$ values, close to +15 ‰, while the thiotrophic mussels had significantly lower $\delta^{34}S$ values, relative to the other mussels. Vestimentiferan tubeworms, indicated by open cross symbols, also had a wide range of $\delta^{13}C$ values (−35 to −12 ‰), indicating that they harbor thioautotrophic endosymbionts with various types of carbon fixation pathways in addition to the Calvin cycle. Certain animal samples (*Alvinocaris* shrimp, *Alaysia* tubeworms at Iheya Ridge field, *Ashinkailepas* barnacles at Iheya North knoll, *Bathymodiolus* mussels at Sumisu caldera, and *Lamellibrachia* tubeworms at Brother seamount) had significantly lower $\delta^{34}S$ values ($<$ −10 ‰), relative to the hydrogen sulfide issuing from the associated hydrothermal vents.

10.3.2 Isotopic Compositions of Animal Samples from Methane Seep Fields

Analytical results for animal soft tissues and issuing fluids are summarized in Table 10.3. Figures 10.4 and 10.5 show relationships comparable to those shown for the hydrothermal fields. Samples without abbreviations represent collections off Hatsushima, in Sagami Bay. Nearly all data were beyond the range of common marine organisms. *Calyptogena* clams, as shown by open circles, were located in the typical thioautotrophic range, as were the specimens obtained from hydrothermal fields, with one exception: *Calyptogena soyoae* off Hatsushima ($\delta^{34}S = +16.8$ ‰). Except for two groups of samples from Kuroshima knoll ($\delta^{34}S = +10.6$, +7.2 for gill tissues), methanotrophic *Bathymodiolus* mussels had high $\delta^{34}S$ values, which are comparable to those of common marine organisms. Some of the bivalves (*Bathymodiolus*, *Calyptogena*, and *Acharax*) showed significantly low $\delta^{15}N$ values < -5 ‰. *Bathymodiolus* mussels also showed significantly low $\delta^{15}N$ values as well as the lowest $\delta^{13}C$ values. It appeared that the $\delta^{13}C$ and $\delta^{15}N$ values of these samples are positively correlated ($R^2 = 0.85$).

10.3.3 Stable Isotopic Composition of the Issuing Fluids Associated with Animal Communities

10.3.3.1 Hydrogen Sulfide

The $\delta^{34}S$ values of hydrogen sulfide dissolved in the hydrothermal fluids ranged from nearly 0 to +12 ‰ (Table 10.2), whereas those from methane-rich seeps were less than −20 ‰, except for the fumarolic gas emitting from Wakamiko submarine volcano (Table 10.3). Thiotrophic animals, which are known to harbor only thioautotrophic endsymbionts or feed on thioautotrophic products, are expected to have $\delta^{34}S$ values close to that of the associated hydrogen sulfide. Therefore, the apparent sulfur isotopic fractionation between the soft tissue of thiotrophic animals and the associated hydrogen sulfide collected from the hydrothermal systems should be zero or nearly zero. As shown in Fig. 10.6, most $\delta^{34}S$ values of the animals were lower than those of the hydrogen sulfides, while some animals showed values slightly higher than those of the hydrogen sulfides. On the other hand, methanotrophic species, which are known to harbor methanotrophic endsymbionts, and heterotrophs relying on phototrophic products are expected to have high $\delta^{34}S$ values, ranging from +15 to +21 ‰, since they assimilate seawater sulfates with $\delta^{34}S$ values of ~+21 ‰. Figures 10.7 and 10.8 show the apparent differences between the $\delta^{34}S$ values of animal soft tissues and seawater-sulfate for samples from hydrothermal systems and methane seeps, respectively. The diagrams show that, with some exceptions, especially bivalves inhabiting methane seeps (*Bathymodiolus japonicas*, *B. platifrons*, *B. hirtus*, and *B. securifornis* in Fig. 10.8), $\delta^{34}S$ values for all animal tissues were significantly lower than that of seawater-sulfate.

Table 10.2 Carbon, nitrogen, and sulfur isotope compositions of benthic animal bodies sampled around hydrothermal fields and associated environmental geochemical data

					Soft body parts								Issuing fluids			
						Carbon		Nitrogen		Sulfur			Methane	Ammonium	Hydrogen sulfide	
Area	Field	Site	Genus (Order or Family)	Species	Tissues	$\delta^{13}C_{VPDB}$ (‰)	SD	$\delta^{15}N_{Air}$ (‰)	SD	$\delta^{34}S_{CDT}$ (‰)	SD	Number	$\delta^{13}C_{VPDB}$ (‰)	$\delta^{15}N_{Air}$ (‰)	$\delta^{34}S_{CDT}$ (‰)	References
Okinawa Trough	Minami-Ensei knoll		(Demospongiae)	?	Bulk	−26.6		−0.6		+6.9	10.6	1	−26.0 to −24.7*	nr	nr	*Kawagucci et al. (2013)
			(Demospongiae)	?	Bulk	−29.7		−0.2		+11.9		1				
			(Demospongiae)	?	Bulk	−26.0		+2.7		+13.6		1				
	Izena Hole	JADE	*Shinkaia*	*crosnieri*	Muscle	−23.1	0.4	+5.2	0.3	−3.8		3	−41.0 to −36.0*	nr	+3.6 to +7.7**	*Ishibashi et al. (1995), **Kim et al. (1989), Sakai et al. (1990), Gamo et al. (2001)
			Paralomis	*verrilli*	Muscle	−24.2		+5.6		−5.4		1				
			Paralomis	?	Muscle	−24.8	1.1	+6.8	1.2	+7.5		2				
			Alvinocaris	*longirostris*	Muscle	−21.0	1.6	+4.3	1.1	−0.7, +2.7		4				
					Egg	−19.7	3.5	+0.5	2.2	+1.1, +1.6		4				
			Opaepele	*loihi*	Muscle	−17.6	0.7	−0.6	0.4	nd		3				
			Bathymodiolus	*platifrons*	Foot	−30.4	0.9	−0.4	1.1	+7.5, +7.7		4				
					Gill	−30.1	0.9	0.0	0.8	+8.5, +9.1		3				
					Gill	−31.5	0.6	nd		+10.6		2				
					Mantle	−31.5	1.1	−0.2		+11.4		2				
			Provanna	?	Bulk	−25.3	0.9	+3.0	2.5	+5.7		4				
			Lepetodrilus	*nux*	Bulk	−20.8	2.3	+2.3	0.4	+3.5		5				
			Bathyacmaea	*secunda*	Bulk	−26.6	1.3	+0.9	1.7	+8.6		4				
			(Zoarcidae)	?	Bulk	−25.7		+7.7		−4.1		1				
			(Goniasteridae)	?	Bulk	−42.3		+8.3		nd		1				
			(Asteroidea)	?	Bulk	−34.4		+8.3		+14.6		1				
			(Demospongiae)	?	Bulk	−21.2		+1.8		+5.6		1				
			(Hexachtinellida)	?	Bulk	−29.6		+7.3		+10.9	7.1	1				
			(Hexachtinellida)	?	Bulk	−30.6		+8.0		+6.9		1				
			(Demospongiae)	?	Bulk	−29.5		+7.9		nd		1				
			(Demospongiae)	?	Bulk	−38.5		−6.6		nd		1				
			Branchipolynoe	*pettiboneae*	Bulk	−29.7	0.6	+6.4	0.5	+8.9		4				
			Paradialychone	?	Bulk	−33.4	1.1	+2.7	0.3	+3.6		3				
		Hakurei	*Shinkaia*	*crosnieri*	Muscle	−22.1	1.4	+4.7	1.3	+0.1		6	−32.0*	nr	+5.5 to +7.8	*Kawagucci et al. (2010)
			Bathymodiolus	*japonicus*	Gill	−31.3	1.3	−3.3	0.1	−8.0		3				
	Iheya Ridge		*Shinkaia*	*crosnieri*	Muscle	−23.7	0.7	+4.4	0.6	−1.1		3	−41.2*	nr	−0.3 to +3.0**	*Ishibashi et al. (1995), **Kim et al. (1990), Gamo et al. (1991)
			Alvinocaris	*longirostris*	Muscle	−26.1	2.0	+6.9	1.1	−21.0		3				
					Egg	−34.7	0.3	+3.3	0.8	−21.0		3				
			Calyptogena	*okutanii*	Gill	−35.2	0.2	+3.1	5.1	+7.7		2				
					Foot	−33.9	1.0	+4.0	2.9	+2.0		3				
			Acharax	?	Bulk	−31.7	0.5	+1.6	2.3	−6.5		3				

(*continued*)

Table 10.2 (continued)

					Soft body parts								Issuing fluids			
						Carbon		Nitrogen		Sulfur			Methane	Ammonium	Hydrogen sulfide	
Area	Field	Site	Genus (Order or Family)	Species	Tissues	$\delta^{13}C_{VPDB}$ (‰)	SD	$\delta^{15}N_{Air}$ (‰)	SD	$\delta^{34}S_{CDT}$ (‰)	SD	Number	$\delta^{13}C_{VPDB}$ (‰)	$\delta^{15}N_{Air}$ (‰)	$\delta^{34}S_{CDT}$ (‰)	References
			Alaysia	?	Bulk	−17.5	0.5	+3.5	0.2	−22.0		3				
	Iheya North Knoll		*Shinkaia*	*crosnieri*	Muscle	−32.4		+4.1		+6.9		1	−54.0 to −52.8*	nr	+8.0 to +12.2**	*Kawagucci et al. (2011), **Yamanaka et al. (2000b)
			Calyptogena	*soyoae*	Gill	**−37.5***		+2.0		**+1.8***		1				*Mae et al. (2007)
					Mantle	**−36.3***		+4.5		**+0.4***		1				*ditto*
			Bathymodiolus	*platifrons*	Gill	−45.2	0.9	−4.4	0.2	+13.3		3				
			Bathymodiolus	*platifrons*	Gill	**−49.2***	**1.6***	**−4.2***	**0.3***	**+13.4***		3				*Mae et al. (2007)
					Mantle	**−49.0***	**2.9***	**−3.7***	**0.5***	**+18.3***		3				*ditto*
			Lamellibrachia	?	Trophosome	−22.3	1.3	+2.9	0.9	nd		6				
			Ashinkailepas	*seepiophilia*	Bulk	−22.8	0.4	+7.2	0.7	−11.0		5				
	Tarama knoll		*Alvinocaris?*	?	Muscle	−15.1		−0.6		+6.8		1	−38.4*	nr		*Inoue and Ueno, personal communication
			Liparis	?	Muscle	−22.3		+9.2		−7.3		1				
			Liparis	?	Muscle	−25.7		+13.6		+7.5		1				
			(Asteroidea)	?	Bulk	−32.4		+15.1		+8.7		1				
			(Hexachtinellida)	?	Bulk	−34.3		+10.6		+5.0		1				
				ditto	Bulk	−35.1		+9.9		+4.8		1				
				ditto	Bulk	−32.1		+7.7		+2.5		1				
			(Alcyonacea)	?	Bulk	−26.3		+11.6		+13.8		1				
			Enypniaster	*eximia*	Bulk	−20.7		+12.8		+14.6		1				
			Benthoctopus	?	Muscle	−23.1		+14.0		+11.5		1				
	Yonaguni knoll		*Shinkaia*	*crosnieri*	Muscle	−22.9	0.0	+3.1	0.1	+5.4		3	−27.3 to −24.8*	nr	+13.0	*Konno et al. (2006)
					Muscle	−17.3		+1.0		+4.6		1				
			Bathymodiolus	*platifrons*	Gill	−25.1	0.1	−7.5	1.4	+13.5		2				
					Mantle	−26.2	0.2	−5.9	1.0	+13.2		2				
			Bathymodiolus	*platifrons*	Gill	**−24.5***		**−6.8***		**+11.1***		1				*Naraoka et al. 2008
	Hatoma knoll		*Shinkaia*	*crosnieri*	Muscle	−24.6	1.6	+5.1	0.7	+8.3		6	−51.3 to −44.3*	nr	+8.0 to +12.0	*Naraoka et al. (2008)
			Alvinocaris	*longirostris*	Muscle	−32.2	5.8	+5.2	1.2	+11.1	3.9	6				
			Lebbeus	*washingtonianus*	Muscle	−30.8	0.1	+5.5	0.0	nd		2				
			Munidopsis	*ryukyuensis*	Muscle	−28.3	0.8	+3.8	0.7	nd		4				
			Paralomis	?	Muscle	−26.7		+9.0		nd		1				
			Bathymodiolus	*platifrons*	Gill	**−44.8***		**−4.4***		**+13.9***		1				*Naraoka et al. (2008)
Izu-Ogasawara arc	Myojin knoll		*Gandalfus*	*yunohana*	Muscle	−15.9	2.2	+8.1	0.4	nd		5	−16.3*	nr	+4.9 to +5.6**	*Tsunogai et al. (2000), **Yamanaka et al. (2000a, 2000b)
			Bathymodiolus	*septemdierim*	Gill	−34.4	0.7	+0.8	0.8	+2.9, +3.1		4				
	Sumisu caldera		*Bathymodiolus*	*septemdierim*	Gill	−34.5		−4.2		−24.4		1	nr	nr	nr	

			Characella	?	Bulk	−34.8		+11.1		−5.9		1				Harboring thioautotrophic endosymbiont (Nishijima et al. (2010)
			Lamellibrachia	?	Trophosome	−12.9		+6.1		−18.5		1				
	Suiyo Seamount		*Bathymodiolus*	*septemdierim*	Gill	−35.3		−2.4		−0.3		1	−7.4 to −5.3*	nr	+3.1**	*Tsunogai et al. (2005), **Yamanaka et al. (2000a, 2000b)
					mantle	−32.8		−1.9		+2.1		1				
					Gill	**−36.0***		**−5.1***		**+4.3***		1				*Naraoka et al. (2008)
					Gill	−34.1	1.1	−1.9	1.7	−0.1		2				
	Kaikata Seamount		*Gandalfus*	*yunohana*	Muscle	−20.2	2.3	+9.9	0.7	nd		12	nr	nr	nr	
			Leptodius	*exaratus*	Muscle	−21.9	0.4	+8.4	0.6	nd		2				
			Symphurus	*orientalis*	Muscle	−17.4		+10.1		nd		1				
South Mariana Trough	Mariana backarc spreading center	Snail site	*Gandalfus*	*yunohana*	Muscle	−21.2	1.8	+9.7	1.2	+7.5	0.6	4	nr	nr	+7.0 - +8.7*	*Kakegawa et al. (2008) (Sulfide minerals)
			Alviniconca	*hessri*	Muscle	−31.3	0.4	+3.6	0.8	+9.8	0.6	4				
		Archaean site	*Phymorhynchus*	?	foot	−30.8		+4.8		+4.4		1	nr	nr	−1.8 to +1.7*	*Kakegawa et al. (2008) (Sulfide minerals)
		Yamanaka site	*Neoverruca*	*brachylepadoformis*	Bulk	−21.8	0.7	+10.4	0.8	nd		5	nr	nr	+5.1 to +6.3*	*Kakegawa et al. (2008) (Sulfide minerals)
			Marianactis	?	Bulk	−17.7		+9.7		+4.6		1				
Kermadic Arc	Brothers volcano	Lower Cone site	*Lamellibrachia*	?	Trophosome	−7.5	1	+1.9	0.4	nd		3	−37.0 to −33.9*	nr	−8.0 to −4.8*	*de Ronde et al. (2011)
			Lamellibrachia	?	Trophosome	−12.9	0.3	+3.7	0.0	nd		3				
			Vulcanolepas	*osheai*	Bulk	−13.0	1.7	+7.8	1.1	nd		4				
Central Indian Ridge	Hakuho Knoll	Kaiko field	*Bathymodiolus*	*marisindicus*	Gill	−31.3*	0.7*	−8.1*	1.5*	+5.3**	0.3**	3	−8.6 to −8.7***	nr	+6.8 to +7.0**	*Van Dover et al. (2001), **Yamanaka et al. (2003a), ***Gamo et al. (2001)

Asterisks on the right shoulder of isotope values indicate cited data appeared in Reference column at the same line.
nr not reported, *nd* not determined

Table 10.3 Carbon, nitrogen, and sulfur isotope compositions of benthic animal bodies sampled around methane seeps and associated environmental geochemical data

					Soft body parts								Issuing fluids				
						Carbon		Nitrogen		Sulfur			Methane	Ammonium	Hydrogen sulfide		
Area	Field	Site	Genus (Order or Family)	Species	Tissues	$\delta^{13}C_{VPDB}$ (‰)	SD	$\delta^{15}N_{Air}$ (‰)	SD	$\delta^{34}S_{CDT}$ (‰)	SD	Number	$\delta^{13}C_{VPDB}$ (‰)	$\delta^{15}N_{Air}$ (‰)	$\delta^{34}S_{CDT}$ (‰)	Note	References
Ryukyu arc	Kuroshima knoll		*Bathymodiolus*	*hirtus*	Gill	−37.6		−1.5		+17.2		1	−43.3 to −38.6*	nr	−22.5 to −21.2	Separate type	*Tsunogai et al. (2010)
					Foot	−39.5		−1.3		+17.4		1				(See text)	
					Mantle	−43.1		−1.4		+17.6		1					
					Adductor	−36.9		−1.0		+17.5		1					
			Bathymodiolus	*hirtus*	Gill	−43.1		0.0		+10.6		1				Mixed type	
					Foot	−41.5		+0.8		+10.7		1				(See text)	
					Mantle	−45.8		nd		+9.8		1					
					Adductor	−45.3		nd		+9.1		1					
			Bathymodiolus	*securiformis*	Gill	−41.6		+0.9		+20.2		1				Separate type	
					Foot	−39.9		+0.5		+20.2		1				(see text)	
					Mantle	−41.5		+1.4		+20.5		1					
					Adductor	−40.7		+1.9		+20.7		1					
			Bathymodiolus	*securiformis*	Gill	−38.3		−0.6		+7.2		1				Mixed type	
					Foot	−36.4		nd		+7.9		1				(See text)	
					Mantle	−42.8		nd		+6.2		1					
					Adductor	−37.5		nd		+4.1		1					
			Calyptogena	*kawamurai*	Gill	−34.1	0.7	+5.3	0.5	−3.2	6.5	4					
					Foot	−33.5	0.2	+6.9	0.2	+2.0	8.1	4					
					Mantle	−34.2	0.5	+6.3	0.3	−0.5	3.9	4					
					Adductor	−33.9	0.3	+7.3	0.5	−4.9	15.8	4					
Kyushu Island	Kagoshima Bay	Wakamiko	*Lamellibrachia*	*satsuma*	Trophosome	−20.5	0.9	+6.4	1.2	−10.0	14.5	8	−27.2	2.7	−33.6 to −27.1*, +6.8, +13.8		*Miura et al. (2002), Mizota and Maki (1998), Yamanaka et al. (2013b)
					Trophosome	nd		nd		−21.2	0.5	4					
Sagami Trough	off Hatsushima		*Alvinocaris*	*longirostris*	Muscle	−31.1	1.0	+0.9	0.5	nd		3	−72.0 to −70.0*	nr	−22.7**		*Hattori et al. (1996), **Sakai et al. (1987)
(Sagami Bay)			*Bathymodiolus*	*platifrons*	Gill	−58.9	3.2	−7.6	0.7	+18.7	1.9	3					
			Bathymodiolus	*japonicus*	Gill	−60.4	0.0	−7.7	1.0	+16.4		3					
			Calyptogena	*okutanii*	Gill	−69.2	1.1	−11.2	1.1	nd		2					
			Calyptogena	*okutanii*	Gill	−36.6	0.3	−9.7	0.2	+16.8	6.5	3					
			Calyptogena	*soyoae*	Gill	−32.1		nd		−23.4*	4.9*	3					*Mizota and Yamanaka (2003)
			Calyptogena	*soyoae*	Gill	−36.6	0.9	−6.6	2.2	nd		6					
			Acharax	*johnsoni*	Gill	−30.4		−11.1		nd		1					
			Acharax	*johnsoni*	Gill	−30.0	0.0	−4.8	0.3	nd		2					

		(Thyasiridae)	?	Gill	−37.6		−7.0		nd		1				
		Conchocela	*bisecta*	Gill	−36.0	0.1	−8.5	0.1	nd		2				
		Provanna	*glabra*	Bulk	−30.7	0.6	−2.3	0.6	nd		2				
		Margarites	*shinkai*	Bulk	−32.9	0.1	−1.7	0.1	nd		2				
		Phymorhynchus	*buccinoides*	Bulk	−58.6	4.4	−4.0	1.2	+13.8		6				
		Bathyacmaea	*nipponica*	Bulk	−25.7		−3.7		nd		1				
		Oenopota	*sagamiana*	Bulk	−30.9	3.6	+2.0	1.5	nd		6				
		(Ophiuroidea)	?	Bulk	−32.8	1.3	−2.6	1.1	nd		4				
		(Actinaria)	?	Bulk	−15.2	0.7	+15.0	0.7	nd		2				
		Lamellibrachia	?	Trophosome	−25.4	0.9	+4.1	0.9	+7.8		3				
		Lamellibrachia	?	Trophosome	−20.2	1.5	−0.1	1.8	−27.9, −17.9						
		Alaysia	?	Trophosome	−19.5	1.1	+4.2	1.1	nd		2				
		Nicomache	*ohtai*	Bulk	−33.3		+1.1		nd		1				
Northern Mariana arc	South Chamorro seamount	*Bathymodiolus*	?	Gill	**−18.9***		**+1.8***		**+10.6***		1	**−14.6***	nr	**−32.3***	*Yamanaka et al. (2003b)
				Foot	nr		nr		**+10.4***		1				
				Mantle	**−21.4***		**+3.1***		**+10.2***		1				
				Adductor	**−19.1***		**+2.7***		nr		1				
				Viscera	**−20.2***		**+2.9***		nr		1				
Southern Mariana arc	Shinkai Seep Field	*Calyptogena*	*mariana*	Gill	**−34.6***	**0.5***	**+4.2***	**1.4***	−9.0	1.0	3	nr	nr	nr	*Ohara et al. (2012)
Sunda Trough	off southwest corner of Java	*Calyptogena*	*garuda*	Gill	−35.5	0.3	−1.5	4.2	−12.3	4.2	2	nr	nr	nr	
				Foot	−34.4	1.2	+2.2	4.4	nd		2				
				Mantle	−34.8	0.8	+1.3	3.6	nd		2				
				Adductor	−34.5	1.1	+2.7	3.9	nd		2				

Asterisks on the right shoulder of isotope values indicate cited data appeared in Reference column at the same line.
nr not reported, *nd* not determined

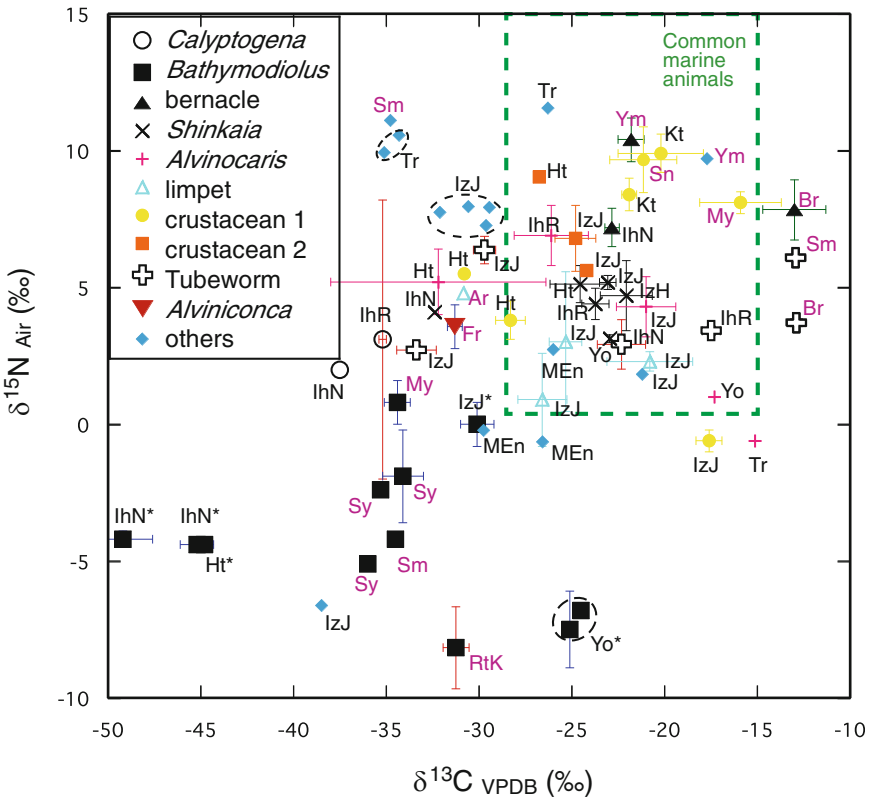

Fig. 10.2 Plot of carbon vs. nitrogen isotopic ratios for animal soft bodies from hydrothermal fields. Numerical data are shown in Table 10.2. Barnacles include *Ashinkailepas* and *Neoverruca*. Crustacean 1 includes two shrimps, *Lebbeus* and *Opaepele*, and three crabs, *Munidopsis*, *Gandalfus*, and *Leptodius*. Crustacean 2 includes the crab, *Paralomis*. Others include sea anemones, soft corals, and sea sponges. Abbreviations in the figures indicate the locations of the samples (*red-colored* abbreviations indicate sediment-starved hydrothermal fields, see Table 10.1)

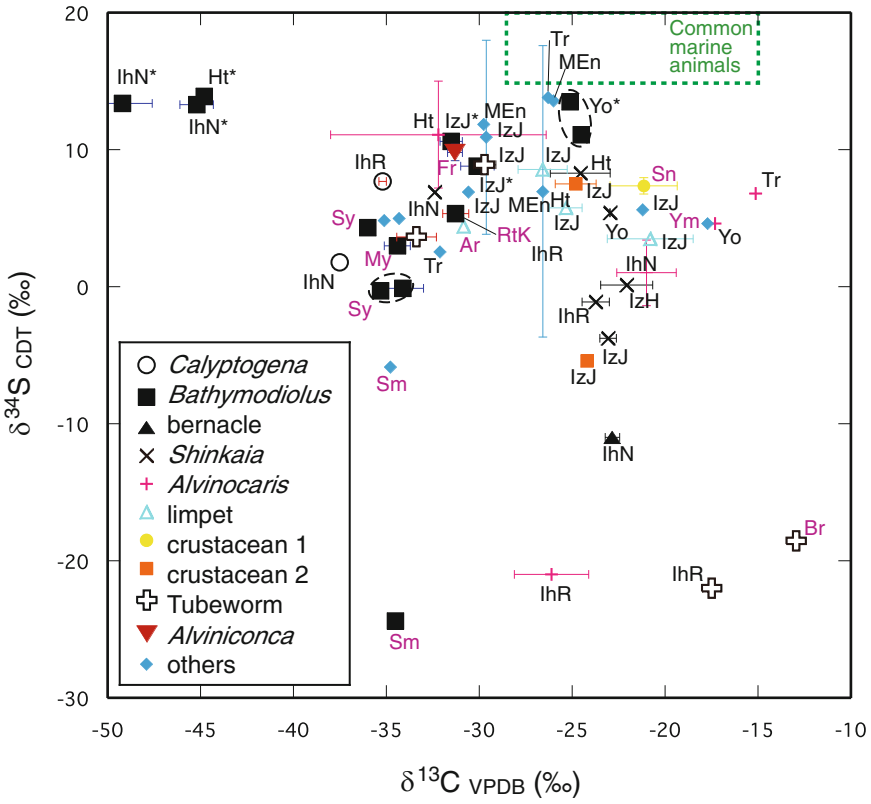

Fig. 10.3 Plot of carbon vs. sulfur isotopic ratios for animal soft bodies from hydrothermal fields. Numerical data are shown in Table 10.2. Barnacles include *Ashinkailepas* and *Neoverruca*. Crustacean 1 includes two shrimps, *Lebbeus* and *Opaepele*, and three crabs, *Munidopsis*, *Gandalfus*, and *Leptodius*. Crustacean 2 includes the crab, *Paralomis*. Others include sea anemones, soft corals, and sea sponges. Abbreviations in the figures indicate the locations of the samples (*red-colored* abbreviations indicate sediment-starved hydrothermal fields, see Table 10.1)

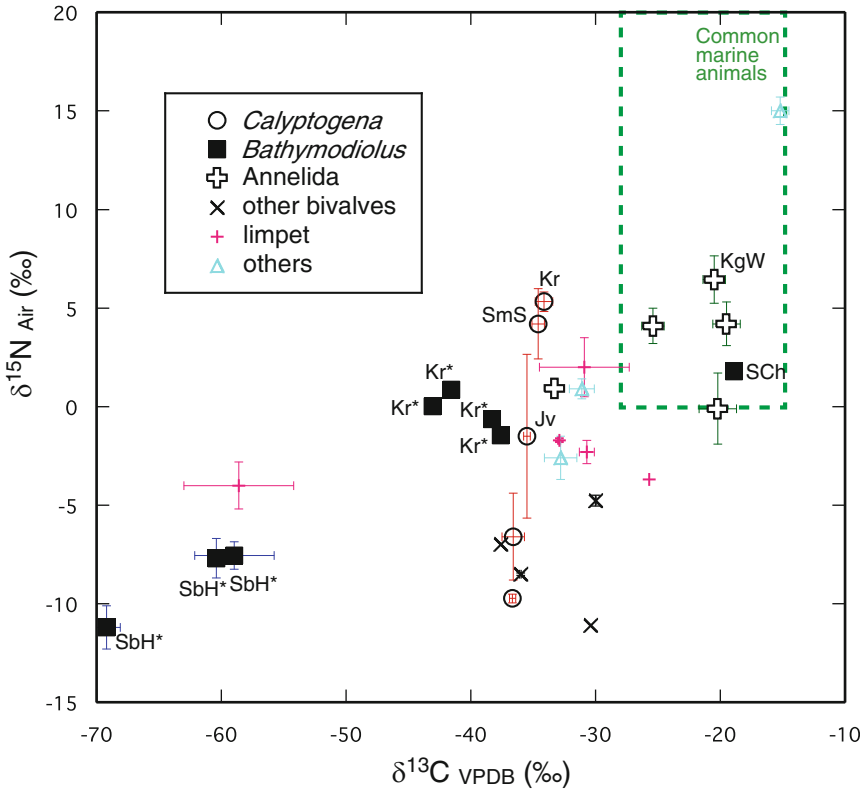

Fig. 10.4 Plot of carbon vs. nitrogen isotopic ratios of animal soft bodies from methane seep fields. Numerical data are shown in Table 10.3. Other bivalves include Thyasiridae, Solemyidae, and Thyasiridae groups. These bivalves harbor thioautotrophic endosymbiots in their gill tissues. Others include *Alviniconca* shrimp, *Actiniaria* sea anemone, and *Ophiuroidea* starfish. Abbreviations in the figures indicate the locations of the samples (see Table 10.1), and plots without abbreviations represent collections off Hatsushima, in Sagami Bay

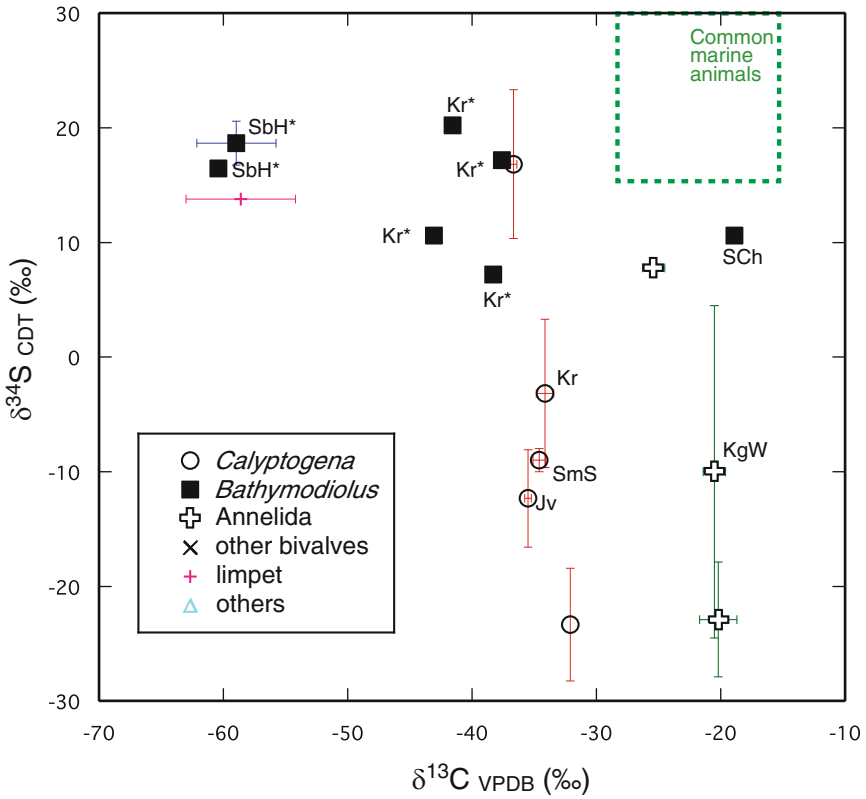

Fig. 10.5 Plot of carbon vs. sulfur isotopic ratios of animal soft bodies from methane seep fields. Numerical data are shown in Table 10.3. Other bivalves include Thyasiridae, Solemyidae, and Thyasiridae groups. These bivalves harbor thioautotrophic endosymbiots in their gill tissues. Others include *Alviniconca* shrimp, *Actiniaria* sea anemone, and *Ophiuroidea* starfish. Abbreviations in the figures indicate the locations of the samples (see Table 10.1), and plots without abbreviations represent collections off Hatsushima, in Sagami Bay

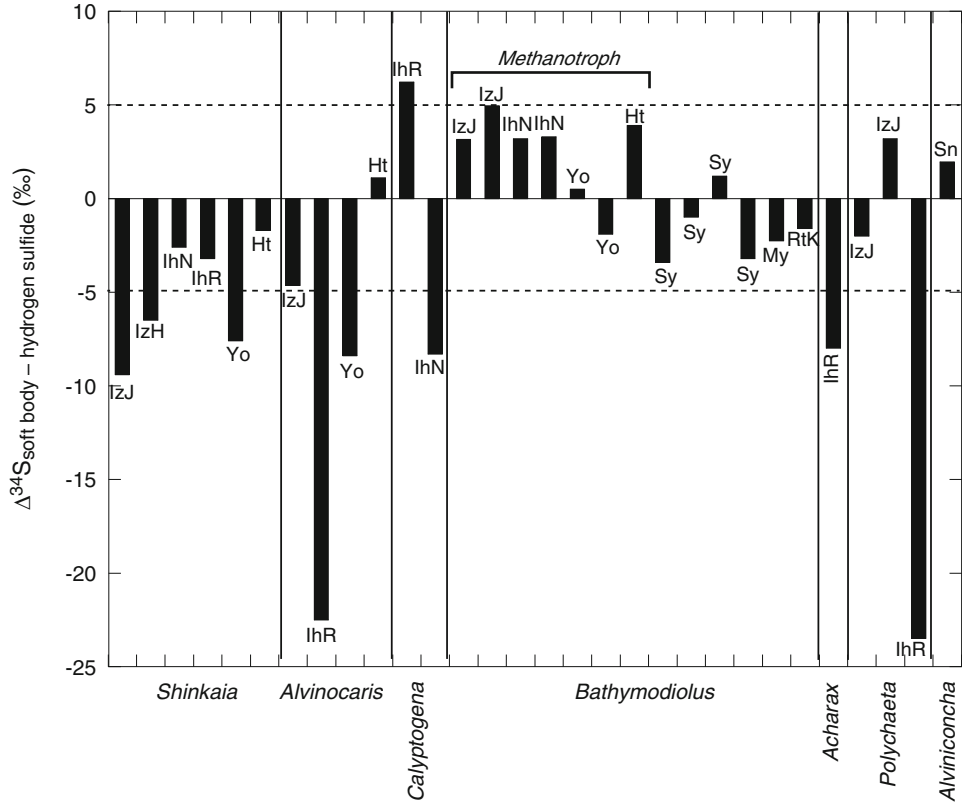

Fig. 10.6 Apparent differences between the $\delta^{34}S$ values of animal soft bodies and issuing hydrogen sulfide from hydrothermal fields. The *two dotted lines* indicate the possible range of variation in $\delta^{34}S$ values of hydrogen sulfide and kinetic isotope fractionation involved with its assimilation. Abbreviations indicate the sample locations shown in Table 10.1

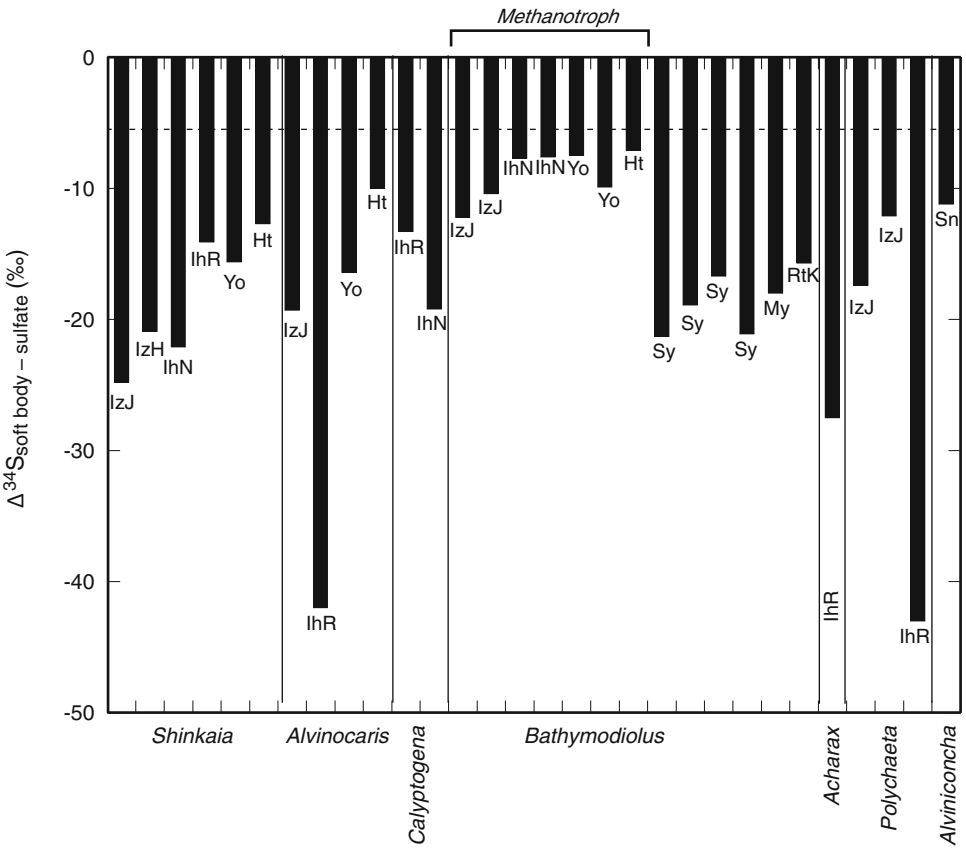

Fig. 10.7 Apparent differences between the $\delta^{34}S$ values of animal soft bodies from hydrothermal fields and seawater sulfate-sulfur ($\delta^{34}S = +21$ ‰). The *dotted line* indicates the possible range of kinetic isotope fractionation involved in the incorporation and subsequent assimilation of sulfates. Abbreviations indicate the sample locations shown in Table 10.1

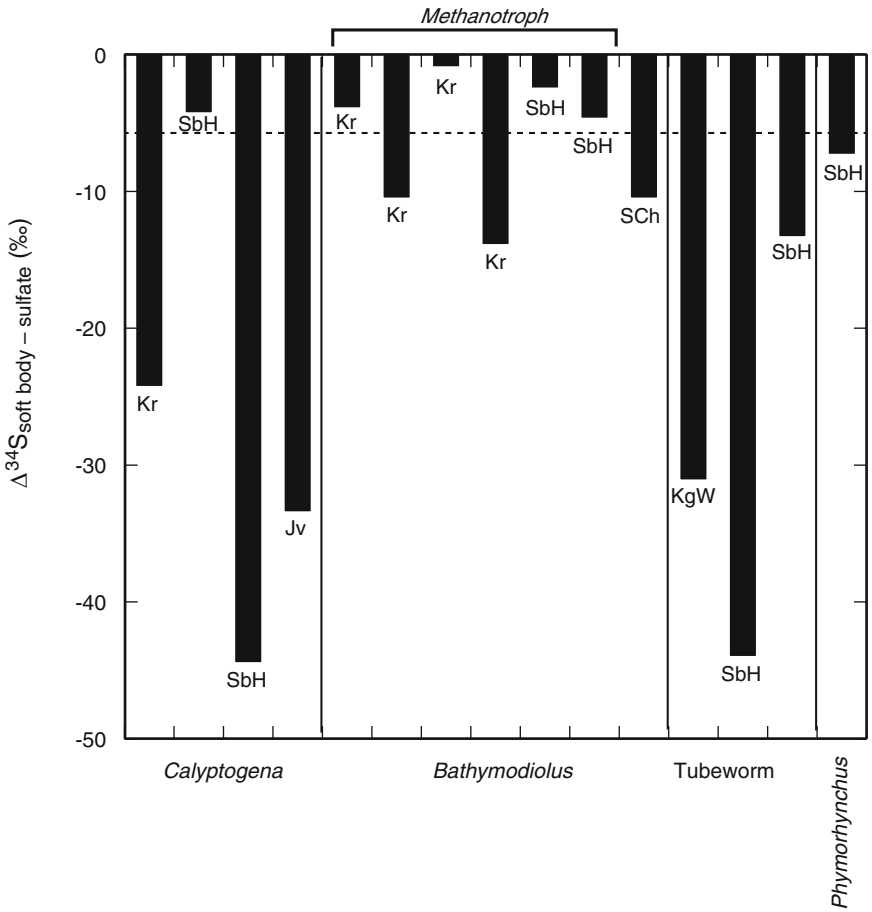

Fig. 10.8 Apparent differences between the $\delta^{34}S$ values of animal soft body parts obtained from methane seep areas and seawater sulfate-sulfur ($\delta^{34}S = +21$ ‰). The *dotted line* indicates the possible range of kinetic isotope fractionation involved with assimilation of sulfate. Abbreviations indicate the sample locations shown in Table 10.1

10.3.3.2 Methane

The $\delta^{13}C$ values of dissolved methane in the venting fluids ranged from −54 to −4 ‰ (Tables 10.2 and 10.3). Methanotrophic species, which are known to harbor methanotrophic endsymbionts, are expected to show $\delta^{13}C$ values close to that of the associated methane. Apparent differences between $\delta^{13}C$ values of animal soft tissues and the associated methane are shown in Figs. 10.9 and 10.10. Most animal samples showed higher $\delta^{13}C$ values relative to those of the associated methane.

10.4 Discussion

10.4.1 The Contribution of Thioautotrophic Nutrition to the Benthic Animal Community

For benthic communities inhabiting the areas around hydrothermal vents and methane seeps, i.e., the discharge zone of TAIGA, major mechanisms that exploit their limited sulfur isotopic fractionation are considered to be a positive assimilation of sulfide-sulfur, since $\delta^{34}S$ values of sulfide are usually lower than +12 ‰. As shown in Figs. 10.3 and 10.5, many animal tissue samples had $\delta^{34}S$ values lower than +15 ‰, suggesting that the animals rely nearly all or in part on thioautotrophic nutrition. Some animals (mostly mussels, such as *Bathymodiolus japonicas*, *B. platifrons*, *B. hirtus*, and *B. securifornis*), which have higher $\delta^{34}S$ values ($\geq$ +15 ‰), are known to harbor methanotrophic endosymbionts in their gill tissue (Fujiwara et al. 2000; Fujikura et al. 2003). These results are quite reasonable, since some of the methanotrophic mussels inhabiting the Okinawa Trough have $\delta^{34}S$ values of slightly less than +14 ‰. *Bathymodiolus* mussels are expected to have preserved their ability to feed via filtration (Page et al. 1990, 1991). Therefore, these results may suggest positive assimilation of thioautotrophic nutrition via filter feeding. Mussels from South Chamorro serpentine seamount also had low $\delta^{34}S$ values (~ +10 ‰). The mussels are considered to harbor both thioautotrophic and methanotrophic endosymbionts (i.e., dual symbiosis) (Yamanaka et al. 2003b). The other heterotrophs, except for vent and seep endemic species, also have $\delta^{34}S$ values of slightly <+15 ‰ (Figs. 10.3 and 10.5), indicating that thioautotrophic nutrition at the vent and seep fields prevails not only with the endemic animals, but also with diverse animals inhabiting areas around the fields.

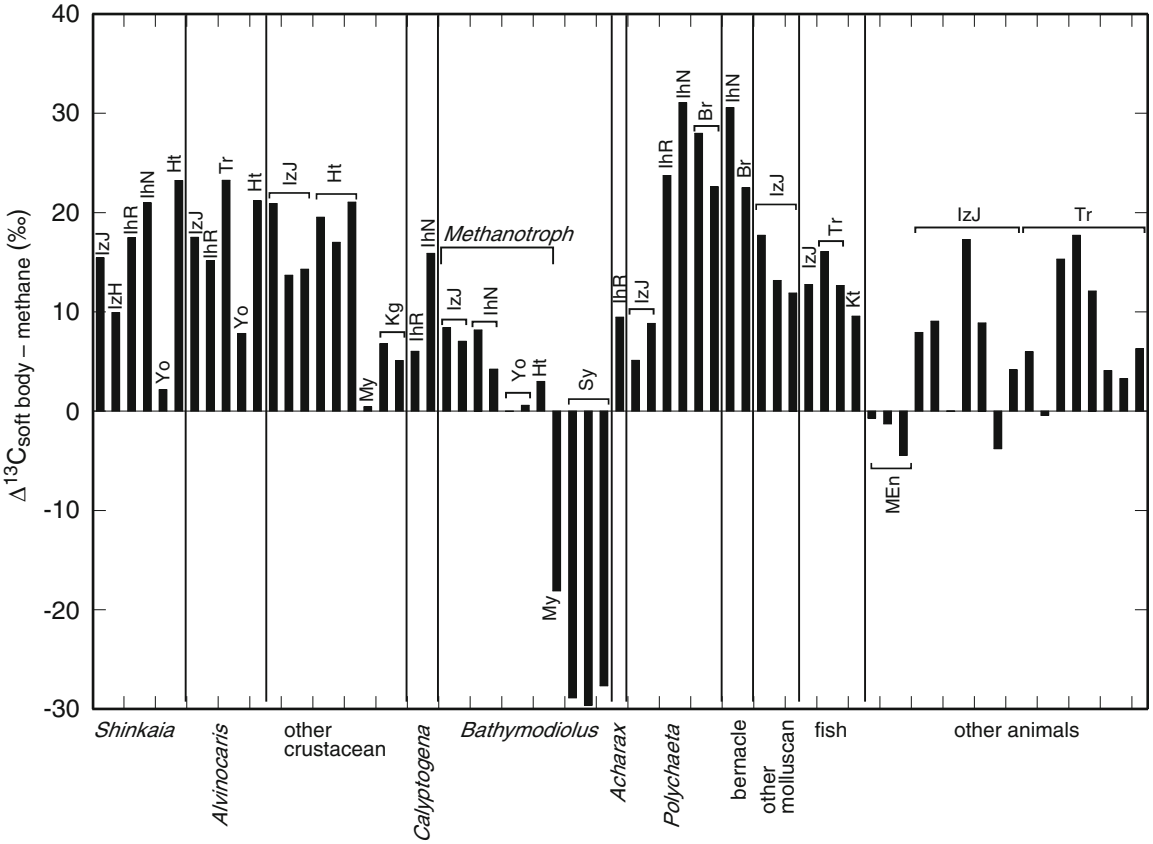

Fig. 10.9 Apparent differences between the $\delta^{13}C$ values of animal soft body parts and associated methane obtained from hydrothermal areas. Abbreviations indicate the sample locations shown in Table 10.1

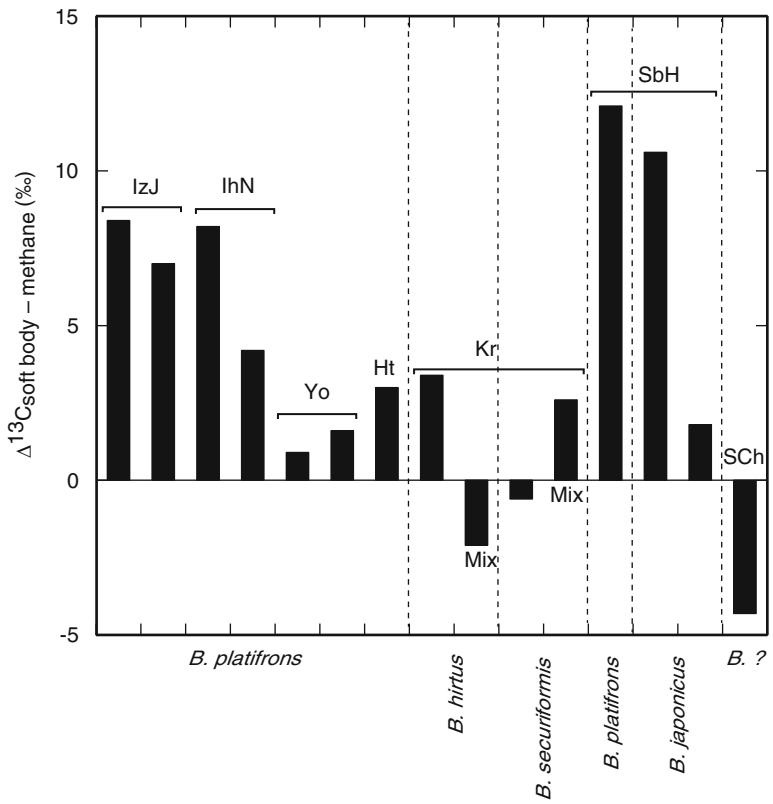

Fig. 10.10 Apparent isotopic fractionation of $\delta^{13}C$ values of animal soft bodies and issuing methane from methane seep fields. The mussels harbor methanotrophic symbionts in their gill tissues. Abbreviations indicate the sample locations shown in Table 10.1. "Mix" indicates that the sample specimens form a mixed colony of *B. hirtus* and *B. securiformis*

One group of *Calyptogena soyoae* from the off Hatsushima site showed quite high $\delta^{34}S$ values (~ +16.5 ± 6.5 ‰). Masuzawa (1996) reported similar high $\delta^{34}S$ values (~ +14 ‰) from other *Calyptogena soyoae* in the area, although the $\delta^{34}S$ value of hydrogen sulfide from that habitat has not been documented. The spatial distribution of $\delta^{34}S$ values for sedimentary sulfide is often heterogeneous within the anoxic environment (e.g., Yamanaka et al. 1999). Paired analysis of sulfur in clams and substrate sediments is required for further study.

The above results also suggest that the sediment-hosted hydrothermal vent and methane-rich seep fields provide thioautotrophic nutrition (i.e., sulfur-oxidizing bacteria and heterotrophic organisms that rely on them) derived from the suspended particles and detritus in the surface sediments. In fact, significant amounts of sulfur-oxidizing microbe cells have been identified in the bottom water around hydrothermal fields in the Okinawa Trough (Yanagawa et al. Chap. 6). Such high biomass flux of the sulfur-oxidizing microbes is supported by microbial sulfide production, suggesting that sub-seafloor bacterial sulfate reduction using methane or sedimentary organic matter as electron donors (Masuzawa et al. 1992) is quite active at the discharge zone of TAIGA.

From the above-mentioned stable isotopic data, it is possible to estimate the contribution of thioautotrophic nutrition to benthic animal communities. Nevertheless, the primary source of hydrogen sulfide is not only hydrothermal but also bacterial. The $\delta^{34}S$ values of bacterial hydrogen sulfide vary widely (e.g., Thode 1988). Therefore, it is difficult to accurately estimate the contribution of thioautotrophic nutrition. The $\delta^{34}S$ values for sulfur of animal soft tissue are less than +10 ‰, indicative of a significant contribution from thioautotrophic nutrition.

10.4.2 Variations in the Carbon Isotopic Ratios of the Benthic Animal Community

The carbon isotopic ratios for the animal soft tissues varied widely (Figs. 10.2, 10.3, and 10.4, and Tables 10.2 and 10.3). This may reflect the variation in $\delta^{13}C$ values of the methane (−71 to −6 ‰) issuing from hydrothermal vents and cold seeps. In particular, $\delta^{13}C$ values of methanotrophic *Bathymodiolus* mussels varied widely, ranging from −70 to −20 ‰. The $\delta^{13}C$ values for most animal soft tissue samples were higher than those of the associated methane (Figs. 10.9 and 10.10). This can be explained by the following two scenarios: (1) the contribution of methane as a carbon source for chemosynthesis-based animals, except for methanotrophic species, is insignificant at many discharge zones or (2) the $\delta^{13}C$ values of methane are increasing due to the selective incorporation of isotopically light methane during biological oxidation (e.g., Silverman and Oyama 1968) before delivery to methanotrophs.

In the former case (1), chemoautotrophs fix CO_2 and therefore do not directly assimilate ^{13}C-depleted methane. Dissolved inorganic carbon (mainly bicarbonate) is usually abundant in the bottom seawater. This means that the signature of ^{13}C-depleted CO_2 originating from ^{13}C-depleted methane oxidation is difficult to detect. In the latter case (2), methane emitted at the sediment-hosted systems undergoes biological oxidation and incorporation during penetration of the sediments, resulting in methane that is enriched in ^{13}C relative to the primary source to be delivered to methanotrophic animals (mainly *Bathymodiolus* mussels).

Another plausible explanation for the methanotrophic species that are enriched in ^{13}C, relative to the associated methane, is the heterotrophic assimilation of organic matter via filter feeding, as demonstrated by Page et al. (1990). The $\delta^{13}C$ values of methane originating from pyrolysis of organic matter and microbial methanogenesis, relative to that of common organic matter, are usually depleted in ^{13}C. Heterotrophic and thiotrophic animals are enriched in ^{13}C compared to methane from these sources. In these cases, the soft tissue is probably depleted in ^{34}S due to the dependence on thioautotrophic nutrition. In fact, the mussels inhabiting the Okinawa Trough were slightly depleted in ^{34}S, suggesting a positive incorporation into thioautotrophic nutrition, as mentioned above.

On the other hand, some animal soft tissues depleted in ^{13}C, relative to the associated methane (Figs. 10.9 and 10.10), were found at the field where emitted methane showed quite high $\delta^{13}C$ values ($\geq$ −10 ‰) in an abiotic source (the sediment-starved Myojin and Suiyo seamounts and serpentine-hosted South Chamorro seamount). Furthermore, the mussels of South Chamorro harbor thioautotrophic endsymbionts in addition to methanotrophs, which assimilate abiotic methane enriched in ^{13}C. Therefore, resulting $\delta^{13}C$ values of the mussels decreased relative to those of the associated methane. Its dual symbiosis has also been supported by their low $\delta^{34}S$ values (+10.6 ‰ for gill tissues), relative to seawater-sulfate (Table 10.3).

Some thiotrophic vestimentiferan tubeworms have slightly higher $\delta^{13}C$ values ($\geq$ −20 ‰). It is known that this animal has another carbon fixation pathway instead of the Calvin cycle (Nelson and Fisher 1995). For example, the rTCA cycle is a process that accompanies the insignificant isotopic fractionation during carbon fixation (Markert et al. 2007). Some heterotrophic animals that have high $\delta^{13}C$ values may feed via mechanisms similar to the tubeworms.

One species of limpet, *Phymorhynchus buccinoides*, obtained from off Hatsushima, has been reported to feed predominantly on the dead bodies of *Bathymodiolus* mussels (Fujikura et al. 2009). Their $\delta^{13}C$ values are significantly lower (~ −60 ‰, Table 10.3) than those of the other

heterotrophs. Although such specific heterotrophs relying on a single vent or seep endemic species have rarely been reported until recently (Van Dover 2000), carnivores, scavengers, and parasites relying on a single vent or seep animals are likely found in the vent and seep communities. In fact, parasitical polychaeta, *Branchipolynoe pettiboneae*, collected from inside the shell of *Bathymodiolus* mussels obtained from JADE site, Izena Hole have similar $\delta^{13}C$ and $\delta^{34}S$ values to the associate mussels with ~6 ‰ enriched in ^{15} N (Table 10.2). With further study, these animals will continue to be identified.

10.4.3 Nitrogen Isotopic Ratios of Symbiotic Bivalves

Nitrogen isotopic ratios of animals have been used for the estimation of trophic levels in studies of food web structures (Minagawa and Wada 1984). Usually, higher trophic levels are believed to have elevated $\delta^{15}N$ values. Such enrichment in ^{15}N with increasing trophic level is also common in vent and seep communities, while symbiotic mussels, such as *Calyptogena* clams and *Bathymodiolus* mussels, still have significantly low $\delta^{15}N$ values (Figs. 10.2 and 10.4). Such trends were recognized in early studies of the chemosynthesis-based animal community, and the reasons for such low values have been debated (e.g., Van Dover 2000), although the detailed mechanism is not well understood. Some plausible explanations have been proposed, e.g., assimilation of ammonium, which prevails in anoxic sediments, may be an important process. During the assimilation of ammonium nutrition, isotopic fractionation may occur (e.g., Hübner 1986; Yoneyama et al. 1993; Lee and Childress 1994). Isotopic fractionation during the assimilation of ammonium depends on its concentration and the types of enzymes used in ammonium assimilation. The reported values range from −20 to +4 ‰ ($\delta^{15}N_{ammonium} - \delta^{15}N_{organism}$) (Hübner 1986; Yoneyama et al. 1993). The $\delta^{13}C$ and $\delta^{15}N$ values of most animal tissues, especially the *Bathymodiolus* mussels inhabiting the methane seeps, are highly correlated ($R^2 = 0.85$) (Fig. 10.4). The increasing $\delta^{13}C$ values may be due to isotopic fractionation during microbial oxidation and/or assimilation of methane nutrition. The $\delta^{15}N$ values of source ammonium are also plausibly increased by microbial consumption, because isotopically light ammonium in preferentially incorporated. Therefore, this implies that $\delta^{15}N$ values of ammonium increase together with $\delta^{13}C$ values of methane due to bacterial isotopic discrimination until the ammonium in source fluids reaches the mussel habitat.

Among the seep fields, the carbon isotopic ratios of methane have reflected the methane origin. However, in our limited data set, *Bathymodiolus* mussels obtained from methane seeps off Hatsushima showed a positive correlation between carbon and nitrogen isotopic ratios. This implies that the $\delta^{13}C$ and $\delta^{15}N$ values of the mussels reflect subsurface microbial processes, which preferentially incorporate isotopically light methane together with ammonium. Ammonium is a plausible source of nitrogen nutrition for methanotrophic communities. Due to a lack of isotopic data for ammonium in this habitat, further studies are needed.

10.4.4 Competition for Energy Sources and the Role of Filter Feeding by *Bathymodiolus* Mussels

Two *Bathymodiolus* species (*B. hirtus* and *B. securiformis*) have been observed at the Kuroshima knoll seep site, where they usually form small colonies composed of one species (separate-type). Nevertheless, some colonies form a mixture of both species (mixed-type). Both species are believed to harbor methanotrophic bacteria as their sole endosymbionts (Fujikura et al. 2003). In fact, sulfur isotopic compositions for specimens from separate-type colonies show a range typical of methanotrophic animals ($\delta^{34}S \geq +15$ ‰). The $\delta^{34}S$ values of specimens from the mixed-type colonies are about 10 ‰ lower than those from the separate-type colonies. Both carbon and nitrogen isotopic ratios for two types of samples are relatively similar. Such low $\delta^{34}S$ values may be due to the assimilation of thioautotrophic nutrition via filter feeding. Mussels of the mixed-type colonies may compete with each other for methane nutrition as an energy source. They may compensate for the shortage of methanotrophic nutrition derived from the endosymbionts by filter feeding.

10.5 Summary

Benthic animal communities supported by thioautotrophic and methanotrophic nourishment are widely distributed over the discharge area of TAIGA, and they have high biodiversity including common marine benthos. As we have summarized the nutritional sources of the benthic animals discussed in this study in the Supplementary document (Suppl. 10.1), microbial methane and hydrogen sulfide generated within the sedimentary layer are important energy sources for microbes, in addition to abiogenic methane and hydrogen sulfide dissolved in the issuing fluids. Although some hydrothermal vent and methane seep endemic species harbor endosymbiotic bacteria and lack digestive organs, *Bathymodiolus* mussels still have ability to feed in the Okinawa Trough and some other methane seep fields. The data suggest that the sediment covered discharge area of TAIGA is also abundant in suspended and/or free-living

microbes, namely thioautotrophs, which support huge biomass production and biodiversity on the deep seafloor.

Acknowledgements We are grateful to Drs. K. Fujikura, Y. Fujiwara, S. Tsuchida, H. Watanabe, D. J. Lindsay, F. Inagaki, and Y. Ohara for providing the animal samples used in this study. We are grateful to Drs. K. Yanagi, S. Kojima, T. Okutani, and T. Yamamoto for identification of the sample animals. We are also indebted to Professor H. Chiba and Dr. S. Kawaguchi for their very useful comments. All of the fluid, water, and chimney samples were obtained through the cooperative efforts of the operation teams of the ROVs *HyperDolphin*, *Dolphin 3 k*, *Kaiko*, and *ROPOS*, the DSV *Shinkai* 2000 and 6500, and the captain and crew of the support ships R/Vs *Natsushima*, *Kaiyo*, *Yokosuka*, and *Thomas Tompson*, to whom we extend our heartfelt thanks. This research was supported by the Ministry of Education, Culture, Sports, Science and Technology of Japan through a Special Coordination Fund 'TAIGA' project (New Scientific Research on Innovative Areas, 20109005) and the Archaean Park Project (International Research Project on Interaction between Sub-Vent Biosphere and Geo-Environments).

References

Berndt ME, Allen DE, Seyfried WE (1996) Reduction of CO_2 during serpentinization of olivine at 300 °C and 500 bar. Geology 24:351–354

Canfield DE (2001) Biogeochemistry of sulfur isotopes, in stable isotope geochemistry. In: Valley JW, Cole DR (eds) Reviews in mineralogy and geochemistry, vol 43. Mineralogical Society of America, pp 607–636. doi:10.2138/gsrmg.43.1.607

Carpenter EJ, Harvey HR, Fry B, Capone DG (1997) Biogeochemical tracers of the marine cyanobacterium Trichodes- mium. Deep Sea Res Part 1 Oceanogr Res Pap 44(1):27–38. doi:10.1016/S0967-0637(96)00091-X

de Ronde CEJ, Massoth GJ, Butterfield DA, Christenson BW, Ishibashi J, Ditchburn RG, Hannington MD, Brathwaite RL, Lupton JE, Kamenetsky VS, Graham IJ, Zellmer GF, Dziak RP, Embley RW, Dekov VM, Munnik F, Lahr J, Evans LJ, Takai K (2011) Submarine hydrothermal activity and gold-rich mineralization at Brothers Volcano, Kermadec Arc, New Zealand. Miner Deposita 46:541–584. doi:10.1007/s00126-011-0345-8

Fiala-Médioni A, Boulègue J, Ohta S, Felbeck H, Mariotti A (1993) Source of energy sustaining the *Calyptogena* populations from deep trenches in subduction zones off Japan. Deep Sea Res Part I 40:1242–1258. doi:10.1016/0967-0637(93)90136-Q

Fisher CR, Childress JJ, Macko SA, Brooks JM (1994) Nutritional interactions in Galapagos Rift hydrothermal vent communities: inferences from stable carbon and nitrogen isotope analyses. Mar Ecol Prog Ser 103:45–55. doi:10.3354/meps103045

Fry B, Gest H, Hayes JM (1983) Sulfur isotopic compositions of deep-sea hydrothermal vent animals. Nature 306:51–52

Fujikura K, Aoki M, Fujiwara Y, Ichibayashi S, Imamura M, Ishibashi J, Iwase R, Kato K, Kosaka A, Machiyama H, Miyake H, Miyazaki J, Mizota C, Morimoto Y, Naganuma T, Nakayama N, Okamoto K, Okoshi K, Sato-Okoshi W, Okutani T, Satoh T, Toth LG, Tsuchida S, Wakamatsu M, Watanabe H, Yamanaka T, Yamamoto H (2003) Report on investigation of vent and methane seep ecosystems by the crewed submersible 'Shinkai 2000' and the ROV 'Dolphin 3 K' on the Hatoma and the Kuroshima Knolls, the Nansei-shoto area, JAMSTEC. J Deep Sea Res 22:21–30 (in Japanese with English abstract)

Fujikura K, Sasaki T, Yamanaka T, Yoshida T (2009) Turrids whelk, *Phymorhynchus buccinoides* feeds on *Bathymodiolus* mussels at a seep site in Sagami Bay, Japan. Plankton Benthos Res 4(1):23–30

Fujikura K, Okutani T, Maruyama T (2012) Deep-sea Life: Biological observations using research submersibles, 2nd edn. Toukai University Press, Toukai (in Japanese with English captions)

Fujiwara Y, Takai K, Uematsu K, Tsuchida S, Hunt JC, Hashimoto J (2000) Phylogenetic characterization of endosymbionts in three hydrothermal vent mussels: influence on host distributions. Mar Ecol Prog Ser 208:147–155. doi:10.3354/meps208147

Gamo T, Sakai H, Kim ES, Shitashima K, Ishibashi J (1991) High alkalinity due to sulfate reduction in the clam hydrothermal field, Okinawa trough. Earth Planet Sci Lett 107:328–338

Gamo T, Chiba H, Yamanaka T, Okudaira T, Hashimoto J, Tsuchida S, Ishibashi J, Kataoka S, Tsunogai U, Kouzuma F, Okamura K, Sano Y, Shinjo R (2001) Chemical characteristics of newly discovered black smoker fluids and associated hydrothermal plumes at the Rodriguez Triple Junction, Central Indian Ridge. Earth Planet Sci Lett 193:371–379. doi:10.1016/S0012-821X(01)00511-8

Glasby GP, Iizasa K, Yuasa M, Usui A (2000) Submarine hydrothermal mineralization on the Izu-Bonin Arc, south of Japan: an overview. Mar Georesources Geotechnol 18(2):141–176. doi:10.1080/10641190009353785

Hashimoto J, Ohta S, Gamo T, Chiba H, Yamaguchi T, Tsuchida S, Okudaira T, Watabe H, Yamanaka T, Kitazawa M (2001) First hydrothermal vent communities from the Indian Ocean Discovered. Zool Sci 18(5):717–721. doi:10.2108/zsj.18.717

Hattori M, Kanie Y, Oba T, Akimoto K (1996) Environmental conditions of carbonates and chemosynthetic animal communities associated with cold seepage zones along the subduction zone in Sagami Bay, central Japan. Kaseki 60:13–22 (in Japanese with English abstract and captions)

Hübner H (1986) Isotope effects on nitrogen in the soil and biosphere. In: Fritz P, Fontes JC (eds) Handbook of environmental isotope geochemistry, vol 2. Elsevier, Amsterdam, pp 361–425

Iizasa K (1993) Assessment of the hydrothermal contribution to seafloor sediments in the Myojinsho submarine caldera, Shichito-Iwojima ridge, Izu-Ogasawara arc, Japan. Mar Geol 114 (1–2):119–132. doi:10.1016/0025-3227(93)90043-U

Ishibashi J, Toki T (2012) Chemistry of deep-sea. In: Fujikura K, Okutani T, Maruyama T (eds) Deep-sea life: biological observations using research submersibles, 2nd edn. Toukai University Press, Toukai, pp 10–23 (in Japanese with English captions)

Ishibashi J, Urabe T (1995) Hydrothermal activity related to arc–backarc magmatism in the western Pacific. In: Taylor B (ed) Backarc basins: tectonics and magmatism. Plenum, New York, pp 451–495

Ishibashi J, Sano Y, Wakita H, Gamo T, Tsutsumi M, Sakai H (1995) Helium and carbon geochemistry of hydrothermal fluids from the Mid-Okinawa Trough Back Arc Basin, southwest of Japan. Chem Geol 123(1–4):1–15. doi:10.1016/0009-2541(95)00051-M

Kakegawa T, Utsumi M, Marumo K (2008) Geochemistry of sulfide chimneys and basement pillow lavas at the Southern Mariana Trough (12.55 degrees N-12.58 degrees N). Resource Geol 58(3):249–266. doi:10.101/j.1751-3928.2008.00060.x

Kato S, Yanagawa K, Sunamura M, Takano Y, Ishibashi J, Kakegawa T, Utsumi M, Yamanaka T, Toki T, Noguchi T, Kobayashi K, Moroi A, Kimura H, Kawarabayasi Y, Marumo K, Urabe T, Yamagishi A (2009) Abundance of Zetaproteobacteria within crustal fluids in back-arc hydrothermal fields of the Southern Mariana Trough. Environ Microbiol 11(12):3210–3222. doi:10.1111/j.1462-2920.2009.02031.x

Kawagucci S, Shirai K, Lan TF, Takahata N, Tsunogai U, Sano Y, Gamo T (2010) Gas geochemical characteristics of hydrothermal

plumes at the HAKUREI and JADE vent sites, the Izena Cauldron, Okinawa Trough. Geochem J 44:507–518

Kawagucci S, Ueno Y, Takai K, Toki T, Ito M, Inoue K, Makabe A, Yoshida N, Muramatsu Y, Takahata N, Sano Y, Narita T, Teranishi G, Obata H, Nakagawa S, Nunoura T, Gamo T (2013) Geochemical origin of hydrothermal fluid methane in sediment-associated fields and its relevance to the geographical distribution of whole hydrothermal circulation. Chem Geol 339:213–225. doi:10.1016/j.chemgeo.2012.05.003

Kelley DS, Karson JA, Früh-Green GL, Yoerger D, Shank TM, Butterfield DA, Hayes JM, Schrenk MO, Olson E, Proskurowski G, Jakuba M, Bradley A, Larson B, Ludwig K, Glickson D, Buckman K, Bradley AS, Brazelton WJ, Roe K, Elend MJ, Delacour A, Bernasconi SM, Lilley MD, Baross JA, Summons RE, Sylva SP (2005) A Serpentinite-hosted ecosystem: the lost city hydrothermal field. Science 307:1428–1434.

Kennicutt MC II, Burke RA Jr, MacDonald IR, Brooks JM, Denoux GJ, Macko SA (1992) Stable isotope partitioning in seep and vent organisms – chemical and ecological significance. Chem Geol 101:293–310. doi:10.1016/0009-2541(92)90009-T

Kim ES, Sakai H, Hashimoto J, Yanagisawa F, Ohta S (1989) Sulfur isotopic-ratios of hydrothermal vent-animals at Ogasawara Arc and Mid-Okinawa Trough – evidence for microbial origin of hydrogen sulfide at low-temperature submarine hydrothermal areas. Geochem J 23:195–208

Kim ES, Sakai H, Gamo T, Hashimoto J, Ohta S, Yanagisawa F (1990) Carbon, nitrogen and sulfur isotopic ratios in hydrothermal vent animals from the mid-Okinawa Trough. JAMSTEC Deesea res 6:129–137 (in Japanese with English abstract and captions)

Konno U, Tsunogai U, Nakagawa F, Nakaseama M, Ishibashi J, Nunoura T, Nakamura K (2006) Liquid CO_2 venting on the seafloor: Yonaguni Knoll IV hydrothermal system, Okinawa Trough. Geophys Res Lett 33, L16607. doi:10.1029/2006GL026115

Lee RW, Childress JJ (1994) Assimilation of inorganic nitrogen by marine invertebrates and their chemoautotrophic and methanotrophic symbionts. Appl Environ Microbiol 60:1852–1858

Letouzey J, Kimura M (1986) The Okinawa Trough: genesis of a back-arc basin developing along a continental margin. Tectonophysics 125:209–230

Mae A, Yamanaka T, Shimoyama S (2007) Stable isotope evidence for identification of chemosynthesis-based fossil bivalves associated with cold-seepages. Palaeogeogr Palaeoclimatol Palaeoecol 245:411–420. doi:10.1016/j.palaeo.2006.09.003

Markert S, Arndt C, Felbeck H, Becher D, Sievert SM, Hugler M, Albrecht D, Robidart J, Bench S, Feldman RA, Hecker M, Schweder T (2007) Physiological proteomics of the uncultured endosymbiont of *Riftia pachyptila*. Science 315:247–250. doi:10.1126/science.1132913

Masuzawa T (1996) Cycling and isotopic composition of sulfur in deep sea cold seep communities. Gekkan Chikyu Gohgai 16:81–86 (in Japanese)

Masuzawa T, Handa N, Kitagawa H, Kusakabe M (1992) Sulfate reduction using methane in sediments beneath a bathyal "cold seep" giant clam community off Hatsushima Island, Sagami Bay, Japan. Earth Planet Sci Lett 110(1–4):39–50. doi:10.1016/0012-821X(92)90037-V

Minagawa M, Wada E (1984) Stepwise enrichment of ^{15}N along food chains: further evidence and the relation between $\delta^{15}N$ and animal age. Geochim Cosmochim Acta 48:1135–1140. doi:10.1016/0016-7037(84)90204-7

Miura T, Nedachi M, Hashimoto J (2002) Sulphur sources for chemoautotrophic nutrition of shallow water vestimentiferan tubeworm in Kagoshima Bay. J Mar Biol Assoc UK 82:537–540. doi:10.1017/S0025315402005854

Mizota C, Yamanaka T (2003) Strategic adaptation of a deep-sea, chemosynthesis-based animal community: an evaluation based on soft body part carbon, nitrogen, and sulfur isotopic signatures. Jpn J Benthol 58:56–69 (in Japanese with English abstract)

Mizota C, Maki Y (1998) Sulfur isotopic variations in soft tissues of Calyptogena soyoae from Sagami Bay, central Japan. Geochem J 32:421–425

Mizota C, Shimoyama S, Yamanaka T (1999) An isotopic characterization of sulfur uptake by benthic animals from Tsuyazaki inlet, northern Kyushu. Jpn Benthos Res 54:81–85

Naraoka H, Naito T, Yamanaka T, Tsunogai U, Fujikura K (2008) A multi-isotope study of deep-sea mussels at three different hydrothermal vent sites in the northwestern Pacific. Chem Geol 255:25–32. doi:10.1016/j.chemgeo.2008.05.015

Nelson DC, Fisher CR (1995) In: Karl DM (ed) Chemoauto- trophic and Methanotrophic Endosymbiotic bacteria at deep-sea vents and seeps: the microbiology of deep-sea hydrothermal vent habitats. CRC, Boca Raton, pp 125–167

Nishijima M, Lindsay DJ, Hata J, Nakamura A, Kasai H, Ise Y, Fisher CR, Fujiwara Y, Kawato M, Maruyama T (2010) Association of Thioautotrophic bacteria with deep-sea sponges. Mar Biotechnol 12:253–260. doi:10.1007/s10126-009-9253-7

Ohara Y, Reagan MK, Fujikura K, Watanabe H, Michibayashi K, Ishii T, Stern RJ, Pujana I, Martinez F, Girard G, Ribeiro J, Brounce M, Komori N, Kino M (2012) A serpentinite-hosted ecosystem in the Southern Mariana Forearc. Proc Natl Acad Sci USA 109 (8):2831–2835. doi:10.1073/pnas.102005109

Okutani T, Soh W (2005) Calyptogena (Archivesicd) garuda, a magnificent new species of Vesicomyid Bivalve from the Java Trench, Indonesia. Venus J Malacol Soc Japan 64(1–2):23–29

Page HM, Fisher CR, Childress JJ (1990) Role of filter-feeding in the nutritional biology of a deep-sea mussel with methanotrophic symbionts. Mar Biol 104(2):251–257. doi:10.1007/BF01313266

Page HM, Fiala-Medioni A, Fisher CR, Childress JJ (1991) Experimental evidence for filter-feeding by the hydrothermal vent mussel, *Bathymodiolus thermophilus*. Deep Sea Res Part A Oceanogr Res Papers 38(12):1455–1461

Rees CE, Jenkins WJ, Monster J (1978) The sulphur isotopic composition of ocean water sulphate. Geochim Cosmochim Acta 42:377–381. doi:10.1016/0016-7037(78)90268-5

Saino T, Ohta S (1989) $^{13}C/^{12}C$ and $^{15}N/^{14}N$ ratios of vesicomyid lams and a vestimentiferan tube worm in the subduction zone east of Japan. Palaeogeogr Palaeoclimatol Palaeoecol 71:169–178. doi:10.1016/0031-0182(89)90036-9

Sakai H, Gamo T, Endow K, Ishibashi J, Ishizuka T, Yanagisawa F, Kusakabe M, Akagi T, Igarashi G, Ohta S (1987) Geochemical study of the bathyal seep communities at the Hatsushima site, Sagami Bay, central Japan. Geochem J 21:227–236

Sakai H, Gamo T, Kim E-S, Shitashima K, Yanagisawa F, Tsutsumi M, Ishibashi J, Sano Y, Wakita H (1990) Unique chemistry of the hydrothermaql solution in the Mid-Okinawa Trough backark basin. Geophys Res Lett 17:2133–2136. doi:10.1029/GL017i012p02133

Schoell M (1988) Multiple origins of methane in the earth. Chem Geol 71:1–10

Silverman MP, Oyama VI (1968) Automatic apparatus for sampling and preparing gases for mass spectral studies of carbon isotope fractionation during methane metabolism. Anal Chem 40:1833–1837

Takano Y, Kobayashi K, Yamanaka T, Marumo K, Urabe T (2004) Amino acids in 308 °C deep-sea hydrothermal sub-vent at the Suiyo Seamount, Izu-Bonin Arc. Pacific Ocean Earth Planet Sci Lett 219:147–153. doi:10.1016/S0012-821X(03)00699-X

Thode HG (1988) Sulphur isotopes in nature and the environment: an overview. In: Krouse HR, Grinenko VA (eds) Stable isotopes: natural and anthropogenic sulphur in the environment. SCOPE43, Wiley, Chichester, pp 7–26

Tsugaru R, Tamaki Y, Sato M, Kimura M, Shimamura K (1991) Report on DELP 1988 cruises in the Okinawa Trough: part 4, preliminary report on the sediment samples. Bull Earthquake Res Inst 66:71–89

Tsunogai U, Yoshida N, Ishibashi J, Gamo T (2000) Carbon isotopic distribution of methane in deep-sea hydrothermal plume, Myojin Knoll Caldera, Izu-Bonin arc: implications for microbial methane oxidation in the oceans and applications to heat flux estimation. Geochim Cosmochim Acta 64:2439–2452. doi:10.1016/S0016-7037(00)00374-4

Tsunogai U, Toki T, Nakayama N, Gamo T, Kato H, Kaneko S (2003) WHATS: a new multi-bottle gas-tight sampler for sea-floor vent fluids. Chikyukagaku (Geochemistry) 37(3):101–109 (in Japanese with English abstract)

Tsunogai U, Nakagawa F, Gamo T, Ishibashi J (2005) Stable isotopic compositions of methane and carbon monoxide in the Suiyo hydrothermal plume, Izu-Bonin arc: Tracers for microbial consumption/production. Earth Planet Sci Lett 237:326–340

Tsunogai UA, Kosaka N, Nakayama DD, Komatsu U, Konno S, Kameyama F, Nakagawa H, Sumino K, Nagao KF, Machiyama H (2010) Origin and fate of deep-sea seeping methane bubbles at Kuroshima Knoll, Ryukyu forearc region, Japan. Geochem J 44 (6):461–476

Van Dover CL (2000) The ecology of deep-sea hydrothermal vents. Princeton University Press, New Jersey, p 424

Van Dover CL, Humphris SE, Fornari D, Cavanaugh CM, Collier R, Goffredi SK, Hashimoto J, Lilley MD, Reysenbach AL, Shank TM, Von Damm KL, Banta A, Gallant RM, Götz D, Green D, Hall J, Harmer TL, Hurtado LA, Johnson P, McKiness ZP, Meredith C, Olson E, Pan IL, Turnipseed M, Won Y, Young CR III, Vrijenhoek RC (2001) Biogeography and ecological setting of Indian Ocean hydrothermal vents. Science 294:818–823. doi:10.1126/science.1064574

Von Damm KL, Edmond JM, Grant B, Measures CI, Walden B, Weiss RF (1985) Chemistry of submarine hydrothermal solutions at 21°N, East Pacific Rise. Geochim Cosmochim Acta 49:2197–2220. doi:10.1016/0016-7037(85)90222-4

Wheat CG et al (2003) Hydrothermal venting in the southernmost portion of the Mariana backarc spreading center at 12°57′N. Eos Trans AGU 84(46), Fall Meet. Suppl., Abstract V32A-0920

Yamanaka T, Murae T, Chiba H (1999) Isotopic fractionation of sulfur in micro zones of tidal flat sediments. Geochem J 33 (2):89–99

Yamanaka T, Shimoyama S, Mizota C (2000a) An evaluation of source sulfur in soft tissues of marine and freshwater benthic animals from Japan using stable isotope analysis. Benthos Res 55:17–22

Yamanaka T, Mizota C, Maki Y, Fujikura K, Chiba H (2000b) Sulfur isotope composition of soft tissues of deep-sea mussels, *Bathymodiolus* spp., in Japanese waters. Benthos Res 55:63–68

Yamanaka T, Mizota C, Fujiwara Y, Chiba H, Hashimoto J, Gamo T, Okudaira T (2003a) Sulfur-isotopic composition of the deep-sea mussel *Bathymodiolus marisindicus* from currently active hydrothermal vents in the Indian Ocean. J Mar Biol Assoc UK 83:841–848. doi:10.1017/S0025315403007872h

Yamanaka T, Mizota C, Satake H, Kouzuma F, Gamo T, Tsunogai U, Miwa T, Fujioka K (2003b) Stable isotope evidence for a putative endosymbiont-based lithotrophic *Bathymodiolus* sp. mussel community atop a serpentine seamount. Geomicrobiol J 20(3):185–197. doi:10.1080/01490450390206674

Yamanaka T, Maeto K, Akashi H, Ishibashi J, Miyoshi Y, Okamura K, Noguchi T, Kuwahara Y, Toki T, Tsunogai U, Ura T, Nakatani T, Maki T, Kubokawa K, Chiba H (2013) Shallow submarine hydrothermal activity with significant contribution of magmatic water producing talc chimneys in the Wakamiko Crater of Kagoshima Bay, southern Kyushu, Japan. J Volcanol Geotherm Res 258:74–84. doi:10.1016/j.jvolgeores.2013.04.007

Yanagisawa F, Sakai H (1983) Thermal decomposition of barium sulfate-vanadium pentaoxide-silica glass mixtures for preparation of sulfur dioxide in sulfur isotope ratio measurements. Anal Chem 55:985–987. doi:10.1021/ac00257a046

Yoneyama T, Kamachi K, Yamaya T, Mae T (1993) Fractionation of nitrogen isotopes by glutamine synthetase isolated from spinach leaves. Plant Cell Physiol 34:489–491

Part II

Central Indian Ridge

Tectonic Background of Four Hydrothermal Fields Along the Central Indian Ridge

11

Kyoko Okino, Kentaro Nakamura, and Hiroshi Sato

Abstract

Since the discovery of the Kairei hydrothermal field at the southernmost end of the Central Indian Ridge (CIR) in 2000, only four active hydrothermal vent fields have subsequently been discovered. These four hydrothermal fields show remarkable diversity in the chemical compositions of fluids and associated ecosystems. Focused geophysical mapping and rock sampling indicate that different tectonic setting constrains the different hydrothermal activity for each field. Two hydrothermal fields in the southern CIR are located on the axial rift-valley wall. The hydrogen-rich Kairei hydrothermal field at 25°19′S is constrained by both basaltic magmatism and detachment faulting that exhume ultramafic rocks on a shallow subsurface, whereas no evidence of ultramafic exposure is recognized in the typical mid-ocean ridge type Edmond hydrothermal field at 23°52′S. Two other hydrothermal fields have been newly discovered in the central CIR. The Solitaire field at 19°33′S is located about 2.6 km away from the neo-volcanic zone and is likely influenced by intra-plate volcanism. The Dodo field at 18°20′S is located at the center of the axial valley floor, where a basaltic sheet-lava flow buries the seafloor. The lava morphology and the existence of an adjacent large off-axis seamount support the idea that excess melt is supplied in this segment. The anomalous magmatism is likely influenced by mantle plume components or by a large-offset transform fault just north of the segment. The large diversity found in the four hydrothermal fields along the CIR provides important insights on the tectonic control of global hydrothermal systems.

Keywords

Geological background • Gravity • Hydrothermal system • Indian Ocean • Magnetics • Morphology • Rock geochemistry

K. Okino (✉)
Atmosphere and Ocean Research Institute (AORI), The University of Tokyo, 5-1-5 Kashiwanoha, Kashiwa, Chiba 277-8564, Japan
e-mail: okino@aori.u-tokyo.ac.jp

K. Nakamura
Department of Systems Innovation, School of Engineering, The University of Tokyo, 7-3-1 Hongo, Bunkyo-ku, Tokyo 113-8656, Japan

Precambrian Ecosystem Laboratory (PEL), Japan Agency for Marine-Earth Science and Technology (JAMSTEC), 2-15 Natsushima, Yokosuka, Kanagawa 237-0061, Japan

Submarine Hydrothermal System Research Group, Japan Agency for Marine-Earth Science and Technology (JAMSTEC), 2-15 Natsushima, Yokosuka, Kanagawa 237-0061, Japan

H. Sato
School of Business Administration, Senshu University, 2-1-1 Higashimita, Tama, Kawasaki, Kanagawa 214-8580, Japan

J.-i. Ishibashi et al. (eds.), *Subseafloor Biosphere Linked to Hydrothermal Systems: TAIGA Concept*,
DOI 10.1007/978-4-431-54865-2_11,

11.1 Introduction

The diversity found in global hydrothermal systems in relation to their size, evolution, fluid geochemistry, and associated ecosystems, is largely constrained by the chemical and physical conditions of the sub-seafloor; in particular, the geological and tectonic settings surrounding the system. The TAIGA project team hypothesize that there are four types of sub-seafloor aquifers (TAIGAs: great rivers in Japanese), which are divided based on their representative chemical energy: compounds of sulfur, carbon (methane), iron, and hydrogen (Urabe et al. 2009; Chap. 1). During the TAIGA project, we study each type of sub-seafloor aquifer, in an attempt to reveal how the geological and tectonic setting controls the hydrothermal activity.

The Central Indian Ridge (CIR) is one of the most intensively-studied fields where unique hydrogen-rich hydrothermal vent is known to exist. At present, only four hydrothermal vent fields have been visually confirmed along the CIR; two of which were newly discovered during the TAIGA project. Other plume anomalies have been reported in the water column along the CIR (e.g., Park 2010) and previous German expeditions reported the fossil hydrothermal sites (e.g., Herzig and Pluger 1988; Halbach et al. 1995) The active hydrothermal vent fields are described as follows.

The Kairei hydrothermal field (KHF), located at the southernmost CIR near the Rodriguez Triple Junction (RTJ), was the first directly-observed hydrothermal field in the Indian Ocean (Gamo et al. 2001). The KHF is a black-smoker-type high temperature field, but fluids have an unusually high concentration of H_2 (2.5–8.5 mmol/kg), despite similarities to typical basalt-hosted mid-ocean ridge hydrothermal fluids in its other mineral and gas element compositions (Van Dover et al. 2001; Gallant and Von Damm 2006; Kumagai et al. 2008). Takai et al. (2004) proposed that the Kairei ecosystem is sustained by the primary production of hydrogenotrophic, hyperthermophilic methanogens, utilizing H_2 and CO_2 as primary energy and carbon sources.

The Edmond field is another high-temperature hydrothermal field located 160 km north of the KHF in the southern CIR (Van Dover et al. 2001). The H_2 concentration in the Edmond fluid is markedly low, and in the range of typical basalt-hosted hydrothermal fluids (Gallant and Von Damm 2006; Kumagai et al. 2008).

Corresponding to a water-column hydrothermal signal discovered as early as the late eighties and recently (Jean-Baptiste et al. 1992; Kawagucci et al. 2008), two new areas of hydrothermal activity with associated chemosynthetic fauna were newly discovered in 2009 on the CIR at 18–20°S (Nakamura et al. 2012). The Solitaire hydrothermal field extends over an area measuring approximately 50 × 50 m, which is comparable to the areas of the KHF and Edmond fields. Several black smoker discharges have been observed, while most of the hydrothermal emissions are clear fluids. The fluid of the Solitaire field is characterized by a high pH (4.8 measured at 25 °C and 1 atm) and K/Cl ratio, compared to those of typical basalt-hosted hydrothermal fluids (Nakamura et al. 2012). The H_2, CH_4 and CO_2 concentrations are within the range of typical basalt-hosted hydrothermal fields, and the biomass and taxonomical richness of the faunal communities are high.

Another new field, the Dodo hydrothermal field, exists 140 km away from the Solitaire field. In 2009, the fluid emissions were observed within an area covering approximately 15 m in diameter, and high temperature black fluid sprouted directly from cracks in the basaltic sheet lava without the formation of mounds. The concentration of H_2 in the Dodo fluids is notably high (>2 mmol/L), while those of CH_4 and CO_2 are comparable with typical hydrothermal fluids. The K/Cl ratio is also high, and comparable with that of the fluid from Solitaire field. In 2009, only a few hydrothermal vent animals were observed, unlike activity in the Solitaire field. When the Dodo field was revisited in 2013, it was found that the fluid emissions had ceased almost entirely (Kawagucci, Pers. Comm.).

In this chapter, we present the general geological background of these four hydrothermal fields along the CIR and discuss how the tectonic setting constrains hydrothermalism in each site. A summary of the geology, fluid chemistry, and faunal communities for each site is described in Nakamura (Chap. 12), and a detailed description of the rock samples is presented in Sato et al. (Chap. 13) and Morishita et al. (Chap. 14).

11.2 Regional Setting

The Central Indian Ridge (CIR) is a slow- to intermediate-rate spreading system bounding the Somalia, the India, and Capricorn Plates. The full spreading rate ranges from 23 mm/year at 10°N, to 47 mm/year at 25°S (MORVEL: DeMets et al. 2010) and the ridge axis is characterized by an axial valley. The CIR meets the Southwest Indian Ridge and the Southeast Indian Ridge at its southern end, forming a ridge–ridge–ridge triple junction (Rodriguez Triple Junction: RTJ). In the southern CIR, the ridge axis trends in an almost NNW–SSE direction and is segmented by several transform faults and non-transform offsets (Parson et al. 1993; Briais 1995). Briais (1995) describes the detailed axial bathymetry between the RTJ and 20°30′S, and defines the axial segmentation using a sequential numbering system that increases northward starting at the RTJ. In accordance with this paper, we follow the nomenclature of ridge segments and use the prefix CIR-Sx (Fig. 11.1).

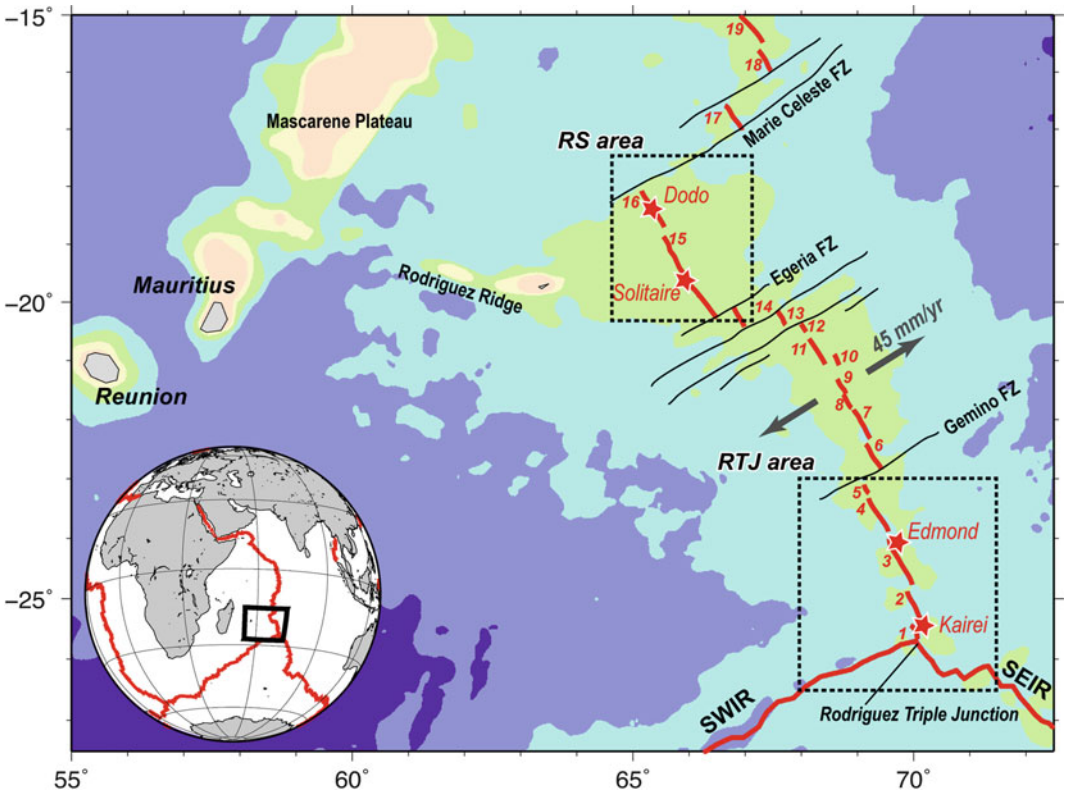

Fig. 11.1 Index map of the Central Indian Ridge (CIR) and adjacent area. *Thick red lines* with numbers indicate segments cited in the text. *Red stars* show the locus of hydrothermal fields. *Two boxes* indicate the areas shown in Figs. 11.2, 11.4, 11.5, and 11.6

The CIR axis gradually shifts westward from CIR-S1 to CIR-S15/S16 and then largely offsets eastward at the Marie Celeste Fracture Zone between CIR-S16 and S17 and further north (Fig. 11.1). CIR-S15 and S16, sometimes known as the Rodrigues Segment (RS), are sandwiched between the Egeria and Marie-Celeste Fracture Zones and both the on- and off-axis areas are shallower than the adjacent normal segments. The unusual elevated and smooth bathymetry, and the geochemical and geophysical characteristics, suggest a hotspot influence on ridge processes, although the Reunion hotspot is presently located 1,000 km away from the CIR (Mahoney et al. 1989; Murton 2005; Nauret et al. 2006; Füri et al. 2011). The Rodrigues Ridge, an WNW-ESE trending volcanic feature (Fig. 11.1), is considered to connect the Reunion-Mauritius hotspot track to the current CIR axis (e.g., Morgan 1978; Dyment et al. 2007).

11.3 Data and Method

11.3.1 Rodriguez Triple Junction (RTJ) Area

Geophysical data were collected during Japanese research cruises KH-93-3, KR00-05, YK01-15, YK05-16, YK09-13, and KH-10-6, from 1993 to 2000. The survey lines are mainly perpendicular to the ridge axis and extend off-axis by 50 km. We compiled all available multibeam bathymetry data to create 50-m grid data. Total geomagnetic field intensity and shipboard gravity data were also obtained along most of the survey lines. We calculated the magnetic anomaly by subtracting the appropriate International Geomagnetic Reference Field models, and then estimated the equivalent magnetization using the three-dimensional inversion method of (Parker and Huestis 1974; Macdonald et al. 1980), assuming a 500-m-thick magnetized layer. We also calculated the free-air gravity anomaly, and then estimated the Mantle Bouguer anomaly by subtracting the predicted gravity effects of the seafloor relief and a 6-km-thick crust from the free-air gravity anomaly (Kuo and Forsyth 1988). Rock samples were also collected along the neo-volcanic zones within the axial valley and on some anomalous off-axis topographic highs, using dredge hauls and submersible dives.

11.3.2 Rodrigues Segment (RS) Area

Bathymetry data were mainly collected during the KH-06-4 cruise and additionally during the cruise of YK13-9.

The off-axis area, located within 50 km from the axis, is covered in CIR-S16, whereas the off-axis coverage is limited in amounts of CIR-S15. We created a 50-m gridded bathymetry for the whole area, and a more precise 25-m grid around two hydrothermal fields. We obtained the total magnetic intensity data mostly along the axial valley, that is not enough to discuss the regional tectonics and calculate the spreading rate. The vector magnetometer data and shipboard gravity data were collected in two cruises but we did not fully analyze the data in TAIGA project. Therefore these are not referred to in this paper. Rock samples were collected along the neo-volcanic zone, using dredge hauls, rock cores, and submersible dives.

11.4 Rodriguez Triple Junction (RTJ) Area

11.4.1 Morphology and Segmentation

Figure 11.2 exhibits the compiled shaded bathymetry map of the Rodriguez Triple Junction (RTJ) area. The present-day ridge axis between the RTJ and 23°S consists of four

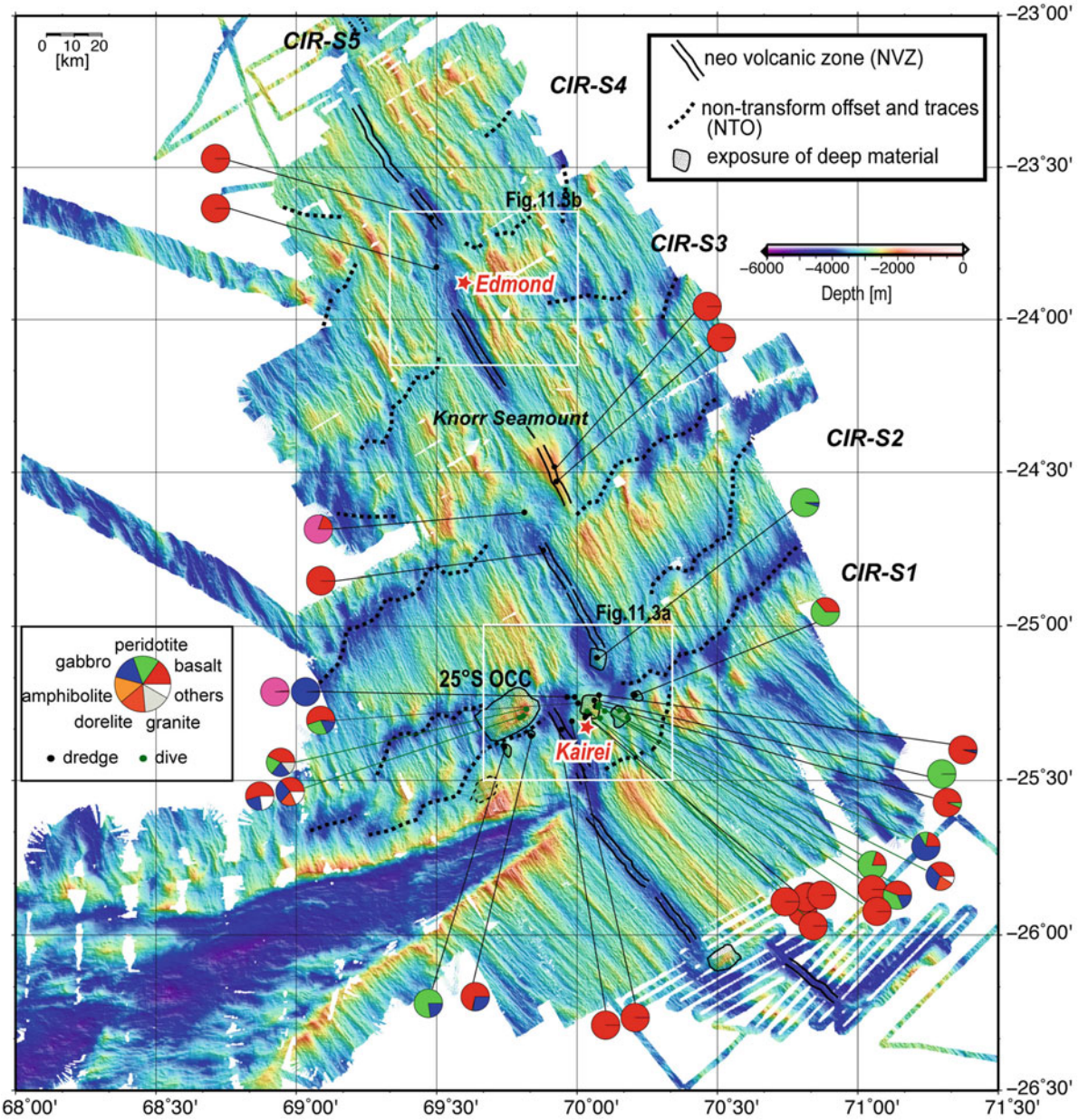

Fig. 11.2 Shaded bathymetry map of the RTJ (Rodriguez Triple Junction) area. Neo-volcanic zone and non-transform offsets are identified for each segment. Both the Kairei and Edmond hydrothermal fields (*red stars*) are located on the axial rift-valley wall. *Pie diagrams* show lithological proportions from dredge and dive collections. *Two white boxes* indicate the areas shown in Fig. 11.3

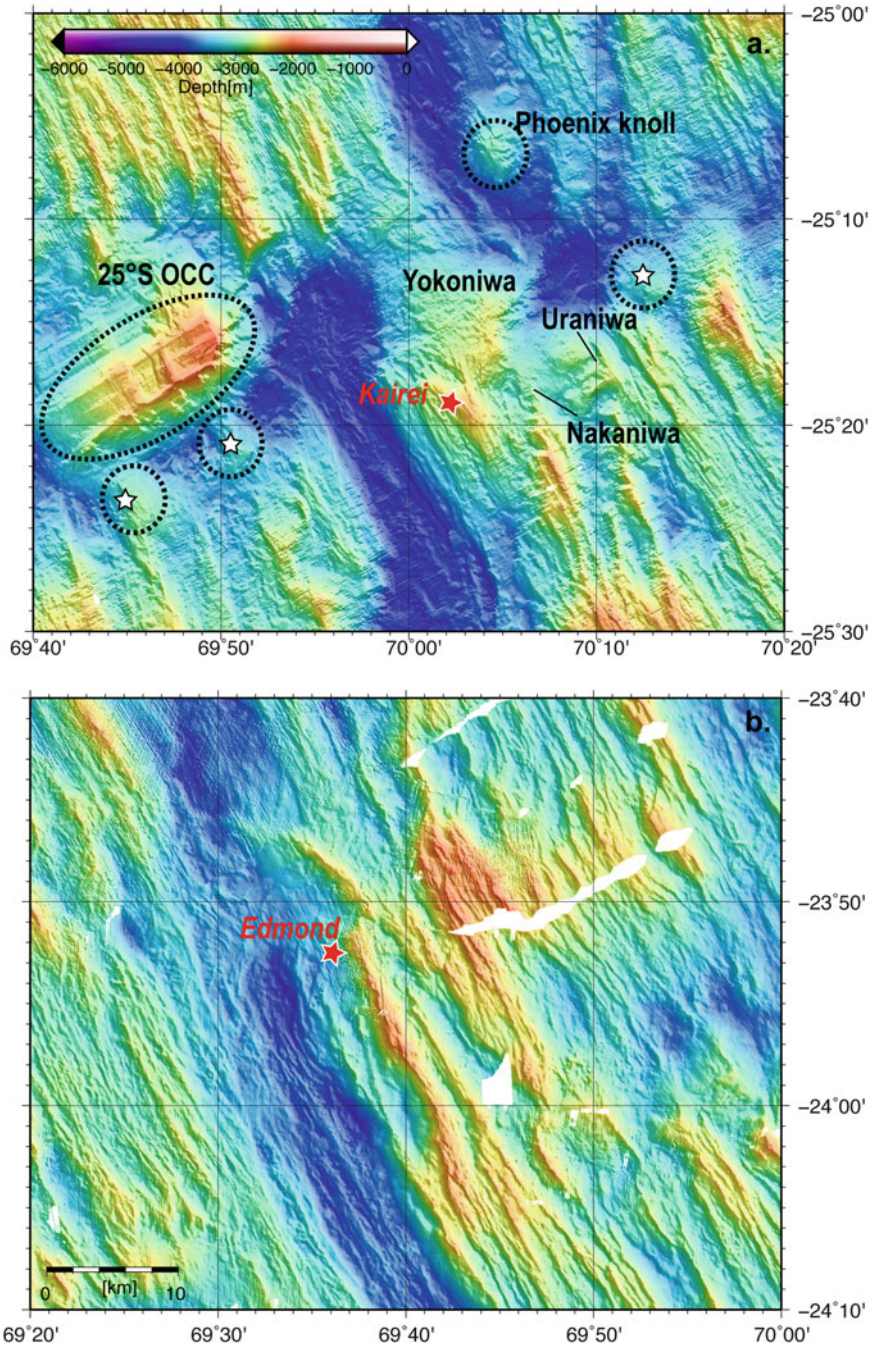

Fig. 11.3 Detailed bathymetry map around the (**a**) Kairei; and (**b**) Edmond, hydrothermal fields. *Dotted circles* are anomalous domed highs near the boundary between CIR-S1 and S2. *White stars* indicate the locations of past NTO massifs where ultramafic rocks were recovered

second-order segments. There is no transform fault in this area and the segments CIR-S1 to S4 are right lateral offset by non-transform discontinuities (NTDs). The axial valley develops at the ridge crest and numerous small, undeformed volcanic cones and flat-topped small volcanic knolls form a neo-volcanic zone.

CIR-S1 is a 20-km segment with a deep axial valley. In contrast to the typical axial morphology, the off-axis area of this segment is highly anomalous. The ridge-parallel abyssal hill pattern is disturbed and several domed highs are distributed along the trace of the NTD between CIR-S1 and S2 (Fig. 11.3a). We recovered deep crust and/or mantle materials on most of these anomalous highs, and interpreted them as modern and remnant NTO (non-transform offset) massifs or oceanic core complexes. They are closely related to the origin of the Kairei hydrothermal field (KHF), and we describe details in Sect. 11.4.4. The segment length shortens, in the farther off-axis, suggesting that the CIR-S1 was newly

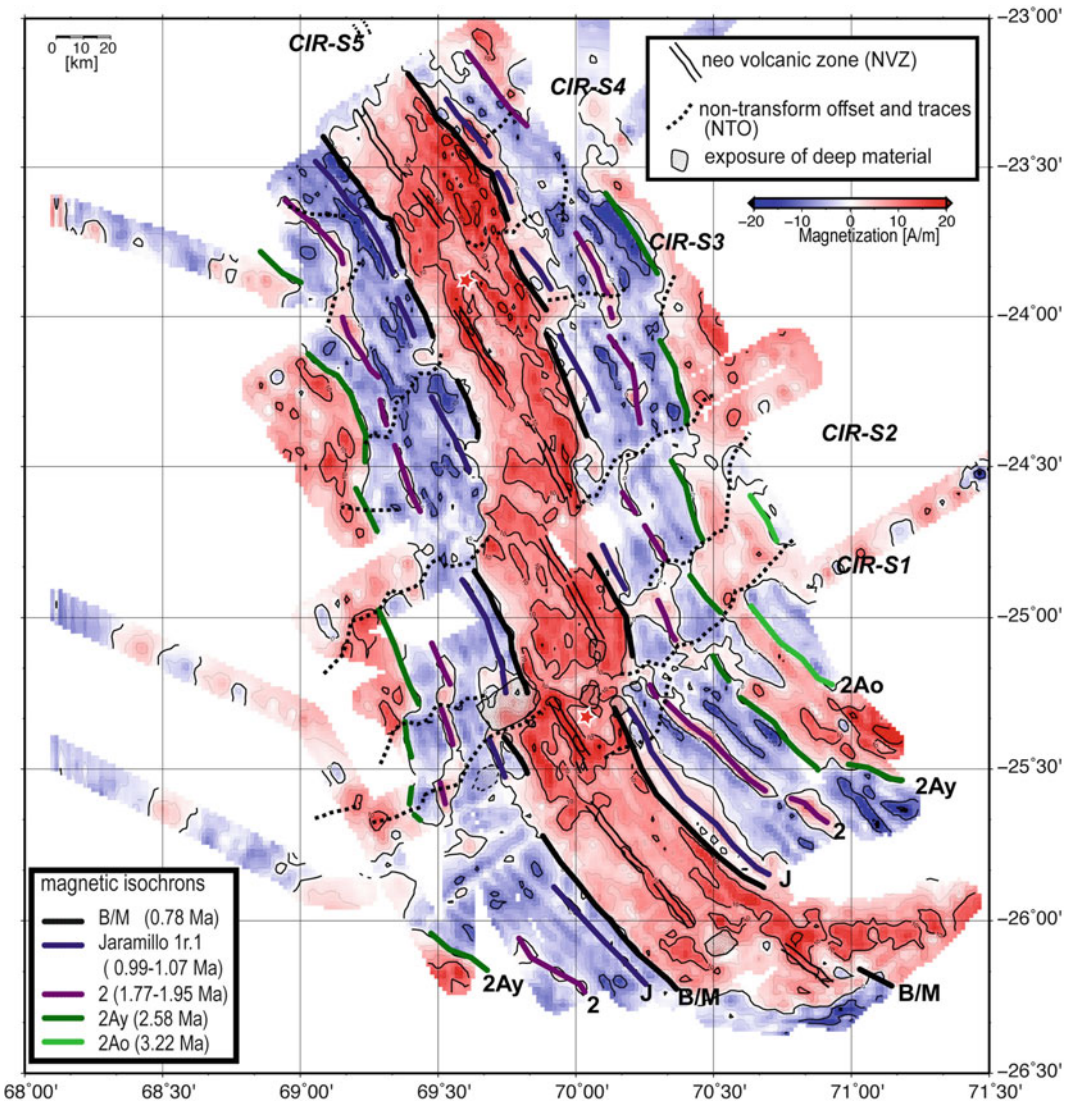

Fig. 11.4 Distribution of magnetization in RTJ area. Contour interval is every 2.5 A/m. Identified magnetic isochrones are superimposed

created during the evolution of the triple junction (Munschy and Schlich 1988; Honsho et al. 1996; Mendel et al. 2000).

CIR-S2 is offset 34 km eastward from CIR-S1. The shallow axial depth around 24°50′S and the concentration of volcanic cones suggest mantle upwelling occurs here. The axial valley appears asymmetric, suggesting a recent jump of neo-volcanic zone eastwards. A unique domed high is located within the southern end of the axial valley, where we recovered fresh and altered peridotite samples (Phoenix knoll in Fig. 11.3a). The off-axis morphology clearly shows that CIR-S2 consisted of two segments in the past. The southern segment progressively shortened and finally vanished, whereas the northern segment lengthened at its expenses. Gac et al. (2006) modeled such a shortening and lengthening of ridge segments. A typical oceanic core complex, the 25°S OCC, was formed in the final phase of the southern segment (Morishita et al. 2009; Sato et al. 2009).

CIR-S3 also shows an anomalous feature at the southern end of the axial valley, where it is filled by the Knorr Seamount, a large triangular-shaped volcano measuring nearly 40-km long (Fig. 11.2). This seamount is volcanic, and a set of parallel rifts has developed at its summit. The off-axis morphology indicates that the segment was also made of two segments in the past, like CIR-S2. The abyssal hill pattern is not symmetric and the magmatic activity appears to be highly variable, particularly in the southern end.

CIR-S4 is only slightly offset from CIR-S3. The axial valley narrows and shallows toward the segment center at

23°20′S, like a typical slow-spreading ridge segment (e.g., Sempéré et al. 1993), suggesting three dimensional mantle upwelling (Lin et al. 1990). Despite the insufficient off-axis coverage, the abyssal hills are shallower in the eastern off-axis near the current segment center.

11.4.2 Magnetics and Gravity

Based on the estimated magnetization distribution (Fig. 11.4), we identified Brunhes/Matuyama (B/M) boundaries (0.78 Ma), the Jaramillo subchron (Chron 1r.1, 0.99–1.07 Ma), Chron 2 (1.77–1.95 Ma) and young and old boundaries of Chron 2A (2.58–3.22 Ma). Chron 2Ao (old) is only recognized in the eastern off-axis of CIR-S1, S2, and in the northernmost segment of SEIR. The neo-volcanic zone in each segment is accompanied by high magnetization stronger than 10 A/m. The neo-volcanic zone of CIR-S1 lies at the center of a positive magnetization zone bounded by the B/M boundaries. In contrast, the neo-volcanic zone with the highest magnetization deviates easterly in CIR-S2, and westerly in CIR-S3 and S4. This observation suggests a recent jump of the volcanic center. In support of this idea, another high magnetization zone is also situated between the eastern B/M boundary and the neo-volcanic zone in CIR-S3 and S4.

The calculated full-spreading rate is 48.5 mm/year in the studied area on average, which is comparable to that of 47 mm/year as predicted by the global plate model (DeMets et al. 2010). A spreading asymmetry is observed for all segments. In CIR-S1, there is no significant difference between our interpretation and that proposed by Mendel et al. (2000). The identification of magnetic isochrones suggests that CIR-S1 was created in ca. Chron 2Ay (2.58 Ma). The off-axis morphology in the northern three segments suggests that the segments each consisted of two segments in the past. Magnetic isochrones support this interpretation, for the isochrones are slightly offset or discontinuous at the traces of the NTDs. Although the exact timing of the amalgamation of the segments differs among the segments, the southern CIR was highly segmented before 1 Ma. This may suggest a change in the mantle upwelling scheme in this region.

The residual mantle Bouguer anomaly map (RMBA, Fig. 11.5) shows a remarkable difference between segments. CIR-S1 is characterized by a high RMBA of around 30 mGal in the off-axis area. This suggests a thin crust and/or a dense material beneath the seafloor, supporting the idea of melt-starved, tectonism dominant, spreading processes. It is also consistent with the existence of an oceanic core complex and other topographic highs with exhumation of mantle materials. The RMBA in CIR-S2 is generally higher in the southern part, and the 25°S oceanic core complex accompanies a very high RMBA. The RMBA is also high at the southern segment end of the present-day ridge axis. CIR-S3 shows a low RMBA along the axial valley. Although we cannot deny the possibility of an inappropriate estimation of plate cooling, we prefer the interpretation that the crust is thicker beneath the Knoll Seamount and recent CIR-S3, and in support of this the abyssal hill morphology also suggests recent robust magmatism in this area. The trace of NTD between CIR-S3 and S4 is clearly accompanied by a high RMBA, suggesting a thinner crust along the segment boundary. CIR-S4 shows relatively a lower RMBA than other segments and clear along-axis variation of RMBA. Although we do not have enough data for the northern segment end, CIR-S4 is a magmatically active slow-spreading type segment, where the mantle upwells at the segment center.

11.4.3 Kairei Hydrothermal Field and Surroundings

The Kairei Hydrothermal Field (KHF) is located about 7 km east of the neo volcanic zone of CIR-S1, on the eastern rift-valley wall (Fig. 11.3a). Due to the presence of a couple of normal faults, the rift-valley wall shows a step-like morphology, and the KHF is located 1,700 m higher than the valley floor on one of these steps. Although the KHF is developed on a typical ridge-parallel structure, the unusual geological features suggest that tectonism-dominant ridge processes spread over the boundary between CIR-S1 and S2.

An anomalous domed high with a corrugated surface was first reported northwest of a deep nodal basin in the northern CIR-S1 (Mitchell et al. 1998) (25°S OCC in Fig. 11.3a). The survey that followed revealed less-deformed serpentinized peridotite exposed on the steep inward slope, and highly deformed rocks widely distributed on the top (Morishita et al. 2009). This observation, and the higher gravity anomaly, support the idea that this domed high is an oceanic core complex (OCC) exposed along a detachment fault. A detailed magnetic analysis showed that the oceanic core complex, known as 25°S OCC, was initiated at the southern inside corner of CIR-S2 during the Matsuyama reversal polarity chron (Sato et al. 2009).

We also discovered another OCC, about 15 km east of the KHF (Fig. 11.3a). Known as Uraniwa Hills, this OCC consists of two domed highs (Kumagai et al. 2008): the northern hill is a rectangular-shaped dome, whereas the southern hill is a more elongated massif with corrugations on the surface. A prominent breakaway ridge bounds the eastern end of this massif. Troctolites and olivine gabbros were sampled at Uraniwa Hills, in addition a dunite (Morishita et al. 2009; Nakamura et al. 2009). A NW-SE trending minor ridge (Nakaniwa Ridge in Fig. 11.3a)

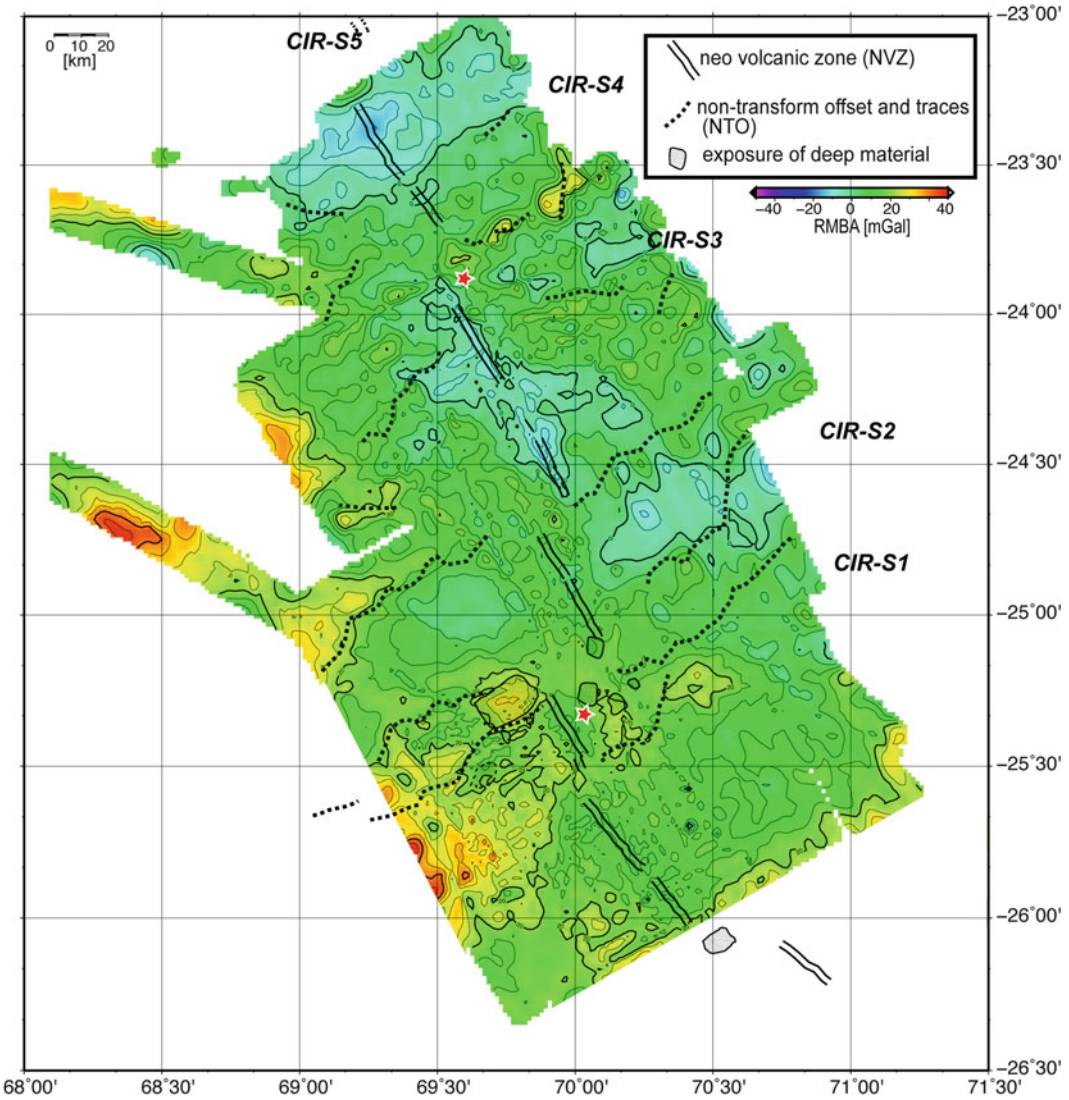

Fig. 11.5 Residual mantle Bouguer anomaly variation of RTJ area. Contour interval is 5 mGal

where gabbroic rocks were also recovered is situated between the Uraniwa Hills and the abyssal hills where the KHF develops.

We observed two deep nodal basins at both the northern segment end of CIR-S1 and at the southern segment end of CIR-S2. Between the two nodal basins, a shallow domed-like massif, has developed. It is 1,700 m high from the rift valley floor and lies oblique-to-parallel to the ridge. High RMBA (Fig. 11.5) and the peridotite exposure on the surface, indicate a very thin magmatic crust beneath this massif and the tectonism-dominant extension of the area. Similar massifs are often observed at NTDs along the Mid-Atlantic Ridge and, are known as NTO (non-transform offset) massifs. Low-angle detachment faults are likely to be the mechanism for the exhumation of deep materials at NTO massifs (Eulalia et al. 2000). The Rainbow and Saldanha hydrothermal sites are located at NTO massifs, where serpentinized peridotite hosts the hydrothermal system supplying hydrogen-rich fluid (Eulalia et al. 2000; Miranda et al. 2003). We named the NTO massif between CIR-S1 and S2 Yokoniwa Rise. During the recent submersible dive, relatively fresh inactive hydrothermal chimneys were discovered on the top. Although the dense CTD tow-yo surveys could not detect any hydrothermal plume anomaly around Yokoniwa, an ultramafic-hosted hydrothermal system probably existed in the recent past.

The Yokoniwa Rise is a current NTO massif, but we also recognized past NTO massifs along the NTD trace between CIR-S1 and S2. One of them is located just south of the 25°S OCC where Hellebrand et al. (2002) reported the exposure of mantle peridotites. The other smaller massifs (white stars in Fig. 11.3a) are also accompanied by ultramafic rocks on the surface, suggesting a common origin of NTO massifs.

Another unusual massif, hereafter known as Phoenix knoll, is located within the axial valley floor of CIR-S2 (Fig. 11.3a). This massif is ~6 km in diameter, with a steeper slope on its western side. We tentatively recognized an ambiguous surface corrugation on the top, but cannot completely deny the possibility of artifact. The dredged samples are mostly serpentinized peridotites. The formation process of the Phoenix knoll is still discussed: Morishita et al. (Chap. 14) propose serpentinite diapirism, whereas the asymmetric structure with its corrugated surface supports the hypothesis of a detachment fault. Ridge-parallel fault scarps cut the massif on its northern slope and undeformed volcanic knolls adjoin the massif. These observations indicate that the segment is now under a normal magmatic spreading phase. The chaotic structure at the current segment boundary and along the NTD trace, strongly suggests an important temporal and spatial variation of the melt supply in this area.

11.4.4 Tectonic Evolution and Hydrothermalism

The hydrothermal fluid of the KHF is unique in its high H_2 and low CH_4 contents (Van Dover et al. 2001; Gallant and Von Damm 2006; Kumagai et al. 2008). In general, the high content of H_2 in the hydrothermal fluid is explained by the generation of H_2 through the serpentinization of ultramafic rocks. Methane is also a product of a series of the serpentinization process, so most H_2 rich hydrothermal fields spout both high H_2 and high CH_4 fluids and are located above the exposure of ultramafic rocks due to tectonic extension. The KHF is just on the ridge-parallel volcanic knoll and is surrounded by basalt lava flows. However, ultramafic rocks are widely exposed around the KHF. Nakamura et al. (2009) proposed that the interaction of seawater with troctolites beneath the Uraniwa Hills explains the composition of the KHF fluids. Their theoretical model predicts that the high H_2, low CH_4, and high Si contents of the KHF fluid can be attributed to serpentinization of the troctolites and the subsequent hydrothermal reactions with basaltic wall rocks under the KHF. Although such an idea explains the KHF fluid geochemistry, it is, however, rather hard to suppose a large scale, across axis circulation from the Uraniwa Hills to the KHF. It is considered likely that a detachment fault exhuming mantle materials on the surface continues to the shallow subsurface beneath the basaltic flow at the KHF, although the fault geometry has to be confirmed. The troctolites and/or other olivine-rich materials may exist in the shallow subsurface beneath the KHF, where the serpentinization process goes on, closely related to the detachment faulting. The relatively high RMBA beneath the KHF supports this idea. The vents of the KHF appear to stand at the foot of an inward facing normal fault scarp. It is likely that the surface normal faults control the position of the upward fluid flow, and that the circulation is driven by the magmatic heat of the neo-volcanic zone. The KHF differs from both the "magma-driven" basalt-hosted hydrothermal fields and the "tectonic-controlled" ultramafic-hosted fields. It is in another category, and is, a magma-assisted, ultramafic hosted, hydrogen-rich hydrothermal system (hydrogen TAIGA).

The Edmond hydrothermal field, located near the northern end of CIR-S3, is similar in that the vent site is located on the eastern rift-valley wall near the NTD (Fig. 11.3b). However, the fluid shows a typical sulfur-rich content, and there is no evidence of ultramafic exposures around the Edmond field (Van Dover et al. 2001; Gallant and Von Damm 2006; Kumagai et al. 2008). Unlike the other hydrothermal fields on fast-spreading ridge, the Edmond filed is not directly linked with the neo-volcanic zone, and the upward fluid path may be controlled by the normal faults of the rift-valley. It is likely that this explains the longevity of the hydrothermal activity (Van Dover et al. 2001), because the circulation path has been constrained by the fault system. The Edmond field is a sulfur-rich hydrothermal system (sulfur TAIGA), hosted by basalt lava and driven by the magmatic heat of the ridge axis, and its circulation path is tectonically controlled.

11.5 Rodrigues Segment (RS) Area: CIR 18-20°S

11.5.1 Morphology and Segmentation

Figure 11.6 exhibits the compiled shaded bathymetry map of the Rodrigues Segment (RS) area. This area is located on the westernmost of the current CIR axis, and is close to the Rodrigues Ridge. The axis is offset by the Marie Celeste Fracture Zone at its northern end, and by the Egeria Fracture Zone at its southern end. Between these two transform faults, the axial valley is relatively continuous. In this area, we were able to define two segments, CIR-S15 and S16, because it was possible to trace the boundary of these segments in the off-axis area. CIR-S15 is a segment measuring ~150-km long, and the axial valley bends at three points. We tentatively named the four parts, CIR-S15A to -S15D.

CIR-S15A shows a slow-spreading ridge morphology, with deep axial valley and well-ordered off-axis abyssal hills. We can easily recognize the continuous neo-volcanic zone at the center of the axial valley. CIR-S15B has an hourglass-shaped axial valley, where the rift-valley narrows toward the center. The axial valley is shallower than in the other parts, suggesting a higher melt supply. The rift-valley wall is extremely asymmetric: the eastern wall consists of steep normal faults and the western side

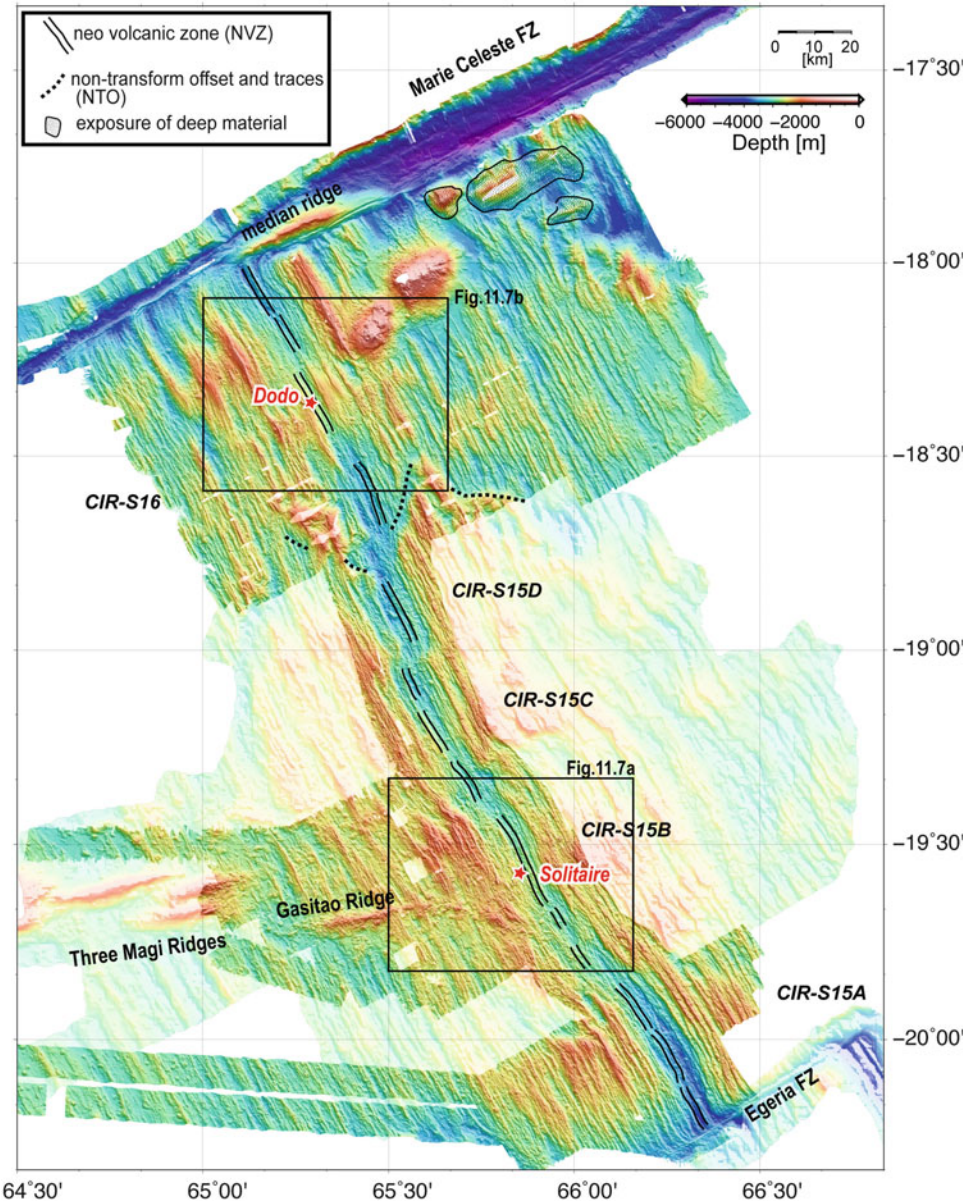

Fig. 11.6 Shaded bathymetry map of the RS (Rodriguez Segment) area. The *pale colored* bathymetry data were collected by previous French cruises (Dyment et al. 1999). Newly discovered Solitaire and Dodo hydrothermal fields are located in a volcanically active zone (*red stars*). *Two black boxes* indicate the areas shown in Fig. 11.7

shows gentle steps on which many small volcanic cones are distributed. An east–west trending volcanic ridge, the Gasitao Ridge (Dyment et al. 1999), exists on the western off-axis of CIR-S15B, and is oblique to both the CIR axis and the direction of plate motion (Fig. 11.6). It appears to erupt above the abyssal hills. The trend and location suggest that the origin of the Gasitao Ridge might be similar to that of the Rodrigues Ridge (Morgan 1978) in the west (Fig. 11.1), and is related to the mantle plume from the Reunion hotspot (Dyment et al. 1999). The Gasitao Ridge ends at 65°40′E to its east, but a zone of small volcanic knolls extends toward the axis of CIR-S15B (Cordier et al. 2010, described in greater detail in Sect. 11.5.3). CIR-S15C and S15D show a more symmetrical morphology. CIR-S15C shows a shallow and narrow axial valley floor at its center, suggesting that S15C is magmatically active at present.

CIR-S16 also shows recent vigorous volcanism. The typical neo-volcanic zone consisting of hummocks and aggregated hummocks (Fig. 11.7b), is developed near the segment ends; the axial depth becomes shallow toward the segment center, where smooth, flat sheet-flow lava buries the whole rift-valley floor. The latter morphology resembles that observed in the fast-spreading ridge crest, suggesting a higher melt supply. The off-axis area is much more anomalous. We discovered a large off-axis seamount east of CIR-S16, with diameter of 15–20 km and a summit depth shallower than 700 m. It is clear that the seamount erupted in the off-axis area, because the volcanic materials cover the underlying abyssal hill fabric and no

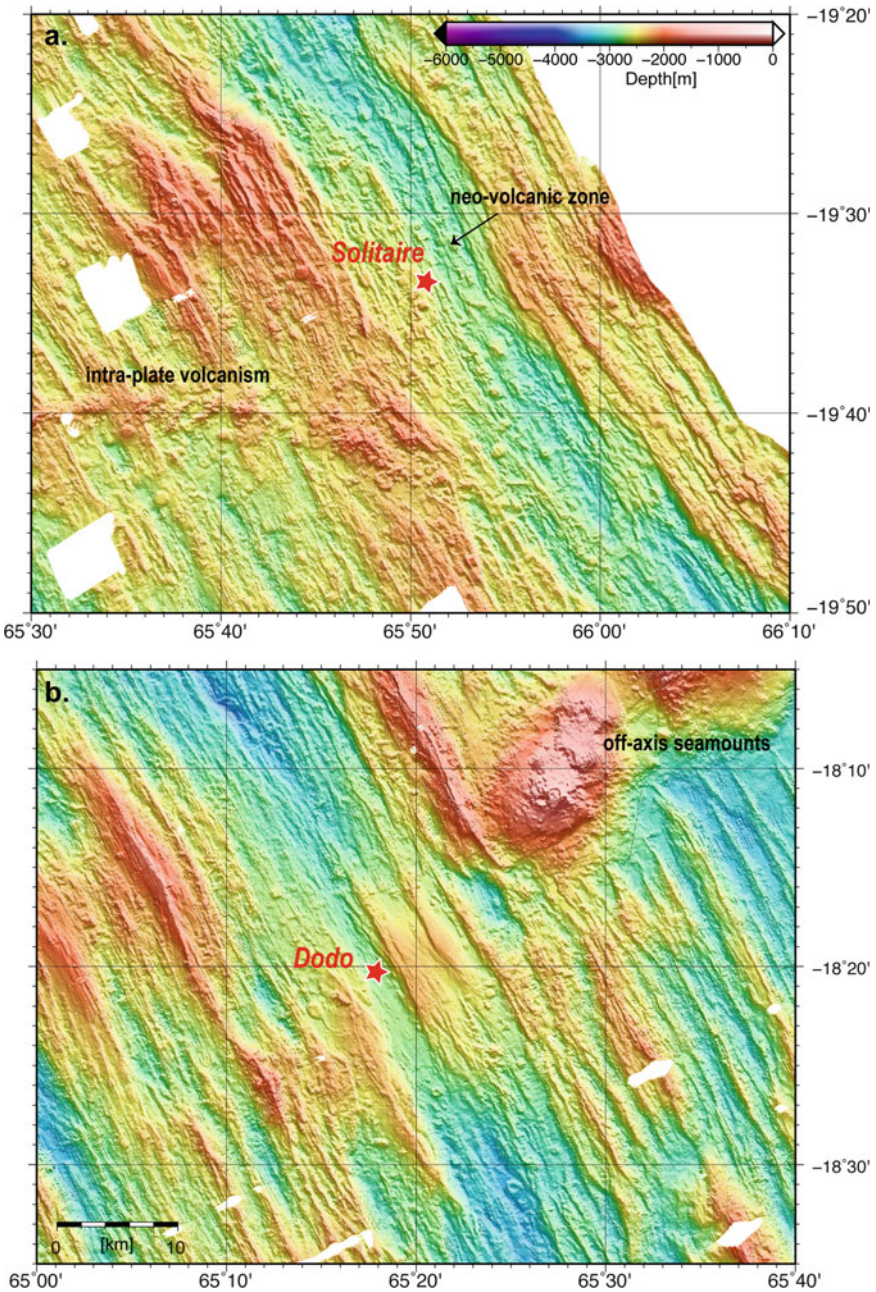

Fig. 11.7 Detailed bathymetry map around the (**a**) Solitaire and (**b**) Dodo hydrothermal fields

ridge-parallel normal faults deform them. Similar large off-axis seamounts, the Lamont Seamounts, have been discovered on the East Pacific Rise near to long-offset transform faults (Fornari et al. 1988) , with a magmatically-active nearby ridge segment (Scheirer and Macdonald 1995). This similarity suggests that a long-offset transform fault may play a key role in transferring water from the seafloor to underneath the mantle, promoting melting. East of the off-axis seamounts we identified a few dome-like (or elongated) highs, with flow-line parallel corrugations on their tops. Although no rock samples were recovered from these massifs, they are interpreted to be oceanic core complexes, where the melt supply is limited and the mantle materials are exhumed along detachment faults. This observation suggests that the temporal variation of melt supply is very large in northern CIR-S16.

11.5.2 Rock Geochemistry

The RS area has been studied as a case of distal hotspot-ridge interaction. The Rodrigues Ridge, Three Magi Ridge and Gasitao Ridge topographically connect the Reunion hotspot track and the CIR and the RS area shows relatively shallow depths suggesting higher melt supply. However the origin of these intra-plate ridges and the style of distal

hotspot-ridge interaction are still the subject of debate. Some previous studies (Mahoney et al. 1989; Murton 2005) proposed that a northward enrichment of incompatible elements and radiogenic isotopes within the basalts in CIR-S15 and S16 suggest the inflow of channelized plume material supplied from the Reunion hotspot. Nauret et al. (2006) showed that Pb isotopes become more radiogenic from south to north, and incompatible trace elements become more enriched, but the composition of Reunion lavas is not a suitable end member for the Pb isotope and Ba/Nb trend. They concluded that the geochemical trend seen along the ridge axis is not related to Reunion-type plume material and the geochemical anomaly on the RS area is a result of mixing of the Reunion plume and depleted mantle. However, their argument is based on only one sample obtained from CIR-S15B. Machida et al. (in press) analyzed a lot of basalt samples from CIR-S15 and S16, and proposed that two melt components mainly control the geochemical signature: a radiogenically enriched component characterized by the Rodrigues Ridge or intermediate series of Mauritius island, and a radiogenically depleted component characterized by the Gasitao Ridge. Their results suggest that the mantle heterogeneity can explain the geochemical anomaly of the RS area but this does not require a channelized plume flow expected from the morphology. Cordier et al. (2010) reported the occurrence of ancient lavas enriched in incompatible elements distributed symmetrically on either side of the ridge whereas on-axis samples are typical N-MORB, using on- and off-axis basalt samples collected across CIR-15B. They proposed that the geochemical variations of zero-age basalts may primarily reflect periodic processes rather than the spatial distribution of mantle heterogeneities. Füri et al. (2011) reported significantly higher $^{3}He/^{4}He$ rations between 19° and 20° along the axis, as well as along the Gasitao Ridge, Three Magi Ridges and Rodrigues Ridge, consistent with lateral flow of hot spot mantle from Reunion toward the CIR. However, basaltic lavas sampled at CIR-15B axis, i.e., the intersection of the CIR and the off-axis volcanic structures, show typical N-MORB-like trace element ratios.

11.5.3 Tectonic Background of Hydrothermal Fields

Two hydrothermal fields were discovered in the RS area in 2009 (Nakamura et al. 2012). The Solitaire field (in CIR-S15B) has been observed to consist mainly of clear smokers with high pH (4.8 measured at 25 °C and 1 atm) fluids and a rich faunal community. The Dodo field (in CIR-S16) is characterized by high temperature (356 °C at a maximum), and H_2 rich fluids (>2 mmol/L) spout directly from cracks in the basalt sheet lava.

The Solitaire field is located at the western flank of the CIR-S15B segment center. It was first predicted by a hydrothermal plume anomaly surveyed in the late 1980s (Jean-Baptiste et al. 1992). As described in Sect. 11.5.1, the segment center shows a highly asymmetric structure. The western rift wall shows a gentle step-like morphology (Fig. 11.7a) and the Solitaire field has developed on the step. We also identified a number of volcanic cones on the step, and these are clearly different from the series of hummocks forming the neo-volcanic zone of the CIR axis. These volcanic cones on the step are undeformed and basalt samples with fresh glass were recovered from one of these cones, supporting the idea that the volcanism has recently occurred. Basalts from the neo-volcanic zone range from 8–53 and 5–10 wt.% in SiO_2 and MgO, respectively, and belong to the subalkaline rock series, whereas basalts from the volcanic cones on the step show higher Na_2O and total alkali compositions (Machida et al. in press). They are considered to be a series of similar volcanic knolls extending from the Gasitao Ridge. These observations suggest that the Solitaire field is influenced by intra-plate volcanism related to the mantle plume or mantle heterogeneity.

The Dodo field, on the other hand, is located just on the neo-volcanic zone of CIR-S16, where smooth sheet-flow lava covers an area of about 70 km^2 (Fig. 11.7b). The lava morphology suggests a high flux of eruption (Gregg and Fink 1995) which is typical of fast-spreading ridges, despite a relatively slow spreading rate (average full rate of ~43 km/Myr). We recognized several fissures on the sheet lava. However, the distribution of vents does not seem to relate to these fissures. The Dodo field was first predicted by the plume anomaly in the water column in 2006 (Kawagucci et al. 2008), and then discovered in 2009 (Nakamura et al. 2012). When we revisited the field in 2013, the fluid venting has already stopped. This observation suggests that the heat supplied by dyke intrusion drives the short-lived hydrothermal circulation, and that the circulation then wanes as the lava cools. The plume anomaly from the Dodo field predicted a high content of hydrogen in the venting fluid (Kawagucci et al. 2008), and this was confirmed by fluid sampling (Nakamura et al. 2012). There are no signs of surface/shallow ultramafic rocks, nor deep-rooted faults, that are usually considered to provide rich hydrogen in hydrothermal fluid. Kawagucci et al. (2008) proposed that serpentinization extensively occurs due to the enormous amount of water supplied from the Marie Celeste fracture zone. However, this idea contradicts the shallow, small-scale circulation at the sheeted basalt sheet-flow, suggested by the geological setting. Although we have not yet understood this type of hydrothermal system, it is a clear illustration of the diversity of hydrogen-rich systems.

11.6 Summary

Four hydrothermal fields along the Central Indian Ridge (CIR) are shown to have different characteristics in their fluid geochemistry and associated ecosystems. Geophysical mapping and rock sampling indicate that the different tectonic setting of each field cause the diversity amongst the hydrothermal systems A summary of the findings of each field is as follows:

1. The Kairei hydrothermal field at 25°19′S is located on the shoulder of the axial valley wall near the northern end of CIR-Seg1. High Bouguer gravity anomaly and the exposures of ultramafic rocks near the KHF suggest that the ultramafic rocks exist below a thin basaltic layer at the KHF. It is likely that the high-H_2 and low-CH_4 contents of the Kairei field are supported by both serpentinization of olivine rich rocks, and a reaction with basalt in the shallow subsurface. The vent site is located at the foot of an inward fault scarp, indicating that the upflow path is controlled by the fault, and it is considered likely that the axial magma drives the circulation.
2. The Edmond hydrothermal field at 23°52′S, located on the shoulder of the axial valley wall at the northern end of CIR-Seg3, is also hosted by basalt. Although the location is similar to that of the Kairei field, no evidence of ultramafic exposure is recognized and the H_2 and CH_4 contents are within the typical range of MOR hydrothermal fluids.
3. The Solitaire field at 19°33′S is located about two miles away from the neo-volcanic zone of CIR-Seg15B. The area shows a unique volcanic environment, where typical MOR neo-volcanic zone activity and intra-plate volcanism coexist at a short distance. The Solitaire field is related to the mantle plume that originated from the Reunion hotspot or to the mantle heterogeneity in this area.
4. The Dodo field at 18°20′S is located at the center of the axial valley floor of CIR-Seg16. The axial valley of the segment center is covered by large-scale basaltic sheet-flow lava, which is distinct from that of typical slow spreading ridges. The morphology and adjacent large off-axis seamounts support the idea that excess melt is supplied in this segment. It is likely that this anomalous magmatism is influenced by mantle plume or by a large-offset transform fault just north of the segment. The concentration of H_2 in the Dodo fluids is notably high, and this is quite atypical for a basalt-hosted hydrothermal system.

The large diversity found among the four known active hydrothermal fields along the southern CIR provides important insights on the tectonic and magmatic control of hydrothermal systems.

Acknowledgements We are grateful to the operation teams of the submersible *SHINKAI 6500* and *AUV r2D4*, and to the crew of the *R/V HAKUHO MARU* and *R/V YOKOSUKA*, for their skilled and proficient acquisition of data. We also thank two reviewers to provide us many valuable comments. The authors wish to thank Prof. Urabe, and members of Project TAIGA, for their collaboration and useful discussions. This study was supported by the Ministry of Education, Culture, Sports, Science and technology (MEXT), Grant-in-Aid for Scientific Research on Innovative Areas "Project TAIGA: Trans-crustal Advection and In-situ biogeochemical process of Global subseafloor Aquifer" (20109002).

References

Briais A (1995) Structural-analysis of the segmentation of the Central-Indian-Ridge between 20-degrees-30′s and 25-degrees-30′s (Rodriguez-Triple-Junction). Mar Geophys Res 17(5):431–467

Cordier C, Benoit M, Hemond C, Dyment J, Le Gall B, Briais A, Kitazawa M (2010) Time scales of melt extraction revealed by distribution of lava composition across a ridge axis. Geochem Geophys Geosyst 11. doi:10.1029/2010gc003074

DeMets C, Gordon RG, Argus DF (2010) Geologically current plate motions. Geophys J Int 181(1):1–80. doi:10.1111/j.1365-246X.2009.04491.x

Dyment J, Gallet Y, The M. 2 Scientific Party (1999) The Magofond 2 cruise: a surface and deep-tow survey on the past and present Central Indian Ridge. InterRidge News 8(1):25–30

Dyment J, Lin J, Baker ET (2007) Ridge–hotspot interactions. Oceanography 20(1):102–115

Eulalia G, Charlou JL, Radford-Knoery J, Parson LM (2000) Non-transform offsets along the Mid-Atlantic Ridge south of the Azores (38 N–34 N): ultramafic exposures and hosting of hydrothermal vents. Earth Planet Sci Lett 177:89–103

Fornari DJ, Perfit MR, Allan JF, Batiza R, Haymon R, Barone A, Ryan WBF, Smith T, Simkin T, Luckman MA (1988) Geochemical and structural studies of the Lamont seamounts: seamounts as indicators of mantle processes. Earth Planet Sci Lett 89(1):63–83. doi:10.1016/0012-821X(88)90033-7

Füri E, Hilton DR, Murton BJ, Hémond C, Dyment J, Day JMD (2011) Helium isotope variations between Réunion Island and the Central Indian Ridge (17°–21°S): new evidence for ridge–hot spot interaction. J Geophys Res 116(B2):B02207. doi:10.1029/2010JB007609

Gac S, Tisseau C, Dyment J, Goslin J (2006) Modelling the thermal evolution of slow-spreading ridge segments and their off-axis geophysical signature. Geophys J Int 164(2):341–358. doi:10.1111/j.1365-246X.2005.02844.x

Gallant RM, Von Damm KL (2006) Geochemical controls on hydrothermal fluids from the Kairei and Edmond Vent Fields, 23°–25°S, Central Indian Ridge. Geochem Geophys Geosyst 7(6):1–24. doi:10.1029/2005GC001067

Gamo T, Chiba H, Yamanaka T (2001) Chemical characteristics of newly discovered black smoker £ uids and associated hydrothermal plumes at the Rodriguez Triple Junction, Central Indian Ridge. Earth Planet Sci Lett 193:371–379

Gregg TKP, Fink JH (1995) Quantification of submarine lava-flow morphology through analog experiments. Geology 23(1):73. doi:10.1130/0091-7613(1995)023<0073:QOSLFM>2.3.CO;2

Halbach P, Blum N, Pluger W, van Gerven M, Erzinger J, S. 92 S. S. Party (1995) The Sonne field – first massive sulfides in the Indian Ocean. InterRidge News 12–15

Hellebrand E, Snow JE, Hoppe P, Hofmann AW (2002) Garnet-field melting and late-stage refertilization in " Residual " abyssal peridotites from the Central Indian Ridge. J Petrol 43 (12):2305–2338

Herzig PM, Pluger WL (1988) Exploration for hydrothermal activity near the Rodriguez triple junction, Indian Ocean. Can Mineral 26:721–736

Honsho C, Tamaki K, Fujimoro H (1996) Three-dimensional magnetic and gravity studies of the Rodriguez Triple Junction in the Indian Ocean. J Geophys Res Solid Earth 101(96):837–848

Jean-Baptiste P, Mantisi F, Pauwells H, Grimaud D, Patriat P (1992) Hydrothermal 3He and manganese plumes at 1939S on the Central Indian Ridge. Geophys Res Lett 19(17):1787–1790

Kawagucci S, Okamura K, Kiyota K, Tsunogai U, Sano Y, Tamaki K, Gamo T (2008) Methane, manganese, and helium-3 in newly discovered hydrothermal plumes over the Central Indian Ridge, 18°–20°S. Geochem Geophys Geosyst 9(10):1–14. doi:10.1029/2008GC002082

Kumagai H et al (2008) Geological background of the Kairei and Edmond hydrothermal fields along the Central Indian Ridge: implications of their vent fluids' distinct chemistry. Geofluids 8 (4):239–251. doi:10.1111/j.1468-8123.2008.00223.x

Kuo BY, Forsyth DW (1988) Gravity-anomalies of the ridge-transform system in the South-Atlantic between 31°S and 34.5°S – upwelling centers and variations in crustal thickness. Mar Geophys Res 10(3–4):205–232

Lin J, Purdy GM, Schouten H, Sempere J-C, Zervas C (1990) Evidence from gravity data for focused magmatic accretion along the Mid-Atlantic Ridge. Nature 344:627–632

Macdonald KC, Miller SP, Huestis SP, Spiess FN (1980) 3-Dimensional modeling of a magnetic reversal boundary from inversion of deep-tow measurements. J Geophys Res 85(NB7):3670–3680

Machida S, Orihashi Y, Magnani M, Neo N, Wilson S, Tanimizu M, Yoneda S, Atsushi Y, Tamaki K (in press) Regional mantle heterogeneity regulates melt production along the Reunion hotspot-influenced Central Indian Ridge. Geochem J

Mahoney JJ, Natland JH, White WM, Poreda R, Bloomer SH, Fisher RL, Bzxter AN (1989), Isotopic and geochemical provinces of the western Indian Ocean Spreading Centers. J Geophys Res Solid Earth 94(88):4033–4052

Mendel V, Sauter D, Patriat P, Munschy M (2000) Evolution of the Central Indian Ridge segmentation with the evolution of the Rodrigues Triple Junction for the past 8 Myr. J Geophys Res 105 (B7):16563–16575

Miranda JM, Silva PF, Lourenço N, Henry B, Costa R, Team S (2003) Study of the Saldanha Massif (MAR, 36° 34 N): constrains from rock magnetic and geophysical data. Mar Geophys Res 23:299–318

Mitchell NC, Escartín J, Allerton S (1998) Detachment faults at mid-ocean ridges garner interest. EOS Trans AGU 79:127

Morgan WJ (1978) Rodriguez, Darwin, Amsterdam, . . ., a second type of hotspot island. J Geophys Res Solid Earth 83(8):5355–5360

Morishita T, Hara K, Nakamura K, Sawaguchi T, Tamura A, Arai S, Okino K, Takai K, Kumagai H (2009) Igneous, alteration and exhumation processes recorded in Abyssal peridotites and related fault rocks from an oceanic core complex along the Central Indian Ridge. J Petrol 50(7):1299–1325. doi:10.1093/petrology/egp025

Munschy M, Schlich R (1988) The Rodriguez Triple Junction (Indian Ocean): structure and evolution for the past one million years. Mar Geophys Res 11:1–14

Murton BJ (2005) Heterogeneity in southern Central Indian Ridge MORB: implications for ridge–hot spot interaction. Geochem Geophys Geosyst 6(3). doi:10.1029/2004GC000798

Nakamura K, Morishita T, Bach W, Klein F, Hara K, Okino K, Takai K, Kumagai H (2009) Serpentinized troctolites exposed near the Kairei Hydrothermal Field, Central Indian Ridge: Insights into the origin of the Kairei hydrothermal fluid supporting a unique microbial ecosystem. Earth Planet Sci Lett 280(1–4):128–136. doi:10.1016/j.epsl.2009.01.024. 21X09000491

Nakamura K et al (2012) Discovery of new hydrothermal activity and chemosynthetic fauna on the central Indian ridge at 18°–20°s. PLoS One 7(3):e32965. doi:10.1371/journal.pone.0032965

Nauret F, Abouchami W, Galer S, Hofmann A, Hemond C, Chauvel C, Dyment J (2006) Correlated trace element-Pb isotope enrichments in Indian MORB along 18–20°S, Central Indian Ridge. Earth Planet Sci Lett 245(1–2):137–152. doi:10.1016/j.epsl.2006.03.015

Park S-H (2010) Korea national report. InterRidge News 9:34

Parker RL, Huestis SP (1974) Inversion of magnetic-anomalies in presence of topography. J Geophys Res 79(11):1587–1593

Parson LM, Patriat P, Searle RC, Briais AR (1993) Segmentation of the Central Indian Ridge between 12-degrees-12′s and the Indian-Ocean Triple Junction. Mar Geophys Res 15(4):265–282

Sato T, Okino K, Kumagai H (2009) Magnetic structure of an oceanic core complex at the southernmost Central Indian Ridge: analysis of shipboard and deep-sea three-component magnetometer data. Geochem Geophys Geosyst 10(6). doi:10.1029/2008GC002267

Scheirer DS, Macdonald KC (1995) Near-axis seamounts on the flanks of the East Pacific Rise, 8°N to 17°N. J Geophys Res 100 (94):2239–2259

Sempéré JC, Lin J, Brown HS, Schouten H, Purdy GM (1993) Segmentation and morphotectonic variations along a slow- spreading center – the Mid-Atlantic Ridge (24°00′N–30°40′N). Mar Geophys Res 15(3):153–200

Takai K, Gamo ÆT, Tsunogai ÆU (2004) Geochemical and microbiological evidence for a hydrogen-based , hyperthermophilic subsurface lithoautotrophic microbial ecosystem (HyperSLiME) beneath an active deep-sea hydrothermal field. Extremophiles 269–282. doi:10.1007/s00792-004-0386-3

Urabe T, Okino K, Sunamura M, Ishibashi J, Takai K, Suzuki K (2009) Trans-crustal advections and in-situ biogeochemical processes of global sub-seafloor aquifer: the Sub-seafloor "TAIGA,". J Geophys Res 118(6):1027–1036

Van Dover CL et al (2001) Biogeography and ecological setting of Indian Ocean hydrothermal vents. Science 294(5543):818–823. doi:10.1126/science.1064574

Indian Ocean Hydrothermal Systems: Seafloor Hydrothermal Activities, Physical and Chemical Characteristics of Hydrothermal Fluids, and Vent-Associated Biological Communities

12

Kentaro Nakamura and Ken Takai

Abstract

In the nearly 40 years since the discovery of the deep-sea hydrothermal vent site at the Galápagos spreading center, more than 300 sites of high-temperature hydrothermal venting have been discovered and investigated around the world. Surprisingly, however, most of these sites are located in the Pacific and Atlantic Oceans, whereas only five hydrothermal vent sites have been discovered in the Indian Ocean. During the TAIGA project, we conducted four research cruises to investigate four of the five Indian Ocean hydrothermal vent sites (two of which were newly discovered during one of the TAIGA cruises) located along the Central Indian Ridge (CIR). The results of geological and geochemical analyses demonstrate wide variation in fluid chemistry, reflecting the diverse geological background of the CIR hydrothermal vent fields. Although the CIR is an intermediate-spreading ridge, the geological and geochemical features of the Kairei hydrothermal field appear to be similar to ultramafic rock-hosted hydrothermal fields found along the slow-spreading Mid-Atlantic Ridge (MAR). By contrast, the Dodo hydrothermal field shares similarities with the hydrothermal vent sites found along the fast-spreading East Pacific Rise. The Solitaire and Edmond hydrothermal fields are characterized by high pH and Cl levels, respectively, although the geological background underlying the unusual chemistry of their hydrothermal fluids is still uncertain. Additionally, extensive microbiological analyses of the Kairei hydrothermal vent site revealed that its microbial communities are affected by the chemical characteristics of the hydrothermal vent fluids. Macrofaunal analyses also revealed new faunal data for the Indian Ocean hydrothermal vents, including novel genera and families that are potentially indigenous to the Indian Ocean hydrothermal systems. In particular, the discovery and characterization of a new morphotype of "scaly-foot" gastropod raises the question of the mechanism and physiological role of iron sulfide mineralization. The results of our investigations extended knowledge of the Indian Ocean hydrothermal systems including geochemical variations of hydrothermal fluids, their relationships to the geological

K. Nakamura (✉)
Precambrian Ecosystem Laboratory (PEL), Japan Agency for Marine-Earth Science and Technology (JAMSTEC), 2-15 Natsushima, Yokosuka, Kanagawa 237-0061, Japan

Submarine Hydrothermal System Research Group, Japan Agency for Marine-Earth Science and Technology (JAMSTEC), 2-15 Natsushima, Yokosuka, Kanagawa 237-0061, Japan

Present address: Department of Systems Innovation, School of Engineering, The University of Tokyo, 7-3-1 Hongo, Bunkyo-ku, Tokyo 113-8656, Japan
e-mail: kentaron@sys.t.u-tokyo.ac.jp

K. Takai
Precambrian Ecosystem Laboratory (PEL), Japan Agency for Marine-Earth Science and Technology (JAMSTEC), 2-15 Natsushima, Yokosuka, Kanagawa 237-0061, Japan

Submarine Hydrothermal System Research Group, Japan Agency for Marine-Earth Science and Technology (JAMSTEC), 2-15 Natsushima, Yokosuka, Kanagawa 237-0061, Japan

Subsurface Geobiology Advanced Research (SUGAR) Project, Japan Agency for Marine-Earth Science and Technology (JAMSTEC), 2-15 Natushima-cho, Yokosuka, Kanagawa 237-0061, Japan

J.-i. Ishibashi et al. (eds.), *Subseafloor Biosphere Linked to Hydrothermal Systems: TAIGA Concept*,
DOI 10.1007/978-4-431-54865-2_12,

background, the biodiversity and biogeography of the hydrothermal vent-associated microbial and faunal communities. This, in turn, will provide important insight into the relationships among geological backgrounds, hydrothermal processes, and biological activities, not only at the Indian Ocean hydrothermal vents but also in global mid-ocean ridge hydrothermal systems.

Keywords
Biodiversity • Fluid chemistry • Geological background • Hydrothermal system • Indian Ocean • Scaly-foot

12.1 Introduction

Since the discovery of deep-sea hydrothermal vents at the Galápagos Rift in 1977 (Corliss et al. 1979), mid-ocean ridge (MOR) hydrothermal systems have attracted attention as key phenomena driving the geochemical cycles of many elements and sustaining unique biological communities in the ocean. A number of geological, geochemical, and biological studies have been conducted at MOR hydrothermal vent sites, providing important insight into the effect of MOR hydrothermal activity on ocean chemistry (e.g., Edmond et al. 1979, 1982; Von Damm et al. 1985a, b; Palmer and Edmond 1989; Elderfield and Schultz 1996), the limit, origin, and early evolution of life (e.g., (Jannasch and Mottl 1985; Nealson et al. 2005; Takai et al. 2006; Takai 2011) as well as the diversity and connections among different biogeographical provinces of hydrothermal vent faunas (e.g., Van Dover et al. 2002; Bachraty et al. 2009; Vrijenhoek 2010). However, most of the hydrothermal vent sites discovered and investigated thus far are located in the Pacific and Atlantic Oceans (German and Von Damm 2004), whereas only a few hydrothermal fields have been identified in the Indian Ocean (Gamo et al. 2001; Hashimoto et al. 2001; Van Dover et al. 2001; Tao et al. 2012; Nakamura et al. 2012). Thus, the geological, geochemical, and biological features of the Indian Ocean hydrothermal system remain poorly understood, and it appears highly uncertain which features are common to global hydrothermal systems and which are unique to the Indian Ocean system.

From 2008 to 2013, an interdisciplinary project (the TAIGA project) focused on interactions between the lithosphere, hydrosphere, and biosphere through the fluid circulation system beneath the seafloor was pursued (Urabe et al. Chap. 1). In this project, the Indian Ocean hydrothermal system was recognized as a major target because, at the beginning of the project, the geological, geochemical, and biological features of the Indian Ocean hydrothermal vent sites were observed to be quite diverse, even though they are located within the quite limited area of the Central Indian Ridge (CIR). In addition, this diversity appeared to be driven by different linkages among geological, geochemical, and biological features (Urabe et al. Chap. 1). During this project, four research cruises using the R/V *Yokosuka*, R/V *Hakuho-maru*, human-occupied vehicle (HOV) *Shinkai 6500*, and autonomous underwater vehicle (AUV) *r2D4* were conducted to investigate the hydrothermal systems of the Indian Ocean. The cruises successfully discovered and explored two new hydrothermal vent sites (the Dodo and Solitaire hydrothermal fields) along the CIR and obtained additional detailed information on the two previously known hydrothermal vent systems (Kairei and Edmond hydrothermal fields). In this paper, we summarize the results of the investigations conducted in these Indian Ocean hydrothermal systems.

12.2 The Four Indian Ocean Hydrothermal Vent Fields Studied in the TAIGA Project

The four hydrothermal vent fields situated along the CIR (the Dodo, Solitaire, Edmond, and Kairei fields) (Fig. 12.1) were studied in the TAIGA project. The Edmond and Kairei hydrothermal fields were discovered previously (Gamo et al. 2001; Hashimoto et al. 2001; Van Dover et al. 2001), whereas the Dodo and Solitaire hydrothermal fields were newly discovered during the TAIGA project (Nakamura et al. 2012). Geological settings and geochemical characteristics of the four hydrothermal vent fields are summarized in Table 12.1.

12.2.1 Dodo Hydrothermal Field

The Dodo hydrothermal field (18°20.1′S, 65°17.9′E; depth of 2,745 m) is located in the Dodo Great Lava Plain in the middle of CIR segment 16 (Fig. 12.2a) (Nakamura et al. 2012). In this field, the active vents are situated on the spreading axis (Fig. 12.2b), in contrast to the hydrothermal vents of the other three hydrothermal vent fields (Solitaire, Kairei, and Edmond), which are all located in the off-axis region. The existence of seafloor hydrothermal activity in

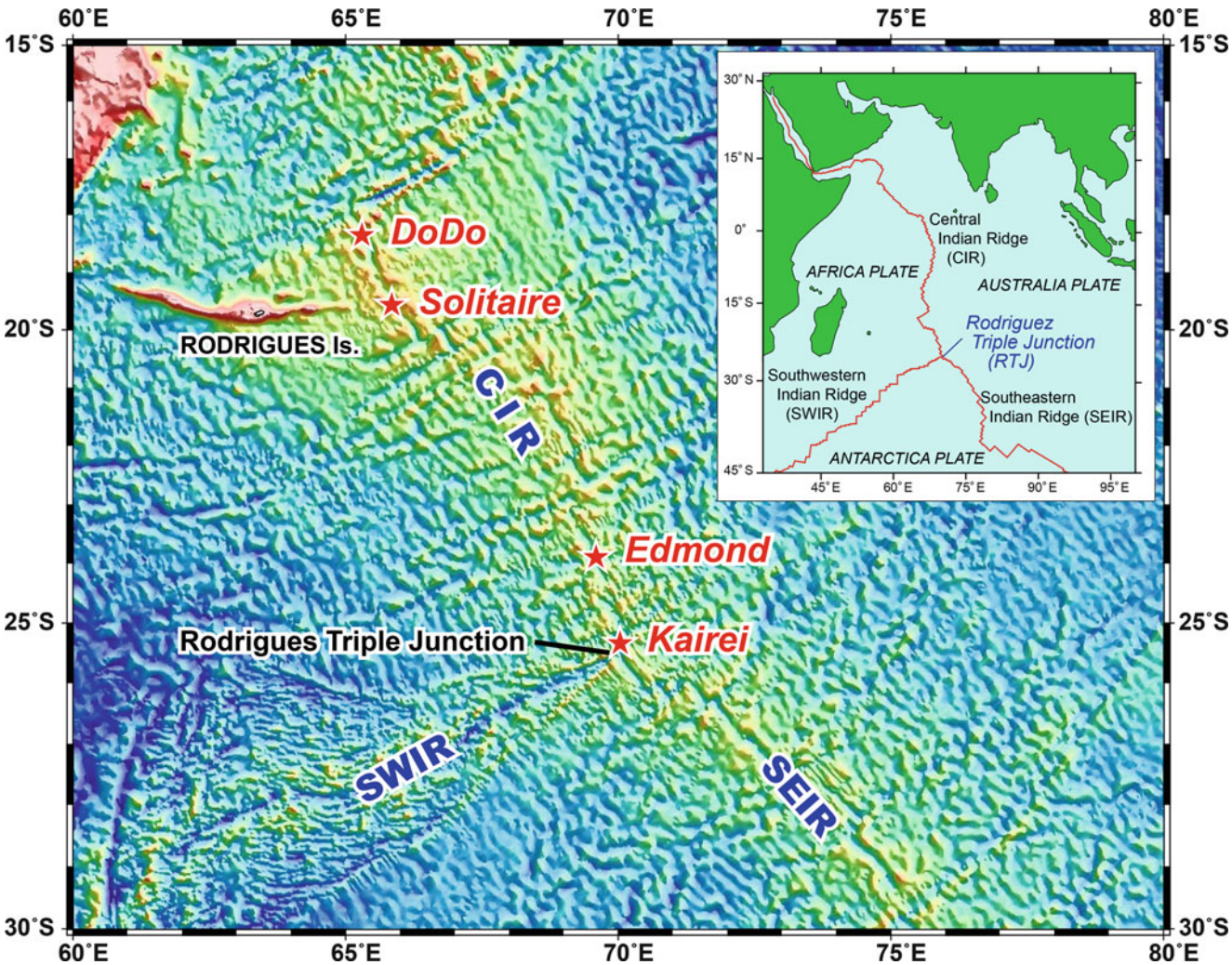

Fig. 12.1 Index map showing the locations of the four hydrothermal vent fields (Dodo, Solitaire, Edmond, and Kairei) along the Central Indian Ridge (CIR)

Table 12.1 Location, host-rock type, and hydrothermal fluid chemistry of the four CIR hydrothermal vent fields

Hydrothermal field	Dodo	Solitaire	Edmond	Kairei
Location	CIR-segment16 on-axis	CIR-segment15 off-axis	CIR-segment4 off-axis	CIR-segment1 off-axis
Host-rock type	E-MORB	E-MORB	N-MORB	Troctolite + D-MORB
Depth (m)	2,745	2,606	3,270–3,303	2,420–2,452
Temperature (°C)	356	296	382	369
pH (25 °C)	3.2	4.8	≤2.97–3.3	3.35–3.60
Cl (mmol/L)	~680	~500	926–973	571–623
H_2 (mmol/L)	~2.4	0.46	0.0556–0.1116	2.48–8.50
CH_4 (mmol/L)	~0.02	~0.05	0.233–0.415	0.123–0.203
CO_2 (mmol/L)	~4	~8	7.19–15.8	4.53–10.1
References	1	1	2, 3	2, 3, 4

CIR central indian ridge, *MORB* mid-ocean ridge basalt, *E-MORB* enriched MORB, *N-MORB* normal MORB, *D-MORB* depleted MORB
1. Nakamura et al. (2012), 2. Gallant and Von Damm (2006), 3. Kumagai et al. (2008), 4. Van Dover et al. (2001)

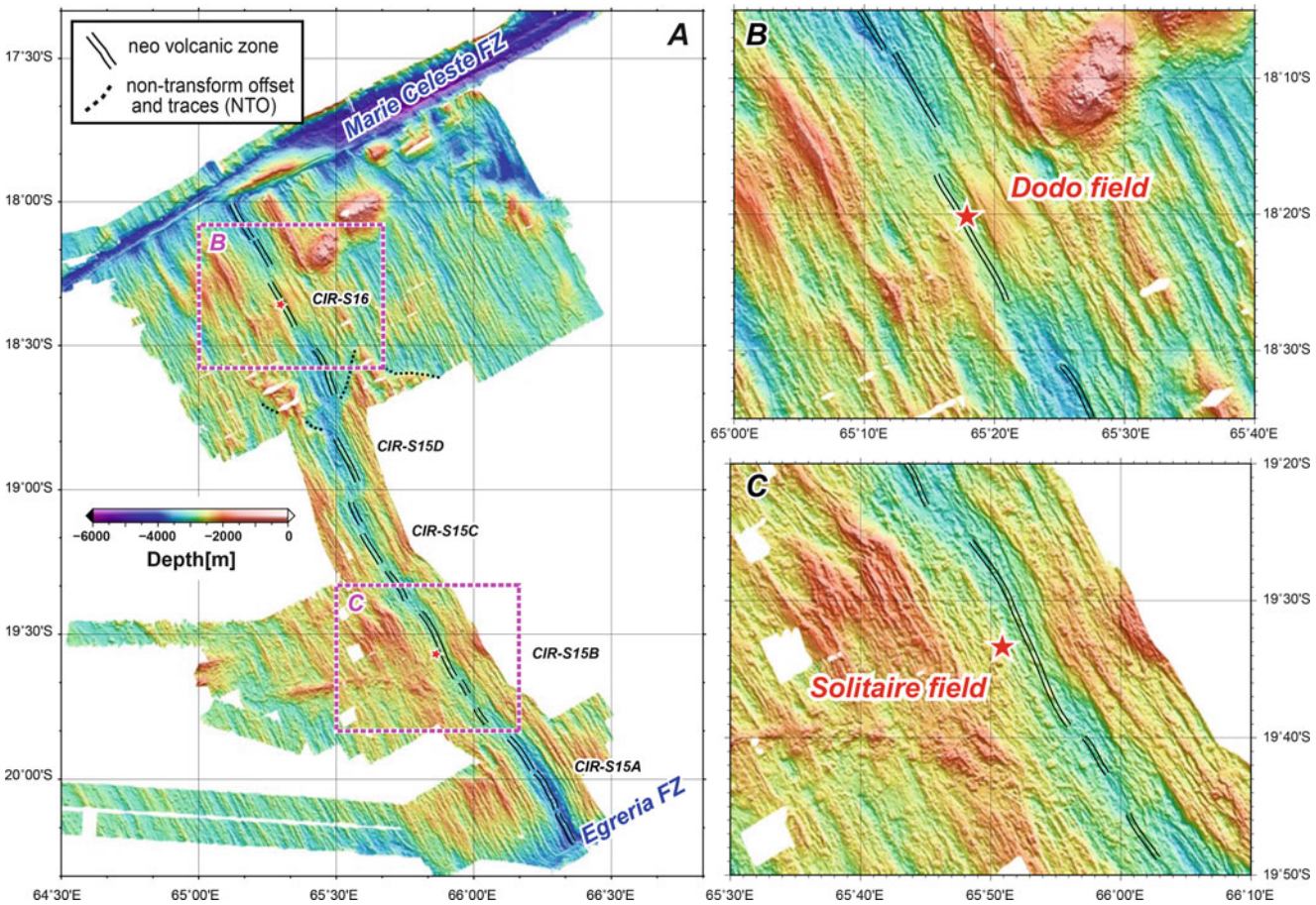

Fig. 12.2 (**a**) Bathymetric map of the Rodriguez segment area and detailed bathymetry maps around the (**b**) Dodo and (**c**) Solitaire hydrothermal fields (after Okino et al. Chap. 11)

the area situated from 18–20°S on the CIR had been suggested by two previous surveys that detected hydrothermal anomalies in the water column (Jean-Baptiste et al. 1992; German et al. 2001). In December 2006, an extensive plume survey was conducted in the CIR region approximately 19°S during the KH 06–4 cruise on the R/V *Hakuho-maru* using vertical and tow-yo hydrocasts and the AUV *r2D4*. During the survey, evident plume signatures of hydrothermally derived CH_4, Mn, and ^3He abundance anomalies and a light transmission signal anomaly were detected in a ridge axial valley of the CIR at 18°20'S within the Dodo Great Lava Plain (Kawagucci et al. 2008). Three years later, in October 2009, detailed observations of the seafloor were performed using a deep-tow camera and the HOV *Shinkai 6500* during the YK 09–13 cruise on the R/V *Yokosuka*. During the cruise, a new hydrothermal field, named the Dodo hydrothermal field, was discovered (Nakamura et al. 2012). The Dodo Great Lava Plain, hosting the Dodo hydrothermal field, is characterized by a flat, smooth seafloor covered with sheet flow lavas stretching over 10 km along the axis, suggestive of high production rates of basaltic melt. These morphological features are similar to those of typical fast-spreading ridges, such as the East Pacific Rise (EPR), rather than that in the spreading centers of the other CIR segments characterized by intermediate spreading rates.

Hydrothermal fluid emissions were observed within a small area (~15 m in diameter) in which many small black smoker chimneys (less than 1 m in height) sprout directly from cracks in the basaltic sheet flow lava. Three main chimney sites were observed: Potsunen, Tsukushi-1, and Tsukushi-2, among which the most vigorous black smoker discharges were observed at the Tsukushi-2 chimney site (Fig. 12.3a). Clear, diffuse fluid flows, either from tiny chimneys or directly from cracks and crevices in the basaltic sheet flow lava, were also detected around the black smoker chimneys. In addition to the active chimneys, several inactive chimneys were found near the Tsukushi-2 chimney site. Interestingly, there are many brownish spots with a small, collapsed crater-like structure on the basaltic sheet flow lava surrounding the hydrothermal vent sites (Fig. 12.3b), and cracks or crevices in pillowed lava and in the interpillow spaces are also stained a brownish color (Fig. 12.3c). The stained area extends more than 50 m along the N–S axis and

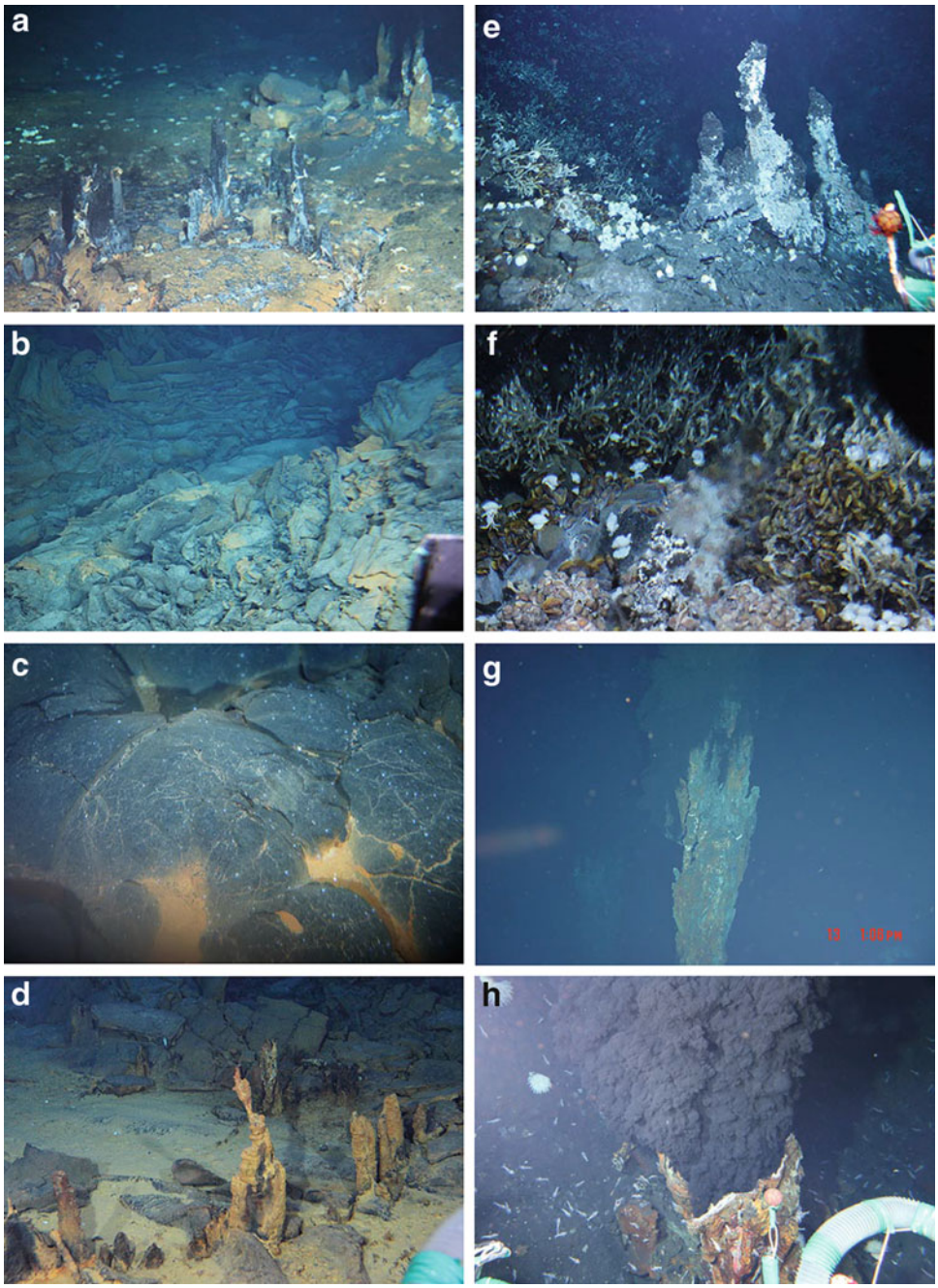

Fig. 12.3 Photographs of (**a**) the Tsukushi-2 chimneys on basaltic sheet flow lava at the Dodo hydrothermal field; (**b**) a brownish spot in the collapsed sheet flow lava; (**c**) cracks and interpillow spaces stained a brownish color; (**d**) inactive chimneys at the Tsukushi-2 chimney site without any fauna present, observed at the Dodo hydrothermal field in 2013; (**e**) the Toukon-3 chimneys in the Solitaire hydrothermal field; (**f**) a diffuse flow area issuing clear fluids in the Solitaire hydrothermal field; (**g**) large black smoker chimneys at the Nura Nura vent site, in the Edmond hydrothermal field; and (**h**) a small black smoker chimney at the Kali vent site, in the Kairei hydrothermal field

at least 200 m along the E–W axis. Recent observations made on the HOV *Shinkai 6500* in 2013 revealed that obvious hydrothermal fluid discharges at the Dodo field had stopped (Fig. 12.3d).

12.2.2 Solitaire Hydrothermal Field

The Solitaire hydrothermal field (19°33.413 S, 65°50.888 E; at a depth of 2,606 m) is located on the Roger plateau on the western ridge flank of CIR segment 15, at approximately 19°33′S (Fig. 12.2a), several kilometers from the ridge axis (Fig. 12.2c) (Nakamura et al. 2012). The location of the Solitaire hydrothermal field is approximately 150 km south of the Dodo hydrothermal field. As for the Dodo field, during the KH 06–4 cruise on the R/V *Hakuho-maru* in December 2006, an extensive plume survey was conducted using vertical and tow-yo hydrocasts and the AUV *r2D4* in the area where the existence of hydrothermal activity had been suggested by previous studies (Jean-Baptiste et al. 1992; German et al. 2001). During the survey, evident plume signatures of anomalies hydrothermally derived CH_4, Mn

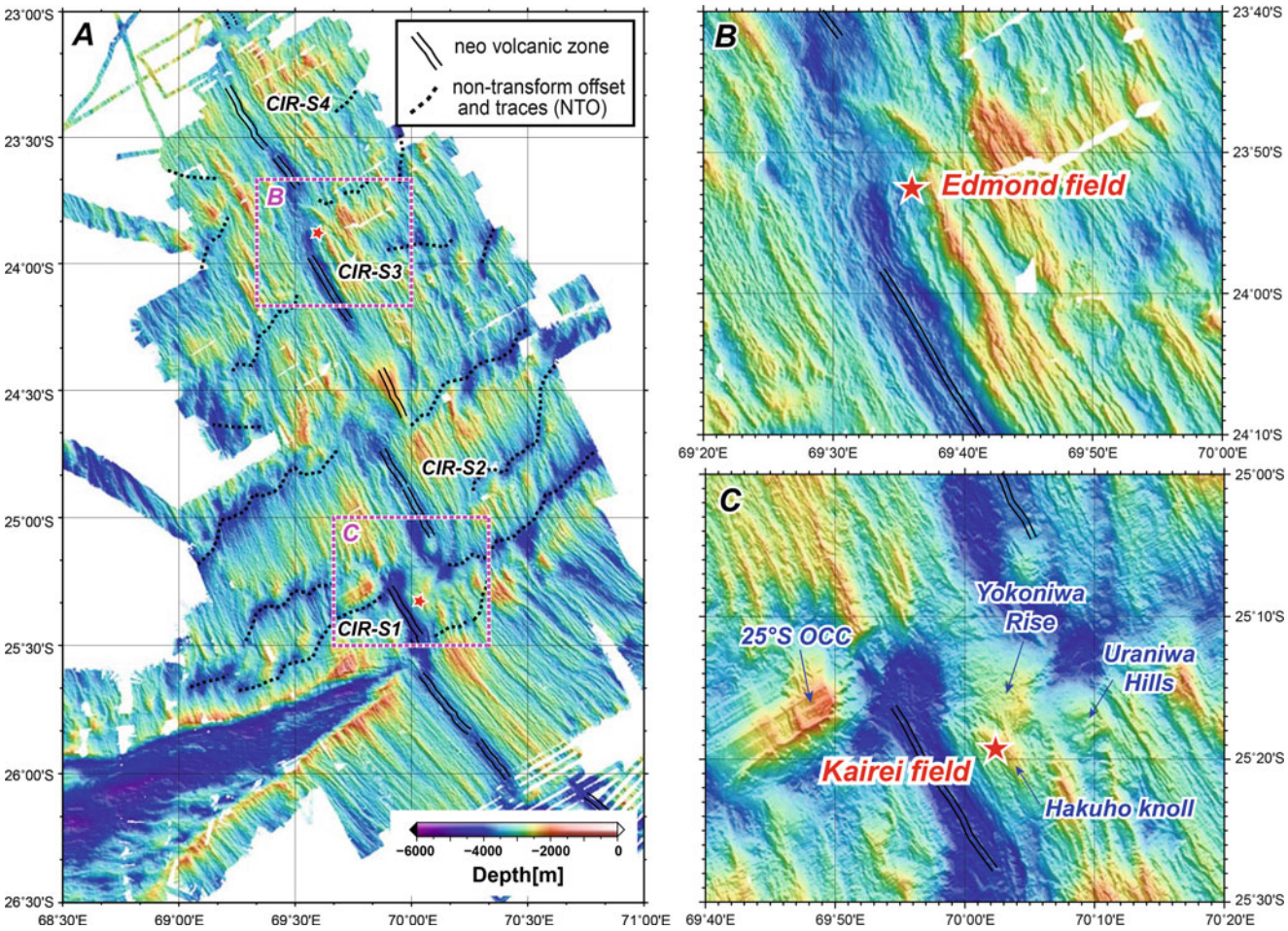

Fig. 12.4 (**a**) Bathymetric map of the CIR-S1 to S4 area and detailed bathymetry maps around the (**b**) Edmond and (**c**) Kairei hydrothermal fields (after Okino et al. Chap. 11).

and ^{3}He abundance and a light transmission signal anomaly were detected along the western off-axis slope of the CIR, at 19°34′S, on the Roger Plateau (Kawagucci et al. 2008). Finally, in October 2009, during the YK 09–13 cruise of the R/V *Yokosuka*, a new seafloor hydrothermal vent site, designated the Solitaire hydrothermal field, was discovered through deep-tow camera surveys and HOV dive observations.

The Solitaire field is situated on the talus at the base of a NNW-SSE-trending steep cliff regarded as a fault scarp. The area of hydrothermal fluid emissions was found to be approximately 50 × 50 m, which is significantly larger than the active venting area of the Dodo hydrothermal field but slightly smaller than those of the Kairei and Edmond hydrothermal fields. In the Solitaire hydrothermal field, three major chimney sites (Toukon-3, Tenkoji, and Liger) were identified. The observed chimneys were less than 5 m in height, with small mounds at their feet (Fig. 12.3e). Although several black smoker discharges were observed at the top of the Toukon-3 chimneys, most of the identified hydrothermal emissions in the Solitaire field consist of clear fluids. In particular, numerous diffuse flow areas issuing clear fluids directly from the talus are a characteristic feature of the Solitaire field (Fig. 12.3f). It is likely that the extensive occurrence of thick and highly permeable talus results in a broad range of mixing zones in the subseafloor environments between the upwelling hydrothermal fluids and the infiltrated seawater.

12.2.3 Edmond Hydrothermal Field

The Edmond hydrothermal field (23°52.68′S, 69°35.80′E; at depths of 3,290–3,320 m) is located at the northern end of CIR segment 3 (Fig. 12.4a) (Van Dover et al. 2001). The location of the Edmond hydrothermal field is approximately 1,000 km south of the Solitaire hydrothermal field. The presence of active seafloor vents in this region was suggested by the results of hydrothermal plume surveys conducted in the 1980s (Herzig and Plüger 1988; Plüger et al. 1990). In

April 2001, detailed geological investigations were conducted through near-bottom water-column surveys by an American research team using the R/V *Knorr* and the remotely operated vehicle (ROV) *Jason*. The investigation resulted in the successful discovery of a hydrothermal vent field in an off-axis region of CIR segment 3 (Van Dover et al. 2001), where typical abyssal hills are observed (Kumagai et al. 2008) (Fig. 12.4b).

The main area of hydrothermal venting in the Edmond hydrothermal field covers ~100 × 60 m (Gallant and Von Damm 2006), which is larger than the other known CIR hydrothermal fields. The black smoker complexes are also larger (up to 35 m tall and 2 m in diameter; Gallant and Von Damm 2006) than any other known CIR hydrothermal field. The most vigorous black-smoker venting is located in discrete clusters of large chimneys at the Nura Nura vent site (Fig. 12.3g) (Kumagai et al. 2008). Similar to the Solitaire hydrothermal field, extensive areas of diffuse flows are present in the Edmond hydrothermal field, suggesting subseafloor seawater entrainment and mixing processes over a broad area. In addition to sulfide structures, orange-brown, iron oxyhydroxide sediments are also commonly observed around the Edmond hydrothermal field.

12.2.4 Kairei Hydrothermal Field

The Kairei hydrothermal field is located in the first segment of the CIR (25°19.23′S, 70°02.42′E; at a depth of 2,415–2,460 m) (Fig. 12.4a) (Gamo et al. 2001). The hydrothermal field was first recognized in 1993 through CTD hydrocasts and tow-yo surveys (Gamo et al. 1996) and was finally discovered by the ROV Kaiko in August 2000 as the first hydrothermal vent site in the Indian Ocean (Gamo et al. 2001). Based on the chemical characteristics of the detected hydrothermal vent fluids as well as basaltic rocks recovered in the vicinity of the hydrothermal vent field, the Kairei hydrothermal field was first recognized as a typical mid-ocean ridge basalt (MORB)-hosted hydrothermal system, despite the unusually high concentrations of H_2 found in its hydrothermal fluids (Gamo et al. 2001; Van Dover et al. 2001; Gallant and Von Damm 2006). However, subsequent bathymetric and visual observations performed using the R/V *Yokosuka* and HOV *Shinkai 6500* revealed that there are two well-defined oceanic core complex (OCC) structures (the 25°S OCC and Uraniwa Hills) consisting of peridotitic and gabbroic rocks within 20 km of the Kairei field (Kumagai et al. 2008) (Fig. 12.4c). More recent observations identified another peridotite-gabbro massif, designated the Yokoniwa Rise, just north of the Hakuho Knoll (Fig. 12.4c). Interestingly, it is generally accepted that OCCs occur only in slow- to ultra-slow-spreading ridges under magma-starved conditions (Escartin et al. 2003; Cannat et al. 2006), whereas the CIR has been classified as an intermediate-spreading ridge with a spreading speed of 47.5 mm/year (DeMets et al. 1994).

The main area of high-temperature vents extends for ~80 m along the rift wall and is ~40 m wide (Gamo et al. 2001; Gallant and Von Damm 2006). Several black smoker complexes with a maximum height of >10 m have been recognized in this area. The most vigorous black smoker discharges were observed at the Kali vent site (Fig. 12.3h) (Kumagai et al. 2008) in the westernmost part of the Kairei hydrothermal field. Although diffuse, lower-temperature flows along the sides and bases of black smoker chimneys are often detectable, broad areas of low-temperature simmering have not been observed in this hydrothermal field. In addition to the large active black smoker chimneys, large accumulations of weathered sulfides and inactive chimneys were also observed in this hydrothermal field.

12.3 Physical and Chemical Characteristics of Hydrothermal Fluids

In the Dodo hydrothermal field, the highest temperature measured was 356 °C, at the Tsukushi-2 chimney site. The lowest pH level of 3.2 was also recorded at this chimney site. These temperature and pH values are comparable with those of typical MOR black smoker fluids (German and Von Damm 2004). The Cl concentration in the hydrothermal fluid was found to be significantly (~20 %) enriched from that in seawater, suggesting subseafloor phase-separation and brine-phase enrichment. A notable feature of the Dodo hydrothermal fluids is their unusually high concentration of H_2 (>2 mmol/L). Such high H_2 contents in hydrothermal fluids are more similar to those found in ultramafic rock-hosted hydrothermal fluids (e.g., in the Rainbow, Logatchev, and Kairei fields), rather than basalt-hosted fluids. However, the morphological features of the Dodo Great Lava Plane clearly suggest a high production rate of basaltic melt, and indeed, no ultramafic rock has been identified around the Dodo hydrothermal field. Kawagucci et al. (2008) suggested a possible involvement of ultramafic rocks exposed in the Marie Celeste Fracture Zone (Hekinian 1982), approximately 50 km north of the Dodo hydrothermal field (Fig. 12.1). Although a model with large-scale hydrothermal circulation is not consistent with the fluid circulation pattern expected for the Dodo field (potentially an EPR-type, short-lived, relatively shallow circulating system), future investigations will be needed to determine the role of large fracture zones in the hydrothermal activity (especially in terms of fluid chemistry) of the neighboring segments. Conspicuous enrichment of K relative to Cl is also a distinctive feature commonly observed in the fluids of the Dodo field (Nakamura et al. 2012). It has been reported that the

basement MORB of the Dodo and Solitaire hydrothermal fields is highly enriched in alkaline and alkaline earth elements compared with typical MORB, due to the influence of plume components derived from the Réunion hot spot (Murton et al. 2005; Nauret et al. 2006). Therefore, it is reasonable to consider the high K/Cl ratio and, likely, other alkali element-to-Cl ratios of the Dodo hydrothermal fluids to reflect the distinct chemistry of the plume-influenced MORB at the base of the hydrothermal field.

In the Solitaire hydrothermal field, a significantly higher pH (4.8) was observed compared to the pH values of typical MOR hydrothermal fluids (3.3 ± 0.5) (German and Von Damm 2004). To explain the relatively high pH detected in MORB-hosted hydrothermal fluids, two primary possibilities are suggested: (1) the existence of highly altered basement rock lacking the ability to buffer the solution pH and (2) the presence of ammonium (NH_3/NH_4^+), serving to buffer the pH at a higher level (German and Von Damm 2004). However, these explanations seem to be unlikely for the Solitaire fluids because (a) the low accumulation of sulfide structures and lack of inactive chimneys imply a relatively young age of the hydrothermal field, and (b) there is no sedimentary component that could produce ammonium in the hydrothermal fluids. Instead, the relatively low temperature (<300 °C) of the Solitaire vent fluids measured at the seafloor suggests another possibility, i.e., that subseafloor mixing between hydrothermal fluids and seawater causes the relatively high pH value of these fluids. The Solitaire fluids exhibit a content of chlorinities that is approximately 10 % lower than the ambient seawater, indicating subseafloor phase separation and segregation of a vapor-rich phase in the discharging fluids. As all of the other CIR hydrothermal systems (Kairei, Edmond, and Dodo fields) exhibit brine-rich hydrothermal fluids with higher chlorinity than the ambient seawater, this constitutes the first observation of discharges of vapor-rich hydrothermal fluids in the Indian Ocean. Despite the vapor enrichment of the Solitaire fluids, their H_2 concentrations (up to 0.46 mmol/L) are generally comparable with typical MOR hydrothermal fluids (McCollom 2008). In addition, similar to the Dodo fluids, the hydrothermal fluids from the Solitaire field are also characterized by a high K/Cl ratio relative to typical MORB-hosted hydrothermal fluids. Indeed, the basement MORB of the Solitaire hydrothermal field is reported to be influenced by the plume components from the Réunion hot spot and, thus, enriched in alkaline and alkaline earth elements (Murton et al. 2005). Therefore, the high K/Cl ratio of the Solitaire fluids is also likely to reflect the chemical characteristic of the plume-influenced MORB at the base of the hydrothermal fields, as in the Dodo hydrothermal field. Because the available hydrothermal fluid samples from the Solitaire field are very limited and the detailed chemical properties of these fluids are still largely unknown, detailed ongoing and future studies of hydrothermal fluid chemistry will provide important insights into the question of how the large- and local-scale geological settings of the Solitaire field affect its unique hydrothermal fluid chemistry.

The maximum temperature of the Edmond hydrothermal fluids (382 °C) (Gallant and Von Damm 2006) is the hottest temperature ever measured in Indian Ocean hydrothermal vents. The pH values of the Edmond fluids range from 2.97 to 3.3 (Gallant and Von Damm 2006; Kumagai et al. 2008), which are slightly lower than the Dodo, Solitaire, and Kairei fluids, but still within the range of typical MORB-hosted hydrothermal fluids (Gallant and Von Damm 2006). The Edmond fluids are characterized by quite high Cl concentrations, which are >70 % higher than in the local ambient seawater, indicating subseafloor phase separation and subsequent brine condensation. The water depth of the Edmond hydrothermal field is ~3,300 m, which corresponds to a hydrostatic pressure of 330 bar. This pressure at the seafloor is above the critical pressure of seawater, indicating that the phase separation of these fluids must occur under supercritical conditions. Furthermore, the data suggest that the temperature of the Edmond fluids must have exceeded 420 °C to have undergone phase separation, even just below the seafloor. In spite of the notable brine enrichment detected, the H_2 concentrations found in the Edmond fluids (0.055–0.111 mmol/kg) (Gallant and Von Damm 2006; Kumagai et al. 2008) are comparable to those of typical MORB-hosted hydrothermal fluids observed elsewhere along the EPR and Mid-Atlantic Ridge (MAR). The vapor and brine phases produced through phase separation are known to be chemically very different from each other and from their parent fluid (e.g., gases are enriched in the vapor-dominated phase and depleted in the brine-dominated phase) (Butterfield et al. 2003). The parent fluid of the Edmond fluids is therefore considered to be more enriched in gases. In contrast to gaseous species, dissolved species that are primarily ionic (e.g., Na^+, Cl^-) are known to show a very strong affinity for the brine phase as a result of phase separation. Indeed, conspicuous enrichment of ionic species was observed in the Edmond fluids (Gallant and Von Damm 2006; Kumagai et al. 2008). However, the Edmond fluids are also characterized by alkali element-to-Cl ratios that are similar to those of typical MORB-hosted hydrothermal fluids (Gallant and Von Damm 2006; Kumagai et al. 2008). Kumagai et al. (Kumagai et al. 2008) reported the chemical composition of the basement basalt of the Edmond hydrothermal field, showing that the contents of alkaline and alkaline earth elements in the Edmond basalt are almost the same as those typically found in MORB (Sun and McDonough 1989).

In the Kairei hydrothermal field, the maximum temperature of the fluid was reported to be 369 °C at the Kali vent

(Kumagai et al. 2008). The pH levels in these high-temperature fluids (3.34 to 3.6) are comparable with those of typical MORB-hosted hydrothermal fluids (Gallant and Von Damm 2006; Kumagai et al. 2008). The Cl concentrations in the endmember fluids are significantly (up to ~14 %) greater than in the local ambient seawater, suggesting subseafloor phase separation and brine-phase enrichment. The first report of the chemical compositions of the Kairei hydrothermal fluids, by Gamo et al. (Gamo et al. 2001), noted a marked similarity between the Kairei fluids and other typical MORB-hosted hydrothermal fluids found along the EPR and MAR (Gamo et al. 2001). However, subsequent studies revealed distinct features of the Kairei hydrothermal fluids (Van Dover et al. 2001), including extraordinarily high H_2 concentrations, of 2.5–8.5 mmol/kg, compared to the concentrations found in typical MORB-hosted hydrothermal fluids (Van Dover et al. 2001; Takai et al. 2004a; Gallant and Von Damm 2006; Kumagai et al. 2008). H_2-enriched, high-temperature hydrothermal vent fluids, similar to the Kairei fluids, have been reported from several hydrothermal vent fields located along the MAR (e.g., the Rainbow, Logatchev I and II, Ashaze I and II, and Nibelungen fields) (Charlou et al. 2002, 2008; Melchert et al. 2008). It has generally been accepted that the H_2 enrichment of hydrothermal vent fluids is attributed to serpentinization of ultramafic rocks (e.g., abyssal peridotite) (Charlou et al. 2002; Douville et al. 2002). However, there was no geological evidence indicating the presence of ultramafic rocks at or near the Kairei hydrothermal field found in the initial investigation (Van Dover et al. 2001; Gallant and Von Damm 2006). Moreover, the Kairei hydrothermal fluids exhibit CH_4 and Si concentrations that are similar to those reported in typical MOR hydrothermal fluids (Gallant and Von Damm 2006), although the peridotite-hosted hydrothermal fluids observed along the MAR generally exhibit higher CH_4 and lower Si concentrations compared to typical basalt-hosted fluids (e.g., Charlou et al. 2002).

In 2006, detailed geological and geophysical investigations were conducted around the Kairei hydrothermal field using the HOV *Shinaki 6500* and R/V *Yokosuka* (YK05-16 cruise). During the research cruise, serpentinized gabbroic rocks (troctolite) were discovered at small topographic highs referred to as the Uraniwa Hills, ~15 km east of the Kairei hydrothermal field (Kumagai et al. 2008). Nakamura et al. (2009) performed geochemical reaction path model calculations to examine whether the reaction of seawater with the troctolitic rocks exposed in the vicinity of the Kairei hydrothermal field explains the high H_2 concentration measured in the hydrothermal fluids. The model results showed that the serpentinization of the Uraniwa troctolite can produce more than 16 mmol/kg of H_2, similar to the H_2 concentrations detected in vent fluids derived from host basement rocks dominated by peridotite (Charlou et al. 2002; Schmidt et al. 2007). To explain the concentrations of the major dissolved components of the vent fluids other than H_2, Nakamura et al. (2009) produced an additional geochemical reaction path model incorporating both troctolite and basalt. The model calculations showed the following two results: (1) even limited interaction between the hydrothermal fluids (reacted with troctolite) and the basaltic wall rock could produce a high-SiO_2 content, similar to those found in basalt-hosted hydrothermal fluids; and (2) H_2 is not predicted to decrease notably during interactions with small amounts of basalt in a hydrothermal upflow zone. This basalt-troctolite hybrid model revealed that troctolite–seawater interactions in recharge and/or reaction zones are responsible for the remarkably high H_2 concentrations observed in the Kairei fluids, whereas the concentrations of other dissolved components of the vent fluids are controlled by the interactions with basalt in the subseafloor hydrothermal fluid flows (particularly in the discharge zone).

The low CH_4 concentration in the Kairei fluids cannot be explained by the hybrid model. Nakamura et al. (2009) noted that the Ni concentrations in olivine-rich gabbroic rocks (e.g., troctolite) are significantly lower than are found in typical mantle peridotite. Because the amount of Ni–Fe alloy directly affects the reaction kinetics of the reduction of CO_2 to CH_4 (Horita and Berndt 1999), the lower concentrations of Ni would reduce the catalytic rate of Fischer–Tropsch-type (FTT) or Sabbatier synthesis in the Uraniwa-Hills rocks, resulting in the lower concentrations of CH_4 relative to H_2 found in the Kairei fluids. However, it should be noted that even in typical peridotite-hosted hydrothermal systems, the CH_4 concentrations are not in equilibrium with the concentrations of H_2 and CO_2, and the real processes controlling CH_4 concentrations in hydrothermal fluids remain uncertain.

The Kairei fluids are also characterized by relatively low ratios of alkaline and alkaline earth elements-to-Cl compared with typical MORB-hosted hydrothermal fluids (Gallant and Von Damm 2006). Kumagai et al. (2008) noted the role of the chemical composition of basement rocks. It is well known that ultramafic rocks (including olivine-rich gabbroic rocks) are depleted in alkaline and alkaline earth elements compared to basaltic rocks. Furthermore, the basaltic rocks present around the Kairei hydrothermal field are also unusually depleted in these elements (Kumagai et al. 2008). Therefore, the chemical characteristics of the Kairei fluids are likely associated with the unique lithology of the Kairei hydrothermal field (involvement of olivine-rich gabbroic rocks and highly depleted basalt).

12.4 Biological Studies Conducted at the Four Hydrothermal Vent Fields

12.4.1 Microbial Communities and Microorganisms Isolated from the CIR Hydrothermal Systems

Among the four deep-sea hydrothermal systems explored along the CIR, only the Kairei field has been extensively studied with respect to the development of the deep-sea vent microbial community. In this section, we therefore summarize the results of the microbiological investigations conducted at the Kairei hydrothermal field thus far. Comprehensive characterizations of the microbial communities in hydrothermal fluids, chimney structures, and planktonic habitats in the mixing zones between the hydrothermal fluids and ambient seawater have been conducted in the Kairei field (Takai et al. 2004a, b; Suzuki et al. 2004; Nakagawa et al. 2004). In addition to microbial community development, the potential biogeochemical functions related to the subseafloor hydrothermal fluid flows and the associated microbial populations have also been addressed in a series of geomicrobiological and biogeochemical investigations (Takai et al. 2004a, 2006; Nakamura et al. 2009; Kawagucci et al. 2010).

The Kairei hydrothermal system exhibits slightly different hydrothermal fluid endmembers, influenced by subseafloor phase separation (Gallant and Von Damm 2006). The Kali vent site is a principal hydrothermal vent site hosting slightly brine-rich fluid, whereas the Fugen chimney site displays relatively gas-rich endmember fluid (Takai et al. 2004a; Gallant and Von Damm 2006). The Fugen chimney is located in the easternmost part of the hydrothermal field and is likely derived from the longest branched hydrothermal fluid path in the predicted subseafloor hydrogeologic structure (Gallant and Von Damm 2006). Although the Fugen chimney fluid is generally enriched with various gas components, the concentration of H_2 in the Fugen chimney fluid is lower than that in the Kali vent fluid (Takai et al. 2004a). The stable isotopic signatures of $\delta D(H_2)$, $\delta^{13}C(CO_2)$, and $\delta^{13}C(CH_4)$ vary between the Kali and Fugen hydrothermal fluids (Takai et al. 2004a; Kawagucci et al. 2010). Together with the observed variation in concentrations, the low $\delta D(H_2)$ value in the Fugen chimney fluid indicates a lower temperature isotopic equilibrium, likely promoted by microbial H_2 consumption. In addition, the high $\delta^{13}C(CO_2)$ value in the Fugen chimney fluid may be explained by isotopic fractionation during microbial consumption, and the significantly low $\delta^{13}C(CH_4)$ level in the Fugen fluid can be attained only through microbial methanogenesis (Takai et al. 2004a). All of these geochemical results are consistent with the composition and metabolic activity of the subseafloor microbial communities revealed through the microbiological characterization of the components entrained from the hydrothermal fluids (Takai et al. 2004a).

The microbial communities in the hydrothermal fluids and the chimney structures of the Kali and Fugen sites were characterized through the quantitative cultivation technique, 16S rRNA gene clone analysis, and FISH analysis (Takai et al. 2004a). Among the microbial communities trapped in the Kali vent and Fugen chimney fluids (the in-situ-colonization-system communities), members of *Thermococcus* and *Pyrococcus* represented the most abundant cultivated populations. The second most abundant cultivated population consisted of thermophilic and hyperthermophilic *Methanococcales* members, all of which represented hydrogenotrophic (H_2-trophic), methanogenic chemolithoautotrophs. The other cultivated microbial components were thermophilic and hyperthermophilic members of *Aquifex* and *Persephonella* (both H_2-trophic and/or thiotrophic chemolithoautotrophs) and *Archaeoglobus* (organotrophic and H_2-trophic, SO_4-reducing chemolithotrophs). *Thermodesulfatator* species were reported to be the dominant, H_2-trophic SO_4-reducing chemolithoautotrophic bacteria in the chimney microbial communities of the Kairei field (Moussard et al. 2004). In addition, certain populations of mesophilic and thermophilic *Epsilonproteobacteria*, such as *Hydrogenimonas* and *Sulfurimonas*, were found in the Fugen chimney fluids. These *Epsilonproteobacteria* are also H_2-trophic and thiotrophic chemolithoautotrophs. The microbial communities found in the Fugen chimney habitats were very similar to the community in the Fugen chimney fluid (Takai et al. 2004a).

Culture-independent molecular analyses (16S rRNA gene cloning and FISH analyses) have generally revealed similar compositions of the microbial communities found in the hydrothermal fluids and chimney structures (Takai et al. 2004a). However, FISH analysis clearly demonstrated the numerical predominance of *Methanococcales* populations in the microbial communities of the Kali and Fugen fluids and strongly suggested that hyperthermophilic H_2-trophic methanogens sustain the microbial communities as primary producers (Takai et al. 2004a). Thus, both geochemical and microbiological characterizations have pointed to the possible existence of a hyperthermophilic subsurface lithotrophic microbial ecosystem (HyperSLiME) beneath the Kairei hydrothermal field (Takai et al. 2004a).

In contrast to the microbial communities that are closely associated with the high-temperature hydrothermal fluid emissions of the Kairei field, the planktonic microbial communities found in the hydrothermal plumes and habitats in the vicinity of this field were not significantly different from those observed in other deep-sea hydrothermal environments (Takai et al. 2004b). Based on examination of the relative abundance of Marine Group I (*Creanarchaeota*

and *Epsilonproteobacteria*) populations in the planktonic microbial communities of the hydrothermal plumes, the communities in the Kairei field showed much less abundant *Epsilonproteobacteria* populations compared to the Iheya North field of the Okinawa Trough. However, microbial populations other than Marine Group I, such as the SUP05 group *Gammaproteobacteria*, a cosmopolitan microbial population that dominates hydrothermal plume communities (Sunamura et al. 2004; Dick and Tebo 2010), were not quantitatively estimated (Takai et al. 2004b). In addition, La Duc et al. (et al. 2007) reported that many of the heterotrophic bacteria isolated from the Kairei hydrothermal plumes displayed high multi-stressor tolerance to desiccation, peroxide exposure, and UV and gamma ray irradiation. However, it is still unclear whether this finding is specifically attributed to the microbial communities of the Kairei hydrothermal plumes or to global hydrothermal plume environments.

In the Edmond field, the microbial community of a sulfide chimney was characterized only via culture-independent, PCR-mediated 16S rRNA gene phylotype analysis (Hoek et al. 2003). The results of this analysis do not provide a quantitative estimation of the microbial community composition or potential functions and represent only qualitative compositional features. Compared to the 16S rRNA gene phylotype compositions obtained from various chimney habitats of the Kairei field, the phylotype composition in the Edmond sulfide chimney, exhibiting relatively high-temperature fluid, consisted mainly of bacterial phylotypes, such as *Epsilonproteobacteria* and *Aquificales*, and archaeal phylotypes, such as the *Aciduliprofundus* and *Thermococcus* genera (Hoek et al. 2003). These phylotypes were quite different from the phylotype compositions found in the Kairei chimneys and fluids, which were dominated by hydrogenotrophic *Methanococcales* and sulfate-reducing chemolithotrophs (Takai et al. 2004a). Although quantitative characterization of the viable populations and metabolic functions of the microbial communities found in various Edmond hydrothermal field habitats remains to be conducted, the different patterns of the microbial phylotype compositions between the Kairei and the Edmond hydrothermal fields are likely associated with the different energy states of the microbially habitable (mixing) zones. These zones are primarily controlled by the physical and chemical characteristics of the endmember hydrothermal fluids, as suggested by Takai and Nakamura (2010, 2011).

Despite the poorly delimited patterns of microbial community development, many novel deep-sea vent microorganisms have been successfully isolated from the CIR deep-sea hydrothermal systems, likely due to the previously unexplored biogeographicity of these systems. Immediately after the discovery of the Kairei hydrothermal field, many new genera and species of deep-sea vent chemolithoautotrophs were isolated and described (L'Haridon et al. 2003; Moussard et al. 2004; Takai et al. 2004c, d, 2008). A hyperthermophilic hydrogenotrophic methanogen, *Methanocaldococcus indicus* (L'Haridon et al. 2003), and an extremely thermophilic hydrogenotrophic methanogen, *Methanotorris formicicus* (Takai et al. 2004c), identified in the Kairei hydrothermal field represent new species of *Methanococcales* and important primary producers of chemolithotrophic microbial communities. A thermophilic hydrogenotrophic sulfate-reducer, *Thermodesulfatator indicus* (Moussard et al. 2004), and a thermophilic hydrogenotrophic epsilonproteobacterium, *Hydrogenimonas thermophila* (Takai et al. 2004d), were new genera of deep-sea vent chemolithoautotrophs originally found in the CIR Kairei field. In addition, although it was not a new taxon of methanogen, the most hyperthermophilic living form identified thus far, *Methanopyrus kandleri* strain 116, was obtained from the Kairei hydrothermal fluid (Takai et al. 2008). The identification of such new taxa of deep-sea vent microorganisms was likely associated with the newly explored biogeographicity of CIR hydrothermal systems, and the unique physiological traits of these chemolithoautotrophs are related to the unique geological setting and hydrothermal fluid chemistry of the Kairei field.

12.4.2 Hydrothermal Vent Fauna and Chemosynthetic Symbioses

The Kairei and Edmond fields have been found to host novel genera and families that are potentially indigenous to CIR hydrothermal systems as well as faunal species common to the Pacific and the Atlantic Oceans (Hashimoto et al. 2001; Van Dover et al. 2001). Based on the limited data obtained from these two hydrothermal vent sites, recent statistical work addressing the connections among biogeographical provinces (Bachraty et al. 2009) and population connectivities (Vrijenhoek 2010) has highlighted similarities between western Pacific and Indian Ocean vent communities. However, as the authors noted, the available information on the Indian Ocean hydrothermal vent faunas is still scarce, and additional faunal data from new Indian Ocean hydrothermal systems is required to improve our knowledge of the biodiversity and biogeography of the global deep-sea hydrothermal vent fauna. During the TAIGA project, we discovered and investigated two new hydrothermal vent sites, the Dodo and Solitaire fields (Nakamura et al. 2012), providing novel information about hydrothermal vent-endemic fauna in the Indian Ocean. The details regarding recent progress in understanding the distribution and genetic diversity of hydrothermal vent fauna and biogeographical and genetic population connectivities in the CIR hydrothermal systems are presented elsewhere in this book (Watanabe and Beedessee, Chap. 16). Here, we briefly

describe the results of the biological studies conducted at the CIR hydrothermal vent fields.

An important finding among the Indian Ocean vent fauna was the existence of two morphotypes of a "scaly-foot" gastropod. Since its first discovery in the Kairei hydrothermal field in 2001 (Van Dover et al. 2001), this gastropod has attracted particular attention because of its distinct features, including unusual black-colored iron sulfide dermal sclerites (Warén et al. 2003; Suzuki et al. 2006), an iron sulfide-plated armor shell structure (Yao et al. 2010), and the unique endo- and epi-symbioses found in its enlarged esophageal gland and sclerites, respectively (Goffredi et al. 2004). In October 2009, during the YK-09-13 cruise, a new morphotype of scaly-foot gastropod was found at the Solitaire hydrothermal field, which exhibits similar morphological and anatomical features to the previously reported type that inhabits the Kairei field but completely lacks an iron sulfide coating on its sclerites (Nakamura et al. 2012).

The new morphotype displays a brown shell and cream-colored sclerites, in contrast to the metallic black shell and sclerites of the type previously known from the Kairei field. Indeed, the sclerites of the Kairei morphotype exhibit the presence of a thick coating of iron sulfide minerals (e.g., greigite or pyrite), as previously reported (Warén et al. 2003; Suzuki et al. 2006), whereas no specific condensation of Fe and S was identified on the sclerites of the Solitaire morphotype. Surprisingly, however, phylogenetic and haplotype analyses clearly demonstrated that the two morphotypes of scaly-foot gastropod of different colors are genetically indistinguishable and should be classified as the same species (Nakamura et al. 2012). Furthermore, the non-iron-sulfide-mineralized sclerites of the Solitaire morphotype show greater mechanical strength of the overall structure compared to those of the Kairei morphotype (Nakamura et al. 2012), despite the fact that the iron sulfide mineralization of sclerites of the Kairei morphotype is believed to harden the sclerites for protection from predation (Suzuki et al. 2006). These findings from the new morphotype of the scaly-foot gastropod demonstrate that the mechanisms and physiological roles of iron sulfide mineralization are still fully uncertain.

A nutritional symbiotic relationship with chemosynthetic bacteria was also observed in the Kairei morphotype of the scaly-foot gastropod (Goffredi et al. 2004). There were different types of symbioses identified in different tissues, such as endosymbiosis of *gammaproteobacterium* in the greatly enlarged esophageal gland and episymbiosis of *Epsilonproteobacteria* and *Deltaproteobacteria* on the iron sulfide-coated sclerites. The nutritional transfer between the chemosynthetic symbiont and the host gastropod is likely sustained by the endosymbiosis in the esophageal gland (Goffredi et al. 2004). Very recently, the complete genome of a gammaproteobacterial endosymbiont found in the Kairei morphotype of the scaly-foot gastropod has been determined (Nakagawa et al. 2013). Notable findings from this study include the presence and transcription of genes for flagellar assembly, through which proteins are potentially exported from the symbiont to the host (Nakagawa et al. 2013). This result indicates the possible nutritional transfer mechanism of this chemosynthetic symbiosis. In addition, the extremely low genetic individuality in the endosymbionts suggests that stringent symbiont selection by the Kairei morphotype of the scaly-foot gastropod prevents random genetic drift in the small population of horizontally transmitted symbionts (Nakagawa et al. 2013). The genomic analysis of the symbiont also suggested that the chemosynthetic symbiosis found in the Kairei morphotype of the scaly-foot gastropod was relatively recently established (Nakagawa et al. 2013).

Another novel chemosynthetic symbiosis was found in a hydrothermal vent gastropod (*Alviniconcha* aff. *hessleri*) predominantly living in the diffusing fluid flow zones of the Kairei field (Suzuki et al. 2005). *Alviniconcha* gastropods belonging to the family *Provannidae* inhabit deep-sea hydrothermal fields at the margins of the western and southwestern Pacific Ocean and along the CIR (Warén and Bouchet 2001; Nakamura et al. 2012). In the gills of the *Alviniconcha* gastropods from the Kairei field, an epsilonproteobacterial endosymbiont was identified for the first time using molecular ecological techniques. It was found that primary production by this species likely supports the nutrition of the host *Alviniconcha* gastropod (Suzuki et al. 2005). The complete genome of the *Alviniconcha* gastropod is being determined, and the energy, carbon metabolism, and nutritional transfer mechanisms of this symbiosis are being investigated through polyphasic physiological and molecular characterizations. The genetic evolution and ecophysiological functions of the chemosynthetic symbiosis found in the *Alviniconcha* gastropods will be clarified through multiple approaches in the future.

12.5 Future Prospects

During the TAIGA project, the exploration and assessment of four Indian Ocean hydrothermal vent fields, including two newly discovered hydrothermal fields, were significantly advanced. As shown in this paper, the results of these investigations greatly extend our knowledge of the geochemical variations of hydrothermal activity and their relationships to the geological background as well as the biodiversity and biogeography of the hydrothermal vent-associated microbial and faunal communities in the Indian Ocean. . The four studied hydrothermal vent sites were all located within the CIR; however, two other MORs in the Indian Ocean (Southeast Indian Ridge: SEIR and Southwest Indian Ridge: SWIR) remain to be explored.

Very recently, a new hydrothermal vent site was discovered along the SWIR and was explored by a Chinese scientific team (Tao et al. 2012). They found hydrothermal vent-endemic fauna, including scaly-foot gastropods at the vent site. However, the fluid chemistry and geological background of this site are still unknown, and detailed descriptions of the vent fauna have yet to be published. Moreover, several hydrothermal plumes indicating the existence of unseen hydrothermal vent sites have also been detected not only at the SWIR (German et al. 1998) but also at the SEIR (Wang et al. 2011). Because similarity between the Indian Ocean and Western Pacific Ocean vent communities has been noted by several researchers, the discovery and investigation of hydrothermal vent sites along the SEIR (a possible corridor for vent communities between Indian and Western Pacific Oceans) are particularly important. In the future, detailed geological, geochemical, and geophysical investigations as well as physiological, genetic, and trophic characterizations of hydrothermal vent-endemic fauna in uninvestigated hydrothermal vent sites will certainly provide important information contributing to our understanding the Indian Ocean MOR hydrothermal system and its relationship to the Pacific and Atlantic Ocean MOR hydrothermal systems.

Acknowledgments We would like to thank the two anonymous reviewers for their constructive and helpful comments and suggestions. This research was financially supported by the Ministry of Education, Culture, Science, and Technology (MEXT) of Japan, through a special coordination fund (Project TAIGA: Trans-crustal Advection and In situ biogeochemical processes of Global subseafloor Aquifer).

References

Bachraty C, Legendre P, Desbruyeres D (2009) Biogeographic relationships among deep-sea hydrothermal vent faunas at global scale. Deep Sea Rese I 56:1371–1378

Butterfield DA, Seyfried Jr. WE, Lilley MD (2003) Composition and evolution of hydrothermal fluids. In: Halbach PE, Tunnicliffe V, Hein JR (eds) Energy and mass transfer in marine hydrothermal systems. Dahlem University Press, Dahlem, pp 123–161

Cannat M, Sauter D, Mendel V, Ruellan E, Okino K, Escartin J, Combier V, Baala M (2006) Modes of seafloor generation at a melt-poor ultraslow-spreading ridge. Geology 34:605–608

Charlou JL, Donval JP, Fouquet Y, Jean-Baptiste P, Holm N (2002) Geochemistry of high H_2 and CH_4 vent fluids issuing from ultramafic rocks at the Rainbow hydrothermal field (36°14′N, MAR). Chem Geol 191:345–359

Charlou JL, Donval JP, Konn C, Birot D, Sudarikov S, Jean-Baptiste P, Fouquet Y, Scientific Party of the SERPENTINE Cruise (2008) High hydrogen and abiotic hydrocarbons from new ultramafic hydrothermal sites between 12°N and 15°N on the Mid Atlantic Ridge-Results of the SERPENTINE cruise. EOS Trans AGU, 88, Fall Meet Suppl, Abstract T51F-04

Corliss JB, Dymond J, Gordon LI, Edmond JM, Von Herzen RP, Ballard RD, Green K, Williams D, Bainbridge A, Crane K, van Andel TH (1979) Submarine thermal springs on the Galapagos Rift. Science 203:1073–1083

DeMets C, Gordon RG, Argus DF, Stein S (1994) Effect of recent revisions to the geomagnetic reversal time scale on estimates of current plate motions. Geophys Res Lett 21:2191–2194

Dick GJ, Tebo BM (2010) Microbial diversity and biogeo- chemistry of the Guaymas Basin deep-sea hydrothermal plume. Environ Microbiol 12:1334–1347

Douville E, Charlou JL, Oelkers EH, Bienvenu P, Jove Colon CF, Donval JP, Fouquet Y, Prieur D, Appriou P (2002) The rainbow vent fluids (36°14′N, MAR): the influence of ultramafic rocks and phase separation on trace metal content in Mid-Atlantic Ridge hydrothermal fluids. Chem Geol 184:37–48

Edmond JM, Measure CI, McDuff RE, Chan LH, Collier R, Grant B, Gordon LI, Corliss JB (1979) Ridge crest hydrothermal activity and the balances of the major and minor elements in the ocean: the Galapagos data. Earth Planet Sci Lett 46:1–18

Edmond JM, Von Damm KL, McDuff RE, Measure CI (1982) Chemistry of hot springs on the East Pacific Rise and their effluent dispersal. Nature 297:187–191

Elderfield H, Schultz A (1996) Mid-ocean ridge hydrothermal fluxes and the chemical composition of the ocean. Annu Rev Earth Planet Sci 24:191–224

Escartin J, Mevel C, MacLeod CJ, McCaig AM (2003) Constraints on deformation conditions and the origin of oceanic detachements: The Mid-Atlantic Ridge core complex at 15°45'N. Geochem Geophys Geosyst 4:1067. doi:10.1029/2002GC000472

Gallant RM, Von Damm KL (2006) Geochemical controls on hydrothermal fluids from the Kairei and Edmond Vent Fields, 23°–25°S, Central Indian Ridge. Geochem Geophys Geosyst 7, Q06018. doi:10.1029/2005GC001067

Gamo T, Nakayama E, Shitashima K, Isshiki K, Obata H, Okamura K, Kanayama S, Oomori T, Koizumi T, Matsumoto S, Hasumoto H (1996) Hydrothermal plumes at the Rodriguez Triple Junction, Indian Ridge. Earth Planet Sci Lett 142:261–270

Gamo T, Chiba H, Yamanaka T, Okudaira T, Hashimoto J, Tsuchida S, Ishibashi J, Kataoka S, Tsunogai U, Okamura K, Sano Y, Shinjo R (2001) Chemical characteristics of newly discovered black smoker fluids and associated hydrothermal plumes at the Rodriguez Triple Junction. Central Indian Ridge Earth Planet Sci Lett 193:371–379

German CR, Von Damm KL (2004) Hydrothermal processes. In: Turekian KK, Holland HD (eds) The oceans and marine geochemistry, treatise on geochemistry, vol 6. Elsevier, New York, pp 181–222

German CR, Baker ET, Mevel C, Tamaki K, the FUJI Science Team (1998) Hydrothermal activity along the southwest Indian ridge. Nature 395:490–493

German CR, Connelly DP, Evans AJ, Murton BJ, Curewitz D Okino K, Statham PJ, Parson LM (2001) Hydrothermal activity along the Central Indian Ridge: ridges, hotspots and philately. Eos Trans AGU 82(47), Fall Meet Suppl, Abstract OS42E–06

Goffredi SK, Warén A, Orphan VJ, Van Dover CL, Vrijenhoek RC (2004) Novel forms of structural integration between microbes and a hydrothermal vent gastropod from the Indian Ocean. Appl Environ Microb 70:3082–3090

Hashimoto J, Ohta S, Gamo T, Chiba H, Yamaguchi T, Tsuchida S, Okudaira T, Watabe H, Yamanaka T, Kitazawa M (2001) First hydrothermal vent communities from the Indian Ocean discovered. Zool Sci 18:717–721

Hekinian R (1982) Petrology of the ocean floor, Elsevier Oceanography Series, 33, Elsevier, Amsterdam, 393 pp

Herzig PM, Plüger WL (1988) Exploration for hydrothermal activity near the Rodriguez Triple Junction, Indian Ocean. Can Mineral 26:721–736

Hoek J, Banta A, Hubler F, Reysenbach A-L (2003) Microbial diversity of a sulphide spire located in the Edmond deep-sea hydrothermal vent field on the Central Indian Ridge. Geobiology 1:119–127

Horita J, Berndt ME (1999) Abiogenic methane formation and isotopic fractionation under hydrothermal conditions. Science 285:1055–1057

Jannasch HW, Mottl MJ (1985) Geomicrobiology of deep-sea hydrothermal vents. Science 229:717–725

Jean-Baptiste P, Mantisi F, Pauwells H, Grimaud D, Patriat P (1992) Hydrotheramal ^{3}He and manganese plumes at 19°29′S on the Central Indian Ridge. Geophys Res Lett 19:1787–1790

Kawagucci S, Okamura K, Kiyota K, Tsunogai U, Sano Y, Tamaki K, Gamo T (2008) Methane, manganese, and helium-3 in newly discovered hydrothermal plumes over the Central Indian Ridge, 18°–20°S. Geochem Geophys Geosyst 9, Q10002. doi:10.1029/2008GC002082

Kawagucci S, Toki T, Ishibashi J, Takai K, Ito M, Oomori T, Gamo T (2010) Isotopic variation of molecular hydrogen in 20–375 °C hydrothermal fluids as detected by a new analytical method. J Geophys Res 115, G03021

Kumagai H, Nakamura K, Toki T, Morishita T, Okino K, Ishibashi J, Tsunogai U, Kawagucci S, Gamo T, Shibuya T, Sawaguchi T, Neo N, Joshima M, Sato T, Takai K (2008) Geological background of the Kairei and Edmond hydrothermal fields along the Central Indian Ridge: implications of their vent fluids' distinct chemistry. Geogluids 8:239–251

La Duc MT, Benardini JN, Kempf MJ, Newcombe DA, Lubarsky M, Venkateswaran K (2007) Microbial diversity of Indian Ocean hydrothermal vent plumes: microbes tolerant of desiccation, peroxide exposure, and ultraviolet and gamma-irradiation. Astrobiology 7:416–431

L'Haridon S, Reysenbach A-L, Banta A, Messner P, Schumann P, Stackebrandt E, Jeanthon C (2003) *Methanocaldococcus indicus* sp. nov., a novel hyperthermophilic methanogen isolated from the Central Indian. Ridge Int J Syst Evol Microbiol 53:1931–1935

McCollom TM (2008) Observation, experimental, and theoretical constraints on carbon cycling. In: Lowell RP, Seewald JS, Metaxas A, Perfit MR (eds) Magma to microbe: modeling hydrothermal processes at Ocean spreading center. AGU Monograph, vol 178. American Geophysical Union, Washington, DC, pp 193–213

Melchert B, Devey CW, German CR, Lackschewitz KS, Seifert R, Walter M, Mertens C, Yoerger DR, Baker ET, Paulick H, Nakamura K (2008) First evidence for high-temperature off-axis venting of deep crustal/mantle heat: the Nibelungen hydrothermal field, southern Mid-Atlantic Ridge. Earth Planet Sci Lett 275:61–69

Moussard H, L'Haridon S, Tindall BJ, Banta A, Schumann P, Stackebrandt E, Reysenbach A-L, Jeanthon C (2004) *Thermodesulfatator indicus* gen. nov., sp. nov., a novel thermophilic chemolithoautotrophic sulfate-reducing bacterium isolated from the Central Indian. Ridge Int J Syst Evol Microbiol 54:227–233

Murton BJ, Tindle AG, Milton JA, Sauter D (2005) Heterogeneity in southern Central Indian Ridge MORB: implications for ridge-hot spot interaction. Geochem Geophys Geosys 6:Q03E20, doi:10.1029/2004GC000798

Nakagawa T, Nakagawa S, Inagaki F, Takai K, Horikoshi K (2004) Phylogenetic diversity of sulfate-reducing prokaryotes in active deep-sea hydrothermal vent chimney structures. FEMS Microbiol Lett 232:145–152

Nakagawa S, Shimamura S, Takaki Y, Suzuki Y, Murakami S, Watanabe T, Fujiyoshi S, Mino S, Sawabe T, Maeda T, Makita H, Nemoto S, Nishimura S, Watanabe H, Watsuji T, Takai K (2013) Allying with armored snails: the complete genome of gammaproteobacterial endosymbiont. ISME J. doi:10.1038/ismej.2013.131

Nakamura K, Morishita T, Bach W, Klein F, Hara K, Okino K, Takai K, Kumagai H (2009) Serpentinized troctolites exposed near the Kairei Hydrothermal Field, Central Indian Ridge: insights into the origin of the Kairei hydrothermal fluid supporting a unique microbial ecosystem. Earth Planet Sci Lett 280:128–136

Nakamura K, Watanabe H, Miyazaki J, Takai K, Kawagucci S, Noguchi T, Nemoto S, Watsuji T, Matsuzaki T, Shibuya T, Okamura K, Mochizuki M, Orihashi Y, Ura T, Asada A, Marie D, Koonjul M, Singh M, Beedessee G, Bhikajee M, Tamaki K (2012) Discovery of new hydrothermal activity and chemosynthetic fauna on the Central Indian Ridge at 18°-20°S. PLoS One 7:e32965. doi:10.1371/journal.pone.0032965

Nauret F, Abouchami W, Galer SJG, Hofmann AW, Hémond C, Chauvel C, Dyment J (2006) Correlated trace element-Pb isotope enrichments in Indian MORB along 18–20°S, Central Indian Ridge. Earth Planet Sci Lett 245:137–152

Nealson KH, Inagaki F, Takai K (2005) Hydrogen-drien subsurface lithoautotrophic microbial ecosystems (SLiMEs): do they exist and why should we care? Trends Microbiol 13:405–410

Palmer MR, Edmond JM (1989) The strontium budget of the modern ocean. Earth Planet Sci Lett 92:11–26

Plüger WL, Herzig PM, Becker KP, Deissmann G, Schöps D, Lange J, Jenisch A, Ladage S, Richnow HH, Schulze T, Michaelis W (1990) Discovery of hydrothermal fields at the Central Indian Ridge. Mar Min 9:73–86

Schmidt K, Koschinsky A, Garbe-Schönberg D, de Carvalho LM, Seifert R (2007) Geochemistry of hydrothermal fluids from the ultramafic-hosted Logatchev hydrothermal field, 15°N on the Mid-Atlantic Ridge: temporal and spatial investigation. Chem Geol 242:1–21

Sun S-S, McDonough WF (1989) Chemical and isotopic systematics of oceanic basalts: implications for mantle composition and processes. In: Saunders AD, Norry MJ (eds) Magmatism in the ocean basins, vol 42. Geological Society of London Special Publication, London, pp 313–345

Sunamura M, Higashi Y, Miyako C, Ishibashi J, Maruyama A (2004) Two bactetia phylotypes are predominant in the Suiyo Seamount hydrothermal plume. Appl Environ Microbiol 70:1190–1198

Suzuki Y, Inagaki F, Takai K, Nealson KH, Horikoshi K (2004) Microbial diversity in inactive chimney structures from deep-sea hydrothermal systems. Microbial Ecol 47:186–196

Suzuki Y, Sasaki T, Suzuki M, Nogi Y, Miwa T, Takai K, Nealson KH, Horikoshi K (2005) Novel chemoautotrophic endosymbiosis between a member of the *Epsilonproteobacteria* and the hydrothermal vent gastropod *Alviniconcha* aff. *hessleri* (*Gastropoda*: *Provannidae*) from the Indian Ocean. Appl Environ Microbiol 71:5440–5450

Suzuki Y, Kopp RE, Kogure T, Suga A, Takai K, Tsuchida S, Ozaki N, Endo K, Hashimoto J, Kato Y, Mizota C, Hirata T, Chiba H, Nealson KH, Horikoshi K, Kirschvink JL (2006) Sclerite formation in the hydrothermal-vent "scaly-foot" gastropod—possible control of iron sulfide biomineralization by the animal. Earth Planet Sci Lett 242:39–50

Takai K (2011) Limits of life and biosphere: Lesson from detection of microorganisms in deep-sea and deep subsurface in the Earth. In: Gargaud M, Lopez-Garcia P, Martin H (eds) Origins and evolution of life: an astrobiological perspective. Cambridge Univeristy Press, Cambridge, pp 469–486

Takai K, Nakamura K (2010) Compositional, physiological and metabolic variability in microbial communities associated with geochemically diverse, deep-sea hydrothermal vent fluids. In: Barton LL, Mandl M, Loy A (eds) Geomicrobiology: molecular and environmental perspective. Springer, Berlin, pp 251–283

Takai K, Nakamura K (2011) Archaeal diversity and community development in deep-sea hydrothermal vents. Curr Opin Microbiol 14:282–291

Takai K, Gamo T, Tsunogai Y, Nakayama N, Hirayama H, Nealson KH, Horikoshi K (2004a) Geochemical and microbiological evidence for a hydrogen-based, hyperthermophilic subsurface lithoautotrophic microbial ecosystem (HyperSLiME) beneath an active deep-sea hydrothermal field. Extremophiles 8:269–282

Takai K, Oida H, Suzuki Y, Hirayama H, Nakagawa S, Nunoura T, Inagaki F, Nealson KH, Horikoshi K (2004b) Spatial distribution of marine crenarchaeota group I in the vicinity of deep-sea hydrothermal systems. Appl Environ Microbiol 70:2404–2413

Takai K, Nealson KH, Horikoshi K (2004c) *Methanotorris formicicus* sp. nov., a novel extremely thermophilic, methane-producing archaeon isolated from a black smoker chimney in the Central Indian Ridge. Int J Syst Evol Microbiol 54:1095–1100

Takai K, Nealson KH, Horikoshi K (2004d) *Hydrogenimonas thermophila* gen. nov., sp. nov., a novel thermophilic, hydrogen-oxidizing chemolithoautotroph within the ε-*Proteobacteria*, isolated from a black smoker in a Central Indian Ridge hydrothermal field. Int J Syst Evol Microbiol 54:25–32

Takai K, Nakamura K, Suzuki K, Inagaki F, Nealson KH, Kumagai H (2006) Ultramafics-Hydrothermalism-Hydrogenesis-HyperSLiME (UltraH^3) linkage: a key insight into early microbial ecosystem in the Archean deep-sea hydrothermal systems. Paleontol Res 10:269–282

Takai K, Nakamura K, Toki T, Tsunogai U, Miyazaki M, Miyazaki J, Hirayama H, Nakagawa S, Nunoura T, Horikoshi K (2008) Cell proliferation at 122 °C and isotopically heavy CH_4 production by a hyperthermophilic methanogen under high-pressure cultivation. Proc Natl Acad Sci U S A 105:10949–10954

Tao C, Lin J, Guo S, Chen YJ, Wu G, Han X, German CR, Yoerger DR, Zhou N, Li H, Su X, Zhu J, the DY115-19 (Legs 1–2) and DY115-20 (Legs 4–7) Science Parties (2012) First active hydrothermal vents on an ultraslow-spreading center: Southwest Indian Ridge. Geology 40:47–50

Van Dover CL, Humphris SE, Fornari D, Cavanaugh CM, Collier R, Goffredi SK, Hashimoto J, Lilley MD, Reysenbach AL, Shank TM, Von Damm KL, Banta A, Gallant RM, Gotz D, Green D, Hall J, Harmer TL, Hurtado LA, Johnson P, McKiness ZP, Meredith C, Olson E, Pan IL, Turnipseed M, Won Y, Young III CR, Vrijenhoek RC (2001) Biogeography and ecological setting of Indian Ocean hydrothermal vents. Science 294:818–823

Van Dover CL, German CR, Speer KG, Parson LM, Vrijenhoek RC (2002) Evolution and biogeograpy of deep-sea vent and seep invertebrates. Science 295:1253–1257

Von Damm KL, Edmond JM, Measures CI, Grant B (1985a) Chemistry of submarine hydrothermal solutions at 21°N. East Pacific Rise Geochim Cosmochim Acta 49:2197–2220

Von Damm KL, Edmond JM, Measures CI, Grant B (1985b) Chemistry of submarine hydrothermal solutions at Guaymas Basin. Gulf California Geochim Cosmochim Acta 49:2221–2237

Vrijenhoek RC (2010) Genetic diversity and connectivity of deep-sea hydrothermal vent metapopulations. Mol Ecol 19:4391–4411

Wang T, Chen YJ, Tao C (2011) Revisit the K-segment of the Southeast Indian Ridge for new evidence of hydrothermal plumes. Chin Sci Bull 56:3605–3609

Warén A, Bouchet P (2001) Gastropoda and monoplacophora from hydrothermal vents and seeps: new taxa and records. Veliger 44:116–231

Warén A, Bengtson S, Goffredi SK, Van Dover CL (2003) A hot-vent gastropod with iron sulfide dermal sclerites. Science 302:1007

Yao H, Dao M, Imholt T, Huang J, Wheeler K, Bonilla A, Suresh S, Ortiz C (2010) Protection mechanisms of the iron-plated armor of a deep-sea hydrothermal vent gastropod. Proc Natl Acad Sci U S A 107:987–992

Petrology and Geochemistry of Mid-Ocean Ridge Basalts from the Southern Central Indian Ridge

13

Hiroshi Sato, Kentaro Nakamura, Hidenori Kumagai, Ryoko Senda, Tomoaki Morishita, Akihiro Tamura, and Shoji Arai

Abstract

Two hydrothermal fields, the Kairei and Edmond hydrothermal fields, are known in the southern Central Indian Ridge (CIR). The Kairei hydrothermal field at 25°19′S is associated with hydrogen-rich hydrothermal activity, whereas the Edmond hydrothermal field at 23°52′S is recognized in the typical mid-ocean ridge type hydrothermal activity. Differences of lithology and geological background between two hydrothermal fields are reflected in the different type of hydrothermal activity. We recovered more than 870 kg of rock samples by dredging from the southern part of the CIR adjacent to the Kairei and Edmond hydrothermal fields during the KH-10-6 cruise. Here, we present new petrological and geochemical data for MORB samples taken between the CIR-S1 and CIR-S4 segments with the aim of constraining distributions of lithology at the southern CIR, and discuss the petrogenesis and the mantle source for these basalts. The MORB melts that formed rocks within the CIR-S1, CIR-S2, and CIR-S4 segments equilibrated with mantle olivine at approximately 10 kbar, and were erupted after undergoing only minor fractionation. MORB samples from the CIR-S4 segment have slightly depleted trace element compositions, whereas MORB samples from the off-ridge part of the CIR-S1 segment are highly depleted. MORB samples from the Knorr seamount have enriched compositions involved a minor amount of hotspot-derived material, as indicated by previous isotope analyses. The presence of a depleted MORB source beneath the off-ridge section of the CIR-S1 segment indicates that the older mantle material at the boundary between the

The online version of this chapter (doi:10.1007/978-4-431-54865-2_13) contains supplementary material, which is available to authorized users.

H. Sato (✉)
School of Business Administration, Senshu University, 2-1-1 Higashimita, Tama-ku, Kawasaki, Kanagawa 214-8580, Japan

K. Nakamura
Precambrian Ecosystem Laboratory (PEL), Japan Agency for Marine-Earth Science and Technology (JAMSTEC), 2-15 Natsushima, Yokosuka, Kanagawa 237-0061, Japan

Department of Systems Innovation, School of Engineering, The University of Tokyo, 7-3-1 Hongo, Bunkyo-ku, Tokyo 113-8656, Japan

H. Kumagai
Institute for Research on Earth Evolution, Japan Agency for Marine-Earth Science and Technology, 2-15 Natsushima-cho, Yokosuka, Kanagawa 237-0061, Japan

R&D Center for Submarine Resources, Japan Agency for Marine-Earth Science and Technology, 2-15 Natsushima-cho, Yokosuka, Kanagawa 237-0061, Japan

R. Senda
Institute for Research on Earth Evolution, Japan Agency for Marine-Earth Science and Technology, 2-15 Natsushima-cho, Yokosuka, Kanagawa 237-0061, Japan

Department of Solid Earth Geochemistry, Japan Agency for Marine-Earth Science and Technology, 2-15 Natsushima-cho, Yokosuka, Kanagawa 237-0061, Japan

T. Morishita • A. Tamura • S. Arai
Faculty of Natural Systems, Institute of Science and Engineering, Kanazawa University, Kakuma, Kanazawa, Ishikawa 920-1192, Japan

J.-i. Ishibashi et al. (eds.), *Subseafloor Biosphere Linked to Hydrothermal Systems: TAIGA Concept*,
DOI 10.1007/978-4-431-54865-2_13,

CIR-S1 and CIR-S2 segments was highly depleted. In turn, this suggests that the source mantle beneath the southern CIR is heterogeneous both along and across the present spreading axis, and that the composition of the mantle in this area is a function of the degree of mixing between depleted and enriched sources.

Keywords
Central Indian Ridge • Geochemistry • Mid-ocean ridge basalts • Petrology

13.1 Introduction

The Indian Ocean hydrothermal fields provide a unique opportunity to improve our understanding of hydrogen production in mid-ocean ridge (MOR) environments. One of these fields, the Kairei hydrothermal field (KHF), is located at the northern end of the first segment of the Central Indian Ridge (CIR-S1, as counted from the Rodriguez Triple Junction (RTJ)) and hosts the only known hydrogen-rich hydrothermal activity outside of slow-spreading ridge environments (Kumagai et al. 2008). The KHF was the first hydrothermal field discovered in the Indian Ocean (Gamo et al. 2001). Recent research by Nakamura et al. (2009) suggested that the high H_2 and Si concentrations within hydrothermal fluids in this field were the result of serpentinization of troctolites at depth, with the derived fluids subsequently undergoing hydrothermal reactions with basaltic wall rocks beneath the KHF. In addition, olivine-rich gabbroic rocks and troctolites, including plagioclase dunites, which are representative of lithologies at deeper parts of the oceanic crust and/or at the crust–mantle boundary, have been recovered from the area around the KHF (Nakamura et al. 2009). This strongly suggests that these deep-forming rocks are exposed in the area around the KHF.

On the other hand, no evidence of ultramafic exposure is recognized in the typical mid-ocean ridge type Edmond hydrothermal field at 23°52′S. Therefore, geological background between the KHF and Edmond hydrothermal field is quite different, and it is estimated that lithology and source mantle compositions along and beneath the southern CIR is heterogeneous. However, petrological and geochemical investigations with systematic sampling have not been performed along the segments of the southern CIR.

Here, we present new petrological and geochemical data for basalts exposed around the KHF with the aim of constraining the distributions of lithology and discuss the characteristics of the source mantle regions for these basalts beneath the southern segments of the CIR. A separate paper in this volume (Okino et al. Chap. 11) presents the general geology of four hydrothermal fields along the CIR and discusses the tectonic setting, with a focus on hydrothermal activity in the area.

13.2 Geological Background and Previous Studies

Details of the tectonic background of the southern CIR (Okino et al. Chap. 11) are summarized here. The CIR is characterized by a narrow axial valley with a slow to intermediate spreading rate (47 mm/year full spreading rate at 25°S) relating to movement of the Somalia and Indian/Capricorn plates. We follow the nomenclature of Briais (Briais 1995) for ridge segments and use the prefix CIR-Sx in this paper.

More than 870 kg of rock samples were recovered by dredging during the KH-10-6 cruise along the CIR-S1 to CIR-S4 segments of the CIR. Several dives by the submersible *Shinkai 6500* were also performed during the YK05-16 cruise (Kumagai et al. 2006, 2008; Morishita et al. 2009), and the compositions of recovered basalt samples are reported in part by Kumagai et al. (Kumagai et al. 2008) and Neo (Neo 2011). Basalt samples from dive sites 6 K#924, 6 K#926, and 6 K#927 are reported and discussed here. In addition, the characteristics of serpentinized peridotites—the dominant lithologies at sites KH-10-6DR19 and KH-10-6DR21—are discussed by Morishita et al. (Chap. 14).

The petrology and geochemistry of MORB around the RTJ that were recovered during the KH-93-3 cruise are reported and discussed by Nakamura et al. (2006). In addition, details of the petrology and geochemistry of MORB from the CIR-S1 segment, including off-ridge samples recovered during the KH-10-6 cruise, will be discussed in future. Previous research (e.g., Price et al. 1986) has also been undertaken in this area, although no studies involving systematic sampling along the southern part of the CIR have been published to date. The locations of dredge and dive sites in this study are given in Table 13.1 and shown in Fig. 13.1, and are described in the following paragraphs.

CIR-S1: Dredge site KH-10-6DR7 is located at the northern part of the CIR-S1 segment, with sites KH-10-6DR6, -DR2, -DR4, -DR3, -DR5, -DR12, -DR11, and -DR10 located to the east of the spreading ridge at the off-ridge area of KH-10-6DR7 along the flow line of plate motion. Basaltic lithologies dominate the rocks recovered from the majority of areas, with serpentinized peridotites recovered from sites KH-10-6DR10, -DR11, and -DR12.

Table 13.1 Locations of dredge sites during KH-10-6 cruise and submersible Shinkai 6500 dive sites during YK05-16 cruise

Segment	Location	Dredge/dive sites	Latitude	Longitude	Water depth (m)	Total weight of samples (g)	Lithology[a]
CIR-S1	Off ridge	KH-10-6DR1	−25°15.00′	70°00.2′	3,115	57,020	B, SP, G, D
CIR-S1	Off ridge	KH-10-6DR2	−25°17.80′	70°01.7′	2,682	18,540	B
CIR-S1	Off ridge	KH-10-6DR3	−25°17.14′	70°02.0′	2,726	5,550	B
CIR-S1	Off ridge	KH-10-6DR4	−25°17.19′	70°01.9′	2,778	2,310	B
CIR-S1	Off ridge	KH-10-6DR5	−25°17.09′	10°02.6′	2,720	51,170	B
CIR-S1	Off ridge	KH-10-6DR6	−25°18.53′	69°58.9′	3,297	84,440	B
CIR-S1	Northern	KH-10-6DR7	−25°20.06′	69°56.6′	4,052	912	B
CIR-S1	Off ridge	KH-10-6DR8	−25°13.79′	69°57.8′	3,886	3,920	B, D
CIR-S1	Off ridge	KH-10-6DR9	−25°13.80′	69°59.5′	3,396	65,840	G, SP, D, B
CIR-S1	Off ridge	KH-10-6DR10	−25°13.46′	70°04.7′	2,966	17,270	B, G, SP
CIR-S1	Off ridge	KH-10-6DR11	−25°14.49′	70°03.7′	2,725	22,510	SP
CIR-S1	Off ridge	KH-10-6DR12	−25°15.69′	70°03.9′	2,551	96,825	B,SP
CIR-S1	Off ridge	KH-10-6DR20	−25°23.48′	69°44.5′	3,160	146,310	SP,G
CIR-S1	Off ridge	KH-10-6DR21	−25°21.39′	69°50.1′	3,275	14,890	B,G,SP
CIR-S1	Off ridge	KH-10-6DR22	−25°13.40′	70°12.4′	3,163	145	SP,B
CIR-S2	Northern	KH-10-6DR17	−24°37.86′	69°48.7′	2,882	8,265	D,B
CIR-S2	Northern	KH-10-6DR18	−24°45.32′	69°52.8′	3,821	1,560	SP,G
CIR-S2	Southern	KH-10-6DR19	−25°06.08′	70°04.3′	3,054	204,810	SP,G
CIR-S2	Center	6K#926	−24°52.50′	69°57.91′	3,545		B
Knorr[b]	Summit	KH-10-6DR15	−24°28.95′	69°55.1′	2,242	67,55	B
Knorr[b]	Summit	KH-10-6DR16	−24°31.77′	69°55.5′	2,268	10,850	B
Knorr[b]	Western flank	6K#924	−24°28.88′	69°49.29′	2,783		B
CIR-S3	Northern end	KH-10-6DR14	−23°49.64′	69°30.0	3,462	24,400	B
CIR-S3	Northern	6K#923	−23°52.93′	69°35.57′	3,547		B
CIR-S3	Center	6K#927	−24°08.06′	69°39.02′	3,592		B
CIR-S4	Southern end	KH-10-6DR13	−23°39.92′	69°28.8′	3,684	28,925	B

[a]Abbreviations for lithology are as follows; *B* basalt, *SP* serpentinized peritotite, *G* gabbro, *D* dorelite
[b]Knorr seamount
Locations for on bottom are shown for both dredge and dive sites

Sites KH-10-6DR20 and -DR21 are located to the west of the CIR-S1 spreading axis at the off-ridge area, and site KH-10-6DR21 is known to contain exposed mantle rocks (Hellebrand et al. 2002). Sites KH-10-6DR1, -DR8, and -DR9 are located at to the east of the spreading axis at the off-ridge part of the northern segment. Basalts and dolerites were recovered from site KH-10-6DR8, and basalts, serpentinized peridotites, and gabbros recovered from sites KH-10-6DR1 and -DR9.

CIR-S2: Site KH-10-6DR19 yielded >150 kg of serpentinized peridotites and is located at the southern end of the CIR-S2 segment, herein referred to as the Phoenix Knoll. The dive site 6 K#926 by the submersible *Shinkai 6500* is within the western part of the axial valley of the central section of the segment. In addition, two dredges were performed during cruise 93 by the R/V *Atlantis II* (Legs 5–5 and 6–10) along the southern part of the CIR-S2 segment (Price et al. 1986), with sites KH-10-6DR17 and -DR18 located within the northern part of the CIR-S2 segment.

Knorr Seamount: The southern end of the CIR-S3 segment hosts a large volcano known as the Knorr Seamount; this volcano is nearly 40 km long by 18 km wide and has a rifted summit that reaches 1,700 m above the rift valley floor. Sites KH-10-6DR15 and -DR16 are located near the summit of the seamount, and dive site 6 K#924 by the *Shinkai 6500*, is located on the western flank of the seamount. In addition, a single dredge was performed during the CIRCE cruise by the R/V *Argo* (Engel and Fisher 1969) at the northern flank of the seamount.

CIR-S3: Dive site 6 K#927 by the *Shinkai 6500* is located at the center of segment CIR-S3, and the trace element compositions of basalts from this site have previously been reported (Kumagai et al. 2008). In addition, dive site 6 K#923 by the *Shinkai 6500* is located within the northern part of the rift valley of segment CIR-S3, close to the Edmond hydrothermal field, and site KH-10-6DR14 is located at the northern end of segment CIR-S3.

CIR-S4: Site KH-10-6DR13 is located at the southern end of the CIR-S4 segment.

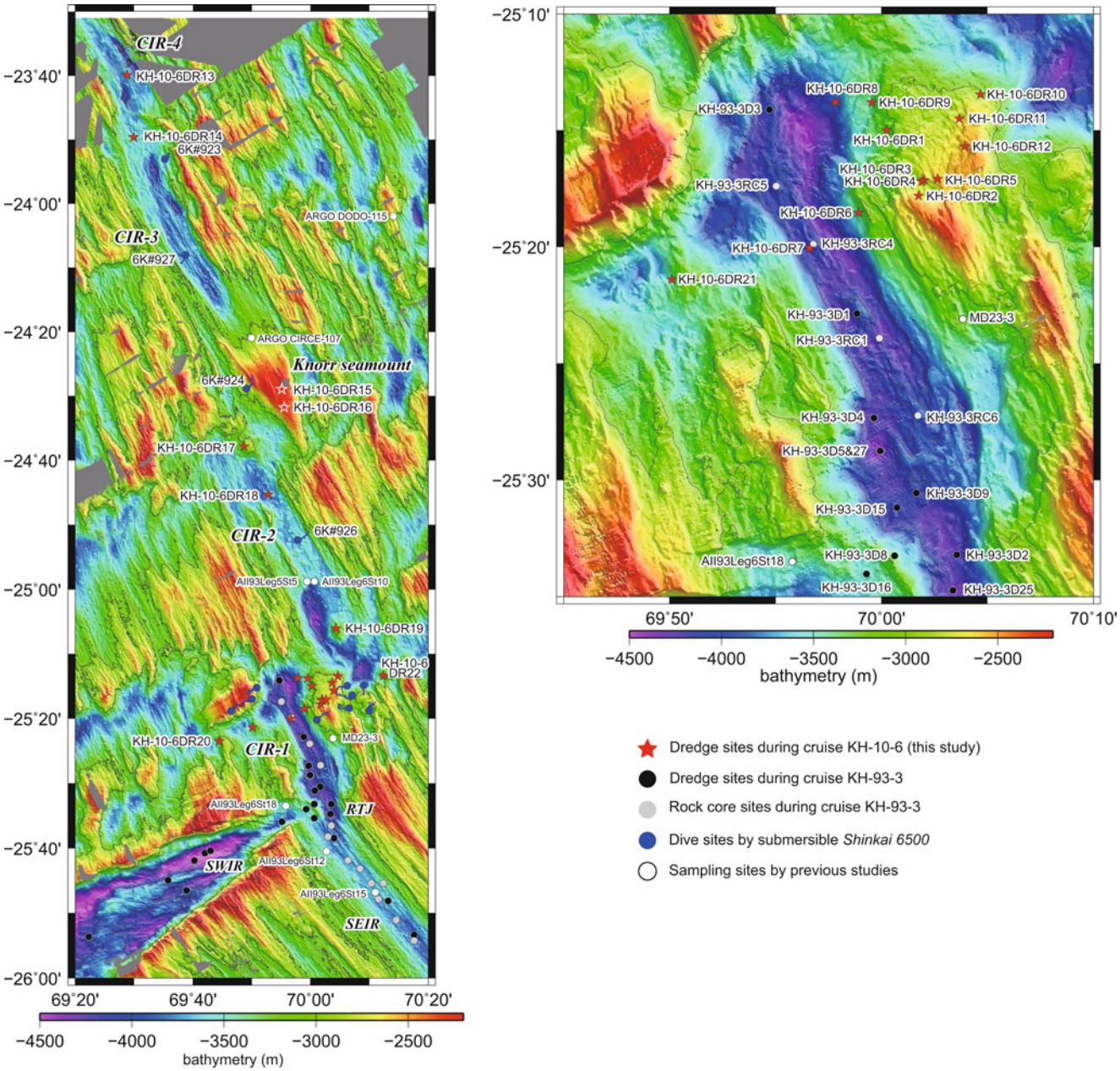

Fig. 13.1 Sampling locations with dredge and rock core samples, and submersible dive sites located on a bathymetric map (Okino et al. Chap. 11). The locations of dredge and rock core sampling undertaken during the KH-93-3 cruise are from Tamaki and Fujimoto (Tamaki and Fujimoto 1995), and the locations sampled by previous studies (Gale et al. 2013; Price et al. 1986) are sourced from the PetDB database (accessed 2013/07/04)

13.3 Petrology and Geochemistry of MORB Along the Southern CIR

Basalts from the southern CIR (CIR-S1 to CIR-S4) are generally plagioclase-olivine phyric to sparsely phyric basalts with glass and/or glassy groundmasses, whereas off-ridge basalts within the CIR-S1 contain significant amounts of olivine phenocrysts with lesser amounts of plagioclase. The major and trace element compositions of these samples were determined by X-ray fluorescence (XRF) and inductively coupled plasma-mass spectrometry (ICP-MS).

13.3.1 Analytical Techniques

The major element compositions of bulk samples were determined using XRF (Rigaku Supermini) housed at Senshu University, Japan. Prior to analysis, samples were

dried at 950 °C before being melted at 1,200 °C in a mixture consisting of 0.9000 g powdered sample and 4.5000 g lithium tetraborate ($Li_2B_4O_7$) flux. XRF calibration lines were determined using the approach of Sato (Sato 2010).

Trace element concentrations within basaltic glass samples were determined using laser ablation–inductively coupled plasma-mass spectrometry (LA-ICP-MS; Agilent 7500S) coupled with a 193 nm ArF excimer MicroLas GeoLas Q-plus laser at Kanazawa University, Japan (Morishita et al. 2005). Each analysis was performed using a 60 μm spot size, a frequency of 5 Hz, and an energy density of 8 J/cm^2 per pulse. A BCR2G (USGS microanalytical reference material) standard was used as the primary calibration standard, with known concentrations obtained from the GeoReM database (Jochum and Nohl 2008). Data reduction was performed using ^{42}Ca as an internal standard, employing CaO contents determined by electron microprobe (EPMA) and the approaches described by Longerich et al. (Longerich et al. 1996).

Trace element concentrations in crystalline MORB samples were analyzed by ICP-MS (Agilent Technologies Agilent 7500ce) at the Japan Agency for Marine-Earth Science and Technology (JAMSTEC). Prior to analysis, powdered samples were digested with a $HClO_4$/HF mixture before undergoing an alkali fusion as outlined in Senda et al. (2014). After reaching dryness, samples were dissolved in 2 % HNO_3 with a trace amount of HF. In and Bi were added to aliquots of samples as internal standards (Senda et al. 2014). Oxide and hydroxide interferences were subtracted from Eu and Gd peaks after analysis.

The results of the major and trace element analyses undertaken during this study are given in Suppl. 13.1 and Suppl. 13.2, respectively.

13.3.2 Major Element Chemistry

The Mg# (=Mg/(Mg + Fe)) values of basalts analyzed during this study range from relatively primitive (Mg# > 65) to relatively evolved (Mg# < 50) compositions (Fig. 13.2). The basalts from the off-ridge of CIR-S1 segment have highly primitive compositions (Mg# > 70). Concentrations of TiO_2, Na_2O, and K_2O negatively correlate with Mg# values, whereas Al_2O_3 concentrations positively correlate with Mg# values. Although variations in each segment could result from the difference of modal compositions of phenocryst in each sample, these trends may represent liquid lines of descent (LLD). Several compositional trends are recognized on Mg# vs. TiO_2, Na_2O, and K_2O diagrams, suggesting that these trends may relate to primary magmas with distinct chemical compositions.

The majority of samples from each dredge have specific major element compositions, indicating that each dredge sampled an individual flow or related flows. The only exceptions are samples from site CIR-S1 and the Knorr Seamount, where dredging appears to have sampled several flows that are exposed at these locations. Some basalt from the Knorr seamount exhibits significant K_2O enrichment. Because they are enriched only in K in terms of trace element chemistry (see below), the enrichment might result from alteration.

Na8 values, calculated as the Na_2O content at an MgO value of 8.0 wt%, are indicative of the degree of partial melting (Klein and Langmuir 1987), where higher Na8 values are indicative of lower average degrees of partial melting, and vice versa. The Na8 values of the majority of basalts from the southern CIR range from 2.5 to 3.0, barring samples from the central CIR-S2 segment and the northern parts of CIR-S3 and CIR-S4, all of which are associated with basalts with Na8 values of <2.5 (Fig. 13.3).

13.3.3 Trace Element Chemistry

Chondrite-normalized rare earth element (REE) and primitive-mantle-normalized trace element variation diagrams for the samples analyzed during this study are shown in Fig. 13.4. Basalts from CIR-S1, -S2, and -S3 have relatively flat REE patterns that are slightly depleted in the light REE (LREE), and have trace element patterns that are slightly depleted in the highly incompatible elements, yielding patterns similar to N-MORB. Crystalline samples (KH-10-6DR18-001 and -DR18-002) obtained from the northern part of segment CIR-S2 have lower highly incompatible element concentrations than N-MORB. Basalts from the central CIR-S3 segment (samples 6 K#927R01, -02, and -04) contain high concentrations of the REE and have minor negative Eu anomalies, suggesting that these basalts are more evolved than other samples analyzed during this study, and have undergone plagioclase fractionation.

Basalts from the CIR-S4 and the off-ridge sections of CIR-S1 are highly depleted in the LREE and highly incompatible trace elements compared with N-MORB (Workman and Hart 2005). In comparison, basalts from the Knorr Seamount have flat patterns or are slightly enriched in both the LREE and the highly incompatible elements.

Trace element ratio values (e.g., La/Sm, Zr/Y, and Zr/Nb) are dependent on the degree of partial melting of the mantle and/or the composition of the mantle, and remain relatively constant during fractionation providing that the melts evolved from the same parental magma. Basalts from the CIR have distinct trace element ratios, as exemplified by changes in Zr/Y ratios for basalts from the study area. Basalts from the CIR-S1 segment have Zr/Y ratios of

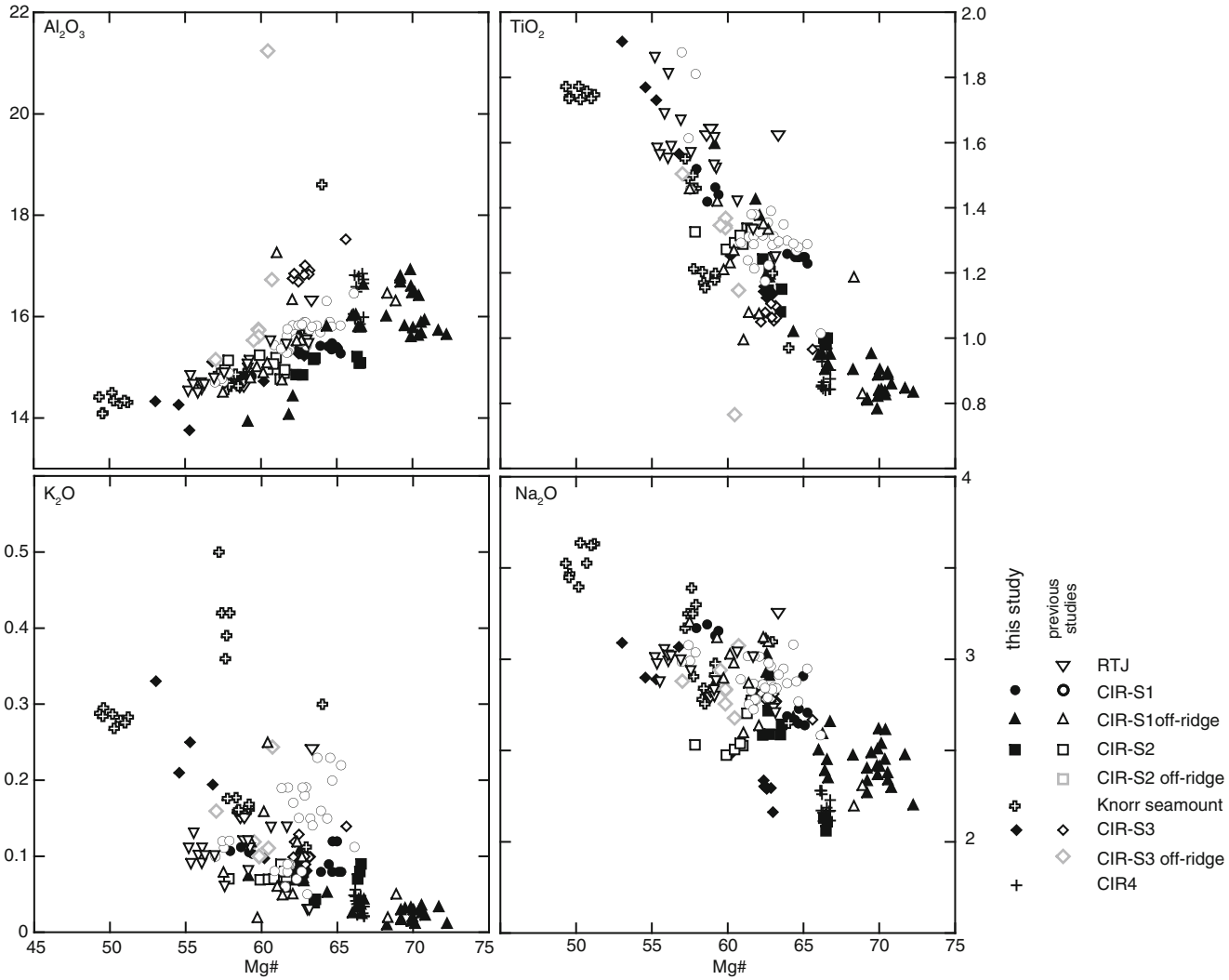

Fig. 13.2 Major element variations in Mg# vs. TiO_2, Na_2O, and K_2O diagrams. The data for previous studies are from Nakamura et al. (2006) for the KH-93-3 cruise and from the PetDB database (accessed 2013/07/04) for all other data, including Hedge et al. (1979), Michard et al. (1986), Price et al. (1986), Engel and Fisher (1975), Engel et al. (1965), Subbarao et al. (1975), Jenner and O'Neill (2012), and Gale et al. (2013)

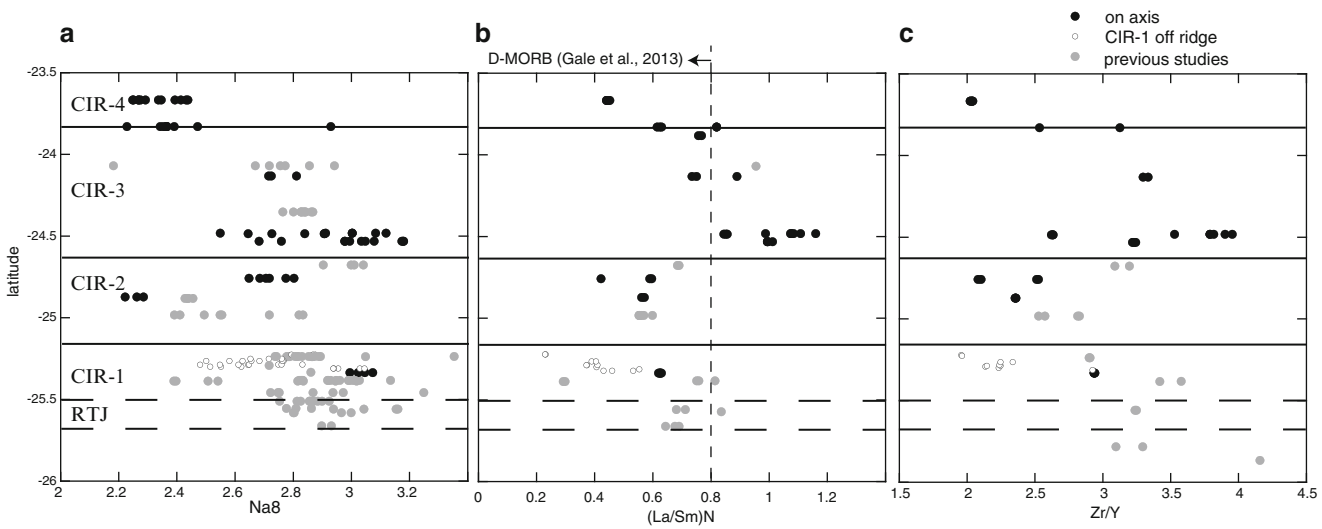

Fig. 13.3 Along-axis variations in chemical compositions of basalts from the southern CIR segments. (**a**) Variations in Na8 (Na_2O contents at MgO = 8 wt%; Klein and Langmuir 1987), indicative of the degree of partial melting if the source mantle is homogeneous; lower Na8 values corresponds to higher degrees of partial melting, and vice versa. Na8 values in this study are calculated based on the equation by Castillo et al. (2000). (**b**) Variations in the La/Sm ratio normalized to N-MORB (Sun and McDonough 1989). (**c**) Variations in the Zr/Y ratio. Data from previous studies were sourced from Nakamura et al. (2006) for samples from the KH-93-3 cruise and the PetDB database (accessed 2013/07/04)

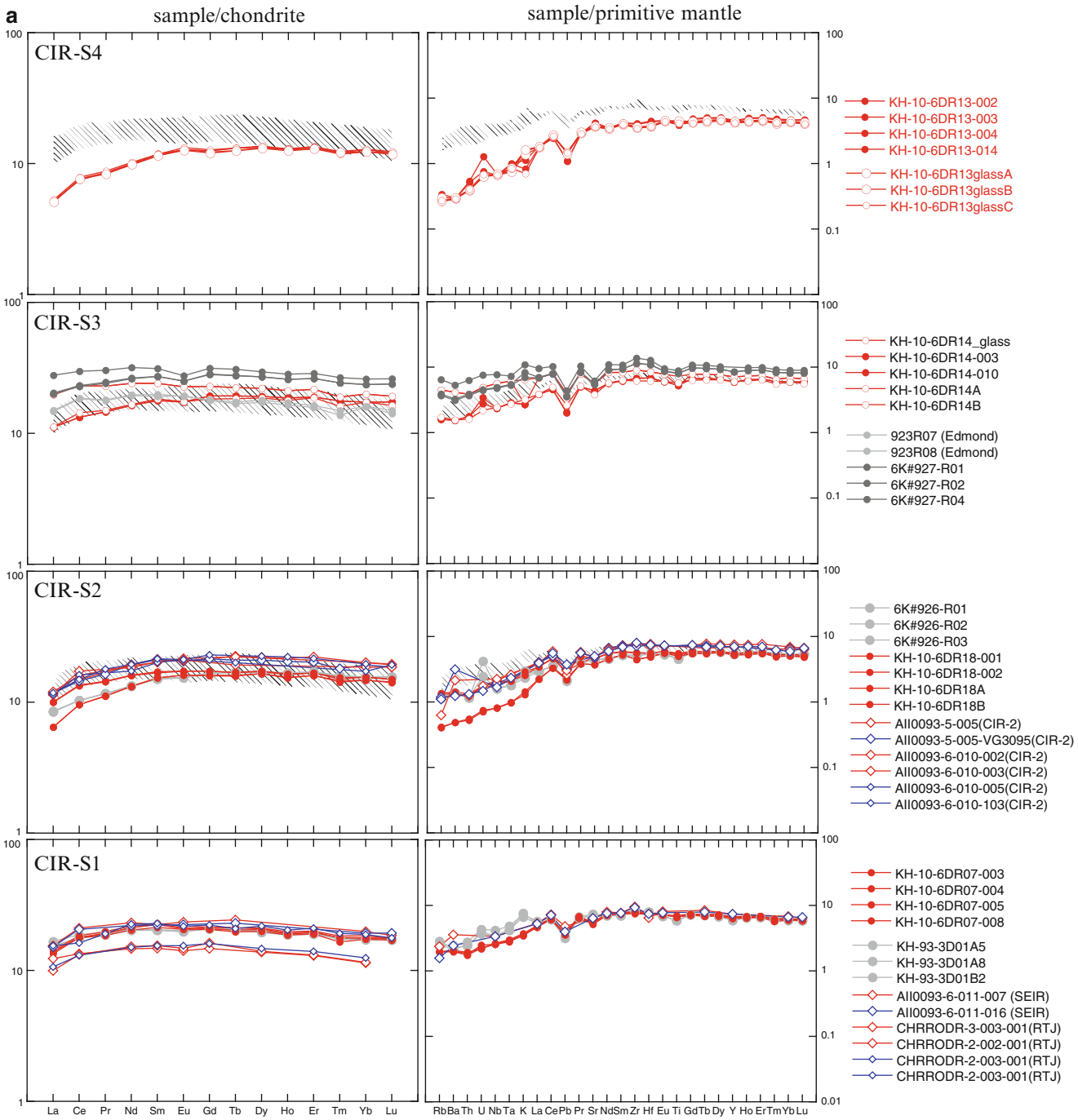

Fig. 13.4 Chondrite-normalized REE and primitive-mantle-normalized trace element variation diagrams (normalized to chondrite and primitive mantle values of Sun and McDonough (1989)). (**a**) MORB from the present-day spreading axis within segments CIR-S1 to CIR-S4. (**b**) Off-ridge MORB from CIR-S1 and the Knorr Seamount, a seamount at the southern end of the CIR-S3; the hatched area indicates the compositional range of MORB from CIR-S1. Data from previous studies were sourced from Nakamura et al. (2006) for samples from the KH-93-3 cruise and the PetDB database (accessed 2013/07/04)

~3.0–3.5, whereas basalts from CIR-S2 have values of 2.0–2.5 (Fig. 13.3), and basalts from CIR-S4 have values around 2.0. In addition, chondrite-normalized La/Sm ratios ($(La/Sm)_N$) for these basalts range from 0.4 to 0.8 except for higher (>1.0) ratios for basalts from the Knorr Seamount. The majority of basalts with $(La/Sm)_N$ ratios of <0.8 are considered to be D-MORB-type basalts according to the recently proposed classification of Gale et al. (2013), suggesting that depleted MORB end-members are widespread throughout the southern part of the CIR.

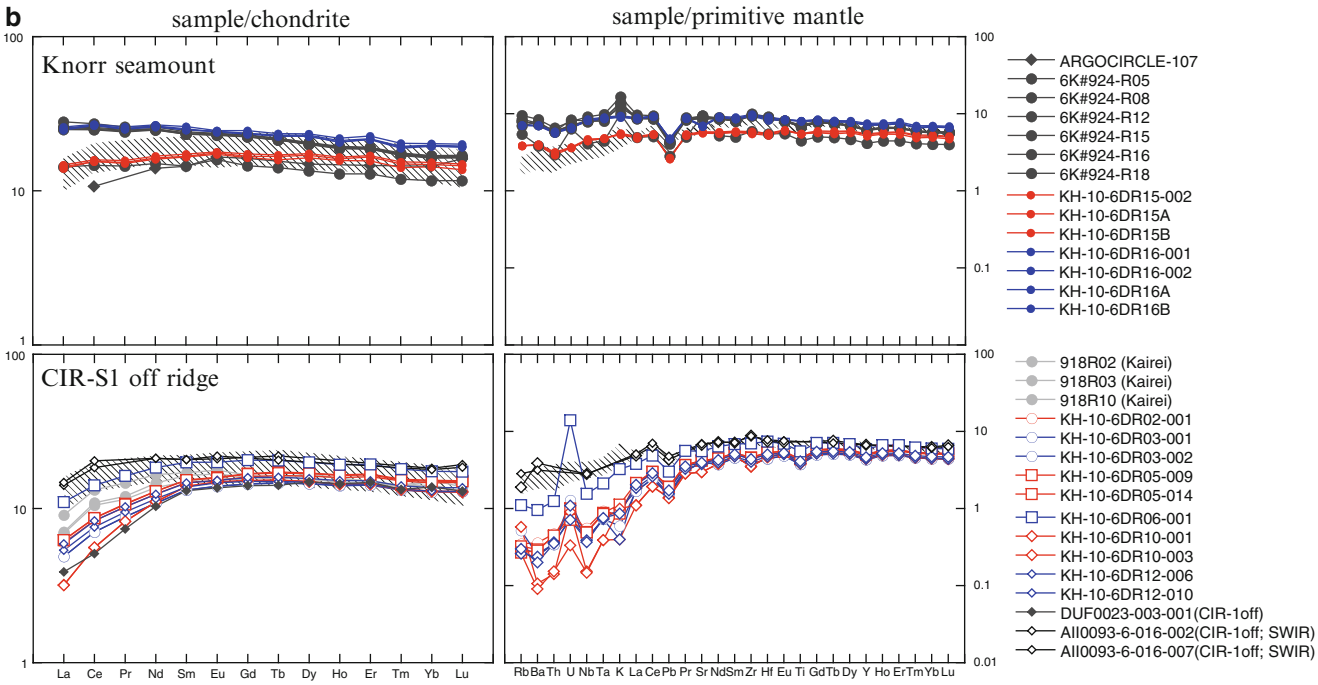

Fig. 13.4 (continued)

13.4 Implications for the Source Mantle Beneath the Southern CIR

13.4.1 Petrogenetic Conditions

The chemical compositions of primary basaltic magmas beneath the CIR were back-calculated from basalt compositions using the olivine maximum fractionation model (e.g., Sato 2004, and references therein). This model calculates the chemical composition of olivine in equilibrium with the basalt using Fe-Mg and Ni-Mg partitioning between olivine and silicate melts. The calculated olivine composition was then added to the original whole-rock composition at a 1:99 weight ratio, with this calculation repeated until the equilibrium olivine had a NiO composition equivalent to that of mantle olivine. The olivine composition that was calculated in each step was fractionated from an original primary magma to yield the basalt compositions analyzed during this study. The whole-rock composition generated by the same number of calculation steps as the olivine composition in equilibrium with the mantle represents the melt composition that was also equilibrated with mantle olivine (i.e., primary magma); the calculations and assumptions involved in this analysis are as presented by Sato (2004).

This calculation assumes that only olivine was fractionated from magma prior to eruption. If plagioclase was fractionated from these magmas, then this calculation would overestimate the MgO concentration of the primary magma, whereas clinopyroxene fractionation would lead to an underestimation of the MgO concentration of the primary magma. This indicates that the starting composition chosen for this modeling should have only crystallized olivine. Therefore, the MgO concentration of the estimated primary magma would be overestimated for basalts containing olivine and plagioclase phenocrysts, The results of these calculations are listed in Table 13.2.

The compositions of basalts from CIR-S1 (including off-ridge samples), CIR-S2, and CIR-S4 are equilibrated with mantle olivine without any significant fractionation. In comparison, the volcanic rocks from CIR-S3 and the Knorr Seamount equilibrated with mantle olivine after several steps of fractionation, suggesting that the MORB compositions at CIR-S1, CIR-S2, and CIR-S4 may represent the compositions of primary melts beneath these segments.

Estimated primary magma compositions are plotted in Fig. 13.5 on an olivine (Ol)-plagioclase (Pl)-quartz (Qz: silica) diagram (Walker et al. 1979) overlain with the isobaric liquid compositional trend of lherzolite determined by Hirose and Kushiro (Hirose and Kushiro 1993). The locations of these primary magmas in the figure represent the pressure (i.e., depth) where melt was fully equilibrated with mantle material or where melt was produced, indicating that off-ridge basalts from CIR-S1 are fully equilibrated with

Table 13.2 Calculated compositions of primary melts and equilibrated olivine

Segment	CIR-S1	CIR-S1 off	CIR-S2	Knorr smt	CIR-S3	CIR-S4
Cruise	KH-93-3	KH-10-6	YK05-16	KH-10-6	YK05-16	KH-10-6
Site	D1	DR12	6K#926	DR15	6K#927	DR13
Sample ID	B2	006	R03	003	R01	003
Step	1	1	1	4	7	1
Equilibrated melt compositions						
SiO_2	51.16	49.78	50.83	51.37	51.29	50.36
TiO_2	1.29	0.84	1.01	1.13	1.66	0.84
Al_2O_3	15.82	15.58	15.29	14.22	13.23	16.57
FeO[a]	8.02	7.91	8.29	9.35	10.38	7.93
MnO	0.14	0.14	0.14	0.17	0.16	0.15
MgO	8.96	12.11	9.78	9.13	10.17	9.46
CaO	11.32	11.36	12.35	11.69	9.94	12.49
Na_2O	2.95	2.19	2.14	2.68	2.78	2.11
K_2O	0.22	0.01	0.09	0.16	0.24	0.03
P_2O_5	0.12	0.08	0.07	0.12	0.14	0.07
Ni (ppm)	148	321	158	90	260	167
Equilibrated olivine compositions						
Mg#[b]	91.3	93.5	91.7	90.2	90.2	91.8
NiO (wt%)	0.295	0.487	0.291	0.173	0.448	0.318

[a]Total Fe as FeO
[b]Mg#=100Mg/(Mg+Fe)

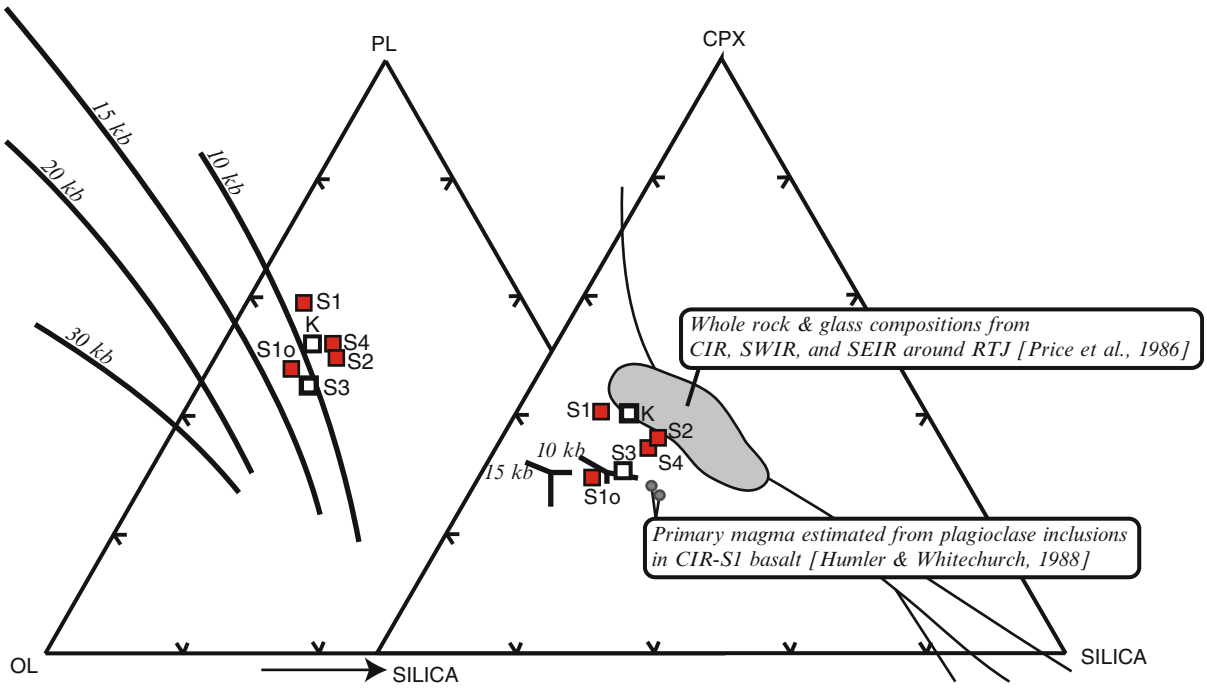

Fig. 13.5 Diagrams showing Ol (olivine)-Pl (plagioclase)-Silica (SiO_2) and Ol (olivine)-CPX (clinopyroxene)-Silica (SiO_2) projections of Walker et al. (1979), indicating the assumed primary magma for MORB from the southern CIR and isobaric liquid compositional trends for dry peridotites (KLB-1 and HK66) determined by Hirose and Kushiro (1993). Also shown are MORB compositions collected near the RTJ by Price et al. (1986) and primary magma compositions for MORB from the CIR-S1 segment (Humler and Whitechurch 1988). S1: CIR-S1, S1o: CIR-S1 off-ridge, S2: CIR-S2, K: Knorr seamount, S3: CIR-S3, S4: CIR-S4

the mantle at slightly greater depths (>10 kbar, equivalent to a depth of 30 km), whereas basalts from other segments are fully equilibrated with the mantle at pressures of <10 kbar. As discussed above, due to possibility of the overestimation of MgO concentration, the estimated pressure might exhibit upper limit value.

13.4.2 Mantle Source Compositions

Differences in the normalized REE and trace element patterns and trace element ratios of basalts can be explained by either differences in the composition of the source mantle for the basalts or by differences in the degree of partial melting of mantle with a similar composition in all cases. The similarities between the REE and trace element compositions of basalts from CIR-S1 to CIR-S3 indicate that these basalts were most likely all derived from a N-MORB-type mantle source, and any variations in Na8, $(La/Sm)_N$, and Zr/Y values for these basalts probably relate to differences in the degree of partial melting. In comparison, basalts from the CIR-S4 segment are more depleted than those from CIR-S1 to -S3. One explanation of this finding is that these depletions are related to higher degrees of partial melting beneath the CIR-S4. Because basalts from the CIR-S4 have similar Na8, $(La/Sm)_N$, and Zr/Y values to basalts from the CIR-S2 segment, the explanation that these basalts formed at similar degrees of partial melting is dismissed. Rather, the more depleted compositions present in CIR-S4 indicate that these basalts were sourced from a mantle region that was slightly more depleted than the mantle beneath areas CIR-S1 to CIR-S3.

Basalts from the off-ridge section of CIR-S1 have more depleted compositions than basalts from the present-day spreading axis. Basalts from near the present-day axis have similar compositions to those at the present-day spreading axis, whereas basalts distal from the spreading axis are more depleted. This suggests that the source mantle beneath the CIR-S1 area was more depleted during formation of the off-ridge basalts in this area compared with the source mantle for more recent (and present-day) basalts.

Although basalts from the Knorr Seamount are significantly enriched when compared with those from the present-day spreading axis, the REE compositions of these seamount basalts provide no lines of evidence of a hotspot influence. Interaction between the Reunion hotspot and CIR segments to the south of 20°S has been proposed by Murton et al. (2005). However, plotting these data on the geochemical discrimination between plume-related and N-MORB/continental magmas of Fitton et al. (1997) indicates that basalts from the

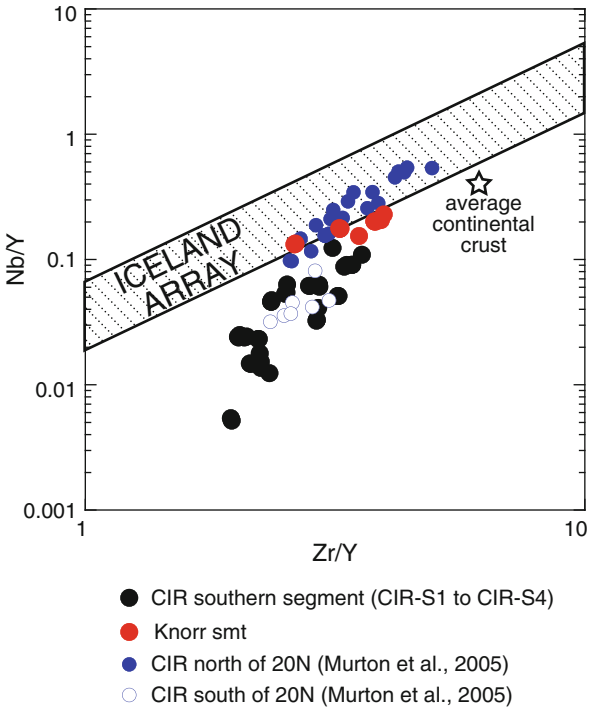

Fig. 13.6 Diagram showing Nb/Y and Zr/Y variations in plume-affected Iceland basalts (Iceland array of Fitton et al. (1997)); N-MORB that is free of plume- or hotspot-influence plots beneath the Iceland array. MORB from the CIR to the north of 20°S (Murton et al. 2005) plots within the array and is therefore considered to have interacted with plume-related material (Murton et al. 2005), whereas MORB from the CIR to the south of 20°S (Murton et al. 2005) and from the southern part of the CIR, including from the Knorr Seamount (this study), plot beneath the array, indicating that these basalts are free of any plume or hotspot influence

southern CIR, including basalts to the south of 20°S as reported by Murton et al. (2005), do not show any plume or hotspot influence (Fig. 13.6). Kumagai et al. (2007) reported He isotope ratios ($^3He/^4He$) of basaltic glasses sampled during the YK05-16 cruise by the *Shinkai* 6500, and these basalts have R_A values well within global MORB variations (7.9 R_A vs. 8 ± 1 R_A for global MORB). In comparison, the majority of basalts around the RTJ, including a segment within the southeast Indian Ridge, have slightly higher He isotope ratios (~8.4 R_A; Kumagai and Kaneoka 2005; Nishio et al. 1998). This indicates that basalts from the Knorr Seamount are not hotspot-related. Furthermore, Hirahara et al. (2007) reported Sr–Nd isotope compositions of basalts from the Knorr Seamount that were sampled during the YK05-16 cruise by the *Shinkai 6500*; these data indicated that the basalts of the Knorr Seamount were probably sourced from a region containing a mix of depleted MORB mantle (DMM) and recycled ancient oceanic crustal material.

13.4.3 Distribution of Depleted and Enriched Mantle

Calculated pressures (i.e., depth) at which melts were fully equilibrated with mantle material or where melts were produced do not change significantly between basalts from segments of the southern CIR (from CIR-S1 to CIR-S4, including the off-ridge area of CIR-S1 and the Knorr Seamount). However, these basalts have distinct trace element compositions, suggesting that the mantle beneath the southern CIR is laterally heterogeneous, with compositional variations present within mantle material at a given depth.

Price et al. (1986) used isotope systematics to determine that depleted components within Indian Ocean MORB are not isotopically homogeneous due to the effects of contamination with different amounts of an ancient (Dupal) component. Recent research into trace element variations in MORB samples from near the RTJ suggests that these variations can be explained by variable contamination of a depleted MORB source mantle by small amounts (up to ~1 %) of lower continental crust-derived melt (Nakamura et al. 2006).

This two-component model, consisting of a large volume of depleted source mantle and a small volume of ancient enriched component, indicates that MORB compositional variations along the southern CIR (from CIR-S1 to CIR-S4) may relate to changes in the degree of mixing between these components. The source mantle beneath the segments between CIR-S1 and CIR-S3 may be compositionally homogeneous, with this mantle representing the proposed mix of voluminous depleted and minor enriched components. In comparison, the off-ridge depleted MORB within the CIR-S1 segment may have been sourced from only the depleted portion of this heterogeneous mantle, whereas basalts from the Knorr Seamount may have been sourced from a region of the mantle that contained an increased amount of the enriched component.

13.4.4 Implications for Tectonic Development of the Southern CIR

An oceanic core complex (OCC), known as 25°S OCC, is exposed along a detachment fault to the west of the northern CIR-S1 (Morishita et al. 2009), with another OCC containing troctolites, olivine gabbros, and dunites reported to the east of the KHF (Kumagai et al. 2008). These OCCs are considered to represent massifs associated with non-transform offsets (NTOs). Observations during recent submersible dives, sample recovery by dredging, and geophysical investigations (Okino et al. Chap. 11) have identified another NTO massif that contains mantle peridotites. The location of this NTO along the segment boundary between CIR-S1 and CIR-S2 suggests that this area has undergone a significant temporal and spatial variation in melt supply, with small amounts of melt supplied during the formation of these NTO massifs.

The formation of the 25°S OCC was initiated at the southern inside corner of CIR-S2 during the Matuyama reversal polarity chron (Sato et al. 2009). A geophysical reconstruction indicates that the majority of the NTO massif, including the 25°S OCC, formed after either the Brunhes-Matuyama boundary or the Jaramillo event (Okino et al. Chap. 11). Therefore, the mantle between CIR-S1 and CIR-S2 may have changed to a more depleted composition, producing the off-ridge basalts in the CIR-S1 area, with present-day mantle beneath the spreading axis being more enriched, producing N-MORB-type basalts at that time.

It is known that the volcanism occur at off-ridge area, and recently large lava fields erupted two to several hundred kilometers off the fast-spreading East Pacific Rise are recognized (Geshi et al. 2007; Umino et al. 2008). The formation age of basaltic rocks from the off-ridge area of the CIR-S1 segment is not clear because no analyses of age determination were performed. The magnetization distribution along the CIR-S1 segment is mostly symmetry (Okino et al. Chap. 11). Therefore, it is plausible that basaltic rocks from the off-ridge area of the CIR-S1 segment might be formed at the ancient spreading center unlike the East Pacific Rise.

13.5 Summary

We investigated the petrology and geochemistry of MORB in segments CIR-S1 to CIR-S4 within the southern part of the CIR, with the aim of constraining the lithological distributions. Our findings are summarized as follows.

(1) MORB from segments CIR-S1 to CIR-S3 have N-MORB-type compositions, and calculated primary melt compositions indicate that the basaltic melts from which these MORB formed, equilibrated with mantle olivine at a pressure of 10 kbar. Particularly, MORB from the CIR-S1, CIR-S2, and CIR-S4 segments derived directly from the primary melts with only minor fractionation.

(2) The trace element compositions of MORB from segments CIR-S1 to CIR-S3 are typical of N-MORB compositions, whereas basalts from the CIR-S4 segment are slightly depleted, indicative of the depletion of the source mantle beneath this segment. Off-ridge basalts from segment CIR-S1 are more depleted than any other MORB within the southern CIR.

(3) MORB from the Knorr Seamount is enriched but has not significantly interacted with hotspot-derived materials, as supported by previous isotope analysis (He, Sr, Nd). It is likely that the enriched magmas within this seamount relate to differences in the abundance of enriched

components within the mantle source for these magmas, rather than the introduction of any plume-related components.

(4) The presence of depleted MORB within the off-ridge section of the CIR-S1 segment indicates that the ancient (i.e., at least as old as the Matuyama reversal polarity chron) source mantle along the boundary between the CIR-S1 and CIR-S2 segments was highly depleted.

Acknowledgements We thank the captain, crew, and scientific party on board the R/V *Hakuho-maru* during cruise KH-10-6. This research was supported by the following grants and programs: the Ministry of Education, Culture, Sports, Science and technology (MEXT), Grant-in-Aid for Scientific Research on Innovative Areas "Project TAIGA: Trans-crustal Advection and In-situ biogeochemical process of Global sub-seafloor Aquifer" (20109002) and a FY2010 Research Fellowship of Senshu University for H.S. H.S. also thanks Ms. K. Komiyama for preparation of thin sections and XRF samples. Maps were drawn using GMT software.

References

Briais A (1995) Structural-analysis of the segmentation of the Central-Indian-Ridge between 20°30′s and 25°30′s (Rodriguez-Triple-Junction). Mar Geophys Res 17(5):431–467. doi:10.1007/BF01371787

Castillo PR, Klein E, Bender J, Langmuir C, Shirey S, Batiza R, White W (2000) Petrology and Sr, Nd, and Pb isotope geochemistry of mid-ocean ridge basalt glasses from the 11°45′N to 15°00′N segment of the East Pacific Rise. Geochem Geophys Geosyst 1:1011. doi:10.1029/1999GC000024

Engel CG, Fisher RL (1969) Lherzolite, anorthosite, gabbro, and basalt dredged from the mid-Indian ocean ridge. Science 166:1136–1141

Engel CG, Fisher RL (1975) Granitic to ultramafic rock complexes of the Indian Ocean ridge system, western Indian Ocean. Geol Soc Am Bull 86:1553

Engel CG, Fischer RL, Engel AE (1965) Igneous rocks of the Indian Ocean Floor. Science 150:605–610

Fitton JG, Saunders AD, Norry MJ, Hardarson BS, Tayler RN (1997) Thermal and chemical structure of the Iceland plume. Earth Planet Sci Lett 153:197–208

Gale A, Dalton CA, Langmuir CH, Su Y, Schilling J-G (2013) The mean composition of ocean ridge basalts. Geochem Geophys Geosyst 14:489–518. doi:10.1029/2012GC004334

Gamo T, Chiba H, Yamanaka T (2001) Chemical characteristics of newly discovered black smoker fluids and associated hydrothermal plumes at the Rodriguez Triple Junction, Central Indian Ridge. Earth Planet Sci Lett 193:371–329

Geshi N, Umino S, Kumagai H, Sinton JM, White SM, Kishimoto K, Hilde TW (2007) Discrete plumbing systems and heterogeneous magma sources of a 24 km^3 off-axis lava field on the western flank of East Pacific Rise 14°S. Earth Planet Sci Lett 258:61–72

Hedge C, Futa K, Engel C, Fisher R (1979) Rare Earth abundances and Rb-Sr systematics of basalts, gabbro, anorthosite and minor granitic rocks from the Indian Ocean Ridge System, Western Indian Ocean. Contrib Mineral Petrol 376:373–376

Hellebrand E, Snow JE, Hoppe P, Hofmann AW (2002) Garnet-field melting and late-stage refertilization in " Residual " abyssal peridotites from the Central Indian Ridge. J Petrol 43 (12):2305–2338

Hirahara Y, Nakamura K, Sato H, Hanyu T, Kumagai H, Suzuki K, Senda R (2007) Origin of the Knoll seamount, the Rodrigues Triple Junction. InterRidge Japan meeting abstract

Hirose K, Kushiro I (1993) Partial melting of dry peridotites at high pressures: determination of compositions of melts segregated from peridotite using aggregates of diamond. Earth Planet Sci Lett 114:477–489

Humler E, Whitechurch H (1988) Petrology of basalts from the Central Indian Ridge (lat. 25°23′S, long. 70°04′E): estimates of frequencies and fractional volumes of magma injections in a two-layered reservoir. Earth Planet Sci Lett 88:169–181

Jenner FE, O'Neill HStC (2012) Analysis of 60 elements in 616 ocean floor basaltic glasses. Geochem Geophys Geosyst 13, Q02005. doi:10.1029/2011GC004009

Jochum KP, Nohl U (2008) Reference materials in geochemistry and environmental research and the GeoReM database. Chem Geol 253:50–53

Klein EM, Langmuir CH (1987) Global correlations of ocean ridge basalt chemistry with axial depth and crustal thickness. J Geophys Res 92:8089–8115

Kumagai H, Kaneoka I (2005) Noble gas signatures around the Rodriguez Triple Junction in the Indian Ocean - Constraints on magma genesis in a ridge system. Geochim Cosmochim Acta 69:5567–5583

Kumagai H, Okino K, Joshima M, Morishita T, Sawaguchi T, Nakamura K, Neo N, Shibuya T, Sato T, Takaesu M, Okada S (2006) Preliminary Cruise Report YK05-16 Leg.1 Yokosuka/Shinkai6500 "URANIWA" Expedition. JAMSTEC

Kumagai H, Joshima M, Morishita T, Nakamura K, Sato H, Arai S, YK05-16Leg1 Shipboard and Shore-Based Scientific Party (2007) An anomalous seamount filling the axial valley of CIR, Indian Ocean: unstable spreading at intermediate-rate spreading ridge. JpGU meeting, J169-012

Kumagai H, Nakamura K, Toki T, Morishita T, Okino K, Ishibashi J-I, Tsunogai U, Kawagucci S, Gamo T, Sshibuya T, Sawaguchi T, Neo N, Joshima M, Sato T, Takai K (2008) Geological background of the Kairei and Edmond hydrothermal fields along the Central Indian Ridge: implications of their vent fluids' distinct chemistry. Geofluids 8:239–251. doi:10.1111/j.1468-8123.2008.00223.x

Longerich HP, Jackson SE, Gunther D (1996) Laser ablation inductively coupled plasma mass spectrometric transient signal data acquisition and analyte concentration calculation. J Anal At Spectrom 11:899–904

Michard A, Montigny R, Schlich R (1986) Geochemistry of the mantle beneath the Rodriguez Triple Junction and the South-East Indian Ridge. Earth Planet Sci Lett 78:104–114

Morishita T, Ishida Y, Arai S (2005) Simultaneous determination of multiple trace element compositions in thin (<30 μm) layers of BCR-2G by 193 nm ArF excimer laser ablation-ICP-MS: implications for matrix effect and element fractionation on quantitative analysis. Geochem J 39:327–340

Morishita T, Hara K, Nakamura K, Sawaguchi T, Tamura A, Arai S, Okino K, Takai K, Kumagai H (2009) Igneous, alteration and exhumation processes recorded in abyssal peridotites and related fault rocks from an oceanic core complex along the Central Indian Ridge. J Petrol 50(7):1299–1325. doi:10.1093/petrology/egp025

Murton BJ, Tindle AG, Milton JA, Sauter D (2005) Heterogeneity in southern Central Indian Ridge MORB: implications for ridge – hot spot interaction. Geochem Geophys Geosyst 6:Q03E20. doi:10.1029/2004GC000798

Nakamura K, Sato H, Sato Y, Ishii T (2006) Petrological and geochemical study of the Indian Ocean MORB from the Rodriguez Triple

Junction, Indian Ocean. EOS Trans AGU 87(52) Fall Meet Suppl, Abstract B31B–1104

Nakamura K, Morishita T, Bach W, Klein F, Hara K, Okino K, Takai K, Kumagai H (2009) Serpentinized troctolites exposed near the Kairei Hydrothermal Field, Central Indian Ridge: insights into the origin of the Kairei hydrothermal fluid supporting a unique microbial ecosystem. Earth Planet Sci Lett 280:128–136

Neo N (2011) Petrology of the basalts of the Central Indian Ridge and regional variations of MORBs along the eastern part of the Southwest Indian Ridge. Dissertation thesis for Doctoral program in Fundamental Sciences, Graduate School of Science and Technology, Niigata University, 99 pp

Nishio Y, Ishii T, Gamo T, Sano Y (1998) Volatile element isotopic systematics of the Rodrigues Triple Junction Indian Ocean MORB: implications for mantle heterogeneity. Earth Planet Sci Lett 170:241–253

Price RC, Kennedy AK, Riggs-Sneeringer M (1986) and F.A. Frey (1986) Geochemistry of basalts from the Indian Ocean triple junction: implications for the generation and evolution of Indian Ocean ridge basalts. Earth Planet Sci Lett 78:379–396

Sato H (2004) Mineral compositions of MORB from the Australian Antarctic Discordance (AAD): implications for mantle source characteristics. In: Pedersen RB, Christie DM, Miller DJ (eds) Proceedings of the ODP, science results, 187 [Online]. http://www-odp.tamu.edu/publications/187_SR/202/202.htm

Sato H (2010) Quantitative analyses with X-ray fluorescence analyzer of major elements for rock samples. Bulletin of the Institute of Natural Sciences, Senshu University, No. 41, pp 15–23 (in Japanese)

Sato T, Okino K, Kumagai H (2009) Magnetic structure of an oceanic core complex at the southernmost Central Indian Ridge: analysis of shipboard and deep-sea three-component magnetometer data. Geochem Geophys Geosyst 10(6). doi:10.1029/2008GC002267

Senda R, Chang Q, Kimura J-I (2014) Evaluation of a rapid, effective sample digestion method for trace element analysis of granitoid samples containing acid-resistant minerals: Alkali fusion after acid digestion. Geochemi J 48:99–103. doi:10.2343/geochemj.2.0280

Subbarao KV, Hekinian R, Chandrasekharam D (1975) Large ion lithophile elements and Sr and Pb isotopic variation in volcanic rocks from the Indian ocean. Ind Ocean Geol Biostratigr Stud Following Deep Sea Drill Legs 9:259–278

Sun S-S, McDonough WF (1989) Chemical and isotopic systematics of oceanic basalts: implications for mantle composition and processes. In: Saunders AD, Norry MJ (eds) Magmatism in the Ocean Basins, vol 42. Geological Society of London, Specical Publication, London, pp 313–345

Tamaki K, Fujimoto H (1995) Rodriguez triple junction expedition in the Indian Ocean: Ocean Research Institute, the University of Tokyo, Tokyo, 183 pp

Umino S, Geshi N, Kumagai H, Kishimoto K (2008) Do off-ridge volcanoes on the East Pacific Rise originate from the Moho transition zone? J Geogr 117:190–219

Walker D, Shibata T, Delong SE (1979) Abyssal tholeiites from the Oceanographer Fracture Zone, II Phase equilibria and mixing. Contrib Mineral Petrol 70:111–125

Workman RK, Hart SR (2005) Major and trace element composition of the depleted MORB mantle (DMM). Earth Planet Sci Lett 231:53–72

Petrology of Peridotites and Related Gabbroic Rocks Around the Kairei Hydrothermal Field in the Central Indian Ridge

14

Tomoaki Morishita, Kentaro Nakamura, Takazo Shibuya, Hidenori Kumagai, Taichi Sato, Kyoko Okino, Hiroshi Sato, Rie Nauchi, Kaori Hara, and Ryo Takamaru

Abstract

Peridotites and related gabbroic rocks are widely exposed in the Central Indian Ridge, where the H_2-rich-fluid-bearing Kairei hydrothermal field exists. We report on petrological and mineralogical characteristics of peridotites and gabbroic rocks recovered from an oceanic core complex at a latitude of 25° South (25°S OCC) and the Yokoniwa Rise around the Kairei hydrothermal field. Gabbros recovered from the 25°S OCC show a wide range of variations in terms of mineral chemistry and mineral assemblages (olivine-gabbro, gabbronorite to highly evolved oxide gabbro) and are similar to those from the Atlantis Bank of the Southwest Indian Ridge, an ultraslow-spreading ocean ridge. Peridotites recovered from 25°S OCC and the Yokoniwa Rise are generally characterized by moderately to highly depleted melt components. The partial melting of these peridotites is followed by chemical modification through interaction with a wide range of melts from relatively less evolved to highly evolved characteristics. Moderately to highly depleted melt components in the studied peridotites can be explained as being either residue after a relatively high-melt productivity period in intermediate-spreading ridges or a geochemically distinctive domain which has suffered from partial melting in the past rather than partial melting beneath the present mid-ocean ridge systems.

Keywords

Central Indian Ridge • Gabbro • Magmatism • Peridotite

14.1 Introduction

It is crucial to understand the generalities and the differences in ocean floor formations as a function of the spreading rate along the mid-ocean ridges within the context of plate

T. Morishita (✉)
School of Natural System, College of Science and Engineering, Kanazawa University, Kakuma, Kanazawa 920-1192, Japan

K. Nakamura • T. Shibuya
H. Kumagai
Precambrian Ecosystem Laboratory (PEL), Japan Agency for Marine-Earth Science and Technology (JAMSTEC), 2-15 Natsushima, Yokosuka, Kanagawa 237-0061, Japan

T. Sato
Geological Survey of Japan, National Institute of Advanced Industrial Science and Technology, Central 7, 1-1-1, Higashi, Tsukuba, Ibaraki 305-8567, Japan

K. Okino
Atmosphere and Ocean Research Institute (AORI), The University of Tokyo, 5-1-5 Kashiwa, Chiba 277-8564, Japan

H. Sato
School of Business Administration, Senshu University, 2-1-1 Higashimita, Tama, Kawasaki, Kanagawa 214-8580, Japan

R. Nauchi • K. Hara • R. Takamaru
School of Natural System, College of Science and Engineering, Kanazawa University, Kakuma, Kanazawa 920-1192, Japan

J.-i. Ishibashi et al. (eds.), *Subseafloor Biosphere Linked to Hydrothermal Systems: TAIGA Concept*,
DOI 10.1007/978-4-431-54865-2_14,

tectonics. The southern end of the Central Indian Ridge (CIR) is characterized by an intermediate-spreading mid-ocean ridge (5 cm/year, full spreading rate) that is different from the Atlantic (slow-spreading) and the Pacific (fast-spreading) ocean ridges. It is, therefore, the southern end of the CIR which will provide us with unique opportunities to study the magmatic and tectonic evolution along an intermediate mid-ocean ridge. One of the difficulties in regard to addressing these questions at oceanic spreading ridges is the paucity of in-situ samples from the seafloor.

Because of the discovery of a H_2-rich-fluid-bearing hydrothermal field (Kairei hydrothermal field) (Hashimoto et al. 2001) coupled with its unique hydrothermal fluid chemistry and vent-endemic ecosystem (Gamo et al. 2001; Van Dover et al. 2001; Van Dover 2002; Takai et al. 2004; Gallant and Von Damm 2006; Kumagai et al. 2008) in the southern end of the CIR, three submersible expeditions of the SHINKAI 6500 and one dredge expedition of the Hakuho-maru were conducted around the Kairei hydrothermal field (Fig. 14.1). This study presents systematic data concerning the mineral compositions of the primary features of peridotites, now highly serpentinized/weathered, and related gabbroic rocks recovered from areas around the Kairei-hydrothermal field.

14.2 Geological Background of the Studied Area

The rate of spreading in the Central Indian Ridge (CIR) increases from slow-spreading of 30 mm/year near the equator to intermediate-spreading with 48 mm/year at the Rodriguez Triple Junction (DeMets et al. 2010). The studied area is the southernmost CIR near the Rodriguez triple junction where three mid-ocean ridges (CIR, Southwestern Indian Ridge, Southeastern Indian Ridge) are intersected. A well-developed axial valley, segmented by fracture zones and non-transform discontinuities are identified in the southern part of the CIR. The ridge segments were identified from south to north, CIR-S1 and CIR-S2, respectively (Briais 1995). The ridge axis of CIR-1 is characterized as 7 km wide at the segment center with the widening to 12–15 km toward segment ends. The axial valley depth ranges from 3,600 to 4,400 m. The ridge axis shows typical slow-spreading ridge morphology, whereas off-axis morphology is rather chaotic. An oceanic core complex, 20 × 10 km in size and 1,000 m higher than the adjacent seafloor, is located off-axis on the western flank of the CIR at a latitude of 25° South (25°S OCC hereafter), between CIR-S1 and CIR-S2 (Mitchell et al. 1998; Kumagai et al. 2008; Morishita et al. 2009; Sato et al. 2009). The Kairei hydrothermal field is located on the eastern axial valley wall of CIR-S1 (Fig. 14.1). The Uraniwa Hills, where gabbros and dunites were mainly recovered from the top of the hill, is located off-axis, about 2 km to the east of the Kairei hydrothermal field (Nakamura et al. 2009). Petrogenesis of dunite-troctolite from the Uraniwa Hills will be shown in a separate paper. Serpentinized peridotites were already sampled at a small hill (Green Rock Hill and called as GRH hereafter), 15 km south of the 25°S OCC (Hellebrand et al. 2002) (Green Rock Hill in Fig. 14.1). Tectonic development of the studied area has been studied by several authors, but there is no clear picture yet (Briais 1995; Honsho et al. 1996; Mendel et al. 2000; Sato et al. 2009). Here we summarize petrological and mineralogical characteristics of peridotites and related gabbros from the 25°S OCC and the Kairei hydrothermal field (Yokoniwa Rise hereafter).

14.3 Petrology

Gabbros from the 25°S OCC are olivine gabbro, gabbro, gabbronorite (granular orthopyroxene-bearing gabbro) and oxide gabbro. The grain sizes of gabbros vary from doleritic fine-grained to coarse-grained rocks (Figs. 14.2 and 14.3). Most of the samples are mainly composed of plagioclase, clinopyroxene and amphibole. Accessory phases are olivine, magnetite, ilmenite, sulfides and apatite. Clinopyroxene usually occurs as a coarse grain (Fig. 14.3a), the interstitial phase interlocking with plagioclase (Fig. 14.3b) and sometimes forming oikocrysts. Orthopyroxene also occurs as a granular grain and is sometimes associated with clinopyroxene, forming a two-pyroxene aggregate (Fig. 14.3d). Olivine tends to occur in fine-grained samples or fine-grained parts of each sample showing variations in grain size within each sample (Fig. 14.4c). Brown and green amphiboles occur heterogeneously in most samples. Brown amphiboles are often gradually changed to green amphiboles, and probably have both igneous and metamorphic origins. Oxide minerals are frequently observed in some samples (Fig. 14.3c). The gabbros have magmatic textures, usually with no or very minor plastic deformation except for very localized millimeter-scale altered zones where green amphibole (tremolitic / actinolitic) and/or chlorite were formed. Chlorite veins and albite veins are also found in the altered zone. Olivine-bearing fine-grained doleritic gabbro cuts gabbronorite with inverted pigeonite (Fig. 14.4c). No troctolitic rocks were found in the 25°S OCC, whereas many troctolitic rocks were recovered from the Uraniwa Hills in the east of the Kairei hydrothermal field (Nakamura et al. 2009). One gabbro (919R09) is cut by a quartz-bearing leucocratic granitic network showing granophyric intergrowth of quartz and feldspar (Fig. 14.2). Amphiboles, both brown-colored and green-colored, are observed at the boundary between the granitic rock and the gabbro. Highly evolved silica-rich granitic rock was also reported from the 25°S OCC (Nakamura et al. 2007).

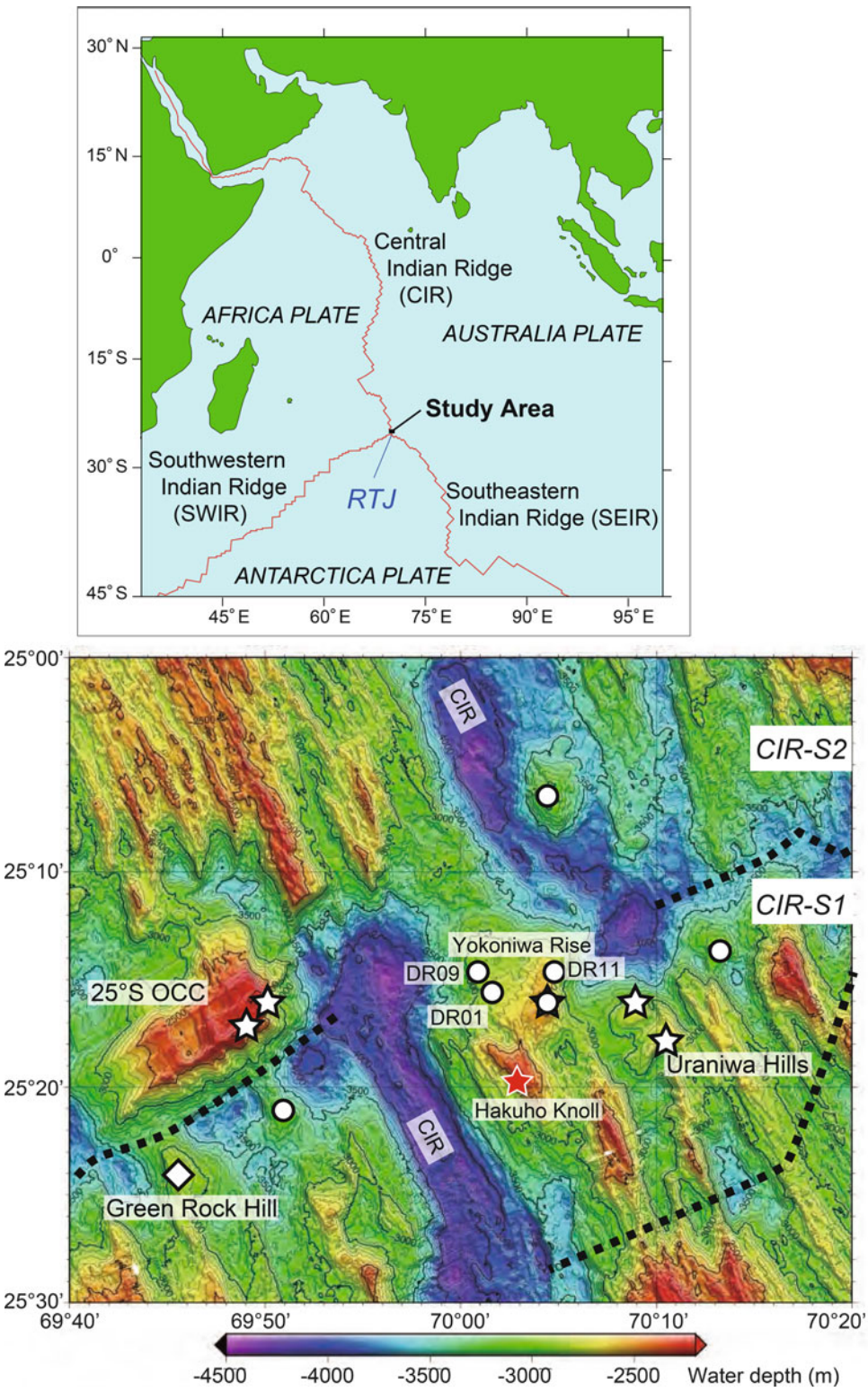

Fig. 14.1 The sample localities of peridotites and related gabbros on bathymetry map around the south end of the Central Indian Ridge (CIR). The *broken lines* represent the estimated non-transform offsets (Okino et al. Chap. 11). The peridotite samples were recovered by the SHINKAI 6500 dives (*star*) and the R/V Hakuho-Maru dredges (*circle*). The *red-filed star* on the Hakuho Knoll is the locality of the Kairei Hydrothermal Field. The Uraniwa Hills (Kumagai et al. 2008), where troctolites and dunites were recovered, is also shown. The peridotite samples from the Green Rock Hill were reported by Hellebrand et al. (2002). *RTJ* Rodriguez Triple Junction

Peridotites sampled from the 25°S OCC are classified into two types: a granular peridotite (clinopyroxene-bearing harzburgite) recovered along the ridge-facing slope and a highly deformed type of rock recovered from the top surface of the 25°S OCC. The latter was formed by interaction between peridotite/gabbro rocks with hydrothermal fluids along the detachment fault (Morishita et al. 2009). Highly deformed samples as found in the 25°S OCC have never been recovered from the Yokoniwa Rise. Petrological characteristics of granular peridotites (clinopyroxene-bearing

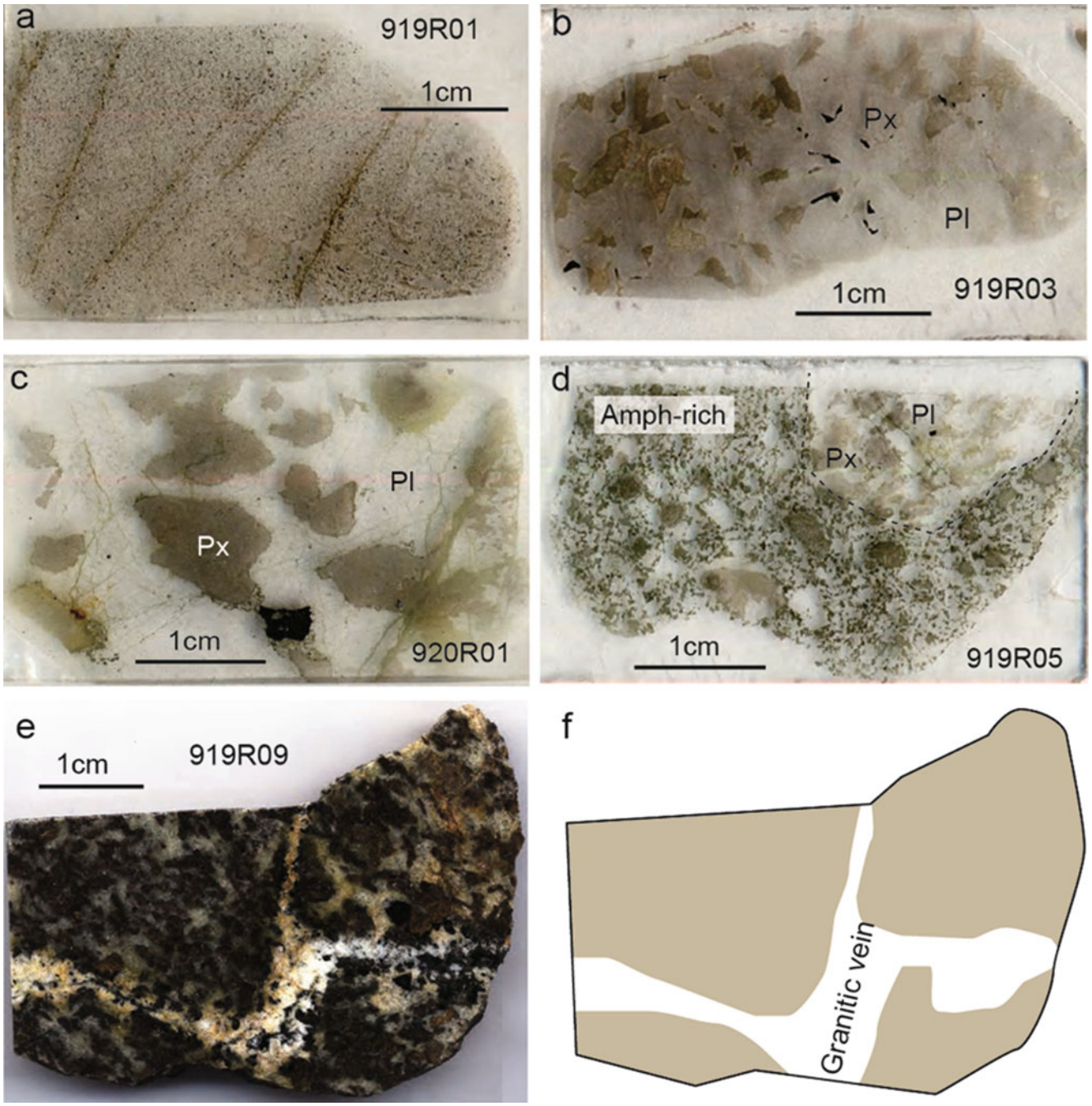

Fig. 14.2 Representative gabbro samples recovered from the 25°S OCC. (**a**) Fine-grained olivine gabbro (919R01). (**b**) Coarse-grained gabbronorite (919R03). (**c**) Coarse-grained gabbronorite (920R01). (**d**) Heterogeneity in grain size showing amphibole-rich domain and gabbroic domain (919R05). (**e**) Quartz-bearing granitic network in gabbro (919R09) and its sketch (**f**). *Pl* plagioclase, *Px* pyroxene

harzburgite to lherzolite) are basically the same between the 25°S OCC and the Yokoniwa Rise. Here we, therefore, briefly describe the petrological characteristics of granular peridotites from the 25°S OCC and the Yokoniwa Rise. Less deformed, granular to weakly deformed peridotites are extensively serpentinized and weathered, >90 % replacement of the primary minerals. Serpentinization and weathering result in variations in the color of samples, such as black, greenish and oranges-like to the naked eye (Fig. 14.5). A part of some samples show white in color, where talc is frequently observed. Bastite textures with relics of orthopyroxene in the core are frequently found in samples. The cores of the orthopyroxene grains frequently contain exsolution lamellae of clinopyroxene. Several samples in both the 25°S OCC and the Yokoniwa Rise were intruded by leucocratic veins (Fig. 14.5), up to 10 mm in thickness, mainly composed of

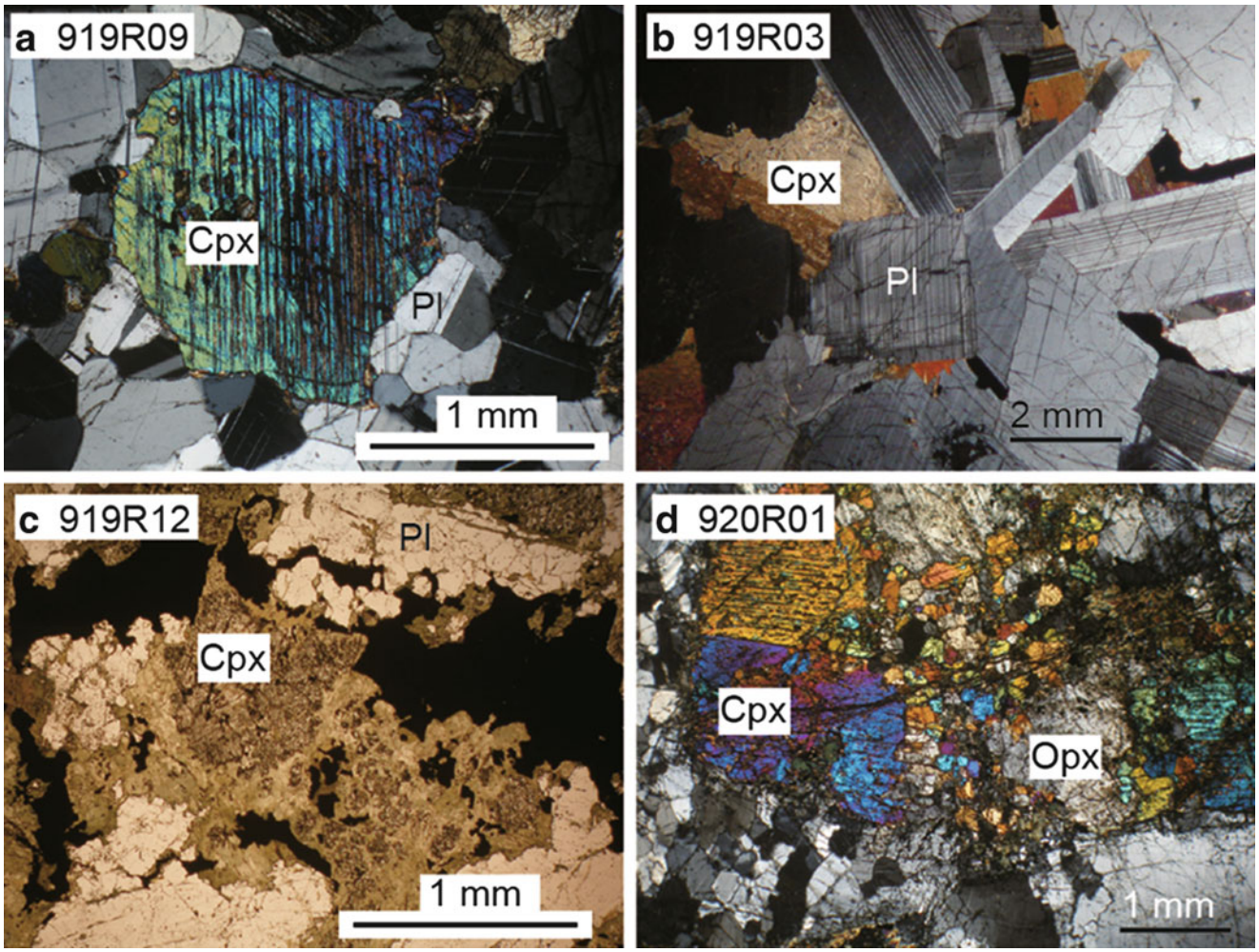

Fig. 14.3 Photomicroscope of gabbro samples recovered from the 25°S OCC. (**a**) Granular clinopyroxene (919R09) (Cross-polarized light). (**b**) Interstitial clinopyroxene (919R03) (Cross-polarized light), (**c**) Oxide-rich gabbro (919R12) (Plane-polarized light), (**d**) Granular orthopyroxene associated with clinopyroxene (920R01) (Cross-polarized light). *Pl* plagioclase, *Cpx* clinopyroxene, *Opx* orthopyroxene

chlorite and tremolite/actinolite with a small amount of ilmenite, zircon and apatite. The area near the thick leucocratic vein tends to be less serpentinized. Plagioclase, now completely altered, was observed in several samples (Fig. 14.5d). Spinel grains without altered plagioclase as well as altered plagioclase without spinel occur in the same thin section (Morishita et al. 2009).

14.4 Mineral Chemistry

14.4.1 Analytical Method

Major element compositions of minerals were analyzed by electron probe microanalysis (EPMA) with a JEOL JXA-8800 Superprobe system at Kanazawa University. The analyses were performed using an accelerating voltage of 15 kV and beam current of 20 nA, using a 3 μm diameter beam. Natural and synthetic mineral standards were employed for all minerals. JEOL software using ZAF corrections was employed (Morishita et al. 2003). We were generally attempting to obtain average compositions for the thin section. However, if the sample showed heterogeneity within each grain and/or each sample, single spot analyses were used as representative analytical data. The mineral chemistry of peridotites recovered from the 25°S OCC had already been described in a previous paper (Morishita et al. 2009). The mineral chemistry of peridotites recovered from the Yokoniwa Rise is similar to that from the 25°S OCC. Representative major element compositions of minerals of gabbroic rocks from the 25°S OCC and peridotites from the Yokoniwa Rise are shown in Tables 14.1, 14.2, 14.3, 14.4, 14.5, 14.6, 14.7, 14.8, and 14.9.

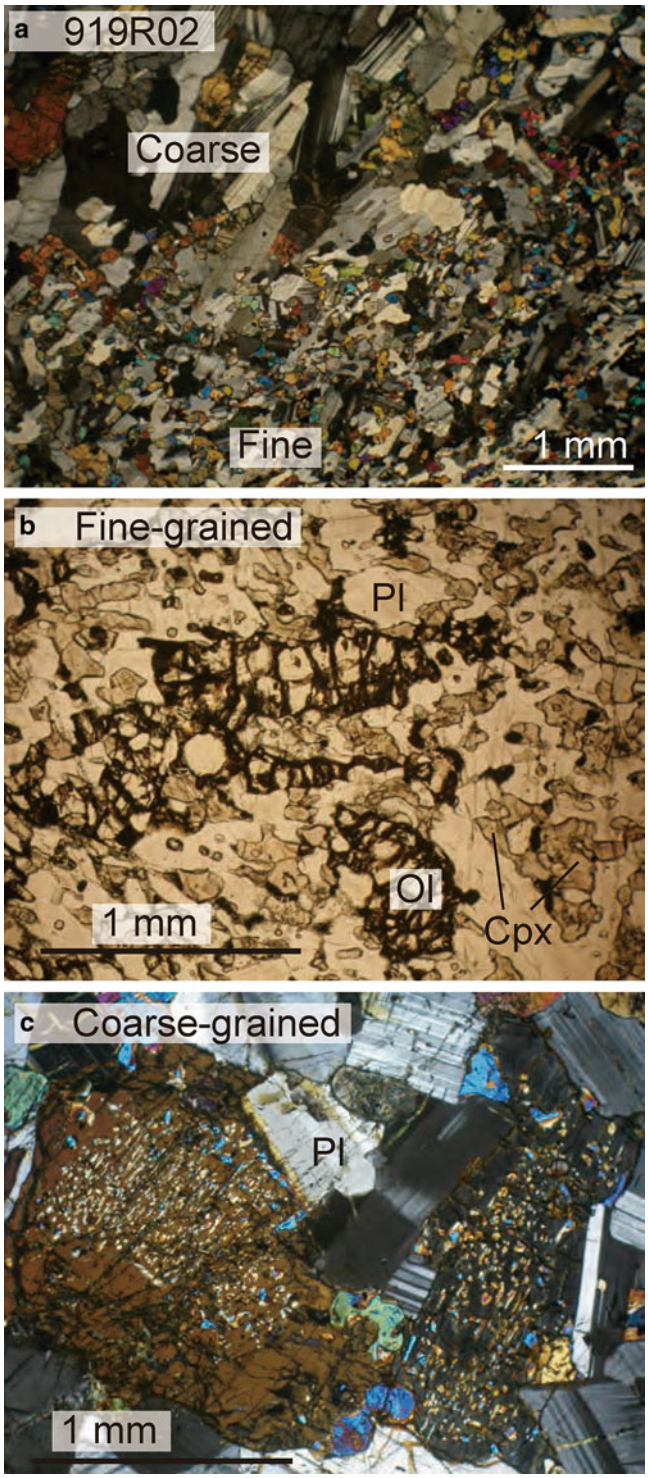

Fig. 14.4 Photomicroscope of heterogeneous gabbro (919R02). (**a**) Contact between fine-grained and coarse-grained parts (Cross-polarized light). (**b**) Fine-grained olivine gabbroic part (Plane-polarized light). (**c**) Coarse-grained part with inverted pegionite (Cross-polarized light).

14.4.2 Gabbros from the 25°S OCC

Mineral compositions in samples with variable grain sizes show different chemical compositions in each domain. The fine-grained part, which usually contains olivine, is higher in Mg# (= Mg/(Mg + Fe^{total}) atomic ratio) than the coarse-grained part within the sample as shown below. We, therefore, analyzed mineral compositions in each domain and describe them as different samples.

Olivine was found in three samples. The forsterite content of olivine is homogeneous within each sample and is 54, 58 and 77, respectively (Table 14.1).

The TiO_2 content of clinopyroxene is first increased with the decreasing of Mg# until around 75 (Fig. 14.6a), as expected for the melt during crystallization of olivine, plagioclase and pyroxenes. The TiO_2 content is then decreased (Fig. 14.6a), probably caused by the crystallization of Ti-bearing oxides, such as ilmenite and titanomagnetite (Table 14.2).

Plagioclase mostly shows normal zoning from the Ca-rich core to the Na-rich rim. The anorthite content of coarse-grained plagioclase ranges from 37 to 59 in the core, whereas more Na-rich plagioclase, down to An6, was found in quartz-bearing granitic veins in gabbro as well as thin veins (albite vein in table) (Table 14.3). There is a good correlation between plagioclase compositions and lithologies, the Ca-rich plagioclase is usually found in olivine-bearing gabbro whereas the Na-rich plagioclase is found in oxide gabbro (Fig. 14.6).

The Mg# of orthopyroxene core ranges from 67 to 76, which is slightly lower than ranges of Mg# of clinopyroxene. The TiO_2 content is usually lower than 0.5 wt.%. The Cr_2O_3 content is low <0.1 wt.% and is usually lower than the detection limit when the Mg# is lower than 70 (Table 14.4).

Brown amphiboles are titaniferous pargastic hornblend (1–4 wt.% TiO_2) (Table 14.5).

14.4.3 Peridotites from the Yokoniwa Rise

Olivine compositions are homogeneous in each sample. The forsterite content and the NiO content are within narrow compositional ranges with 90.8–91.3 and 0.35–0.39 wt.%, respectively (Table 14.6).

The Mg# of orthopyroxene is around 91. The Al_2O_3 content ranges from 2.5 to up to 4 wt.%. The TiO_2 content is lower than detection limit of analyses (<0.06 wt.%) (Table 14.7).

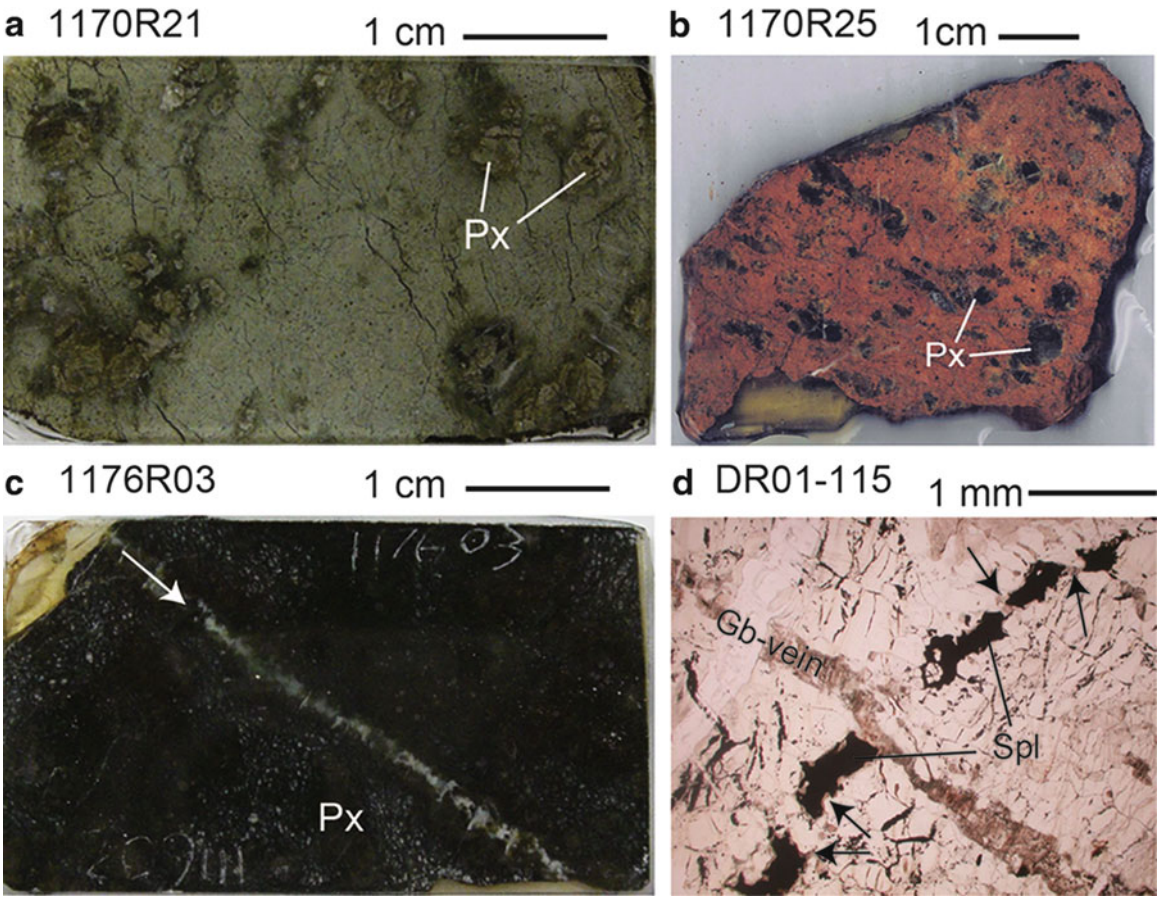

Fig. 14.5 Representative peridotite samples recovered from the Yokoniwa Rise. (**a**) Green-colored (1170R21) (*upper panel*), (**b**) brown-colored (*middle panel*) (1170R25) and (**c**) black-colored with thin leucocratic vein (indicated by *arrow*) (*bottom panel*) (1176R03). (**d**) Spinel trails cut by leucocratic vein (Gb-vein). Note that spinels are surrounded by plagioclase pseudomorph (indicated by *arrows*). *Px* pyroxene, *Spl* spinel

Table 14.1 Representative major element compositions of olivine in gabbroic rocks from the 25°S OCC

Sample	Section	SiO_2	FeO	MnO	MgO	CaO	NiO	Total	Fo
919R01	Average	35.30	36.20	0.48	28.43	0.06	<0.1	100.6	58.3
	STD (N = 4)	0.20	0.22	0.06	0.17	<0.03	–	0.4	0.2
919R02	Average	35.36	38.53	0.54	25.87	0.07	<0.1	100.5	54.5
	STD (N = 2)	0.23	0.03	0.09	0.23	<0.03	–	0.4	0.2
919R05	Average	38.93	21.27	0.32	39.39	0.05	0.14	100.1	76.7
	STD (N = 4)	0.15	0.64	0.04	0.46	<0.03	0.04	0.4	0.7

The Cr_2O_3, TiO_2, Al_2O_3, Na_2O and K_2O contents are mostly lower than detection limit of analyses, <0.08 wt.%, <0.06 wt.%, <0.02 wt.%, <0.03 wt.% and <0.03 wt.%, respectively. *STD* standard deviation, *N* numbers of analyses, *Fo* forsterite content

Clinopyroxene in the samples with leucocratic veins are distinctively higher in Na_2O (0.3–0.5 wt.%) and TiO_2 (0.5–1.3 wt.%) content than those in vein-free samples, usually <0.1 wt.% for both elements (Fig. 14.7).

Chemical compositions of spinels is homogeneous in samples without leucocratic veins, whereas spinels in samples with leucocratic veins show variations within and among grains (Table 14.9). The Cr# and the TiO_2 content of most samples are around 0.35 and <0.1 wt.%, respectively, which are similar to the leucocratic vein-free sample in the 25°S OCC (Fig. 14.8). Both the Cr# and the TiO_2 content of spinels are high in the leucocratic vein-bearing samples and tend to be increased toward the leucocratic veins (Fig. 14.8). YFe^{3+} (= $100Fe^{3+}/(Cr + Al + Fe^{3+})$ atomic ratio) is usually lower than 5 for homogeneous samples, and is relatively higher in high-Ti grains, up to 9 (Table 14.9).

Table 14.2 Representative major element compositions of clinopyroxene in gabbroic rocks from the 25°S OCC

Sample	Note	SiO_2	TiO_2	Al_2O_3	Cr_2O_3	FeO	MnO	MgO	CaO	Na_2O	K_2O	Total	Mg#	Cr#
919R01	Core	50.88	0.91	2.55	0.13	10.82	0.34	14.39	20.43	0.41	<0.03	101.5	70.3	3.3
919R02 (fine)	Core	52.27	0.89	2.28	0.14	8.98	0.26	14.20	20.69	0.36	<0.03	100.1	73.8	3.9
919R02 (coarse)	Core	51.70	0.74	1.84	0.16	11.29	0.28	13.54	20.14	0.39	<0.03	100.1	68.1	5.4
919R03	Core	53.01	0.91	2.61	<0.08	9.15	0.28	14.40	20.96	0.53	<0.03	101.9	73.7	–
919R04 (fine)	Core	53.08	0.62	2.35	<0.08	8.35	0.23	14.81	21.51	0.39	<0.03	101.4	76.0	–
919R04 (coarse)	Core	50.88	0.91	2.55	0.13	10.82	0.34	14.39	20.43	0.41	<0.03	100.9	70.3	3.3
919R05 (ol)	Core	54.22	0.68	2.20	0.26	5.57	0.18	16.26	21.92	0.51	<0.03	101.8	83.9	7.4
919R05 (px)	Core	54.02	0.71	2.17	0.09	6.79	0.19	16.52	20.64	0.32	<0.03	101.5	81.3	2.7
919R05 (amph)	Core	53.17	0.91	2.64	0.15	8.39	0.23	14.78	20.67	0.73	<0.03	101.7	75.8	3.6
91R909	Core	51.96	0.83	2.42	<0.08	7.16	0.23	15.69	21.07	0.39	<0.03	99.8	79.6	–
91R909	Rim	52.45	0.24	0.54	<0.08	11.83	0.39	12.54	21.76	0.13	<0.03	99.9	65.4	–
919R12	Core	52.47	0.23	1.62	<0.08	12.94	0.26	12.33	20.85	0.60	0.05	101.4	62.9	–
919R12	Rim	53.17	0.07	0.38	<0.08	12.05	0.37	12.56	22.46	0.34	<0.03	101.4	65.0	–
920R01	Core	51.95	0.79	2.39	0.09	9.68	0.30	14.92	21.23	0.41	<0.03	101.8	73.3	2.3
920R01	Rim	52.38	0.48	1.58	<0.08	11.01	0.29	14.48	20.74	0.32	<0.03	101.3	70.1	–

The NiO content is mostly lower than 0.1 wt.%. *Fine* fine-grained part, *coarse* coarse-grained part, *ol* olivine-bearing part, *px* olivine-free and amphibole-poor part, *amph* amphibole-rich part, *Mg#* Mg/(Mg + Fe^{total}) atomic ratio, *Cr#* Cr/(Cr + Al) atomic ratio

Table 14.3 Representative major element compositions of plagioclase in gabbroic rocks from the 25°S OCC

Sample	Note	SiO_2	TiO_2	Al_2O_3	FeO	MgO	CaO	Na_2O	K_2O	Total	An
919R01	Core	54.60	0.08	29.35	0.37	0.04	11.71	5.34	0.06	101.6	54.8
919R01	Rim	55.41	<0.05	28.60	0.23	0.03	10.74	5.84	0.08	101.0	50.4
919R02 (fine)		56.91	<0.05	27.44	0.20	0.04	9.46	5.79	0.62	100.5	47.5
919R02 (coarse)		59.18	<0.05	25.80	0.47	0.10	7.95	7.34	0.10	101.0	37.4
919R03	Core	56.92	0.10	26.93	0.37	0.10	9.73	6.16	0.08	100.3	46.6
919R04 (fine)	Core	55.60	<0.05	28.33	0.28	0.04	11.10	5.69	0.03	101.1	51.9
919R04 (fine)	Rim	55.44	<0.05	28.20	0.29	0.04	11.04	5.77	<0.03	100.8	51.4
919R04 (coarse)	Core	57.15	0.14	27.40	0.32	0.03	10.01	6.18	0.08	101.2	47.2
919R05 (ol)		54.50	<0.05	28.80	0.13	0.03	12.20	4.81	0.04	100.5	58.3
919R05 (px)	Core	54.71	<0.05	29.48	0.14	0.02	12.23	5.01	0.03	101.7	57.4
919R05 (px)	Rim	69.59	<0.05	19.82	0.30	<0.02	0.79	11.89	<0.03	102.4	3.5
919R05 (amph)		64.18	<0.05	22.86	0.26	<0.02	4.37	9.65	0.20	101.6	20.0
919R09	Core	53.59	0.05	28.78	0.16	0.02	12.04	4.66	0.07	99.4	58.8
919R09	Rim	52.87	0.05	29.31	0.20	0.05	12.35	4.40	0.08	99.4	60.8
919R09 (granite)		60.86	<0.05	24.00	0.16	0.02	6.08	8.21	0.18	99.5	29.1
919R09 (granite)		67.19	<0.05	20.16	0.00	<0.02	1.25	11.11	0.07	99.9	5.9
919R12	Core	59.27	<0.05	25.69	0.14	<0.02	7.96	7.48	0.16	100.7	37.0
920R01	Core	56.60	<0.05	27.68	0.41	0.04	10.31	5.93	0.03	101.0	49.0
920R01 (ab vein)		66.80	<0.05	21.00	0.00	<0.02	1.62	10.95	0.03	100.5	7.5
920R10	Core	57.29	0.06	26.49	0.11	<0.02	8.85	6.95	0.12	99.9	41.3
921R24	Core	66.77	<0.05	20.68	0.29	<0.02	1.56	11.49	<0.03	100.8	7.0

The Cr_2O_3, MnO and NiO contents are mostly lower than 0.1 wt.%. *Fine* fine-grained part, *coarse* coarse-grained part, *ol* olivine-bearing part, *px* olivine-free and amphibole-poor part, *amph* amphibole-rich part, *granite* granitic vein, *ab vein* albite vein. *An* anorthite content (100 Ca/(Ca + Na) s atomic ratio)

Table 14.4 Representative major element compositions of orthopyroxene in gabbroic rocks from the 25°S OCC

Sample	Note	SiO_2	TiO_2	Al_2O_3	Cr_2O_3	FeO	MnO	MgO	CaO	Na_2O	K_2O	Total	Mg#	Cr#
919R01	Core	53.22	0.56	1.31	<0.08	20.16	0.48	23.45	2.15	<0.03	<0.03	101.4	67.5	–
919R02(coarse)	Core	53.66	0.49	1.18	<0.08	19.61	0.42	23.10	2.63	0.06	<0.03	101.2	67.7	–
919R04 (fine)	Core	54.88	0.36	0.99	<0.08	16.80	0.44	25.91	1.11	<0.03	0.03	100.6	73.3	–
919R04 (coarse)	Core	53.66	0.49	1.18	<0.08	19.61	0.42	23.10	2.63	0.06	<0.03	101.2	67.7	–
919R95 (ol)		55.48	0.29	1.13	0.11	13.88	0.34	27.94	1.10	<0.03	<0.03	100.3	78.2	6.3
919R05(amph)		54.87	0.25	0.80	<0.08	20.39	0.51	23.57	1.27	<0.03	<0.03	101.7	67.3	–
919R09		53.99	0.39	1.03	<0.08	15.27	0.29	26.61	1.64	0.03	<0.03	99.3	75.6	–

The NiO content is mostly lower than 0.1 wt.%. Note that the CaO content might be high because of inevitable contaminations from fine-grained clinopyroxene lamellae. *Fine* fine-grained part, *coarse* coarse-grained part, *ol* olivine-bearing part, *px* olivine-free and amphibole-poor part, *amph* amphibole-rich part, *granite* granitic vein, *ab vein* albite vein, *Mg#* Mg/(Mg+Fe^{total}) atomic ratio, *Cr#* Cr/(Cr+Al) atomic ratio

Table 14.5 Representative major element compositions of brown amphibole in gabbroic rocks from the 25°S OCC

Sample	Note	SiO_2	TiO_2	Al_2O_3	Cr_2O_3	FeO	MnO	MgO	CaO	Na_2O	K_2O	Total	Mg#	Cr#
919R01	Opq	42.81	2.57	10.50	<0.08	15.08	0.20	12.48	11.13	2.61	0.16	97.6	0.596	–
919R01	Fine	44.51	1.36	9.89	0.12	14.01	0.26	13.80	11.24	2.55	0.12	97.9	0.637	0.823
919R02 (fine)	Px	43.96	3.44	10.50	0.61	11.54	0.11	13.62	10.88	2.84	0.13	97.6	0.678	3.739
919R02 (fine)	Bleb	43.21	4.03	10.29	<0.08	14.53	0.18	11.30	11.11	2.98	0.23	97.9	0.581	–
919R02 (fine)	Core	45.63	1.84	8.17	<0.08	18.56	0.23	10.75	10.73	2.15	0.31	98.4	0.508	–
919R02 (coarse)	Core	46.33	1.55	8.61	<0.08	16.25	0.19	12.21	10.74	2.34	0.09	98.4	0.572	–
919R02 (coarse)	Bleb	43.64	4.16	11.13	<0.08	11.26	0.12	13.47	11.18	3.35	0.12	98.4	0.681	–
919R03	Bleb	46.76	1.10	9.28	<0.08	11.98	0.16	14.55	11.23	2.33	0.17	97.6	0.684	–
919R05 (amph)	Pl	44.71	2.83	10.12	0.15	10.92	0.18	14.45	11.20	3.16	0.14	97.9	0.702	1.003
919R05(amph)	Inter	46.41	2.29	8.95	0.54	6.75	0.12	17.38	11.44	2.76	0.17	96.9	0.821	3.892
919R09	Inter	43.46	3.44	11.42	<0.08	8.76	0.08	15.14	11.54	2.89	0.16	97.0	0.755	–
919R09	Px	42.78	3.89	11.11	0.11	8.87	0.19	14.97	11.61	2.87	0.14	96.6	0.750	0.630
919R12	Px	43.72	2.67	9.62	<0.08	17.34	0.32	10.88	10.82	2.83	0.24	98.5	0.528	–

The NiO content is mostly lower than 0.1 wt.%. *Fine* fine-grained part, *coarse* coarse-grained part, *amph* amphibole-rich part, *opq* around opaque mineral, *px* around pyroxene grain, *pl* around plagioclase, *inter* interstitial grain, *Mg#* Mg/(Mg+Fe^{total}) atomic ratio, *Cr#* Cr/(Cr+Al) atomic ratio

Table 14.6 Representative major element compositions of olivine in peridotites from the Yokoniwa Rise

Sample	Note	SiO_2	FeO	MnO	MgO	CaO	NiO	Total	Fo
1170R01	Average	40.92	8.55	0.12	50.49	0.04	0.38	100.5	91.3
	STD (N = 3)	0.36	0.03	0.01	0.64	<0.03	0.01	0.9	0.1
1170R04	Average	40.75	9.03	0.13	50.33	0.04	0.37	100.6	90.9
	STD (N = 6)	0.39	0.07	0.02	0.34	<0.03	0.01	0.7	0.1
1170R09	Average	41.11	9.04	0.13	50.31	<0.03	0.38	101.2	90.8
	STD (N = 13)	0.43	0.09	0.02	0.34	<0.03	0.02	0.7	0.1
1170R21	Average	41.37	8.78	0.13	50.63	0.03	0.39	101.4	91.1
	STD (N = 7)	0.27	0.06	0.03	0.38	<0.03	0.01	0.6	0.1
1170R25	Average	41.10	8.85	0.12	50.43	0.05	0.37	101.0	91.0
	STD (N = 9)	0.17	0.18	0.03	0.42	0.01	0.22	0.7	0.1
1170R27	Average	41.16	8.92	0.13	50.24	<0.03	0.37	100.8	90.9
	STD (N = 20)	0.29	0.13	0.01	0.48	<0.03	0.02	0.7	0.1
1170R28	Average	41.25	8.93	0.13	50.28	0.06	0.37	101.1	90.9
	STD (N = 11)	0.33	0.20	0.04	0.31	<0.03	0.04	0.6	0.2
1176R15	Average	40.77	8.68	0.13	49.30	<0.03	0.35	99.3	91.0
	STD (N = 5)	1.14	0.08	0.02	1.12	<0.03	0.02	2.2	0.2
1176R20	Average	41.25	8.84	0.13	50.38	0.03	0.37	101.0	91.0
	STD (N = 28)	0.31	0.14	0.02	0.41	<0.03	0.02	0.7	0.1
DR01-106	Average	41.15	9.07	0.15	50.55	0.03	0.39	101.4	90.9
	STD (N = 9)	0.36	0.22	0.02	0.48	<0.03	0.02	0.9	0.2
DR11-003	Average	41.60	9.06	0.12	50.28	0.05	0.36	100.6	90.8
	STD (N = 7)	0.57	0.14	0.01	0.53	<0.03	0.02	1.0	0.2

The Cr_2O_3, TiO_2, Al_2O_3, Na_2O and K_2O contents are mostly lower than detection limit of analyses, <0.08 wt.%, <0.06 wt.%, <0.02 wt.%, <0.03 wt.% and <0.03 wt.%, respectively. *STD* standard deviation, *N* numbers of analyses, *Fo* forsterite content

Table 14.7 Representative major element compositions of orthopyroxene in peridotites from the Yokoniwa Rise

Sample	Note	SiO_2	TiO_2	Al_2O_3	Cr_2O_3	FeO	MnO	MgO	CaO	NiO	Total	Mg#	Cr#
1170R04	Core	55.64	<0.05	3.36	0.96	6.00	0.13	33.46	0.89	0.10	100.6	0.909	0.161
1170R09	Core	55.87	<0.05	3.65	0.84	5.97	0.15	33.28	0.95	<0.1	100.8	0.909	0.133
1170R21		56.08	<0.05	3.37	0.87	5.83	0.14	33.46	1.19	<0.1	101.1	0.911	0.148
1170R25	Core	56.38	0.03	3.13	0.81	5.71	0.16	34.02	0.83	<0.1	101.2	0.914	0.148
1170R27		56.20	<0.05	3.00	0.73	5.87	0.06	33.30	1.35	<0.1	100.6	0.910	0.141
1170R28	Core	56.24	<0.05	3.35	0.81	5.72	0.16	32.62	1.14	<0.1	100.2	0.910	0.139
1176R03		56.99	<0.05	2.55	0.78	5.91	0.13	33.79	1.00	<0.1	101.3	0.911	0.171
1176R15		56.14	<0.05	3.41	0.83	5.89	0.14	33.92	0.94	<0.1	101.4	0.911	0.140
DR01-106	Core	54.49	0.06	3.86	0.99	5.84	0.11	32.66	1.35	0.10	99.5	0.909	0.146
DR11-003		55.83	<0.05	3.42	0.79	5.75	0.13	33.05	1.57	0.12	100.7	0.911	0.134

The Na_2O and K_2O contents are lower than detection limit of analyses, <0.03 wt.%. *STD* standard deviation, *N* numbers of analyses, *Mg#* Mg/(Mg+Fe^{total}) atomic ratio, *Cr#* Cr/(Cr+Al) atomic ratio

Table 14.8 Representative major element compositions of clinopyroxene in peridotites from the Yokoniwa Rise

Sample	Note	SiO_2	TiO_2	Al_2O_3	Cr_2O_3	FeO	MnO	MgO	CaO	Na_2O	Total	Mg#	Cr#
1170R01		52.28	0.07	4.48	1.42	2.35	<0.1	16.73	23.53	0.05	101.1	0.927	0.175
1170R04	Average	52.86	0.22	3.03	1.17	2.42	<0.1	17.11	22.95	0.37	100.3	0.927	0.206
	STD(N = 15)	0.78	0.07	0.39	0.21	0.10	<0.1	0.40	0.28	0.08	0.8	0.002	
	Leuco	53.14	0.58	2.20	0.60	2.45	<0.1	17.75	22.53	0.40	99.8	0.928	0.155
	STD(N = 3)	0.48	0.03	0.20	0.10	0.07	<0.1	0.15	0.19	0.07	0.9	0.002	
1170R09	Average	51.92	0.09	4.55	1.39	2.42	<0.1	16.96	22.82	0.07	100.4	0.926	0.170
	STD (N = 3)	0.25	0.01	0.24	0.04	0.16	<0.1	0.48	1.22	0.00	0.4	0.003	
1170R25	Core	51.77	0.11	4.37	1.38	2.82	0.14	17.25	22.37	0.04	100.3	0.916	0.175
1170R27		52.57	0.05	3.57	0.97	2.49	<0.1	17.67	22.65	0.05	100.1	0.927	0.153
1170R28		52.25	0.11	4.29	1.22	2.52	0.12	16.56	23.80	0.08	101.0	0.921	0.160
1176R03		53.69	0.14	2.86	1.21	2.55	<0.1	17.19	22.52	0.34	100.6	0.923	0.222
1176R09		52.14	0.09	4.34	1.46	2.60	0.12	17.07	23.02	0.02	100.9	0.921	0.184
1176R15		52.94	0.09	4.50	1.34	2.89	<0.1	17.42	21.92	0.15	101.4	0.915	0.166
1176R20		53.04	0.11	4.01	1.24	2.08	<0.1	16.64	23.85	0.17	101.2	0.935	0.172
DR01-106		52.43	0.08	3.77	0.95	2.53	<0.1	17.47	23.22	0.06	100.7	0.925	0.145
DR01-115		52.45	1.33	2.86	1.12	2.64	<0.1	17.28	22.34	0.50	100.6	0.921	0.208
DR11-003		52.98	0.06	4.07	1.10	2.71	0.10	17.62	22.48	0.03	101.2	0.921	0.153

The K_2O and NiO contents are lower than detection limit of analyses, <0.03 and <0.1 wt.%, respectively. *STD* standard deviation, *N* numbers of analyses, *Mg#* Mg/(Mg+Fe^{total}) atomic ratio, *Cr#* Cr/(Cr+Al) atomic ratio

14.5 Discussions

14.5.1 Petrogenesis of Gabbros from the 25°S OCC

In-situ samplings of the mid-ocean ridge gabbros provide us with direct insight into their compositions. These data allow us to compare the results from other ocean floors and to discuss models of how the lower oceanic crusts form.

The petrological characteristics of the gabbros in the 25°S OCC are similar to those described from the ultraslow-spreading ocean ridges (Dick et al. 2000), where the magmatic activity is low. There are good correlations between plagioclase and clinopyroxene in the studied samples. This is consistent with chemical trends caused by crystallization of plagioclase and clinopyroxene (+olivine) (Fig. 14.6). Differences in the major-element compositions between the oceans can be seen in the diagram. Gabbros from the ultraslow to slow-spreading ocean ridges (MARK area of the Mid-Atlantic ridge and Atlantis Bank of the Southwest Indian Ridge) have lower plagioclase anorthite contents for a given clinopyroxene Mg# than those in gabbros from the fast-spreading ocean ridge (Hess Deep and/or Pito Deep of East Pacific) (Perk et al. 2007) (Fig. 14.6). Low-anorthite content of plagioclase at the same Mg# of clinopyroxene can be considered as analogues to the parameter Na_8 defined by Klein and Langmuir (1987), which is interpreted to be a good indicator of the extent of partial melting. Since a general trend of an increasing extent of partial melting is moved toward higher Ca, a higher anorthite content of plagioclase is expected to be crystallized from hypothetical

Table 14.9 Representative major element compositions of spinel in peridotites from the Yokoniwa Rise

Sample	Note	TiO_2	Al_2O_3	Cr_2O_3	FeO	MnO	MgO	NiO	Total	Mg#	Cr#	YCr	YAl	YFe^{3+}
1170R01	Average	0.06	36.35	30.42	16.03	0.19	16.24	0.17	99.5	0.694	0.360	34.5	61.5	3.9
	STD (N = 8)	0.01	0.81	0.76	0.54	0.01	0.53	0.02	0.5	0.022	0.011	0.9	1.3	0.6
1170R01 Low-Cr	Average1	<0.05	42.18	25.52	16.42	0.21	15.34	0.19	99.9	0.643	0.289	28.4	70.1	1.5
	STD (N = 3)		0.64	0.48	1.47	0.04	1.99	0.01	0.8	0.075	0.006	0.1	1.8	1.7
1170R04 High-Ti		0.66	22.69	42.66	22.15	0.32	11.42	0.13	100.0	0.524	0.558	53.1	42.1	4.8
1170R04		0.48	22.01	44.16	21.61	0.31	11.90	0.12	100.6	0.545	0.574	54.5	40.5	5.0
1170R04		0.25	23.25	42.81	22.30	0.32	11.23	<0.1	100.3	0.516	0.553	52.7	42.7	4.6
1170R09	Average	<0.05	37.95	29.74	15.33	0.20	16.27	0.17	99.7	0.690	0.345	33.5	63.7	2.8
	STD (N = 15)		1.07	0.68	0.59	0.02	0.47	0.02	0.8	0.013	0.011	1.0	1.2	0.4
1170R09 High-Cr	Average1	<0.05	24.88	41.22	22.66	0.29	10.80	0.08	99.9	0.498	0.526	50.4	45.4	4.2
	STD (N = 2)		0.95	0.79	0.20	0.01	0.09	0.01	0.0	0.002	0.014	1.2	1.5	0.3
1170R21	Average	<0.05	35.56	33.51	13.91	0.20	16.82	0.17	100.2	0.715	0.387	37.8	59.8	2.4
	STD (N = 3)		0.19	0.18	0.18	0.02	0.12	0.02	0.3	0.003	0.000	0.1	0.1	0.1
1170R23	Average	0.05	36.33	31.78	15.65	0.20	16.28	0.17	100.5	0.690	0.370	35.8	61.0	3.2
	STD (N = 21)	0.01	0.74	0.40	0.34	0.02	0.28	0.02	0.9	0.011	0.006	0.5	0.8	0.4
1170R25	Average	0.06	38.25	30.01	14.13	0.18	16.39	0.19	99.2	0.696	0.345	33.9	64.4	1.7
	STD (N = 7)	0.04	0.65	0.44	0.35	0.04	0.21	0.05	0.6	0.010	0.010	0.7	0.7	0.3
1170R027	Average	0.05	35.64	31.96	15.75	0.21	15.89	0.15	99.7	0.682	0.376	36.4	60.5	3.0
	STD (N = 11)	0.01	0.48	1.10	0.82	0.02	0.48	0.03	0.8	0.016	0.010	1.1	0.8	0.5
1170R028	Average	0.07	37.30	30.70	15.25	0.21	16.45	0.17	100.2	0.696	0.356	34.5	62.6	2.9
	STD (N = 4)	0.01	0.65	0.51	0.41	0.02	0.41	0.02	1.4	0.010	0.003	0.4	0.3	0.4
1176R03 High-Ti		0.37	22.14	43.79	19.55	0.27	12.58	0.12	98.9	0.582	0.570	54.4	41.0	4.5
1176R03		0.25	22.38	43.52	19.46	0.29	12.63	0.09	98.6	0.586	0.566	54.0	41.4	4.6
1176R03		0.11	24.50	42.12	18.97	0.32	13.47	0.09	99.6	0.613	0.536	51.0	44.2	4.8
1176R09	Average	<0.05	18.18	16.33	8.50	0.12	7.98	0.09	51.2	0.668	0.376	36.3	60.3	3.4
	STD (N = 14)		18.52	16.65	8.46	0.10	7.85	0.08	51.5	0.337	0.199	19.3	31.3	1.4
1176R15 High-Ti		1.33	19.35	41.42	24.54	0.33	11.39	0.18	98.6	0.534	0.589	53.5	37.2	9.3
1176R15		0.66	26.41	36.22	20.78	0.25	13.96	0.15	98.4	0.630	0.479	44.1	47.9	8.0
1176R15		0.08	35.26	29.43	17.06	0.22	16.03	0.21	98.3	0.695	0.359	33.9	60.6	5.5
1176R20	Average1	0.05	36.05	30.61	15.19	0.20	16.50	0.16	98.8	0.709	0.363	34.9	61.3	3.7
	STD (N = 3)	0.01	0.43	0.26	0.11	0.01	0.09	0.01	0.6	0.002	0.002	0.1	0.3	0.3
1176R22	Average	<0.05	18.33	15.84	7.92	0.10	8.15	0.08	50.5	0.688	0.367	35.5	61.3	3.2
	STD (N = 5)		17.81	15.19	7.56	0.09	8.21	0.08	49.1	0.353	0.181	17.4	30.5	1.7
DR01-106	Average	0.08	36.25	31.04	14.22	0.18	17.30	0.22	99.3	0.736	0.365	35.1	61.1	3.8
	STD (N = 3)	0.01	0.29	0.20	0.20	0.01	0.05	0.04	0.1	0.003	0.003	0.2	0.5	0.4
DR01-106 Low-Cr	Average1	<0.05	39.01	29.28	15.18	0.18	16.69	0.18	100.6	0.699	0.335	32.6	64.7	2.8
	STD (N = 3)		0.39	0.21	0.45	0.02	0.30	0.02	0.5	0.011	0.004	0.4	0.3	0.2
DR01-103 High-Ti		0.23	27.40	41.52	15.33	0.24	15.25	<0.1	100.1	0.674	0.504	49.0	48.3	2.7
DR01-103		0.17	30.85	38.07	14.70	0.22	16.21	0.12	100.3	0.701	0.453	44.0	53.1	2.9
DR01-103		0.10	33.97	34.85	13.78	0.18	16.97	0.16	100.0	0.725	0.408	39.6	57.6	2.8
DR01-115 High-Ti		0.64	29.64	37.62	16.11	0.25	15.66	0.18	100.1	0.681	0.460	44.3	52.0	3.8
DR01-115		0.54	31.11	35.95	15.93	0.19	15.73	0.19	99.7	0.683	0.437	42.1	54.3	3.6
DR01-115		0.25	22.61	46.54	17.30	0.31	13.75	0.12	100.9	0.621	0.580	56.3	40.7	3.0
DR09-19	Average	0.08	26.87	40.83	17.84	0.24	14.66	0.13	100.7	0.650	0.505	48.1	47.2	4.7
	STD (N = 6)	0.02	0.16	0.23	0.32	0.02	0.10	0.01	0.5	0.002	0.002	0.3	0.2	0.4
DR11-003	Average	0.05	38.30	29.51	15.50	0.20	16.47	0.17	100.2	0.694	0.341	33.0	63.9	3.0
	STD (N = 6)	0.02	1.21	0.50	0.84	0.02	0.54	0.02	0.6	0.016	0.011	0.9	1.3	0.4
DR11-008	Average	0.06	37.08	30.63	14.53	0.18	17.06	0.19	101.5	0.722	0.357	34.5	62.2	3.4

The SiO_2, CaO, Na_2O and K_2O are lower than detection limit of analyses, <0.03 wt.%. *Mg#* Mg/(Mg+Fe^{2+}) atomic ratio (Fe^{2+} in spinel was calculated from spinel stoichiometry), *Cr#* Cr/(Cr+Al) atomic ratio, *YCr* Cr/(Cr+Al+Fe^{3+}) atomic ratio, *YAl* Al/(Cr+Al+Fe^{3+}) atomic ratio, YFe^{3+} Fe^{3+}/(Cr+Al+Fe^{3+}) atomic ratio

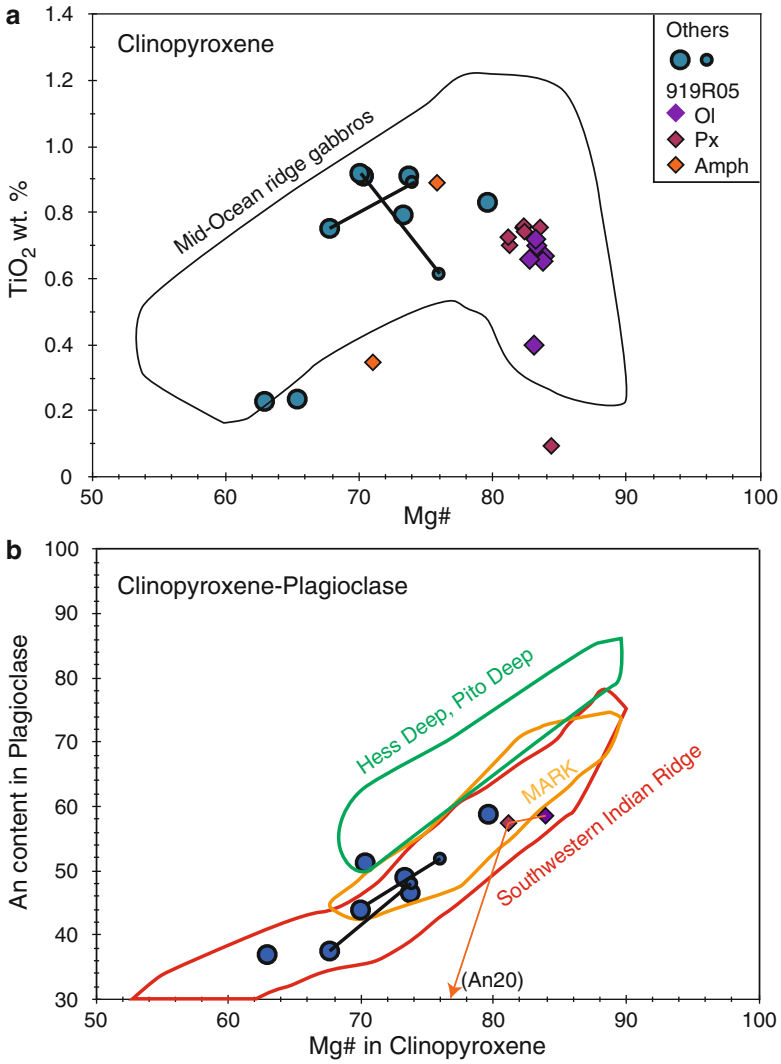

Fig. 14.6 Variations in the major-element compositions of minerals in gabbros from 25°S. (**a**) Relationship between the Mg# and the TiO_2 wt.% in clinopyroxene. (**b**) Relationship between the anorthite content in plagioclase and the Mg# in clinopyroxene. *Tie line* between data indicates the same sample. *Ol* olivine-bearing part, *Px* olivine-free and amphibole-poor part, *Amph* amphibole-rich part. The compositional ranges of main cluster of mid-ocean ridge gabbros (Hess Deep and Pito Deep, MARK = Kane fracture zone of the Mid-Atlantic Ridge, Southwestern Indian Ridge), compiled by Coogan et al. (2007), were also shown.

primitive MORB liquids formed at the fast-spreading ridges than at the slow-spreading ridges. Their Mg#s of mafic minerals in the 25°S OCC are, however, too low to be in equilibrium with mantle compositions. This has been long recognized as a "missing primary cumulate" in the slow-spreading ridges (Dick et al. 2000). On the other hand, oxide gabbros, rich in both ilmenite and magnetite, and their close association with oxide-poor gabbros, are common features at slow-spreading ridges (Dick et al. 2000). Pigeonite-bearing gabbros were also reported from the upper part of the Hole 735B gabbro of the Southwest Indian Ridge (Ozawa et al. 1991). Since the 25°S OCC is located at the segment boundary between CIR-S1 and CIR-S2, fractionated melt compositions can be explained by lateral intrusion of differentiate melt from focused melt flow at the mid-point of the ridge segments. In conclusion, the petrological characteristics of the gabbros in the 25°S OCC were formed while the magmatic activity was low, just as those described from the ultraslow-spreading ocean ridges (Dick et al. 2000).

14.5.2 Effect of Late Modification Due to Infiltration of Multiple Melts on Perdidotites

It is expected that peridotites associated with leucocratic veins were petrologically and geochemically modified during the formation of the leucocratic veins (e.g., Morishita et al. 2009). Leucocratic veins are observed as networks in several peridotites from the 25°S OCC and Yokoniwa Rise. Altered plagioclases, now replaced by fine-grained mineral aggregates (i.e., saussurite), are observed around spinels or as aggregates locally in some peridotites. Samples around the leucocratic veins contain altered plagioclase in spite of the low abundance of clinopyroxenes. Leucocratic vein-bearing peridotites show heterogeneity in minerals within single samples, whereas vein-free samples are basically homogeneous in minerals.

Petrological and geochemical features indicate that plagioclases (±clinopyroxenes) in the studied peridotites

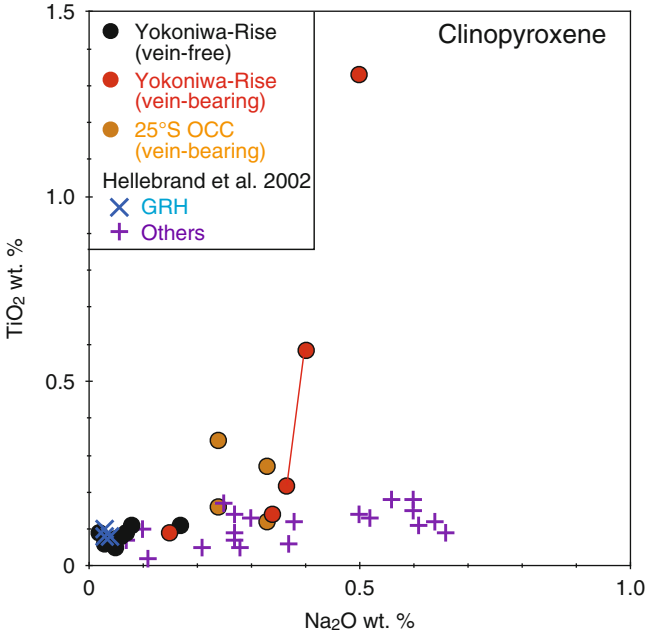

Fig. 14.7 Compositional relationships between TiO_2 wt.% and Na_2O wt.% in clinopyroxene in peridotite samples recovered from the 25°S OCC and Yokoniwa Rise. *Tie line* between data indicates the same sample. *CIR* Central Indian Ridge, *GRH* Green Rock Hill

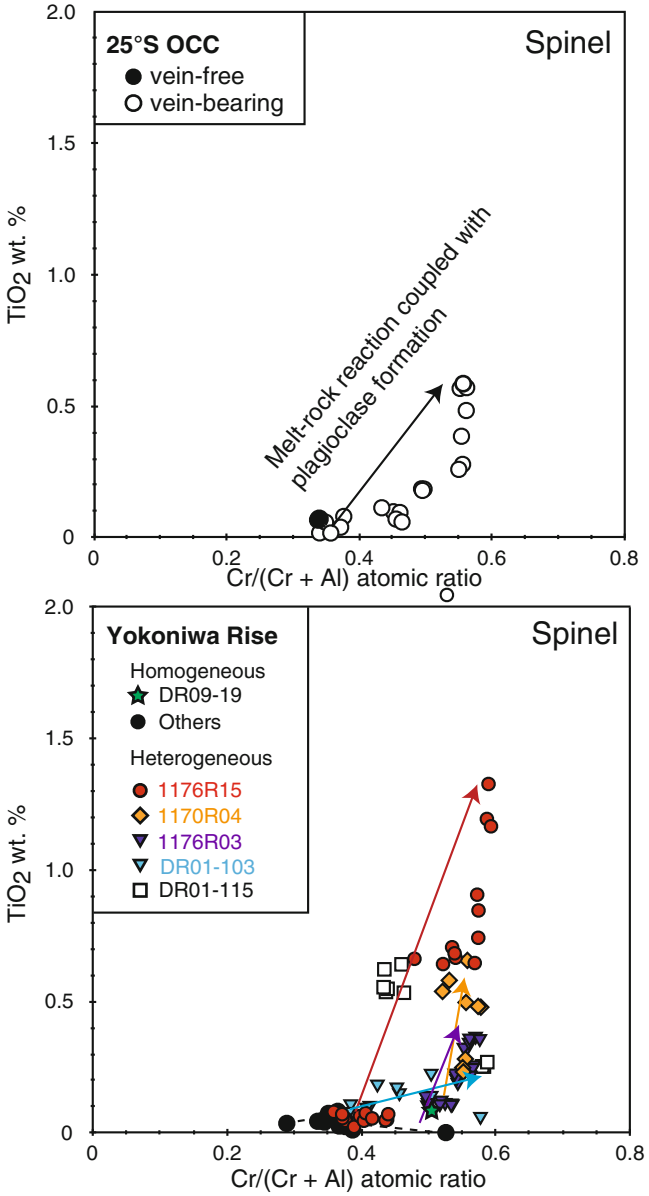

Fig. 14.8 Compositional relationships between Cr/(Cr + Al) (atomic ratio) and TiO_2 wt.% in spinels from 25°S OCC (*upper panel*) (data are from Morishita et al. (2009)) and Yokoniwa Rise (*lower panel*)

both in the 25°S OCC and the Yokoniwa Rise were of magmatic origin related to the formation of leucocratic veins at olivine-plagioclase stability conditions (<0.8 GPa) rather than the metamorphic origin of the subsolidus reaction from pyroxenes and spinel during the exhumation of upper mantle materials from beneath the ocean floor. During the formation of plagioclase, the alumina in the spinels in the peridotites was partly consumed to form plagioclase, and incompatible elements, such as TiO_2 and Na_2O would be added to the precursor minerals (e.g., clinopyroxene) (Figs. 14.7 and 14.8). Clinopyroxenes in the samples with leucocratic veins are, therefore, distinctively higher in both Na_2O and TiO_2 contents (Fig. 14.7) than those in the vein-free samples. The Cr# and TiO_2 contents of the spinels in the peridotites with leucocratic veins show a wide range of variation, 0.3–0.6 for Cr# and up to 1.3 wt.% for TiO_2 (Fig. 14.8). Low Cr# and TiO_2 of the chemical range of spinels from the Yokoniwa Rise are, on the other hand, the same as those from the vein-free samples. Spinels far from the leucocratic vein might, therefore, retain their original geochemical signatures before they were modified by interaction with the melts responsible for the formation of leucocratic vein (Fig. 14.8).

The melts which infiltrated into the peridotite samples had different chemical compositions from less evolved to highly evolved signatures. Although primary plagioclase is not observed in the leucocratic veins, secondary minerals such as chlorite and tremolitic/actinolitic amphibole indicates their original plagioclase-bearing litholoties. Altered plagioclases coupled with the presence of clinopyroxene and brown amphibole in the leucocratic veins suggest their origins from plagioclase-bearing mafic rocks, i.e., gabbroic rocks. On the other hand, zircons in some leucocratic veins indicate highly evolved signatures, such as granitic compositions (Morishita et al. 2009). The variations in the infiltrated melts are also supported by the variations in the maximum TiO_2 contents in minerals along the leucocratic veins in peridotites (e.g., 0.4–1.3 wt.% for spinels with the Cr# around 0.5). During the infiltration of a small amount of melt, the degree of chemical modifications

depends on the combination of an effective melt/rock ratio, melt compositions and P-T conditions on reactions. The size of the leucocratic veins is usually less than 1 cm in thickness. No systematic variations between the size of the leucocratic veins and modified mineral compositions are observed in the studied peridotites. The differences in the TiO_2 contents among those modified minerals are interpreted to be caused by the differences in melt compositions from less evolved to highly evolved compositions rather than the differences in effective melt/rock ratios. The TiO_2 content of melts are generally changed during the fractional crystallization as shown in the chemical variations of clinopyroxene in the 25°S OCC gabbros. Highly evolved gabbroic rocks were reported from both the slow-spreading ridges (Bloomer et al. 1989; Mével et al. 1991; Cannat et al. 1992; Morishita et al. 2004) and the fast-spreading ridges (Constantin 1999). Physical conditions under slow-spreading ridges are characterized by a highly attenuated magma supply and a high rock/melt ratio during melt ascending. We favor the theory that the differences in chemical compositions of the infiltrated melts in the peridotites were formed as an *in-situ* fractionation from a MORB-type melt during the ascent in the mantle while the magmatic activity was low in the intermediate-spreading mid-ocean ridges.

14.5.3 The Primary Features of Peridotites: Implications for the Formation of Serpentine-Dominated Seafloor

The primary features of peridotites recovered from the studied area suggest their relatively depleted signatures in melt components. Leucocratic vein-free samples are basically homogeneous in mineral chemistry at each sample scale. The majority of spinel compositions in the Yokoniwa Rise peridotites is around 0.35 for Cr# and <0.1 wt.% for TiO_2 contents (Fig. 14.8). It should be emphasized that one sample (DR09-19) is distinctively high in Cr# (Fig. 14.8). Low-TiO_2 of mineral compositions in the leucocratic vein-bearing samples are less affected by the chemical modifications, i.e., primary features of peridotite prior to the chemical modifications from the infiltrated melts. Primary spinel compositions of 1176R05 and DR01-103 are around 0.35 for Cr#, whereas those of 1170R04 and 1176R03 are likely to be higher in Cr# than other samples, around 0.5 (Fig. 14.8). Spinels from the 25°S OCC peridotites, leucocratic vein-free and those far from the leucocratic vein-bearing, are also around 0.35 for Cr# and <0.1 wt. % for the TiO_2 content (Fig. 14.8). The composition of the Green Rock Hills is similar to that of the studied samples. The compositional range of these spinels and Al_2O_3 content of orthopyroxene porphyroclasts are overlapped with higher and lower ranges of plagioclase-free CIR abyssal peridotites (Hellebrand et al. 2002), respectively (Fig. 14.9). According to these results, the granular peridotite samples collected from the studied area are residue left after moderate to high degrees of partial melting (13–15 % in the majority and up to 17 % based on the method of Hellebrand et al. (2001)). It should be realized that this study, coupled with previous results, confirms a wide exposure of relatively depleted peridotites on the ocean floor in the studied region.

Niu and Hékinian (1997) reported a correlation between ridge spreading rate and the degree of partial melting in abyssal peridotites, i.e., the idea that the extent of mantle melting beneath normal ocean ridges increases with increasing spreading rate. The studied peridotites are plotted between those from fast-spreading ridges and slow-spreading ridges except for hot-spot related areas (Fig. 14.9). In this context, the moderate to high degree of partial melting of the studied peridotites appears to be consistent with those expected for an "intermediate"-spreading ridge. In particular, the higher compositional range of the Cr# of spinels in peridotites recovered from the southern end of the CIR is also likely consistent with the increase of the spreading rate toward the south along the CIR. Moderately to highly depleted melt components in the studied peridotites can be explained as being residue after a relatively high-melt productivity period in intermediate-spreading ridges.

We also discuss several models for the origin of depleted peridotites in the studied area because peridotites with depleted signatures in melt components were recently reported from oceanic core complexes where fertile peridotites are expected to be recovered (Seyler et al. 2007; Tamura et al. 2008; Dick et al. 2010) (Fig. 14.9). Depleted peridotites were also already recovered from other ultraslow to slow-spreading ridges without a hot spot effect (Bonatti et al. 1992, 2003; Seyler et al. 2003; Brunelli et al. 2006; Morishita et al. 2007; Godard et al. 2008). These studies indicate that large variations in the melting degree of mid-ocean ridge peridotites are probably not simply related to the spreading rate. Several models can be applied for the occurrence of the depleted peridotites even where the degree of partial melting is expected to be low: (i) relics of older partial melting (Seyler et al. 2003, 2007; Liu et al. 2008), (ii) variations of equilibration temperatures probably related to variations of advection velocity below the ridge (Bonatti et al. 2003), and (iii) residue related to the latest melting events, i.e., the present mid-ocean ridge spreading (Morishita et al. 2007). We cannot examine the second case (ii) based on our samples because further samplings in space and time along the CIR are required.

In the last case (iii), we assume that the depleted rocks appear to be very locally formed along main melt conduits. Morishita et al. (2007) described petrological characteristics of a dunite from the ultraslow-spreading Southwest Indian Ridge where fertile clinopyroxene-rich lherzolite is dominant lithology, and reported a relatively depleted sample

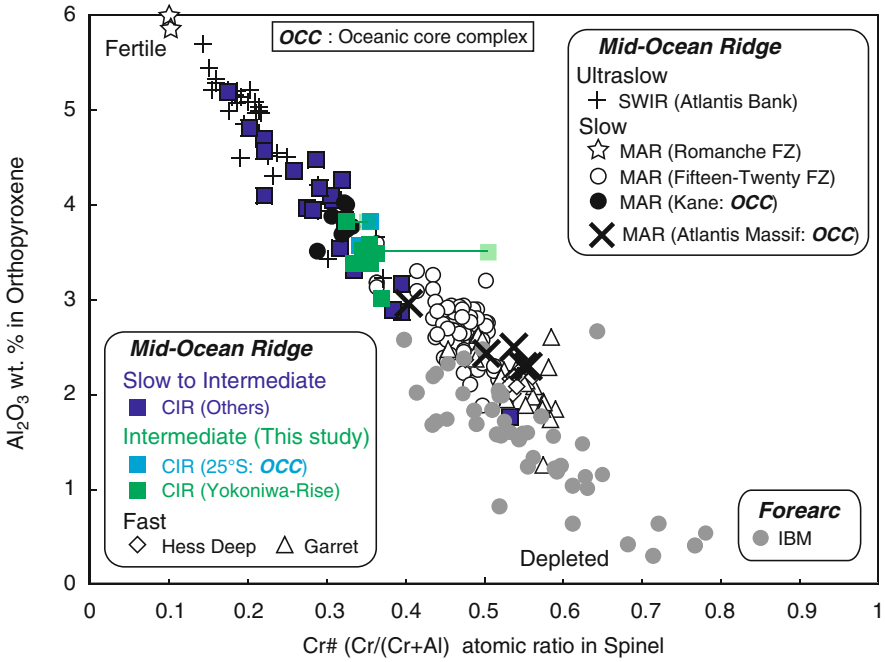

Fig. 14.9 Correlations between Al_2O_3 content (wt.%) in orthopyroxene porphyroclasts and Cr# in spinels. Data of the Southwest Indian Ridge (SWIR) are from Atlantis II Fracture Zone of Dick (Dick 1989) and Seyler et al. (2003). The Central Indian Ridge (CIR) are from Hellebrand et al. (2002), Morishita et al. (2009). The Mid-Atlantic Ridge (MAR) are as follows: Atlantis Massif (Oceanic core complex: OCC) are from Seyler et al. (2007) and Tamura et al. (2008), Romanche fracture zone (FZ) are from Bonatti et al. (1993), Fifteen-Twenty FZ are from Godard et al. (2008), and Kane megamullion (oceanic core complex) are from Dick et al. (2010). The Garret and Hess Deep of East Pacific Rise (EPR) are from Constantin (1999) and Dick and Natland (Dick and Natland 1996), respectively. The Izu-Bonin-Mariana (IBM) forearc are from Parkinson and Pearce (1998) and Zanetti et al. (2006)

(enstatite-poor harzburgite) restrictedly associated with the dunite. Since dunite and depleted peridotite, once formed beneath active ridges, are expected to be later flattened by mantle flow perpendicular to the ridge direction, the uppermost section of oceanic mantle should be more abundant in depleted peridotite than deeper mantle sections. The thickness of residues after relatively high-degree partial melting in the uppermost mantle sequences are expected to be thinner in the slow spreading ridges than in the fast-spreading ridges because the magmatism is more active beneath the fast-spreading ridges than the slow-spreading ridges. In this case, we need additional mechanisms to explain why depleted peridotites are selectively but widely exposed in the studied area.

The ancient melting model (i) can be favored over other model as an explanation for a wide exposure of serpentinized peridotite in the studied area. In this case, depleted peridotites formed as residue, after an ancient partial melting event or evenets, should be survived and would be incorporated beneath a mid-ocean ridge center without significant modifications. Less or no partial melting is expected in the ancient depleted peridotite domain during the upwelling beneath the spreading ridges, resulting in a very limited amount of igneous crust formations at the spreading center. Melts caused by the following partial melting of relatively fertile peridotite beneath the ancient depleted domain might be infiltrated into the upwelled ancient depleted domain, resulting in the formation of gabbroic networks/veins in peridotites. Continuous dragging of the oceanic plate causes fracturing of the uppermost section of the oceanic plate along the ocean ridge. Seawater would have penetrated along the cracks and reacted with peridotites to form serpentinites. Because serpetinized peridotites are less dense than the surrounding host peridotites, serpentinized peridotites can be locally exposed on the seafloor. Further studies on the melting ages of peridotites, such as Os-isotopiec dating, are, however, required to make clear whether or not ancient melting regions are the origin for the studied peridotites.

14.6 Conclusions

We succeeded three submersible expeditions of the SHINKAI 6500 and one dredge expedition of the Hakuho-maru in the south end of the intermediate-spreading Central Indian Ridge, where the Kairei hydrothermal filed is located. Peridotites and their-related gabbroic rocks were widely recovered from the studied region. Here we summarize petrological and mineralogical characteristics the peridottes

and related gabbros from the oceanic core complex at a latitude of 25° South (25°S OCC) and the Yokoniwa Rise around the Kairei hydrothermal field.

Gabbros from the 25°S OCC are olivine gabbro, gabbro, gabbronorite (granular orthopyroxene-bearing gabbro) and oxide gabbro. The petrological characteristics of the gabbros are similar to those described from the ultraslow-spreading ocean ridges. The gabbros in the 25°S OCC were probably formed while the magmatic activity was low.

The peridotites are classified into two types: a granular peridotite and a highly deformed type of rock. The latter was recovered from the top surface of the 25°S OCC. Petrological characteristics of granular peridotites (clinopyroxene-bearing harzburgite to lherzolite) are basically the same between the 25°S OCC and the Yokoniwa Rise. Several samples were intruded by leucocratic veins. Plagioclase, now completely altered, was observed in several samples with thick leucocratic veins. The primary features of peridotites are residue left after moderate to high degrees of partial melting (13–15 % in the majority and up to 17 %). The partial melting of these peridotites is followed by chemical modification through interaction with a wide range of melts from relatively less evolved to highly evolved characteristics. The differences in chemical compositions of the infiltrated melts in the peridotites were probably formed as an *in-situ* fractionation from a MORB-type melt during the ascent in the mantle. Two models for the origin of depleted peridotites in the studied area: (1) residue related to the latest melting events of the present mid-ocean ridge spreading, and (2) residue related to an ancient partial melting event or evenets. In the case (1), the studied peridotites are residue after a relatively high-melt productivity period in intermediate-spreading ridges. In the case (2), the studied peridotites are a geochemically distinctive domain that has suffered from partial melting in the past.

Acknowledgements We are grateful to captains, crews and the scientific parties of the Yokosuka, the SHINKAI team, the R/V Hakuho-maru who contributed to the success of the cruises. This study was partly supported by a Grants-in-Aid for Scientific Research from the Ministry of Education, Culture, Sports, Science and Technology of Japan (MEXT) on Innovative Areas "Project TAIGA: Trans-crustal Advection and In-situ biogeochemical process of Global sub-seafloor Aquifer" led by Prof. Urabe and a Grants-in-Aid for Scientific Research of the MEXT (No. 17740349) to T.M. We also deeply thanks to Shoji Arai, Susumu Umino, Nobu Seama, Tomoyuki Mizukami, Akihiro Tamura and Sumiaki Machi for their discussions. The paper was greatly improved by reviews by two anonymous reviewers. Daniel Gauss improved English in the manuscript.

References

Bloomer SH, Natland JH, Fisher RL (1989) Mineral relationships in gabbroic rocks from fracture zones of Indian Ocean ridges: evidence for extensive fractionation, parental diversity and boundary-layer recrystallization. Geol Soc Spec Pub 42:107–124. doi:10.1144/GSL.SP.1989.042.01.07

Bonatti E, Peyve A, Kepezhinskas P, Kurentsova N, Seyler M, Skolotnev S, Udintsev G (1992) Upper mantle heterogeneity below the Mid-Atlantic Ridge, 0°–15°N. J Geophys Res 97 (B4):4461–4476

Bonatti E, Seyler M, Sushevskaya N (1993) A cold suboceanic mantle belt at the Earth's Eauator. Science 262(5119):315–320. doi:10.2307/2881562

Bonatti E, Ligi MD, Brunelli A, Cipriani P, Fabretti V, Ferrante L, Gasperini L, Ottolini L (2003) Mid-Atlantic Ridge and temporal variations in the formation of oceanic lithosphere. Nature 423 (6939):499–505. doi:10.1038/nature01594

Briais A (1995) Structural-analysis of the segmentation of the Central-Indian-Ridge between 20-degrees-30′s and 25-degrees-30′s (Rodriguez-Triple-Junction). Mar Geophys Res 17(5):431–467. doi:10.1111/j.1365-246X.2009.04491.x

Brunelli D, Seyler M, Cipriani A, Ottolini L, Bonatti E (2006) Discontinuous melt extraction and weak refertilization of mantle peridotites at the Vema lithosphereic section (Mid-Atlantic Ridge). J Petrol 47(4):745–771. doi:10.1093/petrology/egi092

Cannat M, Bideau D, Bougault D (1992) Serpentinized peridotites and gabbros in the Mid-Atlantic Ridge axial valley at 15°37′ and 16°52′N. Earth Planet Sci Lett 109(1–2):87–106. doi:10.1016/0012-821X(92)90076-8

Constantin M (1999) Gabbroic intrusions and magmatic metasomatism in harzburgites from the Garret transform fault: implications for the nature of the mantle-crust transition at fast-spreading ridges. Contrib Mineral Petrol 136(1–2):111–130. doi:10.1007/s004100050527

Coogan LA, Jenkin GRT, Wilson RN (2007) Contrasting cooling rates in the lower oceanic crust at fast- and slow-spreading ridges revealed by geospeedometry. J Petrol 48(11):2211–2231. doi;10.1093/petrology/egm057

DeMets C, Gordon RG, Argus DF (2010) Geologically current plate motions. Geophys J Int 181(1):1–80. doi:10.1111/j.1365-246X.2009.04491.x

Dick HJB (1989) Abyssal peridoties, very slow spreading ridges and ocean ridge magmatism. In: Saunders AD, Norry MJ (eds) Magmatism of Ocean Basins. Geological Society Special Publication, Oxford: Blackwells for the Geological Society, no. 42, pp 71–105

Dick HJB, Natland JH(1996) Late-stage melt evolution and transport in the shallow mantle beneath the East pacific Rise. Proc Ocean Drill Prog 147:103–134

Dick HJB, Natland JH, Alt JC, Bach W, Bideau D, Gee JS, Haggas S, Hertogen JGH, Hirth G, Holm PM, Ildefonse B, Iturrino GJ, John BE, Kelley DS, Kikawa E, Kingdon A, LeRoux J, Maeda PJ, Meyer J, Miller PS, Naslund DJ, Niu HR, Robinson Y-L, Snow PT, Stephen RA, Trimby PW, Worm H-U, Yoshinobu A (2000) A long in situ section of the lower ocean crust: results of ODP Leg 176 drilling at the Southwest Indian Ridge. Earth Planet Sci Lett 179(1):31–51

Dick HJB, Lissenberg CJ, Warren JM (2010) Mantle melting, melt transport, and deliver beneath a slow-spreading ridge: the paleo-MAR from 23°15′N to 23°45′N. J Petrol 51(1–2):425–467

Gallant RM, Von Damm KL (2006) Geochemical controls on hydrothermal fluids from the Kairei and Edmond Vent Fields, 23°–25°S,

Central Indian Ridge. Geochem Geophys Geosyst 7(6):1–24. doi:10.1029/2005GC001067

Gamo T, Chiba H, Yamanaka T, Okudaira T, Hashimoto J, Tsuchida S, Ishibashi J, Kataoka S, Tsunogai U, Okamura K, Sano Y, Shinjo R (2001) Chemical characteristics of newly discovered black smoker fluids and associated hydrothermal plumes at the Rodriguez Triple Junction, Central Indian Ridge. Earth Planet Sci Lett 193 (3–4):371–379

Godard M, Lagabrielle Y, Alard O, Harvey J (2008) Geochemistry of the highly depleted peridotites drilled at ODP Sites 127 and 1274 (Fifteen-Twenty Fracture Zone, Mid-Atlantic Ridge): implications for mantle dynamics beneath a slow spreading ridge. Earth Planet Sci Lett 267(3–4):410–425

Hashimoto J, Ohta S, Gamo T, Chiba H, Yamaguchi S, Tsuchida S, Okudaira T, Watabe H, Yamanaka T, Kitazawa M (2001) First hydrothermal vent communities from the Indian Ocean discovered. Zoolog Sci 18(5):717–721

Hellebrand E, Snow JE, Dick HJB, Hofmann AW (2001) Coupled major and trace elements as indicators of the extent of melting in mid-ocean-ridge peridotites. Nature 410:677–681

Hellebrand E, Snow JE, Hoppe P, Hofmann AW (2002) Garnet-field melting and late-stage refertilization in 'residual' abyssal peridotites from the Central Indian Ridge. J Petrol 43 (12):2305–2338

Honsho C, Tamaki K, Fujimoto H (1996) Three-dimensional magnetic and gravity studies of the Rodriguez Triple Junction in the Indian Ocean. J Geophys Res 101(B7):15837–15848

Klein EM, Langmuir CH (1987) Global correlations of ocean ridge basalt chemistry. J Geophys Res 92(B8):8089–8115

Kumagai H, Nakamura K, Toki T, Morishita T, Okino K, Ishibashi J-I, Tsunogai U, Kawaguchi S, Gamo T, Shibuya T, Sawaguchi T, Neo N, Joshima M, Sato T, Takai K (2008) Geological background of the Kairei and Edmond hydrothermal fields along the Central Indian Ridge: implications of their vent fluids' distinct chemistry. Geofluids 8(4):239–251

Liu C-Z, Snow JE, Hellebrand E, Brügmann G, von der Handt A, Büchl A, Hofmann AW (2008) Ancient, highly heterogeneous mantle beneath Gakkel ridge, Arctic Ocean. Nature 452. doi:10.1038/nature06688

Mendel V, Sauter D, Patriat P, Munschy M (2000) Evolution of the Central Indian Ridge segmentation with the evolution of the Rodrigues Triple Junction for the past 8 Myr. J Geophys Res 105 (B7):16563–16575

Mével C, Cannat M, Gente P, Marion E, Auzende JM, Karson JA (1991) Emplacement of deep crustal and mantle rocks on the west median valley wall of the MARK area (MAR, 23°N0. Tectonophysics 190(1):21–53

Mitchell NC, Escartín J, Allerton S (1998) Detachment faults at mid-ocean ridges garner interest. EOS Trans AGU 79:127

Morishita T, Arai S, Green DH (2003) Evolution of low-Al orthopyroxene in the Horoman peridotite, Japan: an unusual indicator of metasomatising fluids. J Petrol 44(7):1237–1246

Morishita T, Maeda J, Miyashita S, Matsumoto T, Dick HJB (2004) Magmatic srilankite (Ti_2ZrO_6) in gabbroic vein cutting oceanic peridotites: an unusual product of peridotite-melt interactions beneath slow-spreading ridges. Am Mineral 89(5–6):759–766

Morishita T, Maeda J, Miyashita S, Kumagai H, Matsumoto T, Dick HJB (2007) Petrology of local concentration of chromian spinel in dunite from the slow-spreading Southwest Indian Ridge. Eur J Mineral 19(6):871–882

Morishita T, Hara K, Nakamura K, Sawaguchi T, Tamura A, Arai S, Okino K, Takai K, Kumagai H (2009) Igneous, alteration and exhumation processes recorded in abyssal peridotites and related fault rocks from an oceanic core complex along the Central Indian Ridge. J Petrol 50(7):1299–1325

Nakamura K, Morishita T, Chang Q, Neo N, Kumagai H (2007) Discovery of lanthanide tetrad effect in an oceanic plaiogranite from an Ocean Core Complex at the Central Indian Ridge 25°S. Geochem J 41(2):135–140

Nakamura K, Morishita T, Bach W, Klein F, Hara K, Okino K, Takai K, Kumagai H (2009) Serpentinized olivine-rich gabbroic rocks exposed near the Kairei Hydrothermal Field, Central Indian Ridge: Insights into the origin of the Kairei hydrothermal fluid supporting a unique microbial ecosystem. Earth Planet Sci Lett 280(1–4):128–136. doi:10.1016/j.epsl.2009.01.024

Niu Y, Hékinian R (1997) Spreading rate dependence of the extent of mantle melting beneath ocean ridges. Nature 385(6614):326–329

Ozawa K, Meyer PS, Bloomer SH (1991) Mineralogy and textures of iron-titanium oxide gabbros and associated olivine gabbros from Hole 735B. Proc Ocean Drill Prog Sci Rep 118:41–73

Parkinson IJ, Pearce JA (1998) Peridotites from the Izu-Bonin-Mariana forearc (ODP Leg 125): evidence for mantle melting and melt-mantle interaction in a supra-subduction zone setting. J Petrol 39 (9):1577–1618

Perk NW, Coogan LA, Karson JA, Klein EM, Hanna HD (2007) Petrology and geochemistry of primitice lower oceanic crust from Pito Deep: implications for the accretion of the lower crust at the Southern East Pacific Rise. Contrib Mineral Petrol 154(5):575–590. doi:10.1007/s00410-007-0210-z

Sato T, Okino K, Kumagai H (2009) Magnetic structure of an oceanic core complex at the southernmost Central Indian Ridge: analysis of shipboard and deep-sea three-component magnetometer data. Geochem Geophys Geosyst 10(6). doi:10.1029/2008GC002267

Seyler M, Cannat M, Mével C (2003) Evidence for major-element heterogeneity in the mantle source of abyssal peridotites from the Southwest Indian Ridge (52° to 68°E). Geochem Geophys Geosyst 4(2):9101

Seyler M, Loarnd J-P, Dick HJB, Drouin M (2007) Pervasive melt percolatin reactions in ultra-depleted refractory harzburgites at the Mid-Atlantic Ridge, 15°20′N: ODP Hole 1274A. Contrib Mineral Petrol 153(3):303–319

Takai K, Gamo T, Tsunogai U (2004) Geochemical and microbiological evidence for a hydrogen-based, hyperthermophilic subsurface lithoautotrophic microbial ecosystem (HyperSLiME) beneath an active deep-sea hydrothermal field. Extremophiles 269–282. doi:10.1007/s00792-004-0386-3

Tamura A, Arai S, Ishimaru S, Andal ES (2008) Petrology and geochemistry of peridotites from IODP Site U1309 at Atlantis Massif, MAR 30°N: micro- and macro-scale melt penetrations into peridotites. Contrib Mineral Petrol 155(4):491–509

Van Dover CL (2002) Trophic relationships among invertebrates at the Kairei hydrothermal vent field (Central Indian Ridge). Mar Biol 141:761–772

Van Dover CL, Humphris SE, Fornari D, Cavanaugh CM, Collier R, Goffredi SK, Hashimoto J, Lilley MD, Reysenbach AL, Shank TM, Von Damm KL, Banta A, Gallant RM, Götz D, Green D, Hall J, Harmer TL, Hurtado LA, Johnson P, McKiness ZP, Meredith C, Olsen E, Pan IL, Turnipseed M, Won Y, Young CR III, Verijenhoek RC (2001) Biogeography and ecological setting of Indian Ocean hydrothermal vents. Science 294:818–823

Zanetti A, D'Antonio M, Spadea P, Raffone N, Vannucci R, Brugeir O (2006) Petrogenesis of mantle peridotites from the Izu-Bonin-Mariana (IBM) forearc. Ofioliti 31(2):189–206

Distribution and Biogeochemical Properties of Hydrothermal Plumes in the Rodriguez Triple Junction

15

Takuroh Noguchi, Tatsuhiro Fukuba, Kei Okamura, Akira Ijiri, Katsunori Yanagawa, Yoshiyuki Ishitani, Teruo Fujii, and Michinari Sunamura

Abstract

In 2010, we conducted seven surveys for the deep-sea hydrothermal plume through conductivity-temperature-depth profiler (CTD) "tow-yo" cast in the area of the Kairei field. We observed a turbidity anomaly with a maximum thickness of 120 m, the upper limit of which was at 2,150 m water depth, approximately 300 m above the Kairei field hydrothermal vents (~2,440 m). The depth of upper limit of turbidity anomaly around Kairei field was the same height as in previous reports. Because the maximum height of hydrothermal plumes are regulated by the density (temperature and salinity) of the end-member hydrothermal fluid and dilution by the ambient seawater, the height of the plume suggested that the hydrothermal activity of the Kairei field was also the same as 17 years ago. Deep sequencing of microbial 16S rRNA genes showed that the SUP05 phylotypes and *Epsilonproteobacteria*, which are known as the potential sulfur oxidizer and/or possibly hydrogen oxidizer, were propagated in the early stage of the hydrothermal plume and in the hydrothermal fluid–seawater mixing zone near the Kairei hydrothermal vents. Our exploration found a hydrothermal plume at 14 km north of the Kairei field, which had different H_2/CH_4 ratio expected from the end-member hydrothermal fluid of Kairei field and the ambient seawater mixing. The north plume had a lower H_2, higher CH_4 concentration, and higher microbial cell density than those in the hydrothermal plume around Kairei field. The north hydrothermal plume represented too oxic condition to harbor methane production by anaerobic methanogens. In addition, our microbial community structure analysis based on deep sequencing of 16S rRNA genes more than 10,000-amplicon reads per one sample showed no signal of methanogenic archaea. This suggests little in situ methanogenesis from H_2 in the plume. It seems likely that high concentration of methane in the north plume is derived from another hydrothermal plume source rather than the Kairei hydrothermal fluids. Further studies will be needed to understand the cause of high methane concentration in the north plume.

The online version of this chapter (doi:10.1007/978-4-431-54865-2_15) contains supplementary material, which is available to authorized users.

T. Noguchi (✉)
Center for Advanced Marine Core Research, Kochi University, B200 Monobe, Nankoku, Kochi 783-8502, Japan

Marine Technology and Engineering Center, Japan Agency for Marine-Earth Science and Technology, 2-15 Natsushima-cho, Yokosuka, Kanagawa 237-0061, Japan
e-mail: noguchitk@jamstec.go.jp

T. Fukuba
Marine Technology and Engineering Center, Japan Agency for Marine-Earth Science and Technology, 2-15 Natsushima-cho, Yokosuka, Kanagawa 237-0061, Japan

K. Okamura
Center for Advanced Marine Core Research, Kochi University, B200 Monobe, Nankoku, Kochi 783-8502, Japan

A. Ijiri • K. Yanagawa • M. Sunamura
Department of Earth and Planetary Science, The University of Tokyo, 7-3-1 Hongo, Bunkyo-ku, Tokyo 113-0033, Japan

Y. Ishitani
Institute of Biogeoscience, Japan Agency for Marine-Earth Science and Technology, 2-14 Natsushima-cho, Yokosuka, Kanagawa 237-0061, Japan

T. Fujii
Institute of Industrial Science, The University of Tokyo, 4-6-1 Komaba, Meguro-ku, Tokyo 153-8505, Japan

J.-i. Ishibashi et al. (eds.), *Subseafloor Biosphere Linked to Hydrothermal Systems: TAIGA Concept*,
DOI 10.1007/978-4-431-54865-2_15,

Keywords
Hydrothermal plume observation • Microbial population and communities • Plume evolution • Rapid H_2 consumption

15.1 Introduction

Once the venting hydrothermal fluid is sufficiently diluted, it forms a hydrothermal plume with neutral buoyancy that is spread by deep-sea currents. Although the potential density of a neutrally buoyant plume is mostly the same as that of the ambient seawater, some chemical species (e.g., dissolved methane (CH_4), helium (He), and manganese (Mn) and physical properties (e.g., water temperature and turbidity) remain much higher in the hydrothermal plume than in the ambient seawater. In situ sensors and onboard- and onshore-analyses of water samples have been applied to detect these anomalies based on the previous studies of hydrothermal plume surveys (e.g., Baker 1990). These previous studies demonstrated the spatial distribution of hydrothermal plume and the gradation of chemical species. During a spreading process of a hydrothermal plume, chemical composition and stable isotopic composition changes which is termed "chemical evolution of plume". The chemical evolution of a plume is implicated by absorption to particulate materials, sedimentation, and oxidation (German and Von Damm 2003). During the oxidation process in the oxygenated seawater, microbes play an important role for Mn^{2+}, CH_4, and NH_4^+ (e.g. Lam et al. 2004). Raised microbial cell densities in the hydrothermal plumes, compared to in the surrounding ambient seawater, have been reported at several hydrothermal fields (e.g., northern East Pacific Rise, Winn et al. (1986); north Fiji basin, Naganuma et al. (1989)).

During the TAIGA project, we focused on chemical fluxes from hydrothermal vents and its influences to deep-sea ecosystems through a hydrothermal plume investigation. The Kairei field is one of the important targets in our project because the hydrothermal fluids of the Kairei field are characterized by high concentration of H_2. In this chapter, we show the temporal and spatial distribution of chemical species in the hydrothermal plume, and the interaction between the chemical species and the microbial communities base on seven "tow-yo" surveys with conductivity-temperature-depth profiler (CTD) and our developed in situ chemical sensors, together with the water sampling and analysis of geochemistry and microbiology.

15.2 Site Description

Two hydrothermal fields have been discovered on the Central Indian Ridge: the Kairei field (25°19.17′S, 70°02.40′E; 2,450 m water depth) (Hashimoto et al. 2001; Gamo et al. 2001) and the Edmond field (23°52.68′S, 69°35.80′E; 3,290–3,320 m water depth) (Van Dover et al. 2001) (Fig. 15.1a). The geological settings and geochemical characteristics of these hydrothermal fields are described in this book (Okino et al. Chap. 11, Nakamura and Takai, Chap. 12). The end-member chemical and isotopic composition of hydrothermal fluid from the Kairei and Edmond fields are shown in Suppl. 15.1 (supplementary data) summarized from Gallant and Von Damm (2006) and Kumagai et al. (2008). The H_2 concentration of the hydrothermal fluid from the Kairei field is higher than that from the Edmond field or other silicic- to mafic-rock-hosted hydrothermal fields (e.g., East Pacific Rise). Kumagai et al. (2008) and Nakamura et al. (2009) proposed that the high H_2 concentration was derived from the interaction between the hydrothermal fluid and olivine-rich ultramafic rocks.

15.3 Methods

15.3.1 In Situ Sensor Observations and Sampling

Various sensors and water samplers have been used so far in hydrothermal vent surveys (e.g., Baker 1990). During the KH10-6 cruise of R/V *Hakuho-maru* in November 2010, we conducted seven CTD tow-yo surveys in the area of the Kairei field (Fig. 15.1b). In each survey, the following in situ sensors were used: a conductivity-temperature-depth profiler with Carousel Multi-Sampling system (CTDT-CMS; SBE 9*plus* CTD and SBE 32 Carousel Water Sampler, Sea-Bird Electronics Inc.), a backscatter turbidity meter (Seapoint Sensors, Inc.), a glass electrode pH sensor (pH-08, Kimoto Electric Co., Ltd.), an ion-selective field-effective transistor pH sensor (Shitashima et al. 2002), oxidation–reduction potential (ORP) sensors (ORP-08 and ORP-09, Kimoto Electric Co., Ltd.), and a manganese analyzer (TANSAKUN Mn-08, Kimoto Electric Co., Ltd.)

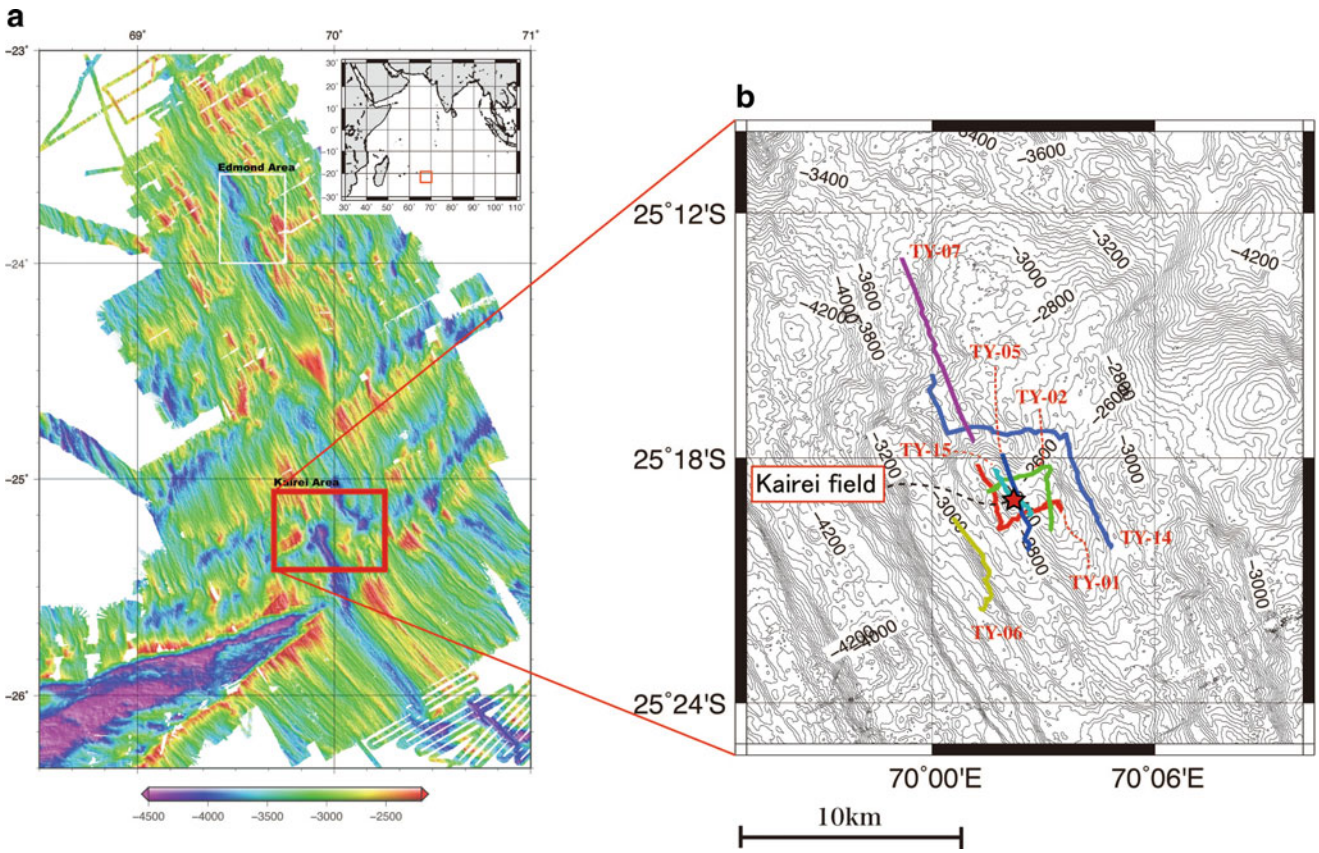

Fig. 15.1 (**a**) Bathymetric map and locations of hydrothermal fields of Central Indian Ridge. (**b**) Tow-yo survey lines around Kairei field during KH10-6 cruise in 2010

(Noguchi et al. 2011). The CTDT-CMS system was controlled onboard ship with a CTD deck unit (SBE 11*plus*, Sea-Bird Electronics Inc.). A total of 22 Niskin-X bottles (12-L sample volume, General Oceanics) were used at each hydrocast for water sampling. A transponder (Kaiyo Densi Co., Ltd.) was used with a Super Short BaseLine (SSBL) sub-navigation system (Model LNS600, Kaiyo Densi Co., Ltd.) to locate the system. All data except for pH and ORP were monitored onboard in real time. The system was towed at a speed of 0.5 to 1 knot, and water samples were collected when the sensors mounted on the CTDT-CMS showed anomalous signals.

15.3.2 Sample Preparation and Measurements

Samples for salinity measurements were collected in amber glass bottles, and salinity was measured with a salinometer (AUTOSAL 8400A, Guildline Instruments). IAPSO standard seawater (Batch P145, Ocean Scientific International Ltd.) was used as the reference sample for standardization (Geiskes et al. 1991). Dissolved oxygen was determined by the Winkler method (Strickland and Parsons 1968), and pH, alkalinity, and dissolved inorganic carbon (DIC) were measured by continuous 0.1 M HCl titration with pH monitoring using an automatic titrator (TLED-09, Kimoto Electric, Co., Ltd.). Alkalinity, DIC, and pH values were determined from the titration data by non-linear least-squares calculations (Dickson et al. 2007). Samples for H_2 and CH_4 were collected in 125 mL volume glass vials without any air bubbles and sterilized by adding 0.5 mL of saturated $HgCl_2$ solution. For the samples for H_2, we used an amber bottle to reduce photochemical oxygenation. Molecular hydrogen was analyzed by a gas chromatograph equipped with a trace reduced gas detector (TRD-1, Round Science Inc.) within 6 h after sample retrieval on board according to an analytical method described in Kawagucci et al. (2010) with a slight modification. The dissolved gas concentration was calculated from the measured gas mixing ratio in the headspace using the solubility coefficient for H_2 (Wiesenburg and Guinasso 1979). The overall analytical uncertainties and detection limits were estimated to be ±10 % and 0.5 nM by repeated analyses of an actual seawater sample and a barometrically diluted commercial standard gas (GL Science). Samples for dissolved CH_4 was stored at 4 °C and brought back to the laboratory. CH_4 in the water samples were analyzed by a gas chromatograph (GC-8A, Shimadzu) equipped with a flame ionization

detector, using a method similar to that described by Tsurushima et al. (1996). The standard deviation, based on repeated analyses of the seawater sample, was <3 % at a concentration of 3 nM.

Microbial cell densities were determined by a flow cytometer (Cell Lab Quanta MPL, Beckman Coulter Inc.) equipped with 488 nm laser. Seawater samples were aseptically transferred to disposable plastic tubes and stored at 4 °C until analysis. Microbial cells in the samples were stained with SYBR Green II at a final concentration of 4× (Molecular Probes Inc.) for 20 min (Marie et al. 1997) and a 50 μL of the sample was injected into the flow cytometer on board.

Microbial phylotype composition in the seawater was determined by the 16S rRNA gene sequencing (Sunamura et al. 2004; Nunoura et al. 2012). Hydrothermal plume samples S05ty-11, S15ty-12, and S14ty-6 and a background/reference sample S06ty-5 were used for deep-sequencing analysis. Sample S05ty-11 was collected closest to the Kairei hydrothermal field, and sample S14ty-11 was collected farthest from the vents. Microbial cells in a 5 L seawater sample were collected on a 0.2-μm-pore-size membrane filter (type GV, Millipore) through filtration. The filter samples were preserved in a deep freezer at −80 °C and brought back to the laboratory. DNA in the cells on the filter samples was extracted by using commercial DNA extraction kits (UltraClean Soil DNA Isolation Kit, MO-Bio Laboratories Inc.) according to the manufacturer's instructions. The 16S rRNA genes were amplified by polymerase chain reaction (PCR) using LA *Taq* (TaKaRa Bio Inc.) with a program of 95 °C for 5 min, followed by 35 cycles of 95 °C for 30 s, 52 °C for 20 s, and 72 °C for 30 s, and a final extension at 72 °C for 10 min. We used the primer set Univ530F and Univ907R, modified from Nunoura et al. (2012). An adaptor sequence for the FLX sequencer and a DNA tag for discrimination of each sample were attached to the 5′ end of the forward primer. Another adaptor sequence for the FLX sequencer was attached to the 5′ end of the reverse primer. After the PCR amplicons were electrophoresed on agarose gel, the target bands were extracted and purified with a QIAquick Gel Purification Kit (Qiagen) according to the manufacturer's instructions. The mixture of purified 16S rRNA gene amplicons were sequenced with an FLX sequencer at Takara Dragon Genomics Center. The sequences were separated by the DNA tags and trimmed and chimeras were removed, and then analyzed using mothur software with the Schloss standard operation procedure (SOP) (Schloss et al. 2009, 2011).

15.4 Results and Discussion

15.4.1 Hydrothermal Plume Around the Kairei Field

Table *15.1* shows the chemical properties and microbial cell densities of seawater samples collected by CTD-CMS sampler. In Fig. *15.2*, we show the two-dimensional distributions of turbidity, temperature, and dissolved Mn anomalies observed by tow-yo survey line S15ty around the Kairei field. The results from the other tow-yo survey lines are also shown in Suppl. 15.2–15.7 (supplementary data). The hydrothermal plume was determined based on the higher turbidity (ΔFTU) in the plume than in the ambient non-plume seawater (Suppl. 15.8).

The hydrothermal plume around Kairei field arose from the seafloor up to approximately 2,150-m water depth below the sea surface and the thickness of the non-buoyant plume was approximately 120 m (Fig. 15.2). Gamo et al. (1996, 2001) and Zhu et al. (2008) detected the hydrothermal plume based on the turbidity anomalies around Kairei field in September 1993 (Gamo et al. 1996), in August 2000 (Gamo et al. 2001), and in December 2005 (Zhu et al. 2008), respectively. The previous studies also reported the upper limit depth of hydrothermal plume at 2,150 m below sea surface (Gamo et al. 1996, 2001; Zhu et al. 2008). The variation of seawater density is caused by the temperature and salinity. Considering that the maximum height of hydrothermal plume is regulated by the density of the end-member hydrothermal fluid and vertical distribution of the density in the ambient seawater, the hydrothermal fluid chemistry and discharging pattern of the Kairei field would have been stable for at least 17 years.

The horizontal distribution of the hydrothermal plume based on the turbidity anomalies showed the Kairei hydrothermal plume was spread to north or northwest direction from the vents in Kairei field (Suppl. 15.2–15.7). Figure 15.3 demonstrated the horizontal distribution of CH_4, H_2, and microbial cell density in the hydrothermal plume (from 2,144 to 3,341 m of water depth) using the water sample collected by the CTD-CMS. The maximum concentration of H_2 in the hydrothermal plume was 87.6 nM observed near the Kairei field (Table 15.1). The H_2 anomaly was observed only close to the hydrothermal vents at Kairei field (Fig. 15.3a). The maximum CH_4 concentration of 12.3 nM was observed approximately 14 km northwest of the Kairei field, which termed "the north plume" (Fig. 15.3b). In this area, we also observed increased microbial cell densities

Table 15.1 Results of chemical analysis and microbial cell density in seawater samples collected from Kairei field during KH10-6 cruise in 2010

CTD cast	Bottle no.	Latitude (°S)	Longitude (°E)	Depth (m)	Time (GMT)	Salinity (PSU)	pH_T	Alkalinity (μM)	TIC (μM)	DO (mg L^{-1})	H_2 (nM)	CH_4 (nM)	Cell count (cell mL^{-1})
S01ty	01	25.31921	70.05670	2,294	15:47	34.711	7.62	2,376	2,280	3.58	0.9	0.1	1.69×10^4
	02	25.31771	70.05296	2,314	16:25	34.712	7.59	2,381	2,296	3.61	0.8	0.7	2.07×10^4
	03	25.31883	70.05117	2,202	16:39	34.711	7.58	2,371	2,287	3.57	0.3	2.0	1.30×10^4
	04	25.32032	70.04932	2,349	17:53	34.710	7.59	2,404	2,316	3.58	37.0	4.0	7.72×10^3
	05	25.32481	70.03033	2,250	18:21	34.711	N.A	N.A	N.A	3.52	14.6	3.2	1.31×10^4
	06	25.31235	70.02707	2,141	19:20	34.710	7.60	2,380	2,291	3.51	13.6	3.1	1.36×10^4
S02ty	01	25.32504	70.05339	2,290	22:18	34.708	7.607	2,380	2,291	3.55	5.8	2.4	1.37×10^4
	02	25.32004	70.05325	2,242	23:01	34.706	7.614	2,380	2,288	3.53	65.5	6.2	1.33×10^4
	03	25.31596	70.05241	2,289	23:22	34.710	7.612	2,377	2,288	3.52	87.6	6.2	1.31×10^4
	04	25.30835	70.03345	2,350	1:44	34.711	7.594	2,376	2,287	3.52	3.2	1.1	9.42×10^3
	05	25.31050	70.03056	2,316	2:01	34.712	7.599	2,375	2,286	3.45	4.4	3.9	1.32×10^4
	06	25.31348	70.02512	2,250	2:26	34.717	7.603	2,376	2,289	3.51	4.9	3.7	8.10×10^3
S05ty	01	25.33348	70.04157	2,750	14:29	34.712	7.668	2,374	2,276	3.51	0.3	0.6	1.01×10^4
	02	25.33343	70.04160	2,750	14:29	34.712	7.669	2,374	2,276	3.56	0.7	0.6	9.48×10^3
	03	25.32855	70.04385	2,620	14:59	34.711	7.662	2,374	2,277	3.57	0.6	0.7	9.32×10^3
	04	25.32740	70.04330	2,250	15:06	34.710	7.657	2,364	2,276	3.49	10.1	1.8	1.06×10^4
	05	25.32318	70.04033	2,360	15:51	34.712	7.645	2,369	2,300	3.48	19.4	7.2	1.06×10^4
	06	25.32047	70.03976	2,320	16:10	34.710	7.654	2,393	2,275	3.49	5.8	3.4	9.32×10^3
	07	25.32014	70.03966	2,260	16:13	34.709	7.65	2,369	2,269	3.55	33.8	2.7	6.34×10^3
	08	25.31882	70.03852	2,320	16:29	34.710	7.651	2,364	2,276	3.51	4.0	2.9	1.12×10^4
	09	25.31609	70.03853	2,320	16:45	34.704	7.657	2,368	2,269	3.48	1.2	2.0	1.41×10^4
	10	25.31402	70.03773	2,310	17:01	34.712	7.664	2,364	2,274	3.51	46.1	3.7	1.13×10^4
	11	25.30945	70.03563	2,320	17:37	34.712	7.642	2,971	2,276	3.48	38.2	4.5	1.77×10^4
	12	25.30918	70.03551	2,260	17:39	34.710	7.657	2,368	2,278	3.48	0.2	4.3	1.76×10^4
	13	25.29885	70.03158	2,260	18:44	34.734	7.67	2,371	2,271	3.50	1.0	3.3	2.48×10^4
S06ty	01	25.36184	70.02345	3,341	21:59	34.714	7.671	2,371	2,272	3.60	BD	0.5	1.38×10^4
	02	25.35187	70.02498	2,260	23:03	34.711	7.663	2,364	2,269	3.49	BD	1.2	1.40×10^4
	03	25.34604	70.02547	2,800	23:38	34.713	7.675	2,376	2,273	3.80	2.9	0.8	9.06×10^3
	04	25.34004	70.02269	2,850	0:19	34.714	7.683	2,368	2,268		BD	0.7	9.14×10^3
S07ty	01	25.30796	70.06516	2,300	18:28	34.709	7.68	2,367	2,270	3.50	0.1	1.8	2.07×10^4
	02	25.28945	70.04014	2,500	21:16	34.711	7.687	2,373	2,272	3.53	BD	1.1	8.44×10^3
	03	25.29034	70.03228	2,460	21:44	34.712	7.682	2,373	2,272	3.52	BD	1.2	1.45×10^4
	04	25.28732	70.02214	2,300	22:22	34.710	7.682	2,368	2,269	3.50	0.7	2.8	1.87×10^4
	05	25.28947	70.00650	2,280	23:01	34.708	7.677	2,366	2,267	3.51	BD	2.5	2.0×10^4
	06	25.28871	70.00615	2,200	23:04	34.708	7.574	2,365	2,281	3.48	0.1	6.5	1.41×10^4
	07	25.27991	70.00283	2,200	23:43	34.710	7.652	2,384	2,290	3.50	BD	2.5	1.65×10^4
	08	25.27262	69.99861	2,168	0:24	34.708	7.688	2,360	2,263	3.50	0.4	3.4	1.74×10^4
	09	25.26683	70.00009	2,200	1:01	34.710	7.667	2,366	2,268	3.56	0.9	3.3	1.95×10^4
S14ty	01	25.26408	70.00490	2,850	17:25	34.904	7.648	2,385	2,292	3.61	0.7	0.94	1.72×10^4
	02	25.25796	70.00176	2,200	18:24	34.709	7.663	2,386	2291	3.62	BD	1.33	1.29×10^4
	03	25.25481	70.00121	2,600	18:50	34.710	7.661	2,386	2,294	3.56	2.5	1.50	1.24×10^4
	04	25.25434	70.00141	2,500	18:53	34.711	7.673	2,376	2,283	3.56	0.5	9.25	2.11×10^4
	05	25.24991	69.99868	2,450	19:31	34.710	7.665	2,384	2,289	3.76	0.3	5.48	1.64×10^4
	06	25.24444	69.99727	2,550	20:06	34.711	7.662	2,385	2,295	3.55	0.5	12.27	2.20×10^4
	07	25.23774	69.99451	2,600	20:44	35.141	7.667	2,451	2,356	4.47	0.5	4.79	4.80×10^4
	08	25.23049	69.99164	2,700	21:20	34.710	7.916	2,323	2,127	3.59	BD	1.57	1.21×10^4
	09	25.21891	69.98633	2,000	22:11	34.694	7.663	2,366	2,275	3.42	BD	1.00	1.02×10^4
S15ty	01	25.32301	70.04336	2,400	14:00	34.709	7.587	2,377	2,274	3.50	1.7	1.50	2.10×10^4
	02	25.32255	70.04448	2,400	14:19	34.705	7.587	2,375	2,274	3.54	0.2	1.37	1.64×10^4
	03	25.32205	70.04413	2,300	14:21	34.706	7.574	2,369	2,272	3.48	0.6	1.31	1.49×10^4
	04	25.32062	70.04308	2,416	14:36	34.709	N.A	2,401	2,276	3.48	1.7	1.65	7.94×10^3
	05	25.31912	70.04133	2,250	14:56	34.707	7.665	2,421	2280	3.47	7.8	2.78	1.55×10^4
	06	25.31732	70.03962	2,270	15:15	34.708	7.660	2,388	2,264	3.46	12.2	2.54	1.54×10^4

(continued)

Table 15.1 (continued)

CTD cast	Bottle no.	Latitude (°S)	Longitude (°E)	Depth (m)	Time (GMT)	Salinity (PSU)	pH_T	Alkalinity (μM)	TIC (μM)	DO (mg L^{-1})	H_2 (nM)	CH_4 (nM)	Cell count (cell mL^{-1})
	07	25.31595	70.03770	2,256	15:35	34.708	7.648	2,389	2,270	3.46	22.0	3.17	1.00×10^4
	08	25.31587	70.03749	2,225	15:36	34.707	7.676	2,419	2,292	3.46	33.5	3.60	6.22×10^3
	09	25.31501	70.03619	2,429	15:49	34.708	7.655	2,397	2,274	3.47	5.7	1.61	9.88×10^3
	10	25.31479	70.03594	2,240	15:53	34.707	7.644	2,389	2,270	3.44	21.6	3.10	1.07×10^4
	11	25.31483	70.03507	2,426	16:07	34.709	7.640	2,385	2,267	3.46	4.4	1.44	7.96×10^3
	12	25.31207	70.03290	2,400	16:30	34.708	7.633	2,388	2,268	3.49	8.9	1.77	9.72×10^3
	13	25.31065	70.03162	2,400	16:48	34.707	N.A	N.A	N.A	3.45	21.5	2.25	1.40×10^4
	14	25.30832	70.03059	2,117	17:11	34.706	7.641	2,390	2,273	3.42	4.2	1.63	1.37×10^4
	15	25.30768	70.02939	2,364	17:25	34.708	7.642	2,383	2266	3.48	10.0		8.68×10^3
	16	25.30585	70.02952	2,400	17:41	34.710	7.661	2,398	2,272	3.46	1.4	1.18	8.90×10^3
	17	25.30573	70.02936	2,370	17:43	34.708	7.623	N.A	2,281	3.47	3.2	1.63	7.32×10^3
	18	25.30560	70.02919	2,340	17:44	34.707	7.658	N.A	N.A	3.43	10.2	2.31	9.22×10^3
	19	25.30548	70.02903	2,310	17:45	34.709	7.618	2,376	2,264	3.43	2.1	1.66	1.19×10^4
	20	25.30536	70.02887	2,280	17:47	34.708	N.A	N.A	N.A	3.49	4.5	1.78	1.17×10^4
	21	25.30524	70.02871	2,250	17:47	34.707	N.A	N.A	N.A	3.49	3.4	1.55	9.50×10^3
	22	25.30511	70.02854	2,220	17:49	34.707	7.609	2,371	2,261	3.45	0.4	1.29	8.22×10^3

N.A not analyze, *BD* below detection limit

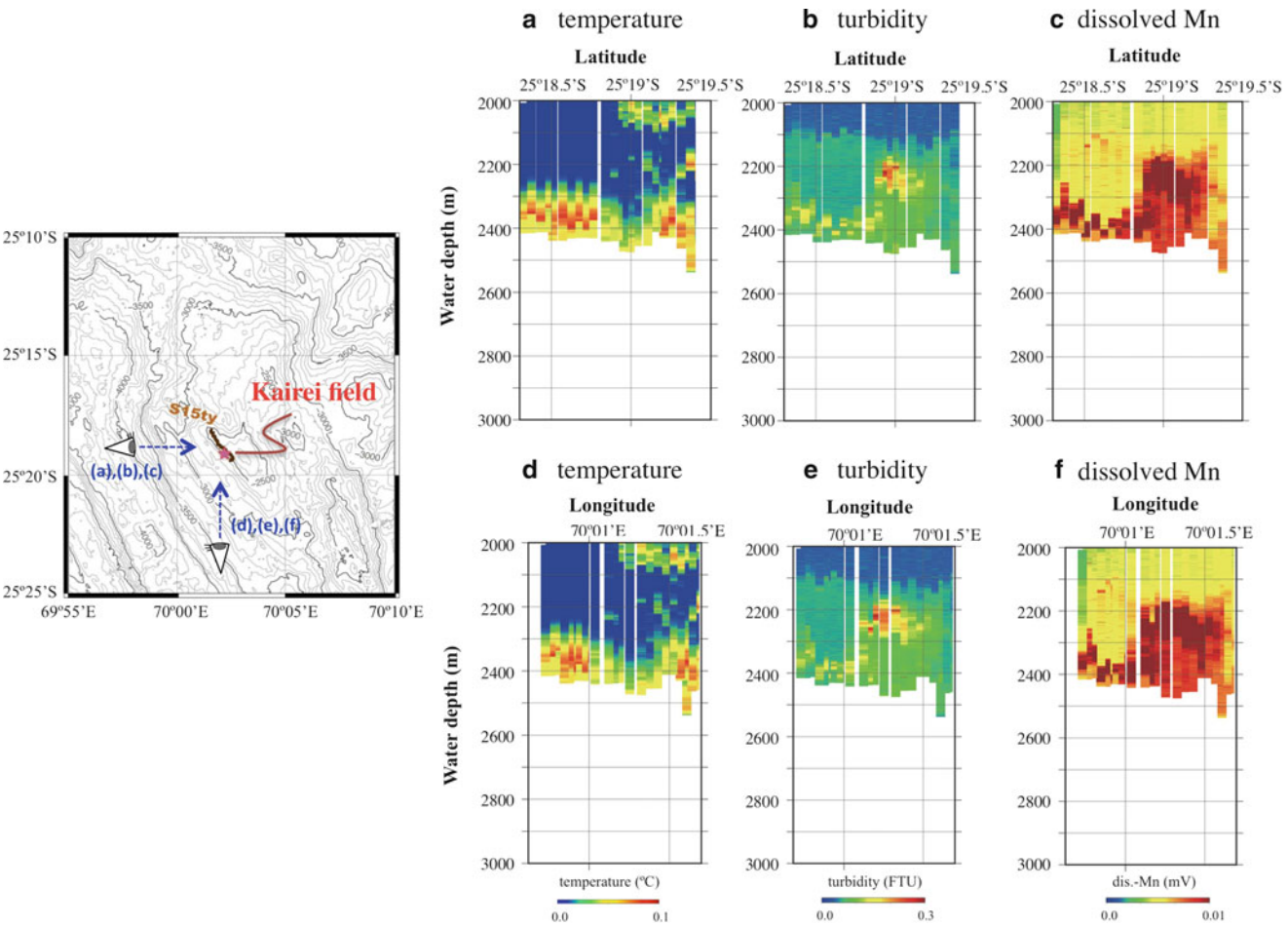

Fig. 15.2 Two-dimensional distribution of temperature (**a**, **d**), turbidity (**b**, **e**), and dissolved manganese (**c**, **e**) anomalies during Tow-yo survey (S15ty) line

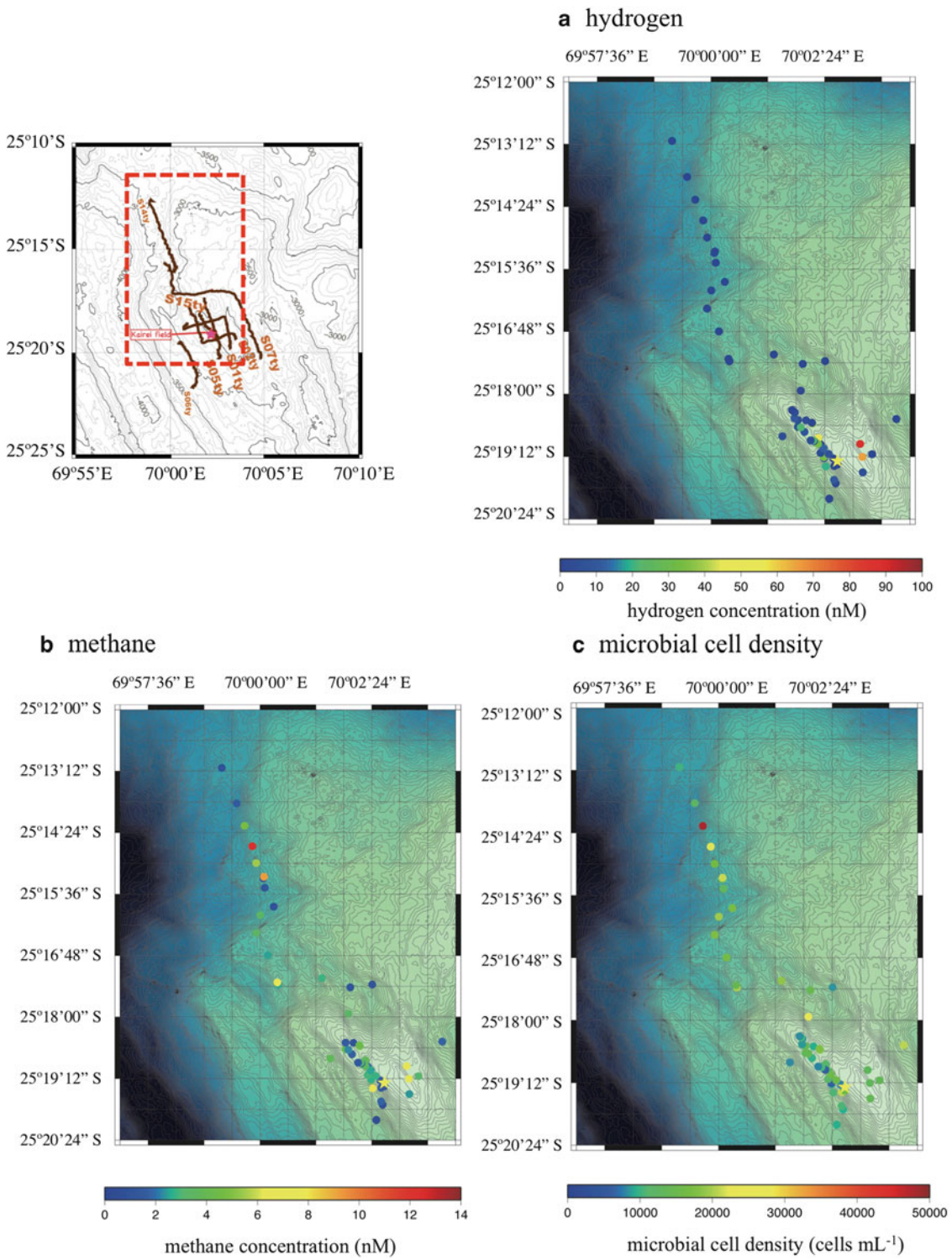

Fig. 15.3 Horizontal distribution of reductive chemical species and microbial cell density around Kairei field, (**a**) H_2, (**b**) CH_4, and (**c**) microbial cell density

(Fig. 15.3c). In the north plume, the H_2/CH_4 ratio in hydrothermal plume sample was completely different from that of the end-member hydrothermal fluid of Kairei field and the plumes near the Kairei field (Fig. 15.4). High and rapid H_2 consumption rate by microorganisms in water column (half time of <1 day) (e.g., Scranton et al. 1984) may cause the restricted distribution of the H_2 anomaly very close to the Kairei field. The CH_4 concentration of the north plume was

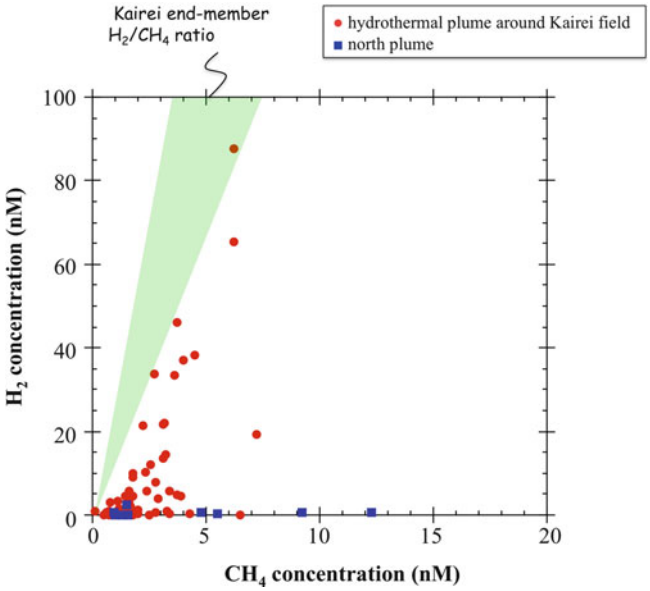

Fig. 15.4 CH_4 concentration vs. H_2 concentration in sub-sampled water taken by Tow-yo survey. H_2/CH_4 ratios of end member compositions of hydrothermal fluids sampled from Kairei Field (15 to 30) were estimated by using the data reported by Kumagai et al. (2008)

higher than those of the plume around Kairei field. One of the possible explanations for the high CH_4 concentration in the north plume would be caused by different hydrothermal end-member fluid. Gamo et al. (2001) predicted the existence of another hydrothermal vent, which has different trend of CH_4 and turbidity ratio, at the north area of Kairei field. The location of north plume, we observed in this time, is farther than that of the plume reported by Gamo et al. (2001). Another possibility of the high CH_4 concentration is in situ CH_4 production under either anaerobic or aerobic conditions. The anaerobic CH_4 production using H_2 and CO_2 may affect the low H_2 and high CH_4 concentration in the north plume, however, this microbial reaction is generally restricted in the strict anaerobic condition. The dissolved oxygen concentration in the plume is more than 3 mg L^{-1}, which indicates that anaerobic methane production is hard to occur. Moreover, our deep-sequencing analysis did not detect any phylotypes related to methanogenic archaea in more than 10,000 amplicons of 16S rRNA gene sequences. Karl et al. (2008) reported that the aerobic CH_4 production in water column via the decomposition of methylphosphonate under the phosphate-depleted condition during microbial growth. The general abyssal seawater is rich in phosphate, however, phosphate in the plume is removed from seawater due to the absorption to the particles of hydrothermal plume (German and Von Damm 2003). We need further exploration for the methylphosphonate concentration and aerobic CH_4 production rate in the hydrothermal plume.

Table 15.2 16S rRNA gene composition of representative microbial community in hydrothermal plumes by deep-sequencing

	S14ty-6 (%)	S15ty-12 (%)	S05ty-1 (%)	S06ty-5 (%)
Specific microbes				
SUP05	2.8	3.2	16.1	8.8
Methylotroph	0.1	0.0	3.1	0.0
Methlylococcus (unclassified)	0.0	0.0	2.8	0.0
Methylobacter	0.1	0.0	0.3	0.0
Methylophilaceae	0.0	0.0	0.0	0.0
Alcanivorax	15.0	17.6	0.8	0.6
Epsiron	4.9	0.8	10.6	1.7

15.4.2 Microbial Populations and Communities

Around the Kairei field, the microbial cell density in seawater samples varied from 0.6×10^4 to 2.5×10^4 cells ml^{-1} (Table 15.1, Fig. 15.3c). At a reference site, where is approximately 80 km north of Kairei field, microbial cell density varied from 0.9×10^4 to 1.4×10^4 cells ml^{-1} (not shown in Table 15.1). The microbial cell density in S05ty-11, S15ty-12, and S14ty-6 was the same as, lower than, and higher than the density in the background/reference S06ty-5 sample, respectively. Microbial cell abundance in the hydrothermal plume was up to three fold higher than that in the abyssal seawater. The increase of microbial cell density was comparable to previous studies (Sunamura et al. 2004; Lam et al. 2004). Samples from near the hydrothermal vents had lower microbial cell densities compared to the reference site, whereas the densities in non-buoyant plume samples were larger than the reference site. The non-buoyant plume was defined based on the horizontal distribution of the turbidity anomaly. We compared the microbial cell densities with physico-chemical properties (e.g. pH, H_2, CH_4, temperature, alkalinity, and dissolved Mn) but we found no strong correlations.

The microbial 16S rRNA gene phylotype compositions showed that the sequences of Phylum *Proteobacteria* accounted for about half of the total sequences in the reference sample (S06ty-5), whereas the proportion was increased in the plume samples (Table 15.2 and Suppl. 15.9). Phylogenetic analysis of 16S rRNA gene sequences suggested that potential chemolitho(auto)trophs such as SUP05 (*Thioglobus*), aerobic methanotrophs (*Methylococcus* and *Methylobacter*), *Epsilonproteobacteria*, and *Alcanivorax* thrived in the plume (Table 15.2). The SUP05 phylotypes, which are known as sulfur oxidizers (Marshall and Morris 2012) and/or possibly hydrogen oxidizers (Petersen et al. 2011; Anantharamana et al.

2013), accounted for 16.1 % of the total 16S rRNA gene sequences in S05ty-11, the sample collected closest to the Kairei vents. The proportion of SUP05 in the total microbial community decreased with distance from the vents, from 16.1 % in S05ty-11 near the vents to 2.8 % in S14ty-6, respectively. The proportion of the epsilonproteobacterial phylotypes, possible sulfur and/or hydrogen oxidizers, was 10.6 %, 0.8 %, and 4.9 % in S05ty-11, S15ty-12, and S14ty-6, respectively. *Alcanivorax* members, which are potential hydrocarbon utilizers and sulfur oxidizers, were rare (0.8 %) in the S05ty-11 plume sample, but it increased to 17.6 % and 15.0 % in Sty15-12 and Sty14-6, respectively. The phylotypes of aerobic methanotrophs were detected in S05ty-11 (3.1 % of the total sequences), but they accounted for less than 0.1 % in the S15ty-12 and S14ty-6 samples. From these results, it is expected that (1) SUP05, *Epsilonproteobacteria*, and methanotrophs dominate in the early stage of the hydrothermal plume and in the hydrothermal fluid–seawater mixing zone near the vents; (2) at a short distance from the vents, microbial cells are diluted or removed from seawater by adsorption onto hydrothermal plume particles and precipitation; and (3) in the non-buoyant and evolved hydrothermal plume far from the vent, small population increase of heterotrophs and sulfur oxidizers such as *Alcanivorax*, *Alphaproteobacteria*, and *Alteromonas* would occur.

15.5 Conclusion

We showed the two different types of hydrothermal plumes during KH10-6 cruise by R/V *Hakuho-maru* in 2010. One was characterized by high H_2 concentration around Kairei field, and the other was identified as low H_2, high CH_4 and high microbial cell density hydrothermal plume named as the "north plume" found in approximately 14 km north of the Kairei field. Although the possibility of in situ aerobic methane production could not be denied, the north plume may originate from the yet unidentified hydrothermal fluid source with high CH_4 concentration end-member. In the north plume, slightly increases of heterotrophs or potential sulfur oxidizers such as *Alcanivorax*, Alpha-proteobacteria, and *Alteromonas* were occured. The little abundance of methanotroph and increased heterotrophs may indicate a chemolithoautotrophic-independent microbial ecosystem in the plume. Removal of chemicals from the hydrothermal plume is one of the important aspects for global chemical flux. Our results showed that microbial cells may be diluted or removed from seawater by adsorption onto hydrothermal plume particles and precipitation in a short distance from the Kairei vents. This indicated that the impacts of the plume microbes on seafloor ecosystem could not be negligible. A H_2 anomaly was observed only close to the Kairei field and SUP05 and Epsilon-proteobacteria, which are known as potential hydrogen oxidizer, propagate in the early stage of the hydrothermal plume and in the hydrothermal fluid–seawater mixing zone near the vents. These indicated the rapid microbial H_2 consumption.

Acknowledgments This work was funded by the Ministry of Education, Culture, Science and Technology (MEXT), Japan, through the Grant-in-Aid for Scientific Research: Project TAIGA (New Scientific Research on Innovative Areas, 20109003) and "Development of new tools for the exploration seafloor resources". We thank the officers and crew of R/V *Hakuho-maru* and the scientists who participated in the KH10-6 cruise for water sample collection.

References

Anantharamana K, Breierb JA, Sheika CS, Dick GJ (2013) Evidence for hydrogen oxidation and metabolic plasticity in widespread deep-sea sulfur-oxidizing bacteria. Proc Natl Acad Sci U S A 110:330–335

Baker ET (1990) Hydrothermal plume prospecting: hydrographic and geochemical techniques. In: McMurray GR (ed) Gorda Ridge. Springer, New York, pp 155–167

Dickson AG, Sabine CL, Christian JR (eds) (2007) Guide to best practices for ocean CO_2 measurements. North Pacific Marine Science Organization, Sidney, British Columbia, pp. 176. (PIECES Special Publication 3)

Gallant RM, Von Damm KL (2006) Geochemical controls on hydrothermal fluids from the Kairei and Edmond Vent Fields, 23–25ºS, Central Indian Ridge. Geochem Geophys Geosys 7(6), Q06018. doi:10.1029/2005GC001067

Gamo T, Nakayama E, Shitashima K, Isshiki K, Obata H, Okamura K, Kanayama S, Oomori T, Koizumi T, Matsumoto S, Hasumoto H (1996) Hydrothermal plumes at the Rodriguez triple junction, Indian ridge. Earth Planet Sci Lett 142:261–270

Gamo T, Chiba H, Yamanaka T, Okudaira T, Hashimoto J, Tsuchida S, Ishibashi J, Kataoka S, Tsunogai U, Okamura K, Sano Y, Shinjo R (2001) Chemical characteristics of newly discovered black smoker fluids and associated hydrothermal plume at the Rodriguez Triple Junction, Central Indian Ridge3. Earth Planet Sci Lett 193:371–379

Geiskes JM, Gamo T, Brumsack H (1991) Chemical methods for interstitial water analysis aboard JOIDES RESOLUTION. ODP Tech. Note 15, Texas A&M University, 60 pp

German CR, Von Damm KL (2003) Hydrothermal processes. In: Henry E (ed) Treatise on geochemistry, vol. 6. Elsevier, 625 pp

Hashimoto J, Ohta S, Gamo T, Chiba H, Yamaguchi T, Tsuchida S, Okudaira T, Watabe H, Yamanaka T, Kitazawa M (2001) First hydrothermal vent communities from the Indian Ocean discovered. Zool Sci 18:717–721

Karl DM, Beversdorf L, Björkman KM, Church MJ, Martinez A, Delong EF (2008) Aerobic production of methane in the sea. Nat Geosci 1:473–478

Kawagucci S, Shirai K, Lan TF, Takahata N, Tusunogai U, Sano Y, Gamo T (2010) Gas geochemical characteristics of hydrothermal plumes at the HAKUREI and JADE vent sites, the Izena Cauldron, Okinawa Trough. Geochem J 44:507–518

Kumagai H, Nakamura K, Toki T, Morishita T, Okino K, Ishibashi J, Tsunogai U, Kawagucci S, Gamo T, Shibuya T, Sawaguchi T, Neo N, Joshima M, Sato T, Takai K (2008) Geological background of Kairei

and Edmond hydrothermal fields along the Central Indian Ridge: Implications of their vent fluid' distinct chemistry. Geofluid 8:239–251
Lam P, Cowen JP, Jones RD (2004) Autotrophic ammonia oxidation in a deep-sea hydrothermal plume. FEMS Microbiol Ecol 47:191–206
Marie D, Partensky F, Jacquet S, Vaulot D (1997) Enumeration and cell cycle analysis of natural populations of marine picoplankton by flow cytome try using the nucleic acid stain SYBR Green I. Appl Environ Microbiol 63:186–193
Marshall KT, Morris RM (2012) Isolation of an aerobic sulfur oxidizer from the SUP05/Arctic96BD-19 clade. ISME J 7(2):452–455
Naganuma T, Otsuki A, Seki H (1989) Abundance and growth-rate of bacterioplankton community in hydrothermal vent plumes of North Fiji Basin. Deep Sea Res A 36:1379–1390
Nakamura K, Morishita T, Bach W, Klein F, Hara K, Okino K, Takai K, Kumagai H (2009) Serpentinized troctolites exposed near the Kairei Hydrothermal Field, Central Indian Ridge: Insights into the origin of the Kairei hydrothermal fluid supporting a unique microbial ecosystem. Earth Planet Sci Lett 280:128–136
Noguchi T, Okamura K, Hatta M, Kimoto H, Suzue T, Ishibashi J, Yamanaka T, Fujii T (2011) Miniaturization of in situ manganese analyzer and its long-term observation at the Wakamiko submarine crater in Kagoshima bay. BUTSURI-TANSA 64(4):291–297 (in Japanese with English abstract)
Nunoura T, Takaki Y, Kazama H, Hirai M, Ashi J, Imachi H, Takai K (2012) Microbial diversity in deep-sea methane seep sediments presented by SSU rRNA gene tag sequencing. Microbs Environ 27(4):382–390
Petersen JM, Zielinski FU, Pape T, Seifert R, Moraru C, Amann R, Hourdez S, Girguis PR, Wankel SD, Barbe V, Pelletier E, Fink D, Borowski C, Bach W, Dubilier N (2011) Hydrogen is an energy source for hydrothermal vent symbioses. Nature 476:176–180
Schloss PD, Westcott SL, Ryabin T, Hall JR, Hartmann M, Hollister EB, Lesniewski RA, Oakley BB, Parks DH, Robinson CJ, Sahl JW, Stres B, Thallinger GG, Van Horn DJ, Weber CF (2009) Introducing mothur: open-source, platform-independent, community-supported software for describing and comparing microbial communities. Appl Environ Microbiol 75(23):7537–7541
Schloss PD, Gevers D, Westcott SL (2011) Reducing the effects of PCR amplification and sequencing artifacts on 16S rRNA-based studies. PLoS One 6(12):e27310
Scranton MI, Novelli PC, Loud PA (1984) The distribution and cycling hydrogen gas in the waters of two anoxic marine environments. Limnol Ocean 29(5):993–1003
Shitashima K, Kyo M, Koike Y, Henmi H (2002) Development of in situ pH sensor using ISFET. In: Proceedings of the 2002 international symposium on underwater technology. IEEE/02EX556, pp 106–108
Strickland JDH, Parsons TR (1968) Determination of dissolved oxygen. In: A practical handbook of seawater analysis, vol 167. Fisheries Research Board of Canada, Bulletin, pp 71–75
Sunamura M, Higashi Y, Miyako C, Ishibashi J, Maruyama A (2004) Two bacteria phylotypes are predominant in the Suiyo Seamount hydrothermal plume. Appl Environ Microbiol 70:1190–1198
Tsurushima N, Watanabe S, Tsunogai U (1996) Methane in the East China Sea Water. J Oceanogr 52:221–233
Van Dover CL, Humphris SE, Fornari D, Cavanaugh CM, Collier R, Goffredi SK, Hashimoto J, Lilly MD, Reysenbach AL, Shank TM, Von Damm KL, Banta A, Gallant RM, Götz D, Green D, Hall J, Harmer TL, Hurtado LA, Johnson P, McKiness ZP, Meredith C, Olson E, Pan IL, Turnipseed M, Won Y, Young III CR, Vrijenhoek RC (2001) Biogeography and ecological setting of Indian Ocean hydrothermal vents. Science 294:818–823
Wiesenburg DA, Guinasso NL (1979) Equilibrium solubilities of methane, carbon–monoxide, and hydrogen in water and sea-water. J Chem Eng Data 24:356–360
Winn CD, Karl DM, Massoth GJ (1986) Microorganisms in deep-sea hydrothermal plumes. Nature 320:744–746
Zhu J, Lin J, Guo S, Chen Y (2008) Hydrothermal plume anomalies along the Central Indian Ridge. Chinese Sci Bull 53(16):2527–2535

Vent Fauna on the Central Indian Ridge

16

Hiromi Watanabe and Girish Beedessee

Abstract

In deep-sea hydrothermal vent fields, faunal distribution is associated with the geochemical environments generated by hydrothermal vent activity. Hydrothermal vent fields on the Central Indian Ridge (CIR) are associated with vent fauna which is thought as a mixture of Atlantic and Pacific and are discretely distributed along the ridge axis of more than 1,000 km apart. In this chapter, faunal distribution in hydrothermal vent fields on the CIR is summarized at the intra- and inter-field levels. The species composition of the vent fauna in the four vent fields hitherto known is reviewed and updated, and faunal resemblance among the four vent fields of the CIR appears to reflect the number of species recorded, indicating that faunal surveys are not sufficient in describing the whole vent fauna on the CIR. All the genetic studies of the CIR vent fauna have indicated a high genetic connectivity among the local populations, despite the many potential dispersal barriers existing between the vent fields. On the basis of the spatial distribution of vent species in a vent field, typical vent fields on the CIR were classified into six zones, of which the central two zones are often covered by *Rimicaris* swarms in the Kairei and Edmond fields. The close relationship between vent fauna from the CIR and the western Pacific, compared to those from other regions, is highlighted. Knowledge of the Indian Ocean vent fauna is limited, and further quantitative information on the biodiversity of vent fauna will provide clues to the formation of biogeographical regions and the dispersal of vent fauna among deep-sea hydrothermal vent fields.

Keywords

Biodiversity • Biogeography • Faunal similarity • Indian Ocean • Zonation

16.1 Background

The Indian Ocean has three spreading ridge branches, the Central Indian Ridge (CIR; see Okino et al. Chap. 11), the Southwest Indian Ridge (SWIR), and the Southeast Indian Ridge (SEIR). Their spreading rates vary from the ultraslow spreading of the SWIR (≤12 mm/year) to the intermediate spreading of the SEIR and CIR (50–60 mm/year) (DeMets et al. 1990; Snow and Edmonds 2007). The biology of CIR hydrothermal vents remains little known, because of inaccessibility. An important physical link between the Mid-Atlantic Ridge (MAR) hydrothermal vents and the western Pacific arc and backarc basins, the CIR hydrothermal vents

The online version of this chapter (doi:10.1007/978-4-431-54865-2_16) contains supplementary material, which is available to authorized users.

H. Watanabe (✉)
Department of Marine Biodiversity Research, Japan Agency for Marine-Earth Science and Technology, Kanagawa 237-0061, Japan
e-mail: hwatanabe@jamstec.go.jp

G. Beedessee
Mauritius Oceanography Institute, France Centre, Victoria Avenue, Quatre-Bornes, Mauritius

Department of Chemistry and Biomolecular Sciences, Macquarie University, Sydney, NSW 2109, Australia

J.-i. Ishibashi et al. (eds.), *Subseafloor Biosphere Linked to Hydrothermal Systems: TAIGA Concept*,
DOI 10.1007/978-4-431-54865-2_16,

consist of a blend of Atlantic and Pacific faunas (Van Dover et al. 2001; Nakamura et al. 2012). Since the discovery of a deep-sea hydrothermal vent field and associated fauna in the Indian Ocean in 2000 at the Kairei vent field near the Rodriguez Triple Junction (RTJ) (Hashimoto et al. 2001), our knowledge of the biogeography of vent fauna at the global level has been improved. Subsequent to the discovery of the Kairei field, three other vent fields were discovered on the CIR; Edmond field by (Van Dover et al. 2001) and DoDo and Solitaire fields by Nakamura et al. (2012). Recently, a hydrothermal vent was discovered on the SWIR (Tao et al. 2012). On the SEIR, hydrothermal plumes have been observed, but vent activity has yet to be observed (Scheirer et al. 1998).

In this chapter, we review the previous studies undertaken on the CIR, provide new insights based on our recent findings, and discuss faunal distributions and its biogeographical relationships.

16.2 Distribution and Connectivity of Vent Fauna

Vent fauna associated with the CIR from the Kairei field has been independently described by Hashimoto et al. (2001) and Van Dover et al. (2001); the latter with a discovery of vent fauna in the Edmond field. Recently, vent fauna was also reported in the Solitaire and DoDo vent fields (Nakamura et al. 2012). Here, we review the original faunal list and provide an updated faunal list of the four vent fields on the CIR (Table 16.1). As described in detail in the later sections of this chapter, the faunal composition of the CIR shows a similarity to the central and southern parts of the Pacific vent fauna, whereas some vent species are endemic to the Indian Ocean. As generally known, sampling effort have made significant effects on the accurate description of the biodiversity (Magurran 2004). Because of the inaccessibility of the Indian Ocean vent fields, the vent fauna is not yet fully described. The biodiversity of the Indian Ocean vent may be underestimated and it causes specificity of vent fauna in the Indian Ocean. In this section, previous reports are reviewed for the three major taxa (Annelida, Arthropoda, and Mollusca), with recent results from TAIGA project.

Annelida. In total, 12 species have been reported in the CIR hydrothermal vent fields, and five genera have been regarded as endemic to this region (Van Dover et al. 2001). No tubeworms have been found in the Indian Ocean vent fields. The absence of alvinellid polychaetes has been regarded as one of the characteristics of Indian Ocean vent fauna; however, in recent investigations, several colonies of alvinellid polychaetes were observed in the Solitaire vent field (Nakamura et al. 2012) as well as in the Edmond field. The genus and species of these alvinellids are still under investigation, and the results will provide a clue to understanding worldwide faunal relationships in deep-sea hydrothermal vent fields.

Archinome jasoni is a recently described polychaete, and it is distributed in the hydrothermal vent fields in the southwestern Pacific, Atlantic, and Indian Oceans (Borda et al. 2013). Phylogenetic analyses of mitochondrial DNA have revealed that the *A. jasoni* on the CIR is more closely related to the *A. jasoni* in the Atlantic vent field than to the *A. jasoni* in the southwestern Pacific vent fields (Borda et al. 2013).

The identification of polychaete species in the Solitaire field is still in progress, and the relationship between the Solitaire and Kairei fields is not yet fully understood. A detailed investigation of the annelid composition of the CIR is required.

Arthropoda. In total, six species have been reported in the CIR hydrothermal vent fields, and they are all appear to be endemic to this region, but the genera are all shared with Pacific and Atlantic vent fauna (Van Dover et al. 2001).

Rimicaris kairei is the most abundant animal in the known vent fields of the Indian Ocean, both on the CIR, and on the SWIR (Nakamura et al. 2012; Tao et al. 2012). No genetic differentiation exists between *R. kairei* populations in the Kairei and Edmond fields (Van Dover et al. 2001). Recently, population genetic analysis of *R. kairei* was undertaken using a partial mitochondrial cytochrome oxidase *c* subunit I (COI) sequence, of the three vent populations on the CIR; again, no genetic differences were detected (Beedessee et al. 2013). The congeneric species *R. exoculata* and *R. hybisae* are found on both the MAR and the Mid-Cayman Rise (MCR) (Nye et al. 2012). The distribution of the *Rimicaris* shrimp may reflect the historical connectivity between these three regions.

Mirocaris indica is the second most abundant crustacean in the CIR vent fields, after *R. kairei*. However, it may sometimes be misidentified as "*Chorocaris*" (Komai et al. 2006); indeed, Hashimoto et al. (2001), Van Dover et al. (2001), and Nakamura et al. (2012) have described it as "*Chorocaris*." Although most *Chorocaris* shrimps are found in the Pacific Ocean, the solitary congeneric species *M. fortunata* is found only on the MAR (Komai and Segonzac 2003). The presence of the *Mirocaris* shrimp on the CIR supports the hypothesized relationship between the vent fauna on the MAR and that on the CIR.

The bythograeid crab *Austinograea rodriguezensis* is a common species found in all four-vent sites of the CIR (Tsuchida and Hashimoto 2002; Nakamura et al. 2012). Its distribution varies from location to location, although it is most abundant in the Kairei and Solitaire fields, and least abundant in the DoDo field. No significant differences were detected in genetic diversity between the Solitaire and Kairei populations (Beedessee et al. 2013), which is consistent with the results of a previous study that found a 0.2 % difference in genetic

Table 16.1 Species list of vent fauna in the Central Indian Ridge (Updated from Van Dover et al. (2001) and Nakamura et al. (2012))

Phylum	Family	Species	Dodo	Solitaire*1	Kairei	Edmond*2
Cnidaria	Actinostolidae	*Marianactis* sp.	+	+	+	+
Arthropoda	Bythograeidae	*A. rodriguezensis*	+	+	+	+
	Alvinocarididae	*Rimicaris kairei*	+	+	+	+
		Mirocaris indica		+	+	+
	Galatheidae	*Munidopsis* sp.		+	+	
	Neolepadidae	Neolepadidae gen et sp.		+	+	
	Chionelasmatidae	*Eochionelasmus* sp.		+	+	
Mollusca	Mitilidae	*Bathymodiolus marisindicus*		+	+	
	Lepetodridae	*Lepetodrilus* sp.		+	+	
		Pseudorimula sp.			+	
	Neolepetopsidae	*Eulepetopsis* sp.		+	+	
	Peltospiridae	Scaly-foot gastropod		+	+	
	Phenacolepadidae	*Shinkailepas* sp.		+	+	
	Provannidae	*Alviniconcha* sp. type 3		+	+	+
		Desbruyeresia sp.		+	+	
	Skeneidae	*Bruceiella* sp.			+	
	Turridae	*Phymorhynchus* sp.		+	+	+
	Simrothiellidae	*Helicoradomenia*? sp.			+	
	Sutilizonidae	*Sutilizona* sp.			+	
	–	Slit limpet sp. 1			+	
	–	Slit limpet sp. 2			+	
Annelida	Alvinellidae	Alvinellid gen et sp.		+		+
	Ampharetidae	*Amphisamytha* sp.			+	
	Amphinomidae	*Archinome jasoni*		+	+	
	Capitellidae	Capitellid sp. 1			+	
	Dorvilleidae	*Ophyotrocha* sp.			+	
	Hesionidae	Hesionoid sp. 1			+	
		Hesionid sp. 2			+	
	Polynoidae	*Branchinotogluma* sp.		+	+	+
		Branchipolynoe sp.			+	
		Harmothoe? sp.			+	
		Levensteiniella? sp.			+	
	Spionidae	*Prionospio* sp.			+	
Echinodermada	–	Apodacean gen et sp.		+		
Chordata	Macroudidae	Macrourid gen et sp.		+		
Nemertea	–	Unidentified		+	+	
Platyhelminthes	–	Unidentified		+	+	
Number of taxaon		37	3	22	34	6

*1: without identification of polychates, *2: compiled from Van Dover et al. (2001), +: presence

diversity between *Austinograea* populations in the Kairei and Edmond fields (Van Dover et al. 2001). Congeneric species are found in the western Pacific vent fields, whereas crabs of different genera are found in the eastern Pacific and MAR vent fields (summarized in Desbruyères et al. 2006).

Other crustaceans are found on the periphery of the vent fields of the CIR. Galatheid crabs of the genus *Munidopsis* are an important component of the macrofauna of the Kairei and Solitaire fields, with *M. laticorpus* being the species found in the Kairei field (Cubelio et al. 2008). *Munidopsis* crabs in the Solitaire field inhabit areas distant from venting chimneys, most likely to avoid predation. *Munidopsis* crabs are distributed globally on the deep-sea floor, not only in vent fields, but also in non-vent environments. Barnacles of the family Neolepadidae and Chionelasmatidae are shown to aggregate in patches at the periphery of the vent fields. The species identification of these barnacles is under investigation, but the congeneric species are all found on the western and eastern parts of the southern Pacific.

Mollusca. In total, 14 species have been reported in the CIR hydrothermal vent fields. Only the scaly-foot gastropod is regarded as an endemic taxon to this region, probably at the genus level, and it is one of the representative animals of

the Indian Ocean vent fauna, both on the CIR and SWIR (Van Dover et al. 2001; Tao et al. 2012). The scaly-foot gastropod was first reported from the Kairei field, and is considered unique because of its iron-coated sclerites (Warén et al. 2003), and the presence of bacterial symbionts in its esophageal gland (Goffredi et al. 2004). Analysis of its population genetics revealed no genetic differences between the scaly-foot populations in the Kairei and Solitaire fields (Nakamura et al. 2012). The symbiotic bacteria of the scaly-foot gastropod, as well as those of *Alviniconcha* gastropods, are summarized with environmental microbial communities in Chap. 12 (Nakamura and Takai).

The genus *Alviniconcha* was first discovered in the Alice Spring vent field of the Mariana Trough, with the only species described to date being *A. hessleri*. The large, hairy *Alviniconcha* snails, which also host bacterial symbionts, are dominant in the vent fields of the Mariana Trough, and in the southernmost vent fields of the western Pacific region, but are less abundant in the Indian Ocean. Several lineages of these gastropods have been detected using molecular approaches (Kojima et al. 2001; Beinart et al. 2012). However, the taxonomic description of this species is still in progress, and only provisional names are used. The population differentiation of this gastropod in the CIR was first examined using a partial sequence of the mitochondrial 16SrRNA gene with no genetic differentiation between the Kairei and Edmond fields (Van Dover et al. 2001), whereas recent investigations have revealed significant genetic differentiation between the local populations in the Edmond and Solitaire fields (Beedessee et al. 2013). *Phymorhynchus*, a globally distributed gastropod genus that inhabits the periphery of vent field, appears to be omnivorous species, as its nitrogen isotopic signature was not high compared to that of other animals without symbionts (Van Dover 2002).

Some gastropods, listed by Hashimoto et al. (2001), have been updated after recent investigation and sample re-examinations. A cancellariid gastropod is now described as *Iphinopsis boucheti*, and a *Provanna* gastropod was re-classified in the related genus *Desbruyeresia* (Okutani et al. 2004). *Bathyacmaea* sp. was probably a misidentification of *Eulepetopsis*, or another limpet (*Bathyacmaea* was listed by Hashimoto et al. (2001) as a collected sample, but only *Lepetodrilus* and *Eulepetopsis* were listed in the database of JAMSTEC biological samples, as well as being in sample storage).

Bathymodiolus marisindicus is a large bivalve with symbiotic bacteria, and is described as an endemic species to the CIR vent fields. However, the previous genetic analysis, based on a partial sequence of the mitochondrial NADH dehydrogenase 4 (*ND4*) gene, revealed that *B. marisindicus* shared a haplotype with the congeneric *B. brevior* in the North Fiji Basin and with *B. septemdierum* in the Myojin Knoll (Kyuno et al. 2009). The sequence of the *ND4* gene is widely used in population genetic analyses as it is contains sufficient information to perform such analyses (Kyuno et al. 2009), therefore, the results of Kyuno et al. (2009) raise the possibility that these three species may be geographic variations of a single species, that has a high dispersal ability.

Other Phyla. A conspicuous red flatworm (probably, a platyhelminth) was observed in the Kairei and Solitaire fields (Van Dover et al. 2001; Nakamura et al. 2012). The occurrence of this animal in the vent fields is unique to the CIR vents, whereas red nemertean worms have been found in the eastern Pacific vent fields (Rogers et al. 1996). An apodacean holothurian was observed in the Kairei and Solitaire fields on the CIR; that in the Kairei field was assigned to the family Synaptidae (Hashimoto et al. 2001). The holothurian *Chiridota hydrothermica* has been found in the Manus Basin hydrothermal vent field, together with large gastropods of the genera *Alviniconcha* and *Ifremeria*, and barnacles (Smirnov et al. 2000). *C. hydrothermica* was also found in both the eastern and western sides of the southern Pacific Ocean, with associated fauna that included mussel clumps (Smirnov et al. 2000). The density of *C. hydrothermica* was significantly affected by lava type (Podowski et al. 2010). Although their geographical distribution has not yet been comprehensively investigated, holothurians may be among the most common animals inhabiting the periphery of hydrothermal vent fields. The sea anemone *Marianactis* was observed consuming *R. kairei*, and this observation was supported by its stable isotopic signature (Van Dover 2002).

16.3 Zonation in a Vent Field

Vent fauna show variation along steep environmental gradients, or patchiness, which is referred to "zonation". In the CIR, two types of vent areas have been recognized; the chimney-rich Kairei and Edmond fields, and the diffuse flow-rich Solitaire field. *R. kairei* swarms near vents are abundant in the chimney-rich vent fields, but are patchily distributed in the diffuse flow-rich vent field. The fauna on the chimney surface, such as the scaly-foot gastropod and the alvinellid polychaetes, are therefore covered by shrimp swarms in the chimney-rich vent fields, but are exposed in the diffuse flow-rich vent field. Therefore, we will describe the zonation in the diffuse flow-rich vent field first, followed by some remarks in the chimney-rich vent fields later.

In the diffuse flow-rich Solitaire field, faunal assemblages are distributed in the following zones: Zone 1, an alvinellid aggregation; Zone 2, a scaly-foot and *Alviniconcha* gastropod-hosted community; Zone 3, a *Bathymodiolus*-hosted community; Zone 4, a peripheral *Phymorhynchus* and *Marianactis* community; Zone 5, a peripheral *barnacle*-dominated community; and Zone 6, a mobile *Rimicaris* aggregation (Fig. 16.1). Alvinellid aggregations are commonly found in the high temperature zone of

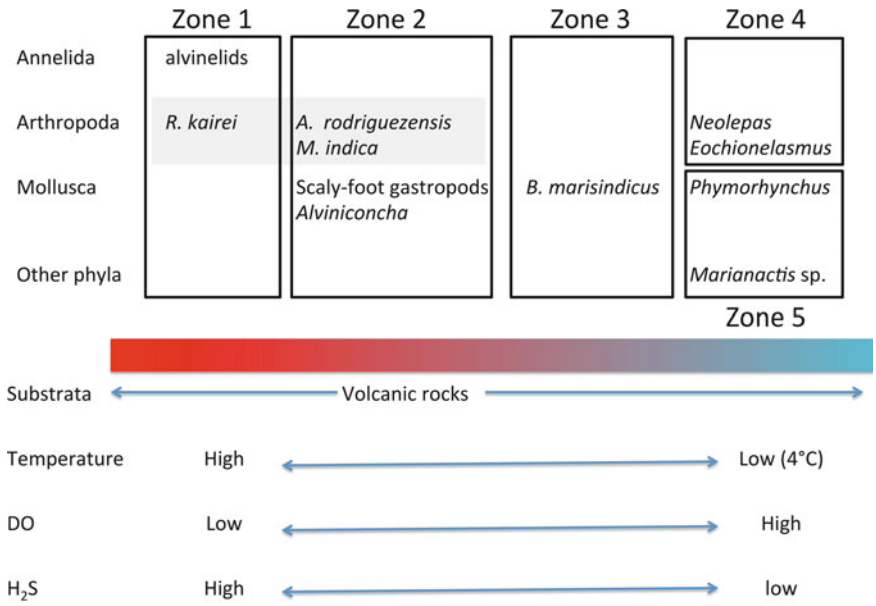

Fig. 16.1 Nonmetric multidimensional scaling (nMDS) plot of faunal similarities among the four vent fields of the Central Indian Ridge based on Table 16.1

hydrothermal vent fields, in both the western and eastern Pacific, but are not abundant on the CIR. Mobile species, such as *R. kairei*, may cover such aggregations in the chimney-rich vent fields. Both scaly-foot and *Alviniconcha* gastropods harbor symbiotic bacteria (Stein et al. 1988; Goffredi et al. 2004), but their distributions are slightly different; scaly-foot gastropods inhabit the diffuse-flow transitional zone, whereas *Alviniconcha* inhabits more gentle environments. *Bathymodiolus*-hosted communities are usually found outside *Rimicaris* aggregations, and are easily observed, even in the chimney-rich vent fields. As for the mobile fauna, *R. kairei* does not only aggregate at the high temperature vents, but also scattered in the diffuse-flow area, in a similar manner as *M. indica* and *A. rodriguezensis*. In *R. kairei* and *A. rodriguezensis*, carapace size, and stable isotopic ratio, are correlated (Van Dover 2002), suggesting that the feeding ecologies of these animals vary according to their growth stage; or that their habitats may be changing.

Some special features of the zonation in the Kairei field are noteworthy. Shed *Rimicaris* molts accumulate at the base of the Monju chimney, just below the *Rimicaris* aggregation. *Archinome* polychaetes are abundant in this area, and its isotope signatures indicates that these polychaetes consumes the *Rimicaris* molts (Van Dover 2002). Flatworm aggregations are also a feature of this region, whereas no such aggregations have been observed in the Solitaire field.

16.4 Inter-Field similarity

To investigate the overall similarity between the vent fauna on the CIR, Jaccard's index of similarity (C_J) was calculated based on the species occurrence data (Table 16.1), and the

Fig. 16.2 Summary of the zonation of vent fauna on the Central Indian Ridge

result was visualized using nonmetric multidimensional scaling (nMDS; Fig. 16.2). Faunal similarity among the four vent fields was less than 50 %; the vent fauna in the Solitaire and Kairei fields were the most similar, despite their geographical locations. However, these results were driven entirely by differences in the number of species observed in each vent field. In total, 42 species were reported on the CIR; 40 and 22 species were reported in the Kairei and Solitaire fields, respectively, but only six and three species were reported in the Edmond and DoDo fields, respectively (Table 16.1). The number of species is generally correlated with the number of investigations carried out and it seemed to be consistent with the result shown as Fig. 16.2. On the other hand, activities of hydrothermal vents were also clearly different between the Edmond and DoDo fields, i.e., active chimneys with flourish vent fauna were observed in the Edmond field but only scattered vent faunas were observed in the DoDo

field (Nakamura et al. 2012). To be accurate, comparative investigation in the Edmond field is required.

16.5 Faunal Similarities with Other Biogeographical Regions

The biogeography of the Indian Ocean vent fauna was first discussed when the second CIR vent field, the Edmond vent field, was discovered (Van Dover et al. 2001). However, knowledge of the vent fauna in the Kairei and Edmond fields was limited and specificity of vent fauna in the Indian Ocean is still under discussion (Bachraty et al. 2009; Rogers et al. 2012). The present review updates the previous dataset, along with those shown in Kojima and Watanabe (Chap. 25) and Watanabe and Kojima (Chap. 34). Similarity among global vent fields at the genus level is shown by the nMDS plot (Fig. 16.3), based on C_J calculated using the species occurrence data in Suppl. 16.1. The results show that the closer relationships of the CIR fauna to the Pacific vent faunas, particularly to those in the Mariana Trough ($C_J = 31.579$) and the Manus Basin ($C_J = 26.667$), than to the Atlantic vent faunas.

Recent discoveries, such as the distribution of alvinellids and holothurians, and the close genetic relationship between *B. marisindicus* and its congeneric relatives in the western Pacific, *B. brevior* and *B. septemdierum*, also indicate that the CIR vent fauna shares a closer relationship with the vent faunas of the western Pacific. On the other hand, an *Archinome* polychaete is found on the CIR, the MAR, and in the western Pacific vent fields, and the *A. jasoni* on the CIR is genetically closer to the *A. jasoni* on the MAR than to the *A. jasoni* found in the Pacific Ocean (Borda et al. 2013). There must be complicated history of biogeography. However, the present results support the hypothesis that the Indian Ocean ridge systems act as a corridor for contemporaneous dispersal between ocean basins (German et al. 1998; Van Dover 2002).

In addition to the CIR, two other ocean ridge systems are found in the Indian Ocean: the SWIR and SEIR. The SWIR is particularly interesting, as it is an ultraslow-spreading ridge system that should act as a corridor for vent faunal gene flow between the Atlantic and Pacific vent fields (German et al. 1998). The recent discovery of a vent field on the SWIR will provide new insights into the biogeography of the Indian Ocean (e.g., the distribution of scaly-foot gastropods on the SWIR (Tao et al. 2012)). On the other hand, the present results suggest that SEIR may not act as a corridor to the Pacific Ocean, as most of the southwestern Pacific vent fauna showed relatively low similarity to the CIR vent fauna, while relatively high similarity was observed between the CIR and the equatorial western Pacific vent faunas. The historical seafloor spreading (Heirtzler et al. 1968) or Indonesian Throughflow (Gordon and Fine 1996) may be among the important factors influencing faunal connectivity between the CIR and western Pacific vent fields.

16.6 Conclusion

More than 10 years of study have provided basic information on the fauna associated with the CIR vent fields, including intra- and inter-field variations. This chapter has described zonation of vent fauna in the CIR vent fields and inter-field similarity of vent fauna. Furthermore, a similarity analysis of global vent fauna suggested close relationships between the CIR and western Pacific vent faunas at the genus level. The CIR vent fields contain a mixture of Atlantic and Pacific vent fauna, although the CIR itself is not connected to any other ridge systems, unlike the SWIR, which is connected to the MAR, or the SEIR, which is

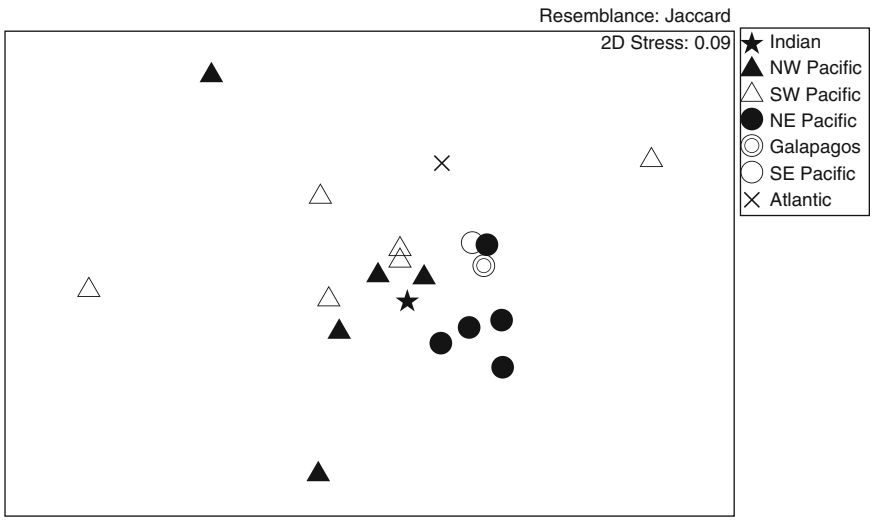

Fig. 16.3 Nonmetric multidimensional scaling (nMDS) plot of faunal similarities among global vent fields based on Suppl. 16.1

connected to the Pacific-Antarctic Ridge. In addition, the spreading rates of the three ridge systems in the Indian Ocean are different. Therefore, elucidating the biogeography of the three ridge systems in the Indian Ocean is important for understanding the global biogeography of vent fauna, not only for the accumulation of information regarding vent fauna distributions but also for elucidating the mechanisms of faunal dispersal and generation of biogeographical regions among vent fields.

Acknowledgments We are grateful to the on-board scientists of the YK09-13 and YK13-02 cruises of the R/V Yokosuka and HOV Shinkai6500, and Drs. Satoshi Mitarai and Dhugal Lindsay for discussion of oceanographic states. This study was supported by the "TAIGA project," which was funded by a Grant-in-Aid for Scientific Research on Innovative Areas (No. 20109001, 20109004, 20109005) from the Ministry of Education, Culture, Sports, Science and Technology (MEXT), Japan, and Canon Foundation.

References

Bachraty C, Legendre P, Desbruyéres D (2009) Biogeographic relationships among deep-sea hydrothermal vent faunas at global scale. Deep Sea Res I 56:1371–1378

Beedessee G, Watanabe H, Ogura T, Nemoto S, Yahagi T, Nakagawa S, Nakamura K, Takai K, Koonjul M, Marie DEP (2013) High connectivity of animal populations in deep-sea hydrothermal vent fields in the Central Indian Ridge relevant to its geological setting. PLoS One 8:e81570

Beinart RA, Sanders JG, Faure B, Sylva SP, Lee RW, Becker EL, Gartman A, Luther GW III, Seewald JS, Fisher CR, Girgius PR (2012) Evidence for the role of endosymbionts in regional-scale habitat partitioning by hydrothermal vent symbioses. Proc Natl Acad Sci USA 109:E3241–E3250

Borda E, Kudenov JD, Chevaldonné P, Blake AJ, Desbruyères D, Fabri MC, Hourdez S, Pleijel F, Shank TM, Wilson NG, Schulze A, Rouse GW (2013) Cryptic species of *Archinome* (Annelida: Amphinomida) from vents and seeps. Proc R Soc B 280:20131876. doi:10.1098/rspb.2013.1876

Cubelio S, Tsuchida S, Watanabe S (2008) New species of *Munidopsis* (Decapoda: Anomura: Galatheidae) from hydrothermal vent areas of Indian and Pacific Oceans. J Mar Biol Ass U K 88:111–117

DeMets C, Gordon RG, Argus DF, Stein S (1990) Current plate motions. Geophys J Int 101:425–478

Desbruyères D, Segonzac M, Bright M (eds) (2006) Handbook of deep-sea hydrothermal vent fauna. Second completely revised edition. Denisia 18:544

German CR, Baker ET, Mevel C, Tamaki K, the FUJI Science Team (1998) Hydrothermal activity along the southwest Indian ridge. Nature 395:490–493

Goffredi SK, Warén A, Orphan VJ, Van Dover CL, Vrijenhoek RC (2004) Novel form of structural integration between microbes and a hydrothermal vent gastropod from the Indian Ocean. App Environ Microbiol 70:3082–3090

Gordon AL, Fine RA (1996) Pathways of water between the Pacific and Indian oceans in the Indonesian seas. Nature 379:146–149

Hashimoto J, Ohta S, Gamo T, Chiba H, Yamaguchi T, Tsuchida S, Okudaira T, Watabe H, Yamanaka T, Kitazawa M (2001) First hydrothermal vent communities from the Indian Ocean discovered. Zool Sci 18:717–721

Heirtzler JR, Dickson GO, Herron EM, Pitman WC III, Le Pichon X (1968) The magnetic anomalies, geomagnetic field reversals and motions of the ocean floor and continents. J Geophys Res 73:2119–2136

Kojima S, Segawa R, Fijiwara Y, Fujikura K, Ohta S, Hashimoto J (2001) Phylogeny of hydrothermal-vent-endemic gastropods *Alviniconcha* spp. from the western Pacific revealed by mitochondrial DNA sequences. Biol Bull 200:298–304

Komai T, Segonzac M (2003) Review of the hydrothermal vent shrimp genus *Mirocaris*, redescription of *M. fortunata* and reassessment of the taxonomic status of the family Alvinocarididae (Crustacea: Decapoda: Caridea). Cah Biol Mar 44:199–215

Komai T, Martin JW, Zala K, Tsuchida S, Hashimoto J (2006) New species of *Mirocaris* (Crustacea: Decapoda: Caridea: Alvinocarididae) associated with hydrothermal vents on the Central Indian Ridge, Indian Ocean. Sci Mar 70:109–119

Kyuno A, Shintaku M, Fujita Y, Matsumoto H, Utsumi M, Watanabe H, Fujiwara Y, Miyazaki J (2009) Dispersal and differentiation of deep-sea mussels of the genus *Bathymodiolus* (Mytilidae, Bathymodiolinae). J Mar Biol. doi:10.1155/2009/625672

Magurran AE (2004) Measuring biological diversity. Blackwell, Massachusetts, Oxford, Victoria, 256 pp

Nakamura K, Watanabe H, Miyazaki J, Takai K, Kawagucci S, Noguchi T, Nemoto S, Watsuji T, Matsuzaki T, Shibuya T, Okamura K, Mochizuki M, Orihashi Y, Ura T, Asada A, Daniel M, Koonjul M, Singh M, Beedessee G, Bhikajee M, Tamaki K (2012) Discovery of new hydrothermal activity and chemosynthetic fauna on the Central Indian Ridge at 18–20°S. PLoS One 7:e32965

Nye V, Copley J, Plouviez S (2012) A new species of Rimicaris (Crustacea: Decapoda: Caridea: Alvinocarididae) from hydrothermal vent fields on the Mid-Cayman Spreading Centre Caribbean. J Mar Biol Ass UK 92:1057–1072

Okutani T, Hashimoto J, Sasaki T (2004) New gastropod taxa from a hydrothermal vent (Kairei field) in the central Indian Ocean. Venus 63:1–11

Podowski EL, Ma S, Luther GW III, Wardrop D, Fisher CR (2010) Biotic and abiotic factors affecting distributions of megafauna in diffuse flow on andesite and basalt along the Eastern Lau Spreading Center. Tonga Mar Ecol Prog Ser 418:25–45

Rogers AD, Gibson R, Tunnicliffe V (1996) A new genus and species of monostiliferous hoplonemertean colonizing an inchoate hydrothermal. Field on Juan de Fuca Ridge. Deep-Sea Res I 43:1581–1599

Rogers AD, Tyler PA, Connelly DP, Copley JT, James R, Larter RD, Linse K, Mills RA, Garabato AN, Pancost RD, Pearce DA, Polunin NVC, German CR, Shank T, Boersch-Supan PH, Alker BJ, Aquilina A, Bennett SA, Clarke A, Dinley RJJ, Graham AGC, Green DRH, Hawkes JA, Hepburn L, Hilario A, Huvenne VAI, Marsh L, Ramirez-Llodra E, Reid WDK, Roterman CN, Sweeting CJ, Thatje S, Zwirglmaier K (2012) The discovery of new deep-sea hydrothermal vent communities in the Southern Ocean and implications for biogeography. PLoS Biol 10:e1001234

Scheirer DS, Baker ET, Johnson KTM (1998) Detection of hydrothermal plumes along the Southeast Indian Ridge near the Amsterdam-St. Paul Plateau. Geophys Res Lett 1998(25):97–100

Smirnov AV, Gebruk AV, Galkin SV, Shank T (2000) New species of holothurian (Echinodermata: Holothuroidea) from hydrothermal vent habitats. J Mar Biol Ass UK 80:321–328

Snow JE, Edmonds HN (2007) Ultraslow-spreading ridges: rapid paradigm changes. Oceanography 20:90–101

Stein JL, Cary C, Hessler RR, Ohta S, Vetter RD, Childress JJ, Felbeck H (1988) Chemoautotrophic symbiosis in a hydrothermal vent gastropod. Biol Bull 174:373–378

Tao C, Lin J, Guo S, Chen YJ, Wu G, Han X, German CR, Yoerger DR, Zhou N, Li H, Su X, Zhu J, the DY115-19 (Leg 1) and DY115-20

(Legs 4–7) Science Parties (2012) First active hydrothermal vents on an ultraslow-spreading center: Southwest Indian Ridge. Geology 40:47–50

Tsuchida S, Hashimoto J (2002) A new species of bythograeid crab, Austinograea rodriguezensis (Decapoda, Brachyura), associated with active hydrothermal vents from the Indian Ocean. J Crust Biol 22:642–650

Van Dover CL (2002) Trophic relationships among invertebrates at the Kairei hydrothermal vent field (Central Indian Ridge). Mar Biol 141:761–772

Van Dover CL, Humphris SE, Fornari D, Cavanaugh CM, Collier R, Goffredi SK, Hashimoto J, Lilley MD, Reysenbach AL, Shank TM, Von Damm KL, Banta A, Gallant RM, Götz D, Green D, Hall J, Harmer TL, Hurtado LA, Johnson P, McKiness ZP, Meredith C, Olsen E, Pan IL, Turnipseed M, Won Y, Young CR III, Verijenhoek RC (2001) Biogeography and ecological setting of Indian Ocean hydrothermal vents. Science 294:818–823

Warén A, Bengtson S, Goffredi SK, Van Dover CL (2003) A hot-vent gastropod with iron-sulfide dermal sclerites. Science 302:1007

Part III

Southern Mariana Trough

The Mantle Dynamics, the Crustal Formation, and the Hydrothermal Activity of the Southern Mariana Trough Back-Arc Basin

17

Nobukazu Seama, Hiroshi Sato, Yoshifumi Nogi, and Kyoko Okino

Abstract

The Southern Mariana Trough back-arc basin is a currently active back arc basin, and it has fast spreading morphologic and geophysical characteristics, suggesting an additional magma supply, even though the full spreading rate is categorized as slow spreading. Five hydrothermal vent sites have been found within 5 km around the spreading axis at 13°N. The Japanese TAIGA Project selected this area as one of three integrated target sites, and TAIGA Project members conducted series of JAMSTEC research cruises for different types of geophysical surveys, together with dive observation and samplings by the submersible Shinkai 6500. We reviewed the results from these geophysical surveys and the volcanic rock samples to summarize the products from the TAIGA Project. The results provide strong constraints on the mantle dynamics and the crustal formation at the Southern Mariana Trough back-arc basin; all the results support that they are influenced by hydration derived from the subducting slab with accompanying the additional magma supply. Furthermore, the results from the geophysical and geological surveys for the five hydrothermal vent sites provide characteristic features on the hydrothermal activity and the features are different between on-axis and off-axis hydrothermal sites. The on-axis hydrothermal site is associated with an episodic diking event followed by fissures in a fourth order ridge segment, and its duration and size vary depending on the episodic diking event and on the fissures following. In contrast, the formation of the off-axis hydrothermal sites is closely related to the residual heat from the volcanism rather than tectonic stresses accompanied by faults, and the off-axis hydrothermal activity is for a long period and in a large scale. We summarized all the evidence to propose our scenario of the mantle dynamics, the crustal formation, and the hydrothermal activity of the Southern Mariana Trough back-arc basin.

N. Seama (✉)
Department of Earth and Planetary Sciences,
Kobe University, 1-1 Rokkodai, Nada, Kobe 657-8501, Japan
e-mail: seama@kobe-u.ac.jp

H. Sato
School of Business Administration, Senshu University,
2-1-1 Higashimita Tama, Kawasaki, Kanagawa 214-8580, Japan

Y. Nogi
National Institute of Polar Research, The Graduate University
for Advanced Studies (Sokendai), 10-3 Midoricho, Tachikawa,
Tokyo 190-8518, Japan

K. Okino
Atmosphere and Ocean Research Institute, The University of Tokyo,
5-1-5 Kashiwanoha, Kashiwa, Chiba 277-8564, Japan

J.-i. Ishibashi et al. (eds.), *Subseafloor Biosphere Linked to Hydrothermal Systems: TAIGA Concept*,
DOI 10.1007/978-4-431-54865-2_17,

Keywords
Back-arc basin • Crustal structure • Hydrothermal activity • Mantle structure • Seafloor spreading • Seismicity

17.1 Introduction

The Mariana Trough back-arc basin is a currently active back-arc basin, where the old Pacific Plate is subducting (Fig. 17.1). The spreading rates of the Mariana Trough back-arc basin increase from the north to the south. Studies of the geomagnetic anomalies using the Matuyama-Brunhes boundary (0.78 Ma) reported the full spreading rates of 10 km/Myr at 22°N in the northern end (Yamazaki et al. 2003) and of ~64 km/Myr in maximum at 13°N in the southern end (Martinez et al. 2000). Repeated GPS surveys in the Mariana Islands show similar trend of the full spreading rates; that is 15.9 ± 6.6 km/Myr at 18.7°N and 44.6 ± 2.7 km/Myr at 13.6°N (Kato et al. 2003). The shape of the subducting slab (Gudmundsson and Sambridge 1998) varies in the subducting angle and strike. The subducting slab is located mostly beneath the active Mariana Island Arc, except for the northern and southern ends where it is located beneath the spreading axes.

The seafloor spreading features also vary from the north to the south, and the Southern Mariana Trough back-arc basin has fast spreading morphologic and geophysical

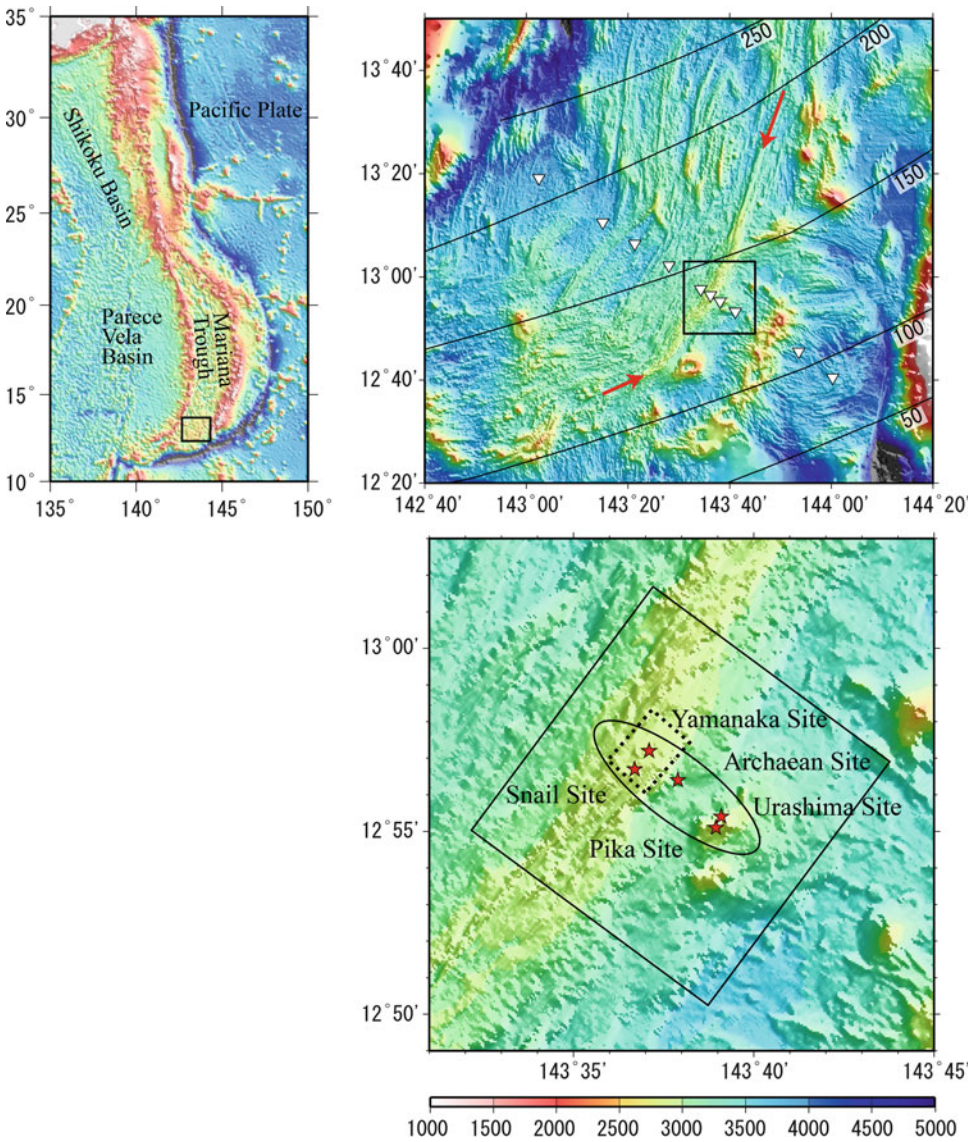

Fig. 17.1 Bathymetry map of the southern Mariana Trough back-arc basin (*top right*) with its location shown by the square in the regional map (*top left*). The *triangles* indicate the locations of the OBEM observations for the marine MT survey. The spreading axis (*arrows*), depth contours to the surface of the subducting slab (*thin solid lines* with their depth in km) inferred from a seismic research (Gudmundsson and Sambridge 1998), and the location of the bottom map (*square*) are also shown. Five hydrothermal vent sites (*stars* with their names) shown in bathymetry map (*bottom*). The *square by solid lines*, the *square by broken lines*, and the *ellipse* indicate the seismic reflection/refraction survey area, the MMR survey area, and the area of the near-bottom acoustic and geomagnetic mapping using the AUV Urashima, respectively

characteristics that are unlike the features of the basin to the north (Martinez et al. 2000). The morphology of the spreading axis of the Southern Mariana Trough back-arc basin shows an axial relief with a broad, smooth cross section, and lacks a deep central graben (Martinez et al. 2000). Kitada et al. (2006) have compiled extensive gravity and bathymetry data for the whole Mariana Trough, and they estimated crustal thickness variation along the spreading axis using the Mantle Bouguer anomalies (MBA), which were calculated by subtracting the predictable gravity signal due to the seawater/crust and crust/mantle density boundaries. Their results show that the two segments in the Southern Mariana Trough (south of 14°22′N) have two characteristic features compared to the other segments in the Mariana Trough; larger individual crustal thickness averages (5.9–6.9 km) and smaller normalized variations in crustal thickness (28–30 m/km). They interpreted these characteristic features as the existence of a sheet-like mantle upwelling with a relatively higher magmatic activity under the spreading axis, suggesting that the spreading process of the Southern Mariana Trough is similar to that of a fast spreading ridge. Becker et al. (2010) conducted a six-channel seismic reflection survey, which consisted of east–west transects spaced 5 nautical miles (9.26 km) apart and oblique (~65°) to the strike of the spreading axis. The seismic reflection data show a magma chamber reflector beneath the southernmost segment of the spreading axis in the Mariana Trough, although it appears only in a single line despite 12 crossings of the ridge axis. They identified a magma chamber at 1.5 s two-way travel time below the crest of the ridge. All these morphologic and geophysical features of the Southern Mariana Trough back-arc basin show fast spreading characteristics, suggesting the additional magma supply, even though the full spreading rate of 45–64 km/Myr is categorized as slow spreading.

A plume survey using standard conductivity-temperature-depth-optical tow-yos between 12°41′N and 13°13′N followed the spreading axes as closely as possible in the Southern Mariana Trough back-arc basin (Baker et al. 2005). Their results show distinct hydrothermal anomalies over six areas, and they found multiple plumes overlying 19 % of the total length of the survey section that is a coverage comparable to mid-ocean ridges spreading at similar rates. The biggest plume anomaly locates between 12°55′N and 12°58 N, and five hydrothermal vent sites have been found within 5 km in the area (Urabe et al. 2004; Nakamura et al. 2013); two sites on the spreading axis, one site at the eastern foot of the axial high, and two sites on an off-axis knoll.

The Japanese TAIGA Project (Urabe, Chap. 1) selected the Southern Mariana Trough back-arc basin including five hydrothermal vent sites as one of three integrated target sites. TAIGA Project members conducted series of JAMSTEC research cruises for different types of geophysical surveys, together with dive observations and samplings by the submersible Shinkai 6500. Furthermore, they conducted a cruise for a Benthic Multicoring System (BMS) to sample the volcanic rock cores. The geophysical surveys consist of (1) surface geophysical surveys, (2) a marine magnetotelluric (MT) survey of a 120 km long transect across the spreading axis using 10 ocean bottom electro-magnetometers (OBEM), (3) a 15 km scale seismic reflection/refraction survey and seismicity observation using nine ocean bottom seismometers (OBS), (4) a magnetometric resistivity (MMR) survey around the on-axis hydrothermal vent sites, and (5) near-bottom acoustic and geomagnetic mapping around the five hydrothermal vent sites using the autonomous underwater vehicle (AUV) Urashima. In this paper, we review results from the geophysical surveys and the volcanic rock samples in the Southern Mariana Trough back-arc basin to summarize the products of the TAIGA Project.

17.2 Asymmetric Seafloor Spreading

A series of JAMSTEC research cruises allowed us to obtain bathymetry and geomagnetic field data in the Southern Mariana Trough back-arc basin. Seama and Okino (Chap. 20) analyzed these data to derive two main features; (1) the seafloor spreading shows high asymmetry and (2) the asymmetric seafloor spreading has two different styles between two ridge segments (we call the northern segment and the southern segment here after, and their locations are shown in Fig. 17.2). The highly asymmetric seafloor spreading is recognized as much faster spreading in the west side of the spreading axis compared to the east side. They estimated the spreading rate of the southern segment as 46 km/Myr with its half rate of 33 km/Myr for the west side and 13 km/Myr for the east side. The full rate of 46 km/Myr is consistent with the present full spreading rate of 44.6 ± 2.7 km/Myr at 13.6°N based on the repeated GPS surveys (Kato et al. 2003).

The asymmetric seafloor spreading has two different styles between the northern segment and the southern segment. Seama and Okino (Chap. 20) proposed that the northern segment is accompanied by an obvious trace of a ridge jump to the east (trench side), while the southern segment is not. The obvious trace of the ridge jump is supported by the bathymetry profiles across the spreading axis, the MBA based on Kitada et al. (2006), and the distribution of the crustal magnetization derived from the total intensity of the geomagnetic anomaly field data (Fig. 17.2). The location of the failed spreading axis due to the ridge jump is suggested at the local symmetry axis in the bathymetry profiles because this local symmetry axis is similar in the bathymetric feature to a spreading axis. This location coincides with the center of the bull's eye feature in the MBA, which is often found

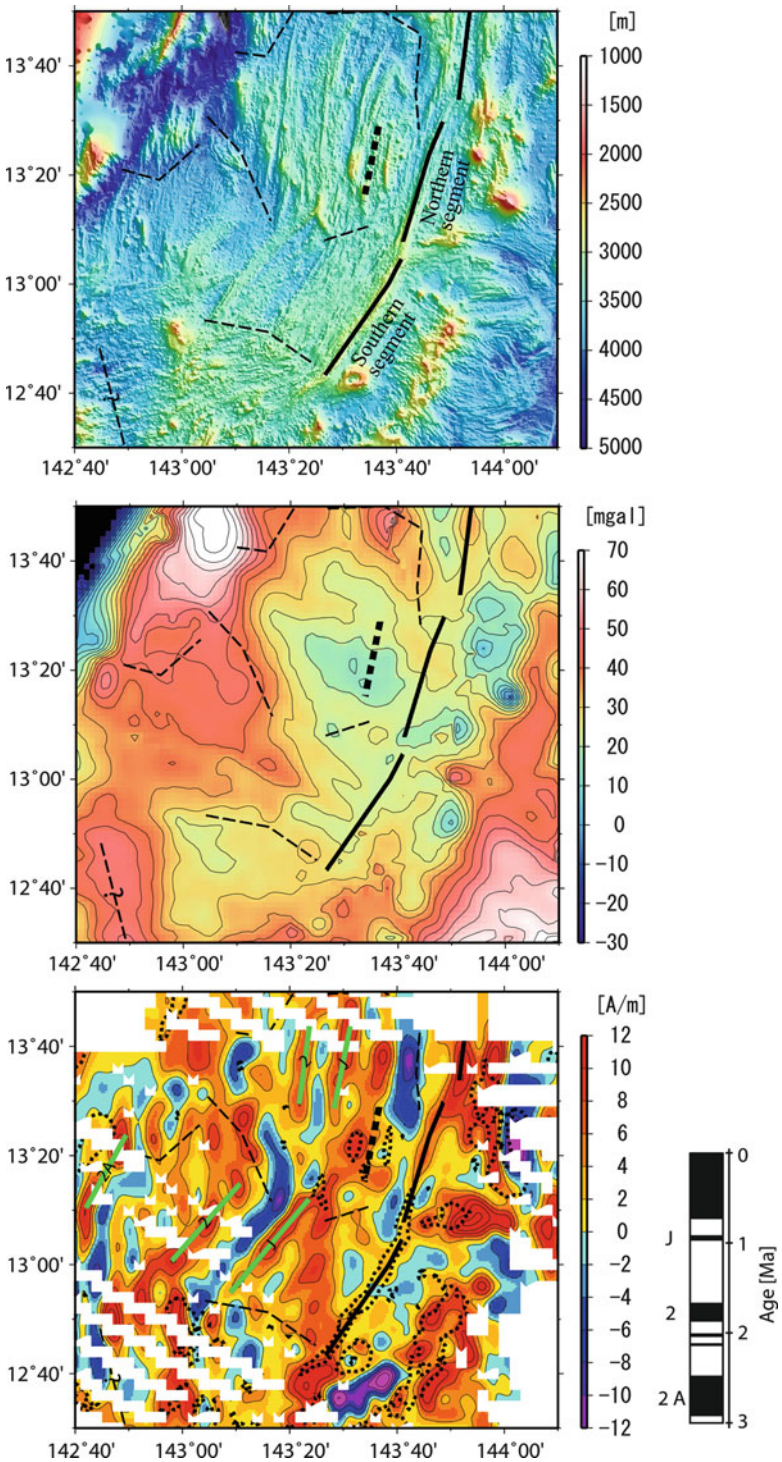

Fig. 17.2 Present spreading axis (*solid lines*), failed spreading axis (*thick broken lines*), and non-transform offset traces determined from seafloor morphology (*thin broken lines*) shown in the bathymetry map (*top*), the Mantle Bouguer anomaly map (*middle*), and the distribution of the crustal magnetization derived from the total geomagnetic anomaly field data (*bottom*). In the bottom figure, the identifications of the geomagnetic anomaly lineations (*green lines* with its geomagnetic anomaly number) and bathymetry contours of 3,000 m depth (*dots*) are also shown. After Seama and Okino (Chap. 20)

at ridge segments of slow spreading axes (e.g. Lin et al. 1990). The crustal magnetization distribution also supports the ridge jump because it can explain the existence of the negative magnetization lineation between the present and the failed spreading axes. They interpreted that the negative magnetization lineation is Matuyama Chron (before 0.78 Ma) made by the failed spreading axis in its east side and that the ridge jump occurred during the Brunhes Chron. If the negative magnetization lineation would be made by the present spreading axis without the ridge jump, the half spreading rate would be 5 km/Myr in maximum (the distance from the present spreading axis to the Matuyama-Brunhes boundary is 4 km in maximum), which is too slow spreading rate to be consistent with other data. The ridge jump leads to the apparent asymmetric seafloor spreading of the northern segment. In contrast, the southern segment shows the asymmetric seafloor spreading without accompanied by an obvious trace of a ridge jump.

17.3 Upper Mantle Structure

Marine magnetotelluric (MT) survey is one of tools to derive upper mantle structure beneath the ocean bottom. Shindo et al. (2012) carried out an electromagnetic experiment with 10 OBEM along a ~120 km long profile across the spreading axis to estimate an electrical resistivity structure, and hence the physical property like temperature, water and melt contents in the upper mantle. The MT method is a base for the OBEM data analysis. In the MT method, magnetic and electric field data observed simultaneously by the OBEM were used to derive the MT responses, which is a transfer function from the magnetic field to the electric field variation in the frequency domain. Then, they corrected seafloor topographic distortions in the MT responses. Finally, a minimum electrical resistivity structure beneath the observation sites was estimated to fit the processed MT responses by performing a smooth model inversion analysis.

A preliminary result of two-dimensional upper mantle electrical resistivity structure from this MT analysis (Fig. 17.3), shows high asymmetry about the spreading axis. The trenchward side shows high resistivity (~300 Ohm-m) at all depths, while the opposite side (the west side) shows that a high resistivity layer (>300 Ohm-m) with ~40 km thick is underlain by a low resistivity (~10 Ohm-m) region. The region under the spreading axis has intermediate resistivity (~100 Ohm-m), which is connected to the low resistivity region in the west side. The subducting slab is well imaged as the higher resistivity region in the trenchward side, which is consistent with the surface of the subducting slab (the black broken line in Fig. 17.3) inferred from a seismic research (Gudmundsson and Sambridge 1998). But it is not imaged in the west side; it is probably because the thick low resistivity region in the shallower depth limits the resolution for the high resistivity region beneath it. The low resistivity region in the west side, which may be connected to the intermediate resistivity region under the spreading axis, is probably influenced by hydration driven by water release from the subducting slab. The uppermost high resistivity layer in the west side is interpreted as a dry lithosphere formed at the spreading axis. The high resistivity region in the trenchward side may result from a cold nose in the mantle wedge where is low temperature as well as the absence of a significant amount of water.

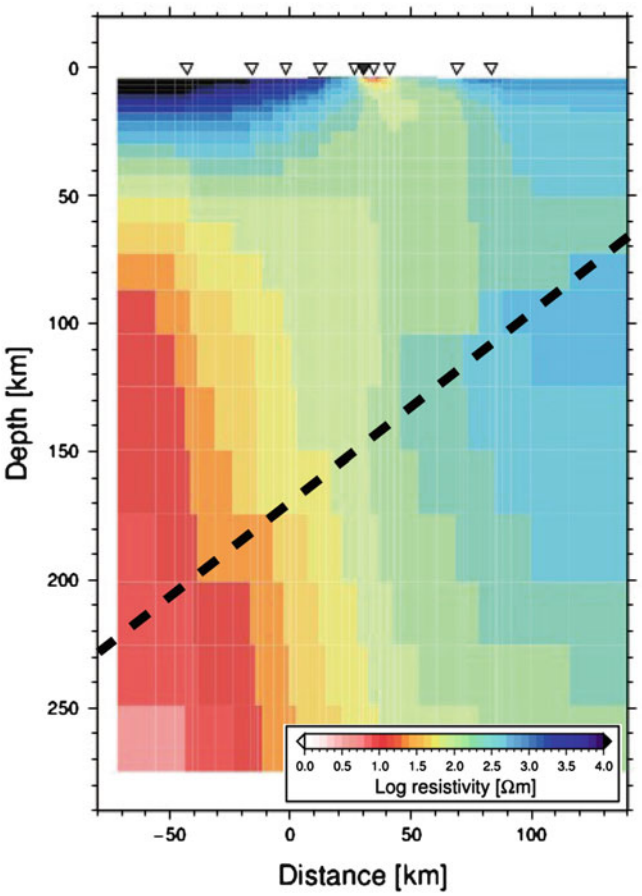

Fig. 17.3 Two-dimensional upper mantle electrical resistivity structure obtained from the marine MT analysis. The locations of the OBEM observations are shown by the *triangles* at the top, and the *triangle* is filled for the location on the spreading axis. The *black broken line* indicates the surface of subducting slab inferred from a seismic research (Gudmundsson and Sambridge 1998). The location of the OBEM in a map view is shown in Fig. 17.1

17.4 Crustal Structure

Crustal structure was investigated using a refraction survey. Sato et al. (Chap. 18) conducted a seismic refraction survey using OBS in the southern segment of the spreading axis in the Mariana Trough back-arc basin. The data analysis allows them to derive a 3-D seismic velocity structure, which indicate three characteristic features (Fig. 17.4); (1) a low-velocity structure just beneath the spreading axis, (2) a high-velocity structure with convex upward beneath an off-axis knoll, and (3) a relatively thicker layer 2 (about 3 km) with lower seismic velocities over the refraction survey area compared with normal mid-ocean ridges. The low seismic velocity structure just beneath the spreading axis suggests that the area beneath the axis is hotter due to magmatic activity. As the seismic reflection profile of Becker et al. (2010) shows no magma chamber reflector in their study area, the low-velocity zone is probably not a magma chamber with abundant melt, but a warm zone with a chamber of crystal-rich mush. Further, the low-velocity zone aligns with the third-order ridge segment that is defined by the bathymetry. These results suggest that sheetlike mantle upwellings beneath the first-order ridge segment on the basis of gravity data (Kitada et al. 2006) can be subdivided into upwellings beneath the third-order ridge segment.

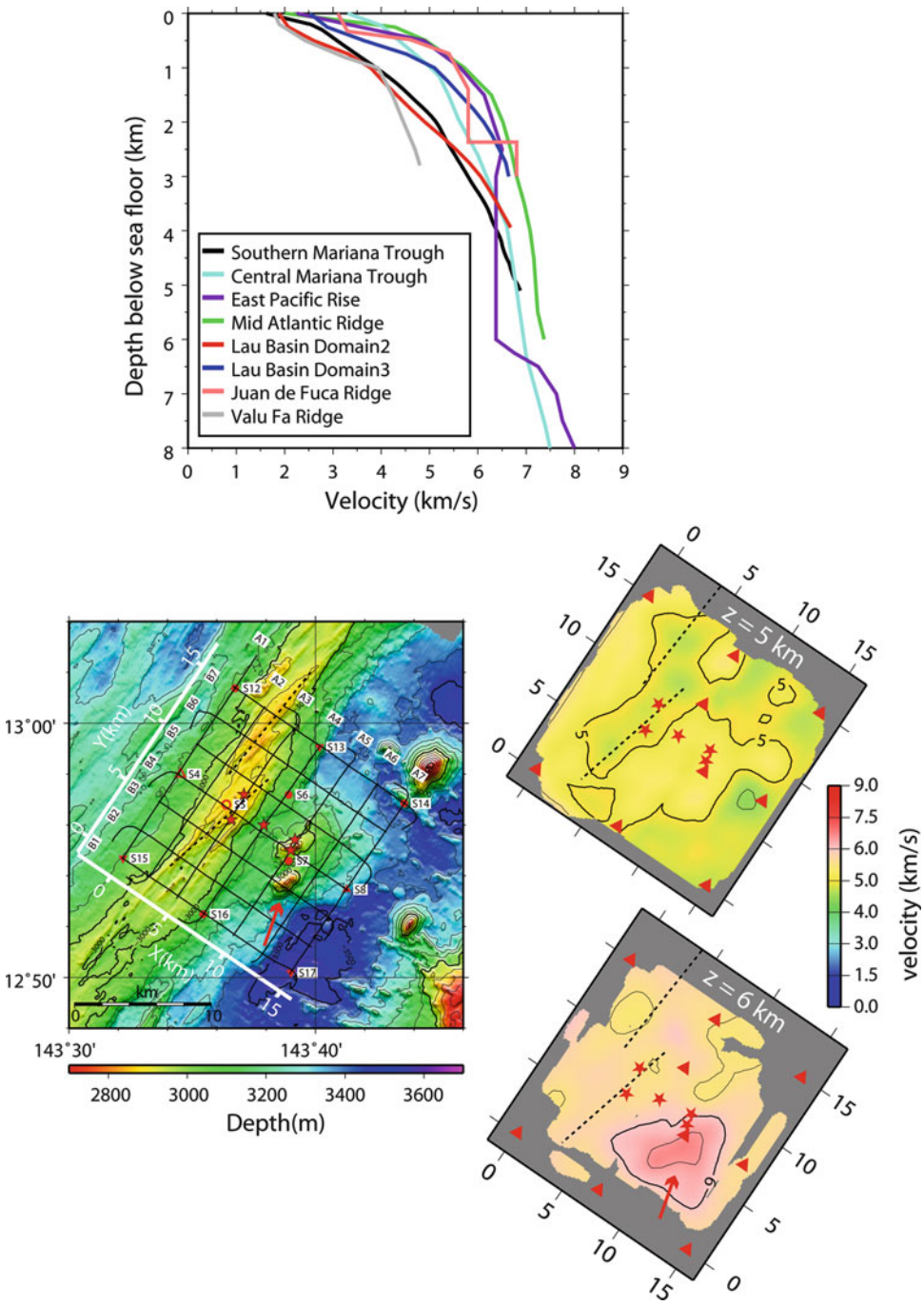

Fig. 17.4 One-dimensional (*top*) and three-dimensional (*bottom right*) crustal velocity structure from the seismic refraction analysis (Sato et al. Chap. 18). The three-dimensional crustal velocity structure is shown in map views with depth (z) from the sea surface. Locations of the five hydrothermal vent sites (*stars*), OBS (*red circles and triangles*), and airgun survey profiles (*black lines*) are also shown in the bathymetry map (*bottom left*). The *broken lines* and the *red arrows* indicate third-order ridge segments and the area of the layer 3 thickening beneath the off-axis knoll, respectively. The location of the survey area is shown in Fig. 17.1

The high-velocity structure with convex upward at the off-axis knoll suggests a thickening of layer 3 beneath the knoll (Sato et al. Chap. 18). They infer that off-axis volcanism once existed there, forming the knoll, and intruded magma became the thickened layer 3. This off-axis volcanism is very young because the knoll is composed of pillow lavas with minor sediment cover (Kakegawa et al. 2008).

Sato et al. (Chap. 18) found that the relatively thicker layer 2 (thickness about 3 km) with lower seismic velocities of the Southern Mariana Trough is similar to those of the Domain II and the Valu Fa Ridge in the Lau basin (Jacobs et al. 2007; Dunn and Martinez 2011), and they suggest that the upwelling mantle beneath the Southern Mariana Trough spreading axis is influenced by subduction because of the similarity to the Lau Domain II and the Valu Fa Ridge. The Southern Mariana Trough is near the subduction zone and the volcanic arc, and the Lau Domain II and the Valu Fa Ridge are also near the subduction slab and the Tonga volcanic arc. Dunn and Martinez (2011) noted that the Lau Domain II and Valu Fa Ridge are formed by magmas with

high volatile contents derived from the subducting plate. The upwelling mantle would have low viscosity due to hydration by water from the subducting slab, and the magmas produced would form thicker crust with lower velocities in the Southern Mariana Trough.

17.5 Hydrothermal Vent Sites

Five hydrothermal vent sites exist within 5 km around the spreading axis at 13°N; two sites on the spreading axis (the Snail and Yamanaka sites), one site at the eastern foot of the axial high (the Archaean site), and two sites on an off-axis knoll (the Pika and Urashima sites). To understand a hydrothermal circulation system, it is important to investigate its heat source, size including pathways, duration, and geological features around the hydrothermal vent site. The crustal structure and the seismicity help to reveal the heat source and the pathways of the hydrothermal circulation related to the geological features (e.g. de Martin et al. 2007). Geophysical surveys using an AUV are effective for near-bottom acoustic and geomagnetic mappings around hydrothermal vent sites. The morphology of the hydrothermal vent site together with dive observation provides us with important constraints on field-scale geological features around the hydrothermal vent site. Near ocean bottom magnetic signatures of active and fossil hydrothermal sites provide information on the size and the duration of the hydrothermal circulation (e.g. Tivey and Johnson 2002). Moreover, near-bottom acoustic and geomagnetic data help to discover a new hydrothermal vent site; a 120 kHz side-scan sonar and a 400 kHz multibeam echo sounder of the AUV Urashima (Kasaya et al. 2011) detected acoustic signals suggesting hydrothermal plumes, and 10 m-scale chimney-like topographic highs within a low magnetization zone, which led to discover the Urashima site (Nakamura et al. 2013). Thus, combination of these geophysical and geological surveys would be important to understand hydrothermal circulation systems.

The information on the heat sources of the hydrothermal sites was provided by the crustal structures. The 3-D seismic velocity structure from the refraction survey in the southern segment of the spreading axis (Sato et al. Chap. 18) covers the area where five hydrothermal vent sites exist. The 3-D seismic velocity structure (Fig. 17.4) shows a low-velocity structure just beneath the third order ridge segment of the spreading axis, suggesting there is some magmatic activity beneath the axis in the form of sheetlike mantle upwellings. These may constitute the hydrothermal heat source at the Snail and Yamanaka sites on the spreading axis. Beneath the off-axis knoll, they have found a high-velocity structure with convex upward that indicates thickening of layer 3, suggesting the presence of ceased off-axis volcanism there. The residual heat may contribute the heat for hydrothermal activity at the Pika and Urashima sites on the off-axis knoll. The heat source for the Archaean site at the eastern foot of the axial high is not clear, but it can be constituted by the magmatic activity beneath the spreading axis, because the horizontal distance to the low-velocity zone beneath the axis is only about 1 km with its depth of 2 km.

The spatial variations of the crustal porosity and the temperature of the fluid within the crust involving a hydrothermal system is estimated using the electrical resistivity structure of the oceanic crust, because the electrical resistivity of the oceanic crust mainly varies with the porosity of the crust and with the connectivity and temperature of the fluid within the crust. The Magnetometric resistivity (MMR) technique using an active (or artificial) electric current source is one of the electromagnetic techniques to reveal the electrical resistivity structure of the uppermost oceanic crust. Matsuno et al. (Chap. 19) carried out a MMR experiment at the Snail and Yamanaka sites on the spreading axis using five ocean bottom magnetometers. The experimental area is almost 4,000 m^2 with a focus on the Snail site (Fig. 17.5). Their results of the MMR data analysis show two main features; (1) an optimal 1-D resistivity structure of

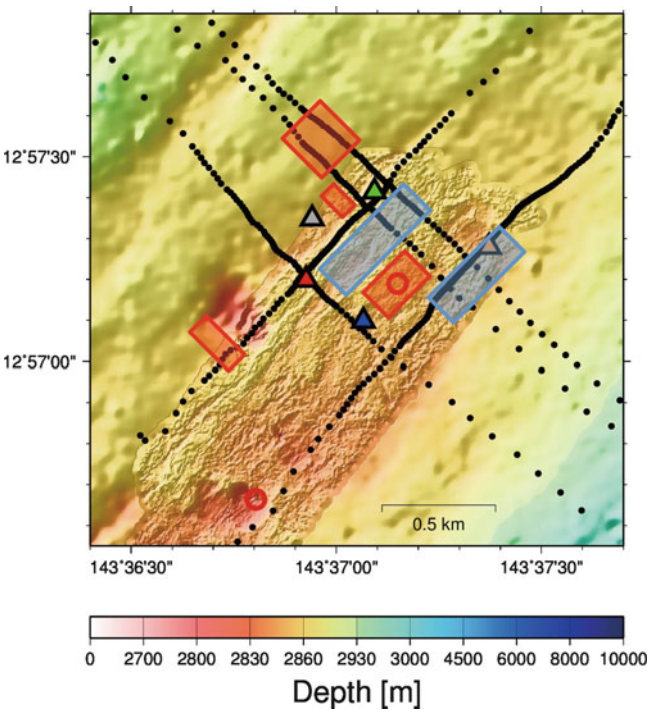

Fig. 17.5 A plan view map of the optimal 3-D resistivity model overlain on the seafloor topography (Matsuno et al. Chap. 19). The *red rectangles* represent conductive anomalies (0.56 Ω-m), and the *blue rectangles* represent resistive anomalies (56 Ω-m). Locations of the hydrothermal sites (*red circles*), the transmission points (*filled black circles*), and the receivers (*color triangles*) are also shown. The Snail site is located near the center of the map. The location of the survey area is shown in Fig. 17.1

the uppermost oceanic crust averaged over the experimental area is a two-layer model, which consists of a 5.6 Ω-m upper layer having a 1,500 m thickness and a 0.1 Ω-m underlying half-space, and (2) small optimal 3-D resistivity structures in the optimal 1-D resistivity model includes a conductive anomaly just below the Snail site, two resistive anomalies adjacent to the conductive anomaly on the across-ridge side, and three conductive anomalies away from the Snail site (Fig. 17.5). They interpreted the optimal 1-D resistivity structure using realistic porosity profiles of the uppermost oceanic crust and the Archie's law (Archie 1942); the resistivity of 5.6 Ω-m at depths ranging from 800 to 1,500 m suggests the presence of high temperature seawater related to the hydrothermal circulation. The resistivity of 0.1 Ω-m below 1,500 m depth may represent a magma mush that is a heat source for the hydrothermal circulation. This low resistivity structure is probably consistent with the low seismic velocity structure beneath the spreading axis (Sato et al., Chap. 18). Further, the 3-D conductive anomaly just below the Snail site suggests the presence of hydrothermal seawater in the shallow crust with its size of approximately 300 m^2 area down to 400 m depth, that is certainly related to the hydrothermal vent.

The style of hydrothermal activity can be investigated by seismicity around the hydrothermal site. A three-month campaign of seismic observations using OBS shows that very low seismicity at the hydrothermal sites (Sato et al. Chap. 18). This result is very different from those of de Martin et al. (2007) and Tolstoy et al. (2008), who found many microearthquakes related to hydrothermal activity. The difference may be because their OBS network had a wider spacing (about 5 km) than the earlier networks (about 1–5 km), and they examined this possibility by checking the seismicity near an OBS, which was less than 1 km from the Pika site. They found that it recorded only three events with S-P time less than 1 s, indicating that the very low seismicity at the hydrothermal sites is not an artifact of their OBS network, but a real feature in the study area. This very low seismicity suggests that hydrothermal activity here is not related to tectonic stresses.

Geomorphological characterization of field-scale geological features associated with the five hydrothermal vent sites are identified using near-bottom swath mapping data collected by the AUV Urashima and dive observation data acquired by the submersible Shinkai 6500 (Yoshikawa et al. 2012). Their results (Fig. 17.6) indicate differences in geomorphological features between the on-axis sites (the Snail and Yamanaka sites) and the off-axis sites (the Archaean, Pika and Urashima sites), and their explanations are as follows. The Snail and Yamanaka sites on the spreading axis are located adjacent to fissures in the volcanically dominant zone, which is characterized by mounds (height, 5–30 m; diameter, 250–320 m) cut by fissures. The mounds probably result from diking events in a fourth order ridge segment, and the on-axis sites are possibly associated with the diking events followed by the fissures. In contrast to the on-axis sites, the off-axis sites show no evidence of faulting, but undeformed features. The Archaean site at the foot of the axial high is characterized by a single mound (height, 50–100; diameter, 250–300 m), pronounced off-axis lava flows, and the presence of high-amplitude rugged seafloor features; the site is located at the top of the mound. Numerous ridge lines (height, mainly 2–6 m) extend radially from the top of the mound, and several chimney-like structures (up to approximately 6 m high) occur on the top and slopes of the mound. The ridge lines appear to have formed as a result of collapse of the slopes and the top of the mound. The Pika and Urashima sites are located on an off-axis knoll, where is characterized by bumpy seabed textures formed by numerous smaller-scale mounds and ridge lines. The three off-axis hydrothermal sites are composed mainly of breccia assemblages that probably originated from hydrothermal activity with black smoker venting. These geomorphological features suggest that the three off-axis sites were identified as localities created by relatively long-term large-scale hydrothermal activity, as compared with the on-axis sites. Moreover, the undeformed features without any faults suggest that the formation and the sustained activity of the off-axis sites are mainly controlled by an off-axis magma upwelling rather than faulting.

Magnetic signatures of active hydrothermal sites are provided by near ocean bottom geomagnetic surveys, which were conducted around the five hydrothermal vent sites using three fluxgate magnetometers attached on the AUV Urashima. Vector geomagnetic anomalies were obtained based on the method of Isezaki (1986) after subtracting the International Geomagnetic Reference Field (IGRF) model. Vector geomagnetic anomaly field data acquired by the three fluxgate-magnetometers were stacked in order to reduce the short wavelength noises. The geomagnetic anomaly field data are upward continued from the uneven AUV tracks to a constant depth. Then, the equivalent magnetization intensity of the seafloor was estimated using the downward component of the geomagnetic anomaly field, because the observation were performed near the geomagnetic equator and the total intensity of the geomagnetic anomaly field is affected by the strike of a magnetic source, but the downward component of the geomagnetic anomaly field is not. The method of Parker and Huestis (1974) was used for this estimation, and it was modified to adapt for the downward component, because the method is generally used for the total intensity of geomagnetic anomaly field. The magnetic source was assumed to have a constant thickness of 250 m. The result of the crustal magnetization distribution (Fig. 17.6) is well related to the locations of the hydrothermal sites; the distribution of low crustal magnetization

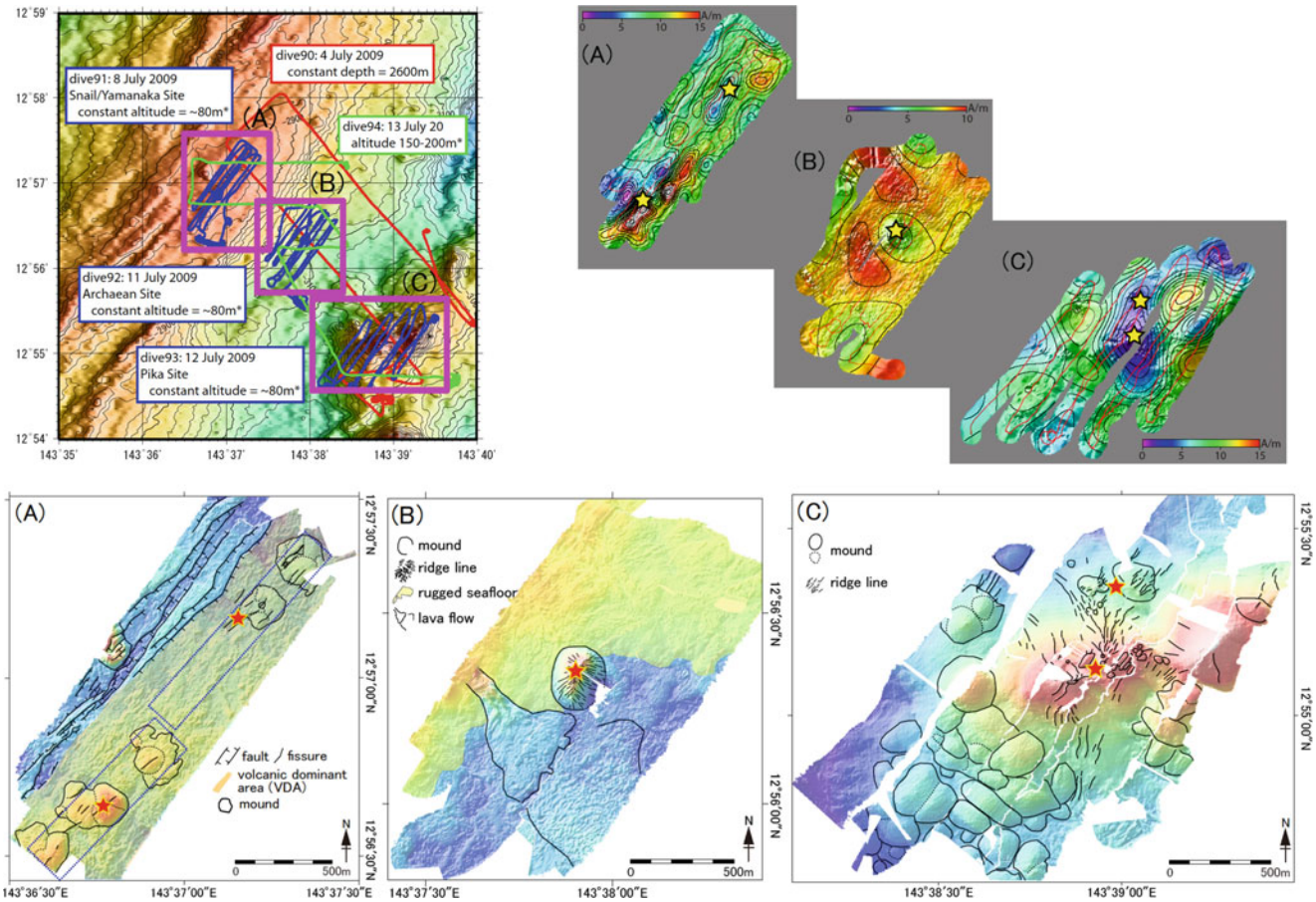

Fig. 17.6 Near-bottom mapping around the five hydrothermal vent sites using the AUV Urashima. Ship tracks of the AUV Urashima (*top left*), crustal magnetization distribution (*top right*), and bathymetry with its interpretation by Yoshikawa et al. (2012) (*bottom*) are shown. The *stars* indicate the locations of the five hydrothermal vent sites; two sites on the spreading axis (the Snail and Yamanaka sites), one site at the eastern foot of the axial high (the Archaean site), and two sites on an off-axis knoll (the Pika and Urashima sites) are located in the areas (*A*), (*B*), and (*C*), respectively. The location of the survey area is shown in Fig. 17.1

coincides mostly with the areas around the hydrothermal sites except for the Yamanaka site on the spreading axis. The low crustal magnetization around the hydrothermal sites most likely indicates a signal that the remanent magnetization of the crust has been reduced through the hydrothermal alternation as suggested by near ocean bottom magnetic signatures of active and fossil hydrothermal sites (e.g. Tivey and Johnson 2002).

17.6 Results from Rock Analysis

Volcanic rocks were recovered by the BMS and submersible dives around the five hydrothermal sites in the Southern Mariana Trough back-arc basin (Nakamura et al. Chap. 45). Their new results of geochemical compositions including both major and trace elements are similar to those reported for the southern Mariana area (e.g. Masuda and Fryer, Chap. 21). These volcanic rocks are classified as basaltic andesite to andesite with 55–60 % of SiO_2. The trace element compositions exhibit enrichment of fluid-mobile elements such as Cs, Rb, Ba, U, and K with remarkable negative Nb and Ta anomaly (Fig. 17.7), suggesting the involvement of subduction components into their parent magmas. These new chemical composition data confirmed the features previously presented for the Southern Mariana Trough by Pearce et al. (2005). They demonstrated that the systematic geochemical mapping for the whole Mariana Trough, and exhibited the distribution of the lithospheric, deep subduction, and shallower subduction components; volcanic glasses from the southern part of the Mariana Trough are influenced by the shallow subduction components while those from 14–15, 17, and 19.5°N segments of the spreading axes contain no subduction components and have true MORB compositions. The new chemical composition data (Nakamura et al. Chap. 45) also support the influence by the shallow subduction components.

The new geochemical composition data indicate slightly different features between the on-axis and off-axis hydrothermal sites (Nakamura et al. Chap. 45). All the volcanic

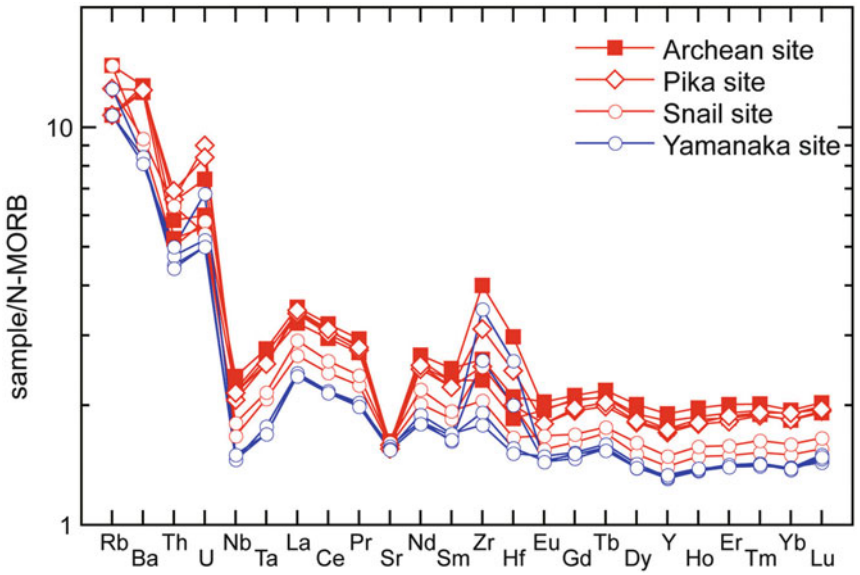

Fig. 17.7 N-MORB normalized multi element plots for the volcanic rocks from the five hydrothermal sites (Nakamura et al. Chap. 45)

rocks from the on-axis hydrothermal sites are within the basaltic andesite field, whereas the volcanic rocks from the off-axis sites have higher silica abundance and fall in the field of andesite. Major element chemical compositions indicate that their compositional variations can be explained by fractionation except for the Pika site, because the volcanic rocks from the Pika site have clearly distinct fractional trend. They interpreted the basement rocks of the Archaean site as a differentiated product of on-axis magma, whereas those of the Pika site are not directly related to the on-axis magma. The volcanic rocks from the off-axis sites contain relatively higher abundance of trace elements than those from the on-axis sites (Fig. 17.7), which is consistent with the more evolved compositions for the volcanic rocks from the off-axis sites shown in major element compositions.

17.7 Discussions and Summary

The results from the geophysical surveys and the volcanic rock samples through the TAIGA Project and those from the previous studies provide strong constraints on the mantle dynamics and the crustal formation at the Southern Mariana Trough back-arc basin; all the results show evidence to support that they are influenced by hydration derived from the subducting slab with accompanying the additional magma supply. The evidence to show dehydration from the subducting slab is only circumstantial evidence, but there is direct evidence to indicate that the additional magma supply and its product of the crust are accompanied by the hydration derived from the subducting slab. The circumstantial evidence to support dehydration from the subducting slab is (1) the shape of the subducting slab, (2) possible low viscosity region in the mantle wedge, and (3) the two-dimensional upper mantle electrical resistivity structure, as listed below:

1. The shape of the subducting slab inferred from a seismic research (Gudmundsson and Sambridge 1998) indicates that the surface of the subducting slab is located at the depth of 120–190 km beneath the spreading axis in the Southern Mariana Trough back-arc basin (Fig. 17.1). The dehydration from the subducting slab is expected to occur at the depths of 110 and 170 km (e.g. Tatsumi and Eggins 1995), and the spreading axis is located where the arc volcanic chains are expected to be located. It is contrast to other spreading axes in the Mariana Trough back-arc basin. Since the subducting slab is divided by a near-vertical tear in the slab striking approximately E-W at 14.5°N (Miller et al. 2006), the subducting slab on the north side of the tear is not located beneath the spreading axes but beneath the active Mariana Island Arc except for the northern end of the Mariana Trough back-arc basin.
2. The analyses of the bathymetry, geomagnetic anomaly, and MBA data, suggest highly asymmetric seafloor spreading; much faster spreading in the west side of the spreading axis compared to the east side (Seama and Okino, Chap. 20). They proposed that an influence of the low viscosity region in the mantle wedge due to hydration driven by water release from the subducting slab leads to the highly asymmetric seafloor spreading; the low viscosity mantle would preferentially captures the mantle upwelling zone beneath the spreading axis as the spreading axis has been kept in the area closed to the low viscosity region in the mantle wedge, resulting in the highly asymmetric seafloor spreading. Further, they proposed that the different styles of the asymmetric seafloor

spreading between the northern segment and the southern segment probably show evidence that the influence varies with the depths to the surface of the subducting slab, which is well related to the distance from the low viscosity region. The subducting slab beneath the Southern Mariana Trough back-arc basin is oblique to the spreading axis, and the depth to the surface of the subducting slab beneath the spreading axis is different, 160–190 km for the northern segment and 120–150 km for the southern segment inferred from a seismic research (Fig. 17.1; Gudmundsson and Sambridge (1998)).

3. Preliminary results of the two-dimensional upper mantle electrical resistivity structure from the MT analysis (Shindo et al. 2012), shows the low resistivity region in the west side. The low resistivity region is probably influenced by hydration driven by water release from the subducting slab; that may result in the additional magma supply to the spreading axis as the low resistivity region may be connected to the intermediate resistivity region under the spreading axis. This result is a contrast to the result from the central Mariana Trough (Matsuno et al. 2010); the two-dimensional upper mantle electrical resistivity structure of the central Mariana Trough shows that the low resistivity region above the subducting slab is not connected to the spreading axis, and the spreading axis is located so far from the subducting slab that there is no evidence to show that the crustal formation has influence of the subducting slab.

The fast spreading morphologic and geophysical characteristics, despite the full spreading rate of about 46 km/Myr being categorized as slow spreading, indicate direct evidence of the additional magma supply that is probably accompanied by the hydration derived from the subducting slab. The fast spreading morphologic and geophysical characteristics appear as following: The morphology of the spreading axis of the Southern Mariana Trough back-arc basin shows an axial relief with a broad, smooth cross section, and lacks a deep central graben (Martinez et al. 2000). The crustal thickness variations along the spreading axis estimated using the MBA show larger individual crustal thickness averages (5.9–6.9 km) and smaller normalized variations in the crustal thickness (28–30 m/km), suggesting a sheetlike mantle upwelling with a relatively higher magmatic activity beneath the first-order ridge segments (Kitada et al. 2006). The seismic velocity structure also supports the sheetlike mantle upwelling but it can be subdivided into upwellings beneath the third-order ridge segments; the low-velocity zone beneath the spreading axis, suggesting a warm zone with a chamber of crystal-rich mush, aligns with the third-order ridge segment (Sato et al. Chap. 18). The low electrical resistivity layer below 1,500 m depth also infers the magma mush beneath the spreading axis (Matsuno et al. Chap. 19). Further, the seismic reflection data show a possible magma chamber reflector beneath the spreading axis (Becker et al. 2010).

The product of the crust that is characterized by the seismic velocity structure and the geochemical composition of the volcanic rocks, shows that the crustal formation at the Southern Mariana Trough back-arc basin is influenced by the hydration derived from the subducting slab. The seismic velocity structure has the thicker layer 2 (thickness about 3 km) with lower seismic velocities over the survey area compared with normal mid-ocean ridges and some back-arc spreading ridges, suggesting that the crust is formed by magmas with high volatile contents derived from the subducting plate (Sato et al. Chap. 18). This result is a contrast to the crustal structure of the central Mariana Trough back-arc basin (Takahashi et al. 2008), which is similar to that of the mid-ocean ridges (Fig. 17.4). The geochemical composition data of the volcanic rocks from the Southern Mariana Trough back-arc basin (Nakamura et al. Chap. 45) indicate that the volcanic rocks are classified as basaltic andesite to andesite with 55–60 % of SiO_2; that is even higher SiO_2 content than those from the Domain II in the Lau basin which was formed by magmas with high volatile contents derived from the subducting plate (Dunn and Martinez 2011). Further, the trace element compositions of the volcanic rocks exhibit enrichment of fluid-mobile elements such as Cs, Rb, Ba, U, and K with remarkable negative Nb and Ta anomaly (Fig. 17.7), suggesting the involvement of the shallow subduction components into their parent magmas (Nakamura et al. Chap. 45).

The results from the geophysical and geological surveys for the five hydrothermal vent sites show different features in the hydrothermal activity between the on-axis hydrothermal sites and the off-axis hydrothermal sites. We propose that the on-axis hydrothermal site is associated with an episodic diking event followed by fissures, and that the duration and size of the on-axis hydrothermal site vary depending on the episodic diking event and on the fissures following. In contrast, the formation of the off-axis hydrothermal sites is closely related to the residual heat from the volcanism rather than tectonic stresses accompanied by faults, and the off-axis hydrothermal activity is for a long period and in a large scale. The two on-axis hydrothermal vent sites (the Snail and Yamanaka sites) are located adjacent to fissures on mounds in the volcanically dominant zone (Yoshikawa et al. 2012), and the heat source for the hydrothermal vent sites is constituted by some magmatic activity beneath the spreading axis in the form of sheetlike mantle upwellings (Sato et al. Chap. 18). Since the mounds probably result from diking events in the fourth order ridge segment, the hydrothermal sites are probably associated with diking events followed by fissures. The present seismicity near the hydrothermal sites is very low (Sato et al. Chap. 18), indicating that the diking is no longer active and that it was probably an

episodic event. The geomagnetic survey results using the AUV show different characters in the magnetization distribution; clear magnetization low at the Snail site but not at the Yamanaka site (Fig. 17.6). This difference suggests that the activity of the on-axis hydrothermal sites has variety in its duration and size. The activity of the Snail site has continued for a long enough period in a wide enough area (a few hundred meter scale) to reduce the magnetic remanence of the crustal rocks, resulting in the clear low magnetization. Further, the distribution of the low crustal magnetization is elongated parallel to the spreading axis, implying that the hydrothermal activity is tectonically controlled possibly with fissures. On the other hand, the magnetization distribution around the Yamanaka Site including its base mound on the spreading axis shows the high magnetization, suggesting that the mound probably results from a 'recent' diking event and that the hydrothermal activity of the Yamanaka Site should be only for a short period and/or in a small scale possibly due to limited number of the fissures after the diking event. The MMR results (Matsuno et al. Chap. 19) support this difference because the conductive anomaly with its size of approximately 300 m^2 area down to 400 m depth is located only at the Snail site, but not at the Yamanaka site; the conductive anomaly suggests the presence of hydrothermal seawater in the shallow depth, that is certainly related to the hydrothermal vent. Thus, the differences between the Snail and Yamanaka sites suggest that the duration and size of the on-axis hydrothermal site vary depending on the episodic diking event and on the fissures following.

In contrast to the on-axis sites, the formation of the off-axis hydrothermal sites is closely related to the residual heat from the volcanism rather than tectonic stresses followed by faults, and the off-axis hydrothermal activity is for a long period and in a large scale. Geomorphological characterization of field-scale geological features associated with the off-axis sites show no evidence of faulting, but undeformed features (Yoshikawa et al. 2012). The low seismicity near the hydrothermal sites also indicates that there are no faults or fractures related to the hydrothermal activity (Sato et al. Chap. 18), and it is in contrast to the high seismicity of the off-axis TAG hydrothermal site that revealed relations between the hydrothermal system and an active detachment fault (deMartin et al. 2007). The heat source of the Pika and Urashima sites is the residual heat of the ceased off-axis volcanism, which is suggested by the low seismicity and the high-velocity structure that indicates thickening of the layer 3 beneath the off-axis knoll (Sato et al. Chap. 18). The heat source for the Archaean site at the eastern foot of the axial high could be constituted by the magmatic activity beneath the spreading axis. The three off-axis sites were identified as localities created by relatively long-term large-scale hydrothermal activity, because the three off-axis hydrothermal sites are composed mainly of breccia assemblages that probably originated from hydrothermal activity with black smoker venting (Yoshikawa et al. 2012). The geomagnetic survey results using the AUV also support that the hydrothermal activity has been for a long period and in a large scale (a few hundred meter scale) to reduce the magnetic remanence of the crustal rocks, because the magnetization distribution shows clear low magnetization at all the off-axis hydrothermal sites.

In summary, all the evidence we presented leads us to propose our scenario of the mantle dynamics, the crustal formation, and the hydrothermal activity of the Southern Mariana Trough back-arc basin: The subducting slab is located at the depth of 120–190 km just beneath the spreading axis that is different from most of the other areas in the Mariana Trough back-arc basin. The hydration driven by water release from the subducting slab, which was inferred from the low resistivity region, probably influences the mantle dynamics beneath the spreading axis accompanied by the additional magma supply to the axis. Further, the low viscosity region in the mantle wedge due to hydration may lead to the highly asymmetric seafloor spreading through capturing mantle upwelling zone within the low viscosity mantle. Moreover, this influence of the hydration is also supported by the geochemical compositions of the volcanic rocks and the seismic velocity structure. The geochemical compositions of the volcanic rocks are classified as basaltic andesite to andesite with 55–60 % of SiO_2 and their trace element compositions exhibit enrichment of fluid-mobile elements, suggesting the involvement of the shallow subduction component into their parent magma. The seismic velocity structure shows the thicker layer 2 with lower seismic velocities, suggesting the crust is formed by magmas with high volatile contents derived from the subducting slab. Furthermore, the additional magma supply accompanied by the hydration results in the fast spreading morphologic and geophysical characteristics despite the full spreading rate of about 46 km/Myr being categorized as a slow spreading. The fast spreading morphologic and geophysical characteristics are the axial relief in morphology, the low electrical resistivity layer and the possible magma chamber reflector beneath the axis, and the sheetlike mantle upwellings beneath the axis suggested by the MBA data and the low-velocity structure. Then, the abundant magma supply leads to the episodic diking events in a fourth order ridge segment supported by the sheetlike mantle upwellings, and to the off-axis volcanism. The two different magmatic activities result in different features between the on-axis and the off-axis hydrothermal sites. The on-axis hydrothermal site is associated with an episodic diking event followed by fissures, and its duration and size vary depending on the episodic diking event and on the fissures following. In contrast, the formation of the off-axis hydrothermal sites is closely related to the residual heat from the volcanism rather

than tectonic stresses accompanied by faults, and the off-axis hydrothermal activity is for a long period and in a large scale.

Acknowledgments We thank all who assisted in the collection of the data and the samples during the JAMSTEC (Japan Agency for Marine-Earth Science and Technology) research cruises and a BMS cruise. This work is supported by the Ministry of Education, Culture, Sports, Science and Technology (MEXT) of Japan for the TAIGA project, Grant-in-Aid for Scientific Research on Innovative Areas (20109002). Two anonymous reviewers provided helpful comments. Kumiko Okumura drew some figures and helped to prepare the manuscript. GMT software (Wessel and Smith 1998) was used to create some figures.

References

Archie GE (1942) The electrical resistivity log as an aid in determining some reservoir characteristics. J Petrol Technol 5:1–8

Baker ET, Massoth GJ, Nakamura K, Embley RW, de Ronde CEJ, Arculus RJ (2005) Hydrothermal activity on near-arc sections of back-arc ridges: results from the Mariana Trough and Lau Basin. Geochem Geophys Geosyst 6, Q09001. doi:10.1029/2005GC000948

Becker NC, Fryer P, Moore GF (2010) Malaguana-Gadao Ridge: identification and implications of a magma chamber reflector in the southern Mariana Trough. Geochem Geophys Geosyst 11: Q04X13. doi:10.1029/2009GC002719

deMartin BJ, Sohn RA, Canales JP, Humphris SE (2007) Kinematics and geometry of active detachment faulting beneath the Trans-Atlantic Geotraverse (TAG) hydrothermal field on the Mid-Atlantic Ridge. Geology 35:711–714

Dunn RA, Martinez F (2011) Contrasting crustal production and rapid mantle transitions beneath back-arc ridges. Nature 469:198–202

Gudmundsson O, Sambridge M (1998) A regionalized upper mantle (RUM) seismic model. J Geophys Res 103(B4):7121–7136

Isezaki N (1986) A new shipboard three-component magnetometer. Geophysics 51:1992–1998

Jacobs AM, Harding AJ, Kent GM (2007) Axial crustal structure of the Lau back-arc basin from velocity modeling of multichannel seismic data. Earth Planet Sci Lett 259:239–255

Kakegawa T, Utsumi M, Marumo K (2008) Geochemistry of sulfide chimneys and basement pillow lavas at the southern Mariana Trough (12.55°N–12.58°N). Resour Geol 58:249–266

Kasaya T, Kanamatsu T, Sawa T, Kinosita M, Tukioka S, Yamamoto F (2011) Acoustic images of the submarine fan system of the northern Kumano Basin obtained during the experimental dives of the Deep Sea AUV URASHIMA. Explor Geophys 42:80–87

Kato T, Beavan J, Matsushima T, Kotake Y, Camacho JT, Nakao S (2003) Geodetic evidence of back-arc spreading in the Mariana Trough. Geophys Res Lett 30(12):1625. doi:10.1029/2002GL016757

Kitada K, Seama N, Yamazaki T, Nogi Y, Suyehiro K (2006) Distinct regional differences in crustal thickness along the axis of the Mariana Trough, inferred from gravity anomalies. Geochem Geophys Geosyst 7, Q04011. doi:10.1029/2005GC001119

Lin J, Purdy GM, Schouten H, Sempere J-C, Zervas C (1990) Evidence from gravity data for focused magmatic accretion along the Mid-Atlantic Ridge. Nature 344:627–632

Martinez F, Fryer P, Becker N (2000) Geophysical characteristics of the southern Mariana Trough, 11°50′N–13°40′N. J Geophys Res 105:16591–16607

Matsuno T, Seama N, Evans R, Chave AD, Baba K, White A, Goto T, Heinson G, Boren G, Yoneda A, Utada H (2010) Upper mantle electrical resistivity structure beneath the central Mariana subduction system. Geochem Geophys Geosyst 11, Q09003. doi:10.1029/2010GC003101

Miller MS, Gorbatov A, Kennett BLN (2006) Three-dimensional visualization of a near-vertical slab tear beneath the southern Mariana arc. Geochem Geophys Geosyst 7, Q06012. doi:10.1029/2005GC001110

Nakamura K, Toki T, Mochizuki N, Asada M, Ishibashi J, Nogi Y, Yoshikawa S, Miyazaki J, Okino K (2013) Discovery of a new hydrothermal vent based on an underwater, high-resolution geophysical survey. Deep Sea Res I 74:1–10

Parker RL, Huestis SP (1974) The inversion of magnetic anomalies in the presence of topography. J Geophys Res 79:1587–1593

Pearce JA, Stern RJ, Bloomer SH, Fryer P (2005) Geochemical mapping of the Mariana arc-basin system: Implications for the nature and distribution of subduction components. Geochem Geophys Geosyst 6, Q07006. doi:10.1029/2004GC000895

Shindo H, Seama N, Matsuno T, Shibata Y, Kimura M, Nogi Y, Okino K (2012) Electrical resistivity structure of the upper mantle in the Southern Mariana Trough. Abstract T51D-2612 presented at 2012 Fall Meeting, AGU, San Francisco, 3–7 Dec

Takahashi N, Kodaira S, Tatsumi Y, Kaneda Y, Suyehiro K (2008) Structure and growth of the Izu-Bonin-Mariana arc crust: 1. Seismic constraint on crust and mantle structure of the Mariana arc–back-arc system. J Geophys Res 113:B01104. doi:10.1029/2007JB005120

Tatsumi Y, Eggins S (1995) Subduction zone magmatism. Blackwell, Boston

Tivey MA, Johnson HP (2002) Crustal magnetization reveals subsurface structure of Juan de Fuca Ridge hydrothermal fields. Geology 30:979–982. doi:10.1130/0091-7613(2002)030<0979:CMRSSO>2.0.CO;2

Tolstoy M, Waldhauser F, Bohnenstiehl DR, Weekly RT, Kim WY (2008) Seismic identification of along-axis hydrothermal flow on the East Pacific Rise. Nature 451:181–184

Urabe T, Ishibashi J, Maruyama A, Marumo K, Seama N, Utsumi M (2004) Discovery and drilling of on- and off-axis hydrothermal sites in backarc spreading center of southern Mariana Trough, western Pacific. Eos Trans AGU 85(47). Fall Meet. Suppl., Abstract V44A-03

Wessel P, Smith WH (1998) New, improved version of the Generic Mapping Tools released. EOS Trans Am Geophys Un 79:579

Yamazaki T, Seama N, Okino K, Kitada K, Joshima M, Oda H, Naka J (2003) Spreading process of the northern Mariana Trough: rifting-spreading transition at 22°N. Geochem Geophys Geosyst 4(9):1075. doi:10.1029/2002GC000492

Yoshikawa S, Okino K, Asada M (2012) Geomorphological variations at hydrothermal sites in the southern Mariana Trough: Relationship between hydrothermal activity and topographic characteristics. Mar Geol 303–306:172–182

Seismic Structure and Seismicity in the Southern Mariana Trough and Their Relation to Hydrothermal Activity

18

Toshinori Sato, Mariko Mizuno, Hiroyoshi Takata, Tomoaki Yamada, Takehi Isse, Kimihiro Mochizuki, Masanao Shinohara, and Nobukazu Seama

Abstract

The Southern Mariana Trough is an active back-arc basin with hydrothermal activity. We investigated relations between the back-arc spreading system and the hydrothermal system in this area by conducting a seismic reflection/refraction survey and a three-month campaign of seismic observations using ocean bottom seismometers. From a 3D seismic velocity structure analysis, we mapped a low-velocity structure just beneath the spreading axis, a high-velocity structure with convex upward beneath an off-axis knoll, and a thickening of layer 2 (to about 3 km) over the refraction survey area compared with normal mid-ocean ridges. We found very low seismicity in the hydrothermal area and high seismicity in areas of high topographic relief that probably represent arc volcanoes. The low-velocity structure at the axis suggests that there is some magmatic activity beneath the axis in the form of sheetlike mantle upwellings. These may constitute the hydrothermal heat source at this site. The high-velocity structure with convex upward at the off-axis knoll suggests the presence of off-axis volcanism there. The very low seismicity suggests that this volcanism may have ceased, thus residual heat of this off-axis volcanism may contribute the heat for hydrothermal activity at this site. A comparison of the velocity structure with other back-arc spreading zones and mid-ocean ridges shows that the Southern Mariana Trough has a relatively thick layer 2 with lower seismic velocities, suggesting that the crust was formed by magmas with high volatile contents, consistent with upwelling mantle influenced by subduction. The very low seismicity at the hydrothermal sites indicates that there are no faults or fractures related to the hydrothermal activity. This suggests that the activity is not related to tectonic stresses there.

Keywords

Back-arc spreading • Crustal structure • Hydrothermal activity • Seismic structure • Southern Mariana Trough

18.1 Introduction

The Mariana Trough is an active back-arc basin in the Philippine Sea plate (Fig. 18.1a). It has opened in the past 6 million years (Fryer 1996) and displays several different features of spreading mechanisms along its strike (e.g., Martinez et al. 2000; Kitada et al. 2006). The northern end of the Mariana Trough (north of 20°35′N) displays a slow-spreading morphology (Martinez et al. 1995), although gravity data indicate the presence of thick crust that may

T. Sato (✉) • M. Mizuno • H. Takata
Department of Earth Sciences, Graduate School of Science, Chiba University, 1-33 Yayoi-cho, Inage-ku, Chiba 263-8522, Japan
e-mail: satot@earth.s.chiba-u.ac.jp

T. Yamada • T. Isse • K. Mochizuki • M. Shinohara
Earthquake Research Institute, University of Tokyo, 1-1-1, Yayoi, Bunkyo-ku, Tokyo 113-0032, Japan

N. Seama
Department of Earth and Planetary Sciences, Kobe University, 1-1 Rokkodai Nada, Kobe 657-8501, Japan

J.-i. Ishibashi et al. (eds.), *Subseafloor Biosphere Linked to Hydrothermal Systems: TAIGA Concept*,
DOI 10.1007/978-4-431-54865-2_18,

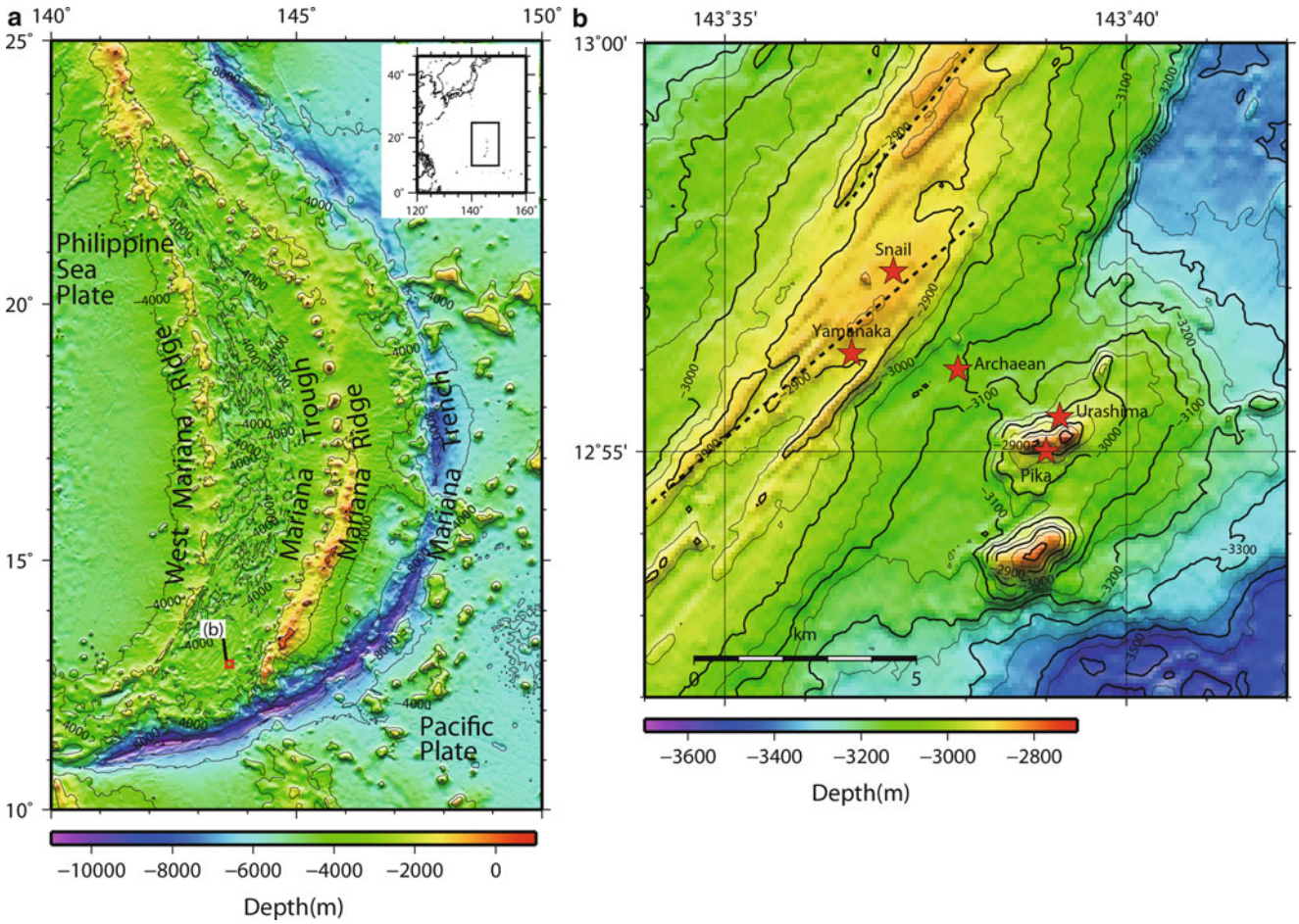

Fig. 18.1 (**a**) Bathymetric map of the Mariana Trough. The *red square* is the location of Fig. 18.1b. Contour interval is 2,000 m. The bathymetry data are from Smith and Sandwell (1997). (**b**) Bathymetric map of hydrothermal sites at the southern end of the Mariana Trough. The *red stars* indicate hydrothermal sites. The *broken lines* indicate ridge axes (Seama and Okino, Chap. 28). Contour interval is 50 m. The bathymetric data are from Seama and Okino (Chap. 28)

reflect an additional magma supply from island arc sources (Yamazaki et al. 2003; Kitada et al. 2006). The northern central part (between 15°38′N and 20°35′N) includes a segment of slow spreading with plume-like mantle upwelling under the axis and a segment of magma-starved slow spreading (Kitada et al. 2006). The southern central part (between 14°22′N and 15°38′N) has thin crust that suggests a very low magma supply (Kitada et al. 2006). In the southern end of the Mariana Trough (south of 14°22′N), although the full spreading rate of 46 km/Myr is categorized as slow spreading (Seama and Okino, Chap. 28), an abundant magma supply is implied by high topographic relief at the spreading axis (Martinez et al. 2000), thick crust (Kitada et al. 2006), and a magma chamber reflector at 13°05′N (Becker et al. 2010).

In the southern end of the Mariana Trough, five hydrothermal sites have been documented (e.g., *YK03-09*, *YK05-09*, and *YK10-10 cruise reports*) (Fig. 18.1b). The Snail and Yamanaka sites are on the spreading axis, the Archaean site is on the eastern foot of the axial high, and the Pika and Urashima sites are on an off-axis knoll about 5 km from the axis. The Snail site is an active hydrothermal system at a mound on pillow lavas cut by fissures (Urabe et al. 2004; Yoshikawa et al. 2012). Reported fluid temperatures are between 248 °C (Wheat et al. 2003) and 116 °C (*YK05-09 cruise report*). The Yamanaka site is an inactive hydrothermal system with a white smoker and several inactive sulfide chimneys (*YK03-09 cruise report*). The Archaean site is an active system at a sulfide mound 50–100 m high (Urabe et al. 2004; Yoshikawa et al. 2012). Reported fluid temperatures there are 213 °C (Ishibashi et al. 2004) and 345 °C (*YK05-09 cruise report*). The Pika site is an active system at the top of an off-axis knoll about 400 m high. The temperature of a black smoker there is 330 °C (Urabe et al. 2004). The Urashima site is at the northern foot of the off-axis knoll, and the reported temperature of a black smoker there is 280 °C (Nakamura et al. 2013). These hydrothermal systems are affected by on- and off-axis magma upwelling systems.

Therefore, they are categorized as "TAIGA of sulfur" in the TAIGA Project (Urabe, Chap. 1), meaning that magma drives the hydrothermal system and degases sulfur species (H_2S, HS^-) that is utilized by microbes.

In studying hydrothermal features, it is important to investigate seismic structures and seismicity. For example, deMartin et al. (2007) used seismic refraction and microseismicity surveys at the TAG segment of the Mid-Atlantic Ridge to document a relationship between a hydrothermal system and an active detachment fault. Tolstoy et al. (2008) delineated along-axis hydrothermal circulation pathways using microearthquake observations on the East Pacific Rise. Using these methods to image melt delivery to spreading axes and off-axis areas, and to trace pathways and heat sources for hydrothermal circulation, can provide important constraints for modeling relations between a spreading system and its related hydrothermal system.

The present study investigated relations between the back-arc spreading system and the hydrothermal system in the Southern Mariana Trough using a seismic reflection/refraction survey and seismicity observations.

18.2 Data Acquisition and Analysis Methods

We conducted a seismic reflection/refraction survey and seismicity observation at the hydrothermal area in the southern end of the Mariana Trough (Fig. 18.2) from August to November 2010 using S/V *Yokosuka* of the Japan Agency for Marine-Science and Technology (JAMSTEC) (*YK10-10 and YK10-15 cruise reports*). We used 17 ocean bottom seismometers (OBSs), an airgun, and a single-channel streamer cable.

The digital OBSs used were of three types. The LTOBS_ERI instrument (used at sites S1–S4 and S8–S11) was deployed in a 50 cm titanium sphere and equipped with a three-component velocity seismometer of 1 Hz natural frequency and a 24-bit analog-to-digital (A/D) converter. The data sampling rate was 200 Hz. The STOBS_ERI instrument (used at sites S5–S7, S12, S14, and S16) was deployed in a 40 cm glass sphere and equipped with a three-component 4.5 Hz velocity seismometer and a 24-bit A/D converter. The data sampling

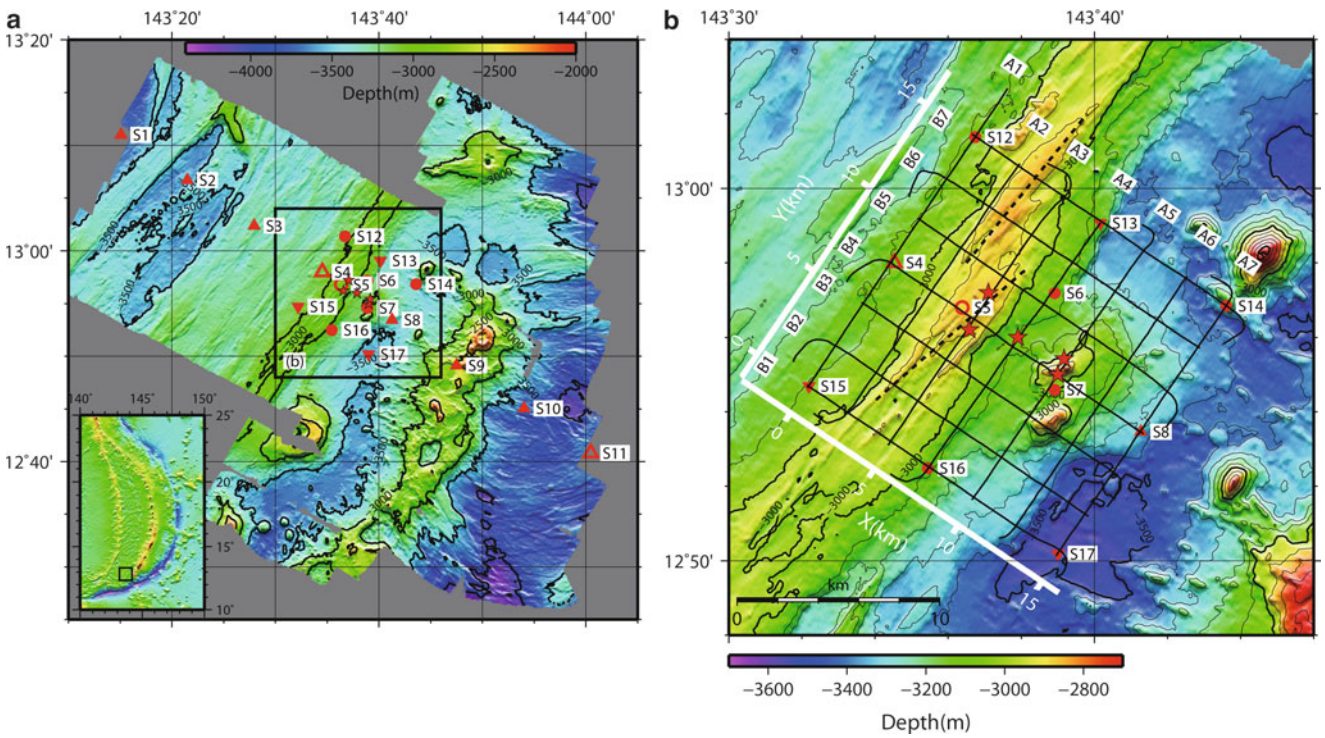

Fig. 18.2 (**a**) Map of OBS locations. The *red triangles* indicate LTOBS_ERI, the *red circles* indicate STOBS_ERI, and the *red inverted triangles* represent STOBS_Chiba instruments. *Filled and open symbols* indicate OBSs with data and no data, respectively. The *red stars* indicate hydrothermal sites. Contour interval is 500 m. The bathymetric data are from Seama and Okino (Chap. 28). (**b**) Profile map of the seismic reflection/refraction survey. The *black lines* indicate airgun survey profiles. *Survey lines* A1–A7 and B1–B7 are shown. The *red triangles*, *circles*, and *inverted triangles* indicate OBSs. The *red stars* indicate hydrothermal sites. The *broken lines* indicate ridge axes. Contour interval is 100 m. Axes in *white* indicate the coordinate system used in the 3D inversion

rate was 200 Hz. The STOBS_Chiba instrument (S13, S15, and S17) used a 40 cm glass sphere equipped with a three-component 4.5 Hz velocity seismometer and a 24-bit A/D converter. The data sampling rate was 125 Hz. All OBSs used a crystal oscillator with a precision greater than 5×10^{-7} s. We determined the location of each OBS at the seafloor through acoustic ranging and ship GPS positions. The accuracy of the OBS positions is estimated to be a few to a few tens of meters. We obtained seismic data from 14 of the 17 OBSs (S1–S3, S6–S10, and S12–S17).

We conducted a seismic reflection/refraction survey of the hydrothermal area to compile a 3D seismic structure image (Fig. 18.2b). Seven lines (A1–A7) ran NE-SW parallel to the spreading axis, and seven lines (B1–B7) ran NW-SE perpendicular to the spreading axis. Lines were 15 km long and the interval between lines was 2.5 km. The airgun was a GI gun with a volume of 355 cu. in. (5.5 L) and air pressure of 13.5 MPa. The shot interval was 40 s, for a shot spacing of about 97 m. We fired 2,519 shots along the profiles. Data from nine OBSs (S6–S8, S12–S17) were used for the seismic refraction analysis. Figure 18.3 shows an example of waveform data obtained by OBSs S12 and S6 from airgun shots. Seismic reflection data were obtained using a single-channel streamer combining 48 hydrophone signals, and the data were recorded with a duration of 16 s and sampling rate of 1,000 Hz for each shot.

To obtain the seismic velocity structure under the hydrothermal area, we carried out 2D traveltime inversions for lines A1, A4, A7, B1, B4, and B7 using first arrivals. We used the progressive model development method (Sato and Kennett 2000) to estimate 2D cross-sections of the seismic velocity structure under each line. Then we constructed a 3D initial seismic velocity model by interpolating among the 2D structures. This initial model also included bathymetric data (Seama and Okino, Chap. 28). Using this initial model, we carried out a tomographic inversion using first arrivals (Zelt and Barton 1998). We also conducted checkerboard tests to assess the reliability of estimated structures.

For analyzing seismicity, we used the WIN processing system for waveform data from microearthquake networks (Urabe and Tsukada 1991). To detect seismic events, we used an event picker algorithm based on the ratio between the short-term average and long-term average of amplitude of recorded wave-form, and duration of events. We extracted events that were recorded at two or more stations. P- and S-wave arrival times were hand-picked. Hypocenters were determined by the HYPOMH algorithm, which uses a maximum-likelihood estimation technique with origin time eliminated (Hirata and Matsu'ura 1987).

18.3 Results

18.3.1 Seismic velocity structure

For the 3D refraction analysis, we used 9028 hand-picked P-wave arrivals. We set the error in P-wave arrivals at 30 ms, as estimated from errors in arrival-time picks (20–30 ms), shot/receiver position (less than 10 ms), and OBS clock drift (less than 5 ms). The initial model for the 3D tomographic inversion (Fig. 18.4a–e) had RMS traveltime residuals between predicted and observed arrivals of 109 ms and showed roughly parallel structures along the spreading ridge axis. In the 3D inversion, we iterated toward a model with a chi-square value χ^2 (normalized RMS of traveltime residuals) of one, which means that the RMS traveltime residual was 30 ms for estimated models. An example of the picked arrivals and synthetic arrivals of the initial and final models is shown in Fig. 18.3.

Figures 18.4f–j and 18.5 show the final model estimated using the 3D tomographic inversion, and Figs. 18.6 and 18.7 show a checkerboard test and ray paths for the final model. For the checkerboard test, we adopted a velocity perturbation of 5 % from the final model and a perturbation grid size of 3 × 3 km horizontal and 1 km vertical for shallower than 5.5 km from the sea surface, and 5 × 5 km horizontal and 1 km vertical for deeper than 5.5 km. We made a set of pseudo-data consisting of synthetic P-wave arrivals with the same source-receiver pairs as the picked data using the test model and random errors with standard deviation of 30 ms. The results of the checkerboard test showed that the pattern of the velocity variation was recovered well at depths shallower than 6.5 km from the sea surface, and ray path coverage shallower than 6.5 km was good over the survey area. Therefore, we confirm that our inversion results can distinguish the three hydrothermal areas (Snail + Yamanaka, Archaean, and Pika + Urashima).

The final model displays four main features of the crustal structure around the back-arc spreading ridge with hydrothermal activity. (1) The average thickness of layer 2 of the oceanic crust in the survey area is about 3 km if we put the boundary between layer 2 and layer 3 at V_P 6 km/s and assume no sedimentary layer around the ridge (Fig. 18.4 k). In general, seismic velocity of layer 2 is about V_P 3–6 km/s with large velocity gradient, and that of layer 3 is about V_P 6–7 km/s with less velocity gradient (e.g., Kearey et al. 2009). Our results show a velocity gradient change at the depth of 6.5 km with V_P 6 km/s. Thus, we set the boundary between layer 2 and layer 3 at V_P 6 km/s. The 3 km thickness of layer 2 means that this area has a thicker layer 2 than in normal oceanic crust, where it is about 1–2 km thick (e.g., Kearey et al. 2009). Moreover, the survey area has a low-velocity layer 2 (~4.0 km/s at

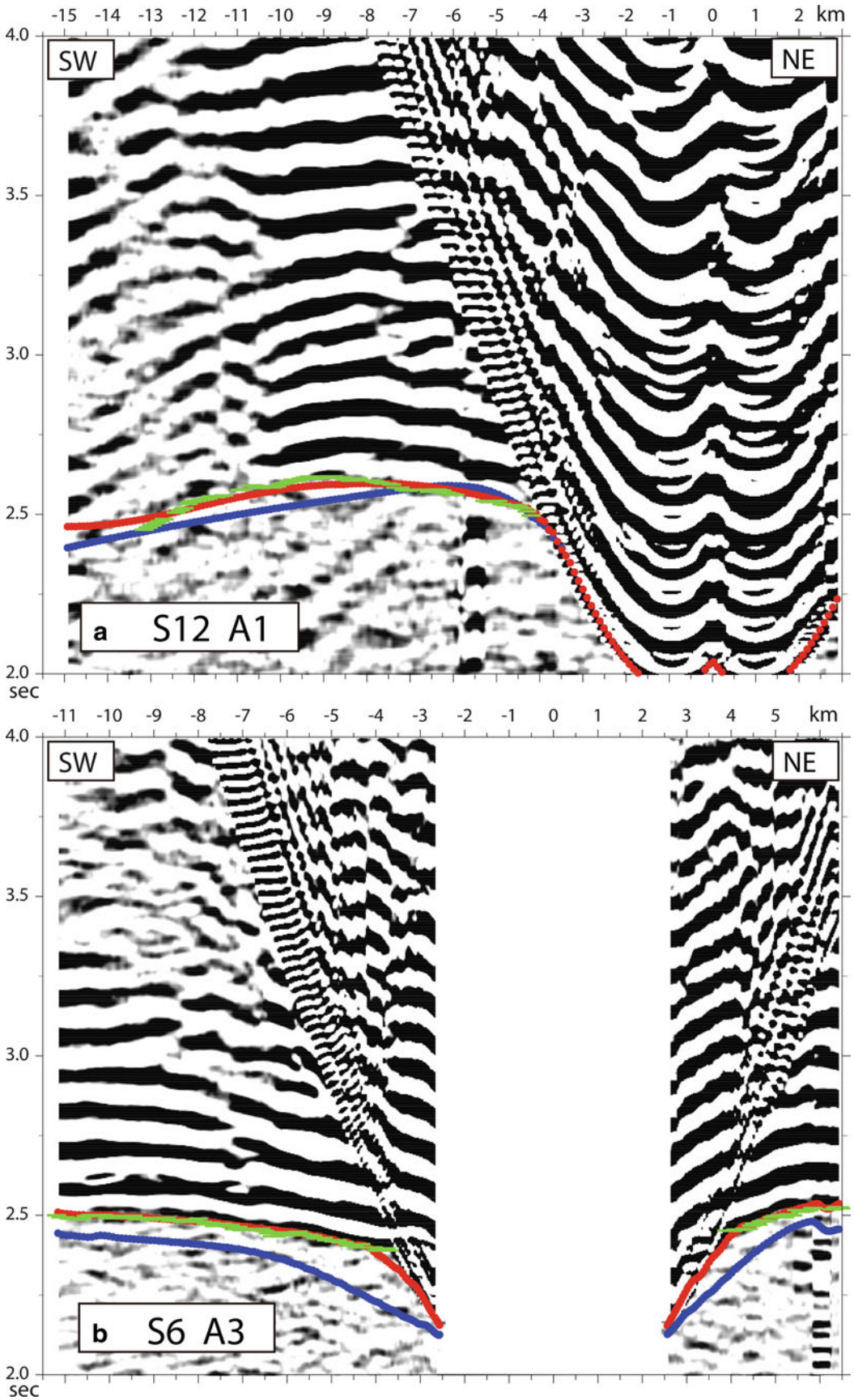

Fig. 18.3 Examples of seismograms. (**a**) Line A1 recorded by OBS S12; (**b**) line A3 recorded by OBS S6. *Horizontal axis* indicates distance from OBS to shots. *Vertical axis* is traveltime. Reduction velocity is 5 km/s. *Green lines* indicate observed (picked) traveltimes. *Blue lines* indicate synthetic traveltimes for the initial model. *Red lines* indicate synthetic traveltimes for the final model

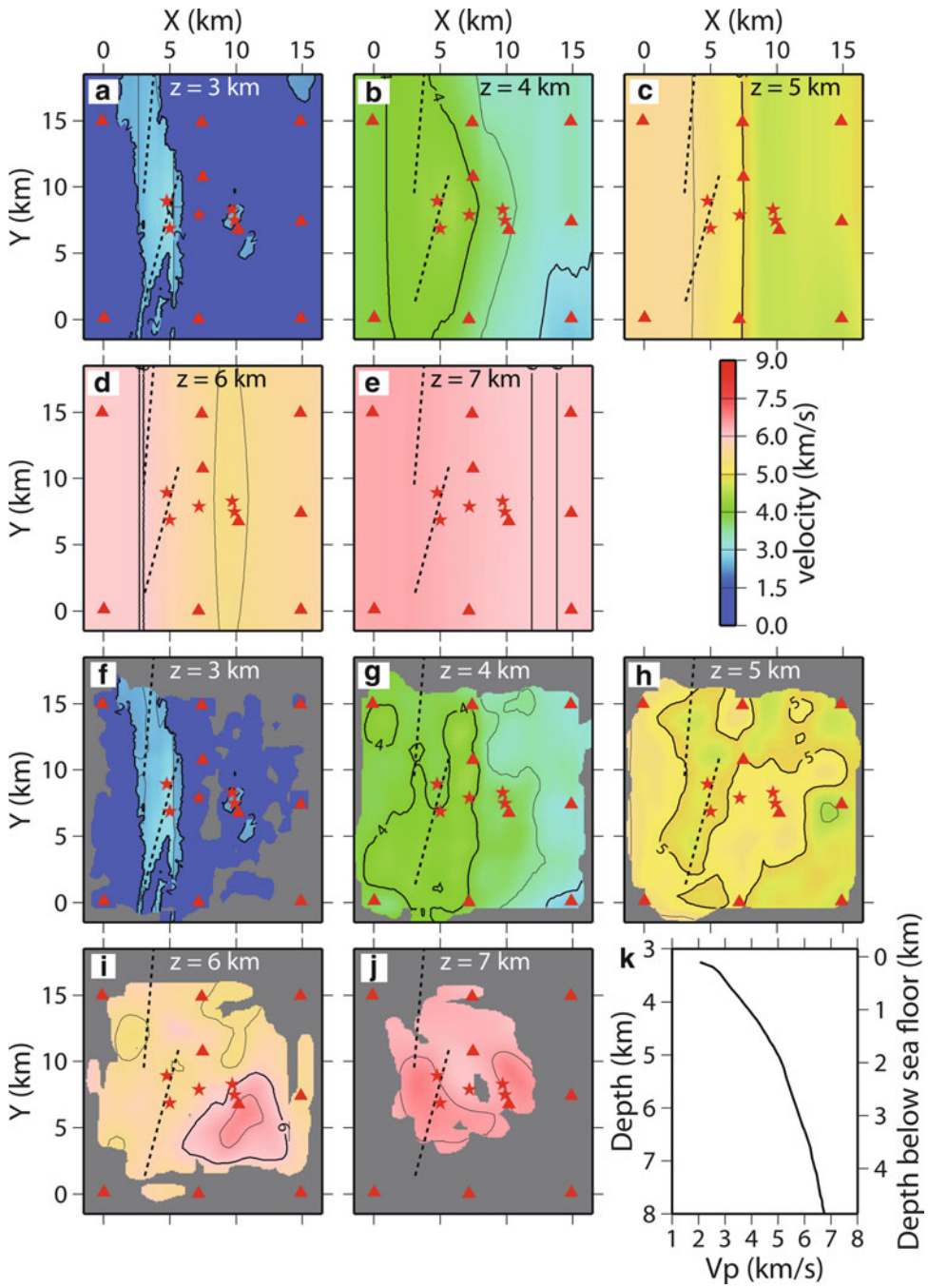

Fig. 18.4 (**a**–**e**) Map views of velocity structure of the initial model. Depth (z) is from the sea surface. Contour interval is 0.5 km/s. The *red triangles* indicate OBSs. The *red stars* indicate hydrothermal sites. The *broken lines* indicate ridge axes. (**f**–**j**) Map views of velocity structure of the final model. *Gray areas* indicate no ray paths. (**k**) 1D average velocity of the final model. Average velocities are taken at each depth below the seafloor

1 km depth below sea floor). (2) The velocity just beneath the spreading ridge is lower than in the surrounding area (see map views at depths of 4 and 5 km in Fig. 18.4g, h and V_P anomalies in Fig. 18.5g–i relative to the 1D average in Fig. 18.4k). This low-velocity zone lies beneath the area including the Snail and Yamanaka hydrothermal sites. (3) There is a high-velocity area just beneath the off-axis knoll (see map view at 6 km depth in Fig. 18.4i). This knoll is the location of the Pika and Urashima hydrothermal sites. Cross-sections through the two hydrothermal sites (Fig. 18.5c, e) show that the boundary between layers 2 and 3 is convex upward beneath the knoll. (4) At the Archaean hydrothermal site, there are no anomalous structures.

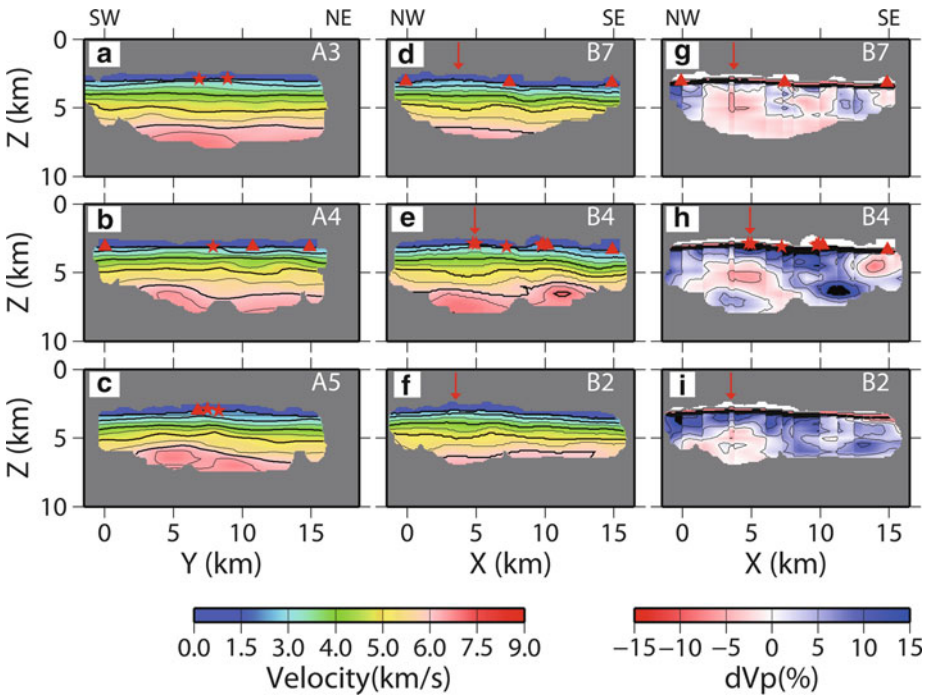

Fig. 18.5 (**a**–**c**) Vertical cross sections of V_P distribution beneath ridge-parallel lines A3, A4, and A5. Contour interval is 0.5 km/s. *Gray areas* indicate no ray paths. The *red triangles* indicate OBSs on the line. The *red stars* indicate hydrothermal sites on the line. (**d**–**f**) Vertical cross sections of V_P distribution beneath ridge-perpendicular lines B7, B4, and B2. The *red arrow* indicates the ridge axis. (g–i) Vertical cross sections of V_P anomalies relative to the 1D average velocity of the final model (Fig. 18.4 k) beneath ridge-perpendicular lines B7, B4, and B2

From the seismic reflection data, we cannot identify reflectors consistent with axial magma chambers. Some data show reflective images at the Pika and Urashima hydrothermal sites, but we cannot distinguish these from scattered returns from the rough surfaces of the off-axis knoll. A multichannel seismic survey would be needed to reveal detailed structures here.

18.3.2 Seismicity

We obtained 3 months of seismicity data at the southern end of the Mariana Trough from 14 of the 17 deployed OBSs. We used a 1D P-wave velocity model (Fig. 18.8) based on the results of this study, the velocity structures of the middle Mariana Trough published by Takahashi et al. (2008), and the IASP91 velocity model (Kennett 1991). We assumed the V_P/V_S ratio to be 1.73.

During the observation period, we determined hypocenters of about 1,700 events (Fig. 18.9). Most events occurred at and around areas of high topographic relief, which are probably arc volcanoes, about 30 km southeast of the spreading ridge. The hydrothermal areas had very few events during the observation period. We determined only two hypocenters within 5 km of the hydrothermal areas.

Some OBSs recorded small tremors like noise. We could not identify these as volcanic tremors, because these tremors were too small to obtain sufficient arrival time data, then we could not determine locations of these tremors. To identify these tremors whether as volcanic or not, we would need more dense OBS arrays.

18.4 Discussion

Our observations revealed a detailed seismic velocity structure and a record of seismicity at and around the hydrothermal areas in the Southern Mariana Trough. We can evaluate the heat sources of the hydrothermal activity from these results.

The spreading axis, where the Snail and Yamanaka hydrothermal sites are located, has lower seismic velocities than the surrounding area. This suggests that the area beneath the axis is hotter due to magmatic activity and thus that the heat source of these sites may be magmatic. Kitada et al. (2006) suggested on the basis of gravity data that there are sheetlike mantle upwellings beneath the first-order ridge segments in the southern end of the Mariana Trough. Our results show more detailed structures. The map view at 5 km depth (Fig. 18.4h) displays that the low-velocity structure

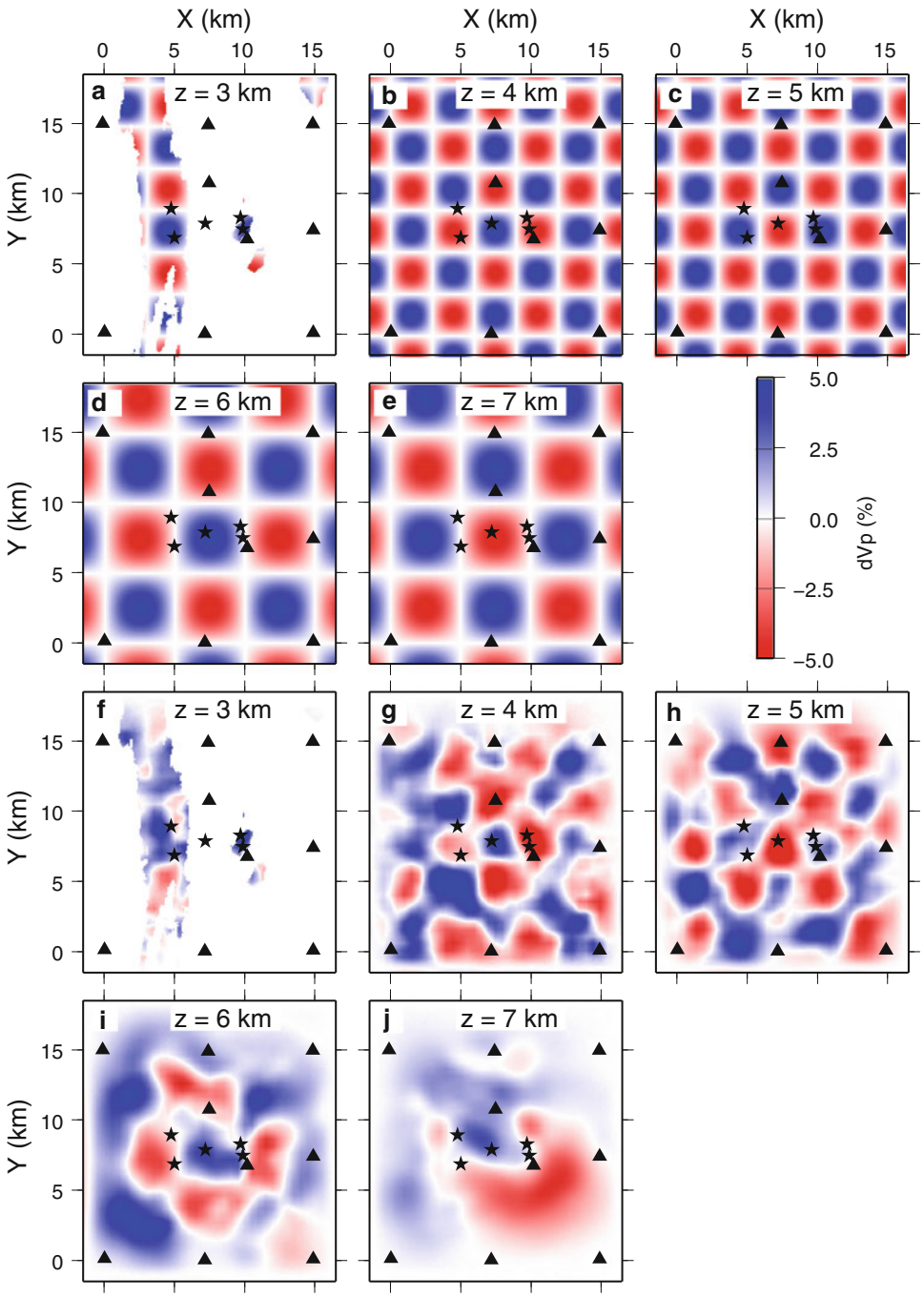

Fig. 18.6 Checkerboard test. (**a**–**e**) Given model. We adopted a velocity perturbation of 5 % from the final model and a perturbation grid size of 3 × 3 km horizontal and 1 km vertical for shallower than 5.5 km from the sea surface, and 5 × 5 km horizontal and 1 km vertical for deeper than 5.5 km. The *triangles* indicate used OBSs. The *stars* indicate hydrothermal sites. (**f**–**j**) Recovered model after the inversion

aligns with the subdivided axes. Our results suggest that the upwellings beneath the first-order ridge segment can be subdivided into upwellings beneath the third-order ridge segment which is pointed by Seama et al. (Chap. 17). The depth of the top of the low-velocity zones is about 4.5 km, or 1.5 km below the seafloor (Fig. 18.5g–i). As the seismic reflection profile of Becker et al. (2010) shows no magma chamber reflector in our study area, the low-velocity zone is probably not a magma chamber with abundant melt, but a warm zone with a chamber of crystal-rich mush.

At the off-axis knoll, where the Pika and Urashima hydrothermal sites are located, we mapped a high-velocity structure with convex upward that suggests a volcanic activity beneath the knoll. We infer that off-axis volcanism once existed there, forming the knoll, and intruded magma was cooled to become layer 3, making the boundary between layers 2 and 3 convex upward. Previous results also support this conclusion. Yoshikawa et al. (2012) interpreted near-bottom swath mapping data showing an undeformed morphology of the knoll to suggest that the knoll is related to an

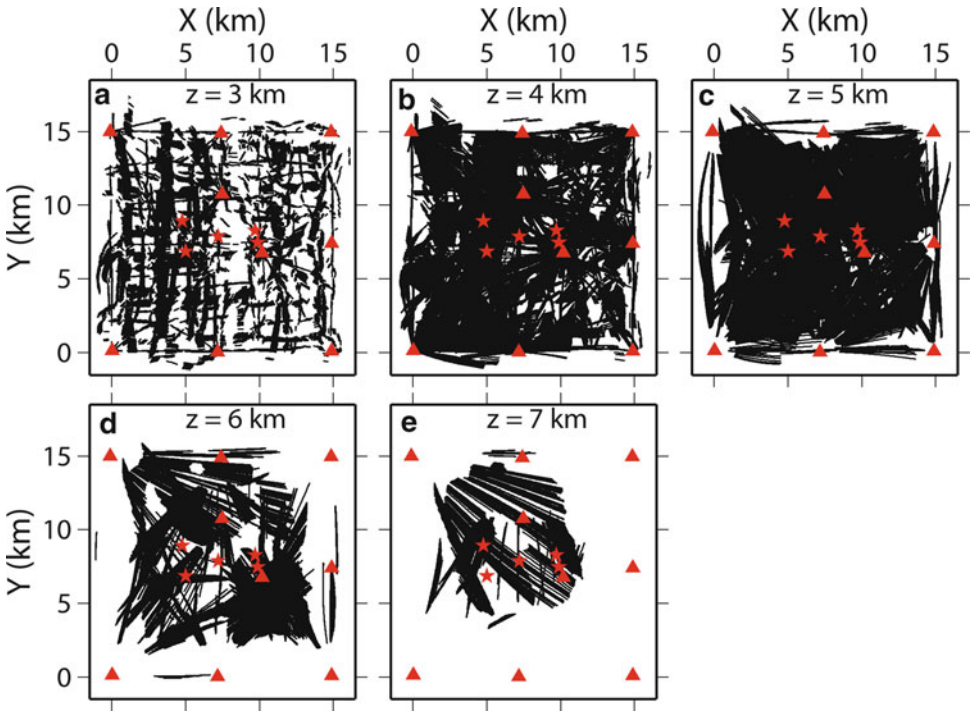

Fig. 18.7 (**a**–**e**) Ray paths of the final model. Each panel shows ray paths within 0.5 km of z. The *red triangles* indicate OBSs. The *red stars* indicate hydrothermal sites

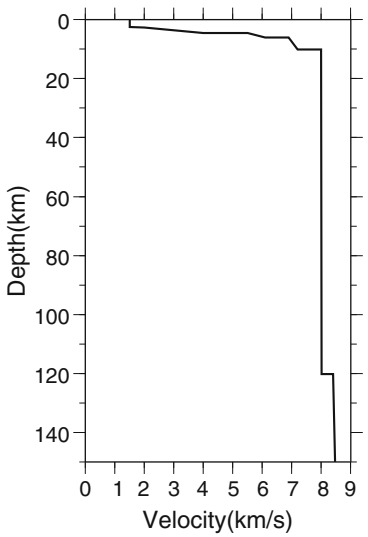

Fig. 18.8 1D velocity structure used for hypocenter determination

off-axis magma upwelling system. Kakegawa et al. (2008) showed that the knoll is composed of pillow lavas with minor sediment cover, indicating that volcanic activity have ceased. The very low seismic activity at the knoll also suggests the cessation. Hence the heat sources of the Pika and Urashima sites may be residual heat from this off-axis magmatic activity.

At the Archaean hydrothermal site, we did not find any anomalous structures like those at the other hydrothermal sites. This site consists of a small mound 250–300 m in diameter and 50–100 m high in a flat basin at the eastern foot of the axial high (Yoshikawa et al. 2012), too small for our seismic survey to reveal any internal structure. A higher-resolution survey is required to obtain a detailed structure at this site.

Our seismic observations found very low seismicity at the hydrothermal sites. This result is very different from those of deMartin et al. (2007) and Tolstoy et al. (2008), who found many microearthquakes related to hydrothermal activity. The difference may be because our OBS network had a wider spacing (about 5 km) than the earlier networks (about 1–5 km). To examine this possibility, we checked the seismicity near OBS S7, which was less than 1 km from the Pika hydrothermal site. Looking at the S–P times of all events recorded by OBS S7 (Fig. 18.10), we found that it recorded only three events with S–P times less than 1 s. This indicates that the very low seismicity was not an artifact of our OBS network, but a real feature in the study area, and it suggests that there are no faults or fractures related to the hydrothermal activity. That in turn suggests that hydrothermal activity here is not related to tectonic stresses. Yoshikawa et al. (2012) likewise reported no fault systems at the off-axis hydrothermal sites Archaean, Pika, and Urashima.

We found a thick layer 2 (thickness about 3 km) with low seismic velocities over the study area. Figure 18.11 shows the 1D velocity profile of this study along with those for the Central Mariana Trough (Takahashi et al. 2008), the Lau basin (Jacobs et al. 2007; Dunn and Martinez 2011), the Juan de Fuca Ridge (Christensen et al. 1993), the East Pacific Rise (Vera et al. 1990), and the Mid-Atlantic Ridge (Magde et al.

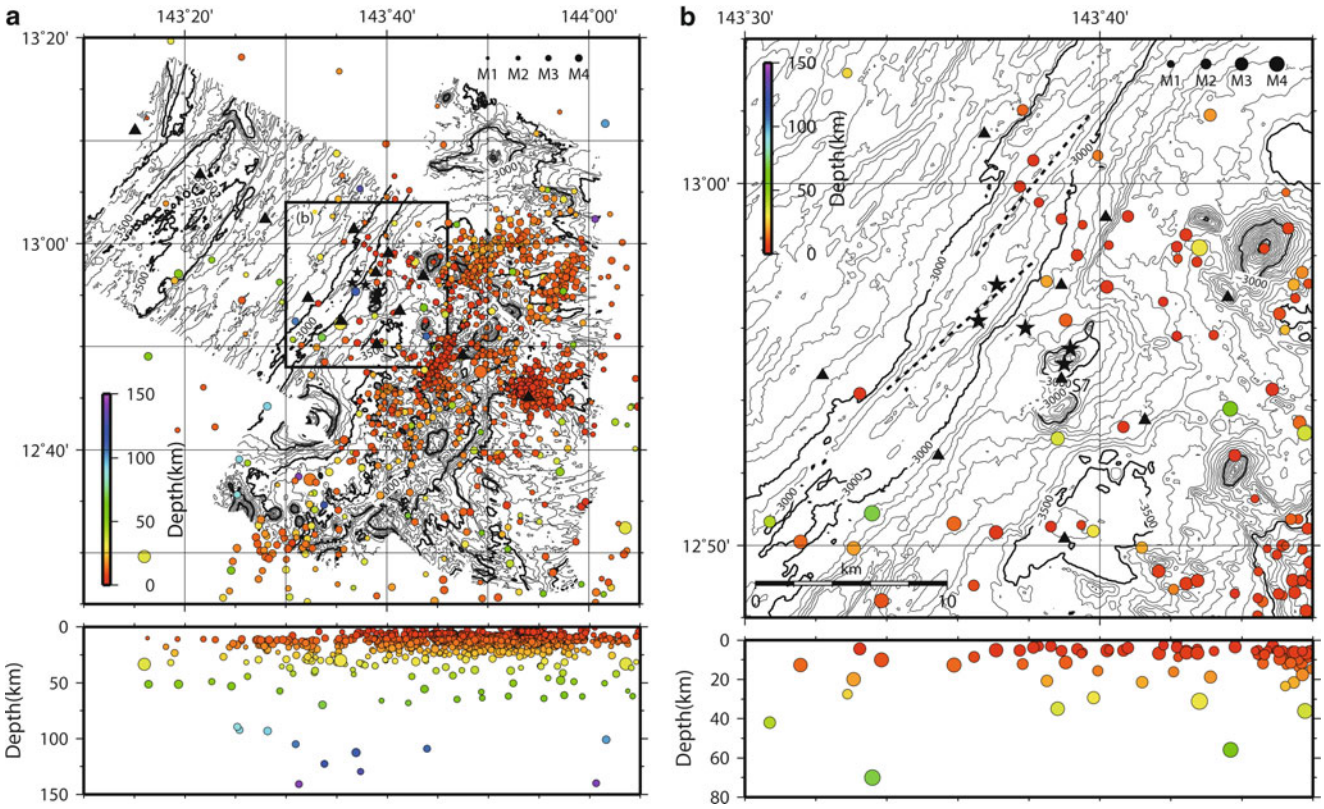

Fig. 18.9 (**a**) Hypocenter distribution at the Southern Mariana Trough during three months of observations by OBSs (*triangles*). The *stars* indicate the hydrothermal sites. Contour interval is 100 m. (**b**) Hypocenter distribution near the hydrothermal sites. Only high-quality hypocenters whose standard error in each of the hypocenter coordinates is less than 5 km are plotted. The *broken lines* indicate ridge axes. Contour interval is 50 m

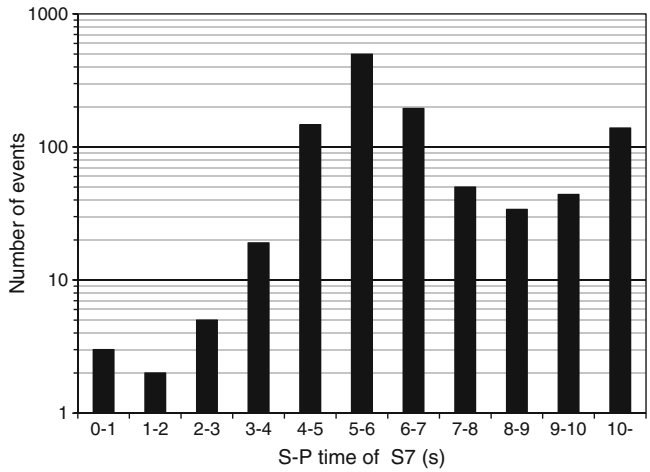

Fig. 18.10 Histogram of S–P times at OBS S7

2000). It shows that the Southern Mariana Trough has a thicker layer 2 and lower seismic velocities than the normal mid-ocean ridges (Juan de Fuca Ridge, East Pacific Rise, and Mid-Atlantic Ridge). In the back-arc spreading ridges, the structures are divided into two groups. One, which includes the Central Mariana Trough and the Lau Domain III, is similar to mid-ocean ridges, and the other, which includes the Southern Mariana Trough, Lau Domain II, and Lau Valu Fa Ridge, has a low-velocity layer 2. Jacobs et al. (2007) and Dunn and Martinez (2011) noted that the low-velocity layer 2 implies high porosities and arc-related mineralogies, and that the Domain II and Valu Fa Ridge in the Lau basin are formed by magmas with high volatile contents derived from the subducting plate, because these areas are near the subduction slab and the Tonga volcanic arc. As the Southern Mariana Trough also is near the subduction zone and the volcanic arc, and as its seismic structure is similar to Lau Domain II and Valu Fa Ridge, we suggest that the upwelling mantle beneath the Southern Mariana Trough spreading axis is influenced by subduction. The upwelling mantle would have low viscosity due to hydration by water from the subducting slab, and the magmas produced would form thicker crust with high porosities (= lower velocities) in the Southern Mariana Trough. The Central Mariana Trough, on the other hand, is far from the subduction zone, hence its crustal structure would be similar to mid-ocean ridges, and there may be no influence of subduction as suggested by the upper mantle electrical resistivity structure reported by Matsuno et al. (2010).

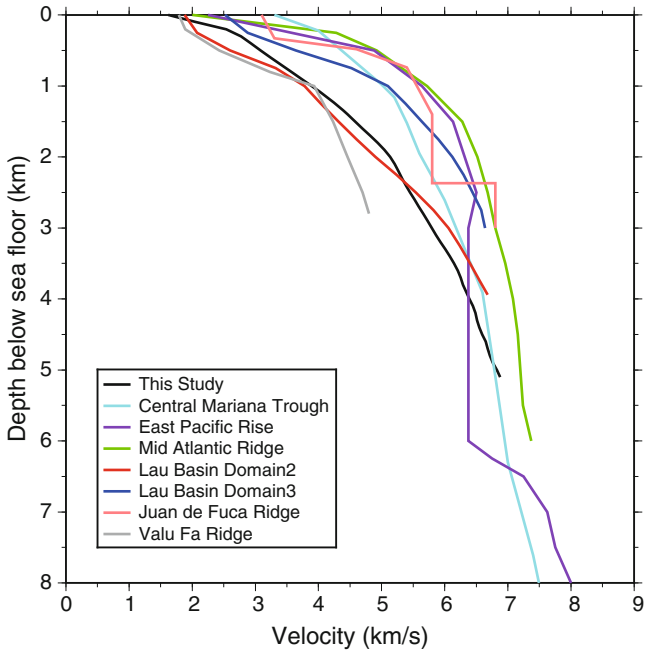

Fig. 18.11 Comparison of 1D velocity structures at spreading ridges of the Southern Mariana Trough (this study), the Central Mariana Trough (Takahashi et al. 2008), East Pacific Rise (Vera et al. 1990), Mid-Atlantic Ridge (Magde et al. 2000), Lau Basin (Dunn and Martinez 2011), Juan de Fuca Ridge (Christensen et al. 1993), and Valu Fa Ridge (Jacobs et al. 2007)

Our seismicity study recorded many microearthquakes beneath the area of high topographic relief that probably represents arc volcanoes. This means that this area is now very active. Fryer et al. (1998) suggested that the morphology of these volcanoes indicates recent activity. More detailed seismicity surveys may reveal this volcanic activity.

18.5 Conclusions

We conducted a seismic reflection/refraction survey and a seismicity observation campaign at the hydrothermal area in the southern end of the Mariana Trough. From a 3D refraction analysis, we found that the spreading axis has a low-velocity structure suggesting the presence of magmatic activity beneath the axis. The low-velocity structure shows sheetlike mantle upwellings beneath the third-order ridge segments that may be the heat sources for the Snail and Yamanaka hydrothermal sites. Beneath an off-axis knoll, we found a high-velocity structure with convex upward that is consistent with off-axis volcanism in the area. The very low seismicity there suggests that this volcanism may have ceased. The heat sources of the Pika and Urashima hydrothermal sites may be residual heat from this off-axis volcanic activity. We detected a thick (about 3 km) layer 2 with low seismic velocities over the survey area. A comparison of this structure with other back-arc spreading centers and mid-ocean ridges suggests that the crust was formed by magmas with high volatile contents, probably due to upwelling mantle influenced by subduction. Our seismic observations documented very low seismicity at the hydrothermal sites, indicating that there are no faults or fractures related to the hydrothermal activity. This suggests that the hydrothermal activity is not related to tectonic stresses.

Acknowledgments We thank the captain and crew of S/V *Yokosuka* of JAMSTEC for their support. This paper has been improved by comments from reviewers. The figures were generated using GMT software (University of Hawaii; *Wessel and Smith* (Wessel and Smith 1998)). This work was supported by Grant-in-Aid for Scientific Research on Innovative Areas of the Ministry of Education, Culture, Sports, Science and Technology (Grant Number 20109002, TAIGA project).

References

Becker NC, Fryer P, Moore GF (2010) Malaguana-Gadao Ridge: identification and implications of a magma chamber reflector in the southern Mariana Trough. Geochem Geophys Geosyst 11: Q04X13. doi:10.1029/2009GC002719

Christensen GL, Purdy GM, Rohr KMM (1993) Structure of the northern symmetrical segment of the Juan de Fuca Ridge. Mar Geophys Res 15:219–240

deMartin BJ, Sohn RA, Canales JP, Humphris SE (2007) Kinematics and geometry of active detachment faulting beneath the Trans-Atlantic Geotraverse (TAG) hydrothermal field on the Mid-Atlantic Ridge. Geology 35:711–714

Dunn RA, Martinez F (2011) Contrasting crustal production and rapid mantle transitions beneath back-arc ridges. Nature 469:198–202

Fryer P (1996) Evolution of the Mariana convergent plate margin system. Rev Geophys 34:89–125

Fryer P, Fujimoto H, Sekine M, Johnson M, Kasahara J, Masuda H, Gamo T, Ishii T, Ariyoshi M, Fujioka K (1998) Volcanoes of the southwestern extension of the active Mariana Island Arc: new swath-mapping and geochemical studies. Isl Arc 7:596–607

Hirata N, Matsu'ura M (1987) Maximum-likelihood estimation of hypocenter with origin time eliminated using nonlinear inversion technique. Phys Earth Planet Inter 47:50–61

Ishibashi J, Yamanaka T, Kimura H, Hirota A, Toki T, Tsunogai U, Gamo T, Utsumi M, Roe K, Miyabe S, Okamura K (2004) Geochemistry of hydrothermal fluids in South Mariana Backarc Spreading Center. Eos Trans AGU 85(47), Fall Meet Suppl, Abstract V44A-05

Jacobs AM, Harding AJ, Kent GM (2007) Axial crustal structure of the Lau back-arc basin from velocity modeling of multichannel seismic data. Earth Planet Sci Lett 259:239–255

Kakegawa T, Utsumi M, Marumo K (2008) Geochemistry of sulfide chimneys and basement pillow lavas at the southern Mariana Trough (12.55°N–12.58°N). Resource Geol 58:249–266

Kearey P, Klepeis KA, Vine FJ (2009) Global tectonics, 3rd edn. Wiley-Blackwell, West Sussex, UK

Kennett BLN (1991) IASPEI 1991 seismological tables, Research School of Earth Sciences, Australian National University, 167 pp

Kitada K, Seama N, Yamazaki T, Nogi Y, Suyehiro K (2006) Distinct regional differences in crustal thickness along the axis of the Mariana Trough, inferred from gravity anomalies. Geochem Geophys Geosyst 7, Q04011. doi:10.1029/2005GC001119

Magde LS, Barclay AH, Toomey DR, Detrick RS, Collins JA (2000) Crustal magma plumbing within a segment of the Mid-Atlantic Ridge, 35°N. Earth Planet Sci Lett 175:55–67

Martinez F, Fryer P, Baker NC, Yamazaki T (1995) Evolution of backarc rifting Mariana Trough 20–24°N. J Geophys Res 100:3807–3827

Martinez F, Fryer P, Becker N (2000) Geophysical characteristics of the southern Mariana Trough, 11°50'N–13°40'N. J Geophys Res 105:16591–16607

Matsuno T, Seama N, Evans R, Chave AD, Baba K, White A, Goto T, Heinson G, Boren G, Yoneda A, Utada H (2010) Upper mantle electrical resistivity structure beneath the central Mariana subduction system. Geochem Geophys Geosyst 11, Q09003. doi:10.1029/2010GC003101

Nakamura K, Toki T, Mochizuki N, Asada M, Ishibashi J, Nogi Y, Yoshikawa S, Okino K (2013) Discovery of a new hydrothermal vent site in the Southern Mariana Trough based on geophysical surveys using the AUV Urashima. Deep-Sea Research Part I 74:1–10

Sato T, Kennett BLN (2000) Two-dimensional inversion of refraction traveltimes by progressive model development. Geophys J Int 140:543–558

Smith WHF, Sandwell DT (1997) Global sea floor topography from satellite altimetry and ship depth soundings. Science 277:1956–1962

Takahashi N, Kodaira S, Tatsumi Y, Kaneda Y, Suyehiro K (2008) Structure and growth of the Izu-Bonin-Mariana arc crust: 1. Seismic constraint on crust and mantle structure of the Mariana arc–back-arc system. J Geophys Res 113:B01104. doi:10.1029/2007JB005120

Tolstoy M, Waldhauser F, Bohnenstiehl DR, Weekly RT, Kim WY (2008) Seismic identification of along-axis hydrothermal flow on the East Pacific Rise. Nature 451:181–184

Urabe T, Tsukada S (1991) A workstation-assisted processing system for waveform data from microearthquake networks (in Japanese). Abstracts of Spring Meeting of Seismological Society of Japan, p 70

Urabe T, Ishibashi J, Maruyama A, Marumo K, Seama N, Utsumi M (2004) Discovery and drilling of on- and off-axis hydrothermal sites in backarc spreading center of southern Mariana Trough, western Pacific. Eos Trans AGU 85(47), Fall Meet Suppl, Abstract V44A-03

Vera EE, Mutter JC, Buhl P, Orcutt JA, Harding AJ, Kappus ME, Detrick RS, Brocher TM (1990) The structure of 0-My to 0.2-My old oceanic-crust at 9°N on the East Pacific Rise from expanded spread profiles. J Geophys Res 95:15529–15556

Wessel P, Smith WHF (1998) New improved version of Generic Mapping Tools released. EOS Trans AGU 79:579

Wheat CG, Fryer P, Hulme SM, Becker NC, Curtis A, Moyer C (2003) Hydrothermal venting in the southern most portion of the Mariana backarc spreading center at 12.57 degrees N. Eos Trans AGU 84 (46), Fall Meet Suppl, Abstract T32A-0920

Yamazaki T, Seama N, Okino K, Kitada K, Joshima M, Oda H, Naka J (2003) Spreading process of the northern Mariana Trough: rifting-spreading transition at 22°N. Geochem Geophys Geosyst 4(9):1075. doi:10.1029/2002GC000492

Yoshikawa S, Okino K, Asada M (2012) Geomorphological variations at hydrothermal sites in the southern Mariana Trough: relationship between hydrothermal activity and topographic characteristics. Marine Geol 303–306:172–182

Zelt CA, Barton PJ (1998) Three-dimensional seismic refraction tomography: a comparison of two methods applied to data from the Faeroe Basin. J Geophys Res 103:7187–7210

Electrical Resistivity Structure of the Snail Site at the Southern Mariana Trough Spreading Center

19

Tetsuo Matsuno, Maho Kimura, and Nobukazu Seama

Abstract

The electrical resistivity of the oceanic crust is sensitive to the porosity of the crust and the fluid temperature within crustal fractures and pores. The spatial variation of the crustal porosity and the fluid temperature that is related to a hydrothermal circulation can be deduced by revealing an electrical resistivity structure of the oceanic crust involving a hydrothermal site. We carried out a magnetometric resistivity experiment using an active source to reveal an electrical resistivity structure of the oceanic crust at the Snail site on the ridge crest of the Southern Mariana Trough. Active source electric currents were transmitted along and across the ridge axis in a 4,000 m^2 area including the Snail site. Five ocean bottom magnetometers were deployed around the Snail site as receivers to measure the magnetic field induced by the transmission of the active source electric currents. The amplitude of the induced magnetic field was calculated by maximizing data density and the signal to error ratio in the data, and locations of the transmissions were determined using several types of calibration data. An optimal 1-D resistivity structure of the oceanic crust, averaged over the experimental area, was deduced by least squares from the data of the amplitude of the magnetic field and the location of the transmission. After calculating magnetic field anomalies, which are deviations of the observed amplitude from the prediction of the optimal 1-D resistivity model, an optimal 3-D resistivity structure was deduced from the magnetic field anomalies through trial and error 3-D forward modeling. The optimal 1-D resistivity structure is a two-layer model, which consists of a 5.6 Ω-m upper layer having a 1,500 m thickness and a 0.1 Ω-m underlying half-space. Using Archie's law and porosity profiles of the oceanic crust, the resistivity of 5.6 Ω-m at depths ranging from 800 to 1,500 m suggests the presence of high-temperature fluid related to the hydrothermal circulation. The resistivity of 0.1 Ω-m below 1,500 m depth may represent a magma mush that is a heat source for the hydrothermal circulation. The optimal 3-D resistivity structure includes a conductive anomaly (0.56 Ω-m in approximately 300 m^2 area down to 400 m depth) immediately below the Snail site, two resistive anomalies (56 Ω-m with slightly larger volumes than the conductive anomaly) adjacent to the conductive anomaly on the across-ridge side, and three conductive anomalies away from the Snail site. The conductive anomaly immediately below the Snail site suggests hydrothermal fluid, and the adjacent resistive anomalies suggest areas of low porosity. The size and distribution of the conductive and resistive anomalies near the Snail site constrains the size and style of the hydrothermal circulation.

T. Matsuno (✉)
National Institute of Polar Research, 10-3 Midoricho, Tachikawa, Tokyo 190-8518, Japan

Earthquake Research Institute, University of Tokyo, 1-1-1 Yayoi, Bunkyo, Tokyo 113-0032, Japan
e-mail: tmatsuno@eri.u-tokyo.ac.jp

M. Kimura • N. Seama
Department of Earth and Planetary Sciences, Kobe University, 1-1 Rokkodai, Nada, Kobe 657-8501, Japan

J.-i. Ishibashi et al. (eds.), *Subseafloor Biosphere Linked to Hydrothermal Systems: TAIGA Concept*,
DOI 10.1007/978-4-431-54865-2_19,

Keywords
Electrical resistivity structure • Hydrothermal circulation • Magnetometric resistivity method • Oceanic crust • Temperature and porosity

19.1 Introduction

The Mariana Trough has been an active back-arc basin since its rifting and subsequent seafloor spreading approximately 6 Ma ago (e.g., Hussong and Uyeda 1982; Fryer 1996). The southern part of the Mariana Trough is inferred to be in an area of high melt production (e.g., Martínez et al. 2000; Kitada et al. 2006). A group of hydrothermal sites, which are called as the Snail, Yamanaka, Archaean, Pika, and Urashima sites, have been discovered on and off the ridge axis of the Southern Mariana Trough at 12°55′ to 12°57′N (e.g., *YK03-09 and YK05-09 cruise reports*; Urabe et al. 2004; Kakegawa et al. 2008). The heat source for hot fluid venting at the hydrothermal sites is expected to come from abundant magma sources. A thicker seismic layer 2 (upper crust) with a lower seismic velocity than other normal mid-ocean ridges in a 15 km^2 area at 12°56′N suggests an abundant melt production under the hydrothermal sites, which is affected by the high content of volatiles derived from the subducted Pacific slab (Sato et al. Chap. 18). A low velocity structure under the on-ridge sites (Snail and Yamanaka) suggests that a heat source is present for hydrothermal circulations at these sites, and a high velocity structure under the off-ridge sites (Archaean, Pika, and Urashima) suggests a thick seismic layer 3 (lower crust) and a residual heat source for hydrothermal circulations (Sato et al. Chap. 18). Low seismicity under the on and off ridge sites indicates that tectonic stresses resulting in faulting are not related to the hydrothermal activity (Sato et al. Chap. 18). In addition to the group of hydrothermal sites, a seismic reflector was observed approximately 15 km northeast along the spreading axis at approximately 3 km depth at 13°05′N, indicating the presence of a magma chamber (Becker et al. 2010).

The Snail site, which is the target of this study, is located at a mound cut by fissures on the ridge crest and is surrounded by unaltered pillow lavas and sheet dykes (Urabe et al. 2004; Yoshikawa et al. 2012; Kakegawa et al. 2008). A diking event is possibly related to development of the site, and hence, the life span of the hydrothermal circulation is inferred to be relatively short (Yoshikawa et al. 2012). Hot fluid at approximately 250 °C was venting at the time of its discovery in May 2003. The temperature of the fluid decreased to ≤116 °C in October 2003 and to 110 °C in July 2005 (Wheat et al. 2003; Kakegawa et al. 2008; *YK05-09 cruise report*). The low temperature of the vent fluid was a result of sub-seafloor mixing of cold seawater and hot fluid (>300 °C) (Ishibashi et al. 2006). Thin sulfide layers having a 3–15 cm thickness covers altered pillow lavas around the northeastern discharging zone, and low temperature fluid at 20–40 °C vents from clay mounds in the southwestern area (Kakegawa et al. 2008). These observations suggest that hydrothermal circulation under the Snail site occurs on a several or more tens of meters scale and that spatial variation in the porosity and permeability, which controls the size and geometry of the hydrothermal circulation, exists on a similar scale.

The electrical resistivity of the oceanic crust changes with the porosity of the crust, the amount and connectivity of fluid within the crust, and the temperature of the crust and the fluid. This property of the electrical resistivity suggests that a spatial variation in the porosity and the temperature of fluid within the crust is deduced by revealing an electrical resistivity structure of the oceanic crust. The magnetometric resistivity (MMR) technique is useful for revealing the electrical resistivity structure of the oceanic crust (e.g., Edwards et al. 1981). The first application of the MMR technique for exploring an electrical resistivity structure of an active hydrothermal system was implemented off the Juan de Fuca Ridge by Nobes et al. (1986), Nobes et al. (1992). Evans et al. (1998) conducted a MMR experiment at the Juan de Fuca Ridge. They determined electrical resistivity structures down to 1 km depth below the seafloor on and off the ridge axis, and concluded that a low resistivity structure found on the ridge axis at 600–800 m depth was related to a recent dike intrusion event and subsequent high-temperature fluid circulation. A MMR experiment at the East Pacific Rise also revealed a low resistivity structure on the ridge axis, suggesting the presence of hot pore-fluids beneath the ridge center (Evans et al. 2002). Tada et al. (2005) conducted a MMR experiment at the Alice Spring Field site on the back-arc spreading ridge in the central Mariana Trough, and discussed the temperature of hydrothermal fluid and the spatial variation of the hydrothermal circulation based on 1-D electrical resistivity profiles on and off ridge axes.

We present a result of a MMR experiment conducted at the Snail site in the Southern Mariana Trough in this contribution. A summary of the MMR experiment and magnetic field data obtained in the experiment is described first. The magnetic field data are analyzed to obtain a 1-D electrical resistivity structure averaged over the experimental area and then to obtain a detailed 3-D electrical resistivity

structure of the experimental area. The resulting 1-D and 3-D electrical resistivity structures are presented, and their features are discussed in terms of the hydrothermal system at the Snail site.

19.2 MMR Experiment

The MMR experiment was conducted at the Snail site from November 21 to 30 in 2003 during the KR03-13 cruise of *R/V Kairei* from the Japan Agency for Marine-Earth Science and Technology (JAMSTEC). Instruments used in the MMR experiment are categorized into transmitter, receiver, and calibrator. The transmitter comprised two electrodes connected by an insulated wire, one of which was set near the sea surface (upper electrode), and the other of which was set near the seafloor (lower electrode). The electrodes were strung out from the stern of the ship. The upper electrode was kept at 7 m below the sea surface and the lower electrode was kept at 20 m above the seafloor. A rectangular alternating current at a period of 16 s, with a peak current of 16 A, was applied between the electrodes for the active source electric current. The receiver comprised five ocean bottom magnetometers (OBMs). The OBMs, which each houses a fluxgate magnetometer, measured the time variation of the three-component magnetic field at a sampling rate of 1 s. The observed magnetic field includes the component induced in the crust by applying the electric current through the transmitter. A two-component tilt meter was equipped on the OBM to measure the instrumental tilt and to correct the tilt for the data analysis. The calibrator comprised a GPS, acoustic transponder, and Super Short Base Line (SSBL) system. The GPS system mounted on the ship was used to determine the location of the ship. The acoustic transponder was attached 100 m above the lower electrode along the insulated wire to measure its own seawater depth and height above the seafloor, as well as the distances between the acoustic transponder, the ship, and the OBM. The SSBL system equipped on the ship bottom was used to locate the lower electrode and the acoustic transponder.

The active source electric current was applied during ship runs along five transmission lines (L1-5) and at ten stationary points on the ends of the lines (Fig. 19.1). The location of the upper electrode was determined from the GPS position of

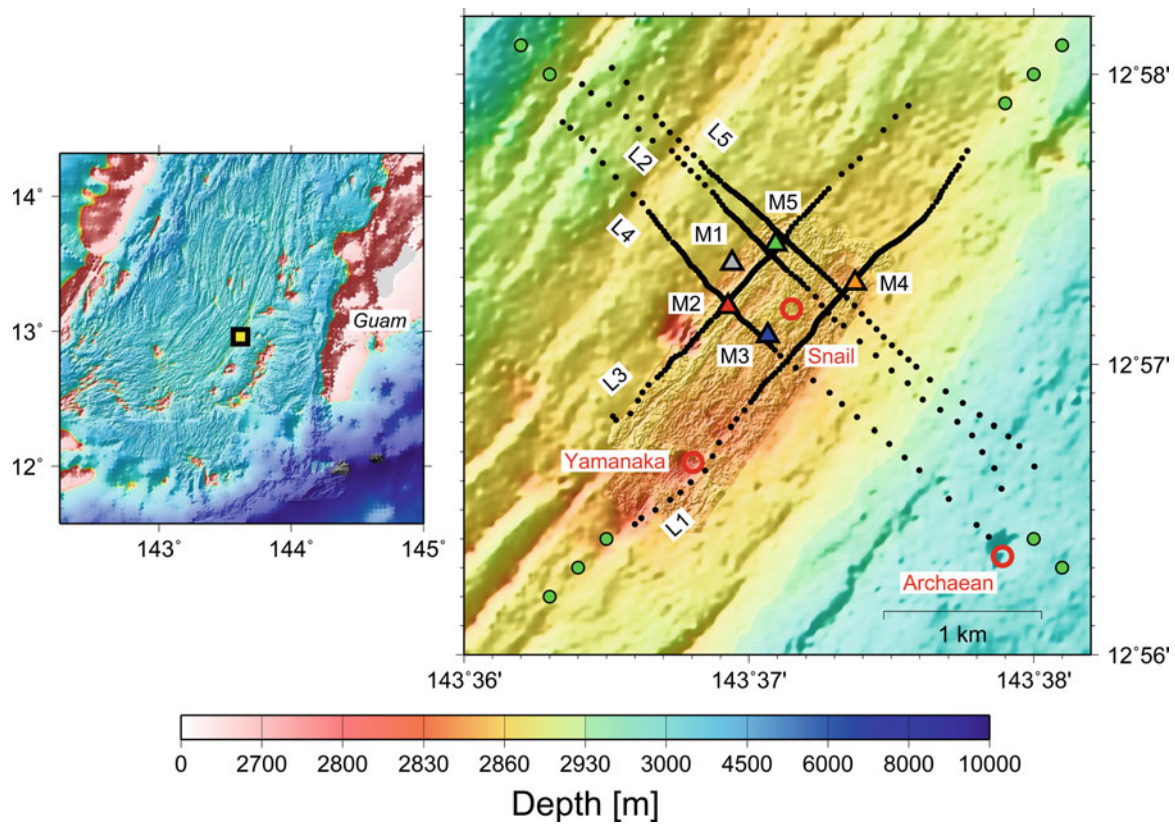

Fig. 19.1 An area map including the MMR experimental area (*left*), and a detailed MMR experimental area map (*right*). The *yellow square* in the left map indicates the location of the experimental area. *Symbols* in the right map denote the followings: *colored triangles* with names, locations of receivers (M); *filled circles*, transmission points during the ship runs along lines; *light green circles* on ends of transmission lines, stationary transmission points; *red circles* with names, locations of known hydrothermal sites. Names for the transmission lines (L) are also shown. High-resolution seafloor topography data on the ridge crest in the right figure are given from Yoshikawa et al. (2012)

Table 19.1 Location and depth of the receiver OBMs determined through a grid search, and RMS misfit distance in the determination of the OBMs' positions

Receiver	Latitude	Longitude	Depth (m)	RMS misfit distance (m)
M1	12°57.348′N	143°36.942′E	2,858	1
M2	12°57.199′N	143°36.927′E	2,862	4
M3	12°57.098′N	143°37.066′E	2,845	4
M4	12°57.280′N	143°37.373′E	2,855	8
M5	12°57.415′N	143°37.094′E	2,858	2

the ship and a visual measurement of the distance to the electrode from the stern. The location of the lower electrodes was determined by using several types of calibration data of the GPS, the acoustic transponder, the OBM, and the SSBL system. The ship speed was kept at 0.5 knots during the transmission along the lines to minimize a horizontal displacement between the upper and lower electrodes as well as the operation time for the experiment. The horizontal displacement between the upper and lower electrodes, which is not avoided as far as the ship runs, may be a problem in the MMR data analysis because the bipole for the source current is assumed to be vertical in the MMR technique theory (e.g., Edwards et al. 1981). The location of the transmission point along the lines is approximated by the horizontal midpoint between the upper and lower electrodes. The validity of this approximation was demonstrated by Seama et al. (2013). The location of the transmission at the stationary points is supposed to be consistent with that of the upper electrode because the ship did not run. The electric current was applied for 30 min at the stationary transmission points.

The five OBMs were deployed on the seafloor as surrounding the Snail site with separations of 300–800 m (Fig. 19.1). The locations of the OBMs were determined by minimizing misfits in slant range between the observation and the prediction through a grid search (Table 19.1). Out of the five OBMs, four OBMs (M2-5) measured the magnetic field during the L1 line transmissions, and the remaining OBM (M1) measured the magnetic field during the L2-5 line transmissions.

19.3 Data Analysis

19.3.1 Processing the Magnetic Field Data

Data measured by the receiver OBM is a three-component magnetic field in the time domain with the instrumental tilt. The instrumental tilt was corrected to retrieve a three-component magnetic field without the influence of the instrumental tilt, and then, a net force of the horizontal two components was obtained. The horizontal net force magnetic field was next processed through the fast Fourier transformation to obtain the amplitude of the magnetic field at a period of 16 s, which is the same period as that of the transmitter electric current. The amplitude of the magnetic field was finally normalized by the peak ampere of the electric current, 16 A.

Six length data segments in the time-domain (32, 64, 128, 256, 512, and 1,024 s) were used to calculate the amplitude of the magnetic field at 16 s. The longer length segment was used for the longer transmitter-receiver separation, and the shorter length segment was used for the shorter separation. Using variable length segments, which has not been done in previous MMR studies, is useful not only to obtain a higher density of amplitudes at the shorter separation but also to ensure a good signal to noise ratio of the amplitude at the longer separation (one datum of the amplitude per approximately 10 m separation with a $10^{-10.7}$ T/A noise level for the 32 s segment, and one datum of the amplitude per approximately 100 m separation with a $10^{-11.5}$ T/A noise level for the 1,024 s segment) (Fig. 19.2). Segments were overlapped by their half length to augment the number of data stacking to obtain a good signal to noise ratio of the amplitude (for example, 32 s segments were overlapped by 16 s). The noise level in the magnetic field amplitude was determined by averaging two adjacent non-transmission data to the 16 s transmission data in the frequency domain.

19.3.2 Obtaining a One-Dimensional Electrical Resistivity Structure

A 1-D electrical resistivity structure under the experimental area was obtained by using the data of the amplitude of the magnetic field and the horizontal separation between the transmitter and the receiver. All data pairs of the transmitter and the receiver were used, meaning that the resulting 1-D resistivity structure should represent a structure averaged over an area covered by all of the pairs of the transmitter and the receiver. An optimal 1-D electrical resistivity structure was determined by a least squares fitting of the model prediction to the observation. The model prediction was obtained from the analytical solution of Edwards et al. (1981).

19.3.3 Obtaining a Three-Dimensional Electrical Resistivity Structure

A 3-D electrical resistivity structure was examined by trial and error forward modeling of magnetic field anomaly for all of the transmission points. The magnetic field anomaly is obtained by subtracting the magnetic field amplitude predicted from the optimal 1-D resistivity structure model $\mathbf{B}_p$ from that observed $\mathbf{B}_o$ in logarithmic scale ($\log |\mathbf{B}_o| - \log |\mathbf{B}_p|$). A program developed by Tada et al. (2011) was

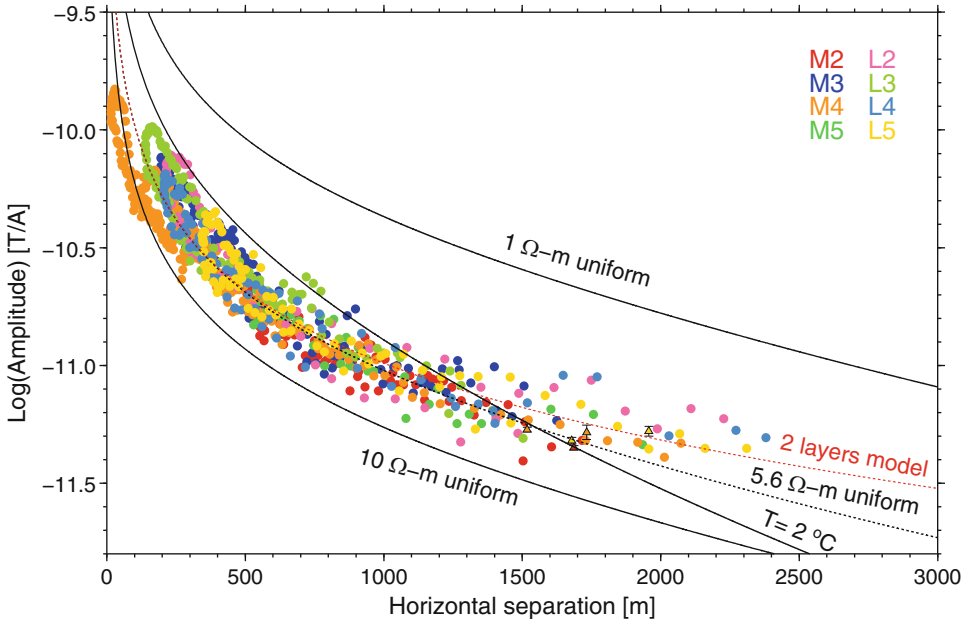

Fig. 19.2 The amplitude of the magnetic field for the horizontal separation between the transmitter and the receiver. Observed amplitudes are represented by *colored circles* and model predictions are shown by *solid and dotted lines*. The names of the receivers and the transmission lines are shown at the *upper right* in the figure. *Circles* with "M" denote each receiver data for the L1 line transmissions, and those with "L" denote data of the M1 receiver for each transmission line. Data at stationary transmission points are shown by *colored triangles* with error bars (one standard deviation) at 1,500–2,000 m horizontal separation. *Solid lines* with "1 Ω-m uniform" and "10 Ω-m uniform" represent analytical solutions of Edwards et al. (1981) for each uniform resistivity structure. A *black dotted line* represents an analytical solution for the 5.6 Ω-m uniform structure that is best fitted to the observations, and a *red dotted line* represents an analytical solution for a best fitting two-layer resistivity structure. The best fitting two-layer model comprises an upper layer with 5.6 Ω-m and a 1,500 m thickness and an underlying 0.1 Ω-m half-space. A *black solid line* with "T = 2 °C" is an analytical solution assuming 2 °C seawater at depths of 800–1,500 m for the bulk resistivity of 5.6 Ω-m, the exponent in Archie's law of 1.2, and a porosity profile from Evans et al. (1998) (Fig. 19.8a); see the discussion section in text

used for the forward modeling. The size of the modeling area was 4,000 × 4,600 × 4,000 m in the x-, y-, and z-axes (the x-axis is parallel to the ridge axis) and was constructed using 80 × 92 × 80 cubes (the dimension of the cube is 50 m). The seafloor depth is a constant 2,900 m, and the sub-seafloor modeling area has a thickness of 1,100 m. The depth of the lower electrode is 2,850 m. The electric current intensity of the active source is 1 A for modeling the magnetic field amplitude normalized by the applied electric current. The resistivity of seawater is 0.3 Ω-m, and that of the crust is 5.6 Ω-m, which is for the optimal 1-D resistivity structure and is described later in detail. Three-dimensional resistivity anomalies examined are cuboid with lower and higher resistivity values than 5.6 Ω-m by one order of magnitude in logarithmic scale (i.e., 0.56 and 56 Ω-m). The actual transmission lines were not strictly straight due to the movement and drift of the ship and the electrodes, but deviations from the straight lines are small as they are almost less than a few tens of meters (Fig. 19.1). Hence, transmission lines are set to be linear in the forward modeling.

19.4 Result

19.4.1 One-Dimensional Electrical Resistivity Structure

The amplitude of the magnetic field at 16 s with the horizontal separation between the transmitter and the receiver is plotted in Fig. 19.2. The amplitudes decay with a larger horizontal separation and are within the predictions of uniform 1-D resistivity models with 1 and 10 Ω-m. The resistivity of the uniform resistivity structure fitted to all of the data was determined to be 5.6 Ω-m (Fig. 19.2). There is a good fit of the prediction of the 5.6 Ω-m uniform resistivity structure to the observed amplitude at $\leq$1,500 m separation, but large misfits are found at >1,500 m separation. A two-layer model improves the fitting at >1,500 m separation (Fig. 19.2); the resistivity of the upper layer down to 1,500 m depth is 5.6 Ω-m, and that of the underlying half-space is 0.1 Ω-m.

19.4.2 Magnetic Field Anomalies and the Three-Dimensional Electrical Resistivity Structure

Magnetic field anomalies for the optimal two-layer 1-D resistivity structure are shown in Figs. 19.3 and 19.4. On the L1 line, the M3 receiver exhibits a positive anomaly (≤0.2 log T/A) at 1,500–2,200 m horizontal separation, and the M4 receiver shows a negative anomaly (≥−0.5 log T/A) at 1,500–2,500 m separation (Fig. 19.3). The M2 and M5 receivers exhibit small variations (≤0.1 log T/A in absolute value) (Fig. 19.3). The M1 receiver has different features on the four transmission lines of L2-5 (Fig. 19.4). Positive anomalies (≤0.3 log T/A) are found at approximately 1,000 m and at 1,800–2,200 m separation on the L3 line, at 1,000–1,500 m separation on the L5 line, at 1,000–1,700 m separation on the L2 line, and at 1,400–1,800 m separation on the L4 line.

A resulting optimal 3-D resistivity structure is shown in Fig. 19.5. The magnitude and variation of the observed magnetic field anomalies (Figs. 19.3 and 19.4) provided a good initial guess for the 3-D resistivity structure, particularly in cross-areas of pairs of the transmitter and the receiver. A remarkable anomaly related to the Snail site is a conductor (C1) immediately below the site. Two resistive anomalies (R1 and R2) extending along the ridge axis sandwich the C1 conductive anomaly. Three other conductive anomalies (C2-4) to the north and west of the Snail site are required by the data. The reliability of the size and distribution of the deduced 3-D anomalies depends on the spatial coverage of transmitter-receiver pairs. The C1-3 and R1 anomalies are well constrained by the data due to good coverage. In contrast, the C4 and R2 anomalies, especially their lengths in the y-axis (across the ridge axis), are not strongly constrained.

Fitting of the prediction of the 3-D resistivity model to the observation in magnetic field anomaly is shown in Figs. 19.6 and 19.7. The optimal 3-D resistivity model explains the M2-M5 receiver data on the L1 line and the M1 receiver data on the L3 line. The misfit is large near the M2 receiver on the L4 line (Fig 19.7). A conductor near the M2 receiver would generate a positive magnetic field anomaly that could improve the fit, and we examined the possibility of such a conductor. However, the conductors tested generate positive magnetic field anomalies not only on the L4 line but also on the L3 line. Predicted positive magnetic field anomalies on the L3 line near the M2 receiver were inconsistent with the observed anomaly, and consequently, we do not believe that a significant conductor exists near the M2 receiver.

The resistivity values used for the 3-D conductive and resistive anomalies in this study are only one pair, 0.56 and 56 Ω-m, and other resistivity values could explain the observation better. Even if there are better resistivity values, the optimal 3-D resistivity structure deduced in this study provides the general sense of the resistivity structure of

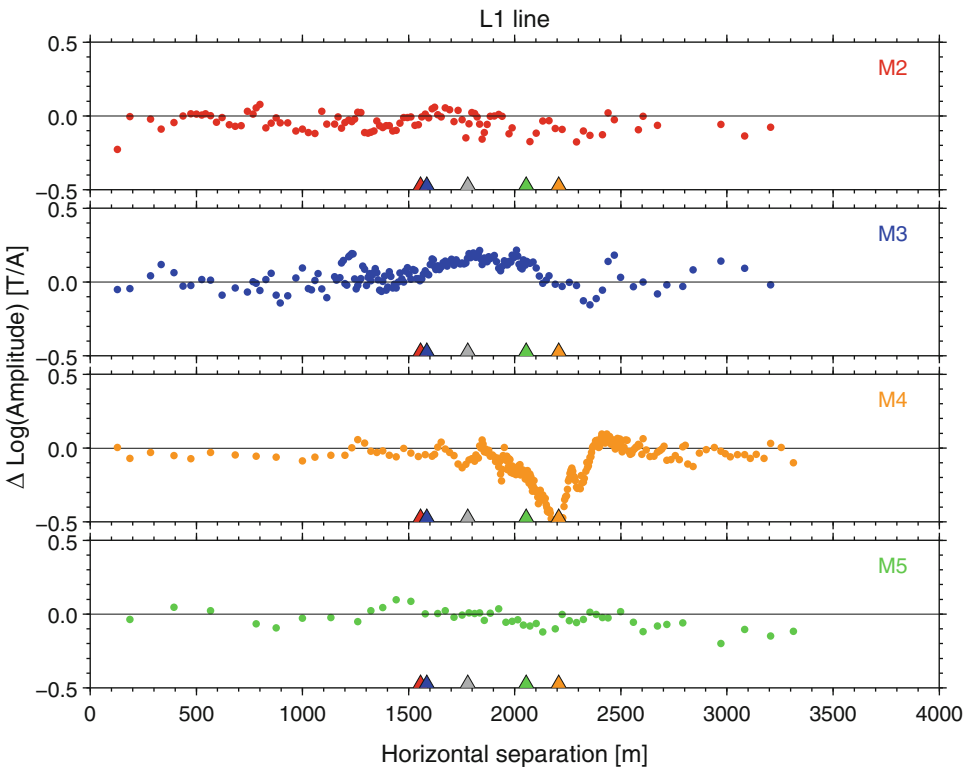

Fig. 19.3 Magnetic field anomalies observed at the M2-5 receivers for the L1 transmission line. The *horizontal axis* shows horizontal separations between the transmitter and the receiver along the L1 line. *Triangles* on the bottom of each panel represent receiver locations projected on the L1 line. The location of the M1 receiver, whose data are not plotted in the figure, is also shown by the *gray triangle* for reference. *Colors* are common for the magnetic field anomaly, the receiver name, and the receiver location

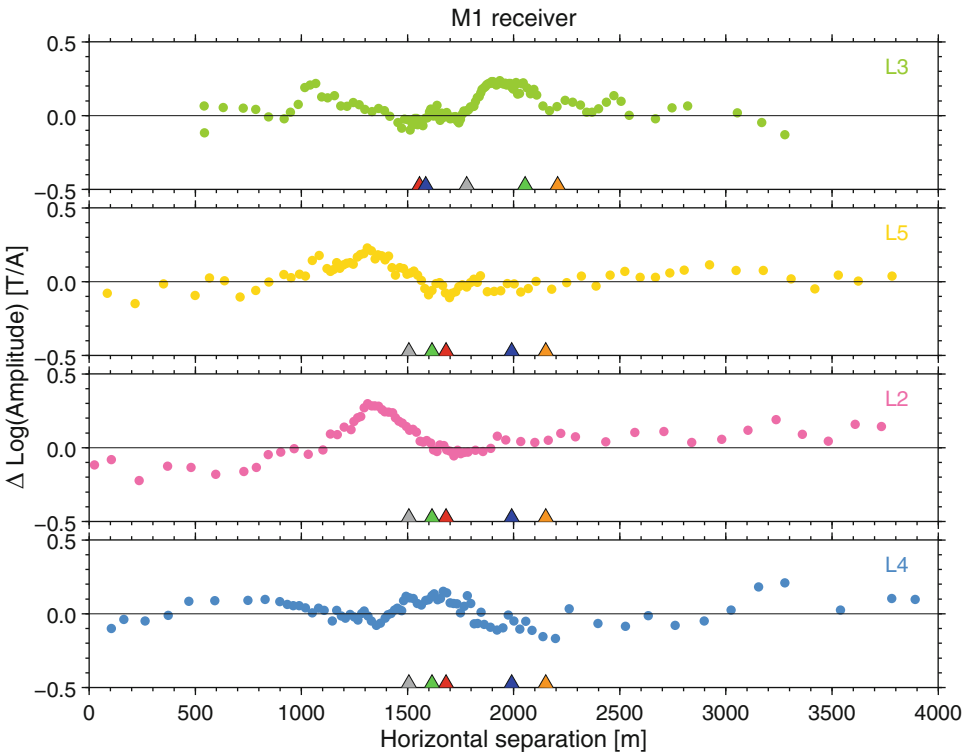

Fig. 19.4 Magnetic field anomalies observed at the M1 receiver from the L2-5 transmission lines. The *horizontal axis* shows horizontal separations between the transmitter and the receiver along each line. A *gray triangle* on the bottom of each panel denotes the location of the M1 receiver projected on each transmission line, and the other *color triangles* denote the locations of the other receivers (M2, *red*; M3, *blue*; M4, *orange*; M5, *light green*) for reference

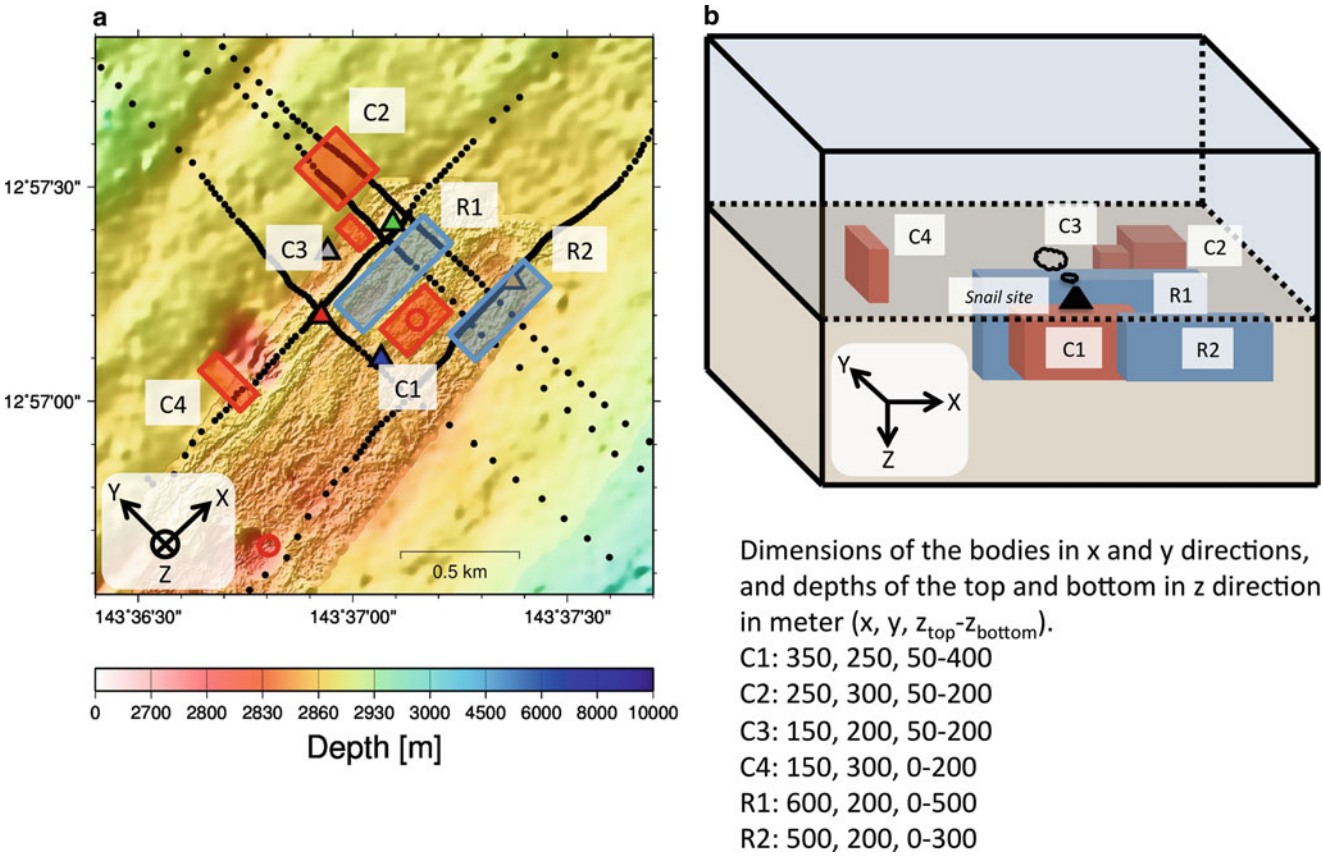

Fig. 19.5 (**a**) A plan view map of the optimal 3-D resistivity model overlain on the seafloor topography. *Red rectangles* represent conductive anomalies (0.56 Ω-m), and *blue rectangles* represent resistive anomalies (56 Ω-m). Locations of the known hydrothermal sites (*red circles*), the receivers (*colored triangles*), and the transmission points (*filled black circles*) are also shown. The Snail site is located near the center of the map. (**b**) A schematic illustration of the optimal 3-D resistivity model viewed from the southeast. The dimensions of the conductive and resistive anomalies are shown below the illustration

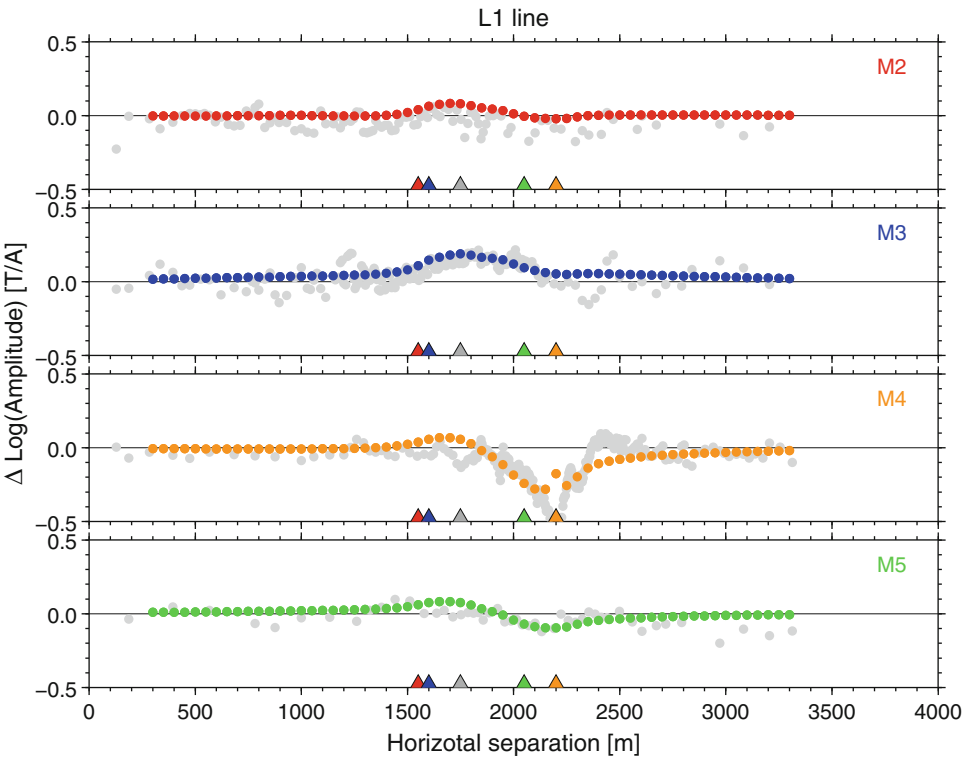

Fig. 19.6 Magnetic field anomalies observed and predicted from the optimal 3-D resistivity model (Fig. 19.5) for the M2-5 receivers on the L1 transmission line. *Colored circles* represent the predictions of the 3-D resistivity model, and *gray circles* behind the *color circles* represent the observation at each receiver. *Triangles* on the bottom of each panel represent locations of receivers projected on the transmission line. The location of the M1 receiver is also shown by *gray triangles* for reference

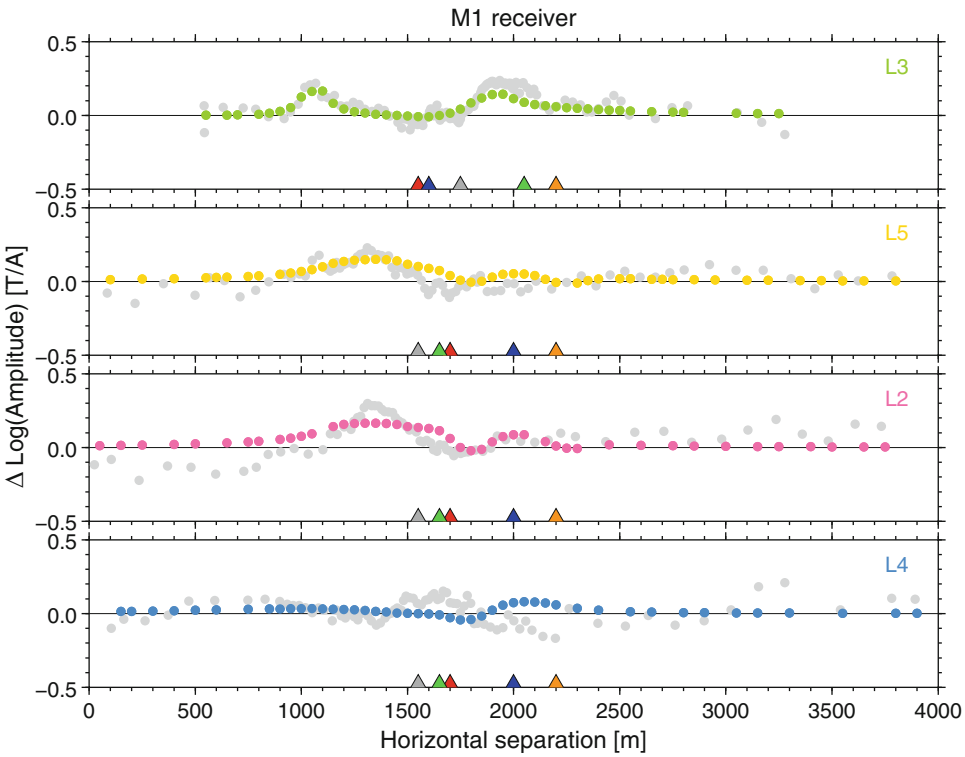

Fig. 19.7 Magnetic field anomalies observed and predicted from the optimal 3-D resistivity model (Fig. 19.5) for the M1 receiver on the L2-5 transmission line. *Colored circles* represent the predictions from the 3-D resistivity model, and gray circles represent the observation at the M1 receiver. *Gray triangles* on the bottom of each figure represent the location of the M1 receiver projected on each transmission line. The locations of the other receivers (M2, *red*; M3, *blue*; M4, *orange*; M5, *light green*) are also plotted for reference

the study area because the equivalency of conductance for different resistivities and different dimensions of a certain anomaly may be valid. As one example for the conductive body, a decrease in resistivity (i.e., the conductive anomaly becomes more conductive) can be compensated by a decrease in size.

19.5 Discussion

The optimal 1-D resistivity structure is the two-layered model (5.6 Ω-m down to 1,500 m depth and 0.1 Ω-m further below). The optimal 3-D resistivity structure exhibits several

lower and higher resistivity anomalies (0.56 and 56 Ω-m) than the basal 1-D resistivity structure at and around the Snail site (Fig. 19.5). The conductive anomaly of C1 is located immediately below the Snail site, and two resistive anomalies of R1 and R2 border the C1 anomaly and extend along the ridge axis. Three other conductive anomalies of C2-4 exist away from the Snail site.

Any resistivity value between 0.56 and 56 Ω-m in the 1-D and 3-D resistivity models is too low to represent the resistivity of basaltic upper oceanic crust without a conductive fluid at geothermal temperature (e.g., Drury and Hyndman 1979). The bulk resistivity of the oceanic crust, including the conductive fluid, has been reasonably explained by Archie's law (Archie 1942)

$$\rho_m/\rho_f = \Phi^{-t} \tag{19.1}$$

where ρ_m is the bulk resistivity of a host (the crust), ρ_f is the resistivity of conductive fluid in the host, Φ is the porosity of the host, and t is a free exponent that has been proven and considered to depend on the interconnected form of the conductive fluid in the host (e.g., Sen et al. 1981; Mendelson and Cohen 1982). The resistivity of the conductive fluid in the oceanic crust changes with temperature, and an empirical relation between ρ_f and fluid temperature, T, is introduced by

$$T = 0.34/\rho_f^2 + 4.2/\rho_f - 16 \tag{19.2}$$

at 2–350 °C after the study of Nesbitt (1993).

Archie's law with the thermal dependence of the resistivity of fluid involves three variables (fluid temperature, porosity, free exponent: T, Φ, t) and one observation (bulk resistivity: ρ_m). A possible range of fluid temperature is supposed to be 2–350 °C. A porosity profile from Evans et al. (1998) is used for the porosity, which is a simplified profile of a DSDP ocean drilling at Hole 504B at the Costa Rica Rift of Becker (1989) (Fig. 19.8a). In the profile, the porosity is 17 % in the top 200 m layer, decreases linearly to 2 % at 200–800 m depth, and is a constant 2 % down to 1,500 m depth (Fig. 19.8a). The porosity of the oceanic crust of the study area could be higher than this profile because less compression is expected for a younger oceanic crust (the seafloor age of the study area is almost 0 Ma, while that of Hole 504B is approximately 6 Ma (Becker 1985)). We consider a hypothetical porosity profile for the newborn seafloor of the study area by assuming that 34 ± 16 %

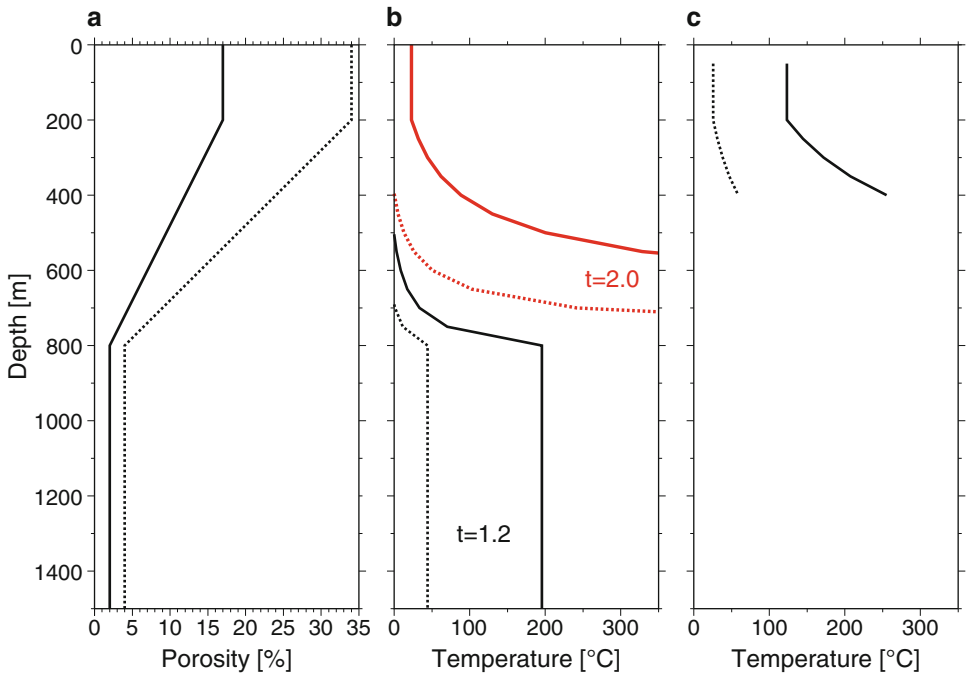

Fig. 19.8 (**a**) A porosity profile of the oceanic crust from Evans et al. (1998) (*solid line*) and a hypothetical profile of the doubled porosity (*dotted line*). (**b**) Profiles of fluid temperature within the crust for the resistivity of 5.6 Ω-m for the optimal 1-D resistivity structure. *Solid lines* represent estimations with the porosity profile from Evans et al. (1998), and *dotted lines* represent estimations with the hypothetical doubled porosity profile. *Black and red colors* show estimations with two exponents of 1.2 and 2.0 in Archie's law, respectively. (**c**) Profiles of fluid temperature within the crust for the conductive anomaly, 0.56 Ω-m. A solid line represents an estimation with the porosity profile from Evans et al. (1998), and a *dotted line* represents an estimation with the hypothetical doubled porosity profile. The exponent in Archie's law is 1.2. The profiles are shown only at depths ranging from 50 to 400 m, which is the depth range of the conductive anomaly

porosity, which was estimated from outcrop rock samples at the northern Gorda Ridge (Pruis and Johnson 2002), is a plausible porosity for the uppermost crust. The hypothetical profile is just double of the porosity profile from Evans et al. (1998), and the highest porosity of the hypothetical profile is 34 % in the uppermost layer (Fig 19.8a).

To determine a t value in Archie's law, two representative exponents of 1.2 and 2.0 are examined, which were extensively used in prior studies (e.g., Becker 1985; Evans 1994). In general, a larger t implies a less interconnected conductive fluid network through the rock (e.g., Evans 1994). With $\rho_m = 5.6$ Ω-m (the optimal 1-D resistivity structure) and the porosity profile from Evans et al. (1998), the fluid temperature for $t = 1.2$ is negative, and that for $t = 2.0$ is less than 200 °C down to 500 m depth (Fig. 19.8b). Below 500 m depth, the fluid temperature for $t = 1.2$ is less than 200 °C and that for $t = 2.0$ is over 350 °C (Fig. 19.8b). With $\rho_m = 5.6$ Ω-m and the hypothetical porosity profile, the fluid temperatures for $t = 1.2$ and $t = 2.0$ both decrease, but the temperature for $t = 2.0$ results in over 350 °C below approximately 700 m depth (Fig. 19.8b). For the possible range of fluid temperatures (2–350 °C), $t = 1.2$ yields more reasonable fluid temperatures for the optimal 1-D resistivity structure than $t = 2.0$. We use $t = 1.2$ in further discussions.

The fluid temperature at depths ranging from 800 to 1,500 m is estimated to be at 44–200 °C (Fig. 19.8b). This temperature is likely supported by the data from the magnetic field amplitude (Fig. 19.2). A prediction of the magnetic field amplitude from a model in which 2 °C seawater was forced to exist at depths of 800–1,500 m (T = 2 °C line in Fig. 19.2) yields a different trend from the observation. The trend is especially different at ≥1,200 m horizontal separation, where the observed data are probably sensitive to the structure at depths of 800–1,500 m (Fig. 19.2). This result suggests that fluid estimated at 44–200 °C is not replaced by 2 °C seawater. Fluid at 44–200 °C and at depths of 800–1,500 m may represent a hydrothermal heating zone, one example of which was deduced at the East Pacific Rise (Tolstoy et al. 2008).

The resistivity of 0.1 Ω-m below 1,500 m depth in the optimal 1-D resistivity structure implies a magma mush under the spreading ridge, which is a heat source for the hydrothermal circulation at the Snail site. The resistivity of 0.1 Ω-m is proper for a basaltic silicic melt (≤1 Ω-m at ≥1,200 °C) (e.g., Tyburczy and Waff 1983). A low seismic velocity below 1,500 m depth on the ridge axis (Sato et al. Chap. 18) likely supports the presence of the heat source. Unfortunately, the conductive structure of 0.1 Ω-m is not reliable because the data for the long horizontal separation, which is sensitive to deeper structures, is sparse (Fig. 19.2).

The conductive anomaly of 0.56 Ω-m immediately below the Snail site (C1 in Fig. 19.5) is examined. The depth of the conductive anomaly is determined to be 50–400 m, and the fluid temperature for the conductive anomaly is estimated to be 120–260 °C for the lower porosity (17–12 %) and 26–59 °C for the higher porosity (34–24 %) at these depths (Fig. 19.8c). These fluid temperatures suggest that there is hydrothermal fluid related to the Snail site activity, although the estimation of temperature changes with porosity.

The two resistive anomalies of 56 Ω-m near the Snail site (R1 and R2 in Fig. 19.5) are examined. Assuming 2 °C seawater, the upper bound of porosity for the resistive anomalies is inferred to be 1 %. This low porosity suggests that these areas would not involve a lot of fluid, potentially because this area is massive and less fractured. The regions of high resistivity could act as barriers for across-axis hydrothermal circulation, leading to preferential along-axis circulation, similar to the observation at the East Pacific Rise (Tolstoy et al. 2008).

The conductive anomalies away from the Snail site (C2-4 in Fig. 19.5) are unlikely to be related to the hydrothermal circulation at the Snail site because of their distance from the Snail vents. There is no evidence for active vents near these conductive anomalies. The conductive anomalies are located in areas dominated by normal faulting (Yoshikawa et al. 2012; Asada et al. Chap. 20). Faulting of the oceanic crust prompts a local increase in permeability (Becker et al. 1994) and may result in high porosity and the conductive anomalies. Weak crustal magnetizations near the conductive anomalies (Seama et al. Chap. 17) could suggest relic hydrothermal systems and low porosity (and low resistivity) due to the presence of past hydrothermal paths.

19.6 Conclusion

We carried out an MMR experiment at the Snail site on the ridge axis of the Southern Mariana Trough, and deduced basal 1-D and detailed 3-D resistivity models of the oceanic crust under the Snail site. The 1-D resistivity model suggests that high-temperature fluid at 44–200 °C exists at depths of 800–1,500 m. The conductive structure below 1,500 m depth in the basal 1-D model implies a magma mush as a heat source for the hydrothermal circulation. The 3-D resistivity model contains a conductive anomaly immediately below the Snail site and two resistive anomalies adjacent to the conductive anomaly. The conductive anomaly immediately below the Snail site suggests the presence of hydrothermal fluid at 26–260 °C that is certainly related to the hydrothermal vent. The size and distribution of the conductive and the resistive anomalies at and around the Snail site give a constraint on the size of the hydrothermal circulation and imply that the circulation preferentially develops along the ridge axis rather than across the ridge axis.

Acknowledgement We thank the captain, the crews, and the scientific members (PI, Toshitsugu Yamazaki) of the KR03-13 cruise of *R/V Kairei* for their strong support to the MMR experiment. Participation of on-board and on-land scientists and marine technicians in the experiment is appreciated: Noriko Tada, Hisanori Iwamoto, Kazuya Kitada, Hitoshi Tanaka, Yutaka Matsuura, Yusuke Sato, Tamami Ueno, Tadanori Goto, and Masashi Shimoizumi. Noriko Tada and Shigenori Otsuka provided program codes for the data analysis, which they developed and improved. This study is partly supported by the scientific program of TAIGA (Trans-crustal Advection and In-situ reaction of Global sub-seafloor Aquifer) sponsored by the Ministry of Education, Culture, Sports, Science and Technology (MEXT) of Japan. Comments and English edit by the reviewers, Rob L. Evans and Yoshifumi Nogi, and editors, Jun-ichiro Ishibashi and Kyoko Okino, were very helpful to improve the manuscript. The GMT software (Wessel and Smith 1998) was used for creating figures. TM was supported by the NIPR project KP-7.

References

Archie GE (1942) The electrical resistivity log as an aid in determining some reservoir characteristics. J Petrol Technol 5:1–8

Becker K (1985) Large-scale electrical resistivity and bulk porosity of the oceanic crust, DSDP Hole 504B, Costa-Rica rift. Initial Rep Deep Sea Drill Proj 83:419–427

Becker K (1989) Measurements of the permeability of the sheeted dikes in Hole 504B. Proc Ocean Drill Program Sci Results 111:317–325

Becker K, Morin RH, Davis EE (1994) Permeabilities in the Middle Valley hydrothermal system measured with packer and flowmeter experiments. Proc Ocean Drill Program Sci Results 139:613–626

Becker NC, Fryer P, Moore GF (2010) Malaguana-Gadao Ridge: identification and implications of a magma chamber reflector in the southern Mariana Trough. Geochem Geophys Geosyst 11: Q04X13. doi:10.1029/2009GC002719

Drury MJ, Hyndman RD (1979) The electrical resistivity of oceanic basalts. J Geophys Res 84:4537–4545. doi:10.1029/JB084iB09p04537

Edwards RN, Law LK, DeLaurier JM (1981) On measuring the electrical conductivity of the oceanic crust by a modified magnetometric resistivity method. J Geophys Res 86:11609–11615. doi:10.1029/JB086iB12p11609

Evans RL (1994) Constraints on the large-scale porosity and permeability structure of young oceanic crust from velocity and resistivity data. Geophys J Int 119:869–879. doi:10.1111/j.1365-246X.1994.tb04023.x

Evans RL, Webb SC, Jegen M, Sananikone K (1998) Hydrothermal circulation at the Cleft-Vance overlapping spreading center: results of a magnetometric resistivity survey. J Geophys Res 103:12321–12338. doi:10.1029/98JB00599

Evans RL, Webb SC, Crawford W, Golden C, Key K, Lewis L, Miyano H, Roosen E, Doherty D, RIFT-UMC Team (2002) Crustal resistivity structure at 9°50′N on the East Pacific Rise: results of an electromagnetic survey. Geophys Res Lett 29(6):6-1-6-4. doi:10.1029/2001GL014106

Fryer P (1996) Evolution of the Mariana convergent plate margin system. Rev Geophys 34(1):89–125. doi:10.1029/95RG03476

Hussong DM, Uyeda S (1982) Tectonic processes and the history of the Mariana arc: a synthesis of the results of Deep Sea Drilling Project Leg 60. Initial Rep Deep Sea Drill Proj 60:909–929

Ishibashi J, Yamanaka T, Kimura H, Toki T, Noguchi T (2006) Time series change of fluid geochemistry in decade scale: case studies for hydrothermal systems in back-arc basin, Japan Geoscience Union, Annual Meeting Program with Abstract, Japan Geoscience Union, Tokyo, J161-014

Kakegawa T, Utsumi M, Marumo K (2008) Geochemistry of sulfide chimneys and basement pillow lavas at the southern Mariana Trough (12.55°N–12.58°N). Resource Geol 58(3):249–266. doi:10.1111/j.1751-3928.2008.00060.x

Kitada K, Seama N, Yamazaki T, Nogi Y, Suyehiro K (2006) Distinct regional differences in crustal thickness along the axis of the Mariana Trough, inferred from gravity anomalies. Geochem Geophys Geosyst 7(4), Q04011. doi:10.1029/2005GC001119

Martínez F, Fryer P, Becker N (2000) Geophysical characteristics of the southern Mariana Trough, 11°50′N–13°40′N. J Geophys Res 105 (B7):16591–16607. doi:10.1029/2000JB900117

Mendelson KS, Cohen MH (1982) The effects of grain anisotropy on the electrical properties of sedimentary rocks. Geophysics 47(2):257–263. doi:10.1190/1.1441332

Nesbitt BE (1993) Electrical resistivities of crustal fluids. J Geophys Res 98(B3):4301–4310. doi:10.1029/92JB02576

Nobes DC, Law LK, Edwards RN (1986) The determination of resistivity and porosity of the sediment and fractured basalt layers near the Juan de Fuca Ridge. Geophys J R Astr Soc 86(2):289–317. doi:10.1111/j.1365-246X.1986.tb03830.x

Nobes DC, Law LK, Edwards RN (1992) Results of a sea-floor electromagnetic survey over a sedimented hydrothermal area on the Juan de Fuca Ridge. Geophys J Int 110(2):333–346. doi:10.1111/j.1365-246X.1992.tb00878.x

Pruis MJ, Johnson HP (2002) Age dependent porosity of young upper oceanic crust: insights from seafloor gravity studies of recent volcanic eruptions. Geophys Res Lett 29(5):20-1-20-4. doi:10.1029/2001GL013977.

Seama N, Tada N, Goto T, Shimoizumi M (2013) A continuously towed vertical bipole source for marine magnetometric resistivity surveying. Earth Planets Space 65:883–891. doi:10.5047/eps.2013.03.007

Sen PN, Scala C, Cohen MH (1981) A self-similar model for sedimentary rocks with application to the dielectric constant of fused glass beads. Geophysics 46(5):781–795. doi:10.1190/1.1441215

Tada N, Seama N, Goto T, Kido M (2005) 1-D resistivity structures of the oceanic crust around the hydrothermal circulation system in the central Mariana Trough using Magnetometric Resistivity method. Earth Planets Space 57(7):673–677

Tada N, Kido M, Seama N (2011) Development of a 3-dimensional forward program for magnetometric resistivity method: application to Alice Springs field. Abstract for workshop on ocean mantle dynamics: from spreading center to subduction zone, Chiba, Japan

Tolstoy M, Waldhauser F, Bohnenstiehl DR, Weekly RT, Kim W-Y (2008) Seismic identification of along-axis hydrothermal flow on the East Pacific Rise. Nature 451:181–184. doi:10.1038/nature06424

Tyburczy JA, Waff HS (1983) Electrical conductivity of molten basalt and andesite to 25 kilobars pressure: geophysical significance and implications for charge transport and melt structure. J Geophys Res 88(B3):2413–2430. doi:10.1029/JB088iB03p02413

Urabe T, Ishibashi J, Maruyama A, Marumo K, Seama N, Utsumi M (2004), Discovery and drilling of on- and off-axis hydrothermal sites in backarc spreading center of southern Mariana Trough, western Pacific. Eos Trans AGU 85(47). Fall Meet. Suppl., Abstract V44A-03

Wessel P, Smith WHF (1998) New, improved version of the Generic Mapping Tools released. Eos Trans AGU 79:579

Wheat CG, Fryer P, Hulme SM, Becker NC, Curtis A, Moyer C (2003). Hydrothermal venting in the southern most portion of the Mariana backarc spreading center at 12.57 degrees N. Eos Trans AGU, 84 (46). Fall Meet. Suppl., Abstract T32A-0920

Yoshikawa S, Okino K, Asada M (2012) Geomorphological variations at hydrothermal sites in the southern Mariana Trough: relationship between hydrothermal activity and topographic characteristics. Mar Geol 303–306:172–182

Asymmetric Seafloor Spreading of the Southern Mariana Trough Back-Arc Basin

20

Nobukazu Seama and Kyoko Okino

Abstract

We compiled multi-narrow beam bathymetric data and geomagnetic field data obtained by a series of JAMSTEC research cruises in the Southern Mariana Trough back-arc basin, where is selected as one of three integrated target sites for the Japanese TAIGA Project. The bathymetric data are used to trace the non-transform offsets that define the ridge segments at the off-axis, and to characterize the seafloor morphology signatures from the bathymetry profiles across the spreading axes of two ridge segments. The geomagnetic field data are used to derive the crustal magnetization distribution and to estimate the spreading rate of the southern segment. Both of the spreading rate and the seafloor deepening rate of the southern segment support highly asymmetric seafloor spreading; much faster spreading in the west side of the spreading axis compared to the east side (trench side). We estimated the full spreading rate as 46 km/Myr with its half rate of 33 km/Myr for the west side and 13 km/Myr for the east side. In contrast to the southern segment, our results indicate that the northern segment has a different style of the asymmetric seafloor spreading; that is accompanied by an obvious trace of a ridge jump to the trench side. The local symmetry axis in the bathymetry profiles locates at a distance of 18 km to the west from the spreading axis, suggesting that it is the failed spreading axis due to the ridge jump. The location of this failed spreading axis coincides with the center of the bull's eye feature in the Mantle Bouguer anomaly, suggesting that the ridge jump to the trench side with an increase in the magma supply. We propose that the influence of the low viscosity region in the mantle wedge due to hydration driven by water release from the subducting slab leads to the highly asymmetric seafloor spreading; the low viscosity mantle would preferentially captures the mantle upwelling zone beneath the spreading axis as the spreading axis has been kept in the area closed to the low viscosity region in the mantle wedge, resulting in the highly asymmetric seafloor spreading. Further, the different styles of the asymmetric seafloor spreading between the northern segment and the southern segment probably show evidence that the influence varies with the distance from the low viscosity region in the mantle wedge.

Keywords

Asymmetric seafloor spreading • Back-arc basin • Bathymetry • Geomagnetic anomaly field • Mantle Bouguer anomaly • Ridge jump

N. Seama (✉)
Department of Earth and Planetary Sciences,
Kobe University, 1-1 Rokkodai, Nada, Kobe 657-8501, Japan
e-mail: seama@kobe-u.ac.jp

K. Okino
Atmosphere and Ocean Research Institute, The University of Tokyo,
5-1-5 Kashiwanoha, Kashiwa, Chiba 277-8564, Japan

20.1 Introduction

The Mariana Trough is a current active back-arc basin with crescent-shaped (Fig. 20.1). Repeated GPS surveys in the Mariana Islands show that the present spreading rates of the

J.-i. Ishibashi et al. (eds.), *Subseafloor Biosphere Linked to Hydrothermal Systems: TAIGA Concept*,
DOI 10.1007/978-4-431-54865-2_20,

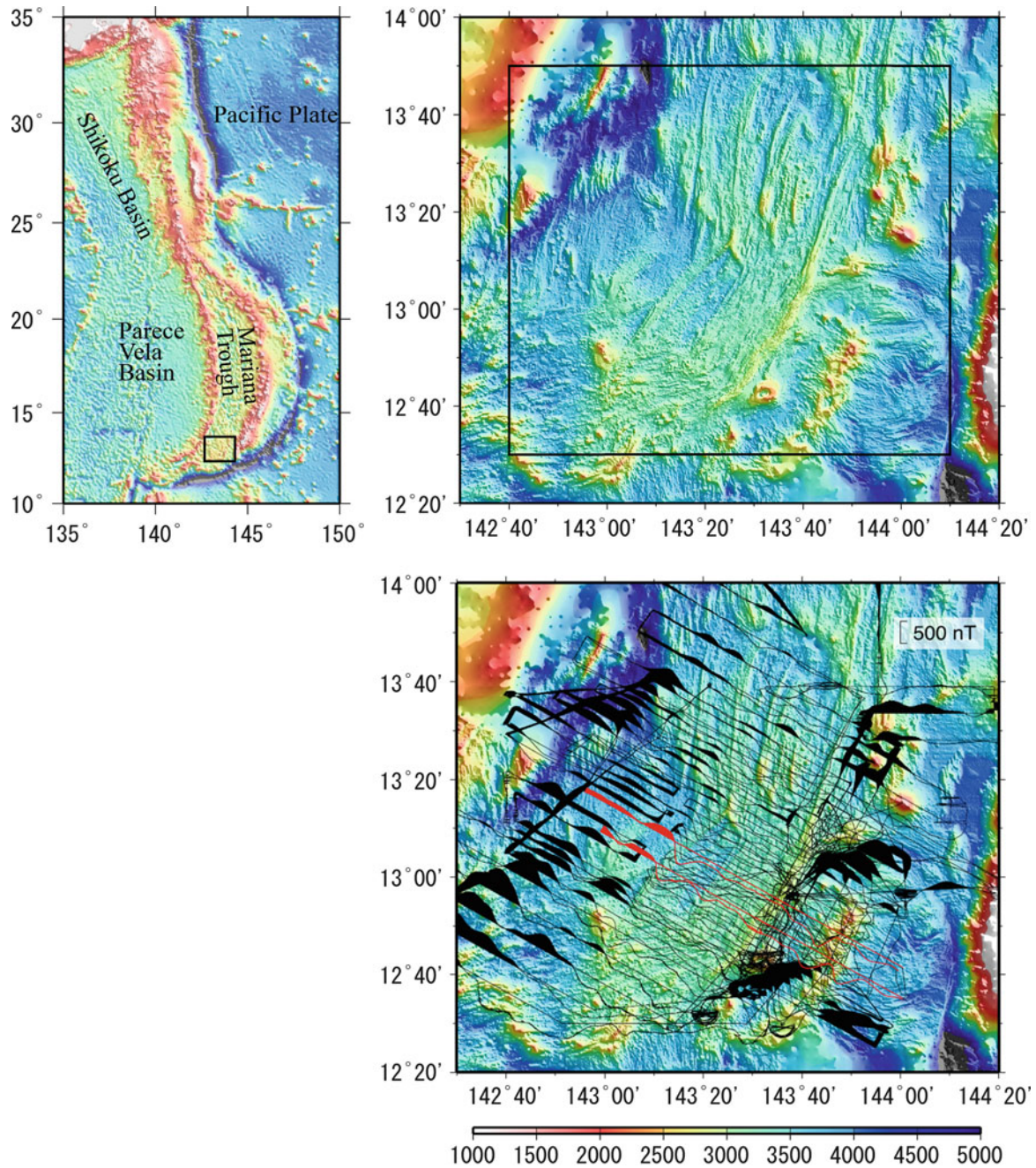

Fig. 20.1 Bathymetry map of the Southern Mariana Trough (*top right*) and its location shown by the *box* in the regional map (*top left*). The *box* in the bathymetry map indicates the location for Figs. 20.2 and 20.3. Profiles of the geomagnetic anomaly field along the ship's track (*bottom*). Positive values are *shaded*. The profiles shown by *red color* are used for a forward modeling to examine the isochrones identifications of the southern segment as shown in Fig. 20.4

Mariana Trough back-arc basin increase from the north to the south; the full spreading rates are 15.9 ± 6.6 km/Myr at 18.7°N and 44.6 ± 2.7 km/Myr at 13.6°N with its Euler pole position being to the south of the junction of the Mariana Arc and the West Mariana Ridge located near 23°N (Kato et al. 2003). The studies of the geomagnetic anomalies using the Matuyama-Brunhes boundary (0.78 Ma) reported the similarity in the spreading trend; the full spreading rates are 10 km/Myr at 22°N in the northern end (Yamazaki et al. 2003) and ~64 km/Myr in maximum at 13°N in the southern end (Martinez et al. 2000). These two different methods show that the full spreading rate of the Southern Mariana Trough back-arc basin ranges 45–64 km/Myr.

The Southern Mariana Trough back-arc basin (Fig. 20.1) has fast spreading morphologic and geophysical characteristics that are unlike the features of the basin to

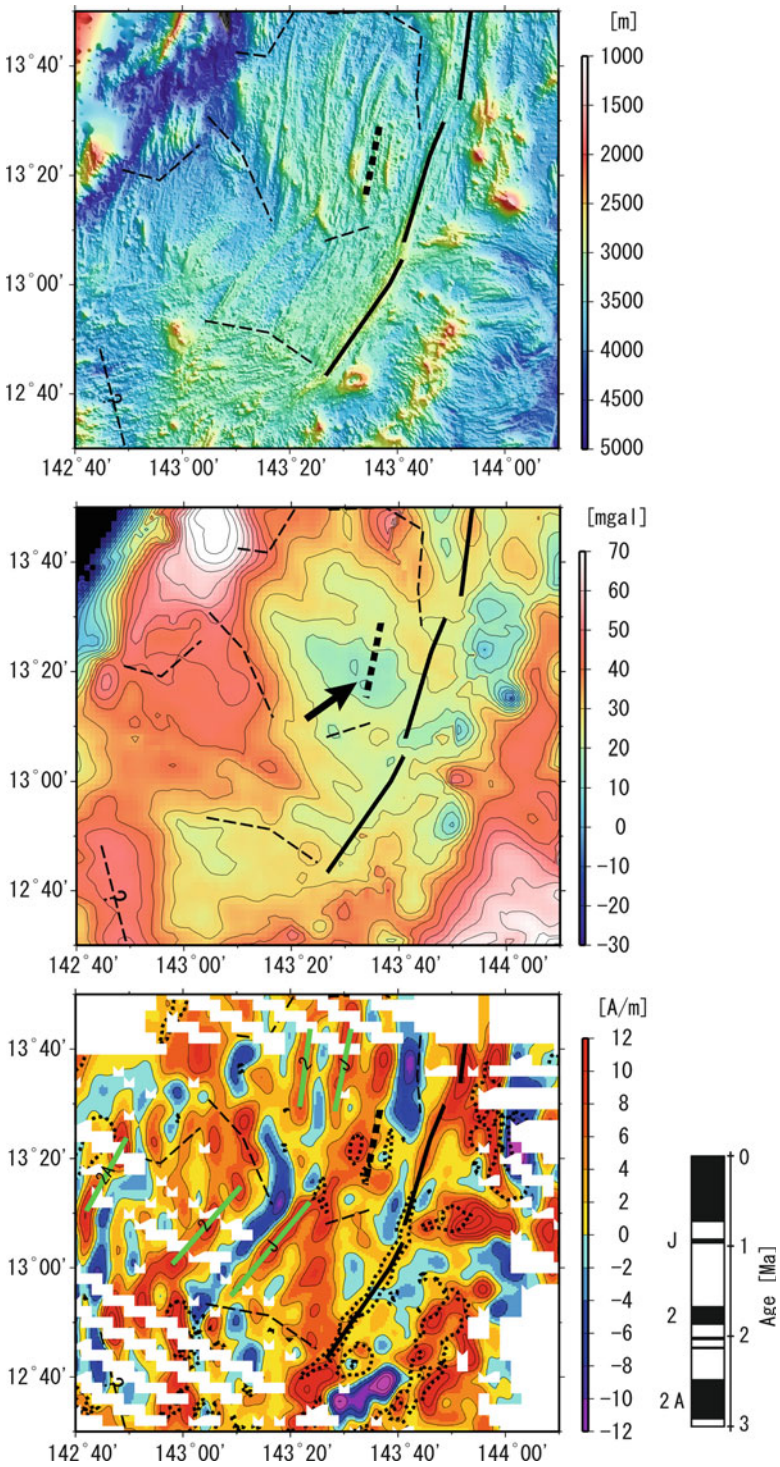

Fig. 20.2 Present spreading axis (*solid lines*), failed spreading axis (*thick broken lines*), and non-transform offset traces determined from seafloor morphology (*thin broken lines*) shown in the bathymetry map (*top*), the Mantle Bouguer anomaly map (*middle*), and the distribution of the crustal magnetization derived from the total geomagnetic anomaly field data (*bottom*). The *arrow* in the middle figure shows the bull's eye feature, in the center of which the failed spreading axis locates. In the bottom figure, our identifications of the geomagnetic anomaly lineations (*green lines* with its geomagnetic anomaly number) and bathymetry contours of 3,000 m depth (dots) are also shown

the north (Martinez et al. 2000), despite the full spreading rate of 45–64 km/Myr being categorized as slow spreading. The morphology of the spreading axis shows an axial relief with a broad, smooth cross section, and lacks a deep central graben (Martinez et al. 2000). The crustal thickness variation along the spreading axis that was estimated using the Mantle Bouguer anomalies shows higher individual crustal thickness averages (5.9–6.9 km) and smaller normalized variations in crustal thickness (28–30 m/km), suggesting a sheetlike mantle upwelling with a relatively higher magmatic activity beneath the ridge segments (Kitada et al. 2006). Further, the seismic reflection data show a possible magma chamber reflector beneath the spreading axis (Becker et al. 2010). All these morphologic and geophysical

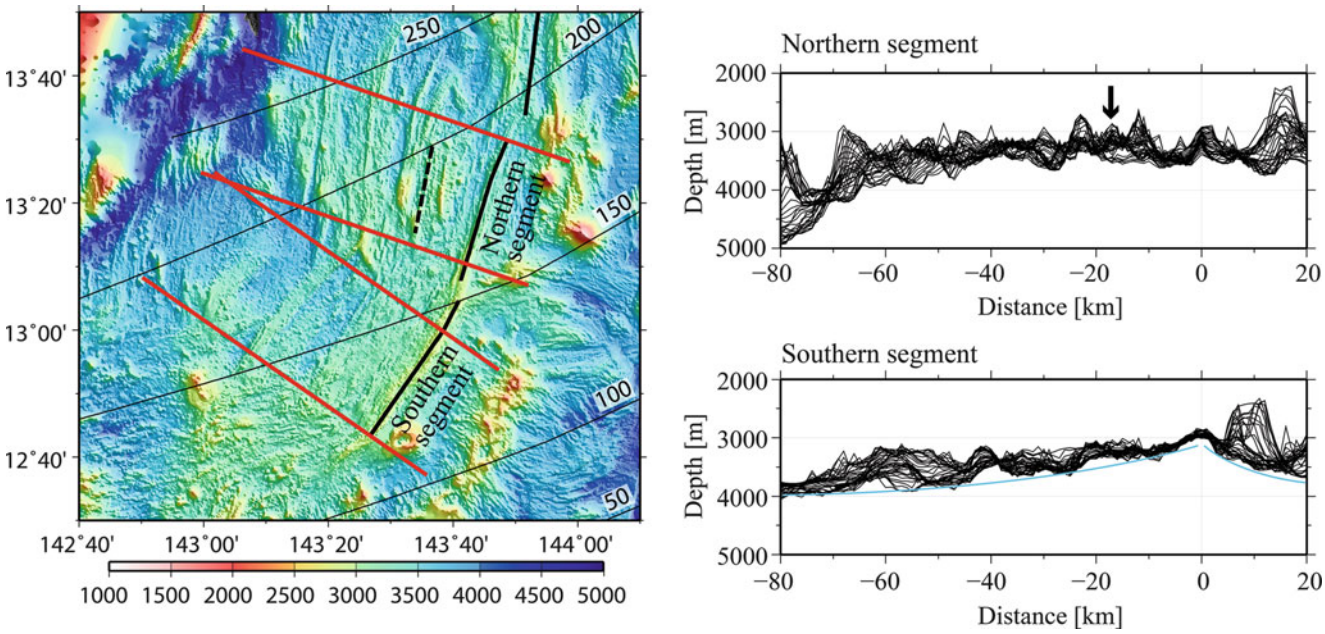

Fig. 20.3 Bathymetry profiles across the spreading axes of the northern segment (*right top*) and the southern segment (*right bottom*). Each bathymetry profile is located between the *two red lines* of each segment in the *left figure*, and it is taken parallel to the *red lines* with interval of 1 km. The distance is shown from the spreading axis and the positive value is to the east. The *arrow* in the northern segment bathymetry profiles shows the symmetry axis of the bathymetry profiles. This symmetry is local within a distance of 10 km with respect to the symmetry axis, but this local symmetry axis is similar in the bathymetric feature to a spreading axis, suggesting that it is the failed spreading axis. The *blue lines* in the southern segment bathymetry profiles show the trends of the water depth changes, which indicate high asymmetry in the seafloor deepening rate as much slower seafloor deepening rate in the west side of the spreading axis compared to the east side. In the *left figure*, the present spreading axis (*solid lines*), failed spreading axis (*broken lines*), and depth contours to the surface of the subducting slab (*thin solid lines* with their depth in km) inferred from a seismic research (Gudmundsson and Sambridge 1998) are also shown

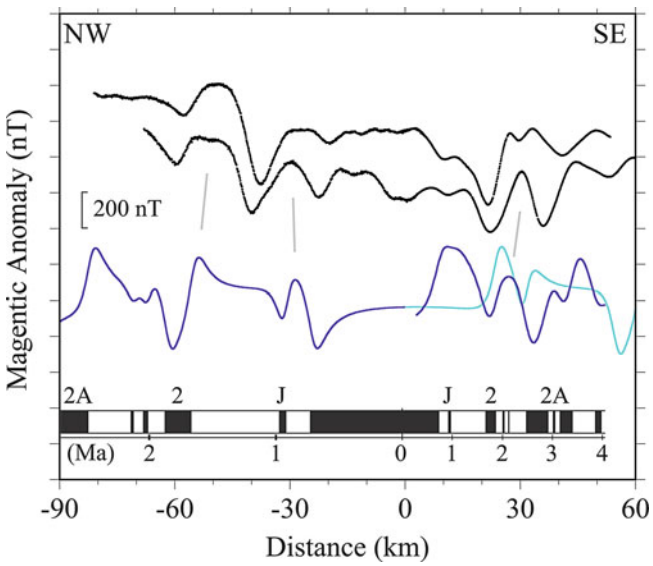

Fig. 20.4 Comparison between observed and calculated geomagnetic anomaly field profiles across the spreading axis of the southern segment. The location of the observed geomagnetic anomaly field profiles (*black*) are shown by *red color* in Fig. 20.1. The calculated geomagnetic anomaly field profiles are based on a forward modeling with its half spreading rates of 33 km/Myr for the west side (*blue*), 13 km/Myr for the east side (*blue*), 33 km/Myr for the east side (*light blue*). The geomagnetic polarity model for the blue profiles is also shown. See text on the forward modeling in detail

features of the Southern Mariana Trough back-arc basin show fast spreading characteristics, suggesting the abundant magma supply, even though the full spreading rate is categorized as slow spreading.

The Japanese TAIGA Project (Urabe, Chap. 1) selected the Southern Mariana Trough back-arc basin as one of three integrated target sites (Seama et al. Chap. 17), and series of JAMSTEC research cruises were conducted by the Japanese research vessel, S/V Yokosuka as well as the Shinkai 6500 submersible operations in this area. Surface geophysical surveys allow us to collect multi-narrow beam bathymetry and geomagnetic field data along with GPS navigation during YK99-11, YK09-08, YK10-10, and YK10-15 cruises, and to characterize tectonic features of the Southern Mariana Trough back-arc basin. Multi-narrow beam bathymetric data were obtained using a SeaBeam 2112 (Swath width 150°; 150 beams with its width and interval of 2°and 1°, respectively). Geomagnetic field data were collected with a ship-towed proton precession magnetometer that measures the intensity of the geomagnetic field. We could cover an approximately 150×150 km area with a nominal 4–11 km track spacing (Fig. 20.1).

In this paper, we first analyze the multi-narrow beam bathymetric data and geomagnetic field data to characterize two ridge segments of the Southern Mariana Trough back-

arc basin. Then, we show different styles of the asymmetric seafloor spreading between the two ridge segments. Finally, we discuss a possible cause for the asymmetric seafloor spreading with relation to the subducting slab.

20.2 Data Analysis and Result

We compiled all the multi-narrow beam bathymetric data to be gridded at 0.1 min spacing using the surface algorithm of Smith and Wessel (1990) with a tension of 0.35. The prediction bathymetry data (Smith and Sandwell 1997) were also used for the outside area surveyed. Then, we traced the non-transform offsets that define the ridge segments at the off-axis using the seafloor morphology signature; ends of lineaments parallel to the spreading axis, commonly troughs, and/or isolated basins (Fig. 20.2). Two major ridge segments are recognized in the Southern Mariana Trough back-arc basin (we call the northern segment and the southern segment here after as shown in Fig. 20.3). We stacked the bathymetry profiles across the spreading axes of the two segments (Fig. 20.3). Each bathymetry profile was obtained from the gridded bathymetry data between the two red lines of each segment in Fig. 20.3, and it is taken parallel to the red lines with interval of 1 km. The results of the bathymetry profiles show different features between the southern segment and the northern segment. The southern segment bathymetry profiles indicate that the shallowest water depth locates at the spreading axis and that the water depth increases as the distance from the spreading axis increases (blue lines in Fig. 20.3) like the age-depth profiles (Parsons and Sclater 1977) except local seamounts. But the seafloor deepening rate shows high asymmetry as much slower seafloor deepening rate in the west side of the spreading axis compared to the east side. The northern segment bathymetry profiles indicate a peak at the spreading axis, but also show symmetric with respect to a point at a distance of 18 km to the west from the spreading axis (arrow in Fig. 20.3). This symmetry is local within a distance of 10 km with respect to the point, but this local symmetry axis (the point) is similar in the bathymetric feature to a spreading axis.

Geomagnetic anomaly field was calculated by subtracting the 11th Generation International Geomagnetic Reference Field (IGRF11; Finlay et al. 2010) from the total intensity geomagnetic field data. We needed to add some values to correct biases depending on which year the data were obtained by examining the geomagnetic anomaly field data at cross over points of the ship's tracks. The biases are probably due to the imperfection of the geomagnetic reference field in the area surveyed. The geomagnetic anomaly field profiles along the ship's tracks are shown in Fig. 20.1.

The geomagnetic anomaly field was inverted for the crustal magnetization. We used the three-dimensional Fourier inversion approach of Parker and Huestis (1974), which also takes into account the effect of bathymetry. The input grid data set was prepared as following. The geomagnetic anomaly field data were gridded at 0.4 min spacing with 256 × 256 points using the surface algorithm of Smith and Wessel (1990) with a tension of 0.25. The bathymetry data were also gridded in a manner similar to geomagnetic data but with a tension of 0.35. The magnetization solution was band-pass filtered with its passband between 5 and 80 km after an each iteration of the calculation to ensure convergence of the inversion solution. The main assumptions of the inversion method are; (1) the magnetization is constant with depth and varies only in the horizontal dimension, (2) the magnetization direction is fixed in the direction of the geocentric axial dipole, and (3) the source region is a magnetized layer of constant thickness (1 km for this study) whose upper boundary is defined by the bathymetry (Fig. 20.2). Inversion for crustal magnetization is an inherently non-unique process. One measure of this non-uniqueness is the annihilator, which is a magnetization that produces no external magnetic field. An infinite amount of annihilator can be added or subtracted from the inversion solution without affecting the resultant magnetic field. We added the annihilator for the magnetization at the present spreading axis to be positive. The computed magnetization result is shown in Fig. 20.2.

We have identified the major isochrones with the crustal magnetization distribution using the polarity timescale of Cande and Kent (1995) (Fig. 20.2), and we examined the isochrones identifications of the southern segment using a forward modeling of the geomagnetic anomaly field. In the forward modeling, we assumed a 1 km thick magnetized layer with its upper depth of 3.5 km. The magnetization of 10 A/m is based on a square wave function constructed with the geomagnetic polarity by Cande and Kent (1995). We changed spreading rates manually to fit the synthetic geomagnetic anomaly with observed one. We applied this method to two profiles of the geomagnetic anomaly field across the spreading axis of the southern segment, which are shown by red color in Fig. 20.1. We obtained a model to reasonably fit observed ones (Fig. 20.4) and confirmed our isochrones identifications of the crustal magnetization distribution (Fig. 20.2). The model allows us to estimate the full spreading rate as 46 km/Myr with its half rate of 33 km/Myr for the west side and 13 km/Myr for the east side. We did not apply this method to the northern segment, because of its specific situation; the northern segment area is near the geomagnetic equator and the strike of magnetic source is expected to be north–south, which is nearly parallel to the present spreading axis. In this situation, the total intensity of the geomagnetic anomaly has almost no signal from the magnetic source and only three-dimensional effect such as bathymetry helps to derive the signal. Thus, the crustal

magnetization distribution calculated by the three-dimensional inversion approach is an only way to identify the geomagnetic anomaly for the northern segment.

20.3 Discussions

Our estimation of the spreading rates based on the geomagnetic anomaly field data shows highly asymmetric seafloor spreading of the southern segment; much faster spreading in the west side of the spreading axis compared to the east side (Fig. 20.4). The bathymetry profiles across the spreading axis of the southern segment also support this highly asymmetric seafloor spreading; the seafloor deepening rate from the spreading axis show high asymmetry as much slower seafloor deepening rate in the west side of the spreading axis compared to the east side (blue lines in Fig. 20.3). We estimated the full spreading rate of 46 km/Myr with its half rate of 33 km/Myr for the west side and 13 km/Myr for the east side, which are based on the crustal magnetization distribution and the forward modeling of the geomagnetic anomaly field. These half spreading rates are also supported by the bathymetry profiles of the spreading axis (Fig. 20.3), because the water depths at both the sides of the spreading axis become the same when the crustal ages inferred from these half spreading rates are the same; both the water depths are about 3,500 m at 1 Ma crustal age with the distance of 33 km to the west and of 13 km to the east side from the spreading axis. Further, the full rate of 46 km/Myr is consistent with the present full spreading rate of 44.6 ± 2.7 km/Myr at 13.6°N based on the repeated GPS surveys (Kato et al. 2003), although the full spreading rate from the geomagnetic anomaly field data is not necessary to be congruent with the present full spreading rate, because it is an average of the full spreading rate for the time scale of the geomagnetic polarity change.

The northern segment shows different features in contrast to the southern segment, and we propose that the northern segment of the spreading axis has a different style of the asymmetric seafloor spreading; that is accompanied by an obvious trace of a ridge jump to the east (trench side). The obvious trace of the ridge jump is supported by the bathymetry profiles across the spreading axis (Fig. 20.3), the Mantle Bouguer anomalies (MBA) based on Kitada et al. (2006), and the distribution of the crustal magnetization derived from the total intensity of the geomagnetic anomaly field data (Fig. 20.2). A local symmetry axis in the bathymetry profiles, which locates at distance of 18 km to the west from the spreading axis, is probably the failed spreading axis due to the ridge jump because the local symmetry axis is similar in the bathymetric feature to a spreading axis. This failed spreading axis is also supported by the MBA because its location coincides with the center of the bull's eye feature in the MBA (arrow in Fig. 20.2), which is often found at ridge segments of slow spreading axes (e.g. Lin et al. 1990). The fact that the bull's eye feature still remains suggests that the ridge jump occurred recently. The crustal magnetization distribution also supports the ridge jump, because the ridge jump can explain the existence of the negative magnetization lineation between the present spreading axis and the failed spreading axis. We interpret that the negative magnetization lineation is Matuyama Chron (before 0.78 Ma) made by the failed spreading axis in its east side and that the ridge jump occurred during the Brunhes Chron (after 0.78 Ma). If the negative magnetization lineation would be made by the present spreading axis without the ridge jump, the half spreading rate would be 5 km/Myr in maximum (the distance from the present spreading axis to the Matuyama-Brunhes boundary is 4 km in maximum), which is too slow spreading rate to be consistent with other data. Our interpretation that the ridge jump occurred during the Brunhes Chron is consistent with the recent ridge jump suggested by the fact that the bull's eye feature still remains. The ridge jump results in the apparent asymmetric seafloor spreading of the northern segment. We have calculated the average half spreading rate for the west side of the north segment and it becomes 27 km/Myr using the distance of 48 km from the present spreading axis to the geomagnetic anomaly isochron 2 (Fig. 20.2). This apparent half spreading rate that includes the ridge jump is slightly slower than 33 km/Myr, the half spreading rate for the west side of the southern segments, but it still shows the apparent asymmetric seafloor spreading if the full spreading rate is 46 km/Myr. It is difficult to estimate the half spreading rate for the east side because some seamounts probably due to the arc volcanism reset and/or mask the original seafloor magnetization as suggested by the positive magnetization distribution with shallow water depth (Fig. 20.2).

Both of the northern and the southern segments show highly asymmetric seafloor spreading, but their styles are different; the northern segment of the spreading axis is accompanied by the obvious trace of the ridge jump to the east (trench side), while the southern segment is not. As a characteristic feature in the northern segment, the seafloor spreading shows a difference between the present spreading axis and the failed spreading axis; the present spreading axis shows fast spreading morphologic and geophysical characteristics (Martinez et al. 2000; Kitada et al. 2006; Becker et al. 2010), but the failed spreading axis shows slow spreading geophysical characteristics of the bull's eye feature in the MBA. Since the full spreading rate of 46 km/Myr is categorized as slow spreading, the failed spreading axis is normal and the present spreading axis should receive the additional magma supply, suggesting that the ridge jump to the trench side with an increase in the magma supply. In contrast, the southern segment shows the asymmetric

seafloor spreading without accompanied by an obvious trace of a ridge jump. Two possible mechanisms for the southern segment are; (1) series of much smaller ridge jumps than that of the northern segment without presenting their obvious traces and/or (2) the asymmetric manner of the crustal accretion itself. The bathymetry profiles (Fig. 20.3) might support the series of small ridge jumps without presenting their obvious traces because the seafloor deepening rate in the west side of the spreading axis does not seem to be constant, but we think further evidence is required to support this.

We propose that an influence of the low viscosity region in the mantle wedge leads the highly asymmetric seafloor spreading, and that the different styles of the asymmetric seafloor spreading show evidence that the influence varies with the distance from the low viscosity region. Several authors suggested the low viscosity mantle in the mantle wedge due to hydration driven by water release from the subducting slab (e.g. Dunn and Martinez 2011). The dehydration from the subducting slab at the depths of 110 km and 170 km leads to arc volcanic chains in subduction zone (e.g. Tatsumi and Eggins 1995), and it also leads to the low viscosity region in the mantle wedge with low yield strength due to effect of water and melt generation for the arc volcanic chains. Since the spreading axis can always be located at the weak arc area with the low viscosity and yield strength in the mantle wedge as suggested by numerical simulation results (Nakakuki and Mura 2013), we suggested that the low viscosity mantle preferentially captures the mantle upwelling zone beneath the spreading axis, which would lead to the highly asymmetric seafloor spreading; the spreading axis has been kept in the area closed to the low viscosity region in the mantle wedge. The influence of the low viscosity region probably varies with the distance from the low viscosity region as Martinez and Taylor (2002) proposed that the spreading center varies with the distance from the arc volcanic front. Although the present arc volcanic chains of the Southern Mariana Trough back-arc basin are not clear and the low viscosity region has not been imaged, the depths to the surface of the subducting slab (we call the slab depth here after) is a suitable indicator for the arc volcanic chains and the low viscosity region, because the slab depth beneath arc volcanic chains in subduction zone is expected to be 110–170 km (e.g. Tatsumi and Eggins 1995). The shape of the subducting slab beneath the Southern Mariana Trough back-arc basin inferred from a seismic research (Gudmundsson and Sambridge 1998), indicates that the subducting slab is oblique to the spreading axis (Fig. 20.3) up to 14.5°N where it is divided by a near-vertical tear in the slab striking approximately E–W (Miller et al. 2006). The slab depth beneath the spreading axis becomes shallower from the north to the south; 160–190 km depth for the northern segment and 120–150 km depth for the southern segment. The morphology of the spreading axis shows narrow cross section of the axial relief in the northern segment while broader cross section in the southern segment (Fig. 20.1), indicating an increase in the magma supply as the slab depth becomes shallower from the north to the south. Furthermore, the ridge jump in the northern segment to the trench side, closer to the mantle wedge, results in the increase in the magma supply as its characteristic features change from the bull's eye feature in the MBA to the axial relief morphology. The failed spreading axis locates above the relatively deeper slab depth and is probably away from the low viscosity region. This ridge jump closer to the mantle wedge with the increase in the magma supply suggests that the mantle upwelling zone that is captured by the low viscosity region in the mantle wedge leads to the ridge jump. In contrast, the spreading axis of the southern segment is closer to the mantle wedge and is probably underlain by the low viscosity region, because the slab depth beneath the spreading axis is 120–150 km that is where the arc volcanic chains are expected to be located. Then, the mantle upwelling zone captured by the low viscosity region probably provides the additional magma to support the broader axial relief, and results in the asymmetric seafloor spreading without accompanies by an obvious trace of a ridge jump. Thus, the different styles of the asymmetric seafloor spreading between the northern segment and the southern segment probably show evidence that the influence varies with the slab depth, which is well related to the distance from the low viscosity region. The transition between the northern segment and the southern segment is not abrupt as suggested at the Lau back-arc basin (Dunn and Martinez 2011), possible because the shape and the size of the low viscosity region of the Southern Mariana Trough back-arc basin are different from those of the Lau back-arc basin due to the differences in the spreading rate and the obliqueness of the subducting slab to the spreading axis. The Southern Mariana Trough back-arc basin shows the slower spreading rate and higher obliqueness of the subducting slab compared to the Lau back-arc basin.

20.4 Conclusion

Our analysis based on the bathymetry, the geomagnetic anomaly field, and the Mantle Bouguer anomaly, suggests highly asymmetric seafloor spreading in the Southern Mariana Trough back-arc basin; much faster spreading in the west side of the spreading axis compared to the east side (trench side). But the style of asymmetric seafloor spreading is different between the northern segment and the southern segment; the northern segment is accompanied by the obvious trace of the ridge jump to the trench side with the increase in the magma supply, while the southern segment

is not. We propose that the influence of the low viscosity region in the mantle wedge due to hydration driven by water release from the subducting slab leads to the highly asymmetric seafloor spreading; the low viscosity mantle would preferentially captures the mantle upwelling zone beneath the spreading axis as the spreading axis has been kept nearly in the area expected to the arc volcanic chains and closed to the low viscosity region, resulting in the highly asymmetric seafloor spreading. Further, the different styles of the asymmetric seafloor spreading between the northern segment and the southern segment probably show evidence that the influence varies with the slab depth, which is well related to the distance from the low viscosity region in the mantle wedge.

Acknowledgments We thank all who assisted in the collection of the geophysical data during the YK99-11, YK09-08, YK10-10, and YK10-15 JAMSTEC (Japan Agency for Marine-Earth Science and Technology) research cruises by the Japanese research vessel, S/V Yokosuka. This work is supported by the Ministry of Education, Culture, Sports, Science and Technology (MEXT) of Japan for the TAIGA project, Grant-in-Aid for Scientific Research on Innovative Areas (20109002). Two anonymous reviewers provided helpful comments. Kumiko Okumura drew some figures and helped to prepare the manuscript. GMT software (Wessel and Smith 1998) was used to create the bathymetry map of the survey area.

References

Becker NC, Fryer P, Moore GF (2010) Malaguana-Gadao Ridge: identification and implications of a magma chamber reflector in the southern Mariana Trough. Geochem Geophys Geosyst 11: Q04X13. doi:10.1029/2009GC002719

Cande SC, Kent DV (1995) Revised calibration of the geomagnetic polarity timescale for the late Cretaceous and Cenozoic. J Geophys Res 100:6093–6095

Dunn RA, Martinez F (2011) Contrasting crustal production and rapid mantle transitions beneath back-arc ridges. Nature 469:198–202

Finlay CC, Maus S, Beggan CD, Hamoudi M, Lowes FJ, Olsen N, Thébault E (2010) Evaluation of candidate geomagnetic field models for IGRF-11. Earth Planets Space 62(10):787–804. doi:10.5047/eps.2010.11.005

Gudmundsson O, Sambridge M (1998) A regionalized upper mantle (RUM) seismic model. J Geophys Res 103(B4):7121–7136

Kato T, Beavan J, Matsushima T, Kotake Y, Camacho JT, Nakao S (2003) Geodetic evidence of back-arc spreading in the Mariana Trough. Geophys Res Lett 30(12):1625. doi:10.1029/2002GL016757

Kitada K, Seama N, Yamazaki T, Nogi Y, Suyehiro K (2006) Distinct regional differences in crustal thickness along the axis of the Mariana Trough, inferred from gravity anomalies. Geochem Geophys Geosyst 7, Q04011. doi:10.1029/2005GC001119

Lin J, Purdy GM, Schouten H, Sempéré J-C, Zervas C (1990) Evidence from gravity data for focused magmatic accretion along the Mid-Atlantic Ridge. Nature 344:627–632

Martinez F, Fryer P, Becker N (2000) Geophysical characteristics of the southern Mariana Trough, 11°50′N–13°40′N. J Geophys Res 105:16591–16607

Martinez F, Taylor B (2002) Mantle wedge control onback-arc crustal accretion. Nature 416:417–420

Miller MS, Gorbatov A, Kennett BLN (2006) Three-dimensional visualization of a near-vertical slab tear beneath the southern Mariana arc. Geochem Geophys Geosyst 7:Q06012. doi:10.1029/2005GC001110

Nakakuki T, Mura E (2013) Dynamics of slab rollback and induced back-arc basin formation. Earth Planet Sci Lett 361:287–297. doi:10.1016/j.epsl.2012.10.031

Parker RL, Huestis SP (1974) The inversion of magnetic anomalies in the presence of topography. J Geophys Res 79:1587–1593

Parsons B, Sclater JG (1977) An analysis of the variation of ocean floor bathymetry and heat flow with age. J Geophys Res 82:803–827. doi:10.1029/JB082i005p00803

Smith WHF, Wessel P (1990) Gridding with continuous curvature splines in tension. Geophysics 55(3):293–305

Smith WHF, Sandwell DT (1997) Global seafloor topography from satellite altimetry and ship depth soundings. Science 277:1956–1962

Tatsumi Y, Eggins S (1995) Subduction zone magmatism. Blackwell, Boston

Wessel P, Smith WHF (1998) New, improved version of the Generic Mapping Tools released. EOS Trans Am Geophys Un 79:579

Yamazaki T, Seama N, Okino K, Kitada K, Joshima M, Oda H, Naka J (2003) Spreading process of the northern Mariana Trough: rifting-spreading transition at 22°N. Geochem Geophys Geosyst 4(9):1075. doi:10.1029/2002GC000492

Geochemical Characteristics of Active Backarc Basin Volcanism at the Southern End of the Mariana Trough

21

Harue Masuda and Patricia Fryer

Abstract

Major and minor chemistry, Sr, Nd and Pb isotope ratios, water content and hydrogen isotope ratios of the backarc basin volcanic rocks taken from the active spreading ridge and surrounding area between 12°40′N and 13°15′N in the southern part of the Mariana Trough indicate a complex regional interplay of suprasubduction-zone magmatic sources.

In this area, active backarc spreading occurs along the eastern side of the Mariana Trough, and discrete seamounts align on two parallel chains east of the backarc spreading center. The spreading-center rocks originated from a typical mid-ocean ridge basalt (MORB)-like source, influenced progressively southwestward by proximity to the arc magmatic source and range from basaltic to dacitic in composition. The volcanic rocks from the seamount chains are explained by the mixing of two types of magmatic sources; one is originally a depleted mantle similar to the arc source for magmas farther north and the other is the MORB-like source of the spreading ridge rocks. The influence of the arc source on magma composition of the seamount chains is higher north of 13°N, indicating heterogeneity of the mantle wedge in this region and the merging of the two sources toward the southwest.

Keywords

Arc volcanisms • Back arc spreading • Hydrogen isotopes • Major and minor element chemistry • Mariana Trough • Submarine volcanoes

21.1 Introduction

As an active subduction factory, where the formation of arc/continental and oceanic crust can be observed, the Mariana convergent plate margin is one of the best documented intraoceanic subduction systems. The backarc spreading forming the Mariana Trough occurs in arc crust that has been thinned by extension related to subduction and roll-back of the Pacific Plate (Karig 1971; Hussong and Uyeda 1981). Because contamination by arc/continental crust and subducting sediments is minimal in this intraoceanic setting, the Mariana Trough is an ideal location to study material cycling and its relation to magmatism in a convergent margin.

Early petrological and geochemical studies of backarc basin rocks of the Mariana Trough concentrated on the central part of the basin at about 18°N, where the backarc basin is widest (e.g., Hart et al. 1972; Hawkins 1977; Fryer et al. 1981; Natland and Tarney 1981; Hawkins et al. 1990). Subsequent studies extended to the northern area between 19° and 24°N, where the active backarc opening terminates where the active Mariana ridge and remnant West Mariana ridge meet (e.g., Jackson 1989; Stern et al. 1990; Hickey-Vargas 1991). These were followed by studies of the southern area, between 18° and 15°N (Gribble et al. 1996). Documentation

The online version of this chapter (doi:10.1007/978-4-431-54865-2_21) contains supplementary material, which is available to authorized users.

H. Masuda (✉)
Department of Geosciences, Osaka City University, 3-3-138, Sugimoto, Sumiyoshi-ku, Osaka 558-8585, Japan
e-mail: harue@sci.osaka-cu.ac.jp

P. Fryer
Hawaii Institute of Geophysics and Planetology, University of Hawaii, 1608, East–west Road, Post 504Honolulu, HI 96822, USA

J.-i. Ishibashi et al. (eds.), *Subseafloor Biosphere Linked to Hydrothermal Systems: TAIGA Concept*,
DOI 10.1007/978-4-431-54865-2_21, © The Author(s) 2015

of the southern Mariana Trough also started in the 1990s (e.g., Johnson et al. 1993; Fryer et al. 1998). A synthesis effort to characterize the arc and backarc composition of the Mariana system on a regional basis as relates to tectonic history of the arc was presented in Pearce et al. (2005).

In this chapter, the geochemical features of the volcanic rocks from the backarc spreading center and discrete chains of volcanoes in the Mariana Trough south of 13°40′N are characterized based on major and trace elements and isotopic compositions. Our data provides a more detailed look at a part of the backarc basin that is different both morphologically and compositionally from the rest of the basin and that lies in a part of the basin influenced by unusual tectonic processes. We discuss the initiation process of backarc opening in this area in relation to the fluids responsible for the magmagenesis and the local tectonic processes.

21.2 Geological Background and Sampling Locations

21.2.1 Bathymetry and Tectonic Setting

The backarc opening of the Mariana Trough has been presumed to have started between the active Mariana and remnant West Mariana arcs at between 5 and 10 Ma from the center of the trough (Hussong and Uyeda 1981; Karig 1971; Bibee et al. 1980; Eguchi 1984; Yamazaki and Stern 1997; Seama et al. 2001). The opening of the northern area was suggested to have started between 2.5 and 3.5 Ma from ~22°N and propagated northward (Yamazaki et al. 1993; Martinez et al. 1995).

The Mariana backarc spreading center between 14° to 22°N shows generally well-developed rift valley morphology, typical of slow spreading centers such as the Mid-Atlantic Ridge (MAR). The southern Trough area south of 14°N (Fig. 21.1) is topographically different from the rest of the basin. The area is generally shallower by about 1 km. Early explanations for such shallow seafloor included diffuse spreading (Hawkins 1977; Smoot 1990), but detailed mapping and sonar imaging (Martinez et al. 2000) led to the discovery that a well-organized spreading center, the Malaguana-Gadau Ridge (MGR hereafter, and in Fig. 21.1). The MGR is located well to the eastern side of the basin and has the typical morphology of fast spreading oceanic ridges like the East Pacific Rise (EPR) (i.e., Kasahara et al. 1994; Fryer et al. 1998) (Fig. 21.1). Such a fast-spreading-ridge morphology formed via higher magmatic activity in this part of the basin than elsewhere (Martinez et al. 2000). Gravity anomaly surveys supported this interpretation; the crust of this area is about 5.9–6.9 km thick, thicker than that of other areas of Mariana Trough (Kitada et al. 2006).

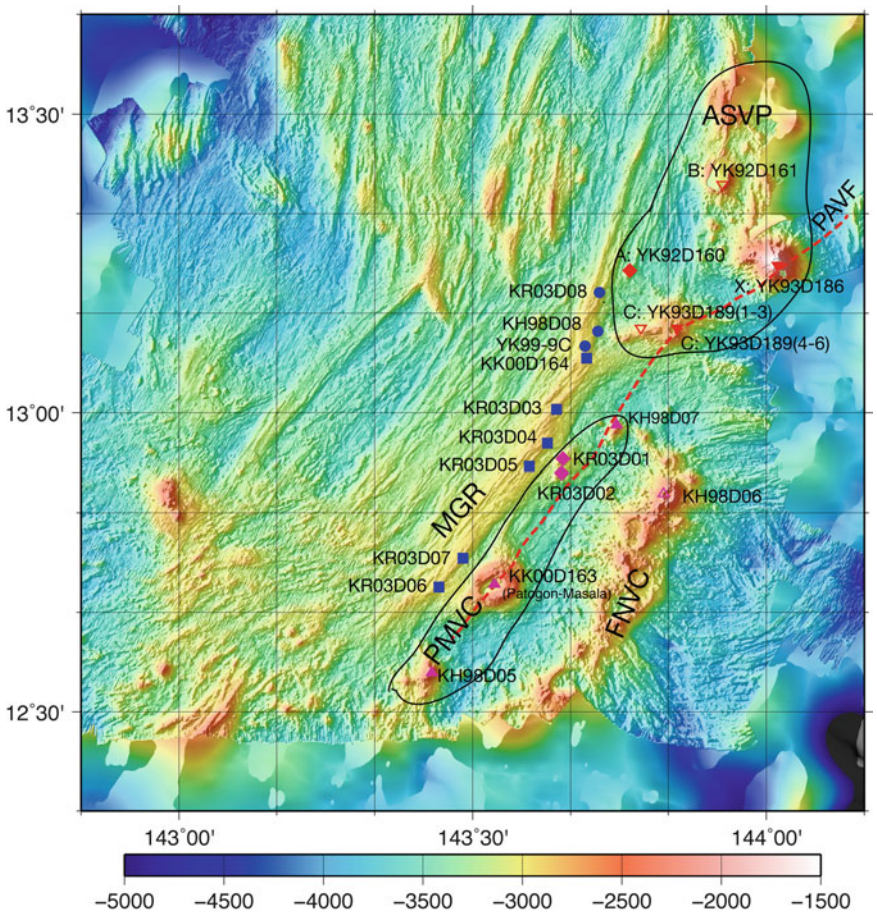

Fig. 21.1 Studied area and locations of rock sampling MGR: active spreading ridge; *Red dotted lines*: Discrete seamount chains (DSC) (PMVC and FNVC indicate west and east lines respectively); *symbols* indicating sample locations categorize the geology and sediments as follows. *Blue circle*: northern segment of MGR; *blue square*: southern segment of MGR; *red and purple diamonds*: off-ridge axis seamount; *red reverse triangle*: northern segment of DSC; *purple normal triangle*: southern segment of DSC

In the southern part of Mariana Trough, opening of the backarc basin was presumably accommodated by stretching of the Mariana forearc associated with accretion of basaltic intrusion/eruption at 3.7–2.7 Ma. This was recently confirmed at the Southeast Mariana Forearc Rift (Ribeiro et al. 2013a), and spreading was presumed to have started 3–3.5 Ma. The spreading center is suggested to have jumped to the present position from 20 km west (Seama et al. 2001). The volcanic activity of the current spreading center was activated during Brunhes Chron (0.7 Ma to present) (Martinez et al. 2000; Seama et al. 2001). Although the ridge shows the EPR-type spreading ridge topography and the spreading rate is higher in the southern Trough than farther north, the rate is still not as great as the EPR. Estimates range <60 to 40–45 mm/year based on magnetic anomalies (Martinez et al. 2000) and ~45 mm/year at 13°N estimated by GPS measurement at Guam (Kato et al. 2003).

Based on submersible and ROV observations, volcanic activity in the northern half of the MGR from 13°12′N seemed to be quiescent at present, since all the sites observed were thinly covered with sediments and only inactive hydrothermal fields were observed. Although much of the MGR south of 13°12′N is volcanically active, the most active area is between 13°05′ and 13°12′N (Mitsuzawa et al. 2000). It is notable that a magma chamber was found by seismic reflection data beneath the spreading ridge at 13°05′N (Becker et al. 2010).

Discrete small seamounts are aligned as two chains in the east and almost parallel to the trend of MGR. The southernmost arc volcano of the Mariana volcanic front was defined to be Tracey seamount at 13°40′N, just northwest of Guam, until these volcanic chains were reported by Fryer et al. (1998). They suggested that the discrete small seamounts, connecting seamounts X, C, KH98D07, and Patgon-Masala (KK00D163) (Line PAVF (presumed volcanic front) in Fig. 21.1), were a continuation of the volcanic front. Small volcanic cones on the east side of the northern half of the MGR were suggested to be formed by diffuse extension of the Mariana Trough (Alphabet Seamount Volcano Province, ASVP in Fig. 21.1, Stern et al. (2013)). Most of the seamounts in between the MGR and PAVF have conical shapes, however, two seamounts (C and Patgon-Masala) have central calderas. The caldera of Patgon-Masala is called TOTO (Gamo et al. 2004). A chain of seamounts having calderas is located in the southeast of our study area (Fina Nagu Volcanic Chain (FNVC), Stern et al. (2013)). The FNVC was reported as a remnant arc volcanoes, which were active before rifting of the southern part of Mariana Trough had started (Becker 2005; Ribeiro et al. 2013b). We term the seamount chain closest to the southern part of MGR the Patgon-Masala Volcanic Chain (PMVC) (Fig. 21.1). Three small seamounts (A: Seamount A (YK92D160), KR03D01 and KR03D02) are included in the ASVP or PMVC, whereas those are categorized as off-ridge seamounts here. When the ASVP, FNVC and PMVC are categorized in the same group hereafter, discrete seamount chains (DSC) will be used as the term indicating the locations.

Active hydrothermal venting was found in many sites along the MGR and in some places on the DSC. A white smoker (>270 °C) was first discovered on the slope of Seamount B (Johnson et al. 1993; Gamo and The Shipboard Scientific Party of the Y9204 cruise 1993), which was named "Forecast Vent" later (Gamo et al., 1997) Then low temperature hydrothermal venting was observed at Seamounts X and C. An active low-temperature hydrothermal area on the MGR was discovered at 12°55′N (Snail Site) (Embley et al. 2004) and observed with Jason 2 (Fryer et al. 2003). Active black smoker venting was found at the edge of southern MGR (Archaean Site) and at one of the off-axis seamounts (KR03D01, Pika Site) (e.g., Utsumi et al. 2004; Ishibashi et al. 2004, 2006; Yoshikawa et al. 2012). In the TOTO caldera of the largest seamount, Patgon-Masala at 12°42′N (KK00D163), white and clear smoker hydrothermal activity and biological communities were found (e.g., Mitsuzawa et al. 2000; Masuda et al. 1993; Gamo et al. 2004).

21.2.2 Sampling Locations of the Volcanic Rocks

The studied rocks were dredged during cruises Hakuho, 1998 (KH98-1 Leg2), and Kairei, 2003 (KR03-11), sampled by using submersible, SHINKAI 6500 in 1992 (YK92-04) and 1993 (YK93-03), and ROV KAIKO in 2000 (KR00-03) (see sampling locations in Fig. 21.1). The rocks from the DSC were taken from 11 sites (ten seamounts) and those of the MGR were taken from nine locations (see Table 21.1 for locations and geologic settings).

21.3 Analytical Methods

In this study, the major and minor elements were measured by X-ray fluorescence photometry (XRF). Quenched glass fragments were picked from the sample surface for the analyses, however, bulk rock samples were also used for XRF analysis when not enough glass could be obtained. Water was extracted from the glass samples by thermal decrepitation in vacuo to determine water content and hydrogen isotope ratios. For the selected glass samples, concentrations of minor and rare earth elements were analyzed by induction-coupled plasma mass spectrometry (ICP-MS) and the isotopes of Pb, Sr and Nd were analyzed by thermal ionization mass spectrometry (TIMS). Detailed procedures are described in the supplementary information (Analytical_Procedures).

Table 21.1 Sampling locations of studied rocks taken from the southern Mariana Trough area

Geologic settings (Segment)	Latitude	Longitude	Remarks[a]
Name[b]			
Back-arc spreading ridge			
(Northern segment MGR)			
KR03D08	13°12′N	143°42′E	
KH98D08	13°08′N	143°42′E	
YK99-9C	13°07′N	143°41′E	
(Southern segment MGR)			
KK00D164	13°06′N	143°41′E	Aphyric obsidian.
KR03D03	13°02′N	143°39′E	
KR03D04	12°56′N	143°37′E	
KR03D05	12°55′N	143°35′E	
KR03D07	12°45′N	143°29′E	
KR03D06	12°43′N	143°27′E	
Off-ridge axis seamount			
(Near ASVP)			
YK92D160 (A)	13°15′N	143°45′E	#160-1,2: Ropy lava on the bottom surface of back-arc basin.
YK92D160 (A)	13°15′N	143°45′E	#160-3-8: Pillow lava from the slope of the seamount.
(Near PMVC)			
KR03D01	12°55′N	143°38′E	
KR03D02	12°54′N	143°38′E	Aphyric obsidian.
Discrete chain seamounts			
(Northern segment)			
(Western chain ASVP)			
YK93D189 (C)	13°08′N	143°45′E	#189-1-3: Pillow lava on the slope of the seamount
YK93D189 (C)	13°08′N	143°50′E	#189-5,6: No quenched glass and bulk rock was analyzed.
(Eastern chain ASVP)			
YK92D161 (B)	13°25′N	143°55′E	
YK93D186 (X)	13°15′N	144°01′E	
(Sothern seamounts)			
(PMVC)			
KK00D163	12°42′N	143°32′E	Bulk rock was analyzed.
(Patgon-Masala)			
KH98D07	12°58′N	143°44′E	
KH98D05	12°33′N	143°25′E	
(FNVC)			
KH98D06	12°51′N	143°50′E	Titanomagnetite including zenolith was recovered with basalt.

[a]Quenched glass rim fragments were used for the analyses except where noted in remarks
[b]The name is the same as those shown in Fig. 21.1
Words in parentheses are the names of seamounts, which are used in the text instead of the site name

21.4 Results

21.4.1 Rock Observations

The rock samples studied are mostly basalt to andesite. Quenched glasses were recovered from most of the sampling sites. However, the rocks without quenched glass rims were obtained from inside the calderas at Seamount C (YK98D189 4–6), site KH98D06 (no name) and TOTO caldera (KK00D163). Aphyric glass was recovered from only two sites, at the center of the MGR (KK00D164) and at one of the off-axis seamounts (KR03D02). The dredged rocks from the latter site were dacitic obsidian.

Plagioclase and minor olivine phenocrysts are common in all of the rocks from the MGR. In addition to plagioclase and olivine, pyroxene occasionally forms phenocrysts in the rocks from the ASVP and PMVC; e.g., orthopyroxene was observed in rocks from Seamounts A and B (Yamatani et al., 1994), and those from the TOTO caldera, and clinopyroxene was observed in those from Seamount B (Yamatani et al. 1994). A gabbroic xenolith including a large amount of titanomagnetite was recovered in basalt from the bottom of the caldera at site KH98D07 (Fig. 21.1).

21.4.2 Major Element Chemical Composition

Analytical results of major and minor element compositions, water contents and δ^2H values are shown in supplementary data (Table 21-S-1). The rock chemistries of DSC are categorized into six groups corresponding to the location of the seamounts as noted above, thus those will be described according to this category; northern segment is abbreviated ASVP, according to the name "Alphabet Seamount Volcanic Chain (Stern et al. 2013), and the sampling sites are sub-grouped as off-ridge axis seamount (ASVP-OR), western seamounts (ASVP-W), and eastern seamounts (ASVP-E); southern segment is divided into two areas, PMVC and FNVC, and the PMVC is sub-divided into off-ridge axis seamounts (PMVC-OR) and western ridge (PMVC-W) (Figs. 21.1, 21.2, 21.3, 21.4, 21.5, 21.6, 21.7, and 21.8).

AFM composition of DSC rocks follows the tholeiite series, subparallel to the MORB trend, while most of the rocks from the MGR fall in the calk-alkaline field between tholeiite series rocks and the so-called "extreme backarc basin rocks" (XBABB) from the Manus Basin (Sinton et al. 2003) (Fig. 21.2). Relationships of major components to SiO_2 show two trends (Fig. 21.3). SiO_2 content of MGR rocks ranges from 53 to 63 %, whereas that of DSC rocks, except off-ridge axis seamounts (ASVP-OR and PMVC-OR), ranges from 51 to 56 %. Except for a few samples, the rocks from the MGR and those from the DSC comprise the two different trends of chemical variation relative to SiO_2 concentration. The rocks from the MGR generally show a roughly linear relationship with increasing SiO_2; e.g., Mg# (Mg/(Mg + Fe)) decreases and $Na_2O + K_2O$ increases with increasing SiO_2. Those linear correlations suggest fractional differentiation of the magma formed from the same source. Sinton et al. (2003) showed that essentially no enrichment of Fe occurred during progressive differentiation of the Manus Basin XBABB. The Fe concentration of rocks from the MGR show a clear negative trend with increasing silica content, suggesting similar controls over differentiation in our study area. Because the total Fe and CaO contents decrease with increasing SiO_2, olivine and anorthite crystallization-precipitation is the main factor affecting major element chemistry.

SiO_2 content of the rocks from ASVP-OR and PMVC-OR has a much broader range, from 49 % (Seamount A) to 68 % (dacitic obsidian from KR03D02), and some of those lie on the trend of those from the MGR. The rocks from the base of Seamount A (D#160-1-2, very close to the northern segment of the MGR) represent an end-member of the MGR composition, whereas the rocks from the upper flanks of this seamount are included in the field of the DSC rocks. Also, the plots of some rocks from MGR, such as KR03D06, give obvious similarity to those of DSC rocks, i.e., they have lower $Na_2O + K_2O$ and TiO_2 contents. The intersection of the MGR and DSC magmas indicates two types of magmatic processes occur in the same place.

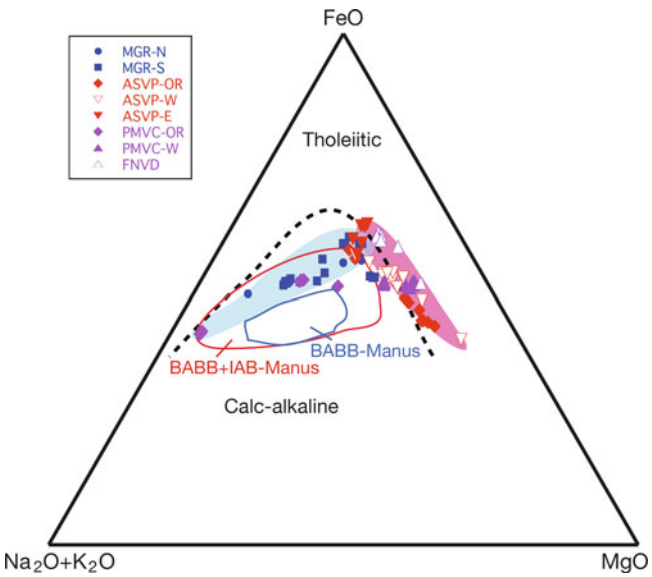

Fig. 21.2 AFM diagram of the submarine volcanic rocks from the southern Mariana Trough area. The boundary between tholeiitic and calc-alkaline rocks (*dashed line*) is after Irvine and Baragar (1971). *Symbols* indicate the sampling locations as in Fig. 21.1. The areas colored *pink* and *blue* are the fields of tholeiite series and BABB rocks

21.4.3 Minor Element Composition

Among the minor elements analyzed here, the relationships between Ti and V and La/Yb and Ba/La characterize two types of magmas in the studied area. The relationship between Ti and V (Fig. 21.4, concentrations are in Table 21.S-1) indicates the redox condition of mantle source regions for magmas and thus for tectonic settings (Shervais 1982). The Ti and V ratios of most of the rocks from the MGR are >20, and thus fall in the fields of backarc basin basalt (BABB), mid-ocean ridge basalt (MORB), and ocean island basalt (OIB). Those that fall in the latter area are highly differentiated MGR rocks. Most samples with SiO_2 content <55 %, including the lavas from the base of Seamount A, fall between Ti/V ratio of 25 and 30. The highly differentiated samples, including those from the TOTO caldera, have much higher ratios, which would reflect precipitation of minerals during differentiation, not the mantle source redox conditions.

Ti/V ratios of the DSC rock are generally <20, indicating the arc nature of these lavas. It is notable that the ranges of Ti/V ratio can be separated into two areas corresponding to the locations of seamounts; i.e., the rocks from the seamounts north from 13°N (ASVP-W and E) have Ti/V ratios between 18 and 22, and those from south (PMVC-W

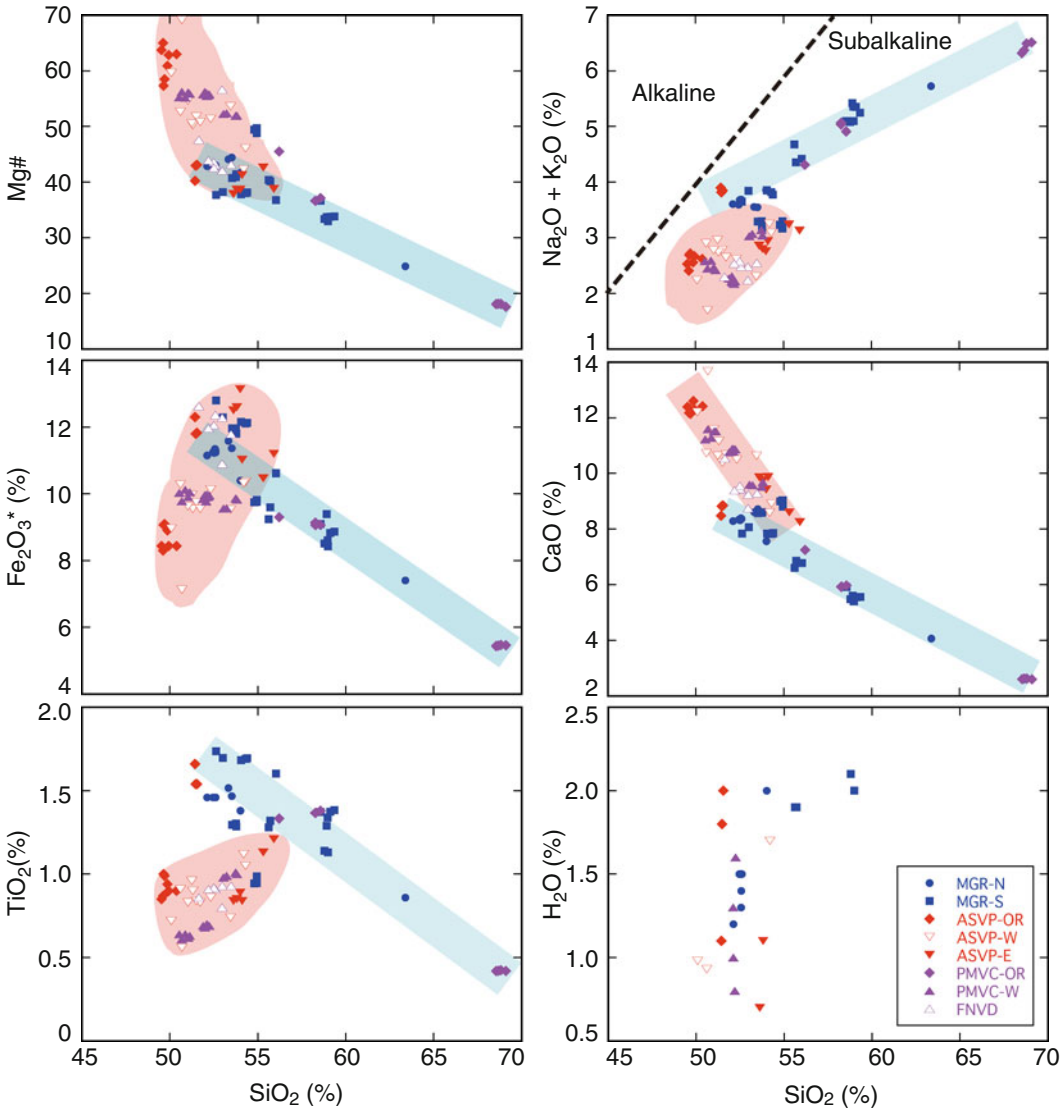

Fig. 21.3 Major element chemistry and water content vs. SiO_2 % of the submarine volcanic rocks from the southern Mariana Trough. The boundary between alkaline and subalkaline rocks (*dashed line*) in the SiO_2 vs. $Na_2O + K_2O$ is after Macdonald (1968). *Symbols* indicate the sampling locations as in Fig. 21.1. *Blue line* shows differentiated compositions of studied rocks mainly sampled from the MGR. The field colored *pink* gives the range of the other group of rocks, probably derived by mixing of n-MORB and depleted mantle source magmas

and FNVC) are between 13 and 15. The rocks from two sites on the MGR (KR03-D06 and D03) also fall within the same area as those from the ASVP. The values of rocks from PMVC-W and FNVC are almost the same as those of Tracey Seamount, the southernmost large arc volcano (Stern et al. 2013). Thus, the source magma of the rocks from the DSC, especially those from the southern DSC, is arc-like rather than BABB-like, based on this figure.

Ba/La vs. (La/Yb)n (Fig. 21.5) is widely used as an indicator of aqueous fluid contribution from source magmas (e.g., McCulloch and Gamble 1991; Hawkesworth et al. 1993). The most primitive rocks of the study area, which have the lowest SiO_2 concentrations, are from the MGR and have the ranges of Ba/La vs. (La/Yb)n ratios closest to that of MORB. It is notable that one of the end-members of the DSC rocks is almost the same as the most primitive rocks of the MGR. The Ba/La and (La/Yb)n ratios of DSC rocks vary in two different trends from the above end-member. Ba concentration of the rocks from ASVP-W and E lie at nearly constant (La/Yb)n values toward the end-member of metazomatized mantle, whereas the rocks from PMVC and FNVC lie at nearly constant Ba/La values.

Minor element compositions including rare earth elements (REE) of selected samples after normalizing with normal MORB (n-MORB) are given in Table 21.S-2 and shown in Fig. 21.6. Among the minor elements, Rb, Ba, Th, U, Pb, and Sr are enriched and Nb is depleted in the studied rocks, indicating that the elements derived from lithosphere

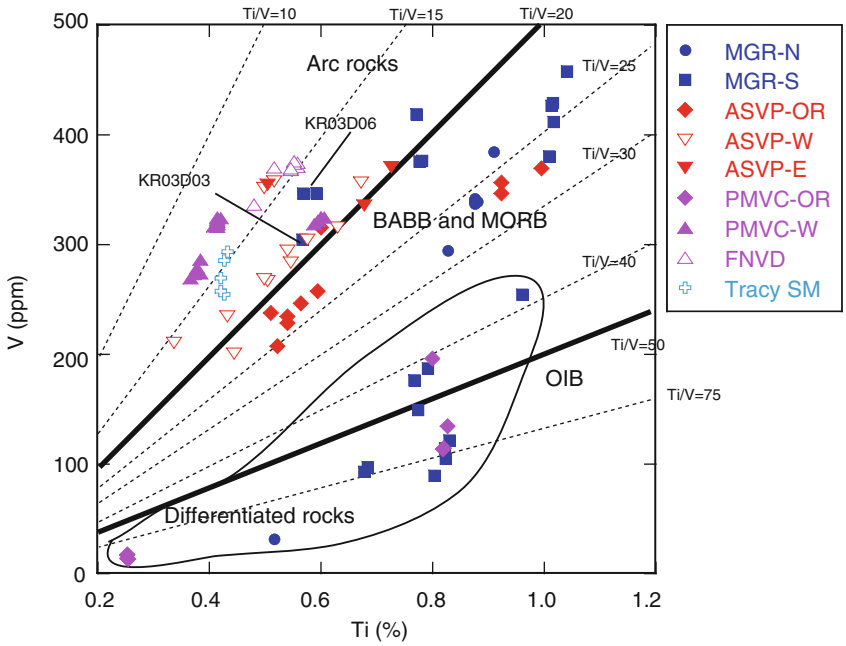

Fig. 21.4 Relationship between Ti and V concentrations of submarine volcanic rocks from the southern Mariana Trough. Tectonic settings designations after Shervais (1982). Heavy lines of Ti/V ratios distinguish the fields of arc lava (Ti/V $<$ 20), backarc-basin basalt (BABB) and mid-ocean ridge basalt (MORB) (20 $<$ Ti/V $<$ 50), vs. ocean island basalt (OIB) (Ti/V $>$ 50). *Symbols* indicate the sampling locations as in Fig. 21.1

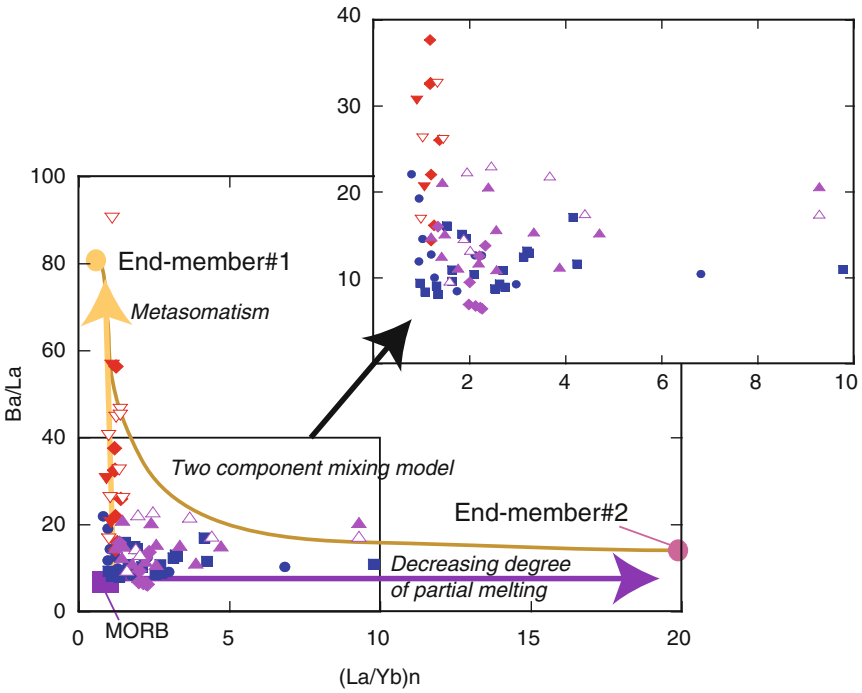

Fig. 21.5 Relationship between Ba/La and (La/Nd)n. The graph is modified after Lin et al. (1989). *Symbols* indicate the sampling locations as in Fig. 21.1

or subduction components are more dominant in the DSC than the MGR. The concentration of Ta from the DSC is extremely high compared with reported rocks from the whole Mariana area. Ta is concentrated in the mantle and behaves in accordance with Nb (Pearce et al. 2005). The normalized concentrations of Nb and Ta of MGR rocks are similar to those of Mariana Trough backarc basin rocks summarized by Pearce et al. (2005), although we cannot explain the enrichment of Ta at present.

21.4.4 Rare Earth Element Compositions

REE compositions normalized to n-MORB are shown in Table 21-S-2 (Supplementary information) and Fig. 21.7. Most of the analyzed rocks from the MGR and DSC have REE patterns similar to that of n-MORB. A rock from the base of Seamount A, which has one of the lowest SiO_2 concentration (51.4 %, Table 21.S-1) among the studied rocks, also shows a pattern similar to that of n-MORB. The

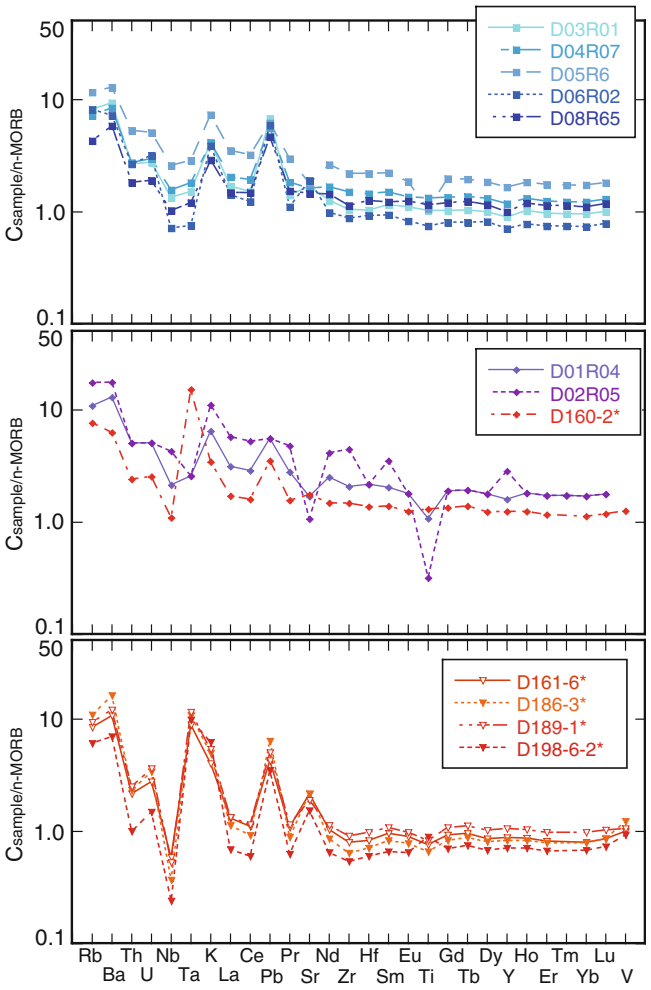

Fig. 21.6 Minor and rare earth element chemistry of selected submarine volcanic rocks from the southern Mariana Trough. The concentrations are normalized to n-MORB (Sun and McDonough (1989) and Sun et al. (1979). The sample name with an asterisk shows that the data used was from Stern et al. (2013)

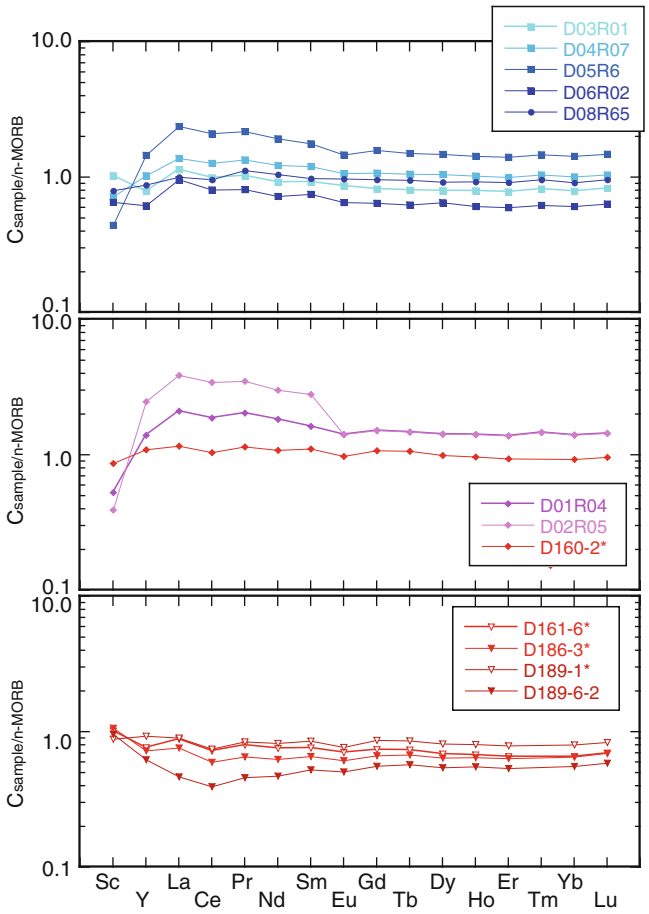

Fig. 21.7 Rare Earth element chemistry of selected submarine volcanic rocks from the southern Mariana Trough. The concentrations are normalized to MORB values published by Sun and McDonough (1989). The sample name with an asterisk shows that the data used was from Stern et al. (2013)

MGR rocks are enriched in LREEs between La and Sm, probably in association with progressive differentiation. There is a slight depletion in LREEs among some of the ASVP rocks (D161-6*, D186-3* and D189-1* in Fig. 21.7). It is notable that a small Ce depletion occurs in all the samples. The minor elements and REE patterns of the rocks studied indicate that one of the end-member magmas originated from a source similar to that of the MGR and DSC, yet the processes responsible for the chemical characteristics are different in each area.

21.4.5 Pb, Sr and Nd Isotopes

Analytical results of Pb, Sr and Nd isotope are in Table 21-S-3 (Supplementary information) and those systematics are shown in Fig. 21.8. Plots of Pb isotopes lie close to the Northern Hemisphere Regression Line (NHRL in Fig. 21.8) (Hart 1984) and the rocks from MGR except for one (KR03D06R02), which has a composition similar to that of DSC rocks as described above, are in the ranges of spreading ridge volcanic rocks reported for the central graben of the northern (Gribble et al. 1998), middle (at 18°N), and southern Mariana Trough (at 14°N) (Volpe et al. 1990; Gribble et al. 1996). Thus, the MGR rocks are derived from a source similar to that of Mariana Trough basalts from farther north.

The relationship between $^{87}Sr/^{86}Sr$ and εNd indicates the trends of two different sources of magmas for the study area more clearly (Fig. 21.8). MGR rocks have a linear negative correlation. The distribution of MGR data points lie in the field of previously reported BABB from the southern and middle Mariana Trough. Most of the DSC rocks have positive correlation. In the figure, end-member #1 is depleted magma (or melt therefrom) with a source similar to MORB that has been metazomatized, and end-member #2 (or melt therefrom) is an LIL- and LREE-enriched OIB-like source

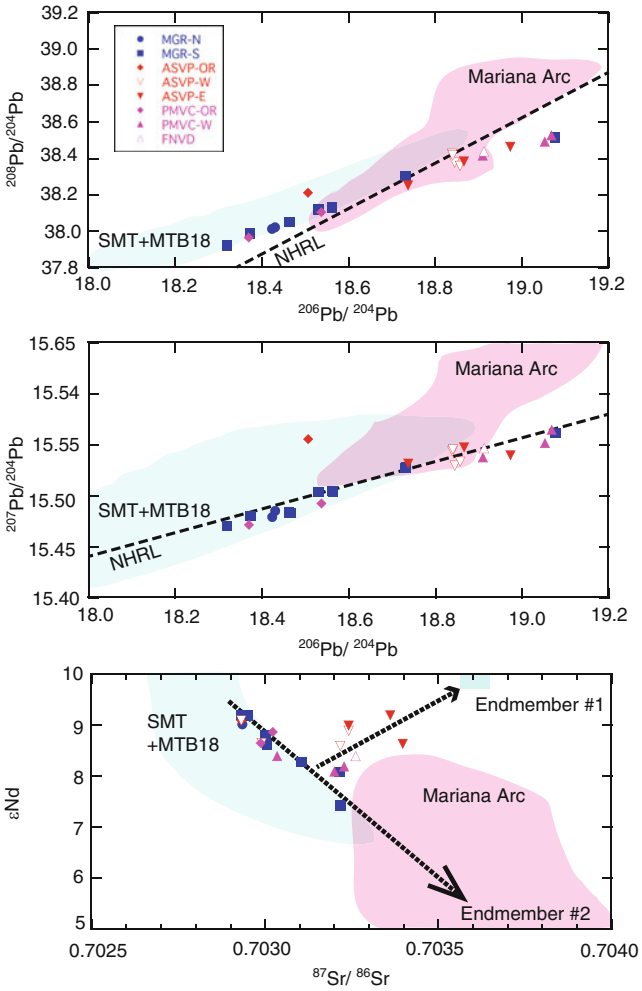

Fig. 21.8 Relationships among Pb isotopes and between Sr and Nd isotopes. The NHRL is Northern Hemisphere Regression Line of Hart (1984). The fields for spreading ridge segments, NMT, SMT, MTB-18 are from Gribble et al. (1998), Volpe et al. (1990) and Gribble et al. (1996). The Mariana arc data are from Gribble et al. (1998) and Stern et al. (1993). End-members #1 and #2 are depleted mantle and OIB (Lin et al. 1989) respectively. *Symbols* indicate the sampling locations as in Fig. 21.1

(Lin et al. 1989). For the rocks studied, the latter would be unlikely. DSC rocks including one from FNVC plausibly are affected by a metazomatized MORB source, as indicated by Ba enrichment noted above. The difference in compositions of rocks from the MGR vs. the DSC is attributed to the compositions of source magma.

21.4.6 Water and Hydrogen Isotope Ratios

Although we have limited data regarding water content and hydrogen isotope ratios for the glasses studied (Table 21-S-1 in Supplementary information), it is possible to make preliminary observations. The water content may show a slight positive correlation with SiO_2 content, especially those from MGR rocks (Fig. 21.3). However, the water content is not related to sampling depth, and is not a simple function of degassing. All five samples that show ~2 % H_2O are from the area of the intersection between the northern and southern MGR. This is also the area in which a magma chamber reflector was resolved on 6-channel seismic reflection data (Becker et al. 2010). Becker et al. (2010) suggested the high R value (contrast in acoustic impedance) of the magma chamber reflector is consistent with a high gas content in the magma chamber.

The hydrogen isotope ratios (δ^2H ‰, VSMOW) are higher in the MGR rocks (−36 to −45 ‰) than in the rocks from the DSC (−45 to −55 ‰). The hydrogen isotope ratios of the MGR rocks are comparable to those reported by Poreda (1985), i.e., values between −32 and −47 ‰ for the Mariana Trough basalts from 18° to 16°N, which are larger than commonly known values of MORB (−80 ± 5 ‰, Kyser and O'Neil 1984) and those of deep-seated mantle (−80 to −60 ‰, Boettcher and O'Neil 1980).

21.5 Discussion

The early studies of petrology suggested that the Mariana Trough basalts originated from melts of a primitive mantle that was enriched in volatiles, alkalis, alkaline earths, and LREE relative to n-MORB because of metasomatic modification of the source mantle (Fryer et al. 1981; Hawkins and Melchior 1985; Sinton and Fryer 1987). Sinton and Fryer (1987) interpreted the enrichment of Ba > Rb > K > LREE > Sr and depletion in Y in the Mariana Trough source to reflect the addition of a depleted suprasubduction-zone mantle component primarily derived by low-degree of melting of the descending eclogitic slab. Based on Sr-Nd-Pb isotope data, magma mixing of depleted MORB source mantle and arc-like lithospheric components were presumed to form heterogenous Mariana backarc basin magmas at about 18°N (Volpe et al. 1987, 1990), whereas the southern Mariana backarc basin basalts have MORB-like compositions modified by a slab-derived fluid (Gribble et al. 1996; Macpherson et al. 2000; Taylor and Martinez 2003). Here, two source magmas and those mixing are obvious; n-MORB type mantle and depleted mantle formed via metasomatism of n-MORB type mantle. In the DVC rocks, occasionally Ba is enriched but not Th or Nb, suggesting that the metazomatized fluid would be derived from the shallower part of descending slab (e. g., Pearce et al. 2005). However, contamination of the source by crustal components including melt of oceanic crust and fluids from the descending slab were not obvious in the MGR rocks, since the Pb, Sr and Nd isotopes do not give any contribution from the metazomatized fluids in those rocks. Enrichment of LREE

in the MGR and off-ridge axis seamounts was likely caused by differentiation or by a low degree of partial melting of n-MORB-type mantle.

The relationship between Ti and V indicates that the DSC magmas had two different redox conditions, both of which lie within the range of arc lavas (Fig. 21.4). Solubility of V in silicate melts is dependent on the redox state of V (V^{3+}/V^{4+}). Because V^{3+} decreases with increasing fO_2 (Canil 1999) and V^{4+} tends to behave as an incompatible element, higher V contents relative to Ti reflect more oxidizing conditions. If this is applicable to our study area, the source magmas in the southern segment of DSC (PMVC and FNVC) are more oxidizing than those in the northern ones (ASVP). As a controlling factor for redox conditions of the magmas formed in the suprasubduction-zone mantle wedge, silicate melt is considered to be a more effective oxidizer than solute-rich hydrous fluid (Parkinson and Arculus 1999). Although the DSC rocks are apparently not affected by subduction components, the more oxidizing condition of the southern than northern DSC magmas, which were more affected by the metazomatizm.

Lower V content in the MGR rocks are in the ranges for backarc basin basalts (Shervais 1982) indicating a more reducing condition in the source magma than in arc magmas. Some of the rocks from the MGR (KR03-R06, KR03-R03) are indistinguishable from the southern DSC (DMVC-W and FNVC) rocks. This would mean that both MGR and DSC magmas have similar source magmas, especially in the southern segments where they merge spatially.

Pearce et al. (2005) explained the complexities of mixing of subduction mobile elements in the mantle sources for Mariana arc lavas, lavas formed during backarc rifting, and the back arc spreading center lavas by plotting deviations from a MORB array, which was defined for the Mariana/Philippine-Sea regions. They used comparison of ratios of various subduction mobile to immobile elements as proxies for total subduction addition. For example, Ba/Yb and Th/Yb vs. Ta/Yb plots are used for detecting the addition of subduction components. The ranges of these ratios for our studied rocks from the MGR are Ba/Yb (1.3–2.3), Th/Yb (0.06–0.14), and Ta/Yb (0.04–0.07), indicating pure mantle source of southern Mariana Trough basalts. The rocks from ASVP give slightly higher Ba/Yb (1.1–4.3), but almost the same Th/Yb (0.06–0.12). None of the samples we report lie within the field of arc lavas from Pearce et al. (2005) with regard to these trace element ratio considerations. This is consistent with the low Ba/La ranges (from 7 to 14) for the MGR and 20.5 to 36.2 for the DSC indicating relatively low slab-fluid contribution to the MGR, consistent with the systematics of Pb, Sr and Nd isotopes as noted above.

Based on Nd and Sr isotope systematics, Lin et al. (1989) proposed that the Mariana island arc lavas represent the mixing of three end-member components; hydrous fluid derived from the subducted sediments, OIB-type mantle and MORB. Lin et al. (1989) explained that the Mariana arc magma was derived from a depleted MORB-like mantle that has been recharged with K, Rb, Sr and Ba by hydrous fluids. Our data of Pb, Sr, and Nd isotopes indicate that the DSC rocks occasionally contained small amount of components derived from metazomatized fluid (Fig. 21.8), probably derived from the shallower part of descending slab. However, unlike the Mariana arc lavas, those rocks would not contain component derived from melted oceanic crust. The FNVC was termed a remnant arc, which was active before opening of the Trough in this area (~3 Ma) (Ribeiro et al. 2013a). However, the Pb, Sr, and Nd isotope systematics do not show any difference from the other rocks of the DSC.

Sources of the water in the samples studied are presumed to be in the mantle wedge, seawater, or they could also have been affected by replenishment from other sources along strike or by mantle-wedge corner flow, but fluids directly from hydrous minerals in the subducting slab are likely minimal in our samples based on δ^2H values. The Mariana Trough rocks are reported to have higher volatile content, including H_2O, than n-MORB (e.g., Garcia et al. 1979; Stolper and Newman 1992, 1994). The studied rocks from the MGR contained higher amounts of H_2O (1.2–2.2 %) than n-MORB (<0.5 %). Higher H_2O content of the BABB than that of the adjacent arc volcanic rocks has been thought to be essential for producing backarc basin magma (e.g., Garcia et al. 1979), because the higher water content acted to lower the melting temperature in the wedge mantle. A small amount of H_2O lowers the melt liquidus temperature and suppresses plagioclase crystallization relative to olivine and clinopyroxene (Fryer et al. 1981; Danyushevsky 2001; Taylor and Martinez 2003). Also, in general, the H_2O content increases with progressive differentiation evidenced by decreasing MgO and increasing Al_2O_3 and FeO* (Danyushevsky 2001), especially at lower temperature; e.g., a larger amount of H_2O than 3 % in the melt causes enrichment in SiO_2 and depletion in MgO at 1,100 °C compared with anhydrous melts (Hirose and Kawamoto 1995). Weakly negative correlation of H_2O content may be present to Mg# and TiO_2 concentration, although it is not clear whether differentiation or partial melting is related to the H_2O content of the source magmas of this area. Kyser and O'Neil (1984) noted that the direct addition of seawater into tholeiite magmas increased water content and hydrogen isotope ratios. They found that Mid-Atlantic Ridge basalts gave a maximum δ^2H value of −35 ‰ with seawater infusion into the source magma. Seawater injection into magma is a plausible mechanism in and around ocean crust, e.g., the heavy hydrogen isotope ratios of granitic rocks at Ascension Island were explained by seawater infusion into the magma (Sheppard and Harris 1985). Seawater infusion into the

MGR magma may explain the heavier δ^2H values than those of MORB and rocks from the DSC. Slightly negative anomalies of Ce would be another evidence of seawater injection into the magma. The widespread faulting associated with a high degree of deformation of the southeastern part of the Mariana forearc (southeast of the DSC) in the study area (Fryer et al. 2003) would provide avenues for intrusion of seawater into the lithosphere of this part of the basin far more readily than elsewhere in the Mariana backarc setting.

Taylor and Martinez (2003) indicated that hydrous fluxing enhances decompression melting of depleted mantle sources just behind the island arc and produces spreading axes with "fast-spreading" morphology. They also suggested that the increasing H_2O and Ba/La ratio were evidence of relationship of slab-derived water affecting backarc magma production in other parts of the Mariana Trough. Based on the U-series isotope characteristics of the rocks in the Valu Fa ridge, a similar mantle chemistry was presumed beneath the arc and backarc spreading areas in the Lau Basin, whereas slab-derived water contributes less in the backarc spreading ridge than in the arc (Peate et al. 2001). The enrichment of Ba in the seamounts north of 13°N (Fig. 21.5) is indicative of the metasomatism by injection of large amounts of fluids derived from the depleted mantle. In this study, the dehydration and dissolution of Ba and the other alkali and alkali-earth elements would explain the water and Ba/La systematics.

Initial rifting of a backarc region most often occurs adjacent to the edge of the volcanic arc, because of concentration of tensional stress along the boundary of the arc crust (Stern et al. 1990). Between the MGR and the DSC sidescan sonar imagery shows high backscatter, numerous small volcanic cones and overlapping lobate flows, indicative of recent resurfacing by volcanism. This is similar to what is observed at the southern end of the Valu Fa ridge, where backarc spreading is propagating into the arc volcanic region (Peate et al. 2001). The most important change in magmatic activity that happens during the formation of a backarc basin is the transition from arc igneous activity to true sea-floor spreading and new lithosphere formation. Because arc magmas are constantly being generated deep in the mantle wedge throughout this process, and backarc opening initially occurs under the control of shallow tectonic stress (Gribble et al. 1998), there is an intermediate period of arc rifting in which magma sources may be influenced by these transitional tectonic phenomena. The FNVC would have been formed at such a tectonic setting. Never-the-less, it is important to mention that the sources of the studied rocks are related to back-arc formation but are not arc volcanoes.

21.6 Conclusions

The major and minor element chemistry and isotope characteristics of the backarc basin rocks from the southern end of Mariana Trough between 12°30 and 13°30′N indicate a progression in interactions between two magmatic sources. The rocks of the backarc spreading center and nearby discrete chains of seamounts are formed mostly from the mantle wedge and have similar compositiosn: n-MORB-type mantle and depleted mantle. The former is the main source of the currently active spreading center, which has the morphology of a fast spreading ridge, such as the EPR, and the latter is the source of discrete seamounts that lie along two parallel chains between the spreading center ridge and the Mariana volcanic arc (FNVC and PMVC). The DSC (FNVC and PMVC) can be separated into two segments, one north of and one south of 13°N. The chemical composition, especially the redox condition of the magmas differs by position north or south of 13°N, not by distance from the active spreading center or the Mariana volcanic arc. The southern segment is more oxidizing than the northern segment, probably due to the depletion of more basic compositions.

We suggest that the center of active backarc extension in the southern Mariana Trough has migrated toward the southeast as the basin opened. The trench-arc system changes from an essentially N-S strike in the north and curves sharply westward at the southern end. The most recent backarc opening in the southernmost part of the Mariana Trough involves not only the active spreading center (MGR) but also the zone between it and an older chain of discrete seamounts (FNVC) This is consistent with southeastward roll-back of the descending slab as suggested by others (Martinez et al. 2000; Fryer et al. 2003; Gvirtzman and Stern 2004).

Acknowledgements The sample rocks for this study were collected during the cruises of R/Vs Yokosuka, Kairei and Hakuho-maru. Crews of those vessels and the operating teams of the Shinaki 6500 submersible and Kaiko ROV are gratefully acknowledged. We thank Dr. M. Kusakabe for guidance to water analyses, and Ms. K. Okazaki, Y. Akioka S. Matsumoto, T. Ueno, and D. Vonderhaar for assistance with the laboratory work, and Dr. K. Okino for providing the bathymetry map Drs. R. Stern and H. Sato are acknowledged for improvement of the manuscript with their review comments. This work was partly supported by the Scientific Fund of the Ministry of Education, Science and Culture (MEXT), Japan, to H. M. (#20109006) This is SOEST contribution no. 9068 and HIGP contribution No. 2024.

References

Baker N, Fryer P, Martinez F (1996) Rifting history of the Northern Mariana Backarc Basin, SeaMARC II and morphology studies. J Geophys Res 101(B5):11427–11455

Becker NC (2005) Recent volcanic and tectonic evolution of the southern Mariana arc, Dissertation, University of Hawai'i, ProQuest, UMI Dissertations Publishing, 2005. 3184487

Becker NC, Fryer P, Moore GF (2010) Malaguana-Gadao ridge: identification and implications of a magma chamber reflector in the southern Mariana Trough. Geochem Geophys Geosyst 11: Q04X13. doi:10.1029/2009GC002719

Bibee LD, Shor GG Jr, Lu RS (1980) Inter-arc spreading in the Mariana Trough. Mar Geol 35:183–197

Boettcher AL, O'Neil JR (1980) Stable isotope, chemical and petrographic studies of high-pressure amphiboles and micas: evidence for metasomatism in the mantle source regions of alkali basalts and kimberlites. Am J Sci 280A:594–621

Canil D (1999) Vanadium partitioning between orthopyroxene, spinel and silicate melt and the redox states of mantle source regions for primary magmas. Geochim Cosmochim Acta 63:557–572

Danyushevsky LV (2001) The effect of small amount of H2O on crystallisation of mid-ocean ridge and backarc basin magmas. J Volcanol Geotherm Res 110:265–280

Eguchi T (1984) Seismotectonics around the Mariana Trough. Tectonophys 102:33–52

Embley RW, Baker ET, Chadwick WW, Lupton JE Jr, Resing JA, Massoth GJ, Nakamura K (2004) Explorations of Mariana arc volcanoes reveal new hydrothermal systems. EOS 85(4):37–44

Fryer P, Sinton JM, Philpotts JA (1981) Basaltic glasses from the Mariana Trough. In Init Rep Deep Sea Drill Proj 60:601–610; US Gov. Print. Office: Washington, DC

Fryer P, Fujimoto H, Sekine M, Johnson L, Kasahara J, Masuda H, Gamo T, Ishii T, Ariyoshi M, Fujioka K (1998) Volcanoes of the southwestern extension of the active Mariana island arc: new swath-mapping and geochemical studies. Island Arc 7(3):596–607

Fryer P, Becker N, Appelgate B, Martinez F, Edwards M, Fryer G (2003) Why is the challenger deep is so deep? Earth Planet Sci Lett 211(3–4):259–269

Gamo T, The Shipboard Scientific Party of the Y9204 cruise (1993) Revisits to the mid-Mariana Trough hydrothermal site and discovery of new venting in the southern Mariana region by the Japanese submersible Shinkai 6500. InterRidge News 12:11–14

Gamo T, Tsunogai U, Ishibashi J, Masuda H, Chiba H (1997) Chemical characteristics of hydrothermal fluids from the Marina Trough. JAMSTEC J Deep Sea Res 69–74; special volume "Deep Sea Research in Subduction Zones, Spreading Centers and Backare Basins

Gamo T, Masuda H, Yamanaka T, Okamura K, Ishibashi J, Nakayama E, Obata H, Nishio K, Shitashima Y, Hasumoto H, Watanabe M, Mitsuzawa K, Seama N, Thusnogai U, Kouzuma F, Sano Y (2004) Discovery of a new hydrothermal venting site in the southernmost Mariana arc: al-rich plumes and white smoker activity associated with biogenic methane. Geochem J 38:527–534

Garcia MO, Lie NWK, Muenow DW (1979) Volatiles in submarine volcanic rocks from the Mariana island arc and Trough. Geochim Cosmochim Acta 43:305–312

Gribble RF, Stern RJ, Bloomer SH, Stüben D, O'Hearn T, Newman S (1996) MORB mantle and subduction components interact to generate basalts in the southern Mariana Trough backarc basin. Geochim Cosmochim Acta 60:2153–2166

Gribble RF, Stern RJ, Newman S, Bloomer SH, O'Hearn T (1998) Chemical and isotopic composition of lavas from the northern Mariana Trough: implications for magmagenesis in back-arc basins. J Petrol 39:125–154

Gvirtzman Z, Stern RJ (2004) Bathymetry of Mariana trench-arc system and formation of the challenger deep as a consequence of weak plate coupling. Tectonics 23, TC2011. doi:10.1029/2003TC001581

Hart SR (1984) A large-scale isotope anomaly in the southern hemisphere mantle. Nature 309:753–757

Hart SR, Glassey WE, Karig DE (1972) Basalts and seafloor spreading behind the Mariana island arc. Earth Planet Sci Lett 15:12–18

Hawkesworth CJ, Gakkagher K, Hergt JM, McDermott F (1993) Mantle and slab contributions in arc magmas. Annu Rev Earth Planet Sci 21:175–204

Hawkins JW (1977) Petrology and geochemical characteristics of marginal basin basalt. In: Hayes DE (ed) Island arcs, deep sea trenches, and backarc basins, vol 23, Geophysics monograph series. AGU, Washington, DC, pp 355–365

Hawkins JW, Melchior JT (1985) Petrology of Mariana Trough and Lau Basin basalts. J Geophys Res 90:11431–11468

Hawkins JW, Lonsdale PF, Macdougall JD, Volpe AM (1990) Petrology of the axial ridge of the Mariana Trough backarc spreading center. Earth Planet Sci Lett 100:226–250

Hickey-Vargas R (1991) Isotope characteristics of submarine lavas from the Philippine sea: implications for the origin of arc and basin magmas of the Philippine plate. Earth Planet Sci Lett 107:290–304

Hirose K, Kawamoto T (1995) Hydrous partial melting of lherzorite at 1 Gps – the effect of H_2O on the genesis of basaltic magma. Earth Planet Sci Lett 133:463–473

Hussong DM, Uyeda S (1981), Tectonic processes and the history of the Mariana arc, a synthesis of the results of deep sea drilling project leg 60. In: Hussong DM, Uyeda S et al (eds) Initial reports of the deep sea drilling project 60, pp 909–929

Irvine TN, Baragar WRA (1971) A guide to the chemical classification of the common volcanic rocks. Can J Earth Sci 8:523–548

Ishibashi J, Yamanaka T, Kimura H, Hirota A, Toki T, Tsunigai U, Gamo T, Utsumi M, Roe K, Miyabe S, Okamura K (2004) Geochemistry of hydrothermal fluids in south Mariana backarc spreading center. EOS Trans AGU 85(47), Fall Meet Suppl, abstract V44A-03

Ishibashi J, Suzuki R, Yamanaka T, Toki T, Kimura H, Noguchi T, Urabe T (2006) Seafloor hydrothermal activity at off-axial seamounts of backarc spreading in southern Mariana Trough. Geochim Cosmochim Acta 70:A279

Jackson M (1989) Petrology and petrogenesis of recent submarine volcanics from the northern Mariana arc and back-arc basin, PhD Dissertation, University of Hawaii at Manoa, Honolulu, HI, United States (USA), 1989

Johnson L, Fryer P, Masuda H, Ishii T, Gamo T (1993) Hydrothermal vent deposits and two magma sources for volcanoes near 13°20′N in the Mariana backarc: a view from Shinkai 6500. EOS Trans AGU 74(43), Fall Meet Suppl., abstract V51C-14

Karig DE (1971) Structural history of the Mariana Island arc system. Geol Soc Am Bull 82:323–344

Kasahara J, Sato T, Fujioka K (1994) Intensive thermal upwelling at a seamount in the southern Mariana Trough observed by ocean bottom seismic instruments using "Shinkai 6500" submersible. JAMSTEC J Deep Sea Res 10:163–174

Kato T, Beavan J, Matsushima T, Karato Y, Camacho J, Nakao S (2003) Geodesic evidence of backarc spreading in the Mariana Trough. Geophys Res Lett 30(27–1):1625. doi:10.1029/2002GL016757

Kitada K, Seama N, Yamazaki T, Nogi Y, Suyehiro K (2006) Distinct regional differences in crustal thickness along the axis of the Mariana Trough, inferred from gravity anomalies. Geochem Geophys Geosyst 7:Q04011. doi:10.1029/2005GC001119

Kyser TK, O'Neil JR (1984) Hydrogen isotope systematics of submarine basalts. Geochim Cosmochim Acta 48:2123–2133

Lin PN, Stern RJ, Bloomer SH (1989) Shoshoniitic volcanism in the northern Mariana arc, 2: large-ion lithophile and rare earth element abundances: evidence for the source of incompatible elemet enrichments in intraoceanic arcs. J Geophys Res 94:4497–4514

Macdonald GA (1968) Composition and origin of Hawaiian lavas. In: Coats RR, Hay RL, Anderson CA (eds) Studies in volcanology: a Memoir in honor of Howel Williams. Geol Soc Am Mem 116

Macpherson CG, Hilton DR, Mattey DP, Sinton JM (2000) Evidence for an ^{18}O-depleted mantle plume from contrasting $^{18}O/^{16}O$ ratios of backarc lavas from the Manus Basin and Mariana Trough. Earth Planet Sci Lett 176:171–183

Martinez F, Fryer P, Baker N, Yamazaki T (1995) Evolution of backarc rifting: Mariana Trough, 20°N-24°N. J Geophys Res 100:3807–3827

Martinez F, Fryer P, Becker N (2000) Geophysical characteristics of the southern Mariana Trough, 11°50'N-13°40'N, *J*. Geophys Res 105:16591–16607

Masuda H, Gamo T, Fryer P, Ishii T, Johnson LE, Tanaka H, Tsunogai U, Matsumoto S, Masumoto S, Fujioka K (1993) Relationship between volcanisms and topography from the major element rock chemistry in the southern Mariana Trough. JAMSTEC J Deep Sea Res 9:181–189 (Japanese with English abstract)

McCulloch MT, Gamble JA (1991) Geochemical and geodynamical constraints on subduction zone magmatism. Earth Planet Sci Lett 102:358–374

Mitsuzawa K, Masuda H, Seama N, Hasegawa Y, Miyamoto M, Togashi N, So A, Yamanobe H (2000) Preliminary report of deep-tow/Yokosuka cruise at hydrothermal areas in the mid and southern Mariana. JAMSTEC Deep Sea Res 17:73–87 (Japanese with English abstact)

Natland JH, Tarney J (1981) Petrologic evolution of the Mariana arc and backarc basin system – a synthesis of drilling results in the south Philippine Sea. In: Hussong DM, Uyeda S (eds) Init Repts DSDP, vol 60. U. S. Govt Printing Office, Washington DC, pp 877–907

Parkinson IJ, Arculus RJ (1999) The redox state of subduction zones: insights from arc-peridotites. Chem Geol 160:409–423

Pearce JA, Stern RJ, Bloomer S, Fryer P (2005) Geochemical mapping of the Mariana arc-basin system: implications for the nature and distribution of subduction components. Geochem Geophys Geosyst 6, Q07006. doi:10.1029/2004GC000895

Peate DW, Kokfelt TF, Hawkesworth CJ, van Calsteren PW, Hergt JM, Pearce JA (2001) U-series isotope data on Lau Basin glasses: the role of subduction-related fluids during melt generation in backarc basins. J Petrol 42:1449–1470

Plank T, Langmuir C (1998) The chemical composition of subducting sediment and its consequence for the crust and mantle. Chem Geol 145:325–394

Poreda R (1985) Helium-3 and deuterium in backarc basalts: Lau Basin and the Mariana Trough. Earth Planet Sci Lett 73:244–254

Ribeiro JM, Stern RJ, Martinez F, Ishizuka O, Merle SG, Kelley K, Anthony EY, Ren M, Ohara Y, Reagan M, Girard G, Bloomer S (2013a) Geodynamics evolution of a forearc rift in the southernmost Mariana arc. Island Arc. doi:10.111/iar.12039

Ribeiro JM, Stern RJ, Kelley K, Martinez F, Ishizuka O, Manton SWI, Ohara Y (2013b) Nature and distribution of slab-derived fluids and mantle sources beneath the Southeast Mariana forearc rift. Geochem Geophys Geosyst. doi:10.1002/ggge.20244

Seama N, Hasegawa Y, Nakase K, Mitsuzawa K, Masuda H, Yamazaki T (2001) Tectonic evolution of central and southern Mariana Trough, 2001 Joint Meeting of Earth and Planetary Science, Abstract A5-001, Tokyo

Sheppard SMF, Harris C (1985) Hydrogen and oxygen isotope geochemistry of Ascension Island lavas and granites: variation with crystal fractionation and interaction with seawater. Contrib Min Petrol 91:74–81

Shervais JW (1982) Ti-V plots and the petrogenesis of modern and ophiolitic lavas. Earth Planet Sci Lett 59:101–118

Sinton JM, Fryer P (1987) Mariana Trough lavas from 18°N: implications for the origin of back arc basin basalts. J Geophys Res 92:12782–12802

Sinton JM, Ford LL, Chappell B, McCulloch MT (2003) Magma genesis and mantle heterogeneity in the Manus backarc basin, Pupua New Guinea. J Petrol 44:159–195

Smoot NC (1990) Mariana Trough by multi-beam sonar. Geo-Mar Lett 10:137–144

Stern RJ, Lin P-N, Morris JD, Jackson MC, Fryer P, Bloomer SH, Ito E (1990) Enriched backarc basalts from the northern Mariana Trough: implications for the magmatic evolution of backarc basins. Earth Planet Sci Lett 100:210–225

Stern RJ, Jackson MC, Fryer P, Ito E (1993) O, Sr, Nd and Pb isotopic composition of Kasuga Cross-Chain in the Mariana Arc: a new perspective on the k–h relationship. Earth Planet Sci Lett 119:459–475

Stern RJ, Tamura Y, Masuda H, Fryer P, Martinez F, Ishizuka O, Bloomer SH (2013) How the Mariana volcanic arc ends in the south. Island Arc 22:133–148

Stolper EM, Newman S (1992) Fluids in the source regions of subduction zone magmas: clues from the study of volatiles in Mariana Trough magmas. Rept Geol Surv Jpn 279:161–169

Stolper EM, Newman S (1994) The role of water in the petrogenesis of Mariana Trough magmas. Earth Planet Sci Lett 121:293–325

Sun S.-S., and W. F. McDonough (1989) Chemical and isotopic systematics of oceanic basalts: Implications for mantle composition and processes. In: Sanders AD, Norry MJ (eds) Magmatism in the ocean basins. Geol Soc London Spec Publ, 42, pp 313–345

Sun S-S, Nesbit RW, Sharaskin AY (1979) Geochemical characterisitcs of mid-ocean ridge basalts. Earth Planet Sci Lett 44:119–138

Taylor B, Martinez F (2003) Back-arc basalt systematics. Earth Planet Sci Lett 210:481–497

Utsumi M, Nakamura K, Kakegawa T, Shitashima K, Kurusu Y, Yamanaka H, Takano Y, Kimura H, Higashi Y, Ishibashi J, Hirota A, Kaneko R, Minabe M, Kasai H, Settsu M (2004) First discovery of hydrothermal vent with black smoker (Pika site) at the southern Mariana Region and its properties, 2004 Joint Meeting of Earth and Planetary Science, Abstract B002-016, Chiba

Volpe AM, MacDougall D, Lugmair GW, Hawkins JW, Lonsdale P (1990) Fine-scale isotopic variation in Mariana Trough basalts: evidence for heterogeneity and a recycled component in backarc basin mantle. Earth Planet Sci Lett 100:251–264

Vople AM, MacDougall JD, Hawkins JW (1987) Mariana Trough basalts (MTB): trace element and Sr-Nd isotopic evidence for mixing between n-MORB-like and Arc-like melts. Earth Planet Sci Lett 82:241–254

Yamatani Y, Masuda H, Amakawa H, Nazaki Y, Gamo T (1994) Rare earth element chemistry of submarine valcanic rocks from a spreading axis, the southern Mariana Trough. JAMSTECJ Deep Sea Res 10:187–193 (Japanese with English abstract)

Yamazaki T, Stern RJ (1997) Topography and magnetic vector anomalies in the Mariana Trough. JAMSTEC J Deep Sea Res 13:31–45

Yamazaki T, Murakami F, Saito E (1993) Mode of seafloor spreading in the northern Mariana Trough. Tectonophys 221:208–222

Yoshikawa S, Okino K, Asada M (2012) Geomorphology variations at hydrothermal sites in the southern Mariana Trough: relationship between hydrothermal activity and topographic characteristics. Mar Geol 303–306:172–182

Mineralogical and Geochemical Characteristics of Hydrothermal Minerals Collected from Hydrothermal Vent Fields in the Southern Mariana Spreading Center

22

Kei Ikehata, Ryohei Suzuki, Kazuhiko Shimada, Jun-ichiro Ishibashi, and Tetsuro Urabe

Abstract

Seafloor hydrothermal mineralization of four active hydrothermal fields (Snail, Yamanaka, Archaean and Pika sites) in the Southern Mariana Trough was investigated to clarify the mineralogical and geochemical characteristics of the hydrothermal minerals. The Snail site and the Yamanaka site are located on the crest of the backarc spreading ridge (on-axis). The Pika site sits atop an off-axial volcano, 4.9 km distant from the spreading axis, while the Archaean site sits on the flank of the spreading ridge, about 1.5 km distant from the axis. In the four hydrothermal sites, chimney and mound sulfides are composed mainly of pyrite, marcasite, sphalerite and chalcopyrite. Conduits and interstices of these sulfide minerals are filled with late barite and anhydrite. Mineralizations of off-axial hydrothermal fields have mineralogical and geochemical signatures (Fe-rich and low f_{S2} condition) similar to those of mineralizations at sediment-free mid-ocean ridge settings. By contrast, mineralizations of on-axial sites show distinctly Zn and Pb-rich (high f_{S2} condition) signatures similar to those found in arc or rifting settings. Sulfur isotopic compositions of collected sulfide minerals show a similar diversity with a mid-ocean ridge range for the off-axial sites and an island-arc range for the on-axial sites. These isotopic signatures could be explained by varying proportions of magmatic sulfur leached from the underlying volcanic rocks and reduced seawater sulfates.

Keywords

Seafloor hydrothermal mineralization • Southern Mariana Trough • Sulfate mineral • Sulfide mineral

22.1 Introduction

Modern seafloor hydrothermal mineralization is mainly found in three types of environments: at mid-ocean ridges, at intraoceanic arc-backarc systems such as the Mariana Trough, and at intracontinental arc-backarc systems such as the Okinawa Trough (Herzig and Hannington 1995; Herzig et al. 2002). Seafloor massive sulfides formed in the subduction-related arc and backarc environments have attracted the attention of economic geologists since these hydrothermal fields are considered to be modern analogues of volcanogenic massive sulfide deposits on land (e.g., Fouquet et al. 1993). Detailed geophysical, geomorphological, geological, mineralogical, geochemical and microbiological analyses of seafloor

K. Ikehata (✉)
Faculty of Life and Environmental Sciences, University of Tsukuba, Ibaraki, Japan
e-mail: ikkei@geol.tsukuba.ac.jp

R. Suzuki • K. Shimada • J.-i. Ishibashi
Faculty of Sciences, Kyushu University, Fukuoka, Japan

T. Urabe
Department of Earth and Planetary Science, The University of Tokyo, Tokyo, Japan

J.-i. Ishibashi et al. (eds.), *Subseafloor Biosphere Linked to Hydrothermal Systems: TAIGA Concept*,
DOI 10.1007/978-4-431-54865-2_22,

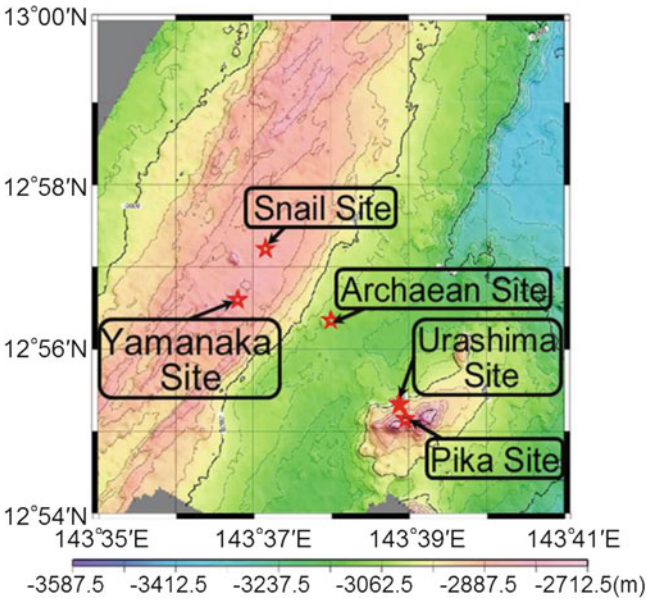

Fig. 22.1 Location of active hydrothermal vent sites on and around the backarc spreading center of the Southern Mariana Trough. The Snail and Yamanaka sites are located on the backarc spreading center (on-axis). The Archaean site is on the flank of the backarc spreading ridge. The Pika and Urashima sites are on an off-axis knoll (volcano). Contours indicate water depth in meter

hydrothermal systems in the Southern Mariana Trough have been carried out within the past 20 years (e.g., Fryer 1995; Ishibashi and Urabe 1995; Ishibashi et al. 2006; Kakegawa et al. 2008; Kato et al. 2009; Yoshikawa et al. 2012; Nakamura et al. 2013; Takamasa et al. 2013; Ishibashi et al. Chap. 23). In this area, five active hydrothermal fields lie in three different geological environments (Fig. 22.1). The Snail and Yamanaka sites are located on the crest of the backarc-spreading ridge (on-axis), while the Pika and Urashima sites are on an off-axis knoll (volcano). The Archaean site lies on the flank of the backarc spreading ridge. The linear array of hydrothermal activities at Snail, Archaean and Pika sites which is almost perpendicular to the arc trend may be related to a structural lineament, although there is no visible tectonic feature connecting them in this area. Yoshikawa et al. (2012) investigated the five hydrothermal sites using near-bottom swath mapping data by the autonomous underwater vehicle *URASHIMA* and dive observation data by the submersible *SHINKAI 6500*. They indicated that the two on-axis sites (Snail and Yamanaka) represent locations of local activity associated with a 4th order spreading segment-scale diking event, in contrast, the three off-axis sites (Archaean, Pika and Urashima) represent locations of sustained large-scale hydrothermal activity related to an off-axis upwelling magma system. Previous studies reported that sulfur isotopic ratios of sulfide minerals are different between on-axis and off-axis sites in the Southern Mariana Trough (Ishibashi et al. 2006; Kakegawa et al. 2008).

In this study, we conducted further detailed descriptions of mineral and chemical compositions in hydrothermal minerals from the Snail, Yamanaka, Archaean and Pika sites to evaluate the geochemical characteristics between on-axis and off-axis seafloor hydrothermal mineralizations.

22.2 Samples

From 2003 to 2005, mineralized samples were collected from the Southern Mariana Trough by submersible diving and shallow drilling. Sample localities are shown in Figs. 22.1, 22.2, 22.3, and 22.4.

Sampling at the Snail site was conducted during YK03-09 cruise. Sulfide crusts (sample #788-1 and #794-3) seen around the hydrothermal discharge were collected. The sample (#788-1) is a piece of hard sulfide crusts with 3–5 cm thickness, showing porous texture. Exterior surface has a thin oxidized layer (Fig. 22.5a). An inactive chimney was sampled from the Yamanaka site during TN167A cruise. The sample (#774-7) has a central conduit and has wall 2–3 cm thick (Fig. 22.5b). From the Archaean site, active and inactive chimneys and massive sulfide breccias were sampled during TN167A and YK05-09 cruises. Samples (#903-2 and #903-4) of active chimneys were obtained from orifice and body of 343 °C black smoker chimney (Fig. 22.5c). Inactive chimneys (sample #903-6) were sampled from the top of a sulfide mound accompanying shimmering of low-temperature fluids. Sample #903-7 is a large flange structure that has many spires on its surface (Fig. 22.5d). Three massive sulfide breccias (sample #903-1, #903-5 and #774-10) were collected from surface of sulfide mounds, which are considered as parts of relict chimneys (Fig. 22.5e). Mineralized samples from the Pika site were collected during YK05-09 and BMS 2004 cruises, and can be categorized in three groups: active chimney, massive sulfide breccia, and drill core. An active chimney sample was obtained from <60 °C clear smoker vent. The sample (#906-2) has tubular structure filled with later sulfides (Fig. 22.5f). Massive sulfide breccias (sample #906-1, #906-3, #906-4 and #906-5) were sampled from bottom and top of the sulfide mound. The samples are characterized by dominance of coarse-grained pyrite (Fig. 22.5g). During BMS 2004 cruise, shallow drilling by BMS (Benthic Multi-coring System, JOGMEC) was performed at the margin of the Pika mound (APM02; Fig. 22.4a). The APM02 hole (subbottom depth = 5.6 m) is entirely composed of massive sulfides beneath thin manganese oxide cover, although recovery of the core was 14 %. Four fragments were subsampled from the APM02 core (Fig. 22.5h).

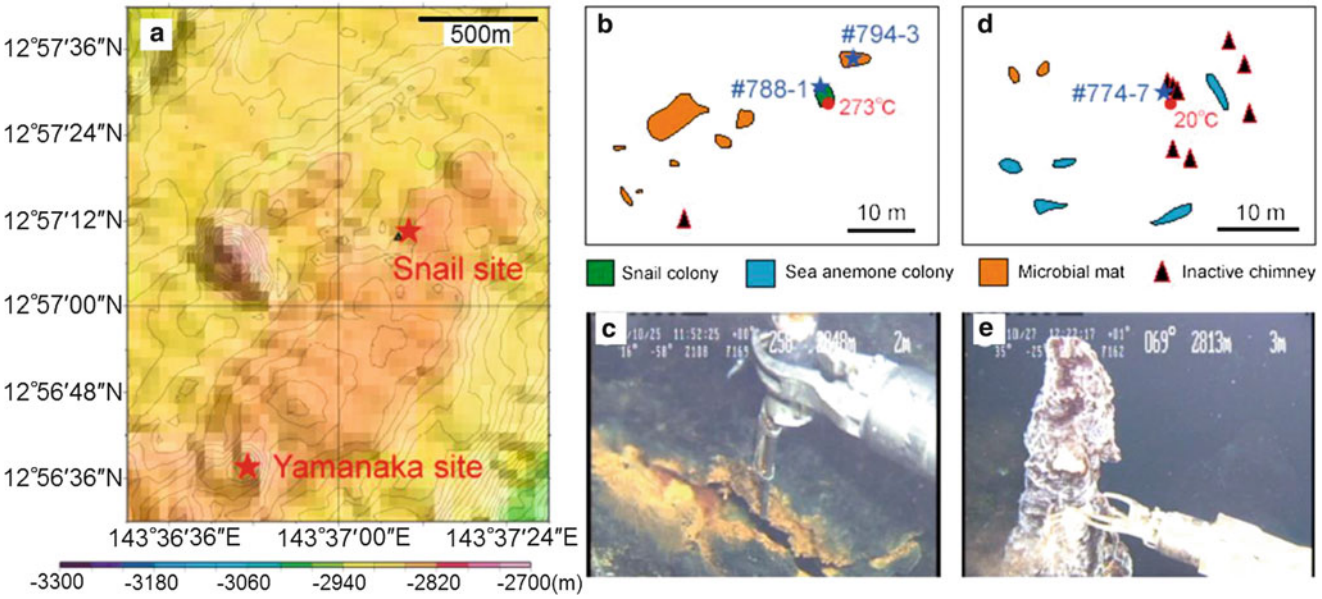

Fig. 22.2 Hydrothermal activity at the Snail and Yamanaka sites. (**a**) Bathymetric map of the crest of the backarc spreading ridge, showing locations of the Snail and Yamanaka sites. *Contours* indicate water depth in meter. (**b**) Distribution of hydrothermal activity of the Snail site is modified after the Cruise Report of YK03-09. *Blue stars* indicate the sampling points of hydrothermal mineralization. Number in degrees Celsius is the maximum temperature of the discharging fluid. (**c**) Hydrothermal discharge through a crack of hydrothermal sulfide crust at the Snail site. The yellowish material lined along the crack is microbial mat. Width of view is ~50 cm. (**d**) Distribution of hydrothermal activity of the Yamanaka site is modified after the Cruise Report of YK03-09. *Blue star* indicates the sampling point of hydrothermal mineralization. Number in degrees Celsius is the maximum temperature of the discharging fluid. (**e**) Inactive chimney covered by whitish microbial mat observed at the Yamanaka site. Width of view is ~1 m

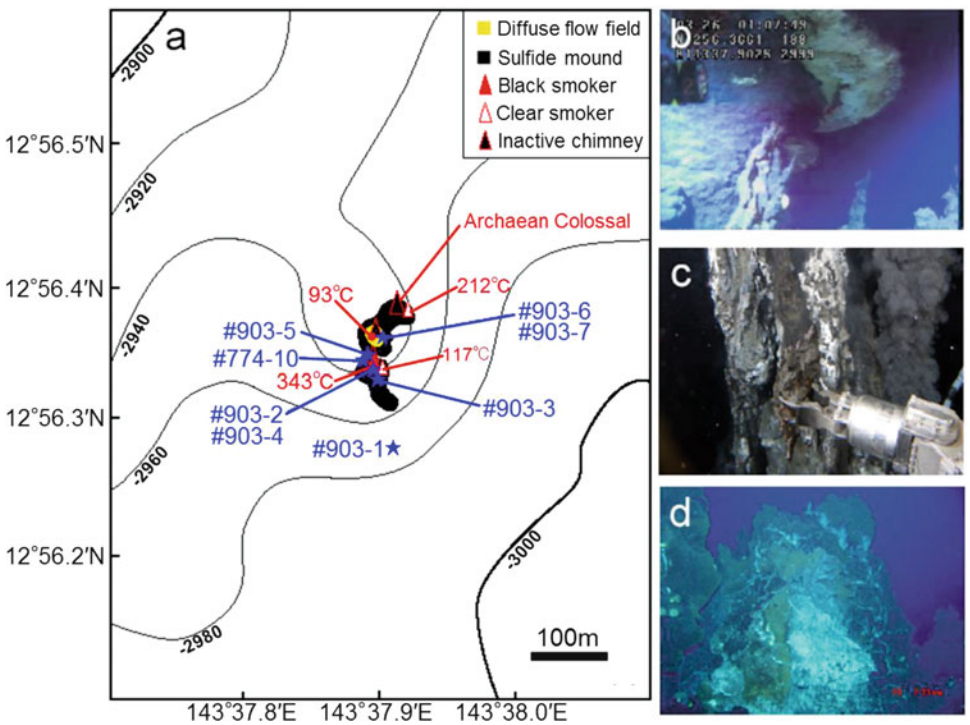

Fig. 22.3 Hydrothermal activity at the Archaean site. (**a**) Bathymetry and distribution of hydrothermal activity of the Archaean site constructed from video logs of the dive #903 during the YK05-09. *Contours* indicate water depth in meter. Numbers in degrees Celsius are the maximum temperatures of the discharging fluids. *Blue stars* indicate the sampling points of hydrothermal mineralization. (**b**) Large flange structure seen at the middle part of the Archaean Colossal. Width of view is ~3 m. (**c**) Actively hydrothermal venting at the 343 °C black smoker chimney. Width of view is ~50 cm. (**d**) Shimmering of 93 °C hydrothermal fluids from the sulfide mound. Width of view is ~3 m

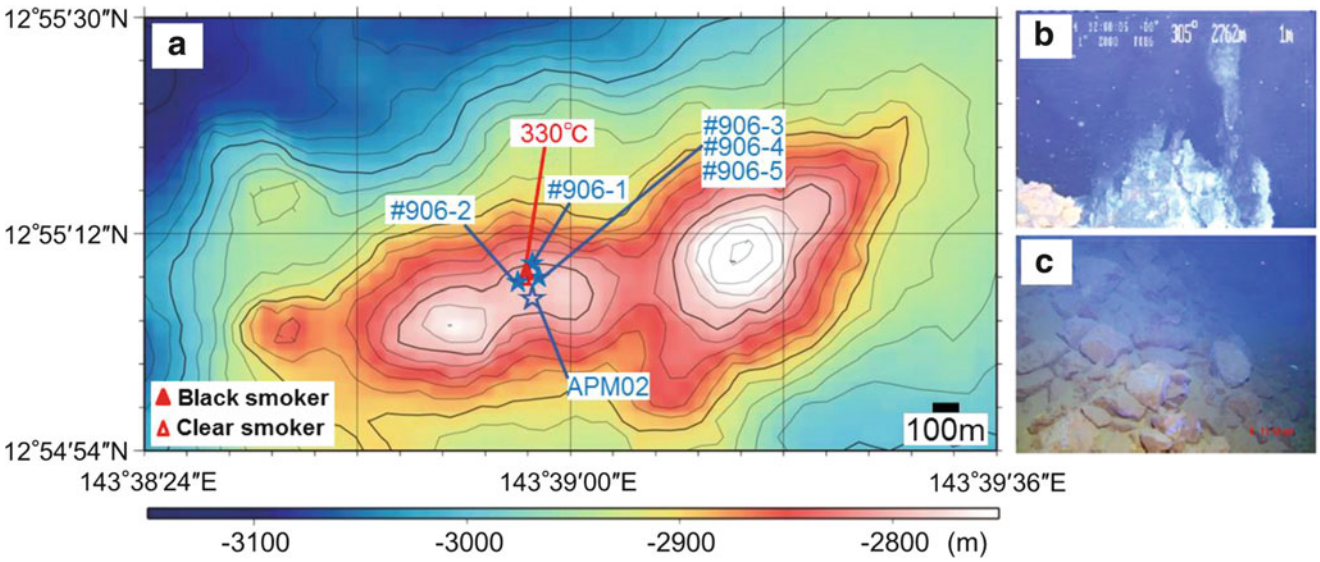

Fig. 22.4 Hydrothermal activity at the Pika site. (**a**) Bathymetry and distribution of hydrothermal activity of the Pika site (modified after the Cruise Report of YK03-09). Contours indicate water depth in meter. Number in degrees Celsius is the maximum temperature of the discharging fluids. *Solid blue stars* indicate the sampling points of hydrothermal mineralization. *Open blue star* indicates the position of the drill hole APM02 by BMS. (**b**) Several black smokers at the top of the sulfide mound. Width of view is ~3 m. (**c**) Piles of massive sulfide breccias and sulfide debris seen at the bottom of the Pika mound. Width of view is ~2 m

22.3 Analytical Methods

22.3.1 Electron Probe X-ray Microanalysis

Chemical compositions of sulfide minerals were determined on a JEOL JCXA-733 electron probe X-ray microanalyzer at Kyushu University, using the thin sections for microscopy after dried in an oven (~80 °C) overnight and coated with evaporated carbon film. This instrument operates with a 20 kV acceleration voltage and a 10 nA specimen current.

22.3.2 Geochemistry of Hydrothermal Ores

Mineralized sample was subsampled (10–50 g), washed with deionized water, dried in air overnight, and ground to powder in an agate mortar. About 0.5 g of the powder sample was decomposed with 20 mL conc. HNO_3 and 2 mL 31 % H_2O_2 on a hot plate with a temperature of about 80 °C. Soon after evaporated to dryness, the precipitates were dissolved in 10 mL 5 N HNO_3. The solution was diluted to proper concentration and conditioned to 1 N HNO_3. Analyses were performed using a Shimadzu AA-680 atomic absorption/flame emission spectrophotometer at Kyushu University.

22.3.3 Fluid Inclusion Microthermometry

Doubly polished thick sections of sphalerite, barite, anhydrite and gypsum were prepared for fluid inclusion study. Microthermometric measurements of fluid inclusions were performed under near infrared (IR) light using Olympus BX51-IR1. Heating and freezing were run using Linkam TH-600, calibrated using synthetic fluid inclusions.

22.3.4 Sulfur Isotope Measurement

Sulfur isotopic compositions of sulfide and barite samples were measured at the University of Tokyo using a Thermo Finnigan DELTAplus mass spectrometer. To prepare SO_2 for mass spectrometry, thermal decomposition of $BaSO_4$ with V_2O_5 and SiO_2 described by Yanagisawa and Sakai (1983) was employed. Sulfur isotopic compositions are reported as $\delta^{34}S$ notation relative to CDT (Canyon Diablo Troilite).

22.4 Results and Discussion

22.4.1 Mineralogy, Fluid Inclusion Microthermometry and Mineral Parageneses

Sulfide crust samples from the Snail site show moderately zoned texture from interior to exterior. The inner layer is enriched in colloform marcasite with minor amount of pyrite overgrowing barite. Small blebs of chalcopyrite are rarely seen. The intermediate layer, which occupies large part of the crust, consists of predominant sphalerite, common marcasite, barite and amorphous silica, and minor pyrite,

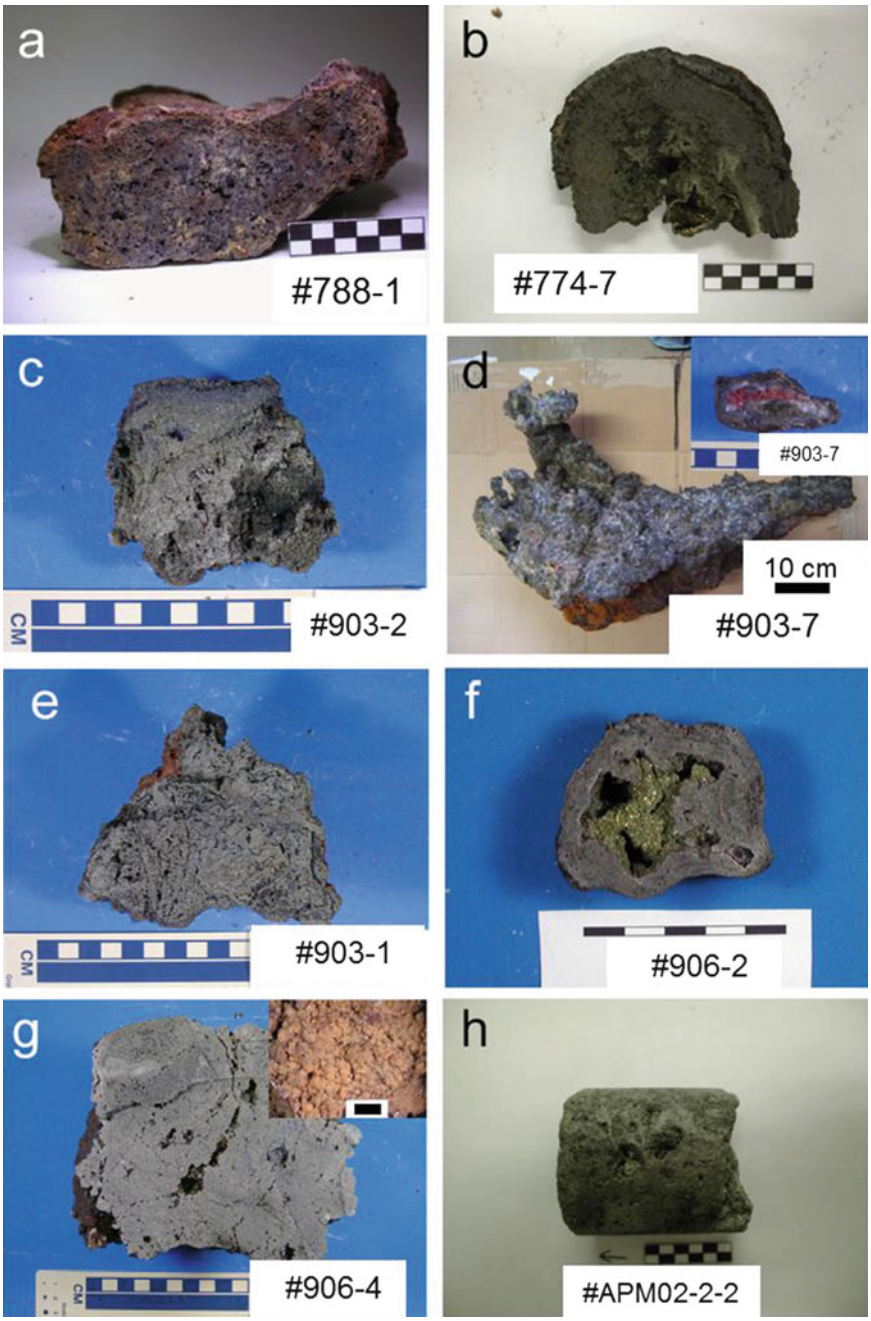

Fig. 22.5 Sample photographs of typical mineralization from the Southern Mariana Trough. (**a**) Sulfide crust from the Snail site (sample #788-1). The upper side is the surface of the crust. (**b**) Cross cut of an inactive chimney sampled from the Yamanaka site (sample #774-7). Chalcopyrite lines the central conduit. (**c**) Piece of active chimney from the Archaean site (sample #903-2). The upper side is the exterior surface. (**d**) Large inactive flange structure collected from the Archaean site (sample #903-7). The inset is a cross cut of a spire grown on the surface of the flange structure. The conduit is filled with barite (*white*) and Fe oxides (*brown*). (**e**) Massive sulfide breccia found on the hydrothermal mound of the Archaean site (sample #903-1). (**f**) Cross cut of an active chimney sampled from the Pika site (sample #906-2). (**g**) Massive sulfide breccia from the Pika mound (sample #906-4). The inset is a surface texture characterized by occurrence of millimetric pyritohedrons. (**h**) Drill core sample APM02-2-2 collected from beneath the Pika mound. *Scale bar* in each photograph is 1 cm except that Figs. 22.5a, b, h are 5 mm

chalcopyrite, galena and tennantite. Sphalerite contains small inclusions of chalcopyrite, galena and tennantite (Fig. 22.6a). Galena and tennantite are common in seafloor hydrothermal minerals on arc and backarc environments (Herzig et al. 2002). Marcasite and pyrite occur as blebs in sphalerite and barite. Some early barite was replaced by sulfides such as sphalerite and marcasite, and some late barite cuts sphalerite, marcasite and pyrite. Yet much of barite appears to be precipitated contemporary with sulfide mineralization. The outermost zone is composed of fine-grained barite with little sulfides. Sulfides and barite are mantled by amorphous silica.

Paragenetic sequence for mineralization at the Snail site is shown in Fig. 22.7a. Fine-grained barite is the first mineral to precipitate. At a higher temperature, small blebs of marcasite and sphalerite are associated with barite (stage I). An isotopic equilibrium temperature (cf., Sect. 22.4.4) of 224 °C was obtained for the mineral assemblage marcasite and sphalerite of the stage I. A ratio of sulfides and barite and crystallinity of sulfides increase with increasing temperature, and replacement of sphalerite by tennantite and chalcopyrite occurs (stage II). Precipitation of galena is confined to the stage II, suggesting that galena is precipitated at a higher temperature. A sphalerite-hosted fluid inclusion from stage

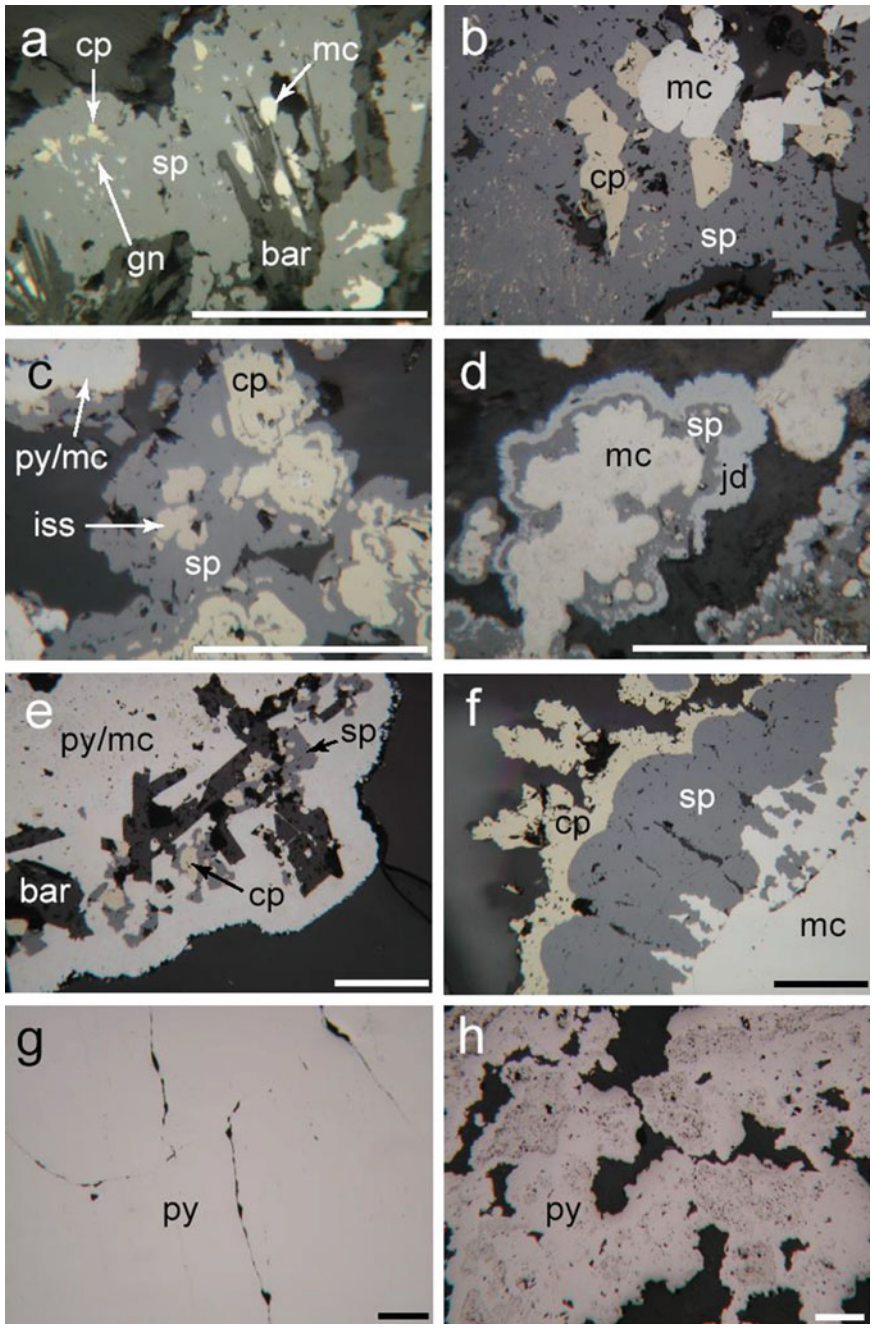

Fig. 22.6 Reflected light photomicrographs of typical mineral assemblages from the Southern Mariana Trough. (**a**) Sphalerite contains chalcopyrite and galena as inclusions seen in sample #788-1. (**b**) Assemblage of sphalerite, chalcopyrite and marcasite seen in sample #774-7. Chalcopyrite disease is frequently found (see lower left of the photomicrograph). (**c**) Intermediate solid solution associated with sphalerite, chalcopyrite and pyrite seen in sample #903-2. (**d**) Typical mineral assemblage seen in inactive chimney from the Archaean site. Marcasite is mantled by sphalerite, which is in turn mantled by jordanite (sample #903-6). (**e**) Typical mineral assemblage seen in massive sulfide breccias from the Archaean site (sample #903-1). Sphalerite and chalcopyrite is partly replaced by marcasite, and later barite overgrows sulfides. (**f**) Zonation of marcasite, sphalerite and chalcopyrite seen in sample #906-2. (**g**) Photomicrograph of massive sulfide breccia (sample #906-4). No sulfide mineral is found other than pyrite. (**h**) Photomicrograph of sample APM02-2-2. The sample consists only of pyrite, but more porous and less mature texture than the massive sulfide breccia samples from the mound (cf., Fig. 22.6g). *Scale bar* in each photomicrograph is 100 μm. *bar* barite, *cp* chalcopyrite, *gn* galena, *iss* intermediate solid solution, *jd* jordanite, *mc* marcasite, *py* pyrite, *sp* sphalerite

II mineralization yielded trapping temperature of 261 °C, which is about 10 °C lower than maximum vent fluid temperature recorded in May 2003. At the waning stage, barite is precipitated in open spaces as relatively coarse crystals. These barites have fluid inclusions with trapping temperatures 188 and 200 °C. Amorphous silica fills the interstices of sulfides and barite at the last (stage III).

Inactive chimney collected from the Yamanaka site is enriched in sphalerite, marcasite and chalcopyrite. Marcasite and lesser amount of pyrite frequently form dendritic and/or colloform aggregates. Pyrite in the inner wall occasionally exhibits cubic morphology. Chalcopyrite disease (Barton and Bethke 1987) in sphalerite is common (Fig. 22.6b). Wurtzite is identified under transmitted polarized light using its anisotropy. Lining of chalcopyrite, which replaces sphalerite, is predominant along central conduit. The exterior surface has a thin layer composed of marcasite, pyrite, sphalerite and barite, which would be formed by fluid seepage through the chimney body.

Paragenetic sequence for mineralization at the Yamanaka site is shown in Fig. 22.7b. Fine-grained barite and dendritic and/or framboidal marcasite are the first mineral assemblage to precipitate, followed by precipitation of sphalerite, marcasite, pyrite and chalcopyrite (stage I). Wurtzite, which can

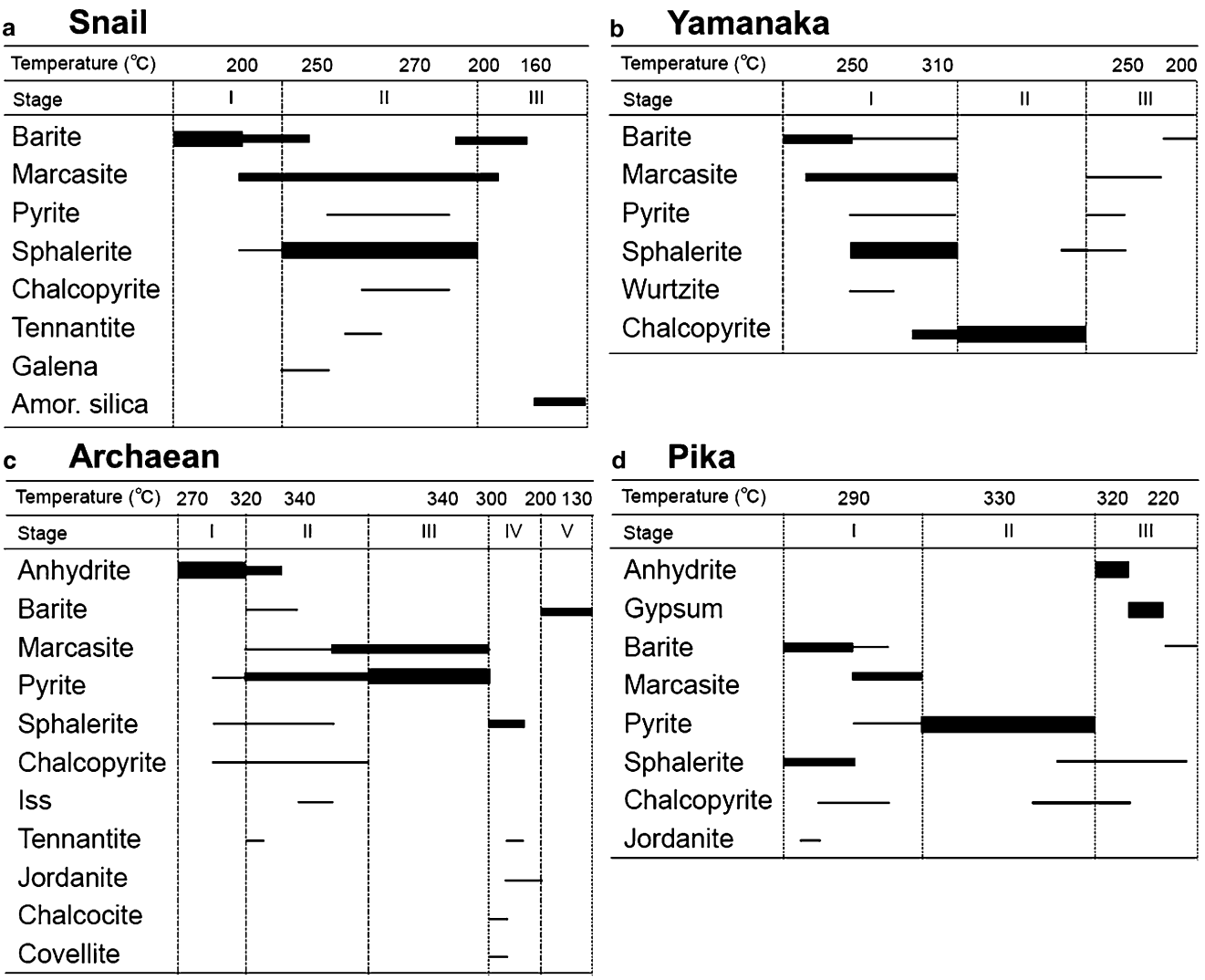

Fig. 22.7 Paragenetic sequence of hydrothermal mineralization in the Southern Mariana Trough. (**a**) Snail site; (**b**) Yamanaka site; (**c**) Archaean site; (**d**) Pika site. *Iss* intermediate solid solution, *Amor. silica* amorphous silica

be precipitated by rapid cooling of hydrothermal fluids as a metastable phase, would be associated with relatively early mineralization. An isotopic equilibrium temperature (cf., Sect. 22.4.4) of 306 °C was obtained for the assemblage pyrite/marcasite and sphalerite. This temperature is about 50 °C higher than a trapping temperature of sphalerite-hosted fluid inclusion (256 °C), but may be closer to the maximum temperature of mineralization at the Yamanaka site. Much of chalcopyrite in the Yamanaka sample extensively replaces sphalerite and marcasite/pyrite (stage II). Reactions for the replacement would be written as follows (Ohmoto 1996):

$$2\mathrm{ZnS\,(s)} + \mathrm{H^+} + \mathrm{Cu^+} + \mathrm{Fe^{2+}} = \mathrm{CuFeS_2(s)} + 2\mathrm{Zn^{2+}} + 1/2\mathrm{H_2(aq)} \quad (22.1)$$

$$2\mathrm{ZnS\,(s)} + \mathrm{FeS_2(s)} + 2\mathrm{Cu^+} + \mathrm{Fe^{2+}} = 2\mathrm{CuFeS_2(s)} + 2\mathrm{Zn^{2+}} \quad (22.2)$$

These reactions can take place when hydrothermal fluid is undersaturated with respect to sphalerite but saturated with respect to chalcopyrite. These conditions would be satisfied by increase in temperature of the hydrothermal fluid. Smaller amounts of marcasite, pyrite, sphalerite and barite would be precipitated at the waning stage (stage III).

Active chimneys from the base of 343 °C black smoker at the Archaean site consist of abundant pyrite and marcasite, common sphalerite and chalcopyrite, and minor barite, iss (intermediate solid solution), tennantite, jordanite, chalcocite and covellite. Intermediate solid solution is associated with sphalerite, chalcopyrite and pyrite (Fig. 22.6c).

Tennantite and jordanite occur locally as tiny blebs in sphalerite. Barite occurs only in outermost part of the chimney, where colloform marcasite is predominant. The inner part has abundant pyrite and chalcopyrite, and lacks marcasite. Anhydrite-hosted fluid inclusions from the 343 °C vent orifice have trapping temperatures ranging from 276 to 349 °C. This temperature range can be explained by precipitation mechanism of anhydrite by mixing of vent fluids with seawater. Salinities of these inclusions have a wide range between 3.2 and 5.4 wt% NaCl. Inactive chimneys from the Archaean mounds contain abundant marcasite, common pyrite, sphalerite and barite, and minor tennantite and jordanite. Marcasite and pyrite occur as cryptocrystalline or colloform aggregates. Sphalerite mantles colloform marcasite, and the sphalerite is in turn mantled by jordanite (Fig. 22.6d). Much of barite occurs as late-stage infillings of conduits and interstices. Massive sulfide rubbles from the Archaean mound are predominated by cryptocrystalline pyrite and marcasite with lesser amounts of sphalerite, chalcopyrite and barite, which are relatively simple mineralogy. Pyrite and marcasite intimately coexist and seem to have replaced much of sphalerite and chalcopyrite. Tabular barite is precipitated within interstices of sulfides and even replacing sulfides (Fig. 22.6e). Chalcocite and covellite occur as secondary minerals.

Mineralization from the Archaean site has five paragenetic successions (Fig. 22.7c). Anhydrite disseminated with pyrite, sphalerite and chalcopyrite is the first mineral assemblage to precipitate from black smoker fluids (stage I). According to the maturity of the chimney, sulfide mineralization involving pyrite, marcasite, sphalerite and chalcopyrite becomes predominant (stage II). Here, iss is precipitated at a temperature higher than 340 °C. Sphalerite precipitated under such a high-temperature condition. Replacement of sphalerite and pyrite/marcasite by chalcopyrite (reactions 1 and 2) would also occur at the Archaean site. However, resulting chalcopyrite would be, in turn, replaced by pyrite/marcasite by the following reaction (Ohmoto 1996):

$$2CuFeS_2(s) + 4H^+ = 2Cu^+ + Fe^{2+} + FeS_2(s) + 2H_2S\,(aq) \quad (22.3)$$

High-temperature acidic hydrothermal fluids undersaturated with chalcopyrite can drive this reaction. The product H_2S can cause direct precipitation of pyrite/marcasite by the following reaction (Ohmoto 1996):

$$Fe^{2+} + 2H_2S\,(aq) = FeS_2(s) + 2H^+ + H_2(aq) \quad (22.4)$$

Much of the assemblage sphalerite + pyrite/marcasite + chalcopyrite is consequently replaced by pyrite/marcasite by the reactions 3 and 4 (stage III). At the waning stage, sphalerite (trapping temperature = 300 °C) is the predominant mineral to precipitate with accessory minerals such as tennantite and jordanite. Barite is the last mineral to precipitate under a temperature between 208 and 130 °C (salinities = 3.2–5.2 wt% NaCl).

Active chimney sampled from the Pika site consists of abundant cryptocrystalline marcasite and pyrite, common sphalerite and chalcopyrite, and rare jordanite and barite. Zonation of marcasite/pyrite, sphalerite and chalcopyrite is well developed (Fig. 22.6f). Massive sulfide breccias from the Pika mound are composed of coarse-grained euhedral pyrite so called pyritohedrons, which coalesce each other to form massive pyrite breccia (Fig. 22.6g). Cryptocrystalline texture of pyrite is rarely seen, and no sulfide phase other than pyrite is recognized. Cracks within massive sulfide breccias are locally filled with gypsum and lesser amount of anhydrite. A thin rind of Fe-oxides and sulfate is also found on their exterior. Fluid inclusions in anhydrite filling cracks of massive sulfides yielded trapping temperature ranges between 306 and 328 °C for primary inclusions and 232 and 278 °C for secondary inclusions. Trapping temperatures of primary inclusions are mostly within a range between 320 and 330 °C, which is well consistent with a maximum vent fluid temperature. The primary inclusions hosted by anhydrite yielded a wide salinity range between 3.5 and 5.4 wt% NaCl, while the secondary inclusions yielded salinities from 4.2 to 4.3 wt% NaCl. Pyrite is an only component of drill core samples recovered from the APM02 hole at the Pika site. Pyrite of these samples is characterized by cryptocrystalline texture (Fig. 22.6h), which can be recognized as formed under relatively low-temperature conditions (e.g., Ramdohr 1980). In addition, these core samples represent relatively porous texture.

Figure 22.7d shows the mineral paragenesis for the Pika mineralization. Barite, marcasite, pyrite, chalcopyrite and sphalerite (trapping temperatures = 291 and 296 °C) with accessory jordanite are the early sulfide phases (stage I). Replacement of sphalerite by the reaction 1 is common in this stage. At the main stage of mineralization, sphalerite and chalcopyrite are significantly replaced by pyrite by the reaction 3 (stage II). When the chimney composed of massive pyrite is cracked, anhydrite is precipitated to fill the cracks. Subsequently, anhydrite is hydrated by ambient seawater to form gypsum, followed by precipitation of barite at the waning stage (stage III).

22.4.2 Characteristics of Chemical Compositions for Selected Minerals

The FeS contents in sphalerite grains from the Southern Mariana Trough are shown in Fig. 22.8. Sphalerite from the Snail site has a narrow range of FeS contents between

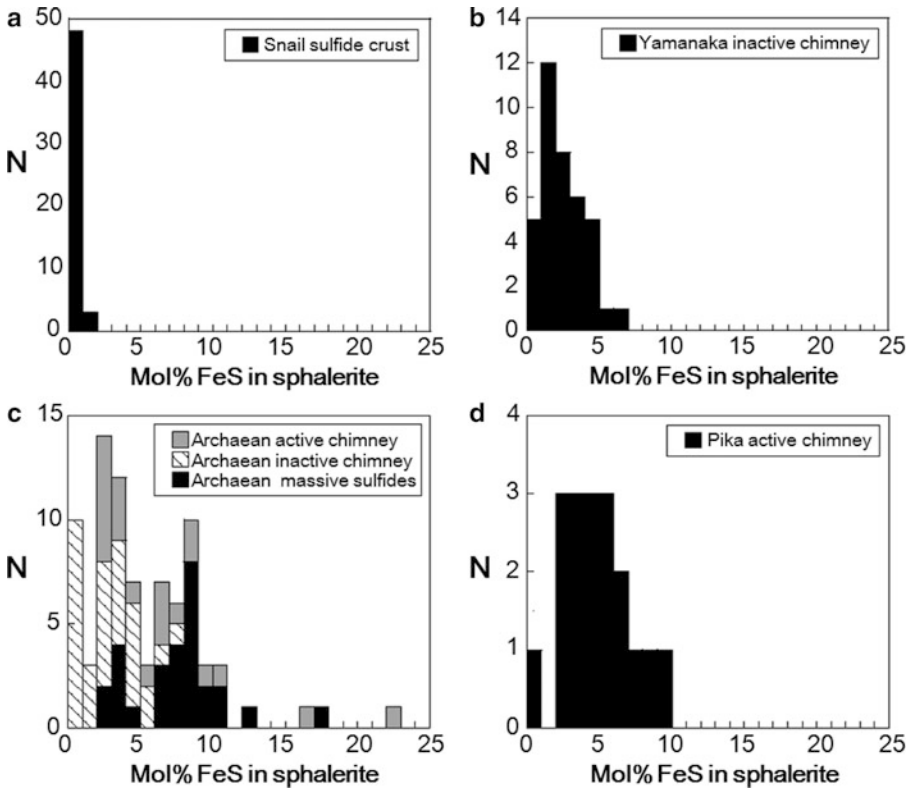

Fig. 22.8 Histograms of FeS content in sphalerite from the Southern Mariana Trough. (**a**) Snail site; (**b**) Yamanaka site; (**c**) Archaean site; (**d**) Pika site

nil and 1.8, and 0.4 mol% on average. FeS contents in sphalerite/wurtzite from the Yamanaka site range between 0.3 and 6.9 mol%, averaging 2.5 mol%. On the other hand, sphalerite from the off-axial sites has wider ranges of FeS contents. Sphalerite in active chimneys from the Archaean site contains 2.2–22.5 mol% FeS and has average FeS content of 6.5 mol%. Sphalerite in inactive chimneys has FeS contents ranging from nil to 7.3, and 2.7 mol% on average. Sphalerite in massive sulfide breccias contains 2.0–17.3 mol % FeS and has average FeS contents of 7.5 mol%. For sphalerite from the Pika site, FeS contents have a range between 0.8 and 9.1 mol% and an average value of 4.8 mol%.

The sulfur fugacity (f_{S2}) of hydrothermal fluids for each site was determined using the FeS content in sphalerite and a formation temperature of the sphalerite (Scott and Barnes 1971). The calculated f_{S2} of hydrothermal systems in the Southern Mariana Trough is low for off-axial sites and high for on-axial sites. The mineralizations from the Archaean and Pika sites yielded lower f_{S2}, plotted near the equilibrium between pyrite and pyrrhotite. In sediment-free mid-ocean ridge systems, the pyrite-pyrrhotite buffer controls the f_{S2} condition (e.g., Hannington et al. 1995). The Snail site is plotted near the sulfidation equilibrium between tennantite and enargite. Compared with the Snail site, the Yamanaka site shows a slightly lower f_{S2}, although higher than those of off-axial sites. High f_{S2} condition in a hydrothermal system hosted by an arc volcano can be indicative of contribution of magmatic SO_2 that disproportionates and generates H_2S (de Ronde et al. 2005).

Trace metal contents in pyrite/marcasite differ by locality and sample type. Pyrite/marcasite from the Snail and Yamanaka sites have relatively high Zn (~0.23 wt%) and As (~0.08 wt%) contents. Pyrite/marcasite in chimney and massive sulfide samples from the Archaean and Pika sites have lower Zn (~0.05 wt%) and As (~0.03 wt%) contents. Copper contents in pyrite/marcasite, however, make little difference by locality and sample type. Intermediate solid solution from 343 °C black smoker at the Archaean site has chemical composition close to that of stoichiometric cubanite, and is moderately zinciferous (~1.42 wt%).

22.4.3 Comparison of Bulk Chemical Compositions for Mineralized Samples

Bulk chemical concentrations of mineralized samples are given in Table 22.1. Mineralized samples from the Snail and Yamanaka sites are relatively rich in Zn (11.9–48.2 wt %) and poor in Fe (0.88–9.07 wt%). These results reflect the sphalerite-dominant mineralogy of the samples. Sea-floor hydrothermal mineralization formed in island arc settings can be normally differentiated from those on mid-ocean ridges by major element geochemistry. On the Cu-Zn-Fe diagram (Fig. 22.9a), mineralizations recovered from the Snail and Yamanaka sites are plotted in the arc-setting field. On the other hand, mineralized samples from the Archaean and Pika sites are characterized by higher Fe concentrations (21.3–42.9 wt%), which arise

Table 22.1 Geochemistry of hydrothermal precipitate samples from the Southern Mariana Trough, determined by atomic absorption spectrometry

Site	Sample	Type	Fe (wt%)	Cu	Zn	Pb (ppm)	Mn	Cd	Sb	Ag
Snail	#788-1-a	Sulfide crust (outer)	9.07	0.39	22.7	5616	1703	104	<200	98
	#788-1-b	Sulfide crust (inner)	0.88	0.69	43.3	3053	258	404	<200	116
	#794-3	Sulfide crust	5.63	0.23	11.9	8755	783	70	281	275
Yamanaka	#774-7	Inactive chimney	8.00	4.90	48.2	1410	670	1288	284	74
Archaean	#774-10	Massive sulfides	42.9	0.88	0.48	236	21	13	<200	<30
	#903-1	Massive sulfides	38.9	0.59	2.20	1346	46	42	147	50
	#903-2	Active chimney	33.0	7.51	0.44	240	188	18	n.a.	31
	#903-4	Active chimney	37.3	0.66	0.77	169	53	25	n.a.	32
	#903-5	Massive sulfides	37.5	0.03	0.26	462	21	10	n.a.	<30
	#903-6	Inactive chimney	24.1	0.03	13.4	4997	1628	90	n.a.	65
	#903-7	Inactive chimney	21.3	0.02	13.2	5477	161	86	n.a.	59
Pika	APM02-1-a	Drill core	41.0	0.21	0.04	84	<20	<10	<200	<30
	APM02-2-2	Drill core	36.2	0.20	0.04	71	<20	<10	<200	<30
	APM02-3-1	Drill core	37.5	0.28	0.09	198	49	<10	<200	<30
	APM02-4-1	Drill core	38.8	0.33	0.08	145	59	<10	<200	<30
	#906-1	Massive sulfides	36.1	0.10	0.03	77	n.a.	<10	n.a.	<30
	#906-2	Active chimney	32.1	1.78	5.75	1167	32	194	229	63
	#906-3	Massive sulfides	34.8	0.02	0.07	96	n.a.	<10	<200	<30
	#906-4	Massive sulfides	35.5	0.02	0.08	90	n.a.	<10	<200	<30
	#906-5	Massive sulfides	36.3	0.03	0.05	81	<20	<10	<200	<30

n.a. not analyzed

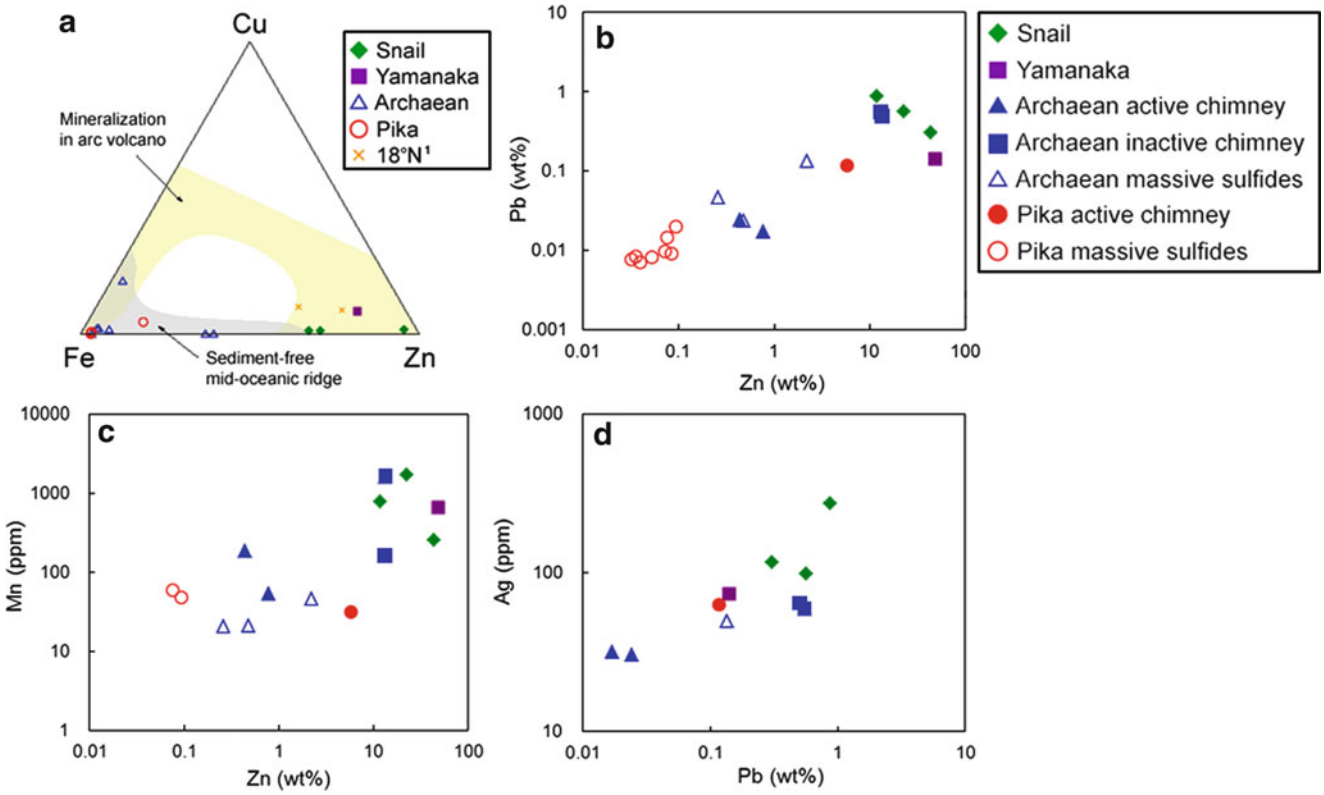

Fig. 22.9 (**a**) Cu-Fe-Zn ternary diagram showing the geochemistry of hydrothermal mineralization in the Southern Mariana Trough compared with those on sediment-free mid-ocean ridges (Hannington et al. 1991) and arc volcanoes (Watanabe et al. 1995; de Ronde et al. 2005). 1: Hannington (1989). (**b**) Log/log plot of Zn versus Pb concentrations in precipitate samples from the Southern Mariana Trough. Pika massive sulfides include drill core samples from the APM02 hole. (**c**) Log/log plot of Zn versus Mn concentrations in precipitate samples from the Southern Mariana Trough. Pika massive sulfides include drill core samples from the APM02 hole. (**d**) Log/log plot of Pb versus Ag concentrations in precipitate samples from the Southern Mariana Trough

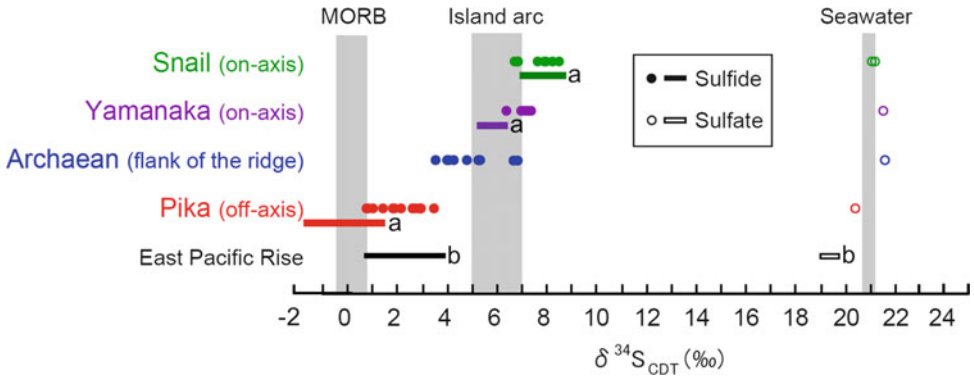

Fig. 22.10 Compilation of sulfur isotopic ratios ($\delta^{34}S_{CDT}$‰) of sulfides and sulfates from the Southern Mariana Trough compared with those from mid-ocean ridge and island arc settings. MORB: Sakai et al. (1984); Island arc volcanic rock: Ueda and Sakai (1984); Seawater: Rees et al. (1978). **a**: Kakegawa et al. (2008); **b**: Styrt et al. (1981) and Kerridge et al. (1983)

from pyrite- and marcasite-rich mineral compositions. This mineral assemblage as well as bulk chemical compositions are similar to massive pyrite ore on sediment-free mid-ocean ridges (Herzig et al. 2002) (Fig. 22.9a), although is devoid of pyrrhotite. Hydrothermal fluids from the Pika site have pH of 2.9, which is somehow acid compared with the range of mid-ocean ridge fluids (Ishibashi et al. 2006; Toki et al. Chap. 45). Therefore the solubility is enhanced and temperatures of mineral precipitation decrease, compared with those of the East Pacific Rise. As a result, pyrite is the only mineral to precipitate in high-temperature condition, and mineralization becomes enriched in Fe (Fig. 22.9a). Copper is poor in most samples (<1 wt%) except for three chimney samples. The Snail and Yamanaka samples, as well as the Archaean inactive chimneys and Pika active chimney, are rich in Pb (1,167–8,755 ppm). Occurrence of galena and jordanite and Pb-bearing sphalerite can account for the enrichment of Pb in these samples. Lead, Cd and Mn moderately to strongly correlate with Zn (Fig. 22.9b, c and Table 22.1). Samples from the Snail and Yamanaka sites have higher Pb and Zn compositions than those from the Archaean and Pika sites (Fig. 22.9b). Correlation between Mn, Cd and Zn can be explained by formation of solid solution as sphalerite. But precipitation of Mn oxyhydroxide during the low-temperature mineralization would contribute to Mn geochemistry. Correlation between Pb and Zn may be attributed to the mineralogy that sphalerite contains Pb-bearing minerals as invisible inclusions. Silver correlates more strongly with Pb (Fig. 22.9d), suggesting that Ag is incorporated in galena.

22.4.4 Source of a Range in Sulfur Isotopic Compositions for Sulfide and Sulfate Minerals from the Southern Mariana Trough

The hydrothermal minerals from the Southern Mariana Trough show variable $\delta^{34}S$ values, ranging from +0.8 to +8.5 ‰ (Fig. 22.10). Sulfides from the Snail sulfide crust samples have $\delta^{34}S$ values between +6.8 and +8.5 ‰ for sphalerite and between +6.9 and +7.9 ‰ for pyrite/marcasite. These $\delta^{34}S$ ranges are consistent with the reported values ($\delta^{34}S = +7.0 - +8.7$ ‰) for sulfide crust samples from the Snail site (Kakegawa et al. 2008). Inner parts of the samples have lower $\delta^{34}S$ values than the outer parts. An equilibrium temperature of 224 °C is calculated using the sphalerite-pyrite fractionation equation of Smith et al. (1977). Sulfides from the Yamanaka inactive chimney have $\delta^{34}S$ values between +7.1 and +7.4 ‰ for sphalerite, between +7.0 and 7.2 ‰ for chalcopyrite and +6.4 ‰ for pyrite/marcasite. These $\delta^{34}S$ ranges are slightly higher than those ($\delta^{34}S = +5.1 - +6.3$ ‰) for sulfide chimney samples from the Yamanaka site (Kakegawa et al. 2008). Sulfides from the inner wall of chimney have lower $\delta^{34}S$ values than those from the outer wall. The pyrite-sphalerite geothermometer yields 306 °C for pyrite/marcasite-sphalerite assemblage. Sulfides from the Archaean site yielded $\delta^{34}S$ values ranging from +4.1 to +4.3 ‰ for sphalerite and from +3.6 to +6.9 ‰ for pyrite/marcasite. Sulfides from the Pika site have $\delta^{34}S$ values between +0.8 and +3.5 ‰ for pyrite/marcasite and +1.0 ‰ for sphalerite. These $\delta^{34}S$ ranges are slightly higher than those ($\delta^{34}S = -1.8 - +1.7$ ‰) for sulfide chimney samples from the Pika site (Kakegawa et al. 2008). Sulfur isotope ratios of drill core samples ($\delta^{34}S = +2.8 - +3.5$ ‰) are slightly higher than those of massive sulfide samples ($\delta^{34}S = +1.4 - +3.0$ ‰). Barites from the Southern Mariana Trough ($\delta^{34}S = +20.4 - +21.6$ ‰) are isotopically close to seawater sulfate, indicating that mixing of hydrothermal fluids with seawater brought about barite precipitation. The fact that $\delta^{34}S$ value (+20.4 ‰) of the Pika barite is slightly lower than that of the ambient seawater indicates mixing of hydrothermal fluids with a small amount of seawater and subsequent oxidation of hydrothermal sulfide. Sulfides from the on-axial sites (Snail and Yamanaka) obviously have higher $\delta^{34}S$ values than those from the off-axial site (Pika). In addition, $\delta^{34}S$ values of sulfides from the Archaean site, which is situated between the Snail and Pika sites, are approximately intermediate between those of the Snail and Pika sites.

There can be several processes that cause isotopic fractionation and develop a wide range in $\delta^{34}S$ values within a single hydrothermal field. It is possible that higher $\delta^{34}S$ values obtained from the Snail and Yamanaka sulfides are attributed to the incorporation of seawater sulfate-derived sulfur without isotopic fractionation during reducing process in a seafloor environment. Sulfur occurs as sulfate in seawater with $\delta^{34}S$ values of about +21 ‰ (Rees et al. 1978). So the incorporation of seawater sulfate-derived sulfur reduced without isotope fractionation can increase the $\delta^{34}S$ values. However, the theoretical modeling shows that mixing of hydrothermal fluids with seawater at the seafloor cannot generate $\delta^{34}S$ value heavier than +4.5 ‰ (Janecky and Shanks 1988). Thus, this process cannot explain the range in the $\delta^{34}S$ values of the Snail and Yamanaka sites. Around seafloor hydrothermal sites, heating (150–200 °C) of seawater during downflow in upper oceanic crust commonly results in the formation of anhydrite (Shanks et al. 1981; Janecky and Shanks 1988). At high-temperature conditions of above 200 °C, the anhydrite (SO_4^{2-}) is subsequently dissolved, and partially reduced to sulfide (H_2S) without isotope fractionation (Shanks et al. 1981; Shanks and Seyfried 1987). Therefore, the degree of mixing of this isotopically heavy sulfur with magmatic sulfur can account for the variation of $\delta^{34}S$ values of sulfide minerals in the four hydrothermal sites. The other possible cause of the sulfur isotopic range is the variety in the $\delta^{34}S$ values of the host rocks under each vent site. The incorporation of sulfur into hydrothermal fluids by leaching of igneous sulfides proceeds with little isotopic fractionation, therefore the fluid H_2S should have $\delta^{34}S$ values similar to footwall rock values (Shanks et al. 1995). The $\delta^{34}S$ values of mid-ocean ridge basalt (MORB) vary within a narrow range of +0.1 ± 0.5 ‰ (Sakai et al. 1984). In contrast, island arc magma has higher $\delta^{34}S$ values of up to +7 ‰ due to the presence of a subduction-related seawater sulfate component in the subarc mantle source (Ueda and Sakai 1984). The $\delta^{34}S$ values of backarc magma lie between those of MORB and island arc rocks (Alt et al. 1993). In the Southern Mariana Trough, the close proximity of arc volcanoes to the spreading center may be responsible for the axial high of the spreading center. The proximity, as well as the radial faulting pattern of the eastern backarc basin south of 13°10′N, may facilitate channeling of arc magma to the spreading center (Fryer 1995; Fryer et al. 1998). Martinez et al. (2000) proposed that the well-developed spreading system, in contrast to the rifting-stage system of the Northern Mariana Trough, channels arc magma efficiently along the backarc-spreading axis. They also suggested that the small arc seamounts in the Southern Mariana Trough may also support the derivation of the arc magmatic budget to the spreading center. Although there are no sulfur isotopic data of footwall volcanic rocks from the Snail, Yamanaka, Archaean and Pika sites, basement rocks from the four hydrothermal fields have geochemical signatures of slab-derived components (Nakamura et al., Chap. 41). Moreover, our data show that mineralizations from the on-axial sites tend to have an arc-like geochemical signatures compared with those from the off-axial sites. Therefore, at the moment, we cannot rule out the possibility that the sulfur isotope variations of sulfide minerals from the four hydrothermal sites are influenced by sulfur isotopic characteristics of volcanic rocks under each vent site.

Acknowledgments We wish to thank *SHINKAI 6500* and ROV *ROPOS* team members, crews of the R/V *YOKOSUKA* and R/V *Thomas G. Thompson*, and onboard scientists for their skillful support during the YK03-09, YK05-09 and TN167A cruises. We also thank crews of the R/V *Hakurei-Maru No.2* during the BMS2004 cruise for their cooperation. Profs. Hitoshi Chiba and Shunichi Nakai are thanked for their constructive comments that helped improve the manuscript. This study was supported by the Ministry of Education, Culture, Sports, Science and Technology (MEXT) of Japan through a Special Coordination Fund "Archaean Park Project" and a Grant-in-Aid for Scientific Research on Innovative Areas "TAIGA project". This study was also financially supported by JSPS and NSF, respectively.

References

Alt JC, Shanks WC III, Jackson MC (1993) Cycling of sulfur in subduction zones: the geochemistry of sulfur in the Mariana island arc and back-arc Trough. Earth Planet Sci Lett 119:477–494

Barton PB, Bethke PM (1987) Chalcopyrite disease in sphalerite: pathology and epidemiology. Am Mineral 72:451–467

de Ronde CEJ, Hannington MD, Stoffers P, Wright IC, Ditchburn RG, Reyes AG, Baker ET, Massoth GJ, Lupton JE, Walker SL, Greene RR, Soong CW, Ishibashi J, Lebon GT, Bray CJ, Resing JA (2005) Evolution of a submarine magmatic-hydrothermal system: Brothers volcano, southern Kermadec arc, New Zealand. Econ Geol 100:1097–1133

Fouquet Y, von Stackelberg U, Charlou JL, Erzinger J, Herzig PM, Mühe R, Wiedicke M (1993) Metallogenesis in back-arc environments; the Lau Basin example. Econ Geol 88:2154–2181

Fryer P (1995) Geology of the Mariana Trough. In: Taylor B (ed) Backarc basins: tectonics and magmatism. Springer, New York, pp 237–279

Fryer P, Fujimoto H, Sekine M, Johnson LE, Kasahara J, Masuda H, Gamo T, Ishii T, Ariyoshi M, Fujioka K (1998) Volcanoes of the southwestern extension of the active Mariana island arc: new swath-mapping and geochemical studies. Island Arc 7:596–607

Hannington MD (1989) The geochemistry of gold in modern sea-floor hydrothermal systems and implications for gold mineralization in ancient volcanogenic massive sulfides, PhD thesis, University of Toronto, p 554

Hannington MD, Herzig PM, Scott SD, Thompson G, Rona P (1991) Comparative mineralogy and geochemistry of gold-bearing sulfide deposits on the mid-ocean ridges. Mar Geol 101:217–248

Hannington MD, Jonasson IR, Herzing PM, Petersen S (1995) Physical and chemical processes of seafloor mineralization at mid-ocean ridges. In: Humphris SE, Zierenberg RA, Mullineaux LS,

Thomson RE (eds) Seafloor hydrothermal systems: physical, chemical, biological, and geological interactions. Geophysical monograph series, vol 91, Am Geol Union, pp 115–157

Herzig PM, Hannington MD (1995) Polymetallic massive sulfides at the modern seafloor: a review. Ore Geol Rev 10:95–115

Herzig PM, Hannington MD, Petersen S (2002) Polymetallic massive sulphide deposits at the modern seafloor and their resource potential. In: Polymetallic massive sulphides and cobalt-rich ferromanganese crusts: status and prospects, international seabed authority technical study 2, Report on the UN Workshop on Seafloor Mineral Resources 2000, Kingston, Jamaica, pp 8–35

Ishibashi J, Urabe T (1995) Hydrothermal activity related to arc-backarc magmatism in the Western Pacific. In: Taylor B (ed) Tectonics and magmatism. Plenum Press, New York, pp 451–495

Ishibashi J, Suzuki R, Yamanaka A, Toki T, Kimura H, Noguchi T, Urabe T (2006) Seafloor hydrothermal activity at off-axial seamounts of backarc spreading in Southern Mariana Trough. Geochim Cosmochim Acta 70:A279

Janecky DR, Shanks WC III (1988) Computational modeling of chemical and sulfur isotopic reaction processes in seafloor hydrothermal systems: chimney, massive sulfides, and subjacent alteration zones. Can Mineral 26:805–825

Kakegawa T, Utsumi M, Marumo K (2008) Geochemistry of sulfide chimneys and Basement pillow lavas at the Southern Mariana Trough (12.55°N-12.58°N). Res Geol 58:249–266

Kato S, Kobayashi C, Kakegawa T, Yamagishi A (2009) Microbial communities in iron-silica-rich microbial mats at deep-sea hydrothermal fields of the Southern Mariana Trough. Environ Microbiol 11:2094–2111

Kerridge JF, Haymon RM, Kastner M (1983) Sulfur isotope systematics at the 21°N site, East Pacific Rise. Earth Planet Sci Lett 66:91–100

Martinez F, Fryer P, Becker N (2000) Geophysical characteristics of the Southern Mariana Trough, 11°50′N-13°40′N. J Geophys Res 105:16591–16607

Nakamura K, Toki T, Mochizuki N, Asada M, Ishibashi J, Nogi Y, Yoshikawa S, Miyazaki J, Okino K (2013) Discovery of a new hydrothermal vent based on an underwater, high-resolution geophysical survey. Deep Sea Res I 74:1–10

Ohmoto H (1996) Formation of volcanogenic massive sulfide deposits: the Kuroko perspective. Ore Geol Rev 10:135–177

Ramdohr P (1980) The ore minerals and their intergrowth. Pergamon Press, Oxford, p 1205

Rees CE, Jenkins WJ, Monster J (1978) The sulfur isotopic composition of ocean water sulfate. Geochim Cosmochim Acta 42:377–381

Sakai H, Des Maris DJ, Ueda A, Moore JG (1984) Concentrations and isotope ratios of carbon, nitrogen, and sulfur in ocean-floor basalts and volcanic gases at Kilauea volcano, Hawaii. Geochim Cosmochim Acta 48:2433–2441

Scott SD, Barnes HL (1971) Sphalerite geothermometry and geobarometry. Econ Geol 66:653–669

Shanks WC III, Böhlke JK, Seal RR II (1995) Stable isotopes in mid-ocean ridge hydrothermal systems: interactions between fluids, minerals and organisms. In: Humphris SE, Zierenberg RA, Mullineaux LS, Thomson RE (eds) Seafloor hydrothermal systems: physical, chemical, biological, and geological interactions. Geophysical monograph series, vol 91, Am Geol Union, pp 194–221

Shanks WC III, Seyfried WE Jr (1987) Stable isotope studies of vent fluids and chimney minerals, southern Juan de Fuca Ridge. Sodium metasomatism and seawater sulfate reduction. J Geophys Res 92:11387–11399

Shanks WC III, Bischoff JL, Rosenbauer RJ (1981) Seawater sulfate reduction and sulfur isotope fractionation in basaltic systems: interaction of seawater with fayalite and magnetite at 200–350 °C. Geochim Cosmochim Acta 45:1977–1995

Smith JW, Doolan S, McFarlane EF (1977) A sulfur isotope geothermometer for the trisulfide system galena-sphalerite-pyrite. Chem Geol 19:83–90

Styrt MM, Brackmann AJ, Holland HD, Clark BC, Pisutha-Arnond V, Eldridge CS, Ohmoto H (1981) The mineralogy and the isotopic composition of sulfur in hydrothermal sulfide/sulfate deposits on the East Pacific Rise, 21°N latitude. Earth Planet Sci Lett 53:382–390

Takamasa A, Nakai S, Sato F, Toyoda S, Banerjee D, Ishibashi J (2013) U–Th radioactive disequilibrium and ESR dating of a barite-containing sulfide crust from South Mariana Trough. Quart Geochron 15:38–46

Ueda A, Sakai H (1984) Sulfur isotope study of Quaternary volcanic rocks from the Japanese island arc. Geochim Cosmochim Acta 48:1837–1848

Watanabe K, Shibata A, Kajimura T (1995) Comparison of the bulk chemical composition between hydrothermal sulfides from Suiyo Seamount and sea-floor hydrothermal sulfides from the other areas. JAMSTEC J Deep Sea Res 11:351–361

Yanagisawa F, Sakai H (1983) Thermal decomposition of barium sulfate-vanadium pentaoxide-silica glass mixtures for preparation of sulfur dioxide in sulfur isotope ratio measurements. Anal Chem 55:985–987

Yoshikawa S, Okino K, Asada M (2012) Geomorphological variations at hydrothermal sites in the Southern Mariana Trough: relationship between hydrothermal activity and topographic characteristics. Mar Geol 303–306:172–182

Dating of Hydrothermal Mineralization in Active Hydrothermal Fields in the Southern Mariana Trough

23

Jun-ichiro Ishibashi, Kazuhiko Shimada, Fumihiro Sato, Ai Uchida, Shin Toyoda, Asako Takamasa, Shun'ichi Nakai, Hironobu Hyodo, Keiko Sato, Hidenori Kumagai, and Kei Ikehata

Abstract

Ages of sulfide and sulfate mineralized samples collected from active hydrothermal fields in the Southern Mariana Trough were determined. In addition to samples collected from active and inactive chimneys, and sulfide breccia during dive expeditions, massive sulfide ores obtained by shallow drilling were studied. We applied $^{230}Th/^{234}U$ radioactive disequilibrium dating technique to sulfide minerals, as the collected mineralized samples were dominated by marcasite, pyrite and sphalerite. In addition, electron spin resonance (ESR) dating was applied to a few barite-rich samples, for comparison purpose. A laser step heating ^{39}Ar-^{40}Ar dating of the basement volcanic rock samples was also attempted.

Sulfide chimneys and ores collected from a hydrothermal mound located beside the spreading axis range in age from <100 to 3,520 years old, without notable hiatus. The growth rate of the massive sulfide ore body is calculated to be 0.12–1.5 mm year^{-1} based on results of the core samples. This age range is comparable for those previously reported for giant hydrothermal mounds of a few 100 m in diameter. These results suggest >1,000 years of continuous hydrothermal activity would be necessary for the formation of a massive sulfide deposit.

Sulfide chimneys and breccia collected from two hydrothermal fields located on an off-axis knoll are up to 9,000 years old. Sulfide breccia collected from an active site on the spreading axis are 2,740 and 7,190 years old. Geophysical studies provided evidence for abundant magma supply in the Southern Mariana Trough, which would have fueled hydrothermal activities in this area for long duration. While geophysical evidence for crustal velocity anomaly below the off-axis knoll suggests mineralization at the off-axis sites is considered to be in the late-stage of the hydrothermal activity, the discrete ages from the on-axis site might reflect episodic hydrothermal activities related to diking events proposed by geophysical and geological studies.

The online version of this chapter (doi:10.1007/978-4-431-54865-2_23) contains supplementary material, which is available to authorized users.

J.-i. Ishibashi (✉) • K. Shimada
Faculty of Sciences, Kyushu University, Fukuoka, Japan
e-mail: ishibashi.junichiro.779@m.kyushu-u.ac.jp

F. Sato • A. Uchida • S. Toyoda • H. Hyodo
Okayama University of Science, Okayama, Japan

A. Takamasa
Earthquake Research Institute, The University of Tokyo, Tokyo, Japan

National Institute of Radiological Sciences, Chiba, Japan

S. Nakai
Earthquake Research Institute, The University of Tokyo, Tokyo, Japan

K. Sato
Institute for Research on Earth Evolution (IFREE), Japan Agency for Marine-Earth Science and Technology (JAMSTEC), Yokosuka, Japan

Research and Development (R&D) Center for Submarine Resources, Japan Agency for Marine-Earth Science and Technology (JAMSTEC), Yokosuka, Japan

Okayama University of Science, Okayama, Japan

H. Kumagai
Institute for Research on Earth Evolution (IFREE), Japan Agency for Marine-Earth Science and Technology (JAMSTEC), Yokosuka, Japan

K. Ikehata
Faculty of Life and Environmental Sciences, University of Tsukuba, Tsukuba, Japan

J.-i. Ishibashi et al. (eds.), *Subseafloor Biosphere Linked to Hydrothermal Systems: TAIGA Concept*,
DOI 10.1007/978-4-431-54865-2_23,

Keywords
BMS shallow drilling • Massive sulfide deposits • U-Th disequilibrium dating

23.1 Introduction

Studies dating of hydrothermal mineralization provide key information for understanding formation processes of seafloor massive sulfide deposits, since prolonged hydrothermal activity is undoubtedly required to accumulate metals needed to form an economic ore deposit. Application of radiometric dating technique to studies dating of hydrothermal mineralization has attempted since 1980s (e.g., Lalou and Brichet 1987). Many of pioneering studies, however, reported age data only for a limited numbers of samples collected from one or two hydrothermal fields, and the age data were simply attributed to be a sign for active and resting stages of episodic hydrothermal activity (e.g. Lalou et al. 1995). Recent improvements in analytical techniques have contributed to reduce both sample volume and analysis time, which enabled us to conduct a systematic study to discuss linkage between a series of chronological data and records of geologic events (e.g., You and Bickle 1998; Ditchburn et al. 2012). Jamieson et al. (2013) conducted a dating study of mineralized samples collected from inside slope and outside of the axial valley of the Juan de Fuca ridge. They revealed temporal and spatial history of hydrothermal activity, which appears to have been closely related to evolution of the axial valley. de Ronde et al. (2011) conducted a dating study of chimney samples divided into some parts and compared the age data with geochemical data. They revealed how episodic magmatic input into the system affects the accumulation of metals based on a relationship between fluctuating geochemical data along ages.

During the TAIGA project, we have developed application of two different techniques; $^{230}Th/^{234}U$ radioactive disequilibrium and electron spin resonance (ESR) to hydrothermal minerals (Takamasa et al. 2013, Kumagai et al. Chap. 5). The $^{230}Th/^{234}U$ radioactive disequilibrium technique is applied to sulfide minerals. When sulfide minerals precipitate from the hydrothermal fluid, U is usually incorporated into them but Th is completely absent. Once sulfide mineral precipitated, ^{230}Th accumulates due to radioactive decay of ^{234}U, and $^{230}Th/^{234}U$ ratio gradually approaches to the radioactive equilibrium with time. From the half-lives of ^{230}Th and ^{234}U, this technique is applicable to dating an age range from 10^2 to 10^5 years. The ESR dating is based on the idea that paramagnetic defects with unpaired electrons are created by natural radiation and accumulates with time since mineral precipitation. Okumura et al. (2010) first practically applied this technique to barite in samples collected from the seafloor, by determining signal intensities of the paramagnetic defects with SO_3^- radical. Toyoda et al. (2011) estimated an age range of application of the ESR dating for barite from 10^2 to 10^5 years based on estimation for stability of paramagnetic defects. This age range (from 10^2 to 10^5 years) cannot relate with a time series change which visual observation records, but would cover broad spectra of events related to hydrothermal activity such as formation of a massive sulfide deposit (Kumagai et al. Chap. 5). For longer time range, $>10^4$ years, ^{39}Ar-^{40}Ar dating technique is well known as an established technique for volcanic rock samples. Application of ^{39}Ar-^{40}Ar dating technique directly for hydrothermal minerals is difficult, mainly due to too much activation during irradiation for ^{39}Ar production. Recently, micro scale analysis combined with a laser step heating is often adopted to avoid influence of alteration processes, especially for volcanic rock samples collected from the seafloor. We have attempted this technique for dating some volcanic rocks during the TAIGA project.

We have conducted a systematic dating study of four hydrothermal sites in the Southern Mariana Trough. A range in geochemical compositions and mineralogical assemblages have been shown within hydrothermal sites located both on- and off-axis, along a single tectonic lineament (Seama et al. Chap. 17; Ikehata et al. Chap. 22). Results of the dating study could provide information for discussion on temporal and spatial history of hydrothermal activity in this area. Moreover, a series of ore samples from massive sulfide deposit was obtained by shallow drilling conducted in this area (Nakamura et al. Chap. 41), which provide a good opportunity to apply dating study to discuss the duration of deposit formation. For the majority of samples, $^{230}Th/^{234}U$ radioactive disequilibrium dating was applied to sulfide minerals because the collected samples are dominated by marcasite, pyrite and sphalerite. In addition, electron spin resonance (ESR) dating was applied to a few barite-rich samples, for cross comparison purpose. Other than these, a laser step heating ^{39}Ar-^{40}Ar method was applied to volcanic basement samples in order to constrain the upper age limit for hydrothermal activity in the area.

23.2 Hydrothermal Activity in the Southern Mariana Trough at 13°N

Hydrothermal fields targeted in this study include a series of active hydrothermal sites located in the Southern Mariana Trough, at 13°N (Fig. 23.1). The geologic setting of this

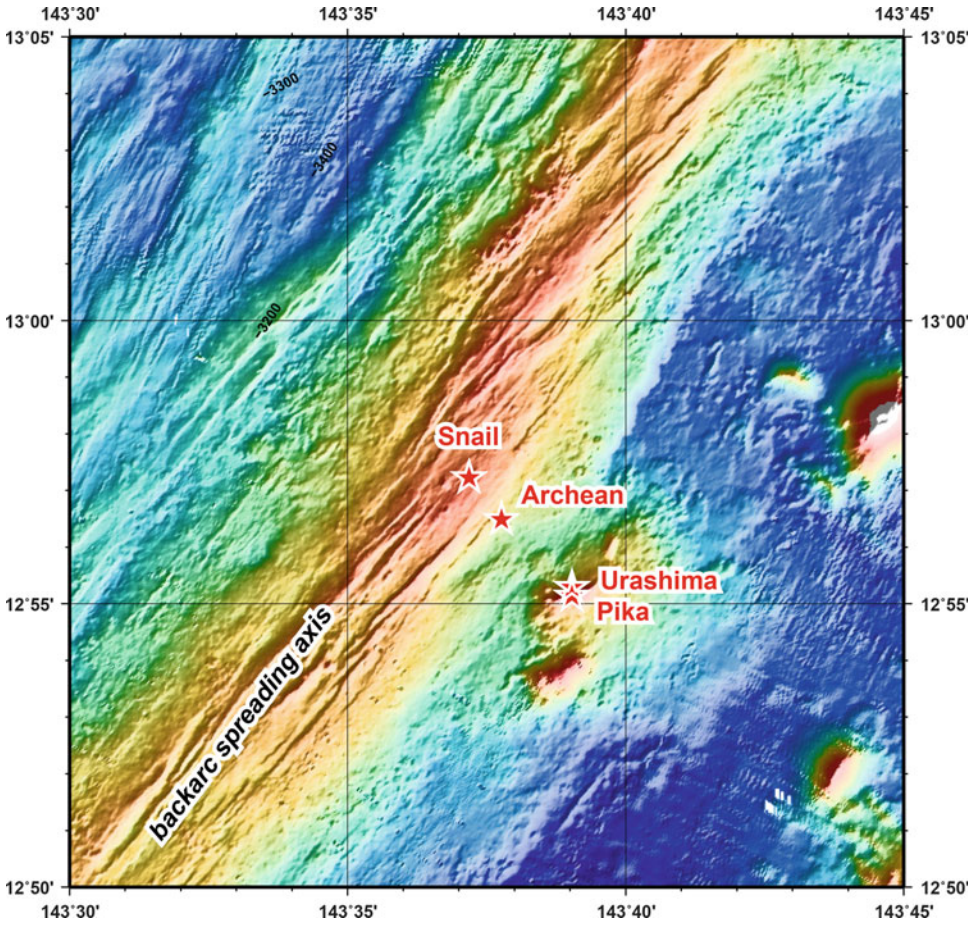

Fig. 23.1 Bathymetric maps of the Southern Mariana Trough, around 13ºN. Localities of the hydrothermal sites studied are given by the *star symbols*

area is described in detail elsewhere in this volume (Seama et al. Chap. 17) and also in previous papers (Yoshikawa et al. 2012; Nakamura et al. 2013). The essential points are summarized below.

The Archaean site is located at the foot of an axial high, at water depths between ~2,980 and 3,030 m. This site is located on a single conical shaped mound with a diameter of 250–300 m and a height above the seafloor of 50–100 m (Yoshikawa et al. 2012). Although the shape of the mound was attributed to an off-axis lava dome, its surface is dominantly covered by sulfidic ores, which are commonly hosted by breccia assemblages (Yoshikawa et al. 2012). Active and inactive chimneys have been observed in several places atop the mound. The highest measured temperature for the venting fluid is 343 °C (Toki et al. Chap. 45).

The Pika site is located at the top of an off-axis knoll, 4.9 km southeast of the spreading axis. This site covers an area about 100 × 400 m on the seafloor. Slightly shifted from the active vent area, a breccia assemblage consisting of sulfide ore was commonly seen. Hydrothermal activity of the Pika site is represented by black smokers with the highest measured fluid temperature of 320 °C and areas of diffuse flow, as well as many inactive chimney structures and spires (Toki et al. Chap. 45).

The Urashima site, a recently discovered active field, is located at the northern slope of the same knoll as the Pika site, but about 500 m to the north (Nakamura et al. 2013). This site covers an area about 300 × 300 m. Hydrothermal activity is characterized by clusters of active and inactive chimneys that are 5 m tall, or more. The highest fluid temperature measured from an active vent was 280 °C (Nakamura et al. 2013).

The Snail hydrothermal site is located on the spreading axis, at water depth of ~2,850 m. This site is characterized by abundant volcanic mounds consisting of mainly pillow lavas that are cut by fissures (Yoshikawa et al. 2012). Venting of 100–150 °C transparent fluid associated with hydrothermal mounds was observed outcropping on the slope of 5 m tall volcanic mound.

23.3 Material and Methods

23.3.1 Sample Collection

Hydrothermal mineralized samples were obtained using the manned submersible *SHINKAI 6500* during the YK10-11 cruise of the *R/V Yokosuka* conducted in August 2010. These samples were collected from clusters of active or

inactive chimneys, or from small mounds, using a manipulator on the submersible. Brecciated sulfide blocks that amassed on the slope as talus were collected by the submersible and formed part of this study. Samples recovered by the submersible are summarized in Table 23.1.

Other samples were recovered by drilling using a BMS (Benthic Multi-coring System) during the TAIGA10 cruise of the *R/V Hakurei-Maru No.2* conducted in June 2010. Detailed information of operations during this cruise is reported in other chapter (Nakamura et al. Chap. 41). Core samples were obtained from four drilled sites; BMS02, BMS03 and BMS07 from the Archean Site, and BMS09 from the Pika Site. These cores provided a continuous record of sulfide mineralization at these sites and highlight the success of drilling into massive sulfide deposits. The samples obtained by BMS drilling are given in Table 23.2.

Other than mineralized samples, some volcanic rock samples were also provided for a ^{39}Ar-^{40}Ar dating study. A list of these samples is given as Table 23.3.

Table 23.1 Samples collected during submersible dive expeditions

Sample ID	Sampling date	Sampling position Latitude (N)	Sampling position Longitude (E)	Water Depth (m)	Description
Archaean site					
6K903 R07-2[a]	7/29/2005	12° 56.3625′	143° 37.9000′	2,974	Sulfide crust
6K1221 R05-1	9/5/2010	12° 56.3255′	143° 37.8875′	3,014	Inactive chimney
6K1221 R07-1	9/5/2010	12° 56.3627′	143° 37.9022′	2,970	Active chimney
6K1223 R03-1	9/7/2010	12° 56.3795′	143° 37.9206′	3,000	Active chimney
6K1224 R02	9/9/2010	12 56.3643′	143° 37.8954′	2,972	Active chimney
Pika site					
6K1226 R02	9/12/2010	12° 55.1628′	143° 38.9482′	2,782	sulfide breccia
Urashima site					
6K1222 R06-1	9/6/2010	12° 55.2839′	143° 38.8726′	2,919	Active chimney
6K1222 R07-1	9/6/2010	12° 55.2667′	143° 38.8686′	2,905	Inactive chimney
6K1226 R03	9/12/2010	12° 55.2969′	143° 38.8756′	2,926	Active chimney
Snail site					
6K1227 R01	9/13/2010	12° 57.1978′	143° 37.1756′	2,848	Sulfide breccia
6K1228 R03	9/14/2010	12° 57.1902′	143° 37.1487′	2,847	Sulfide breccia

[a]Dating results presented in a previous study (Takamasa et al. 2013) are discussed together

23.3.2 Mineralogical Analysis

The samples collected by the submersible were cut into slabs of ~5 × 5 cm in size, whereas the core samples recovered by the BMS drilling (core diameter is 4.9 cm) were cut into sections a few cm in thickness. In parallel with dating analysis, mineralogy of the samples was determined by X-ray diffraction (XRD) after powdered. Texture of mineral was observed and determined using a thin section by microscope and Electron Probe Micro Analyzer (EPMA), which was conducted using JXA-8530F (JEOL) at 20 kV of accelerated voltage.

23.3.3 Dating Analysis

Analytical protocol for ^{230}Th/^{234}U radioactive disequilibrium dating followed our previous study (Takamasa et al. 2013). Aliquots of ~2 g of crushed samples were treated in 13 M nitric acid heated at 85 °C for 3 days to dissolve sulfide minerals and to separate them from insoluble minerals (mainly barite). After purification by column separation procedures using AG1-X8 and U/TEVA resins sequentially, U and Th isotope measurements were conducted using a multi-collector ICP mass spectrometer (MC-ICP-MS).

Analytical procedures for ESR dating followed our previous studies (Okumura et al. 2010; Toyoda et al. 2011). Aliquots of crushed powder were prepared separately from the same sample as used in the ^{230}Th/^{234}U dating. Barite was separated from sulfide minerals by leaching with 12 M hydrochloric acid and 13 M nitric acid, sequentially. After rinsing, the residue was collected by filtration and prepared for measurements of radiation. Signal intensity due to paramagnetic defect of the SO_3^- radical was measured using an ESR spectrometer, after the samples were irradiated using a ^{60}Co gamma ray source at the Takasaki Advanced Radiation Research Institute of the Japan Atomic Energy Agency. Concentration of ^{226}Ra was determined separately by gamma-ray spectrometry.

Analytical procedures for ^{39}Ar-^{40}Ar method with a laser step heating are described below. At a hand specimen scale, very fresh portions of the rock samples were crushed and sieved (#20–40 mesh). After confirmed no phenocrysts included, a few fragments (~1 mm in diameter) of groundmass were handpicked, and irradiated in the core of the Kyoto University Research Reactor. In this study, only pyroxene was identified as phenocryst in sample BMS03-02C, which was analyzed separately as BMS03-02C Px1 for comparison. Once the radioactivity had decreased, the irradiated samples were placed into a vacuum-sealed sample chamber and heated by a 5 W argon ion continuous laser with a defocused beam for stepwise heating. Temperatures were measured to a precision of 5 K utilizing monitoring and feedback controls through an infrared thermometer

Table 23.2 Samples collected by BMS drilling

Sample ID	Sampling date	Sampling position		Water	Sample depth below the seafloor (cmbsf)
		Latitude (N)	Longitude (E)	Depth (m)	
Archaean site					
BMS02 2 19–30	6/16/2010	12° 56.3696′	143° 37.9599′	3,073	26–37
BMS02 2 53–57	*ditto*	*ditto*	*ditto*	*ditto*	60–64
BMS02 2 75–80	*ditto*	*ditto*	*ditto*	*ditto*	82–87
BMS03 2B 08–42	6/16/2010	12° 56.3627′	143° 37.9036′	3,024	133–167
BMS03 2B 42–65	*ditto*	*ditto*	*ditto*	*ditto*	167–190
BMS03 2C 03–20	*ditto*	*ditto*	*ditto*	*ditto*	220–237
BMS03 2C 40–56	*ditto*	*ditto*	*ditto*	*ditto*	257–273
BMS03 2C 58–80 (a)	*ditto*	*ditto*	*ditto*	*ditto*	275
BMS03 2C 58–80 (b)	*ditto*	*ditto*	*ditto*	*ditto*	284
BSM03 2C 58–80 (c)	*ditto*	*ditto*	*ditto*	*ditto*	297
BMS07 1 61–71	6/20/2010	12° 56.3783′	143° 37.9187′	3,008	17–27
BMS07 2B 12–20	*ditto*	*ditto*	*ditto*	*ditto*	164–172
BMS07 2B 27–40	*ditto*	*ditto*	*ditto*	*ditto*	179–192
BMS07 2B 44–55 (a)	*ditto*	*ditto*	*ditto*	*ditto*	196
BMS07 2B 44–55 (b)	*ditto*	*ditto*	*ditto*	*ditto*	207
Pika site					
BMS09 2B 23–31	6/21/2010	12° 55.1368′	143° 38.9333′	2,804	165–173
BMS09 2B 45–58 (a)	*ditto*	*ditto*	*ditto*	*ditto*	184
BMS09 2B 45–58 (b)	*ditto*	*ditto*	*ditto*	*ditto*	200
BMS09 2B 65–71	*ditto*	*ditto*	*ditto*	*ditto*	207–213

Table 23.3 Volcanic rock samples

Sample ID	Sampling date	Sampling position		Water Depth (m)
		Latitude (N)	Longitude (E)	
Archaean site				
6K1221 R02	9/5/2010	12° 56.2201′	143° 37.8993′	3,082
BMS6C 62–75	6/19/2010	12° 56.3358′	143° 37.0094′	3,108
BMS6D 44–45	6/19/2010	12° 56.3222′	143° 38.0042′	3,115
Urashima site				
6K1226 R01	9/6/2010	12° 55.2962′	143° 39.0282′	2,917

(Hyodo 2008). The argon isotopes were then measured on a custom made mass spectrometer with a mass resolution of approximately 400 at the Research Institute of Natural Sciences, from which the Ar isotope ratio, ages, and correction factors were calculated. Typical blanks for argon isotopes in the extraction system were 6.2×10^{-14}, 8.7×10^{-14}, 3.8×10^{-14}, 5.2×10^{-14}, and 2.6×10^{-12} cm^3 for ^{36}Ar, ^{37}Ar, ^{38}Ar, ^{39}Ar, and ^{40}Ar, respectively. All errors shown are at the 2σ level.

23.4 Results

Pictures of representative mineralized samples are shown in Fig. 23.2, together with back scatter electron (BSE) images of the polished section prepared from the same samples. Marcasite, pyrite and sphalerite were recognized as dominant sulfide minerals in most of the collected samples in this study. Barite was identified in several samples as a minor amount, and chalcopyrite was identified mainly in chimney samples. These occurrences of sulfide and sulfate minerals are consistent with results of mineralogical study for the same hydrothermal sites reported in other Chapter (Ikehata et al. Chap. 22). As remarkable features in mineral texture, significant void spaces are noticeable in the chimney samples (Fig. 23.2a, b). On the other hand, less but still some void spaces are recognized in the ore samples recovered by the BMS drilling (Fig. 23.2c, d), suggesting mineralization have occurred repeatedly filling up the void to form a massive sulfide deposit.

Results of $^{230}Th/^{234}U$ radioactive disequilibrium dating are summarized in Table 23.4. Concentrations of U and Th are calculated relative to the total weight of the sample (including other minerals such as barite). Consequently, U and Th abundance in the analyzed sulfide fraction would likely be higher than the reported values. $^{230}Th/^{234}U$ disequilibrium ages were calculated using the following equation from the radioactivity ratio,

$$t = -\frac{1}{\lambda^{230}Th}\ln\left(1 - \frac{^{230}Th}{^{234}U}\right)$$

where $\lambda^{230}Th$ is the decay constant of ^{230}Th ($\lambda^{230}Th = 9.1577 \times 10^{-6}$ $year^{-1}$). This equation assumes the absence of ^{230}Th at the time of sulfide mineral precipitation.

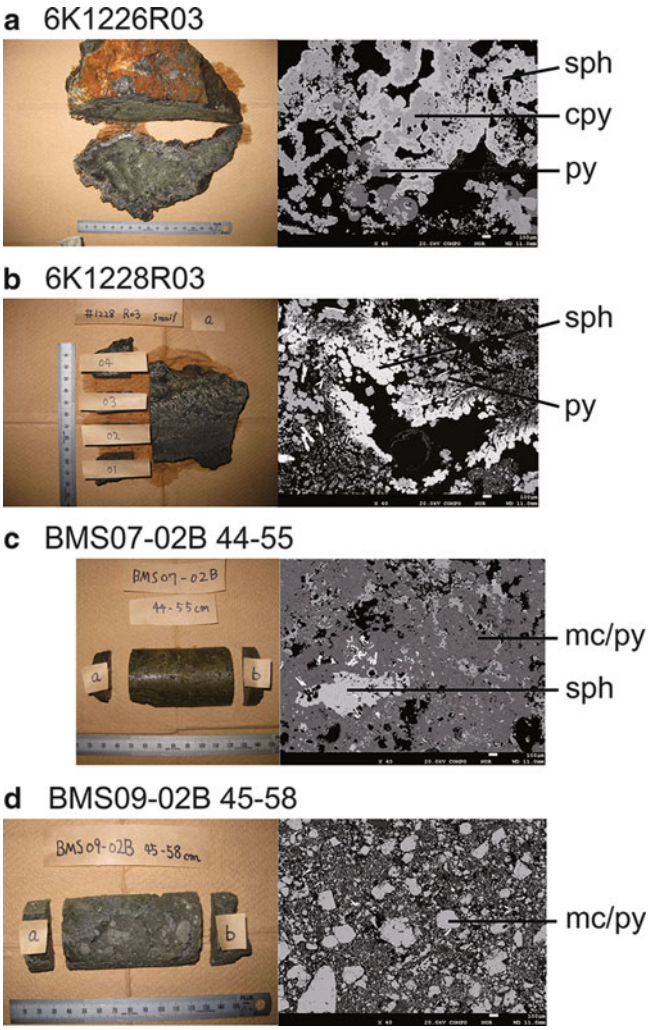

Fig. 23.2 Pictures of selected mineralized samples (*left*) and back scatter electron (BSE) images of the polished section from the same samples (*right*); (**a**) sample 6K1226R03 from the Urashima site, (**b**) sample 6K1228R03 from the Snail site, (**c**) sample BMS07-02B 44–55 from the Archaean site, and (**d**) sample BMS09-02B 45–58 from the Pika site. Abbreviations for minerals are *sph* sphalerite, *cpy* chalcopyrite, *py* pyrite, *mc* marcasite

As in an earlier study (Takamasa et al. 2013), we also corrected $^{230}Th/^{234}U$ ages for possible contribution of silicate minerals derived from sediment, as this would cause a shift of the initial $^{230}Th/^{234}U$ ratio away from zero. Corrected $^{230}Th/^{234}U$ values and corrected ages are shown in Table 23.4. Uncertainties of the calculated age are estimated as 3 %, based on analytical uncertainties of the $^{230}Th/^{232}Th$ and $^{234}U/^{232}Th$ values. Where there was insufficient Th in a sample to allow for a reliable analysis, we abandoned plans to date that sample. Based on preliminary tests, this method can be applied to samples with ages as young as ~100 years. On the other hand, substantial depletion in the abundance of U is likely to be attributed to sulfide having suffered from U loss due to hydrothermal alteration. In such a scenario, the apparent age should be much older. Corrected U-Th ages are <100 to 3,520 years old for the samples collected from the Archaean site, from 300 to 8,950 years old for the Pika site, from 250 to 9,130 years old for the Urashima site, and 2,740 and 7,190 years old for the Snail site.

Results of ESR dating are presented in Supplementary Data (Suppl. 23_S1). Accumulated natural radiation dose is estimated by the additive dose method. At first, dose response was examined for each sample by measuring ESR signal intensity due to the paramagnetic defects, as a function of additive dose by artificial gamma ray irradiation. Then, the dose response was fitted and extrapolated to the zero ordinate to determine an originally had accumulated dose for the sample, which is given as an equivalent dose in the table. To deduce age, the equivalent dose is subsequently divided by dose rate. Preliminary tests by Okumura et al. (2010) found that Ra is the only important source of radiation located in barite crystals and that the dose rate is estimated from ^{226}Ra content in the barite. The dose rates of alpha, beta and gamma rays (D_α, D_β, and $D\gamma$) were calculated according to the method adopted by Okumura et al. (2010) and given in the table. Age uncertainties are calculated by standard error propagation. Obtained ESR ages are 1,110 years old for one sample from the Archaean site, from 180 to 4,580 years old for the Pika site, and 110 and 390 years old for the Snail site.

Results of ^{39}Ar-^{40}Ar dating are presented in Supplementary Data (Suppl. 23_S2), and ^{39}Ar-^{40}Ar age spectra on plots of cumulative ^{39}Ar versus apparent ages were shown in Supplementary file (Suppl. 23_S3). In this study, no ^{39}Ar-^{40}Ar age spectra formed "plateau". A plateau is a sequence formed by more than two contiguous temperature steps containing more than 50 % of the total released ^{39}Ar, which provides one criteria for a reliable ^{39}Ar-^{40}Ar age from the sample (e.g., Baksi 1999). In general, only one thirds or less of submarine lava samples show clear plateau, partially due to their high Ca but low K signature (e.g. Wanke et al. 2012). In many cases, irradiation produced nuclei from Ca largely contribute into ^{36}Ar, which results in a negative age due to over-corrections (McDougall and Harrison 1999). In this study, rather disturbed spectra were obtained, meaning difficult to deduce fully reliable ^{39}Ar-^{40}Ar age. Samples "6K1221R02MT1" and "6K1221R02MT3" collected from near the Archaean site showed fair release of ^{36}Ar in high temperature fractions; these two samples gave 16–0 Ma as their total ages and interpreted ages are calculated as 6–0 Ma after the corrections of possible irradiation produced ^{36}Ar. We cannot exclude possibility that these interpreted ^{39}Ar-^{40}Ar ages may be rejuvenated by later alteration, however, it seems to be consistent with 1–2 Ma of the seafloor age estimated from spreading rate in the area.

Table 23.4 Results of radioactive disequilibrium dating of sulfide mineralization

Sample ID	Fraction	U (ppb)[a]	Th (ppb)[a]	$^{234}U/^{238}U$	$^{230}Th/^{232}Th$	$^{230}Th/^{234}U$	Age (years)	$^{230}Th/^{234}U$ corr.[b]	Age (years) corr.[b]
Archaean site									
BMS02 219-30		9.34E+02	4.67E-02	6.35E-05	5.63E-03	1.48E-02	1.63E+03	1.48E-02	1,630
BMS02 253-57		8.13E+02	6.43E-02	6.34E-05	u. d.	–	–	–	–
BMS02 275-80	nm	2.69E+03	9.49E-02	6.25E-05	7.82E-03	1.48E-02	1.63E+03	1.48E-02	1,630
	mag	3.04E+03	5.33E-02	6.10E-05	1.31E-02	1.24E-02	1.37E+03	1.24E-02	1,370
BMS03 2B 08-42		6.11E+01	4.16E-03	6.38E-05	u. d.	–	–	–	–
BMS03 2B 42-65 (a)		1.87E+02	1.66E-02	6.32E-05	2.34E-03	1.10E-02	1.21E+03	1.10E-02	1,210
BMS03 2B 42-65 (b)		3.03E+02	5.74E-02	6.33E-05	2.98E-04	2.99E-03	3.27E+02	2.94E-03	320
BMS03 2C 03-20 (a)		2.25E+02	2.93E-02	6.32E-05	3.07E-03	2.12E-02	2.33E+03	2.11E-02	2,330
BMS03 2C 40-56 (a)		2.16E+03	1.18E-01	6.31E-05	3.87E-03	1.13E-02	1.24E+03	1.13E-02	1,240
BMS03 2C 58-80 (a)	nm100	6.27E+02	6.91E-01	4.69E-05	3.88E-04	3.05E-02	3.38E+03	3.02E-02	3,350
	mg100	7.60E+02	8.82E-02	6.19E-05	4.09E-03	2.57E-02	2.84E+03	2.56E-02	2,840
	nm250	6.12E+02	4.73E-02	4.78E-05	4.74E-03	2.56E-02	2.84E+03	2.56E-02	2,830
BMS03 2C 58-80 (b)	nm250	4.80E+02	4.55E-02	5.83E-05	4.34E-03	2.18E-02	2.41E+03	2.18E-02	2,400
	mg250	3.90E+02	8.06E-02	6.20E-05	2.31E-03	2.56E-02	2.83E+03	2.55E-02	2,820
BSM03 2C 58-80 (c)	nm100	2.06E+02	7.06E-02	6.24E-05	1.36E-03	2.46E-02	2.72E+03	2.46E-02	2,720
	nm250	2.13E+02	2.77E-01	6.24E-05	3.70E-04	2.55E-02	2.82E+03	2.52E-02	2,790
BMS07 1 61-71 (a)		3.00E+03	1.15E-01	5.78E-05	2.72E-04	6.05E-04	6.61E+01	5.64E-04	61
BMS07 1 61-71 (b)		1.61E+03	1.56E-01	5.93E-05	3.05E-05	1.67E-04	1.82E+01	1.43E-04	15
BMS07 2B 12-20		4.95E+02	1.03E-01	6.38E-05	u. d.	–	–	–	–
BMS07 2B 27-40		8.59E+03	2.04E-02	6.31E-05	8.31E-02	1.05E-02	1.15E+03	1.05E-02	1,150
BMS07 2B 44-55 (b)	run 1	5.65E+03	2.27E-02	6.32E-05	5.16E-02	1.10E-02	1.20E+03	1.10E-02	1,200
	run 2	6.31E+03	3.51E-02	6.33E-05	3.80E-02	1.12E-02	1.23E+03	1.12E-02	1,230
6K1221 R05-1	mg250	5.98E+02	1.55E-01	6.22E-05	2.28E-03	3.17E-02	3.52E+03	3.17E-02	3,520
	mg100	3.57E+02	2.50E-01	5.98E-05	6.24E-04	2.45E-02	2.71E+03	2.43E-02	2,690
	nm100	7.95E+01	4.59E-02	5.74E-05	3.04E-04	1.02E-02	1.12E+03	1.01E-02	1,110
6K1221 R07-1	nm250	1.62E+02	1.17E-01	6.18E-05	5.41E-04	2.11E-02	2.33E+03	2.10E-02	2,320
6K1223 R03-1	mg250	2.64E+02	4.03E-02	5.04E-05	8.06E-04	8.18E-03	8.96E+02	8.13E-03	890
	mg100	2.54E+02	4.94E-02	5.75E-05	4.86E-04	5.50E-03	6.02E+02	5.45E-03	600
6K1224 R02 (a)	run 1	2.71E+03	7.01E-02	6.27E-05	3.02E-03	4.16E-03	4.56E+02	4.16E-03	460
	run 2	1.74E+03	1.50E-01	6.28E-05	1.86E-03	8.58E-03	9.41E+02	8.56E-03	940
Pika site									
BMS09 2B 23-31	run 1	8.74E+02	3.73E-02	6.30E-05	1.21E-03	2.74E-03	3.00E+02	2.73E-03	300
	run 2	3.11E+02	3.43E-02	6.29E-05	4.59E-03	2.69E-02	2.97E+03	2.68E-02	2,970
BMS09 2B 45-58 (a)	run 1	2.73E+02	2.26E-01	6.11E-05	1.08E-03	4.90E-02	5.48E+03	4.88E-02	5,460
	run 2	3.38E+02	1.71E-01	5.87E-05	1.65E-03	4.78E-02	5.35E+03	4.77E-02	5,340
BMS09 2B 45-58 (b)		2.17E+02	6.17E-01	6.24E-05	5.20E-04	7.93E-02	9.03E+03	7.87E-02	8,950
BMS09 2B 65-71		4.82E+03	2.48E-02	6.32E-05	1.13E-01	3.07E-02	3.40E+03	3.07E-02	3,400
6K1226 R02	a	1.67E+03	5.60E-02	6.28E-05	2.72E-03	4.86E-03	5.32E+02	4.86E-03	530
	b	2.54E+03	3.53E-02	6.22E-05	6.85E-03	5.14E-03	5.62E+02	5.13E-03	560
	d	6.79E+02	4.13E-02	6.29E-05	1.76E-03	5.69E-03	6.23E+02	5.68E-03	620
6K1222 R06-1	a nm100	9.86E+01	1.10E-01	5.78E-05	1.95E-04	1.26E-02	1.38E+03	1.23E-02	1,350
6K1222 R07-1	a all	1.23E+02	6.47E-02	5.63E-05	6.80E-04	2.13E-02	2.35E+03	2.11E-02	2,330
	b nm100	2.28E+01	7.93E-02	6.04E-05	4.20E-04	8.10E-02	9.22E+03	8.02E-02	9,130
	b nm250	2.00E+01	2.99E-02	6.17E-05	4.38E-04	3.55E-02	3.95E+03	3.52E-02	3,910
	b mg100	6.48E+01	1.25E-01	6.01E-05	1.53E-04	1.64E-02	1.81E+03	1.60E-02	1,760
	b mg250	3.77E+01	1.24E-01	6.17E-05	4.38E-04	7.81E-02	8.88E+03	7.73E-02	8,790
6K1226 R03	a nm250	8.44E+02	3.65E-02	6.24E-05	9.91E-04	2.30E-03	2.51E+02	2.29E-03	250
	a nm500	2.62E+01	8.70E-03	6.20E-05	1.24E-03	2.23E-02	2.46E+03	2.22E-02	2,460
	b nm500	4.83E+02	2.76E-02	6.24E-05	1.24E-03	3.82E-03	4.18E+02	3.81E-03	420
	b mg500	1.23E+03	4.26E-02	6.25E-05	1.63E-03	3.03E-03	3.31E+02	3.02E-03	330

(*continued*)

Table 23.4 (continued)

Sample ID	Fraction	U (ppb)[a]	Th (ppb)[a]	$^{234}U/^{238}U$	$^{230}Th/^{232}Th$	$^{230}Th/^{234}U$	Age (years)	$^{230}Th/^{234}U$ corr.[b]	Age (years) corr.[b]
Snail site									
6K1227 R01	anm1000	3.30E+00	2.20E-02	6.11E-05	4.97E-04	1.83E-01	2.20E+04	1.81E-01	_[c]
	bnm 250	4.17E+01	1.29E-02	6.25E-05	1.50E-03	2.49E-02	2.75E+03	2.48E-02	2,740
	anm 500	2.87E+00	7.06E-03	5.61E-05	2.11E-03	3.10E-01	4.05E+04	3.09E-01	_[c]
6K1228 R03	a01nm250	1.18E+00	1.24E-01	5.94E-05	1.16E-04	6.91E-01	1.28E+05	6.65E-01	_[c]
	b03nm250	1.22E+01	1.22E-02	5.09E-05	9.73E-04	6.40E-02	7.22E+03	6.37E-02	7,190

Each age has an about 5% error for samples with ($^{234}U/^{232}Th$) of a few hundreds and a few % error for samples with ($^{234}U/^{232}Th$) of a few thousands

[a]U and Th abundances are calculated relative to total weight of a sample

[b]Corrected for possible involvement of silicate minerals derived from sediment

[c]Samples with * have low U abundances and they may have suffered alteration events. Their ages were not calculated

23.5 Discussion

23.5.1 Evaluation of Results of Dating Mineralization

A cross check of results between the $^{230}Th/^{234}U$ radioactive disequilibrium dating and ESR dating was examined only for five samples, because minor mineralization of sulfate (barite) made difficult to conduct the ESR dating. Sample "BMS09 2B 65–71" showed fairly good agreement; 3,400 years by the U-Th dating and 3,447 years by the ESR dating. Sample "6K1226 R03" showed agreement with one exception; 250–420 years with one exceptional age 2,460 years by the U-Th dating, and 180–360 years by the ESR dating. On the other hand, Sample "BMS 07 1 61–71" showed discrepancy; 15–61 years by the U-Th dating, and 1,110years by the ESR dating. Sample "6K1227R01" showed reversed discrepancy; 2,740 years by the U-Th dating and 110 years by the ESR dating. Sample "6K1228R03" showed largest discrepancy among them; 7,190 years by the U-Th dating and 390years by the ESR dating. Cross checks between the two methods including other data obtained during the TAIGA project are also discussed in other chapter (Kumagai et al. Chap. 5).

It is important to remind that both $^{230}Th/^{234}U$ radioactive disequilibrium and ESR dating methods require at least a few grams of sulfide or sulfate mineralized sample. This means that the calculated ages should be considered as homogeneous values, or average ages for sulfide or sulfate minerals included in the sample. As well as in the previous study (Takamasa et al. 2013), mineral textures of the sample in this study suggest that the sulfide and sulfate minerals have repeatedly been precipitated from hydrothermal fluid (Fig. 23.2). The obtained results would correspond not to specific events but to intermediates of duration for continuing mineralization. Or, they may represent apparent average ages of some episodic mineralization events. For example, discrepancy in the age data is found among fractions from Sample "6K1226R03"; 250–2,460 years for Fraction a, 330–420 years for Fraction b, and 4,580 years for Fraction c by the ESR method. This discrepancy could be interpreted as a result of different incorporation ratio between previously deposited minerals and recently deposited minerals for each analyzed fraction. Moreover, incorporation ratio for sulfide and sulfate minerals can be different because mineralization of these minerals do not occur simultaneously, which would cause discrepancy between the ages obtained by the $^{230}Th/^{234}U$ radioactive disequilibrium and ESR dating methods. For example, the discrepancy found in Sample "BMS 07 1 61–71" might be explained as a result of recent mineralization exclusively of sulfides, considering that the ESR age of 1,110 years obtained for this sample well agrees with the U-Th age of the samples collected from deeper portion of the same drilled hole (Samples "BMS07 2B 12–20", "BMS07 2B 27–40", "BMS07 2B 44–55").

As disturbance in highly reliable dating by these two methods, some other factors could be considered. Involvement of silicate minerals would cause a shift of the initial $^{230}Th/^{234}U$ ratio away from zero, because we did not eliminate this fraction during the chemical preparation process. We have corrected this effect and the correction was not so large, because ^{230}Th content was high enough in many samples. On the other hand, if the mineralized samples have experienced alteration since the mineralization, it would cause severe problem for $^{230}Th/^{234}U$ dating because the apparent age become older by U loss. We have excluded results from the samples of less than 10 ppm U in this study, however, this threshold was arbitrarily assumed. We cannot exclude possibility for that two samples collected from Snail site (Samples "6K1227R01" and "6K1228R03") suffer from this effect, since most of the fractions from these two samples showed relatively low U content. For the ESR dating, estimation of the dose rate would have uncertainties, because the calculation has assumed several parameters

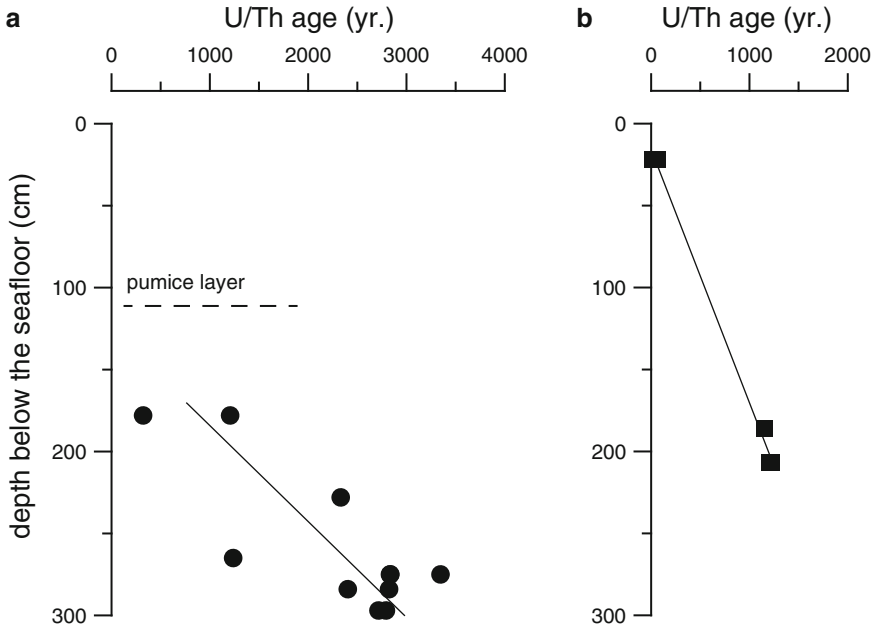

Fig. 23.3 Dating results for the core samples from (**a**) BMS03 and (**b**) BMS07

(for example, size and geometry of barite crystals), as discussed in Okumura et al. (2010).

From above factors, it may be difficult to obtain good agreement from one-by-one cross check. At present, we do not have additional data to endorse or withdraw the age data presented here. More detailed studies including consideration for chemical preparations of mineralized samples would be necessary to increase reliability of dating.

In spite of these possible uncertainties, our previous study showed common spatial distribution patterns of ages determined by the two methods, among ten blocks divided from a sulfide crust adjacent to an acitve chimney from the Achaean site (Takamasa et al. 2013). We believe that trend recognized among a series of samples would have high reliability, because they would have similar mineral composition and texture. In this respect, core samples recovered by the BMS drilling from massive sulfide deposits provide a good opportunity to apply dating study.

23.5.2 Estimation of Growth Rate for Massive Sulfide Mineralization

Results of dating the massive sulfide ores cored from two drilled holes in the Archaean site are shown in Fig. 23.3. The $^{230}Th/^{234}U$ disequilibrium ages are plotted against depth below the seafloor where the core section was assigned. Data points for the BMS03 samples which ages range from 320 to 3,350 years show a crude trend of older ages with depth (Fig. 23.3a). Although the data are somewhat scattered, they do not suggest a hiatus between the measured ages. Linear regression of these 10 data points gives a slope of 17 years per 1 cm. According to this relationship, the depth of a zero age sulfide is calculated as 125 cmbsf (centimeters below the sea floor). We consider this intercept value reasonable, since the top of the massive sulfide was found at 112 cmbsf and only pumiceous materials were found in the shallowest layer by the drilling. Similarly, a slope derived from five data points for the BMS07 samples range from <100 to 1,230 years gives an estimated as 6.6 years per 1 cm (Fig. 23.3b).

As discussed in the previous section, ages of sulfide mineralization should be carefully considered, as they accumulate over a period of time and not instantaneous but constantaneous. We are not confident of estimating growth rates for massive sulfide deposits by simple linear regression. However, the calculated growth rates of 0.59 mm $year^{-1}$ for core BMS03 and 1.5 mm $year^{-1}$ for core BMS07, respectively, would provide basic age information, when discussing the formation history of this type of mineralization. Previously, we dated a sulfide crust adjacent to an active chimney at the Archaean site, in a water depth of 2,974 m, and estimated its growth rate as 0.12 mm $year^{-1}$ (Takamasa et al. 2013). These three estimates of growth rates fall within about a range of one order-of-magnitude, which we believe represent the growth rate of massive sulfide mineralization at this site.

The distribution of ages for all the samples collected from the Archaean Site, including the results of the previous study, is compiled in Fig. 23.4. Here, ages for sulfides both recovered by the BMS drilling and by submersible *SHINKAI 6500* are plotted against water depth of the sampling sites. Although the BMS samples were recovered from below the seafloor, their drilled depths were only a few

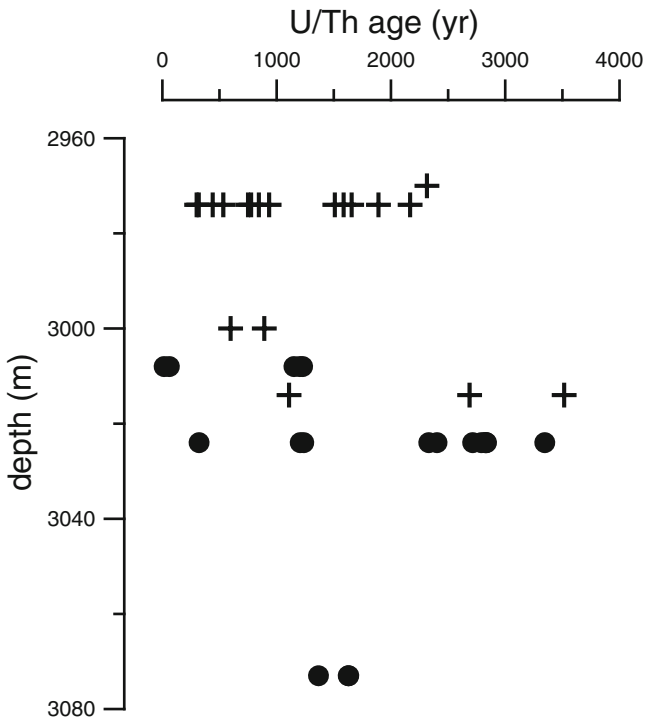

Fig. 23.4 Compilation of dating results for the samples collected from the Archean Site, by the BMS drilling (*closed circles*) and by the submersible *SHINKAI 6500* (*cross marks*)

meters and not expressed in this figure. Sulfides from the Archaean site range in age from <100 to 3,520 years. BMS02 was drilled at a water depth of 3,072 m, that is not on the hydrothermal mound, but on the seafloor adjacent to the mound. Thus, the cored sulfides are attributed to be collapse materials derived from the mound, as Yoshikawa et al. (2012) suggested based on the topography. There is no clear relationship between age and water depth of sampling. Even sulfides collected at water depths shallower than 3,000 m, which is close to the top of the mound, have ages ranging up to 2,310 years. These results are consistent with the hypothesis that seafloor hydrothermal ore deposits grow continuously filling up void spaces. Irrespective, we believe that hydrothermal activity at the Archaean site has a history of >1,000 years accumulating massive hydrothermal mineralization all the time.

23.5.3 History of Hydrothermal Activity in Off-Axis Knolls

Sulfides collected from the Pika site range in age from 300 to 8,950 years (Table 23.4). The oldest sample occurs within the core samples BMS09. Sulfides collected from the Urashima site range in age from 250 to 9,130 years. Sample "6K1226R03" was a part of an active chimney as young as a few 100 years old, whereas Sample "6K1222R07" is from an inactive chimney and is up to 9,000 years old. Good agreement between the maximum sulfide ages from these two sites would be reasonable, consistent with both sites being located on the same off-axis knoll. Hydrothermal activity at these sites cannot be attributed to magmatic activity related to spreading but to off-axis magmatic activity. Based on estimated local half spreading rate of 13 mm year^{-1} (Seama and Okino Chap. 20), the Pika and Urashima sites are considered to be located on the oceanic crust of 0.38 Ma. It is difficult to continue relationship between hydrothermal activity and heat source magma for such long time duration. On the other hand, a recent seismic refraction survey under the TAIGA project studied 3-D seismic velocity structure in this area, and located a high-velocity region suggesting a cool 'extinct' magma body just beneath the off-axis knoll where these two sites located (Sato et al. Chap. 18). For example, maximum sulfide ages of 9,000 years would be consistent with the time taken for a magma body to cool after emplacement. Hydrothermal activity at the Pika and Urashima sites is therefore considered to be 'late stage' and related to the cooling of a magma body.

The maximum sulfide age from the Archaean site is ~3,500 years, which is much younger than those from the Pika or Urashima sites. Since no geophysical evidence for a magma body to exist beneath this site, a heat source of hydrothermal activity at the Archaean site could be related to magmatic activity beneath the spreading axis that is located at ~1 km distance (Seama et al. Chap. 17). Such style of heat supply may contribute to continuous hydrothermal activity at the same mound for >1,000 years.

Ages of the sulfide breccia collected from the hydrothermal mound in the Snail site, based on the U-Th dating method, are 2,740 and 7,190 years, while ages for sulfates obtained by the ESR dating method are much younger (110 and 390 years). The U-Th sulfide ages for the Snail site are comparable to those for off-axis sites (Pika and Urashima sites), although we cannot exclude the possibility that these values are affected by hydrothermal alteration.

Geophysical studies during the TAIGA project have shown evidence to support that mantle dynamics and crustal formation in this area are influenced by hydration derived from the subducting slab with accompanying the additional magma supply (Seama et al. Chap. 17). The abundant magma supply is considered to lead to the episodic diking events on the spreading axis and to the off-axis volcanism, both of which supply heat source for hydrothermal activity on the seafloor. The discrete ages from the Snail site may reflect hydrothermal activities fueled by episodic diking events, while the ages from the Pika and Urashima site would be attributed to be related to cooling off-axis magma as mentioned above. In both cases, abundant magma supply in this area would be an important factor

for long duration of hydrothermal activities, although we need future studies with dating more samples for better understanding the history.

23.5.4 Comparison with Other Seafloor Massive Sulfide Deposits

Previous studies have attempted to estimate the age of giant hydrothermal mounds developed within, or just outside, a spreading axis of the mid-ocean ridge. For example, the TAG mound at 26ºN on the Mid-Atlantic Ridge is located 2.4 km east of the ridge axis, near the base of the east wall of the rift valley, and is the most well-studied giant hydrothermal mound. Sulfides collected from the TAG mound by submersible dives have yielded ages up to 48,000 years (Lalou et al. 1995), whereas sample recovered by drilling from inside of the mound gave ages from 2,200 to 15,000 years, with exception of two samples dated at 37,000 ± 1,000 years (You and Bickle 1998). These studies demonstrated that the distribution of ages correlates with the stratigraphy of hydrothermal mound, with the oldest material found in a middle layer through the center of the deposit. Both groups of researchers suggest that the activity necessary to accumulate sulfide deposits of the TAG mound has not been continuous, but has been interrupted by several periods of extended quiescence. Together with results from our studies, we believe that an order of 10^4–10^5 years of continuous hydrothermal activity may be necessary for the formation of giant hydrothermal mounds.

Another comparable set of age data are reported for an off-axial structure on the East Pacific Rise, near 12°43′N (Lalou et al. 1985; Fouquet et al. 1996). Sulfides collected from an off-axial seamount (SE Seamount), at located 6 km east of the spreading axis yielded ages from 11,600 to 30,500 years. This is in contrast to sulfides collected from an active hydrothermal mound 70 m high and 200 m in diameter located at 2 km east of the axis yielded ages of ~2,000 years. The reported range of sulfide ages are similar to our results, which may suggests a common tectonic condition to form both off-axial structures and hydrothermal mounds. As proposed by these earlier studies, off-axis seamounts are localized areas with high magmatic budget able to drive hydrothermal systems in the same place for long periods of time, enabling sulfide ore mineralization to accumulate. The age data presented in this study would support this hypothesis.

Acknowledgments We are grateful to Captain Morio Endo and crew of the *R/V Hakurei-Maru No.2*, and also to team leader Tadashi Sato and members of the BMS operation team for their professional skill and careful consideration for collecting core samples during the TAIGA10 cruise. We wish to thank members of *SHINKAI 6500* team and crew of the *R/V Yokosuka* for their skillful support during the YK10-11 cruise. We are grateful to the staff of Kyoto University Research Reactor (KUR) for neutron irradiation of the samples used for laser fusion ^{39}Ar-^{40}Ar dating, and also to the staff of Takasaki Advanced Radiation Research Institute, Japan Atomic Energy Agency (JAEA) for gamma ray irradiation of the sample used for ESR dating. This study was partially supported by the "TAIGA project," which was funded by a Grant-in-Aid for Scientific Research on Innovative Areas (#20109004) from the Ministry of Education, Culture, Sports, Science and Technology (MEXT), Japan. A part of this study was supported also by the Inter-University Program for the Joint Use of JAEA Facilities. This manuscript benefited from constructive comments from Tatsuo Nozaki and Cornel de Ronde.

References

Baksi AK (1999) Reevaluation of plate motion models based on hotspot tracks in the Atlantic and Indian oceans. J Geol 107:13–26

de Ronde CEJ, Massoth GJ, Butterfield DA, Christenson BW, Ishibashi J, Ditchburn RG, Hannington MD, Brathwaite RL, Lupton JE, Kamenetsky VS, Graham IJ, Zellmer GF, Dziak RP, Embley RW, Dekov VM, Munnik F, Lahr J, Evans LJ, Takai K (2011) Submarine hydrothermal activity and gold-rich mineralization at Brothers Volcano, Kermadec arc, New Zealand. Miner Deposita 46:541–584

Ditchburn RG, de Ronde CEJ, Barry BJ (2012) Radiometric dating of volcanogenic massive sulfides and associated iron oxide crusts with an emphasis on ^{226}Ra/Ba and ^{228}Ra/^{226}Ra in volcanic and hydrothermal processes at intraoceanic arcs. Econ Geol 107:1635–1648

Fouquet Y, Knott R, Cambon P, Fallick A, Rickard D, Desbruyeres D (1996) Formation of large sulfide mineral deposits along fast spreading ridges. Example from off-axial deposits at 12°43′N on the East Pacific Rise. Earth Planet Sci Lett 144:147–162

Hyodo H (2008) Laser probe ^{40}Ar/^{39}Ar dating: history and development from a technical perspectivem. Gondwa Res 14:609–616

Jamieson JW, Hannington MD, Clague DA, Kelley DS, Delaney JR, Holden JF, Tivey MK, Kimpe LE (2013) Sulfide geochronology along the Endeavour segment of the Juan de Fuca Ridge. Geochem Geophys Geosyst 14. doi:10.1002/ggge20133

Lalou C, Brichet E (1987) On the isotopic chronology of submarine hydrothermal deposits. Chem Geol 65:197–207

Lalou C, Brichet E, Hekinian R (1985) Age dating of sulfide deposits from axial and off-axial structures on the East Pacific Rise near 12°50′N. Earth Planet Sci Lett 75:59–71

Lalou C, Reyss J-L, Brichet E, Rona PA, Thompson G (1995) Hydrothermal activity on a 10^5-year scale at a slow-spreading ridge, TAG hydrothermal field, mid-Atlantic Ridge 26°N. J Geophys Res 100:17855–17862

McDougall I, Harrison TM (1999) Geochronology and thermochronology by the ^{40}Ar/^{39}Ar method. Oxford University Press, Oxford, p 269

Nakamura K, Toki T, Mochizuki N, Asada M, Ishibashi J, Nogi Y, Yoshikawa S, Okino K (2013) Discovery of a new hydrothermal vent site in the Southern Mariana Trough based on geophysical surveys using the AUV Urashima. Deep Sea Res I 74:1–10

Okumura T, Toyoda S, Sato F, Uchida A, Ishibashi J, Nakai S (2010) ESR dating of barite in chimneys deposited from hydrothermal vents. Geochronometria 37:57–61

Takamasa A, Nakai S, Sato F, Toyoda S, Banerjee D, Ishibashi J (2013) U-Th radioactive disequilibrium and ESR dating of a barite-containing sulfide crust from South Mariana Trough. Quater Geochronol 15:38–46

Toyoda S, Sato F, Banerjee D, Ishibashi J (2011) Characteristics of the radiation induced ESR signals in barite. Adv ESR Appl 27:4–6

Wanke M, Portnyagin M, Hoernle K, Werner R, Hauff F, van den Bogaard P, Garbe-Schöberg D (2012) Bowers Ridge (Bering Sea): an Oligocene-early Miocene island arc. Geology 40:687–690

Yoshikawa S, Okino K, Asada M (2012) Geomorphological variations at hydrothermal sites in the southern Mariana Trough: relationship between hydrotherm alactivity and topographic characteristics. Mar Geol 303–306:172–182

You C-F, Bickle MJ (1998) Evolution of an active sea-floor massive sulphide deposit. Nature 394:668–670

Intra-Field Variation of Prokaryotic Communities On and Below the Seafloor in the Back-Arc Hydrothermal System of the Southern Mariana Trough

24

Shingo Kato, Moriya Ohkuma, and Akihiko Yamagishi

Abstract

Deep-sea hydrothermal vents harbor diverse prokaryotes. There are a variety of habitat types in a deep-sea hydrothermal field, e.g., active and inactive chimneys, iron-rich mats, venting fluid and hydrothermal plume. Numerous studies have shown the diversity and composition of prokaryotic communities in individual habitats. However, it is still unclear whether and how the characteristics of prokaryotic communities in their respective habitats are different. Previously, we reported 16S rRNA genes in a variety of habitats, i.e., hydrothermally active and inactive chimneys, iron-rich mats, a vent fluid, crustal fluids from boreholes, as well as ambient seawater in a back-arc basin hydrothermal field of the Southern Mariana Trough. Here we summarize the prokaryotic communities in the collected samples at higher taxonomic resolution (up to family level) using the detected 16S rRNA gene sequences and compare them using recently developed bioinformatics tools. The comparative analysis clearly highlights differences in prokaryotic communities among the habitat types on and below the seafloor in the Southern Mariana Trough. Furthermore, descriptions of cultured species and environmental clones close to the detected sequences provide valuable information for understanding of their distribution and potential of ecological roles in deep-sea hydrothermal fields.

Keywords

16S rRNA gene • Archaea • Back-arc basin • Bacteria • Chemosynthetic ecosystem • Deep-sea hydrothermal vents • Prokaryotic community

24.1 Introduction

Deep-sea hydrothermal vents are oases for organisms on the vast seafloor. Hydrothermal fluids are rich in reduced chemical species, such as hydrogen, hydrogen sulfide, methane and ferrous iron, which support the growth of chemolithoautotrophs as energy sources. Chemolithoautotrophs are the primary producers in the chemosynthetic ecosystem in TAIGA, which is designated a great sub-seafloor river (Urabe et al. Chap. 1). Numerous studies have characterized the prokaryotic community structures in various habitat types, such as hydrothermally active chimneys (e.g., Flores et al. 2012a; Kato et al. 2010; Kormas et al. 2006; Nakagawa et al. 2005; Schrenk et al. 2003; Takai and Horikoshi 1999), inactive chimneys (Kato et al. 2010; Suzuki et al. 2004;

The online version of this chapter (doi:10.1007/978-4-431-54865-2_24) contains supplementary material, which is available to authorized users.

S. Kato
Japan Collection of Microorganisms, RIKEN BioResource Center, Tsukuba, Ibaraki, Japan

Department of Molecular Biology, Tokyo University of Pharmacy and Life Science, 1432-1 Horinouchi, Hachioji, Tokyo 192-0392, Japan

M. Ohkuma
Japan Collection of Microorganisms, RIKEN BioResource Center, Tsukuba, Ibaraki, Japan

A. Yamagishi (✉)
Department of Molecular Biology, Tokyo University of Pharmacy and Life Science, 1432-1 Horinouchi, Hachioji, Tokyo 192-0392, Japan
e-mail: yamagish@toyaku.ac.jp

J.-i. Ishibashi et al. (eds.), *Subseafloor Biosphere Linked to Hydrothermal Systems: TAIGA Concept*,
DOI 10.1007/978-4-431-54865-2_24,

Sylvan et al. 2012), iron-rich mats (e.g., Davis and Moyer 2008; Fleming et al. 2013; Forget et al. 2010; Kato et al. 2009a), and crustal fluids (Cowen et al. 2003; Huber et al. 2006; Kato et al. 2009b, 2013; Orcutt et al. 2011), in various deep-sea hydrothermal fields. Through such studies, inter-field variation between prokaryotic community structures in deep-sea hydrothermal system habitats has been revealed (e.g., Takai et al. 2006; Flores et al. 2012a). However, intra-field variation of prokaryotic community structures among these habitat types is still poorly understood.

The Southern Mariana Trough (SMT) is an actively spreading back-arc basin that is located at the southern extension of the Izu-Bonin Arc (Seama et al. Chap. 17). Hydrothermal vents have been found on the back-arc spreading ridge and off-ridge seamounts in the SMT. Furthermore, in this field, several boreholes have been drilled by a seafloor-drilling instrument, the Benthic Multi-coring System (BMS) (Marumo et al. 2008). The tectonics and geology of the SMT and geochemistry of its hydrothermal fluids have been well studied (Seama et al. Chap. 17; Toki et al. Chap. 45). Therefore, the SMT is a model field for studying the relationships among tectonics, geology, geochemistry, and microbial ecology in many habitats including sub-seafloor environments.

We analyzed the prokaryotic community structures in a variety of samples collected in the SMT, such as active and inactive chimneys, iron-rich mats, hydrothermal fluid from an active vent and boreholes, and ambient seawater (Kato et al. 2009a, b, 2010). In particular, the chemosynthetic ecosystem supported by ferrous iron was found in the iron-rich mats and crustal fluids (Kato et al. 2012). However, comprehensive comparative analyses of the prokaryotic community structures among the SMT samples have not been carried out. In this review, we summarize the prokaryotic community structures in the SMT samples at higher taxonomic resolution (up to family level) based on the 16S rRNA gene sequences and compare them using recently developed bioinformatics tools. The results highlight the differences of prokaryotic communities on and below the seafloor in the SMT.

24.2 Re-Analysis of 16S rRNA Gene Sequences

The 16S rRNA gene sequences were recovered from iron-rich mats (YS16 and YS18) (Kato et al. 2009a), active (AFhm, APcsc, APbsc, AAcs) and inactive chimneys (IPltc, IYdc, Inoc) (Kato et al. 2010; Kato et al. Chap. 9), crustal fluids obtained from boreholes (Fapm1a, Fapm1b, Papm3, F2apm1), a natural vent fluid (Fnv) and ambient seawater (Pasw and Fasw) (Kato et al. 2009b) in the SMT hydrothermal fields, i.e., Snail, Pika, Archaean, Kaiko and Yamanaka sites (Suppl. 24.1). The map for these sampling sites is shown in previous reports (Kato et al. 2009a, b, 2010) and Seama et al. (Chap. 17). The crustal fluid samples of Fapm1a, Fapm1b and F2apm1 were collected from the same borehole APM01 in the Snail site. Fapm1a and Fapm1b were collected in March 2004. F2apm1 was collected in August 2005. The 16S rRNA gene sequences were analyzed using QIIME version 1.7.0 (Caporaso et al. 2010) for clustering into OTUs at a 97 % similarity cut-off and for taxonomic affiliation of the OTUs. Any improper taxonomic affiliations by QIIME were modified manually as judged by the phylogenetic analysis described in previous reports (Kato et al. 2009a, b, 2010). It should be noted that the taxonomy within *Archaea* has not been standardized yet, and the affiliation for some archaeal groups based on the QIIME-equipped reference database is doubtful: for example, pMC1A4 and the related clones in Marine Benthic Group E (MBGE) was affiliated with *Methanobacteriales*. Therefore, the taxonomic affiliation of the detected clones was modified manually based on the archaeal phylogenetic tree as shown in Suppl. 24.2, which is provided in SILVA-Ref-NR database release 111 (Quast et al. 2012). A maximum-likelihood phylogenetic tree for Zetaproteobacteria was constructed by PhyML version 3.0 (Guindon et al. 2010). Coverage for each clone library was calculated using mothur version 1.2.8 (Schloss et al. 2009). Bacterial and archaeal community structures were compared by principal coordinate analysis (PCoA) using unweighted UniFrac (Lozupone and Knight 2005) equipped with QIIME. The sequencing process, i.e., DNA extraction, PCR, cloning and sequencing, was almost identical for all samples (Kato et al. 2009a, b, 2010). PCR was performed using a prokaryote-universal PCR primer set, Uni516F and Uni1406R, and an archaea-universal primer set, Arc8F and Uni1406R. Bacterial 16S rRNA gene sequences were dominant in the clone library data constructed using the prokaryote-universal PCR primer set (Kato et al. 2009a, b, 2010). Only the bacterial 16S rRNA gene sequences were extracted and used for bacterial community analyses in this study. To obtain more archaeal clones, we performed PCR clone analysis using the archaea-universal primer set in the previous studies (Kato et al. 2009a, b, 2010).

24.3 Bacterial Community Structures

Bacterial community structures in the SMT samples are summarized in Fig. 24.1. The relative abundance of each taxon in the libraries at the phylum level is shown in Fig. 24.1a. For *Proteobacteria*, the relative abundance in the class level (i.e., *Alpha-, Beta-, Gamma-, Delta-, Epsilon-* and *Zetaproteobacteria*) is shown in Fig. 24.1b. For each proteobacterial class except *Beta-* and *Zetaproteobacteria*,

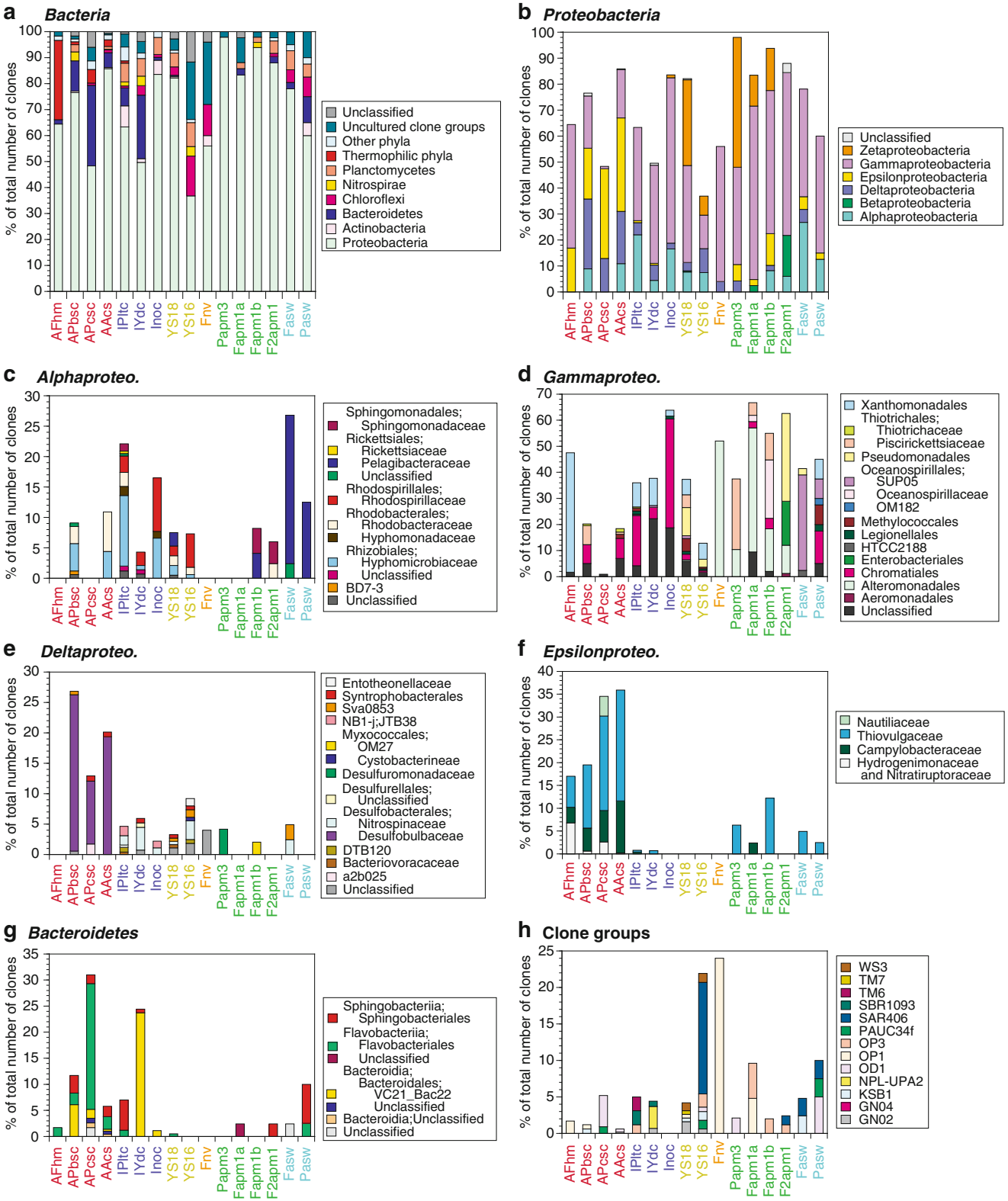

Fig. 24.1 Bacterial community structures based on the 16S rRNA gene clone libraries. The detection frequency of each taxon for (**a**) *Bacteria*, (**b**) *Proteobacteria*, (**c**) *Alphaproteobacteria*, (**d**) *Gammaproteobacteria*, (**e**) *Deltaproteobacteria*, (**f**) *Epsilonproteobacteria*, (**g**) *Bacteroidetes*, and (**h**) Uncultured clone groups are shown. (**a**) "Thermophilic phyla" include *Aquificae*, *Calditrhix*, *Deinococcus-Thermus*, *Thermodesulfobacteria* and *Thermotogae*, and "Other phyla" include *Chlamydiae*, *Chlorobi*, *Acidobacteria*, *Cyanobacteria*, *Firmicutes*, *Fusobacteria*, *Gemmatimonadetes*, *Spirochaetes* and *Verrucomicrobia*. *Colors* of the sample ID indicate the sample types: *red*, active chimney; *purple*, inactive chimney; *yellow*, iron-rich mat; *orange*, natural vent fluid; *green*, crustal fluid; *sky-blue*, ambient seawater. See also Suppl. Table 24.1 for the sample description

Table 24.1 Summary of dominant bacterial and archaeal taxa for each sample type

Sample type	Temperature (°C)[a]	pH[a]	Abundant bacterial taxa[b]	Abundant archaeal taxa[b]	Inorganic energy sources[c]
Active chimney	19–270	2.9–6.4	*Aquificae*, *Thiovulgaceae* (ε), *Campylobacteraceae* (ε), *Desulfobulbaceae* (δ), *Xanthomonadales* (γ), *Flavobacteriales* (Bact)	*Thermococci*, *Archaeoglobi*, *Thermoprotei*, *Aciduliprofundaceae*, THSCG, *Korarchaeota*	H_2, H_2S
Inactive chimney	2–3	7.6–8.1	*Chromatiales* (γ), VC21_Bac22 (Bact)	MGI, DHVEG-6	FeS_2, NH_4
Iron-rich mat	33–116	5.8–6.7	*Zetaproteobacteria*, SAR406	MCG, MBGE	Fe^{2+}
Crustal fluid	6–40	6.4–7.3	*Zetaproteobacteria*, *Piscirickettsiaceae* (γ), *Oceanospirillaceae* (γ), *Alteromonadales* (γ), *Pseudomonadales* (γ)	MCG, MGI	Fe^{2+}, H_2S, NH_4
Natural vent fluid	63–69	6.2–6.3	*Alteromonadales* (γ), OP1	MCG, MGBE, MGI	H_2
Ambient seawater	2–3	7.6–8.1	*Pelagibacteraceae* (α), SUP05 (γ)	MGI	H_2S, NH_4

[a]Temperature and pH of the venting fluids for active chimneys and iron mat and those of the seawater for inactive chimneys are shown. Data from Toki et al. (Chap. 45)
[b]Abundant taxa in the libraries (>20 % of the total number of clones) are shown. Greek letters in parentheses indicate proteobacterial classes. "Bact" in parentheses indicates the phylum *Bacteroidetes*
[c]Inferred from the physiological characteristics of the cultured species in the taxa

the relative abundance in the order or family level is shown in Fig. 24.1c–f. The relative abundance in *Bacteroidetes* and uncultured clone groups are shown in Fig. 24.1g, h. The dominant taxonomic groups for each sample type are summarized in Table 24.1 along with their environmental characteristics.

24.3.1 Zetaproteobacteria

Zetaproteobacteria were detected in the two iron-rich mat samples (YS16 and YS18), three crustal fluid samples (Papm3, Fapm1a and Fapm1b) and one inactive chimney sample (Inoc) (Fig. 24.1b). The relative abundance was up to 50 % of the total number of clones. Davis and Moyer (2008) also detected *Zetaproteobacteria* in an iron-rich mat sample from the Snail site. McAllister et al. (2011) have shown that most of the zetaproteobacterial clones detected in the crustal fluids are not clustered with the other clones detected in the other samples, suggesting the presence of endemic zetaproteobacterial members in the crustal fluids in the SMT (Suppl. 24.3). Quantitative analyses have shown that *Zetaproteobacteria* is abundant (up to 30 % of total prokaryotic cells) in prokaryotic communities in iron-rich mats and crustal fluids in the SMT (Kato et al. 2009a, b). The sole cultured species in *Zetaproteobacteria* was *Mariprofundus ferrooxydans*, a neutrophilic iron-oxidizing chemolithoautotroph (Emerson et al. 2007). Given that all or most of the *Zetaproteobacteria* are iron-oxidizers (Emerson et al. 2010; Fleming et al. 2013), any microbial ecosystem dominated by *Zetaproteobacteria* is supported by ferrous iron as the energy source (i.e., "iron-based ecosystem"). This is consistent with the thermodynamic calculation of bioavailable energy yields based on geochemical characteristics of the environments: the energy yield obtained from iron oxidation is comparable to or higher than that from oxidation of other reduced chemical species, such as hydrogen, hydrogen sulfide and methane (Kato et al. 2012).

Remarkably, iron-based ecosystems were found at both the Snail and Pika sites, even though their geological settings (on and off-ridge) are different (Seama et al. Chap. 17). Iron-based ecosystems also occur in deep-sea hydrothermal fields with other geological characteristics, such as the Loihi Seamount of Hawaii (Fleming et al. 2013), Tonga–Kermadec Arc (Forget et al. 2010; Hodges and Olson 2009), Lau basin (Li et al. 2012), Juan de Fuca Ridge (Davis et al. 2009) and Mohns Ridge (Øvreås et al. 2007). Thus, the development of iron-based ecosystems seems to be independent of these geological differences. Kato et al. (2012) have suggested that higher concentration of ferrous iron than hydrogen sulfide, which can supply more energy for the growth of iron-oxidizers than sulfide-oxidizers, is needed for the development of iron-based ecosystems. In addition, the continuous supply of ferrous iron, the chemical conditions that make ferrous iron dissolve stably (i.e., low pH, low Eh and low concentration of sulfide), and the temperature at which the iron-oxidizers can grow may be also important for the development of iron-based ecosystems. Iron-based ecosystems are likely to be widely distributed in environments that fulfill the above conditions on and below the seafloor.

24.3.2 Alphaproteobacteria

The relative abundance of each family level taxon of *Alphaproteobacteria* differed among the sample types (Fig. 24.1c). *Hyphomicrobiaceae* were relatively abundant in some solid samples, i.e., active and inactive chimneys and iron-rich mats (Fig. 24.1c). Most of the clones in the *Hyphomicrobiaceae* were not close to the cultured species (<92 % of 16S rRNA gene similarity) and clustered with environmental clones detected in deep-sea basaltic rocks and sulfide chimneys (Kato et al. 2013; Santelli et al. 2008). *Rhodospirillaceae* were relatively abundant in the iron-rich mat and inactive chimney samples, but not detected in the active chimney samples (Fig. 24.1c). One of the closest cultured species for the clones in the *Rhodospirillaceae* was a magnetotactic bacterium *Magnetovibrio blakemorei* with 92 % similarity (Bazylinski et al. 2013). The physiology of the uncultured bacteria in *Hyphomicrobiaceae* and *Rhodospirillaceae* was unclear; however, considering the sample types (i.e., sulfide chimneys, iron-rich mats and rocks on the seafloor) where they were detected, their presence was probably related to the presence of iron and/or sulfide minerals (such as goethite, pyrite, chalcopyrite and sphalerite (Ikehata et al. Chap. 22; Kakegawa et al. 2008; Masuda and Fryer, Chap. 21)).

In contrast, *Sphingomonadaceae* were relatively abundant in two crustal fluid samples (Fig. 24.1c). The detected clones of *Sphingomonadaceae* were close to *Sphingomonas* species (>97 % similarity) including oligotrophs, which are widely distributed in nature. In the crustal aquifer, they can survive with low concentrations of nutrients.

24.3.3 Gammaproteobacteria

Piscirickettsiaceae were relatively abundant in crustal fluid samples (Fig. 24.1d). This family contains chemolithoautotrophic sulfur-oxidizing bacteria such as *Thiomicrospira* spp. and *Thioalkalimicrobium* spp. The detected clones in the *Piscirickettsiaceae* were closest to *Thiomicrospira* spp. with up to 96 % similarity. In contrast, *Chromatiales* were relatively abundant in active and inactive chimney samples (Fig. 24.1d). The closest cultured species to the clones in *Chromatiales* were *Thiohalomonas* spp. or *Thioalkalispira* spp. (up to 94 % similarity), which are chemolithoautotrophic sulfur-oxidizing bacteria. Members in *Chromatiales* are facultative anaerobes, which can grow using nitrate as an electron acceptor. In contrast, *Thiomicrospira* spp. within the *Piscirickettsiaceae* are strict aerobes. Therefore, the availability of electron acceptors is likely to lead to differences in the relative abundance of the two taxa of sulfur-oxidizing bacteria.

Alteromonadales were relatively abundant in crustal fluid samples and the natural vent fluid sample (Fig. 24.1d). The detected clones in the *Alteromonadales* were close to *Alteromonas* spp., *Pseudoalteromonas* spp., *Marinobacter* spp., etc. (up to 99 % similarity). These cultured species are mainly chemoorganoheterotrophs. These species may thrive in warm crustal fluids (<40 °C) under the seafloor using organic carbon produced by chemolithoautotrophs. The gammaproteobacterial population of the F2apm1 sample differed from those of the other crustal fluid samples (Fig. 24.1d).

24.3.4 Deltaproteobacteria

Deltaproteobacteria accounted for over 10 % of the total number of clones in 3 out of 4 active chimney samples (Fig. 24.1b, e). Most of the deltaproteobacterial clones from the active chimney samples were affiliated with the *Desulfobulbaceae*, of which members grow depending on the reduction of oxidized sulfur species (such as sulfate and thiosulfate) or sulfur disproportionation. The closest cultured species to these clones are *Desulfobulbus* spp., *Desulfocapsa* spp., etc. (92–97 % similarity). *Desulfobulbaceae* have been also detected in active chimneys in other hydrothermal fields, such as the hydrothermal fields in the Okinawa Trough, Suiyo Seamount and 9°N EPR (Kato et al. 2013; Kormas et al. 2006; Nakagawa et al. 2004). In contrast, *Desulfobulbaceae* were rarely detected in the other SMT samples and in inactive chimneys in other hydrothermal fields, such as the hydrothermal fields in the Okinawa Trough, Central Indian Ridge (CIR) and 9°N EPR (Suzuki et al. 2004; Sylvan et al. 2012). These facts suggest that the detected members in *Desulfobulbaceae* prefer conditions in the active chimneys.

In contrast, *Nitrospinaceae* were detected in all of the inactive chimneys and iron-rich mat samples (Fig. 24.1e). A nitrite-oxidizing bacterium, *Nitrospina gracilis* is the sole cultured species in *Nitrospinaceae* (Watson and Waterbury 1971). It should be noted that a novel phylum, *Nitrospinae* has been proposed on the basis of a detailed phylogenetic analysis of the genome sequence of *N. gracilis* (Lücker et al. 2013). The detected members in the *Nitrospinaceae* may use nitrite as an electron donor. Nitrate reducers, e.g., members in Chromatiales, can produce nitrite. Remarkably, both *Nitrospinaceae* and *Chromatiales* were relatively abundant in the inactive chimney samples, suggesting that redox cycling of nitrogen species is potentially driven by the combination of nitrite oxidizers in the *Nitrospinaceae* and nitrate reducers in the *Chromatiales*.

24.3.5 Epsilonproteobacteria

Epsilonproteobacteria accounted for over 15 % of the total number of clones in all the active chimney samples (Fig. 24.1b, f). They are likely to play a significant role as primary producers in the ecosystem within the active chimneys in the SMT. This class contains chemolithoautotrophs using hydrogen and/or reduced sulfur species as electron donors (Campbell et al. 2006). The high proportions of *Epsilonproteobacteria* and *Desulfobulbaceae* in the *Deltaproteobacteria* in the clone libraries from the active chimney samples suggest that they contribute to the redox cycling of sulfur.

Epsilonproteobacteria were also detected in some crustal fluid samples (Fig. 24.1b, f). Hydrogen sulfide was detected in the crustal fluids (~5 μM; Toki et al. Chap. 45). These results suggest that, in addition to iron, the reduced sulfur species is used as an energy source for prokaryotic communities in the crustal fluids below the seafloor. In contrast, *Epsilonproteobacteria* were rarely detected in the iron-rich mat samples, suggesting that hydrogen and reduced sulfur species are not available in these habitats. Instead, iron may be the major energy source for prokaryotic communities in the iron-rich mats as mentioned above.

Epsilonproteobacteria were detected but only in low numbers in two inactive chimney samples, even though reduced sulfur species were rich in the chimneys. This suggests that the detected *Epsilonproteobacteria* cannot use the reduced sulfur species in the inactive chimneys surveyed. Alternatively, conditions, such as temperature, pH and Eh, in the inactive chimneys might not be suitable for *Epsilonproteobacteria*. In fact, autotrophs within the *Epsilonproteobacteria* use the reductive tricarboxylic acid cycle for carbon fixation, and this cycle appears to be the dominant pathway in habitats characterized by warm (over 20 °C) and anaerobic (or microaerobic) conditions (Nakagawa and Takai 2008; Hügler and Sievert 2010).

24.3.6 Bacteroidetes

Bacteroidetes were relatively abundant in the clone libraries from the active and inactive chimney samples (Fig. 24.1a, g). In particular, most of the clones detected in one inactive chimney (IYdc) were classified as belonging to the VC21_Bac22 group. This group was also detected in some of the other active and inactive chimney samples (Fig. 24.1g). The clones in this group are distant from the closest cultured species (<90 % similarity). The group was found to be relatively abundant in some inactive chimneys at other hydrothermal fields (Suzuki et al. 2004; Sylvan et al. 2012). Furthermore, this group was also relatively abundant in the clone libraries from massive sub-seafloor sulfide deposits collected in the SMT using BMS (S. Kato, in preparation). These results imply that the appearance of this group is related to the presence of sulfide minerals.

24.3.7 Uncultured Bacterial Clone Groups

The uncultured clone groups detected in the SMT samples were affiliated with GN02, GN04, KSB1, NPL-UPA2, OD1, OP1, OP3, PAUC34f, SAR406, SBR1093, TM6, TM7 and WS3. Metagenomic analyses have shown the metabolic potential of some groups, i.e., OD1 (Wrighton et al. 2012), OP1 (Takami et al. 2012), TM6 (McLean et al. 2013) and TM7 (Marcy et al. 2007). Furthermore, a recent study has reported the near-complete genomes of GN02, OP3, SAR406 and WS3, in addition to OD1 and OP1, using single-cell genomic analysis; however, details of metabolic potential have not been described yet (Rinke et al. 2013). Further cultivation or metagenomic analysis is needed to elucidate the metabolic function of the uncultured groups detected in the SMT.

24.4 Archaeal Community Structures

Diverse archaeal 16S rRNA gene sequences were detected in the SMT samples (Fig. 24.2 and Suppl. 24.2). In addition to cultured thermophilic *Euryarchaeota* and *Crenarchaeota* that are typical in deep-sea hydrothermal vents, the following groups were detected: Marine benthic groups A and E (MBGA and MBGE), Marine groups I, II and III (MGI, MGII and MGIII), Marine hydrothermal vent groups (MHVG and MHVG-1), Deep-sea euryarchaeotic group (DSEG), Deep-sea hydrothermal vent euryarchaeotic group (DHVEG) and Terrestrial hot spring crenarchaeotic group (THSCG). The dominant taxonomic groups for each sample type are shown in Table 24.1.

24.4.1 Thermophilic Archaea and Related Groups

Clones closely related to cultured thermophiles in the *Euryarchaeota* and *Crenarchaeota*, such as members in *Thermococci*, *Archaeoglobi* and *Thermopreotei*, were detected only in the active chimney samples (Fig. 24.2a). These cultured archaea include hydrogen-oxidizers, S^0-reducers, sulfate-reducers and fermenters. In addition, *Korarchaeota* were detected only in one active chimney sample (AFhm). Whole genome analyses have revealed that the *Korarchaeota* contains peptide fermenters (Elkins et al. 2008). THSCG was also detected in all of the active chimney samples (Fig. 24.2a). A metagenomic analysis has

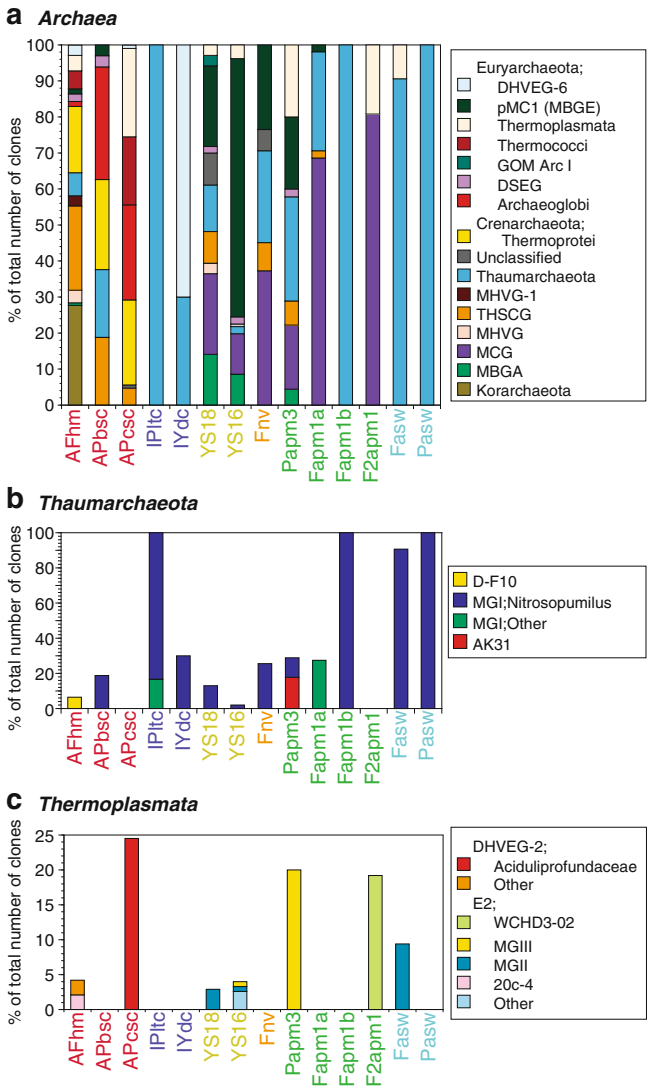

Fig. 24.2 Archaeal community structures based on the 16S rRNA gene clone libraries. The detection frequency of each taxon for (**a**) *Archaea*, (**b**) *Thaumarchaeota*, and (**c**) *Thermoplasmata* are shown. *Colors* of the sample ID indicate the sample types: *red*, active chimney; *purple*, inactive chimney; *yellow*, iron-rich mat; *orange*, natural vent fluid; *green*, crustal fluid; *sky-blue*, ambient seawater. See also Suppl. Table 24.1 for the sample description

suggested that THSCG contains a hydrogen- or CO-utilizing acetogen (Nunoura et al. 2011). These thermophilic archaea have been widely detected in active chimneys within various hydrothermal fields (Takai et al. 2006).

24.4.2 Thaumarchaeota and Related Groups

Thaumarchaeota were detected in most of the samples (Fig. 24.2a). All of the clones of *Thaumarchaeota* detected in the ambient seawater, the iron-rich mat and the natural vent fluid samples were closely related to *Nitrosopumilus maritimus*, an ammonia-oxidizer belonging to MGI (Könneke et al. 2005). In contrast, the clones that were not affiliated with MGI but placed in deeper positions within the *Thaumarchaeota* (AK31 and D-F10 clusters; Suppl. 24.2) were detected in one active chimney (AFhm) and one crustal fluid samples (Papm3) (Fig. 24.2b). These clones are relatively close to the ammonia-oxidizers, e.g., *Nitrososphaera* spp. (Tourna et al. 2011) or *Candidatus* "Nitrosocaldus yellowstonii" (De La Torre et al. 2008) (Suppl. 24.2). Furthermore, MBGA were detected in the two iron-rich mat samples and one crustal fluid sample (Papm3) (Fig. 24.2a). This group is related to the pSL12 clade that may contain ammonia oxidizers (Mincer et al. 2007). These putative ammonia-oxidizing archaea potentially play a role as primary producers in prokaryotic ecosystems in the SMT, which is consistent with the high bioavailable energy yields obtained from ammonia oxidation (Kato et al. 2012).

24.4.3 Thermoplasmata

Thermoplasmata accounted for over 15 % of the total number of clones in one active sulfide (APcsc) and two crustal fluid samples (Papm3 and F2apm) (Fig. 24.2a, c). Although *Thermoplasmata* contains methanogens (Dridi et al. 2012; Iino et al. 2013), the detected clones were distant from the methanogens (Suppl. 24.2).

DHVEG-2 was detected in two of the active chimney samples (AFhm and APcsc; Fig. 24.2c). DHVEG-2 is an ubiquitous group in deep-sea hydrothermal vents and contains a thermoacidophilic sulfur- and iron-reducing chemoorganoheterotroph, *Aciduliprofundum boonei* (Flores et al. 2012b; Reysenbach et al. 2006). The detected members in DHVEG-2 are probably thermophiles as well as *Archaeoglobi*, *Thermopreotei* and THSCG.

All of the *Thermoplasmata* clones detected in two crustal fluid samples (Papm3 and F2apm1) were affiliated with MGIII or the WCHD3-02 cluster, respectively (Fig. 24.2c). Considering the temperature of the habitats where these clones in MGIII and the WCHD3-02 cluster were detected, they may not be thermophiles.

24.4.4 Other Archaeal Clone Groups

MBGE accounted for 20 % or higher of the total number of clones in the two iron-rich mats, the natural vent and one of the crustal fluid samples (Papm3), and it was also detected in two active chimney samples (AFhm and APbsc) and another crustal fluid sample (Fapm1a) (Fig. 24.2a). MBGE has been detected in deep-sea sediments including marine hydrothermal fields (e.g., (Nercessian et al. 2005; Vetriani et al. 1999). MBGE was not detected in the inactive chimney samples of

the SMT, although they dominated in the libraries from inactive chimneys collected from some hydrothermal fields in the Okinawa Trough and CIR (Suzuki et al. 2004).

MCG was detected in the iron-rich mat, the natural vent fluid and the crustal fluid samples except Fapm1b (Fig. 24.2a). The relative abundance was high (11.2–80.8 %) in each clone library. MCG is abundant and widely distributed in marine sediments (Kubo et al. 2012). Single-cell genome-sequencing analyses suggest that MCG includes an anaerobic protein-degrader (Lloyd et al. 2013). However, the detected MCG clones show up to 83 % similarity with the 16S rRNA gene in the MCG genome. Further cultivation or metagenomic analysis is needed to know the ecophysiology of the MCG in the SMT.

DHVEG-6 dominated in the clone library from one inactive chimney sample (IYdc) and was also detected in two active chimney samples (AFhm and APcsc) (Fig. 24.2a). DHVEG-6 has been detected in various environments including acid mines and marine hydrothermal fields (e.g., Baker et al. 2010; Takai and Horikoshi 1999). The metagenome analyses of *Candidatus* Parvarchaeum spp. in DHVEG-6 suggest that they are aerobic host-associated/symbiotic archaea interacting with members of cell wall-less *Thermoplasmatales* (Baker et al. 2010). However, clones related to the cell wall-less *Thermoplasmatales* spp. were not detected in the SMT samples.

24.5 Comparison of Community Structures

The PCoA shows that bacterial community structures are similar within the same sample type, except F2apm1 (Fig. 24.3a). This result is generally consistent with the detection pattern of each taxon (Fig. 24.1), especially of each dominant taxon (Table 24.1). In other words, the bacterial community structures are different among the sample types, i.e., habitat types. *Epsilonproteobacteria* (putative hydrogen-oxidizers and sulfide-oxidizers) were dominant in the libraries from active chimneys, *Zetaproteobacteria* (putative iron-oxidizers) were dominant in those from iron-rich mats, and both *Zetaproteobacteria* and *Epsilonproteobacteria* were mainly detected in crustal fluids (Fig. 24.1, Table 24.1). Members of the *Zetaproteobacteria* and *Epsilonproteobacteria* may use H_2S or Fe^{2+} dissolved in the venting hydrothermal fluids. Our previous study has shown that the diversity in bacterial community structures is consistent with the thermodynamic calculation of bioavailable energy yields from oxidation of reduced chemical species, such as hydrogen, hydrogen sulfide and iron, for each habitat (Kato et al. 2012).

In addition, the bacterial community structures clearly differed between active and inactive chimney samples (Fig. 24.3a). *Epsilonproteobacteria* and thermophilic

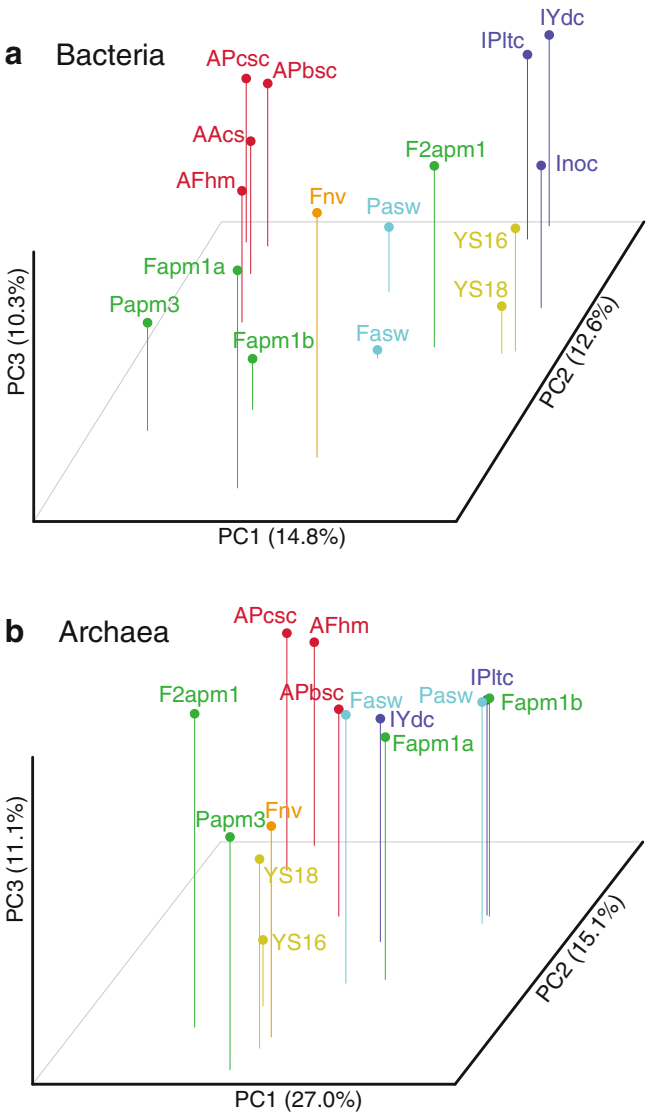

Fig. 24.3 Comparison of (**a**) bacterial and (**b**) archaeal community structures by PCoA. The percentages in the axis labels represent the percentages of variation explained by the principal coordinates. *Colors* of the sample ID indicate the sample types: *red*, active sulfide chimney; *purple*, inactive sulfide chimney; *yellow*, iron-rich mat; *orange*, natural vent fluid; *green*, crustal fluid; *sky-blue*, ambient seawater. See also Suppl. Table 24.1 for the sample description

bacteria (e.g., *Aquificae*) were rarely detected in the inactive chimneys; *Chromatiales* in *Gammaproteobacteria* (putative sulfide-oxidizers) was relatively abundant (Fig. 24.1, Table 24.1). The members in *Chromatiales* potentially use sulfide minerals such as pyrites, which are the main component of the chimneys (Kakegawa et al. 2008; Ikehata et al., Chap. 22), as their energy sources, even if the supply of hydrothermal fluids ceases. The difference between active and inactive chimney samples may reflect the temporal change before and after the cease of hydrothermal activity, i.e., temperature, pH and Eh, in addition to availability of

reduced chemical species (Kato et al. 2010), which is consistent with the previous study of 9°N EPR (Sylvan et al. 2012).

In contrast to the bacterial community structures, the archaeal community structures seems not to be clearly distinguished by the sample types, especially for inactive chimneys, some borehole fluids and ambient seawater samples (Fig. 24.3b). MGI was dominant in the libraries from these samples (Fig. 24.2); however, for the present, it is difficult to identify whether the MGI is indigenous in the samples or arises through contamination from the ambient seawater. At the least, archaeal community structures in the active chimneys can be distinguished from those in the other samples (Fig. 24.3b). Thermophilic archaea (e.g., *Thermococci* and *Archaeoglobi*) were dominant in the libraries from the active chimney samples (Fig. 24.2, Table 24.1). The detection of thermophilic archaea is consistent with the high temperature of venting fluids from the active chimneys. In contrast, they were rarely detected in the iron-rich mat and crustal fluid samples; MBGE and MCG are mainly detected there (Fig. 24.2, Table 24.1). In addition to temperature, the difference in pH, Eh and availability of reduced chemical species may cause the observed difference in the archaeal communities between the active chimneys and the others, as per the case of the bacterial communities.

24.6 Concluding Remarks

These comprehensive comparative analyses show the differences in the prokaryotic community structures among the habitat types on and below the seafloor in the SMT. These differences are likely to be associated with the relative abundance of putative chemolithoautotrophs. The geological difference between the on- and off-ridge hydrothermal sites might not constrain the community structures. Detailed phylogenetic analysis suggests the presence of endemic taxa for each habitat type. The detected prokaryotes are likely to play a significant role in the cycling of carbon, nitrogen, sulfur and/or iron in these habitats. Our results indicate that the prokaryotic community structure in sulfide chimneys dramatically changes before and after cessation of hydrothermal venting. In addition, diverse yet-uncultured bacteria and archaea were detected in the SMT hydrothermal fields. However, DNA-based molecular analyses targeting 16S rRNA genes cannot provide direct evidence for physiology, activity or productivity of prokaryotes. Further studies using RNA-based analyses, in situ incubation experiments, isolation and cultivation are needed to understand prokaryotic ecology within the hydrothermal fields.

Acknowledgements We are grateful to two anonymous reviewers for valuable comments and suggestions. This research was funded by the Ministry of Education, Culture, Science, and Technology (MEXT), Japan, through a special coordination fund (Archaean Park Project: International Research Project on Interaction between Sub-Vent Biosphere and Geo-Environments) and a Grant-in-Aid for Scientific Research on Innovative Areas (Project TAIGA, #20109006), and partially by the RIKEN Special Postdoctoral Researchers Program.

References

Baker BJ, Comolli LR, Dick GJ, Hauser LJ, Hyatt D, Dill BD, Land ML, VerBerkmoes NC, Hettich RL, Banfield JF (2010) Enigmatic, ultrasmall, uncultivated archaea. Proc Natl Acad Sci U S A 107 (19):8806–8811. doi:10.1073/pnas.0914470107

Bazylinski DA, Williams TJ, Lefèvre CT, Trubitsyn D, Fang J, Beveridge TJ, Moskowitz BM, Ward B, Schübbe S, Dubbels BL, Simpson B (2013) *Magnetovibrio blakemorei* gen. nov., sp. nov., a magnetotactic bacterium (*Alphaproteobacteria*: *Rhodospirillaceae*) isolated from a salt marsh. Int J Syst Evol Microbiol 63(Pt 5):1824–1833. doi:10.1099/ijs.0.044453-0

Campbell BJ, Engel AS, Porter ML, Takai K (2006) The versatile epsilon-proteobacteria: key players in sulphidic habitats. Nat Rev Microbiol 4(6):458–468

Caporaso JG, Kuczynski J, Stombaugh J, Bittinger K, Bushman FD, Costello EK, Fierer N, Pena AG, Goodrich JK, Gordon JI, Huttley GA, Kelley ST, Knights D, Koenig JE, Ley RE, Lozupone CA, McDonald D, Muegge BD, Pirrung M, Reeder J, Sevinsky JR, Turnbaugh PJ, Walters WA, Widmann J, Yatsunenko T, Zaneveld J, Knight R (2010) QIIME allows analysis of high-throughput community sequencing data. Nat Method 7(5):335–336. doi:10.1038/nmeth.f.303

Cowen J, Giovannoni S, Kenig F, Johnson H, Butterfield D, Rappé M, Hutnak M, Lam P (2003) Fluids from aging ocean crust that support microbial life. Science 299(5603):120–123

Davis R, Moyer C (2008) Extreme spatial and temporal variability of hydrothermal microbial mat communities along the Mariana island arc and southern Mariana back-arc system. J Geophys Res 113: B08S15. doi:10.1029/2007JB005413

Davis RE, Stakes DS, Wheat CG, Moyer CL (2009) Bacterial variability within an iron-silica-manganese-rich hydrothermal mound located off-axis at the Cleft Segment, Juan de Fuca Ridge. Geomicrobiol J 26(8):570–580. doi:10.1080/01490450902889080

De La Torre JR, Walker CB, Ingalls AE, Könneke M, Stahl DA (2008) Cultivation of a thermophilic ammonia oxidizing archaeon synthesizing crenarchaeol. Environ Microbiol 10(3):810–818. doi:10.1111/j.1462-2920.2007.01506.x

Dridi B, Fardeau M-L, Ollivier B, Raoult D, Drancourt M (2012) *Methanomassiliicoccus luminyensis* gen. nov., sp. nov., a methanogenic archaeon isolated from human faeces. Int J Syst Evol Microbiol 62(Pt 8):1902–1907. doi:10.1099/ijs.0.033712-0

Elkins JG, Podar M, Graham DE, Makarova KS, Wolf Y, Randau L, Hedlund BP, Brochier-Armanet CL, Kunin V, Anderson I, Lapidus A, Goltsman E, Barry K, Koonin EV, Hugenholtz P, Kyrpides N, Wanner G, Richardson P, Keller M, Stetter KO (2008) A korarchaeal genome reveals insights into the evolution of the archaea. Proc Natl Acad Sci U S A 105(23):8102–8107. doi:10.1073/pnas.0801980105

Emerson D, Rentz JA, Lilburn TG, Davis RE, Aldrich H, Chan C, Moyer CL (2007) A novel lineage of proteobacteria involved in formation of marine Fe-oxidizing microbial mat communities. PLoS One 2(8):e667. doi:10.1371/journal.pone.0000667

Emerson D, Fleming EJ, McBeth JM (2010) Iron-oxidizing bacteria: an environmental and genomic perspective. Ann Rev Microbiol 64 (1):561–583. doi:10.1146/annurev.micro.112408.134208

Fleming EJ, Davis RE, McAllister SM, Chan CS, Moyer CL, Tebo BM, Emerson D (2013) Hidden in plain sight: discovery of sheath-forming, iron-oxidizing *Zetaproteobacteria* at Loihi Seamount, Hawaii, USA. FEMS Microbiol Ecol 85(1):116–127. doi:10.1111/1574-6941.12104

Flores GE, Shakya M, Meneghin J, Yang ZK, Seewald JS, Geoff Wheat C, Podar M, Reysenbach AL (2012a) Inter-field variability in the microbial communities of hydrothermal vent deposits from a back-arc basin. Geobiology 10(4):333–346. doi:10.1111/j.1472-4669.2012.00325.x

Flores GE, Wagner I, Liu Y, Reysenbach A-L (2012b) Distribution, abundance, and diversity patterns of the thermoacidophilic "Deep-sea hydrothermal vent euryarchaeota 2" (DHVE2). Front Microbiol 3. doi:10.3389/fmicb.2012.00047

Forget NL, Murdock SA, Juniper SK (2010) Bacterial diversity in Fe-rich hydrothermal sediments at two South Tonga Arc submarine volcanoes. Geobiology 8(5):417–432. doi:10.1111/j.1472-4669.2010.00247.x

Guindon S, Dufayard J-F, Lefort V, Anisimova M, Hordijk W, Gascuel O (2010) New algorithms and methods to estimate maximum-likelihood phylogenies: assessing the performance of PhyML 3.0. Syst Biol 59(3):307–321. doi:10.1093/sysbio/syq010

Hodges TW, Olson JB (2009) Molecular comparison of bacterial communities within iron-containing flocculent mats associated with submarine volcanoes along the Kermadec Arc. Appl Environ Microbiol 75(6):1650–1657. doi:10.1128/aem.01835-08

Huber JA, Johnson HP, Butterfield DA, Baross JA (2006) Microbial life in ridge flank crustal fluids. Environ Microbiol 8(1):88–99

Hügler M, Sievert SM (2010) Beyond the calvin cycle: autotrophic carbon fixation in the ocean. Ann Rev Mar Sci 3(1):261–289. doi:10.1146/annurev-marine-120709-142712

Iino T, Tamaki H, Tamazawa S, Ueno Y, Ohkuma M, Suzuki K, Igarashi Y, Haruta S (2013) *Candidatus* Methanogranum caenicola: a novel methanogen from the anaerobic digested sludge, and proposal of *Methanomassiliicoccaceae* fam. nov. And *Methanomassiliicoccales* ord. nov., for a methanogenic lineage of the class *Thermoplasmata*. Microbes Environ 28(2):244–250

Kakegawa T, Utsumi M, Marumo K (2008) Geochemistry of sulfide chimneys and basement pillow lavas at the Southern Mariana Trough (12.55°N–12.58°N). Res Geol 58:249–266

Kato S, Kobayashi C, Kakegawa T, Yamagishi A (2009a) Microbial communities in iron-silica-rich microbial mats at deep-sea hydrothermal fields of the Southern Mariana Trough. Environ Microbiol 11(8):2094–2111

Kato S, Yanagawa K, Sunamura M, Takano Y, Ishibashi J, Kakegawa T, Utsumi M, Yamanaka T, Toki T, Noguchi T, Kobayashi K, Moroi A, Kimura H, Kawarabayasi Y, Marumo K, Urabe T, Yamagishi A (2009b) Abundance of *Zetaproteobacteria* within crustal fluids in back-arc hydrothermal fields of the Southern Mariana Trough. Environ Microbiol 11(12):3210–3222

Kato S, Takano Y, Kakegawa T, Oba H, Inoue K, Kobayashi C, Utsumi M, Marumo K, Kobayashi K, Ito Y, Ishibashi J, Yamagishi A (2010) Biogeography and biodiversity in sulfide structures of active and inactive vents at deep-sea hydrothermal fields of the Southern Mariana Trough. Appl Environ Microbiol 76(9):2968–2979. doi:10.1128/aem.00478-10

Kato S, Nakamura K, Toki T, Ishibashi J, Tsunogai U, Hirota A, Ohkuma M, Yamagishi A (2012) Iron-based microbial ecosystem on and below the seafloor: a case study of hydrothermal fields of the Southern Mariana Trough. Front Microbiol 3. doi:10.3389/fmicb.2012.00089

Kato S, Nakawake M, Kita J, Yamanaka T, Utsumi M, Okamura K, Ishibashi J, Ohkuma M, Yamagishi A (2013) Characteristics of microbial communities in crustal fluids in a deep-sea hydrothermal field of the Suiyo Seamount. Front Microbiol 4. doi:10.3389/fmicb.2013.00085

Könneke M, Bernhard AE, de la Torre JR, Walker CB, Waterbury JB, Stahl DA (2005) Isolation of an autotrophic ammonia-oxidizing marine archaeon. Nature 437(7058):543–546

Kormas KA, Tivey MK, Von Damm K, Teske A (2006) Bacterial and archaeal phylotypes associated with distinct mineralogical layers of a white smoker spire from a deep-sea hydrothermal vent site (9°N, East Pacific Rise). Environ Microbiol 8(5):909–920. doi:10.1111/j.1462-2920.2005.00978.x

Kubo K, Lloyd KG, Biddle JF, Amann R, Teske A, Knittel K (2012) Archaea of the miscellaneous crenarchaeotal group are abundant, diverse and widespread in marine sediments. ISME J. doi:10.1038/ismej.2012.37

Li J, Zhou H, Peng X, Wu Z, Chen S, Fang J (2012) Microbial diversity and biomineralization in low-temperature hydrothermal iron–silica-rich precipitates of the Lau Basin hydrothermal field. FEMS Microbiol Ecol 81(1):205–216. doi:10.1111/j.1574-6941.2012.01367.x

Lloyd KG, Schreiber L, Petersen DG, Kjeldsen KU, Lever MA, Steen AD, Stepanauskas R, Richter M, Kleindienst S, Lenk S, Schramm A, Jorgensen BB (2013) Predominant archaea in marine sediments degrade detrital proteins. Nature 496(7444):215–218. doi:10.1038/nature12033

Lozupone C, Knight R (2005) UniFrac: a new phylogenetic method for comparing microbial communities. Appl Environ Microbiol 71(12):8228–8235. doi:10.1128/aem.71.12.8228-8235.2005

Lücker S, Nowka B, Rattei T, Spieck E, Daims H (2013) The genome of *Nitrospina gracilis* illuminates the metabolism and evolution of the major marine nitrite oxidizer. Front Microbiol 4. doi:10.3389/fmicb.2013.00027

Marcy Y, Ouverney C, Bik EM, Losekann T, Ivanova N, Martin HG, Szeto E, Platt D, Hugenholtz P, Relman DA, Quake SR (2007) Dissecting biological "Dark matter" with single-cell genetic analysis of rare and uncultivated TM7 microbes from the human mouth. Proc Natl Acad Sci U S A 104(29):11889–11894. doi:10.1073/pnas.0704662104

Marumo K, Urabe T, Goto A, Takano Y, Nakaseama M (2008) Mineralogy and isotope geochemistry of active submarine hydrothermal field at Suiyo Seamount, Izu–Bonin Arc, west Pacific Ocean. Res Geol 58(3):220–248. doi:10.1111/j.1751-3928.2008.00059.x

McAllister SM, Davis RE, McBeth JM, Tebo BM, Emerson D, Moyer CL (2011) Biodiversity and emerging biogeography of the neutrophilic iron-oxidizing *Zetaproteobacteria*. Appl Environ Microbiol 77(15):5445–5457. doi:10.1128/aem.00533-11

McLean JS, Lombardo M-J, Badger JH, Edlund A, Novotny M, Yee-Greenbaum J, Vyahhi N, Hall AP, Yang Y, Dupont CL, Ziegler MG, Chitsaz H, Allen AE, Yooseph S, Tesler G, Pevzner PA, Friedman RM, Nealson KH, Venter JC, Lasken RS (2013) Candidate phylum TM6 genome recovered from a hospital sink biofilm provides genomic insights into this uncultivated phylum. Proc Natl Acad Sci U S A. doi:10.1073/pnas.1219809110

Mincer TJ, Church MJ, Taylor LT, Preston C, Karl DM, DeLong EF (2007) Quantitative distribution of presumptive archaeal and bacterial nitrifiers in Monterey Bay and the North Pacific Subtropical Gyre. Environ Microbiol 9(5):1162–1175. doi:10.1111/j.1462-2920.2007.01239.x

Nakagawa S, Takai K (2008) Deep-sea vent chemoautotrophs: diversity, biochemistry and ecological significance. FEMS Microbiol Ecol 65(1):1–14

Nakagawa T, Nakagawa S, Inagaki F, Takai K, Horikoshi K (2004) Phylogenetic diversity of sulfate-reducing prokaryotes in active deep-sea hydrothermal vent chimney structures. FEMS Microbiol Lett 232(2):145–152

Nakagawa S, Takai K, Inagaki F, Chiba H, Ishibashi J, Kataoka S, Hirayama H, Nunoura T, Horikoshi K, Sako Y (2005) Variability in microbial community and venting chemistry in a sediment-hosted

backarc hydrothermal system: impacts of subseafloor phase-separation. FEMS Microbiol Ecol 54(1):141–155

Nercessian O, Fouquet Y, Pierre C, Prieur D, Jeanthon C (2005) Diversity of bacteria and archaea associated with a carbonate-rich metalliferous sediment sample from the rainbow vent field on the Mid-Atlantic Ridge. Environ Microbiol 7(5):698–714

Nunoura T, Takaki Y, Kakuta J, Nishi S, Sugahara J, Kazama H, Chee G-J, Hattori M, Kanai A, Atomi H, Takai K, Takami H (2011) Insights into the evolution of archaea and eukaryotic protein modifier systems revealed by the genome of a novel archaeal group. Nucl Acids Res 39(8):3204–3223. doi:10.1093/nar/gkq1228

Orcutt BN, Bach W, Becker K, Fisher AT, Hentscher M, Toner BM, Wheat CG, Edwards KJ (2011) Colonization of subsurface microbial observatories deployed in young ocean crust. ISME J 5 (4):692–703. doi:10.1038/ismej.2010.157

Øvreås L, Johannessen T, Jorgensen S, Thorseth IH, Pedersen RB (2007) Diversity of microorganisms associated with low temperature iron deposits at the 71°N hydrothermal vent field along the arctic mid-ocean ridge. Eos Trans AGU 88(52) Fall Meet Suppl, Abstract OS43A-0992

Quast C, Pruesse E, Yilmaz P, Gerken J, Schweer T, Yarza P, Peplies J, Glöckner FO (2012) The SILVA ribosomal RNA gene database project: improved data processing and web-based tools. Nucl Acids Res. doi:10.1093/nar/gks1219

Reysenbach A-L, Liu Y, Banta AB, Beveridge TJ, Kirshtein JD, Schouten S, Tivey MK, Von Damm KL, Voytek MA (2006) A ubiquitous thermoacidophilic archaeon from deep-sea hydrothermal vents. Nature 442(7101):444–447

Rinke C, Schwientek P, Sczyrba A, Ivanova NN, Anderson IJ, Cheng J-F, Darling A, Malfatti S, Swan BK, Gies EA, Dodsworth JA, Hedlund BP, Tsiamis G, Sievert SM, Liu W-T, Eisen JA, Hallam SJ, Kyrpides NC, Stepanauskas R, Rubin EM, Hugenholtz P, Woyke T (2013) Insights into the phylogeny and coding potential of microbial dark matter. Nature 499(7459):431–437. doi:10.1038/nature12352

Santelli CM, Orcutt BN, Banning E, Bach W, Moyer CL, Sogin ML, Staudigel H, Edwards KJ (2008) Abundance and diversity of microbial life in ocean crust. Nature 453(7195):653–656

Schloss PD, Westcott SL, Ryabin T, Hall JR, Hartmann M, Hollister EB, Lesniewski RA, Oakley BB, Parks DH, Robinson CJ, Sahl JW, Stres B, Thallinger GG, Van Horn DJ, Weber CF (2009) Introducing mothur: open-source, platform-independent, community-supported software for describing and comparing microbial communities. Appl Environ Microbiol 75 (23):7537–7541. doi:10.1128/aem.01541-09

Schrenk MO, Kelley DS, Delaney JR, Baross JA (2003) Incidence and diversity of microorganisms within the walls of an active deep-sea sulfide chimney. Appl Environ Microbiol 69(6):3580–3592

Suzuki Y, Inagaki F, Takai K, Nealson KH, Horikoshi K (2004) Microbial diversity in inactive chimney structures from deep-sea hydrothermal systems. Microb Ecol 47(2):186–196

Sylvan JB, Toner BM, Edwards KJ (2012) Life and death of deep-sea vents: bacterial diversity and ecosystem succession on inactive hydrothermal sulfides. MBio 3(1):e00279-11. doi:10.1128/mBio.00279-11

Takai K, Horikoshi K (1999) Genetic diversity of archaea in deep-sea hydrothermal vent environments. Genetics 152(4):1285–1297

Takai K, Nakagawa S, Reysenbach AL, Hoek J (2006) Microbial ecology of mid-ocean ridges and back-arc basins. Geophys Monogr 166:185–213

Takami H, Noguchi H, Takaki Y, Uchiyama I, Toyoda A, Nishi S, Chee G-J, Arai W, Nunoura T, Itoh T, Hattori M, Takai K (2012) A deeply branching thermophilic bacterium with an ancient acetyl-CoA pathway dominates a subsurface ecosystem. PLoS One 7(1): e30559. doi:10.1371/journal.pone.0030559

Tourna M, Stieglmeier M, Spang A, Könneke M, Schintlmeister A, Urich T, Engel M, Schloter M, Wagner M, Richter A, Schleper C (2011) *Nitrososphaera viennensis*, an ammonia oxidizing archaeon from soil. Proc Natl Acad Sci U S A 108(20):8420–8425. doi:10.1073/pnas.1013488108

Vetriani C, Jannasch HW, MacGregor BJ, Stahl DA, Reysenbach A-L (1999) Population structure and phylogenetic characterization of marine benthic archaea in deep-sea sediments. Appl Environ Microbiol 65(10):4375–4384

Watson S, Waterbury J (1971) Characteristics of two marine nitrite oxidizing bacteria, *Nitrospina gracilis* nov. gen. nov. sp. and *Nitrococcus mobilis* nov. gen. nov. sp. Arch Mikrobiol 77 (3):203–230. doi:10.1007/bf00408114

Wrighton KC, Thomas BC, Sharon I, Miller CS, Castelle CJ, VerBerkmoes NC, Wilkins MJ, Hettich RL, Lipton MS, Williams KH, Long PE, Banfield JF (2012) Fermentation, hydrogen, and sulfur metabolism in multiple uncultivated bacterial phyla. Science 337(6102):1661–1665. doi:10.1126/science.1224041

Vent Fauna in the Mariana Trough

25

Shigeaki Kojima and Hiromi Watanabe

Abstract

The Mariana Trough is a back-arc basin in the Northwestern Pacific. To date, active hydrothermal vent fields associated with the back-arc spreading center have been reported from the central to the southernmost region of the basin. In spite of a large variation of water depth, no clear segregation of vent faunas has been recognized among vent fields in the Mariana Trough and a large snail *Alviniconcha hessleri* dominates chemosynthesis-based communities in most fields. Although the Mariana Trough approaches the Mariana Arc at both northern and southern ends, the fauna at back-arc vents within the trough appears to differ from arc vents. In addition, a distinct chemosynthesis-based community was recently discovered in a methane seep site on the landward slope of the Mariana Trench. On the other hand, some hydrothermal vent fields in the Okinawa Trough backarc basin and the Izu-Ogasawara Arc share some faunal groups with the Mariana Trough. The Mariana Trough is a very interesting area from the zoogeographical point of view.

Keywords

Alvinoconcha hessleri • Chemosynthetic-based communities • Hydrothermal vent • Mariana Arc • Mariana Trough

25.1 Introduction

The Mariana Trough is a back-arc basin in the Northwestern Pacific (Fig. 25.1). The present hydrothermal activity in the Mariana Trough is estimated to have started about 7 million years ago (Ma) (Stern et al. 2003) and some dating studies reported records of mineralization in this region since 12,000 years ago (Stüben et al. 1994; Takamasa et al. 2013; Ishibashi et al. Chap. 23).

S. Kojima (✉)
Graduate School of Frontier Sciences, The University of Tokyo, Chiba 277-8563, Japan

Atmosphere and Ocean Research Institute, The University of Tokyo, Chiba 277-8564, Japan
e-mail: kojima@aori.u-tokyo.ac.jp

H. Watanabe
Japan Agency for Marine-Earth Science and Technology, Kanagawa 237-0061, Japan

The first hydrothermal vent field discovered in the Mariana Trough was the Alice Springs, in the Central Mariana Trough (18° 13′ N, 144° 43′ E: 3,600 m depth) in 1987 (Craig et al. 1987). Although an unnamed vent field was discovered 20 km south of the Alice Springs (18° 03′ N, 144° 45′ E: 3,660 m depth), biological research have not yet conducted there (Hessler and Lonsdale 1991). Next vent field was discovered at the Forecast Vent site (13° 24′ N, 143° 55′ E: 1,470 m depth) in 1992 (Johnson et al. 1993). This site has been classified as an arc-related vent (e.g. Embley et al. 2007), however a recent study proposed that volcanic style in the region around the Forecast seamount reflects strong extension in the back-arc basin (Stern et al. 2013). Although the geologic setting of the Forecast site would be considered as in transition, vent fauna of this field is more similar to other vent fields in the Mariana Trough than arc vents as mentioned below, and we treat it as a vent field in the Mariana Trough in this paper.

In the southernmost region of the Mariana Trough, various hydrothermal vent fields have been discovered

J.-i. Ishibashi et al. (eds.), *Subseafloor Biosphere Linked to Hydrothermal Systems: TAIGA Concept*,
DOI 10.1007/978-4-431-54865-2_25,

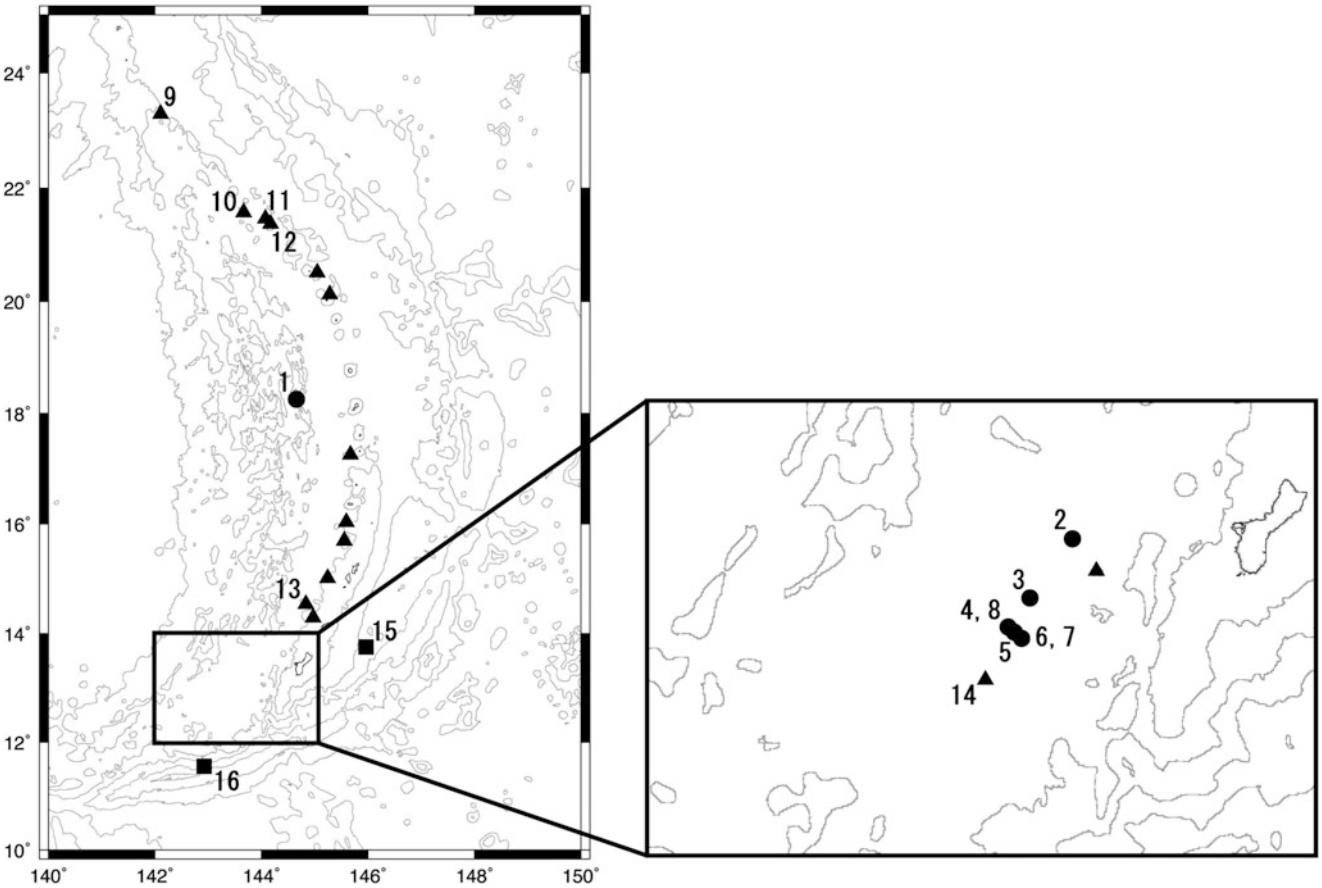

Fig. 25.1 A map of hydrothermal vent fields in the Mariana Trough (*closed circles*) and the Mariana Arc (*Closed triangles*), and a methane seep sites in the Mariana Trench (*closed squares*). Bathymetrical contour intervals are 2,000 m. *1*, Alice Springs and an unnamed vent field; *2*, Forecast Vent site; *3*, 13°N Ridge site; *4*, Snail site; *5*, Archaean site; *6*, Pika site; *7*, Urashima site; *8*, Yamanaka site; *9*, Nikko Seamount; *10*, Dai-ni (second) Kasuga Seamount; *11*, NW Eifuku Seamount; *12*, Daikoku Seamount; *13*, NW Rota-1 Seamount; *14*, TOTO Caldera; *15*, South Chamorro Seamount; *16*, Shinkai Seep Field

(Yoshikawa et al. 2012). First in this region, a low-temperature vent site (the 13°N Ridge site) was discovered at 13°06′N on the Backarc Spreading Center (13°06′N, 143°41′E, 2,945 m depth) in 1999 (Mitsuzawa et al. 2000; Masuda et al. 2001b). Thereafter, an active vent field was discovered at the Snail site (=Fryer site; 12°57′N, 143°37′E, 2,850 m depth), which is also situated on the back-arc spreading center, in 2003 (Wheat et al. 2003). The Yamanaka site (=Y site; 12°57′N, 143°37′E, 2,826 m depth), which is about 1.1 km SW of the Snail site, was also discovered on the spreading center in 2003 (Kakegawa et al. 2008). The Pika site (12°55′N, 143°39′E, 2,770 m depth) and the Archaean site (12°56′N, 143°38′E, 2,990 m depth) were discovered on off-axis seamounts in 2003 (Urabe et al. 2004; Ishibashi et al. 2004). The newest hydrothermal vent field was discovered at the Urashima site (12°55′N, 143°39′E, 2,922 m depth), which is situated about 0.5 km north of the Pika site, in 2010 (Nakamura et al. 2012). The Snail, Archaean, Pika, and Urashima sites are distributed almost on a straight line from ridge axis to the off-ridge, which suggests that the locality of hydrothermal activity is controlled by tectonic fractures.

25.2 Vent Fauna of the Mariana Trough

25.2.1 Research History

Hessler and Lonsdale (1991) report 30 species from the chemosynthetic communities at the Alice Springs site (Table 25.1). They pointed out faunal affinity at the genus level between vent fields of the Mariana Trough and the central ridges in the Eastern Pacific Ocean, although they stated that eight genera were known only from the western Pacific vents. After 6 years, Fujikura et al. (1997) and Hasegawa et al. (1997) summarized vent faunas at the Alice Springs and Forecast sites based on specimens collected using the submersible *SHINKAI 2000* in 1996 (Table 25.1). In spite of a large difference in water depth

Table 25.1 List of animals collected in hydrothermal vent fields in the Mariana Trough

Phylum	Class	Family	Species	Sites[a]	Description	Remarks
Porifera	Demospongiae	Cladorhizidae	*Abyssocladia* sp.	4		
Cnidaria	Actinulida	Actinostolidae	*Marianactis bythios*	1, 2	Fautin and Hessler (1989)	
			Small sea anemone	1		Hessler and Lonsdale (1991), photograph only
			White sea anemone	7		Video and photograph only
			Actinostolid-like anemone	4		Video and photograph only
			Anemone	3, 5		Video and photograph only
Plathyhelminthes	Polycladida		unidentifid species	2		Fujikura et al. (1997)
Annelida	Polychaeta	Alvinellidae	*Paralvinella hessleri*	1	Desbruyères and Laubier (1989)	
		Polynoidae	*Branchinotogluma burkensis*	1, 2	Pettibone (1989)	
		Polynoidae	*Branchinotogluma marianus*	1, 2		Described as *Opisthotrochopodus marianus*
		Lepidonotopodinae	*Lepidonotopodium minutum*	1		
		Lepidonotopodinae	*Levensteiniella raisae*	1		
		Hesionidae	*Hesiocaeca hessleri*	1	Blake (1991)	*Hesiocaeca* sp. in Hessler and Lonsdale (1991)
		Maldanidae	*Nicomache* sp.	1		*Nicomache arwidssoni* in Hessler and Lonsdale (1991); *Nicomache* cf. *ohtai* in Desbruyères et al. (2006)
		Ampharitidae	*Amphisamytha galapagensis*	1	Zottoli (1983)	
			unidentified species	1, 2		Fujikura et al. (1997)
Mollusca	Aplacophora	Simrothiellidae	undescribed species	1		Hessler and Lonsdale (1991)
	Bivalvia	Mytilidae	*Bathymodiolus* sp.	1, 2		It forms a monophyletic group with *B. septemdierum*, *B. brevior*, and *B. marisindicus* (Fujita et al. 2009).
		Malletiidae	undescribed species (*Malletia* sp.?)	2		Fujikura et al. (1997)
	Gastropoda	Provannidae	*Alviniconcha hessleri*	1, 2, 3, 4, 5	Okutani and Ohta (1988)	
		Provannidae	*Provanna nassariaeformis*	1	Okutani (1990)	
		Provannidae	*Desbruyeresia marianaensis*	1, 2		Described as *Provanna marianaensis*
		Provannidae	*Desbruyeresia* cf. *mariaensis*	4, 5 6		
		Provannidae	*Desbruyeresia* cf. *spinosa*	2		Hasegawa et al. (1997)
		Neomphalidae	*Symmetromphalus regularis*	1, 2	McLean (1990)	
		Lepetodrilidae	*Lepetodrilus* aff. *schrolli*	1, 2		*L. elevatus* in Hessler and Lonsdale (1991); Johnson et al., (2008)
		Lepetodrilidae	*Lepetodrilus* sp.	4		
		Phenacolepadidae	*Shinkailepas* spp.	1, 2, 3, 4, 5, 6		*Shinkailepas* cf. *kaikatensis* in Hessler and Lonsdale (1991) and Fujikura et al. (1997)
		Acmaeidae	Undescribed species	1		Hessler and Lonsdale (1991)

(continued)

Table 25.1 (continued)

Phylum	Class	Family	Species	Sites[a]	Description	Remarks
		Turridae	*Phymorhynchus* cf. *starmeri*	1, 2, 5		Fujikura et al. (1997), probably Buccinidae indet. in Hessler and Lansdale (1991)
		Turridae	*Phymorhynchus* sp.	3, 5		
		Clypeosectidae	*Pseudorimula marianae*	1, 2	McLean (1990)	
		Skeneidae	*Ventsia* cf. *tricarinata*	1, 2		Fujikura et al. (1997)
		Peltospiridae	*Pachydermia* cf. *sculpta*	2		
		Peltospiridae	*Lirapex* sp.	5		
		Scissurellidae	*Anatoma* sp.	4		
		Acmaeidae	*Bathyacmaea* sp.	4		
			Protobranchia sp.	6		
			Unidentified gastropod	4, 5, 6		
Arthropoda	Pycnogonida	Ammotheidae	*Sericosura cochleifovea*	1	Child (1989)	
	Copepoda	Dirivultidae	*Stygiopontius pectinatus*	1	Humes (1987)	
		Dirivultidae	*Stygiopontius stabilitus*	1	Humes (1990)	
		Dirivultidae	*Chasmatopontius thescalus*	1		
	Amphipoda		Amphipoda gen. et sp.	2		Fujikura et al. (1997)
	Cirripedia	Neoverrucidae	*Neoverruca brachylepadoformis*	1, 2, 3, 4, 5	Newman and Hessler (1989)	
			Scalpellomorpha gen. et sp.	1		Hessler and Lonsdale (1991), photograph only
	Decapoda	Galatheidae	*Munidopsis marianica*	1, 2	Williams and Baba (1989)	
		Galatheidae	*Munidopsis* sp.	3, 5, 6		
		Bythogreidae	*Austinograea williamsi*	1, 2, 3, 4, 5, 6	Hessler and Martin (1989)	
		Alvinocarididae	*Chorocaris vandoverae*	1, 2, 3, 4, 5, 6	Martin and Hessler (1990)	
		Alvinocarididae	*Chorocaris* sp.	3, 5, 6		

[a]1, Alice Springs site; 2, Forecast site; 3, Snail site; 4, Archaean site; 5, Pika site; 6, Urashima site; 7, Yamanaka site

between two sites (3,600 vs. 1,470 m), they reported that the faunas are quite similar to each other (Fujikura et al. 1997).

During 2000s, vent fields in the southernmost region of the Mariana Trough were surveyed in the second stage of the Archaean project (2003–2004) and the NOAA VENTS program. As few macrobiologists joined these projects, little information on their vent faunas was available. Wheat et al. (2003) reported they sampled a provannid snail *Alviniconcha hessleri* and crabs from the Snail site. An abundant anemone colony was observed in the southern part of the Yamanaka site (Kakegawa et al. 2008).

As an activity of the TAIGA Project, we collected biological specimens at four vent sites in the southernmost region of the Mariana Trough, namely, the Snail, Archaean, Pika, and Urashima sites, during the cruise YK10-11 of the R/V *YOKOSUKA* and the submersible *SHINKAI 6500* of Japan Agency for Marine-Earth Science and Technology (JAMSTEC). Results obtained from the sampling are also shown in Chap. 26.

At the Snail site, the largest animal community was observed around the chimney with fringe structure. The center of the community was dominated by *A. hessleri* assemblage and accompanied with *Shinkailepas* limpets, *Austinograea* crabs, and *Chorocaris* shrimps. Further apart from the chimney, only a few shrimp and crab were observed. The outermost part of the vent field was occupied by the turrid snail *Phymorhynchus* sp., two kinds of sea anemones, and ophidiiformes. At the Archaean site, only

small and scattered animal communities were observed. On the steep terrain of the mound, galatheid crabs, brisingids, actinostolid-like anemones, and Abyssocladia sponges were observed. Around active chimneys, *Shinkailepas* limpets were abundant and attached to the vertical surface. *Alviniconcha hessleri* inhabits the narrow place coved with white bacterial mat. We observed a wide size range of galatheids and small bythograeids, actinostolid-like anemones in diffuse flow, and shrimp and crabs were abundant in the shimmering flow of the vent itself. Two large bivalves were found in a crevice at the base of the chimney but could not be collected. *Chorocaris* shrimps and *Austinograea* crabs were also common. On the steep slope of the Pika mound, a few white bythograeid crabs are distributed and many empty shells of *Alviniconcha* seemed to have fallen from above. With approaching to the summit, *Phymorhynchus* snails, galatheid and bythograeid crabs, and *Desbruyeresia* gastropods appeared although the fauna was very sparse there. We noticed a small population of *A. hessleri* on the side of a chimney. Shrimps were swimming around them. There were also scattered limpets. At the Urashima site, vent fauna was not so abundant, although shrimps, galatheid crabs, anemones and a few small gastropods were distributed in a place with strong diffuse flow. In total 19 species were observed and collected in these four hydrothermal vent sites. Although the most flourishing fauna was observed at the Snail site on-axis, the number of species was highest at off-axis Pika and Archaean sites. During this cruise, the sampling of larvae of vent animals was carried out around vent fields using plankton pump systems for the first time in the southernmost region of the Marana Trough and 13 and 15 morphotypes of polychaete and gastropod larvae were sampled, respectively (Beaulieu et al. 2011; Sasaki et al. unpublished data).

We also revisited the Yamanaka site where abundant white sea anemones were observed on pillow lavas. This site was thought to have passed its peak of hydrothermal activity (Yoshikawa et al. 2012).

Unfortunately, no detailed faunal information is available for the 13°N Ridge site with the exception of observation of animals around hydrothermal vents by the Deep Tow Camera system and the ROV *KAIKO* (Mitsuzawa et al. 2000; Masuda et al. 2001b).

25.2.2 Mollusca

The most dominant species of the communities in hydrothermal vent fields in the Mariana Trough is a large provannid gastropod *Alviniconcha hessleri* (Okutani and Ohta 1988). To date, this species is known only from the Mariana Trough, and *Alvinoconcha* gastropods inhabiting the Manus, North Fiji, and Lau Basins, and the Indian Ocean are thought to be other undescribed species (Kojima et al. 2001; Suzuki et al. 2006). Although no genetic differentiations between the Alice Springs and the Forecast Vent site were detected for this species (Kojima et al. 2001), our more detailed analysis showed a slight difference between populations of the Central and Southern Mariana Trough (Hidaka et al. Chap. 26). By using the DNA barcoding, two larvae of this species were identified in the specimens collected by plankton pump systems mentioned above (Sasaki et al. unpublished data). Based on shell morphology, they are judged to be planktotrophic as Warèn and Bouchet (1993) concluded based on young adult specimens of an undescribed *Alviniconcha* species from the Lau Basin. Sulfur-oxidizing endosymbiotic bacteria were discovered in specialized gill cells (bacteriocytes) of *A. hessleri* (Stein et al. 1988; Endow and Ohta 1989). They belong to the gammaproteobacteria, although some undescribed *Alvinoconcha* species endosymbiose with epsilonproteobacteria (Suzuki et al. 2005, 2006). Wittenberg and Stein (1995) reported that the gill of *A. hessleri* contents hemoglobin at a comparable concentration to endosymbiont-retaining solemyid, lucinid, and vesicomyid clams. Sulfur stable isotope ratios of *A. hessleri* showed sulfide in hydrothermal fluid is the major source of assimilated sulfur, which is supplied by endosymbiotic bacteria (Maki and Mizota 1997).

Two small provannid gastropod species were described by Okutani (1990). They are classified into the genus *Provanna* as *P. nassariaeformis* and *P. marianensis*, and the latter was transferred to the genus *Desbryuesia* in Warèn and Bouchet (1993).

Vrijenhoek et al. (1997) showed that a limpet of the genus *Lepetodrilus* from the Mariana Trough, which had been thought to be conspecific to that in the Eastern Pacific, is genetically distinct from East Pacific species. Johnson et al. (2008) analyzed phylogenetic relationships among *Lepetodrilus* limpets and showed those of the Mariana Trough form a species complex with *L. schrolli* from the Manus Basin and unidentified individuals from the North Fiji and Lau Basins. Limpets of the genus *Shinkailepas* also dominate vent fields in the Mariana Trough as well as the Izu-Ogasawara Arc. Although *Shinkailepas* limpets of the Mariana Trough resemble to *S. kaikatensis* of which the type locality is the Kaikata Seamount in the Izu-Ogasawara Arc and were referred as *Shinkailepas* cf. *kaikatensis* in Hessler and Lonsdale (1991) and Fujikura et al. (1997), DNA barcoding and detailed morphological examination clearly showed those of the Mariana Trough are not *S. kaikatensis* which was described based on specimens from the Izu-Ogasawara Arc (Kano et al., unpublished data).

Genetic analysis with mitochondrial DNA also showed little genetic deviation among morphologically-distinct

species, namely, *Bathymodiolus septemdierum* from the Izu-Ogasawara Arc, *Bathymodiolus* sp. from the Mariana Trough, *B. brevior* from the North Fiji and Lau Basins, and *B. marisindicus* from the Indian Ocean (Fujita et al. 2009). If they are a single species with extremely high ability of larval dispersion, the situation is very similar to that of a vestimentiferan *Paraescarpia echinospica*, which are distributed from the Nankai Trough in the northwestern Pacific to the Java Trench in the Indian Ocean but not in the Mariana Trough (Kojima et al. 2002).

25.2.3 Arthropoda

A bythograeid crab, *Austinograea williamsi*, which was described by Hessler and Martin (1989) is also a representative vent-endemic species in the Mariana Trough. Its heterochely, relative growth and gonad morphology were reported in Tsuchida and Fujikura (2000).

To date, all alvinocarid shrimps collected in the Mariana Trough have been classified into the genus *Chorocaris*. Besides a dominant alvinocarid shrimp *Chorocaris vandoverae*, we collected some specimens of an undescribed *Chorocaris* shrimp at the Snail, Pika, and Urashima sites. Based on sulfur stable isotope ratio analysis, Maki and Mizota (1997) reported that *C. vandoverae* is supplied sulfur from hydrogen sulfide in hydrothermal fluid.

A hydrothermal vent-endemic barnacle *Neoverruca brachylepadoformis* is closely related to an undescribed species inhabiting the Okinawa Trough, Izu-Ogasawara Arc, and the Mariana Arc. Their ancestors were estimated to have migrated from the Mariana Trough to the Izu-Ogasawara Arc and the Mariana Arc via the Okinawa Trough based on the molecular phylogenetic and phylogeoraphic analyses (Watanabe and Kojima 2009; Watanabe et al. 2005).

25.2.4 Annelida

Paralvinella hessleri is one of the dominant annelid species. This species is also thought to inhabit the Okinawa Trough and the Izu-Ogasawara Arc. A molecular phylogenetic analysis using the mitochondrial COI gene showed that populations of the Okinawa Trough and the Izu-Ogasawara Arc are almost deviated from each other (Pradillon et al., unpublished data). As no molecular data is available for the Mariana Trough population and we cannot deny the possibility that *Paralvinella* annelids of the Okinawa Trough and the Izu-Ogasawara Arc are another cryptic species of *P. hessleri*.

25.3 Vent/Seep Faunas of Neighboring Sea Areas

25.3.1 Mariana Arc, Izu-Ogasawara Arc, and Okinawa Trough

The Mariana Trough approaches to the Mariana Arc at both northern and southern ends (Fig. 25.1). Along the Mariana Arc, hydrothermal activities were discovered on 13 submarine volcanoes at the depths from 50 to 3,000 m, and chemosynthetic-based communities was reported from the Nikko, Daini (second) Kasuga, NW Eifuku, Daifuku, and NW Rota-1 Seamounts and TOTO Caldera (Fujikura et al. 1998; Masuda et al. 2001a; Embley et al. 2007). At the northern end, the Mariana Arc connects with the Izu-Ogasawara Arc. Although the Mariana Trough also adjoins the Mariana Arc at the northern end, the recent hydrothermalism has not yet been discovered in the northern region of the Mariana Trough. Indeed, the vent fauna of the Mariana Trough is rather similar to that of the Okinawa Trough (Fig. 25.2). As planktonic materials can be transported by the North Equatorial Current and the Kuroshio Current from the Mariana Trough to the Okinawa Trough, historical larval migration might have occurred along this route (Watanabe et al. 2005).

An *Alviniconcha* snail, which is a representative vent-endemic taxon of the Mariana Trough, has not been reported north of the Mariana Trough with the exception of a single specimen collected from the Suiyo Seamount, the Izu-Ogasawara Arc. It phylogenetically differs from *A. hessleri* and all other *Alviniconcha* lineages (Fujiwara et al. 2013) and is suspected to have immigrated to this vent field accidentally. Habitat(s) of this undescribed species may be situated in other vent fields in the Izu-Ogasawara and/or Mariana Arcs. Although small gastropods of the genera *Provanna, Desbruyeresia, Lepetodrilus* and *Shinkailepas* inhabit vent fields in both the Mariana Trough and neighboring sea areas, the existence of endemic species to the Mariana Trough was shown for each genus. Vesicomyid clams were collected in the TOTO Caldera and identified as *Calyptogena nautilei* (Kojima et al., unpublished data).

Alvinocaris shrimps have not yet been reported from the Mariana Trough while an undescribed species of this genus was discovered in two vent fields of the Mariana Arc, namely, NW Rota (Limén et al. 2006) and NW Eifuku, which will be described as a new species (Tsuchida, personal communication). Four *Alvinocaris* shrimps, namely, *A. longirostris, A. dissimilis, A. brevitelsonis*, and an undescribed species inhabit the Okimawa Trough (Komai and Segonzac 2005; Fujikura et al. 2012; Yahagi et al., unpublished data). This undescribed species was also

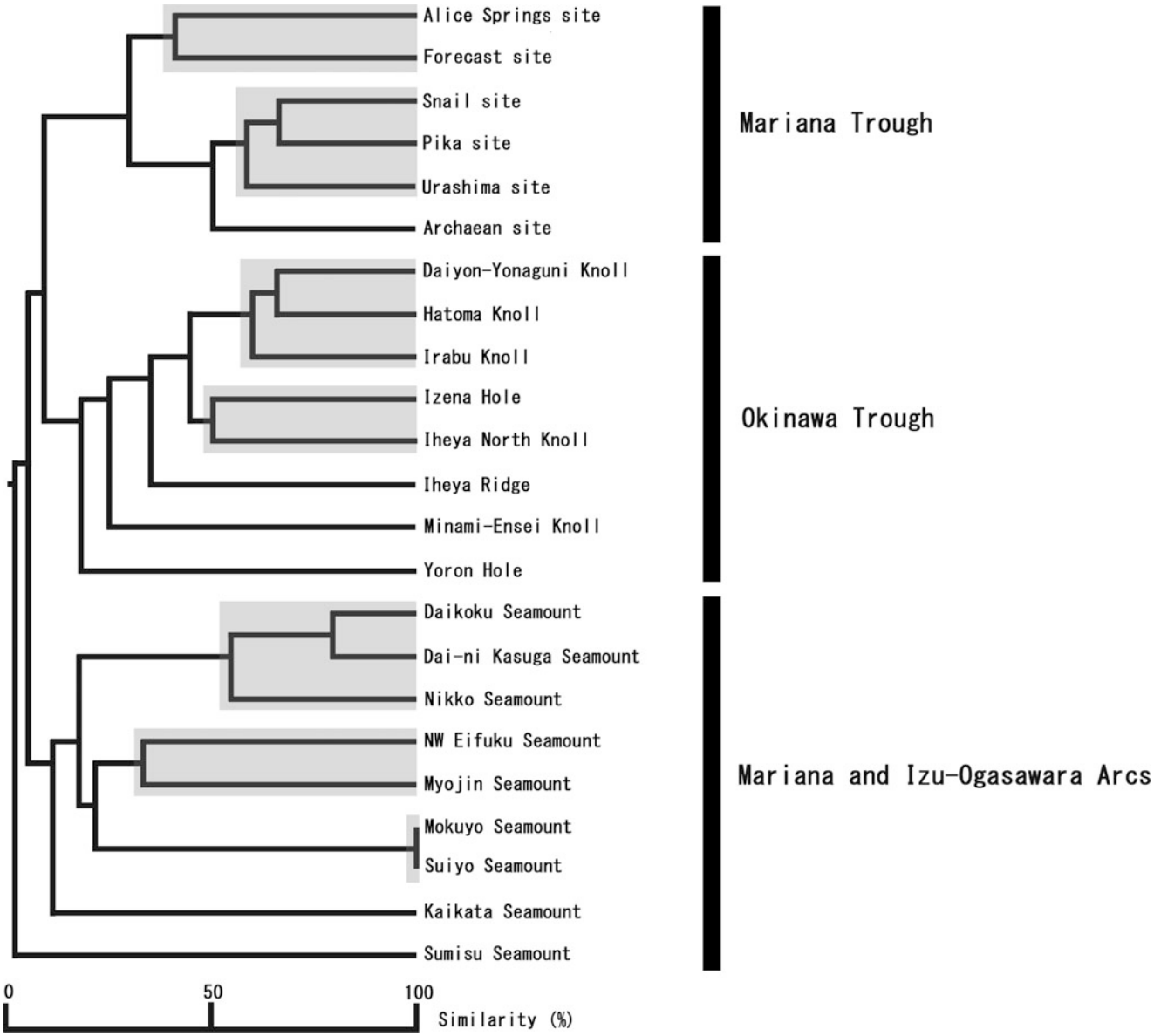

Fig. 25.2 A cladogram of hydrothermal vent faunas in the Mariana Trough, Mariana Arc, Izu-Ogasawara Arc, and Okinawa Trough, generated by the group average method using the Jaccard similarity coefficient based on genera. Data of Table 25.1 were used for the Mariana Trough, data of the Mariana Arc, Izu-Ogasawara Arc, and Okinawa Trough were updated from those in Watanabe et al. (2010), and only data of identified genera were used. Among faunas in gray areas, no significant difference ($p > 0.05$) was detected by the SIMPROF (similarity profile) test with 1,000 permutations

collected from the Suiyo Seamount in the Izu-Ogasawara Arc (Yahagi et al., unpublished data). *Austinograea williamsi* is an endemic species to the Mariana Trough and differs from bythograeid crabs from the Izu-Ogasawara and Mariana Arcs at the genus level. *Munidopsis marianica* is also endemic to the Mariana Trough while some congeneric species inhabit vent fields in the Mariana Arc, Izu-Ogasawara Arc, and/or Okinawa Trough. For *Neoverruca* barnacles, significant genetic differences were shown among specimens from the Mariana Trough, the Okinwa Trough, and the Izu-Ogawsawara Arc (Watanabe 2004). Individuals of the Izu-Ogasawara Arc were further shown to form a monophyletic group with those from the Mariana Arc (Watanabe et al., unpublished data).

Vestimentiferan tube worms, which form one of representative groups of hydrothermal vent fields in the Okinawa Trough and the Manus Basin, has not yet been reported from the Mariana Trough. They are also rare in the Mariana Arc where two species are found; *Lamellibrachia satsuma* from the Nikko and Daikoku Seamounts (Black et al. 1997; Kojima et al. 2012) and *L. juni* from the TOTO Caldera (Kojima et al. 2006). The former is known from the seep

area around the Japanese Islands at shallower depths than 330 m. The absence of this species in the Mariana Trough might be attributable to the absence of such a shallow vent site. The latter is also known from the DESMOS site in the Manus Basin and the Brothers Caldera in the Kermadec Arc (Kojima et al. 2006). All of three habits of this species are characterized by extreme acidic hydrothermal fluids (around pH 2). If this species has been specialized to such a harsh environment, it may explain its absence in the Mariana Trough.

While symphurine tonguefish are distributed in the Mariana Arc, the Izu-Ogasawara Arc, and the Okinawa Trough, they have not been reported from the Mariana Trough. Tunnicliffe et al. (2010) reported that a symphurine tonguefish *Symphurus thermophilus* inhabiting vent fields at the Daikoku, Nikko, and Daini (second) Kasuga Seamounts is genetically distinct from those of the Kermadic arc in spite of no morphological difference between them and suggested the possibility that the latter is a cryptic species. The type locality of *S. thermophilus* is the Kaikata Samount of the Izu-Ogasawara Arc (Munroe and Hashimoto 2008) and individuals in the Mariana Arc might be classified into another cryptic species. Unfortunately, no molecular information is available for symphurines of the Izu-Ogasawara Arc and the Okinawa Trough.

25.3.2 Mariana Forearc and Mariana Trench

Many serpentinite mud volcanoes are known in the Mariana forearc between the Mariana volcanic island arc and the Mariana Trench. In 1997, a methane seep area with a highly alkaline fluid was discovered on one of those mud volcanoes, the South Chamorro Seamount (Fryer and Mottl 1997). *Bathymodiolus* mussels inhabiting this field were shown to be genetically distinct from those of the Mariana Trough (Fujita et al. 2009). Vesicomyid clams collected in this area were identified as *Calyptogena nautilei* (Kojima et al., unpublished data). Although Fryer and Mottl (1997) also reported "tube worms" from this site, their detailed information is not available.

A distinct chemosynthesis-based community was recently discovered in a methane seep area (Shinkai Seep Field) on the landward slope of the Mariana Trench (Ohara et al. 2012). From there, a new species of vesicomyid clams *Calyptogena mariana* was described (Okutani et al. 2013). This species was classified into the subgenus *Abyssogena* and shown to be more related to species of the abyssal depths such as *C. kaikoi* from seep areas in the Nankai Trough off the Japanese mainland than inhabitants of the Mariana Arc. To date, no species of the Mariana Trough have been reported from methane seep areas around Japan.

25.3.3 Backarc Basins in the South Pacific

Hydrothermal vent fields in backarc basins in the South Pacific, namely, the Manus Basin, the North Fiji Basin, and the Lau Basin, share *Alviniconcha* snails as a dominant species with the Mariana Trough. Those of the South Pacific were estimated to have speciated into two different undescribed species. *Ifremeria nautilei* is also a large snail with endosymbiotic chemoautotrophic bacteria. Although this species forms a monophyletic group with *Alviniconcha* snails, it is not distributed in the Mariana Trough. Chemosynthesis-based communities of the Mariana Basin lack vestimentiferan annelids and *Calyptogena* clams, while the former is distributed in the Manus Basin and the Lau Basin (Desbruyères et al. 2006) and the later is distributed at a single site (the DESMOS caldera) in the Manus Basin (Hashimoto et al. 1999). Bythograeid crabs of the genus *Austinograea* are known from the Mariana Trough (*A. williamsi*), the South Pacific (*A. alayseae*), and the Indian Ocean (*A. rodriguezensis*).

25.4 Conclusion

Diversity of hydrothermal environments and vent faunas in the western Pacific is probably due to their various backgrounds and two-dimensional distribution, which results in complicated connectivity between vent sites, in addition to proximity of vent areas with different geological settings as well as cold seep areas. In contrast, hydrothermal vent fields in the eastern Pacific, Atlantic and Indian Oceans are distributed along the mid-oceanic ridges and essentially aligned. Thus, the western Pacific is expected to offer interesting subjects for researches of dispersal, genetic deviation, and speciation processes of animals endemic to chemosynthesis-based communities. Comparative studies between the western Pacific and other sea areas are important for understanding evolution and ecology of vent fauna.

The Mariana Trough is situated in the central position in hydrothermal areas in the northwestern Pacific, surrounded by the Okinawa Trough, the Izu-Ogasawara Arc, the Mariana Arc, and the Manus Basin. Chemosynthesis-based communities in the Mariana Trough are characterized by the absence of vestimentiferans and *Calyptogena* clams, which are dominant in both vent and seep sites around the Ryuykyu and Japan Islands, the dominance of *Alviniconcha* snails and *Austinograea* crabs, which is shared with the South Pacific and the Indian Ocean. Phylogeographic analyses showed *Neoverruca* barnacles have historically migrated from the Mariana Trough to the Izu-Ogasawara Arc and the Mariana Arc via the Okinawa Trough (Watanabe and Kojima 2009; Watanabe et al. 2005). They were further estimated to have deviated from a common ancestor species which inhabited

the Manus Basin (Watanabe 2004), which suggest the primary historical migration in the western Pacific occurred in the northward direction. Similar suggestions have been noted for *Alviniconcha* snails (Kojima et al. 1999) and *Alaysia*-like vestimentiferans (Kojima et al. 2003).

A very interesting issue is a biogeographic break of the vent fauna between the Mariana Trough and the Izu-Ogasawara and Mariana Arcs. It may be attributable to directions of surface currents, namely, the North Equatorial Current and the Kuroshio Current, and/or the absence of active vent sites in the northernmost region of the Mariana Trough where the trough is adjacent to the arcs. In the southernmost region, extreme acidic hydrothermal fluids of the TOTO Caldera might prevent the vent fauna of the Mariana Trough from colonizing to the arc area.

The Mariana Trough is a key place connecting various vent and seep sites in the western Pacific. Exhaustive survey in this area with joint research using phylogeographic and larval ecological methodologies will provide fruitful results for understanding organization mechanisms of vent communities.

Acknowledgements The authors are grateful to the operation teams of the submersible *SHINKAI 6500*, the crew of the support ship *Yokosuka*, and onboard scientists of the YK10-11 cruise of *Yokosuka* for help in sampling. We also thank Drs. Takashi Okutani, Jun Hashimoto, Shinji Tsuchida, Yasunori Kano, and Takuya Yahagi for taxonomic information. Thanks are also extended to two reviewers for comments that improved manuscript. This study was conducted as an activity of the scientific research on innovative areas "TAIGA (Trans-crustal Advection & In situ bio-geochemical processes of Global sub-seafloor Aquifer)" which is sponsored by Ministry of Education, Culture, Sports, Science and Technology (MEXT), Japan (No. 20109004). We also referred to results by KAKENHI (No. 23370040).

References

Beaulieu SE, Mills S, Mullineaux L, Pradillon F, Watanabe H, Kojima S (2011) International study of larval dispersal and population connectivity at hydrothermal vents in the southern Marianas Trough. InterRidge News 20:50–54

Black MB, Halanych KM, Mass PAY, Hoeh WR, Hashimoto J, Desbruyères D, Lutz RA, Vrijenhoek RC (1997) Molecular systematics of vestimentiferan tubeworms from hydrothermal vents and cold-water seeps. Mar Biol 130:141–149

Blake JA (1991) A new species of Hesiocaeca (Polychaeta: Hesionidae) from hydrothermal vents at the Mariana Back-Arc Basin with notes on other polychaetes. Proc Biol Soc Wash 104:175–180

Child CA (1989) Pycnogonida of the western Pacific islands VI. *Sericocura cochleifovea*, a new hydrothermal vent species from the Mariana Back-Arc basin. Proc Biol Soc Wash 102:732–737

Craig H, Horibe Y, Farley KA, Welhan JA, Kim K, Hey RN (1987) Hydrothermal vents in the Mariana Trough: results of the first Alvin dives. Eos Trans AGU 68:1531

Desbruyères D, Laubier L (1989) *Paralvinella hessleri*, new species of Alvinellidae (Polychaeta) from the Mariana Bach-Arc Basin hydrothermal vents. Proc Biol Soc Wash 102:761–767

Desbruyères D, Hashimoto J, Fabri M-C (2006) Composition and biogeography of hydrothermal vent communities in western Pacific back-arc basins. In: Christie DM, Fisher CR, Lee S-M, Givens S (eds) Back-arc spreading systems: geological, biological, chemical, and physical interactions. The American Geophysical Union, Washington, DC, pp 215–234

Embley RW, Baker ET, Butterfield DA, Chadwick WW Jr, Lupton JE, Resing JA, De Ronde CDJ, Nakamura K, Tunnicliffe V, Dower JF, Merle SG (2007) Exploring the submarine ring of fire: Mriana Arc – Western Pacific. Oceanography 4:68–79

Endow K, Ohta S (1989) The symbiotic relationship between bacteria and a mesogastropod snail, *Alviniconcha hessleri*, collected from hydrothermal vents of the Mariana Back-Arc Basin. Bull Jap Soc Microbial Ecol 3:73–82

Fautin DG, Hessler RR (1989) *Marianactis bythios*, a new genus and species of actinostolid sea anemone (Coelenterata: Actiniaria) from the Mariana vents. Proc Biol Soc Wash 102:761–767

Fryer P, Mottl MJ (1997) "Shinkai 6500" investigations of a resurgent mud volcano on the southern Mariana forearc. JAMSTEC J Deep Sea Res 13:103–114

Fujikura K, Yamazaki T, Hasegawa K, Tsunogai U, Stein RJ, Ueno H, Yamamoto H, Maki Y, Tsuchida S, Kodera T, Yamamoto H, Sun C, Okutani T (1997) Biology and earth scientific investigation by the submersible "Shinkai 2000" system of deep-sea hydrothermalism and lithosphere in the Mariana Back-Arc Basin. JAMSTEC J Deep Sea Res 13:1–20 (in Japanese with English abstract)

Fujikura K, Tsuchida S, Ueno H, Ishibashi J, Gaze W, Maki Y (1998) Investigation of the deep-sea chemosynthetic ecosystem and submarine volcano at the Kaguga 2 and 3 Seamounts in the Northern Mariana Trough, Western Pacific. JAMSTEC J Deep Sea Res 14:127–138

Fujikura K, Okutani T, Maruyama T (eds) (2012) Deep-sea life; biological observations using research submersibles, 2nd edn. Tokai University Press, Kanagaawa (in Japanese with English figure captions)

Fujita Y, Matsumoto H, Fujiwara Y, Hashimoto J, Galkin SV, Ueshima R, Miyazaki J (2009) Phylogenetic relationships of deep-sea *Bathymodiolus* mussels to their mytilid relatives from sunken whale carcasses and wood. Venus 67:123–134

Fujiwara Y, Okutani T, Kimura H (2013) First occurrence of *Alviniconcha* from Japanese waters (Gastropoda: Provannidae). Venus 71:217–219

Hasegawa K, Fujikura K, Okutani T (1997) Gastropod fauna associated with hydrothermal vents in the Mariana Back-Arc Basin: summary of the results of 1996 "Shinkai 6500" dives. JAMSTEC J Deep Sea Res 13:69–83

Hashimoto J, Ohta S, Fiala-Médione A, Auzende J-M, Kojima S, Segonzac M, Fujiwara Y, Hunt JC, Gena K, Miura T, Kikuchi T, Yamaguchi T, Toda T, Chiba H, Tsuchida S, Ishibashi J, Henry K, Zbinden M, Pruski A, Inoue A, Kobayashi H, Birrien J-L, Naka J, Yamanaka T, Laporte C, Nishimura K, Yeats C, Malagun S, Kia P, Oyaizu M, Katayama T (1999) Hydrothermal vent communities in the Manus Basin, Papua New Guinea: results of the BIOACCESS cruises'96 and'98. InterRidge News 8(2):12–18

Hessler RR, Lonsdale PF (1991) Biogeography of Mariana Trough hydrothermal vent communities. Deep-Sea Res 38:185–199

Hessler RR, Martin WM (1989) *Austinograea williamsi*, new genus, new species, a hydrothermal vent crab (Decapoda: Bythograeidae) from the Mariana Back-Arc Basin, western Pacific. J Crust Biol 9:645–661

Humes AG (1987) Copepoda from deep-sea hydrothermal vents. Bull Mar Sci 41:645–788

Humes AG (1990) Copepoda (Siphonostomatoida) from a deep-sea hydrothermal vent at the Mariana Back-Arc Basin in the Pacific, including a new genus and species. J Nat Hist 24:289–304

Ishibashi J, Yamanaka T, Kimura H, Hirota A, Toki T, Tsunogai U, Gamo T, Utsumi M, Roe K, Miyabe S, Okamura K (2004) Geochemistry of hydrothermal fluids in South Mariana backarc spreading center. EOS Trans AGU 85, Fall Meet Suppl, F1908

Johnson L, Fryer H, Matsuda H, Ishii T, Gamo T (1993) Hydrothermal deposits and two magma sources for volcanoes near 13°20′N in the Mariana backarc: a view from Shinkai 6500. EOS Trans AGU 74, Fall Meet Suppl, p 381

Johnson SB, Warén A, Vrijenhoek RC (2008) DNA barcoding of *Lepetdrilus* limpets reveals cryptic species. J Shellfish Res 27:43–51

Kakegawa T, Utsumi M, Marumo K (2008) Geochemistry of sulfide chimneys and basement pillow lavas at the southern Mariana Trough (12.55ºN-12.58ºN). Res Geol 58:249–266

Kojima S, Ohta S, Fujiwara Y, Fujikura K, Hashimoto J (1999) Speciation of gastropods of the genus *Alviniconcha* in the South Pacific. JAMSTEC J Deep Sea Res 14:501–505 (in Japanese with English abstract)

Kojima S, Segawa R, Fujiwara Y, Fujikura K, Ohta S, Hashimoto J (2001) Phylogeny of hydrothermal vent-endemic gastropods *Alviniconcha* spp. from the Western Pacific revealed by mitochondrial DNA sequences. Biol Bull 200:298–304

Kojima S, Ohta S, Yamamoto T, Miura T, Fujiwara Y, Fujikura K, Hashimoto J (2002) Molecular taxonomy of vestimentiferans of the Western Pacific and their phylogenetic relationship to species of the Eastern Pacific. II. Families Escarpiidae and Arcovestiidae. Mar Biol 141:57–64

Kojima S, Ohta S, Yamamoto T, Yamaguchi T, Miura T, Fujiwara Y, Fujikura K, Hashimoto J (2003) Molecular taxonomy of vestimentiferans of the Western Pacific and their phylogenetic relationship to species of the Eastern Pacific. III. Families *Alaysia*-like vestimentiferans and relationships among families. Mar Biol 142:625–635

Kojima S, Watanabe H, Tsuchida S, Fujikura K, Rowden AA, Takai K, Miura T (2006) Phylogenetic relationships of a tube worm (*Lamellibrachia juni*) from three hydrothermal vent fields in the South Pacific. J Mar Biol Assoc UK 86:1357–1361

Kojima S, Murakami S, Nemoto S, Watanabe H, Miyake H, Tsuchida S (2012) Genetic diversity and population structure of a vestimentiferan annelid *Lamellibrachia satsuma* in Japanese and northern Mariana waters. Plankton Benthos Res 7:146–150

Komai T, Segonzac M (2005) A revision of the genus *Alvinocaris* Williams and Chase (Crustacea: Decapoda: Caridea: Alvinocarididae), with descriptions of a new genus and a new species of *Alvinocaris*. J Nat History 39:1111–1175

Limén H, Juniper SK, Tunnicliffe V, Clément M (2006) Benthic communities on two peaks of an erupting seamount: Northwest Rota-1 Volcano, Mariana Arc, western Pacific. Cah Biol Mar 47:457–463

Maki Y, Mizota C (1997) Sulfur isotopic comparison of *Alviniconcha hessleri* and *Chorocaris vandoverae* from Mariana Back-Arc Basin. JAMSTEC J Deep Sea Res 13:63–67 (in Japanese with English abstract)

Martin JW, Hessler RR (1990) Chorocaris vandoverae, a new genus and species of hydrothermal vent shrimp (Crustacea, Decapoda, Bresiliidae) from the western Pacific. Contr Sci Nat His Mus Los Angeles Country 417:1–11

Masuda H, Mitsuzawa K, Seama N, Masumoto S, YK-99-11 Shipboard Scientific Party (2001a) Bathymetry and hydrothermal activities in the southern Mariana Trough – reconnaissance results of YK-99–11. JAMSTEC J Deep Sea Res 18:83–88 (In Japanese with English abstract)

Masuda H, Nakagawa S, The Shipboard Scientific Party of KK-00-03 (2001b) Newly found low temperature hydrothermal activities at the southern Mariana back arc basin – summary of Dive #164 during KK-00-03. JAMSTEC J Deep Sea Res 18:89–93 (In Japanese with English abstract)

McLean JH (1990) A new genus and species of neomphalid limpet from the Mariana vents, with a review of current understanding of relationships among Neomphalacea and Peltospiracea. The Nautilus 104:77–86

Mitsuzawa K, Matsuda H, Seama N, Hasegawa Y, Miyamoto M, Togashi N, So A, Yamanobe H (2000) Preliminary report of Deep-Tow/Yokosuka Cruise at hydrothermal areas in the Mid and Southern Mariana. JAMSTEC J Deep Sea Res 17:73–87 (in Japanese with English abstract)

Munroe TA, Hashimoto J (2008) A new Western Pacific Tonguefish (Pleuronectiformes: Cynoglossidae): the first Pleuronectiform discovered at active hydrothermal vents. Zootaxa 1839:43–59

Nakamura K, Toki T, Mochizuki N, Asada M, Ishibashi J, Nogi Y, Yoshikawa S, Miyazaki J, Okino K (2012) Discovery of a new hydrothermal vent based on an underwater, high-resolution geophysical survey. Deep Sea Res I 74:1–10

Newman WA, Hessler RR (1989) A new abyssal hydrothermal verrucomorphan (Cirripedia; Sessilia): the most primitive living sessile barnacle. Trans San Diego Soc Nat Hist 21:259–73

Ohara Y, Reagan M, Fujikura K, Watanabe H, Michibayashi K, Ishii T, Stern R, Pujana I, Martinez F, Girard G, Ribeiro J, Brounce M, Komori N, Kino M (2012) A serpentinite-hosted ecosystem in the southern Mariana Forearc. Proc Natl Acad Sci USA 109:2831–2835

Okutani T (1990) Two new species of *Provanna* (Gastropoda: Cerithiacea) from "snail pit" in the hydrothermal vent site at the Mariana Back-Arc Basin. Venus (Jpn J Malac) 59:83–101

Okutani T, Ohta S (1988) A new gastropod mullusk associated with hydrothermal vents in the Mariana Back-Arc Basin, Western Pacific. Venus (Jpn J Malac) 47:211–218

Okutani T, Fujikura K, Watanabe H, Ohara Y (2013) *Calyptogena* (*Abyssogena*) *mariana*: Discovery of a new vesicomyid clam from the Mariana Trench. Venus 71:39–47

Pettibone MH (1989) New species of scale-worms (Polychaeta: Polynoidae) from the hydrothermal rift-area of the Mariana Back-Arc Basin in the western central Pacific. Proc Biol Soc Wash 102:137–153

Stein JL, Cary SC, Hessler RR, Ohta S, Vetter RD, Childress JJ, Felbeck H (1988) Chemoautotrophic symbiosis in a hydrothermal vent gastropod. Biol Bull 174:373–378

Stern RJ, Fouch MJ, Klemperer SL (2003) An overview of the Izu-Bonin-Mariana subduction factory. In: Eiler J, Hirschmann M (eds) Inside the subduction factory. American Geological Union, Washington, DC, pp 175–222

Stern RJ, Tamura Y, Masda H, Fryer P, Martinez F, Ishizuka O, Bloomer SH (2013) How the Mariana volcanic arc ends in the south. Island Arc 22:133–148

Stüben D, Taibi NE, McMurtry GM, Scholten J, Stoffers P, Zhang D (1994) Growth history of a hydrothermal silica chimney from the Mariana backarc spreading center (southwest Pacific, 18°21′N). Chem Geol 113:273–296

Suzuki Y, Sasaki T, Suzuki M, Nealson KH, Horikoshi K (2005) Molecular phylogenetic and isotopic evidence of two lineages of chemoautotrophic endosymbionts distinct at the subdivision level harbored in the one host-animal type: the genus *Alviniconcha* (Gastropoda: Provannidae). FEMS Microbiol Lett 249:105–112

Suzuki Y, Kojima S, Sasaki T, Suzuki M, Utsumi T, Watanabe H, Urakawa H, Tsuchida S, Nunoura T, Hirayama H, Takai K, Nealson KH, Horikoshi K (2006) Host-symbiont relationships in hydrothermal vent gastropods of the genus *Alviniconcha* from the South West Pacific. Appl Environ Microbiol 72:1388–1393

Takamasa A, Nakai S, Sato F, Toyoda S, Banerjee D, Ishibashi J (2013) U-Th radioactive disequilibrium and ESR dating of a barite-containing sulfide crust from South Mariana Trough. Quat Geochronol 15:38–46

Tsuchida S, Fujikura K (2000) Heterochely, relative growth, and gonopod morphology in the bythograeid crab, *Austinograea williamsi* (Decapoda, Brachyura). J Crust Res 20:407–414

Tunnicliffe V, Koop BF, Tylerand J, So S (2010) Flatfish at seamount hydrothermal vents show strong genetic divergence between volcanic arcs. Mar Ecol 31(Suppl 1):158–167

Urabe T, Ishibashi J, Maruyama A, Marumo K, Seama N, Utsumi M (2004) Discovery and drilling of on- and off-axis hydrothermal sites in backarc spreading center of southern Mariana Trough, western Pacific. EOS Trans AGU 85, Fall Meet Suppl, F1907

Vrijenhoek RC, Feldman RA, Lutz RA, Craddock C, Hashimoto J (1997) Genetic characterization of *Lepetodrilus* limpets from hydrothermal vents in the Mariana Trough. JAMSTEC J Deep Sea Res (special volume "Deep sea research in subduction zones, spreading centers and backarc basins) pp 111–116

Warèn A, Bouchet P (1993) New records, species, genera, and a new family of gastropods from hydrothermal vents and hydrocarbon seeps. Zool Scr 22:1–90

Watanabe H (2004) Larval ecology and genetic differentiation of hydrothermal vent-endemic barnacles of the family neoverrucidae. PhD. thesis, Dep. of Biol. Sci., Univ. of Tokyo, Tokyo, Japan

Watanabe H, Kojima S (2009) Dispersal and speciation of faunal groups endemic to hydrothermal vent fields. In: Nishida M (ed) Evolution in the sea: molecular phylogenetic approaches to the marine diversity. Tokai University Press, Kanagawa, pp 244–260 (in Japanese)

Watanabe H, Tsuchida S, Fujikura K, Yamamoto H, Inagaki F, Kyo M, Kojima S (2005) Population history associated with hydrothermal vent activity inferred from the genetic structure of neoverrucid barnacles around Japan. Mar Ecol Prog Ser 288:233–240

Watanabe H, Fujikura K, Kojima S, Miyazaki J, Fujiwara Y (2010) Vents and seeps in close proximity. In: Kiel S (ed) The vent and seep biota, Topics in geobiology, vol 33. Springer, Dordrecht, pp 379–401

Wheat CG, Fryer P, Hulme SM, Becker NC, Curtis A, Moyer C (2003) Hydrothermal venting in the southern most portion of the Mariana backarc spreading center at 12.57 degrees N. EOS Trans AGU 84, Fall Meet Suppl, F1399

Williams AB, Baba K (1989) New squat lobsters (Galatheidae) from the Pacific Ocean: Mariana Back Arc Basin, East Pacific Rise, and Cascadia Basin. Fish Bull 87:899–910

Wittenberg JB, Stein JL (1995) Hemoglobin in the symbiont harboring gill of the marine gastropod *Alviniconcha hessleri*. Biol Bull 188:5–7

Yoshikawa S, Okino K, Asada M (2012) Geomorphological variations at hydrothermal sites in the southern Mariana Trough: relationship between hydrothermal activity and topographic characteristics. Mar Geol 303–306:172–182

Zottoli R (1983) *Amphisamytha galapogensis*, a new species of ampharetid polychaete from the vicinity of abyssal hydrothermal vents in the Galápagos Rift, and the role of this species in rift ecosystems. Proc Biol Soc Wash 96:379–391

Population History of a Hydrothermal Vent-Endemic Gastropod *Alviniconcha hessleri* in the Mariana Trough

26

Hiroka Hidaka, Tomomi Ogura, Hiromi Watanabe, Yasunori Kano, and Shigeaki Kojima

Abstract

Molecular evolutionary rate of the COI (cytochrome *c* oxidase subunit I) gene in the vent endemic genus *Alviniconcha* (Gastropoda: Provannidae) was estimated to be 0.69 % per million year based on GTR (General time-reversible) + G (Gamma) + I (Proportion Invariant) distances and hypothesized divergence dates of 59–64 Ma (million years ago) between *Alviniconcha* and its sister genus *Ifremeria*. The population history of *A. hessleri*, an endemic species to the Mariana Trough, the northwestern Pacific, was reconstructed by analyzing the nucleotide sequences of two fragments of mitochondrial DNA and an intron region of a nuclear gene for ATPS β (ATP Synthetase subunit β) and by extrapolating the estimated COI rate. Two genetically deviated *A. hessleri* groups with different patterns of geographical distribution were recognized in the analysis of the mitochondrial DNA and their age of divergence was estimated to be 0.91 Ma by the coalescent theory-based analysis of the nuclear gene data. The present geographical distributions of the two groups suggest that their ancestral populations were isolated in the central and southern Mariana Trough, respectively. Rapid expansion (increase of the population size) was suggested to have occurred in both groups at 0.26 and 0.17 Ma, respectively. Periodical changes of hydrothermal activity have apparently controlled the isolation and expansion of the local populations.

Keywords

Alviniconcha hessleri • ATP Synthetase subunit β • Hydrothermal vent • Intron • Mitochondrial DNA • Phylogeography

H. Hidaka • S. Kojima (✉)
Graduate School of Frontier Sciences, The University of Tokyo, Chiba 277-8563, Japan

Atmosphere and Ocean Research Institute, The University of Tokyo, Chiba 277-8564, Japan
e-mail: kojima@aori.u-tokyo.ac.jp

T. Ogura
Japan Agency for Marine-Earth Science and Technology, Kanagawa 237-0061, Japan

Graduate School of Marine Science and Technology, Tokyo University of Marine Science and Technology, Tokyo 108-8477, Japan

H. Watanabe
Japan Agency for Marine-Earth Science and Technology, Kanagawa 237-0061, Japan

Y. Kano
Atmosphere and Ocean Research Institute, The University of Tokyo, Chiba 277-8564, Japan

J.-i. Ishibashi et al. (eds.), *Subseafloor Biosphere Linked to Hydrothermal Systems: TAIGA Concept*,
DOI 10.1007/978-4-431-54865-2_26,

26.1 Introduction

Since the discovery of the first deep-sea hydrothermal field in the late 1970s, many hydrothermal-vent endemic species have been reported from various vent fields over the world (Rogers et al. 2012). Hydrothermal vent fields are generally unstable environments; the activities sometimes rapidly abate, cease or increase to cause the catastrophic explosion and the longevity of a single vent is estimated to be no more than 10,000 years (Vrijenhoek 2010). Thus, species endemic to such environments are expected to have abilities to disperse and colonize other vent sites. Comparison of the population history of vent-endemic faunal groups would provide valuable information to understand mechanisms underlaying the evolution of such animals. Recent development of phylogeographic analyses including the coalescent theory-based methodologies has enabled us to investigate population history in more detail (Kuhner 2008; Ho and Shapiro 2011). On the other hand, new geochemical analyses of hydrothermal sulfides and sulfate minerals, which reflect magmatic activities of their places of production, are also being developed to reconstruct the historical changes of hydrothermal activities more precisely (Ishibashi et al. 2009, Chap. 23). Results obtained from biological and geochemical evidences need to be integrated for more accurate understanding of history of hydrothermal ecosystems and for the improvement of each method (Kumagai et al. Chap. 5).

In this chapter, the population history of a hydrothermal vent-endemic snail *Alviniconcha hessleri* is reconstructed. *Alviniconcha* snails have highly specialized morphological and ecological characteristics to adapt the vent environments with chemoautosynthtic endosymbiotic gamma- or epsilon-proteobacteria (Suzuki et al. 2006). *Alviniconcha hessleri* dominates as an endemic species in hydrothermal areas in the Mariana Trough, the northwestern Pacific. This species was described based on specimens collected at the Alice Springs site (3,600 m depth) in the central Mariana Trough (Okutani and Ohta 1988). The second habitat of this species was discovered at the Forecast Vent site (1,470 m depth) in the southern Mariana Trough (Johnson et al. 1993). During the first decade of the twenty-first century, various hydrothermal vent fields have been discovered in the southernmost part of the Mariana Trough. Among them, *A. hessleri* has been reported from three sites, namely, the Snail (=Fryer), Archaean, and Pika sites. The Snail site (2,850 m depth) is situated on the South Mariana Backarc Spreading Center while the Archaean (2,990 m depth) and Pika (2,770 m depth) sites were discovered on off-axis seamounts (Wheat et al. 2003; Urabe et al. 2004; Kakegawa et al. 2008; Yoshikawa et al. 2012). These vent sites are distributed almost on a straight line from the ridge axis to the off-ridge. Although the present hydrothermal activity of the Mariana Trough is estimated to have started about 7 Ma (Stern et al. 2003), detailed historical changes in the activity have been traced back only to 12,000 years ago by the geochemical approach (Stüben et al. 1994; Takamasa et al. 2013; Ishibashi et al., Chap. 23).

Johnson et al. (2010) estimated phylogenetic relationships and deviation dates among provannid gastropods including *Alviniconcha* snails, with the Bayesian evolutionary analysis on the basis of nucleotide sequences from the mitochondrial COI (cytochrome *c* oxidase subunit I), 12S and 16S ribosomal RNA (rRNA) genes and nuclear Histone H3 and 18S and 28S rRNA genes. They calibrated molecular clocks based on a hypothetical age of vicariance between the Pacific and Atlantic deep-sea faunas at 15–16 Ma in prior to the closure of the Isthmus of Panama, or fossil records that suggest the divergence between *Provanna* and *Desbruyeresia* at 93–100 Ma and two outgroup *Neptunea* species at 33–37 Ma. Using this clock, the population history of *A. hessleri* can be estimated. However, the intraspecific molecular evolutionary rate is expected to be higher than intergeneric rates, as the estimate of rate decrease with enlargement of time-scale investigated due to the saturation of genetic mutations, which results in the overestimation of ages. The present study attempted to decrease this problem by calculating rates based on genetic distances between congeneric species.

This chapter report population history of *A. hessleri* in the Mariana Trough from 1 to 0.2 Ma revealed by phylogeographic analyses using adequate molecular evolutionary rate mentioned above and discuss changes of the hydrothermal activity during this period, which might have greatly contributed to the population dynamics of vent-endemic species.

26.2 Materials and Methods

26.2.1 Evolutionary Rate of COI Gene in *Alviniconcha*

The molecular evolutionary rate of the COI gene in *Alviniconcha* was estimated by analyzing sequences from additional species of the genus and other provannids under the GTR (General time-reversible) + G (Gamma) + I (Proportion Invariant) distances model and by extrapolating suggested divergence dates between *Alviniconcha* and *Ifremeria* in Johnson et al. (2010). Seven COI sequences published in Suzuki et al. (2006) were incorporated with 18 representative sequences from Johnson et al. (2010) and 25 operational taxonomic units (OTUs) with the length of 530 base pair (bp) were used in the succeeding Bayesian phylogenetic analysis. The genus *Alviniconcha* was represented by all the five known species (Hidaka et al.

Table 26.1 List of samples used for population genetic analyses

No.	Site	Coordinates	Depth (m)	Dive#	Date	*N*[a]
1	Alice Springs	18°13′ N, 144°43′E	3,600	6 K153	9 November 1992	20[b] (18)
2	Forecast	13°24′ N, 143°55′E	1,470	6 K186	22 October 1993	20[b] (13)
3	Snail	12°57′ N, 143°37′E	2,850	6 K1228	22 September 2010	20 (18)
4	Archaean	12°56′ N, 143°38′E	2,990	6 K1224	9 September 2010	20 (14)
5	Pika	12°55′N, 143°39′E	2,770	6 K1225	10 September 2010	20 (18)

[a]Numbers of specimens used for sequencing the ATP Synthetase subunit β gene are shown in parentheses
[b]Nucleotide sequences of mitochondrial DNA were reported in Hidaka et al. (2013)

2013) to better correct the genetic distances between these ingroup OTUs, while only three conspecific individuals were included for the monotypic *Ifremeria*.

Bayesian tree reconstruction was performed with MrBayes 3.1.2 (Ronquist and Huelsenbeck 2003). The shape, proportion of invariant sites, state frequency and substitution rate parameters were estimated for each codon position separately. Two parallel runs were made for 10,000,000 generations (with a sample frequency of 1,000), using the default value of four Markov chains. The first 5,000 trees for each run were discarded to ensure the four chains reached stationarity by referring to the average standard deviation of split frequencies (Ronquist and Huelsenbeck 2003). The consensus tree and posterior probabilities (PP) were computed from the remaining 10,000 trees (5,000 trees, 2 runs).

26.2.2 Population History of *Alviniconcha hessleri*

The specimens of *A. hessleri* used for population genetic analyses in this study were collected by the submersible *SHINKAI 6500* of the Japan Agency for Marine-Earth Science and Technology (JAMSTEC; Table 26.1). Sampling at the Snail, Archaean, and Pika sites in the southernmost area of the Mariana Trough was conducted as a part of the TAIGA Project. Total genomic DNA was extracted from the foot tissue of sixty specimens from the three sites with a DNeasy Tissue Extraction Kit (Qiagen, Valencia, CA). DNA samples from a previous study (Kojima et al. 2001) were used for populations at the Alice Springs and Forecast sites. The extracted DNA was treated with GeneReleaser (BioVenture Inc., Murfreesboro, TN) to sequester the products of cell lysis that might have inhibited polymerase activity.

Three fragments were amplified for each of the newly collected specimens from the southernmost Mariana Trough by polymerase chain reaction (PCR) with the extracted DNA as a template and *Takara Ex Taq* Hot Start Version (Takara Bio Inc., Shiga, Japan). These included two mitochondrial DNA fragments for the cytochrome *c* oxidase subunits I (COI) and a region spanning from the $tRNA^{Met}$ gene to the 12S rRNA gene, as well as an intron region of a nuclear gene for ATP Synthetase subunit β (ATPSβ). The COI fragment was amplified using primers LCO1490 (5′-GGTCAACAAATCATAAAGATATTGG-3′) (Folmer et al. 1994) and COI-6 (5′-GGRTARTCNSWRTANCGNCGNGGYAT-3′) (Shimayama et al. 1990). The second fragment, which contains the $tRNA^{Met}$, $tRNA^{Trp}$, $tRNA^{Tyr}$, $tRNA^{Cys}$, $tRNA^{Gln}$, $tRNA^{Gly}$, $tRNA^{Glu}$, and 12S rRNA genes and six non-coding regions, was amplified using a primer set AlIfCOII-1 (5′-GGGCATCARTGATAYTGRAG-3′) (Hidaka et al. 2013) and AlIf12S-1R (5′-GTCTAAAGCACCGCCAAGCCC-3′) (Hidaka et al. 2013) or another set AlIfATP6-1 (5′-TATACAATTTTTGARTTYGG-3′) (Hidaka et al. 2013) and AlIf12S-2R (5′-TATAYTTWYAAGTCAGAGCCAAGC-3′) (Hidaka et al. 2013). This region has been shown to provide much more information about the genetic structure of *A. hessleri* than the COI gene does (Hidaka et al. 2013). PCR conditions for the two mitochondrial DNA fragments were as follows: incubation at 94 °C for 2 min, followed by 40 cycles of incubation at 92, 50, and 72 °C for 40 s, 1 min, and 90 s, respectively, and a final extension at 72 °C for 7 min. DNA fragments containing the intron region of the nuclear ATPSβ gene were amplified using a primer ATPSβf1 (5′-CGTGAGGGNAAYGATTTHTACCATGAGATGAT-3′) (Jarman et al. 2002) in combination with either ATPSβr1 (5′-TACTTGCTTGGNGGDCCRCGGGCACGGGC-3′) (Jarman et al. 2002) or ATPSβr2 (5′-ACACCTGCACAAATCACCAC-3′; synthesized on the basis of determined sequences). PCR conditions for this fragment were as follows: incubation at 94 °C for 2 min, followed by 35 cycles of incubation at 94, 54, and 72 °C for 20 s, 1 min, and 1 min, respectively. For specimens from the Alice Springs and Forecast Vent sites, only the third fragment was newly amplified as nucleotide sequences of two mitochondrial DNA fragments have been determined and published elsewhere (Kojima et al. 2001; Hidaka et al. 2013).

Each PCR product was incubated with ExoSAP-IT (United States Biochemical, Cleveland, OH) at 37 °C for 15 min to digest the unused primers and nucleotides and at 80 °C for 15 min to deactivate ExoSAP, used in cycle sequencing reactions performed with a BigDye Terminator Cycle Sequencing Kit Version 3.0 (Applied Biosystems Inc., Foster City, CA), and sequenced on an automated sequencer

(ABI3130; Applied Biosystems) with the same primers as used in PCR. Low quality ends were trimmed from the obtained sequences and the final dataset comprised 491 bp and 631–633 bp for the COI gene and the region spanning from the $tRNA^{Met}$ gene to the 12S rRNA gene, respectively. The ATPSβ intron dataset was represented by nucleotide sequences of 194–226 bp from a limited number of individuals, where genotype could be determined through direct-sequencing; those yielded multiple amplicons with more than one substitutions and/or indels were excluded from the succeeding coalescence theory-based analyses. The nucleotide sequences determined in the current study were deposited in the DDBJ/EMBL/GenBank databases under the accession numbers AB874407–874415 (COI), AB874416–874443 ($tRNA^{Met}$–12SrRNA), and AB874444–874468 (ATPSβ).

Haplotype networks were constructed on the basis of differences in the nucleotide sequences of the mitochondrial datasets with the median-joining method implemented in Network version 4.6.1.0 (Bandelt et al. 1999). Differences in the frequencies of haplotypes between populations were evaluated using the exact test of population differentiation (Raymond and Rousset 1995) in the Arlequin software package version 3.5.1.2 (Excoffier and Lischer 2010). This software package was also used to estimate the unbiased fixation index, F_{ST} (Weir and Cockerham 1984) and to test the significance of the F_{ST} values by nonparametric permutation with 10,000 runs.

The same mitochondrial datasets were also analyzed to infer the demographic history of the species based on the distribution of pairwise sequence differences. Historical population expansion (a rapid increase of population size) was assessed by performing mismatch distribution analysis (Rogers and Harpending 1992; Rogers 1995) in Arlequin. Whether or not a given population has recently experienced a sudden expansion was evaluated by testing the null hypothesis that the mismatch distribution expected under the sudden expansion model is different from the observed distribution. If the population was considered to have recently experienced a sudden expansion, the time from the expansion (t) was estimated according to the relationship $\tau = 2tu$, where τ is the mode of the distribution and u is the mutation rate of a sequence calculated as $u = \mu k$ (where μ is the mutation rate per nucleotide and k is the number of nucleotides) (Rogers and Harpending 1992). Moreover, Tajima's D test (Tajima 1983) and Fu's F_s test (Fu 1997) of neutrality were performed in Arlequin to further evaluate the possible events during population expansion. A population that has experienced expansion generally shows a significant negative Tajima's D value; F_s is also sensitive to population expansion, which generally leads to large negative F_s values (Fu 1997).

The distribution of the posterior probabilities for the deviation date between populations of *A. hesssleri* were estimated using the ATPSβ intron dataset and Bayesian coalescent inference (Hey and Wakeley 2001) implemented in the program IM (Hey and Nielsen 2007). The prior distributions of parameters were adjusted as a function of what was observed in the first run with the default settings according to the program documentation. Replicate runs with different seed numbers were conducted to ensure each run had approximately the same results. Ten million steps were sampled for each run after a burn-in of 1,000,000 steps. The converged ten runs with the complete posterior distributions of all parameters within the prior distributions were used for the final divergence time estimates.

The mutation rates of the $tRNA^{Met}$–12S rRNA and ATPSβ intron regions were approximated by comparing Kimura-corrected average pairwise distances (Kimura 1980) for these regions and the COI gene among the individuals of *A. hessleri* and by extrapolating the estimated evolutionary rate for the latter gene in the entire *Alviniconcha* (see above).

26.3 Results

26.3.1 Evolutionary Rate of COI Gene in *Alviniconcha*

The Bayesian phylogenetic reconstruction under the GTR + G + I model estimated COI genetic distances between the six individuals of *Alviniconcha* and three of *Ifremeria nautilei* to be 0.8088–0.8514 with an average of 0.8264 (Fig. 26.1). The divergence date for the split between *Alviniconcha* and *Ifremeria* was estimated either at 64.4 Ma (31.4–98.9 Ma: 95 % highest probability density interval) or 59.2 Ma (18.8–74.5 Ma) using fossil calibration points or the hypothesized vicariance of deep-sea taxa across the Isthmus of Panama, respectively (Johnson et al. 2010). Assuming that reasonably well corrected distances were observed in the present Bayesian phylogram and the two lineages leading to *Alviniconcha* and *Ifremeria* evolved at an equal pace, the substitution rate of their COI gene was calculated to be 0.64 % per million years (My) (95 % confidence range: 0.42–1.32 %/My) with the fossil dates or 0.70 %/My (0.55–2.19 %/My) with the vicariance calibration. As the two estimates were similar to each other, the average value (0.67 %/My) was used in the following assessment of population history of *A. hessleri*. This average value roughly corresponded to the lower limit of the range of COI evolutionary rates for animal lineages (0.7–1.2 %/My) reviewed by Wilke (2003).

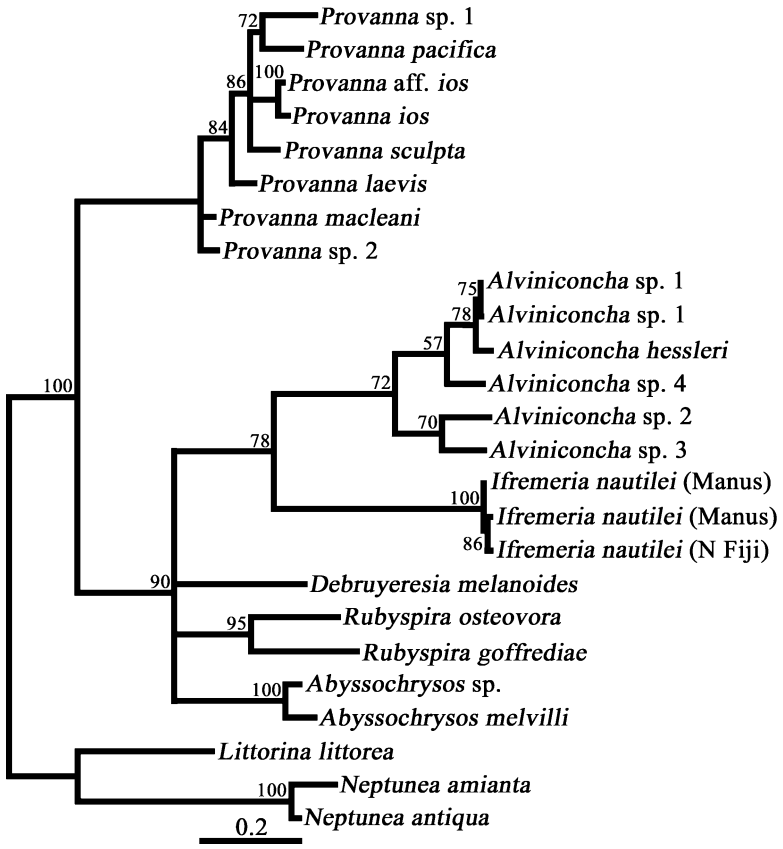

Fig. 26.1 Bayesian phylogram of 22 provannid and three outgroup gastropods, reconstructed from the 530-bp alignment of the cytochrome *c* oxidase subunit I gene. Numerals on branches indicate Bayesian posterior probabilities, shown as percentage for values above 50 %. See Johnson et al. (2010) and Hidaka et al. (2013) for the details of the study specimens

Table 26.2 The genetic diversity of five populations of *Alviniconcha hessleri* estimated from two mitochondrial regions

Region	Vent site	*N*	Haplotype	Gene diversity	Nucleotide diversity
COI	Alice Springs	20	10	0.85 ± 0.06	0.00322 ± 0.00223
	Forecast	20	10	0.91 ± 0.04	0.00398 ± 0.00263
	Snail	20	6	0.52 ± 0.13	0.00177 ± 0.00145
	Archaean	20	9	0.80 ± 0.09	0.00268 ± 0.00195
	Pika	20	6	0.64 ± 0.12	0.00241 ± 0.00180
$tRNA^{Met}$–12SrRNA	Alice Springs	20	11	0.76 ± 0.10	0.01385 ± 0.00894
	Forecast	20	12	0.92 ± 0.04	0.02729 ± 0.01576
	Snail	20	11	0.89 ± 0.05	0.01894 ± 0.01154
	Archaean	20	13	0.91 ± 0.05	0.01891 ± 0.01152
	Pika	20	13	0.88 ± 0.07	0.01978 ± 0.01197

26.3.2 Population History of *Alviniconcha hessleri*

Twenty-five and 53 types of sequences (haplotypes) were identified among a hundred individuals of *A. hessleri* in the COI gene and the fragment spanning from the $tRNA^{Met}$ gene to the 12S rRNA gene, respectively. The COI region contained 21 variable sites, eight of which were parsimoniously informative; the $tRNA^{Met}$–12S rRNA region had 50 variable and 26 parsimoniously-informative sites. The genetic diversity of populations of *Alviniconcha hessleri* at different five hydrothermal sites was estimated from two mitochondrial regions (Table 26.2). The unbiased F_{ST} and exact tests of population differentiation for a combined dataset of the two mitochondrial regions showed no significant genetic difference among populations from the five vent sites ($p > 0.05$) except between the Snail and Pika sites in the latter test ($p = 0.047$).

The above comparison between the two gene regions showed that the $tRNA^{Met}$–12S rRNA fragment contained more informative signals than the COI gene as noted in a previous study (Hidaka et al. 2013). Indeed, genetically distinct groups were recognized only in the haplotype network of the former gene region: seven haplotypes construct a group (Group 2 in Fig. 26.2b), which is separated from another group constructed by 46 other haplotypes (Group 1 in Fig. 26.2b), by three substitutions. The two groups

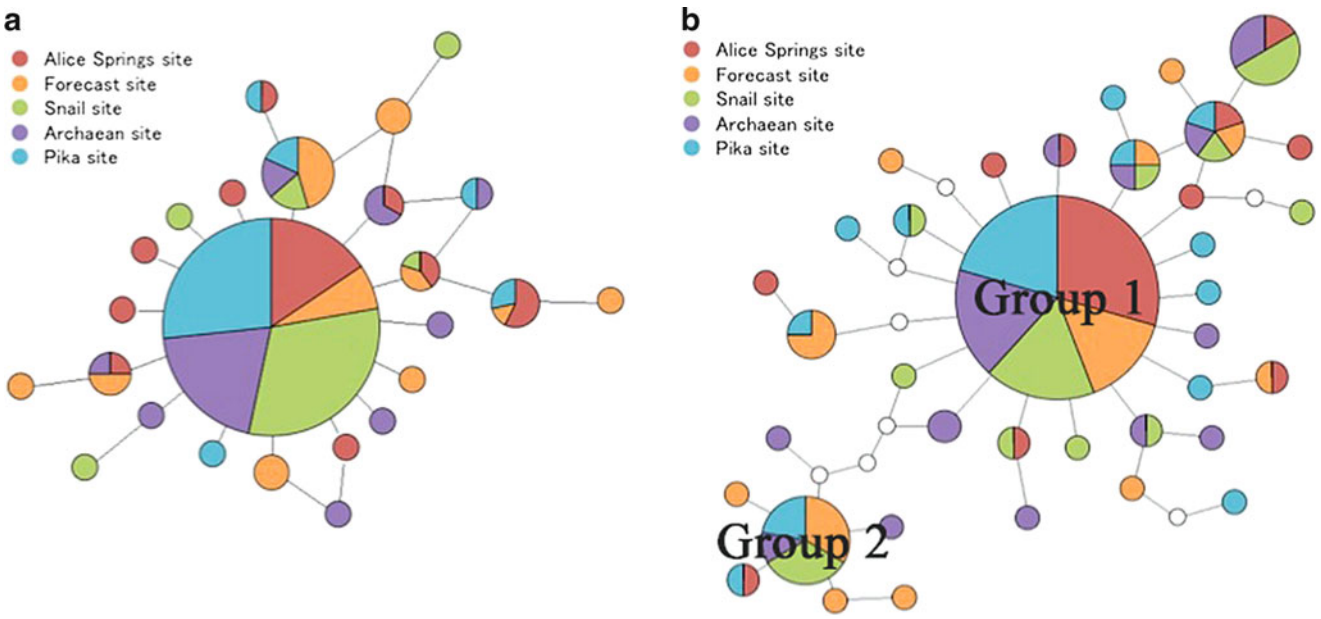

Fig. 26.2 Median-joining networks connecting haplotypes found in the five populations of *Alviniconcha hessleri* for the cytochrome *c* oxidase subunit I gene (**a**) and the region spanning from the $tRNA^{Met}$ gene to the 12S rRNA gene (**b**). *Open circles* denote missing haplotypes. The areas of the *colored circles* are proportional to the frequency of each haplotype: the smallest ones represent single individuals. Two haplotype groups (separated by three missing haplotypes) were recognized in the network shown in (**b**)

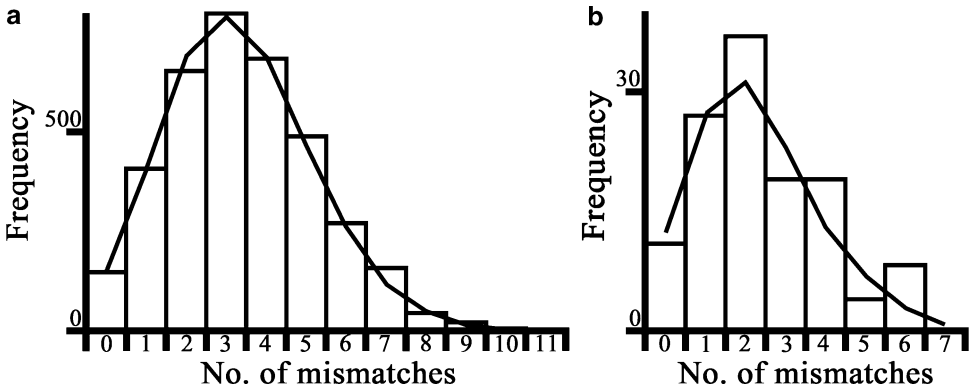

Fig. 26.3 Mismatch distributions for two groups of *Alviniconcha hessleri*, the Group 1 (**a**) and Group 2 (**b**), based on combined nucleotide sequences of the gene for the cytochrome *c* oxidase subunits I and the region spanning from the $tRNA^{Met}$ gene to the 12S rRNA gene. *Lines*: expected distribution for the sudden expansion model; *bars*: observed distribution

showed an apparent difference in geographic distribution. While the Group 1 was evenly distributed over the five study sites, the Group 2 was rare at the northernmost Alice Springs site. An average genetic distance of 0.015 (K2P) between the two haplotype groups was larger than the average distance between all pairs of individuals (0.007). By applying the average distance of 0.003 for the COI gene between the same pairs and its suggested rate of 0.67 %/My (see above), the evolutionary rate for the $tRNA^{Met}$–12S rRNA region was calculated to be 1.56 %/My and hence the divergence between the Groups 1 and 2 at 0.958 Ma.

The mismatch distribution analysis showed that the Group 1 (mismatch observed mean = 3.413, $\tau = 3.479$, $\theta_0 = 0.040$, $\theta_1 = 100.625$, SSD = 0.0001, $p = 0.980$) and the Group 2 (mismatch observed mean = 2.250, $\tau = 2.270$, $\theta_0 = 0.004$, $\theta_1 = 99{,}999.000$, SSD = 0.0080, $p = 0.480$) have recently experienced sudden expansions in population size (Fig. 26.3). Using the calculated rates of the COI gene and the $tRNA^{Met}$–12S rRNA region, the expansions of the Group 1 and the Group 2 were estimated to have occurred at 0.264 and 0.172 Ma, respectively. Tajima's D (−2.071 and −1.700, respectively) and Fu's F_s (−27.34 and −3.446, respectively) were significantly negative for both groups ($p < 0.05$), also suggesting the recent expansions.

The average and standard deviation of mode values of the distributions of the posterior probabilities for the deviation date between the Groups 1 and 2 (i.e., the most probable estimates) among 10 runs was 5.23 ± 3.52 and seven of ten replicate runs showed the mode values around 5.0. The average genetic distance between all pairs of available

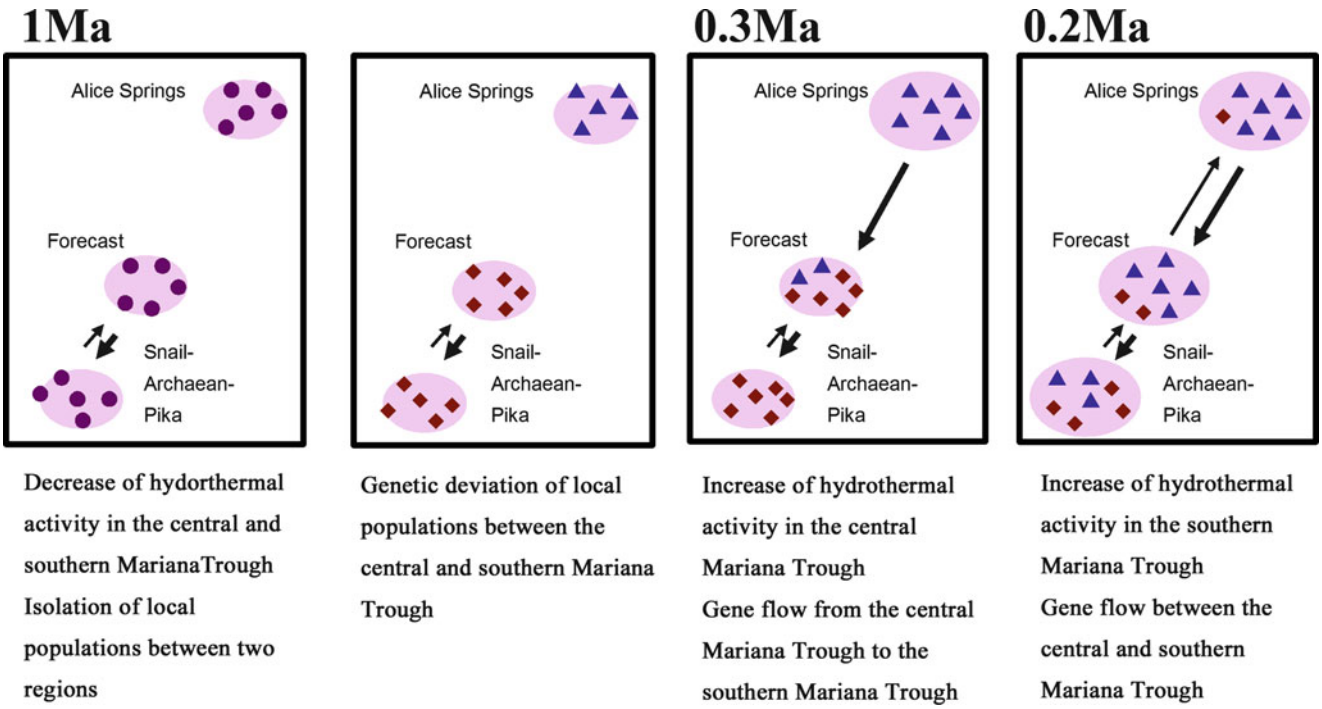

Fig. 26.4 Estimated population history of *Alviniconcha hessleri* in the Mariana Trough between 1 and 0.2 million years ago (Ma)

individuals was 0.011 for the ATPSβ gene. Extrapolation of the average distance and substitution rate for the COI gene implied that this intron region has a rate of 2.46 %/My. The estimated age of divergence between the two groups, 0.937 Ma, agreed well with the result inferred from the average genetic distance for the $tRNA^{Met}$–12S rRNA region (0.958 Ma).

26.4 Discussion

The genetic distances estimated based on nucleotide sequences of the COI gene from the six individuals of *Alviniconcha* and three of *Ifremeria nautilei*, were approximately 1.9 times larger than that based on a single species for each genus (0.44) (Johnson et al. 2010), which suggests the saturation of genetic distance due to multiple substitutions at the same sites since the split between *Alviniconcha* and *Ifremeria*. The molecular evolutionary rate calculated based on such a more reasonable estimation is expected to enable reconstruction of reliable population history of *Alviniconcha hessleri*.

Population dynamics of hydrothermal-vent endemic species such as *A. hessleri* are thought to be controlled primarily by fluctuating hydrothermal activity. A decline in the activity results in the reduction of population size which accelerates divergence between local populations. In contrast, recovery of the activity causes an expansion of population size, fusion of isolated populations, and secondary contact between genetically differentiated individuals. Population divergence around 1 Ma and expansions around 0.3 and 0.2 Ma, which were estimated for *A. hessleri* in the present study, are also attributable to changes in the hydrothermal activity (Fig. 26.4). Hydrothermal activities in the Mariana Trough, which started around 7 Ma (Stern et al. 2003), are thought to have been more intense during its young stage than the present and therefore *A. hessleri* might have been distributed over a wider area in the trough. The present results showed genetic differentiation between populations in the central and southern parts of the Mariana Trough at around 1 Ma. The decline in hydrothermal activity might have resulted in the reduction of local populations of the species and loss of connectivity between them, which possibly represent the origin of the Groups 1 and 2.

The mismatch distribution analysis suggested that the Groups 1 and 2 expanded at 0.3 and 0.2 Ma, respectively. These expansion events might be attributable to the recovery of the local hydrothermal activity. In that case, the increase of the activity in the central Mariana Trough preceded that in the southern Mariana Trough and gene flow from expanding central population into southern ones might have predominated for about a 100,000 years and resulted in ubiquitous distribution of individuals of the Group 1. In contrast, the more recent increase of the population size in the southern Mariana Trough might have resulted in the uneven geographical distribution of individuals of the Group 2 (Fig. 26.3).

The snails of *Alviniconcha* are one of the representative animal groups in the hydrothermal vent fields of the Pacific and Indian Oceans. Due to their dominance and strict endemism to the hydrothermal vent environment, which means their local populations change reflecting hydrothermal activities clearly, they are expected to be useful model animals for the evaluation of effects of artificial or natural environmental change such as those by the hydrothermal deposit mining or volcanic eruption on this deep-sea ecosystem. The general biology and natural history of these species have been the subject of several studies. For example, their spatial distribution within a single vent field and species compositions at different fields have been reported in the Lau Basin in the southern Pacific (Podowski et al. 2009; Beinart et al. 2012). Similar studies have been conducted for the closely related *Ifremeria nautilei* in the Manus Basin (Thaler et al. 2011). Information about the effects of the past environmental changes on the populations of such model species will be very useful for the interpretation of results of monitoring their genetic characteristics after the environmental change.

The history of hydrothermal ecosystems can be better reconstructed by comparing and integrating estimates of past environmental changes from biological and geochemical methodologies. Such studies are expected to contribute to more accurate reconstruction of history of hydrothermal ecosystems. Unfortunately, the present results cannot be compared with geochemical evidence. The historical fluctuation in the hydrothermal activity of the Mariana Trough have been traced back only to 12,000 years ago by the geochemical approach (Stüben et al. 1994; Takamasa et al. 2013, Ishibashi et al., Chap. 23), while our results suggested environmental changes between 1 to 0.2 Ma. Future progress in both methodologies will enable us to further explore the hypothesis that historical changes in hydrothermal activity promote genetic structuring of hydrothermal vent-endemic species.

26.5 Acknowledgements

Acknowledgements The authors are grateful to the operation teams of the submersible *SHINKAI 6500*, the crew of the support ship *Yokosuka*, and the onboard scientists of the YK10-11 cruise of *Yokosuka* for their help in sampling. This study was conducted as an activity of the scientific research innovative areas "TAIGA (Trans-crustal Advection & In situ bio-geochemical processes of Global sub-seafloor Aquifer)" which is sponsored by Ministry of Education, Culture, Sports, Science and Technology (MEXT), Japan (No. 20109004).

References

Bandelt HJ, Forster P, Röhl A (1999) Median-joining networks for inferring intraspecific phylogenies. Mol Biol Evol 16:37–48

Beinart RA, Sanders JG, Faure B, Sylva SP, Lee RW, Becker EL, Gartman A, Luther GW III, Seewald JS, Fisher CR, Girguis PR (2012) Evidence for the role of endosymbionts in regional-scale habitat partitioning by hydrothermal vent symbioses. Proc Natl Acad Sci USA 109:E3241–E3250

Excoffier L, Lischer HEL (2010) Arlequin suite ver 3.5: a new series of programs to perform population genetics analyses under Linux and Windows. Mol Ecol Resour 10:564–567

Folmer O, Black M, Hoeh W, Lutz RA, Vrijenhoek RC (1994) DNA primers for amplification of mitochondrial cytochrome c oxidase subunit I from diverse metazoan invertebrates. Mol Mar Biol Biotech 3:294–299

Fu YX (1997) Statistical tests of neutrality of mutations against population growth, hitchhiking and background selection. Genetics 147:915–925

Hey J, Nielsen R (2007) Integration within the Felsenstein equation for improved Markov chain Monte Carlo methods in population genetics. Proc Natl Acad Sci USA 104:2785–2790

Hey J, Wakeley J (2001) Distinguishing migration from isolation: a Markov Chain Monte Carlo approach. Genetics 158:885–896

Hidaka H, Watanabe H, Kano Y, Kojima S (2013) Mitochondrial genome rearrangement in a hydrothermal vent-endemic lineage of provannid gastropods provides a new DNA marker for phylogeographical studies. J Mar Biol Assoc UK 93:1053–1058

Ho SYW, Shapiro B (2011) Skyline-plot methods for estimating demographic history from nucleotide sequences. Mol Ecol Resour 11:423–434

Ishibashi J, Nakai S, Toyoda S, Kumaga H, Noguchi T, Ishizuka O (2009) Geochemical and geochronological studies on the evolution of submarine hydrothermal systems. J Geogr 118:1186–1204 (in Japanese with English abstract)

Jarman SN, Ward RD, Elliott NG (2002) Oligonucleotide primers for PCR amplification of coelomate introns. Mar Biotechnol 4:347–355

Johnson L, Fryer H, Masuda H, Ishii T, Gamo T (1993) Hydrothermal deposits and two magma sources for volcanoes near 13°20′N in the Mariana backarc: a view from *Shinkai 6500*. EOS Trans AGU 74, Fall Meet Suppl, 381

Johnson SB, Warén A, Lee RW, Kano Y, Kaim A, Davis A, Strong EE, Vrijenhoek RC (2010) *Rubyspira*, a new genus and two new species of bone-eating deep-sea snails with ancient habits. Biol Bull 219:166–177

Kakegawa T, Utsumi M, Marumo K (2008) Geochemistry of sulfide chimneys and basement pillow lavas at the southern Mariana Trough (12.55ºN-12.58ºN). Res Geol 58:249–266

Kimura M (1980) A simple method for estimating evolutionary rate of base substitutions through comparative studies of nucleotide sequence. J Mol Evol 16:111–120

Kojima S, Segawa R, Fujiwara Y, Fujikura K, Ohta S, Hashimoto J (2001) Phylogeny of hydrothermal vent-endemic gastropods *Alviniconcha* spp. from the Western Pacific revealed by mitochondrial DNA sequences. Biol Bull 200:298–304

Kuhner MK (2008) Coalecent genealogy samples: window into population history. Trends Ecol Evol 24:86–93

Okutani T, Ohta S (1988) A new gastropod mollusk associated with hydrothermal vents in the Mariana Back-Arc Basin, western Pacific. Venus (Jap J Malac) 47:1–9

Podowski EL, Moore TS, Zelnio KA, Luther GW III, Fisher CR (2009) Distribution of diffuse flow and megafauna in two sites on the Eastern Lau Spreading Center, Tonga. Deep-Sea Res I 56:2041–2056

Raymond M, Rousset F (1995) An exact test for population differentiation. Evolution 49:1280–1283

Rogers AR (1995) Genetic evidence for a Pleistocene population explosion. Evolution 49:608–615

Rogers AR, Harpending H (1992) Population growth makes waves in the distribution of pairwise genetic differences. Mol Biol Evol 9:552–569

Rogers AD, Tyler PA, Connelly DP, Copley JT, James R, Larter RD, Linse K, Mills RA, Garabato AN, Pancost RD, Pearce DA, Polunin NVC, German CR, Shank T, Boersch-Supan XPH, Alker BJ, Aquilina A, Bennett SA, Clarke A, Dinley RJJ, Graham AGC, Green DRH, Hawkes JA, Hepburn L, Hilario A, Huvenne VAI, Marsh L, Ramirez-Llodra E, Roterman CN, Thatje S, Zwirglmaier K (2012) The discovery of new deep-Sea hydrothermal vent communities in the southern ocean and implications for biogeography. PLoS One 10:e1001234

Ronquist F, Huelsenbeck JP (2003) MRBAYES 3: Bayesian phylogenetic inference under mixed models. Bioinformatics 19:1572–1574

Shimayama T, Himeno H, Sasuga J, Yokobori S, Ueda T, Watanabe K (1990) The genetic code of a squid mitochondrial gene. Nucleic Acids Symp Ser 22:77–78

Stern RJ, Fouch MJ, Klemperer SL (2003) An overview of the Izu-Bonin-Mariana subduction factory. In: Eiler J, Hirschmann M (eds) Inside the subduction factory. American Geological Union, Washington, DC, pp 175–222

Stüben D, Taibi NE, McMurtry GM, Scholten J, Stoffers P, Zhang D (1994) Growth history of a hydrothermal silica chimney from the Mariana backarc spreading center (southwest Pacific, 18°21′N). Chem Geol 113:273–296

Suzuki Y, Kojima S, Sasaki T, Suzuki M, Utsumi T, Watanabe H, Urakawa H, Tsuchida S, Nunoura T, Hirayama H, Takai K, Nealson KH, Horikoshi K (2006) Host-symbiont relationships in hydrothermal vent gastropods of the genus *Alviniconcha* from the Southwest Pacific. Appl Environ Microbiol 72:1388–1393

Tajima F (1983) Statistical method for testing the neutral mutation hypothesis by DNA Polymorphism. Genetics 105:585–595

Takamasa A, Nakai S, Sato F, Toyoda S, Banerjee D, Ishibashi J (2013) U-Th radioactive disequilibrium and ESR dating of a barite-containing sulfide crust from South Mariana Trough. Quat Geochronol 15:38–46

Thaler AD, Zelnio K, Saleu W, Shultz TF, Carlsson J, Cunnungham C, Vrijenhoek RC, Van Dover CL (2011) The spatial scale of genetic subdivision in populations of *Ifremeria nautilei*, a hydrothermal-vent gastropod from the southwest Pacific. BMC Evol Biol 11:372

Urabe T, Ishibashi J, Maruyama A, Marumo K, Seama N, Utsumi M (2004) Discovery and drilling of on- and off-axis hydrothermal sites in backarc spreading center of southern Mariana Trough, western Pacific. EOS Trans AGU 85, Fall Meet Suppl, F1907

Vrijenhoek RC (2010) Genetic diversity and connectivity of deep-sea hydrothermal vent metapopulations. Mol Ecol 19:4391–4411

Weir BS, Cockerham CC (1984) Estimating *F*-statistics for the analysis of population structure. Evolution 38:1358–1370

Wheat CG, Fryer P, Hulme SM, Becker NC, Curtis A, Moyer C (2003) Hydrothermal venting in the southern most portion of the Mariana backarc spreading center at 12.57 degrees N. EOS Trans AGU 84, Fall Meet Suppl, F1399

Wilke T (2003) *Salenthydrobia* gen. nov. (Rissooidea: Hydrobiidae): a potential relic of the Messinian salinity crisis. Zool J Linn Soc 137:319–336

Yoshikawa S, Okino K, Asada M (2012) Geomorphological variations at hydrothermal sites in the southern Mariana Trough Relationship between hydrothermal activity and topographic characteristics. Mar Geol 303–306:172–182

Part IV

Okinawa Trough

Hydrothermal Activity in the Okinawa Trough Back-Arc Basin: Geological Background and Hydrothermal Mineralization

27

Jun-ichiro Ishibashi, Fumihiko Ikegami, Takeshi Tsuji, and Tetsuro Urabe

Abstract

The Okinawa Trough is a back-arc basin behind the Ryukyu trench-arc system and located along the eastern margin of the Eurasian continent. Sulfide and sulfate mineralization associated with hydrothermal activity has been recognized in ten hydrothermal fields in the Okinawa Trough. Hydrothermal mineralization recognized in these fields is commonly represented by coexisting occurrence of zinc- and lead-enriched polymetallic sulfides and abundant sulfate minerals. The mineralogy and geochemical signatures present has led researchers to suggest these areas may be a modern analogue for the formation of ancient Kuroko-type volcanogenic massive sulfide (VMS) deposits. Recent seafloor drilling during IODP (Integrated Ocean Drilling Program) Expedition 331 documented the subseafloor structure of a hydrothermal system at the Iheya North Knoll. Mineral textures and hydrothermal assemblages present in the drilled cores obtained from a hydrothermal mound in the proximal area are consistent with Kuroko-type mineralization. Based on geochemical studies, the intra-field diversity of mineralization commonly recognized in the Okinawa Trough can be explained by subseafloor phase separation of the hydrothermal fluid, which reflects shallow water depth (from 700 to 1,600 m). The subseafloor phase separation may. play an important role to accumulate metal elements beneath the seafloor. Based on geophysical and geological studies, the Okinawa Trough is considered a back-arc basin in the rifting stage. Such a tectonic setting is characterized by development of normal faulting in brittle continental crust and frequent intrusion of a magma, which can be expected to provide favorable environment for development of a hydrothermal system

Keywords

Back-arc rifting • Kuroko-type deposit • Mineralization • Phase separation • Volcanic massive sulfide

J.-i. Ishibashi (✉)
Department of Earth and Planetary Sciences, Faculty of Sciences, Kyushu University, Fukuoka 812-8581, Japan

Submarine Resources Research Project (SRRP), Japan Agency for Marine-Earth Science and Technology (JAMSTEC), Yokosuka 237-0061, Japan
e-mail: ishibashi.junichiro.779@m.kyushuu.ac.jp

F. Ikegami
Department of Earth and Planetary Sciences, Graduate School of Sciences, Kyushu University, Fukuoka 812-8581, Japan

T. Tsuji
International Institute for Carbon-Neutral Energy Research (I2CNER), Kyushu University, Fukuoka 819-0395, Japan

Submarine Resources Research Project (SRRP), Japan Agency for Marine-Earth Science and Technology (JAMSTEC), Yokosuka 237-0061, Japan

T. Urabe
Department of Earth and Planetary Science, Graduate School of Science, The University of Tokyo, Tokyo 113-0033, Japan

J.-i. Ishibashi et al. (eds.), *Subseafloor Biosphere Linked to Hydrothermal Systems: TAIGA Concept*,
DOI 10.1007/978-4-431-54865-2_27,

27.1 Introduction

Since the initial discovery in 1988 (Halbach et al. 1989), seafloor hydrothermal activity of the Okinawa Trough has been considered a modern analog to ancient Kuroko-type VMS (volcanogenic massive sulfide) deposits. Fouquet et al. (1991) proposed seafloor massive sulfide deposits in a back-arc setting showed more resemblance to the Kuroko-type deposits compared with those in the mid-ocean ridge. Halbach et al. (1993) studied in detail mineralogy of sulfide ore samples collected from the Jade field in the Okinawa Trough, and concluded that the seafloor sulfide deposit is a modern analogue of the Kuroko-type deposits, based on strong similarities in the mineralogical and chemical composition of the polymetallic (zinc and lead enriched) sulfides present. Several researchers followed this idea in their reports for description of hydrothermal mineralization (e.g., Nakamura et al. 1989). Marumo and Hattori (1999) showed similarities are also found in occurrence of clay minerals formed by hydrothermal alteration. Glasby et al. (2008) argued that sulfide ore samples collected from hydrothermal fields in submarine volcanoes of the Izu-Bonin Arc showed greater similarities in chemical composition to that of the Kuroko-type deposits, although they recognized hydrothermal fields in the Okinawa Trough showed resemblance in the tectonic setting. In 2010, IODP Expedition 331 drilled through the active hydrothermal field at the Iheya North Knoll hydrothermal field, providing a unique opportunity to directly access the hydrothermal system below the seafloor (Takai et al. 2011, 2012). Mineral textures and assemblages present in the drilled cores obtained from a hydrothermal mound in the proximal area were consistent with those recognized in ancient Kuroko-type mineralization (Yeats et al. 2012; Yeats and Hollis 2013). Moreover, stratabound occurrences of base-metal mineralization and widespread hydrothermal alteration were documented across an area of over 500 m extent, which are comparable to ancient Kuroko-type deposits (Ishibashi et al. 2013).

The northeast (NE) Honshu is the type locality for Kuroko-type VMS deposits, where the Hokuroku District is especially known as many large deposits are concentrated. The Kuroko-type deposits are located in a narrow zone parallel to the arc and associated with a specific litho-tectonic domain that mainly consists of Neogene submarine volcanic rocks (e.g., Sato 1974). Numerous studies were devoted to understand formation of Kuroko-type VMS deposits which represent a significant crustal source of Zn-Pb-Cu-Ag-Au in Japan, based on analysis of samples collected during the mining boom period of 1960s (e.g., Ishihara 1974; Ohmoto and Skinner 1983). They established a concept that the Kuroko-type deposits formed at the discharge sites of submarine hydrothermal systems associated with silicic magmatic activity (e.g., Ohmoto 1996). However, several conflicting ore formation models have been proposed, and provoked continuing debate (e.g., Urabe and Marumo 1991; Ohmoto 1996). The Kuroko-type deposits are characterized by strata-bound and massive mineralization of diverse sulfide and sulfate minerals. However this style is difficult to be simply explained by the hydrogeology of a hydrothermal system. To make matters worse, the Kuroko mines in the northeast Japan were shut down during the 1980–1990s. Since then, samples are available only from archives (Glasby et al. 2008), and only a few studies have been published (e.g., Shikazono 2003; Urabe and Kubota 2004).

If it is the case that hydrothermal activity in the Okinawa Trough is a preferable modern analog to ancient Kuroko-type deposits, it would provide a rare window into the formation of Kuroko-type VMS deposits. In this Chapter, we review previous studies on hydrothermal mineralization in the Okinawa Trough to verify how it is analogous to characteristics of mineralization of the Kuroko-type deposits, which would be useful for further discussion on links between VMS mineralization and the regional geology of the Okinawa Trough back-arc basin. Tectonic activities, geological features (including the nature of volcanism), and its evolution are discussed in Sect. 27.2. Case studies on seafloor hydrothermal mineralization are introduced in Sect. 27.3. The characteristics and style of mineralization are discussed in relation to the tectonic setting of the Okinawa Trough back-arc basin in Sect. 27.4.

27.2 Geological Setting of the Okinawa Trough

27.2.1 Tectonic Overview

The Okinawa Trough is one of many back-arc basins located along the eastern margin of the Eurasian continent (Fig. 27.1). It extends for more than 1,200 km from the Japanese mainland to Taiwan along the Ryukyu Arc, and is characterized by active rifting structures and magmatism along the depression (Letouzey and Kimura 1986). In contrast to the other back-arc basins in western Pacific, previous study has shown that the Okinawa Trough lacks oceanic lithosphere (Nagumo et al. 1986; Hirata et al. 1991; Oshida et al. 1992). A recent seismic study revealed a minimum crustal thickness of only 8 km at the southernmost part (Klingelhoefer et al. 2009). Although this thickness might be thin compared with typical continental crust, the velocity gradient of the layer is too low to be interpreted as oceanic crust. From these lines of evidence, the Okinawa Trough is considered still to be in the nascent stage of back-arc basin formation. The slow extensional rate (3.7 ± 0.06 cm/year)

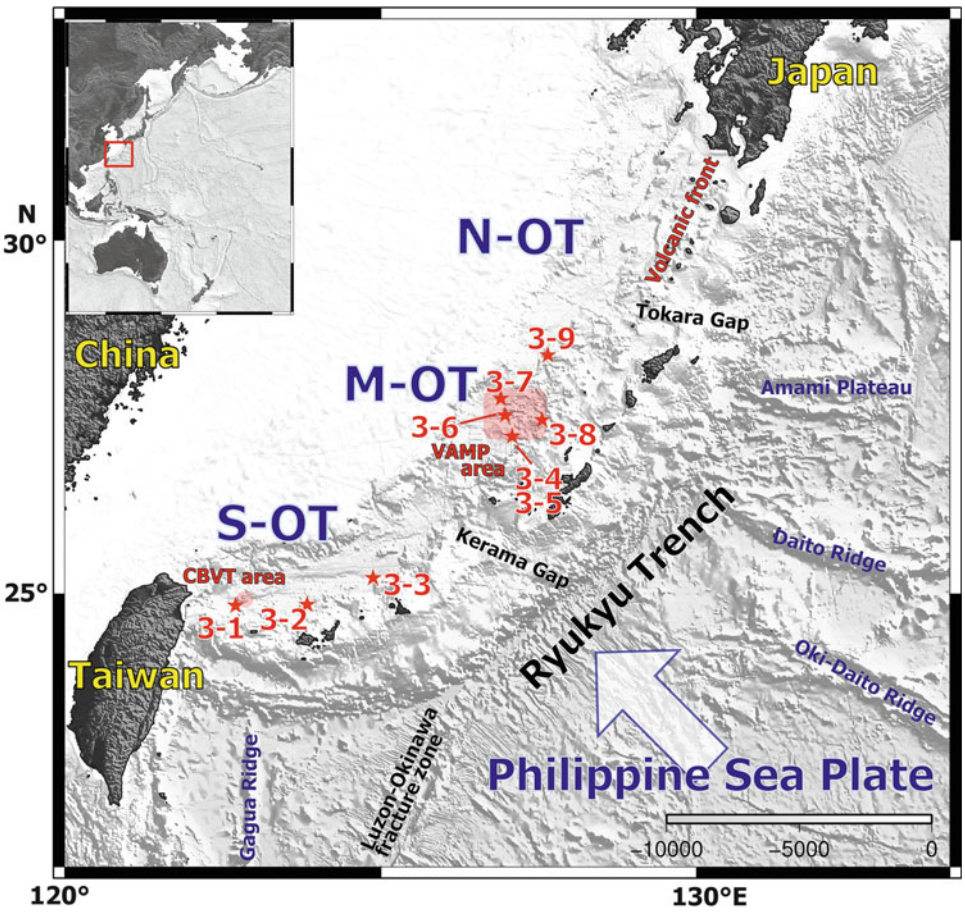

Fig. 27.1 Tectonic setting of the Okinawa Trough back-arc basin. N-OT, M-OT, and S-OT represent the northern, middle, and southern Okinawa Trough, respectively. *Star marks* indicate localities of active hydrothermal fields, which are associated with subsection numbers in this text. Two *red shaded areas* represent the VAMP (Volcanic Arc Migration Phenomenon) area (Sibuet et al. 1987) and CVST (Cross-Backarc Volcanic Trail) area (Sibuet et al. 1998)

observed by means of the Global Navigation Satellite System, or GNSS (Kotake 2000) is also consistent with the view that seafloor spreading has not yet commenced.

27.2.2 Geological Features and Volcanism

Recent seismic profiles (Oikawa et al. 2009) have shown the Okinawa Trough is geologically complex both along and across its length (Fig. 27.2). The northern to middle part of the trough, which lies along the Kyushu to Amami Islands, consists of numerous half-grabens within and/or next to the massive Tokara Sub-Basin (Sibuet et al. 1987). The stratigraphy of this area was documented by the borehole "TO-KA1" (Nash 1979). On the basis of following correlations, the Shimajiri Group (SG) comprising Late Miocene to Pliocene terrigenous deposits, lies as the basement of the trough not only in the northern part but along its length (Kimura 1985). Such half-grabens rotated the Shimajiri Group, and they were later overlain by onlapping trough-infill deposits (Fig. 27.2a). The northern half of the trough had been long considered to be devoid of active volcanism (e.g. Kimura 1996). However, based on recent detailed mappings together with results of petrologic studies, Yokose et al. (2010) proposed that a chain of submarine knolls along the North Okinawa Trough would be assigned as an extension of the volcanic front of the Ryukyu Arc that is identified as volcanoes in the Tokara Islands.

In the middle to southern Okinawa Trough, there is a remarkable change in the topography of the trough. The trough floor is lowered and the continental slope becomes steeper (Fig. 27.1). Such a topographical change is accompanied by en echelon intra-trough grabens (Kimura 1985). While the volcanic front in the Ryukyu Arc disappears from the sea-surface in west area of the Iwo-Torishima Is., an area of extensive intra-trough volcanism along the Iheya Graben occurs in the middle of the Okinawa Trough. Sibuet et al. (1987) inferred this was a product of the volcanic arc migrating into the back-arc basin, and named it the Volcanic Arc Migration Phenomenon, or VAMP area. Although the volcanism takes place within the Okinawa Trough, its compositions consistently vary from rhyolite to basalt (Ishikawa et al. 1991; Shinjo and Kato 2000). As a result of such extensive volcanism, the VAMP area is spotted with regions of anomalously high heat flow (Yamano et al. 1986) and several hydrothermal fields (Ishibashi and Urabe 1995).

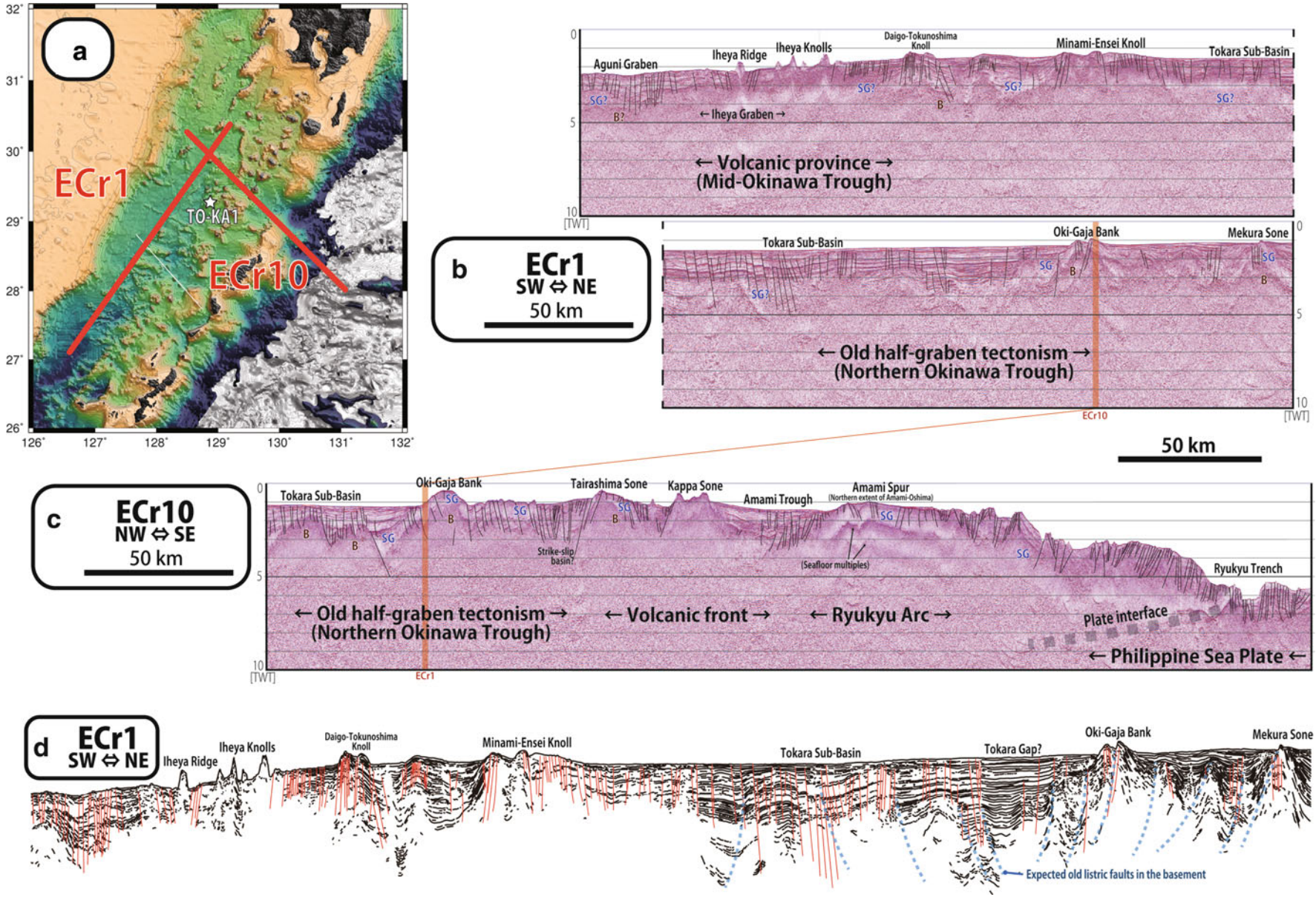

Fig. 27.2 Seismic reflection profiles in the northern to middle of the Okinawa Trough after (Oikawa et al. 2009). (**a**) Bathymetry map of the region (Ryan et al. 2009), in which two survey lines are superimposed. (**b**) Seismic image of the along-axis survey line ECr1. In the Tokara Sub-Basin in the northern Okinawa Trough (in the *lower image*), thick stratified deposits and vast flat-surfaced seafloor are prominent. While this feature is sporadic in the mid-Okinawa Trough (in the *upper image*). (**c**) Seismic image of the NW-SE transect survey line ECr10 for the northern Okinawa Trough. Extensive half-graben forming listric rotation of the basement (B) and Shimajiri Group (SG) is observed in the Tokara Sub-Basin and its vicinities. However the rotation would not be active in the present, because their displacements are covered by onlapping recent deposits. (**d**) Interpretative drawing of the along-axis profile ECr1. The fault planes are shown as *red lines*. The faulting in the stratified deposits has different sense against the listric rotations for the old basement

The southernmost area which is close to Taiwan Is. has the topographically lowermost trough floor throughout the Okinawa Trough (Fig. 27.1). Previous surveys on the crustal thickness in the area documented the thinned nature of the continental crust, which is less than 20 km thick (Lee et al. 1980; Hirata et al. 1991; Klingelhoefer et al. 2009), whereas thicker crust occurs in the middle (Murauchi et al. 1968; Nagumo et al. 1986) and northern parts (Iwasaki et al. 1990) of the trough. Such geophysical evidence suggests that back-arc basin formation is most pronounced in the southernmost part of the Okinawa Trough. This area hosts major volcanic alignment which crosses the central graben, and called as the Cross-Backarc Volcanic Trail, or CBVT (Sibuet et al. 1998). Chronological variations of the volcanism suggest complex backgrounds related to the collision in Taiwan (Shinjo 1999; Shinjo et al. 1999). Lin et al. (2004) inferred that a slab window originated from the subducting Gagua Ridge on the Philippine Sea Plate was the cause of such volcanism. Possible signs of magma chambers at the lower crust beneath the CBVT have been observed (Lin et al. 2009).

27.2.3 Origin and Evolution

Multiple stages of evolution were proposed to explain the origin of the Okinawa Trough (e.g. Lee et al. 1980; Kimura 1996; Miki 1995). The geographical order and timing of the initiation of rifting still remains quite controversial. The geological reconstruction proposed by Kimura (1985, 1990, 1996) provided a schematic evolution for the entire Okinawa Trough, with two stages of rifting in the Pliocene (6–4 Ma) and Pleistocene to present (2–0 Ma). Kimura (1985, 1990, 1996) argued that extensive rifting took place between the area of the current continental shelf and Ryukyu Arc in the first stage. The deposition of Shimajiri Group, which was widely prograding from the continental shelf to Ryukyu Trench (Sibuet et al. 1998; Park et al. 1998) took place during this event. Across the unconformity that was associated with subaerial exposure (Kimura 2000), the second stage of rifting was marked by the rapid subsidence and deposition of onlapping thick trough-infills which eventually shaped the present Okinawa Trough. Submarine channels and meanders at the trough floor (Kimura et al. 2001), as well as limestone outcrops discovered from a water depth of ~1,400 m (Shinjo et al. 2001), indicate the remarkable rate of the subsidence. At least in the southernmost area of Okinawa Trough, this stage is thought to be still in progress with the westward migration towards Taiwan (Wang et al. 2000).

On the other hand, the onshore studies have shown that the recent advances on the studies of coral development in Pleistocene provided the spatiotemporal yield for the back-arc basin formation, which is possibly comparable to the second stage of the rifting. Formation of the back-arc basin would disturb the terrigenous supply from the continent and enable the growth of coral reefs in the arc. In fact, the oldest reef deposits in the Ryukyu Islands formed at 1.45–1.65 Ma in the northern to middle part of the Islands, while the dating never predates 1 Ma at the southernmost Yaeyama Islands (Iryu et al. 2006). It is therefore assumed that the subsidence of the Okinawa Trough started at the northern to middle part in the Early Pleistocene, prior to development in the south. A paleostress study supports such a view of southwestward migration of the rifting (Otubo and Hayashi 2003). In the Ryukyu Islands, however, it is believed that a large scale environmental change from the marginal highlands to the island chain took place somewhat coincidentally. Pollen analysis in the Okinawa Island spotted the disappearance in the mountains of 1,000–1,500 m height which apparently enabled the vegetation of cool climate trees in 1.2–0.8 Ma (Kuroda and Ozawa 1996). Phylogenetic reconstruction of insects also provided an implication for the timing of the isolation of the islands as in the form of group. It is estimated that Amami-Okinawa, Yaeyama and Taiwan were likely to be branched simultaneously around 1.55 Ma (Osozawa et al. 2013). Although the detailed context of events and their localities may still require further investigations, the ongoing tectonics in the Okinawa Trough can be well understood within the framework of a developing Quaternary back-arc basin.

27.3 Case Studies in Hydrothermal Activity and Mineralization in the Okinawa Trough

27.3.1 Daiyon-Yonaguni Knoll Hydrothermal Field

The Daiyon-Yonaguni Knoll hydrothermal field is situated in an elongated valley with a length of approximately 1,000 m and a width of approximately 500 m, and lies adjacent to the Daiyon-Yonaguni Knoll (one of the seamounts that delineate a volcanic belt) (Fig. 27.3). Active hydrothermal sites align north–south, which may be related to a fault control on hydrothermal flow. Observations during dive surveys indicate the elongated valley is covered mainly with muddy sediment, except for active hydrothermal sites, and that the northern slope of the valley has volcanic breccia (Suzuki et al. 2008).

A diverse style of fluid emanations occurs within the Daiyon-Yonaguni Knoll hydrothermal field (Inagaki et al. 2006; Konno et al. 2006; Suzuki et al. 2008). A large chimney-mound complex called the Tiger site, which is approximately 10-m high, is located near the boundary between the slope of the knoll and sediment seafloor at water depth of ~1,370 m. Vigorous venting of blackish-smoky fluids

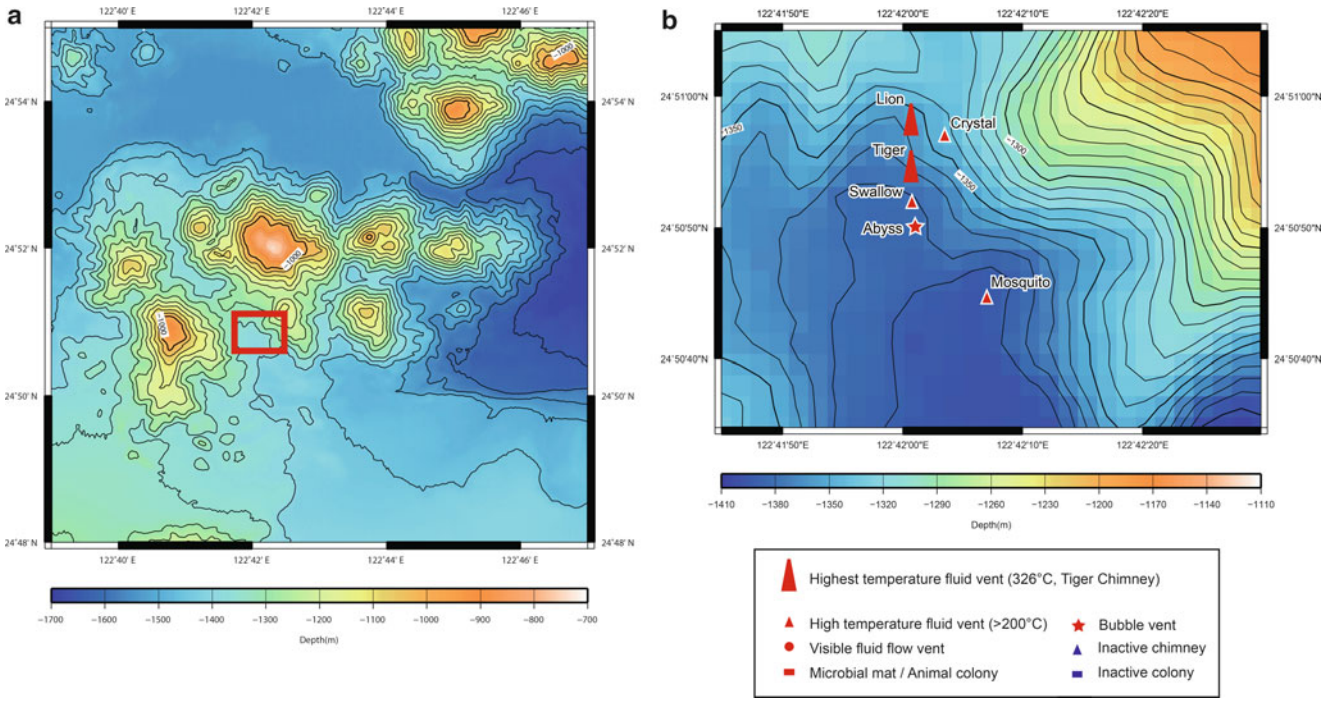

Fig. 27.3 (**a**) Topography of the Daiyon-Yonaguni Knoll (**b**) Localities of active fluid venting in the Daiyon-Yonaguni Knoll hydrothermal field

up to 328 °C has been recorded from the basal part of the mound complex, which seems to mark the central part of the present hydrothermal activity in the field. On the other hand, clear fluid venting with the highest temperature of 310 °C was observed at the top of the same chimney at the Tiger site at water depth of 1,362 m. Another large chimney-mound complex called the Lion site (located at just 50 m north of the Tiger site) hosts smokers venting vigorously similar blackish smoky fluid at 326 °C. Another mound structure (named as Crystal Site) at about 100 m east of the Tiger site was recognized by dense colony of vent specific animals. Venting of clear fluid with the highest temperature of 220 °C was observed at the foot of the mound, which was accompanied with discharge of significant amount of liquid CO_2 droplets. Liquid CO_2 emanation from altered sediment has been observed in many places around the active hydrothermal mounds (Inagaki et al. 2006; Konno et al. 2006). In the southern part of the hydrothermal field (the Abyss Vent site), diffusive fluid venting was observed from the seafloor which is covered with sediment associated whitish hydrothermal crusts (Inagaki et al. 2006). Further south, inactive or diffuse venting from small chimney structures has been recognized, although the area has not been well explored.

Mineralization in the Daiyon-Yonaguni Knoll hydrothermal field was studied in detail by Suzuki et al. (2008). According to this study, the diverse range of sulfide and sulfate mineral deposits can be classified into five groups; (i) anhydrite-rich chimneys, immature precipitates including sulfide disseminations in anhydrite; (ii) massive Zn-Pb-Cu sulfides, consisting of sphalerite, wurtzite, galena, chalcopyrite, pyrite, and marcasite; (iii) Ba-As chimneys, composed of barite with sulfide disseminations, sometimes associated with realgar and orpiment overgrowth; (iv) Mn-rich chimneys, consisting of carbonates (calcite and magnesite) and sulfides (sphalerite, galena, chalcopyrite, alabandite, and minor amount of both tennantite and enargite); and (v) pavement, silicified sediment including abundant native sulfur or barite.

Suzuki et al. (2008) demonstrated a link between the mode of sulfide/sulfate mineralization and geochemistry of fluid emanations. The sulfide/sulfate mineralization (groups i–iii) was dominantly observed in chimney-mound structures in the proximal area (the Tiger site and Lion site), which often host vigorous venting of high temperature and slightly Cl-enriched fluid (Cl concentration of the fluid is higher than that of seawater). In contrast, the sulfide/carbonate mineralization (group iv) and the silicified sediment (group v) were found in the distal area, which are associated with clear fluid venting and/or diffusive fluid emanation. These fluids showed Cl-depleted chemistry and sometimes were associated with discharge of CO_2 liquid droplets. Cl-depleted clear fluid venting was exceptionally observed in the proximal area, at the very top of the chimney at Tiger site. And in the same chimney, carbonate minerals were identified, which follows the same link between the mineralization and fluid chemistry. In addition, Gena et al.

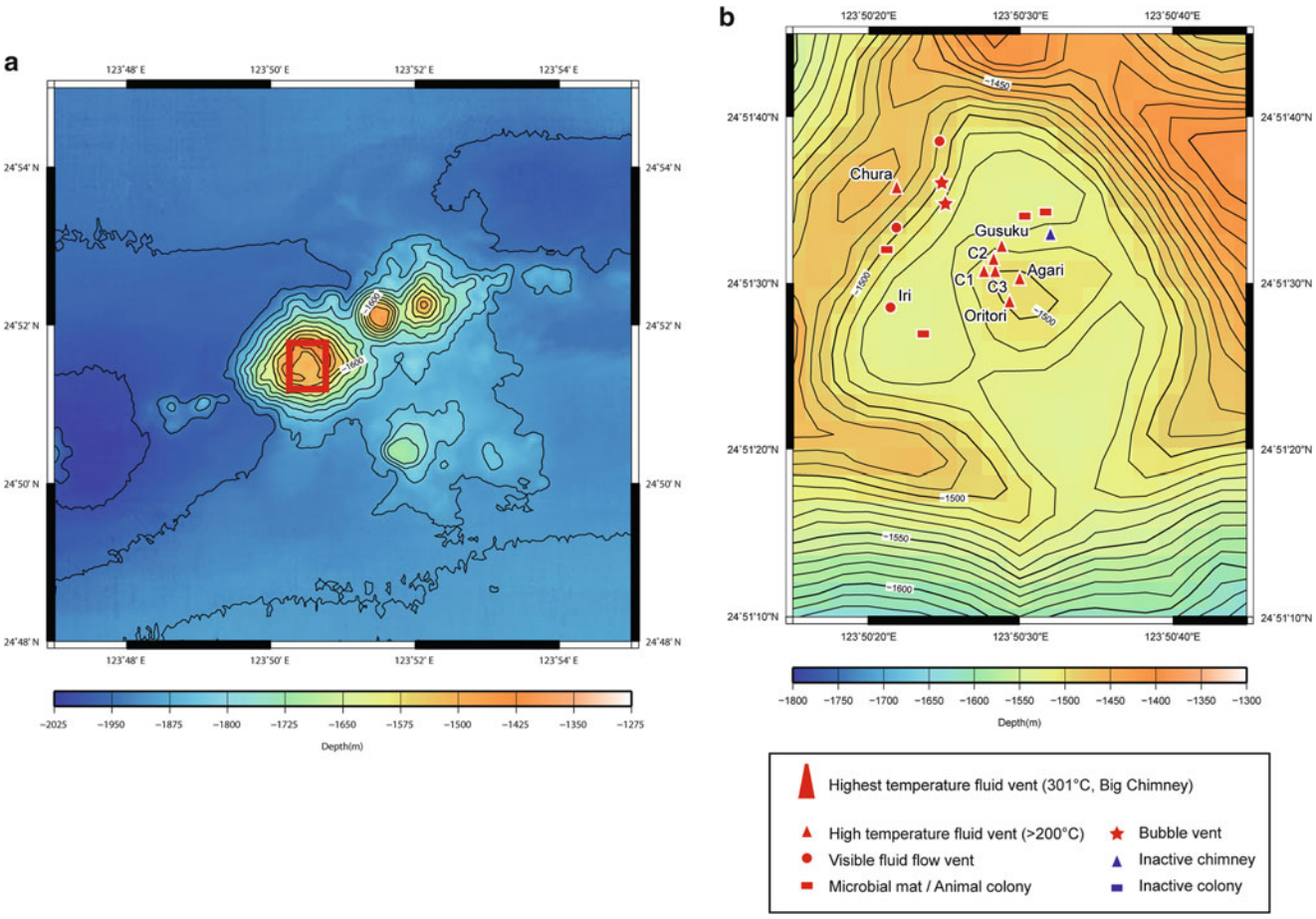

Fig. 27.4 (**a**) Topography of the Hatoma Knoll (**b**) Localities of active fluid venting in the Hatoma Knoll hydrothermal field

(2013) documented occurrence of Pt-Cu-Fe-bearing bismuthinite and Sn-bearing chalcopyrite in the active chimney at the Tiger site. They were attributed to have precipitated as metastable phase at a temperature above 300 °C based on the fluid inclusion data.

27.3.2 Hatoma Knoll Hydrothermal Field

The Hatoma Knoll hydrothermal field is located inside the summit crater of the Hatoma Knoll (Fig. 27.4). At the center of the summit crater, which is approximately 600 m in diameter, a dacite cone hosting large active chimney structure was recognized at a water depth of 1,470–1,485 m (Watanabe 2001). Hydrothermal activity has also been observed in several sites surrounding the central cone at water depth about 1,490 m, where the seafloor is covered with (altered) sediment. Vigorous venting of clear hydrothermal fluid up to 301 °C at the central cone seems to mark the central part of the present hydrothermal activity in the field. Emanation of liquid CO_2 droplets was observed at several active sites including the central cone (Shitashima et al. 2007).

According to the previous study (Okamoto et al. 2002; Nakano et al. 2008), mineralization in the Hatoma Knoll field can be classified into three groups; (i) anhydrite-rich chimneys, immature precipitates including sulfides (sphalerite and pyrite) disseminations in anhydrite; (ii) massive Zn-Pb-Cu sulfides, consisting of sphalerite, wurtzite, galena, tennantite-tetrahedrite, chalcopyrite and pyrite, and sometimes associated with non-stoichiometric As-sulfide; and (iii) Ba-As chimneys, composed of barite and sulfides disseminations sometimes associated with As-sulfide and/or kermesite which is likely to be secondary minerals originated from stibnite. Other than these sulfide/sulfate minerals, glob of native sulfur was sometimes recognized as attached to the ore samples.

The association between the mode of sulfide/sulfate mineralization and geochemistry of fluid emanations is relatively simple. All of the active chimneys venting high temperature fluids are predominantly composed of anhydrite, and the fluid chemistry was Cl-depleted without any exception. Barite bearing chimneys were always inactive chimneys. On the other hand, the abundant occurrences of sulfides have only been found in massive blocks which were

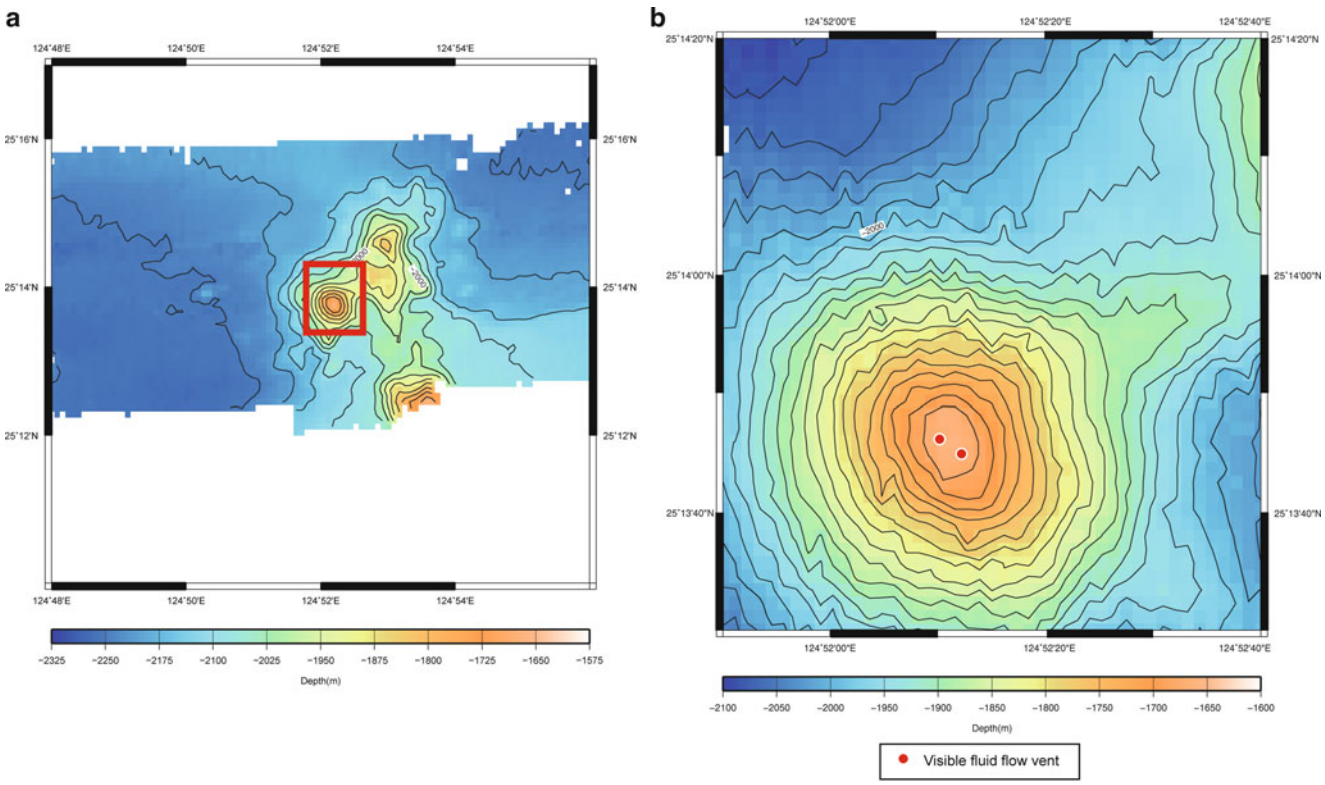

Fig. 27.5 (**a**) Topography of the Irabu Knoll (**b**) Localities of active fluid venting in the Irabu Knoll hydrothermal field

sampled from the mound structure, sometimes half buried in the seafloor.

There is a report that a Cu-rich sulfide sample approximately 5 cm in size was dredged from a small knoll (24°46.0′N, 123°59.0′E, water depth = 1,474 m) near the Hatoma Knoll (Watanabe et al. 1995). In addition, east of the Hatoma Knoll, Tarama Knoll (25°06′ N, 124°32′ E, water depth = 1,490 m) has been known as to host Fe-rich oxides mineralization in more than 100 m wide area (Yamanaka et al., Chap. 40).

27.3.3 Irabu Knoll Hydrothermal Field

Hydrothermal activity has been observed both at the top of West seamount and at the summit depression of the East seamount (Fig. 27.5). More intense activity was observed on the West seamount, where clear fluid emanations with the temperature of 151 °C were recorded in 2000 (Matsumoto et al. 2001) and 67 °C was recorded in 2011 (Fukuba et al., Chap. 39). Along a steep slope of both the West and East seamounts, continuous exposures of fresh basaltic pillow lava were observed (Matsumoto et al. 2001). Magmatism of the Irabu Knoll has been considered to occur at the cross point of an axial part of the Yaeyama Central Graben and the volcanic front of the Ryukyu trench-arc-backarc system.

Mineralization in the Irabu Knoll field was studied with great interest, since the hydrothermal activity is probably hosted by a basaltic magma (Watanabe et al. 2006). Massive sulfide samples collected from the West seamount consist of dominant sphalerite, with subordinate amounts of chalcopyrite, galena and tennantite-tetrahedrite and with some realgar. Chimney-like samples and gangue minerals-rich samples were also recovered. In a sample of massive sulfide collected from the East seamount, primary bornite and secondary covellite were identified. In summary, mineral associations of the sulfide samples did not show distinctive characteristics from other hydrothermal fields in the Okinawa Trough, with exception for a few minor minerals (Watanabe et al. 2006).

27.3.4 Hakurei Hydrothermal Field in the Izena Hole

The Hakurei field is located at the bottom of the depression of the Izena Hole (which has also been termed as the Izena Cauldron), at water depths of 1,600–1,610 m (Fig. 27.6a, b). The Izena Hole is situated along the southwestern continuation of a chain of Quaternary volcanoes of the Ryukyu arc (Shinjo et al. 1999), while its location can also be considered as the

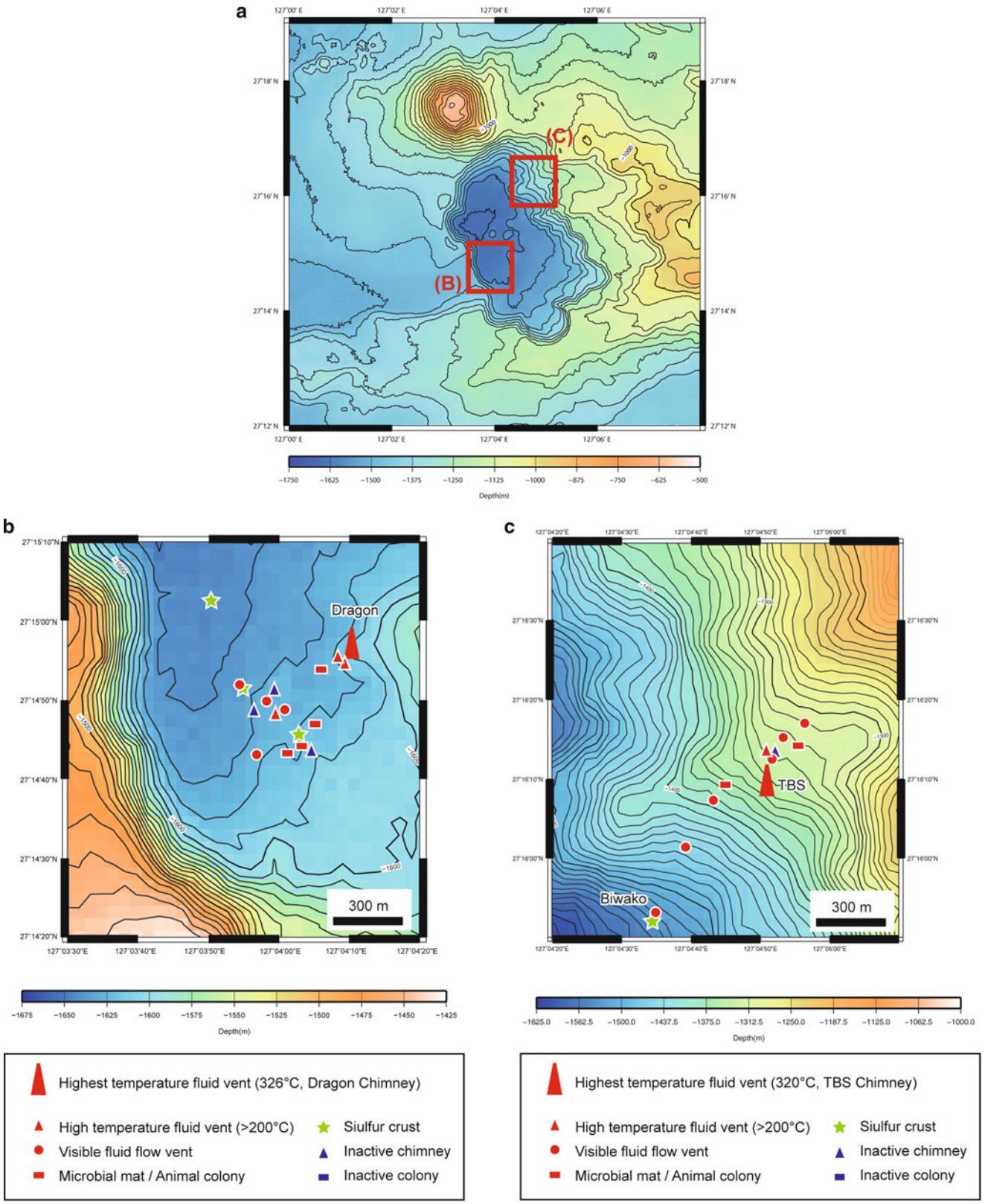

Fig. 27.6 (**a**) Topography of the Izena Hole (**b**) Localities of active fluid venting in the Hakurei field (**c**) Localities of active fluid venting in the in the Jade field

eastern end of the Aguni rift graben segment (Halbach et al. 1993). The Izena Hole is a rectangular shaped depression about 6 × 3 km. Abundant tuff breccia and woody pumice exposed on the slopes, and a center-cone like small knoll consisted of dacitic lava recognized at the center of the Hole, are evidence for recent magmatic activity (Kato et al. 1989; Kato 1990).

Hydrothermal activity has been observed over an area exceeding 500 m length during ROV studies (Ishibashi et al. 2014). Vigorous high temperature fluid venting in the Hakurei field was often associated with a complex chimney structure which was more than 10 m in height and equipped with well-developed flange structure. Effluent of high temperature fluid up to 326 °C was observed from the edges of a few meters long flange at the "Dragon" chimney located at a water depth of 1,600 m.

The Hakurei field has been explored intensively by JOGMEC (Japan Oil, Gas and Metals National Corporation) under a framework of the ocean energy and mineral resources development program since 2008. More than a hundred of drillings with BMS (Benthic Multi-coring System) have been conducted, and Zn-rich polymetallic sulfide mineralization was extensively recognized in the Hakurei field (METI 2013). BMS drilling was also conducted for scientific purpose during the TAIGA project (Ishibashi et al., Chap. 42). A sequence of core samples of 6 m length was successfully obtained and occurrence of Cu-rich sulfide mineralization was recognized (Yoshizumi et al., Chap. 43).

27.3.5 Jade Hydrothermal Field in the Izena Hole

The Jade field is located at an inside slope of the north-eastern wall of the Izena Hole (Cauldron) at a water depth of 1,550–1,300 m (Fig. 27.6a, c). This field is named as "JADE" in commemoration of Japan-Deutche collaboration during the SO-56 cruise of German Research Vessel *Sonne*, which accomplished the first discovery for the seafloor hydrothermal activity around Japan (Halbach et al. 1989). Hydrothermal activity was recognized in an area of 500 × 300 m. Venting of hydrothermal fluid up to 320 °C at the TBS chimney at water depth of 1,350 m seems to mark the central part of the present hydrothermal activity in the field. Active chimneys associated with moderate to high temperature fluid venting are concentrated in around the TBS chimney. Diffusive shimmering vents and inactive chimneys have been recognized, along the active venting, in a NE-SW direction (Nakamura et al. 1989). Emission of liquid CO_2 was identified at both extensions of the chimney line (Sakai et al. 1990). At the southwestern extension of the chimney line, thick layered consolidated structure plausibly consisted of amorphous silica and native sulfur was recognized at ~500 m apart from the TBS chimney. In the vicinity, diffusive venting of hydrothermal fluid of 104 °C associated with liquid CO_2 bubble was located, which was named as the Biwako vent (Ishibashi et al. 2014). About 3 km southwest of the Biwako Vent, the Hakurei field is located; however, the sandwiched area between the Jade and Hakurei fields has not been explored.

Mineralization in the Jade field was studied at first using massive samples collected by a TV-controlled deep-sea grab system during SO-56 cruise (Halbach et al. 1989). Sphalerite and galena were the principal minerals, which are accompanied by pyrite, marcasite, chalcopyrite, tetrahedrite-tennantite, barite, amorphous silica and anglesite. Halbach et al. (1993) distinguished five ore types from the collected samples; (i) Zn-Pb-rich sulfide ore, massive sulfide composed of sphalerite, galena, pyrite, and chalcopyrite; (ii) Ba-Zn-Pb sulfide ore, consists of a matrix of euhedral to anhedral barite with sphalerite and tennantite-tetrahedrite; (iii) Massive Zn-Cu-rich sulfide slabs, dominated by sphalerite and chalcopyrite, but contain pyrite, marcasite, covellite, realgar, galena and a Ag-Cu-sulfide; (iv) Fe-rich replacement ore, which represents fragments of mature chimneys and (v) Zn-Pb-rich impregnation ore consists of thin stringers and veinlets filled with coarse-grained sulfides in strongly altered siliceous host rocks.

Several geochemical studies have been conducted for these mineral deposits. Systematic studies on fluid inclusions (Lüders et al. 2001, 2002; Lüders and Niedermann 2010) demonstrated evidence for subseafloor phase separation and its influence on the mineralization. Lead isotope data from ores, igneous rocks and sediments suggested that both surrounding sediments and volcanic rocks contributed comparable amounts of lead to the deposit (Halbach et al. 1997). Zeng et al. (2009) reported minor elements composition and U-series isotope data of sulfide/sulfate deposits. Noguchi et al. (2011) reported $^{87}Sr/^{86}Sr$ data for barite collected from the Jade and Hakurei fields, which suggest a significant contribution of sediment.

27.3.6 Clam Hydrothermal Field Along the Iheya Ridge

The Clam hydrothermal field is located at a small depression along the eastern part of the Iheya Ridge where basalt breccia occurs (Fig. 27.7). In 1988, the Clam Site was the second discovery of high temperature hydrothermal activity in the Okinawa Trough. A deep-tow TV camera survey at this site revealed the presence of a clam colony. Intensely hydrothermally altered and sometimes consolidated sediment was recognized in a small area (100 × 50 m) at a water depth of 1,392 m (Nakashima et al. 1995). In some areas, forests of small chimneys (less than 10 cm in height) were recognized along the fissure, where calm diffusive emanations of clear fluids occur. The landmark feature of

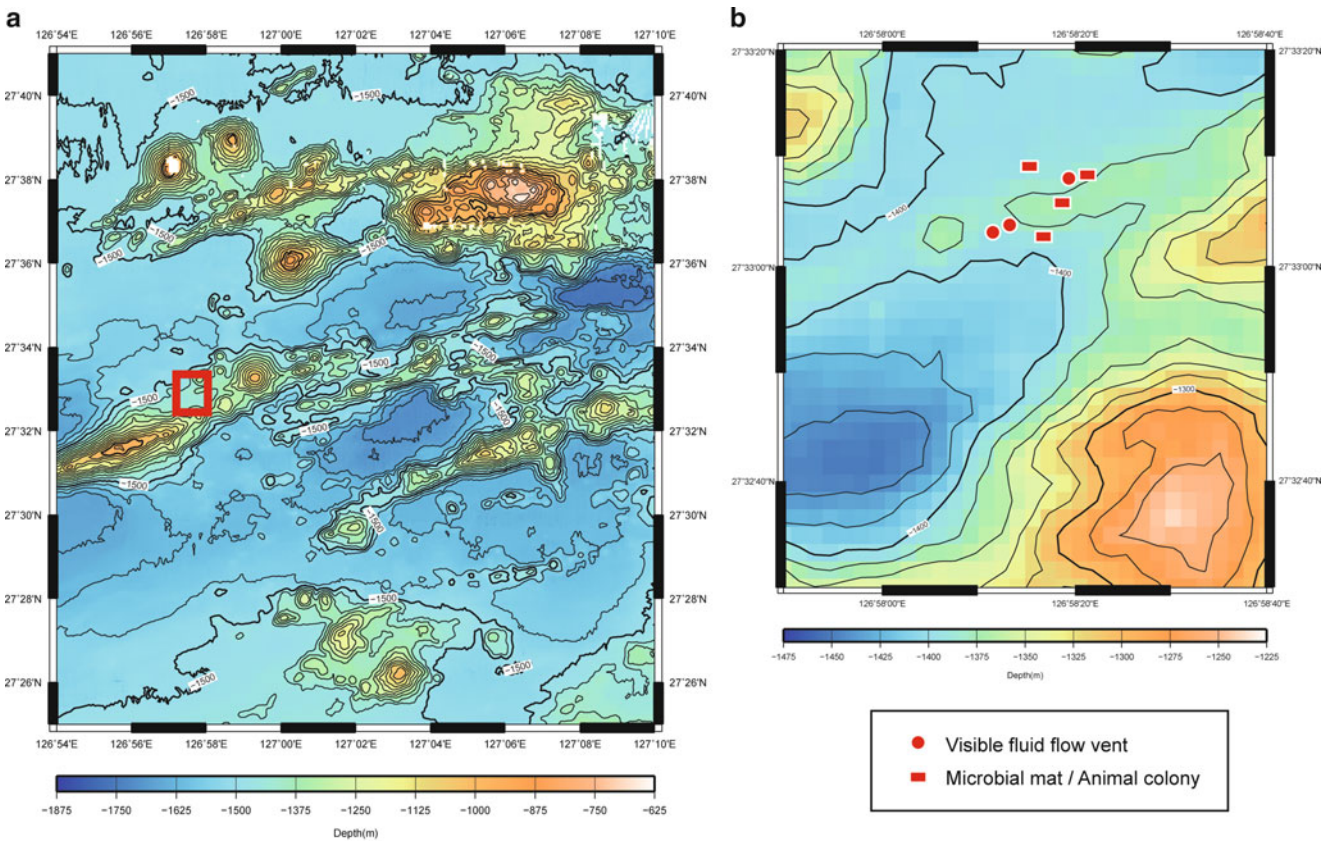

Fig. 27.7 (**a**) Topography of the Iheya Ridge (**b**) Localities of active fluid venting in the Clam hydrothermal field. Note that map (**a**) is not the same scale as other figures

the Clam hydrothermal field, 2 m high cone-shaped chimney structure called the Pyramid chimney discharged hydrothermal fluid from the foot part of the structure. The fluid temperature fluctuated year to year of sampling, and the highest temperature was recorded as 220 °C in 1988. Venting was ceased in 1990, and since then, dive studies have not been conducted in this field.

Mineralization in the Clam field was characterized by carbonate precipitates (Nakashima et al. 1995). The carbonates collected from the chimney structure consisted of manganoan calcite, rhodochrosite, anhydrite, and amorphous silica, with only trace amounts of sulfides including wurtzite, pyrrhotite, chalcopyrite, isocubanite and realgar present as disseminations (Izawa et al. 1991). Native sulfur was also recovered from the outer region of the field. Carbonates precipitation should be related to high alkalinity of the hydrothermal fluid, which is accompanied with increase of ammonium ion and ^{34}S-enriched sulfate (Gamo et al. 1991). As they demonstrated, this fluid chemistry would be attributed to be affected by sulfate reduction utilizing supplied hydrothermal methane and/or organic matter decomposition in the sediment layer, which in turn induces carbonate mineralization. This idea is supported by microscopic observations where replacement of anhydrite and gypsum by carbonate or sulfide minerals was recognized by the crystal texture (Nakashima et al. 1995).

At the summit area of the Natsushima 84–1 knoll (water depth of 1,540 m), which is located about 15 km east extension of the Iheya Ridge, low-temperature hydrothermal activity was first discovered in 1986 in the middle Okinawa Trough (Kimura et al. 1988). Shimmering water from one of the mounds has a temperature 2–3 °C higher than that of the ambient seawater, while methane and manganese anomalies were detected. The mound was covered with a yellowish brown deposit of Fe-rich smectite and Fe-Mn oxyhydroxide (Masuda et al. 1987).

27.3.7 Iheya North Knoll Hydrothermal Field

The Iheya North Knoll hydrothermal field is located along the eastern slope (at water depth about 1,000 m) of a small knoll which constitutes a volcanic complex of the Iheya North Knoll (Fig. 27.8). Seismic studies around the Iheya North Koll demonstrated relatively disordered seismic reflectors as deep as 400–500 mbsf (meters below the

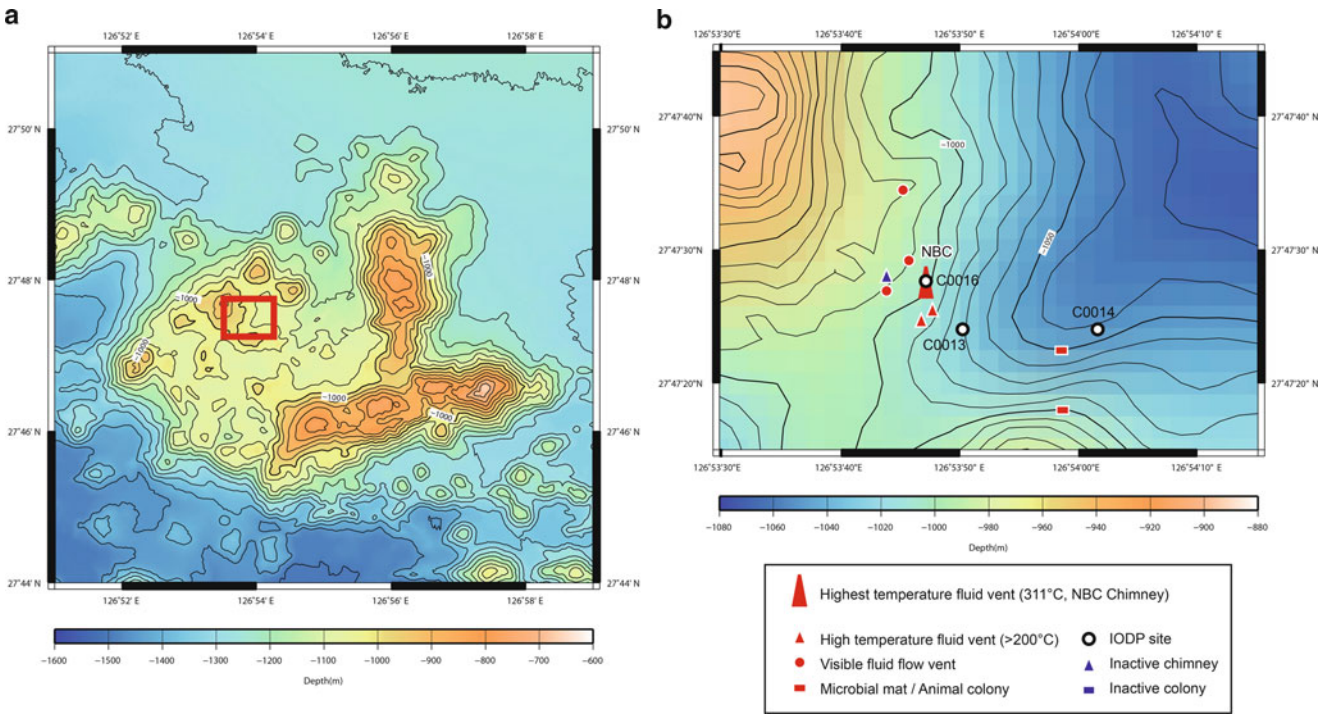

Fig. 27.8 (**a**) Topography of the Iheya North Knoll (**b**) Localities of active fluid venting in the Iheya North Knoll hydrothermal field

seafloor) in the Central Valley that were surrounded by small knolls (Tsuji et al. 2012). This suggested presence of pumiceous volcaniclastic flow deposits below surficial hemipelagic sediments, rather than massive igneous rocks. Indeed, previous geological studies using gravity cores have recovered a large volume of pumiceous volcaniclastic sediment in the Central Valley.

About ten of the active hydrothermal mounds are concentrated in a small region, aligned north to south. Many of the mounds host active fluid venting and sulfide/sulfate mineralization. A large mound of more than 30 m height associated with vigorous venting of clear fluid with the highest temperature of 311 °C (called NBC (North Big Chimney) mound) appears to mark a center of the hydrothermal activity at the Iheya North Knoll (Nakagawa et al. 2005). A diversity of fluid chemistry and temperature within the hydrothermal field has been attributed to subseafloor phase separation (Kawagucci et al. 2011).

Mineralization in the Iheya North Knoll was studied based on analysis of active and inactive chimneys collected from the seafloor (Ueno et al. 2003). Main sulfide minerals are sphalerite, wurtzite, galena, pyrite, marcasite, chalcopyrite and tennantite-tetrahedrite. Luzonite and freieslebenite and covellite were identified in a few samples. Gangue sulfates consist mainly of barite, gypsum and anhydrite.

During scientific drilling by IODP Expedition 331, a variety of hydrothermal sulfide/sulfate deposits were successfully recovered from below the seafloor (Takai et al. 2011, 2012; Yeats et al. 2012; Ishibashi et al. 2013). Blocks of massive sphalerite-(pyrite-chalcopyrite)-rich sulfides, coarsely crystalline anhydrite aggregate and silicified rocks disseminated with veins contained pyrite were identified in the core drilled at the flank of the NBC (North Big Chimney) hydrothermal mound. Sulfide mineralization was identified also within intensively altered sediment at two drilled sites, 100 and 450 m east of the NBC mound. Occurrence of sulfides in the upper portions was characterized by detrital grains which included euhedral fragments of sphalerite and pyrite. In the core at greater depths, quartz-sulfide veins were present among silicified volcanic breccia, some of which contained chalcopyrite, sphalerite and galena.

27.3.8 Yoron Hole Hydrothermal Field

The Yoron Hole hydrothermal field is located on the northeastern slope of a small depression termed as the Yoron Hole (Fig. 27.9). This caldera-like depression approximately 3 km in a diameter was recently identified by detailed mapping (Horisako et al. 2010). Hydrothermal activity was only observed at two small areas at water depths of 560–590 m (Fukuba et al., Chap. 38). All of the active smokers discharged clear fluid, with the highest temperature of 247 °C.

Active chimney samples collected from the Yoron Hole hydrothermal field consisted of dominantly barite associated

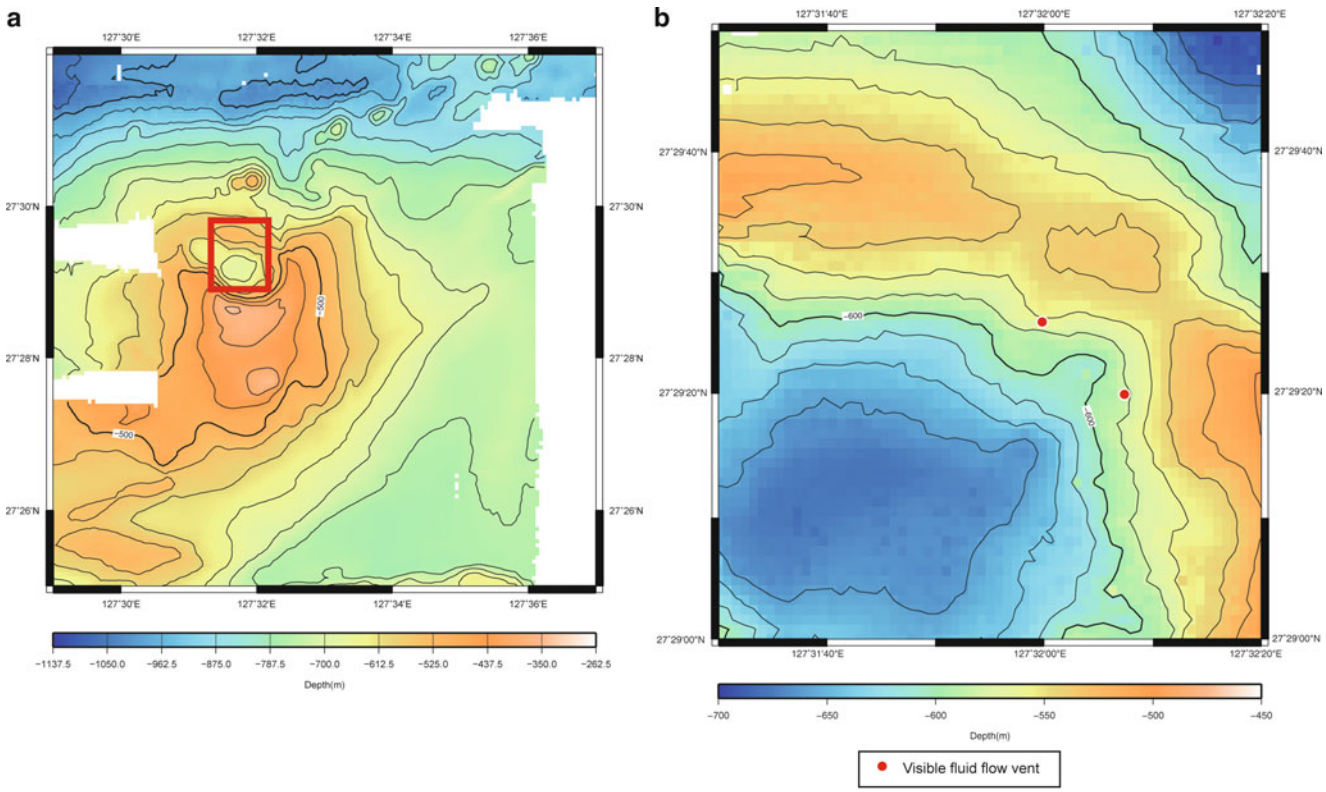

Fig. 27.9 (**a**) Topography of the Yoron Hole (**b**) Localities of active fluid venting in the Yoron Hole hydrothermal field

with sulfide minerals of sphalerite, galena pyrite tetrahedrite-tennantite or associated with combination of stibnite, orpiment and Pb-Ag-Sb sulfide (Ooki et al. 2012). The latter mineral assemblage could be attributed to low temperature mineralization. Massive sulfide was recognized only at one site, which mineral association was composed of dominant sphalerite and pyrite, minor chalcopyrite, stibnite, covellite and tetrahedrite-tennantite.

27.3.9 Minami-Ensei Knoll Hydrothermal Fields

The Minami-Ensei Knoll hydrothermal field is located in one of small depressions (named as C depression) of the Minami-Ensei Knoll (Fig. 27.10). This knoll is characterized by complicated topography which includes small hills and depressions within a circular rim of 2 km radius. Poorly vesciculated pumice, diorite, and granite samples were recovered from this knoll implying the knoll is a volcanic complex. The "C depression" of 300 × 100 m in size is located on the western slope of the knoll at a water depth of ~700 m. Several rather small chimneys were recognized as aligned along an N–S direction. Many of them discharged transparent fluids with the highest temperature of 278 °C (Chiba et al. 1993).

According to Nakashima et al. (1995), mineralization in the Minami-Ensei Knoll field can be classified into four types; (i) anhydrite-rich chimneys, immature precipitates of anhydrite and/or gypsum including sulfide disseminations consisting of chalcopyrite, sphalerite, pyrite, galena, anglesite; (ii) massive Zn-Pb-Cu sulfides, consisting of pyrite, sphalerite, galena and chalcopyrite; (iii) clastic layers consist of both volcanic and hydrothermal particles. Volcanic material is mainly pumiceous fragments which were filled up with sulfide minerals including sphalerite, pyrite, chalcopyrite, galena, tetrahedrite-tennantite, realgar, and stibnite. All of the active chimneys are fragile anhydrite or gypsum chimney, and massive or sheeted sulfide are collected only from the seafloor.

27.3.10 Hydrothermal Mineralization in the North Okinawa Trough

The northern Okinawa Trough had been long considered be devoid of active volcanism (e.g. Kimura 1996), while the volcanic front is obviously recognized as a series of the Tokara volcanic islands. Yokose et al. (2010) proposed that this volcanic chain extends in a southwest direction to submarine knolls along the North Okinawa Trough, based on

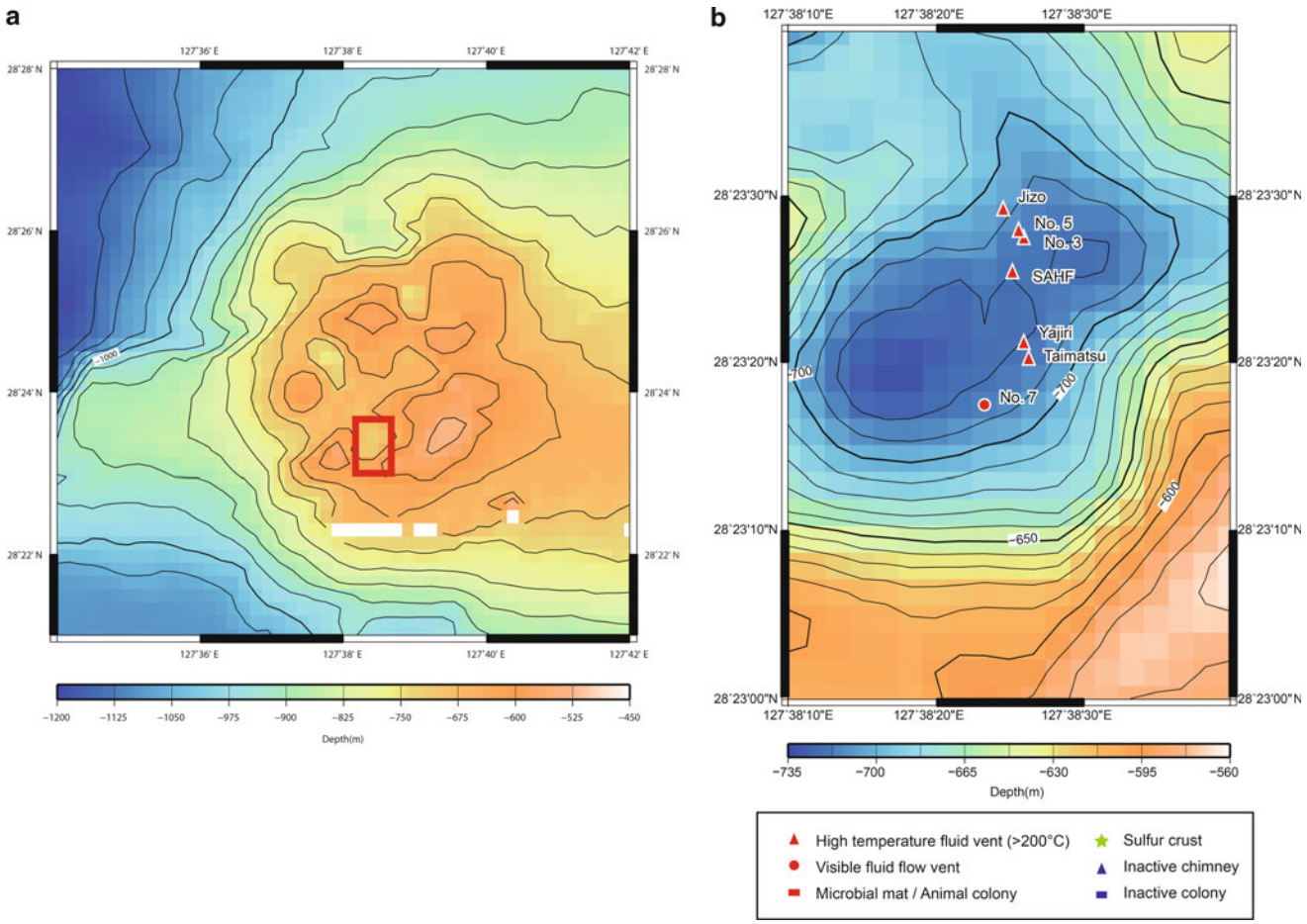

Fig. 27.10 (**a**) Topography of the Minami-Ensei Knoll (**b**) Localities of active fluid venting in the Minami-Ensei Knoll hydrothermal field

petrologic study together with detailed mapping. They also recognized some submarine caldera structures in the volcano chain, from where subangular to angular cobble-boulder fragments of lava, scoria and pumice of volcanic rocks were abundantly recovered by dredging. As mineralized samples, Fe-Mn oxide crusts enriched in As and Mo were documented as dredged from the Amami caldera, one of the submarine calderas (Yokose et al. 2009). The northern Okinawa Trough has become one of target regions for recent exploration of seafloor hydrothermal deposits.

27.4 Characteristics of Hydrothermal Mineralization in the Okinawa Trough

27.4.1 Chemical Signature of Hydrothermal Ores

As described in the previous section, a diverse range of mineralization has been recognized in most of the hydrothermal fields in the Okinawa Trough. For sulfide mineralization, sphalerite and galena are the principal minerals in most of the fields. Pyrite, chalcopyrite, marcasite, and/or tetrahedrite-tennantite are also commonly identified. Sulfates such as anhydrite, gypsum and barite are also recognized abundantly in all the fields. On the other hand, carbonate has only been recognized in two fields, the Daiyon-Yonaguni Knoll and Clam field.

To confirm this common signature, bulk chemical composition of mineralized samples collected from the hydrothermal fields in the Okinawa Trough is compiled in Fig. 27.11. A plus symbol in the figure indicates an average grade of 392 drilled core samples from the Hakurei field (METI 2013); which was reported as Cu = 0.51 wt%, Pb = 3.49 wt%, Zn = 9.69 wt%, Fe = 30.68 wt%, Au = 3.2 g/t and Ag = 250 g/t. The data plot is likely to be shifted to Fe-rich; however this is mainly because a significant amount of pyrite in the alteration zone was included. Sulfide ores from the Okinawa Trough are notably enriched with Zn and Pb compared with sulfide samples collected from seafloor hydrothermal fields in the mid-ocean ridge setting. As several researchers have pointed out, above signatures of mineralization found in the Okinawa Trough is similar to that of Kuroko-type deposits which are usually polymetallic

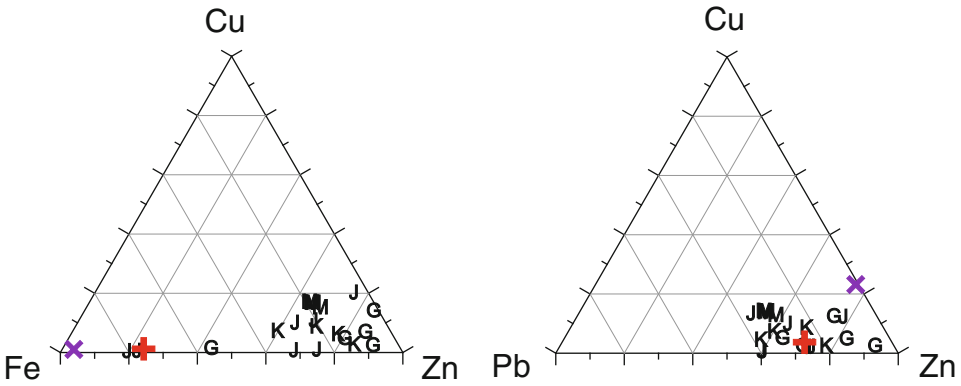

Fig. 27.11 Ternary diagrams for major chemical composition of hydrothermal ore samples collected from the hydrothermal fields in the Okinawa Trough. A *red cross mark* plots an averaged value of 392 drilled core samples from the Hakurei field (METI 2013). A *purple cross mark plots* an averaged value of drilled cores obtained from the Bent Hill massive sulfide deposit in the Middle Valley of the Juan de Fuca Ridge during ODP Leg 169 (Lawrie and Miller 2000). *Alphabetical symbols* represent a name of a hydrothermal field where samples were collected, *G*: Daiyon-Yonaguni Knoll field (Suzuki et al. 2008), *M*: Hatoma Knoll field (Okamoto et al. 2002), *J*: Jade site in the Izena Hole (Halbach et al. 1993), *K*: Iheya North Knoll field (Ueno et al. 2003)

(Zn-Pb-Cu-Ag-Au, with trace metal associations). It is notable that the common signature in the bulk chemical composition is recognized in spite of a diverse range of a water depth and geologic setting where the hydrothermal activity is hosted. This signature can be attributed to reflect the chemical signature of the ore fluid which transports metals. It is reasonable to expect enrichment in Pb in the hydrothermal ores from the Okinawa Trough, compared with those from the mid-ocean ridge setting, as both island arc magma and surrounding continental crust are enriched in Pb (e.g. Halbach et al. 1997).

Enrichment in some specific trace elements such as As, Sb and Ag has been noticed in sulfide ores from the Okinawa Trough both by geochemical studies (e.g., Noguchi et al. 2007) and mineralogical studies (e.g., Halbach et al. 1989). Sulfide minerals of these elements have been considered as precipitated in the later low-temperature stages based on their occurrence often found in the outer part of the ores (Halbach et al. 1989). Enrichment in these elements is observed also in the Kuroko-type deposits, but not so much considerable (Glasby et al. 2008). However, this difference has not been well discussed.

27.4.2 Style of Mineralization Below the Active Hydrothermal Field

Although several studies have described the characteristics of hydrothermal mineralization at sites across the Okinawa Trough, most of them were based on analytical results of mineralized samples collected from above the seafloor using a submersible or dredge. This situation is quite different from that our knowledge about Kuroko-type deposits has been accumulated by studying numerous core samples drilled for underground exploration. Because the stratabound mineralization is one of important characteristics for the Kuroko-type deposits, our present understanding of mineralization in the Okinawa Trough might be distorted due to the sampling bias. Deep drilling during IODP Expedition 331 provided the first opportunity to overcome this problem by revealing the subseafloor hydrothermal structure at the Iheya North Knoll (Takai et al. 2012).

Lithologies at the Iheya North Knoll field are characterized by a complex mixed sequence of coarse pumiceous volcaniclastic and fine hemipelagic sediments, overlying dacitic to rhyolitic volcanic substrate (Yeats et al. 2012). Together with the seismic image obtained by previous investigation (Tsuji et al. 2012), these lithologies are likely to be horizontally continuous between the drilled sites up to 1 km (Takai et al. 2012). Sulfide occurrences are shown in a compilation of vertical profiles at two drilled sites; C0013 located at 100 m east of the central mound and C0014 at 450 m east, in Fig. 27.12a. Sulfide mineralization at these two sites was characterized by the occurrence of detrital grains which included euhedral crystals of sphalerite and pyrite in the upper portions of sediment, 0–12 mbsf at C0013 and 0–19 mbsf at C0014 (Takai et al. 2012; Ishibashi et al. 2013). Sediment in some sections collected from Site C0013E was heavily mineralized, with layers up to 10 cm in thickness probably exceeding 50 % total sulfide, while the sulfidic grits were relatively scarce at Site C0014. In the core at greater depths (26–28 mbsf at C0013 and, 109–113 mbsf and 127 mbsf at C0014), quartz-sulfide veins among silicified volcanic breccia were present; some of them contained chalcopyrite, sphalerite and galena. Sulfate minerals, anhydrite and/or gypsum were abundant in the intermediate layer (6–24 mbsf at C0013 and 57–100 mbsf at C0014), sometimes breccia with euhedral anhydrite clasts were noted.

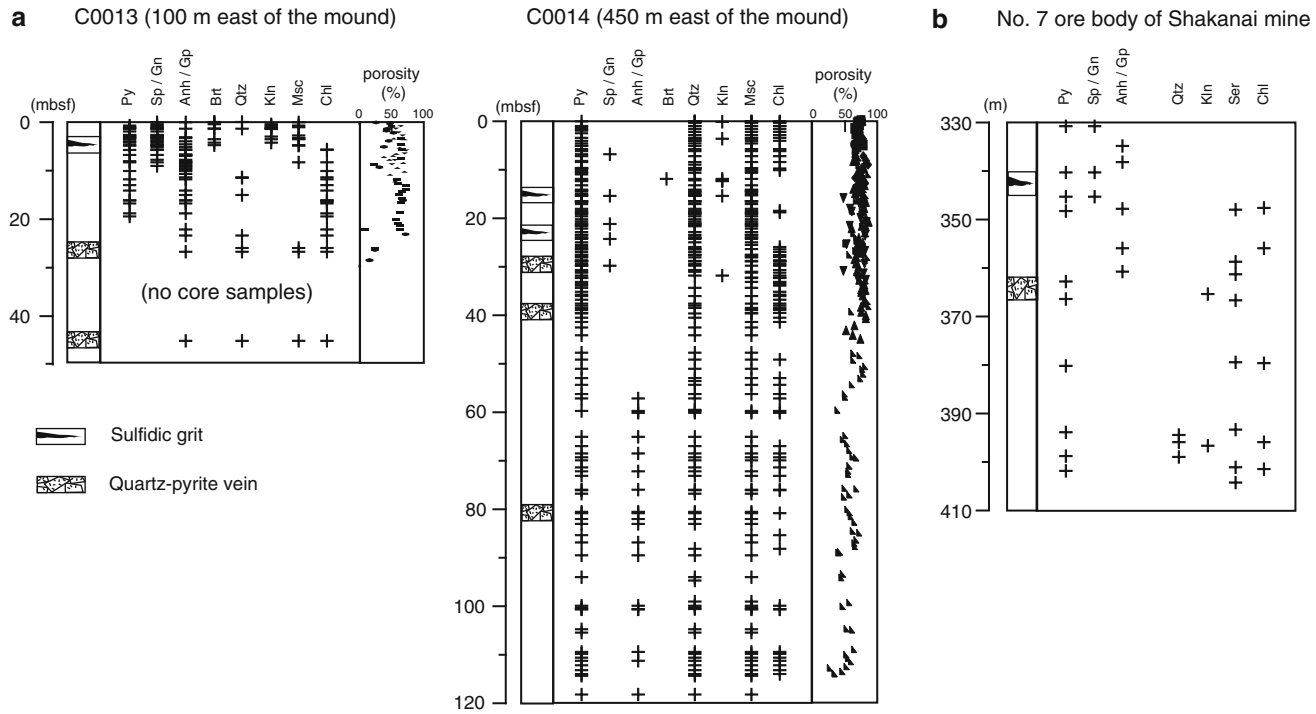

Fig. 27.12 Comparison of occurrence of dominant sulfide, sulfate and clay minerals between (**a**) cores obtained from Sites C0013 and C0014 on the Iheya North Knoll during IODP Expedition 331, based on results of onboard XRD analysis (Takai et al. 2011), and (**b**) cores obtained from the No. 161 borehole that penetrated the No.7 ore body of the Shakanai mine, a typical Kuroko-type deposit in northeast Japan (modified after Iijima 1974). In Fig. 27.12a, profiles of porosity of the core samples determined by onboard physical property measurements are shown together (Takai et al. 2011). In Fig. 27.12b, a depth of 330 m corresponded to the top of the Shakanai Formation of Nishikurosawa Stage in middle Miocene. Abbreviation for mineral names: *Py* pyrite, *Sp*/*Gn* sphalerite and/or galena, *Anh*/*Gp* anhydrite and/or gypsum, *Brt* barite, *Qtz* quratz, *Kln* kaolinite, *Ms* muscovite, *Chl* chlorite, *Ser* sericite (mainly muscovite)

By drilling into the flank part of the active hydrothermal mound (NBC mound) at Site C0016, a variety of mineralization styles were successfully recovered (Takai et al. 2011; Yeats et al. 2012). Blocks of massive and semi massive sulfide were obtained from the first core (0–9 mbsf). Underlying recovered lithologies included snow-white, coarsely crystalline anhydrite aggregate with a dark vein of pyrite (9–27 mbsf), along with silicified and variably altered volcanic rocks. Shipboard work by Yeats et al. (2012) demonstrated that recovered massive sulfides show clear evidence for formation by both surface detrital and subsurface chemical processes, with some sphalerite precipitation in void spaces. Sulfide and sulfate paragenesis is consistent with an evolving system, where early sphalerite mineralization is overprinted by pyrite and then chalcopyrite as the temperature increases, prior to late sphalerite precipitation as it cools (Yeats et al. 2012). Late coarse anhydrite is consistent with final seawater influx (Yeats et al. 2012). Quartz-muscovite/illite and quartz-chlorite alteration of underlying lithologies (Takai et al. 2011; Yeats et al. 2012) are consistent with proximal hydrothermal alteration associated with Kuroko-type VMS deposits.

The vertical profiles of mineral occurrence documented for the obtained cores are directly compared to those from Kuroko-type deposits in Fig. 27.12b. A typical Kuroko-type VMS deposit, according to the classic study by Sato (1974), is usually composed of gypsum ore, siliceous ore, yellow ore, black ore, barite ore and ferruginous chert ore in stratigraphically ascending order. As well as the sphalerite-rich massive sulfides, the sulfidic grits in the upper portion sediment could correspond to “black ore”. The siliceous volcanic breccia with sulfide veins may correspond to the “siliceous ore”. Material reminiscent of Kuroko-type “yellow ore” was not identified in the cores. The interval of thick hydrothermal alteration with abundant anhydrite may be corresponded to the “gypsum ore”, but may also represent seawater influx into the system. The agreement in the 2-D structure both in vertical and horizontal scale supports the idea that mineralization recognized at the Iheya North Knoll is associated with a hydrothermal system similar to that formed Kuroko-type VMS deposits.

Another important success during the IODP drilling was recovery of the sphalerite-rich massive sulfide blocks that strongly resemble the “black ore” of Kuroko-type deposits

(Yeats et al. 2012). Clastic textures comprising fragments of hydrothermal clay and siliceous volcanic material were recognized by microscopic observation, which is attributed to be formed by subsurface chemical processes involving surface detrital material. On the other hand, chimneys collected from active or inactive vents on the seafloor often showed distinctive mineral texture that is explained by a result of precipitations during quench process, such as colloforms mainly consists of pyrite, dendritic growth texture, and also by small grain size (Ueno et al. 2003). These textures have been rarely recognized in Kuroko-type deposits, as demonstrated by Shikazono and Kusakabe (1999). It is notable that the mineralization observed in the drilled cores collected from 100 to 450 m apart from the hydrothermal mound is characterized by occurrence of sulfidic detrital grains. By microscopic observation, euhedral crystals of sphalerite and pyrite were identified as closely associated with abundant clay minerals (Ishibashi et al. 2013). This texture is also quite distinctive from the texture recognized in chimneys collected from active or inactive vents.

27.4.3 Diverse Range of Mineralization and Fluid Chemistry

Active hydrothermal fields in the Okinawa Trough are located in rather shallow water depth from 700 to 1,600 m. Moreover, the highest temperatures of venting fluids are close to the boiling temperature of the seawater at pressure corresponding to the water depth of the seafloor in many fields. Geochemical studies of venting fluids indicated evidence for subseafloor phase separation in several hydrothermal fields in the Okinawa Trough (Kawagucci, Chap. 30). Evidence for subseafloor phase separation was also recognized by a systematic study of fluid inclusions in the Jade field (Lüders et al. 2001, 2002). As several previous studies pointed out that phase separation should play important roles in mineralization process, because it causes drastic change in fluid chemistry (e.g. Drummond and Ohmoto 1985).

As described in the Sect. 27.3.1, the relationship between a diverse range of mineralization styles and intra-field variation of fluid chemistry was recognized in the Daiyon-Yonaguni Knoll hydrothermal field, and attributed to influence of subseafloor phase separation (Suzuki et al. 2008). Sulfide mineralization was dominantly observed in chimney-mound structures in the proximal area where vigorous venting of high temperature and slightly Cl-enriched fluid are concentrated. Carbonate mineralization was found in the distal area where Cl-depleted and transparent fluid venting sometimes associated with discharge of CO_2 liquid droplets was observed. Similar intra-field diversity in fluid chemistry was recognized also in the Jade field (Ishibashi et al. 2014). Such a geographical distribution of hydrothermal discharge is similar to the diversity of fluid discharges observed in a subaerial geothermal field. As Giggenbach et al. (1994) documented for a geothermal field in New Zealand, high-temperature Na-Cl type springs from the brine phase are located in the central area and acid-sulfate type springs originated from the vapor phase are located in the peripheral area in many cases. Since the phase separation of the hydrothermal fluids in the Okinawa Trough occurs in the sub-critical condition, hydrological behavior of two phases should be similar to the case of boiling occurs in an on land geothermal system rather than that of super-critical phase separation in the deep region (e.g. in the vicinity of a magma body).

Venting of hydrothermal fluids experienced boiling (phase separation in the sub-critical condition) has been documented by several studies (e.g. Butterfield et al. 1990; Takai et al. 2008). They demonstrated diversity of observed fluid chemistry is almost quantitatively explained by participation of chemical species during the subseafloor boiling; gas species such as CO_2 and H_2S into the vapor phase, while ion species such as Cl and Na into the liquid phase. They also mentioned that hydrothermal fluid in natural systems discharges from the seafloor before physical segregation of vapor and liquid phases completes, because phase separation usually occurs during rapid fluid ascending. In the Daiyon-Yonaguni Knoll hydrothermal system, the high temperature Cl-enriched hydrothermal fluids are interpreted as the mainstream of the ascending fluid which has experienced vapor loss during the boiling, while Cl-depleted hydrothermal fluids are condensate of the vapor-rich phase which has branched (Suzuki et al. 2008).

Participation of ore-forming elements during phase separation (both in subcritical and supercritical conditions) was discussed in detail in a review by Heinrich (2007). Elements which forms chloride-complex such as Na, Fe, Zn, Pb partition more into the liquid phase, basically in proportion to Cl enrichment (Pokrovski et al. 2005). Behavior of Cu is unique; Cu follows the same trend as Zn under S-free condition, while addition of S into the system as an additional complexing ligand causes enrichment in Cu in favor of the vapor phase (Nagaseki and Hayashi 2008). Hydroxy-complexed elements including As, Sb and Au reach relatively higher concentrations in the vapor phase. These results indicate fractionation between vapor and liquid phases is highly element-specific, suggesting phase separation can be an important step in the segregation of elements to form certain types of ore deposits (Heinrich 2007). In natural systems, also drastic pH change should associate with phase separation due to favorable participation of gas species in the vapor phase (Drummond and Ohmoto 1985). Because the solubility of metal elements is substantially controlled by fluid pH, this effect makes the behavior of metals during phase separation more complex. Irrespective

of such complex behaviors, the sulfide mineralization associated with vigorous venting of high temperature and slightly Cl-enriched fluid in the Daiyon-Yonaguni field is reasonable, because influence of phase segregation would be limited based on the observed Cl concentration slightly higher than the seawater (Suzuki et al. 2008).

On the other hand, it is notable that only Cl-depleted hydrothermal fluid was recognized in the Hatoma Knoll and Minami-Ensei Knoll hydrothermal fields. All the active chimneys in these two fields are anhydrite dominant sulfate chimney, in which sulfide minerals are identified only as disseminated. Exclusive anhydrite mineralization observed in the entire hydrothermal field could be explained by less participation of metals into the vapor phase during the subseafloor phase separation, although cooling of the ascending hydrothermal fluid should be another important factor which induces low solubility of metal elements, especially for Cu. Similar significant metal loss associated with fluid phase separation was documented for a subaerial but seawater-dominated geothermal system in Iceland (Hardartóttir et al. 2009). While hydrothermal fluids collected from in situ wells at 1,350–1,500 m depth contained sub-millimolar order of Fe, Cu and Zn, samples collected at the surface of the same wells had orders of magnitude lower metal concentrations. This significant difference was attributed to precipitation caused by boiling during depressurization, which was confirmed by occurrence of Cu-rich scales deposit at the orifice of the well (Hardartóttir et al. 2010). Based on this result, they proposed that subseafloor mineralization associated with phase separation may occur in some submarine hydrothermal systems where boiling of fluids occur before discharging from seafloor vents. If it is the case applicable to the hydrothermal fields in the Okinawa Trough, subseafloor mineralization could be one of important processes for formation of VMS deposits. This idea may be supported by an observation of post-drilling changes after IODP Expedition 331 (Kawagucci et al. 2013), which documented rapid growth of sulfide-sulfate chimney structure on the artificial vent drilled as Hole C0016A into the NBC mound (Nozaki et al. 2013). They reported occurrence of sulfide minerals (mainly composed of chalcopyrite, sphalerite, and galena) inside of the newly grown chimney associated with venting of Cl-enriched hydrothermal fluid after drilling, while only a small anhydrite chimney had been observed as active vents on the NBC mound associated with Cl-depleted fluid emanation.

The diverse range of mineralization in the hydrothermal fields in the Okinawa Trough is also recognized in a compilation of the FeS content in sphalerite/wurtzite (Fig. 27.13). Many of collected samples show significant low FeS content in ZnS less than 5 mol%. On the other hand, higher FeS content in ZnS than 10 mol% was recognized in the samples collected from the Daiyon-Yonaguni and Jade field, where

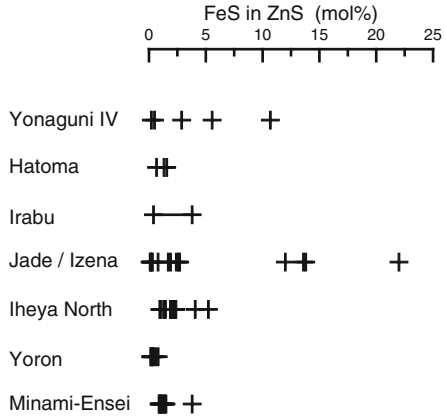

Fig. 27.13 Comparison of FeS content in sphalerite/wurzite (mol%) for samples collected from the Okinawa Trough. Data sources are as bellows; Daiyon-Yonaguni Knoll field (Suzuki et al. 2008), Hatoma Knoll field (Nakano et al. 2008), Irabu Knoll field (Watanabe et al. 2006), Jade field in the Izena Hole (Halbach et al. 1993), Iheya North Knoll field (Ueno et al. 2003), Yoron Hole and Minami-Ensei Knoll fields (Ooki et al. 2012)

brine-rich hydrothermal fluid venting was observed on the seafloor. In these samples, the high FeS sphalerite was associated with sulfide minerals formed under reductive environment such as pyrrohtite. These two groups are likely to correspond to mineralization under Cl-depleted (gas-rich) and Cl-enriched (gas-lost) hydrothermal fluids, as discussed in the previous study (Suzuki et al. 2008). However, the compiled FeS/ZnS ratio is rather low compared with that observed in VMS deposits, which may be distorted due to the sampling bias in the seafloor studies. Previous studies on VMS deposit (e.g. McLeod and Stanton 1984) have demonstrated systematic change in FeS/ZnS in stratiform ores. Systematic sampling preferably including drilled core samples would be required to discuss geochemical environment for mineralization.

27.4.4 Tectonic Setting Favorable for Effective Formation of Volcanogenic Massive Sulfide Deposits

As discussed in the Sect. 27.2, the Okinawa Trough is a back-arc basin in the rifting stage. Development of hydrothermal systems would be stimulated by fault networks that act as fluid conduits and the frequent intrusion of a magma that supplies a heat source. Thick accumulations of terrigenous and/or volcanic sediment on the seafloor could be another important geological feature which favorable for ore deposit formation. The sulfide occurrence within the sediment layer revealed by IODP Expedition 331 suggests highly porous volcaniclastic materials provide sufficient space for fluid flow and mineral precipitation (Ishibashi

et al. 2013). As shown in Fig. 27.12a, the porosity of hydrothermally altered sediment drastically decreased in the layer of anhydrite formation, but remained high in the layer of clay minerals alteration which includes the layers of sulfide mineralization. This advantage would be endorsed by comparison with mineralization found in drilled core samples obtained during previous scientific drillings. During ODP Leg 193 conducted in the Pacmanus field in the East Manus Basin, only minor mineralization was observed in fissures of dacite lava dome as vein type inlet (Binns et al. 2007). On the other hand, drilling during ODP Legs 139 and 169 conducted in the Middle Valley revealed formation of massive sulfide ore body below the seafloor in a tectonic setting of sedimented ridge where axial valley of terminated spreading ridge is covered with thick terrigenous turbidite (Zierenberg and Miller 2000; Goodfellow and Franklin 1993).

Considering these points, geological structure of a depression associated with magmatic intrusions is considered favorable for formation of massive sulfide deposits. A large size caldera volcano would provide such an environment in an island-arc setting. In the early rifting stage, a depression structure formed by graben surrounded by faulting would be alternative candidate. This idea has been proposed by several researchers, for formation of Kuroko-type deposits (e.g. Ohmoto 1996). The Jade and Hakurei fields in the Izena Hole would be listed as the top of such examples, although volcanic activity in this hole has not been well studied. Some previous studies pointed out geographic distribution of hydrothermal mounds in the Izena Hole could be comparable to distribution of ore deposits in the Hokuroku Basin in the northeast Japan (e.g. Nakamura et al. 1989).

As Glasby and Notsu (2003) noted, several active hydrothermal fields have been discovered in clusters in the middle Okinawa Trough, where is called as the VAMP area (the Volcanic Arc Migration Phenomenon) by Sibuet et al. (1998) (Fig. 27.1). Although artificial bias of exploration efforts cannot be excluded as a possible reason, some ideas have been proposed for explanation. Halbach et al. (1989) noticed this area is a kind of overlapping area of two axial graben structures. Sibuet et al. (1998) emphasized subduction of the Daito Ridge extending beneath the VAMP area has induced stress at the base of the arc with the result that cracks propagated through the overlying brittle lithosphere acted as conduits for magmas with arc affinities to erupt at the seafloor (Fig. 27.1). Yokose et al. (2010) pointed out a series of a large size seafloor caldera structure in the North Okinawa Trough, as an extension of volcanoes of Kyushu Islands-Tokara islands. Although the volcanic front becomes unclear in the middle Okinawa Trough, the VAMP area would be assigned as the extension of this arc caldera chain.

A recent study discussed evolution of the geologic setting of the northeast Honshu arc from Early Eocene to Early Miocene (Yamada and Yoshida 2011). They proposed that extensive volcanism in the rifting stage from 21 to 14 Ma which hosted formation of Kuroko-type deposits around the Hokuroku area (in its final period) is related to the back-arc spreading stage before 21 Ma at the Yamato Basin located at several hundred km west, and recognized an eastward migration of volcanic activity with time (Yamada and Yoshida 2011). As discussed in the Sect. 27.2, geologic setting of the Okinawa Trough is considered as still in the rifting stage and evidence for the late stage in the rifting activity was appeared in the South Okinawa Trough. We may speculate about a forward stage when spreading of the Okinawa Trough starts from the southern end. If similar eastward migration of volcanic activity with time occurs in the Okinawa Trough, the middle Okinawa Trough might be the area where extensive volcanism in the rifting stimulates significant formation of VMS deposits.

27.5 Summary

Mineralization recognized in the seafloor hydrothermal systems of the Okinawa Trough have been considered analogous to the formation of ancient Kuroko-type VMS deposits. Mineralogical and geochemical compositions of polymetallic (zinc and lead enriched) sulfide assemblage is commonly recognized among the hydrothermal fields, which strongly resemble Kuroko-type deposits. On the other hand, microscopic observation revealed texture of the sulfide minerals collected from above the seafloor showed distinctive feature. Deep drilling into the Iheya North Knoll hydrothermal field during IODP Expedition 331 provided additional evidence for this analogy. Sulfide blocks of sphalerite-rich massive sulfides ("black ore") collected from a hydrothermal mound inside shows clear evidence for formation by both surface detrital and subseafloor chemical processes, with some sphalerite precipitation in void spaces. Moreover, vertical profiles of mineral occurrence revealed subseafloor hydrothermal structure directly comparable to that of Kuroko-type deposits both in horizontal and vertical scales. On the other hand, geochemical studies of hydrothermal fluid venting from the seafloor demonstrated that the recognized diverse range of sulfide and sulfate mineralization could be related to subseafloor geochemical processes such as phase separation and probably mineralization. These results highlighted importance of subseafloor processes for formation of VMS deposits. Drilling studies targeting a hydrothermal field, as well as integration of geological, geophysical and hydrological studies of background environment, would significantly promote our

understanding of dynamic processes for formation of VMS deposits.

Acknowledgement We appreciate for crew, submersible team members, drilling operators and onboard scientists of all of the research cruises conducted in the Okinawa Trough. Especially, onboard and offshore scientists of the IODP Expedition 331 inspired the authors in several aspects. Discussion with the IGCP-502 program members, especially during the field excursion in the Hokuroku Basin in the northeast Japan provided the first author (J. Ishibashi) several important clues to understand the analogy with Kuroko-type deposits. Discussion with Ken Takai, Shinsuke Kawagucci, and Tatsuo Nozaki of SRRP, JAMSTEC was fruitful for the authors. Earlier version of the manuscript was significantly improved by constructive comments by Fernando Tornos and Steven Hollis. We gratefully acknowledge Japan Coast Guard (JCG) for permission of the use of their seismic profiles in this chapter. This study was partially supported by the "TAIGA project," which was funded by a Grant-in-Aid for Scientific Research on Innovative Areas (#20109004) from the Ministry of Education, Culture, Sports, Science and Technology (MEXT), Japan. T. Tsuji gratefully acknowledges the support of the I^2CNER, sponsored by the World Premier International Research Center Initiative (WPI), MEXT, Japan.

References

Binns RA, Barriga FJAS, Miller DJ (2007) Leg 193 synthesis: anatomy of an active felsic-hosted hydrothermal system, eastern Manus Basin, Papua New Guinea. In: Barriga FJAS, Binns RA, Miller DJ, Herzig PM (eds) Proc ODP Sci Res 193: College Station, TX (Ocean Drilling Program), pp 1–17. doi:10.2973/odp.proc.sr.193.201.2007

Butterfield DA, Massoth GJ, McDuff RE, Lupton JE, Lilley MD (1990) Geochemistry of hydrothermal fluids from axial seamount hydrothermal emissions study vent field, Juan de Fuca Ridge: subseafloor boiling and subsequent fluid-rock interaction. J Geophys Res 95:12895–12921. doi:10.1029/JB095iB08p12895

Chiba H, Nakashima K, Gamo T, Ishibashi J, Tsunogai U, Sakai H (1993) Hydrothermal activity at the Minami-Ensei Knoll, Okinawa Trough: chemical characteristics of hydrothermal solutions. JAMSTEC Deepsea Res 9:271–282 (in Japanese with English abstract)

Drummond SE, Ohmoto H (1985) Chemical evolution and mineral deposition in boiling hydrothermal systems. Econ Geol 80:126–147

Fouquet Y, Von Stackelberg U, Charlou JL, Donval JP, Erzinger J, Foucher JP, Herzig P, Mühe R, Soakai S, Wiedicke M, Whitechurch H (1991) Hydrothermal activity and metallogenesis in the Lau back-arc basin. Nature 349:778–781

Gamo T, Sakai H, Kim E-S, Shitashima K, Ishibashi J (1991) High alkalinity due to sulfate reduction in the CLAM hydrothermal field, Okinawa Trough. Earth Planet Sci Lett 107:328–338

Gena K, Chiba H, Kase K, Nakashima K, Ishiyama D (2013) The tiger sulfide chimney, Yonaguni knoll IV hydrothermal field, southern Okinawa Trough, Japan: the first reported occurrence of Pt-Cu-Fe-bearing bismuthinite and Sn-bearing chalcopyrite in an active seafloor hydrothermal system. Res Geol 63:360–370

Giggenbach WF, Sheppard DS, Robinson BW, Stewart MK, Lyon GL (1994) Geochemical structure and position of the Waiotapu geothermal field, New Zealand. Geothermics 23:599–644

Glasby GP, Notsu K (2003) Submarine hydrothermal mineralization in the Okinawa Trough, SW of Japan: an overview. Ore Geol Rev 23:299–339. doi:10.1016/j.oregeorev.2003.07.001

Glasby GP, Iizasa K, Hannington M, Kubota H, Notsu K (2008) Mineralogy and composition of Kuroko deposits from northeastern Honshu and their possible modern analogues from the Izu-Ogasawara (Bonin) Arc south of Japan: implications for mode of formation. Ore Geol Rev 34:547–560. doi:10.1016/j.oregeorev.2008.09.005

Goodfellow WD, Franklin JM (1993) Geology, mineralogy, and chemistry of sediment-hosted clastic massive sulfides in shallow cores, Middle Valley, northern Juan de Fuca Ridge. Econ Geol 88:2037–2068

Halbach P, Nakamura K, Wahsner M, Lange J, Sakai H, Kaselitz L, Hansen R-D, Yamano M, Post J, Prause B, Seifert R, Michaelis W, Teichmann F, Kinoshita M, Marten A, Ishibashi J, Czerwinski S, Blum N (1989) Probable modern analogue of Kuroko-type massive sulphide deposits in the Okinawa Trough back-arc basin. Nature 338:496–499. doi:10.1038/338496a0

Halbach P, Pracejus B, Märten A (1993) Geology and mineralogy of massive sulfide ores from the Central Okinawa Trough, Japan. Econ Geol 88:2210–2225

Halbach P, Hansmann W, Köppel V, Pracejus B (1997) Whole-rock and sulfide lead-isotope data from the hydrothermal JADE field in the Okinawa back-arc trough. Min Deposita 32:70–78

Hardartóttir V, Brown KL, Fridriksson T, Hedenquist JW, Hannington MD, Thorhallson S (2009) Metals in deep liquid of the Reykjanes geothermal system, southwest Iceland: implications for the composition of seafloor black smoker fluids. Geology 37:1103–1106

Hardartóttir V, Hannington MD, Hedenquist JW, Kjarsgaard I, Hoal K (2010) Cu-rich scales in the Reykjanes geothermal system, Iceland. Econ Geol 105:1143–1155

Heinrich C (2007) Fluid-fluid interactions in magmatic-hydrothermal ore formation. Rev Min Geochem 65:363–387

Hirata N, Kinoshita H, Katao H, Baba H, Kaiho Y, Koresawa S, Ono Y, Hayashi K (1991) Report on DELP 1988 cruises in the Okinawa Trough Part 3. Crustal structure of the southern Okinawa Trough. Bull ERI Univ Tokyo 66:37–70

Horisako J, Dojun S, Tanaka K, Otonari Y, Hashimoto T (2010) Preliminary report of the bathymetric survey in the region to the northwest of Okinawa Island. Rep Hydrogr Oceanogr Res 46:87–91 (in Japanese with English abstract)

Iijima A (1974) Clay and zeolitic alteration zones surrounding kuroko deposits in the Hokuroku district, northern Akita, as submarine hydrothermal-diagenetic alteration products. Min Geol Spec Issue 6:267–289

Inagaki F, Kuypers MMM, Tsunogai U, Ishibashi J, Nakamura K, Treude T, Ohkubo S, Nakaseama M, Gena K, Chiba H, Hirayama H, Ninoura T, Takai K, Jørgensen BB, Horikoshi K, Boetius A (2006) Microbial community in a sediment-hosted CO_2 lake of the southern Okinawa Trough hydrothermal system. Proc Natl Acad Sci U S A 103:14164–14169

Iryu Y, Matsuda H, Machiyama H, Piller WE, Quinn TM, Mutti M (2006) Introductory perspective on the COREF project. Island Arc 15:393–406. doi:10.1111/j.1440-1738.2006.00537.x

Ishibashi J, Urabe T (1995) Hydrothermal activity related to arc-backarc magmatism in the western Pacific. In: Taylor B (ed) Backarc basins tectonics and magmatism. Plenum, New York, pp 451–495

Ishibashi J, Miyoshi Y, Inoue H, Yeats C, Hollis SP, Corona JC, Bowden S, Yang SY, Southam G, Masaki Y, Hartnett H, IODP Expedition 331 Scientists (2013) Subseafloor structure of a submarine hydrothermal system within volcaniclastic sediments: a modern analogue for 'Kuroko-type' VMS deposits. In: Proceedings of the 12th Biennial SGA Meeting, 12–15 August 2013, Uppsala, Sweden, ISBN 978-91-7403-207-9, pp 542–544

Ishibashi J, Noguchi T, Toki T, Miyabe S, Yamagami S, Onishi Y, Yamanaka T, Yokoyama Y, Oomori E, Takahashi Y, Hatada K, Nakaguchi Y, Yoshizaki M, Konno U, Shibuya T, Takai K, Inagakai F, Kawagucci S (2014) Diversity of fluid geochemistry affected by processes during fluid upwelling in active hydrothermal fields in the Izena Hole, the middle Okinawa Trough back-arc basin. Geochem J 48:357–369. doi:10.2343/geochemj.2.0311

Ishihara S (ed) (1974) Geology of Kuroko deposits. Min Geol Spec Issue 6:435

Ishikawa M, Sato H, Furukawa M, Kimura M, Kato Y, Tsugaru R, Shimamura K (1991) Report on DELP 1988 cruises in the Okinawa Trough Part 6: petrology of volcanic rocks. Bull ERI Univ Tokyo 66:151–177

Iwasaki T, Shimamura H, Kanazawa T, Hirata T, Suehiro K, Urabe T (1990) Results of the 1984 Japan Germany joint seismic study on Ryukyu Arc. Chikyu Month 12(5):254–261 (in Japanese)

Izawa E, Motomura Y, Tanaka T, Kimura M (1991) Hydrothermal carbonate chimneys in the Iheya Ridge of the Okinawa Trough. JAMSTEC Deepsea Res 7:185–192 (in Japanese with English abstract)

Kato Y (1990) Geology and topography on the ridge south of the active hydrothermal deposits of the Izena Hole –the results of diving survey in 1989–. JAMSTEC Deepsea Res 6:27–31 (in Japanese with English abstract)

Kato Y, Nakamura K, Iwabuchi Y, Hashimoto J, Kaneko Y (1989) Geology and topography in the Izena Hole of the middle Okinawa Trough – the results of diving surveys in 1987 and 1988. JAMSTEC Deepsea Res 5:163–182 (in Japanese with English abstract)

Kawagucci S, Chiba H, Ishibashi J, Yamanaka T, Toki T, Muramatsu Y, Ueno Y, Makabe A, Inoue K, Yoshida N, Nakagawa S, Nunoura T, Takai K, Takahata N, Sano Y, Narita T, Teranishi G, Obata H, Gamo T (2011) Hydrothermal fluid geochemistry at the Iheya North field in the mid-Okinawa Trough: implication for origin of methane in subseafloor fluid circulation systems. Geochem J 45:109–124

Kawagucci S, Miyazaki J, Nakajima R, Nozaki T, Takaya Y, Kato Y, Shibuya T, Konno U, Nakaguchi Y, Hatada K, Hirayama H, Fujikura K, Furushima Y, Yamamoto H, Watsuji T, Ishibashi J, Takai K (2013) Post-drilling changes in fluid discharge pattern, mineral deposition, and fluid chemistry in the Iheya North hydrothermal field, Okinawa Trough. Geochem Geophys Geosyst 14:4774–4790

Kimura M (1985) Back-arc rifting in the Okinawa Trough. Mar Petrol Geol 2:222–240

Kimura M (1990) Genesis and formation of the Okinawa Trough, Japan. Mem Geol Soc Jap 34:77–88

Kimura M (1996) Active rift system in the Okinawa Trough and its northeastern continuation. Bull Disas Prev Res Inst Kyoto Univ 45:27–38

Kimura M (2000) Paleogeography of the Ryukyu Islands. Tropics 10 (1):5–24

Kimura M, Uyeda S, Kato Y, Yamano M, Gamo T, Sakai H, Kato S, Izawa E, Oomori T (1988) Active hydrothermal mounds in the Okinawa Trough backarc basin, Japan. Tectonophysics 145:319–324

Kimura M, Matsumoto T, Shinjo R, Nakamura M, Motoyama I, Machiyama H, Toyama G, Yagi H (2001) Meanders recognized in the southwestern part of the Okinawa Trough and its significance. JAMSTEC Deepsea Res 18:103–120

Klingelhoefer F, Lee C-S, Lin J-Y, Sibuet J-C (2009) Structure of the southernmost Okinawa Trough from reflection and wide-angle seismic data. Tectonophysics 446:281–288. doi:10.1016/j.tecto.2007.11.031

Konno U, Tsunogai U, Nakagawa F, Nakaseama M, Ishibashi J, Nunoura T, Nakamura K (2006) Liquid CO_2 venting on the seafloor: Yonaguni knoll VI hydrothermal system, Okinawa Trough. Geophys Res Lett 33, L16607

Kotake Y (2000) Study on the tectonics of western Pacific region derived from GPS data analysis. Bull ERI Univ Tokyo 75:229–334

Kuroda T, Ozawa T (1996) Paleoclimatic and vegetational changes during the Pleistocene and Holocene in the Ryukyu Islands inferred from pollen assemblages. Jpn J Geogr 105:328–342

Lawrie D, Miller DJ (2000) Sulfide mineral chemistry and petrography from Bent Hill, ODP Mound, and TAG massive sulfide deposits. In: Zierenberg RA, Fouquet Y, Miller DJ, Normark WR (eds) Proc ODP Sci Res 169: College Station, TX (Ocean Drilling Program), pp 1–34

Lee C-S, Shore GG, Bebee LD, Lu RS, Hilde T (1980) Okinawa Trough: origin of a back-arc basin. Mar Geol 35:219–241

Letouzey J, Kimura M (1986) The Okinawa Trough: genesis of a back-arc basin developing along a continental margin. Tectonophysics 125:209–230

Lin J-Y, Hsu S-K, Sibuet J-C (2004) Melting features along the Ryukyu slab tear, beneath the southwestern Okinawa Trough. Geophys Res Lett 31, L19697. doi:10.1029/2004GS020862

Lin J-Y, Sibuet J-C, Lee C-S, Hsu S-K, Klingelhoefer F, Auffret Y, Pelleau P, Crozon J, Lin C-H (2009) Microseismicity and faulting in the southwestern Okinawa Trough. Tectonophysics 466:268–280. doi:10.1016/j.tecto.2007.11.030

Lüders V, Niedermann S (2010) Helium isotope composition of fluid inclusions hosted in massive sulfides from modern submarine hydrothermal systems. Econ Geol 105:443–449

Lüders V, Pracejus B, Halbach P (2001) Fluid inclusion and sulfur isotope studies in probable modern analogue Kuroko-type ores from the JADE hydrothermal field (Central Okinawa Trough, Japan). Chem Geol 173:45–58

Lüders V, Banks DA, Halbach P (2002) Extreme Cl/Br and ^{37}Cl isotope fractionation in fluids of modern submarine hydrothermal systems. Min Deposita 37:765–771

Marumo K, Hattori K (1999) Seafloor hydrothermal clay alteration at Jade in the back-arc Okinawa Trough: mineralogy, geochemistry and isotope characteristics. Geochim Cosmochim Acta 63 (18):2785–2804

Masuda H, Ishibashi J, Kato Y, Gamo T, Sakai H (1987) Oxygen isotope ratio and trace element composition of hydrothermal sediments from Okinawa Trough, collected with SHINKAI2000, dive 231. JAMSTEC Deepsea Res 3:225–231 (in Japanese with English abstract)

Matsumoto T, Kinoshita M, Nakamura M, Sibuet J-C, Lee C-S, Hsu S-K, Oomori T, Shinjo R, Hashimoto Y, Hosoya S, Imamura M, Ito M, Tukuda K, Yagi H, Tatekawa K, Kagaya I, Hokakubo S, Okada T, Kimura M (2001) Volcanic and hydrothermal activities and possible "segmentation" of the axial rifting in the westernmost part of the Okinawa Trough -preliminary results from the YOKOSUKA/SHINKAI6500 Lequios Cruise. JAMSTEC Deepsea Res 19:95–107 (in Japanese with English abstract)

METI (2013) Report for the first stage of the program. Development of deep-sea mineral resources (in Japanese). http://www.meti.go.jp/press/2013/07/20130705003/20130705003-2.pdf

Miki M (1995) Two-phase opening model for the Okinawa Trough inferred from paleomagnetic study of the Ryukyu arc. J Geophys Res 100:8169–8184. doi:10.1029/95JB00034

Murauchi S, Den N, Asano S, Hotta H, Yoshii T, Asanuma T, Hagiwara K, Ichikawa K, Sato T, Lutwig WJ, Ewing JT, Edger NT, Houtz RE

(1968) Crustal structure of the Philippine Sea. J Geophys Res 73:3153–3171
Nagaseki H, Hayashi K (2008) Experimental study of the behavior of copper and zinc in a boiling hydrothermal system. Geology 36:27–30
Nagumo S, Kinoshita H, Kasahara J, Ouchi T, Tokuyama H, Asanuma T, Koresawa S, Akiyoshi H (1986) Report on DELP 1984 cruises in the middle Okinawa Trough Part 2: seismic structural studies. Bull ERI Univ Tokyo 61:167–202
Nakagawa S, Takai K, Inagaki F, Chiba H, Ishibashi J-I, Kataoka S, Hirayama H, Nunoura T, Horikoshi K, Sako Y (2005) Variability in microbial community and venting chemistry in a sediment-hosted backarc hydrothermal system: impacts of subseafloor phase-separation. FEMS Microbiol Ecol 54:141–155. doi:10.1016/j.femsec.2005.03.007
Nakamura K, Kato Y, Kimura M, Ando M, Kyo M (1989) Occurrence and distribution of the hydrothermal ore deposits at the Izena Hole in the Okinawa Trough – summary of the knowledge in 1988–. JAMSTEC Deepsea Res 5:183–189 (in Japanese with English abstract)
Nakano H, Okamoto K, Ishibashi J-I, Noguchi T (2008) Chemical signature of submarine hydrothermal deposits collected from the Hatoma Koll in southern Okinawa trough backarc basin. Abstract, MRD03316P, 33rd International Geological Congress, Oslo, August 6–14, 2008
Nakashima K, Sakai H, Yoshida H, Chiba H, Tanaka Y, Gamo T, Ishibashi J, Tsunogai U (1995) Hydrothermal mineralization at the Okinawa Trough. In: Sakai H, Nozaki Y (eds) Biogeochemical processes and ocean flux in the Western Pacific. Terra Scientific Publication, Tokyo, pp 487–508
Nash DF (1979) The geological development of the North Okinawa Trough area from Neogene times to recent. J Japan Assoc Petrol Tech 44:109–119
Noguchi T, Oomori T, Tanahara A, Taira N, Takada J, Taira H (2007) Chemical composition of hydrothermal ores from Mid-Okinawa Trough and Suiyo Seamount determined by neutron activation analysis. Geochem J 41:141–148
Noguchi T, Shinjo R, Ito M, Takada J, Oomori T (2011) Barite geochemistry from hydrothermal chimneys of the Okinawa Trough: insight into chimney formation and fluid/sediment interaction. J Min Petrol Sci 106:26–35
Nozaki T, Ishibashi J, Shimada K, Takaya Y, Kato Y, Kawagucci S, Shibuya T, Takai K (2013) Geochemical signature of the "zero-age chimney" formed on artificial hydrothermal vents created by IODP Exp. 331 in the Iheya North field, Okinawa Trough, Proceedings of the 12th Biennial SGA Meeting, 12–15 August 2013, Uppsala, Sweden, ISBN 978-91-7403-207-9, p 561
Ohmoto H (1996) Formation of volcanogenic massive sulfide deposits: the Kuroko next term perspective. Ore Geol Rev 10:135–177. doi:10.1016/0169-1368(95)00021-6
Ohmoto H, Skinner BJ (eds) (1983) The Kuroko and related volcanogenic massive sulfide deposits. Econ Geol Monogr 5:604
Oikawa M, Nishizawa A, Kaneda K, Horiuchi D (2009) Seismic crustal structure along the Okinawa Trough axis. Abstract, The Seismological Society of Japan (SSJ) 2009 Fall Meeting, Kyoto, Oct 21–23, 2009
Okamoto K, Ishibashi J, Motomura Y, Yamanaka T, Fujikura K (2002) Mineralogical studies of hydrothermal deposits collected from the Dai-Yon Yonaguni Knoll and the Hatoma Knoll in the Okinawa Trough. JAMSTEC Deepsea Res 21:75–81 (in Japanese with English abstract)
Ooki M, Miyoshi Y, Shimada K, Ishibashi J-I, Nozaki T (2012) Mineralogy and geochemistry of hydrothermal ores collected from active hydrothermal fields in shallow water depth. In: Proceedings of Japan Geoscience Union Meeting 2012, BBG21-P09 (abstract)
Oshida A, Tamaki K, Kimura M (1992) Origin of the magnetic anomalies in the southern Okinawa Trough. J Geomag Geoelectr 44:345–359
Osozawa S, Su Z-H, Oba Y, Yagi T, Watanabe Y, Wakabayashi J (2013) Vicariant speciation due to 1.55 Ma isolation of the Ryukyu islands, Japan, based on geological and GenBank data. Entomolog Sci 16:267–277. doi:10.1111/ens.12037
Otubo M, Hayashi D (2003) Neotectonics in southern Ryukyu arc by means of paleostress analysis. Bull Fac Sci Univ Ryukyus 76:1–73
Park J-O, Tokuyama H, Shinohara M, Suyehiro K, Taira A (1998) Seismic record of tectonic evolution and backarc rifting in the southern Ryukyu island arc system. Tectonophysics 294:21–42
Pokrovski GS, Roux J, Harrichoury JC (2005) Fluid density control on vapor–liquid partitioning of metals in hydrothermal systems. Geology 33:657–660
Ryan BF, Carbotte SM, Coplan JO, O'Hara S, Melkonian A, Arko R, Weissel RA, Ferrini V, Goodwillie A, Nitsche F, Bonczkowski J, Zemsky R (2009) Global multi-resolution topography synthesis. Geochem Geophys Geosyst 10, Q03014. doi:10.1029/2008GC002332
Sakai H, Gamo T, Kim E-S, Tsutsumi M, Tanaka T, Ishibashi J, Wakita H, Yamano M, Oomori T (1990) Venting of carbon dioxide-rich fluid and hydrate formation in mid-Okinawa Trough Backarc Basin. Science 248:1093–1096
Sato T (1974) Distribution and geological setting of the Kuroko deposits. Min Geol Spec Issue 6:1–9
Shikazono T (2003) Geochemical and tectonic evolution of arc-backarc hydrothermal systems implication for the origin of kuroko and epithermal vein-type mineralizations and the global geochemical cycle. Elsevier, Amsterdam, p 466
Shikazono T, Kusakabe M (1999) Mineralogical characteristics and formation mechanism of sulfate-sulfide chimneys from Kuroko area, Mariana Trough and mid-ocean ridges. Res Geol Spec Issue 20:1344–1698
Shinjo R (1999) Geochemistry of high Mg andesites and the tectonic evolution of the Okinawa Trough-Ryukyu arc system. Chem Geol 157:69–88
Shinjo R, Kato Y (2000) Geochemical constraints on the origin of bimodal magmatism at the Okinawa Trough, an incipient back-arc basin. Lithosphere 54:117–137
Shinjo R, Chung S-L, Kato Y, Kimura M (1999) Geochemical and Sr-Nd isotopic characteristics of volcanic rocks from the Okinawa Trough and Ryukyu Arc: implications for the evolution of a young, intracontinental back arc basin. J Geophys Res 104:10591–10608. doi:10.1029/1999JB900040
Shinjo R, Machiyama H, Maki Y, Motoyama I, Toyama G, Hokakubo S, Chung S-L (2001) Outline of SHINKAI-2000 dive surveys at the westernmost part of the Okinawa Trough and the Kuroshima Knoll - preliminary report of the NT00-06 Leg-1 Cruise. JAMSTEC Deepsea Res 19:109–121 (in Japanese with English abstract)
Shitashima K, Maeda Y, Koike Y, Ohsumi T (2007) Natural analogue of the rise and dissolution of liquid CO_2 in the ocean. Int J Greenhouse Gas Control 2:95–104. doi:10.1016/S1750-5836(07)00092-8
Sibuet J-C, Letouzey J, Barbier F, Charvet J, Foucher J-P, Hilde T, Kimura M, Ling-Yun C, Marsset B, Muller C, Stephan J-F (1987) Back arc extension in the Okinawa Trough. J Geophys Res 92:14041–14063. doi:10.1029/JB092iB13p14041
Sibuet J-C, Deffontaines B, Hsu S-K, Thareau N, Le Formal J-P, Liu C-S, ACT Party (1998) Okinawa trough backarc basin: early tectonic and magmatic evolution. J Geophys Res 103:30245–30267
Suzuki R, Ishibashi J-I, Nakaseama M, Konno U, Tsunogai U, Gena K, Chiba H (2008) Diverse range of mineralization induced by phase separation of hydrothermal fluid: a case study of the Yonaguni IV hydrothermal field in the Okinawa Trough Backarc Basin. Res Geol 58:267–288. doi:10.1111/j.1751-3928.2008.00061.x

Takai K, Nunoura T, Ishibashi J-I, Lupton J, Suzuki R, Hamasaki H, Ueno Y, Kawagucci S, Gamo T, Suzuki Y, Hirayama H, Horikoshi K (2008) Variability in the microbial communities and hydrothermal fluid chemistry at the newly discovered Mariner hydrothermal field, southern Lau Basin. J Geophys Res 113, G02031. doi:10.1029/2007JG000636

Takai K, Mottl MJ, Nielsen SH, The Expedition 331 Scientists (2011) Proceedings of IODP, 331: Tokyo (Integrated Ocean Drilling Program Management International, Inc.). doi:10.2204/iodp.proc.331.2011

Takai K, Mottl MJ, Nielsen SH, The Expedition 331 Scientists (2012) IODP expedition 331: strong and expansive subseafloor hydrothermal activities in the Okinawa Trough. Sci Dril 13:19–27. doi:10.2204/iodp.sd.13.03.2011

Tsuji T, Takai K, Oiwane H, Nakamura Y, Masaki Y, Kumagai H, Kinoshita M, Yamamoto F, Okano T, Kuramoto S (2012) Hydrothermal fluid flow system around the Iheya North Knoll in the mid-Okinawa trough based on seismic reflection data. J Volcanol Geotherm Res 213–214:41–50

Ueno H, Hamasaki H, Murakawa Y, Kitazono S, Takeda T (2003) Ore and gangue minerals of sulfide chimneys from the North Knoll, Iheya Ridge, Okinawa Trough, Japan. JAMSTEC Deepsea Res 22:49–62

Urabe T, Kubota H (2004) About this issue: Kuroko deposits revisited after the discovery of their modern analogues on submarine arc volcanoes. Res Geol 54:385–386

Urabe T, Marumo K (1991) A new model for Kuroko-type deposits of Japan. Episodes 14:246–251

Wang C, Yang M-L, Chou C-P, Chang Y-C, Lee C-S (2000) Westward extension of the Okinawa Trough at its western end in the northern Taiwan area: bathymetric and seismological evidence. Terrest Atmos Ocean 11:459–480

Watanabe K (2001) Mapping the hydrothermal activity area on the Hatoma Knoll in the southern Okinawa Trough. JAMSTEC Deepsea Res 19:87–94 (in Japanese with English abstract)

Watanabe K, Shibata A, Furukawa H, Kajimura T (1995) Topography of submarine volcanoes off the North-Northeast Coast of Iriomote island, the Ryukyu Islands. Kazan Ser 2(40):91–97 (in Japanese with English abstract)

Watanabe M, Hoshino K, Shiokawa R, Takaoka Y, Fukumoto H, Shibata Y, Shinjo R, Oomori T (2006) Metallic mineralization associated with pillow basalts in the Yaeyama Central Graben, Southern Okinawa Trough, Japan. JAMSTEC Rep Res Dev 3:1–8

Yamada R, Yoshida T (2011) Relationships between Kuroko volcanogenic massive sulfide (VMS) deposits, felsic volcanism, and island arc development in the northeast Honshu arc. Jpn Min Deposita 46:431–448

Yamano M, Uyeda S, Kinoshita H, Hilde TWC (1986) Report on DELP 1984 cruises in the middle Okinawa Trough Part 4: heat flow measurements. Bull ERI Univ Tokyo 61:251–267

Yeats C, Hollis SP (2013) Actively forming Kuroko-style massive sulfide mineralisation and hydrothermal alteration at Iheya North, Okinawa Trough. Abstract, Goldschmidt Conference 2013, Florence, August 25–30, 2013

Yeats C, Hollis S, Corona JC, Expedition 331 Shipboard Scientific Party (2012) Actively forming Kuroko-style massive sulfide mineralization and hydrothermal alteration at Iheya North, Okinawa Trough -key petrological results of IODP Expedition 331. Abstract, 34th International Geological Congress, Brisbane, August 5–10, 2012

Yokose H, Sato H, Kobayashi T, Yoshimura H, Morii Y, Yamawaki N (2009) Evidence of recent hydrothermal activity in the Amami caldera: discovery of Fe-Mn oxide crusts enriched in As and Mo. Proceedings of Japan Geoscience Union Meeting 2009, R219-008 (abstract)

Yokose H, Yoshimura H, Morii Y, Kobayashi T (2010) Volcanic chain of the western Okinawa Trough margin: discovery of a quaternary shoshonitic rock. In: Proceedings of Japan Geoscience Union Meeting 2011, SCG086-28 (abstract)

Zeng ZG, Yu SX, Yin XB, Wang XY, Zhang GL, Wang XM, Chen DG (2009) Element enrichment and U-series isotopic characteristics of the hydrothermal sulfides at Jade site in the Okinawa Trough. Sci China Ser D Earth Sci 52:913–924. doi:10.1007/s11430-009-0107-y

Zierenberg RA, Miller DJ (2000) Overview of ocean drilling program Leg 169: sedimented ridges II. In: Zierenberg RA, Fouquet Y, Miller DJ, Normark WR (eds) Proc ODP Sci Res 169: College Station, TX (Ocean Drilling Program), pp 1–39

Active Rifting Structures in Iheya Graben and Adjacent Area of the Mid-Okinawa Trough Observed Through Seismic Reflection Surveys

28

Fumihiko Ikegami, Takeshi Tsuji, Hidenori Kumagai, Jun-ichiro Ishibashi, and Ken Takai

Abstract

The mid-Okinawa Trough is recognized as an area with extensive volcanism and hydrothermal activity. The Iheya Graben is a depression in the mid-Okinawa Trough, extending approximately 100 km in an ENE-WSW strike. The graben lies 200 m below the surrounding flat-surfaced trough floor (from −1,400 to −1,600 m below sea level). The latest seismic profiles in the western Iheya Graben and adjacent areas reveal numerous normal faults, possibly in association with the rifting activity of the Okinawa Trough. The faulting of the Iheya Graben is non-listric syn-depression faulting, in contrast with dense listric faulting of the adjacent trough floor. The faulting in both areas consists of numerous seafloor-reaching active faults; however, recent activity is concentrated within the Iheya Graben. Non-listric faulting in the Iheya Graben shapes its present structure with large displacements. The displacements and fault propagations indicate the depression of the Iheya Graben was created with an abrupt flexural subsidence followed by extension with normal faulting. The event occurred largely before the formation of the overlying Iheya Ridge, which was reported to be at least 0.2 Ma. Such a significant event may be related to the present extensive volcanism in the region by means of rifting tectonics and magmatism.

Keywords

Back-arc basin • Okinawa Trough • Rifting • Seismic reflection survey

F. Ikegami (✉)
Graduate School of Sciences, Kyushu University,
6-10-1 Hakozaki, Higashi-ku, Fukuoka 812-8581, Japan
e-mail: ikegami@kyudai.jp

T. Tsuji
International Institute for Carbon-Neutral Energy Research (I2CNER),
Kyushu University, 744 Motooka, Nishi-ku, Fukuoka 819-0395, Japan

Submarine Resources Research Project (SRRP),
Japan Agency for Marine-Earth Science and Technology (JAMSTEC),
2-15 Natsushima-Cho, Yokosuka 237-0061, Japan

H. Kumagai
R&D Center for Submarine Resources, Japan Agency for Marine-Earth Science and Technology (JAMSTEC), 2-15 Natsushima-Cho,
Yokosuka 237-0061, Japan

Institute for Research on Earth Evolution (IFREE), Japan Agency for Marine-Earth Science and Technology (JAMSTEC), 2-15 Natsushima-Cho, Yokosuka 237-0061, Japan

Precambrian Ecosystem Laboratory, Japan Agency for Marine-Earth Science and Technology (JAMSTEC), 2-15 Natsushima-cho,
Yokosuka 237-0061, Japan

J.-i. Ishibashi
Faculty of Sciences, Kyushu University,
6-10-1 Hakozaki, Higashi-ku, Fukuoka 812-8581, Japan

Submarine Resources Research Project (SRRP),
Japan Agency for Marine-Earth Science and Technology (JAMSTEC),
2-15 Natsushima-Cho, Yokosuka 237-0061, Japan

K. Takai
Department of Subsurface Geobiological Analysis and Research (D-SUGAR) and Research and Development (R&D), Center
for Submarine Resources, Japan Agency for Marine-Earth Science
and Technology (JAMSTEC), 2-15 Natsushima-Cho,
Yokosuka 237-0061, Japan

J.-i. Ishibashi et al. (eds.), *Subseafloor Biosphere Linked to Hydrothermal Systems: TAIGA Concept*,
DOI 10.1007/978-4-431-54865-2_28,

28.1 Introduction

The Okinawa Trough (Fig. 28.1a) is a NE-SW elongated back-arc basin located behind the Ryukyu Arc in the East China Sea. The Ryukyu Arc marks the convergent margin of the Eurasia and Philippine Sea Plates. The mid-Okinawa Trough is situated at the transitional settings between the shallow northern Okinawa Trough and the deep southern Okinawa Trough (Fig. 28.1a), in association with the occurrences of en echelon aligned intra-trough "grabens" (Kimura 1990). One such feature is the Iheya Graben (Iheya Depression/Iheya Deep (Ueda et al. 1985; Kimura et al. 1987)), an ENE-WSW elongated depression situated at the mid-Okinawa Trough (Fig. 28.1c). The Iheya Graben is 100 km long and 200 m deep when compared with the adjacent trough floor (Fig. 28.1c). Numerous volcanic knolls and active hydrothermal sites are distributed along the Iheya Graben and its vicinities, including the Iheya-North Knoll, the CLAM site of Iheya Ridge, and the Izena Hole (Glasby and Notsu 2003). Sibuet et al. (1987) inferred that the migration of the volcanic front into the back-arc basin resulted such an extensive volcanism in the region.

The Okinawa Trough is considered to be the only present representation of a submerged marginal rift in the nascent stage (Letouzey and Kimura 1986). However, the detailed structure and evolution of the Okinawa Trough still remains unveiled. Several seismic studies have been conducted since the 1970s to investigate these questions (Lee et al. 1980; Letouzey and Kimura 1986), however the recent surveys with modern advanced equipments were only conducted at the southern part of the Okinawa Trough (Furukawa et al. 1991; Sibuet et al. 1998; Park et al. 1998). Recent implications with other approaches such as geomagnetic (Miki 1995), paleostress (Otubo and Hayashi 2003), and coral reef studies (Iryu et al. 2006) indicate that the Okinawa Trough has experienced geographically heterogenetic evolution in multiple stages (Ishibashi et al., Chap. 27). Using the latest seismic reflection data, this study investigates the geological structures within the mid-Okinawa Trough in order to understand the evolution of the Okinawa Trough back-arc basin.

28.2 Data

In the 2000s, a number of seismic reflection surveys were conducted in the mid-Okinawa Trough in order to characterize the sedimentary and hydrogeologic structures of this region (Tsuji et al. 2012). In this study, four seismic profiles (Table 28.1) were used to investigate the geological structure of the Iheya Graben (< −1,600 m below sea level) and adjacent trough floor (from −1,400 to −1,600 m below sea level; Fig. 28.1c). The longest seismic profile, "Line 1" (Fig. 28.2), transects the trough floor and the Iheya graben, and was obtained on the KY02-11 cruise. The "INH10-A2" seismic profile (Fig. 28.3) transects the northern trough floor, and was obtained with a large-volume source on the KR10-02 cruise, which passes through the flat-surfaced area near the Iheya-North Knoll (Fig. 28.3). Two parallel cross sections, "Line 6" and "Line 7" (Fig. 28.4), describe the Iheya Ridge, and were obtained on the YK12-16 cruise.

28.3 Results

28.3.1 Iheya Graben

The Iheya Graben appears as an ENE-WSW elongated depression within the trough floor (Fig. 28.1). At the center of the depression, the Iheya Ridge (Fig. 28.1c) extends for more than 15 km. Three stratigraphic units: IHG-A, IHG-B, and IHG-C in descending order were defined using the seismic profiles of Line 6 and 7 (Fig. 28.4). The topmost unit, IHG-A, is an onlapping unit with weak-amplitude stratified reflectors. It has a maximum thickness of ~0.27 s in acoustic two-way travel time. This thickness is equivalent to ~200 m when the acoustic velocity is set at 1,500 m/s (Fig. 28.4e, f). The second unit, IHG-B, has similar weak-amplitude stratified facies, although its reflectors are dipping towards the center of the depression (Fig. 28.4c, d). The transition of such geometries between IHG-A and IHG-B marks an unconformity seen in Line 7 (Fig. 28.4c), and is more subtly expressed in Line 6 (Fig. 28.4d). The lowermost IHG-C is an acoustic basement in the depression, the top of which is defined by the basal strong reflectors highlighted by the dashed line (Fig. 28.4c–f).

Faulting in the Iheya Graben is divided into two groups depending upon whether it cuts the IHG-A unit. The former are seafloor-reaching active faults, which cut both IHG-B and IHG-A units, and generate large displacement (up to tens of meters) on the seafloor (Fig. 28.4c, d). The latter, however, are the inactive counterpart and cut only the IHG-B unit and below. Although the latter did not cause displacement in the IHG-A, some reflector hiatuses are seen in the IHG-A unit (Fig. 28.4c). Most of the faulting occurs as non-listric normal faults, although compressional features consisting of multiple reverse faults are observed in the southern edge of the Iheya Graben (Fig. 28.4e, f).

28.3.2 Trough Floor

The trough floor is characterized by flat-surfaced thick deposits, and is divided north to south by the Iheya Graben (Fig. 28.1). The northern part of the trough floor lies west

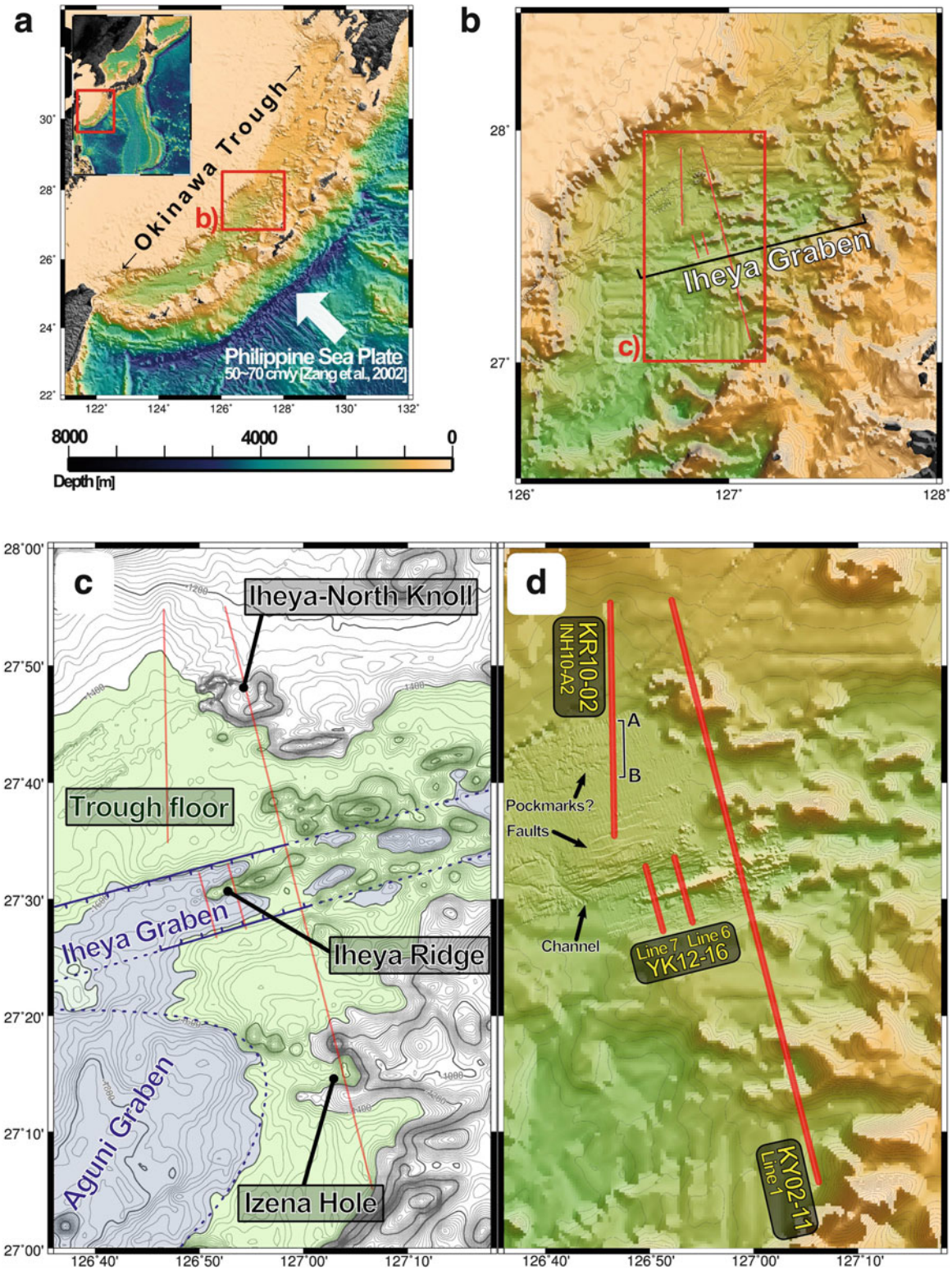

Fig. 28.1 (**a**) Geographical setting of the Okinawa Trough. Basemaps are from Global Multi-Resolution Topography (Ryan et al. 2009). (**b**) An enlarged bathymetry map of the mid-Okinawa Trough. The *red box shows* the survey area of this study. (**c**) Contoured bathymetry map with geological features highlighted. The *green area* is the flat-surfaced trough floor, which is bounded by the trough edge on the −1,400 m contour line. The *blue areas* are depressions in the trough floor that are lower than −1,600 m. (**d**) Shaded bathymetry map with high-resolution data in the western Iheya Graben (Kumagai 2012). The *red lines* are the seismic profiles used in this study. The section A–B along the INH10-A2 profile highlights where the profile intersects pockmark-like structures, and corresponds to the A–B section in Fig. 28.3

Table 28.1 List of survey cruises and equipment used for seismic data acquisition

	Fig. 28.2	Fig. 28.3	Fig. 28.4
Year	2002	2010	2012
Cruise	KY02-11	KR10-02	YK12-16
Lines	Line 1	INH10-A2	Line 6 and 7
Vessel	R/V Kaiyo	R/V Kairei	R/V Yokosuka
Streamer	24 ch/600 m	360 ch/4,500 m	Single channel
Source	~2.5 L (150 cu in) G-I gun	~54 L (3,300 cu in) Tuned gun	~2.5 L (150 cu in) G-I gun

of the Iheya-North Knoll (Fig. 28.1c). Although Line 1 transects the Iheya-North Knoll, this portion of the profile did not provide detailed subsurface structures for the area possibly because of numerous volcanics, which attenuate the acoustic wave energy (Fig. 28.2a, b). However, the INH10-A2 survey, located ~15 km west of the volcanic area (Fig. 28.1), was conducted with a large volume source, and it provided a detailed subsurface image (Fig. 28.3; Tsuji et al. 2012). The southern part of the trough floor features the Iheya and Aguni Grabens,

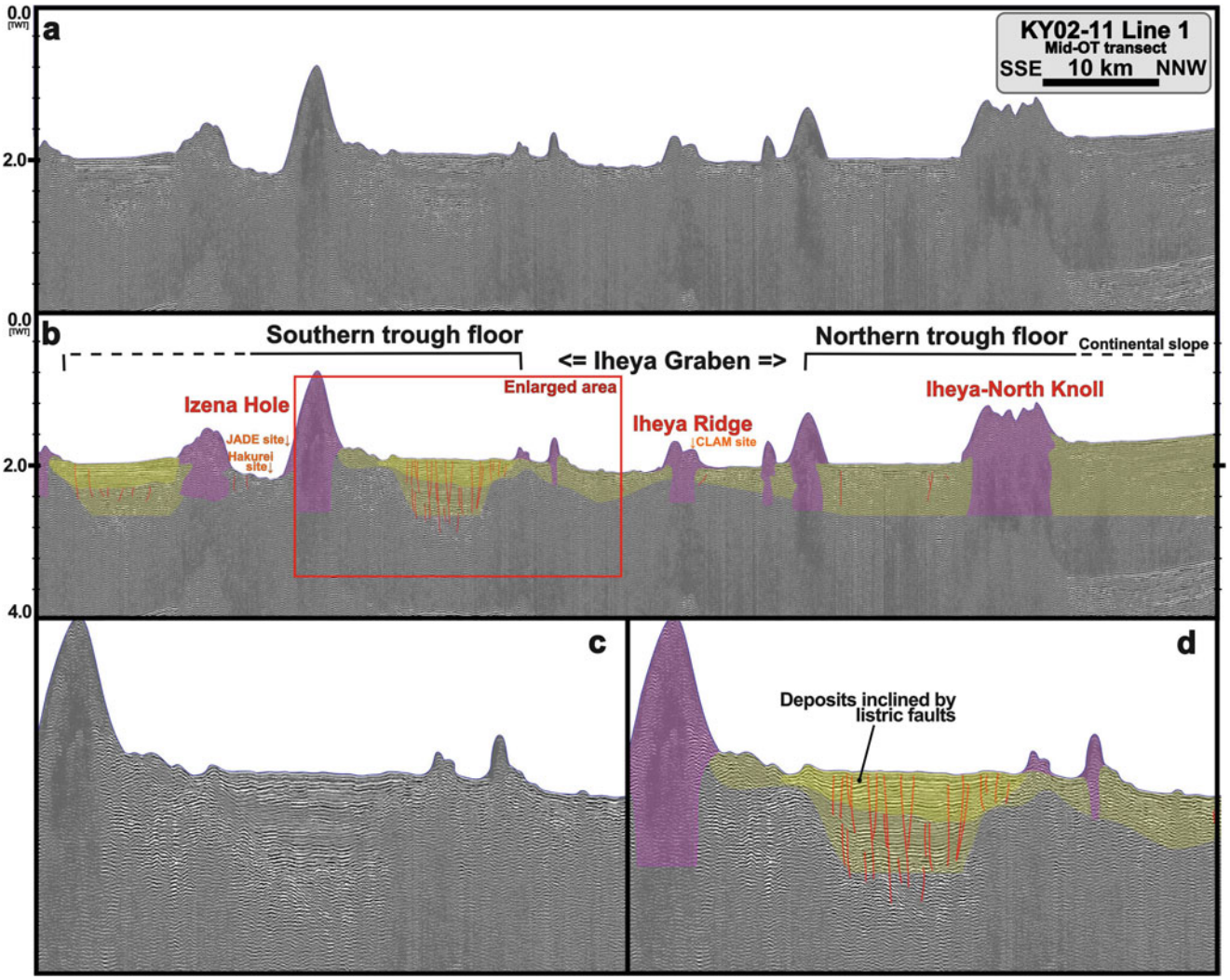

Fig. 28.2 (**a**) SSE-NNW seismic profile transecting the mid-Okinawa Trough obtained on the KY02-11 cruise. (**b**) Interpretation of the profile. The *purple areas* represent volcanic edifices, while the *yellow areas* show the approximate location of the stratified deposits. The onlapping deposits are emphasized in *dark yellow*. The *red* and *orange labels* show the approximate position of previously known volcanic and hydrothermal sites. (**c**) An enlarged image of the southern trough floor basin. (**d**) An interpretation of the enlarged image of the southern trough floor basin. The *red lines* highlight the fault planes of listric normal faults, which have cut and slightly rotated the stratified deposits

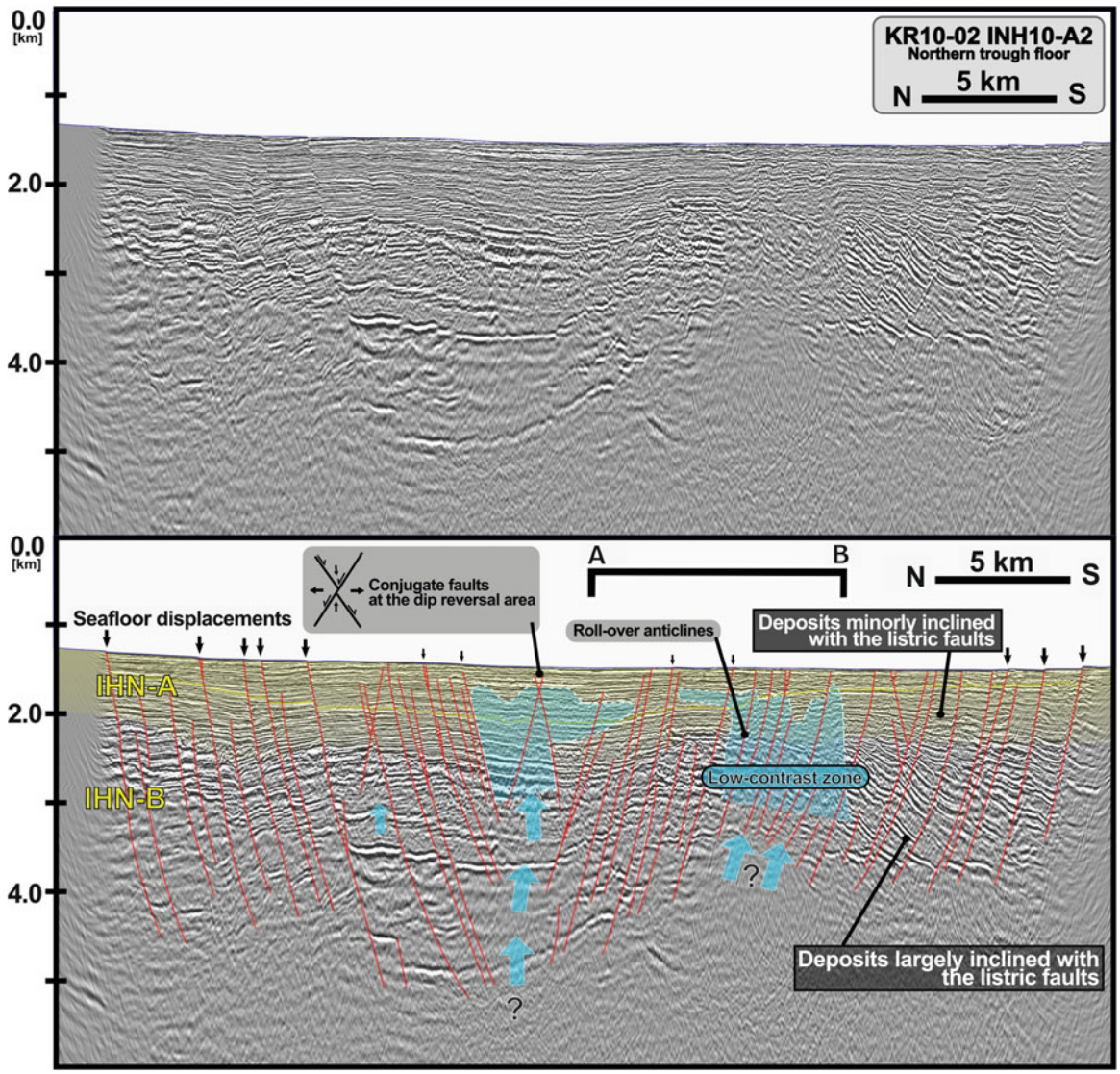

Fig. 28.3 Large volume sourced seismic profile of the northern flat-surfaced trough floor obtained on the KR10-A2 cruise (Tsuji et al. 2012). The *yellow fill* highlights poorly inclined recent deposits (IHN-A), while the *red lines* highlight listric normal faults. The *blue regions* and *blue arrows* are fluid-indicative anomalous low-contrast zones located below the A–B section shown in Fig. 28.1c

and was transected by the southern portion of Line 1 (Fig. 28.2c, d).

The depth-migrated seismic profile of the INH10-A2 line (Fig. 28.3) in the northern trough floor shows thick stratified deposits that were cut and inclined by densely spaced listric normal faults. The dips of those faults reverse at the center of the profile, forming a conjugate fault system, where the profile is neighboring the Iheya-North Knoll. The deposits are divided into IHN-A and IHN-B based on the change in degree of inclination. The reflectors in the upper IHN-A are almost parallel to the seafloor, while the reflectors in IHN-B increase their inclination along the depth. The reflectors in both IHN-A and B deposits often become ambiguous in multiple kilometer-scale "low-contrast zones," which strongly indicate the presence of fluid activity in the region, as previously reported by Tsuji et al. (2012).

Meanwhile, the resolution of the Line 1 did not allow for precise examination of the subsurface structures of the southern trough floor, it is similar to its northern counterpart with thick stratified deposits that are cut and inclined with numerous listric faults. The dip-reversal occurs at the center of the basin as well. The inclination of the southern trough floor deposits are small and uniform throughout the top to bottom of the deposits.

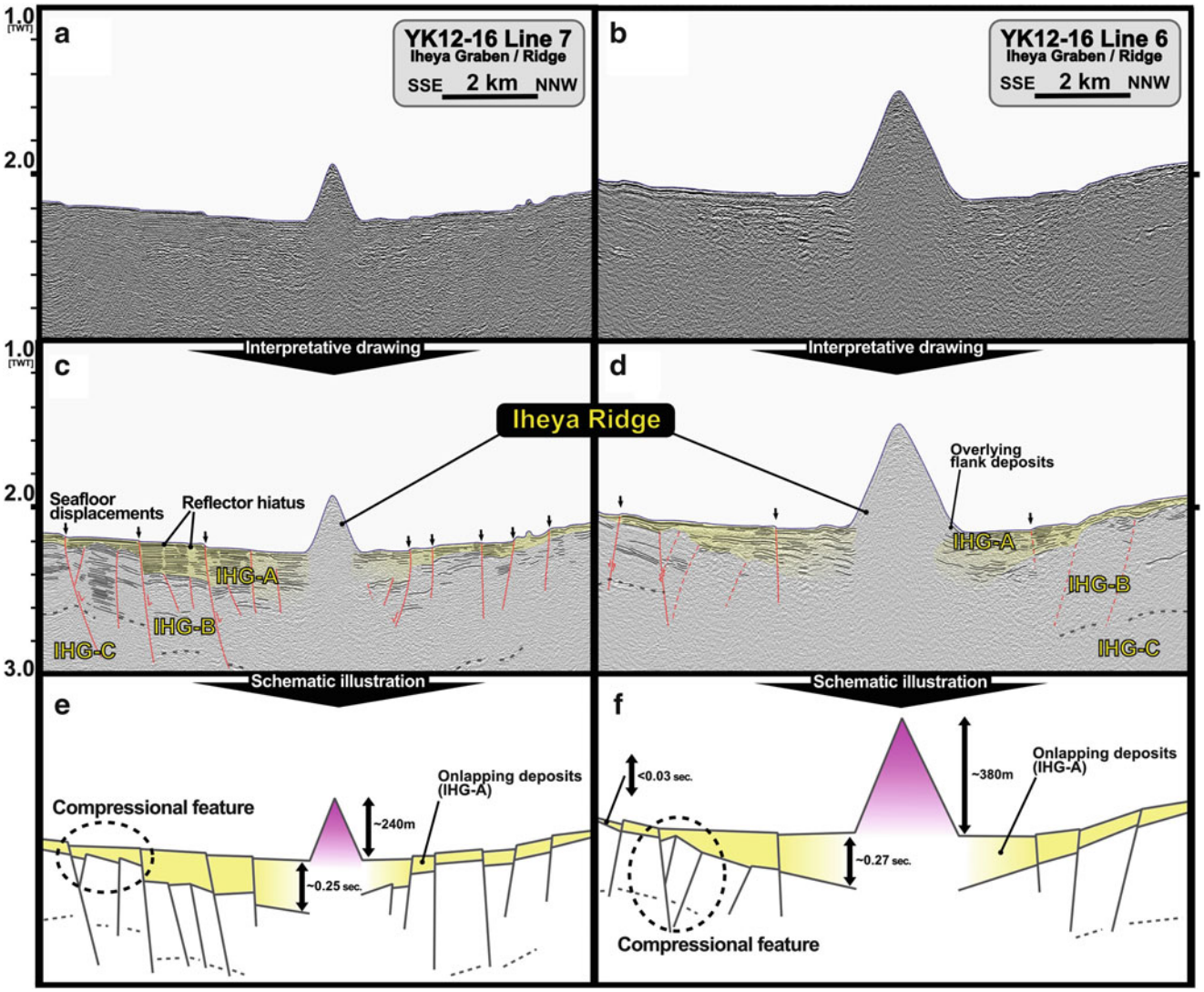

Fig. 28.4 (**a**, **b**) SSE-NNW single-channel seismic cross-sections in the western Iheya Graben obtained on the YK12-16 Cruise (Kumagai 2012). The knoll in the center of each section is the Iheya Ridge, which is located at the center of the Iheya Graben. (**c**, **d**) Interpretative drawings of the previous images. The onlapping facies (IHG-A) are highlighted in *yellow*, and fault planes are shown with *red lines*. (**e**, **f**) Schematic of the two profiles based on the interpretations of the previous images. The thicknesses of the IHG-A deposits were measured from (**c**) and (**d**), while the height of the Iheya Ridge was estimated from high-resolution bathymetry data (Kumagai 2012)

28.4 Discussion

28.4.1 Structure of the Iheya Graben and Adjacent Trough Floor

The geologically prominent feature in the survey area of the Okinawa Trough is the Iheya Graben. It is presently filled with onlapping IHG-A deposits (Fig. 28.4b, d). Such a "basin-filling" depositional configuration suggests that the depression structure of the Iheya Graben existed before the deposition of the IHG-A. On the other hand, the IHG-B deposits have shaped the base of the Iheya Graben with inwardly rotated beds. The compressional "hinge" structures present in the IHG-B unit in the southern margin of the Iheya Graben (Fig. 28.4e, f) indicate that such rotations were formed by flexural subsidence of the IHG-B and its basement beneath. The cause of the flexure cannot be determined from the seismic data in this study however, magmatism in the region is the likely candidate. Previous study on crustal velocities in this region reported high-attenuation zone at ~10 km beneath the sea surface, which could be interpreted as the lower crust with high thermal elasticity or melt content (Nagumo et al. 1986).

Both the northern and southern trough floors are flat-surfaced and extensively cut by listric faults (Figs. 28.2 and 28.3).

Similarly, each section has a dip-reversal in the middle of the basin. The difference between the two parts is marked with whether the deposits have uniform inclination or not. This indicates that each section of the basin has experienced a different tectonic history. Kimura (1990) previously suggested that the center of older rift basin which was present before the Pleistocene, was at the western margin of the Okinawa Trough, based on his interpretations for seismic profiles. The highly inclined IHN-B deposits as well as the distinct faults geometry in the northern trough floor would be the remnant of such a past rifting activity.

28.4.2 Age of the Iheya Graben Initiation

The chronology of intra-trough "grabens" are thought to be important in determining the evolution of the Okinawa Trough. Kimura (2000) assumed that the "grabens" in the Okinawa Trough have formed since 1 Ma, although the detailed ages of each graben remain unknown. Because the flank of the Iheya Ridge overlies the IHG-A deposits and is almost exposed to the seafloor (Fig. 28.4d), the Iheya Ridge edifice must have formed after the Iheya Graben had been filled. Using K–Ar dating of basalt samples, Kimura et al. (1986) reported an age of 0.42 ± 0.19 Ma for the Iheya Ridge. Therefore, the initiation of the Iheya Graben formation and subsequent deposition of the IHG-A unit must have occurred before 0.2 Ma.

Submarine channels flowing into the Iheya Graben can be seen in the high-resolution bathymetry map (Fig. 28.1d). These channels occur at a depth of 1,550–1,650 m and cut the faulted seafloor of the Iheya Graben. Similar features are observed in the intra-trough Yonaguni Graben, located in the southernmost part of the Okinawa Trough, and occur at approximately same depth (Sibuet et al. 1998). However, the meandering channels observed in the Yaeyama Graben are cut by faults, unlike the un-faulted channels of the Iheya Graben. Through dives #458–459, observations by remotely operated vehicle Dorphin-3 K, Kimura et al. (2001) determined that the channels in the Yonaguni Graben are presently not active because of the lack of erosional features on the surface, and hypothesize that they were formed in one of the glacial periods in the late Quaternary. They suggest the Riss Glaciation (0.2–0.12 Ma) was likeliest based on the previously known stratigraphic unconformities in the East China Sea. However, as previously noted, the depression of the Iheya Graben should be formed and filled with 200 m thick deposits prior to 0.2 Ma. Therefore, when it is assumed that they were formed together, both the channels in the Iheya Graben and the meander in the southern Okinawa Trough might be the products of an older, lower sea level. It also indicates that the Iheya Graben in the mid-Okinawa Trough is older, or less active than the Yaeyama Graben in the southernmost Okinawa Trough.

28.4.3 Present Rifting Status in the Iheya Graben Area of the Mid-Okinawa Trough

The present status of rifting-related tectonism in the Iheya Graben area can be evaluated through the propagation and displacement of faults. Despite abundant active listric and non-listric normal faulting throughout the Okinawa Trough, topographical displacements on the seafloor are clearly weighted along the Iheya Graben (Fig. 28.1). The poorly rotated recent IHN-A deposits in the northern trough floor basin indicate low slip rates because the abrupt change that marks the boundary of IHN-A and B occurred (Fig. 28.3). The listric faulting in the southern part of the trough on the other hand has not caused significant displacement (Figs. 28.1 and 28.2). Therefore, the active tectonics in the area may have been concentrated in the Iheya Graben because the Iheya Graben was initially formed with the rapid flexural subsidence. As the compressional faulting at the "hinge" area is not propagated into the upper IHG-A deposits, the flexural subsidence was thought to be an abrupt and short-lived activity. Instead, simple syn-depression normal faulting contributes to the latest growth of the Iheya Graben, as large displacements are exposed on the seafloor (Fig. 28.4).

28.5 Conclusion

The seismic reflection profiles in the Iheya Graben and adjacent areas of the mid-Okinawa Trough reveal geological structures that allow for the chronological ordering of events in the region. Extensive listric faulting in the thick deposits takes place throughout the flat-surfaced trough floor, although the rate of slip is presently negligible. The most recent major event in the area was the formation of the Iheya Graben, which was initiated with abrupt flexural subsidence followed by the growth with normal faulting. The age of the Iheya Graben is older than that of the Iheya Ridge, which is at least 0.2 Ma. The formation of the Iheya Graben and volcanism afterwards raise the possibility that the large-scale magmatism beneath the Iheya Graben is the present driving force of back-arc rifting in the region.

Acknowledgements This study was supported by the "TAIGA project," which was funded by a Grant-in-Aid for Scientific Research on Innovative Areas (No. 20109004) from the Ministry of Education, Culture, Sports, Science and Technology (MEXT), Japan.

The YK12-16 Cruise was conducted as a part of the Submarine Resources Research Project, JAMSTEC. Dr. H, Machiyama and

Y. 'Nishio supported the survey as on-board scientists. Other seismic data we used in this study were also acquired by JAMSTEC.

We thank K. Okino (University of Tokyo) and M. Asada (JAMSTEC) for their constructive review comments. Our manuscript is well improved by their comments.

T. Tsuji gratefully acknowledges the support of the I2CNER, sponsored by the World Premier International Research Center Initiative (WPI), MEXT, Japan. T. Tsuji is also partially supported for this work by Sumitomo Foundation.

References

Furukawa M, Tokuyama H, Abe S, Nishizawa A, Kinoshita H (1991) Report on DELP 1988 cruises in the Okinawa Trough Part 2. Seismic reflection studies in the southwestern part of the Okinawa Trough. Bull ERI Univ Tokyo 66:17–36

Glasby GP, Notsu K (2003) Submarine hydrothermal mineralization in the Okinawa Trough, SW of Japan: an overview. Ore Geol Rev 23:299–339. doi:10.1016/j.oregeorev.2003.07.001

Iryu Y, Matsuda H, Machiyama H, Piller WE, Quinn TM, Mutti M (2006) Introductory perspective on the COREF project. Island Arc 15:393–406. doi:10.1111/j.1440-1738.2006.00537.x

Kimura M (1990) Genesis and formation of the Okinawa Trough, Japan. Memoirs Geol Soc Japan 34:77–88

Kimura M (2000) Paleogeography of the Ryukyu Islands. Tropics 10 (1):5–24

Kimura M, Kaneoka I, Kato Y, Yamamoto S, Kushiro I, Tokuyama H, Kinoshita H, Isezaki N, Masaki H, Oshida A, Uyeda S, Hilde T (1986) Report on DELP 1984 cruises in the middle Okinawa Trough. Part 5: topography and geology of the central grabens and their vicinity. Bull ERI Univ Tokyo 61:269–310

Kimura M, Kato Y, Tanaka T, Naka J, Gamou T, Yamano M, Ando M, Uyeda S, Sakai H, Oomori T, Izawa E, Kanenaga M, Ono T, Oshida A (1987) Submersible SHINKAI 2000 study in the central rift in the Middle Okinawa Trough. JAMSTEC Deepsea Res 3:165–196

Kimura M, Matsumoto T, Shinjo R, Nakamura M, Motoyama I, Machiyama H, Toyama G, Yagi H (2001) Meanders recognized in the southwestern part of the Okinawa Trough and its significance. JAMSTEC Deepsea Res 18:103–120

Kumagai H (2012) Yokosuka/Urashima "Cruise Report" YK12-16, JAMSTEC. http://www.godac.jamstec.go.jp/catalog/data/doc_catalog/media/YK12-16_all.pdf

Lee C-S, Shore GG, Bebee LD, Lu RS, Hilde T (1980) Okinawa Trough: origin of a back-arc basin. Marine Geol 35:219–241

Letouzey J, Kimura M (1986) The Okinawa Trough: genesis of a back-arc basin developing along a continental margin. Tectonophysics 125:209–230

Miki M (1995) Two-phase opening model for the Okinawa Trough inferred from paleomagnetic study of the Ryukyu arc. J Geophys Res 100(B5):8169–8184. doi:10.1029/95JB00034

Nagumo S, Kinoshita H, Kasahara J, Ouchi T, Tokuyama H, Asamuma T, Koresawa S, Akiyoshi H (1986) Report on DELP 1984 cruises in the middle Okinawa Trough Part 2: seismic structural studies. Bull ERI Univ Tokyo 61:167–202

Otubo M, Hayashi D (2003) Neotectonics in southern Ryukyu arc by means of paleostress analysis. Bull Fac Sci Univ Ryukyus 76:1–73

Park J-O, Tokuyama H, Shinohara M, Suyehiro K, Taira A (1998) Seismic record of tectonic evolution and backarc rifting in the southern Ryukyu island arc system. Tectonophysics 294:21–42

Ryan BF, Carbotte SM, Coplan JO, O'Hara S, Melkonian A, Arko R, Weissel RA, Ferrini V, Goodwillie A, Nitsche F, Bonczkowski J, Zemsky R (2009) Global multi-resolution topography synthesis. Geochem Geophys Geosyst 10(3), Q03014. doi:10.1029/2008GC002332

Sibuet J-C, Letouzey J, Barbier F, Charvet J, Foucher J-P, Hilde T, Kimura M, Ling-Yun C, Marsset B, Muller C, Stephan J-F (1987) Back arc extension in the Okinawa Trough. J Geophys Res 92 (B13):14041–14063. doi:10.1029/JB092iB13p14041

Sibuet J-C, Deffontaines B, Hsu S-K, Thareau N, Le Formal J-P, Liu C-S, ACT Party (1998) Okinawa trough backarc basin: early tectonic and magmatic evolution. J Geophys Res 103(B12):30245–30267

Tsuji T, Takai K, Oiwane H, Nakamura Y, Masaki Y, Kumagai H, Kinoshita M, Yamamoto F, Okano T, Kuramoto S (2012) Hydrothermal fluid flow system around the Iheya North Knoll in the mid-Okinawa trough based on seismic reflection data. J Volc Geotherm Res 213:41–50. doi:10.1016/j.jvolgeores.2011.11.007

Ueda S, Kimura M, Tanaka T, Kaneoka I, Kato Y, Kushiro I (1985) Spreading center of the Okinawa Trough. JAMSTEC Deepsea Res 1:123–142

Zang SX, Chen QY, Ning JY, Shen ZK, Liu YG (2002) Motion of the Philippine Sea plate consistent with the NUVEL-1A model. Geophys J Int 150(3):809–819

ESR Dating of Barite in Sea-Floor Hydrothermal Sulfide Deposits in the Okinawa Trough

29

Taisei Fujiwara, Shin Toyoda, Ai Uchida, Jun-ichiro Ishibashi, Shun'ichi Nakai, and Asako Takamasa

Abstract

ESR (electron spin resonance) ages were determined for barite crystals extracted from hydrothermal sulfide deposits taken at Daiyon-Yonaguni Knoll field, Hatoma Knoll field, Iheya North Knoll field, Hakurei Site of Izena Hole field, Yoron Hole field of the Okinawa Trough. The ages range from 4.1 to 16,000 years, being consistent with detection of ^{228}Ra in younger samples and radioactive equilibrium/disequilibrium between radium and daughter nuclei. The variation of the ages within each sample is mostly within the statistical error range. The relative order of the ages is consistent with the result of ^{226}Ra-^{210}Pb method, but the determining absolute ages is still an issue. The order of ages of the 5 hydrothermal fields would be arranged, from young to old as follows; Yoron Hole field, Daiyon-Yonaguni Knoll field, Hatoma Knoll field, being nearly equal to Iheya North Knoll field.

Keywords

Barite • Dating • Electron spin resonance • Hydrothermal activities

29.1 Introduction

There have been many scientific efforts devoted for studies on active sea-floor hydrothermal fields found in Okinawa Trough (Ishibashi et al. Chap. 23). The evolution of these hydrothermal fields is one of the important issues. Dating methods have been employed for hydrothermal sulfide deposits, such as the U-Th disequilibrium method (e.g. You and Bickle 1998) applicable for the age range more than several thousand years, and ^{226}Ra-^{210}Pb and ^{228}Ra-^{228}Th method (e.g. Noguchi et al. 2011) for the range less than 150 years. The age range of several hundred years is essential to estimate the life time of hydrothermal activities. However, dating methods for the age range are lacking.

Okumura et al. (2010) made the first practical application of ESR dating technique to a sample of seafloor hydrothermal barite to obtain ages of 300 and 3,620 years, while Kasuya et al. (1991) first pointed out that barite can be used for ESR dating. Toyoda et al. (2011) determined the optimum ESR condition while Sato et al. (2011) confirmed that the signal is thermally stable enough for an age range of several thousand years.

Seafloor massive sulfide deposits are composed of sulfide minerals such as pyrite, sphalerite, chalcopyrite and galena, and also include sulfate minerals such as anhydrite and barite. The sulfate minerals precipitate by mixing of hydrothermal fluid and seawater, while the sulfide minerals precipitate from the hydrothermal fluid mainly by cooling (Hannington et al. 1995). It is generally considered that a combination and/or switch of these two modes of hydrothermal precipitation lead to growth of sulfide structures such as a chimney and mound and that of large hydrothermal

T. Fujiwara • S. Toyoda (✉) • A. Uchida
Okayama University of Science, Okayama, Japan
e-mail: toyoda@dap.ous.ac.jp

J.-i. Ishibashi
Kyusyu University, Fukuoka, Japan

S. Nakai
University of Tokyo, Tokyo, Japan

A. Takamasa
National Institute of Radiological Sciences, Chiba, Japan

J.-i. Ishibashi et al. (eds.), *Subseafloor Biosphere Linked to Hydrothermal Systems: TAIGA Concept*,
DOI 10.1007/978-4-431-54865-2_29,

deposits (e.g. Tivey 2007). Takamasa et al. (2013) determined ESR ages for barite in sulfide deposits in the South Mariana Trough hydrothermal field, and concluded that the ages are consistent with U-Th ages. In this study, the ages of various hydrothermal sulfides in the Okinawa Trough are determined by ESR dating.

29.2 Material and Methods

The sulfide deposit samples were obtained in the 6 research cruises; NT01-05, NT02-07, YK04-05, NT11-20, NT12-06, and NT12-10 operated by the Japan Agency for Marine-Earth Science and Technology (JAMSTEC) from Daiyon-Yonaguni Knoll field, Hatoma Knoll field, Iheya North Knoll field, Hakurei field of Izena Hole field, Yoron Hole field of the Okinawa Trough (Figs. 29.1 and 29.2, and Table 29.1). After blocks of sulfide sample were cut into pieces (Fig. 29.3), approximately 2.0 g of the pieces was crushed. The samples were soaked in 12 M hydrochloric acid for approximately 24 h. Then, 13 M nitric acid was added. Finally, after rinsing in distilled water, the sample was filtered and dried. Mineral grains other than barite were removed by handpicking. The purified mineral grains were determined by an X-ray diffraction and confirmed that the grains are pure barite.

The barite grains extracted from each sample were separated into 100–250 μm aliquots for gamma ray irradiation up to about 10 kGy with a dose rate of 404.4 Gy/h made at Takasaki Advanced Radiation Research Institute, Japan Atomic Energy Agency (JAEA). The sample aliquots were measured at room temperature with an ESR spectrometer (JES-PX2300) with a microwave power of 1 mW, and the magnetic field modulation amplitude of 0.1 mT as indicated by Toyoda et al. (2011) to be the best measurement conditions. The equivalent natural radiation doses were obtained by extrapolating the obtained dose response curve of the SO_3^- signal to the ordinate intercept.

The bulk radium (^{226}Ra and ^{228}Ra) concentrations were measured by the low background pure Ge gamma ray spectrometer. Assuming that Ra is populated only in barite as confirmed by Okumura et al. (2010), the internal and external dose rates of alpha, beta and gamma rays given to the barite minerals were calculated (Toyoda et al. 2014). The alpha effectiveness of 0.043 was adopted (Toyoda et al. 2012). Corrections were made for water content, beta ray attenuation for grain sizes (a plane with 20 μm in thickness as confirmed by thin section). In the present paper, a new formula is proposed to obtain the ages which takes into account the decays of ^{226}Ra (a half life of 1,600 years) and ^{228}Ra (a half life of 5.75 years) with disequilibrated daughter nuclei as the following.

29.3 The Dose Rate Conversion Factors and the Decay Corrections for ^{226}Ra and ^{228}Ra

It is the most important feature of hydrothermal barite in the aspect of dose rate estimation that the only source of the radiation is internal radium (Okumura et al. 2010; Toyoda et al. 2014). The dose rate was calculated from the concentrations of radium and its daughter nuclei as the following.

The newest dose rate conversion factors, which are to be multiplied to the concentrations of U, Th, K to obtain dose rate, were reported by Guérin et al. (2011) for U and Th in radioactive equilibrium and for K together with the contributions of each nucleus in the decay chains. Toyoda et al. (2014) obtained the dose rate conversion factors from their table for ^{226}Ra only in the case of radioactive equilibrium. By summing up the energy contributions of the nuclei in the chains listed in Guérin et al. (2011), the dose rate conversion factors for ^{226}Ra and ^{228}Ra were calculated so that the dose rate can be obtained in the case of radioactive disequilibrium as shown in Table 29.2.

When the dose rate varies with time in the past, the equivalent dose, D_E, obtained by the ESR measurements is expressed by the integration of a time dependent dose rate, D (t), as the following,

$$D_E = \int_0^T D(t)dt \tag{29.1}$$

As the source of the dose is Ra which decays with time, the decay has to be taken into account for the does rate, D(t). For the decay of ^{226}Ra, Toyoda et al. (2014) obtained a formula as

$$T = \frac{1}{\lambda}\ln\left(\lambda\frac{D_E}{D} + 1\right) \tag{29.2}$$

This formula is valid for the samples with ages over 200 years where the daughter nucleus with second longest half life (^{210}Pb, 22.3 years) in the decay series is equilibrated. However, for the younger samples, the radioactive disequilibrium and contributions from the decay series starting from ^{228}Ra have to be considered.

When the number of nuclei of ^{226}Ra or ^{228}Ra is N_1, and that of the daughter nuclei with second longest life (^{210}Pb or ^{228}Th) is N_2, those are expressed as,

$$N_1 = N_{10}\,e^{-\lambda_1 t} \tag{29.3}$$

$$N_2 = \frac{\lambda_1}{\lambda_2 - \lambda_1}N_{10}\left(e^{-\lambda_1 t} - e^{-\lambda_2 t}\right) \tag{29.4}$$

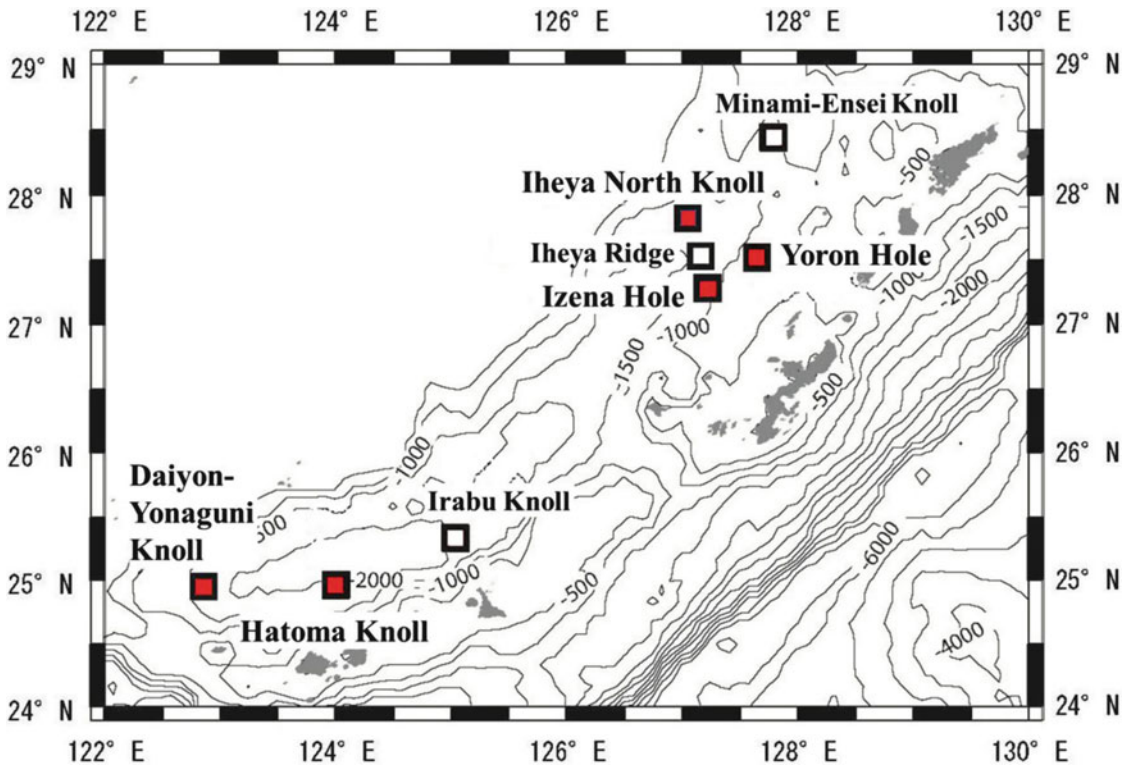

Fig. 29.1 A bathymetric map of the known hydrothermal fields and sampling fields in the Okinawa Trough. *Red triangles* indicate the sampling fields; Daiyon-Yonaguni Knoll field, Hatoma Knoll field, Iheya North Knoll field, Hakurei field of Izena Hole field, Yoron Hole field

where N_{10} is the initial number of parent nuclei, λ_1 and λ_2 are the decay constant of the parent and the daughter nuclei, respectively, and it is assumed that initially no daughter nuclei are present. We only know the number of nuclei at present, N_{1p}, expressed as,

$$N_{1p} = N_{10}e^{-\lambda_1 T}$$

where T is the age of the sample. Therefore, Eqs. (29.3) and (29.4) are written as,

$$N_1 = N_{1p}e^{\lambda_1(T-t)} \tag{29.5}$$

$$N_2 = \frac{\lambda_1}{\lambda_2 - \lambda_1}N_{1p}e^{\lambda_1 T}\left(e^{-\lambda_1 t} - e^{-\lambda_2 t}\right) \tag{29.6}$$

respectively.

The dose rate, D(t), given by the parent and daughter nuclei is written as,

$$D(t) = Q_1\lambda_1 N_1(t) + Q_2\lambda_2 N_2(t) \tag{29.7}$$

where Q_1 and Q_2 are the dose rate conversion factors for the nuclei from the parent to the one just before the daughter with the second longest life time in the decay series, and for those from that daughter and after, respectively. Please note that a conversion factor is given per unit activity, λN. From Eqs. (29.5)–(29.7) is written as,

$$D(t) = \lambda_1 N_{1p}e^{\lambda_1 T}\left\{e^{-\lambda_1 t}\left(Q_1 + Q_2\frac{\lambda_2}{\lambda_2 - \lambda_1}\right) - Q_2 e^{-\lambda_2 t}\right\} \tag{29.8}$$

The D_E is given by integrating the dose rate as the following,

$$D_E = \int_0^T D(t)dt$$
$$= \lambda_1 N_{1p}e^{\lambda_1 T}\left\{\frac{1}{\lambda_1}\left(Q_1 + Q_2\frac{\lambda_2}{\lambda_2 - \lambda_1}\right)\left(1 - e^{-\lambda_1 T}\right) - \frac{Q_2}{\lambda_2}\left(1 - e^{-\lambda_2 T}\right)\right\} \tag{29.9}$$

For the present case, two decay series have to be taken into account, one starting from ^{226}Ra (half life: 1,600 years) where the daughter nucleus with the second longest life time is ^{210}Pb (22.3 years), and the other from ^{228}Ra (5.75 years) where the daughter is ^{228}Th (1.91 years). In the present work, the dose rates from both series are summed and T is obtained by Eq. (29.9) where the present radium activities ($\lambda_1 N_1$) were used.

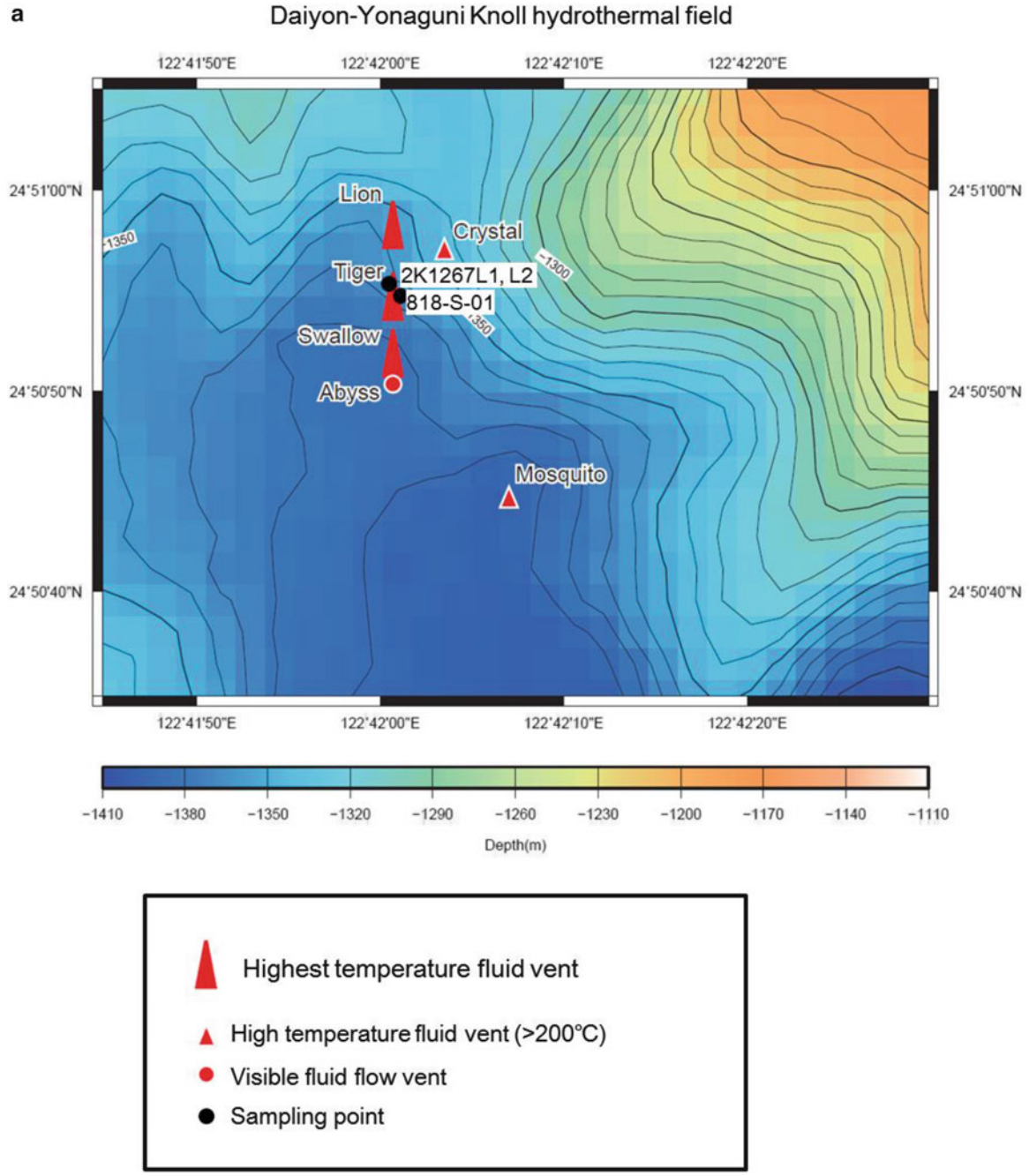

Fig. 29.2 Sampling location at the five hydrothermal fields in the Okinawa Trough. (**a**) Daiyon-Yonaguni Knoll field, (**b**) Hatoma Knoll field, (**c**) Iheya North Knoll field, (**d**) Hakurei field of Izena Hole field, (**e**) Yoron Hole field

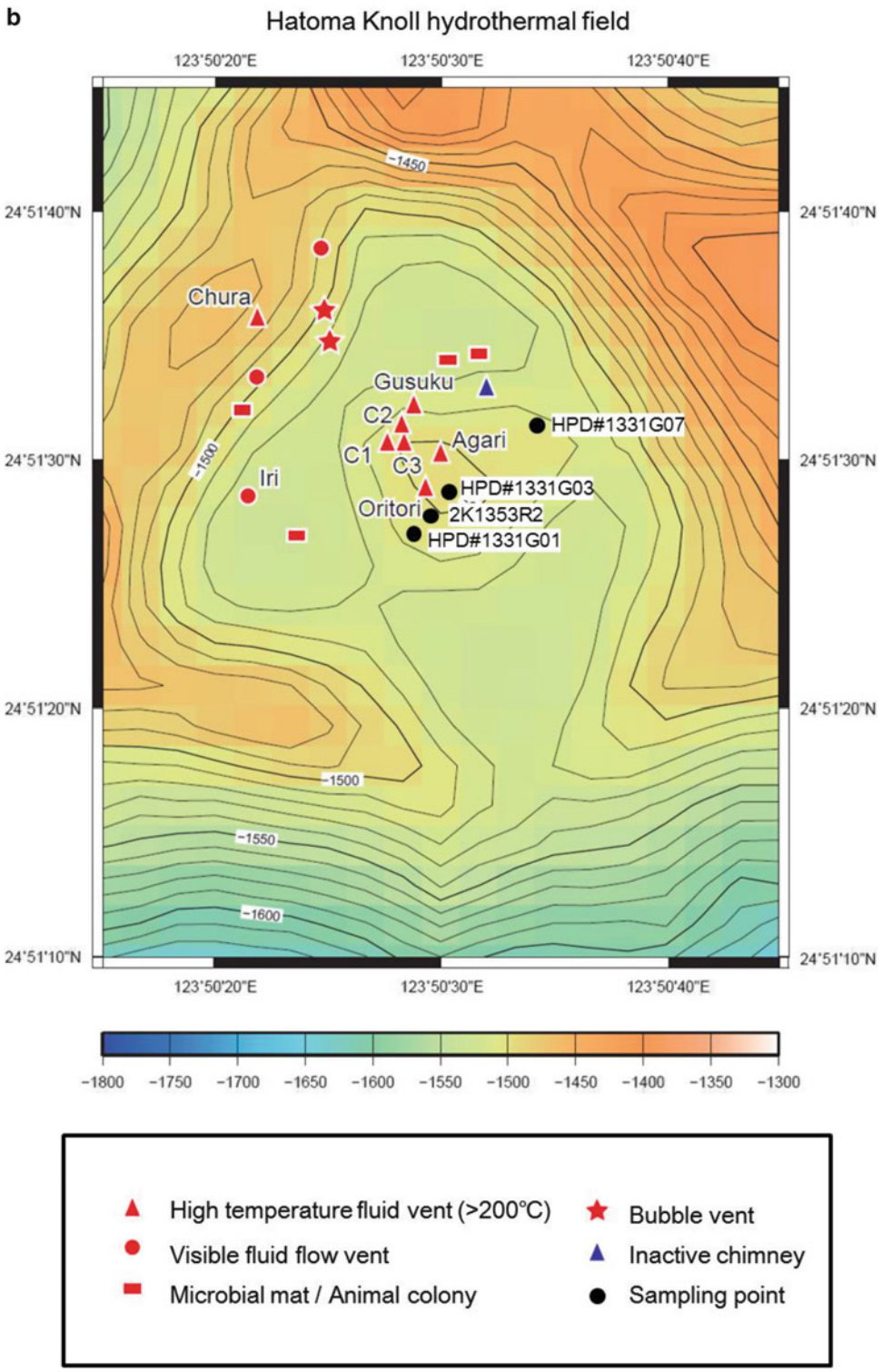

Fig. 29.2 (continued)

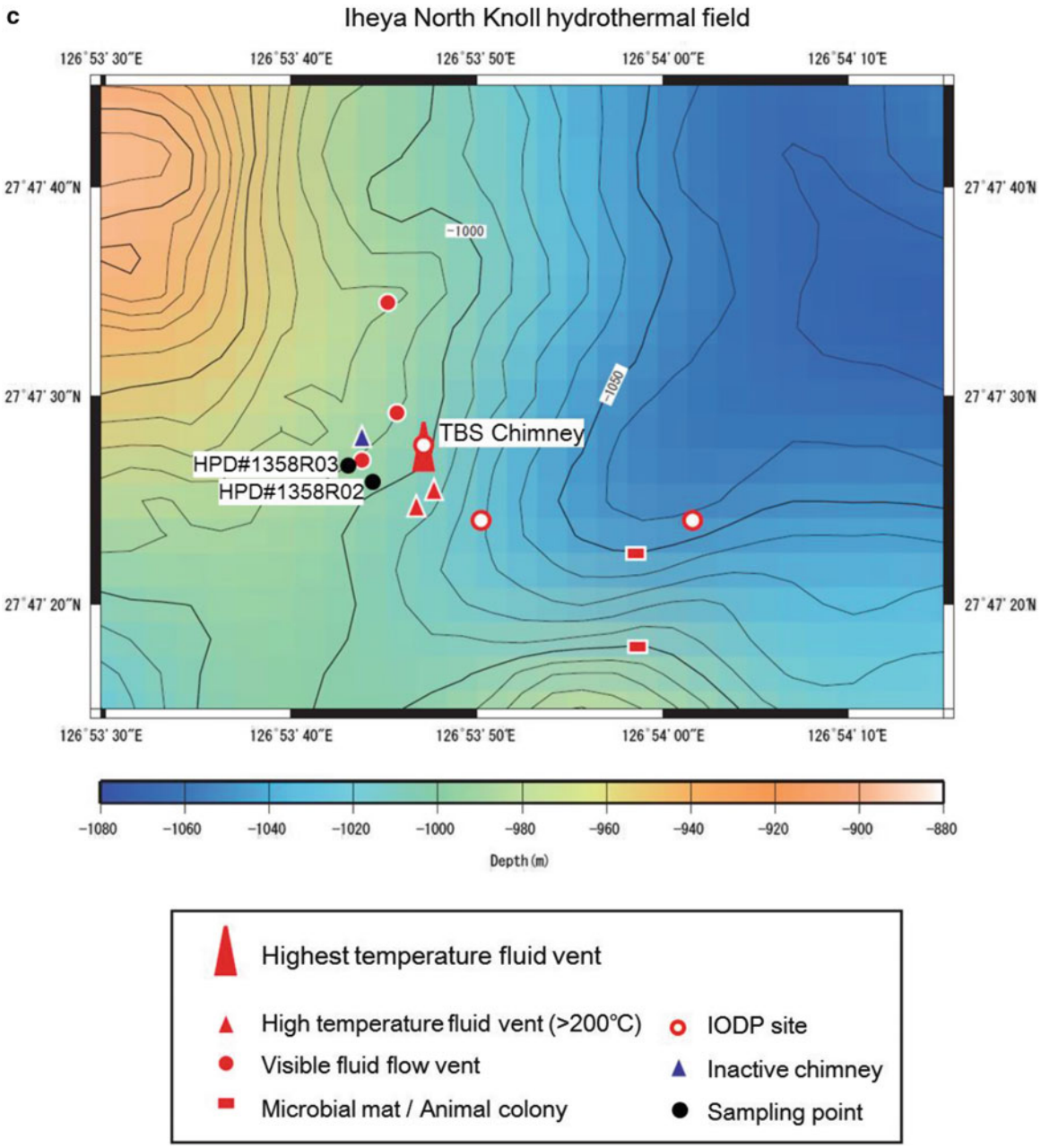

Fig. 29.2 (continued)

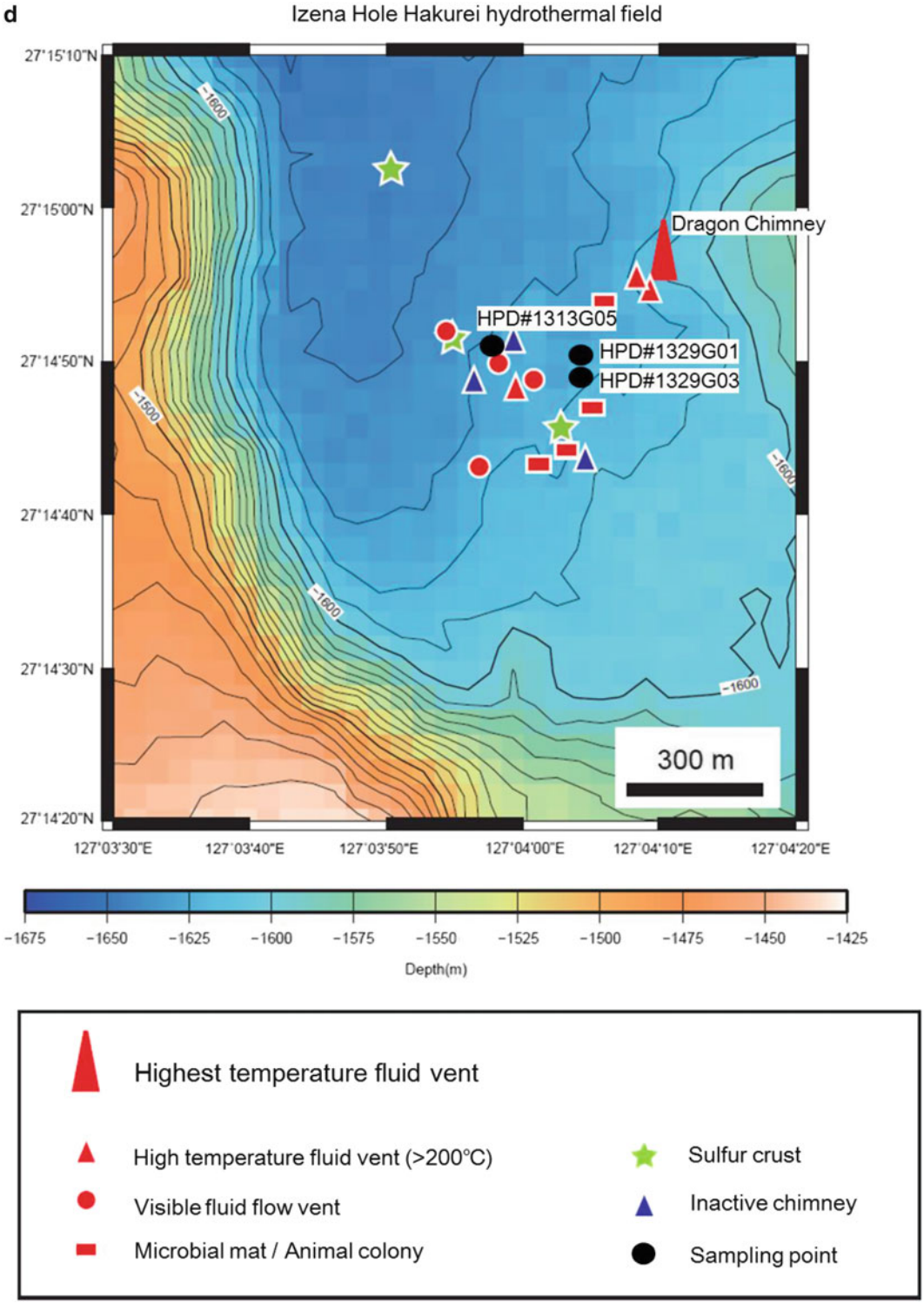

Fig. 29.2 (continued)

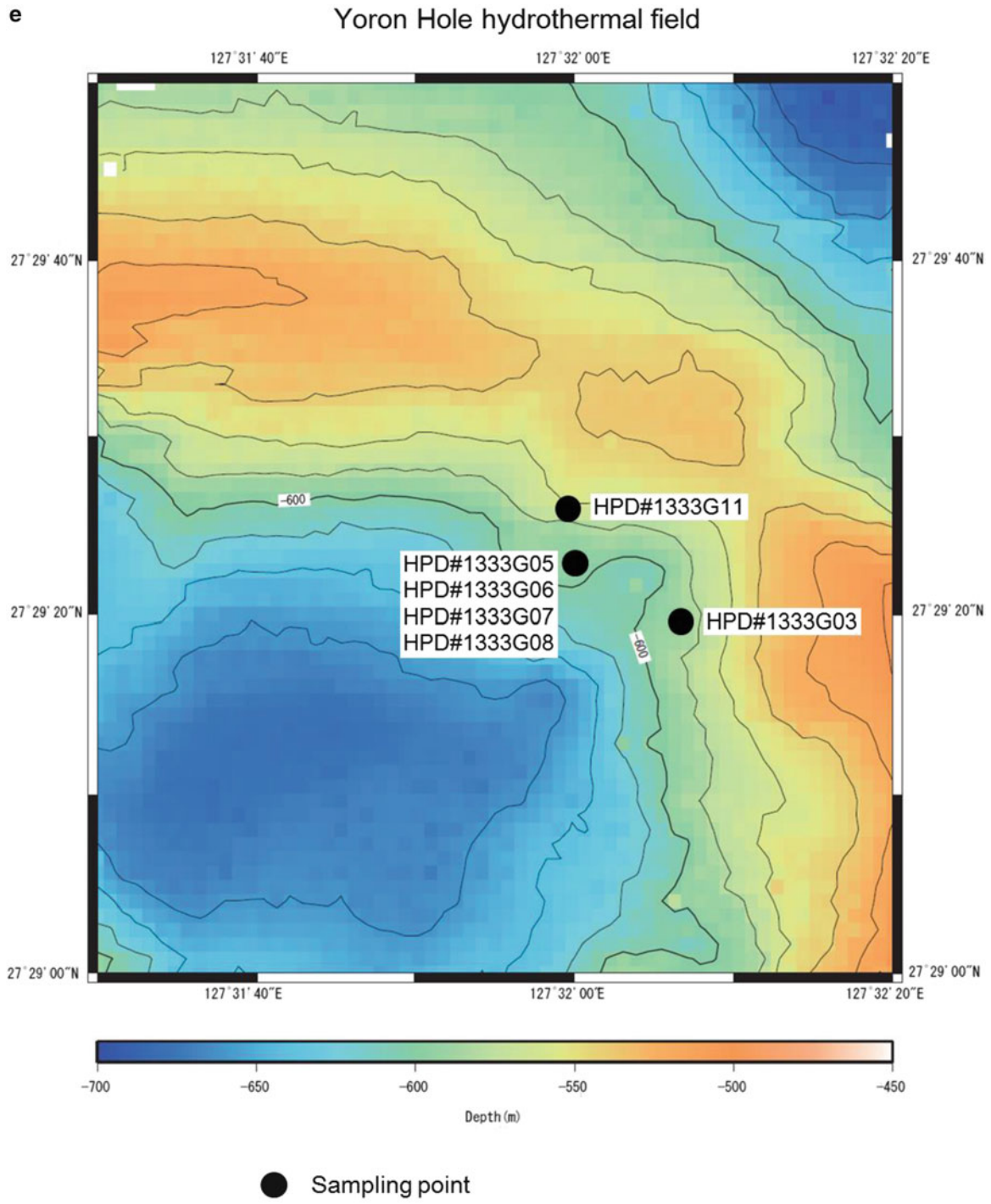

Fig. 29.2 (continued)

Table 29.1 List of samples analyzed in the present study

Sample No.	Sampling position		Depth (m)	Sampling	Sampling	Description
	Latitude (N)	Longitude (E)		Date	Tool	
Yonaguni Knoll field-Daiyon						
818-S-01	24°50.893′	122°42.020′	1,363	5/28/2004	SHINKAI6500	Active chimney
2K1267L1	24°50.934′	122°42.012′	1,366	5/16/2001	SHINKAI2000	Active chimney
2K1267L2	24°50.934′	122°42.012′	1,366	5/16/2001	SHINKAI2000	Active chimney
Hatoma Knoll field						
HPD#1331G01	24°51.450′	123°50.478′	1,499	10/8/2011	Hyper Dolphyn	Inactive chimney
HPD#1331G03	24°51.477′	123°50.508′	1,477	10/8/2011	Hyper Dolphyn	Sulfide mound
HPD#1331G07	24°51.520′	123°50.559′	1,490	10/8/2011	Hyper Dolphyn	Active chimney
2K1353R2	24°51.455′	123°50.477′	1,488	5/28/2002	SHINKAI2000	Active chimney
Iheya North Knoll field						
HD#1358R2	27°47.438′	126°53.736′	990	3/21/2012	Hyper Dolphyn	Sulfide mound
HD#1358R3	27°47.460′	126°53.730′	982	3/21/2012	Hyper Dolphyn	Inactive chimney
Izena Hole field						
HPD#1313G05	27°14.856′	127°03.962′	1,613	8/22/2011	Hyper Dolphyn	Active chimney
HPD#1329G01	27°14.838′	127°04.093′	1,620	10/5/2011	Hyper Dolphyn	Inactive chimney
HPD#1329G03	27°14.815′	127°03.093′	1,617	10/5/2011	Hyper Dolphyn	Inactive chimney
Yoron Hole field						
HPD#1333G03	27°29.328′	127°32.124′	580	10/10/2011	Hyper Dolphyn	Active chimney
HPD#1333G05	27°29.382′	127°32.004′	591	10/10/2011	Hyper Dolphyn	Active chimney
HPD#1333G06	27°29.382′	127°32.004′	591	10/10/2011	Hyper Dolphyn	Active chimney
HPD#1333G07	27°29.382′	127°32.004′	591	10/10/2011	Hyper Dolphyn	Active chimney
HPD#1333G08	27°29.382′	127°32.004′	591	10/10/2011	Hyper Dolphyn	Active chimney
HPD#1333G11	27°29.424′	127°31.998′	566	10/10/2011	Hyper Dolphyn	Active chimney

29.4 Results and Discussions

A typical ESR spectrum is shown in Fig. 29.4. The principal g factors are calculated from this powder spectrum to be 1.9995, 2.0023, and 2.0031, being consistent with the g factors for SO_3^- radical obtained by Krystec (1980), which are 1.9995, 2.0023, and 2.0032. The peak-to-peak height of the spectrum (Fig. 29.4) was used as the signal intensity. An example of dose response of the signal intensity is shown in Fig. 29.5. Extrapolating the dose response to the zero ordinate, being fitted by a saturating exponential curve, the equivalent doses are obtained as shown in Table 29.3.

The ^{226}Ra and ^{228}Ra concentrations were measured by a low background pure germanium gamma ray spectrometer for bulk samples as shown in Table 29.3. The ^{226}Ra concentrations were obtained from the peak counts for ^{214}Bi (609, 1,120, 1,765 keV) and for ^{214}Pb (295 and 352 keV) in comparison with a standard uranite sample with radioactive equilibrium with known uranium concentration. The ^{228}Ra concentrations were from the peak counts for ^{228}Ac (338, 911, 969 keV) (Yonezawa et al. 2002). The ages of the samples were determined using the Eq. (29.6) as shown in Table 29.3.

The ages ranged from 4.1 to 16,000 years while the ages of pieces from a sample varies more than estimated analytical errors (Table 29.3). As discussed by Toyoda et al. (2014), microscopic observation revealed that sulfide minerals with various size and various occurrence fill the spaces among barite crystals, suggesting repeated stages of mineralization, which starts with sulfate precipitation and followed by sulfide precipitation. Thus the samples would consist of minerals in various ages. It would be more probable that the determined ages are somewhat "averaged" within the portion of the sample, implying that the variation in ages corresponds to the ratio of the younger to older crystals. Therefore, when the ages vary within a sample portion, it would mean that repeated hydrothermal activities have formed the sample at the time of around those ages. If this is the case, the oldest age would correspond to the youngest limit of the oldest activity.

The determined ESR ages are young up to 56 years for those samples in which ^{228}Ra is detected. It is consistent that younger samples contain ^{228}Ra with a short half life of 5.75

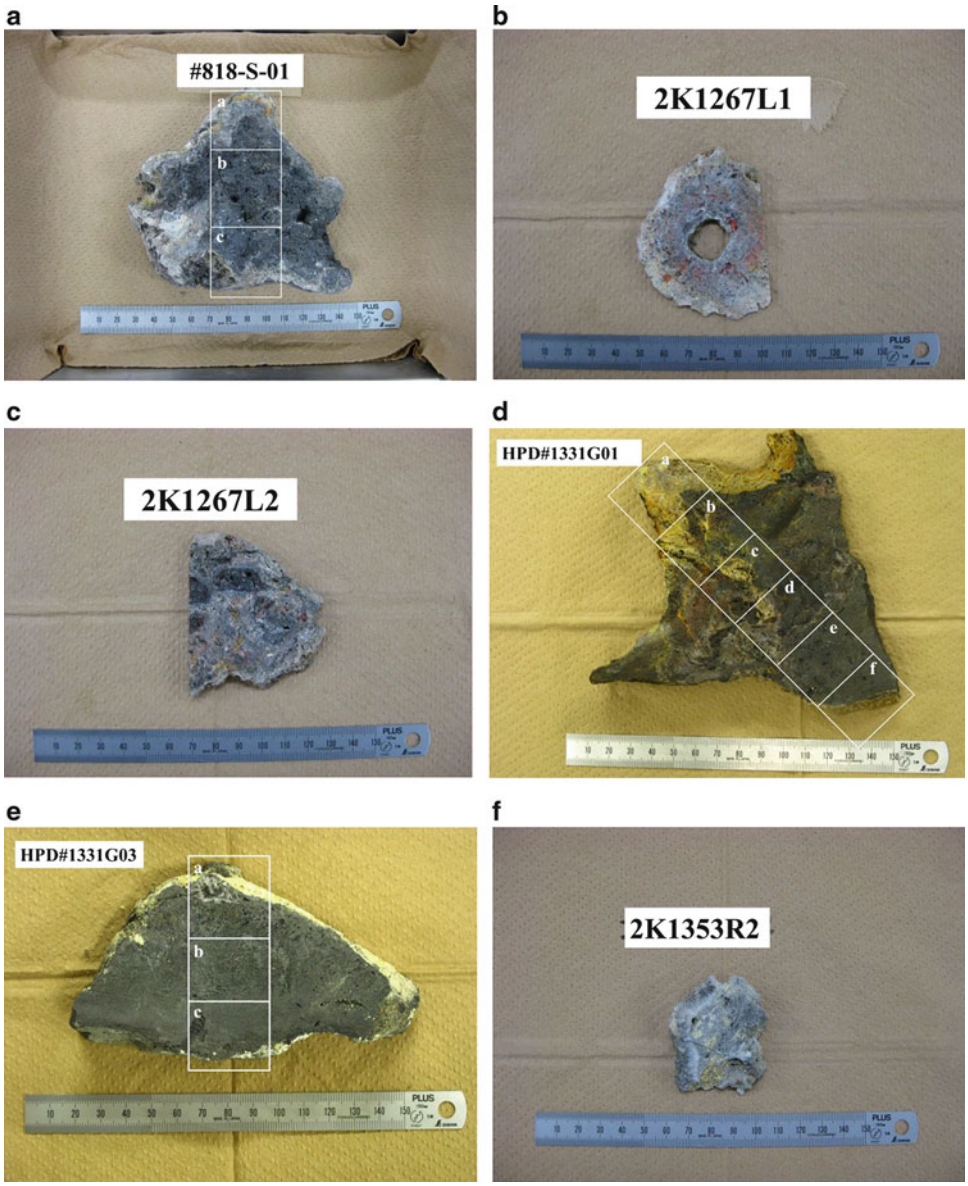

Fig. 29.3 Overview of sulfide samples and analyzed parts in each sulfide

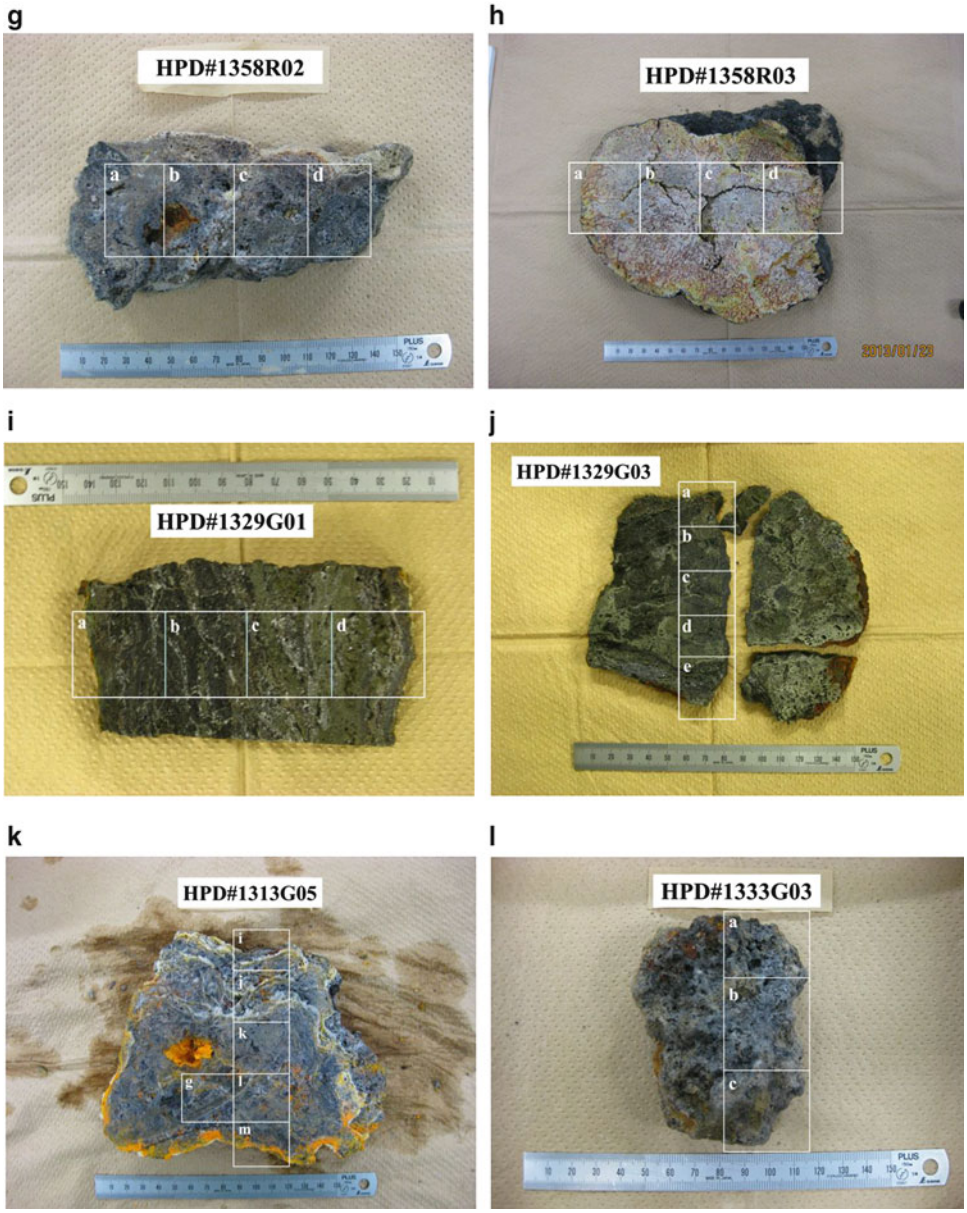

Fig. 29.3 (continued)

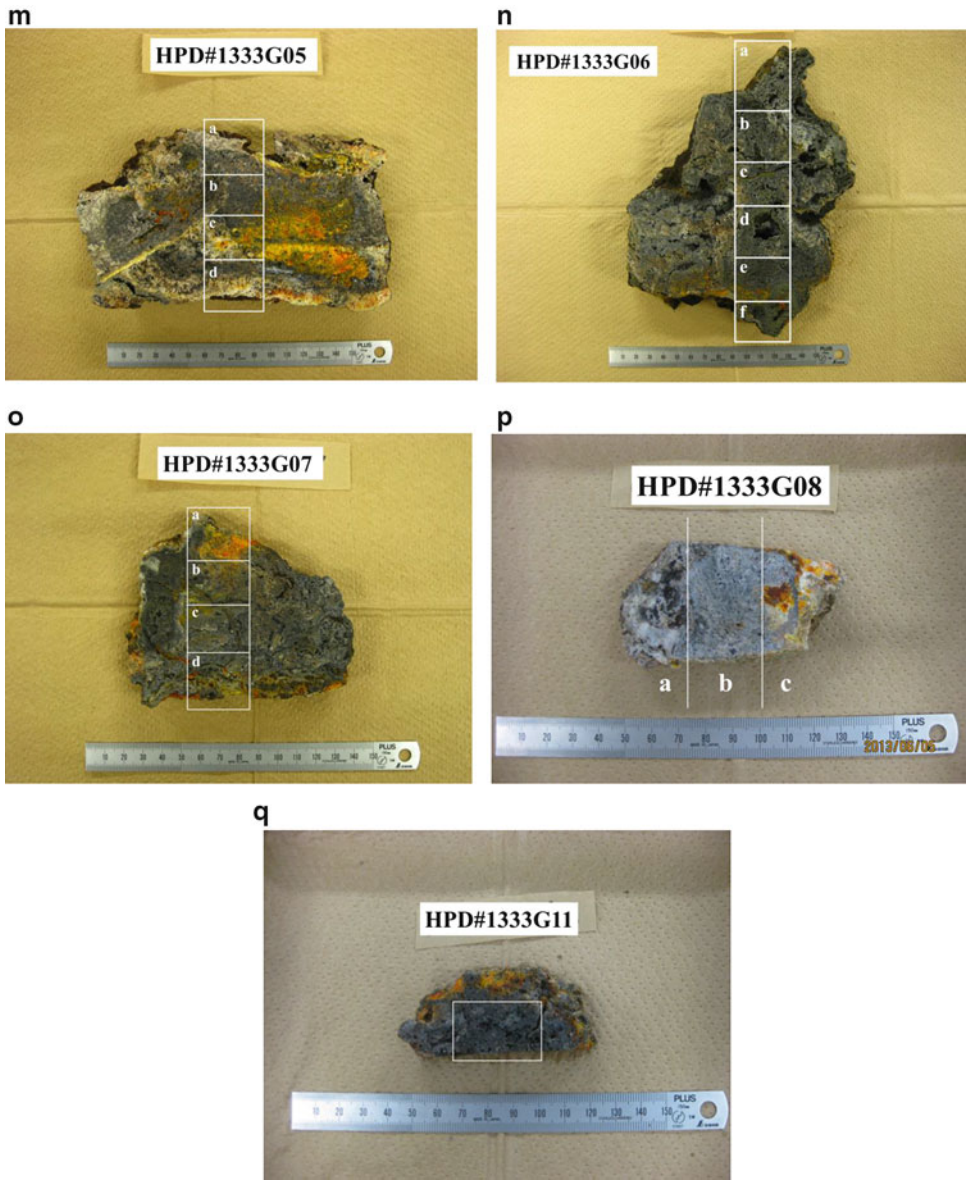

Fig. 29.3 (continued)

years. It is also reasonable that the all ESR ages for sulfide samples of active vent site are younger than those for sulfide samples of inactive vent site. ^{226}Ra-^{210}Pb and ^{228}Ra-^{228}Th ages obtained for part of the present samples are discussed in comparison with the present ESR ages by Uchida et al. (Chap. 47).

29.4.1 Daiyon-Yonaguni Knoll Field

The age of active chimney (818-S-01) from an active vent site ranges from 580 to 990 years, while the samples from active vent sites (2K1267L1, 2) show younger ages, 200 and 260 years.

29.4.2 Hatoma Knoll Field

The ESR ages of inactive chimney (HPD#1331G01) were 2,400–3,700 years, which are statistically indistinguishable. ^{210}Pb in this sample was in radioactive equilibrium with ^{226}Ra. One piece from sulfide mound sample, HPD#1331G03, shows an age of 990 years, which was statistically younger than other two ages of 3,000 and

5,700 years. The age of 2K1353R2 was determined to be 970 years. The age of HPD#1331G07 taken from an active chimney was determined to be of 7.1 years. U-Th ages were determined for sulfide minerals extracted from three pieces of HPD#1331G01, but they vary much more than ESR ages.

Table 29.2 The dose rate conversion factors in mGy/y calculated, summing up the energy contributions of the nuclei in the chains listed in Guérin et al. (2011), the dose rate conversion factors for ^{226}Ra and ^{228}Ra were calculated so that the dose rate can be obtained in the case of radiative disequilibrium

mGy/y	D_α	D_β	D_γ
^{226}Ra-^{210}Tl			
per 1 Bq/g of ^{226}Ra	120.9	4.789	8.703
per 1 ppm of virtually equilibrated ^{238}U	1.505	0.0596	0.1083
^{210}Pb-^{206}Pb			
per 1 Bq/g of ^{226}Ra	26.76	2.138	0.0241
per 1 ppm of virtually equilibrated ^{238}U	0.333	0.0266	0.0003
^{228}Ra-^{228}Ac			
per 1 Bq/g of ^{228}Ra	0	2.177	4.353
per 1 ppm of virtually equilibrated ^{232}Th	0	0.0088	0.0176
^{228}Th-^{208}Pb			
per 1 Bq/g of ^{228}Ra	162.1	4.600	7.470
per 1 ppm of virtually equilibrated ^{232}Th	0.6554	0.0186	0.0302

29.4.3 Iheya North Knoll Field

A sample from an inactive chimney (HPD#1358R3) shows ages from 3,000 to 4,300 years, while the other sample taken from a sulfide mound (HPD#1358R2) shows younger age 560–1,000 years, which are also statistically indistinguishable.

29.4.4 Izena Hole Field

Two samples from an inactive chimney (HPD#1329G01, G03) show ages over 10,000 years. On the other hand, a sample from an active chimney (HPD#1313G05) shows statistically consistent ages from 12 to 16 years, in which ^{228}Ra was also detected. ^{228}Th was equilibrated with ^{228}Ra.

29.4.5 Yoron Hole Field

The samples analyzed in the present study were all from active chimneys. Older ages over 70 years were determined for HPD#1333G05 and G06 in which no ^{228}Ra was detected while younger ages up to 56 years were determined for HPD#1333G03, G07, G08 and for HPD#1333G11 in

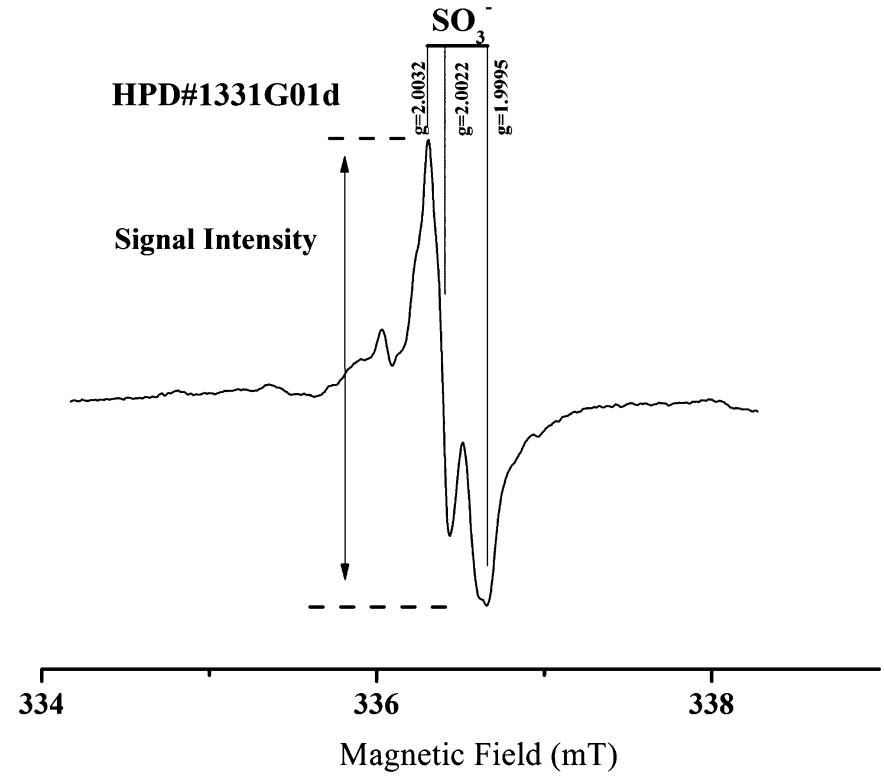

Fig. 29.4 A typical ESR spectrum in hydrothermal barite (natural sample of HPD#1331G01d)

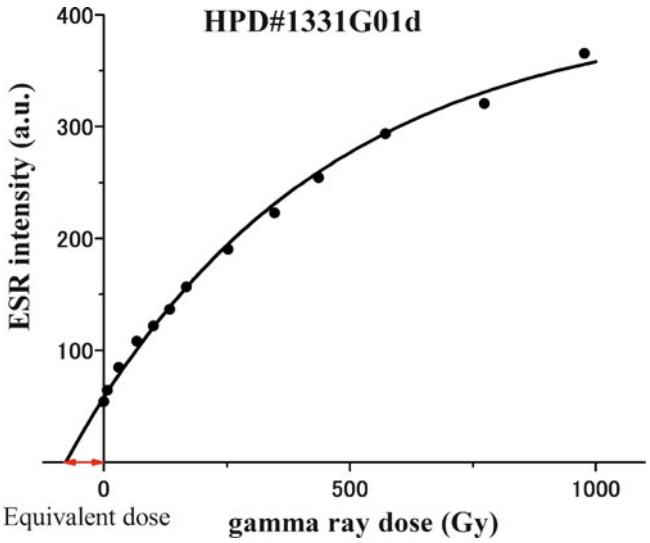

Fig. 29.5 A typical dose response of the SO_3^- signal on gamma ray dose (HPD#1331G01d)

which ^{228}Ra was detected. The two consistent ages of 400 years were determined from two pieces of the sample, HPD#1333G05, however, the age of 200 years from one piece is significantly younger than these ages. Another age of 330 years between these ages was also determined. It seems that there are two distinct ages of 70–80 and 120–150 years in HPD#1333G06, which are statistically distinct. U-Th ages for this sample were less than 20 or 80 years, younger than ESR ages. ^{226}Ra-^{210}Pb ages were determined for these two samples using the same barite samples for ESR measurements. The ages were 71–77 years for HPD#1333G05 and 23–27 years for HPD#1333G06, significantly younger than ESR ages, but the relative order is consistent. The ESR ages of 200–400 years for HPD#1333G05 are older than 70–150 years for HPD#1333G06, while ^{226}Ra-^{210}Pb ages for HPD#1333G05 are 71–77 years, older than 23–27 years for HPD#1333G06 (Uchida et al. Chap. 47).

The sample HPD#1333G03 shows consistent ESR ages of 4.1–5.2 years, while ^{228}Ra-^{228}Th ages were 4.5–5.2 years, being coincided with ESR ages. Three ESR ages of HPD#1333G07 were in agreement between 50 and 56 years while one piece shows significantly younger age of 28 years. ^{228}Th was in radioactive equilibrium with ^{228}Ra in these samples, which is consistent with the results that ESR ages are older than HPD#1333G03, in which ^{228}Ra and ^{228}Th are in disequilibrium. Two ESR ages, 35 and 39 years, of HPD#1333G08 are statistically consistent but one age of 27 years is younger, for which ^{228}Ra-^{228}Th was determined to be 4.2 years. ^{228}Th was in radioactive equilibrium with ^{228}Ra in the former two pieces, being consistent with ESR results.

29.4.6 ESR Ages of Hydrothermal Field in the Okinawa Trough

Figure 29.6 shows the determined ESR ages plotted as a geographical position of longitude of the hydrothermal fields. The order of ages of the 5 hydrothermal fields would be arranged, from young to old as follows; Yoron Hole field < Daiyon-Yonaguni Knoll field < Hatoma Knoll field ≒ Iheya North Knoll field < Izena Hole field. The samples from Hakurei site showed the high variation of ESR ages, indicating possible variation in the age of the hydrothermal fields, therefore, a conclusion based on analysis of a few samples from active sites may not be appropriate. More systematic dating works are necessary in each specific hydrothermal field in order to reconstruct the history of the hydrothermal activities.

29.4.7 ESR Dating of Hydrothermal Barite

Our attempt is the first study to determine such a large number of ESR ages using hydrothermal barite of many sulfide breccia samples. The results indicate that ESR dating of barite would be practically useful to investigate the history of sea-floor hydrothermal systems. The technique determines the ages more promptly than using isotopes, and is especially useful in the range from 100 to 10,000 years where ^{226}Ra-^{210}Pb method is not applicable. The present study showed that the method reveals relative order of the ages among the samples, however, additional efforts should be needed to establish the method for absolute age determination through further comparative dating studies. Moreover, it is also necessary to investigate the relationship and between the variation in ages and the occurrence of the minerals.

Acknowledgements The work was supported by TAIGA project, Grant-in-Aid for Scientific Research on innovative Areas (20109004) funded by the Ministry of Education, Culture, Sports, Science and Technology (MEXT), partly by MEXT-Supported Program for the Strategic Research Foundation at Private Universities (2011–2015, S1101036), and also by the Inter-University Program for the Joint Use of JAEA Facilities.

Table 29.3 Dating results of sulfide samples

Sample No.	Barite (%)	^{226}Ra (Bq/g)	^{228}Ra (Bq/g)	^{226}Ra Dose rate (mGy/y)				^{228}Ra Dose rate (mGy/y)				Equivalent dose (Gy)		Age (year)		U-Th	^{226}Ra-^{210}Pb	^{228}Ra-^{228}Th
				D_α	D_β	$D\gamma$	D_{total}	D_α	D_β	$D\gamma$	D_{total}							
Daiyon-Yonaguni Knoll																		
818-S-01																		
a	44.0	18.5	ud.	182	119	124	424	ud.	ud.	ud.	ud.	280	+40/−30	580	+75/−60	nm.	nm.	nm.
b	3.95	2.56	ud.	220	33.1	16.5	269	ud.	ud.	ud.	ud.	332	+90/−60	990	+210/−150	nm.	nm.	nm.
c	40.9	17.6	ud.	180	112	116	408	ud.	ud.	ud.	ud.	424	+60/−150	860	+100/−280	nm.	nm.	nm.
2K1267L1	58.3	36.6	ud.	340	264	278	882	ud.	ud.	ud.	ud.	231	+40/−30	200	+40/−30	nm.	nm.	nm.
2K1267L2	58.4	30.2	ud.	280	217	229	727	ud.	ud.	ud.	ud.	284	+30/−50	260	+140/−50	nm.	nm.	nm.
Hatoma Knoll																		
HPD#1331G01																		
a	85.3	0.773	ud.	5.47	5.42	5.87	16.8	ud.	ud.	ud.	ud.	157	+18/−15	3,700	+880/−750	18,600	—	—
b	82.9	0.925	ud.	6.68	6.50	7.03	20.2	ud.	ud.	ud.	ud.	153	+17/−15	3,300	+710/−600	nm.	—	—
c	84.8	0.858	ud.	6.09	6.01	6.51	18.6	ud.	ud.	ud.	ud.	103	+9.4/−8.2	2,800	+510/−450	nm.	—	—
d	82.9	0.831	ud.	6.00	5.84	6.31	18.1	ud.	ud.	ud.	ud.	79.2	+6.3/5.6	2,400	+300/−280	nm.	—	—
e	71.5	0.735	ud.	5.88	5.21	5.58	16.7	ud.	ud.	ud.	ud.	111	+10/−8.7	3,100	+550/−480	<20	—	—
f	56.6	0.977	ud.	9.28	7.05	7.42	23.8	ud.	ud.	ud.	ud.	106	+9.5/−8.3	2,500	+380/−340	111	—	—
HPD#1331G03																		
a	13.1	3.14	ud.	105	29.1	23.8	158	ud.	ud.	ud.	ud.	196	+130/−57	990	+680/−345	nm.	nm.	—
b	9.89	0.122	ud.	5.31	1.23	0.93	7.47	ud.	ud.	ud.	ud.	187	+90/−50	5,700	+2,100/−1,500	nm.	nm.	—
c	10.6	0.489	ud.	20.0	4.83	3.71	28.5	ud.	ud.	ud.	ud.	175	+75/−40	3,000	+1,400/−900	nm.	nm.	—
HPD#1331G07	60.8	13.3	14.8	266	166.0	199	630	146	70.4	98.5	315	7.33	+0.50/−0.47	7.05	+0.44/−0.42	nm.	nm.	nm.
2K1353R2	78.0	12.0	ud.	90.2	84.6	91.1	266	ud.	ud.	ud.	ud.	321	+50/−40	970	+117/−97.8	nm.	nm.	nm.
Iheya North Knoll																		
HD#1358R2																		
a	65.8	55.9	ud.	409	352	378	1,139	ud.	ud.	ud.	ud.	1,200	+440/−260	890	+250/−160	nm.	nm.	—
b	60.2	53.5	ud.	406	331	354	1,091	ud.	ud.	ud.	ud.	1,400	+650/−340	1,000	+360/−210	nm.	nm.	—
c	44.4	52.8	ud.	514	340	353	1,207	ud.	ud.	ud.	ud.	770.0	+200/−140	560	+130/−90	nm.	nm.	—
d	43.5	44.7	ud.	458	297	307	1,062	ud.	ud.	ud.	ud.	790.0	+220/−140	650	+150/−100	nm.	nm.	—
HD#1358R3																		
a	70.2	7.84	ud.	63.5	55.6	59.5	179	ud.	ud.	ud.	ud.	1,200	+500/−280	3,200	+620/−430	nm.	nm.	—
b	83.1	7.27	ud.	52.3	51.0	55.2	159	ud.	ud.	ud.	ud.	1,000	+720/−300	3,000	+970/−560	nm.	nm.	—
c	80.3	7.33	ud.	54.0	51.6	55.7	161	ud.	ud.	ud.	ud.	1,200	+990/−380	3,300	+1,100/−620	nm.	nm.	—
d	77.8	7.35	ud.	55.4	51.8	55.8	163	ud.	ud.	ud.	ud.	2,000	+1,270/−810	4,300	+1,500/−930	nm.	nm.	—

(*continued*)

Table 29.3 (continued)

Sample No.	Barite (%)	^{226}Ra (Bq/g)	^{228}Ra (Bq/g)	^{226}Ra Dose rate (mGy/y)				^{228}Ra Dose rate (mGy/y)				Equivalent dose (Gy)		Age (year)		U-Th	^{226}Ra-^{210}Pb	^{228}Ra-^{228}Th
				D_α	D_β	$D\gamma$	D_{total}	D_α	D_β	$D\gamma$	D_{total}							
Izena Hole																		
HPD#1313G05																		
g	49.0	15.4	16.9	141	99.2	104	344	169	106	159	435	20	+5.5/−3.7	14	+1.9/−1.5	nm.	nm.	9.3
i	71.4	17.1	20.9	118	107	116	342	158	128	196	482	18	+4.9/−3.3	12	+1.8/−1.4	nm.	nm.	7.6
j	70.9	16.8	18.4	119	107	116	342	143	114	176	432	27	+10/−5.8	16	+2.6/−2.0	nm.	nm.	8.3
k	54.3	13.1	13.5	115	86.3	91.2	292	130	87.1	131	348	18	+4.5/−3.1	15	+1.8/−1.4	nm.	nm.	11
l	65.0	14.7	14.6	115	97.1	104	316	124	93.8	143	361	15	+3.4/−2.4	13	+1.5/−1.3	nm.	nm.	9.2
m	61.1	16.5	13.9	135	110	117	362	124	89.8	136	350	18	+4.6/−3.1	14	+1.8/−1.5	nm.	nm.	10
HPD#1329G01																		
a	7.79	0.147	ud.	7.96	1.60	1.09	10.6	ud.	ud.	ud.	ud.	2,600	+600/−400	10,000	+460/−400	nm.	—	—
b	8.01	0.218	ud.	11.5	2.34	1.61	15.4	ud.	ud.	ud.	ud.	8,000	+5,700/−2,400	13,000	+1,200/−800	nm.	—	—
c	10.9	0.286	ud.	11.0	2.73	2.11	15.8	ud.	ud.	ud.	ud.	15,000	+26,000/−5,000	14,000	+2,300/−1,000	nm.	—	—
d	15.3	0.410	ud.	11.3	3.56	3.03	17.9	ud.	ud.	ud.	ud.	10,000	+20,000/−3,700	13,000	+2,500/−1,100	nm.	—	—
HPD#1329G03																		
a	14.0	0.175	ud.	5.23	1.55	1.29	8.07	ud.	ud.	ud.	ud.	3,900	+3,000/−1,200	12,000	+1,300/−860	nm.	—	—
b	6.29	0.099	ud.	6.64	1.18	0.733	8.55	ud.	ud.	ud.	ud.	8,000	+6,500/−2,500	14,000	+1,300/−850	nm.	—	—
c	5.49	0.103	ud.	7.87	1.30	0.757	9.92	ud.	ud.	ud.	ud.	6,000	+2,200/−1,300	13,000	+750/−580	nm.	—	—
d	4.96	0.081	ud.	6.83	1.07	0.595	8.50	ud.	ud.	ud.	ud.	6,500	+3,300/−1,600	13,000	+950/−690	nm.	—	—
e	25.0	0.242	ud.	4.08	1.89	1.79	7.76	ud.	ud.	ud.	ud.	25,000	+30,000/−14,000	16,000	+5,900/−1,800	nm.	—	—
Yoron Hole																		
HPD#1333G03																		
a	79.5	35.8	64.5	217	212	232	661	426	372	578	1,377	11.6	+0.88/−0.82	4.6	+0.29/−0.27	nm.	nm.	4.5
b	66.4	31.4	54.5	241	207	222	669	458	350	533	1,341	9.75	+0.79/−0.73	4.1	+0.27/−0.26	nm.	nm.	4.9
c	68.4	32.1	55.7	233	205	221	659	443	347	531	1,320	13.1	+0.99/−0.93	5.2	+0.31/−0.30	nm.	nm.	5.2
HPD#1333G05																		
a	75.0	26.0	ud.	201	184	198	583	ud.	ud.	ud.	ud.	210	+40/−30	330	+60/−45	nm.	71	—
b	70.1	19.4	ud.	157	138	147	443	ud.	ud.	ud.	ud.	191	+35/−27	400	+66/−51	nm.	74	—
c	72.2	17.5	ud.	139	124	133	396	ud.	ud.	ud.	ud.	170	+29/−22	400	+60/−48	nm.	nm.	—
d	73.0	36.2	ud.	285	256	275	817	ud.	ud.	ud.	ud.	163	+27/−21	200	+30/−24	nm.	77	—

HPD#1333G06																	
a	83.8	29.0	ud.	208	204	221	633	ud.	ud.	ud.	ud.	51.1	+6.8/−5.6	80	+12/−10	<20	nm.	—
b	89.4	33.3	ud.	228	233	253	714	ud.	ud.	ud.	ud.	51.3	+6.7/−5.5	70	+10/−9	<20	25	—
c	87.2	30.4	ud.	212	213	231	656	ud.	ud.	ud.	ud.	56.0	+7.2/5.9	80	+12/−10	<20	nm.	—
d	81.0	26.9	ud.	197	189	204	590	ud.	ud.	ud.	ud.	89.5	+16/−12	150	+30/−23	80	23	—
e	82.5	27.4	ud.	198	193	208	599	ud.	ud.	ud.	ud.	81.7	+13/−10	130	+25/−19	<20	nm.	—
f	82.9	28.5	ud.	206	200	217	623	ud.	ud.	ud.	ud.	76.6	+12/−9.2	120	+21/−17	<20	27	—
HPD#1333G07																		
a	63.9	31.0	0.621	241	202	216	658	5.27	3.94	5.99	15.2	88.7	+13/−10	50	+1.6/−1.6	nm.	nm.	nm.
b	67.5	30.4	0.702	230	200	214	644	5.81	4.49	6.86	17.2	106	+17/−14	52	+1.7/−1.6	nm.	nm.	nm.
c	68.8	24.1	0.557	180	158	170	507	4.54	3.55	5.43	13.5	121	+24/−18	56	+1.8/−1.7	nm.	nm.	nm.
d	78.2	32.1	9.43	207	199	216	622	66.4	56.9	88.0	211	65.8	+8.9/−7.4	28	+1.2/−1.2	nm.	nm.	nm.
HPD#1333G08																		
a	70.1	32.2	2.64	239	212	228	680	21.4	17.0	25.9	64.3	81.8	+11/−9.6	39	+1.4/−1.4	nm.	nm.	nm.
b	66.1	29.6	4.03	229	196	210	635	34.1	26.0	39.6	99.6	78.6	+11/−9.4	35	+1.4/−1.3	nm.	nm.	nm.
c	59.1	27.1	12.5	213	170	182	565	107	76.6	116	300	79.1	+11/−9.9	27	+1.2/−1.2	nm.	nm.	5.8
HPD#1333G11	67.5	33.6	42.7	218	193	210	620	303	239	369	911	20.3	+1.7/−1.6	9.0	+0.51/−0.49	nm.	nm.	nm.

ud. : under detection limit
— : radioactive equilibria
nm. : not measured

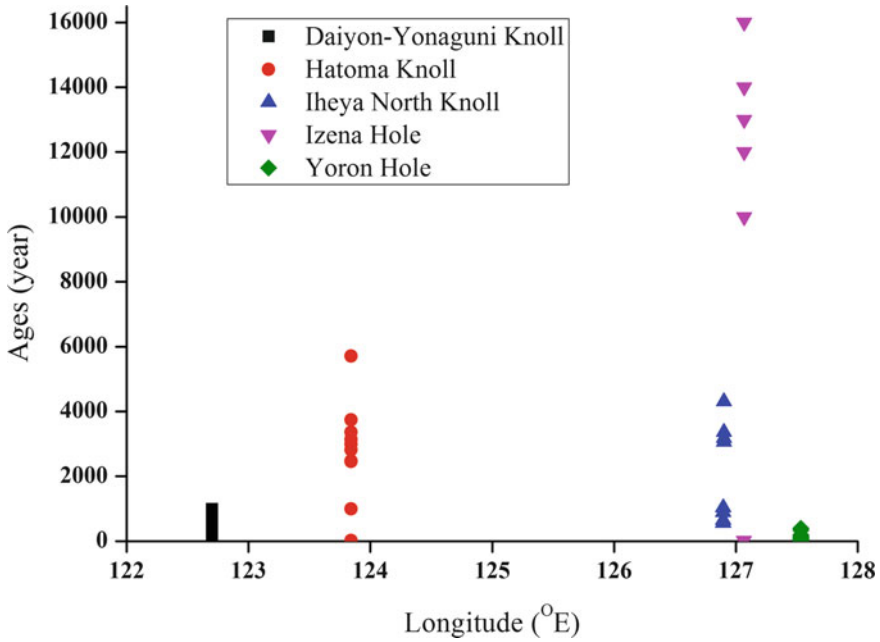

Fig. 29.6 The obtained ESR ages plotted as a function of longitude of the hydrothermal fields

References

Guérin G, Mercier N, Adamiec G (2011) Dose-rate conversion factors: update. Ancient TL 29:5–8

Hannington MD, Jonasson IR, Herzig PM, Petersen S (1995) Physical and chemical processes of seafloor mineralization at mid-ocean ridges. In: Humphris SE et al (eds) Seafloor hydrothermal systems; physical, chemical, biological, and geological interactions. American Geophysical Union Geophysical Monograph, vol 91, pp 115–157

Kasuya M, Kato M, Ikeya M (1991) ESR signals of natural barite ($BaSO_4$) crystals: possible application to geochronology. In Essay in Geology, Prof. Nakagawa Commemorative Volume: 95–98

Krystec M (1980) ESR measurements from X-ray irradiated $BaSO_4$ single crystals. Phys Status Solidi A 57:171–178

Noguchi T, Shinjo R, Ito M, Takada J, Oomori T (2011) Barite geochemistry from hydrothermal chimneys of the Okinawa Trough: insight into chimney formation and fluid/sediment interaction. J Mineral Petrol Sci 106:26–35

Okumura T, Toyoda S, Sato F, Uchida A, Ishibashi J, Nakai S (2010) ESR dating of marine barites in chimneys deposited from hydrothermal vents. Geochronometria 37:57–61

Sato F, Toyoda S, Banerjee D, Ishibashi J (2011) Thermal stability of ESR signals in hydrothermal barites. Radiat Meas 46:866–870

Takamasa A, Nakai S, Sato F, Toyoda S, Banerjee D, Ishibashi J (2013) U-Th radioactive disequilibrium and ESR dating of a barite-containing sulfide crust from South Mariana Trough. Quat Geochronol 15:38–46

Tivey MK (2007) Generation of seafloor hydrothermal vent fluids and associated mineral deposits. Oceanography 20:50–65

Toyoda S, Sato F, Banerjee D, Ishibashi J (2011) Characteristics of the radiation induced ESR signals in barite. Adv ESR Appl 27:4–6

Toyoda S, Sato F, Nishido H, Kayama M, Ishibashi J (2012) The alpha effectiveness of the dating ESR signal in barite. Radiat Meas 47:900–902

Toyoda S, Fujiwara T, Uchida A, Ishibashi J, Nakai S, Takamasa A (2014) ESR dating of barite in sulfide deposits formed by the sea floor hydrothermal activities. Radiat Prot Dosimetry 159:203–211

Yonezawa N, H. Matsue, Y. Miyamoto, D. Suzuki, K. Yasuda, J. Inagawa, Y. Saito (2002) Handbook for practical gamma ray spectrometry (Japanese title translated), Nikkan Kogyo, Japan. (Translation of Gilmore and Hemingway, 1995, Practical gamma-ray spectrometry, Wiley, Chichester/New York/Brisbane/Toronto/Singapore)

You CF, Bickle MJ (1998) Evolution of an active sea-floor massive sulphide deposit. Nature 394:668–671

Fluid Geochemistry of High-Temperature Hydrothermal Fields in the Okinawa Trough

30

Shinsuke Kawagucci

Abstract

This review compiles fluid chemistries of the six known high-temperature hydrothermal fields in the Okinawa Trough (OT) and compares them to global representative fields with various tectonic/geologic backgrounds. The comparisons indicate that the chemical characteristics of the OT hydrothermal fluids are explained by linkages between (1) shallow water depth that constrains the maximum fluid temperature, (2) back-arc tectonic setting that introduces magmatic volatiles into the fluid, (3) probable silicic rock-based fluid-mineral interaction at the hydrothermal reaction zone, and (4) seafloor sediment around the vents that provides both compounds derived from sedimentary organic matter and biogenic compounds, such as methane, produced by microbial ecosystems in the sedimentary environment.

To explain the highly diverse gas compositions and stable isotope ratios of methane among the OT hydrothermal fields, "fluid-sediment interaction" has been further classified into several types with respect to processes (microbial or chemical) and stages of subseafloor fluid circulation (recharge or discharge). This concept, called the Microbial Methanogenesis at Recharge stage (MMR) model, enables us not only to deduce the geochemical origins of the hydrothermal fluid CH_4 in each OT field but also to estimate the geographical distribution of hydrothermal fluid circulation via a two-dimension schematic illustration. The model, which links the fluid geochemistry with the subseafloor fluid migration path, will serve as a base for future studies also for any subseafloor geofluid systems that include hydrothermal systems, subseafloor methane hydrate, and seismogenic fault zone.

Keywords

High-temperature hydrothermal fluid geochemistry • Inter-field comparison • Okinawa trough • Origin of methane

30.1 Introduction

Active hydrothermal systems in the Okinawa Trough (OT) are representative of one of the four TAIGAs, i.e., the 'TAIGA of Methane' (Urabe et al. Chap. 1). Numerous cruises for more than two decades have investigated the hydrothermal activities and fluid geochemistry of high-temperature hydrothermal fields within the OT, such as Minami-Ensei (Chiba et al. 1993; Kawagucci et al. 2013a), Iheya North (Nakagawa et al. 2005; Kawagucci et al. 2011,

S. Kawagucci (✉)
Institute of Biogeosciences (Biogeos), Japan Agency for Marine-Earth Science and Technology (JAMSTEC), 2-15 Natsushima-cho, Yokosuka, Kanagawa 237-0061, Japan

Precambrian Ecosystem Laboratory (PEL), Japan Agency for Marine-Earth Science and Technology (JAMSTEC), 2-15 Natsushima-cho, Yokosuka, Kanagawa 237-0061, Japan

Submarine Resources Research Project (SRRP), Japan Agency for Marine-Earth Science and Technology (JAMSTEC), 2-15 Natsushima-cho, Yokosuka, Kanagawa 237-0061, Japan
e-mail: kawagucci@jamstec.go.jp

J.-i. Ishibashi et al. (eds.), *Subseafloor Biosphere Linked to Hydrothermal Systems: TAIGA Concept*,
DOI 10.1007/978-4-431-54865-2_30,

2013b), Jade (Sakai et al. 1990a, 1990b; Ishibashi et al. 1995), Hakurei (Ishibashi et al. 2014), Hatoma (Nakano et al. 2001; Saegusa et al. 2006; Kawagucci et al. 2010b; Toki et al., in preparation), and Daiyon-Yonaguni (Yonaguni IV) (Kishida et al. 2004; Konno et al. 2006; Suzuki et al. 2008). The most notable characteristics of the fluid chemistry of the OT hydrothermal fields are abundant millimolar levels of CH_4 (Fig. 30.1 and Table 30.1). This is why the OT hydrothermal systems are representative of the 'TAIGA of Methane.'

The chemical characteristics of venting hydrothermal fluid are primarily constrained by high-temperature fluid-rock interactions at deep hydrothermal reaction zones (Seewald and Seyfried 1990; Seyfried et al. 2003; German and von Damm 2003). Phase separation and subsequent phase segregation occurring at deep high-temperature region also affect the chemistry of the venting fluid (Gamo 1995). Furthermore, certain microbial and chemical effects on hydrothermal chemistry have been identified in the branched low-temperature diffusing fluid in the discharge stage (Butterfield et al. 2004; von Damm and Lilley 2004; Toki et al. 2008). These key processes, however, have been hypothesized to occur in the high-temperature hydrothermal reaction zones and during the discharge stage, not in the fluid recharge stage, where cool seawater penetrates into the subsurface and its chemistry changes with increasing temperature via relevant (bio)geochemical processes.

Recently, I and my colleagues have claimed that chemical and biological processes occurring in the recharge stage significantly affect the chemical composition of the venting fluid in the case that the product is inert under the conditions of the high-temperature hydrothermal reaction zone, such as methane (Kawagucci et al. 2011, 2013a). From this point of view, we have considered Microbial Methanogenesis at Recharge stage (MMR) in hydrothermal circulation as a possible predominant source of CH_4 in the high-temperature venting fluid, and refer to the concept as the 'MMR model' (Kawagucci et al. 2011). The MMR model is relevant particularly in a sediment-associated hydrothermal system, where the recharge stage of hydrothermal fluid circulation is expected to include an organic-rich sedimentary environment that promotes the widespread occurrence of functionally active microbial communities and impacts on fluid chemistry. Although the characteristic fluid chemistry in sediment-associated hydrothermal systems has occasionally been explained by equivocal 'fluid-sediment interaction', the MMR model argues that "fluid-sediment interaction" has been further classified into three types with respect to processes (microbial or chemical) and stages of subseafloor fluid circulation (recharge or discharge) (Kawagucci et al. 2013a).

In this chapter, I attempt to discover how and where the 'TAIGA of Methane' forms mainly based on fluid chemistry, following the recently proposed MMR model (Kawagucci et al. 2011, 2013a). For this purpose, general characteristics of the hydrothermal fluid chemistry of the OT fields are reviewed at first and then compared with those of other hydrothermal systems in Sect. 30.2. After assessing the utility of geochemical tracers to deduce the origin of hydrothermal fluid methane in Sect. 30.3, I discuss the geochemical origins of CH_4 dissolved in hydrothermal fluid in each OT field and their relevance with the geological setting and geographical distribution of hydrothermal fluid circulation in Sect. 30.4.

30.2 Major Fluid Chemistry

30.2.1 General View of the OT Hydrothermal Fluids

The OT hydrothermal fluids show significant enrichment of not only CH_4 but also of some other components (e.g., CO_2, K, NH_4, etc.) compared to hydrothermal fluids collected from sediment-starved Mid-Ocean Ridge (MOR) fields. Pioneering works (Sakai et al 1990a, 1990b; Gamo et al. 1991; You et al. 1994; Ishibashi et al. 1995) noted that the distinctive chemistry of the OT hydrothermal fluids is linked with the organic-rich continent-derived sediment filling the OT seafloor and the volatile-rich dacitic-rhyolitic (silicic) magma beneath the OT. Moreover, relatively shallow water depths of the OT hydrothermal systems (Fig. 30.1) serve as a physical factor that induces frequent boiling (subcritical phase separation) and subsequent phase segregation (Fig. 30.2), which results in chemical compositions of the venting hydrothermal fluids that are quite different from the deep source fluid (Gamo 1995). Phase separation forces volatile species into the resulting 'vapor' phase and leaves ion species in the 'liquid' phase. The source hydrothermal fluid composition prior to the phase separation can be estimated by a simple correction using the venting fluid chlorine concentration (i.e., the ion-element/Cl ratio) (Butterfield et al. 2003). Despite potential influences of multiple factors due to the geological and tectonic backgrounds of the OT, limited observations at each sediment-associated basalt-hosted MOR system and sediment-starved silicic rock-hosted arc-back-arc (ABA) system in the early 1990s inhibited the understanding of how the sediment filling the OT seafloor and volatile-rich silicic host rocks impact the OT hydrothermal fluid chemistry. Over the 35 years since the discovery of deep-sea hydrothermal activity in 1977, the current global dataset of hydrothermal fluid chemistry has enabled us to compare the fluid chemistry of the OT fields with that of hydrothermal systems of various geological and tectonic backgrounds. Field-to-field variations (inter-field variation) of fluid

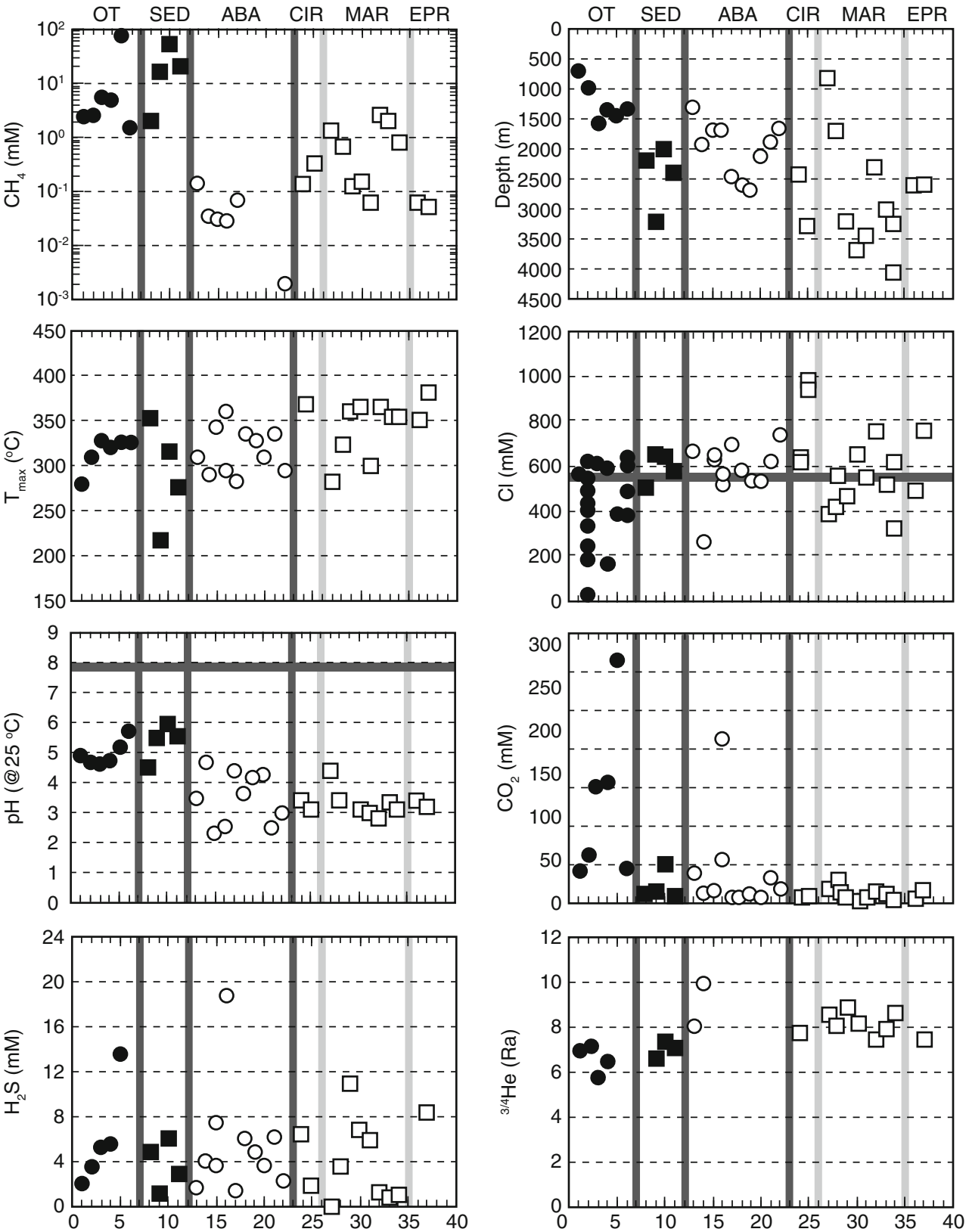

Fig. 30.1 Compilation of the physical properties and fluid chemistry of the Okinawa Trough and global hydrothermal fields. The vertical axis (methane concentration) is in logarithm scale. Horizontal axes are common for all panels and represent each hydrothermal field as follows: 1-Minami-Ensei, 2-Iheya North, 3-Hakurei, 4-Jade, 5-Hatoma, 6-Daiyon-Yonaguni, 7-vacant, 8-Endeavour, 9-Escanaba, 10-Guaymas, 11-Middle Valley, 12-vacant, 13-Suiyo, 14-North Fiji, 15-Roman Ruins, 16-Satanic Mills, 17-Vienna Woods, 18-Kilo Moana, 19-Tow Cam, 20-ABE, 21-Mariner, 22-Brother, 23-vacant, 24-Kairei, 25-Edmond, 26-vacanct, 27-Manez Gwen, 28-Lucky Strike, 29-Broken Spur, 30-TAG, 31-Snake Pit, 32-Rainbow, 33-Logatchev, 34-Ashadze, 35-vacant, 36-EPR21N, 37-EPR13N. *Vertical dark* and *light gray bars* separate different geological/tectonic settings. *Horizontal gray bars* in several panels represent seawater levels. References for this figure are presented in Sect. 30.2.2

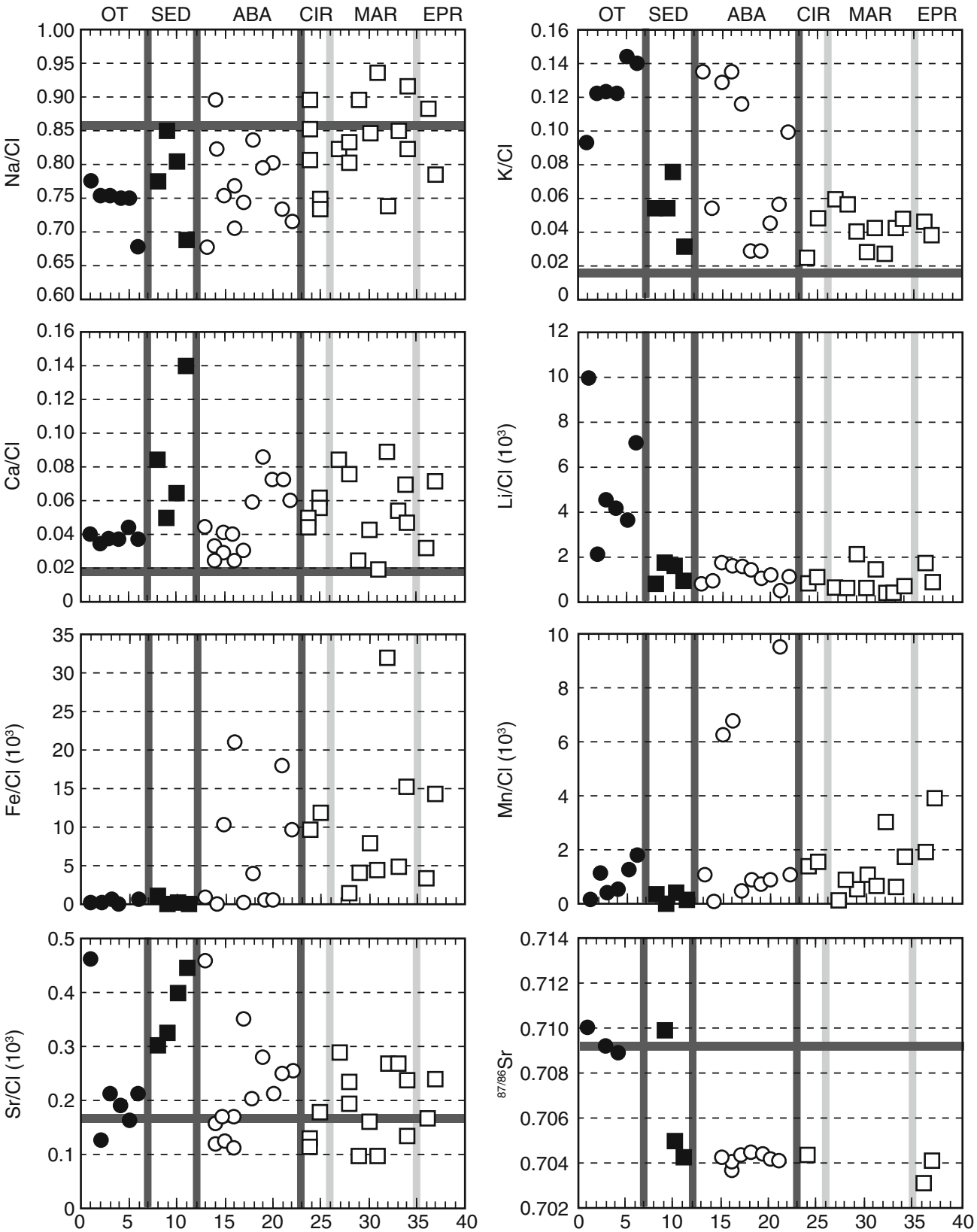

Fig. 30.1 (continued)

Table 30.1 Fluid chemistry of the Okinawa Trough hydrothermal fields

		Iheya North		Izena Hall			Hatoma	Daiyon-Yonaguni		
Field vent	Minami Ensei (whole)	NBC 2011	Variation	Jade	Hakurei	Biwako	Gusuku	Lion	Variation	Seawater
Depth (m)	700	980		1,350	1,600	1,525	1,473	1,360		
T_{max} (°C)	280	309	<311	320	326	104	325	325	<328	
pH	4.9	4.65	>4.65	4.7	4.7	4.8	5.2	5.7	5.7–6.8	7.8
Alk. (mM)	3.3	1.3	0.2–3.3	1.5	1.5		4.7	0.25	0.25–2.95	2.3
Cl (mM)	562	599	16–634	590	608	167	381	614	376–635	559
Na (mM)	436	451	8–479	442	458	173	285	416	254–433	480
K (mM)	53	73	7–82	72	75	12	55	86	55.3–90.1	10
Ca (mM)	23	21.1	0–25	22	23	4.3	17	23.2	14.3–26.1	11
Si (mM)	11.1	11.9	3.1–13.8	11.8	11.3	11	12	11.3	11.3–13.2	0.18
B (mM)	3.8	1.97	0.44–2.3	3.2	3.7	1	3.3	3.9	2.93–4.31	0.43
Li (mM)	5.6	1.32	0.11–1.52	2.5	2.8		1.4	4.4		0.026
Fe (μM)	120	121	31–142	31	445		8.6	410	80–410	0.001
Mn (μM)	99	694	115–694	341	290		483	1,120	700–1,250	0.003
Ba (μM)		31	9.7–44	65	120					0.15
Al (μM)	4.7	11.0								0.04
Sr (μM)	260	77		115	129	27	62	130		91
$^{87/86}Sr$	0.71			0.7089	(0.7094)					0.70918
F (μM)		209								70
Br (μM)		952								860
I (μM)	30	44.8								0.5
Mo (nM)							7			107
W (nM)		320					123			0.07
Zn (μM)		94								0.01
Se (nM)		73		40–150	50–100					2.3
CH_4 (mM)	2.4	2.5	0.2–7.0	4.9	6.8		80	1.6	1.2–13.5	0.0000001
$\delta^{13}C_{CH4}$ (‰)	−25	−54.1	−58.2 to −54.0	−30.8	−32.1		−50	−26.9	−27.3 to −24.8	
δD_{CH4} (‰)	−112	−124	−132 to −113	−113	−113					
H_2 (mM)	0.04	0.10	0.03–0.2	0.06	1.4		0.2	1.0	0.8–5.5	0.0000001
δD_{H2} (‰)	−420	−394	−430 to −394	−381	−379		−386			
CO_2 (mM)	42	63	27–228	156	151		315	47	22–329	2.3
$\delta^{13}C_{CO2}$ (‰)	−5.1	−9.6	−10.8 to −8.8	−6.2	−6.2		−7.9	−7.3	−8.0 to −7.2	−8
δD_{H2O} (‰)		−1.0		−0.3	−0.6					0
$\delta^{18}O_{H2O}$ (‰)		+1.2		+1.8	+1.6					0
NH_4^+ (mM)	5.4	2.1	1.6–3.9	4.2	4.4	5	7.2	14.7	8.6–14.7	
H_2S (mM)	2	3.6	1.8–3.9	5.6	5.2	23	13.5			0.0000001
$\delta^{34}S_{H2S}$	+3.6	+11		+3.6 to +7.7	+5.5 to +7.8					
C_2H_6 (uM)	<1	<1		0.33	2.5					
CO (uM)				30	63					0.0001
He (uM)	0.68			0.72	0.53					
$^{3/4}He$ (R_{atm})	6.99	7.1		6.5	5.81					1

chemistry among the global hydrothermal fields help to clarify the characteristic fluid chemistries of the OT hydrothermal fluids and their relationships with geological and tectonic backgrounds.

This chapter discusses only the 'endmember' high-temperature fluid chemistry, estimated by a Mg-diagram and extrapolation of Mg concentrations to zero (von Damm et al. 1985), to avoid losing focus on the inter-field comparison. Thus this chapter does not discuss secondary chemical modification associated with either low-temperature hydrothermal fluid discharges through the sedimentary environment (Gamo et al. 1991; Kawagucci et al. 2013b; Yokoyama et al. Chap. 31) or the liquid CO_2 emersion and the relevant microbial ecosystems (Inagaki et al. 2006; Yanagawa et al.

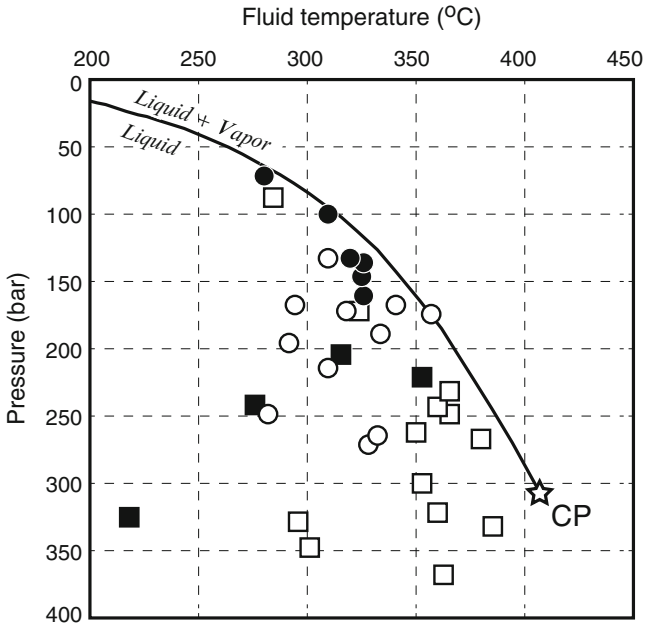

Fig. 30.2 Two-phase curve for seawater. Each symbol represents P-T conditions of venting fluids at each field from the Okinawa Trough (*filled circles*), sediment-associated systems (*filled squares*), sediment-starved ABA systems (*open circles*), and sediment-starved MOR systems (*open squares*). An open star (CP) represents a critical point of seawater. References for this figure are presented in Sect. 30.2.2

2013). In addition, trace elements (Mo, W, REE, etc.) measured in some OT hydrothermal fluids (Kishida et al. 2004; Hongo et al. 2007; Kawagucci et al. 2013b) are also not included in this chapter because the limited available dataset prohibits global comparison.

30.2.2 Inter-Field (Field-to-Field) Variation and the OT Characteristics

Figure 30.1 shows the physical properties and the Mg-corrected endmember chemistries of high-temperature hydrothermal fluids in (1) the six OT fields (Table 30.1), (2) four sediment-associated MOR fields (Lilley et al. 1993, 2003; Proskurowski et al. 2004, 2006; von Damm et al. 2005; McCollom 2008; Ishibashi et al. 2002; Pearson et al. 2005; Gieskes et al. 2002; Butterfield et al. 1994; and references therein), (3) ten sediment-starved ABA fields (Tsunogai et al. 1994, 2005; Toki et al. 2008; Kishida et al. 2004; Ishibashi et al. 1994a, 1994b; 2002b; Grimaud et al. 1991; Reeves et al. 2011; Mottl et al. 2011; de Ronde et al. 2011; and references therein), and (4) twelve sediment-starved MOR fields (Gamo et al. 2001; Kumagai et al. 2008; Gallant and von Damm 2006; Fouquet et al. 2010; Charlou et al. 2010; Von Damm et al. 1985; Merlivat et al. 1987; and references therein). The hydrothermal fields shown in Fig. 30.1 represent global variations in host rock chemistry (silicic, mafic, and ultramafic) and geographical distribution (the Indian Ocean, the Pacific Ocean, the Atlantic Ocean, and the adjacent seas). The endmember Cl concentrations are deviated from seawater Cl levels in almost all the hydrothermal fields (Fig. 30.1), demonstrating alteration in fluid chemistry due to the phase separation. For ion species, element/Cl ratios are used instead of concentrations to eliminate the effect of phase separation (Fig. 30.1).

The highest measured temperatures of hydrothermal fluids (T_{max}) in the OT hydrothermal fields range between 280 and 326 °C, which are lower than typical T_{max} of the MOR fields (approximately 350 °C). Fluid temperature is very likely constrained by pressure, which determines the fluid boiling temperature (Fig. 30.2). Because the water depths of the OT hydrothermal fields range between 700 and 1,600 m and are generally shallower than other hydrothermal systems (Fig. 30.1), the pressure condition (the potential of T_{max}) is lower. In fact, the fluid pressure-temperature conditions of the OT fields are very close to the two-phase boundary (Bischoff and Rosenbauer 1984) (Fig. 30.2).

The hydrothermal fluid pH of the OT fields, measured at 25 °C in an onboard laboratory, range from 4.65 to 5.7. This pH range is generally comparable with that in the sediment-associated MOR systems (pH = 4.5–5.9) but higher than the pH ranges of sediment-starved ABA and MOR systems (pH = 2–5) (Fig. 30.1). In addition, a low-temperature hydrothermal fluid with an extremely low pH (≤2.1) due to direct emission of magmatic SO_2 to the seafloor has been observed in the DESMOS field in the eastern Manus Basin, Western Pacific (Gamo et al. 1997). The moderately acidic pH of the OT fluids despite the ABA tectonic background suggests that some components from sedimentary organic matter decomposition, such as millimolar levels of NH_3/NH_4^+ (Table 30.1), buffer the pH. The presence of NH_3/NH_4^+ in high-temperature hydrothermal fluids is known to yield a high pH at the 25 °C measurement but a lower pH at in situ hydrothermal conditions (Tivey et al. 1999). The OT hydrothermal fluids contain abundant CO_2 (>40 mM) of magmatic origin, based on the carbon isotope ratios of the CO_2 (Ishibashi et al. 1995; Kawagucci et al. 2011, 2013a). In contrast, the concentrations of H_2S, another major component of the magma-derived volatiles, are similar between the OT and other fields, regardless of the geological/tectonic backgrounds (Fig. 30.1). The helium isotope ratios ($^{3/4}$He) of the OT hydrothermal fluids are ≤7.1 and are similar to those in the sediment-associated MOR fluids (Fig. 30.1). This $^{3/4}$He range, which is slightly lower than the typical sediment-starved MOR value of 8 (Sano and Fischer 2013), implies a contribution of crustal ^{4}He-enriched helium.

The lower Na/Cl ratios of the OT fluids (0.68–0.78) compared to the seawater Na/Cl ratio (0.86) suggest Na

uptake into the solid phase during subseafloor fluid circulation (Fig. 30.1). High K/Cl ratios are typical characteristics of hydrothermal fields in ABA systems, including the OT fields (>0.09) (Fig. 30.1). The K enrichment in the ABA fluids is attributed to probable K enrichment in surrounding rocks, with which fluid interacts during fluid circulation (Sakai et al. 1990a). The magnitudes of Na-loss and K-gain in each OT field seem consistent between each other (Fig. 30.1), implying quantitative exchange of Na for K during fluid-mineral interaction. In addition, a geographical trend in the K/Cl variation within the OT is also found: higher K/Cl ratios in southern OT fields (Daiyon-Yonaguni and Hatoma) than in northern OT fields (particularly Minami-Ensei). This trend may reflect a difference in the K content of the basement rocks, although there is little data on the host rock chemistry of the OT hydrothermal fields (Shinjo and Kato 2000). The Ca/Cl ratios are lower in the OT fields (<0.05) than in the others, including sediment-associated MOR fields (Fig. 30.1). The Li/Cl ratios are substantially higher in all of the OT fields (>0.002) than in the other fields. Because of the almost quantitative partitioning of alkali elements into the fluid phase during high-temperature fluid-rock (-sediment) interactions, the high Li/Cl ratios in the OT fluids suggest Li enrichment in the OT basement rocks and/or the OT-filling sediment. Low Fe/Cl ratios (<0.001) are typical in the sediment-associated fields while the low Fe/Cl ratios of the OT fluids may be associated with low T_{max}. The Mn/Cl ratios are similar regardless of tectonic/geological background, excluding several ABA fields where the Mn/Cl ratios are extremely high. The Sr/Cl ratios so far observed in hydrothermal fluids vary among the fields regardless of tectonic/geological backgrounds. The hydrothermal fluid Sr/Cl range, higher or lower than the seawater Sr/Cl ratio in each field, indicates that both net gain and loss of Sr from the starting seawater during the hydrothermal fluid circulation is possible. Strontium isotope ratios ($^{87/86}$Sr) are high (≥0.709) in the OT Minami-Ensei and Jade fields (Noguchi et al. 2011) and a sediment-covered Escanaba field but low (approximately 0.704) in sediment-starved MOR and ABA fields and sediment-covered Guaymas and Middle Valley fields. The high $^{87/86}$Sr ratios of the OT fluids are attributed to those in the OT-filling sedimentary component (Noguchi et al. 2011).

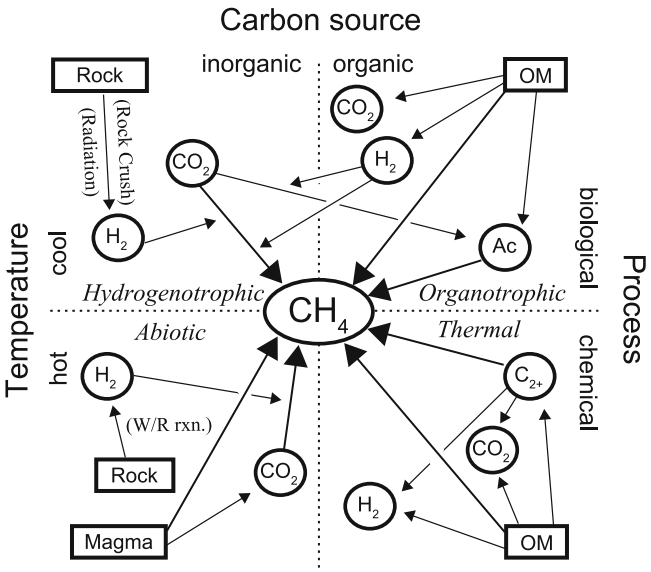

Fig. 30.3 Schematic illustrating methanogenic pathways in subseafloor geofluid systems. Ac, C_{2+}, and OM represent acetate, hydrocarbons with carbon numbers >2, and organic matter, respectively. After Kawagucci et al. (2013a) with minor modification

30.3 Gas Species Chemistry

30.3.1 Methane Sources in Hydrothermal System

The chemical origins of subseafloor CH_4 are typically classified by a combination of the carbon source (inorganic or organic) and the generation process (chemical or biological, which approximately correspond to high-temperature or low-temperature environments) (Fig. 30.3). This classification distinguishes three types: so-called abiotic CH_4 (e.g., McCollom 2013), thermogenic CH_4 (e.g., Welhan and Lupton 1987), and biogenic CH_4 (e.g., Valentine et al. 2004). Abiotic CH_4 has been considered to be the predominant source of hydrothermal fluid CH_4 in typical sediment-starved hydrothermal systems. However, in almost all the sediment-starved hydrothermal fields so far observed, the measured CH_4 concentrations are several orders of magnitude greater (or smaller) than the CH_4 concentrations that are thermodynamically predicted from the H_2 and CO_2 concentrations and fluid temperature of the venting fluid (McCollom 2008). While the excess could be explained by the loss of H_2 and/or CO_2 during fluid upwelling from the deep zone where abiotic methanogenesis has actually occurred, CH_4 derived from other sources could also account for the excess. Thermogenic CH_4 has been thought to be the predominant source for abundant CH_4 in hydrothermal systems occurring close to sedimentary organic-rich environments, such as the OT fields (Ishibashi et al. 1995). Even if the seafloor has a sediment-starved appearance, organic matter buried beneath the seafloor is assumed to be a source for thermogenic CH_4 (Lilley et al. 1993). Biogenic CH_4 includes methane generated by both hydrogenotrophic and organotrophic methanogenesis. The microbial syntrophic relationship between fermentative hydrogenogenesis and hydrogenotrophic methanogenesis is expected in the sedimentary environment (Fig. 30.3). Biogenic CH_4 could be incorporated into hydrothermal fluid

only in the recharge stage of the whole fluid circulation process because the reaction zone and the discharge stage are too hot for any microbes to be active (Takai et al. 2008). The recharge stage environment, where the penetrating seawater becomes reduced and warm, is very likely suitable for anaerobic and/or thermophilic microbes.

The MMR model, which we have proposed in recent papers (Kawagucci et al. 2011, 2013a), describes the origin of hydrothermal fluid CH_4 in not only geochemical terms but also geographical aspects. This model claims that CH_4 in high-temperature hydrothermal fluid can originate from CH_4 that is generated biologically and incorporated into the fluid in the low-temperature recharge stage of hydrothermal fluid circulation. The MMR model is emphasized particularly in the sediment-associated hydrothermal systems where the recharge stage of hydrothermal fluid circulation is expected to include an organic-rich sedimentary environment. Even if the sedimentary recharge zone is absent, methanogenic ecosystems in the crustal recharge zone might be fueled by abiotic H_2 generated from serpentinization (McCollom and Bach 2009), water radiolysis (Lin et al. 2005), and/or fault activity (Hirose et al. 2011). Moreover, abiotic methanogenesis associated with serpentinization of ultramafic rocks in the recharge stage cannot be ruled out because of its kinetic and thermodynamic favorability at temperatures of 200–315 °C (McCollom and Bach 2009). Consequently, all three types of CH_4 generation and their occurrence through each stage of the whole fluid circulation system should be considered to deduce the origins of CH_4 in venting hydrothermal fluid.

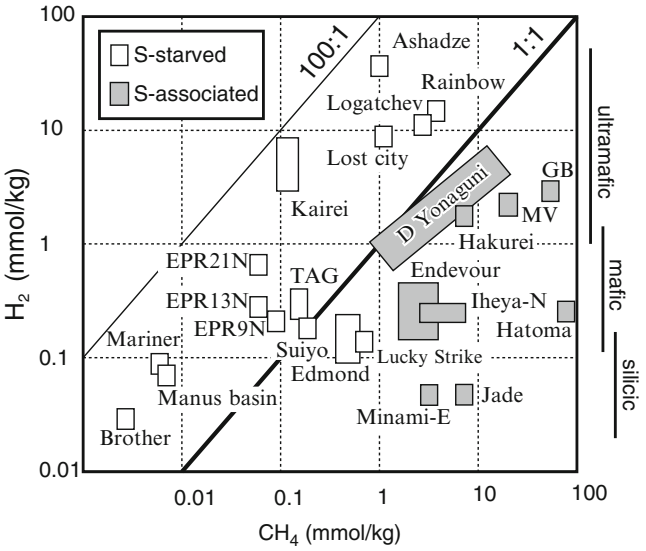

Fig. 30.4 Plots of H_2 concentration versus CH_4 concentration in hydrothermal fluids. *Open* and *gray squares* represent sediment-starved and sediment-associated fields, respectively. *Vertical bars* indicate typical H_2 concentrations in reaction zone fluids for silicic, mafic, and ultra-mafic basement systems. Labels GB and MV are Guaymas Basin and Middle Valley, respectively. After Kawagucci et al. (2013a) with minor modification

30.3.2 Geochemical Tracers to Deduce the Origin of Methane

The origin of hydrothermal fluid CH_4 can be deduced by using geochemical tracers, and the multiple tracers approach allows us to more accurately deduce the origin of hydrothermal fluid CH_4. Although several tracers have been proposed and indeed utilized, the indications of the tracers include uncertainties in some circumstances and should be assessed carefully. This issue has already been discussed in previous papers on stable hydrogen isotope ratios (δD_{CH4}) (Kawagucci et al. 2011), stable carbon isotope ratios ($\delta^{13}C_{CH4}$), relative abundances of CH_4 to non-methane hydrocarbons (C_1/C_{2+}), and H_2 concentrations (Kawagucci et al. 2013a). Here, a summary of the previous discussion with some additional information is presented.

30.3.2.1 Methane Concentration and $CH_4/^3He$ Ratio

The concentration of CH_4 in the venting fluid is a fundamental piece of information in deducing the origin of the CH_4. The global dataset of high-temperature hydrothermal fluid compositions illustrates two approximate relationships between CH_4 concentrations and geological settings. First, CH_4 concentrations are significantly higher in hydrothermal fields located in sedimentary locations (Figs. 30.1 and 30.3). This type of CH_4 enrichment typically accompanies enrichment in certain other components, such as ammonium, suggesting anoxic organic matter decomposition for its origin. Second, CH_4 concentrations are approximately related to the redox state of the rocks exposed around the vents: higher CH_4 concentrations are associated with more reduced rocks (Figs. 30.1 and 30.4). Although, again, measured CH_4 concentrations are not consistent with thermodynamic predictions (McCollom 2008), more reducing conditions in the reaction zone are advantageous for abiotic methanogenesis.

The relative abundance of CH_4 with ^3He ($CH_4/^3He$) differentiates mantle-derived CH_4 from crust- and sediment-derived CH_4 because juvenile ^3He should be derived from the mantle. $CH_4/^3He$ ratios higher than 10^7 (mol/mol) are typically found in sediment-associated hydrothermal fields (Lilley et al. 1993; Ishibashi et al. 1995) and sediment-starved slow-spreading MOR fields (Charlou et al. 2000), while ratios of 10^6 are reported for moderate- to fast-spreading MOR hydrothermal fields (Kawagucci et al. 2008; and references therein).

30.3.2.2 Carbon and Hydrogen Isotope Ratios of Methane

The $\delta^{13}C_{CH4}$ value is the geochemical indicator most widely used to deduce the origins of environmental CH_4. Expected ranges of $\delta^{13}C_{CH4}$ values for each of the three types have been investigated in laboratory experiments (Fig. 30.5). The $\delta^{13}C_{CH4}$ values of abiotic CH_4 in the experiments (−40 to −20 ‰) (e.g., Horita and Berndt 1999; McCollom and Seewald 2006; McCollom et al. 2010) are quite different from those frequently observed in the sediment-starved hydrothermal fields (−20 to −5 ‰). The inconsistency in abiotic $\delta^{13}C_{CH4}$ values remains unresolved. I suspect the reason may be due to some experimental artifacts, such as unnatural catalysts of Fe-Ni alloy, for example. Thermogenic CH_4 generated from sedimentary organic matter ($\delta^{13}C_{org}$ = −25 to −20 ‰) likely results in $\delta^{13}C_{CH4}$ values between −30 and −20 ‰ because of small isotope fractionation, based on experiments (Seewald et al. 1994). However, larger fractionations at lower temperature (Hoefs 2009) and intra-molecular ^{13}C depletion in the methyl-carbon of long-chain hydrocarbons (Gilbert et al. 2013) imply possibly more ^{13}C-depleted thermogenic CH_4. Although a broad $\delta^{13}C_{CH4}$ range (−50 to −20 ‰) was proposed for thermogenic CH_4 based on the compilation of field observations (Whiticar 1999), such a broad range may result from the mixing of 'pure' thermogenic CH_4 described above with ^{13}C-depleted biogenic CH_4 (−100 to −40 ‰) (Kawagucci et al. 2013a and references therein). The $\delta^{13}C_{CH4}$ values at the time of generation might be modified by certain processes occurring during subseafloor fluid migration (e.g., carbon isotope exchange between CO_2-CH_4), but the $\delta^{13}C_{CH4}$ modifications are expected to be negligible in terms of both reaction kinetics and/or magnitudes of the fractionation (see Kawagucci et al. 2013a for details). Consequently, the $\delta^{13}C_{CH4}$ value is a robust and useful indicator for deducing the origin of subseafloor CH_4.

The δD_{CH4} value has been used as an indicator to deduce the origin of environmental CH_4, in addition to the $\delta^{13}C_{CH4}$ value (Fig. 30.6). Many incubation experiments using both microbial isolates and bulk ecosystems (e.g., soil) revealed that biogenic CH_4 displayed a typically D-depleted isotope signature (−350 to −250 ‰) (Sugimoto and Wada 1995; Valentine et al. 2004) at the case that the δD_{H2O} value is +0 ‰. These incubations also revealed that the empirical $\delta D_{CH4}/\delta D_{H2O}$ ratio is approximately 0.75 for hydrogenotrophic methanogenesis and approximately 0.25 for aceticlastic methanogenesis. In contrast, past compilations of observations from sediment, oil fields, and natural gases (Nakai et al. 1974; Whiticar 1999) proposed a broader range of δD_{CH4} values (−450 to −150 ‰) as the "biogenic methane signature." The proposed biogenic δD_{CH4} characteristics from the compilation should be followed with care because environmental CH_4 may result from the mixing of multiple CH_4 sources and may have been partly consumed that results in increase of δD_{CH4} value. Nevertheless, all hydrothermal δD_{CH4} values measured so far have fallen into a narrow range (−130 to −96 ‰), regardless of the types of hydrothermal systems (Proskurowski et al. 2006; Kawagucci et al. 2011, 2013a; Reeves et al. 2011). This narrow range is very likely caused by hydrogen isotopic equilibrium between CH_4 and H_2O in the high-temperature fluids (>250 °C and δD_{H2O} = +0 ‰) that lead to δD_{CH4} values of approximately −130 ‰ (Proskurowski et al. 2006) although the certain reaction kinetics of hydrogen isotope exchange between CH_4 and H_2O toward isotopic equilibrium have never been

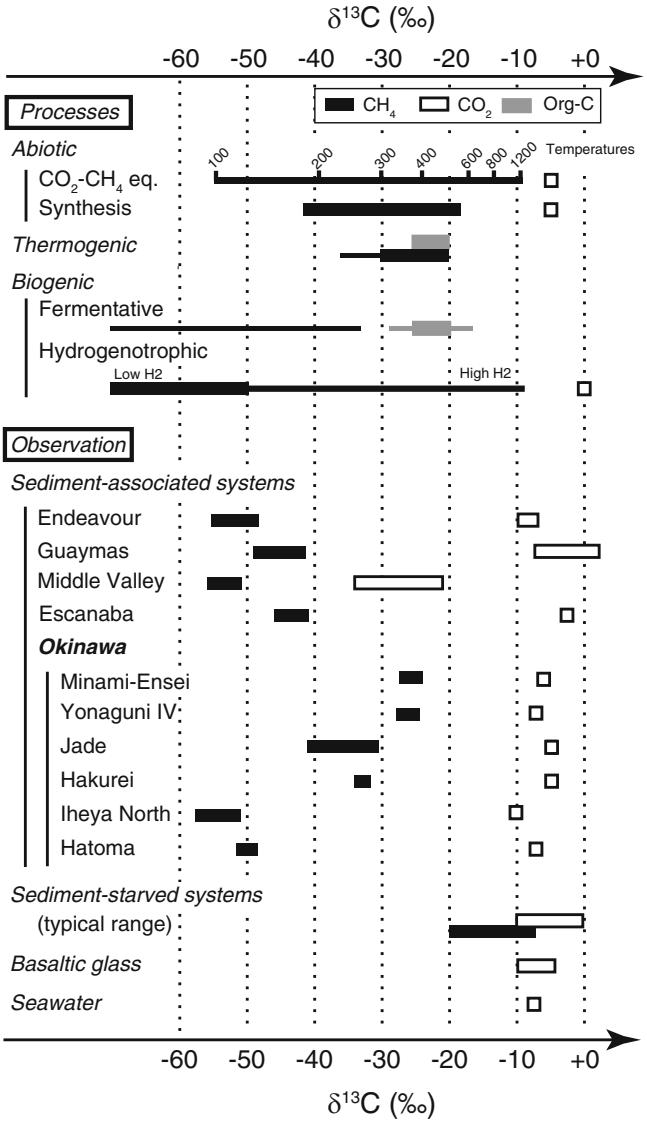

Fig. 30.5 $\delta^{13}C$ values of CH_4 (*black bars*), CO_2 (*white boxes*), and organic carbon (*gray bars*) considered typical for each process based on experimental and theoretical studies and observations in hydrothermal fluids. After Kawagucci et al. (2013a) with minor modification

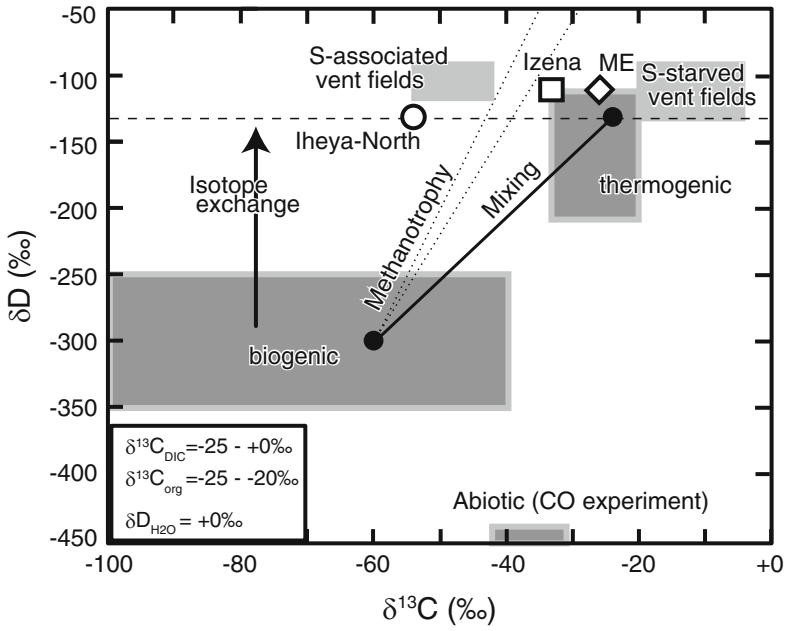

Fig. 30.6 Plots of δD_{CH4} values versus $\delta^{13}C_{CH4}$ values. *Open symbols* represent the observations in the Okinawa Trough (ME: Minami-Ensei; Izena: Jade and Hakurei). *Light gray areas* represent typical ranges of sediment-starved and -associated fields as labeled. *Dark gray areas* represent the expected ranges for thermogenic, biogenic, and abiotic methane, where the values of $\delta^{13}C_{DIC}$ (−25 to +0 ‰), $\delta^{13}C_{org}$ (−25 to −20 ‰), and δD_{H2O} (+0 ‰) are assumed for a methanogenic environment (see literature for details). An *arrow* and a *horizontal break line* represent the direction of δD_{CH4} change on the hydrogen isotope exchange between H_2O and CH_4 and the value at the isotope equilibrium, respectively. *Diagonal dotted lines* represent typical co-variation of $\delta^{13}C$-δD in microbial methane consumption ($\Delta\delta D/\Delta\delta^{13}C = 8–10$) (Feisthauer et al. 2011)

constrained (Reeves et al. 2012). While no experiment has yet verified the δD_{CH4} value of thermogenic CH_4, the δD_{CH4} values would be dominated by subsequent isotope exchange resulting in the isotopic equilibrium due to the obligatory high temperature. In addition, experimentally estimated δD_{CH4} values for abiotic CH_4 (e.g., approximately −500 ‰) (McCollom et al. 2010) (Fig. 30.6) are quite different from the isotopically equilibrated δD_{CH4} values, despite high-temperature condition for the methanogenesis. The presence of both equilibrated δD_{CH4} values and non-equilibrated $\delta^{13}C_{CH4}$ values in a CH_4 reservoir would be reasonable because the molecular geometry of CH_4 (carbon as a central atom and hydrogen as terminal atoms) suggests more rapid exchange of hydrogen. Consequently, the δD_{CH4} value is, in general, not useful in deducing the origin of hydrothermal fluid CH_4 due to the predominance of secondary isotope exchange. However, co-variation of $\delta^{13}C$ and δD ($\Delta\delta D/\Delta\delta^{13}C = 8–10$) has been identified in microbial methanotrophic activity (Feisthauer et al. 2011). Therefore, combination measurements between δD_{CH4} and $\delta^{13}C_{CH4}$ for a series of fluid samples provides supporting information for discussion of whether the $\delta^{13}C_{CH4}$ values of the samples have been altered by microbial methanotrophy (Fig. 30.6).

The radioactive carbon in CH_4 ($\Delta^{14}C_{CH4}$) is a possible tracer. Because magma-derived carbon should be ^{14}C-dead, detectable ^{14}C in hydrothermal fluid CH_4 indicates carbon input from seawater or young sediment. Therefore, detectable ^{14}C in the hydrothermal fluid CH_4, if present, implies microbial methanogenesis in the recharge stage of hydrothermal fluid circulation as a dominant CH_4 source. As far as the author is aware, only one study, which used samples from the sediment-covered Guaymas hydrothermal field, has reported ^{14}C measurements of high-temperature hydrothermal fluid CH_4 (Pearson et al. 2005) that revealed ^{14}C-dead CH_4 in hydrothermal fluid.

30.3.2.3 Molecular Hydrogen and Non-methane Hydrocarbons

The concentration of H_2 in hydrothermal fluid primarily depends on the redox conditions of the high-temperature hydrothermal reaction zone. In fact, a clear relationship between the host rock type (ultramafic to silicic) and the measured H_2 concentration has been identified in sediment-starved fields (Fig. 30.4). The relationship is also found even in several sediment-associated fields, such as the OT Minami-Ensei and Jade fields (Fig. 30.4). Because H_2 is likely buffered in the reaction zone by rapid reaction kinetics, additions of H_2 in the recharge stage of hydrothermal fluid circulation would be diminished in the reaction zone and never detectable in the venting fluid. In turn, because sub-millimolar levels of H_2 are expected from mafic host rocks, the measured millimolar levels of H_2 in hydrothermal fluids in the fully sediment-covered mafic-hosted Guaymas and Middle Valley fields are attributed to thermogenic H_2 input during the discharge stage of hydrothermal fluid circulation. Consequently, the H_2 concentration of the venting fluid is a useful indicator in determining whether thermal fluid-sediment interaction occurred in the discharge stage.

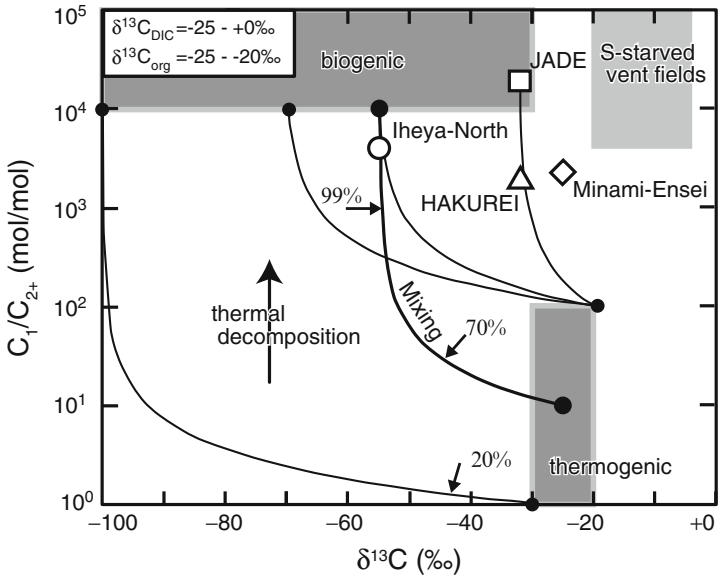

Fig. 30.7 A diagram of C_1/C_{2+} ratios versus $\delta^{13}C_{CH4}$ values. *Gray areas* represent the expected ranges of each hydrocarbon source, estimated by assuming $\delta^{13}C_{DIC}$ (−25 ‰ to +0 ‰) and $\delta^{13}C_{org}$ (−25 to −20 ‰) (see Kawagucci et al. (2013a)). Abiotic methane range is not described. Five curves demonstrate bimodal mixing scenarios between biogenic and thermogenic hydrocarbons. The *bold curve* is considered the most likely scenario for subseafloor environments in sediment-associated hydrothermal systems at this time. *Arrows* with percentages present contributions of biogenic methane at the arrowed points of the bimodal mixing curves. *Open symbols* represent the measured values in each Okinawa Trough hydrothermal field. After Kawagucci et al. (2013a) with minor modification

The C_1/C_{2+} ratio has been often utilized to deduce the origins of subseafloor CH_4 (Fig. 30.7). Although hydrothermal experiments demonstrating abiotic CH_4 generation have shown broad ranges of C_1/C_{2+} ratios of $>10^3$ (Horita and Berndt 1999) and approximately 3 (McCollom and Seewald 2006; McCollom et al. 2010), the observed range in sediment-starved hydrothermal fields is typically $>10^3$ (McCollom 2008 and references therein). The difference may be due to experimental artifacts, such as the use of unnatural catalysts of native iron, for example. Microbial methanogenesis accompanies little C_{2+} hydrocarbon generation and is expected to feature C_1/C_{2+} ratios of $>10^4$ (Kawagucci et al. 2013a; and references therein). While the C_1/C_{2+} ratios of thermogenic hydrocarbons under high-temperature hydrothermal conditions have not yet been experimentally verified, a C_1/C_{2+} ratio of $<10^2$ has been practically used as a thermogenic hydrocarbon signature (e.g., Whiticar 1999). It should be noted that thermal decomposition of C_{2+} hydrocarbons to CH_4 would likely occur under deep-sea hydrothermal conditions due to both thermodynamic and kinetic aspects and could result in increasing C_1/C_{2+} ratios as high as those of abiotic/biogenic CH_4 (Kawagucci et al. 2013a). It should also be noted that a C_1/C_{2+} ratio resulting from bimodal mixing between typical thermogenic hydrocarbons and biogenic CH_4 is not linearly correlated with the mixing ratio of CH_4 between these hydrocarbons (Fig. 30.7). Consequently, low C_1/C_{2+} ratios ($<10^3$) are a definite indication of thermogenic hydrocarbons contributions to the fluid, whereas higher C_1/C_{2+} ratios ($>10^3$) do not rule out involvement of thermogenic hydrocarbons.

30.4 Estimation of Fluid Circulation Path: Implications of Methane Geochemistry

By using the multiple tracers discussed above, the geochemical origins of the hydrothermal fluid CH_4 in each OT field and the relationships with the geological settings can be modeled in two-dimension schematic illustrations (Fig. 30.8). This modeling enables us to deduce the geographical distribution of hydrothermal fluid circulation (Kawagucci et al. 2013a). I attempt to discover the geographical distribution of fluid circulations for all six OT hydrothermal fields, with the addition of the OT bathymetry. It should be noted that almost all of the hydrothermal fluid vents of the OT fields are hosted in volcanic bodies that outcrop from the sediment that fills the OT.

30.4.1 Iheya North

The Iheya North hydrothermal fluid features low $\delta^{13}C_{CH4}$ values (−58 to −51 ‰), high C_1/C_{2+} ratios (>3,700), equilibrated δD_{CH4} values (−130 ‰), and low H_2

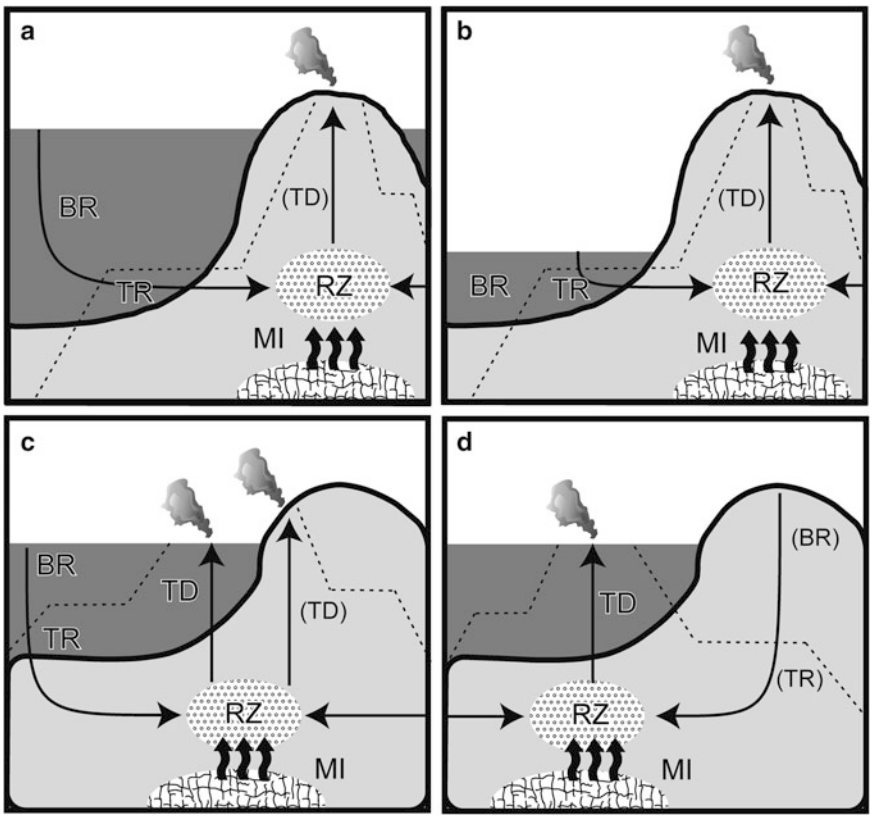

Fig. 30.8 Schematic illustrations of the 2D model representing methane origins based on the MMR model (after Kawagucci et al. (2011, 2013a) with minor modification). The geological setting and possible processes controlling fluid geochemistry, along with fluid circulation, are described (not to scale). *White*, *dark-gray*, and *light-gray fields* represent the seawater column, seafloor sediment, and rock basement, respectively. *Arrows* represent hydrothermal fluid migration paths. The two character designations represent the following: *BR* biological processes during the Recharge stage, *TR* thermal fluid-sediment interaction during the Recharge stage, *MI* magmatic volatile Inputs, *RZ* reaction zone, and *TR* thermal fluid-sediment interaction during the Discharge stage. *Dashed lines* are conceptual isotherms indicating the boundary between the microbial activity-dominated region and the thermochemical reaction-dominated region. Panels correspond to the models for describing (**a**) Iheya North and Hatoma, (**b**) Minami-Ensei, (**c**) Jade and Hakurei, and (**d**) Daiyon-Yonaguni

concentrations (~0.2 mM) (Kawagucci et al. 2011, 2013b). The low $\delta^{13}C_{CH4}$ values strongly suggest biogenic CH_4 as the dominant geochemical origin. The high C_1/C_{2+} ratios and the low H_2 concentrations eliminate the possibility of thermal fluid-sediment interaction during the discharge stage. All these geochemical indications can be consistently explained by dominance of microbial methanogenesis in the recharge stage as the origin of hydrothermal fluid CH_4 (Kawagucci et al. 2011) (Fig. 30.8a). Carbon mass balance calculations for the Iheya North hydrothermal system, as well as subseafloor hydrogeological structures revealed by geophysical study (Tsuji et al. 2012), suggest that the recharge stage of the Iheya North hydrothermal system includes the spatially abundant OT-filling sediments surrounding the Iheya North Knoll. This requires more than several kilometers of subseafloor hydrothermal fluid migration from the OT-filling sediment to the NBC vent (Fig. 30.9a).

30.4.2 Minami-Ensei

The Minami-Ensei hydrothermal fluid features high $\delta^{13}C_{CH4}$ values (−25 ‰), high C_1/C_{2+} ratios (>1,710), nearly equilibrated δD_{CH4} values (−105 ‰), and low H_2 concentrations (0.04 mM) (Fig. 30.4) (Kawagucci et al. 2013a). The high $\delta^{13}C_{CH4}$ values strongly suggest predominance of thermogenic CH_4 as its geochemical origin while the low H_2 concentrations rule out thermal fluid-sediment interaction during the discharge stage. These geochemical indications can be explained by dominance of thermal fluid-sediment interaction occurring in the recharge stage and reaction zone of hydrothermal fluid circulation as the origin of hydrothermal fluid CH_4 (Kawagucci et al. 2013a) (Fig. 30.8b). Less biogenic CH_4 contribution in the Minami-Ensei fluid implies a laterally shrunken hydrothermal fluid circulation that minimizes incorporation of biogenic CH_4 from the OT-filling sediment. This model seems

consistent with the large volcanic body of the Minami-Ensei Knoll (approximately 700 m in height and 5 km in radius) (Fig. 30.9b).

30.4.3 Izena Hall (Jade and Hakurei)

The Jade and Hakurei hydrothermal fluids are known to have identical fluid geochemistry, including moderate $\delta^{13}C$ values (−32 ‰) and the nearly equilibrated δD values (−113 ‰) (Table 30.1) (Ishibashi et al. 2014). However, there are significant differences in C_2H_6 concentrations ($C_1/C_{2+} = 14{,}900$ for Jade and $C_1/C_{2+} = 2{,}730$ for Hakurei) and H_2 concentrations (0.06 mM for Jade and 1.4 mM for Hakurei). The almost identical fluid geochemistry can be explained by the fact that the Jade and Hakurei fluids likely share a common fluid reservoir, which means that they share a common fluid circulation system for the recharge stage and reaction zones (Fig. 30.8c) (Ishibashi et al. 2014). This model does not conflict with the identical $\delta^{13}C_{CH4}$ and δD_{CH4} values at the case that the hydrothermal fluid CH_4 of these fields are mainly derived from the recharge stage of hydrothermal fluid circulation. The moderate $\delta^{13}C_{CH4}$ value suggests concomitant biogenic and thermogenic CH_4 in the recharge stage. In turn, the relatively low C_1/C_{2+} ratios (Fig. 30.7) and high H_2 concentrations of the Hakurei fluid (Fig. 30.4) suggest thermal fluid-sediment interaction during the discharge stage. Because the sedimentary settings of the discharge stages are quite different between the fields (thick sediment-covered Hakurei field and sediment-starved Jade field), it is reasonable that thermogenic hydrocarbons and molecular hydrogen entrained into the upwelling fluid occur only in the Hakurei field (Fig. 30.8c) (Kawagucci et al. 2010a; Ishibashi et al. 2014). Hydrothermal fluid reservoir underlying the southern part of the bottom and north-eastern inner wall of the Izena Hall imply that the fluid recharge occurs not only within the Izena Cauldron but also in the volcanic body of the Izena Hall and the OT-filling sediment surrounding the Izena Hall, >4 km from the vents (Fig. 30.9c).

30.4.4 Daiyon-Yonaguni

The Daiyon-Yonaguni hydrothermal fluids have high $\delta^{13}C$ values (−26 ‰) and high H_2 concentrations (0.8–5.5 mM), but no C_1/C_{2+} ratios or δD values have been reported (Konno et al. 2006). The millimolar levels of H_2 concentration, despite the most likely silicic rock-hosted hydrothermal system (Fig. 30.4), suggest thermal fluid-sediment interaction occurs in the discharge stage (Fig. 30.8d). This interpretation is consistent with the high $\delta^{13}C$ values that indicate that thermogenic CH_4 is the dominant CH_4 source. The geochemical origin of the hydrothermal fluid CH_4, particularly less biogenic CH_4, implies that the outcropping knolls surrounding the fluid venting area serve as the recharge zone of hydrothermal fluid circulation: Such fluid recharge reduces incorporation of biogenic CH_4 from the sediment surrounding the Daiyon-Yonaguni knoll (Fig. 30.8d). Seafloor sediment of the fluid venting area, a valley of the small knolls, hosts thermal fluid-sediment interaction during fluid upwelling, which increases H_2 in the fluid (Fig. 30.8d). Assuming the above model, the lateral extent of the hydrothermal fluid circulation is <4 km in radius from the vents (Fig. 30.9d).

30.4.5 Hatoma

The Hatoma hydrothermal fluids feature low $\delta^{13}C$ values (−50 ‰) (Saegusa et al. 2006) and low H_2 concentrations (0.3 mM) (Kawagucci et al. 2010b). Although no C_1/C_{2+} ratios or δD values have been reported, the geochemical origin of CH_4 in the Hatoma fluid can be explained by a model similar to that of the Iheya North field: Biogenic CH_4 is incorporated during the recharge stage of fluid circulation while there is little involvement of thermogenic compounds (Fig. 30.8a). Because the Hatoma Knoll is small (approximately 1 km in radius) compared with the other OT knolls hosting high-temperature hydrothermal fields (Fig. 30.9), the OT-filling sediments surrounding the Hatoma Knoll are likely the recharge stage for hydrothermal fluid circulation and the source of biogenic CH_4 in the vent fluid (Fig. 30.9e).

30.5 Concluding Remarks

This chapter provides a compilation of high-temperature hydrothermal fluid geochemistry from the OT hydrothermal fields. The generation of the 'TAIGA of Methane' (in other words, how and where fluid-sediment interaction occurs within a hydrothermal system) is classified by the geochemical and geographical origins of the venting methane into three patterns: (1) microbial methanogenesis in the sedimentary environment during the recharge stage, (2) thermal degradation of sedimentary organic matter during the recharge stage, and (3) thermal degradation of sedimentary organic matter during high-temperature hydrothermal fluid upwelling through the sediment layer beneath the vent (Fig. 30.8). The discussion of the origins of CH_4 provides implications for the lateral extents of hydrothermal fluid circulation in each OT field (Fig. 30.9), such as larger contribution of biogenic CH_4 relating to more widespread recharge zone. However, this remains highly speculative. To strengthen the model, an understanding of subseafloor hydrogeological conditions via analysis of seismic reflection

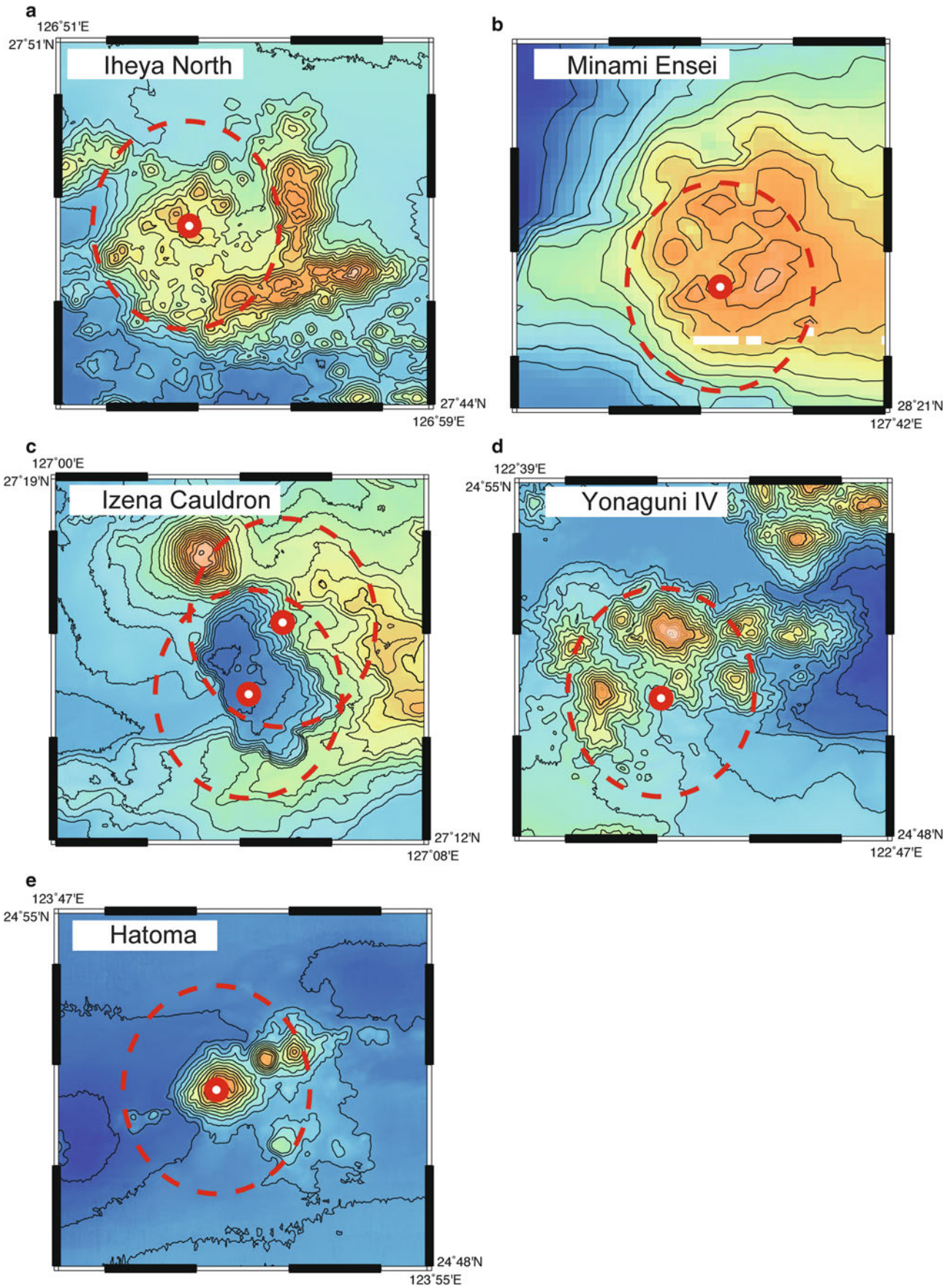

Fig. 30.9 Bathymetry maps of the six high-temperature hydrothermal fields at the same horizontal scale (coloring of depths is independent among the maps). *Broken red circles* on the maps represent the 2-miles radius from the main vent for each hydrothermal field

data and measurement of the permeability of cored rocks from seafloor drilling is essential. Nevertheless, the multiple geochemical tracer approach, when combined with interdisciplinary geological and microbiological investigations, will be a great breakthrough in clarifying the geochemical and geographical origins of CH_4 and associated hydrocarbons not only in deep-sea hydrothermal systems but also in the other sub(sea)floor geofluid systems, including subseafloor methane hydrate.

Acknowledgements I appreciate Ken Takai and the members of the TAIGA project for their valuable collaboration in studying deep-sea hydrothermal activity in the Okinawa Trough.

References

Bischoff JL, Rosenbauer RJ (1984) The critical-point and 2-phase boundary of seawater, 200–500°˜C. Earth Planet Sci Lett 68 (1):172–180

Butterfield DA, Mcduff RE, Mottl MJ, Lilley MD, Lupton JE, Massoth GJ (1994) Gradients in the composition of hydrothermal fluids from the endeavor segment vent field – phase-separation and brine loss. J Geophys Res Solid Earth 99(B5):9561–9583

Butterfield DA, Seyfried WE Jr, Lilley MD (2003) Composition and evolution of hydrothermal fluids. In: Halbach PE, Tunnicliffe V, Hein JR (eds) Energy and mass transfer in marine hydrothermal systems. Dahlem University Press, Germany, pp 124–161

Butterfield DA et al (2004) Mixing, reaction and microbial activity in the sub-seafloor revealed by temporal and spatial variation in diffuse flow vents at axial volcano. In: Wilcock WSD, Delong EF, Kelley DS, Baross JA, Cary CS (eds) The subseafloor biosphere at mid-ocean ridges. AGU, Washington, DC, pp 269–289

Charlou JL, Donval JP, Douville E, Jean-Baptiste P, Radford-Knoery J, Fouquet Y, Dapoigny A, Stievenard M (2000) Compared geochemical signatures and the evolution of menez Gwen (37°50′N) and lucky strike (37°17′N) hydrothermal fluids, south of the Azores triple junction on the Mid-Atlantic ridge. Chem Geol 171 (1–2):49–75

Charlou JL, Donval JP, Konn C, Ondréas H, Fouquet Y, Jean-Baptiste P, Fourré E (2010) High production and fluxes of H_2 and CH_4 and evidence of abiotic hydrocarbon synthesis by serpentinization in ultramafic-hosted hydrothermal systems on the Mid-Atlantic Ridge. In: Rona PA, Devey CW, Dyment J, Murton BJ (eds) Diversity of hydrothermal systems on slow spreading ocean ridges, vol 188, Geophysics monograph series. AGU, Washington, DC, pp 265–296

Chiba H et al (1993) Hydrothermal activity at the Minami-Ensei Knoll. Okinawa Trough: chemical characteristics of hydrothermal solutions. JAMSTECTR Deep Sea Res 9:271–282 (in Japanese with English abstract)

de Ronde CEL et al (2011) Submarine hydrothermal activity and gold-rich mineratization at Brother Volcano, Kermadec Arc, New Zealand. Miner Deposita. doi:10.1007/s00126-00011-00345-00128

Feisthauer S, Vogt C, Modrzynski J, Szlenkier M, Kruger M, Siegert M, Richnow HH (2011) Different types of methane monooxygenases produce similar carbon and hydrogen isotope fractionation patterns during methane oxidation. Geochim Cosmochim Acta 75 (5):1173–1184

Fouquet Y et al (2010) Geodiversity of hydrothermal processes along the Mid-Atlantic Ridge and ultramafic-hosted mineralization: a new type of oceanic Cu-Zn-Co-Au volcanogenic massive sulfide deposit. In: Rona PA, Devey CW, Dyment J, Murton BJ (eds) Diversity of hydrothermal systems on slow spreading ocean ridges, vol 188, Geophysics monograph series. AGU, Washington, DC, pp 321–368

Gallant RM, Von Damm KL (2006) Geochemical controls on hydrothermal fluids from the Kairei and Edmond Vent Fields, 23°-25°˜S, Central Indian Ridge. Geochem Geophys Geosyst 7

Gamo T (1995) Wide variation of chemical characteristics of submarine hydrothermal fluids due to the secondary modification processes after high temperature water-rock interaction: a review. In: Sakai H, Nozaki Y (eds) Biogeocheimical processes and ocean flux in the western pacific. Terra Scientific Publishing Company (TERRAPUB), Tokyo, pp 425–451

Gamo T, Sakai H, Kim ES, Shitashima K, Ishibashi J (1991) High alkalinity Due to sulfate reduction in the clam hydrothermal field, Okinawa Trough. Earth Planet Sci Lett 107(2):328–338

Gamo T, Okamura K, Charlou JL, Urabe T, Auzende JM, Ishibashi J, Shitashima K, Chiba H, Shipboard Scientific Party (1997) Acidic and sulfate-rich hydrothermal fluids from the Manus back-arc basin, Papua New Guinea. Geology 25:139–142

Gamo T et al (2001) Chemical characteristics of newly discovered black smoker fluids and associated hydrothermal plumes at the Rodriguez Triple Junction, Central Indian Ridge. Earth Planet Sci Lett 193(3–4):371–379

German CR, Von Damm KL (2003) 6.07 – hydrothermal processes. In: Heinrich DH, Karl KT (eds) Treatise on geochemistry. Pergamon, Oxford, pp 181–222

Gieskes JM, Simoneit BRT, Goodfellow WD, Baker PA, Mahn C (2002) Hydrothermal geochemistry of sediments and pore waters in Escanaba Trough – ODP Leg 169. Appl Geochem 17 (11):1435–1456

Gilbert A, Yamada K, Yoshida N (2013) Exploration of intramolecular ^{13}C isotope distribution in long chain n-alkanes (C11–C31) using isotopic ^{13}C NMR. Org Geochem 62:56–61

Grimaud D, Ishibashi J, Lagabrielle Y, Auzende JM, Urabe T (1991) Chemistry of hydrothermal fluids from the 17°˜S active-site on the north Fiji basin ridge (Sw pacific). Chem Geol 93(3–4):209–218

Hirose T, Kawagucci S, Suzuki K (2011) Mechanoradical H_2 generation during simulated faulting: implications for an earthquake-driven subsurface biosphere. Geophys Res Lett 38:L17303. doi:10.1029/2011GL048850

Hoefs J (2009) Stable isotope geochemistry, 6th edn. Springer, Berlin, p 285

Hongo Y, Obata H, Gamo T, Nakaseama M, Ishibashi J, Konno U, Saegusa S, Ohkubo S, Tsunogai U (2007) Rare earth elements in the hydrothermal system at Okinawa Trough back-arc basin. Geochem J 41:1–15

Horita J, Berndt ME (1999) Abiogenic methane formation and isotopic fractionation under hydrothermal conditions. Science 285 (5430):1055–1057

Inagaki F et al (2006) Microbial community in a sediment-hosted CO_2 lake of the southern Okinawa Trough hydrothermal system. Proc Natl Acad Sci U S A 103(38):14164–14169

Ishibashi JI, Wakita H, Nojiri Y, Grimaud D, Jeanbaptiste P, Gamo T, Auzende JM, Urabe T (1994a) Helium and carbon geochemistry of hydrothermal fluids from the north Fiji basin spreading ridge (southwest pacific). Earth Planet Sci Lett 128(3–4):183–197

Ishibashi J, Grimaud D, Nojiri Y, Auzende JM, Urabe T (1994b) Fluctuation of chemical-compositions of the phase-separated hydrothermal fluid from the North Fiji Basin Ridge. Mar Geol 116 (1–2):215–226

Ishibashi J, Sano Y, Wakita H, Gamo T, Tsutsumi M, Sakai H (1995) Helium and carbon geochemistry of hydrothermal fluids from the mid-Okinawa trough back-arc basin, southwest of Japan. Chem Geol 123(1–4):1–15

Ishibashi J, Sato M, Sano Y, Wakita H, Gamo T, Shanks WC (2002) Helium and carbon gas geochemistry of pore fluids from the sediment-rich hydrothermal system in Escanaba Trough. Appl Geochem 17(11):1457–1466

Ishibachi J et al (2002b) Concentration of biologically important chemical species in hydrothermal fluids from submarine arc volcano suiyo seamount. Eos Trans AGU 83(47), Fall Meets. Suppl., Abstract #V11C-05

Ishibashi J-I, Noguchi T, Toki T, Miyabe S, Yamagami S, Onishi Y, Yamanaka T, Yokoyama Y, Omori E, Takahashi Y, Hatada K, Nakaguchi Y, Yoshizaki M, Konno U, Shibuya T, Takai K, Inagaki F, Kawagucci S (2014) Diversity of fluid geochemistry affected by processes during fluid upwelling in active hydrothermal fields in the Izena Hole, the middle Okinawa Trough back-arc basin. Geochem J 48(3):357–369

Kawagucci S, Okamura K, Kiyota K, Tsunogai U, Sano Y, Tamaki K, Gamo T (2008) Methane, manganese, and helium-3 in newly discovered hydrothermal plumes over the Central Indian Ridge, 18°-20°˜S. Geochem Geophys Geosyst 9:Q10002. doi:10.1029/2008GC002082

Kawagucci S, Shirai K, Lan TF, Takahata N, Tsunogai U, Sano Y, Gamo T (2010a) Gas geochemical characteristics of hydrothermal plumes at the HAKUREI and JADE vent sites, the Izena Cauldron, Okinawa Trough. Geochem J 44(6):507–518

Kawagucci S, Toki T, Ishibashi J, Takai K, Ito M, Oomori T, Gamo T (2010b) Isotopic variation of molecular hydrogen in 20–375°˜C hydrothermal fluids as detected by a new analytical method. J Geophys Res Biogeosci 115, G03021. doi:10.1029/2009JG001203

Kawagucci S et al (2011) Hydrothermal fluid geochemistry at the Iheya North field in the mid-Okinawa Trough: implication for origin of methane in subseafloor fluid circulation systems. Geochem J 45 (2):109–124

Kawagucci S et al (2013a) Geochemical origin of hydrothermal fluid methane in sediment-associated fields and its relevance to the geographical distribution of whole hydrothermal circulation. Chem Geol 339:213–225

Kawagucci S et al (2013b) Post-drilling changes in fluid discharge pattern, mineral deposition, and fluid chemistry in the Iheya North hydrothermal field, Okinawa Trough. Geochem Geophys Geosyst 14:4774–4790

Kishida K, Sohrin Y, Okamura K, Ishibachi J (2004) Tungsten enriched in submarine hydrothermal fluids. Earth Planet Sci Lett 222 (3–4):819–827

Konno U, Tsunogai U, Nakagawa F, Nakaseama M, Ishibashi JI, Nunoura T, Nakamura KI (2006) Liquid CO_2 venting on the seafloor: Yonaguni knoll IV hydrothermal system, Okinawa Trough. Geophys Res Lett 33:L16607

Kumagai H et al (2008) Geological background of the Kairei and Edmond hydrothermal fields along the Central Indian Ridge: implications of their vent fluids' distinct chemistry. Geofluids 8 (4):239–251

Lilley MD, Butterfield DA, Olson EJ, Lupton JE, Macko SA, Mcduff RE (1993) Anomalous CH_4 and NH_4^+ concentrations at an unsedimented mid-ocean-ridge hydrothermal system. Nature 364 (6432):45–47

Lilley MD, Butterfield DA, Lupton JE, Olson EJ (2003) Magmatic events can produce rapid changes in hydrothermal vent chemistry. Nature 422(6934):878–881

Lin LH, Slater GF, Lollar BS, Lacrampe-Couloume G, Onstott TC (2005) The yield and isotopic composition of radiolytic H-2, a potential energy source for the deep subsurface biosphere. Geochim Cosmochim Acta 69(4):893–903

McCollom TM (2008) Observation, experimental, and theoretical constraints on carbon cycling in mid-ocean ridge hydrothermal systems. In: Lowell RP, Seewald JS, Metaxas A, Perfit MR (eds) Magma to microbe: modeling hydrothermal processes at ocean spreading centers. American Geophysical Union, Washington, DC, pp 193–213

McCollom TM (2013) Laboratory simulations of abiotic hydrocarbon formation in Earth's deep subsurface. Rev Min Geochem 75:467–494

McCollom TM, Seewald JS (2006) Carbon isotope composition of organic compounds produced by abiotic synthesis under hydrothermal conditions. Earth Planet Sci Lett 243(1–2):74–84

McCollom TM, Bach WG (2009) Thermodynamic constraints on hydrogen generation during serpentinization of ultramafic rocks. Geochim Cosmochim Acta 73(3):856–875

McCollom TM, Lollar BS, Lacrampe-Couloume G, Seewald JS (2010) The influence of carbon source on abiotic organic synthesis and carbon isotope fractionation under hydrothermal conditions. Geochim Cosmochim Acta 74(9):2717–2740

Merlivat L, Pineau F, Javoy M (1987) Hydrothermal vent waters at 13°˜N on the east pacific rise – isotopic composition and gas concentration. Earth Planet Sci Lett 84(1):100–108

Mottl MJ et al (2011) Chemistry of hot springs along the eastern Lau spreading center. Geochim Cosmochim Acta 75 (4):1013–1038

Nakagawa S, Takai K, Inagaki F, Chiba H, Ishibashi J, Kataoka S, Hirayama H, Nunoura T, Horikoshi K, Sako Y (2005) Variability in microbial community and venting chemistry in a sediment-hosted backarc hydrothermal system: Impacts of subseafloor phase-separation. FEMS Microbiol Ecol 54(1):141–155

Nakai N, Yoshida N, Ando N (1974) Isotopic studies on oil and gas fields in Japan. Chikyu Kagaku 7:87–98 (in Japanese with English abstract)

Nakano A, Matsumura M, Ishibashi J (2001) Geochemistry of hydrothermal fluids from the Hatoma Knoll in the South Okinawa Trough. JAMSTEC J Deep Sea Res 18:139–144

Noguchi T, Shinjo R, Ito M, Takada J, Oomori T (2011) Barite geochemistry from hydrothermal chimneys of the Okinawa Trough: insight into chimney formation and fluid/sediment interaction. J Mineral Petrol Sci 106(1):26–35

Pearson A, Seewald JS, Eglinton TI (2005) Bacterial incorporation of relict carbon in the hydrothermal environment of Guaymas Basin. Geochim Cosmochim Acta 69(23):5477–5486

Proskurowski G, Lilley MD, Brown TA (2004) Isotopic evidence of magmatism and seawater bicarbonate removal at the endeavour hydrothermal system. Earth Planet Sci Lett 225(1–2):53–61

Proskurowski G, Lilley MD, Kelley DS, Olson EJ (2006) Low temperature volatile production at the Lost City Hydrothermal Field, evidence from a hydrogen stable isotope geothermometer. Chem Geol 229(4):331–343

Reeves EP, Seewald JS, Saccocia P, Bach W, Craddock PR, Shanks WC, Sylva SP, Walsh E, Pichler T, Rosner M (2011) Geochemistry of hydrothermal fluids from the PACMANUS, Northeast Pual and Vienna Woods hydrothermal fields, Manus Basin, Papua New Guinea. Geochim Cosmochim Acta 75(4):1088–1123

Reeves EP, Seewald JS, Sylva SP (2012) Hydrogen isotope exchange between n-alkanes and water under hydrothermal conditions. Geochim Cosmochim Acta 77:582–599

Saegusa S, Tsunogai U, Nakagawa F, Kaneko S (2006) Development of a multibottle gas-tight fluid sampler WHATS II for Japanese submersibles/ROVs. Geofluids 6(3):234–240

Sakai H, Gamo T, Kim ES, Tsutsumi M, Tanaka T, Ishibashi J, Wakita H, Yamano M, Oomori T (1990a) Venting of carbon-dioxide rich

fluid and hydrate formation in mid-Okinawa Trough Backarc Basin. Science 248(4959):1093–1096

Sakai H et al (1990b) Unique chemistry of the hydrothermal solution in the mid-Okinawa Trough Backarc Basin. Geophys Res Lett 17 (12):2133–2136

Sano Y, Fischer TP (2013) The analysis and interpretation of noble gases in modern hydrothermal systems. In: Burnard P (ed) The noble gases as geochemical tracers, advances in isotope geochemistry. Springer, Berlin/Heidelberg, pp 249–317

Seewald JS, Seyfried WE (1990) The effect of temperature on metal mobility in subseafloor hydrothermal systems – constraints from basalt alteration experiments. Earth Planet Sci Lett 101 (2–4):388–403

Seewald JS, Seyfried WE, Shanks WC (1994) Variations in the chemical and stable-isotope composition of carbon and sulfur species during organic-rich sediment alteration – an experimental and theoretical-study of hydrothermal activity at Guaymas Basin, Gulf of California. Geochim Cosmochim Acta 58(22):5065–5082

Seyfried WE, Seewald JS, Berndt ME, Ding K, Foustoukos DI (2003) Chemistry of hydrothermal vent fluids from the main Endeavour field, northern Juan de Fuca Ridge: geochemical controls in the aftermath of June 1999 seismic events. J Geophys Res Solid Earth 108(B9):2429

Shinjo R, Kato Y (2000) Geochemical constraints on the origin of bimodal magmatism at the Okinawa Trough, an incipient back-arc basin. Lithos 54:117–137

Sugimoto A, Wada E (1995) Hydrogen isotopic composition of bacterial methane – CO_2/H_2 reduction and acetate fermentation. Geochim Cosmochim Acta 59(7):1329–1337

Suzuki R, Ishibashi JI, Nakaseama M, Konno U, Tsunogai U, Gena K, Chiba H (2008) Diverse range of mineralization induced by phase separation of hydrothermal fluid: case study of the Yonaguni Knoll IV hydrothermal field in the Okinawa Trough back-arc basin. Res Geol 58(3):267–288

Takai K, Nakamura K, Toki T, Tsunogai U, Miyazaki M, Miyazaki J, Hirayama H, Nakagawa S, Nunoura T, Horikoshi K (2008) Cell proliferation at 122°C and isotopically heavy CH_4 production by a hyperthermophilic methanogen under high-pressure cultivation. Proc Natl Acad Sci U S A 105(31):10949–10954

Tivey MK, Stakes DS, Cook TL, Hannington MD, Petersen S (1999) A model for growth of steep-sided vent structures on the Endeavour Segment of the Juan de Fuca Ridge: results of a petrologic and geochemical study. J Geophys Res Solid Earth 104 (B10):22859–22883

Toki T, Tsunogai U, Ishibashi J, Utsumi M, Gamo T (2008) Methane enrichment in low-temperature hydrothermal fluids from the Suiyo Seamount in the Izu-Bonin Arc of the western Pacific Ocean. J Geophys Res Solid Earth 113:B08s13. doi:10.1029/2007jb005476

Tsuji T, Takai K, Oiwane H, Nakamura Y, Masaki Y, Kumagai H, Kinoshita M, Yamamoto F, Okano T, Kuramoto S (2012) Hydrothermal fluid flow system around the Iheya North Knoll in the mid-Okinawa trough based on seismic reflection data. J Volcanol Geoth Res 213:41–50

Tsunogai U, Ishibashi J, Wakita H, Gamo T, Watanabe K, Kajimura T, Kanayama S, Sakai H (1994) Peculiar features of Suiyo seamount hydrothermal fluids, Izu-Bonin arc – differences from subaerial volcanism. Earth Planet Sci Lett 126(4):289–301

Tsunogai U, Nakagawa F, Gamo T, Ishibashi J (2005) Stable isotopic compositions of methane and carbon monoxide in the Suiyo hydrothermal plume, Izu-Bonin arc: tracers for microbial consumption/production. Earth Planet Sci Lett 237(3–4):326–340

Valentine DL, Chidthaisong A, Rice A, Reeburgh WS, Tyler SC (2004) Carbon and hydrogen isotope fractionation by moderately thermophilic methanogens. Geochim Cosmochim Acta 68 (7):1571–1590

Von Damm KL, Lilley MD (2004) Diffuse flow hydrothermal fluids from 9°50′N east pacific rise: origin, evolution and biogeochemical controls. In: Wilcock WSD, Delong EF, Kelley DS, Baross JA, Cary CS (eds) The subseafloor biosphere at mid-ocean ridges. AGU, Washington, DC, pp 245–268

Von Damm KL, Edmond JM, Measures CI, Grant B (1985) Chemistry of submarine hydrothermal solutions at Guaymas Basin, Gulf of California. Geochim Cosmochim Acta 49(11):2221–2237

Von Damm KL, Parker CM, Zierenberg RA, Lilley MD, Olson EJ, Clague DA, McClain JS (2005) The Escanaba Trough, Gorda ridge hydrothermal system: temporal stability and subseafloor complexity. Geochim Cosmochim Acta 69(21):4971–4984

Welhan JA, Lupton JE (1987) Light hydrocarbon gases in Guaymas Basin hydrothermal fluids: thermogenic versus abiogenic origin. Am Assoc Petrol Geol Bull 71:215–223

Whiticar MJ (1999) Carbon and hydrogen isotope systematics of bacterial formation and oxidation of methane. Chem Geol 161 (1–3):291–314

Yanagawa K et al (2013) Metabolically active microbial communities in marine sediment under high-CO_2 and low-pH extremes. ISME J 7 (3):555–567

You CF, Butterfield DA, Spivack AJ, Gieskes JM, Gamo T, Campbell AJ (1994) Boron and Halide systematics in submarine hydrothermal systems – effects of phase-separation and sedimentary contributions. Earth Planet Sci Lett 123(1–4):227–238

Sediment–Pore Water System Associated with Native Sulfur Formation at Jade Hydrothermal Field in Okinawa Trough

31

Yuka Yokoyama, Yoshio Takahashi, Youko Miyoshi, Jun-ichiro Ishibashi, and Shinsuke Kawagucci

Abstract

The subsurface sediment–pore water system in the Jade hydrothermal field was investigated along with pore water chemistry and X-ray absorption fine structure analysis for sediment samples. Sediments were collected by coring near the TBS vent (Core 1186MBL) and from near the Biwako vent (Core 1188MB), which are active hydrothermal vents with high (320 °C) and low (90 °C) temperature fluids, respectively. Core 1186MBL is characterized by occurrences of chimney fragments in the shallow part (2–9 cmbsf) and native sulfur in the deep part (6–19 cmbsf). The results of chemical analyses of the pore water suggest a seawater recharge from the seafloor into Core 1186MBL. This hydraulic characteristic of the pore water, which is commonly observed near active submarine hydrothermal vents, leads to oxidation of sulfide minerals in chimney fragments in the shallow part by the oxic recharged seawater. The resulting acidic and suboxic pore water is transported downward, and can form native sulfur in the deeper part of Core 1186MBL. Core 1188MB shows a wide distribution of native sulfur, and its pore water chemistry indicates anaerobic oxidation of methane below 8 cmbsf and a mixing of seawater and hydrothermal fluid below 10 cmbsf. The mixing of acidic and anoxic hydrothermal fluid and seawater allows the precipitation of native sulfur in Core 1188MB, and the uniform circumneutral pH condition despite the input of acidic hydrothermal fluid. The native sulfur deposits in the arc–back-arc hydrothermal fields provide important geochemical information that is useful to understand the subsurface sediment–pore water system involving hydrothermal fluids

Keywords

Native sulfur • Pore water chemistry • Seafloor hydrothermal system • XAFS

Y. Yokoyama (✉)
Department of Earth and Planetary Systems Science,
Graduate School of Science, Hiroshima University,
1-3-1 Kagamiyama, Higashi-Hiroshima, Hiroshima 739-8526, Japan
e-mail: yoshiyukasris@gmail.com

Y. Takahashi
Department of Earth and Planetary Systems Science,
Graduate School of Science, Hiroshima University,
1-3-1 Kagamiyama, Higashi-Hiroshima, Hiroshima 739-8526, Japan

Department of Earth and Planetary Science,
Graduate School of Science, The University of Tokyo,
7-3-1 Hongo, Bunkyo-ku, Tokyo 113-0033, Japan

Y. Miyoshi • J.-i. Ishibashi
Department of Earth and Planetary Sciences,
Graduate School of Sciences, Kyushu University, 6-10-1 Hakozaki,
Higashi-ku, Fukuoka 812-8581, Japan

S. Kawagucci
Precambrian Ecosystem Laboratory (PEL), Japan Agency
for Marine-Earth Science and Technology (JAMSTEC),
2-15 Natsushima-cho, Yokosuka, Kanagawa 237-0061, Japan

J.-i. Ishibashi et al. (eds.), *Subseafloor Biosphere Linked to Hydrothermal Systems: TAIGA Concept*,
DOI 10.1007/978-4-431-54865-2_31,

31.1 Introduction

The Jade hydrothermal field is located at the northeast of the Izena Hole in the mid-Okinawa Trough back-arc basin behind the Ryukyu arc-trench system. The site has been the subject of numerous studies (Halbach et al. 1989; Sakai et al. 1990a, b; Ishibashi et al. 1995; Kinoshita and Yamano 1997; Marumo and Hattori 1999). The strong enrichment of volatiles (e.g., H_2O, CO_2, and SO_2) in arc–back-arc magmas results in an input of these volatiles in the hydrothermal fluid of the arc–back-arc hydrothermal systems (Gamo et al. 2006). Considerable SO_2 input into the hydrothermal fluid produces acidic fluid, often resulting in native sulfur deposits in arc–back-arc hydrothermal systems (Marumo and Hattori 1999; Nakagawa et al. 2006; Embley et al. 2007; de Ronde et al. 2011).

In seafloor hydrothermal system, a mixing of anoxic hydrothermal fluid with oxic seawater produces a significant gradient of environmental factors such as pH and redox conditions at and below seafloor. These environmental factors in sediment–pore water system are, therefore, helpful in understanding seafloor hydrothermal circulation. The specific pH and redox conditions associated with hydrothermal fluid is often recorded by mineral compositions in sediment. The Jade field is characterized by layered or massive native sulfur (sulfur crust) (Marumo and Hattori 1999; Ishibashi et al. 2014). Precipitation of native sulfur can occur under a limited Eh-pH condition, or under high acidity and suboxic conditions close to the sulfide–sulfate boundary with a sufficient concentration of sulfur (Brookins 1987). This suggests that the presence of native sulfur indicates the limited pH and redox conditions of the system. Chemical speciation of redox-sensitive elements such as sulfur is also a useful method for estimating the redox condition of the system that includes the elements. In the last two decades, X-ray Absorption Fine Structure (XAFS) spectroscopy has become a common speciation technique for various natural materials because of its high elemental selectivity without sample destruction (Tsuji et al. 2012). In this study, XAFS spectroscopy was applied for speciation of sulfur (S), iron (Fe), and selenium (Se) in sediments to understand the subsurface redox system in the Jade hydrothermal field. In addition, by combining pore water chemistry with the speciation study, the sediment–pore water system involving hydrothermal fluids was investigated in relation to the native sulfur formation.

31.2 Sampling and Analyses

The research site, Jade field, is located along the northeastern slope of the Izena Hole at water depths of 1,300–1,550 m. The detailed geological settings of this area are summarized in Ishibashi et al. (Chap. 27). In the hole, one black smoker venting chimney was discovered with Mg^{2+}-free fluids of 320 °C at 1,350 m depth (TBS vent) (Sakai et al. 1990a; Ishibashi et al. 2014). At the southwest distal part of the Jade field, the seafloor is covered with sulfur crust, and an active hydrothermal vent was found at a depth of 1,520 m (Biwako vent); the hydrothermal vent fluid is 90 °C and associated with emanation of liquid CO_2 bubbles. Sediment samples were collected by short coring using the Remotely Operated Vehicle (ROV) *Hyper Dolphin* during the NT10-17 cruise of the *R/V Natsushima* in September 2010. Sediment cores were collected at 50 m southwest of the TBS vent (1186MBL), and adjacent to the Biwako vent (1188MB) using an MBARI-type corer 30 cm in length with bottom seawater. The sampling locations of the two sediment cores are shown in Fig. 44.1 (Miyoshi et al., Chap. 44).

After the recovery of the ROV, the MBARI core samples were cut horizontally into 1 to several cm in length, and the outer rim of the core in each layer was removed to avoid possible contamination and artifacts. A sediment subsample of several cm^3 in volume was taken from each cut sediment core section and pressed to drain the pore water using a disposal syringe with a 0.45 μm pore-size filter. The remaining portion of each subsample was stored in an air-tight polyethylene bag with N_2 gas at 4 °C for onshore analyses. Aliquots of the filtered pore water and bottom seawater samples were acidified by HNO_3 for onshore ICP-AES analysis to prevent mineral precipitation and microbial activities, and stored in a refrigerator with the other unacidified aliquots for onshore analysis. The following parameters for the filtered pore water and bottom seawater were measured onboard: pH was determined using a pH meter (Horiba pH meter and glass electrode); alkalinity was measured by potentiometric titration with 0.1 M HCl; ammonium ion (NH_4^+) concentration was determined using the indophenol blue colorimetric method (Solorzano 1969); and hydrogen sulfide (H_2S) concentration was determined by the methylene blue colorimetric method (Cline 1969). The analytical precisions were estimated to be within 0.5 % for pH, 5 % for alkalinity, 7 % for NH_4^+, and 5 % for H_2S.

In the onshore laboratory, the collected sediment samples were treated in an anaerobic glove box (Coy Laboratory Products) purged with an atmosphere of Ar/H_2 (95:5) mixture, in which the oxygen content was monitored and kept below 0.01 mg/L. The mineralogy of the sediment samples was analyzed using a powder X-ray diffracometer (XRD; MultiFlex, Rigaku Co.). To determine the bulk mineralogy, each sediment sample was ground and homogenized using agate mortar after drying in the glove box. The mineral phase identification was carried out by matching the XRD patterns to reference materials from the International Center for Diffraction Data (ICDD) database.

For speciation analysis by XAFS, the sediment samples were re-packed into airtight polyethylene bags in the glove box without drying and stored at 4 °C until the XAFS measurements. The XAFS spectra were obtained at beamlines BL-9A and BL-12C at the KEK Photon Factory (Tsukuba, Japan). The measurements were carried out at room temperature under ambient conditions. Iron and Se K-edge XAFS spectra of the reference compounds were collected in transmission mode, whereas those of the sediment samples were obtained in fluorescence yield (FY) mode using a 19-element germanium semiconductor detector positioned at 90° to the incident beam. In the fluorescence mode, the samples were positioned at 45° with respect to the incident beam. Sulfur K-edge XAFS spectra were collected both by the fluorescence and conversion electron yield (CEY) modes in a chamber purged with helium to minimize the attenuation of incident X-rays by air. For the sulfur K-edge CEY-XAFS measurement, each sediment sample was directly attached to carbon double-faced tape on a sample holder and set in the chamber soon after taking it out of the polyethylene bag. The XAFS data were analyzed using the Athena program (Ravel and Newville 2005). XAFS consists of X-ray Absorption Near Edge Structure (XANES) and Extended X-ray Absorption Fine Structure (EXAFS). Analysis of XANES spectra based on least-square Linear Combination Fitting (LCF) provides information about the oxidation state and coordination chemistry of the absorbing atom. The quality of the LCF is given by the residual value (R) defined by

$$R(\%) = \frac{\sum\{I_{\mathrm{dat}}(E) - I_{\mathrm{cal}}(E)\}^2}{\sum\{I_{\mathrm{dat}}(E)\}^2} \times 100 \qquad (31.1)$$

where I_{dat} is the absorption of the experimental spectra and I_{cal} is the absorption calculated from the reference spectra. By a similar LCF technique, EXAFS provides information on the structural environment of the absorbing atom and complements the XANES analysis. The LCF was performed on the k^3-weighted EXAFS data using reference spectra by minimizing the residual of the fit. The quality of the fitting is given by the goodness-of-fit parameter R, defined as

$$R(\%) = \frac{\sum\{k^3\chi_{\mathrm{dat}}(k) - k^3\chi_{\mathrm{cal}}(k)\}^2}{\sum\{k^3\chi_{\mathrm{dat}}(k)\}^2} \times 100 \qquad (31.2)$$

where $\chi_{\mathrm{dat}}(k)$ and $\chi_{\mathrm{cal}}(k)$ are the experimental and calculated data points, respectively.

Chloride (Cl^-) and sulfate (SO_4^{2-}) concentrations in the unacidified pore water and bottom seawater were determined by ion chromatography with up to 5 % errors. The concentration of magnesium (Mg) in the acidified pore water and bottom seawater was measured by ICP-AES within 3 % error.

31.3 Results

31.3.1 Mineralogy in the Sediments

Core 1186MBL (19 cm in length) collected near the TBS vent mainly consists of mud matrix and is black (Fig. 31.1a). This black sediment is characterized by the appearance of black lumps at 2–9 cm below the seafloor (cmbsf) and yellow lumps 17–19 cmbsf, which were identified as sulfide minerals (sphalerite and galena) and native sulfur, respectively, by XRD analysis (Table 31.1). The sulfide lumps found 2–9 cmbsf are considered to be chimney fragments from the many sulfide inactive chimneys around the TBS vent. The results of the bulk XRD analysis showed common occurrences of quartz throughout the entire core, while their concomitant minerals show a vertical compositional variation: barite at 0–4 cmbsf, sphalerite (ZnS) and galena (PbS) at 2–9 cmbsf, and native sulfur and pyrite (FeS_2) at 6–19 cmbsf (Table 31.1). Core 1188MB (23 cm in length) obtained adjacent to the Biwako vent can be visually divided into two units. The top layer (0–2 cmbsf)

Fig. 31.1 Photograph of (**a**) Core 1186MBL collected near the TBS vent and (**b**) Core 1188MB obtained adjacent to the Biwako vent

Table 31.1 Occurrences of minerals in the Core 1186MBL and Core 1188MB observed by bulk XRD analyses

Depth (cmbsf)	Quartz	Native sulfur	Pyrite	Sphalerite	Galena	Barite	Illite	Smectite	Kaolinite	Chlorite
Core 1186MBL										
0–2	xxx			x	x	xx	x	xx	xx	
2–4	xx			xxx	x	xx	x	xx	xx	
4–6	x			xxx	xxx		x	xx	xx	
6–9	xx	x	x	xxx	xx		xx	xx	xx	
9–11	xxx	xxx	x				xx	xx	xx	
11–13	xxx	xxx	x				xx	xx	xx	
13–15	xxx	xxx	x				xx	xx	xx	
15–17	xxx	xxx	x				xx	xx	xx	
17–19	xxx	xxx	x				xx	xx	xx	
Core 1188MB										
0–2	xxx	x	x				xx	xx		xx
2–4	xxx	xx	x				x	xx		xx
4–6	xxx	xx	x				x	xx		xx
6–8	xxx	xxx	x				x	xx		xx
8–10	xxx	xxx	x				x	xx		xx
10–11	xxx	xxx	x				x	xx		xx
11–14	xxx	xxx	x				x	xx		xx
14–17	xxx	xxx	x				x	xx		xx
17–20	xxx	xxx	x				x	xx		xx
20–23	xxx	xxx	x				x	xx		xx

Details of the clay mineralogy can be found in Miyoshi et al. (Chap. 44)
Mineral abundances determined by semi-quantitative XRD analysis: xxx, abundant (>25 %); xx, common (>10 %); x, minor (>3 %).

appears grayish black, while the subsurface layer (2–23 cmbsf) was grayish white with a thin yellow layer (Fig. 31.1b). This grayish sediment is composed of quartz, native sulfur, and pyrite (Table 31.1). The native sulfur and pyrite are minor in the top layer compared with the subsurface layer. In addition to our bulk XRD analysis, Miyoshi et al. (Chap. 44) carefully identified the clay minerals for these two sediments. Their results showed that several clay minerals occur over the whole sediment sample (illite, smectite, and kaolinite in Core 1186MBL; illite, smectite, and chlorite in Core 1188MB), which were produced by hydrothermal alteration (Miyoshi et al. Chap. 44).

31.3.2 XAFS

31.3.2.1 Sulfur K-Edge XANES

Sulfur K-edge XANES can distinguish the oxidation states of sulfur by peak-energy positions, as well as identify the species by the post-edge structure (Pingitore et al. 1995) (Fig. 31.2a). Since the total sulfur concentration in the sediment sample is high, the FY-XANES spectra for the sediment samples tended to be distorted because of the thickness effect or self-absorption effect (Schroeder 1996; Manceau et al. 2002). Therefore, the speciation of sulfur for the sediment samples was conducted based on the XANES spectra collected mainly by the CEY mode.

The results of the sulfur XANES analysis of Core 1186MBL indicated three types of XANES spectra along with sediment depth (Fig. 31.2b). The fractions of sulfur species for each spectrum are listed in Table 31.2. The XANES spectra for the upper-layer sediments (0–4 cmbsf) show a prominent peak of sulfate species with post-edge structure of barite and with minor contribution of sphalerite. The abundances of barite and sphalerite are, however, almost equivalent because the peak intensity of barite is generally higher than that of sphalerite (Fig. 31.2a). In the intermediate layer sediments (4–9 cmbsf), sphalerite is the dominant sulfur species, but minor contributions of native sulfur and sulfate species were also found in the XANES spectra. Although identification of this sulfate species was difficult because of the absence of post-edge structure in the spectra, the spectrum of barite was used as a reference to determine the fraction of the sulfate species. Inconsistency between the observed and fitting curve around 2,470 eV for the 4–6 cmbsf sediment cannot be explained by the reference spectra of native sulfur and pyrite, and may have been caused by the thickness effect or self-absorption effect in the FY mode measurement. The sulfur species below 9 cmbsf were completely identified as native sulfur. The transition of the sulfur species with increasing depth is roughly consistent with the XRD data.

The sulfur XANES spectra for Core 1188MB show a peak originating from the native sulfur for all the depths studied here (Fig. 31.2c). Only the top layer of the sediment (0–2 cmbsf) contains a considerable amount of sulfate

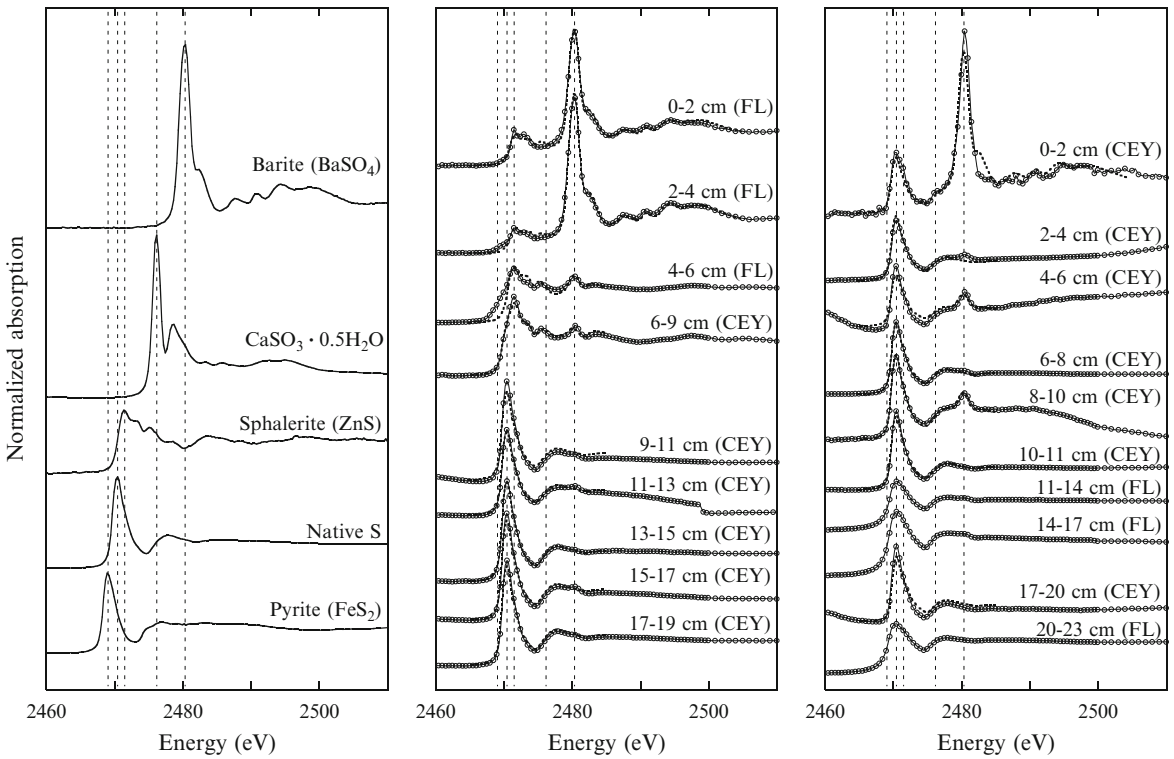

Fig. 31.2 Normalized sulfur K-edge XANES spectra for (**a**) sulfur reference materials, (**b**) Core 1186MBL, and (**c**) Core 1188MB. *Dotted curves* show the spectra simulated by the least-square fitting

Table 31.2 Linear combination fitting (LCF) results obtained by sulfur XANES for Core 1186MBL and Core 1188MB

Depth (cmbsf)	Native sulfur	Spharelite	Barite	Data collection mode
Core 1186MBL				
0–2	–	50	50	FY
2–4	–	40	60	FY
4–6	–	90	10[a]	FY
6–9	25	70	5[a]	CEY
9–11	100	–	–	CEY
11–13	100	–	–	CEY
13–15	100	–	–	CEY
15–17	100	–	–	CEY
17–19	100	–	–	CEY
Core 1188MB				
0–2	44	–	56	CEY
2–4	100	–	–	CEY
4–6	87	–	13[a]	CEY
6–8	100	–	–	CEY
8–10	89	–	11[a]	CEY
10–11	100	–	–	CEY
11–14				FY
14–17				FY
17–20	100	–	–	CEY
20–23				FY

[a]Barite spectrum was used as a reference of sulfate species without post-edge structure in XANES spectra

species, which was identified as barite based on the post-edge structure. The XANES spectra for the sediments from 11–14, 14–17, and 20–23 cmbsf could not be fitted with native sulfur or pyrite reference spectra. These spectra, which are distorted compared with other CEY-XANES spectra, are caused by the thickness or self-absorption effect in the FY mode. Judging from the peak energy of the spectra, native sulfur is likely to be dominant in these sediments.

31.3.2.2 Iron K-Edge XAFS

Iron K-edge XANES and EXAFS analyses are effective in iron speciation (O'Day et al. 2004). Three samples representing the top, intermediate, and bottom layers were selected from the sediment cores for the iron XANES and EXAFS measurement (Figs. 31.3 and 31.4). The fractions of each iron species obtained by LCF analysis by combinations of end-member spectra in the XANES and EXAFS analyses were similar (Table 31.3), suggesting that these fitting results are relatively reliable, since the XANES and EXAFS spectra have different physical-chemical origin and provide qualitatively different information. In Core 1186MBL, about half of the iron was estimated to be in the clay minerals (illite and chlorite); the remaining fraction of the iron is ferrihydrite in the top layer (0–2 cmbsf), and pyrite in the intermediate (6–9 cmbsf) and bottom

(17–19 cmbsf) layers. Since the XRD analysis did not confirm the presence of chlorite in Core 1186MBL, chlorite seems to be a minor component in the sediment. The chlorite identified by iron XAFS analysis is likely to correspond to Fe-Mg-chlorite of detrital origin (Marumo and Hattori 1999). Core 1188MB also contains ferrihydrite only in the top layer (0–2 cmbsf). Pyrite and chlorite were found at all the depths. The smaller fraction of pyrite in the top layer relative to the deeper layer agrees with the result from the XRD analysis. Considering the absence of pyrite in the sulfur XANES spectra, the amount of pyrite in the two sediments is significantly lower than that of the native sulfur at any depths studied here.

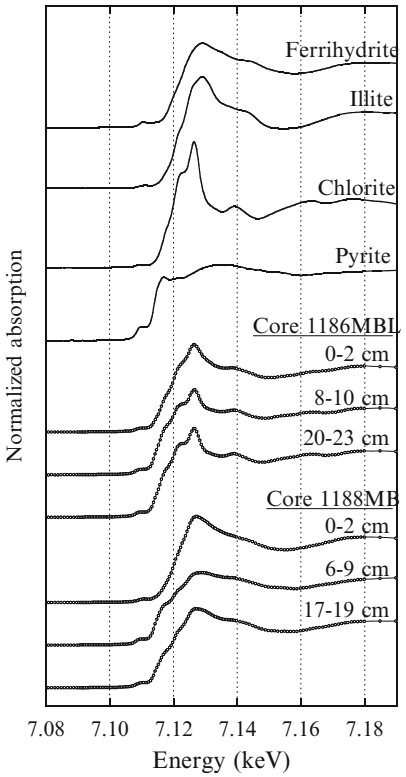

Fig. 31.3 Normalized iron K-edge XANES spectra for iron reference materials, Core 1186MBL, and Core 1188MB

31.3.2.3 Selenium K-Edge XANES

Selenium XANES spectra were measured for sediment samples representing the top, intermediate, and bottom layers in the sediment cores. The selenium K-edge position is generally sensitive to the valence of the selenium (e.g., Pickering et al. 1995); however, previous studies have indicated that

Table 31.3 Linear combination fitting results obtained by iron EXAFS for Core 1186MBL and Core 1188MB

Depth (cmbsf)	Pyrite	Illite	Chlorite	Ferrihydrite	*R* factor (%)
Core 1186MBL					
0–2	–	0.29 (0.10)	0.15 (0.19)	0.56 (0.72)	6.1
6–9	0.56 (0.65)	0.33 (0.24)	0.11 (0.12)	–	6.9
17–19	0.40 (0.50)	0.46 (0.34)	0.14 (0.16)	–	5.5
Core 1188MB					
0–2	0.18 (0.29)	–	0.42 (0.39)	0.40 (0.32)	7.2
8–10	0.50 (0.55)	–	0.50 (0.45)	–	7.7
20–23	0.44 (0.49)	–	0.56 (0.51)	–	8.0

Fraction of iron species determined by iron XANES analysis are shown in brackets. The *R* values (the residual of the LCF in the iron XANES analysis) were <1 %

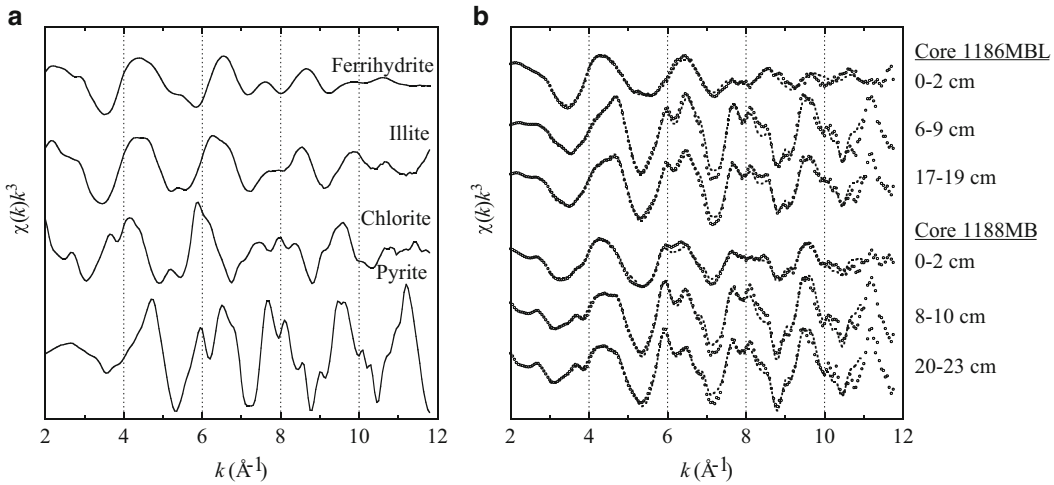

Fig. 31.4 Normalized k^3-weighted background-subtracted EXAFS data for (**a**) iron reference materials and (**b**) Core 1186MBL and Core 1188MB. *Dotted curves* show the spectra simulated by the least-square fitting

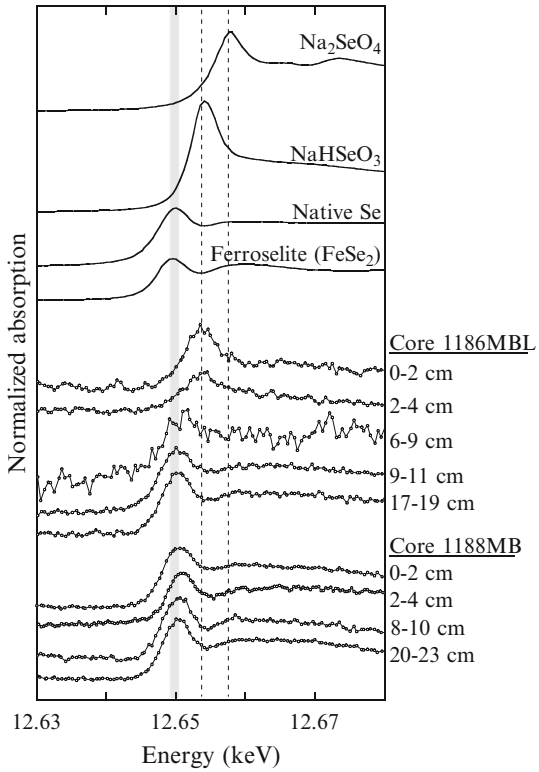

Fig. 31.5 Normalized selenium K-edge XANES spectra for selenium reference materials, Core 1186MBL, and Core 1188MB

selenium K-edge XANES spectroscopy cannot easily distinguish between native selenium (Se^0) and selenide species (Se^{-I} and Se^{-II}) because of their close peak positions within 2 eV (van Hullenbusch et al. 2007; Scheinost and Charlet 2008). In our analysis, the spectra of the native selenium and ferroselite ($FeSe_2$) also showed similar peak positions and structures (Fig. 31.5), indicating that native selenium and ferroselite cannot be distinguished clearly by selenium XANES spectra in this study. Most of the selenium XANES spectra of the sediment samples exhibited structures similar to those of native selenium and ferroselite (Fig. 31.5). The fact that the spectra showing native selenium and ferroselite were obtained for the samples below 6 cmbsf in Core 1186MBL and for the samples in Core 1188MB is in good agreement with the distributions of native sulfur and pyrite determined by XRD, sulfur XANES, and iron XAFS analyses. Selenite (Se^{IV}) was identified only in the upper layer (0–4 cmbsf) of Core 1186MBL.

31.3.3 Pore Water Chemistry

The results of pore water analyses for Core 1186MBL and Core 1188MB are summarized in Table 31.4 with the chemical composition of the Biwako hydrothermal fluid (Biwako fluid) reported by Ishibashi et al. (2014). The H_2S concentrations in most of the pore water samples were below the detection limit (0.6 μmol/L).

Table 31.4 Chemical composition in pore water for Core 1186MBL and Core 1188MB with that of Biwako hydrothermal fluid estimated by Ishibashi et al. (2014)

Depth (cmbsf)	pH	Mg (mmol/L)	Cl (mmol/L)	SO_4^{2-} (mmol/L)	Alkalinity (mmol/L)	NH_4^+ (mmol/L)	H_2S (mmol/L)
Core 1186MBL							
0[a]	7.6	53.8	569	29.9	2.42	0.007	<DL
0–2	7.6	56.0	567	27.3	2.63	0.031	<DL
2–4	7.6	59.8	588	30.5	2.21	0.027	<DL
4–6	7.2	58.3	578	29.6	0.84	0.039	<DL
6–9	5.1	57.8	569	28.5	0.07	0.034	<DL
9–11	4.4	56.2	567	28.6	–	0.028	<DL
11–13	4.3	54.2	575	28.7	–	0.040	<DL
13–15	4.3	55.6	731	36.1	–	0.035	<DL
15–17	4.8	55.7	613	29.1	0.06	0.036	<DL
17–19	4.4	64.8	572	28.8	–	0.025	<DL
Core 1188MB							
0[a]	7.6	50.3	609	24.8	5.0	0.062	0.074
0–2	7.6	56.7	581	26.8	4.8	–	<DL
2–4	7.5	53.0	575	25.9	3.9	0.054	<DL
4–6	7.6	52.4	586	24.7	5.4	–	<DL
6–8	7.5	53.3	601	25.4	6.6	–	<DL
8–10	7.6	54.0	561	21.6	8.3	–	<DL
10–17	7.4	47.4	534	11.5	17.3	0.43	<DL
17–23	8.0	39.5	470	1.8	25.6	–	<DL
Biwako hydrothermal fluid							
	4.8	0	167	0	–	5	23

[a]Bottom seawater

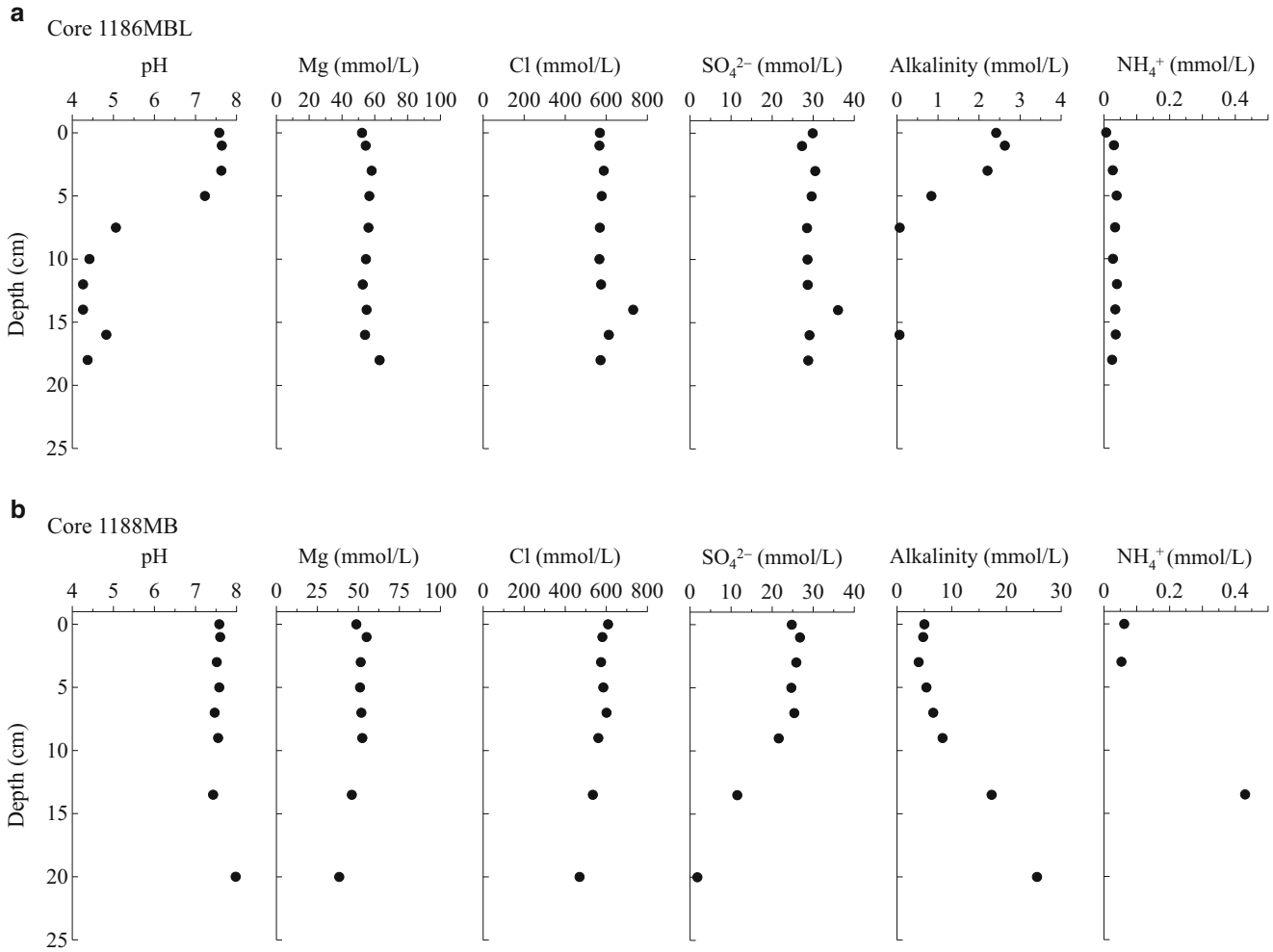

Fig. 31.6 Vertical profiles of pH, alkalinity, and concentrations of NH_4^+, sulfate, chloride, and magnesium in the pore water for (**a**) Core 1186MBL and (**b**) Core 1188MB

The pore water chemistry of Core 1186MBL is characterized by decreasing pH and alkalinity with increasing depth, and lower pH and alkalinity levels than those of the ambient seawater (pH 7.6 and 2.4 mmol/L of alkalinity) (Fig. 31.6a). The alkalinity could not be determined for pore water with a pH below 4.8. The NH_4^+ concentration in the pore water did not rise above 50 μmol/L at any depth. Noteworthy, the pore water in the deeper layer (9–19 cmbsf) shows a pH of 4.2–4.9, suggesting that this unique pore water chemistry is unlikely to be explained only by a simple mixing between high-temperature hydrothermal fluid and ambient seawater, because the pH of the high-temperature hydrothermal fluid obtained from the TBS vent (Jade fluid) does not go below 4.7 (Sakai et al. 1990b; Ishibashi et al. 2014). The concentrations of sulfate, chloride, and magnesium in the deeper layer pore water are comparable to the ambient seawater levels, which also indicates a low contribution of hydrothermal fluid since depletions of sulfate and magnesium are common in the hydrothermal fluid (Ishibashi et al. 2014).

The pore water of Core 1188MB shows a profile characterized by significantly increased alkalinity and NH_4^+ concentration and decreased sulfate, chloride, and magnesium concentrations with increasing depth (Fig. 31.6b). The alkalinity (up to 25.6 mmol/L) is the highest among previously reported values for hydrothermal fluids and sediment pore water around vents in the Okinawa Trough hydrothermal systems (Gamo et al. 1991; Kawagucci et al. 2011). The pH values are maintained at the ambient seawater value throughout Core 1188MB.

31.4 Discussion

31.4.1 Core 1186MBL Collected Around the Black Smoker Vent

Core 1186MBL contains abundant native sulfur below 6 cmbsf without any evidence of contribution of hydrothermal fluid in the pore water. The depth of the occurrence of

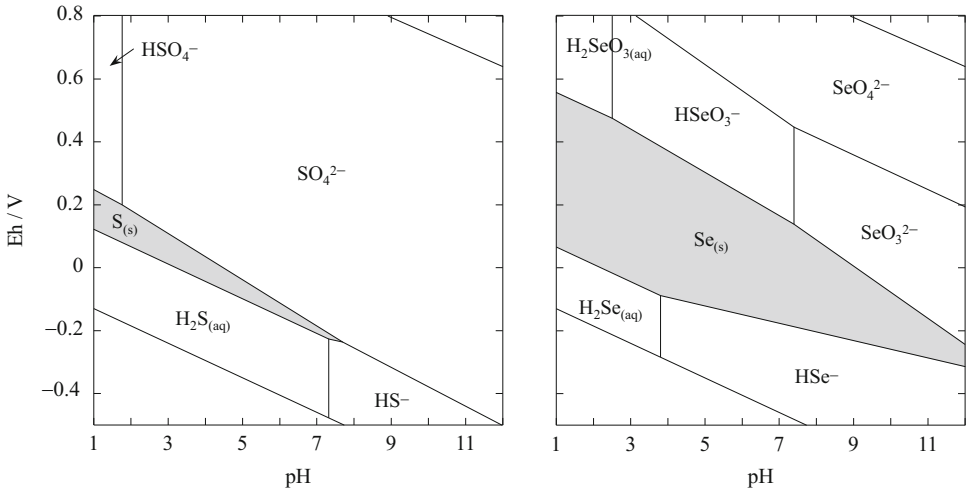

Fig. 31.7 Eh-pH diagrams for sulfur and selenium species at 5 °C and 150 bar total pressure. The 30 mmol/L of total sulfur and 1 nmol/L of total selenium concentrations correspond to seawater level and simulate the pore water condition in Core 1186MBL (i.e., recharging seawater). Diagrams were constructed by ACT2 module of the Geochemist's Workbench software with the "thermo.com.v8.r6+" database (Bethke 2011)

native sulfur is concomitant with significantly acidic pore water. This is reasonable considering that the acidic condition is one of the restrictions for the formation of native sulfur (Fig. 31.7). One possible interpretation of the acidic condition is that the pore water contains acidic volatiles. In the Jade hydrothermal system, both magmatic volatiles and the vapor phase resulting from hydrothermal fluid boiling are known to include substantial amount of CO_2 with H_2S (Sakai et al. 1990b). The vapor involvement into the pore water results in a decrease in pH as follows:

$$CO_{2(g)} + H_2O \rightarrow HCO_3^- + H^+ \quad (31.3)$$

$$H_2S_{(g)} \rightarrow HS^- + H^+ \quad (31.4)$$

In addition, the involvement of the vapor phase produced by the boiling of hydrothermal fluid would lead to lower chloride concentrations of the pore water than that of the ambient seawater because of the chloride depletion in the vapor phase resulting from subcritical phase separation (Butterfield et al. 2003). However, the vertical chloride profile retains the ambient seawater chloride level. Therefore, input of the acid volatiles into the pore water is not likely to occur in Core 1186MBL. The mineral component also showed minor hydrothermal alteration in Core 1186MBL. The hydrothermal alteration of epiclastic sediments at the Jade site is characterized by the common occurrence of hydrothermal clay minerals, e.g., Mg-rich chlorite (Marumo and Hattori 1999). However, careful study of the XRD analysis for the clay minerals shows an absence of Mg-rich chlorite in Core 1186MBL (Miyoshi et al. Chap. 44). Alternatively, Core 1186MBL still contains detrital Fe-Mg-chlorite as shown by the iron XAFS analysis, suggesting that typical hydrothermal alteration at the Jade site is not widespread in Core 1186MBL.

Seawater level concentrations of sulfate, chlorite, and magnesium in the pore water in the deeper layer suggest the process of recharging of seawater into the subsurface sediments. Near active fluid venting site, such as TBS vent, pressure gradients associated with venting is known to induce the seawater recharge and to produce secondary fluid circulation cell below the seafloor (Stein and Fisher 2001). Incorporating oxic seawater into the subsurface sediments may retain a low concentration of NH_4^+, which is usually found under anoxic condition. The recharging seawater is acidified to pH 4.4 within the intermediate layer (4–9 cmbsf). This acidifying layer corresponds to the occurrence of sulfide lumps. Acidification associated with sulfide oxidation is well known process in drainage from sulfidic mine (Nordstrom 1982; Moses et al. 1987). The oxic recharging seawater could lead to the oxidation of the sulfide lumps, such as sphalerite and galena:

$$ZnS + 2O_2 \rightarrow Zn^{2+} + SO_4^{2-} \quad (31.5)$$

$$PbS + 2O_2 \rightarrow Pb^{2+} + SO_4^{2-} \quad (31.6)$$

However, oxidation of these minerals shows no contribution to the acidification. In sphalerite, iron can significantly substitute for zinc up to 15 mol% (Baumgartner et al 2008). If iron substitutes for zinc, the sulfide oxidation occurs in a similar way as pyrrhotite (FeS):

$$FeS + 2O_2 \rightarrow Fe^{2+} + SO_4^{2-} \quad (31.7)$$

In addition, oxidation of ferrous iron (Fe^{2+}) to ferric iron (Fe^{3+}) and precipitation of iron hydroxide under oxic condition acidify the pore water:

$$Fe^{2+} + \frac{1}{4}O_2 + \frac{5}{2}H_2O \rightarrow Fe(OH)_{3(s)} + 2H^+ \quad (31.8)$$

Thus, sphalerite containing iron could be acid generator. Oxidation of pyrite is also known to be efficient acid producer by reaction in Eq. (31.9), followed by reaction in Eq. (31.8):

$$FeS_2 + \frac{7}{2}O_2 + H_2O \rightarrow Fe^{2+} + 2SO_4^{2-} + 2H^+ \quad (31.9)$$

Although the occurrence of pyrite is found only below 6 cmbsf, pyrite could contribute the acidification as one of sulfide minerals in the sulfide lumps. The absence of pyrite in the upper layer (0–6 cmbsf) may suggest that most of pyrite in the chimney fragments is dissolved. The oxidations of sulfide minerals in the acidifying layer decrease the alkalinity of pore water from seawater level (2.4 mmol/L) to almost zero due to the productions of protons and sulfate ions.

The secondary fluid circulation transports the acidified pore water downward. Under acidic and suboxic conditions, stability of native sulfur increases because of its grater insolubility at low pH (Fig. 31.7). Thus, the native sulfur formation appearing below the acidifying layer is induced by the supply of acidic and suboxic pore water, and by simultaneous pyrite oxidation:

$$FeS_2 + \frac{1}{2}O_2 + 2H^+ \rightarrow 2S_{(s)} + Fe^{2+} + H_2O \quad (31.10)$$

Ferric iron is produced by oxidation of ferrous iron readily under acidic condition, and thus the ferric iron may become additional oxidant of pyrite, as follows:

$$Fe^{2+} + \frac{1}{4}O_2 + H^+ \rightarrow Fe^{3+} + \frac{1}{2}H_2O \quad (31.11)$$

$$FeS_2 + 2Fe^{3+} \rightarrow 2S_{(s)} + 3Fe^{2+} \quad (31.12)$$

Precipitation of native sulfur has the potential to form an inert layer on the pyrite surface, which inhibits the diffusion of oxidants to the surface and further dissolution of pyrite (Nordstrom 1982). The remaining pyrite in the native sulfur layer might be protect from acidic pore water by the native sulfur. The formation of native sulfur may extend below 19 cmbsf as long as oxygen remains because of the downward flow of the acidic pore water. Hence, the native sulfur is considered to be formed by the supply of acidic and suboxic pore water, resulting from the oxidation of sulfide minerals by the recharging seawater, below 9 cmbsf in Core 1186MBL (native sulfur formation zone).

The redox transition from oxic to suboxic conditions also affects the chemical species of redox-sensitive elements in the sediment. The upper layer (0–4 cmbsf) is characterized by the occurrences of iron oxyhydroxide (ferrihydrite), sulfate mineral (barite), and selenite, which are stable under the (relatively) oxic condition. These species are not found below 6 cmbsf with the redox transition to suboxic condition. According to Eh-pH diagrams of sulfur and selenium, stable conditions of native sulfur fall within those of the native selenium under acidic condition (Fig. 31.7). The presence of native sulfur in the sediment supports that of native selenium, although distinguishing between native selenium and ferroselite was difficult by selenium K-edge XANES.

Kaolinite found in Core 1186MBL is generally formed under acidic condition. Marumo and Hattori (1999) indicated that the simple mixing of seawater and hydrothermal fluids in the Jade site is not sufficient to produce the acidic condition required for the formation of kaolinite. On the other hand, our analysis suggests that the sulfide oxidation process could produce pore water that is more acidic than the hydrothermal fluid, and thus may lead to the formation of kaolinite in Core 1186MBL.

31.4.2 Core 1188MB Collected near the Biwako Vent

The decreased magnesium, chloride, and sulfate concentrations with increasing depth imply a contribution of hydrothermal fluid below 10 cmbsf (Fig. 31.6b). The decreasing chloride concentrations within the deeper layer (8–23 cmbsf) are correlated with the decrease in the magnesium concentration along the mixing line between the seawater (Mg: 55 mmol/L; Cl: 560 mmol/L) and the Biwako fluid (Mg: 0 mmol/L; Cl: 167 mmol/L) endmembers (Fig. 31.8a). It suggests input of Biwako fluid into the pore water below 10 cmbsf. The Biwako fluid originates mainly from the vapor phase produced by the phase separation of the original hydrothermal fluid (Jade fluid) (Ishibashi et al. 2014). Since Core 1188MB was located adjacent to the Biwako vent, it is reasonable to expect the input of Biwako fluid in the sample. Based on a decreasing rate of magnesium concentration between the seawater and the pore water at 10–17 cmbsf (47.4/55 = 0.86), the NH_4^+ concentration in the pore water at 10–17 cmbsf could be predicted as 0.75 mmol/L (=5 × (1 − 0.86) + 0.058), where the NH_4^+ concentration in the Biwako fluid is 5 mmol/L and the average NH_4^+ concentration in the pore water above 10 cmbsf is 0.058 mmol/L (Table 31.4). This predicted value

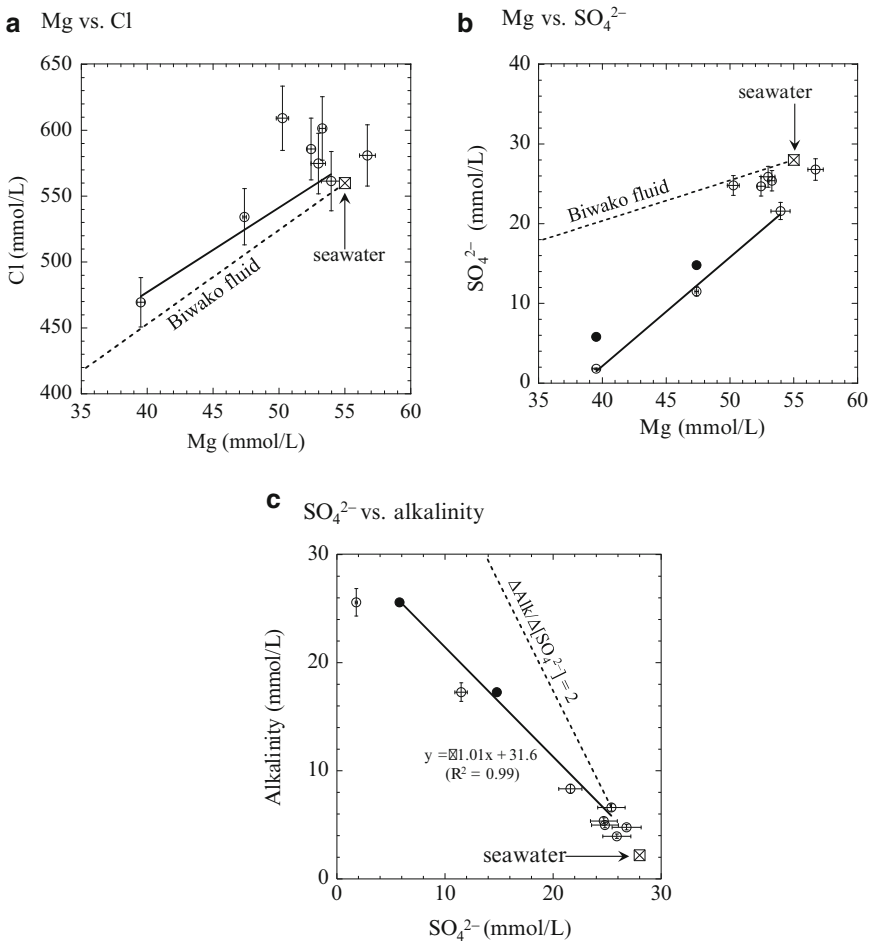

Fig. 31.8 (**a**) Magnesium versus chloride concentrations and (**b**) magnesium versus sulfate concentrations in the pore water of Core 1188MB. The *dotted line* extending from the seawater value represents the mixing line between seawater and the Biwako hydrothermal fluid. *Solid lines* are the linear regression lines for three datasets (8–23 cmbsf) showing the input of the Biwako fluid into the pore water. (**c**) Relationship between sulfate concentration and alkalinity in the pore water of Core 1188MB. The *dotted line* (extending from the data of 6–8 cmbsf) represents the increase in alkalinity with decreasing sulfate in $\Delta Alk/\Delta[SO_4^{2-}] = 2$, which is based on ideal SR and AOM processes. The *filled circles* in (**b**) and (**c**) are the estimated values for sulfate concentration in pore water below 10 cmbsf excluding the contribution of the Biwako fluid. The *solid line* in (**c**) represents the linear regression line for the two measured data (6–10 cmbsf) and the two predicted data without the contribution of the Biwako fluid (10–23 cmbsf)

is somewhat larger but of the same order as the NH_4^+ concentration observed at 10–17 cmbsf (0.43 mmol/L), suggesting that the increase in NH_4^+ concentration in the deeper layer is attributed to the input of Biwako fluid into the pore water. The input of Biwako fluid can cause a decrease in the sulfate concentration in the pore water because of the absence of sulfate in the Biwako fluid. However, three pore water samples within the deeper layer (8–23 cmbsf) significantly deviate from the mixing line between the seawater and the Biwako hydrothermal fluid endmembers (Fig. 31.8b). This suggests that another sulfate removal process occurs below 8 cmbsf in Core 1188MB.

Since alkalinity in the Biwako hydrothermal fluid has not been reported previously, it is difficult to estimate the effect of the input of the Biwako fluid on the alkalinity of the pore water. As mentioned before, however, the alkalinity in the pore water of Core 1188MB (up to 25.6 mmol/L) far exceeds the alkalinity in the surrounding hydrothermal fluid (e.g., 1.5 mmol/L in the Jade fluid (Sakai et al. 1990b)). The significant increase in alkalinity with increasing depth may be related to another sulfate removal process described above. Along with the depth, the alkalinity profile is inversely correlated with the sulfate concentration profile (Fig. 31.8c). Note that the apparent decrease in sulfate concentration is partially caused by the mixing with Biwako fluid below 10 cmbsf. This mixing effect could be estimated based on the decreasing rate of magnesium concentration within 8–23 cmbsf, and is excluded from the data to discuss another sulfate removal process (plotted as filled circles in Fig. 31.8b, c). After this elimination of the mixing

component, the ratio of increased alkalinity (Alk) and decreased sulfate concentrations ($=\Delta Alk/\Delta[SO_4^{2-}]$) is estimated as 1.01 in atomic ratio (Fig. 31.8c).

The simultaneous decrease of sulfate concentration and increase of alkalinity toward the deeper parts at the sedimentary seafloor have often been interpreted as the effect of sulfate reduction (SR) and anaerobic oxidation of methane (AOM) (e.g., Gamo et al. 1991; Chatterjee et al. 2011). The Biwako fluid is characterized by high contents of volatile species originating from the Jade fluid. Since the Jade fluid is enriched in methane (7.6 mmol/L) (Ishibashi et al. 1995), the methane is expected to be supplied along with the Biwako fluid to Core 1188MB. Stoichiometry of SR for sedimentary organic matter is frequently described as follows, using the Redfield ratio (C:N:P = 106:16:1 by atoms), which represents the ideal composition of phytoplankton (Redfield 1958):

$$(CH_2O)_{106}(NH_3)_{16}(H_3PO_4) + 53SO_4^{2-} \rightarrow 106HCO_3^- + 16NH_4^+ + 53HS^- + H_3PO_4 + 37H^+ \quad (31.13)$$

The ratio of the produced alkalinity and consumed sulfate concentrations ($=\Delta Alk/\Delta[SO_4^{2-}]$) during SR is estimated as 2 (=(106 + 53–16–37)/53). However, the increased NH_4^+ concentration at 10–17 cmbsf could be explained only by the input of the Biwako fluid into the pore water as described above. Therefore, SR is not considered to be associated with another sulfate removal process observed below 8 cmbsf in Core 1188MB. The other sulfate-consuming reaction, AOM, can be expressed as

$$CH_4 + SO_4^{2-} \rightarrow HCO_3^- + HS^- + H_2O \quad (31.14)$$

which can increase the alkalinity without changing the NH_4^+ concentration in the pore water. The increase in alkalinity corresponds to releases of bicarbonate and hydrogen sulfide (HS^-), resulting in a $\Delta Alk/\Delta[SO_4^{2-}]$ ratio of 2 in the AOM. Assuming that AOM occurs, the increase in alkalinity below 8 cmbsf in Core 1188MB ($\Delta Alk/\Delta[SO_4^{2-}] = 1.01$) is stoichiometrically insufficient (Fig. 31.8c). This inconsistency of the $\Delta Alk/\Delta[SO_4^{2-}]$ ratio can be explained by considering the presence of native sulfur in Core 1188MB, as described below.

The sulfate consumption by AOM releases dissolved hydrogen sulfide to the pore water in Core 1188MB. Simultaneously, the input of the Biwako fluid raises the concentration of hydrogen sulfide in the pore water because of its high concentration in the Biwako fluid (23 mmol/L). Under the pH condition in Core 1188MB (pH >7.4), hydrogen sulfide could be dissolved as HS^- (Fig. 31.7). The concentration of HS^-, however, was considerably low throughout Core 1188MB. Furthermore, the pH of the pore water remains at seawater-level pH value over the whole sediment core despite the mixing with the acidic Biwako fluid (pH 4.8). These apparent inconsistencies in terms of HS^- and pH in the pore water can be explained by the precipitation of native sulfur, which was found throughout Core 1188MB. When the acidic and anoxic Biwako fluid encounters the relatively oxic sediment pore water, the HS^- in the Biwako fluid and sulfate in the pore water are converted into intermediate valence sulfur, i.e., native sulfur, as follow:

$$3HS^- + SO_4^{2-} + 5H^+ \rightarrow 4S_{(s)} + 4H_2O \quad (31.15)$$

The reaction in Eq. (31.15) could inhibit the acidification of the pore water by the consumption of protons supplied from the acidic Biwako fluid. In addition, HS^- originating from the Biwako fluid and AOM can be consumed by reaction in Eq. (31.15), resulting in depletion of HS^- in the pore water.

A previous sulfur isotope study has suggested that the sulfur crust near the Biwako vent was formed by disequilibrium precipitation of native sulfur during exhalation of hydrothermal fluid into cold seawater on the seafloor (Marumo and Hattori 1999). In the case of Core 1188MB, this encounter of hydrothermal fluid and seawater occurs within the subsurface sediment deeper than 10 cmbsf at present, and the resulting native sulfur formation could occur extensively below Core 1188MB. However, native sulfur was found immediately below the seafloor in Core 1188MB. This wide distribution of native sulfur, as well as the commonly-found hydrothermal clay minerals (illite, smectite, and chlorite), may reflect the past fluid input into the sediment. The presence of iron oxyhydroxide (ferrihydrite) and sulfate (barite), which were identified by XAFS analysis for Core 1188MB, indicate that the oxic condition is maintained only in the shallowest sediment near the seafloor.

When the HS^- is removed from the pore water by the precipitation of native sulfur, only the release of bicarbonate during reaction in Eq. (31.14) contributes to the increase in alkalinity in AOM. The net $\Delta Alk/\Delta[SO_4^{2-}]$ ratio is expected to be 1 (Eq. 31.14), which agrees with the $\Delta Alk/\Delta[SO_4^{2-}]$ ratio below 8 cmbsf in Core 1188MB (=1.01). Hence, the formation of native sulfur in Core 1188MB can be associated with AOM below 8 cmbsf and the input of the Biwako fluid into the sediment below 10 cmbsf.

31.5 Summary

The sediment samples collected by coring from two active hydrothermal vents are characterized by the common occurrence of native sulfur; however, the two sediments show

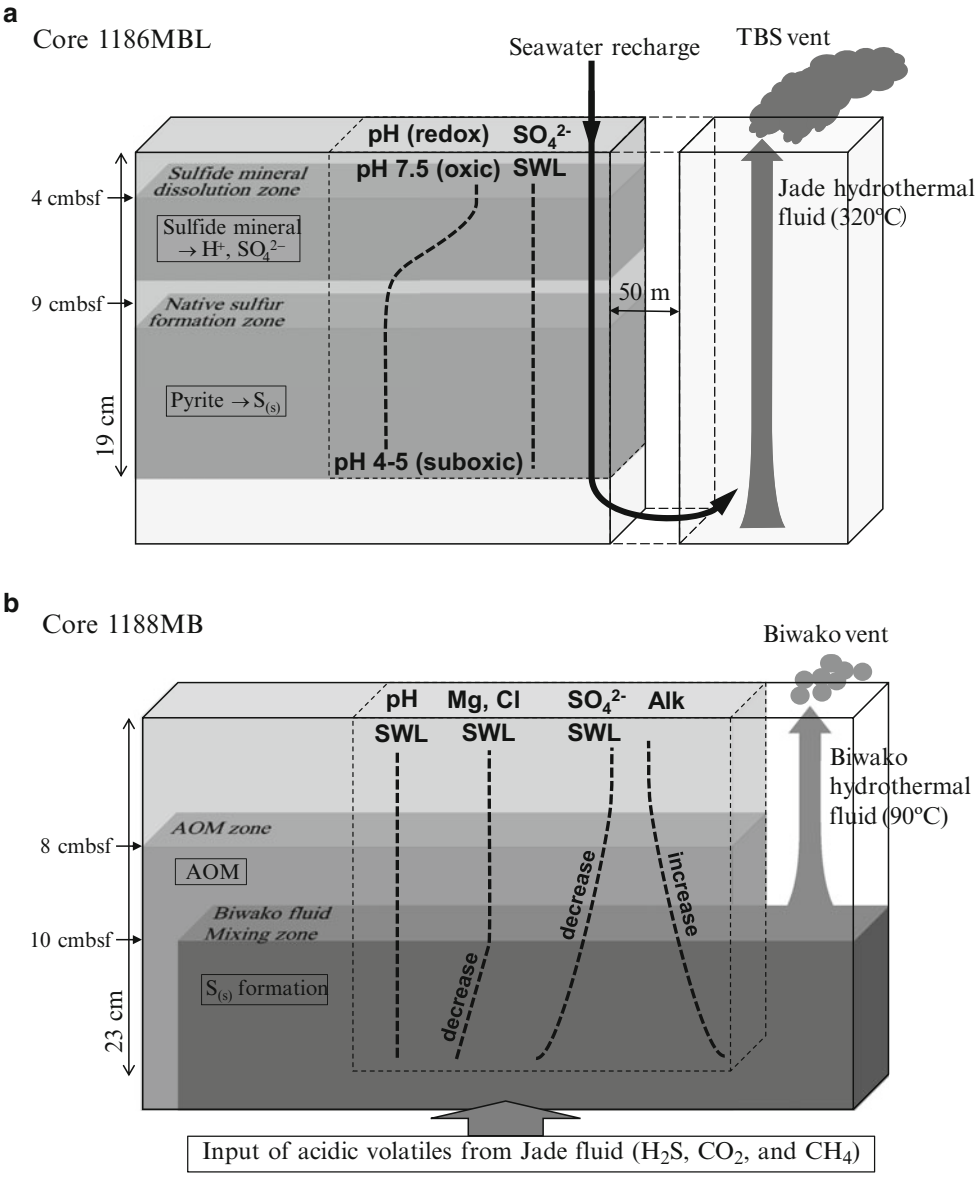

Fig. 31.9 Schematic models of subsurface sediment–pore water system involving native sulfur formation in the Jade hydrothermal field. (**a**) The seawater recharge system observed in Core 1186MBL. (**b**) The hydrothermal fluid–seawater mixing system observed in Core 1188MB. *SWL* sea water level

quite different pore water chemistry (Fig. 31.9). The sediment collected near the TBS vent (Core 1186MBL) is characterized by chimney fragments in the shallower part (2–9 cmbsf) and native sulfur in the deeper part (6–19 cmbsf). The chemical composition of the pore water implies that seawater penetrates into the sediment downward to form secondary fluid circulation cell. This seawater could oxidize and dissolve sulfide minerals in the chimney fragments at the shallower part, resulting in the transport of acidic and suboxic pore water toward the deeper part. The precipitation of native sulfur in the deeper part is considered to be derived from the acidic and suboxic pore water. The other sediment collected near the Biwako vent (Core 1188MB) shows the involvement of the Biwako fluid in the pore water below 10 cmbsf, and the AOM below 8 cmbsf. The active AOM could be explained by the input of the volatile-rich vapor phase produced by subcritical phase separation, which raises pore water alkalinity significantly with increasing depth. The uniform pH condition and depletion of hydrogen sulfide in the pore water throughout Core 1188MB despite the input of hydrothermal fluid and AOM may be attributed to the precipitation of native sulfur. The wide distribution of native sulfur throughout the sediment core may reflect past fluid input into the sediment. The roles of native sulfur formation in the sediment–pore water systems are obviously different between the two sediment cores. The native sulfur formation in Core 1186MBL is the result of the acidic condition created by the sulfide dissolution, while the precipitation of the native sulfur maintains the circumneutral pH condition in Core 1188MB. The occurrence of native sulfur also implies

the seawater recharge in Core 1186MBL, and the input of hydrothermal fluid to the sediment and AOM in Core 1188MB. These are common events in sub-seafloor hydrothermal systems, and native sulfur might be an indicator of these important geochemical events in the sediment–pore water system of arc–back-arc hydrothermal fields.

Acknowledgments This study was supported by a Grant-in-Aid for Scientific Research on Innovative Areas from the Ministry of Education, Culture, Sports, Science and Technology (MEXT) of Japan including the "TAIGA" project accepted as a Scientific Research on Innovative Areas (Grant Number: 20109004), and by the JSPS Research Fellowships for Young Scientists. This work has been performed with the approval of KEK (Proposal No. 2012G111 and 2013G052) and SPring-8/JASRI (2011B1673, 2012B1564, and 2013B1116).

References

Baumgartner R, Fontboté L, Vennemann T (2008) Mineral zoning and geochemistry of epithermal polymetallic Zn-Pb-Ag-Cu-Bi mineralization at Cerro de Pasco, Peru. Econ Geol 103:493–537. doi:10.2113/gsecongeo.103.3.493

Bethke C (2011) The Geochemist's workbench software package (version 9.0). University of Illinois, Urbana-Champaign

Brookins DG (1987) Eh-pH diagrams for geochemistry. Springer, Berlin

Butterfield DA, Seyfried WE, Lilley MD (2003) Composition and evolution of hydrothermal fluids. In: Halbach PE et al (eds) Energy and mass transfer in marine hydrothermal systems. Dahlem University Press, Germany, pp 124–161

Chatterjee S, Dickens GR, Bhatnagar G, Chapman WG, Dugan B, Snyder GT, Hirasaki GJ (2011) Pore water sulfate, alkalinity, and carbon isotope profiles in shallow sediment above marine gas hydrate systems: a numerical modeling perspective. J Geophys Res 116, B09103. doi:10.1029/2011JB008290

Cline JD (1969) Spectrophotometric determination of hydrogen sulfide in natural waters. Limnol Oceanogr 14:454–458

de Ronde CEJ, Massoth GJ, Butterfield DA, Christenson BW, Ishibashi J, Ditchburn RG, Hannington MD, Brathwaite RL, Lupton JE, Kamenetsky VS, Graham IJ, Zellmer GF, Dziak RP, Embley RW, Dekov VM, Munnik F, Lahr J, Evans LJ, Takai K (2011) Submarine hydrothermal activity and gold-rich mineralization at Brothers Volcano, Kermadec Arc, New Zealand. Miner Deposita 46:541–584. doi:10.1007/s00126-011-0345-8

Embley RW, Baker ET, Butterfield DA, Chadwick WW Jr, Lupton JE, Resing JA, de Ronde CEJ, Nakamura K, Tunnicliffe V, Dower JF, Merle SG (2007) Exploring the submarine ring of fire: Mariana Arc – Western Pacific. Oceanography 20(4):68–79. doi:10.5670/oceanog.2007.07

Gamo T, Sakai H, Kim ES, Shitashima K, Ishibashi J (1991) High alkalinity due to sulfate reduction in the CLAM hydrothermal field, Okinawa Trough. Earth Planet Sci Lett 107(2):328–338. doi:10.1016/0012-821X(91)90080-2

Gamo T, Ishibashi J, Tsunogai U, Okamura K, Chiba H (2006) Unique geochemistry of submarine hydrothermal fluids from arc-back-arc settings of the western Pacific. In: Christie DM et al (eds) Back-arc spreading systems: geological, biological, chemical and physical interactions, vol 166, Geophysical monograph. AGU, Washington, DC, pp 147–161. doi:10.1029/166GM08

Halbach P, Nakamura K-I, Wahsner M, Lange J, Sakai H, Käselitz L, Hansen R-D, Yamano M, Post J, Prause B, Seifert R, Michaelis W, Teichmann F, Kinoshita M, Märten A, Ishibashi J, Czerwinski S, Blum N (1989) Probable modern analogue of Kuroko-type massive sulphide deposits in the Okinawa Trough back-arc basin. Nature 338(6215):496–499. doi:10.1038/338496a0

Ishibashi J, Sano Y, Wakita H, Gamo T, Tsutsumi M, Sakai H (1995) Helium and carbon geochemistry of hydrothermal fluids from the mid-Okinawa Trough back-arc basin, Southwest of Japan. Chem Geol 123(1–4):1–15. doi:10.1016/0009-2541(95)00051-M

Ishibashi J, Noguchi T, Toki T, Miyabe S, Yamagami S, Onishi Y, Yamanaka T, Yokoyama Y, Omori E, Takahashi Y, Hatada K, Nakaguchi Y, Yoshizaki M, Konno U, Shibuya T, Takai K, Inagaki F, Kawagucci S (2014) Diversity of fluid geochemistry affected by processes during fluid upwelling in active hydrothermal fields in the Izena Hole, the middle Okinawa Trough back-arc basin. Geochem J 48(3):357–369. doi:10.2343/geochemj.2.0311

Kawagucci S, Chiba H, Shibash J, Yamanaka T, Toki T, Muramatsu Y, Ueno Y, Makabe A, Inoue K, Yoshida N, Nakagawa S, Nunoura T, Takai K, Takahata N, Sano Y, Narita T, Teranishi G, Obata H, Gamo T (2011) Hydrothermal fluid geochemistry at the Iheya North field in the mid-Okinawa Trough: implication for origin of methane in subseafloor fluid circulation systems. Geochem J 45(2):109–124

Kinoshita M, Yamano M (1997) Hydrothermal regime and constraints on reservoir depth of the Jade site in the Mid-Okinawa Trough inferred from heat flow measurements. J Geophys Res 102 (B2):3183–3194. doi:10.1029/96JB03556

Manceau A, Marcus MA, Tamura N (2002) Quantitative speciation of heavy metals in soils and sediments by synchrotron X-ray techniques. In: Fenter PA, Rivers ML, Sturchio NC, Sutton SR (eds) Applications of synchrotron radiation in low-temperature geochemistry and environmental science, vol 49. Reviews in Mineralogy and Geochemistry, Mineralogical Society of America. pp 341–428, doi:10.2138/gsrmg.49.1.341

Marumo K, Hattori KH (1999) Seafloor hydrothermal clay alteration at JADE in the back-arc Okinawa Trough: mineralogy, geochemistry and isotope characteristics. Geochim Cosmochim Acta 63 (18):2785–2804. doi:10.1016/S0016-7037(99)00158-1

Moses CO, Nordstrom DK, Herman JS, Mills AL (1987) Aqueous pyrite oxidation by dissolved oxygen and by ferric iron. Geochim Cosmochim Acta 51(6):1561–1571. doi:10.1016/0016-7037(87)90337-1

Nakagawa T, Takai K, Suzuki Y, Hirayama H, Konno U, Tsunogai U, Horikoshi K (2006) Geomicrobiological exploration and characterization of a novel deep-sea hydrothermal system at the TOTO caldera in the Mariana Volcanic Arc. Environ Microbiol 8 (1):37–49. doi:10.1111/j.1462-2920.2005.00884.x

Nordstrom DK (1982) Aqueous pyrite oxidation and the consequent formation of secondary iron minerals. In: Kittrick JA, Fanning DS, Hossner LR (eds) Acid sulfate weathering. Soil Science Society of America Special Publication 10, Madison, pp 37–46

O'Day PA, Rivera N, Root R, Carroll SA (2004) X-ray absorption spectroscopic study of Fe reference compounds for the analysis of natural sediments. Am Mineral 89(4):572–585

Pickering IJ, Brown GE, Tokunaga TK (1995) Quantitative speciation of selenium in soils using X-ray absorption spectroscopy. Environ Sci Technol 29(9):2456–2459. doi:10.1021/es00009a043

Pingitore NE, Meitzner G, Love KM (1995) Identification of sulfate in natural carbonates by X-ray absorption spectroscopy. Geochim Cosmochim Acta 59(12):2477–2483. doi:10.1016/0016-7037(95)00142-5

Ravel B, Newville M (2005) ATHENA, ARTEMIS, HEPHAESTUS: data analysis for X-ray absorption spectroscopy using IFEFFIT. J Synchrotoron Rad 12(4):537–541. doi:10.1107/s0909049505012719

Redfield AC (1958) The biological control of chemical factors in the environment. Am Sci 46(3):205–221

Sakai H, Gamo T, Ishibashi J, Shitashima K, Kim E-S, Yanagisawa F, Tsutsumi M, Sano Y, Wakita H, Tanaka T, Matsumoto T, Naganuma T, Mitsuzawa K (1990a) Unique chemistry of the hydrothermal solution in the mid-Okinawa Trough Backarc Basin. Geophys Res Lett 17(12):2133–2136. doi:10.1029/GL017i012p02133

Sakai H, Gamo T, Kim E-S, Tsutsumi M, Tanaka T, Ishibashi J, Wakita H, Yamano M, Oomori T (1990b) Venting of carbon dioxide-rich fluid and hydrate formation in mid-Okinawa Trough Backarc Basin. Science 248(4959):1093–1096. doi:10.1126/science.248.4959.1093

Scheinost AC, Charlet L (2008) Selenite reduction by mackinawite, magnetite and siderite: XAS characterization of nanosized redox products. Environ Sci Technol 42(6):1984–1989. doi:10.1021/es071573f

Schroeder SLM (1996) Towards a 'universal curve' for total electron-yield XAS. Solid State Commun 98(5):405–409. doi:10.1016/0038-1098(96)00035-X

Solorzano L (1969) Determination of ammonia in natural waters by the phenol hypochlorite method. Limnol Oceanogr 14(5):799–801

Stein JS, Fisher AT (2001) Multiple scales of hydrothermal circulation in Muddle Valley, northern Juan de Fuca Ridge: physical constraints and geologic models. J Geophys Res 106:8563–8580. doi:10.1029/2000JB900395

Tsuji K, Nakano K, Takahashi Y, Hayashi K, Ro C-U (2012) X-ray spectrometry. Anal Chem 84(2):636–668. doi:10.1021/ac202871b

van Hullenbusch E, Farges F, Lenz M, Lens P, Brown GE (2007) Selenium speciation in biofilms from granular sludge bed reactors used for wastewater treatment. AIP Conf Proc 882(1):229–231. doi:10.1063/1.2644483

Comparative Investigation of Microbial Communities Associated with Hydrothermal Activities in the Okinawa Trough

32

Ken Takai, Satoshi Nakagawa, and Takuro Nunoura

Abstract

In the Okinawa Trough, microbial communities in deep-sea hydrothermal vent chimneys have been extensively studied in the Iheya North (Iheya North Knoll) and the Yonaguni Knoll IV (Daiyon-Yonaguni Knoll) fields. In comparison of the microbial community patterns in geographically and geologically diverse deep-sea hydrothermal systems all the world, the Okinawa Trough deep-sea vent microbial communities have been known to be distinctive and to be associated with the unique hydrothermal fluid chemistry commonly observed in the Okinawa Trough systems. However, this implication is based only on the data from the above two hydrothermal systems. Here, we further show the microbial community patterns of Minami-Ensei (Minami-Ensei Knoll), Izena Hole Jade and Hakurei fields in the Okinawa Trough, using data by culture-dependent techniques. The comparison of the microbial community patterns determined in typical chimney habitats of representative Okinawa Trough hydrothermal systems including new data points that the diversity and abundance of cultivated microbial populations are significantly relevant with intra-field variation of hydrothermal fluid chemistry induced by the subseafloor phase-separation and -partition processes rather than with inter-fields variability in the endmember fluid chemistry. Inter-fields variability in potential microbial community development in the Okinawa Trough hydrothermal systems may be caused by other possible bases in the microbial community development such as the physical mode of hydrothermal fluid discharges, the age of hydrothermal system and the hydrogeological complexity of subseafloor hydrothermal fluid flow structures. Nevertheless, the correlation between the H_2 concentration in hydrothermal fluid and the culturable population size of

K. Takai (✉)
Department of Subsurface Geobiological Analysis and Research (D-SUGAR) and Research and Development (R&D) Center for Submarine Resources, Japan Agency for Marine-Earth Science and Technology (JAMSTEC), 2-15 Natsushima-cho, Yokosuka 237-0061, Japan
e-mail: kent@jamstec.go.jp

S. Nakagawa
Department of Subsurface Geobiological Analysis and Research (D-SUGAR), Japan Agency for Marine-Earth Science and Technology (JAMSTEC), 2-15 Natsushima-cho, Yokosuka 237-0061, Japan

Division of Applied Biosciences, Graduate School of Agriculture, Kyoto University, 3-1-1 Minato-cho, Hakodate, Hokkaido 041-8611, Japan

T. Nunoura
Research and Development Center for Marine Biosciences, Japan Agency for Marine-Earth Science and Technology (JAMSTEC), 2-15 Natsushima-cho, Yokosuka 237-0061, Japan

J.-i. Ishibashi et al. (eds.), *Subseafloor Biosphere Linked to Hydrothermal Systems: TAIGA Concept*,
DOI 10.1007/978-4-431-54865-2_32,

H_2-trophic methanogens is reinforced by the new results obtained from the Izena Hole Hakurei chimney habitat hosting the H_2-enriched hydrothermal fluid. It seems very likely that the H_2 concentration in the hydrothermal fluid is still a very important chemical factor to control the chemolithotrophic microbial community development essentially in the global deep-sea hydrothermal systems.

Keywords
Chemolithoautotroph • Deep-sea hydrothermal vents • Epsilonproteobacteria • Methane • Okinawa Trough

32.1 Introduction

Deep-sea hydrothermal vent environments represent one of the most physically and chemically diverse biomes in Earth. The chemical and thermal gradients provide a wide range of niches for microbial communities living there (Huber and Holden 2008; Nakagawa and Takai 2008; Nakamura and Takai 2014; Reysenbach et al. 2000; Takai et al. 2006; Takai and Nakamura 2010, 2011). Phylogenetically and physiologically diverse microorganisms thrive by chemolithoautotrophy or heterotrophy, utilizing abundant available inorganic and organic chemical energy, carbon and other element sources. They reside as free-living and biofilm-forming lifestyles in the rocky and sedimentary mixing interfaces between hot, highly reductive hydrothermal fluids (high-temperature endmember hydrothermal fluids) and ambient seawaters beneath and at the seafloor and within the lower-temperature diffuse fluids mainly resulting from subseafloor mixing between endmember hydrothermal fluids and ambient seawaters, and as facultative or obligate symbiotic lifestyle on and within the invertebrate hosts (Nakamura and Takai 2014; Takai et al. 2006; Takai and Nakamura 2010, 2011).

Over the past two decades, microbiologists have gained significant insights into the compositional and functional diversity of microbial communities in these unique ecosystems. In particular, the microbial communities have been extensively explored in the chimney structures and using the artificial habitats (e.g., in situ colonization devices) associated with high-temperature endmember-like hydrothermal fluid discharges (Takai et al. 2006; Takai and Nakamura 2010, 2011). The early research was conducted in the several deep-sea hydrothermal systems in the Mid Ocean Ridges (MORs), however recently, as the greater heterogeneity of the physical and chemical characteristics of hydrothermal fluids in the Volcanic Arcs (VAs) and Backarc Basins (BABs) and even of hydrothermal fluids in the ultramafic rocks-associated systems recently found in the MORs, many studies have demonstrated the great inter-fields heterogeneity of the microbial communities, particularly present in the chimney structures among a variety of fields (Nakamura and Takai 2014; Takai et al. 2006; Takai and Nakamura 2010, 2011). These results have suggested the impact of endmember-like hydrothermal fluid chemistry on the compositions and functions of proximal microbial communities in the subseafloor as well as at the seafloor habitats including chimneys. In addition, several disciplines of approaches begin to clarify the geochemical-microbial interrelation based on the thermodynamic modeling of microbially available energy potentials by various chemolithotrophic metabolisms in the hydrothermal mixing zones and the inter-fields comparisons of functionally active microbial communities coupled with hydrothermal inputs of energy sources (McCollom 2007; McCollom and Shock 1997; Nakamura and Takai 2014; Shock and Holland 2004; Takai and Nakamura 2010, 2011; Nakamura and Takai Chap. 2).

The thermodynamic calculations have clearly predicted that the hydrothermal fluid chemistry variation leads to different patters and compositions of chemolithotrophic microbial communities, particularly in chimney habitats (Nakamura and Takai 2014; Takai and Nakamura 2010, 2011). In the model, the S-trophic (thiotrophic) chemolithotrophy would be always predominant in any types of deep-sea hydrothermal systems while the H_2-trophic (hydrogenotrophic) methanogenesis, SO_4-reduction and S-reduction should be fostered particularly in high temperature zones of H_2-enriched deep-sea hydrothermal systems (Nakamura and Takai 2014; Takai and Nakamura 2010, 2011). These predictions are indeed supported by the estimated population abundances of the S-trophic and H_2-trophic chemolithotrophs using quantitative cultivation analyses (Nakamura and Takai 2014; Takai and Nakamura 2010, 2011). In addition, the thermodynamic model have pointed to unique composition of chemolithotrophic microbial communities that would be driven by psychrophilic to hyperthermophilic aerobic methanotrophs and ammonia-oxidizers and hyperthermophilic anoxic methanotrophs in the Okinawa Trough deep-sea hydrothermal systems (Nakamura and Takai 2014; Takai and Nakamura 2010,

2011). Although the microbiological characterizations have not fully justified the formation of unique chemolithotrophic communities in the Okinawa Trough deep-sea hydrothermal systems, the development of a great phylogenetic and physiological diversity of chemolithotrophic microbial communities has been demonstrated by the previous cultivation-dependent and even the molecular ecological methods (Nakagawa et al. 2005; Nunoura and Takai 2009; Takai et al. 2006). However, these implications have been based only on the results of microbiological characterizations in two hydrothermal systems, Iheya North (Iheya North Knoll) and Yonaguni Knoll IV (Daiyon-Yonaguni Knoll) fields of the Okinawa Trough.

The Okinawa Trough is a "rifting phase" of Backarc Basin covered with thick terrigenous sediments (Letouzey and Kimura 1986) and is now known to host seven active deep-sea hydrothermal fields, of which the seafloor hydrothermal activities have been verified by the seafloor observation and the hydrothermal fluid and mineral samples have been investigated (Glasby and Notsu 2003; Ishibashi et al. Chap. 27). The Izena Hole Jade and Hakurei fields and the Iheya Ridge Clam field were discovered in the late 1980s, the Minami-Ensei (Minami-Ensei Knoll) field in 1990, the Iheya North field in 1995, and finally the Yonaguni Knoll IV field and the Hatoma Knoll fields were explored in 1999 (Glasby and Notsu 2003; Ishibashi et al. Chap. 27). Since the discovery of these Okinawa Trough hydrothermal systems, more than 300 dives of manned submersibles and remotely operative vehicles have been organized, and the geochemical analyses of hydrothermal fluids and mineral deposits and the microbiological characterizations have been extensively conducted (Glasby and Notsu 2003; Ishibashi et al. Chap. 27). At present, the detail physical and chemical characteristics of hydrothermal fluids have been determined in the Iheya North field (Kawagucci et al. 2011), the Yonaguni Knoll IV field (Konno et al. 2006; Suzuki et al. 2008), the Minami-Ensei field (Kawagucci et al. 2013) and the Izena Hole Jade and Hakurei fields (Ishibashi et al. 2014; some data summarized in Kawagucci Chap. 30). Thus, if the compositions and functions of microbial communities in the chimney habitats are characterized with a combination of the detail physical and chemical characteristics of the proximal hydrothermal fluids, the new data provide important insights into understanding the inter-fields and intra-field features of microbial community development patterns and geochemical-microbial interrelation in the Okinawa Trough hydrothermal systems. In this chapter, we show the microbial community patterns in the chimney habitats characterized mainly by using culture-dependent techniques in the Minami-Ensei, Izena Hole Jade and Hakurei fields of the Okinawa Trough. The overall comparison of the microbial community patterns points to the conventional and unique aspects of the geochemical-microbial interrelation in the Okinawa Trough hydrothermal systems.

32.2 Materials and Methods

32.2.1 Site Summary, Seafloor Sampling and Onboard Processes

For Jade and Hakurei fields of the Izena Hole, all samples used in this study were obtained by means of a manned submersible *Shinkai 2000* and its mother research vessel *Natsushima* in the cruise of August 2003 (JAMSTEC cruise NT03-08). Bulks of chimney structures (>100 g) were obtained from high-temperature hydrothermal fluid discharge vent sites (TBS chimney site at the Jade field and 214 chimney site at the Hakurei field). For the Minami-Ensei (Minami-Ensei Knoll) field, all samples used in this study were obtained by a remotely operative vehicle (ROV) *Hyper Dolphin* and its mother research vessel *Natsushima* in the cruise of July 2007 (JAMSTEC cruise NT07-11). In both cruises, the obtained hydrothermal fluids were investigated by onboard and onshore measurements, sample preparations and geochemical analyses, and the detail physical and chemical properties of the high-temperature and the endmember hydrothermal fluids were reported in the previous studies (Table 32.1) (Ishibashi et al. 2014; Kawagucci et al. 2013).

The chimney structures examined in this study were TBS chimney at the Izena Hole Jade field, 214 chimney at the Izena Hole Hakurei field, and Jizo and No. 7 chimneys at the Minami-Ensei field (Table 32.1). Each of the recovered chimney samples was further divided and subjected to nucleic acid extraction, microscopic observation and liquid serial dilution culture as previously reported by Nakagawa et al. (2005) and Nunoura and Takai (2009). For liquid serial dilution culture experiments, the subsamples of the chimneys (about 10 g wet weight) were slurried with sterile MJ synthetic seawater (30 mL) (Takai et al. 1999) containing neutralized Na_2S solution at a final concentration of 0.05 % (wt/vol) under N_2 atmosphere, and stored at 4 °C in the dark until they were used. For microscopic observation, the subsamples (about 2 g) were fixed with sterile MJ synthetic seawater (10 mL) containing 3.7 % (wt/vol) of formaldehyde for 24 h and then stored at −80 °C. The remaining subsamples were stored at −80 °C for nucleic acid extraction.

In the Izena Hole Hakurei field, an in situ colonization system (ISCS) (Takai et al. 2003; Nakagawa et al. 2005) was deployed for 5 days in the vent orifice of the 214 chimney that hosted high-temperature hydrothermal fluid. After 5 days incubation, the ISCS was recovered onboard and the substratum was subsampled for the nucleic acid extraction,

Table 32.1 Physical and chemical characteristics of hydrothermal fluids in different deep-sea hydrothermal fields of Okinawa Trough

Field	Iheya North			Yonaguni Knoll IV		Izena Hole Jade	Izena Hole Hakurei	Minami-Ensei		Ambient seawater
Vent site	NBC	CBC	E18	BTC	CTC	TBS	214	Jizo	No. 7	
Temp. (°C)	311	311	311	330	330	320	326	280	280	2
Depth (m)	980	990	1,000	1,369	1,362	1,340	1,600	710	722	
pH	4.8	5.3	4.6[a]	5.3[b]	4.7[a]	4.7	4.7	4.9	4.9	7.8
H_2 (mM)	0.229	0.135[c]	0.346[c]	0.8	2.4	0.06	1.4	0.029	0.033	0.0000004
H_2S (mM)	4.5	2.7[c]	6.8[c]	19.7[a]	38.3[a]	5.6	5.3	0.40	0.92[a]	0
CH_4 (mM)	3.7	2.2[c]	5.6[c]	1.8	9.1	4.9	5.8	2.3	2.6	0.0000003
CO_2 (mM)	230	136[c]	347[c]	71	318	156	151	39	46	2.3
N_2 (mM)	0.0346[b]	0.0189[c]	0.0487[c]	1.5[a]	2.0[a]	1.5[a]	1.5[a]	0.35	2.2	0.59
CO (mM)	<0.0001[b]	<0.0001[b]	<0.0001[b]	<0.0001[a]	<0.0001[a]	0.03	0.063	<0.0001[b]	<0.0001[b]	0
SO_4 (mM)	0	0	0	0	−1.6	0	0	0	0	27.9
NH_4 (mM)	1.7	1.85[b]	1.85	8.6	20.7	4.2	4.4	5.4	5.4	0.00005
Na (mM)	432	745	288	433	254	442	458	436	436	464
Cl (mM)	544	864	338	635	376	590	608	562	562	546
Ca (mM)	16.1	19.9	11.9	26.1	14.3	22	23	23	23	10.2
Mg (mM)	0	0	0	0	0	0	0	0	0	52.7
K (mM)	72	79	56.2	90.1	55.3	72	75	53	53	9.8
Fe (mM)	0.251[b]	0.424[c]	0.167[c]	0.2	0.1	0.031	0.445	<0.12	<0.12	0.0000015
Mn (mM)	0.619	0.46	0.445	1.25	0.7	0.341	0.29	0.099	0.099	0
NO_3 (mM)	0	0	0	0	0	0	0	0	0	0.03
Si (mM)	10.1	11.6	6.9	13.2	12.5	11.8	11.3	11.1	11.1	0.16
$\delta D(H_2)$	−430	n.d.	n.d.	n.d.	n.d.	−381	−379	−642	−405	
$\delta^{13}C$ (CO_2)	−9.7	n.d.	n.d.	−7.6	−7.6	−6.2	−6.2	−5.0	−5.3	
$\delta^{13}C$ (CH_4)	−53.8	n.d.	n.d.	−25.9	−26.6	−30.8	−32.1	−25.1	−25.3	
$\delta^{34}S$ (H_2S)	+12[b]	n.d.	n.d.	n.d.	n.d.	+3.8 ~ +8.0	+5.5 ~ +7.8	+3.6	+3.6	
Reference	Kawagucci et al. (2011)	Kawagucci et al. (2011)	Kawagucci et al. (2011)	Suzuki et al. (2008)	Suzuki et al. (2008)	Ishibashi et al. (2014)	Ishibashi et al. (2014)	Kawagucci et al. (2013)	Kawagucci et al. (2013)	McCollom (2007)
	Nakagawa et al. (2005)	Nakagawa et al. (2005)	Nakagawa et al. (2005)	Konno et al. (2006)	Konno et al. (2006)	Kawagucci (Chap. 30)	Kawagucci (Chap. 30)			

[b]Unpublished data

[a]Values taken from a similar hydrothermal fluid: for E18 site in Iheya North field from a gas-rich fluid in the Yonaguni Knoll IV field (unpublished); for BTC and CTC in Yonoguni Knoll IV field from Cl-enriched and -depleted fluids in Hatoma Knoll field (unpublished); for Minami Ensei field (No. 7 site) from Minami Ensei field (Taimatsu site) (Kawagucci et al. 2013)

[c]Values calculated according to a simple phase-separation ratio that is linearly reproduced by the deviation of chloride concentrations in the hydrothermal fluids

n.d. not determined

the microscopic observation and the liquid serial dilution culture as previously reported by Nakagawa et al. (2005).

32.2.2 Total Direct Cell Counts

Microbial cell densities in the sub-samples extracted from the chimney structures were determined by 4′,6-diamidino-2-phenylindole (DAPI)-staining direct counting. The thawed, formaldehyde-fixed chimney subsample was vigorously suspended with a vortex mixer. After 5 min, 1 mL of formaldehyde-fixed supernatant was added to 1 mL of filter-sterilized phosphate-buffered saline (PBS, pH 7.2) containing DAPI (10 μg/mL), and incubated at room temperature for 30 min. After the mixture was filtered, each filter was rinsed twice with 2 mL of filter-sterilized PBS. The filters were observed under epifluorescence using a phase-contrast Olympus BX51 microscope with the Olympus DP71 digital camera system. An average total cell count was obtained from more than 100 microscopic fields from three separate filters.

32.2.3 Nucleic Acid Extraction and 16S rRNA Gene Clone Analysis

Nucleic acids were extracted from the chimney outer surfaces and the chimney inside walls with the Ultra Clean Mega Soil DNA kit (MO Bio Laboratory, Solana Beach, CA, USA), following the manufacturer's instructions. A blank tube (with no sample added) was processed as a negative control. Extracted nucleic acids were stored at −80 °C.

Bacterial and archaeal 16S rRNA genes were amplified from DNA extracts from subsamples and controls by PCR using LA Taq polymerase with GC buffer (TaKaRa, Kyoto, Japan). The oligonucleotide primers used were Bac27F and 1492R (Lane 1991) for the bacterial rRNA gene in the samples from both the Izena Hole and the Minami-Ensei fields, and Arch21F and Arch958R (DeLong 1992) in the cases of the Minami-Ensei field's samples, and Arch21F and 1492R in the cases of Izena Hole fields' samples. Thermal cycling was performed under the following conditions: 30–50 cycles of 96 °C for 25 s, 50 °C for 45 s and 72 °C for 120 s for the archaeal 16S rRNA gene and 20–40 cycles of 96 °C for 25 s, 54 °C for 45 s and 72 °C for 120 s for the bacterial 16S rRNA gene. The PCR cycle numbers represent almost the minimum cycle numbers providing enough amplified products for the cloning based on the preliminary PCR amplification experiments using the same templates. The amplified rRNA gene products from several separate reactions at the least number of thermal cycles were pooled and purified as previously described (Takai et al. 2001). Cloning and sequencing were also followed by the procedure described by Takai et al. (2001). The Bac27F (Lane 1991) or Arch21F (DeLong 1992) primer was used in partial sequencing analysis.

Single-strand sequences of approximately 500 nucleotides in length were determined. The sequence similarity was analyzed by the FASTA component program of DNASIS (Hitachi software, Tokyo, Japan). The rRNA gene sequences having ≥97 % similarity by FASTA were assigned to the same phylotype. The partial sequences of the representative phylotypes were determined for both strands (>800 bp), and were applied to sequence similarity analysis against the non-redundant nucleotide sequence databases of GenBank, EMBL and DDBJ using the gapped-BLAST.

32.2.4 Phylogenetic Analysis

The sequences of the representative phylotypes from the clone analysis and the isolates were manually realigned according to the secondary structures using ARB (Ludwig et al. 2004). Phylogenetic analyses were restricted to nucleotide positions that could be chosen using the *Bacteria* and *Archaea* filters for the bacterial and archaeal 16S rRNA gene sequences (Hugenholtz 2002). Evolutionary distance matrix analysis (using the Jukes & Cantor correlation method) and neighbor-joining analysis were performed using PHYLIP package (http://evolution.genetics.washington.edu/phylip.html). In this study, the phylogenetic analysis was conducted only to identify the phylogenetic affiliation of 16S rRNA gene phylotypes and the isolated strains to the previously known phylogenetic groups, potentially corresponding to the appropriate phylum, order, family and genus levels of taxonomic hierarchy.

32.2.5 Quantitative PCR Analysis

Determination of the proportion of the archaeal 16S rRNA genes in the whole microbial DNA assemblage was performed by the quantitative fluorescent PCR method using TaqMan probes as described elsewhere (Takai and Horikoshi 2000). A dilution series of each of the DNA samples was prepared and the samples were assayed using the universal 16S rRNA gene mixture and the archaeal 16S rRNA gene mixture as the respective standards (Takai and Horikoshi 2000).

32.2.6 Liquid Serial Dilution Cultures

To estimate the abundance of culturable microorganisms (viable counts) represented by a variety of physiological

and metabolic characteristics, a series of serial dilution cultures were done from each of the chimney subsamples under the various cultivation conditions. All the cultivation experiments to estimate the viable counts were performed within 3 months after the sample collection. The cultivation experiments were conducted in the order of experiments for the strictly anaerobic chemolithoautotrophs, for the strictly anaerobic heterotrophs, for facultative anaerobic chemolithoautotrophs, for facultative anaerobic chemolithoautotrophs and for microaerobic chemolithoautotrophs. These conditions are also similar with those in the previous studies (Nakagawa et al. 2005; Nunoura and Takai 2009; Takai et al. 2008, 2009). In the cases of Izena Hole fields' samples, the media and the cultivation conditions for quantitative cultivation analysis were conducted in the same manner as described in Nakagawa et al. (2005). In the cases of Minami-Ensei field's samples, the media and the cultivation conditions for quantitative cultivation analysis were conducted in the same manner as described in Nunoura and Takai (2009). The microorganism present in the most diluted series of each medium at each temperature was isolated by the subsequent extinction–dilution method (Takai et al. 2000). The partial sequences of the 16S rRNA genes (approx. 700–1,000 bp) of the isolates were determined as described elsewhere (Takai et al. 2004). Although the purity of the isolates was not substantial in this study, it was checked by the cellular morphology on the microscopic observation and the 16S rRNA gene partial sequence. In addition, as it has been often pointed out, the elaborate quantitative cultivations even using numerous media under various growth conditions do not escape from the strong experimental biases and still fail to estimate considerable amounts of various important populations for the microbial communities.

32.3 Results

32.3.1 Fluid Chemistry

The physical properties and the chemical compositions of the endmember hydrothermal fluids being expelled from the TBS chimney at the Izena Hole Jade field, the 214 chimney at the Izena Hole Hakurei field, and the Jizo and No. 7 chimneys at the Minami-Ensei (Minami-Ensei Knoll) field are summarized in Table 32.1 together with the physical-chemical characteristics of the other endmember hydrothermal fluids in the Okinawa Trough. All of the data in Table 32.1 were already reported in the previous studies (Ishibashi et al. 2014; Kawagucci Chap. 30; Kawagucci et al. 2011, 2013; Konno et al. 2006; Nakagawa et al. 2005; Suzuki et al. 2008; Takai and Nakamura 2010).

As a whole, the high-temperature hydrothermal fluids in the Okinawa Trough deep-sea hydrothermal systems including the Izena Hole Jade and Hakurei fields and the Minami-Ensei field have unique common chemical features represented by the relatively neutral pH and high concentrations of K, NH_3, CO_2 and CH_4, which are tightly associated with the geological settings of Okinawa Trough (Kawagucci, Chap. 30). In the Iheya North and Yonaguni Knoll IV fields, many high-temperature hydrothermal fluids in different chimney sites are affected by the subseafloor phase-separation and -partition processes, and thus, the abundance of gas components in the endmember hydrothermal fluids is highly variable. In contrast, it has been demonstrated that the endmember hydrothermal fluids in the Izena Hole Jade and Hakurei fields and the Minami-Ensei field are little affected by the subseafloor phase-separation and -partition processes (Ishibashi et al. 2014; Kawagucci et al. 2013).

Notably, the most recent geochemical analysis of various hydrothermal fluids obtained from the Izena Hole Jade and Hakurei fields has led the following interpretation of the hydrothermal activities (Ishibashi et al. 2014): the endmember hydrothermal fluids of both the Jade and Hakurei fields would have the same primary fluid source derived from the common, deep subseafloor hydrothermal reaction zone, while the two major branched fluid paths in the course of the upwelling source fluid flow would generate the two geographically distant, geochemically slightly deviated hydrothermal systems (Jade and Hakurei fields) at the seafloor of the Izena Hole area. The most deviated chemical properties between the endmember hydrothermal fluids of Jade and Hakurei fields are dissolved H_2 and C_2H_6 concentrations (Table 32.1), which are induced by the presence and the absence of the hydrothermal fluid reaction with sediments (in other words, the thermal decomposition of sedimentary organic compounds) in the subseafloor upwelling hydrothermal fluid flow zones (the presence of sediments in the Hakurei field and the absence of sediments in the Jade field) (Ishibashi et al. 2014). Thus, the different physical and chemical characteristics of hydrothermal fluids and even the different microbial community development patterns would be interpreted as a sort of intra-field variation.

In contrast, although no apparent difference in the Cl concentration is observed in the high-temperature hydrothermal fluids, the abundance of gas components is found to be slightly variable among the different hydrothermal vent sites of the Minami-Ensei field (Kawagucci et al. 2013). Since the seafloor observation by ROV clearly verified boiling of hydrothermal fluid in several vent sites of the Minami-Ensei field, it seems likely that the phase-separation occurs in the relatively shallow deep-sea hydrothermal system of Minami-Ensei field with a water depth range of 710–730 m. Probably, the boiling of hydrothermal fluid occurs at the seafloor or at

around the very shallow subseafloor zones. The quite local phase-separation and -partition would provide a little variability in the hydrothermal fluid chemistry at different vent sites of the Minami-Ensei field.

32.3.2 Biomass in the Hydrothermal Chimney Habitats

The prokaryotic cell density determined by direct counting of each chimney subsample is listed in Table 32.2. The direct counts of the Minami-Ensei Jizo and No. 7 chimneys were quite difficult due to the very low cell densities recovered from the subsamples and were estimated to be below estimation limit of 10^4 cells/g wet weight (Table 32.2). The quite low cell densities of the Minami-Ensei Jizo and No. 7 chimneys were also expected from the negative results of PCR amplification of bacterial and archaeal 16S rRNA genes: none of the bacterial and archaeal 16S rRNA gene fragments was recovered from the DNA extracts of the subsamples in these chimney structures. In addition, the quantitative PCR analysis using different PCR primer sets showed that the amounts of whole microbial and archaeal 16S rRNA genes in these chimney habitats were also below detection limits (<0.1 fg/g).

In contrast, the directly counted cell densities of the chimney habitats in the Izena Hole Jade and Hakurei fields were comparable with the microbial cell populations previously found in typical chimney habitats of other Okinawa Trough hydrothermal systems (Nakagawa et al. 2005; Nunoura and Takai 2009). In the chimney surface habitats, microbial cell populations with more than 10^7 cells/g wet weight were detected, and slightly lower or similar cell densities were obtained even from the interior parts of the chimney structures (Table 32.2). In addition, microbial cell population with more than 10^7 cells/g wet weight was estimated in the ISCS deployed in the 214 chimney hydrothermal fluid of the Izena Hole Hakurei field for 5 days (Table 32.2). The recovery of relatively high density of microbial population in the ISCS deployed in the 214 chimney high-temperature hydrothermal fluid is comparable with those in the ISCSs deployed in various vent sites of Iheya North field (Nakagawa et al. 2005) and in the Kali vent site of Kairei field (Takai et al. 2004), but is different from the pattern in the case of ISCS at the Mariner field (Lau Basin) (Takai et al. 2008). Since the ISCS collects the microbial populations entrained by the hydrothermal fluid flow from the subseafloor microbial communities and the microbial population abundance trapped in the ISCS could be relevant with the microbial population abundance entrained by the hydrothermal fluid, the recovery of relatively high density of microbial population in the ISCS at the 214 chimney site may represent the potential population abundance and spatially widespread distribution of subseafloor microbial communities beneath the Izena Hole Hakurei field.

Although microbial cell populations with more than 10^7 cells/g wet weight were detected in the surface habitats of both the TBS and 214 chimneys, the quantitative PCR analysis provided 4.2×10^5 copies/g wet weight and 1.5×10^5 copies/g wet weight for whole prokaryotic 16S rRNA gene numbers at the TBS and 214 chimney surface habitats, respectively. In the chimney interior parts, although relatively higher microbial cell densities were obtained from the microscopic observation, only 5.2×10^3 and 5.6×10^3 copies/g wet weight for whole prokaryotic 16S rRNA gene numbers were obtained from the TBS and 214 chimneys, and 1.4×10^3 copies/g wet weight for total 16S rRNA gene number was found in the ISCS deployed at the 214 chimney. The proportion of archaeal 16S rRNA gene number against the bacterial counterpart was quite low among all the chimney habitats (Table 32.2), which are comparable with any of the previously known values of the chimney habitats in various deep-sea hydrothermal systems.

32.3.3 Bacterial and Archaeal Phylotypes in the Chimney Habitats

The archaeal and bacterial 16S rRNA gene phylotype compositions of the chimney habitats are shown in Tables 32.3 and 32.4. The phylogenetic affiliation of the phylotype is characterized by the phylogenetic analysis of representative phylotype sequences. The archaeal 16S rRNA genes were only successfully amplified from the samples of the 214 chimney and ISCS at the Hakurei field (Table 32.3). The predominant archaeal 16S rRNA gene phylotypes from the 214 chimney surface habitat were all closely related with the previously known (hyper)thermophilic archaeal genera such as *Methanothermococcus*, *Methanocaldococcus*, *Methanopyrus*, *Thermococcus* and *Pyrodictium* (Table 32.3). In the ISCS deployed at the high-temperature hydrothermal fluid for 5 days, only one phylotype of *Methanothermococcus* dominated the archaeal 16S rRNA phylotype composition and three representative phylotypes related with *Nanoarchaeota* occupied the archaeal 16S rRNA phylotype composition in the interior part of the 214 chimney (Table 32.3). These archaeal 16S rRNA gene phylotypes are closely related with the (hyper)thermophilic archaeal populations that have been frequently identified in the global deep-sea hydrothermal vent environments although these archaeal 16S rRNA gene phylotypes represent quite low fractions of whole prokaryotic 16S rRNA gene assemblages (Table 32.2).

The bacterial 16S rRNA gene phylotypes were obtained from the TBS chimney and the 214 chimney and its ISCS of the Jade and Hakurei fields (Table 32.4). However, the

Table 32.2 Microbiological characteristics of each chimney subsample

Sample ID	Sample description	Prokaryotic community density (cells/g)	Strains obtained from dilution-cultivation test in the medium of						Proportion of rRNA gene for Bacteria (%)
			MJYPGS[a]	MMJ[a]	MMJHS[a]	MMJHS	MMJHS	MJAIS[a]	
			Gas A[b]	Gas B[b]	Gas B	Gas C[b]	Gas D[b]	Gas B	
TBS-S	Izena Hole Jade field surface part of TBS chimney	1.0×10^7	TBS-SBI70Tc (9.1×10^4 cells/g)	n.d.[c]	TBS-SBI25e-1 (1.3×10^4 cells/g)	n.d.	nn.a.[d]	TBS-SBI55Des (7.6×10^1 cells/g)	100
					TBSSulfide37e-1 (1.4×10^3 cells/g)			TBS-SBI37Des (2.6×10^4 cells/g)	
TBS-I	Izena Hole Jade field interior part of TBS chimney	1.5×10^7	TBSblackin70Tc (7.0×10^2 cells/g)	n.d.	TBSBlackIn25e-1 (4.9×10^3 cells/g)	n.d.	n.a.	n.d.	100
214-S	Izena Hole Hakurei field surface part of 214 chimney	1.5×10^8	214OrangeS70Tc (4.8×10^5 cells/g)	214OrangeS70Mc (7.2×10^4 cells/g)	214OS37e-1 (1.5×10^3 cells/g)	n.d.	n.a.	214OS55Des (7.2×10^4 cells/g)	96.6
				214OrangeS85Mc (1.0×10^4 cells/g)	214OS25e-1 (3.0×10^1 cells/g)			214OS70Des (2.1×10^2 cells/g)	
214-I	Izena Hole Hakurei field interior part of 214 chimney	2.5×10^6	214BI70Tc (2.6×10^3 cells/g)	214BI70Mc (4.2×10^2 cells/g)	214BI37e-1 (2.9×10^3 cells/g)	n.d.	n.a.	214WhiteIn70Des (3.0×10^1 cells/g)	100
				214BI85Mc ($1.3 \times 10^\circ$ cells/g)	214BI25e-1 ($2.4 \times 10^\circ$ cells/g)				
215-ISCS	Izena Hole Hakurei field ISCS deployed for 5 days at 214 chimney	1.8×10^7	215ISCS70Tc (2.8×10^3 cells/g)	215ISCS85Mc (1.3×10^4 cells/g)	215ISCS25e-1 (2.0×10^4 cells/g)	n.d.	n.a.	214ISCS55Des (2.8×10^5 cells/g)	99.9
				215ISCS70Mc (1.9×10^3 cells/g)	215ISCS37e-1 ($8.3 \times 10^\circ$ cells/g)				
Jizo-S	Minami Ensei field surface part of Jizo chimney	$<10^4$	689-S-T-70 (1.0×10^1 cells/g)	n.d.	n.d.	689-S-1 %-55 (1.0×10^2 cells/g)	n.d.	n.d.	n.d.
Jizo-I	Minami Ensei field	$<10^4$	n.d.	n.d.	689-I-0 %-37	689-I-1 %-37	689-I-5 %-37	n.d.	n.d.

[a]MJYPG and MJAIS media (Nakagawa et al., 2005); MMJ medium (Takai et al., 2002); MMJHS medium (Takai et al. 2003)
[b]Gas A = 100 % N_2 (2 atm); Gas B = 80 % H_2 + 20 % CO_2 (2 atm); Gas C = 79 % H_2 + 20 % CO_2 + 1 % O_2 (2 atm); Gas D = 79 % H_2 + 20 % CO_2 + 5 % O_2 (2 atm)
[c]n.d.; not detected
[d]n.a.; not attempted

Table 32.3 Distribution of representative archaeal 16S rRNA gene phylotypes in the various chimney subsamples

	Number of clones from		
Phylogenetic affiliation	214-S	214-I	215-ISCS
Nanoarchaeota	–	29	–
Crenarchaeota			
Desulfurococcales	1	–	–
Euryarchaeota			
Methanopyrales	2	–	–
Methanococcales	22	–	45
Thermococcales	19	–	–
Total	44	29	45

Table 32.4 Distribution of representative bacterial 16S rRNA gene phylotypes in the various chimney subsamples

	Number of clones from				
Phylogenetic affiliation	TBS-S	TBS-I	214-S	214-I	215-ISCS
Aquificae					
Aquifex group	–	–	1	–	–
Desulfurobacteria group	–	–	4	–	–
CFB Group	–	–	–	–	3
Chloroflexi	16	1	–	–	–
Planctmycetes	8	–	–	1	
Actinobacteria	15	2	–	13	3
Firmicutes	–	1	–	1	4
Proteobacteria					
Alphaproteobacteria	–	1	–	7	3
Betaproteobacteria	–	3	–	8	12
Gammaproteobacteria					
Thiomicrospira group	1	–	–	–	–
Deltaproteobacteria	1	–	–	–	–
Epsilonproteobacteria					
Nautiliaceae	–	–	14	–	–
Campylobacteraceae, Sulfurospirillum group	–	–	1	–	–
Thiovulgaceae, Sulfurovum group	1	–	5	–	–
Nitratiruptor group	–	–	12	–	–
Thioreductor group	–	–	4	–	–
Total	42	8	35	30	25

bacterial 16S rRNA gene phylotype compositions in the TBS chimney interior habitat, the 214 chimney interior habitat and the 214 ISCS were not likely derived from the indigenous microbial communities in the in situ habitats (Table 32.4). Most of the predominant bacterial phylotypes from these samples were closely related with previously cultured and uncultured members of *Actinobacteria*, *Alphaproteobacteria* and *Betaproteobacteria* obtained from non-hydrothermal environments and not from marine environments. Considering the quite low numbers of whole prokaryotic 16S rRNA genes recovered by the quantitative PCR, it seems very likely that these bacterial 16S rRNA gene phylotypes do not represent the predominant bacterial components in the indigenous microbial communities associated with the high-temperature hydrothermal fluid flows. Rather, these bacterial 16S rRNA gene phylotypes may be derived from the contaminants from other environments such as seawater and onboard and onshore laboratory environments. In contrast, the bacterial 16S rRNA gene phylotype compositions in the TBS chimney and the 214 chimney surface habitats seemed to represent the predominant bacterial components in the indigenous microbial communities (Table 32.4). All the bacterial 16S rRNA gene phylotypes obtained from the 214 chimney surface were closely related with the members of *Aquificae* and *Epsilonproteobacteria*, predominant microbial populations in many of the deep-sea hydrothermal environments. Similarly, the bacterial 16S rRNA gene phylotype composition in the TBS chimney surface hosted the bacterial phylotypes related with the deep-sea vent epsilon-, delta- and gamma-proteobacterial components although the clonal abundances of these phylotypes were low (Table 32.4). Other than these typical deep-sea vent proteobacterial components, in the TBS chimney surface habitats, the bacterial phylotypes within the *Chloroflexi*, *Planctomycetes* and *Actinobacteria* dominated the clone library (Table 32.4). Most of these *Chloroflexi*, *Planctomycetes* and *Actinobacteria* phylotypes were phylogenetically related with the bacterial phylotypes detected in the inactive chimneys or the active but highly weathered chimney outer surface parts of the Okinawa Trough, Indian Ocean and Lau Basin (Suzuki et al. 2004; Takai et al. 2008). Thus, the bacterial 16S rRNA gene phylotype composition in the TBS chimney surface is likely derived from the indigenous microbial community in the in situ surface habitat of the TBS chimney of the Jade field.

32.3.4 Cultivation Analyses of Microbial Components

We attempted to estimate the viable counts of potentially predominant microbial components living in the chimney environments by means of a liquid serial dilution cultivation technique. The viable count of each strain and the estimated population size of each taxonomic group are shown in Table 32.2 and Fig. 32.1, respectively.

As a whole, very diverse cultivated microbial populations were obtained from four chimney habitats of the Izena Hole and Minami-Ensei hydrothermal fields and the great variability in the abundance and diversity of cultivated microbial community was evident between the chimney sites (Fig. 32.1). The most diverse cultivated microbial populations were found in the 214 chimney of the Izena Hole Hakurei field. Nine different genera of mesophilic to

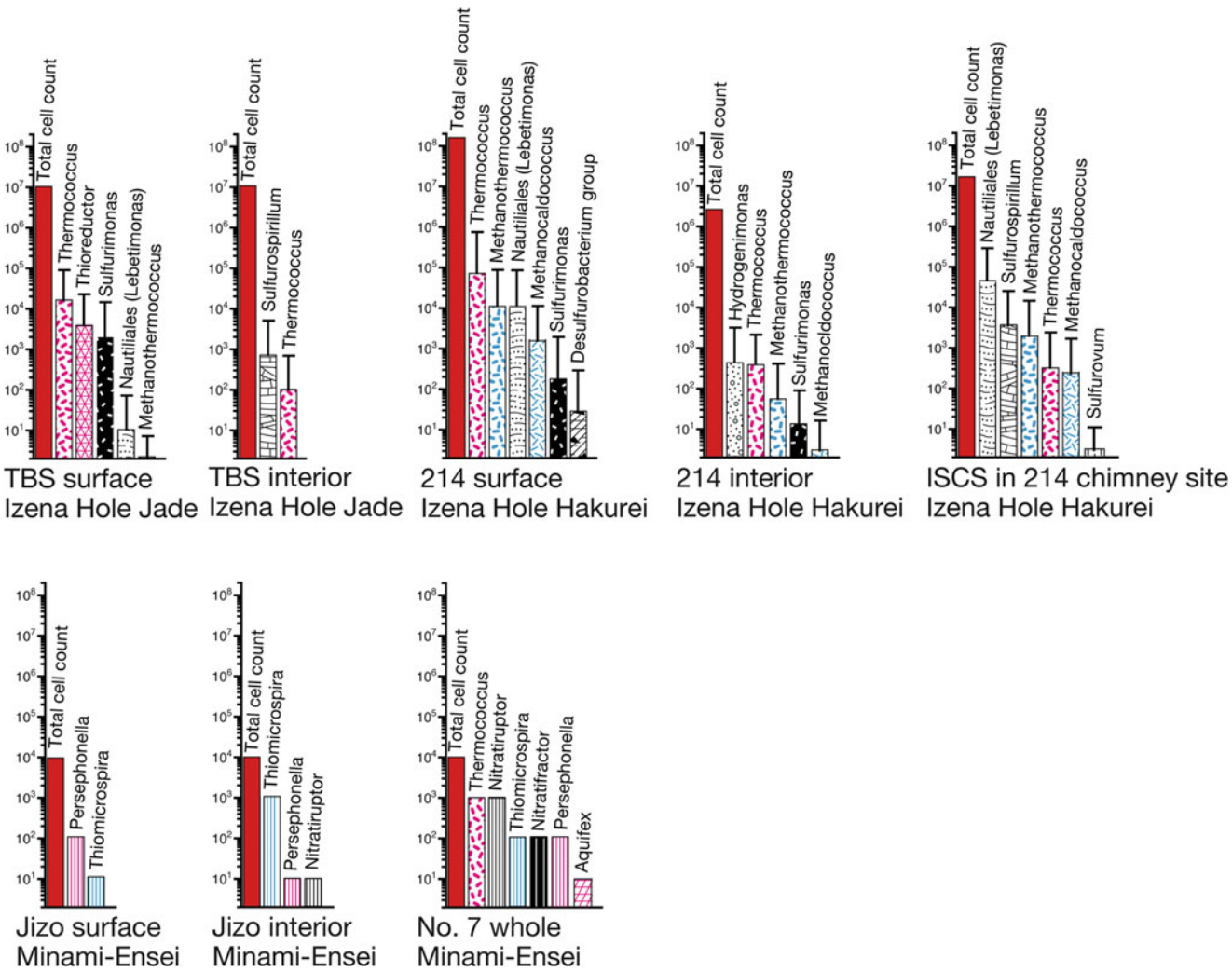

Fig. 32.1 Total cell count and viable count determined using DAPI staining and serial dilution cultivation in chimney habitats. The phylogenetic affiliation of isolates was delineated from the phylogenetic tree analysis. The abundances of cultivated microbial populations in the Izena Hole Jade and Hakurei chimneys are shown with the minimum estimation (*column*) and the maximum estimation (*bar*). The abundances of cultivated microbial populations in the Minami-Ensei chimneys are shown only with the maximum estimation (*column*)

hyperthermophilic deep-sea vent-endemic microbial populations were cultivated from the chimney habitats (Fig. 32.1). It was interesting that most of the cultivated components were common in between the TBS and 214 chimney sites of Izena Hole Jade and Hakurei fields or in between the Jizo and No. 7 chimneys of the Minami-Ensei field, while the cultivated components were significantly distinct in between the Izena Hole fields and the Minami-Ensei field (Fig. 32.1).

In the Izena Hole fields, the predominant cultivated microbial populations were *Thermococcus*, *Nautiliales*, *Hydrogenimonas*, *Thioreductor*, *Sulfurimonas* and *Sulfurospirillum* members (Fig. 32.1). Among these members, the predominant occurrence of cultivated *Hydrogenimonas*, *Thioreductor* and *Sulfurospirillum* populations was atypical in the deep-sea hydrothermal environments other than the Okinawa Trough, and the predominant cultivation of *Sulfurospirillum* population was unique in the Izena Hole hydrothermal fields, although the considerable population of *Sulfurospirillum* members has been cultivated from the chimney habitats and the polychaetes colonies of the Iheya North and Yonaguni Knoll IV fields using a specific mixotrophic media enriched with formate (unpublished data). The *Sulfurospirillum* members are known to be psychrophilic to slightly thermophilic chemolithomixotrophs and to require formate and simple organic acids in addition H_2 as the primary energy sources (Campbell et al. 2006). The first detection of *Sulfurospirillum* members as one of the predominant cultivated microbial populations in the Izena Hole fields, particularly in the Hakurei field, may be associated with the hydrothermal fluid chemistry, e.g., relative enrichment of formate in the hydrothermal fluids as

observed in the thermogenic hydrocarbons compared to other deep-sea hydrothermal fluids in the Okinawa Trough and the MOR, systems. However, the significant difference was found in the comparison of cultivated microbial community structures between the two Izena Hole fields, which should be an intra-field variability as described above. The cultivated population abundances of (hyper)thermophilic hydrogenotrophic methanogens such as *Methanothermococcus* and *Methanocaldococcus* were significant in the Hakurei field but were quite little in the Jade field (Fig. 32.1). This was the most outstanding intra-field difference of the cultivated microbial community structures in the Izena Hole hydrothermal system.

In the Minami-Ensei field, the cultivated microbial communities consisted of members of *Thermococcus*, *Aquifex*, *Persephonella*, *Nitratiruptor*, *Nitratifractor* and *Thiomicrospira* (Fig. 32.1). Among these members, the *Thermococcus*, *Aquifex* and *Persephonella* populations have been very often detected as predominant cultivated populations in many of the deep-sea hydrothermal environments including the Okinawa Trough systems (Takai and Nakamura 2010, 2011), and the *Nitratiruptor* and *Nitratifractor* members also represent typical cultivated populations in the Iheya North chimney habitats (Nakagawa et al. 2005). However, the predominant occurrence of cultivated *Thiomicrospira* population has been observed only in the S^0 chimney of the TOTO caldera field, the Mariana Volcanic Arc (Nakagawa et al. 2006), and may be a unique feature of the microbial communities in the chimney habitats of the Minami Ensei field (Fig. 32.1).

32.4 Discussion

32.4.1 Intra-Field Variability in Hydrothermal Fluid Chemistry and Microbial Community Development

In two hydrothermal fields of the Izena Hole area, the physical and chemical characteristics of the endmember hydrothermal fluids are quite similar other than the dissolved H_2 and C_2H_6 concentrations, probably due to the occurrence of the common, deep subseafloor hydrothermal reaction zones (Table 32.1) (Ishibashi et al. 2014). However, it is very likely that the dissolved H_2 concentration has a great impact on the microbial community development in the chimney habitats associated with the high-temperature hydrothermal fluids. The significant variability in the cultivated population abundances of (hyper)thermophilic hydrogenotrophic methanogens such as *Methanothermococcus* and *Methanocaldococcus* in the chimney habitats is evident (Fig. 32.1). The predominant occurrence of these (hyper) thermophilic hydrogenotrophic methanogens' populations in the microbial communities of the chimney habitats is also in part supported by the cultivation-independent 16S rRNA gene clone analyses, in which their 16S rRNA gene sequences are recovered only from the 214 chimney and the ISCS habitats in the Izena Hole hydrothermal system (Table 32.3), although the 16S rRNA gene clone analyses do not very much provide the quantitative insight into the microbial phylotype compositions. It is empirically justified and statistically supported by the geochemical analysis of dissolved H_2 concentration in the proximal hydrothermal fluids and the quantitative estimation of cultivated (hyper) thermophilic hydrogenotrophic methanogens' populations (Takai and Nakamura 2010, 2011). Not only the increased cultivated population abundances of (hyper)thermophilic hydrogenotrophic methanogens but also the greater diversity of cultivated microbial populations in the Izena Hole hydrothermal system are likely affected by the enrichment of dissolved H_2 in the adjacent hydrothermal fluids (Fig. 32.1). This can be theoretically justified by the thermodynamic estimation of potential energy yields of various chemolithotrophic energy metabolisms in the hydrothermal mixing zones of habitats (Nakamura and Takai 2014; Takai and Nakamura 2010, 2011; Nakamura and Takai Chap. 2). Most of potential energy yields of thiotrophic chemolithotrophic metabolisms in the hydrothermal mixing zones are constrained by the dissolved O_2 concentration in the ambient seawater while those of hydrogenotrophic metabolisms are proportionated by the dissolved H_2 concentration in the hydrothermal fluid due to much greater abundances and availability of electron acceptors such as CO_2 and sulfate other than O_2 in the mixing zones (Nakamura and Takai 2014, Chap. 2). Thus, it is predicted that the intra-field variability in the hydrothermal fluid H_2 concentration much more significantly affects the microbial community development in the chimney habitat than the intra-field variability in concentrations of other hydrothermal fluid gas components.

Similarly, the intra-field variability in the microbial community development is perceived in the chimney habitats of the Minami-Ensei field (Fig. 32.1). The abundance and diversity of cultivated microbial communities (e.g., *Thermococcus*, *Nitratiruptor*, *Nitratifractor*, *Persephonella* and *Aquifex* populations) were greater in the No. 7 chimney than in the Jizo chimney (Fig. 32.1). In the Minami-Ensei field, it has been suggested that the hydrothermal fluid chemistry of endmember hydrothermal fluid is little affected by the subseafloor phase-separation and -partition processes (Kawagucci et al. 2013). However, there is found the slight deviation of dissolved gas concentrations in the hydrothermal fluids at different chimney sites probably due to the phase-separation and -partition near the seafloor (Table 32.1) (Kawagucci et al. 2013). Indeed, the dissolved H_2, H_2S and CH_4 concentrations in the hydrothermal fluid are slightly

higher at the No. 7 chimney site than at the Jizo chimney site (Table 32.1). The cultivated microbial populations that represent the intra-field variation of abundance and incidence are known to be capable of growth with hydrogenotrophic and thiotrophic chemolithoautotrophy except for *Thermococcus* (Fig. 32.1). The intra-field variability in the active microbial community significantly associated with phase-separation-induced chemical variation has been demonstrated in the case studies of the Iheya North (Iheya North Knoll) field (Nakagawa et al. 2005) and the Yonaguni Knoll IV (Daiyon-Yonaguni Knoll) field (Nunoura and Takai 2009). Thus, as observed in the Iheya North (Nakagawa et al. 2005) and the Yonaguni Knoll IV fields (Nunoura and Takai 2009), despite the slight differences, the intra-field variation in the hydrothermal fluid gas chemistry may lead to the intra-field variability in the microbial community development in the Minami-Ensei field.

32.4.2 Inter-Fields Variability in Microbial Community Development in the Okinawa Trough

This study shows variability in the microbial communities in the microbial habitats associated with the endmember-like high-temperature hydrothermal fluids in the Izena Hole and Minami-Ensei hydrothermal fields of the Okinawa Trough. Combining the physical and chemical characteristics of hydrothermal fluids determined in the previous studies (Ishibashi et al. 2014; Kawagucci et al. 2013) and the microbial community patterns delineated from this study with the accumulated information in other deep-sea hydrothermal systems of the Okinawa Trough (Tables 32.1 and 32.5), the inter-fields variability in microbial community development is discussed here.

As compared to the cultivated microbial community patterns in the Iheya North and Yonaguni Knoll IV chimney habitats, the abundance and diversity of cultivated microbial community in the Izena Hole Hakurei chimney are comparable with those in the chimney habitats hosting the gas-enriched hydrothermal fluids in the Iheya North and Yonaguni Knoll IV fields (Tables 32.1 and 32.5). These chimney habitats that represent the greater abundance and diversity of cultivated microbial community are characterized by relatively high concentrations of H_2 in the adjacent hydrothermal fluids (0.23 to 2.4 mM H_2) (Table 32.1). In contrast, the cultivated microbial communities in the Minami-Ensei chimney habitats are less abundant and diverse as compared to the cultivated microbial communities in the chimney habitats of other Okinawa Trough deep-sea hydrothermal systems (Table 32.5) and even other global deep-sea hydrothermal systems such as the TOTO Caldera field in the Mariana Volcanic Arc (Nakagawa et al. 2006), the Mariner field in the Lau Basin (Takai et al. 2008) and the Brother Caldera field in the Kermadec Arc (Takai et al. 2009). The less abundant and diverse cultivated microbial communities in the Minami-Ensei field may be caused by the much lower concentration of H_2S in the hydrothermal fluids (<1 mM) as compared to other deep-sea hydrothermal systems. However, the relatively low concentrations of hydrothermal fluid H_2S have been known in the Middle Valley field of the Juan de Fuca Ridge (1.1–1.5 mM) (Von Damm 1995), Rainbow field (1.2 mM) and Logatchev field (0.5–0.8 mM) (Charlou et al. 2002), whereas the occurrences of quite diverse and highly active microbial communities in these deep-sea hydrothermal environments have been strongly pointed by the multidisciplinary biogeochemical and microbiological characterizations (Flores et al. 2011; Frank et al. 2013; Perner et al. 2007, 2013). Rather than the hydrothermal fluid chemistry, the physical properties of the chimney structures and the physical behavior of hydrothermal fluid flow in the chimneys may more significantly affect the indigenous microbial community development. In the Minami-Ensei field, all the chimney structures were very fragile and porous, and the high-temperature hydrothermal fluid discharges were found not from the focused orifices of the chimneys but from whole surface areas of the chimneys. In such chimney structures, it is expected that the hydrothermal mixing is very fluctuated and the microbiologically habitable zones are temporally and spatially unstable due to the frequent exposure to high-temperature hydrothermal fluid flows that would be lethal to the development of indigenous microbial community or the frequent collapse of chimney structures. Indeed, only the quite low abundances of microbial cell density and 16S rRNA gene number were obtained from the chimney structures in the Minami-Ensei field (Table 32.2). The reproduction rate and pattern of microbial communities in the newly created chimney habitats would be influenced by the abundance and diversity of seed microbial populations mainly entrained by the hydrothermal fluids from the ambient hydrothermal mixing fluids and the potential subseafloor microbial communities. Thus, the microbial community development in the deep-sea hydrothermal vent chimneys may be relevant with the age of hydrothermal system and the hydrogeological complexity of subseafloor hydrothermal fluid flow structures that would sustain the potential resilience of chimney and other seafloor microbial communities in the deep-sea hydrothermal systems.

The previous investigations have demonstrated the statistically supported correlation between the dissolved H_2 concentration in hydrothermal fluid and the total culturable population abundance of (hyper)thermophilic hydrogenotrophic methanogens (Takai and Nakamura 2010, 2011). In the analysis including new data obtained in

Table 32.5 Viable cell estimation of each microbial population in chimney microbial communities among different hydrothermal fields in the Okinawa Trough

	Iheya North			Yonaguni		Izena Hole		Minami-Eansei	
	NBC	CBC	E18	Knoll IV	Knoll IV	Jade	Hakurei	Jizo	No. 7
Population density (cells/g)	Chimney & ISCS	Chimney & ISCS	ISCS	BTC & LC	CTC & SW	TBS chimney & ISCS	214 chimney & ISCS	Chimney	Chimney
Thermococcus	5×10^6–3.5×10^7	2.5×10^5–1.8×10^6	100–720	4×10^5–3×10^6	1×10^5–1×10^6	1.3×10^4–9.1×10^4	6.9×10^4–4.8×10^5	1–10	100–1,000
Pyrococcus	20–140	2–15	3–20	20–200	300–2,000	<1	1–8	<1	<1
Methanococcales	90–650	10–70	3,800–2.6×10^4	900–8,000	300–3,000	1–7	1×10^4–7.2×10^4	<1	<1
Archaeoglobus	1.2×10^5–8×10^5	<10	<15	<4	<4	<1	<1	<1	<1
Aquifex	230–1,600	<10	<15	<4	<4	<1	<1	<1	1–10
Persephonella	1.6×10^6–1.2×10^7	7–50	<15	10^4–10^5	300–2,000	2–14	1–7	10–100	10–100
Desulfurobacteria group	<4	6–38	3–20	<4	20–200	<1	30–210	<1	<1
Thermaceae	<4	500–3,500	<15	<4	<4	n.d.	n.d.	n.d.	n.d.
Deferribacter	<4	<10	<15	<4	<4	n.d.	n.d.	n.d.	n.d.
Rhodothermus	<4	<10	<15	<4	<4	n.d.	n.d.	n.d.	n.d.
Tepidibacter	25–180	<10	<15	<4	<4	n.d.	n.d.	n.d.	n.d.
Nautiliales	8×10^4–5.6×10^5	<10	<15	7,000–6×10^4	10^5–10^6	10–76	4×10^4–2.8×10^5	<1	<1
Hydrogenimonas	<4	25–180	<15	900–8,000	2×10^4–2×10^5	<1	410–2,900	<1	<1
Nitratiruptor	2.2×10^5–1.5×10^6	37–260	<15	10^4–10^5	2×10^4–2×10^5	<1	<1	1–10	100–1,000
Nitratifractor	<4	33–230	<15	<4	300–2,000	<1	<1	<1	1–10
Sulfurovum	1.4×10^4–7.3×10^5	7–50	<15	<4	<4	<1	1.2–8.3	<1	<1
Sulfurimonas	5.6×10^5–3.9×10^6	1,800–1.3×10^4	2,500–1.7×10^4	10^7–10^8	7×10^6–6×10^7	1,900–1.3×10^4	210–1,500	<1	<1
Thioreductor	<4	<10	600–4,300	<4	<4	3,700 × 2.6 × 10^4	<1	<1	<1
Sulfurospirillum	<4	<10	<15	<4	<4	700–4,900	3×10^3–2×10^4	<1	<1
Thiomicrospira	<4	<10	<15	<4	300–2,000	<1	<1	100–1,000	10–100
Others	n.d.	n.d.	n.d.	200–2,000	1,000–9,000	n.d.	n.d.	n.d.	n.d.
Reference	Nakagawa et al. (2005)	Nakagawa et al. (2005)	Nakagawa et al. (2005)	Nunoura and Takai (2009)	Nunoura and Takai (2009)	This study	This study	This study	This study

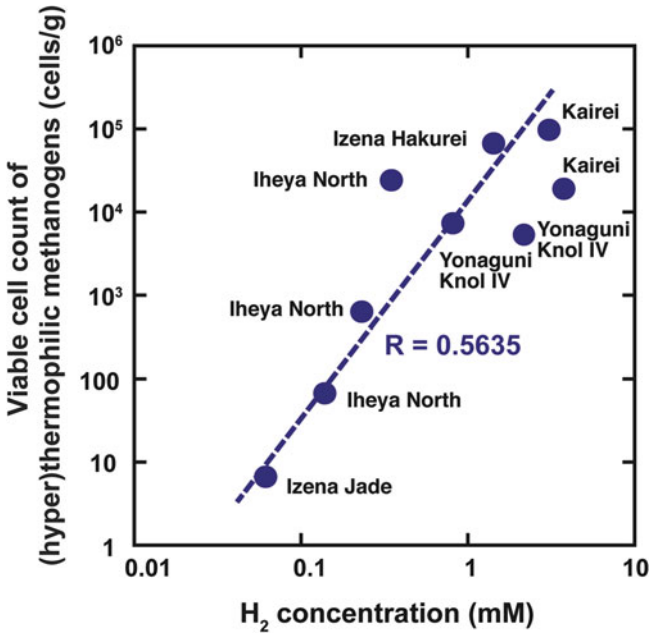

Fig. 32.2 Correlation between cultivated population of the (hyper) thermophilic hydrogenotrophic methanogens and dissolved H_2 concentration in adjacent endmember hydrothermal fluid. Moderate correlation is found between them (*dot line*)

this study (Fig. 32.2), the correlation is statistically validated with a higher regression constant than in the previous studies (Fig. 32.2) (Takai and Nakamura 2010, 2011). The correlation between the dissolved H_2 concentration in hydrothermal fluid and the culturable population abundance of (hyper) thermophilic hydrogenotrophic methanogens can be predicted by the thermodynamic estimation of potential energy yields of various chemolithotrophic energy metabolisms in the hydrothermal mixing zones of habitats (Nakamura and Takai 2014, Chap. 2). The potential energy available for hydrogenotrophic methanogenesis in the hydrothermal mixing zones is primarily dependent on the H_2 input from the hydrothermal fluids since the electron acceptor and carbon source (CO_2) can be supplied both from the hydrothermal fluids and ambient seawater and be more abundant in the hydrothermal mixing zones than H_2 (Nakamura and Takai 2014, Chap. 2). Only if the dissolved O_2, which is lethal to most of the methanogens, is fully removed from the microbial habitats in hydrothermal mixing zones, the productivity of hydrogenotrophic methanogens would be primarily controlled by H_2 concentration in the adjacent hydrothermal fluids. Although greater number of deep-sea vent examples and data will be essential for future study to justify the linkages between microbial community development and chemical characteristics in deep-sea hydrothermal ecosystems, it seems very likely that the H_2 concentration in the hydrothermal fluid is the only chemical factor directly to control the thermodynamic energy potential and the existent biomass and production of the (hyper) thermophilic hydrogenotrophic methanogens in the global deep-sea hydrothermal environments.

Acknowledgments We are grateful to the captain and crews of the research vessel *Natsushima* and the operation teams of the manned submersible *Shinkai 2000* and the remotely operative vehicle *Hyperdolphin* for their technical expertise and safety at sea. We wish to thank onboard scientists of the cruises for their support. This work was supported in part by Grand-in-Aid for Science Research of TAIGA project (No. 20109005) from MEXT, Japan.

References

Campbell BJ, Engel AS, Porter ML, Takai K (2006) The versatile epsilon-proteobacteria: key players in sulphidic habitats. Nat Rev Microbiol 4:458–468

Charlou JL, Donval JP, Fouquet Y, Jean-Baptiste P, Holm N (2002) Geochemistry of high H_2 and CH_4 vent fluids issuing from ultramafic rocks at the rainbow hydrothermal field (36°14′, MAR). Chem Geol 191:345–359

DeLong EF (1992) Archaea in coastal marine environments. Proc Natl Acad Sci U S A 89:5685–5689

Flores GE, Campbell JH, Kirshtein JD, Meneghin J, Podar M, Steinberg JI, Seewald JS, Tivey MK, Voytek MA, Yang ZK, Reysenbach A-L (2011) Microbial community structure of hydrothermal deposits from geochemically different vent fields along the Mid-Atlantic Ridge. Environ Microbiol 13:2158–2171

Frank KL, Rogers DR, Olins HC, Vidoudez C, Girguis PR (2013) Characterizing the distribution and rates of microbial sulfate reduction at Middle Valley hydrothermal vents. ISME J 7:1391–1401

Glasby GP, Notsu K (2003) Submarine hydrothermal mineralization in the Okinawa Trough, SW of Japan: an overview. Ore Geol Rev 23:299–339

Huber JA, Holden JF (2008) Modeling the impact of diffuse vent microorganisms along Mid-Ocean Ridges and Flanks. In: Magma to microbe: modeling hydrothermal processes at oceanic spreading centers, Geophysics Monograph. AGU, Washington, DC, pp 215–231

Hugenholtz P (2002) Exploring prokaryotic diversity in the genomic era. Genome Biol 3, reviews0003.1-0003.8

Ishibashi J, Noguchi T, Toki T, Miyabe S, Yamagami S, Ohnishi Y, Yamanaka T, Yokoyama Y, Omori R, Takahashi Y, Hatada K, Nakaguchi J, Yoshizaki M, Konno U, Shibuya T, Takai K, Inagaki F, Kawagucci S (2014) Similarity and diversity of fluid geochemistry in active hydrothermal fields in the Izena Cauldron, in the middle Okinawa Trough back-arc basin. Geochem J 48:357–369

Kawagucci S, Chiba H, Ishibashi J, Yamanaka T, Toki T, Muramatsu Y, Ueno Y, Makabe A, Inoue K, Yoshida N, Nakagawa S, Nunoura T, Takai K, Takahata N, Sano Y, Narita T, Teranishi G, Obata H, Gamo T (2011) Hydrothermal fluid geochemistry at the Iheya North field in the mid-Okinawa Trough: implication for origin of methane in subseafloor fluid circulation systems. Geochem J 45:109–124

Kawagucci S, Ueno Y, Takai K, Toki T, Ito M, Inoue K, Makabe A, Yoshida N, Muramatsu Y, Takahata N, Sano Y, Narita T, Teranishi G, Obata H, Nakagawa S, Nunoura T, Gamo T (2013) Geochemical

origin of hydrothermal fluid methane in sediment-associated fields and its relevance to the geographical distribution of whole hydrothermal circulation. Chem Geol 339:213–225

Konno U, Tsunogai U, Nakagawa S, Nakaseama M, Ishibashi J, Nunoura T, Nakamura K (2006) Liquid CO_2 venting on the seafloor: Yonaguni Knoll IV hydrothermal system, Okinawa Trough. Geophys Res Lett 33, L16607

Lane DJ (1991) 16S/23S sequencing. In: Stackebrandt E, Goodfellow M (eds) Nucleic acid techniques in bacterial systematics. Wiley, New York, pp 115–176

Letouzey J, Kimura M (1986) The Okinawa Trough: genesis of a back-arc basin developing along a continental margin. Tectonophys 125:209–230

Ludwig W, Strunk O, Westram R, Richter L, Yadhukumar HM, Buchner A, Lai T, Steppi S, Jobb G, Förster W, Brettske I, Gerber S, Ginhart AW, Gross O, Grumann S, Hermann S, Jost R, König A, Liss T, Lüßmann R, May M, Nonhoff B, Reichel B, Strehlow R, Stamatakis A, Stuckmann N, Vilbig A, Lenke M, Ludwig T, Bode A, Schleifer KH (2004) ARB: a software environment for sequence data. Nucleic Acids Res 32:1363–1371

McCollom TM (2007) Geochemical constraints on sources of metabolic energy for chemolithoautotrophy in ultramafic-hosted deep-sea hydrothermal systems. Astrobiol 7:933–950

McCollom TM, Shock EL (1997) Geochemical constraints on chemolithoautotrophic metabolism by microorganisms in seafloor hydrothermal systems. Geochim Cosmochim Acta 61:4375–4391

Nakagawa S, Takai K (2008) Deep-sea vent chemoautotrophs: diversity, biochemistry and ecological significance. FEMS Microbiol Ecol 65:1–14

Nakagawa S, Takai K, Inagaki F, Chiba H, Ishibashi J, Kataoka S, Hirayama H, Nunoura T, Horikoshi K, Sako Y (2005) Variability in microbial community and venting chemistry in a sediment-hosted backarc hydrothermal system: impacts of subseafloor phase-separation. FEMS Microbiol Ecol 54:141–155

Nakagawa T, Takai K, Suzuki Y, Hirayama H, Konno U, Tsunogai U, Horikoshi K (2006) Geomicrobiological exploration and characterization of a novel deep-sea hydrothermal system at the TOTO caldera in the Mariana Volcanic Arc. Environ Microbiol 8:37–49

Nakamura K, Takai K (2014) Theoretical constraints of physical and chemical properties of hydrothermal fluids on variations in chemolithotrophic microbial communities in seafloor hydrothermal systems. Prog Earth Plant Sci 1:1–24

Nunoura T, Takai K (2009) Comparison of microbial communities associated with phase-separation-induced hydrothermal fluids at the Yonaguni Knoll IV hydrothermal field, the Southern Okinawa Trough. FEMS Microbiol Ecol 67:351–370

Perner M, Kuever J, Seifert R, Pape T, Koschinsky A, Schmidt K, Strauss H, Imhoff JF (2007) The influence of ultramafic rocks on microbial communities at the Logatchev hydrothermal field, located 15 degrees N on the Mid-Atlantic Ridge. FEMS Microbiol Ecol 61:97–109

Perner M, Hansen M, Seifert R, Strauss H, Koschinsky A, Petersen S (2013) Linking geology, fluid chemistry, and microbial activity of basalt- and ultramafic-hosted deep-sea hydrothermal vent environments. Geobiol 11:340–355

Reysenbach A-L, Banta AB, Boone DR, Cary SC, Luther GW (2000) Microbial essentials at hydrothermal vents. Nature 404:835–845

Shock EL, Holland ME (2004) Geochemical energy sources that support the subsurface biosphere. In: Wilcock WSD, Delong EF, Kelley DS, Baross JA, Cary SC (eds) The subseafloor biosphere at mid-ocean ridges, vol 144, Geophysics monograph series. AGU, Washington, DC, pp 153–165

Suzuki Y, Inagaki F, Takai K, Nealson KH, Horikoshi K (2004) Microbial diversity in inactive chimney structures from deep-sea hydrothermal systems. Microbial Ecol 47:186–196

Suzuki R, Ishibashi J, Nakaseama M, Konno U, Tsunogai U, Gena K, Chiba H (2008) Diverse range of mineralization induced by phase separation of hydrothermal fluid: case study of the Yonaguni Knoll IV hydrothermal field in the Okinawa Trough back-arc basin. Res Geol 58:267–288

Takai K, Horikoshi K (2000) Rapid detection and quantification of members of the archaeal community by quantitative PCR using fluorogenic probes. Appl Environ Microbiol 66:5066–5072

Takai K, Nakamura K (2010) Compositional, physiological and metabolic variability in microbial communities associated with geochemically diverse, deep-sea hydrothermal vent fluids. In: Barton LL, Mandl M, Loy A (eds) Geomicrobiology: molecular and environmental perspective. Springer, New York, pp 251–283

Takai K, Nakamura K (2011) Archaeal diversity and community development in deep-sea hydrothermal vents. Curr Opin Microbiol 14:282–291

Takai K, Inoue A, Horikoshi K (1999) *Thermaerobacter marianensis* gen. nov., sp. nov., an aerobic extremely thermophilic marine bacterium from the 11,000 m deep Mariana Trench. Int J Syst Bacteriol 49:619–628

Takai K, Inoue A, Horikoshi K (2000) *Thermosipho japonicus* sp. nov., an extremely thermophilic bacterium isolated from a deep-sea hydrothermal vent in Japan. Extremophiles 4:9–17

Takai K, Moser DP, Deflaum M, Onstott TC, Fredrickson JK (2001) Archaeal diversity in waters from deep South African gold mines. Appl Environ Microbiol 67:5750–5760

Takai K, Inoue A, Horikoshi K (2002) *Methanothermococcus okinawensis* sp. nov., a thermophilic, methane-producing archaeon isolated from a Western Pacific deep-sea hydrothermal vent system. Int J Syst Evol Microbiol 52:1089–1095

Takai K, Inagaki F, Nakagawa S, Hirayama H, Nunoura T, Sako Y, Nealson KH, Horikoshi K (2003) Isolation and phylogenetic diversity of members of previously uncultivated epsilon-*Proteobacteria* in deep-sea hydrothermal fields. FEMS Microbiol Lett 218:167–174

Takai K, Gamo T, Tsunogai U, Nakayama N, Hirayama H, Nealson KH, Horikoshi K (2004) Geochemical and microbiological evidence for a hydrogen-based, hyperthermophilic subsurface lithoautotrophic microbial ecosystem (HyperSLiME) beneath an active deep-sea hydrothermal field. Extremophiles 8:269–282

Takai K, Nakagawa S, Reysenbach AL, Hoek J (2006) Microbial ecology of mid-ocean ridges and back-arc basins. In: Christie DM, Fisher CR, Lee SM, Givens S (eds) Back-arc spreading systems: geological, biological, chemical and physical interactions, vol 166, Geophysics monograph series. AGU, Washington, DC, pp 185–213

Takai K, Nunoura T, Ishibashi J, Lupton J, Suzuki R, Hamasaki H, Ueno Y, Kawagucci S, Gamo T, Suzuki Y, Hirayama H, Horikoshi K (2008) Variability in the microbial communities and hydrothermal fluid chemistry at the newly-discovered Mariner hydrothermal field, southern Lau Basin. J Geophys Res 113, G02031

Takai K, Nunoura T, Horikoshi K, Shibuya T, Nakamura K, Suzuki Y, Stott M, Massoth GJ, Christenson BW, de Ronde CEJ, Butterfield DA, Ishibashi J, Lupton JE, Evans LJ (2009) Variability in microbial communities in black smoker chimneys at the NW caldera vent field, Brothers volcano, Kermadec arc. Geomicrobiol J 26:552–569

Von Damm KL (1995) Diffuse flow hydrothermal fluids from 9°50′N East Pacific rise: origin, evolution and biogeochemical controls. In: Humphris SE, Zierenberg RA, Mullineaux LS, Thomson RE (eds) Seafloor hydrothermal systems, vol 144, Geophysics monograph series. AGU, Washington, DC

In Situ Determination of Bacterial Growth in Mixing Zone of Hydrothermal Vent Field on the Hatoma Knoll, Southern Okinawa Trough

33

Hiroyuki Yamamoto, Tomoko Maruyama, László G.-Tóth, Kenji Kato, Yasuo Furushima, Naoto Taira, Yoshiaki Maeda, and Kiminori Shitashima

Abstract

The doubling time of indigenous bacteria in mixing-zone of hydrothermal fluid and seawater was determined using a diffusion chamber unit deployed on the field of Hatoma Knoll (24° 51.50′N, 123° 50.50′ E), which is a submarine volcano located on southern Okinawa Trough. The diffusion chamber is a reliable tool to incubate and to directly measure the microbial growth under in situ condition of deep-sea, although an operation of submersible and a complicated preparation of seed water became the technical constraints. The doubling time at non-vent site distant from active vent site was estimated from 86 to 110 h, while at active vent sites more rapid doubling time, 21–32 h, were estimated. A potential sulfur-oxidizing bacteria belonging to *Epsilonproteobacteria* dominated the population grew in the chambers, which were incubated using the plume water obtained from the mixing zone between the vent fluid and seawater, and Bathymodiolus colony, while no detection of *Gammaproteobacteria*. The methane-oxidizing bacteria were detected only from gill and digestive tract of *Bathymodiolus platifrons*, and could not be detected from the chamber, although the chamber was placed on Bathymodiolus colony. The results of this study suggested that chemolithoautotrophic growth near by the hydrothermal vent is sustained by the rapid doubling time of *Epsilonproteobacteria* using chemical species dissolved in fluid and provides the chemo-autotrophic product to deep-sea benthopelagic community, as well as a microbial products in hydrothermal vent plume.

Keywords

Diffusion chamber • Hydrothermal vent • Microbial growth rate • Okinawa Trough

The online version of this chapter (doi:10.1007/978-4-431-54865-2_33) contains supplementary material, which is available to authorized users.

H. Yamamoto (✉)
Environmental Impact Assessment Research Group, R&D Center for Submarine Resources, Japan Agency for Marine-Earth Science Technology (JMSTEC), 2-15 Natsushima-Cho, Yokosuka, Kanagawa 237-0061, Japan

T. Maruyama • K. Kato
Faculty of Science, Shizuoka University, Shizuoka, Japan

L. G.-Tóth
Faculty of Science, Balaton Limnological Research Institute of the Hungarian Academy of Sciences, Tihany, Hungary

Y. Furushima
Environmental Impact Assessment Research Group, R&D Center for Submarine Resources, Japan Agency for Marine-Earth Science Technology (JMSTEC), Kanagawa, Japan

N. Taira
University of the Ryukyus, Okinawa, Japan

Y. Maeda
Civil Engineering Research and Environmental Studies (CERES Inc.), Chiba, Japan

K. Shitashima
International Institute for Carbon-Neutral Energy Research, Kyushu University, Fukuoka, Japan

J.-i. Ishibashi et al. (eds.), *Subseafloor Biosphere Linked to Hydrothermal Systems: TAIGA Concept*,
DOI 10.1007/978-4-431-54865-2_33,

33.1 Introduction

The discovery of high-density animal aggregations in the vicinity of hydrothermal vents of the Galapagos Rift (Corliss et al. 1979; Lonsdale 1977) raised many questions for the mechanism to sustain the ecosystem, especially for the source of primary production. Chemosynthesis of prokaryotes, depending on the inorganic chemical reaction between hydrothermal fluid and seawater, has been recognized major energy source of primary production in the hydrothermal ecosystems (Jannasch and Mottl 1985; Karl et al. 1980). Growth rate of microbial community in hydrothermal system is most useful data to qualify a primary production by chemosynthesis.

Potential chemical energy for the chemolithoautotrophic growth has been calculated by chemical thermodynamics based on geochemical data of hydrothermal fluids (Amend and Shock 1998; Jannasch and Mottl 1985; McCollom 2000; McCollom and Shock 1997; Schmidt et al. 2008). The primary production based on chemical energy sustains the huge biomass in megafauna and their rapid growth rate, for examples, 85 cm/year determined by tube length of *Riftia pachyptila* (Lutz et al. 1994), 10 cm/year growth and long lived of *Lamellibrachia* sp. (Bergquist et al. 2000), a biomass of the mussel bed exceeded 70 kg/m^2 of weight at Logatchev area (Gebruk et al. 2000). The biomass of endosymbiotic bacteria in such invertebrates determined by quinone biomarker suggested sustainable power of chemosynthetic primary production (Yamamoto et al. 2002), despite no data of microbial growth rate directly measured from the symbionts.

Investigation of in situ growth of free-living microbial community in ocean habitats is difficult yet due to the non-culturable or slow growing physiology in majority of marine prokaryotes. Several parameters without traditional cultivation methods have been used to estimate microbial growth rate, e.g. microscopic cell density and cell size, adenosine 5′-triphosphate (ATP), assimilation rate of isotope labeled substrates (Karl et al. 1980; Kirchman 2001; Malmstrom et al. 2005; Torrton and Dufour 1996), microbial mat formation based on time-series observation (Taylor et al. 1999), frequency of dividing cells (Newell and Christian 1981), macromolecular synthesis (Torrton and Dufour 1996), whole-genome microarray analysis (Holmes et al. 2013). These methods were applied in the hydrothermal environments (Jannasch and Mottl 1985; Karl et al. 1980) as well as general oceanic environments, and the calibration methods to convert growth rate or doubling time from these parameters have been developed (Kirchman 2001; Sherr et al. 1999; Torrton and Dufour 1996; Yokokawa et al. 2004).

Another technical issue to determine microbial growth rate in deep-sea hydrothermal vent is an incubation method under in situ physical and chemical conditions. The so-called pressure simulated in situ incubation system equipped in laboratory was used to determine the indigenous heterotrophic marine bacteria isolated from 75 to 5,550 m depth (Carlucci and Williams 1978; Williams and Carlucci 1976). The in situ chamber approach is a convenient method to incubate the indigenous microbes under original habitat condition. It has been applied in deep-sea expeditions for hydrothermal vents, and successfully isolated and/or accumulated novel chemolithotrophic bacteria (Higashi et al. 2004; Reysenbach et al. 2000; Takai et al. 2003). Of theses several types of in situ chambers, a diffusion chamber is a very useful apparatus for in situ physiological experiments of microbes (Bollmann et al. 2007; McFeters and Stuart 1972; Vasconcelos and Swartz 1976), in situ determination of growth rate of phytoplankton (Furnas 1991) and thermophiles in alkaline geothermal pool (Kimura et al. 2010).

In this study, in situ experiments using a diffusion chamber unit were carried out on Hatoma Knoll in southern Okinawa Trough to estimate the state of microbial growth in mixing-zone of hydrothermal vent area on the knoll.

33.2 Materials and Methods

33.2.1 Sample Collection

The in situ incubation experiments were conducted during three cruises, NT01-05, NT02-07, and NT04-03 at hydrothermal and methane seep areas on the southern Ryukyu Archipelago. In these cruise, water samples were collected and prepared for the in situ experiments using diffusion chamber, and deployed the chambers in the following sites; a vent field of the Hatoma Knoll (24° 51.500′ N, 123° 50.500′ E) and a methane seep field of the Kuroshima Knoll (24° 8.000′ N, 124° 11.500′ E). Hatoma Knoll is a submarine volcano located in the southern Okinawa Trough of the southwestern Ryukyu arc. Hydrothermal activity of the Hatoma Knoll has been discovered at a rim and a center mound of horse-shoe shaped caldera on the knoll at 1,490–1,530 m in the deep-sea expedition of 1999 and 2000 (Watanabe 2001). Prominent hydrothermal activity occurs over a central mound and created two big-chimneys with discharge of high temperature fluid up to max. 300 °C (Table 33.1, Suppl. 33.1). These two big-chimneys collapsed in July of 2006. Kuroshima Knoll is a methane seep field located in the south of Ishigaki-island and isolated from island shelf. It was used as reference site for in situ growth chamber experiments in NT04-03 cruise. The gas bubbles were rising from the Bathymodiolus colony of deep-sea mussels at seafloor of 600–700 m in water-depth.

Table 33.1 Physicochemical profile and microbial cell counts in the water column on hydrothermal vent area of Hatoma Knoll determined in the dive expedition of HPD#295, NT04-03

Depth (m)	Temp. (°C)	Salinity (‰)	pH	SiO_2 (mM)	H_2S (mM)	CH_4 (nmol/kg)	delta^{13}C-CH_4 (‰)	total-Hg (ppt)	Turbidity (FTU)	TDC (cells/mL)
5	25.36	34.55	nd	nd	nd	nd	nd	nd	nd	1.9×10^5
1,365	3.94	34.54	7.65	0.112	<1	40	−45.2	14	15	1.4×10^4
1,365	3.93	34.48	7.60	0.109	<1	62	−43.5	13	19	2.4×10^4
1,400	3.91	34.54	7.60	0.089	<1	324	−49.5	24	36	9.6×10^3
1,400	3.91	34.54	7.54	0.126	<1	5,870	−49.5	56	92	2.2×10^4
1,400	3.97	34.54	7.35	0.092	2.021	4,550	−49.7	17	88	1.0×10^4
1,435	3.90	34.54	7.53	0.088	<1	3,120	nd	18	103	1.7×10^4
1,435	3.89	34.54	7.44	0.125	<1	3,140	nd	18	158	1.9×10^4
1,435	3.88	34.54	7.58	0.101	<1	135	nd	16	23	2.5×10^4
1,436	3.89	34.54	7.58	0.096	<1	354	nd	15	22	1.8×10^4
1,461	3.86	34.52	7.52	0.123	<1	1,760	−49.4	25	168	2.0×10^4
1,468	3.86	34.54	7.64	0.094	<1	742	nd	nd	143	nd
1,476	6.24	33.20	6.36	0.132	2.134	45,100	−49.9	37	156	2.8×10^4
1,475	300	nd	5.08	2.157	10.437	nd	nd	nd	nd	nd

nd no data

The water samples were collected either by a Niskin bottle sampler, ORI manifold sampler or syringe type water sampler using the human occupied vehicle (HOV) Shinkai 2000, or remotely operated vehicle (ROV) Hyper-Dolphin 3000. The sample of deep-sea mussel, *Bathymodiolus platifrons*, was collected in NT03-09 to analyze the microbial flora of gill and digestive tract. The video footages recorded whole operations on the experiment sites of NT01-05 and NT02-07 were accessible at the JAMSTEC E-library of Deep-sea Images (http://www.godac.jamstec.go.jp/jedi). The identification codes for video clips are "2K1270SHDB4028", and "2K1353SHDB6021" for Shinkai 2000 dives, respectively. The video clips of ROV dives of 2003 and 2004 are yet preparing in 2013.

33.2.2 Preparation and In Situ Experiment Using a Diffusion Chamber

The diffusion-chamber based approach was applied for determination of microbial growth under in situ condition of deep-sea hydrothermal vent field. The chamber was designed to make a cultivation space (ca. 35 mL) sealed with polycarbonate membrane filter (0.2 μm-pore-size), which permit to exchange chemicals and organic matters between inside and outside of the chamber (Fig. 33.1). The chamber was filled with 0.2 μm filter-sterilized seawater, which was collected from the experimental site. No artificial supplement was added in the chamber. Both of the prepared chamber and the seeds-water were preserved in 4 °C until the time to next dive for chamber experiment. Just before a dive the chambers were inoculated with the seed-water (Fig. 33.1), the chambers set in the canister were settled in the payload container filled with cold seawater, transported by the deep-sea submersibles, and placed on the experiment sites. For this experiment, three kinds of seeds-water specimens were collected respectively from the mixing zone of 1 m heights on vent, within the Bathymodiolus colony, and the surface seawater as negative reference. In the growth experiment, a seed-water filtered by 1 μm pore size membrane filter was prepared to examine an effect of protista predation on microbial growth rate. In the cruise of NT04-03, compact thermometer (MDS-MkV/T, JFE Advantech Co., Ltd.) was attached on the canister for determination of temperature fluctuation during in situ incubation experiments (Suppl. 33.2).

33.2.3 Microbial Population and Growth

The cells fixed with 1 % paraformaldehyde were collected on polycarbonate membrane (0.2 μm-pore-size), and stained with acridine orange or DAPI (Hobbie et al. 1977). The microbial cells were observed using epifluorescence microscopy (BX50, Olympus Corp.) and counted 100 microscopic fields per filter sample.

Doubling time and growth rate constant are index for microbial growth rate, and generally calculated from the data during the exponential growth phase having a constant interval of cell dividing (Powell 1956). Our experiment did not provide the time course population growth and we could not determine the exponential growth phase precisely. In this study, we used the initial and final microbial cell densities by regarding that they were in exponential phase. The incubation time was counted from the time of the chamber deployed on seafloor. The generation time, doubling time,

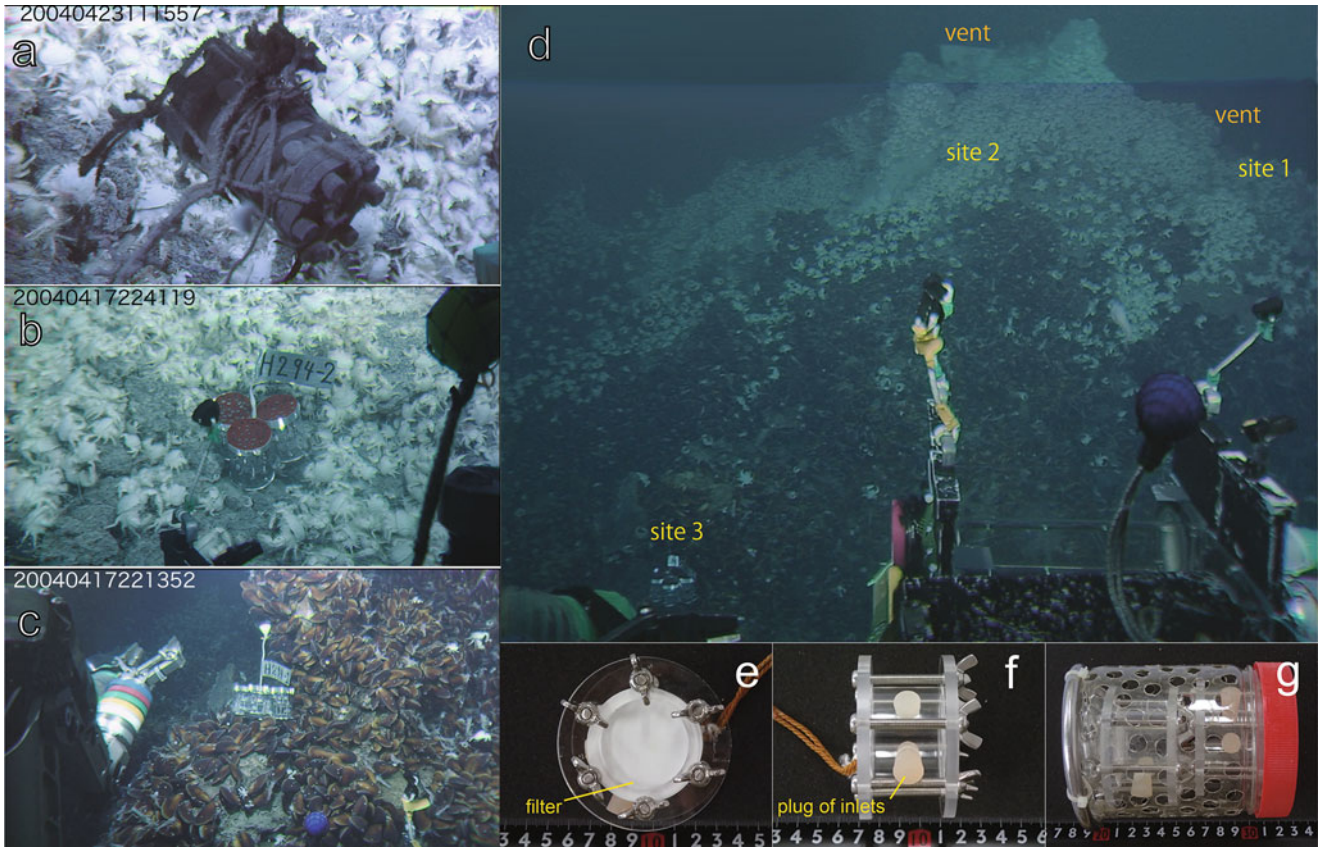

Fig 33.1 In situ experiment conducted in NT04-03 cruise at hydothermal vent of Hatoma Knoll. (**a**) Chamber on hydrothermal vent (site 1), (**b**) canisters contained chambers in aggregation of *Shinkaia crosnieri* (site 2), (**c**) canisters contained chambers settled in Bathymodiolus colony (site 3), (**d**) location of hydrothermal vents and experiments sites on the moud, (**e**, **f**) profile of chamber with membrane filter, and (**g**) punched canisters contained chambers

and growth rate constant are calculated from the following equation:

$$generations = \frac{log_{10}N_t - log_{10}N_0}{log_{10}2}$$

$$doubling\ time = \frac{incubation\ time}{generations}$$

$$growth\ rate\ constant\ (\mu) = \frac{\ln 2}{doubling\ time}$$

N_0: initial cell density, N_t: cell density at the end of indubation

33.2.4 16S rRNA Gene Based Analysis by DGGE and DNA Sequencing

The chamber-incubated-microbes were precipitated by centrifugation. Crude DNA of the microbial cell was extracted by phenol-chloroform-isoamylalcohol solution and purified with a GFX genomic blood DNA purification kit (Amersham Pharmacia biotech, USA). Digestive tract contents and gill tissue specimens were collected from dissected sample of *Bathymodiolus platifrons,* and washed in TE-buffer (10 mM Tris-hydrochloride, 1 mM EDTA (pH 8.0)) and DNA was extracted according to a previously described method (Yamamoto et al. 2002). Denaturing gradient gel electrophoresis (DGGE) was performed on a D-code apparatus (Bio-Rad, Hercules, Calif.). Extracted and purified DNA was used as templates for amplification by the universal DGGE primers targeted to V3 region of 16S rRNA gene of domain Bacteria (341F-GC: 5′-CGCCCGCCGCGCGCGGCGGGCGGGGCG GGGGCACGGGGGGCCTACGGGAGGCAGCAG and 53 4R: 5′-ATTACCGCGGCTGCTGG). The annealing temperature was set at 10 °C above the expected annealing temperature and lowered with 1 °C every second cycle until a touchdown at 55 °C (30 cycle) (Muyzer et al. 1993). PCR products were loaded onto 10 % (wt/vol) polyacrylamide gels (37.5:1, acrylamide-bisacrylamide) in 1× Tris-acetate-EDTA (TAE), (containing 40 mM Tris, 20 mM acetic acid, and 1 mM EDTA) with a denaturing gradient ranging from 30 to 55 % denaturant (100 % denaturant contains 7 M urea and 40 % (vol/vol) formamide in 1× TAE). The PCR amplicons were electrophoresed at 60 °C and 200 V for 3.5 h. The gel was

stained with SYBR Green I (Molecular Probes) for 30 min. DGGE bands were excised from the gel and re-amplified using the aforementioned primer set. The PCR products were purified using a QIAquick PCR purification kit (Qiagen, Germany). The sequences of the DGGE bands were determined for both strands using an ABI model 377 (Applied Biosystems, USA) or a CEQ2000XL DNA analysis system (Beckman Coulter, USA). The sequence data were checked for chimeric artifacts and were analyzed by a modular system for evolutionary analysis, MESQUITE v2.75 (http://mesquiteproject.org) (Maddison 2004).

33.2.5 Physicochemical Conditions

The conductivity, temperature, and pressure were determined by SBE 911 plus (Sea-Bird Electronics, Inc.) or Micro-CTD (Falmouth Scientific, Inc.). The turbidity was measured by turbidity meter (Seapoint, Inc.). We also used a pH sensor which uses an ion-sensitive field- effect transistor (ISFET) as the pH electrode, and a chloride ion selective electrode (Cl-ISE) as the reference electrode (Shitashima et al. 2008). The concentration of H_2S was measured with colorimetry using the methylene blue method (Guenther et al. 2001). Determination of CH_4 was conducted using an automated CH_4 analysis system (DKK corporation, GAS-1061), which consists of a purge unit, a trap unit, and a gas chromatograph with FID (flame ionization detector) after separation by a packed column (Porapak Q 60/80 mesh, 3 mm i.d. × 4 m) (Ishibashi et al. 1997). Sensitivity of the FID was calibrated every day using a working standard gas from which CH_4 concentration had determined. Dissolved total mercury was determined by cold-vapor atomic absorption spectrometry (CVAAS). Dissolved mercury is reduced to zerovalent Hg (Hg^0) by $SnCl_2$ under the acid condition. The zerovalent mercury ion has low solubility and rapidly vaporized by air bubbling. Vaporized mercury is introduced to detection cell and measured the absorbance in 253.7 nm. We used a CVAAS system (RA-3220, Nippon Instruments Co.) and vaporized procedure was modified with Bloom and Crecelius (1983) (Bloom and Crecelius 1983). 5 mL of seawater sample were mixed with 0.5 mL of 50 % H_2SO_4 (analytical grade, Kanto Chemical) and 0.5 mL of 10 % $SnCl_2$ (analytical grade, Kanto Chemical) in closed glass vial. We started the bubbling with mercury free air and logging of Hg^0 absorbance (253.7 nm) just after the reagents addition. 1,000 ppm $HgCl_2$ standard solution for atomic absorption spectrometry (Kanto Chemical) diluted for calibration. To prevent mercury oxidation and/or reduction during storage of standard solution, L-cysteine was added into each standard solution.

33.2.6 Nucleotide Sequence Accession Numbers

The nucleotide sequences of 16S rRNA genes amplified from the DGGE bands (150–190 bp) have been deposited in the DDBJ database under accession numbers AB207847 to AB207866.

33.3 Results

33.3.1 Environmental Conditions of Hydrothermal Vent Site

Physicochemical factors were measured in NT04-03 cruise. Ambient temperature during in situ incubation on vent fauna habitat fluctuated between 3.9 °C and 4.9 °C with an interval corresponding to tidal cycle (Suppl. 33.2). High concentration of methane (45 μmol kg^{-1}) and hydrogen sulfide (2 mM) dissolved in the vent fluid were detected in the mixing zone of vent side and in the plume of Hatoma Knoll (Table 33.1). The vent plume at 1-m height from vent showed physical and chemical anomaly in cell count, turbidity, total Hg and methane. The high concentration of hydrogen sulfide was detected in the vent fluid and two samples of the hydrothermal plum from 1,476 and 1,400 m. The 324 nmol kg^{-1} of methane concentration was detected, and $\delta^{13}C$ of the methane was range within 49 ‰. A 56 ppt of total Hg was detected even at 1,400 m in water depth. The signatures of hydrothermal fluid clearly declined at water depth of 1,365 m.

33.3.2 Estimation of the Growth Rate Using Diffusion Chamber System

The in situ incubation experiments using the diffusion chambers were carried out in three cruises under different settings (Table 33.2). The onboard preservation time of a prepared chamber and a seeds-water was varied from 16 to 18 h for next submersible dive to deploy the chambers onto seafloor. In the result of NT01-05 cruise, the filtered seed-water induced an effect to shorten the doubling time, and similar effect was detected in the following experiments in NT04-03. The results of NT02-07 showed longer doubling time, 31–32 h, in two times longer incubation days than the case of NT01-05. The results of NT04-03 showed that the most rapid rate, 21 h, was recorded from the chambers placed at vent side, while the growth rate slowed down significantly to 110 h at Bathymodiolus colony in 3–5 m distance from hydrothermal vent (Fig. 33.1). The microbial growth in the chambers inoculated with seed-water from the surface (5 m depth) failed completely under hydrothermal

Table 33.2 In situ experiments of diffusion chamber for determination of microbial growth

Origin of seed-water	Incubation sites	Depth (m)	Temp. (°C)	TDC (cells/mL)		Incubation (day)	DT (h)	GR (day^{-1})
				At initial	At end			
Hatoma Knoll								
NT01-05 (2K1270)								
Colony	Vent side	1,523	150 [*1]	1.9×10^4	3.4×10^6	7	22.5	0.74
Colony	Vent side	1,523	150 [*1]	1.9×10^4	3.7×10^6	7	22.2	0.75
f-colony	Vent side	1,523	150 [*1]	1.6×10^4	3.4×10^6	7	21.9	0.76
f-colony	Vent side	1,523	150 [*1]	1.6×10^4	3.6×10^6	7	21.6	0.77
NT02-07 (2K1354)								
Plume	Vent side	1,473	80 [*1]	4.3×10^3	4.5×10^6	13	31.2	0.53
Plume	vent side	1,473	80 [*1]	4.3×10^3	3.2×10^6	13	32.8	0.51
NT04-03 (HPD294)								
Plume	Vent side	1,477	97.27[*1]	9.2×10^3	9.7×10^5	6	21.4	0.78
Plume	Shinkia site	1,477	4.17	9.2×10^3	2.9×10^4	6	86.6	0.19
Plume	Bathymodiolus site	1,479	3.93	9.2×10^3	2.3×10^4	6	109.8	0.15
Colony	Shinkia site	1,477	4.20	5.5×10^3	1.4×10^4	6	110.2	0.15
f-colony	Shinkia site	1,477	4.20	5.5×10^3	1.7×10^4	6	89.6	0.19
Colony	Bathymodiolus site	1,479	3.90	5.5×10^3	1.5×10^4	6	100.4	0.17
f-colony	Bathymodiolus site	1,479	3.90	5.5×10^3	1.2×10^3	6	−67.6	−0.25
Surface	Bathymodiolus site	1,479	3.90	1.5×10^4	4.7×10^3	6	−86.1	−0.19
f-surface	Bathymodiolus site	1,479	3.90	1.5×10^4	4.4×10^3	6	−81.0	−0.21
Kuroshima Knoll								
NT04-03 (HPD291)								
Seep	Bathymodiolus site	641	7.56	3.3×10^4	5.7×10^6	10	32.4	0.51
Colony	Bathymodiolus site	641	7.56	7.9×10^3	4.5×10^6	10	26.2	0.63
Surface	Bathymodiolus site	641	7.56	3.0×10^4	2.1×10^6	10	39.0	0.43
f-seep	Bathymodiolus site	641	7.56	1.3×10^4	6.8×10^5	10	42.4	0.39
f-colony	Bathymodiolus site	641	7.56	7.8×10^3	5.6×10^6	10	25.3	0.66
f-surface	Bathymodiolus site	641	7.56	4.7×10^4	5.1×10^5	10	69.8	0.24

f-: filtrated by 1 μm pore-sized-filter
TDC total direct count, *DT* doubling time, *GR* growth rate constant
NT: cruise ID of R/V Natsushima, 2K: dive ID of Shinkai 2000, HPD: dive ID of Hyper-Dolphin 3000
[*1]The temperature records on vent side were measured in vent orifice, not in the chamber

vent conditions in 1,449 m depth on Hatoma Knoll, while they grew under methane seep field in 641 m depth on Kuroshima Knoll.

33.3.3 Phylogenetic Analysis of Indigenous Bacteria

The seed-waters contained many bacterial taxon groups and the physicochemical condition in mixing zone accelerated the growth of several group in the chambers (Fig. 33.2). The bacterial phylogeny of 16S rRNA gene isolated in the DGGE bands from the samples of incubated chambers and the specimens of *B. platifrons* shown that three taxa, *Mollicutes*, *Gammaproteobacteria*, and *Epsilonproteobacteria* were dominant groups (Fig. 33.3). The 16S rRNA gene sequences belonging to *Mollicutes* were found only in the specimens from digestive tract of *B. platifrons*. The 16S rRNA gene sequences belonging to methanotroph of *Gammaproteobacteria* were only isolated from *B. platifrons*, and no thioautotroph type of *Gammaproteobacteria* appeared in the chambers incubated under the condition of mixing zone on the vent area. The 16S rRNA gene sequences belonging to *Epsilonproteobacteria* were discovered from specimens of the digestive tract and the chambers incubated with seed water from plume and Bathymodiolus colony.

33.4 Discussion

The data of microbial growth rate of deep-sea zone were previously determined by a simulated in situ incubation system equipped in laboratory. As shown in Table 33.3, the microbial growth rate in ocean gradually declined with water depth (Carlucci and Williams 1978; Lochte and Turley 1988). The oligotrophic growth of indigenous bacteria in unsupplemented seawater of North Pacific Ocean was quite longer doubling time, 145 h, under 1,500 m depth pressured

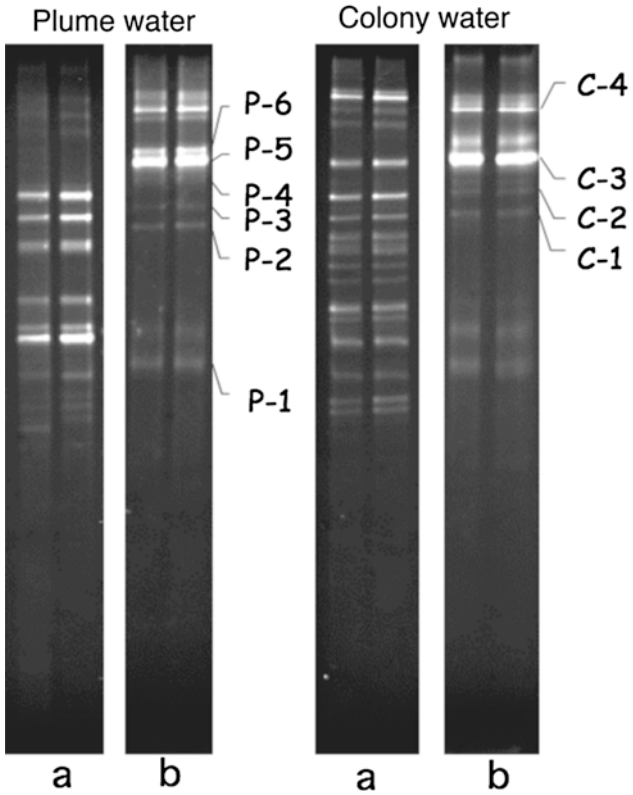

Fig 33.2 DGGE band patterns of the water sample before (**a**) and after (**b**) the incubation with the seeds water collected from plume and Bathymodiolus colony. P is meaning "plume water", C is meaning "colony water". The DGGE bands with ID numbers, P- and C-, in the lane (**b**) were applied to DNA sequencing

condition (Carlucci and Williams 1978). In the same depth zone of hydrothermal vent area in Hatoma Knoll, the doubling time at non-vent site distant from the active vent were estimated from 86 to 110 h, while at active vent sites 21–32 h doubling time were estimated. The phytodetritus and marine snow provides eutrophic microhabitat for microbial community. The microbial growth determined in such microhabitats under simulated deep-sea condition showed quite rapid doubling times from 10 to 11 h (Lochte and Turley 1988). The photosynthetic product is an effective substrate of bacterial community in pelagic ocean, but its efficiency to sustain the population size declined with water depth (Steinberg et al. 2008).

The bacterivorous protozoa are common member of microbial community even in deep-sea zone (Turley and Carstens 1991; Turley et al. 1988). In this study, although any protozoa by microscopic observation could not be observed, probably due to small population size in the sample, the evidence of bacterivorous activity in hydrothermal system was detected as rapid growth rate in the result of chamber incubation inoculated with filtered seedwater, which was eliminated protozoan sized cells. The microbes of surface seawater did not grow in the chambers placed on the hydrothermal vent field, while grow on the methane seep area on Kuroshima Knoll. The toxicity of hydrogen sulfide and mercury (Pracejus and Halbach 1996) in hydrothermal fluid may be an effective agent to regulate the microbial growth, rather than the water depth and temperature.

The growth rate of thermophiles inhabiting an 85 °C geothermal pool has been measured by the similar in situ diffusion chamber tool, and recorded a range from 20 to 39 h doubling time under 0.2 mM sulfide in geothermal fluid (Kimura et al. 2010). This range was a comparable result determined in 2 mM sulfide in the hydrothermal vent of Hatoma Knoll. While the phylogenetic composition and the physical conditions are quite different between geothermal and hydrothermal systems, they showed very similar range of the doubling times.

The onboard preservation time of the prepared chamber and the seeds-water was unavoidable technical issue of deep-sea submersible operation. This factor may induce unlike physiological condition and be affected the results of growth rate estimation, although the inoculation of seeds-water was performed just before each dive operation. To determine accurate growth rate, the time course in situ experiment with frequent sampling will be needed.

The the 16S rRNA gene sequences of potential sulfur-oxidation bacteria belonging to *Epsilonproteobacteria* were detected in the chambers incubated with plume water and colony water (Fig. 33.3), while the sequences of *Gammaproteobacteria* appeared in the chamber incubated with the colony water. The *Epsilonproteobacteria* have been known as common member discovered from benthic mixing zone of hydrothermal system (Campbell et al. 2006), and a majority of epibiotic microbial community on *Sinkaia crosnieri* (Tsuchida et al. 2010; Watsuji et al. 2010). The free-living *Gammaproteobacteria*, SUP05 potential sulfur oxidizing phylotype, dwelled in hydrothermal system have been discovered as common member in chemoautotrophic group of hydrothermal plume (Dick et al. 2013; Sunamura et al. 2004). The different ecophysiological functions between *Epsilonproteobacteria* and *Gammaproteobacteria* probably induced the habitat segregation within hydrothermal system (Nakagawa and Takai 2008; Yamamoto and Takai 2011).

The clade of *Epsilonproteobacteria* consists of many ecotypes include symbiont with marine invertebrates (Dubilier et al. 2008; Tokuda et al. 2008; Tsuchida et al. 2010), pathogen or normal flora of animals, and free-livings (Campbell et al. 2006). In this study, the 16S rRNA gene sequences of *Epsilonproteobacteria* from a digestive tract of the Bathymodiolus have either possibility of a feed from mixing-zone bacterial population or a member of normal flora (Egas et al. 2012; Van Horn et al. 2011).

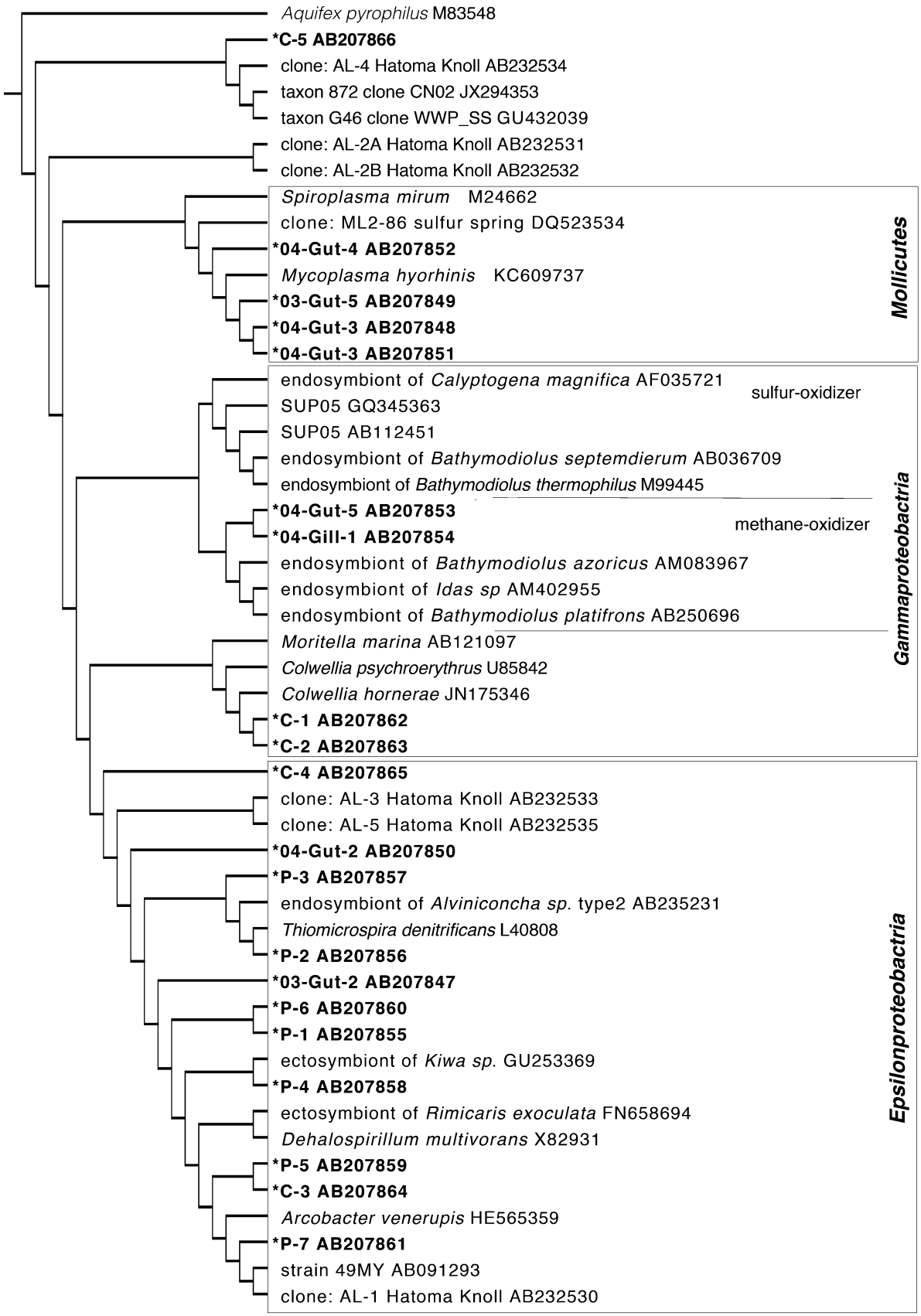

Fig 33.3 Cladogram of phylogenetic clusters for 16S rRNA sequences. The sequences with *asterisk* are DNA from DGGE gel in this study. Abbreviation of the sequences: "Gill" is the gill tissue, "Gut" is the content of digestive tract, "P" is the chamber samples incubated with seed-water of plume, "C" is the chamber samples incubated with seed-water from Bathymodiolus colony

Table 33.3 Comparison between bacterial growth rates and aquatic environments

Site	Incubation methods	Depth (m)	Temp. (°C)	Incubation (day)	DT (h)	GR (day^{-1})	References
Vent sides	In situ incubation	1,477–1,523	80–150	6–13	21–33	0.77–0.50	This study
Colony	In situ incubation	1,477–1,479	3.9–4.8	6	86–110	0.15–0.92	This study
Methane seep	In situ incubation	641	6.5–9.5	10	26–39	0.63–0.42	This study
Geothermal pool	In situ incubation	Terrestrial	84–88	3	20–38	0.43–0.82	Kimura et al. (2010)
Pacific Ocean	Simulated incubation	Surface	22.6	nd	14	1.18	Carlucci and Williams (1978)
Pacific Ocean	Simulated incubation	500	7.5	nd	67	0.24	Carlucci and Williams (1978)
Pacific Ocean	Simulated incubation	1,500	2.5	nd	145	0.11	Carlucci and Williams (1978)
Phytodetritus	Simulated incubation	4,500	2	1	11.5	1.45	Lochte and Turley (1988)
Phytodetritus	Simulated incubation	Surface	15	1	10.1	1.50	Lochte and Turley (1988)
Oregon coast	Simulated incubation	Surface	10	2–3	19.1	0.86	Sherr et al. (1999)
Oregon coast	Simulated incubation	Surface	15	2–3	38.3	0.43	Sherr et al. (1999)
Oregon coast	Simulated incubation	Surface	18	2–3	43.3	0.38	Sherr et al. (1999)
Delaware estuary	Simulated incubation	Surface	11.9–27.6	3	nd	1.7–3.0	Yokokawa et al. (2004)
Delaware estuary	Simulated incubation	Surface	12.8–28.5	3	nd	0.4–3.5	Yokokawa et al. (2004)

Another digestive tract associated the 16S rRNA gene sequences belonging to *Mollicute* were probably parasitic or potential pathogenic group for mollusks (King et al. 2012; Van Horn et al. 2011; Waltzek et al. 2012).

Methane is proposed as a significant energy source of microbial growth in hydrothermal system (McCollom 2000). The 16S rRNA gene sequence of methane-oxidizing bacteria were detected only from gill and digestive tract, and could not detect from the chamber, despite the chamber was placed on the Bathymodiolus colony. The reasons why the chamber incubation did not allow the growth of methane-oxidizing bacteria was unknown whether caused by methane-permeability of membrane filter or environment constrain for proliferation, or some others.

In conclusion, the results of this study suggested that chemoautotrophic growth in the hydrothermal vent area has an equivalent primary production in the surface seawater. Although an extent of vigorous chemosynthetic growth is constrained to the size of hydrothermal system, the primary production from the growth continuously delivers by hydrothermal plume and bottom current into deep-sea benthopelagic environments. Thus, the microbial growth sustained by chemosynthesis is an important element to estimate the productivity of marine ecosystem.

Acknowledgement We thank the captain and crew of R/V *Natsushima* and the deep-sea submersible operation teams of Hyper-Dorphin 3000 and Shinkai 2000 for helping us to complete sample collection and in situ experiments. This work was partially supported by a Grant-in-Aid for Scientific Research on Innovative Areas (no. 20109003) and the Archaean Park Program from the Ministry of Education, Culture, Sports, Science and Technology of Japan (MEXT). Thanks are also due to the Japan Society for the Promotion of Science (JSPS) for the stay of L. G. Tóth.

References

Amend JP, Shock EL (1998) Energetics of amino acid synthesis in hydrothermal ecosystems. Science 281(5383):1659–1662

Bergquist DC, Williams FM, Fisher CR (2000) Longevity record for deep-sea invertebrate. Nature 403:499–500

Bloom NS, Crecelius EA (1983) Determination of mercury in seawater at sub-nanogram per liter levels. Mar Chem 14:49–59

Bollmann A, Lewis K, Epstein SS (2007) Incubation of environmental samples in a diffusion chamber increases the diversity of recovered isolates. Appl Environ Microbiol 73(20):6386–6390

Campbell BJ, Engel AS, Porter ML, Takai K (2006) The versatile epsilon-proteobacteria: key players in sulphidic habitats. Nat Rev Microbiol 4(6):458–468

Carlucci AF, Williams PM (1978) Simulated in situ growth rates of pelagic marine bacteria. Naturwissenschaften 65:541–542

Corliss JB et al (1979) Submaraine thermal springs on the Galapagos Rift. Science 203(4385):1073–1083

Dick GJ, Anantharaman K, Baker BJ, Li M, Reed DC, Sheik CS (2013) The microbiology of deep-sea hydrothermal vent plumes: ecological and biogeographic linkages to seafloor and water column habitats. Front Microbiol 4:124

Dubilier N, Bergin C, Lott C (2008) Symbiotic diversity in marine animals: the art of harnessing chemosynthesis. Nat Rev Microbiol 6 (10):725–740

Egas C, Pinheiro M, Gomes P, Barroso C, Bettencourt R (2012) The transcriptome of *Bathymodiolus azoricus* gill reveals expression of genes from endosymbionts and free-living deep-sea bacteria. Mar Drugs 10(8):1765–1783

Furnas MJ (1991) Net in situ grwoth rates of phytoplankton in an oligotrophic, troical shelf ecosystem. Limnol Ecanogr 36 (1):13–29

Gebruk AV, Chevaldonne P, Shank T, Lutz RA, Vrijenhoek RC (2000) Deep-sea hydrothermal vent communities of the Logatchev area: diverse biotopes and high biomass. J Mar Biol Assoc UK 80:383–393

Guenther EA, Johnson KS, Coale KH (2001) Direct ultraviolet spectrophotometric determination of total sulfied and iodide in natural waters. Anal Chem 73(14):3481–3487

Higashi Y, Sunamura M, Kitamura K, Nakamura K-I, Kurusu Y, Ishibashi J-I, Urabe T, Maruyam A (2004) Microbial diversity in hydrothermal surface to subsurface environments of Suiyo Seamount, Izu-Bonin Arc, using a catheter-type in situ growth chamber. FEMS Microbiol Ecol 47:327–336

Hobbie JE, Daley RJ, Jasper S (1977) Use of nucleopore filters for counting bacteia by fluorescence microscopy. Appl Environ Microbiol 33:1225–12228

Holmes DE, Giloteaux L, Barlett M, Chavan MA, Smith JA, Williams KH, Wilkins M, Long P, Lovley DR (2013) Molecular analysis of the in situ growth rates of subsurface Geobacter species. Appl Environ Microbiol 79:1646–1653

Ishibashi J-I, Wakita H, Okamura K, Nakayama E, Feely RA, Lebon GT, Baker ET, Marumo K (1997) Hydrothermal methane and manganese variation in the plume over the superfast-spreding southern east pacific rise. Geochim Cosmochim Acta 61 (3):485–500

Jannasch HW, Mottl MJ (1985) Geomicobiology of deep-sea hydrothermal vents. Science 229:717–725

Karl DM, Wirsen CO, Janasch HW (1980) Deep-sea primary production at the Galapagos hydrothermal vents. Science 207:1345–1347

Kimura H, Mori K, Nashimoto H, Hattori S, Yamada K, Koba K, Yoshida N, Kato K (2010) Biomass production and energy source of thermophiles in a Japanese alkaline geothermal pool. Environ Microbiol 12(2):480–489

King GM, Judd C, Kuske CR, Smith C (2012) Analysis of stomach and gut microbiomes of the eastern oyster (Crassostrea virginica) from coastal Louisiana, USA. PLoS One 7(12):e51475

Kirchman DL (2001) Measuring bacterial biomass production and growth rates from leucine incorporation in natural aquatic environments. Method Microbiol 30:227–237

Lochte K, Turley CM (1988) Bacteria and cyanobacteria associated with phytodetritus in deep sea. Nature 333:67–69

Lonsdale P (1977) Clustering of suspension-feeding macrobenthos near abyssal hydrothermasl vents at oceanic spreding centers. Deep Sea Res 24:857–863

Lutz RA, Shank TM, Fornari DJ, Haymon RM, Lilley MD, Von Damm KL, Desbruyeres D (1994) Rapid growth at deep-sea vents. Nature 371:663–664

Maddison DR (2004) Are strepsipterans related to flies? Exploring long branch attraction. Study 2 in Mesquite: a modular system for evolutionary analysis, version 1.04. http://mesquiteproject.org

Malmstrom RR, Cottrell MT, Elifantz H, Kirchman DL (2005) Biomass production and assimilation of dissolved organic matter by SAR11 bacteria in the Northwest Atlantic Ocean. Appl Environ Microbiol 71(6):2979–2986

McCollom TM (2000) Geochemical constraints on primary productivity in submarine hydrothermal vent plumes. Deep Sea Res I 47:85–101

McCollom TM, Shock EL (1997) Geochemical constraints on chemolithoautotrophic metabolism by microorganisms in seafloor hydrothermal systems. Geochim Cosmochim Acta 61 (20):4375–4391

McFeters GA, Stuart DG (1972) Survval of coliform bacteria in natural waters: field ad laboratory studies with membrane-filter chambers. Appl Microbiol 24(5):805–811

Muyzer G, De Waal EC, Uitterlinden AG (1993) Profiling of complex microbial population by denaturing gradient gel eclectrophoresis analysis of polymerase chain reaction- amplified genes coding for 16S rRNA. Appl Environ Microbiol 59(3):695–700

Nakagawa S, Takai K (2008) Deep-sea vent chemoautotrophs: diversity, biochemistry and ecological significance. FEMS Microbiol Ecol 65(1):1–14

Newell SY, Christian RR (1981) Frequency of dividing cells as an estimator of bacterial productivity. Appl Environ Microbiol 42 (1):23–31

Powell EO (1956) Growth rate and generation time of bacteria, with special reference to continuous culture. J Gen Microbiol 15:492–511

Pracejus B, Halbach P (1996) Do marine moulds infuluence Hg and Si precipitation in the hydrothermal JADE field (Okinawa Trough)? Chem Geol 130(87–99)

Reysenbach AL, Longnecker K, Kirshtein J (2000) Novel bacterial and Archaeal lineages from an in situ growth chamber deployed at a mid-Atlantic Ridge hydrothermal vent. Appl Environ Microbiol 66 (9):3798–3806

Schmidt C, Vuillemin R, Le Gall C, Gaill F, Le Bris N (2008) Geochemical energy sources for microbial primary production in the environment of hydrothermal vent shrimps. Mar Chem 108 (1–2):18–31

Sherr EB, Sherr BF, Sigmon T (1999) Activity of marine bacteria under incubated and in situ conditions. Aquat Microb Ecol 20:213–223

Shitashima K, Maeda Y, Koike Y, Ohsumi T (2008) Natural analogue of the rise and dissolution of liquid CO_2 in the ocean. Int J Greenhouse Gas Control 2(1):95–104

Steinberg DK, Van Mooy BAS, Buesseler KO, Boyd PW, Kobari T, Karl DM (2008) Bacterial vs. zooplankton control of sinking particle flux in the ocean's twilight zone. Limnol Ecanogr 53 (4):1327–1338

Sunamura M, Higashi Y, Miyako C, Ishibashi JI, Maruyama A (2004) Two bacteria phylotypes are predominant in the Suiyo seamount hydrothermal plume. Appl Environ Microbiol 70(2):1190–1198

Takai K, Inagaki F, Nakagawa S, Hirayama H, Nunoura T, Sako Y, Nealson KH, Horikoshi K (2003) Isolation and phylogenetic diversity of members of previously uncultivated epsilon-Proteobacteria in deep-sea hydrothermal felds. FEMS Microbiol Lett 218:164–174

Taylor CD, Wirsen CO, Gaill F (1999) Rapid microbial production of filamentous sulfur mats at hydrothermal vents. Appl Environ Microbiol 65(5):2253–2255

Tokuda G, Yamada A, Nakano K, Arita NO, Yamasaki H (2008) Colonization of Sulfurovum sp. on the gill surfaces of Alvinocaris longirostris, a deep-sea hydrothermal vent shrimp. Mar Ecol 29 (1):106–114

Torrton J-P, Dufour P (1996) Bacterioplankton production determined by DNA synthesis, protein synthesis, and frequency of dividing cells in Tuamotu Atoll Lagoons and surounding ocean. Microb Ecol 32:185–202

Tsuchida S, Suzuki Y, Fujiwara Y, Kawato M, Uematsu K, Yamanaka T, Mizota C, Yamamoto H (2010) Epibiotic association between filamentous bacteria and the vent-associated galatheid crab, Shinkaia crosnieri (Decapoda: Anomura). J Mar Biol Assoc U K 91(01):23–32

Turley CM, Carstens M (1991) Pressure tolerance of oceanic flagellates: implications for remineralization of organic matter. Deep Sea Res 38:403–413

Turley CM, Lochte K, Patterson DJ (1988) A barophilic flagellate isolated from 4500 m in the mid-North Atlantic. Deep Sea Res 35 (7):1079–1092

Van Horn DJ, Garcia JR, Loker ES, Mitchell KR, Mkoji GM, Adema CM, Takacs-Vesbach CD (2011) Complex intestinal bacterial communities in three species of planorbid snails. J Molluscan Stud 78(1):74–80

Vasconcelos GJ, Swartz RG (1976) Sruvival of bacteria in seawater using a diffusion chamber apparatus in situ. Appl Environ Microbiol 31(6):913–920

Waltzek TB, Cortes-Hinojosa G, Wellehan JF Jr, Gray GC (2012) Marine mammal zoonoses: a review of disease manifestations. Zoonoses Public Health 59(8):521–535

Watanabe K (2001) Mapping the hydrothermal activity area on the Hatoma Knoll in the southern Okinawa Trough. JAMSTEC J Deep Sea Res 19:87–94

Watsuji T-O, Nakagawa S, Tsuchida S, Toki T, Hirota A, Tsunogai U, Takai K (2010) Diversity and function of epibiotic microbial

communities on the Galatheid Crab, Shinkaia crosnieri. Microb Environ 25(4):288–294

Williams PM, Carlucci AF (1976) Bacterial utilisation of organic matter in the deep sea. Nature 262:810–811

Yamamoto M, Takai K (2011) Sulfur metabolisms in epsilon- and gamma-proteobacteria in deep-sea hydrothermal fields. Front Microbiol 2:192

Yamamoto H, Fujikura K, Hiraishi A, Kato K, Maki Y (2002) Phylogenetic characterization and biomass estimation of bacterial endosymbionts associated with invertebrates dwellin in chemosynthetic communities of hydrothermal vent and cold seep fields. Mar Ecol Prog Ser 245:61–67

Yokokawa T, Nagata T, Cottrell MT, Kirchman DL (2004) Growth rate of the major phylogenetic bacterial groups in the Delaware estuary. Limnol Ecanogr 49(5):1620–1629

Vent Fauna in the Okinawa Trough

34

Hiromi Watanabe and Shigeaki Kojima

Abstract

In deep-sea hydrothermal vent fields, faunal distribution is associated with geochemical environments generated by hydrothermal vent activity. The Okinawa Trough is located between the Eurasian Continent and the Ryukyu Arc, and is characterized by sediment-associated fauna associated with vents. In this chapter, the faunal distribution in hydrothermal vent fields in the Okinawa Trough is summarized at inter- and intra-field levels, and its relationship with geochemical environments and species-specific ecologies is discussed. Although the zonation of sediment-associated fauna is not distinct, the fauna on rocky seabed can be categorized into four zones based on thermal conditions. Genetic connectivity among conspecific populations in the Okinawa Trough appears to be common; further, a few faunal groups, such as tubeworms, show connectivity to regions outside of the Okinawa Trough. The faunal composition of vent communities in the Okinawa Trough has been categorized into three groups: the Minami-Ensei Knoll, Yoron Hole, and middle-southern Okinawa Trough. To determine more precisely the relationships between faunal composition and environmental factors in the Okinawa Trough vent fields, both generalized and vent-specific environmental factors should be measured simultaneously with quantitative faunal sampling for analyses.

Keywords

Biodiversity • Connectivity • Faunal similarity • Zonation

34.1 Background

Deep-sea hydrothermal vents are among the most flourishing deep-sea environments, due to the associated chemosynthetic bacterial productivity. The Okinawa Trough is a backarc basin located between the Eurasian continent and the Ryukyu island arc. The first hydrothermal vent field in the Okinawa Trough was discovered in the 1980s at the JADE site, Izena Hole (Halbach et al. 1989), and geological and geochemical knowledge has been accumulated since then. In total, eight hydrothermal vent fields, i.e. the Minami-Ensei Knoll, the Yoron Hole, the Iheya Ridge, the Iheya North Knoll, the Izena Hole, Irabu Knoll, the Hatoma Knoll and the Daiyon-Yonaguni Knoll, have been discovered to date in the Okinawa Trough, and exploration is still in progress (see Fukuba et al. Chaps. 38 and 39; Yanamaka

H. Watanabe (✉)
Department of Marine Biodiversity Research,
Japan Agency for Marine-Earth Science and Technology,
Kanagawa 237-0061, Japan
e-mail: hwatanabe@jamstec.go.jp

S. Kojima
Graduate School of Frontier Sciences, The University of Tokyo,
Chiba 277-8563, Japan

Atmosphere and Ocean Research Institute, The University of Tokyo,
Chiba 277-8564, Japan

J.-i. Ishibashi et al. (eds.), *Subseafloor Biosphere Linked to Hydrothermal Systems: TAIGA Concept*,
DOI 10.1007/978-4-431-54865-2_34,

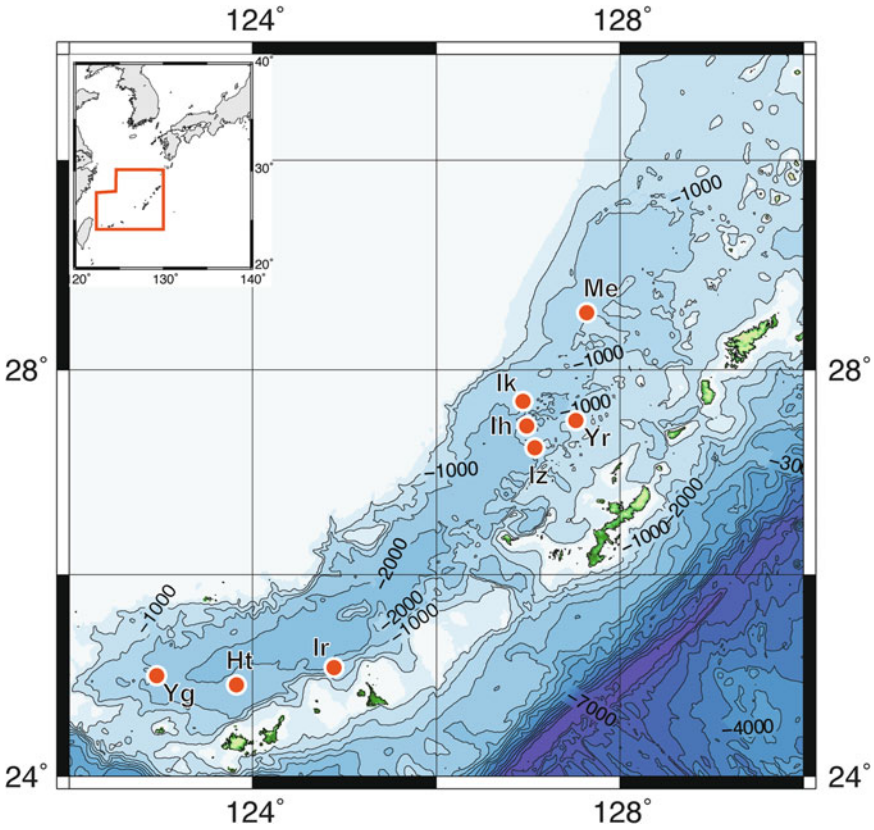

Fig. 34.1 Distribution of deep-sea hydrothermal vent fields in the Okinawa Trough. *Me* Minami-Ensei Knoll (D = 600–800 m), *Yr* Yoron Hole (D = 580 m), *Ik* Iheya North Knoll (D = 900–1,000 m), *Ih* Iheya Ridge (D = 1,300–1,500 m), *Iz* Izena Hole (D = 1,300–1,600 m), *Ir* Irabu Knoll (D = 1,650 m), *Ht* Hatoma Knoll (D = 1,400–1,530 m), *Yg* Daiyon-Yonaguni Knoll (D = 1,320–1,387 m)

et al. Chap. 40). Rifting of the Okinawa Trough appears to have started from the southern end. In terms of water columns, the Kuroshio Current flows from the southern end of the Okinawa Trough to the Kerama Gap or to the Japan Sea. The details of the vent fields in the Okinawa Trough are summarized by Ishibashi et al. (Chap. 29).

The faunal assemblages associated with hydrothermal vents in the Okinawa Trough were first summarized for the Iheya Ridge (Ohta 1991; Kim and Ohta 1991) and updated by Hashimoto et al. (1995) with extensive descriptions of the vent fauna in the Minami-Ensei Knoll and comparisons with vent fauna in the north (Minami-Ensei Knoll) and middle (Iheya Ridge) parts of the Okinawa Trough (Fig. 34.1). In the early 2000s, reports described vent fauna in the southern part of the Okinawa Trough (Tsuchida et al. 2000; Fujikura et al. 2001). On the basis of these descriptions, the fauna associated with hydrothermal vent fields in the Okinawa Trough appear to show similarities to those in methane seep sites in Sagami Bay due to the dense sedimentation (Fujikura et al. 1995; Watanabe et al. 2010).

In this paper, we summarize the previous research and recent results from the TAIGA project on vent fauna in the Okinawa Trough, to focus on (1) species distribution and population connectivity among the vent fields, (2) the zonation of fauna around vents, and (3) faunal similarities among vent fields in the Okinawa Trough.

34.2 Distribution and Connectivity of Vent Fauna in the Okinawa Trough

Vent fauna in the Okinawa Trough have been summarized previously (Kojima 2002; Fujikura et al. 2008; Watanabe et al. 2010); however, the community structure is not yet fully understood due to a lack of quantitative information. Recent comprehensive DNA barcoding analyses have revealed the existence of cryptic species, or morphologically similar species, particularly among the polychaetes and small gastropods. On the other hand, the possibility of synonymy is arising. Therefore, verification of the distributional records of vent fauna in the Okinawa Trough is still in progress. To date, a total of 109 species has been reported in and near vent fields in the Okinawa Trough (summarized in Table 34.1). In this section, previous reports are briefly summarized for the three major taxa (Annelida, Arthropoda, and Mollusca), together with recent distributional remarks and results of genetic analyses from the TAIGA project, which infer population connectivity.

Annelida. In total, 36 species have been reported in the Okinawa Trough hydrothermal vent fields, but as yet no species strictly endemic to the region have been recognized. Vestimenteiferan tubeworms are among the conspicuous

Table 34.1 Species list of vent fauna in the Okinawa Trough

		Minami-Ensei Knoll	Yoron Hole	Iheya North Knoll	Iheya Ridge	Izena Hole	Irabu Knoll	Hatoma Knoll	Daiyon-Yonaguni Knoll
Porifera	Rossellidae gen. et sp.				+				
	Pheronema ijimai	+			+	+			
	Pheronema sp.	+							
	Euplectella spp.	+			+				
	Poecilosclerida gen. et sp.	+							
Mollusca (Gastropoda)	*Leptochiton tenuidontus*				+				
	Thermochiton undocostatus				+				
	Bathyacmaea secunda	+		+	+	+	+	+	+
	Bathyacmaea tertia			+					
	Pyropelta ryukyuensis							+	+
	Lepetodrilus japonicus	+							
	Lepetodrilus nux	+		+	+	+	+	+	+
	Puncturella parvinobilis	+		+		+			
	Puncturella rimaizenaensis					+			
	Margarites ryukyuensis			+	+	+	+	+	+
	Margarites shinkai					+			
	Iheyaspira lequios			+	+	+			
	Iheyaspira sp.	+							
	Peltospiridae gen. et sp.								+
	Cantrainea jamsteci	+		+		+			
	Cantrainea nuda	+							
	Shinkailepas kaikatensis		+						
	Shinkailepas aff. myojinensis	+	+			+			
	Shinkailepas sp.			+					
	Provanna aff. glabra (MO1)		+	+	+	+	+	+	+
	Provanna sp., MO2					+	+	+	
	Provanna sp., MO3	+							
	Desbruyeresia sp.					+			
	Oenopota sp.			+					
	Eosipho desbruyeresi nipponensis			+					
	Neptunea insularis robusta	+							
Mollusca (Bivalvia)	*Eulimella* sp.			+					
	Solemya flava				+				
	Bathymodiolus aduloides	+			+				
	Bathymodiolus japonicus	+		+					
	Bathymodiolus platifrons			+	+	+		+	+
	Calyptogena okutanii			+	+				
	Calyptogena nankaiensis			+					
	Calyptogena kawamurai	+							

(continued)

Table 34.1 (continued)

		Minami-Ensei Knoll	Yoron Hole	Iheya North Knoll	Iheya Ridge	Izena Hole	Irabu Knoll	Hatoma Knoll	Daiyon-Yonaguni Knoll
Annelida	*Capitella* sp.	+							
	Nicomache ohtai					+			
	Maldanidae gen. et sp.	+							
	Paraonidae gen. et sp.	+							
	Brachipolynoe pettiboneae				+	+			+
	Brachipolynoe spp.			+		+		+	+
	Branchinotogluma (=*Opisthotrochopodus*) sp.			+		+			
	Shinkai longipedata			+	+				
	Shinkai semilonga			+					
	Mytilidiphila enseiensis	+							
	Mytilidiphila okinawaensis	+			+				
	Iheyomytilidicola tridentatus				+				
	Ophryotrocha sp.	+							
	Schistomeringos sp.	+							
	Eunice masudai	+							
	Eunice northioidea	+							
	Eunice spp.	+	+			+		+	
	Sabellidae gen. et sp.	+							
	Lamellibrachia sp. L1			+	+				
	Paraescrpia echinospica				+				
	Escarpia sp. E2				+				
	Alaysia sp. A2								+
	Alaysia sp. A4			+	+	+	+		
	Cirratulidae gen. et sp.			+					
	Paralvinella aff. hessleri		+	+	+	+		+	+
	Paralvinella aff. unidentata							+	+
	Amphisamytha aff. galapagogensis			+	+	+	+		
	Amphisamytha sp.					+		+	
	Glyphanostomum? sp.					+		+	
	Ampharetidae gen. et sp.	+			+	+		+	+
	Terebellidae gen. et sp.	+							
	Hesionidae gen. et sp.					+			
	Nephtyidae gen. et sp.		+			+			
	Cerviniidae gen. et sp.	+							
	Hyphalion sp.	+							
Arthropoda	*Ashinkailepas seepiophila*			+	+				
	Leucolepas longa			+	+				+
	Neoverruca sp.			+	+	+	+	+	+
	Alvinocais brevitelsonis	+							
	Alvinocais dissimilis	+							
	Alvinocais longirostris			+	+	+	+	+	+
	Alvinocais sp. type SM						+		
	Shinkaicaris leurokolos	+	+	+		+	+	+	+
	Glyphocrangon sp.							+	
	Paracrangon sp.	+							
	Lebbeus shinkaiae	+	+		+	+	+	+	+

(continued)

Table 34.1 (continued)

		Minami-Ensei Knoll	Yoron Hole	Iheya North Knoll	Iheya Ridge	Izena Hole	Irabu Knoll	Hatoma Knoll	Daiyon-Yonaguni Knoll
	Stylodactylus major							+	
	Munidopsis ryukyuensis					+	+	+	
	Munidopsis naginata							+	
	Shinkaia crosnieri	+		+	+	+	+	+	+
	Munida sp.				+				
	Paralomis jamsteci	+							
	Paralomis verrilli				+			+	
	Paralomis multispina	+							
	Gandulfus yunohana	+							
	Geryon aff. granulatus	+							
	Xanthidae sp.		+						
	Gnathiidae sp.		+						
Echinodermata	*Ceranaster misadiensis*	+							
	Synallactidae gen. et sp.				+	+			
Chordata	*Eptatretus okinoseanus*	+			+				
	Myxine garmani	+							
	Synaphobranchus affinis				+				
	Ilyophis brunneus				+				
	Aldvovandia affinis				+				
	Zoarcidae gen. spp.	+		+	+	+			+
	Psychrolutes inermis	+							
	Symphurus cf. *orientalis*	+							
	Liparidae sp.					+			

Updated from Fujikura et al. 2008

fauna in the vent fields. Three species have been separately reported in the Okinawa Trough vent fields, but these are also found in the methane seep faunas: *Lamellibrachia* sp. in the Iheya Ridge and the Iheya North Knoll; *Paraescarpia echinospica* in the Iheya Ridge; and two lineages of *Alaysia*, A2 in the Daiyon-Yonaguni Knoll and A4 in the Iheya Ridge, the Iheya North Knoll and the Izena Hole (Fujikura et al. 2008). Two unidentified species of tubeworm were reported in Depression B of the Minami-Ensei Knoll (Hashimoto et al. 1995; Fig. 34.2a). The tubeworm clump possibly consisted of *Alaysia* and *Lamellibrachia*; however, identification to the species level has been impossible. Population genetic analyses of tubeworms showed no differences among the populations in the Okinawa Trough, or from those of populations outside of the Okinawa Trough (Watanabe et al. 2010).

Other than tubeworms, the connectivity among populations of annelids has yet to be examined. For the polychaetes, classification of the collected animals is not sufficient for a comparison of the faunal composition among the vent fields. Ampharetid polychaetes are, however, abundant in the middle and southern parts of the Okinawa Trough, and are frequently associated with a squat lobster, *Shinkaia crosnieri* (Fig. 34.2). Recent DNA barcoding indicates the existence of at least three different clusters ampharetid polychaetes in the Okinawa Trough (data not shown), probably including the "ampharetid sp." reported by Hashimoto et al. (1995). Two *Eunice* species have been described (*E. masudai* and *E. northioidea*), and the existence of further species in this genus has been indicated (Hashimoto et al. 1995). As most of the species-level composition of polychaete fauna in the Okinawa Trough is still incomplete, we have only identified them to the genus level. However, it is apparent that the diversity of vent polychaetes in the Okinawa Trough is underestimated, and a detailed re-examination is accordingly required.

Arthropoda. In total, 23 species have been reported in the Okinawa Trough hydrothermal vent fields, and three dominant species, *Shinkaia crosnieri*; a shrimp with a pair of unfused dorsal eyes, *Shinkaicaris leurokolos*; and a shrimp with stalked eyes, *Lebbeus shinkaiae*, are treated as endemic to this region. No bythograeid crabs have been reported.

Shinkaia crosnieri has been observed in most vent fields and is among the representative animals of the Okinawa Trough, although its abundance decreases in shallower vent fields such as the Minami-Ensei Knoll and it is absent from the Yoron Hole. *S. crosnieri* harbors bacterial symbionts in its ventral side (Watsuji et al. 2010) and the ecological characteristics are similar to those of *Kiwa* (Roterman et al. 2013). Genetic diversity is relatively high (Kumagai et al., Chap. 5), probably due to its high abundance caused by frequent reproduction to sustain a huge biomass.

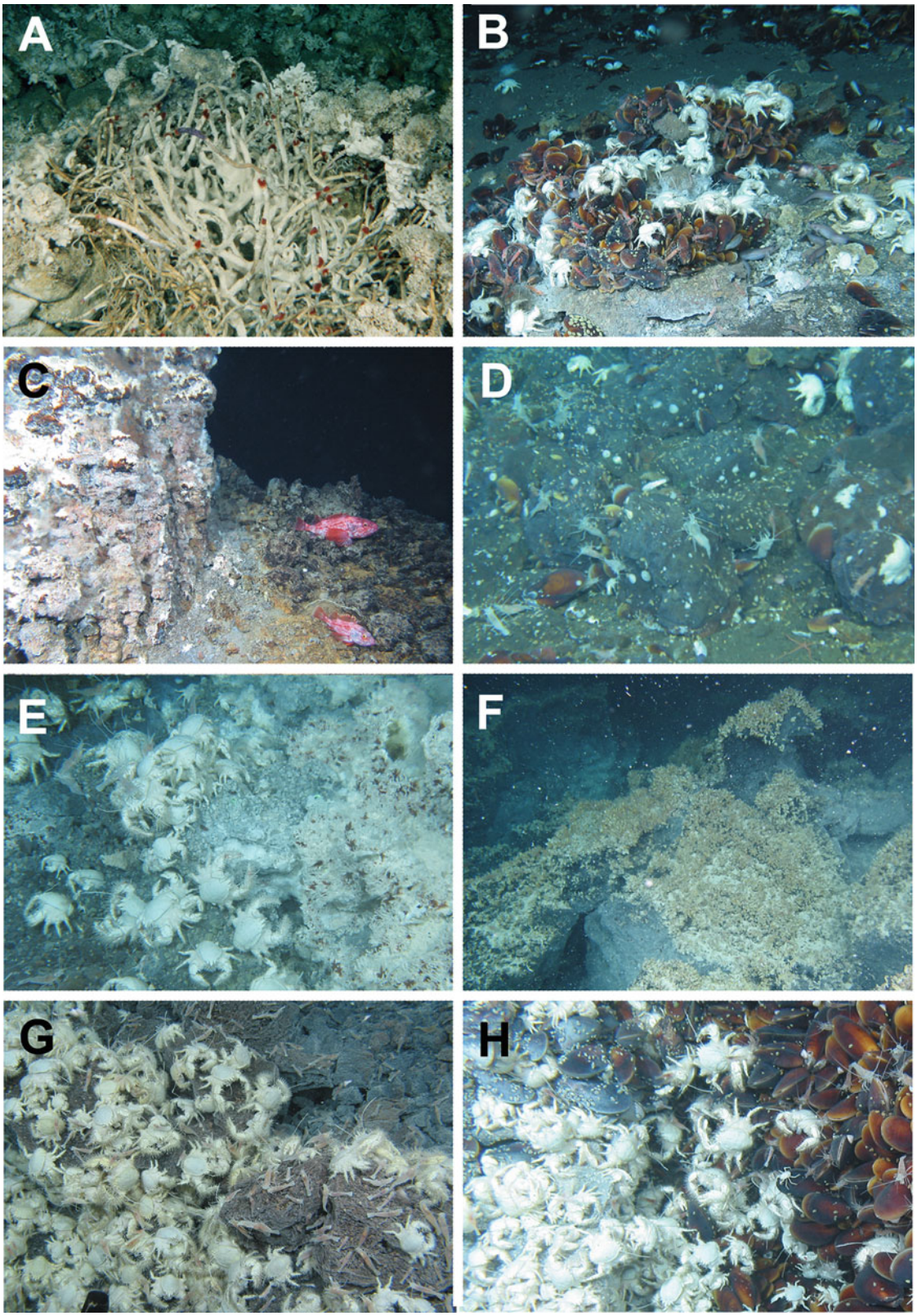

Fig. 34.2 Typical vent fauna in the Okinawa Trough. (**A**) tubeworm clump in the Minami-Ensei Knoll, (**B**) typical rocky fauna in the Minami-Ensei Knoll, (**C**) vent associated fauna in the Yoron Hole, (**D**) peripheral vent fauna in the Izena Hole, (**E**) high-temperature vent fauna in the Izena Hole, (**F**) barnacle-dominated zone in the Irabu Knoll, (**G**) typical rocky fauna in the Irabu Knoll, (**H**) typical rocky fauna in the Hatoma Knoll

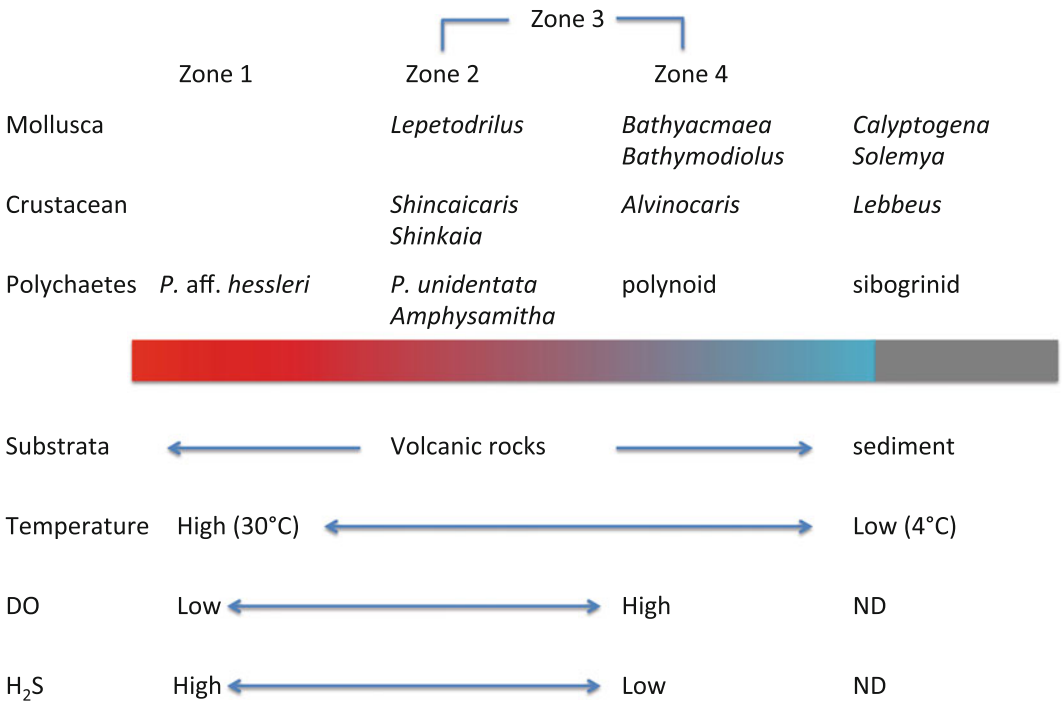

Fig. 34.3 Summary of zonation of vent fauna in the Okinawa Trough. *ND* not determined

Alvinocaridid shrimps are the second most dominant crustaceans in the Okinawa Trough vent fields; however, the two reported genera, *Alvinocaris* and *Shinkaicaris*, have different distributions (Komai and Segonzac 2005). The *Alvinocaris* shrimps have been reported in a wide area in the Okinawa Trough: *A. dissimilis* in the Minami-Ensei Knoll, and *A. longirostris* in all the other vent fields except for the Yoron Hole (Fujikura et al. 2008). On the other hand, *Shinkaicaris leurokolos*, whose distribution was thought to be restricted to the Minami-Ensei Knoll, now appears to be distributed in all the known vent fields in the Okinawa Trough (Yahagi per. com).

Lebbeus shinkaiae, which is a recently described shrimp, but which has also been reported as *Lebbeus washingtonius* or *Lebbeus* sp. (Komai et al. 2012), is also widely distributed, but is only reported from the Okinawa Trough. This shrimp is not aggregated and is commonly distributed near peripheral areas of vent fields.

A barnacle of the genus *Neoverruca* is patchily but abundantly distributed in all the Okinawa Trough vent fields except for the Minami-Ensei Knoll and Yoron Hole. Among the local populations in the Okinawa Trough, no genetic differences have been detected and their population expansion date has been estimated to be earlier than that in the Izu-Ogasawara Arc vent fields (Watanabe et al. 2005). Rearing experiments on larvae of this barnacle revealed that high temperature surface water may act as a dispersal barrier for this species (Watanabe et al. 2006).

Mollusca. In total, 34 species have been reported in the Okinawa Trough hydrothermal vent fields, and most vent gastropod species are thought to be endemic to this region.

Large clams of the genus *Calyptogena* s.l. are distributed only in sedimentary fields (Kim and Ohta 1991) in the hydrothermal vent fields of Minami-Ensei Knoll and Iheya Ridge and Iheya North Knoll in the Okinawa Trough. Hitherto, three species have been reported, and the population genetic structure has been examined for *C. kawamurai* and *C. okutanii* (Watanabe et al. 2010, based on the data in Kojima et al. 2001, 2006). In both cases, populations in the Okinawa Trough were significantly different from those outside of the Okinawa Trough. No differences were detected between *C. okutanii* populations in vent fields of the Iheya Ridge and Iheya North Knoll.

Bathymodiolus mussels are among the representative animals of the Okinawa Trough, and three species are distributed in the different ranges: *B. japonicus* in Minami-Ensei Knoll (Fig. 34.2b), *B. aduloides* in the Minami-Ensei Knoll and Iheya Ridge, and *B. platifrons* in all the vent fields except for the Minami-Ensei Knoll and Yoron Hole (Fig. 34.2, Table 34.1). The population connectivity of *B. platifrons* was examined using partial sequences of mitochondrial NADH dehydrogenase 4 (ND4), and the most dominant haplotype was shared between populations inside and outside of the Okinawa Trough (Kyuno et al. 2009), inferring connectivity between the populations.

Provanna snails are the most abundant macrofauna in the Okinawa Trough vent fields. They are associated with both

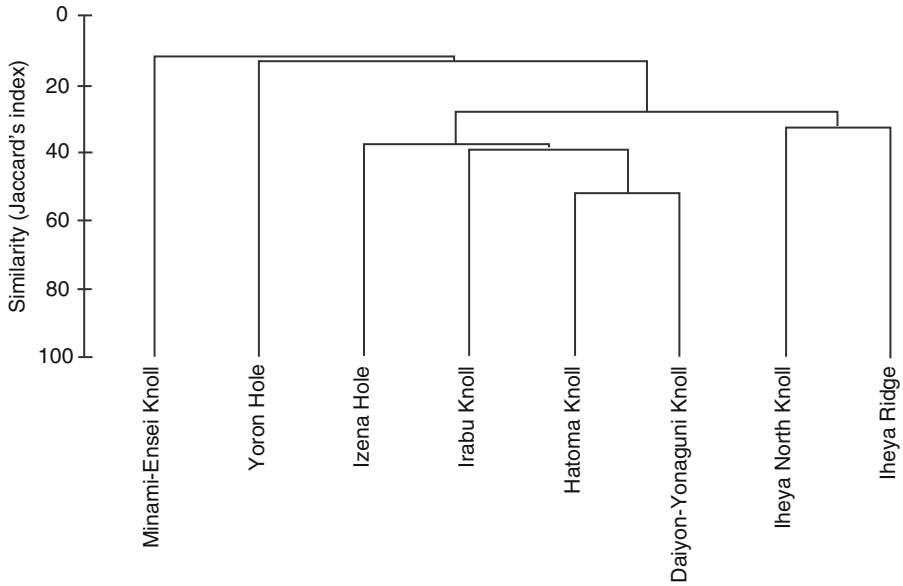

Fig. 34.4 Results of clustering analysis of faunal similarity among the eight vent fields listed in Table 34.1

hard and soft substrata, both in vents and seeps (Fujikura et al. 2008). The *Provanna* gastropods in vent fields in the Okinawa Trough were first referred to as *P. glabra* based on the populations in Sagami Bay, but certain morphological differences were identified; therefore, they have been referred to as *P.* aff. *glabra* for more than 10 years (Fujikura et al. 2008). Morphometric and DNA barcoding analyses is now in progress and it shows the possibility that more than 2 lineages of *Provanna* gastropods are distributed in the Okinawa Trough.

A small limpet, *Lepetodrilus nux*, is a species endemic to the Okinawa Trough and has been found in all of the vent fields except for the Yoron Hole. It is sometimes associated with *S. crosnieri* and *B. platifrons*, but can also be found on inorganic hard substrata. *Lepetodrilus japonicus* was described from a vent field in the Minami-Ensei Knoll, but a recent investigation could not determine its distribution in Depression C of the knoll. On the other hand, *L. nux* appears to be distributed in the Minami-Ensei Knoll in addition to the previously known vent fields (Nakamura et al. 2014).

A small snail, *Iheyaspira lequios*, is a species only found in hydrothermal vent fields in the Okinawa Trough. Recently, a second species of the genus *Iheyaspira*, *I. bathycodon*, was reported from the Mid-Cayman Rise in the Caribbean Sea (Nye et al. 2013). This patchy worldwide distribution of a vent-endemic genus is quite rare, as there are many vent fields located between the Okinawa Trough and the Caribbean Sea. *Iheyaspira* gastropods are usually smaller than 5 mm in shell width, in the Okinawa Trough, and may be missed or misidentified due to their small size. A detailed examination of both morphology and genetics is required to understand the distributional pattern of *Iheyaspira* gastropods, not only in the Okinawa Trough but also on a global scale.

Other Phyla. Poriferans, anthozoans, echinoderms, and fishes are common marine fauna but not well described for the areas near vent fields in the Okinawa Trough. Poriferans are abundant in the Minami-Ensei Knoll (Fig. 34.2a), but to date no species have been identified. Some echinoderms such as *Ceramaster* asteroids and unidentified ophiuroids have been reported in Depression B in the Minami-Ensei Knoll and the CLAM site in the Iheya Ridge (Hashimoto et al. 1995; Kim and Ohta 1991). Recently, the reproduction of a liparid fish, *Careproctus rhodomelas*, in the Hatoma Knoll was reported (Takemura et al. 2010); however, for the other fishes, almost nothing has been reported due to the difficulty of sampling. These fauna may be important as predators in such ecosystems, and detailed observations are required for elucidating trophic interactions.

34.3 Faunal Zonation in a Vent Field

Vent fauna show variation along steep environmental gradients, or patchiness, which is referred to "zonation." In the Okinawa Trough, hydrothermal vents host two types of fauna: rocky seabed fauna associated with direct vent activity (rock-associated fauna), and epi- and infauna indirectly supported by vents (sediment-associated fauna). Generally, faunal composition differs among substrata (Tunnicliffe et al. 2003). These differences in the vent fields in the Okinawa Trough were first mentioned by Kim and Ohta (1991) based on the observation of vent fauna in the CLAM (sedimentary) and PYRAMID (rocky) sites of the Iheya Ridge. Subsequently, two neighboring vent sites with differing fauna were reported in Depression B (sedimentary) and C (rocky) in the Minami-Ensei Knoll (Hashimoto et al. 1995). This

section summarizes zonations in the rocky and sedimentary habitats in the vent fields in the Okinawa Trough.

Rock-Associated Fauna. Rocky fauna are generally dominant in deep-sea hydrothermal vent fields. The zonation sequence of epifauna on the rocky substrata has been categorized into 4 zones in the Iheya North Knoll: Zone 1 (<0.2 m from vent), no fauna except for occasional invasion by shrimps; Zone 2 (0.2–0.8 m from vent), *Shinkaia crosnieri* aggregation with shrimps; Zone 3 (0.8–2.5 m from vent), co-occurrence of *S. crosnieri* and *Bathymodiolus platifrons* with two limpets (*Bathyacmaea secunda* and *Lepetodrilus nux*) and shrimps; and Zone 4 (>2.5 m from vent), *B. platifrons* without *S. crosnieri* (Tokeshi 2011). Additional observations have updated the faunal composition of each zone (Figs. 34.2 and 34.3). Zone 1, nearest to hydrothermal venting, is inhabited by a dense assemblage of *Paralvinella* aff. *hessleri* with white tubes (Fig. 34.2e), although congeneric *P.* aff. *unidentata* without tubes are scattered near vents. The surrounding area (Zone 2) is inhabited by *Shinkaicaris leurokolos* and *S. crosnieri*. *S. crosnieri* is sometimes associated with *L. nux* and ampharetid polychaetes and red copepods. Outside of the *S. leurokolos–S. crosnieri* assemblage (Zone 4), *B. platifrons*-hosted fauna are distributed. *Alvinocaris longirostris*, a shrimp without a dorsal eye, and the limpets *B. secunda* and *L. nux* are associated with this fauna. The transitional zone from Zone 2 to Zone 4 is Zone 3, which shares fauna with both zones.

For the zonation associated with hydrothermal vents, temperature must be an important factor. There is some evidence to show that temperature contributes to controlling faunal zonation. For instance, in the Okinawa Trough, the difference in temperature effects was also observed for two vent barnacles; *Ashinkailepas seepiophila* was found on a dead chimney and *Neoverruca* sp. on an active chimney, as the effects of rearing temperature on larval duration of these two species were different (Yorisue et al. 2013). Other environmental factors, such as salinity, dissolved oxygen (DO), and the concentration of H_2S, may contribute to the zonation, but there is no supportive evidence for this from the northwestern Pacific. In vent fields in the southwestern Pacific, sulfide concentration and DO, in addition to temperature, appear to contribute to the gradient distribution of vent fauna (Podowski et al. 2010).

Sediment-Associated Fauna. Sedimentary fauna associated with vents is found in the northern and middle part of the Okinawa Trough. This fauna differentiate the vent fauna in the Okinawa Trough from that of other vent fields in the northwestern Pacific and contribute to the species diversity of the Okinawa Trough. The zonation sequence of sediment-associated fauna is still unclear as it is difficult to stratify sediment with infauna to determine the relationships between environmental gradients and faunal distribution in a vertical spectrum. On the other hand, horizontal zonation has been observed in some methane seep sites. The relationships between the concentration of methane and faunal distribution have been discussed both from the perspective of a toxin for animals and as a substrate for chemosynthetic production (e.g. Barry et al. 1997). However, in general, faunal distribution in marine environments is explained by more generalized factors, such as temperature, salinity, and the concentration of DO. Indeed, the distribution of *Calyptogena* s.l. assemblages associated with hydrothermal vents and methane seeps in the Okinawa Trough and Sagami Bay could be explained by temperature and salinity (Watanabe et al. 2013). Although the vertical distribution of infauna is still unclear, the importance of infauna as a disturber of sediment has been noted in deep-sea reducing environments (Seike et al. 2012).

Vesicomyid or *Calyptogena* s.l. clams and solemiyd clams, along with tubeworms, are dominant in the sedimentary fauna in the Okinawa Trough vent fields. Recently, *Solemya flava* was described from a sedimentary vent field in the Iheya Ridge (Sato et al. 2013). The main difference from rocky fauna is that most sedimentary fauna are shared between methane seep sites in Sagami Bay and Nankai Trough (Watanabe et al. 2010). This can be attributed to the similarity of vent fauna in the Okinawa Trough to the methane seep fauna, in addition to the high concentration of methane and CO_2 in vent fluids (Sakai et al. 1990).

34.4 Faunal Resemblance in the Okinawa Trough

To show the overall similarity among the vent fauna in the Okinawa Trough, Jaccard's similarity index was calculated based on the species occurrence data (Table 34.1), and the results were presented using group-average clustering analysis (Fig. 34.4). Faunal similarity was lower than 60 % between all the vent fields, but the vent fauna was divisible into three groups at the 20 % similarity index: the Minami-Ensei Knoll, the Yoron Hole, and the others locations in the middle to the southern Okinawa Trough. Recent research has suggested that, although some fauna appear to be shared between the vent faunas in the Minami-Ensei Knoll and the other vent fields in the Okinawa Trough (e.g., *Shinkaicaris leurokolos* and *Lepetodrilus nux*), the fauna in the Minami-Ensei Knoll still retains high endemicity. However, the information on the sediment-associated fauna in the Minami-Ensei Knoll (Depression B) was not sufficient to examine the faunal resemblance. In the middle to southern Okinawa Trough, the faunal composition was relatively similar to the neighboring vent fields. The cluster of the

Iheya Ridge and Iheya North Knoll vent fauna is distinguished from those in the Izena Hole and Irabu, Hatoma and Daiyon Yonaguni Knolls because it included sediment-associated fauna.

There are several factors that contribute to inter-field faunal resemblance. In general, the diversity of deep-sea fauna varies according to depth (Rex and Etter 2010). Similar observation was made for deep-sea bivalves in chemosynthetic environments because the species show restricted ranges of vertical distribution (Fujikura et al. 2008). Indeed, the clusters of vent fauna in the Okinawa Trough are correlated with the depth range of each vent field (Fig. 34.4). The depth variation may act as both a dispersal barrier (pre-settlement) and physiological barrier (post-settlement). General oceanographic factors such as ambient temperature, salinity, and DO, are more important than the concentration of reduced chemicals in endmember fluid to field-level similarity, as the latter are quickly diluted by ambient seawater and seem to contribute to the species microdistribution in a vent field. To determine more precisely the relationships between faunal composition and environmental factors in the vent fields, both generalized and vent-specific environmental factors should be measured simultaneously for the analyses.

34.5 Conclusions

In this chapter, we summarized and updated the information on vent fauna in the Okinawa Trough. A total of 109 species are listed here; however, that number may be either an over- or under-estimate. Detailed morphological and genetic examination of vent fauna, particularly for polychaetes and small gastropods such as *Iheyaspira*, are required to confirm the existence of synonymous or cryptic species. The composition of sediment-associated fauna is genetically similar to that in methane seep sites outside of the Okinawa Trough, but its zonation is still unclear, as it's elucidation requires 3-dimensional observation of the sediment. On the other hand, the zonation of rock-associated fauna has been clearly determined, and most endemic species of the Okinawa Trough are found among the rock-associated fauna. The total diversity of vent fauna in the Okinawa Trough is attributable to the associated sediment-associated fauna and the wide depth range causing variation in both ambient temperature and that near hydrothermal vents. Although more than 20 years have passed since the discovery of vent fauna in the Okinawa Trough, further investigation is still required to understand their local biogeography.

Acknowledgements We are grateful to the on-board scientist of the NT11-20 cruise for providing an overview of the faunal assemblages in the Okinawa Trough vent fields, Mr. Naoto Jimi and Ms. Mai Karasawa, for their great help with our polychaete identification, Dr. Hidenori Kumagai kindly provided us the map of Okinawa Trough, using free mapping software, GMT (Wessel and Smith 1998) based on the global data set of topography model, ETOPO1 (Amante and Eakins 2009). This study was supported by the "TAIGA project," which was funded by a Grant-in-Aid for Scientific Research on Innovative Areas (No. 20109004) from the Ministry of Education, Culture, Sports, Science and Technology (MEXT), Japan, and the Canon Foundation.

References

Amante C, Eakins BW (2009) ETOPO1 1 arc-minute global relief model: procedures, data sources and analysis, NOAA technical memorandum NESDIS NGDC-24, National Geophysical Data Center, Boulder, Colorado, p 19

Barry JP, Kochevar RE, Baxter CH (1997) The influence of porewater chemistry and physiology on the distribution of vesicomyid clams at cold seeps in Monterey Bay: implications for patterns of chemosynthetic community organization. Limnol Oceanogr 42:318–328

Fujikura K, Hashimoto J, Fujiwara Y, Okutani T (1995) Community ecology of the chemosynthetic community at Off Hathushima site, Sagami Bay, Japan. JAMSTEC J Deep Sea Res 11:227–241 (In Japanese with English abstract and captions)

Fujikura K, Fujiwara Y, Ishibashi J, Katayama S, Komatsu T, Maezawa Y, Maki Y, Miyazaki J-I, Miyake H, Okamoto K, Okoshi K, Toth LG, Tsuchida S, Yamaguchi T, Yamanaka T, Watabe H, Watanabe H, Zielinski S, Kato K (2001) Report on investigation of hydrothermal vent ecosystems by the crewed submersible 'Shinkai 2000' on the Dai-yon (No. 4) Yonaguni Knoll and the Hatoma Knoll, the Okinawa Trough. JAMSTEC J Deep Sea Res 19:141–154 (In Japanese with English abstract and captions)

Fujikura K, Okutani T, Maruyama T (2008) Deep-sea life – biological observations using research submersibles. Tokai University Press, Kanagawa

Halbach P, Nakamura K, Wahsner M, Lange J, Sakai H, Käselitz L, Hansen RD, Yamano M, Post J, Prause B, Seifert R, Michaelis W, Teichmann F, Kinoshita M, Märten A, Ishibashi J, Czerwinski S, Blum N (1989) Probably modern analogue of Kuroko-type massive sulphide deposits in the Okinawa Trough back-arc basin. Nature 338:496–499

Hashimoto J, Ohta S, Fujikura K, Miura T (1995) Distribution pattern and biogeography of the hydrothermal vent communities of the Minami-Ensei Knoll in the Mid-Okinawa Trough, Western Pacific. Deep Sea Res I 42:577–598

Kim DS, Ohta S (1991) Submersible observations and comparison of the biological communities of the two hydrothermal vents on the Iheya Ridge of the Mid-Okinawa Trough. JAMSTEC Tech Rep Deep Sea Res 221–253 (In Japanese with English abstract and captions)

Kojima S (2002) Deep-sea chemosynthesis-based communities in the northwestern Pacific. J Oceanogr 58:343–363

Kojima S, Ohta S, Yamamoto T, Miura T, Fujiwara Y, Hashimoto J (2001) Molecular taxonomy of vestimentiferans of the western Pacific and their phylogenetic relationship to species of the eastern Pacific. I. Family Lamellibrachiidae. Mar Biol 139:211–219

Kojima S, Tsuchida E, Numanami H, Fujikura K, Okutani T (2006) Synonymy of *Calyptogena solidissima* with *Calyptogena*

kawamurai (Bivalvia: Vesicomyidae) and its population structure revealed by mitochondrial DNA sequences. Zool Sci 23:835–842

Komai T, Segonzac M (2005) A revision of the genus *Alvinocaris* Williams and Chace (Crustacea: Decapoda: Caridea: Alvinocarididae), with descriptions of a new genus and a new species of *Alvinocaris*. J Nat History 39:1111–1175

Komai T, Tsuchida S, Segonzac M (2012) Records of species of the hippolytid genus *Lebbeus* White, 1847 (Crustacea: Decapoda: Caridea) from hydrothermal vents in the Pacific Ocean, with descriptions of three new species. Zootaxa 3241:35–63

Kyuno A, Shintaku M, Fujita Y, Matsumoto H, Utsumi M, Watanabe H, Fujiwara Y, Miyazaki J-I (2009) Dispersal and differentiation of deep-sea mussels of the genus *Bathymodiolus* (Mytilidae, Bathymodiolinae). J Mar Biol. doi:10.1155/2009/625672, Article ID 625672

Nakamura M, Watanabe H, Sasaki T, Ishibashi J, Fujikura K, Mitarai S (2014) Life history traits of Lepetodrilus nux in the Okinawa Trough, based upon gametogenesis, shell size, and gene variability. Mar Ecol Prog Ser 505:109–130

Nye V, Copley J, Linse K, Plouviez S (2013) *Iheyaspira bathycodon* new species (Vetigastropoda: Trochoidae: Turbinidar: Skeneinae) from the Von Damm vent field, Mid-Cayman spreading center, Caribbean. J Mar Biol Assoc UK 93:1017–1024

Ohta S (1991) Deep-sea submersible survey of the hydrothermal vent community on the northern slope of the Iheya Ridge, the Okinawa Trough. JAMSTEC Tech Rep Deep Sea Res 145–156 (In Japanese with English abstract and captions)

Podowski EL, Ma S, Luther GW III, Wardrop D, Fisher CR (2010) Biotic and abiotic factors affecting distributions of megafauna in diffuse flow on andesite and basalt along the Eastern Lau Spreading Center, Tonga. Mar Ecol Prog Ser 418:25–45

Rex MA, Etter RJ (2010) Deep-sea biodiversity: pattern and scale. Harvard University Press, Cambridge, p 354

Roterman CN, Copley JT, Linse KT, Tyler PA, Rogers AD (2013) The biogeography of the yeti crabs (Kiwaidae) with notes on the phylogeny of the Chirostyloidea (Decapoda: Anomura). Proc Roy Soc B. doi:10.1098/rspb.2013.0718

Sakai H, Gamo T, Ki ES, Tsutsumi M, Tanaka T, Ishibashi J, Wakita H, Yamano M, Oomori T (1990) Venting of carbon dioxide-rich fluid and hydrate formation in mid-Okinawa Trough backarc basin. Science 248:1093–1096

Sato K, Watanabe H, Sasaki T (2013) A new species of Solemya (Bivalvia: Protobranchia: Solemyidae) from a hydrothermal vent in the Iheya Ridge in the mid-Okinawa Trough, Japan. Nautilus 127:93–100

Seike K, Genkins RG, Watanabe H, Nomaki H, Sato K (2012) Novel use of burrow casting as a research tool in deep-sea ecology. Biol Lett 8:648–651

Takemura A, Tamotsu S, Miwa T, Yamamoto H (2010) Preliminary results on the reproduction of a deep-sea snailfish *Careproctus rhodomelas* around the active hydrothermal vent on the Hatoma Knoll, Okinawa, Japan. J Fish Biol 77:1709–1715

Tokeshi M (2011) Spatial structures of hydrothermal vents and vent-associated megafauna in the back-arc basin system of the Okinawa Trough, western Pacific. J Oceanogr 67:651–665

Tsuchida S, Watanabe K, Ishibashi J, Miyake H, Watabe H, Yamaguchi T, Kitajima T, Nakano A, Matsumura M, Watanabe H (2000) Preliminary report of a biological, geological, and geochemical survey on hydrothermalism at the Hatoma and Minna Knolls. JAMSTEC J Deep Sea Res 17:35–42

Tunnicliffe V, Juniper K, Sibuet M (2003) Reducing environments of the deep-sea floor. In: Tyler PA (ed) Ecosystems of the deep oceans, vol 28, Ecosystems of the world. Elsevier, Amsterdam, pp 81–110

Watanabe H, Tsuchida S, Fujikura K, Yamamoto H, Inagaki F, Kyo M, Kojima S (2005) Population history associated with hydrothermal vent activity inferred from genetic structure of neoverrucid barnacles around Japan. Mar Ecol Prog Ser 288:233–240

Watanabe H, Kado R, Kaida M, Tsuchida S, Kojima S (2006) Dispersal of vent-barnacle (genus *Neoverruca*) in the Western Pacific. Cah Biol Mar 47:353–357

Watanabe H, Fujikura K, Kojima S, Miyazaki J-I, Fujiwara Y (2010) Japan: vents and seeps in close proximity. In: Kiel S (ed) The vent and seep biota. Topics in geobiology, vol 33, pp 379–401

Watanabe H, Seo E, Takahashi Y, Yoshida T, Kojima S, Fujikura K, Miyake H (2013) Spatial distribution of sister species of vesicomyid bivalves *Calyptogena okutanii* and *Calyptogena soyoae* along an environmental gradient in chemosynthetic biological communities in Japan. J Oceanogr 69:129–134

Watsuji T, Nakagawa S, Tsuchida S, Toki T, Hirota A, Tsunogai U, Takai K (2010) Diversity and function of epibiotic microbial communities on the galatheid crab, Shinkaia crosnieri. Microbes Environ 25:288–294

Wessel P, Smith WH (1998) New, improved version of the generic mapping tools released. EOS Trans Am Geophys Union 79:579

Yorisue T, Kado R, Watanabe H, Hoeg JT, Inoue K, Kojima S, Chan BKK (2013) Influence of water temperature on the larval development of *Neoverruca* sp. and *Ashinkailepas seepiophila*—implications for larval dispersal and settlement in the vent and seep environments. Deep Sea Res I 71:33–37

Part V

Appendix I: Site Reports

Brief Report of Side-Scan Sonar Observations Around the Yokoniwa NTO Massif

35

Miho Asada, Kyoko Okino, Hisashi Koyama, Akira Asada, and Tamaki Ura

Abstract

We conducted the side-scan sonar observations of the Yokoniwa Rise, a non-transform offset massif at the southern Central Indian Ridge using the autonomous underwater vehicle AUV-*r2D4* fitted with a 100 kHz sidescan sonar system. We identified two terrain types with high backscattering signals; one terrain type exhibited typical volcanic features, while the other appeared to correspond to peridotite outcrops. The orientation of linear features identified in the survey area was highly variable, but appeared to be affected by local bathymetry. The standard deviations of the orientation and average length of these linear features were larger and smaller, respectively, than those of similar features observed along the East Pacific Rise. These observations showed that the linear features on the sonar image were likely to be flow channels or areas of the seafloor that had experienced gravitational collapse. A few small chimney-like structures were also detected.

Keywords

Peridotite outcrops • Side-scan sonar • Yokoniwa rise

35.1 Introduction

The Yokoniwa Rise is a non-transform offset massif (NTO) situated along the southern Central Indian Ridge (CIR), immediately north of the Rodriguez Triple Junction in the Indian Ocean. It is a rectangular-shaped topographic high located at the boundary between CIR segments 1 and 2 to the north of the Kairei Hydrothermal Field (Fig. 35.1) (Okino et al., Chap. 11). A dive by the submersible *Shinkai6500* in 2009 discovered a group of inactive chimneys and widely exposed peridotite outcrops on the eastern slope and top of the Yokoniwa Rise (*YK09-13_leg2 cruise report* available at http://www.godac.jamstec.go.jp/darwin/cruise/yokosuka/yk09-13_leg2/e), suggesting past activity of ultramafic-hosted hydrothermal system in this area. Surveys of this area will improve our understanding of the geological control of ultramafic-hosted hydrothermal activity. Here we present the results of a sidescan sonar survey of the Yokoniwa Rise using the autonomous underwater vehicle AUV-*r2D4* fitted with a 100 kHz interferometric sidescan sonar system that was conducted on cruise KH-10-06 in 2010, and geological maps produced from the obtained acoustic data set.

M. Asada (✉)
Research and Development Center for Earthquake and Tsunami (CEAT), Japan Agency for Marine-Earth Science and Technology (JAMSTEC), 2-15 Natsushima, Yokosuka, Kanagawa 237-0061, Japan
e-mail: asadam@jamstec.go.jp

K. Okino
Atmosphere and Ocean Research Institute (AORI), The University of Tokyo, 5-1-5 Kashiwanoha, Kashiwa, Chiba 277-8564, Japan

H. Koyama
Mitsui Engineering & Shipbuilding Co., Ltd, 1-1, Tama 3-chome, Tamano, Okayama 706-8651, Japan

A. Asada
Institute of Industrial Science (IIS), The University of Tokyo, 4-6-1 Komaba, Meguro-ku, Tokyo 153-8505, Japan

T. Ura
Center for Socio-Robotic Synthesis, Kyusyu Institute of Technology, 2-4, Hibikino, Wakamatsu-ku, Kita Kyusyu, Fukuoka 808-0196, Japan

J.-i. Ishibashi et al. (eds.), *Subseafloor Biosphere Linked to Hydrothermal Systems: TAIGA Concept*,
DOI 10.1007/978-4-431-54865-2_35,

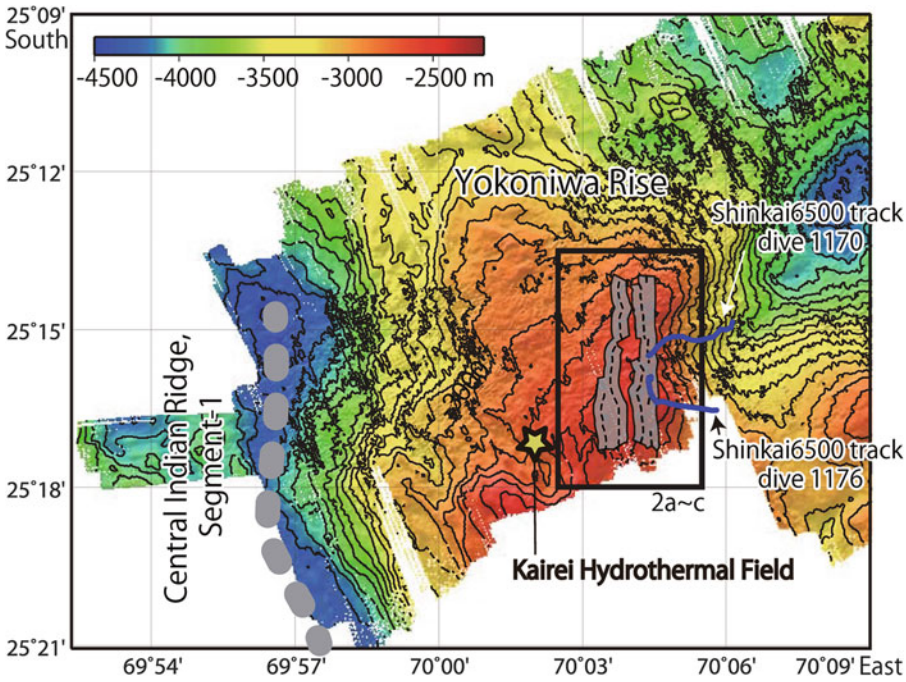

Fig. 35.1 Bathymetry data of the surveyed area were obtained by the Seabeam2120 system on the R/V *Hakuho-Maru* during cruise KH10-06 (Okino et al., Chap. 11). *Inset* is shown in Fig. 35.2a–c. The *gray areas* and the *two blue lines* indicate coverage of sidescan sonar imagery obtained by AUV-*r2D4* in 2010, and the *track lines* of the *Shinkai6500* submersible (dives 1170 and 1176) in 2009, respectively

35.2 Data Acquisition

35.2.1 Description of Sidescan Sonar System and Processing Procedures

Dive 68 of AUV-*r2D4* was conducted above the Yokoniwa Rise (Fig. 35.1). The *r2D4* is equipped with a 100/500 kHz dual frequency sidescan sonar system (Klein System). The half swath range of the sonar image is 300 m and an L-shaped hydrophone array is used to calculate interferometric bathymetry with high accuracy (Koyama et al. 2007).

We conducted a 19 km survey of the top of the Yokoniwa Rise in a north–south direction along four subparallel survey lines that covered an area of 6.3 km (north–south) × 2.4 km (east–west) (Fig. 35.1). The vehicle altitude during the dive was kept at 30–150 m above the seafloor during the survey.

We first converted the file format from that of the vendor (*.5kd) to a generalized XTF format, and then applied the necessary corrections to produce a mosaic image of the area using software. The resulting sonar image is shown in Fig. 35.2a. Correction and processing of the interferometric bathymetry data were conducted using proprietary software (Koyama et al. 2007). The processed interferometric bathymetry data covered 18 % of the total survey area (Fig. 35.2b). The results of the 500 kHz sonar survey data will be presented in future.

35.2.2 Data Limitations and Considerations

The sonar image was distorted in several places, possibly due to issues related to the stability and heading of the AUV. In addition, wedge-shaped acoustic noises, likely attributed to communication signals between the vehicle and the mother ship at 10-second intervals, were also observed (see Fig. 35.3). Since gain modification was occasionally inappropriate during data acquisition, comparisons of backscattering intensity between the port and the starboard sides require careful consideration.

35.3 Observed Results

As shown in Fig. 35.2, the sidescan sonar imagery revealed the presence of numerous areas with high backscattering signals. The boundaries between these areas and terrain with low backscattering were indistinct. Terrains with high backscattering signals covered 42.5 % of the study area and can be classified into two types. One type was characterized by facies with volcanic features typically associated with the neo-volcanic zones of mid-ocean ridges, such as hummocky and sheet lava patterns (Smith et al. 1995; Briais et al. 2000; Sauter et al. 2002; Cann and Smith 2005; Searle et al. 2010). This type of terrain was found in the west of the observed area, on the gentle west-facing slope near the top of the Yokoniwa Rise (Fig. 35.3a). The second type of high backscattering terrain was not

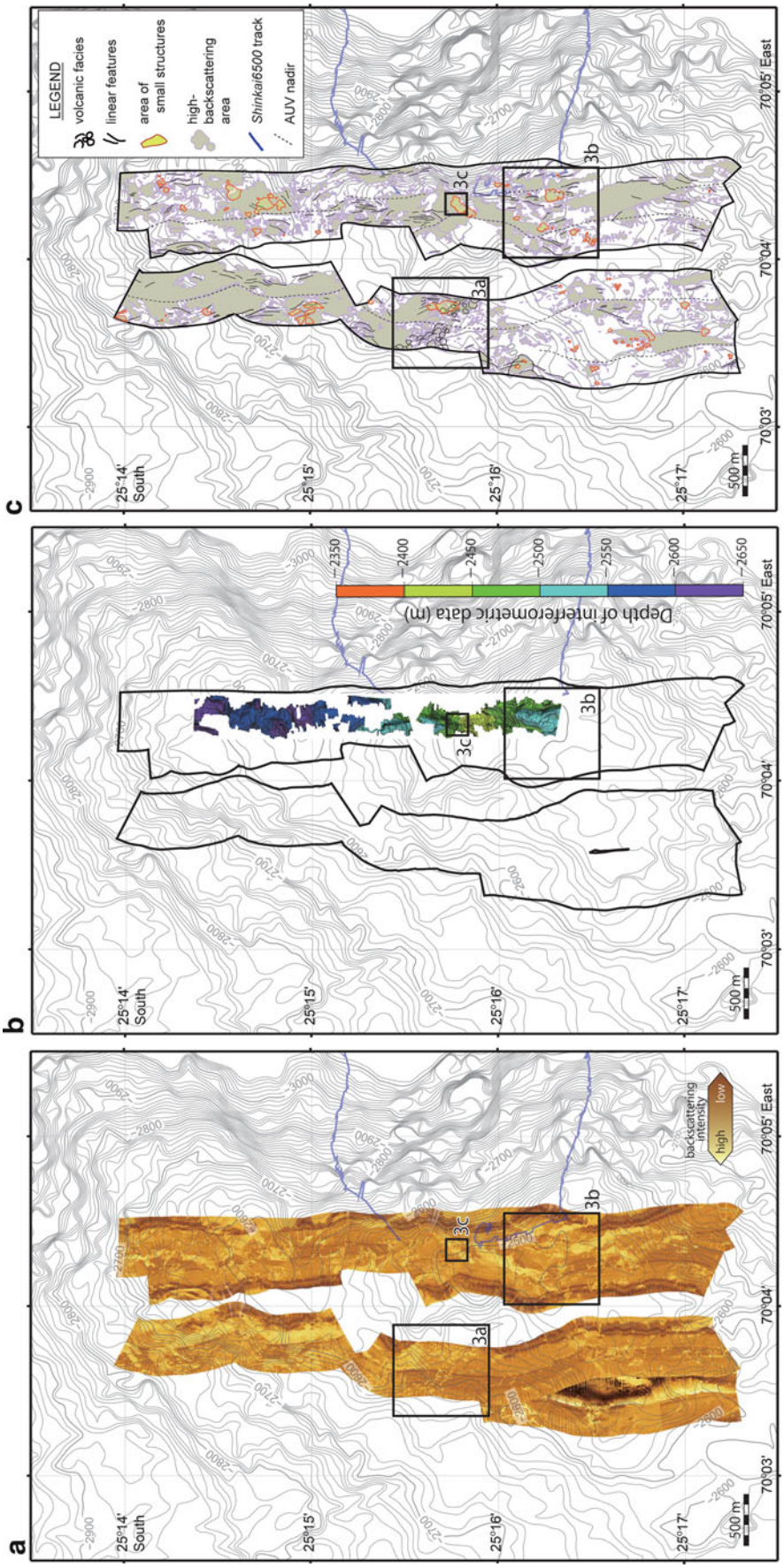

Fig. 35.2 (**a**) Sidescan sonar imagery collected by the AUV-*r2D4*. Contours show shipboard multibeam bathymetry data. Areas with high backscattering intensity appear lighter in color. *Blue lines* indicate the tracks of the *Shinkai6500* submersible (*YK09-13_leg2 cruise report*, 2009). *Boxes* indicate the areas shown in Fig. 35.3. (**b**) Shipboard multibeam bathymetry overlaid with interferometric bathymetry data (color). *Boxes* indicate the areas shown in Fig. 35.3. (**c**) Interpretation map of the sidescan sonar imagery. High backscattering terrains are colored *pale green*. Locations where the small, chimney-like, columnar structures were observed are shown by *red circles*. *Boxes* indicate the areas shown in Fig. 35.3

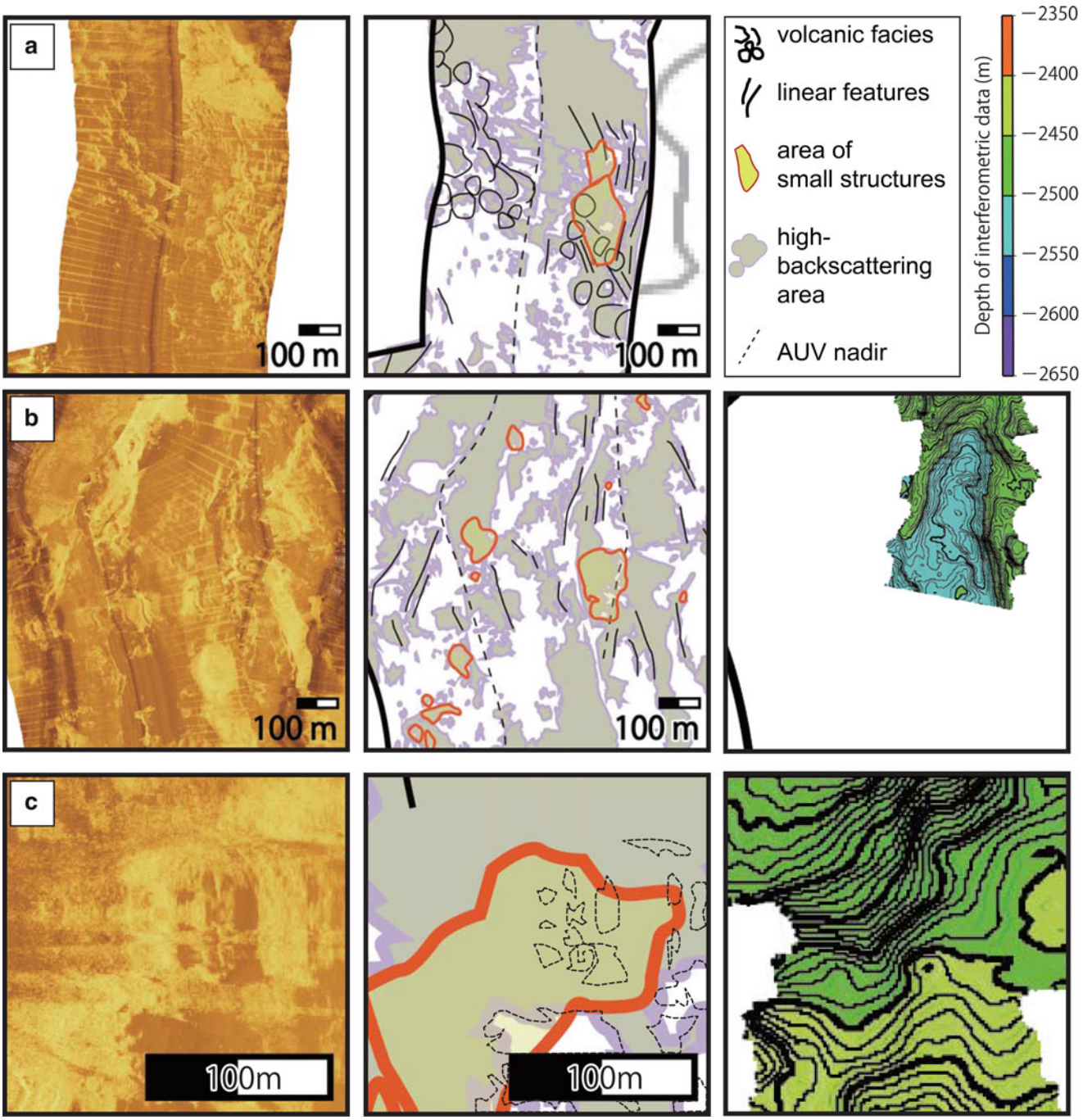

Fig. 35.3 Enlarged sidescan sonar images (*left*), interpretation map (*center*), and interferometric bathymetry data (*right*). The legend is the same as that used in Fig. 35.2c. The wedge-shaped lines of high backscattering across tracks are acoustic noise. (**a**) Volcanic features, (**b**) linear features in a region of high backscattering without acoustic shadows, and (**c**) small, columnar, structures with acoustic shadows. *Dotted circles* in interpretation map indicate acoustic shadows

associated with any obvious acoustic shadows, suggesting that these areas consisted of flat seafloor (Fig. 35.3b). This type of terrain was distributed throughout the survey area, and might be indicative of flat areas with peridotite outcrops covered by either no or little sediment. Video image of peridotite outcrops covered by little sediment was recorded (dive 1176 of *Shinkai6500*) in this type of terrain (Fig. 35.4) (Nakamura and Onboard Scientists 2009). The indistinct boundary between the terrains with high and low backscattering signals might reflect a gradual change in the degree of sedimentation between these areas.

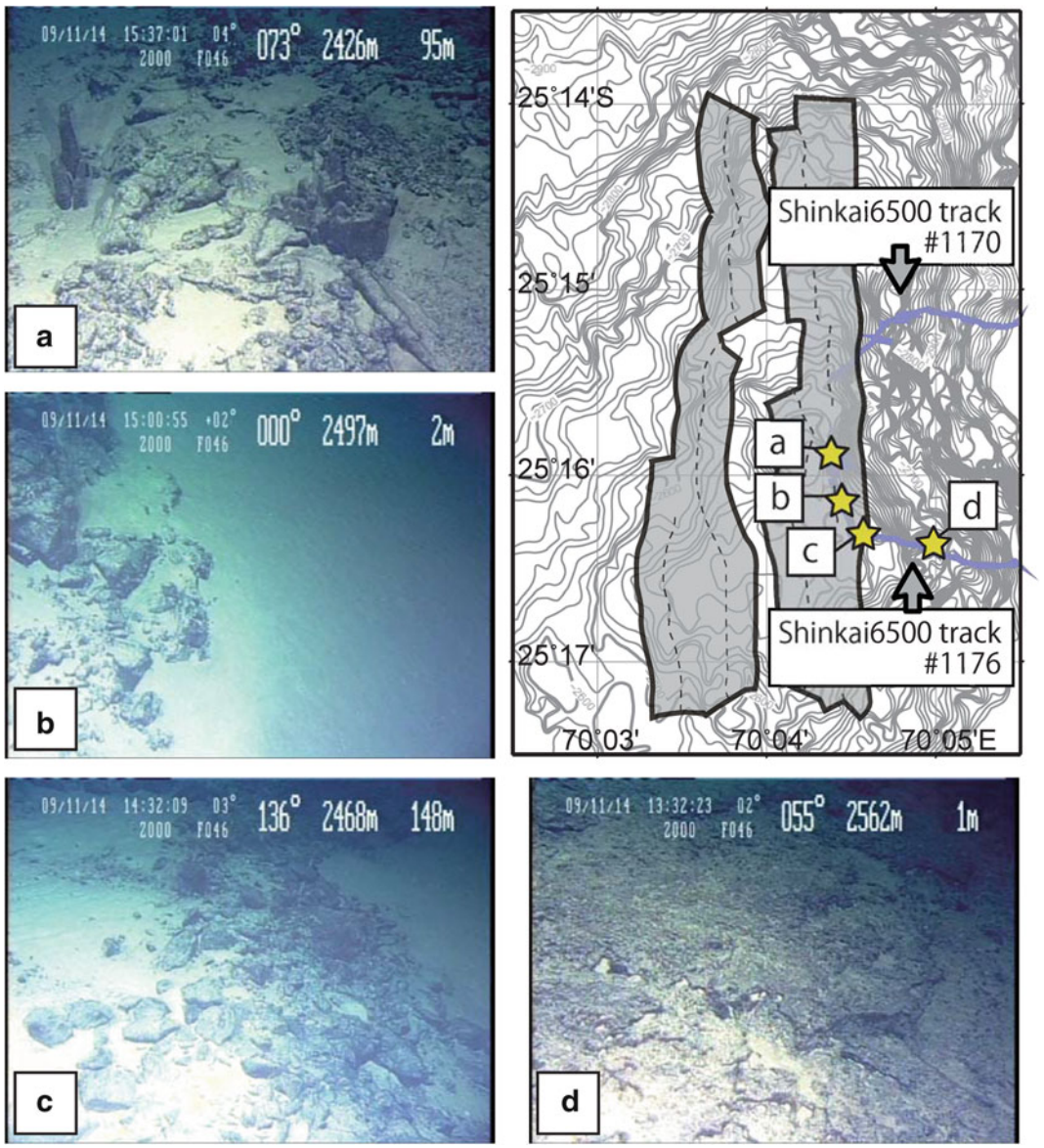

Fig. 35.4 Photographs taken by *Shinkai6500* in 2009 from database of YK09-13_leg2 cuise. The location of each photo is indicated by a *star* on the index map (*top right*). Plates **a**–**d** show flat outcrops surrounded by sediment at the locations indicated by the stars on the bathymetry map. The tops of the outcrops were level with the seafloor

Linear features were identified in both types of terrain in the study area (Fig. 35.3a, b). We identified a total of 216 linear features and measured their orientation and length. The orientation of these linear features was primarily parallel or orthogonal to local bathymetric variation (based on bathymetry data obtained by the *Seabeam2112* system), and not in the direction of plate motion. Average and standard deviation of the elongation direction were N1°W ± 20°. And average length of the linear features was 0.14 km. At 20°, the standard deviation of the direction was larger than the value of 7.94° along the East Pacific Rise (EPR) 9°05′–10°03′N (based on DSL-120 data, which is 120 kHz sidescan sonar observation data; Asada unpublished data). In addition, the average length of the linear features was less than that along the EPR (0.2 km). These observations suggest that the linear features would not attribute to be tectonic origin, but to reflect either flow channels or gravitationla collapse.

We also observed small columnar structures with acoustic shadows in terrains with high backscattering signals (Fig. 35.3c). Although these structures were interpreted to be hydrothermal chimneys, we did not observe any other indication of hydrothermal activity such as hydrothermal mounds or acoustic anomaly in water column in the observed images.

Acknowledgements We thank the officers and crew of the R/V *Hakuho-Maru*, members of the *r2D4* technical support team, and scientists onboard cruise KH-10-06 for their assistance with the collection of the survey data. We thank the two anonymous reviewers and the editorial board of this e-book for their suggestions regarding improvements to the manuscript. This research was financially supported by the Ministry of Education, Culture, Science, and Technology (MEXT) of Japan, through a special coordination fund (Project TAIGA: Trans-crustal Advection and In situ biogeochemical processes of Global subseafloor Aquifer, FY 2008–2012).

References

Briais A, Sloan H, Parson LM, Murton BJ (2000) Accretionary process in the axial valley of the Mind-Atlantic Ridge 27°N-31°N from TOBI side-scan sonar images. Mar Geophys Res 21:87–119

Cann JR, Smith DK (2005) Evolution of volcanism and faulting in a segment of the Mid-Atlantic Ridge at 25°N. Geochem Geophys Geosyst 6:Q09008. doi:10.1029/2005GC000954

Koyama H, Asada A, Ura T, Han J, Obata T, Nagahashi K (2007) Bathymetric survey at hydrothermal site by L-array Interferometric sonar mounted on AUV-r2D4. In: Underwater technology and workshop on scientific use of submarine cables and related technologies, pp 156–161, 10.1109/UT.2007.370845, 17–20 April, Tokyo

Nakamura K, Onboard Scientists (2009) YK09-13_leg2 cruise report. http://www.godac.jamstec.go.jp/darwin/cruise/yokosuka/yk09-13_leg2/e

Sauter D, Parson L, Mendel V, Rommevaux-Jestin C, Gomez O, Briais A, Mevel C, Tamaki K, The FUJI Scientific Team (2002) TOBI sidescan sonar imagery of the very slow-spreading Southwest Indian Ridge: evidence for along-axis magma distribution. Earth Planet Sci Lett 199:81–95

Searle RC, Murton BJ, Achenbach K, LeBas T, Tivey M, Yeo I, Cormier MH, Carlut J, Ferreira P, Mallows C, Morris K, Schroth N, van Calsteren P, Waters C (2010) Structure and development of an axial volcanic ridge: Mid-Atlantic Ridge, 45 degrees N. Earth Planet Sci Lett 299:228–241

Smith DK, Cann J, Dougherty ME, Lin J, Spencer S, Macleod C, Keeton J, Mcallister E, Brooks B, Pascoe R, Robertson W (1995) Mid-Atlantic Ridge volcanism from deep-towed side-scan sonar images, 25°-29°N. J Volcano Geotherm Res 67:233–262

Examination of Volcanic Activity: AUV and Submersible Observations of Fine-Scale Lava Flow Distributions Along the Southern Mariana Trough Spreading Axis

36

Miho Asada, Shuro Yoshikawa, Nobutatsu Mochizuki, Yoshifumi Nogi, and Kyoko Okino

Abstract

A high-resolution acoustic investigation using the AUV *Urashima* has revealed detailed volcanic and tectonic features along the neo-volcanic zone of the intermediate-rate spreading Southern Mariana Trough, where the high magma flux forms fast-spreading type axial high morphology. Side-scan sonar imagery suggests that the survey area mainly consists of two types of terrain: high-backscattering lumpy terrain occupies the majority of the neo-volcanic zone, and low-backscattering terrain is scattered over the entire area to form various bathymetric features. Visual observations by the submersible *Shinkai 6500* show that the former corresponds to bulbous pillow lava and the latter to jumbled or wrinkled sheet lavas. The estimated proportion of sheet lava with respect to study area is approximately 10 %. Pillow lavas are flatly distributed and do not form the pillow mounds that are common in the slow-spreading Mid-Atlantic Ridge. Furthermore, we did not observe any pillars, collapse features, or axial summit troughs, all of which are frequently reported in the fast-spreading East Pacific Rise.

Keywords

AUV *Urashima* • Low-backscattering terrain • Lumpy terrain • Pillow and sheet lavas • Side-scan sonar

36.1 Introduction

Melt generation and the resulting volcanic activity associated with a seafloor spreading axis generally depend on the spreading rate (e.g., Small 1998; Macdonald 1998). Along back-arc ridges, the correlation between spreading rate and volcanism is more complex owing to the influence of plate subduction processes (Martinez and Taylor 2002; Taylor and Martinez 2003). Taylor and Martinez (2003) systematically analyzed global back-arc basin basalt and proposed that melt generation along back-arc ridges can vary markedly with distance from the volcanic front, mainly due to subduction-induced compositional changes in the mantle rather than the seafloor spreading rate itself. The spreading center of the Southern Mariana Trough shows an axial high morphology similar to fast-spreading ridges, despite its slow to intermediate spreading rate. The back-arc spreading center is very close to the volcanic arc in

M. Asada (✉)
Research and Development Center for Earthquake and Tsunami (CEAT), Japan Agency for Marine-Earth Science and Technology (JAMSTEC), 2-15 Natsushima, Yokosuka, Kanagawa 237-0061, Japan
e-mail: asadam@jamstec.go.jp

S. Yoshikawa
Department of Mathematical Science and Advanced Technology, Japan Agency for Marine-Earth Science and Technology (JAMSTEC), 2-15 Natsushima, Yokosuka, Kanagawa 237-0061, Japan

N. Mochizuki
Priority Organization for Innovation and Excellence, Kumamoto University, Kumamoto, Japan

Y. Nogi
National Institute of Polar Research, 10-3 Midoricho, Tachikawa, Tokyo 190-8518, Japan

K. Okino
Atmosphere and Ocean Research Institute (AORI), the University of Tokyo, 5-1-5 Kashiwanoha, Kashiwa, Chiba 277-8564, Japan

J.-i. Ishibashi et al. (eds.), *Subseafloor Biosphere Linked to Hydrothermal Systems: TAIGA Concept*,
DOI 10.1007/978-4-431-54865-2_36,

this region, although the volcanic front is not clear south of 12°30′N. Previous studies have shown that the magmatic budget increases along the spreading axes in the Southern Mariana Trough because the spreading axis possibly captures heat and melt supply from the volcanic front (e.g., Martinez et al. 2000; Fryer 1996; Taylor and Martinez 2003).

Although previous studies have shown a high magma budget in the Southern Mariana Trough, the style of volcanism (e.g., the distribution of the volcanic product) and lava morphology and texture have not yet been studied. During the TAIGA project, we conducted fine-scale acoustic observations using the AUV *Urashima* and visual observations using the submersible *Shinkai 6500* in the hydrothermal areas of the Southern Mariana Trough (Seama et al., Chap. 17). One of the target areas is the axial zone of back-arc spreading, where it is possible to observe the most recent volcanic activity and active hydrothermal vents. In this chapter, we show the microbathymetry and side-scan sonar imagery collected by the AUV together with photographs taken during the submersible dives. We describe the fine-scale volcanic and tectonic features in the area. This survey gives us the first sub-meter scale observations with ground references along the Southern Mariana Trough, and enables us to obtain a better understanding of volcanism at back-arc spreading centers under the considerable influence of arc volcanism.

36.2 Geological Background

The Mariana Trough is a back-arc basin located behind the Mariana Trench, where the Pacific Plate subducts under the Philippine Sea Plate. The current rate of spreading is approximately 40 mm/year near Guam (13°24′N) (Kato et al. 2003; Martinez et al. 2000) and, based on this spreading rate, the ridge has been categorized as a slow to intermediate spreading ridge.

The spreading axis lies in the eastern part of the basin, indicating asymmetric seafloor accretion (Yamazaki et al. 2003; Deschamps and Fujiwara 2003; Deschamps et al. 2005; Asada et al. 2007). Abyssal hills have not been clearly observed in the eastern off-axis area owing to thick sedimentary coverage and/or overprinting of later arc volcanism (Fryer 1996; Martinez et al. 2000). North of 14°N, the spreading center of the Mariana Trough is morphologically similar to slow-spreading mid-ocean ridges, having a deep crustal graben flanked by a zone of abyssal hills (Seama et al. 2002; Yamazaki et al. 2003), as expected from its slow spreading rate. However, the southern part of the Mariana Trough, where the back-arc spreading axis approaches the volcanic arc (within 10 km at around 13°20′N) (Martinez et al. 2000), shows a broad and smooth morphological cross section and lacks a deep crustal graben (Fig. 36.1). The morphology of this spreading axis is thus similar to that of fast-spreading ridges (Martinez et al. 2000; Martinez and Taylor 2002).

The similarity in morphology to fast-spreading ridges suggests that the spreading ridge of the Southern Mariana Trough receives a considerably higher magma supply than elsewhere along the trough (e.g., Fryer 1996; Martinez et al. 2000; Becker et al. 2010). The highly inflated region along the Southern Mariana Trough is centered at 12°57′N, where the axis forms a broad shallow plateau almost a kilometer wide. The high magma supply in the area is also supported by the existence of a thick crust determined from gravity analysis (Kitada et al. 2006) and by the existence of a melt lens detected by a multi-channel reflection survey (Becker et al. 2010).

Our study area is the neo-volcanic zone of the axial high between 12°56′30″N and 12°57′30″N (Box in Fig. 36.1). The area is the most inflated part along the spreading axis (Martinez et al. 2000; Baker et al. 2005). In the study area, there are two known sites of hydrothermal activity: the Snail site and the Yamanaka site (Fig. 36.2). The Snail site (12°57′12″N, 143°37′12″E) was discovered by an American group using the remotely operated vehicle *Jason* (Wheat et al. 2003). The site is characterized by several high- and low-temperature hydrothermal vents with clear fluid coming up through cracks in outcrops. The Yamanaka site (12°56′42″N, 143°36′48″E) is located approximately a kilometer southwest of the Snail site and was discovered by a Japanese group using the *Shinkai 6500* (Kakegawa et al. 2008). Inactive chimneys and low-temperature simmering have been observed at the Yamanaka site (Kakegawa et al. 2008).

36.3 Data Acquisition

Meter-scale, high-resolution, bathymetric and side-scan sonar data were acquired by the AUV *Urashima* (JAMSTEC), which was built in 1998 (Tsukioka et al. 2005; Kasaya et al. 2011). The AUV *Urashima* is fitted with a 120 kHz side-scan sonar (SSS) for obtaining backscattering intensity data, a 1–6 kHz charp sub-bottom profiler (SBP) for obtaining sub-seafloor sediment information (EdgeTech2200). It is also fitted with a 400 kHz multi-beam echo sounder (MBES) to obtain meter-scale bathymetry data and backscattering intensity data simultaneously (Seabat7125), a depth meter, an altimeter, and a conductivity, temperature, depth, and dissolved oxygen level (CTDO) sensor.

The *Urashima* Dive-91 was conducted at the back-arc spreading center between 12°56′30″N and 12°57′30″N (Fig. 36.2) during the YK09-08 cruise in 2009 (Okino and

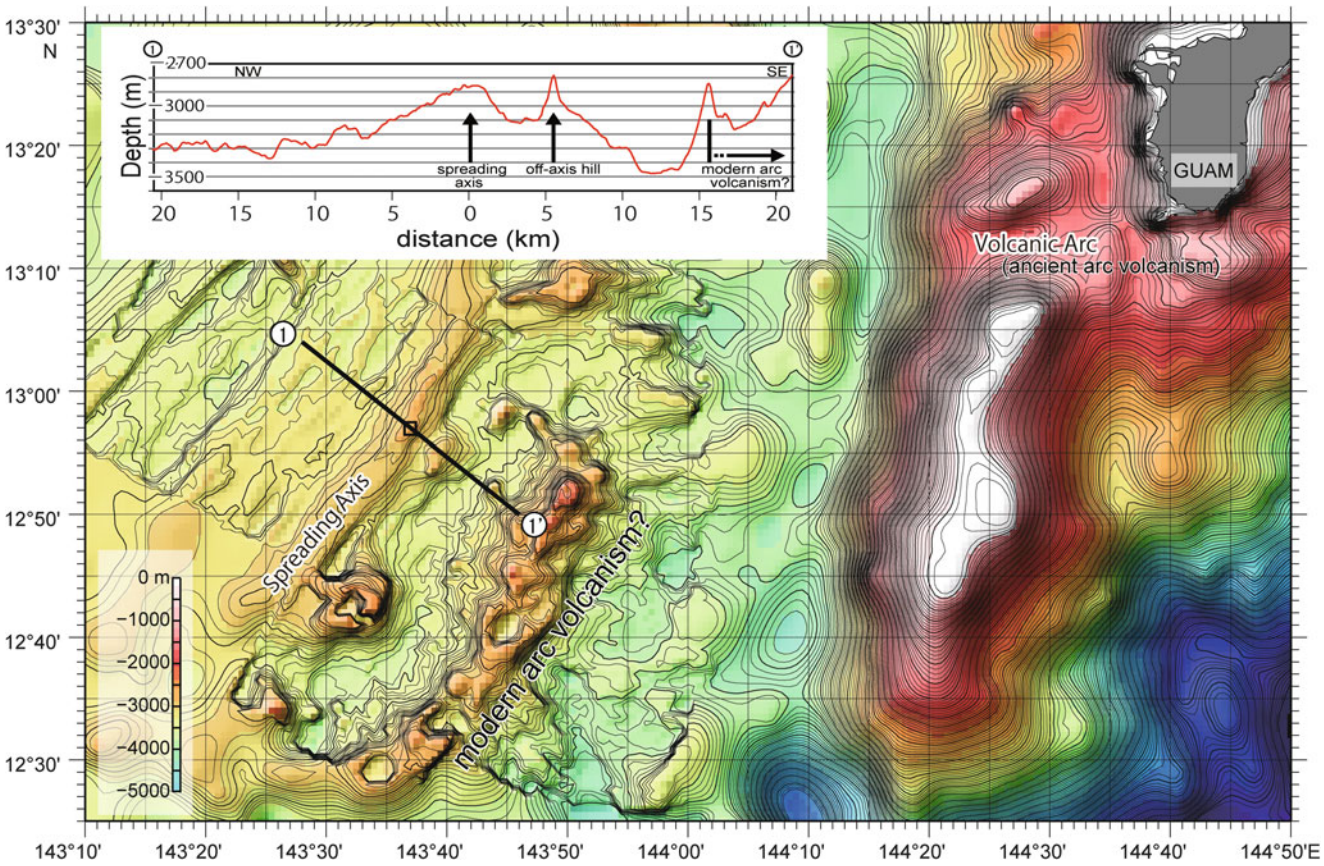

Fig. 36.1 Regional map of the Southern Mariana Trough. The bathymetry data obtained using a *SeaBeam 2112* system on cruise YK09-08 aboard the R/V *Yokosuka* are superimposed on the ETOPO1 dataset (Amante and Eakins 2009). The *box* on transect shows the area shown in Fig. 36.2. The *inset* shows the cross section along the *black line* $1 - 1'$

Shipboard scientific party 2009). The survey was done along seven ~2 km long survey lines parallel to the spreading axis at intervals of roughly 100 m. The obtained data cover an area approximately 2 km long and 1 km wide that includes the neo-volcanic zone. The average survey altitude and speed of the AUV during the YK09-08 cruise were about 100 m and 2 knots, respectively. The expected across-track resolutions for the AUV's acoustic imagery are several meters for the 400 kHz MBES and approximately 7.5 cm for the 120 kHz SSS (when acoustic velocity in seawater is 1,500 m/s). The acoustic beam along-track footprint is 2–5 m (beam width is 0.5° for MBES and 0.9° for SSS). The data processing method is described in Asada et al. (Chap. 37).

In this area, the *Shinkai 6500* submersible performed a total of six dives in 2003 and 2005, and then three more dives after the AUV observation during the YK10-11 cruise in 2010 (Kojima and Shipboard scientific party 2011). We utilized video images and photographs obtained during the dives as ground references for the acoustic imagery data.

36.4 Results and Discussion

36.4.1 Overview of the Survey Area

The micro-bathymetry collected by the AUV-attached 400 kHz multibeam sonar is shown in Fig. 36.2. The northwestern part of the survey area is characterized by well-developed faults; on the contrary, the southeastern part is shallower and dominated by volcanic structures. Hereafter, we refer to these parts as the western and eastern areas following the nomenclature of Yoshikawa et al. (2012) (Fig. 36.2). The mosaic image of the 120 kHz side-scan sonar data and its geological interpretation are shown in Fig. 36.3a and b, respectively.

The western area occupies approximately 30 % of the surveyed area. The side-scan sonar image shows the existence of extensive linear features (Fig. 36.3a, b). These linear features, sometimes associated with acoustic shadows, are generally interpreted as faults, fissures, lava flow channels, and levees. A 30 m high, rectangular hill lies in

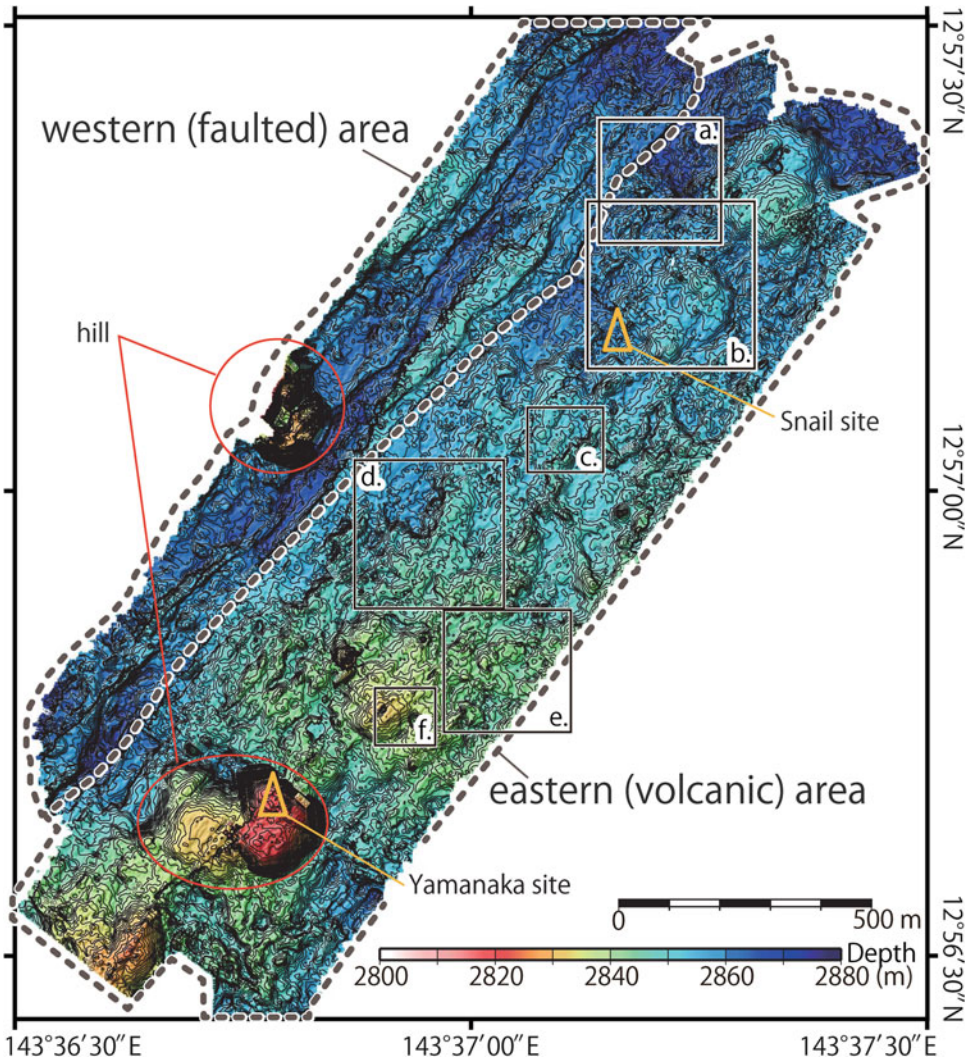

Fig. 36.2 Bathymetry map obtained by the 400 kHz multibeam system mounted on the AUV *Urashima*. Contour interval is 1 m. The enlarged views in *boxes a–f* are shown in Fig. 36.5. *Triangles* indicate the locations of two hydrothermal sites

the area (Fig. 36.2) and is cut by the linear features. The orientation of the linear features is typically NNE–SSW to NE–SW and corresponds well with the orientation of the ridge axis. Both side-scan sonar intensity and SBP data suggest that the sediment cover is very thin or absent in this area.

The eastern area occupies approximately 70 % of the surveyed area. The bathymetry map (Fig. 36.2) shows that this area consists of several mounds, ring-shaped craters, and minor ridges. These volcanic structures are mostly undeformed by faults and are aligned in the NNE–SSW direction, forming the neo-volcanic zone. The relative elevation of these features is 5–10 m. On the side-scan sonar image, we recognize a few linear features that are mostly not associated with acoustic shadows (Fig. 36.3). Generally, such linear features are interpreted as faults or fissures with small vertical throw. Two hydrothermal sites lie in the eastern area (Fig. 36.2). We were unable to recognize any chimney-like structures at and around the Snail site (Fig. 36.4a). A small chimney-like feature was observed on the sonar image at the Yamanaka site (triangle in Fig. 36.4b). The Yamanaka site is situated on an approximately 25 m-high, flat-topped mound (Fig. 36.2), that adjoins another flat-topped mound to the southwest. Other several chimney-like structures were also recognized in between two mounds (circle in Fig. 36.4b). The surface of these mounds corresponds to high backscattering and lumpy terrain (described in the next paragraph) on the sonar imagery. Both side-scan sonar intensity and the SBP data suggest that the sediment cover is very thin or absent in this area, too.

36.4.2 High-Backscattering Lumpy and Smooth Terrains

We categorize the high-backscattering terrain into two groups: lumpy terrain and smooth terrain. Figure 36.5 shows the typical facies of these terrains on the sonar

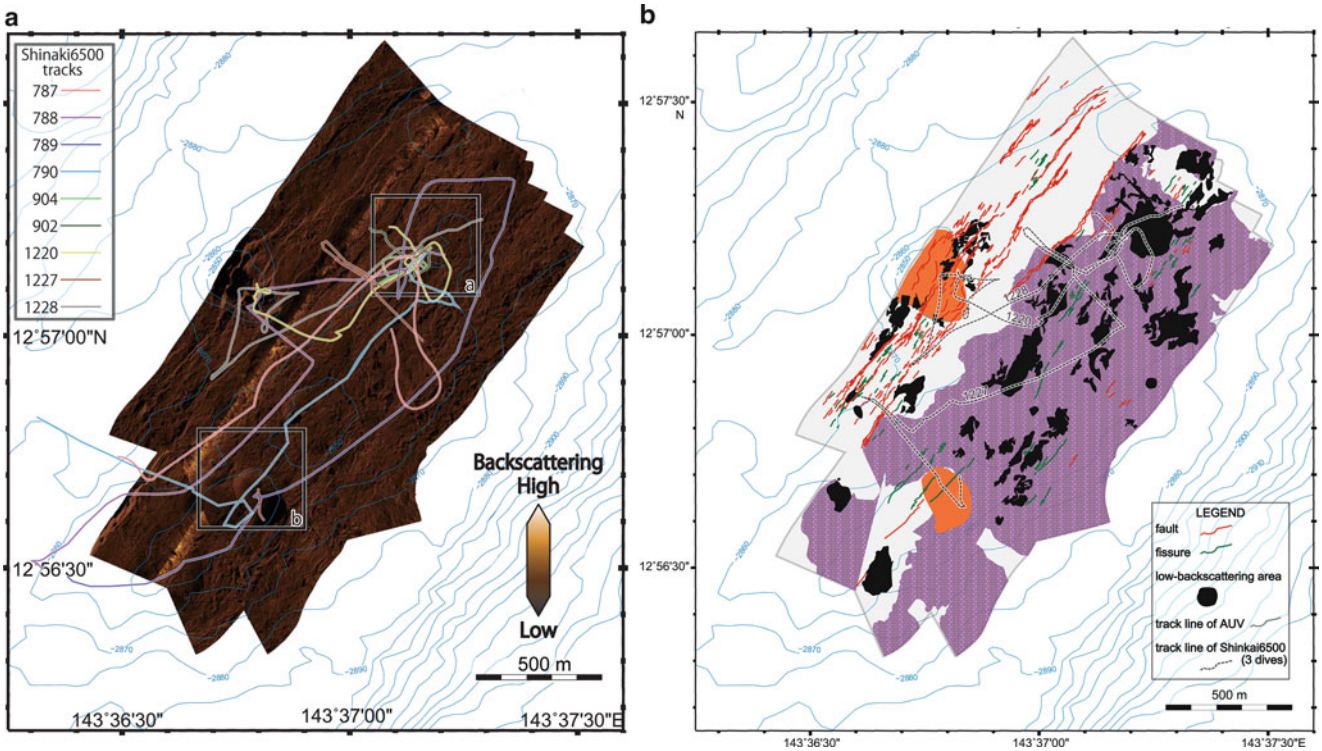

Fig. 36.3 (**a**) Mosaic imagery of 120 kHz side-scan sonar data. *Darker color* indicates lower backscattering intensity. Bathymetry is shown by contours. Tracks of nine submersible dives used for ground reference are indicated. *Boxes a* and *b* indicate the locations of Fig. 36.4a and b, respectively. (**b**) Map showing the interpretation of the side-scan sonar imagery. High-backscattering lumpy terrain and low-backscattering terrain are indicated by *purple* and *black colors*, respectively. *Orange areas* indicate relatively large hills and *gray areas* indicate smooth terrain. *Boxes* indicate the same as in (**a**)

image, and the distribution of these terrains is shown in Fig. 36.3b.

The lumpy terrain is characterized by densely spaced small-scale bumps (lumps) (Figs. 36.5d, g). The typical size of each bump is 20–30 m and the relief is less than a few meters. No dominant direction is recognized for each bump or the distribution pattern. The lumpy terrain occupies most part of the eastern area (Fig. 36.3b).

The smooth terrain is the area exhibiting a smooth surface with finer dots (Figs. 36.5e, h). The terrain shows relatively high backscattering intensity and has no prominent pattern on the sonar image. The smooth terrain covers a large part of the western area (Fig. 36.3b)

36.4.3 Low-Backscattering Terrains

We recognized at least 49 sites of smooth surfaces with low-backscattering signatures on the side-scan image (Fig. 36.3b). These sites, which we refer to as low-backscattering terrain, can be distinguished from the lumpy terrain (Fig. 36.5f, i). The low-backscattering terrain appears as a very fine and homogeneous pattern with few acoustic shadows. The boundaries between the low-backscattering terrain and the lumpy terrain are distinct in some places but ambiguous in others. This variation may be attributed to the differences in age and/or morphological relationships between them. The relative proportion of low-backscattering terrain to lumpy terrain within the observed area was approximately 10 %. The low-backscattering terrains were observed in both the eastern and western areas (Fig. 36.3b). Figure 36.6 shows close up views of the low-backscattering terrains with a sonar intensity profile across these terrains. The low-backscattering terrains are observed in areas with various morphologies: on the top and slope of several mounds, minor ridges, and the slope and bottom of ring-shaped craters.

36.4.4 Visual Observation Using the Manned Submersible, *Shinkai 6500*

The submarine lava shows various surface forms depending on the physical and chemical property of magma, effusion rate, and local surface morphology (Griffiths and Fink 1992; Gregg et al. 1996; Fink and Griffiths 1998; Umino et al. 2000;

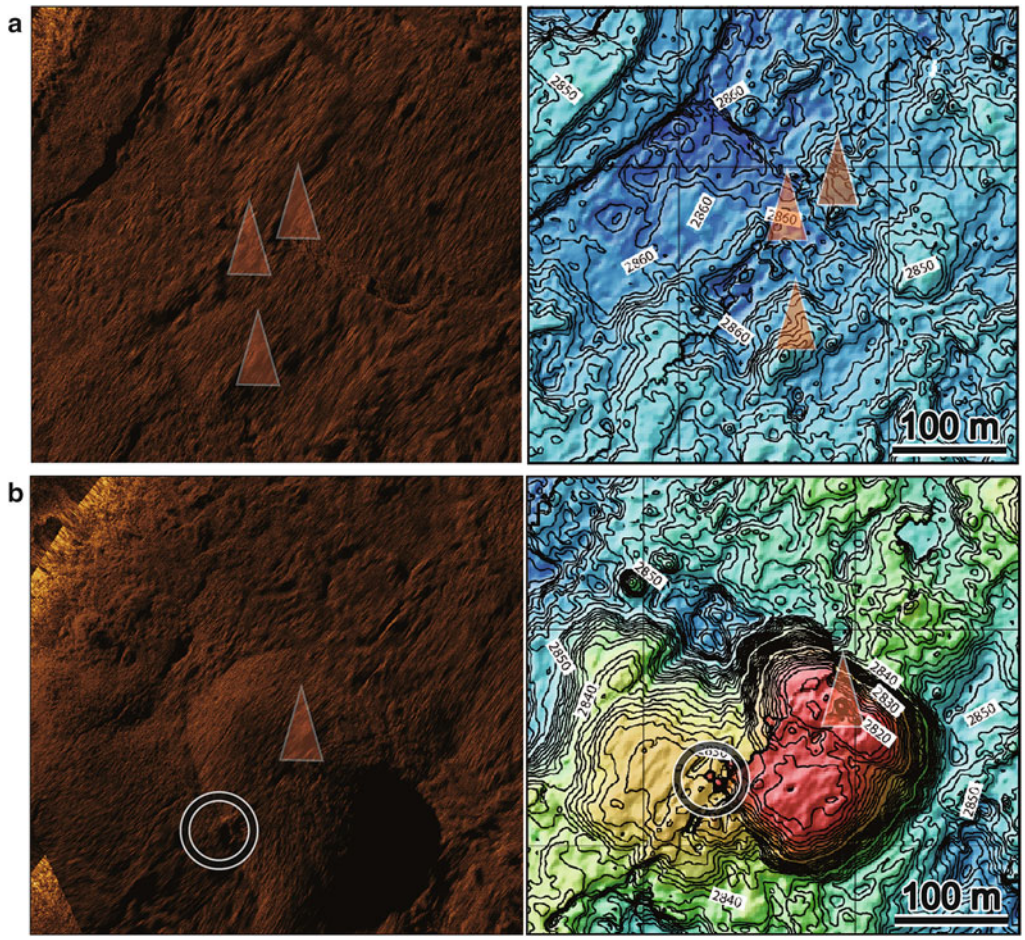

Fig. 36.4 The 120 kHz side-scan sonar images (*left*) and 400 kHz multibeam bathymetry (*right*) of two hydrothermal sites: (*top*) Snail site, (*bottom*) Yamanaka site. The locations of maps are shown by *boxes* in Fig. 36.3a. *Orange triangles* indicate the active hydrothermal areas recognized by visual observation. *Circle* in the *bottom figure* (Yamanaka site) indicate the location at which we recognized a few chimney-like structures on the sonar imagery

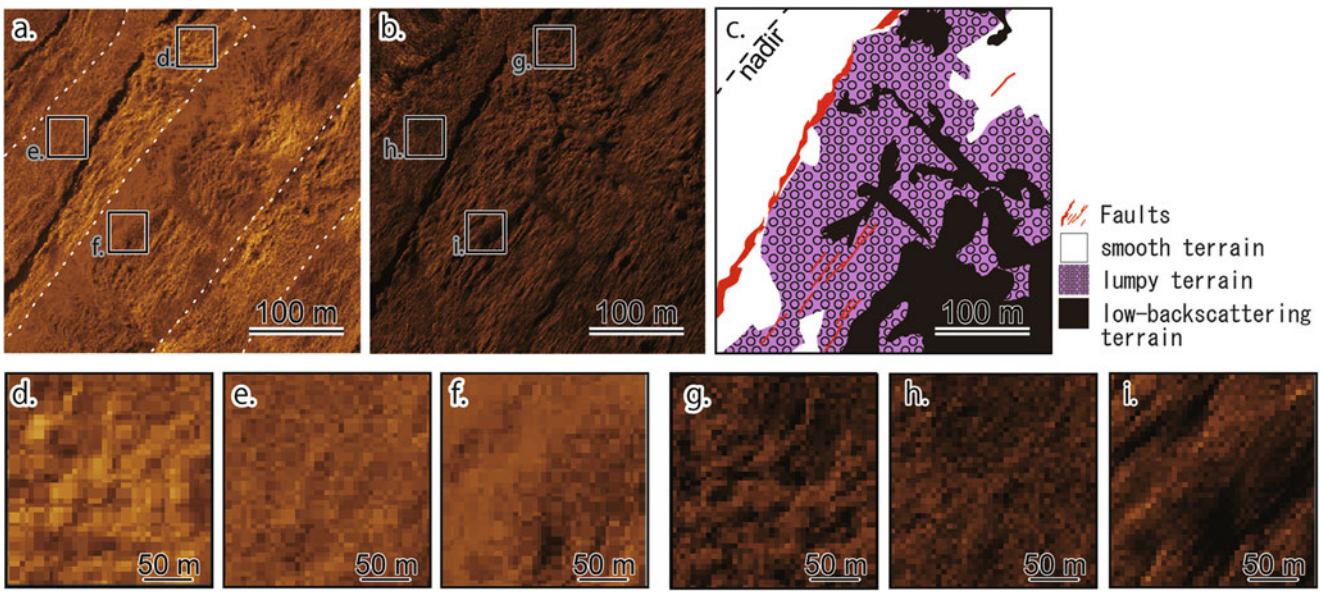

Fig. 36.5 Lumpy, smooth, and low-backscattering terrains on the side-scan sonar image. (**a**) 400 kHz side-scan sonar imagery, (**b**) 120 kHz side-scan sonar imagery, (**c**) interpretation image of the 120 kHz side-scan sonar imagery, (**d**) lumpy terrain (400 kHz), (**e**) smooth terrain (400 kHz), (**f**) low-backscattering terrain (400 kHz), (**g**) lumpy terrain (120 kHz), (**h**) smooth terrain (120 kHz), and (**i**) low-backscattering terrain (120 kHz). *White dotted lines* on the 400 kHz side-scan sonar image indicate the edge of the swath

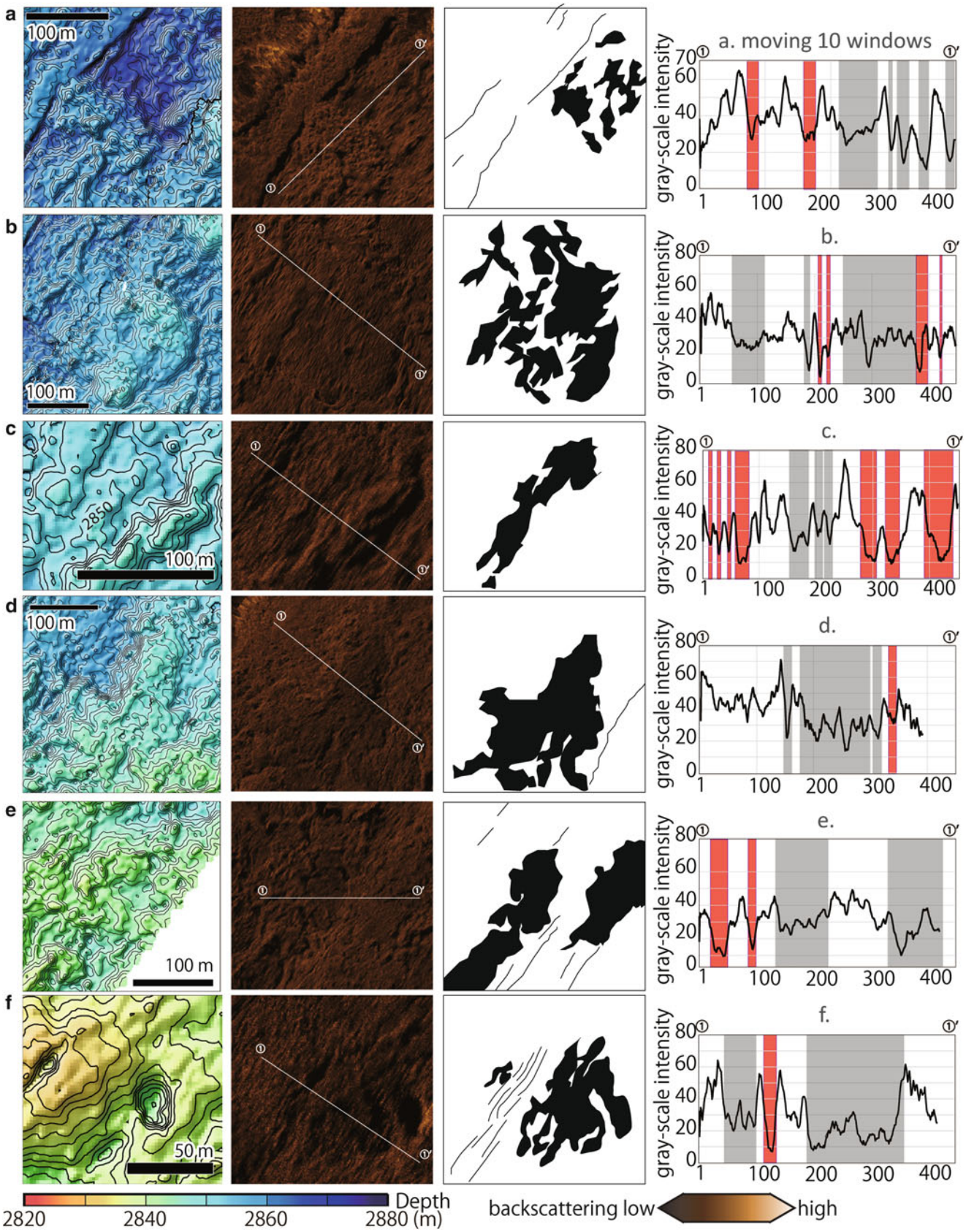

Fig. 36.6 Detailed view of bathymetric features of the low-backscattering terrains. From *left* to *right*, panels show multibeam bathymetry maps, side-scan sonar imagery, interpretation images of side-scan sonar imagery, and intensity along lines shown on the side-scan sonar images. Locations of maps are shown in Fig. 36.2. *Red*- and *gray-colored* areas in graphs indicate the positions of acoustic shadow and low-backscattering terrain, respectively. The *horizontal* and *vertical axes* are pixel number and gray-scale intensity (*darker shades* indicate lower number)

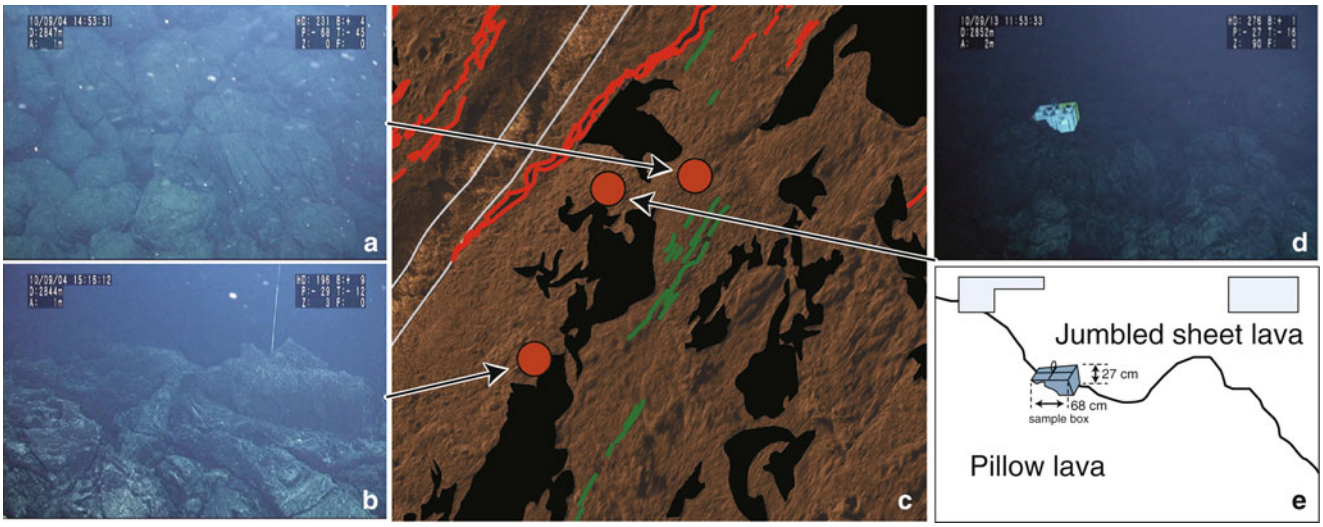

Fig. 36.7 Photos taken by submersible showing a large variety in lava morphology and the corresponding side-scan sonar imagery. (**a**) Photo of pillow lava in lumpy terrain. (**b**) Jumbled sheet lava in low-backscattering terrain. (**c**) Geological interpretation of side-scan sonar imagery. Low-backscattering terrains are shown in *black*. *Red line*, *green line*, and *white line* indicate fault, fissure, and nadir of AUV track and edge of swath, respectively. (**d**) Photo of the boundary of pillow and sheet lava. (**e**) Schematic interpretation of photo (**d**)

Tominaga and Umino 2010). Pillow lavas display bulbous, spherical, or elongate tubular patterns and sheet flows exhibit smooth, lobate, rippled, wrinkled, ropy, whorly, hackly, or jumbled configurations (Fox et al. 1998; Gregg and Fink 1995; Kennish and Lutz 1998; Fundis et al. 2010). Along our observed nine transects of the *Shinkai 6500* dives, the seafloor was mostly covered by bulbous pillow lava with sporadic jumbled, wrinkled, and/or partially fractured (or hackly) types of sheet lava. No axial summit troughs, pillars, or collapse features were observed, even though these features are frequently observed along the fast-spreading East Pacific Rise (Gregg and Chadwick 1996; Gregg and Fornari 1998; Kennish and Lutz 1998; Gregg et al. 2000; White et al. 2002; Haymon and White 2004; Tanaka et al. 2007).

The lumpy terrain on the sonar image corresponds to the flatly distributed bulbous pillow lava (Fig. 36.7a). We found jumbled or wrinkled (and partly hackly) sheet lava in areas consisting of low-backscattering terrains (Fig. 36.7b). We can recognize fragmented pillow lavas in the smooth terrain. We carefully investigated the boundaries between the low-backscattering terrain and the lumpy terrain in the visual records but could not recognize the age difference between theses terrains (Fig. 36.7d, e). Because of the little sedimentary cover over both terrains, differences in backscattering strength likely correspond to differences in the surface morphologies of lava.

Linear features on a hill in the western area (Fig. 36.3b) are faults, which displace the surrounding pillow lavas. Thin sedimentary cover, which was not detected by SBP observations, was observed on the seafloor in the western area. Although turbid water was observed at the foot of the hill, we did not discover any hydrothermal signature in the western area.

Very little sediment was observed in the eastern area. At the Snail site, a hydrothermal plume appeared to be coming up through the cracks of large rocky outcrops, but we did not find any chimney-like structures. The Snail site is located in a valley surrounded by three small mounds. The flat-topped hill on which the Yamanaka site is developed is covered by bulbous pillows at the top and elongated pillows on the slope. These geologic features are consistent with our interpretation of acoustic observations.

36.5 Conclusions

1. We observed the axial zone of the back-arc spreading center in the Southern Mariana Trough using the AUV *Urashima* and the *Shinkai 6500* submersible. The neovolcanic zone is mostly occupied by lumpy terrain with high backscattering intensity. The lumpy terrain consists of flatly distributed pillow lava.
2. Our high-resolution AUV observations using side-scan sonar imagery revealed the existence of low-backscattering signatures. These low-backscattering terrains are associated with a variety of bathymetric features. The submersible observations revealed that the terrain mostly consists of wrinkled and/or jumbled sheet lava, and the edges of the low-backscattering terrains are coincident with the boundaries of pillow and sheet lava types.

3. The proportion of low-backscattering terrain within our observed area is estimated to be approximately 10 %. Since the low-backscattering is interpreted as sheet lava and lumpy/smooth terrains are as bulbous or fractured pillow lavas, the sheet lava occupied ~10 % of seafloor when it is assumed that all of the low-backscattering areas indicate the occurrence of sheet lava.
4. We did not observe axial summit troughs, pillars, or collapse features, all of which are common along the fast spreading East Pacific Rise, in our study area. We also observed a few pillow mounds, which are commonly observed along the intermediate spreading Mid Atlantic Ridge

Acknowledgements We thank the officers and crew of the R/V *Yokosuka*, members of the AUV *Urashima* technical support team, and the scientists onboard the vessel during the YK09-08 and YK10-11 cruises for their help during the collection of the survey data. We appreciate an anonymous reviewer and the editorial board of this e-book for improvement of the manuscript. This research was financially supported by the Ministry of Education, Culture, Science, and Technology (MEXT) of Japan, through a special coordination fund (Project TAIGA: Trans-crustal Advection and In situ biogeochemical processes of Global subseafloor Aquifer, FY 2008–2012).

References

Amante C, Eakins BW (2009) ETOPO1 1 arc-minute global relief model: procedures, data sources and analysis, national geophysical data center, NOAA Technical Memorandum NESDIS NGDC-24, 19 pp, March 2009

Asada M, Deschamps A, Fujiwara T, Nakamura Y (2007) Submarine lava flow emplacement and faulting in the axial valley of two morphologically distinct spreading segments of the mariana back-arc basin from Wadatsumi side-scan sonar images. Geochem Geophys Geosyst 8:Q04001. doi:10.1029/2006GC001418

Baker ET, Massoth GJ, Nakamura K, Embley RW, de Ronde CEJ, Arculus RJ (2005) Hydrothermal activity on near-arc sections of back-arc ridges: results from the Mariana Trough and Lau Basin. Geochem Geophys Geosyst 6:14

Becker NC, Fryer P, Moore GF (2010) Malaguana-Gadao Ridge: identification and implications of a magma chamber reflector in the southern Mariana Trough. Geochem Geophys Geosyst 11:11

Deschamps A, Fujiwara T (2003) Asymmetric accretion along the slow-spreading Mariana Ridge. Geochem Geophys Geosyst 4:8622. doi:10.1029/2003GC000537

Deschamps A, Fujiwara T, Asada M, Montesi L, Gente P (2005) Faulting and volcanism in the axial valley of the slowspreading center of the Mariana back arc basin from Wadatsumi side-scan sonar images. Geochem Geophys Geosyst 6:Q05006. doi:10.1029/2004GC000881

Fink JH, Griffiths R (1998) Morphology, eruption rates, and rheology of lava domes: Insights from laboratory models. J Geophys Res 103:527–545

Fox CG, Murphy KM, Rmble RW (1998) Automated display and statistical analysis of interpreted deep-sea bottom photographs. Mar Geol 78:199–216

Fryer P (1996) Evolution of the Mariana convergent plate margine system. Rev Geophys 34:89–125

Fundis AT, Soule SA, Fornari DJ, Perfit MR (2010) Paving the seafloor: volcanic emplacement processes during the 2005–2006 eruptions at the fast spreading East Pacific Rise, 9 degrees 50′ N. Geochem Geophys Geosyst 11:20. doi:10.1029/2010GC003058

Gregg TKP, Chadwick WW Jr (1996) Submarine lava-flow inflation: a model for the formation of lava pillars. Geology 24:981–984

Gregg TKP, Fink JH (1995) Quantification of submarine lava-flow morphology through analog experiments. Geology 23:73–76

Gregg TKP, Fornari DJ (1998) Long submarine lava flows: observations and results from numerical modeling. J Geophys Res 103:27517–27531

Gregg TKP, Fornari DJ, Perfit MR, Haymon RM, Fink JH (1996) Rapid emplacement of a mid-ocean ridge lava flow on the East Pacific Rise at 9 degrees 46′-51′N. Earth Planet Sci Lett 144:1–7

Gregg TKP, Fornari DJ, Perfit MR, Ridley WI, Kurz MD (2000) Using submarine lava pillars to record mid-ocean ridge eruption dynamics. Earth Planet Sci Lett 178:195–214

Griffiths RW, Fink J (1992) Solidification and morphology of submarine lavas—a dependence on extrusion rate. J Geophys Res 97:19729–19737

Haymon RM, White SM (2004) Fine-scale segmentation of volcanic/hydrothermal systems along fast-spreading ridge crests. Earth Planet Sci Lett 226:367–382

Kakegawa T, Utsumi M, Marumo K (2008) Geochemistry of sulfide chimneys and basement pillow lavas at the Southern Mariana Trough (12.55 degrees N–12.58 degrees N). Res Geol 58:249–266

Kasaya T, Kanamatsu T, Sawa T, Kinoshita M, Tukioka S, Yamamoto F (2011) Acoustic images of the submarine fan system of the northern Kumano basin obtained during the ecperimental dives of the deep sea AUV URASHIMA. Explor Geophys 42:80–87

Kato T, Beavan J, Matsushima T, Kotake Y, Camacho JT, Nakao S (2003) Geodetic evidence of back-arc spreading in the Mariana Trough. Geophys Res Lett 30:1625. doi:10.1029/2002GL016757

Kennish MJ, Lutz RA (1998) Morphology and distribution of lava flows on mid-ocean ridges: a review. Earth Sci Rev 43:63–90

Kitada K, Seama N, Yamazaki T, Nogi Y, Suyehiro K (2006) Distinct regional differences in crustal thickness along the axis of the Mariana Trough, inferred from gravity anomalies. Geochem Geophys Geosyst 7, Q04011. doi:10.1029/2005GC001119

Kojima S, Shipboard Scientific Party (2011) Cruise report on YK10-11 "SHINKAI6500, the southern Mariana Trough". http://www.godac.jamstec.go.jp/catalog/data/doc_catalog/media/YK10-11_all.pdf

Macdonald KC (1998) Linkages between faulting, volcanism, hydrothermal activity and segmentation on fast spreading centers. In: Buck WR, Delaney PT, Karson JA, Lagabrielle Y (eds) Faulting and magmatism at mid-ocean ridges, vol 106. American Geophysical Union, Washington DC

Martinez F, Taylor B (2002) Mantle wedge control on back-arc crustal accretion. Nature 416:417–420

Martinez F, Fryer P, Becker N (2000) Geophysical characteristics of the southern Mariana Trough, 11 deg.50′N-13 deg.40′N. J Geophys Res 105:16591–16607

Okino K, Shipboard Scientific Party (2009) Cruise report on YK09-08 "URASHIMA survey dives". http://www.godac.jamstec.go.jp/catalog/data/doc_catalog/media/YK09-08_all.pdf

Seama N, Yamazaki T, Iwamoto H, Kitada K, Yamamoto M, Fujiwara T, Nogi Y, Okino K, Suyehiro K (2002) Tectonic features of the Mariana Trough, Eos Trans, vol 83, Fall Meet. Suppl., abstract T71F-08, American Geophysical Union, Washington DC

Small C (1998) Global systematics of mid-ocean ridge morphology. In: Buck WR, Delaney PT, Karson JA, Lagabrielle Y (eds) Faulting

and magmatism at mid-ocean ridges, vol 106. American Geophysical Union, Washington DC, pp 1–25

Tanaka A, Rosat S, Kisimoto K, Urabe T (2007) High-resolution bathymetry using Alvin scanning sonar at the Southern East Pacific Rise and its implication to the formation of collapsed lava lakes. Earth Planet Space 59:245–249

Taylor B, Martinez F (2003) Back-arc basin basalt systematic. Earth Planet Sci Lett 210:481–497

Tominaga M, Umino S (2010) Lava deposition history in ODP Hole 1256D: insights from log-based volcanostratigraphy. Geochem Geophys Geosyst 11:19. doi:10.1029/2009GC002933

Tsukioka S, Aoki T, Yoshida H, Hyakudome T, Sawa T, Ishibasi S, Mizuno M, Tahara J, Ishikawa A (2005) The PEM fuel cell system for autonomous underwater vehicles. Mar Tech Soc J 39:56–64

Umino S, Lipman PW, Obata S (2000) Subaqueous lava flow lobes, observed on ROV KAIKO dives off Hawaii. Geology 28:503–506

Wheat CG, Fryer P, Hulme S, Becker N, Curtis A, Moyer C (2003) Hydrothermal venting in the southern most portion of the Mariana backarc spreading center at 12.57°N, EOS Trans, T32A-0920, Fall Meeting 2003. American Geophysical Union, Washinton DC

White SM, Haymon RM, Fornari DJ, Perfit MR, Macdonald KC (2002) Correlation between volcanic and tectonic segmentation of fast-spreading ridges: evidence from volcanic structures and lava flow mrphology on the East Pacific Rise at 9°–10°N. J Geophys Res 107. doi:10.1029/2001JB000571

Yamazaki T, Seama N, Okino K, Kitada K, Joshima M, Oda H, Naka J (2003) spreading process of the northern Mariana Trough: rifting-spreading transition at 22°N. Geochem Geophys Geosyst 4. doi:10.1029/2002GC000492

Yoshikawa S, Okino K, Asada M (2012) Geomorphological variations at hydrothermal sites in the southern Mariana Trough: relationship between hydrothermal activity and topographic characteristics. Mar Geol 303:172–182

Brief Report of Side-Scan Sonar Imagery Observations of the Archaean, Pika, and Urashima Hydrothermal Sites

37

Miho Asada, Shuro Yoshikawa, Nobutatsu Mochizuki, Yoshifumi Nogi, and Kyoko Okino

Abstract

A high-resolution acoustic investigation using AUV-*Urashima* reveals the geological features of three off-axis hydrothermal sites at the Southern Mariana Trough. They are developed ~5 km in distance from backarc spreading axis. The *Archaean* site is developed at the foot of axial horst and forms 60 m-high mound. Hydrothermal chimneys in the site are arrayed along the ridge of the mound. Our acoustic observations detect small structures along the ridge which could be interpreted as the chimneys. To the south of the *Archaean* mound, the seafloor is characterized by rough and elongated fabrics approximately trending in NE–SW direction, which coincides with the strike of background seafloor slope. Visual observation indicates that the area consists of lava tube slightly covered by sediment. The *Pika* and the *Urashima* sites are developed on top and at foot of a ~1,800 m-high off-axis knoll. Unprocessed sidescan sonar imagery above the *Pika* and the *Urashima* sites shows anomalous backscattering signatures in water column. A series of hills with convex shape develops on the southwestern slope of the off-axis knoll. It shows unique facies that is rough surface with high-backscattering intensity on the sonar imagery. Tube lavas are recognized in corresponding seafloor by visual observation.

Keywords

Hydrothermal signature • Side-scan sonar • Southern Mariana Trough

37.1 Introduction

The southern Mariana Trough is one of the intensive study areas of TAIGA project (Chap. 1). Three active off-axis hydrothermal sites are known in this area (Kakegawa et al. 2008; Nakamura et al. 2013) as well as two other sites on the backarc spreading axis. The *Archaean* site is located at foot of the axial high (Fig. 37.1), the *Pika* site and the *Urashima* site are located at the top and the foot of an off-axis knoll (Fig. 37.4). These sites are found within 5 km from

M. Asada (✉)
Research and Development Center for Earthquake and Tsunami (CEAT), Japan Agency for Marine-Earth Science and Technology (JAMSTEC), 2-15 Natsushima, Yokosuka, Kanagawa 237-0061, Japan

S. Yoshikawa
Department of Mathematical Science and Advanced Technology, Japan Agency for Marine-Earth Science and Technology (JAMSTEC), 2-15 Natsushima, Yokosuka, Kanagawa 237-0061, Japan

N. Mochizuki
Priority Organization for Innovation and Excellence, Kumamoto University, 2-40-1 Kurokami Chuo-ku, Kumamoto City 860-8555, Japan

Y. Nogi
National Institute of Polar Research, 10-3 Midoricho, Tachikawa, Tokyo 190-8518, Japan

K. Okino
Atmosphere and Ocean Research Institute (AORI), The University of Tokyo, 5-1-5 Kashiwanoha, Kashiwa, Chiba 277-8564, Japan

J.-i. Ishibashi et al. (eds.), *Subseafloor Biosphere Linked to Hydrothermal Systems: TAIGA Concept*,
DOI 10.1007/978-4-431-54865-2_37,

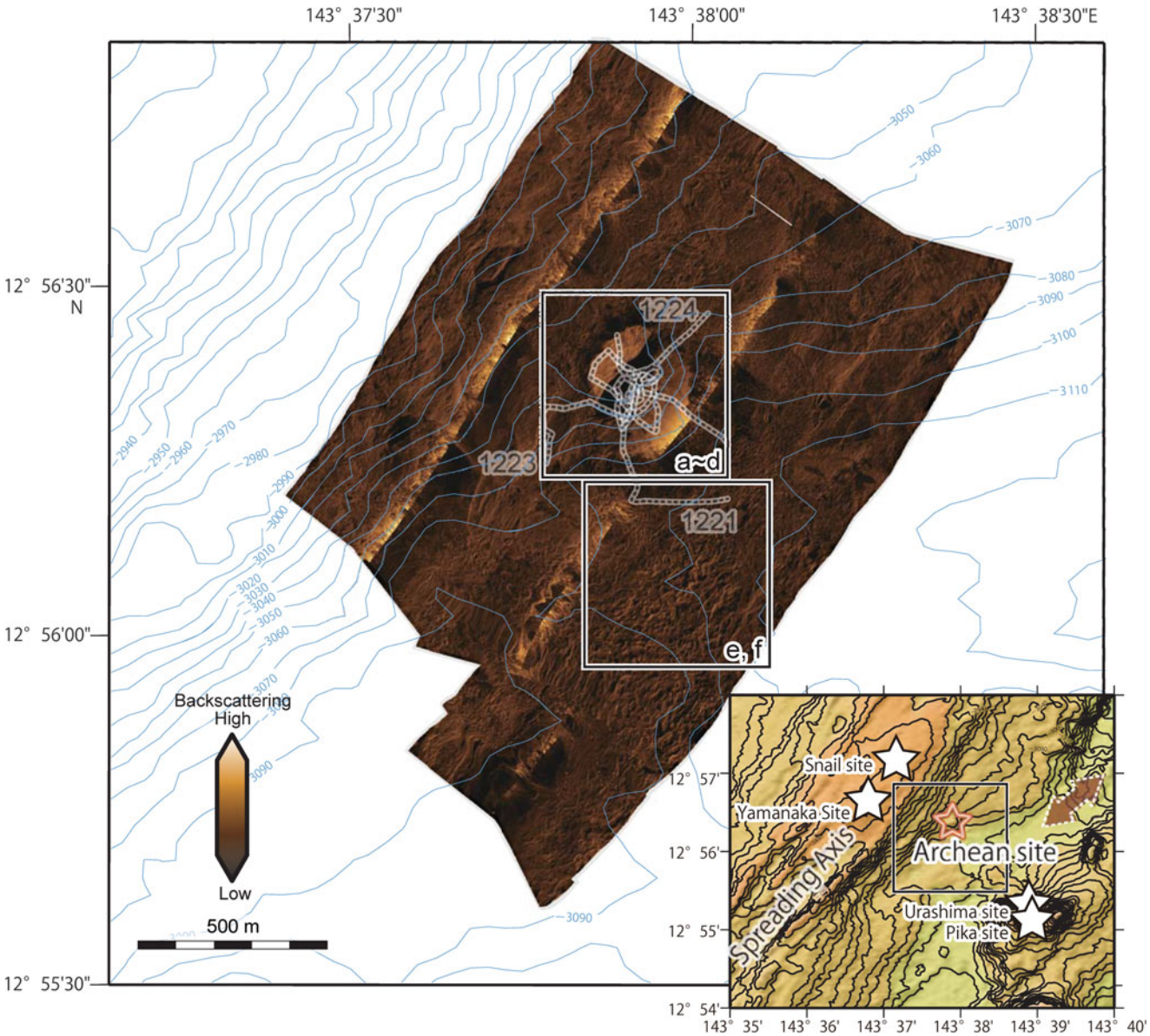

Fig. 37.1 Sidescan sonar imagery of the *Archaean* hydrothermal site and surrounding seafloor obtained using an *Edgetech2200* system (120 kHz) mounted on the AUV-*Urashima*. *Darker color* indicates lower backscattering intensity. *Dotted lines* indicate tracks of the submersible-*Shinkai6500* during cruise YK10-11 in 2010. *Blue lines* and *annotations* show background bathymetry obtained by a *Seabeam2112* system (11 kHz) mounted on R/V *Yokosuka*, for reference. *Squares* are locations of Fig. 37.2. *Inset* (*right*, *down*) is location map of hydrothermal sites in this area. On- and off-axis hydrothermal sites are indicated by *stars*. A *double-headed arrow* roughly indicates local trend of valley on the background bathymetry

spreading axis, and along single line nearly perpendicular to the spreading axis. There are two on-axis hydrothermal sites, the Snail and the Yamanaka sites, near these off-axis sites, and the Snail site is located on the same line linking the off-axis sites. To investigate the geological background of these hydrothermal sites and to understand the if these sites are related to each other in terms of the heat source and/or tectonic background, we conducted high-resolution acoustic observations using the AUV-*Urashima* in 2009 and visual observations using the submersible *Shinkai6500* in 2010. In this report, we present the survey results at the three off-axis hydrothermal sites (the *Archaean*, *Pika*, and *Urashima* sites). The results on two on-axis sites are reported in Asada et al. (Chap. 36).

37.2 Data Acquisition

Meter-scale, high-resolution, bathymetric and sidescan sonar data were acquired by the AUV-*Urashima* (JAMSTEC), which was developed in 1998 (Tsukioka et al. 2005; Kasaya et al. 2011). The AUV-*Urashima* is equipped with a 400 kHz multi-beam echo sounder (MBES) for meter-scale bathymetry data (*Seabat7125*), a 120 kHz sidescan sonar (SSS) for backscattering strength data, and a 1–6 kHz (charp) sub-bottom profiler (SBP) for subseafloor information (*EdgeTech2200*). Dive-92 around the *Archaean* site (Fig. 37.1) and Dive-93 around the off-axis knoll on which the *Urashima* and the *Pika* sites (Fig. 37.4) are conducted. In each dive, the AUV collected the data along nine, parallel, NE–SW trending lines roughly 100 m (Dive-92) and 140 m (Dive-93) intervals. The average survey altitude and speed of the AUV were about 100 m and 2 knots, respectively. The along-track width of acoustic beam is 0.5° for MBES and 0.9° for SSS, equivalent to 2–5 m on the seafloor. The resolutions for the 120 kHz SSS is approximately 7.5 cm (when acoustic velocity in seawater is 1,500 m/s). The 400 kHz MBES bathymetry data are gridded at interval of 2 m.

Visual observation using the *Shinkai6500* submersible was performed in YK10-11 cruise in 2010. We utilized the videos and photographs recorded along the dive tracks as ground references for the acoustic imagery.

37.3 Processing Methods

Acoustic data sets obtained by the AUV-*Urashima* are extracted from data logger on board. The converted SSS data is processed and mosaiced using software CleanSweep3 (Oceanic Imaging Consultants, Inc.). Bathymetric data were processed using software HIPS and SHIPS (Caris) and plotted using the Generic Mapping Tools software program (Wessel and Smith 1991).

Deficiencies and artifacts in the bathymetric data occur near the top of the *Archaean* mound and the off-axis knoll where the *Pika* site is located. The quality of SSS imagery is also low in the same part of the survey lines. They are caused by unstable attitude control of the AUV during these dives, mainly due to mal-function of DVL (Doppler Velocity Log).

We interpreted the patterns on the sonar imagery as geological features, referring to many previous studies on mid-ocean ridges (Smith et al. 1995; Briais et al. 2000; Sauter et al. 2002; Cann and Smith 2005; Searle et al. 2010). Generally, lava outcrops have high backscattering signatures while seafloor covered by sediment has lower backscattering signatures. A seafloor covered by rabbles shows higher backscattering intensity rather than a flat lava. Acoustic shadows are used to estimate the height of seafloor structures. Geological information can be obtained from facies which are identified based on backscattering intensity and patterns of the acoustic shadows and distributions.

37.4 Results

37.4.1 Observation of the *Archaean* Site

The *Archaean* site is located on an approximately 60 m-high conical mound at the foot of the axial high (Fig. 37.1). The facies of the conical mound was generally smooth with a wavy surface texture and the backscattering intensities are high (Fig. 37.2a–d). Visual observations from the *Shinkai6500* submersible revealed that the surface of the mound was extensively covered by sulfide deposits (Fig. 37.3ii). Our SSS and MBES data detect small structures with acoustic shadow along the ridge of the conical mound (Fig. 37.2a–d). The positions of the small structures are confirmed by visual observation by submersible observation. The distribution of the small structures on the SSS imagery could be useful as an indication of chimneys on the seafloor.

The facies of the seafloor to the south of the mound was characterized by the presence of rough and elongated fabrics approximately trending in NE–SW direction (Fig. 37.2e, f), which coincides with the strike of background seafloor slope (see bathymetry map in Fig. 37.1). Visual observations revealed the presence of relatively old tube lavas covered with sediment (Fig. 37.3iv). This characteristic fabrics appears to develop on the surrounding seafloor and the distribution does not show any connection to the current spreading axis nor the *Archaean* mound, suggesting the possibility of off-axis volcanism further to the south.

37.4.2 Observation of the *Urashima* Site and *Pika* Site

The *Pika* site, discovered in 2003 (Kakegawa et al. 2008), is characterized by high-temperature black and clear smokers. The site develops at a part of the western top of the off-axis knoll, which is ~5 km east from spreading axis. The Urashima site was newly discovered in 2010 at the northern foot of the same knoll, following the detection of acoustic and geomagnetic anomalies during our AUV survey (Nakamura et al. 2013).

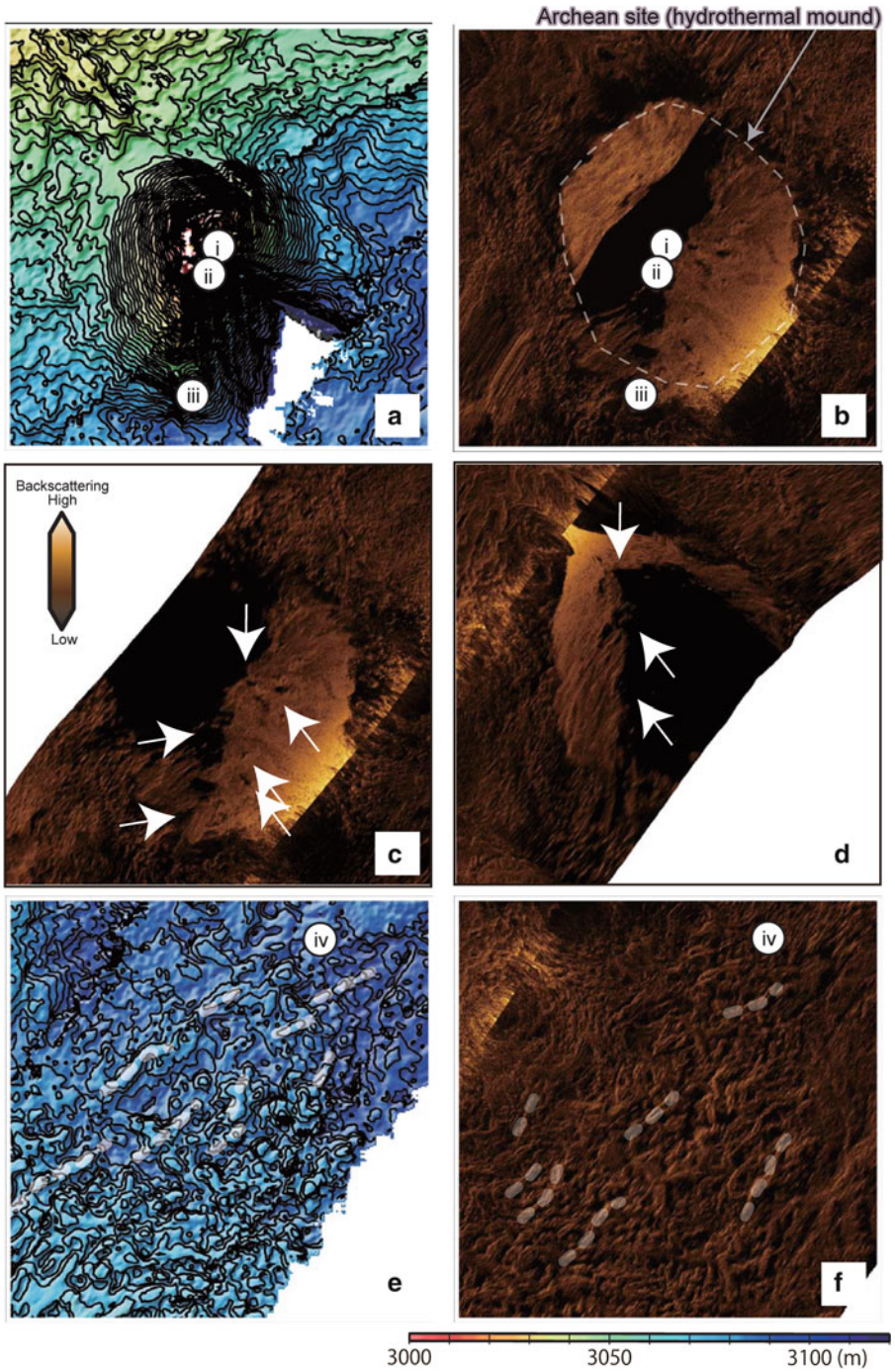

Fig. 37.2 Detailed views of sidescan sonar imagery and bathymetry. (**a**) Bathymetry map obtained by the *Seabat7125* system (400 kHz) mounted on the AUV-*Urashima*. (**b**) Sidescan sonar imagery of the the hydrothermal sulfide mound of the *Archaean* site. (**c**) Single swath of sidescan sonar imagery taken from south of the mound. *White arrows* indicate small structures with acoustic shadow. (**d**) Single swath of sidescan sonar taken from the north of the mound. *White arrows* indicate small structures. (**e**) Bathymetry map of seafloor lies at southern sides of the mound. *White transparent dotted lines* indicate suggested trend of represented examples of the rough and elongated fabrics. (**f**) Sidescan sonar image of the seafloor. *White transparent dotted lines* indicate suggested trend of represented examples of the rough and elongated fabrics, too. (*i*)–(*iv*) are locus of photographs shown in Fig. 37.3

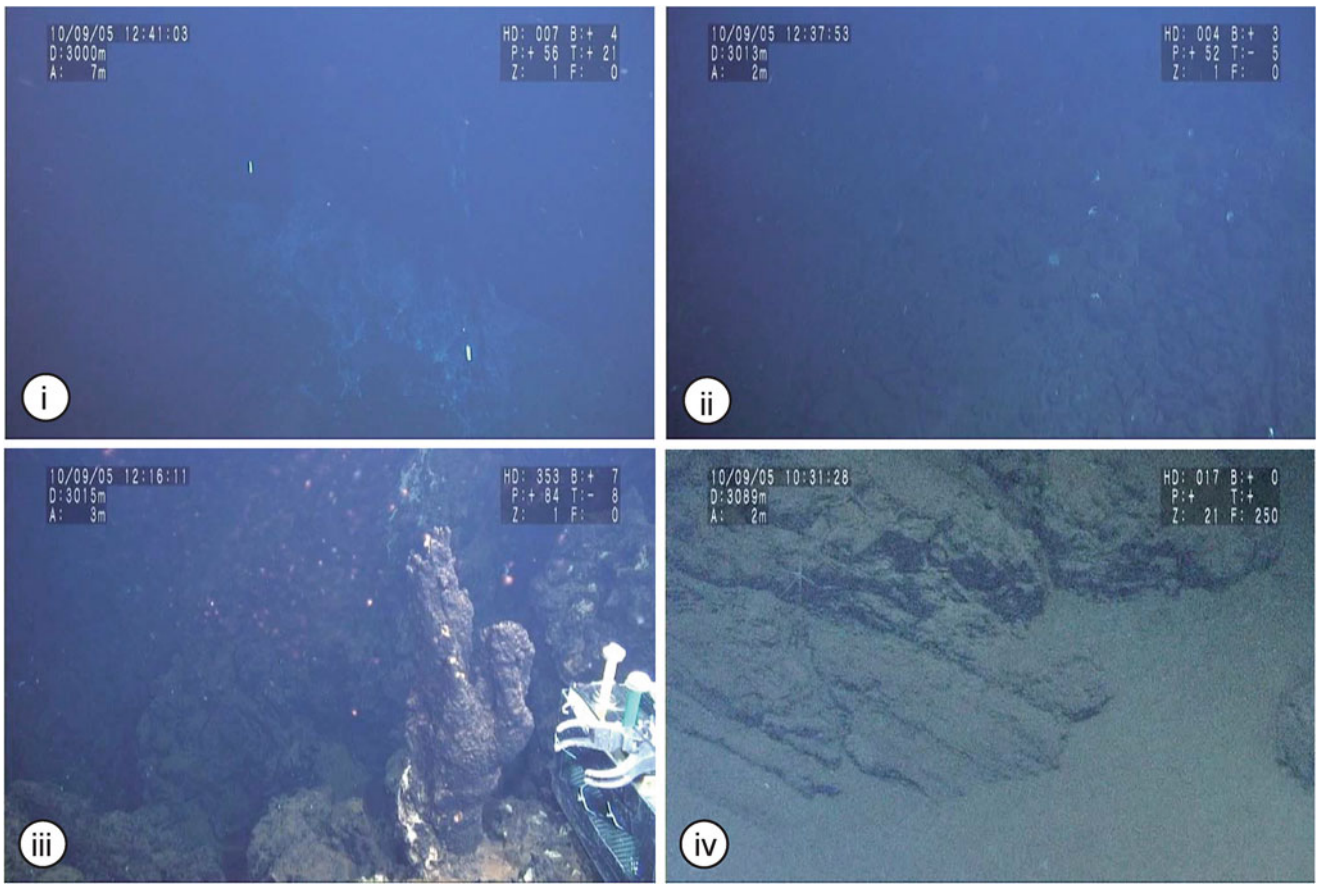

Fig. 37.3 Photographs taken at (*i*)–(*iv*) shown in Fig. 37.2. (*i*) Active hydrothermal chimney on the top of a mound, (*ii*) rubbles at the foot of a hydrothermal chimney, (*iii*) active hydrothermal chimney at the foot of the mound, and (*iv*) seafloor lies at southern ~ southwestern sides of the mound, showing lava covered by sediment

We detected anomalous backscattering signals in the water column by SSS above the *Pika* and the *Urashima* sites (Fig. 37.5c, d), where the active hydrothermal chimneys are observed (Fig. 37.6i, ii).

A series of hills with a convex shape (Figs. 37.5e, f, 37.6iii) extend from the southern to the southwestern sides of the off-axis knoll. The diameter and relative elevation of the hills are approximately 100 m and several tens of meters, respectively. SSS imagery shows unique facies, that is rough surface with high-backscattering intensity. Dive photos show that the surface of the hills is covered by tube lavas (Fig. 37.6v) with thin sediment. The tops of the hills are flat and partially covered by sediment, and a rocky outcrop with a web-like surface structure was observed (circle in Fig. 37.6iii, iv). SBP data shows obscured image of sediment layers in this area, meaning that the thickness of the sediment layer is less than catalogue resolution of 1–6 kHz (~15 cm in vertical) acoustic signals.

The SSS imagery shows relatively high-backscattering terrain over the area of western top of the off-axis knoll, although the *Pika* site is recognized at the limited area. Due to higly distorted SSS imagery, we could not estimate distribution of high-backscattering terrain, small structures, and linear features in detail.

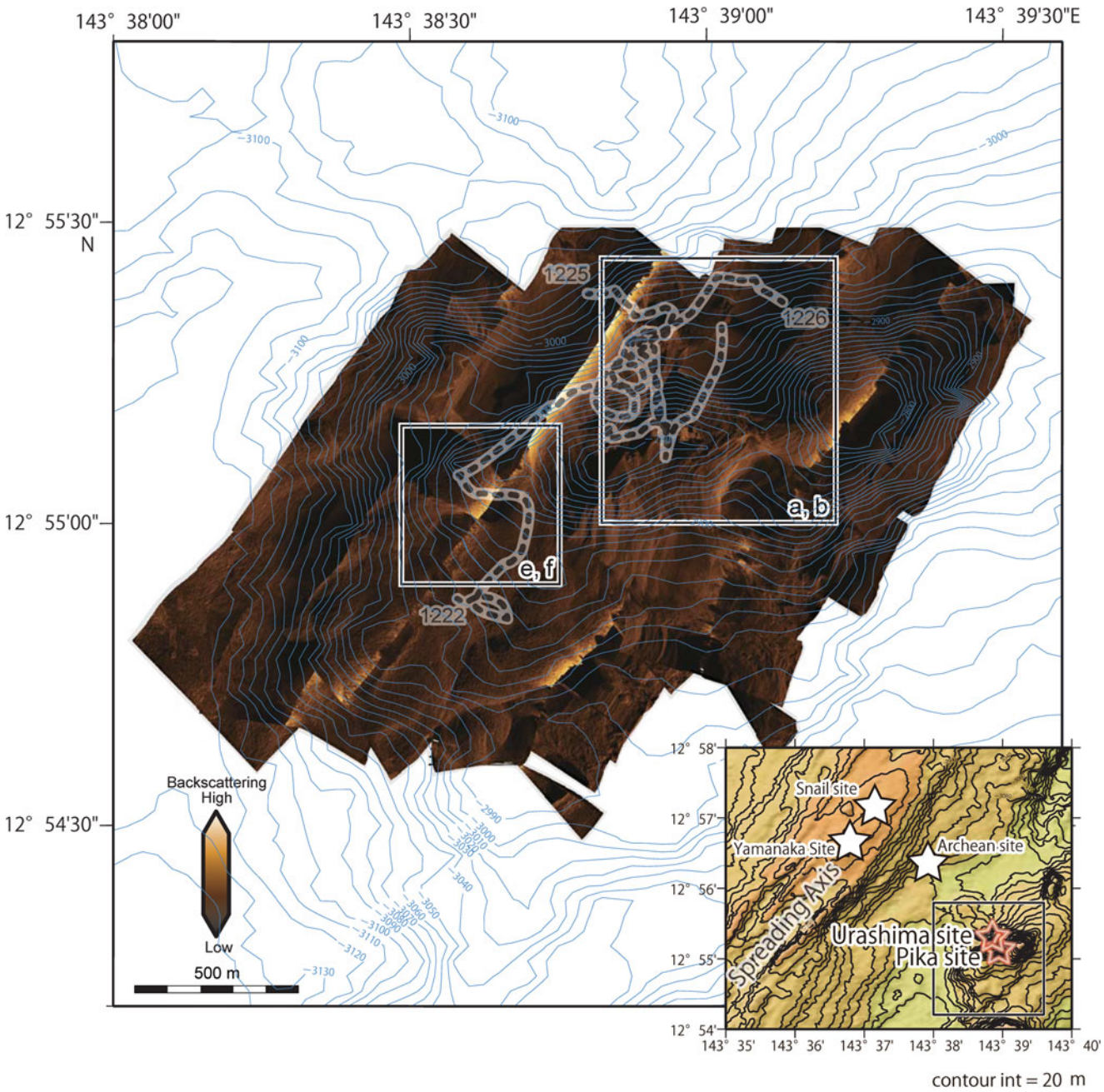

Fig. 37.4 Sidescan sonar imagery of the off-axis seamount on which the *Pika* site and the *Urashima* site. See Fig. 37.1 for description

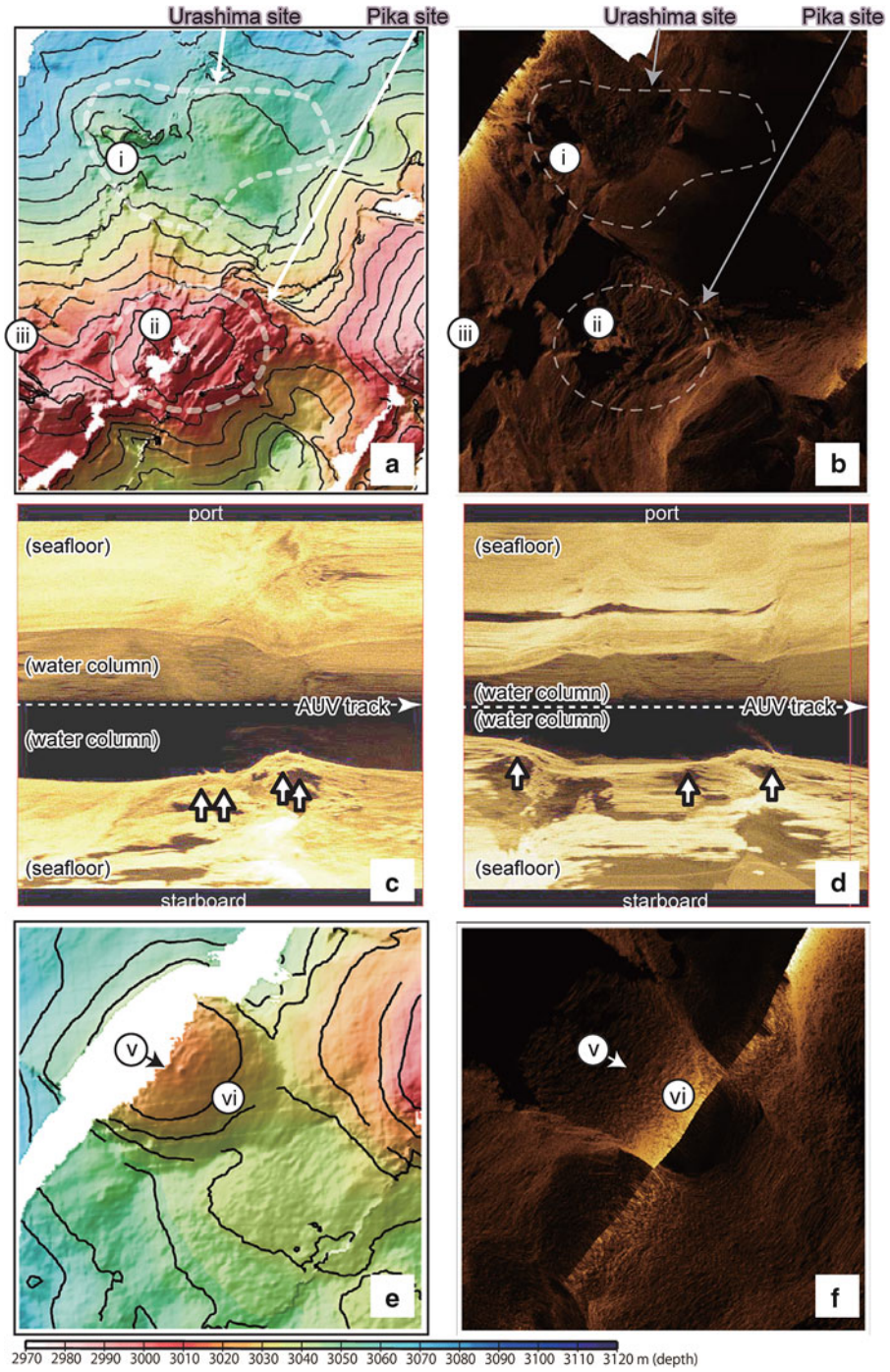

Fig. 37.5 Sidescan sonar imagery, bathymetry of the *seabat7125* system at a same location to the sidescan sonar image, and unprocessed sidescan sonar imageries plotted along time. (**a**) Bathymetry map of *seabat7125* system. *Dashed areas* indicate approximate locations of the *Pika* site and the *Urashima* site. (**b**) Sidescan sonar imagery of the location shown in (**a**). (**c**) Unprocessed sidescan sonar data obtained above the *Urashima* site. Backscattering signals in water column suggest the presence of materials associated with hydrothermal activity. (**d**) Unprocessed sidescan sonar data above the *Pika* site and showing backscattering signals in the water column. (**e**) Bathymetry map of southwestern foot of the off-axis seamount. (**f**) Sidescan sonar imagery of the location shown in (**e**). (*i*), (*ii*), (*iv*) and (*v*) are locus of photographs shown in Fig. 37.6

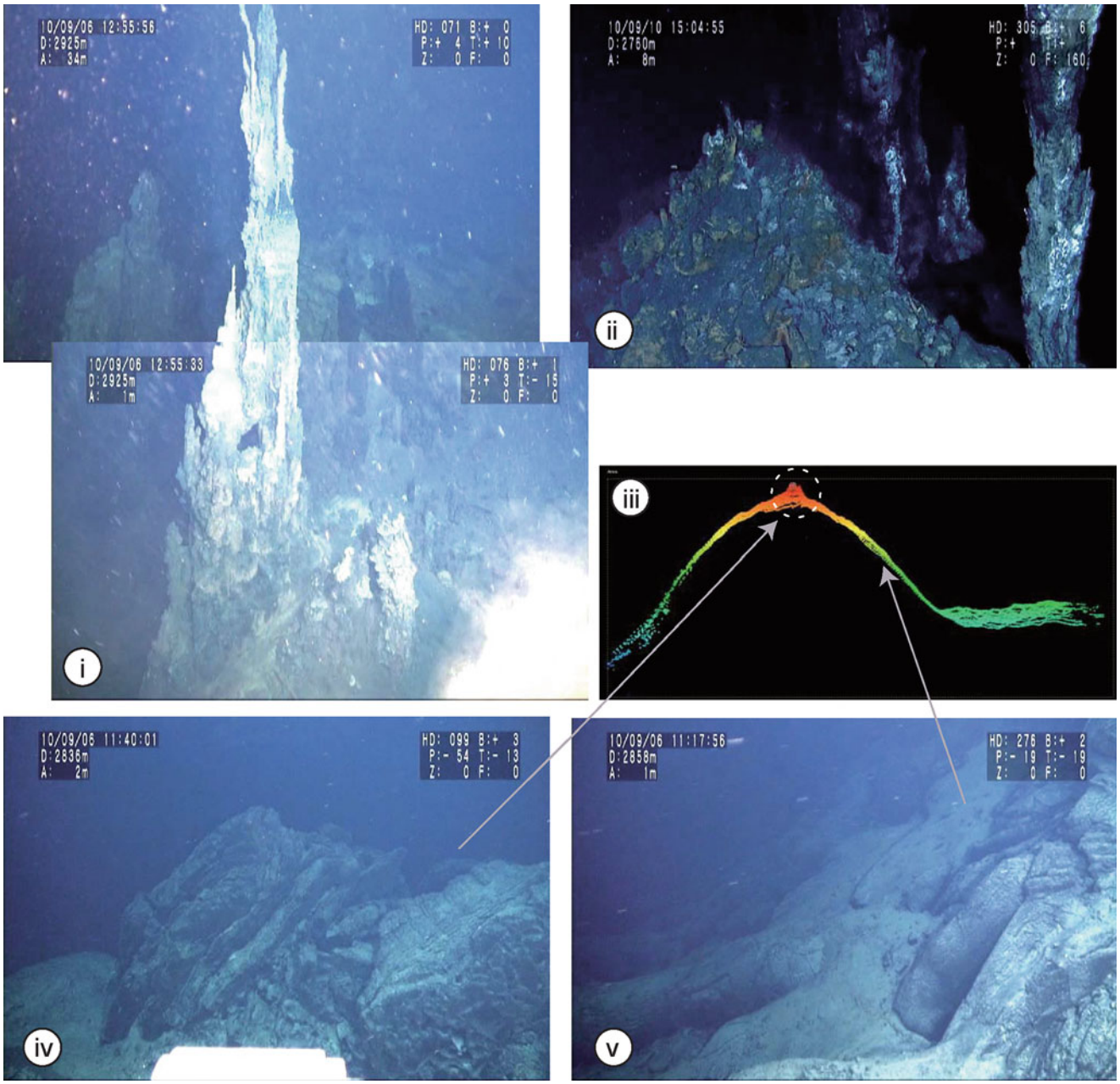

Fig. 37.6 Photographs of locations (*i*), (*ii*), (*iv*), and (*v*) in Fig. 37.5, and (*iii*) snapshot of unprocessed multi-beam bathymetry data. (*i*) Active hydrothermal chimney at the Urashima site. (*ii*) Active hydrothermal chimney at the Pika site. (*iii*) unprocessed bathymetry data consisting of 50 pings of *seabat7125* system, showing a cross-section of hill with a *convex* shape. (*iv*) Rocky outcrop with the "web structure" on surface sitting at top of the hill with a *convex* shape. (*v*) Example of tube lava covering slope of the hill with a convex shape

Acknowledgements We thank the officers and crews of the R/V Yokosuka, member of AUV-*Urashima* technical support team, and onboard scientists of YK09-08 and YK10-11 cruises for their help during the collection of the survey data. We appreciate anonymous reviewer and editorial board of this e-book for improvement of the manuscript. This research was financially supported by the Ministry of Education, Culture, Science, and Technology (MEXT) of Japan, through a special coordination fund (Project TAIGA: Trans-crustal Advection and In situ biogeochemical processes of Global subseafloor Aquifer, FY 2008–2012).

References

Briais A, Sloan H, Parson LM, Murton BJ (2000) Accretionary process in the axial valley of the Mind-Atlantic Ridge 27°N-31°N from TOBI side-scan sonar images. Mar Geophys Res 21:87–119

Cann JR, Smith DK (2005) Evolution of volcanism and faulting in a segment of the Mid-Atlantic Ridge at 25°N. Geochem Geophys Geosyst 6, Q09008. doi:10.1029/2005GC000954

Kakegawa T, Utsumi M, Marumo K (2008) Geochemistry of sulfide chimneys and basement pillow lavas at the Southern Mariana Trough (12.55 degrees N–12.58 degrees N). Res Geol 58:249–266

Kasaya T, Kanamatsu T, Sawa T, Kinoshita M, Tukioka S, Yamamoto F (2011) Acoustic images of the submarine fan system of the northern Kumano basin obtained during the experimental dives of the deep sea AUV URASHIMA. Explor Geophys 42:80–87

Nakamura K, Toki T, Mochizuki N, Asada M, Ishibashi J, Nogi Y, Yoshikawa S, Miyazaki J, Okino K (2013) Discovery of a new hydrothermal vent based on an underwater, high-resolution geophysical survey. Deep-Sea Res 174:1–10

Sauter D, Parson L, Mendel V, Rommevaux-Jestin C, Gomez O, Briais A, Mevel C, Tamaki K, The FUJI Scientific Team (2002) TOBI sidescan sonar imagery of the very slow-spreading Southwest Indian Ridge: evidence for along-axis magma distribution. Earth Planet Sci Lett 199:81–95

Searle RC, Murton BJ, Achenbach K, LeBas T, Tivey M, Yeo I, Cormier MH, Carlut J, Ferreira P, Mallows C, Morris K, Schroth N, van Calsteren P, Waters C (2010) Structure and development of an axial volcanic ridge: mid-Atlantic Ridge, 45 degrees N. Earth Planet Sci Lett 299:228–241

Smith DK, Cann J, Dougherty ME, Lin J, Spencer S, Macleod C, Keeton J, Mcallister E, Brooks B, Pascoe R, Robertson W (1995) Mid-Atlantic Ridge volcanism from deep-towed side-scan sonar images, 25°–29°N. J Volcano Geotherm Res 67:233–262

Tsukioka S, Aoki T, Yoshida H, Hyakudome T, Sawa T, Ishibasi S, Mizuno M, Tahara J, Ishikawa A (2005) The PEM fuel cell system for autonomous underwater vehicles. Mar Tech Soc J 39:56–64

Wessel P, Smith WHF (1991) Free software helps map and display data. EOS Trans, American Geophysical Union, p 72

The Yoron Hole: The Shallowest Hydrothermal System in the Okinawa Trough

38

Tatsuhiro Fukuba, Takuroh Noguchi, and Teruo Fujii

Abstract

During NT10-16 cruise with R/V NATSUSHIMA and ROV HYPER-DOLPHIN in 2010, a new hydrothermal vent community was discovered at the Yoron Hole, where is the shallowest hydrothermal system in the known hydrothermal site found in the Okinawa Trough. The maximum temperature of clear smoker fluid was 247 °C, which was slightly lower than the boiling temperature (275 °C) of the seawater at the water pressure of 560-m water depth (5.6 MPa). Hydrothermal chimneys are composed of barite, sphalerite, galena, pyrite, chalcopyrite, and tetrahedrite. Although crustaceans and polychaetes were found around the hydrothermal vent, the diversity and population density were lower than that of the Iheya North Knoll and the Izena Hole hydrothermal sites.

Keywords

Chemosynthetic ecosystem • Hydrothermal site survey • The Yoron Hole

38.1 Location and Geological Settings

The Yoron Hole locates in the adjacent seamount to the well-studied deep-sea hydrothermal systems such as the Iheya Ridge, the Iheya North Knoll, and the Izena Hole, in the northwest region of the Okinawa Island, and was formed by arc-backarc volcanisms in the Okinawa Trough (Fig. 38.1, left). The seamount of the Yoron Hole has approximately 500 m of the relative height and it has a clearly recognizable crater at the north flank of the seamount (Fig. 38.1, right). Diameter of the crater has area of 3 km east to west and 2 km north to south, and relative depth is approximately 350 m. Hydrothermal vents are localized on the northeast slope of the crater.

38.2 Survey History

The Yoron Hole was firstly discovered by underwater topographic survey operations of Japan Coast Guard during a series of cruises from July 2008 to march 2009, and reported as an underwater volcanic crater (Horisako et al. 2010). Detailed scientific survey on hydrothermal activity of the Yoron Hole was intensively performed by a joint research group of the University of Tokyo, Kochi University, Central Research Institute of Electric Power Industry (CRIEPI), and Japan Agency for Marine-Earth Science and Technology (JAMSTEC) using R/V NATSUSHIMA and ROV HYPER-DOLPHIN (JAMSTEC) during NT10-16 cruise in 2010 (Fukuba 2010). In NT10-16, physicochemical anomaly caused by the hydrothermal plume was detected with in situ chemical sensors, and the shallowest hydrothermal site in the Okinawa Trough was discovered at the northeastern slope of the crater. The following scientific cruises have

The online version of this chapter (doi:10.1007/978-4-431-54865-2_38) contains supplementary material, which is available to authorized users.

T. Fukuba (✉) • T. Noguchi
Marine Technology and Engineering Center,
Japan Agency for Marine-Earth Science and Technology,
2-15 Natsushima-cho, Yokosuka, Kanagawa 237-0061, Japan
e-mail: bafuk@jamstec.go.jp

T. Fujii
Institute of Industrial Science, The University of Tokyo,
4-6-1 Komaba, Meguro-ku, Tokyo 153-8505, Japan

J.-i. Ishibashi et al. (eds.), *Subseafloor Biosphere Linked to Hydrothermal Systems: TAIGA Concept*,
DOI 10.1007/978-4-431-54865-2_38,

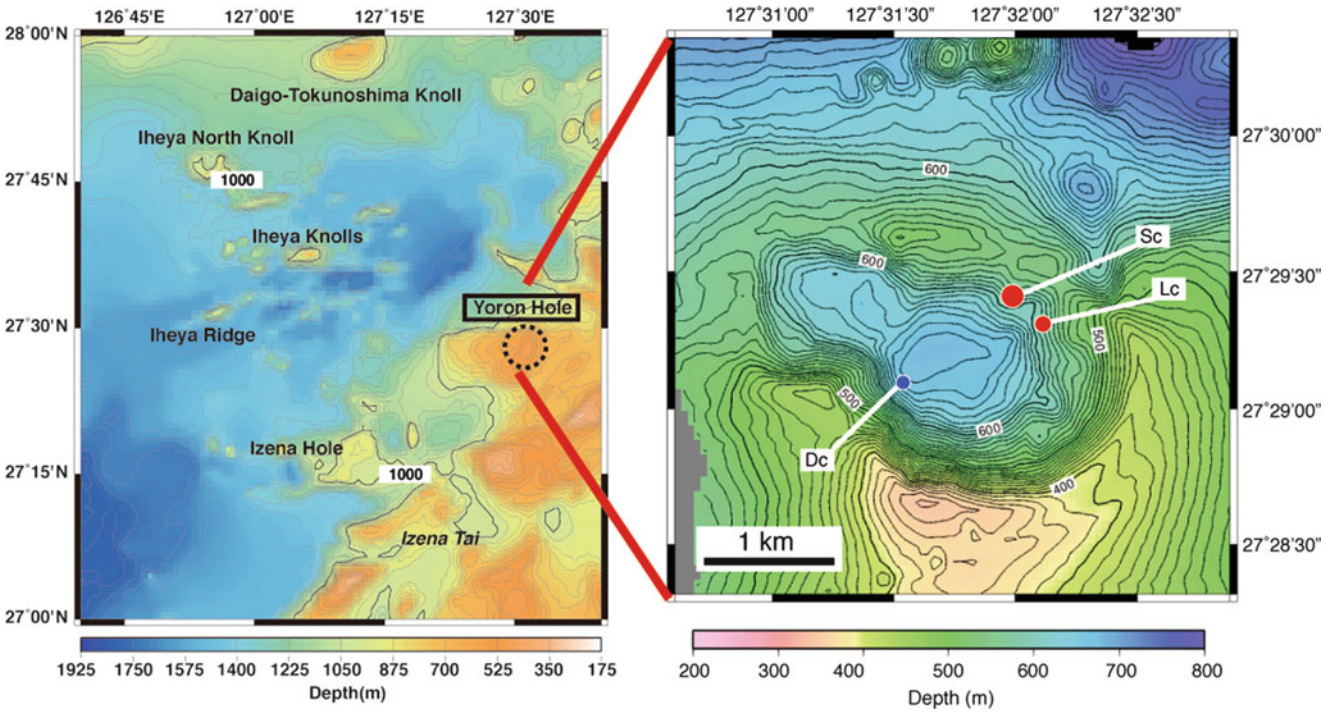

Fig. 38.1 Bathymetric map of the Mid-Okinawa Trough and location of hydrothermal vents at the Yoron Hole. *Sc* hydrothermal vent with small chimneys, *Lc* the largest chimney and simmering, *Dc* dead chimneys

conducted for other hydrothermal vent survey and biogeochemical studies (e.g. NT11-17 and NT11-20 using R/V NATSUSHIMA and ROV HYPER-DOLPHIN) (Fukuba 2011; Ishibashi 2011). The area including the Yoron Hole and the surrounding volcanic topographies was provisionally named as the North–East (NE) Izena or the Yoron Knoll. The formal name, the Yoron Hole, was inscribed in the IHO-IOC GEBCO Gazetteers of Undersea Feature Names in 2012 (General Bathymetric Chart of the Ocean 2012).

38.3 Hydrothermal Activity and Biogeochemical Properties

The anomalies of seawater temperature, pH, pCO_2, ORP, and Mn concentration detected by in situ sensor observation (Provin et al. 2013) had focal points on the east to the northeast slope of the hole at depth of 500–600 m. The observation according to the detail camera survey in the anomaly area, multiple hydrothermal vents were recognized around a gorge on the northeast slope in the hole, and their water depth were ranged between 560 to 590 m (Fig. 38.2a, b). There are some small clear smoker chimneys (10–30 cm tall) at the north slope of the gorge, and measured maximum hydrothermal fluid temperature was 247 °C. In the south slope of the gorge, there is a large active chimney gushing clear hydrothermal fluid whose maximum temperature was 85 °C (Suppl. 38.1a). Around the large chimney, there are some white colored hydrothermally altered area with shimmering fluid (maximum temperature of 121 °C) (Suppl. 38.1b). Dead chimneys (Suppl. 38.1c) were discovered on the bottom of the southwestern slope of the hole. Active hydrothermal vents were discovered in a limited area on northeastern slope of the hole, therefore, it seems to be the center of a hydrothermal discharge zone in the Yoron Hole.

Although chemosynthetic ecosystems formed around the active hydrothermal vents, the population density and diversity were scant in comparison to fauna of the Iheya Knoll or the Izena Hole. Small numbers of crustacean are living around the active vents (Fig. 38.2c, d). Alvinelid polychaeta formed patchy colonies on the foot part of the active chimneys (Fig. 38.2e). Surface of the chimneys had partially covered with yellowish-white filamentous mats, probably be made from bacteria (Fig. 38.2f).

Major geological features in the Yoron Hole are shown in Suppl. 38.1d,e. Surface of the slope was composed of volcanic detritus, and partially covered by thin sediment. The center of the hole was flat plain covered by sandy sediment. The analysis on geological features of rocks, massive sulfides, and chimneys are undergoing yet (Fujiwara et al. 2013; Takamasa et al. 2013). Preliminary result for mineral composition of the hydrothermal chimneys shows that barite is a dominant mineral and sphalerite, galena, pyrite, chalcopyrite, and tetrahedrite are included as minor contents. Ishibashi et al. (2013) suggested that the arsenic and silver contents in the tetrahedrite are slightly higher than those in

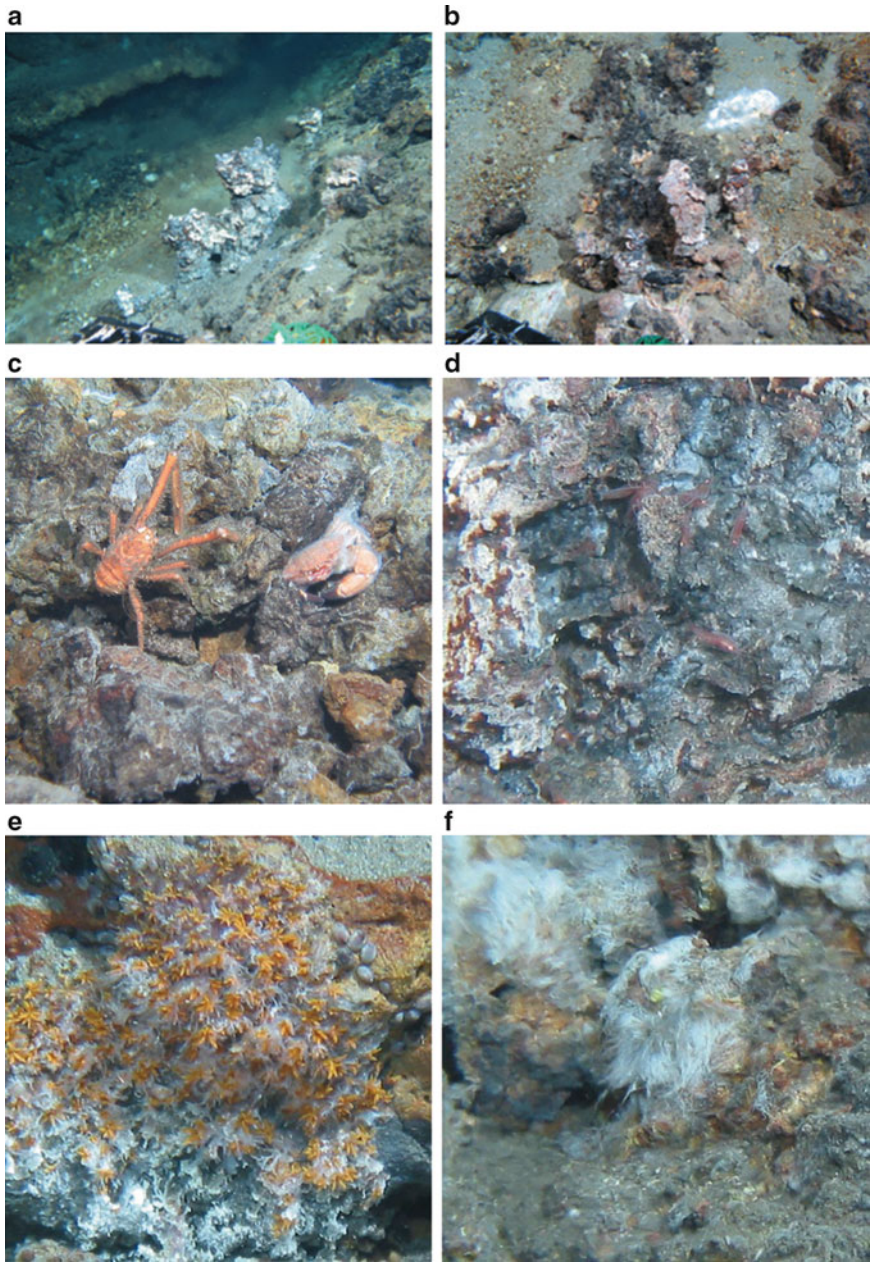

Fig. 38.2 Digital camera images of hydrothermal vents and surrounding biological communities (NT10-16 cruise, 2010). (**a**) and (**b**): Small active chimneys emitting clear fluid, (**c**–**f**): Biological members observed in the Yoron Hole. (**c**) *Munidopsis* sp. and a xanthid crab, (**d**) Alvinocaridid shrimps, (**e**) Alvinelid polychaetes, and (**f**) Filamentous bacteria mat

tetrahedrite samples from the other hydrothermal field in the Okinawa Trough, which might be reflected by geophysical parameters (e.g. temperature, pH, water depth, etc.).

Acknowledgement Part of the bathymetric data was supplied from Japan Oceanographic Data Center (JODC). This work was partially supported by a Grant-in-Aid for Scientific Research on Innovative Areas (Project TAIGA, no. 20109003).

References

Fujiwara T, Toyoda S, Ishibashi J, Nakai S, Uchida A, Takamasa A (2013) ESR dating of barite in sea-floor hydrothermal sulfide deposits. In: Proceedings of Japan Geoscience Union Meeting 2013 (May 19–24, 2013, Chiba, Japan), SGL40-P07

Fukuba T (2010) A study on novel hydrothermal ore mine survey by *in situ* multi parameter measurement, Cruise report of NT10-16. http://www.godac.jamstec.go.jp/darwin/cruise/NATSUSHIMA/nt10-16/e

Fukuba T (2011) A study on a hydrothermal plume mapping and a novel hydrothermal ore mine survey by *in situ* multi parameter measurements, Cruise report of NT11-17. http://www.godac.jamstec.go.jp/darwin/cruise/NATSUSHIMA/nt11-17/e

General Bathymetric Chart of The Ocean (2012) 25th GEBCO Sub-Committee on Undersea Feature Names (SCUFN) Meeting Report, New Zealand, pp 23–27, Oct 2012. http://www.gebco.net/data_and_products/undersea_feature_names/documents/gebco_scufn25.pdf

Horisako J, Dojun S, Tanaka K, Otonari Y, Hashimoto T (2010) Preliminary report of the bathymetric survey in the region to the northwest of Okinawa Island. Rep Hydrogr Oceanogr Res 46:87–91 (Japanese with English abstract)

Ishibashi J (2011) History of hydrothermal activities and associated biological communities in the Okinawa Trough, Cruise report of NT11-20. http://www.godac.jamstec.go.jp/darwin/cruise/NATSUSHIMA/nt11-20/e

Ishibashi J, Oshiro M, Shimada K, Nozaki T, Yoshizumi R, Urabe T, Sato H (2013) Diversity of seafloor massive sulfide ores in the Okinawa Trough. In: Proceedings of Japan Geoscience Union Meeting 2013 (May 19–24, 2013, Chiba, Japan), BBG21-07

Provin C, Fukuba T, Okamura K, Fujii T (2013) An integrated microfluidic system for manganese anomaly detection based on chemiluminescence: description and practical use to discover hydrothermal plumes near the Okinawa Trough. IEEE J Ocean Eng 38:178–185

Takamasa A, Nakai S, Ishibashi J, Sato F, Toyoda S, Fujiwara T (2013) U-Th radioactive disequilibrium dating of hydrothermal vent of Okinawa and South Mariana Trough. In: Proceedings of Japan Geoscience Union Meeting 2013 (May 19–24, 2013, Chiba, Japan), BBG21-P06

The Irabu Knoll: Hydrothermal Site at the Eastern Edge of the Yaeyama Graben

39

Tatsuhiro Fukuba, Takuroh Noguchi, and Teruo Fujii

Abstract

The Irabu Knoll hydrothermal vents were first discovered in 2000 during YK00-06 cruise using R/V YOKOSUKA and manned submersible SHINKAI 6500. The Irabu Knoll consists of three seamounts from 1,680 to 1,970-m in water depth. The Irabu Knoll is located in the Southern Okinawa Trough and is constructed from basalt as the host rock. Two hydrothermal venting sites have been found at East and West seamount. Sulfide deposit of the Irabu Knoll hydrothermal system consists of barite, sphalerite, pyrite, and chalcopyrite. Major taxa in the vent ecosystem are *Shinkaia crosnieri, Munidopsis* sp., and *Ashinkailepsas* sp.

Keywords

Basaltic pillow lava • Chemosynthetic ecosystem • Hydrothermal plume • The Irabu Knoll

39.1 Location and Geological Settings

The Irabu Knoll was first recognized through comprehensive geological and geophysical surveys in 1988 (Oshima et al. 1988; Kimura et al. 1991; Shinjo 1999). It locates at 55 km off the northwest of the Miyako Island on the eastern edge of the Yaeyama Graben in the Southern Okinawa Trough (Fig. 39.1). The Southern Okinawa Trough characterized by an active rifting of the Asian continental margin and the Yaeyama Graben is considered to be a key area to understand tectonics and evolution of back-arc basins. The Irabu Knoll consists of three major seamounts, East, West, and South seamounts. The East seamount has a caldera-like elliptic depression with an opening on its northwest face. The major and minor axis of the depression is ca. 600 and 400 m, respectively. The water depth at the bottom of the depression is 1,970 m. The West seamount has a truncated cone feature and the water depth of the seamount is ca. 1,680 m. The South seamount has been reported as EW-elongated structure by Matsumoto et al. (2001), but the accurate water depth is not determined yet. In 2000, several dives using manned submersible SHINKAI 6500 revealed the existence of hydrothermal activities at the East and the West seamounts, however, no dive has been carried out at the South seamount (Matsumoto et al. 2001). Former two seamounts were composed of fresh basaltic pillow lava, and thin sediments were covered on the pillow lava in the flank of the seamounts (Fig. 39.2a). Hydrothermal vents are located on the south face of the East seamount (25°14.10′N, 124°52.89′E; water depth = 1,876 m) and at the summit of the West seamount (25°13.76′N, 124°52.16′E; water depth = 1,648 m). Sulfide deposits collected from the West seamount are likely to be composed under rather higher sulfidation state and are mineralogically similar to those of the Kuroko deposits rather than the Bessi-type deposits (Watanabe et al. 2006). Existence of indium in the sulfide chimney, revealed using neutron activation analysis (Noguchi 2007), is consistent with geochemical

The online version of this chapter (doi:10.1007/978-4-431-54865-2_39) contains supplementary material, which is available to authorized users.

T. Fukuba (✉) • T. Noguchi
Marine Technology and Engineering Center,
Japan Agency for Marine-Earth Science and Technology,
2-15 Natsushima-cho, Yokosuka, Kanagawa 237-0061, Japan
e-mail: bafuk@jamstec.go.jp

T. Fujii
Institute of Industrial Science, The University of Tokyo,
4-6-1 Komaba, Meguro-ku, Tokyo, Japan

J.-i. Ishibashi et al. (eds.), *Subseafloor Biosphere Linked to Hydrothermal Systems: TAIGA Concept*,
DOI 10.1007/978-4-431-54865-2_39, © The Author(s) 2015

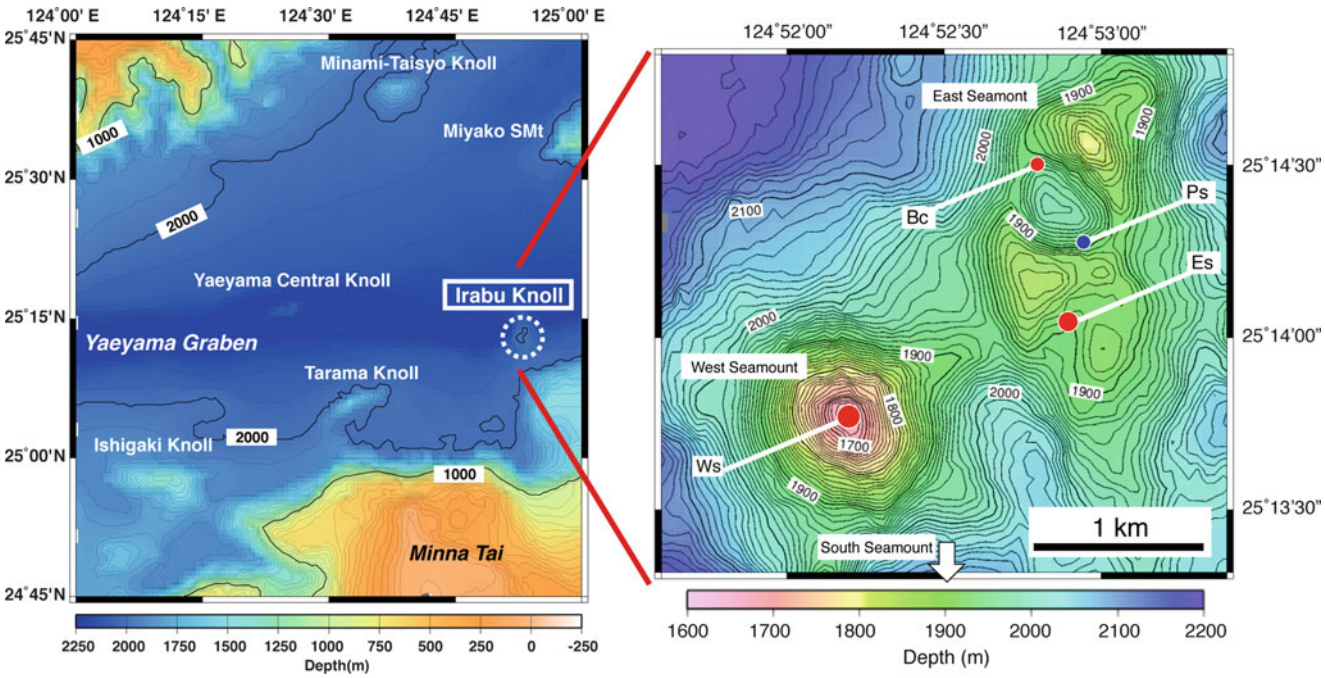

Fig. 39.1 Bathymetry of the Southern Okinawa Trough and location of the hydrothermal vents at the Irabu Knoll. *Ws* hydrothermal vents on the West seamount, *Ns* hydrothermal vents on the East seamount, *Bc* Mytiloidea colonies with weak seepage, *Ps* Previously reported site (Matsumoto et al. 2001). The South seamount is not shown in the bathymetric map

characteristic common on the basaltic lava hosted hydrothermal fields (e.g. the East Pacific Rise and the Southern Mariana Trough). To observe the hydrothermal plumes and to collect the rocks, sulfide minerals, and biological samples for geochronological studies, following three cruises were conducted in 2011 and 2012, NT11-17 (R/V NATSUSHIMA and ROV HYPER-DOLPHIN, JAMSTEC) (Fukuba 2011), NT11-20 scientific cruise in 2011 (R/V NATSUSHIMA and ROV HYPER-DOLPHIN), and YK12-05 (R/V YOKOSUKA and manned submersible SHINKAI 6500, JAMSTEC).

39.2 Hydrothermal Activity and Biogeochemical Properties

Clear hydrothermal fluid venting was found at the summit of the West seamount. A grid survey of hydrothermal plume using ROV HYPER-DOLPHIN found the temperature anomalies at three points around the rugged summit of the seamount (Suppl. 39.1). White-fluffy precipitates were observed in hydrothermal plume and covered a part of the massive sulfides and chimney structures. The highest fluid temperature in the Irabu Knoll, 67 °C, was recorded at a clear smoker vent on the West seamount during 2011 survey (Fukuba 2011). Dense and diverse populations of Crustaceans dominated by *Shinkaia crosnieri, Munidopsis* sp. (Fig. 39.2b–d), and *Ashinkailepsas* sp. (Fig. 39.2d) were observed around the active chimneys. Hydrothermal chimney structures and sulfide deposits at the East seamount were smaller than those of the West seamount. The chimneys were distributed on flat terraces and cliffs at the south face of the caldera-like depression. Clear hydrothermal fluid was venting from the chimneys and gaps between rocks on cliffs. The other hydrothermal site with seepage was found at northern inside face of the depression. Small colonies of bivalves were interspersed on a rocky slope covered by thin sediment (Fig. 39.2e).

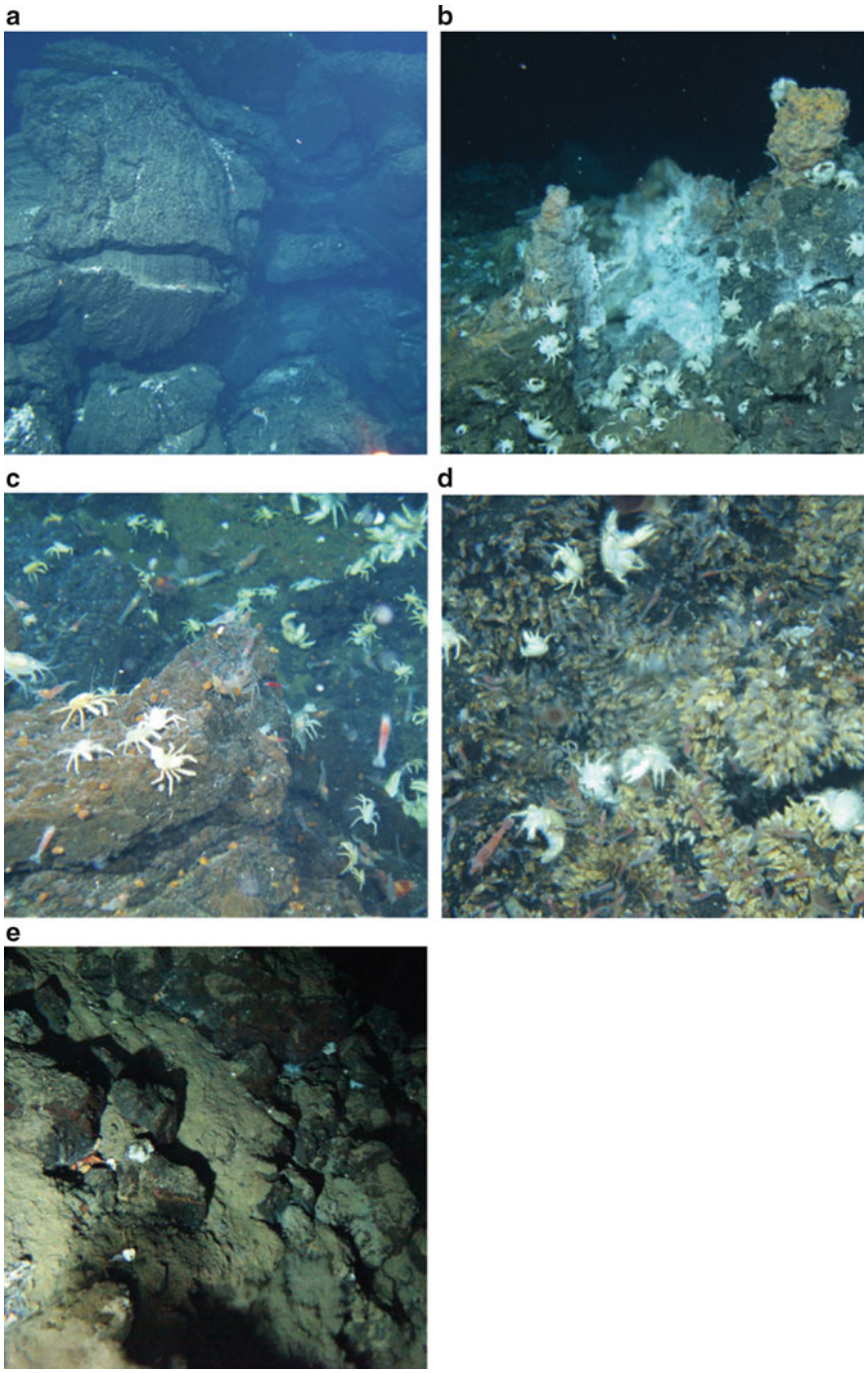

Fig. 39.2 Pictures of geological and biological feature at the Irabu Knoll. (**a**) Fresh basaltic pillow lava, (**b**) Active hydrothermal site at the West seamount, (**c**) Crustaceans dominated by *Shinkaia crosnieri* and *Munidopsis* sp., (**d**) Dense colony of *Ashinkailepsas* sp. (**e**) A small colony of bivalves on the northern inside slope

Acknowledgement Part of the bathymetric data was supplied from Japan Oceanographic Data Center (JODC). This work was partially supported by a Grant-in-Aid for Scientific Research on Innovative Areas (Project TAIGA, no. 20109003).

References

Fukuba T (2011) Hydrothermal plume mapping by *in situ* multi parameter measurements at the Yoron Knoll and the Irabu Knoll, NATSUSHIMA Cruise Report. http://www.godac.jamstec.go.jp/catalog/data/doc_catalog/media/NT10-16_all.pdf

Kimura M, Furukawa M, Izawa E, Ishikawa M, Kuramoto S, Sakai H, Uyeda S, Markris J (1991) Report of DELP 1988 cruises in the Okinawa Trough. Part 7. Geologic investigation of the central rift in the middle to southern Okinawa Trough. Bull Earthq Res Instit Univ Tokyo 66:179–209

Matsumoto T, Kinoshita M, Nakamura M, Sibuet JC, Lee CS, Hsu SK, Oomori T, Shinjyo R, Hashimoto Y, Hosoya S, Imamura M, Ito M, Tsukuda K, Yagi H, Tatekawa K, Kagaya I, Hokakubo S, Okada T, Kimura M (2001) Volcanic and hydrothermal activities and possible "segmentation" of the axial rifting in the westernmost part of the Okinawa Trough. Preliminary results from the YOKOSUKA/SHINKAI 6500 Lequios Cruise. JAMSTEC J Deep Sea Res 19:95–107 (in Japanese with English abstract)

Noguchi T (2007) Geochemical study on the deep and shallow submarine hydrothermal activities, Ph.D. thesis, University of the Ryukyus, Okinawa, Japan

Oshima S, Takanashi M, Kato S, Uchida M, Okazaki I, Kasuga S, Kawashiri C, Kaneko Y, Ogawa M, Kawai K, Seta H, Kato Y (1988) Geological and geophysical survey in the Okinawa Trough and the adjoining seas of Nansei Syoto. Rep Hydr Res 24:19–43 (in Japanese with English abstract)

Shinjo R (1999) Geochemistry of high Mg andesites and the tectonic evolution of the Okinawa Trough—Ryukyu arc system. Chem Geol 157:69–88

Watanabe M, Hoshino K, Shinokawa R, Takaoka Y, Fukumoto H, Shibata Y, Shinjo R, Oomori T (2006) Metallic mineralization associated with pillow basalts in the Yaeyama Central Graben, Southern Okinawa Trough, Japan. JAMSTEC Rep Res Dev 3:1–8

The Tarama Knoll: Geochemical and Biological Profiles of Hydrothermal Activity

40

Toshiro Yamanaka, Hiromi Nagashio, Ryu Nishio, Kazuna Kondo, Takuroh Noguchi, Kei Okamura, Takuro Nunoura, Hiroko Makita, Kentaro Nakamura, Hiromi Watanabe, Kazuhiro Inoue, Tomohiro Toki, Kouichiro Iguchi, Urumu Tsunogai, Ryoichi Nakada, Shogo Ohshima, Shin Toyoda, Jun Kawai, Naohiro Yoshida, Akira Ijiri, and Michinari Sunamura

Abstract

Tarama Knoll is located about 60 km north of Tarama Island, Sakishima Islands, southwestern Japan. The knoll has an almost conical shape, with foot and summit depths of 2,000 and 1,490 m (total relief = 510 m) from the sea surface, respectively. This area has been identified as a possible active submerged volcano called "Tarama Knoll" (Otani et al. 2004). However, there are actually two separate knolls in the area. This knoll is located northeast of the other, which is named Tarama Hill. During the KT05-26 cruise on the R/V

T. Yamanaka (✉) • H. Nagashio • R. Nishio • K. Kondo
Graduate School of Natural Science and Technology, Okayama University, 1-1, Naka-3-chome Kita-ku, Okayama 700-8530, Japan
e-mail: toshiroy@cc.okayama-u.ac.jp

T. Noguchi
Center for Advanced Marine Core Research, Kochi University, B200 Monobe, Nankoku, Kochi 783-8502, Japan

Marine Technology and Engineering Center, Japan Agency for Marine-Earth Science and Technology, 2-15 Natsushima-cho, Yokosuka, Kanagawa 237-0061, Japan

K. Okamura
Center for Advanced Marine Core Research, Kochi University, B200 Monobe, Nankoku, Kochi 783-8502, Japan

T. Nunoura
Subsurface Geobiology Advanced Research (SUGAR) Project, Japan Agency for Marine-Earth Science and Technology (JAMSTEC), 2-15 Natsushima-cho, Yokosuka 237-0061, Japan

Marine Functional Biology Group, Research and Development (R&D) Center for Marine Biosciences, Japan Agency for Marine-Earth Science & Technology, 2-15 Natsushima-cho, Yokosuka 237-0061, Japan

H. Makita
Subsurface Geobiology Advanced Research (SUGAR) Project, Japan Agency for Marine-Earth Science and Technology (JAMSTEC), 2-15 Natsushima-cho, Yokosuka 237-0061, Japan

K. Nakamura
Precambrian Ecosystem Laboratory (PEL), Japan Agency for Marine-Earth Science and Technology (JAMSTEC), 2-15 Natsushima-cho, Yokosuka 237-0061, Japan

Department of Systems Innovation, School of Engineering, The University of Tokyo, 7-3-1 Hongo, Bunkyo-ku, Tokyo 113-8656, Japan

H. Watanabe
Department of Marine Biodiversity Research, Japan Agency for Marine-Earth Science and Technology (JAMSTEC), 2-15 Natsushima-cho, Yokosuka 237-0061, Japan

K. Inoue • N. Yoshida
Deptartment of Environmental Chemistry & Engineering, Department of Environmental Science & Technology, The Research Center for the Evolving Earth & Planets, Tokyo Institute of Technology G1-17, 4259 Nagatsuta, Midori-ku, Yokohama 226-8502, Japan

T. Toki
Faculty of Science, University of the Ryukyus, 1 Senbaru, Nishihara, Okinawa 903-0213, Japan

K. Iguchi
Faculty of Science, Hokkaido University, Kita-10 Nishi-8 Kita-ku, Sapporo 060-0810, Japan

U. Tsunogai
Faculty of Science, Hokkaido University, Kita-10 Nishi-8 Kita-ku, Sapporo 060-0810, Japan

Graduate School of Environmental Studies, Nagoya University, Furo-cho, Chikusa-ku, Nagoya 464-8601, Japan

R. Nakada
Graduate School of Science, Hiroshima University, Higashi-Hiroshima, Hiroshima 739-8526, Japan

Earth-Life Science Institute, Tokyo Institute of Technology, 2-12-1 Ookayama, Meguro, Tokyo 152-8550, Japan

S. Ohshima
Graduate School of Science, Kyushu University, 6-10-1, Hakozaki, Higashi-ku, Fukuoka 812-8581, Japan

J.-i. Ishibashi et al. (eds.), *Subseafloor Biosphere Linked to Hydrothermal Systems: TAIGA Concept*,
DOI 10.1007/978-4-431-54865-2_40,

Tanseimaru, a methane anomaly was detected near the seafloor around the area and was considered to be of possible hydrothermal origin. Based on visual observation of the seafloor and its bathymetry, this knoll is considered a pumice cone. Dense turbid water is often observed around summit of the knoll, and a methane anomaly was detected in the water. These observations suggest that the turbid water is a hydrothermal plume. An iron-rich, red-brown sediment-covered area was discovered at a depth of 1,510–1,540 m on the southwestern slope near the summit. At the red-brown sediment area, a weak shimmering of clear fluid could be observed, and the fluid temperature reached 20 °C. Sampled shimmering fluid showed a high silica concentration (≥1 mM), indicating an interaction between the fluid and the surrounding rock. These chemical data support the occurrence of active hydrothermal circulation at Tarama Knoll.

Keywords
Hydrothermal activity • Hydrothermal plume • Southern Okinawa Trough • Tarama Knoll

40.1 Location and Bathymetric Features of Tarama Knoll

Tarama Knoll is located at 25°05.50′N, 124°32.50′E (Fig. 40.1). The knoll lies almost at the foot of the south fault scarp in the rift graben of the southern Okinawa Trough (Letouzey and Kimura 1986). The knoll has an almost conical shape and an additional small peak on the northern slope (Fig. 40.2). The depths of the main summit and foot are 1,490 and about 2,000 m from the sea surface, respectively, and the total relief from the foot to summit is 510 m. The average steepness is *c*. 18°, and the steepness does not change significantly from the foot to the summit. Another smaller knoll named Tarama Hill is located about 4 km southwest of Tarama Knoll.

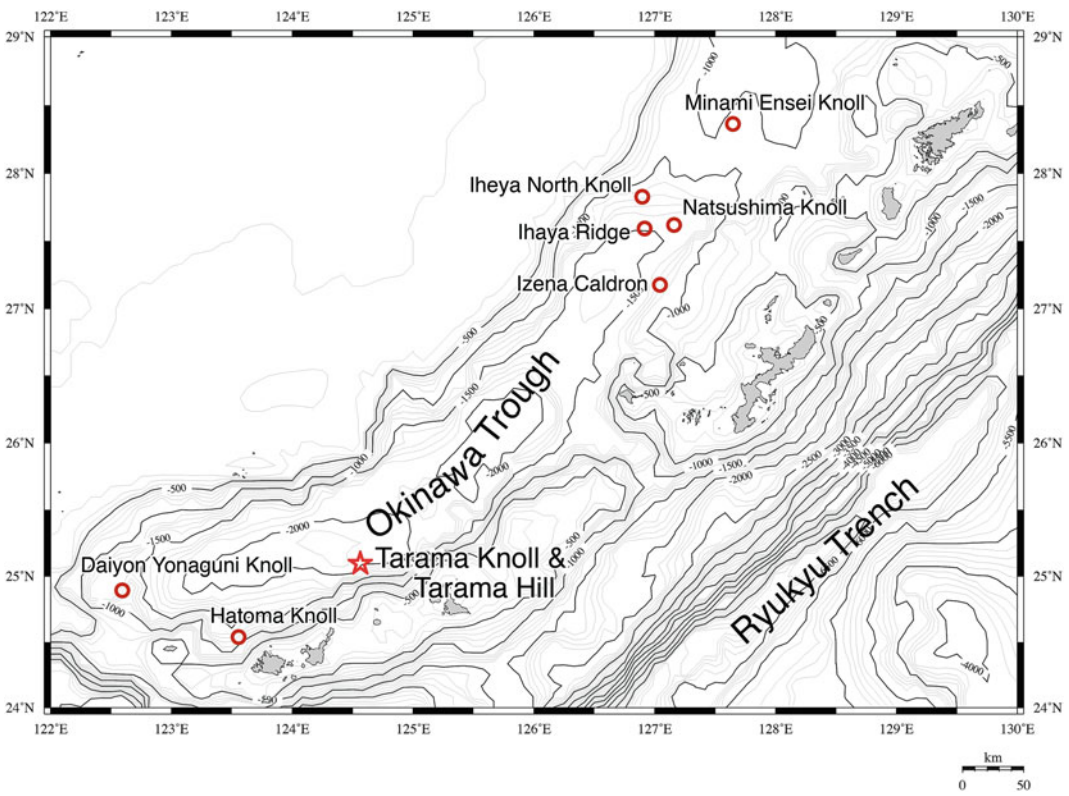

Fig. 40.1 Locations of Tarama Knoll and Tarama Hill and other hydrothermal fields in the Okinawa Trough

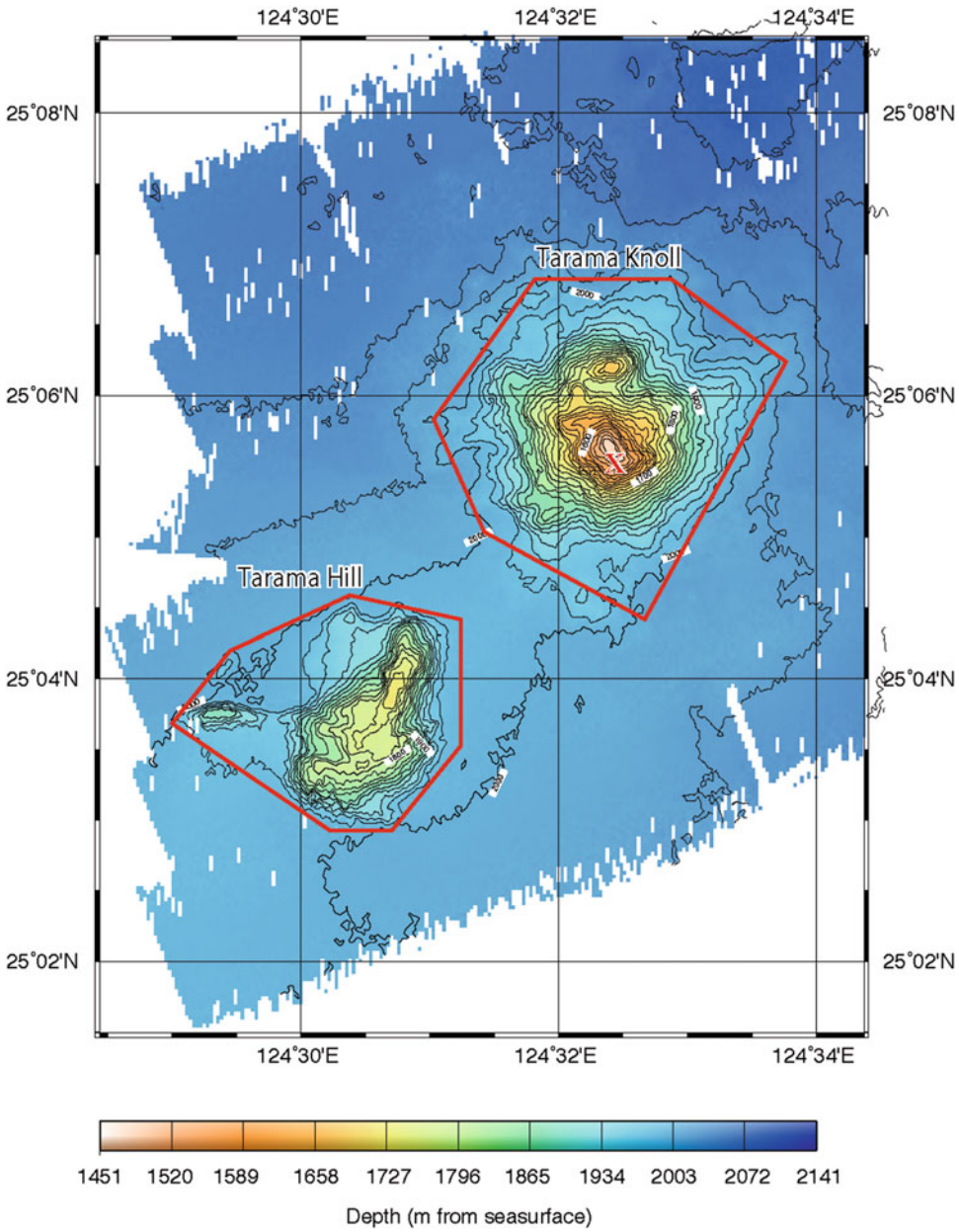

Fig. 40.2 Bathymetric map of Tarama Knoll and Tarama Hill obtained by the SeaBat 8160 multibeam echosounder on the R/V *Natsushima* during NT09-10 Leg. 2 and NT10-06 Leg. 2 cruises. The X indicates the sampling point during the KT05-26 cruise

40.2 Observation History of Tarama Knoll

Tarama Knoll was originally described as a single-summit active volcano based on low-resolution seismic and geomagnetic observations carried by the Hydrographic Surveys Division of Japan Coast Guard (Otani et al. 2004). Tarama Knoll and Tarama Hill were then identified as one elongated knoll due to insufficient resolution (Fig. 40.2). This area was visited by the R/V *Tanseimaru* during the KT05-26 cruise, and a methane anomaly was detected near the seafloor that was considered of possible hydrothermal origin (Fig. 40.3). During the NT09-10 Leg. 2 cruise in 2009, a high-resolution seismic survey was done by the R/V *Natsushima* (which belongs to JAMSTEC) using a SeaBat 8160 multibeam echosounder, and the results showed two independent knolls. A methane anomaly was detected near the Tarama Knoll, and therefore dive surveys using the ROV/*HyperDolphin* were carried out at the knoll in 2009, 2010, and 2011.

40.3 Dive Observations at Tarama Knoll

Since 2009, we have done seven dives using the ROV/*HyperDolphin* (which belongs to JAMSTEC) at the Tarama Knoll (Table 40.1). All dive tracks are shown in Fig. 40.4. During the dives, we often observed dense turbid water

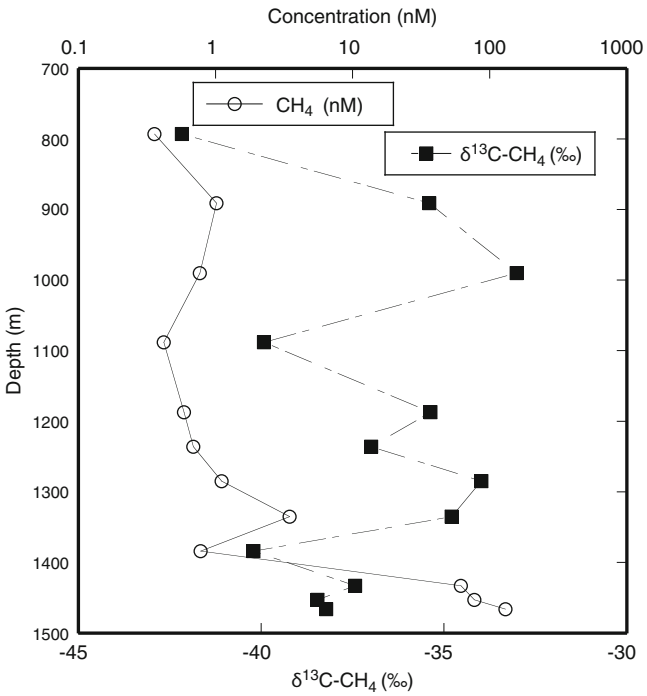

Fig. 40.3 Vertical profiles of the methane concentrations and $\delta^{13}C$ values of methane dissolved in seawater. Samples were obtained during the KT05-26 cruise

resembling hydrothermal plumes, and many planktonic tunicates were observed in the water. As such planktonic tunicates have often been observed in hydrothermal plumes emitted by active hydrothermal vents in the Okinawa Trough (Miyake et al. 2009), hydrothermal venting from a nearby area was expected. However, no active venting site has yet been found. Visual observation of the seafloor indicated rubble and angular gravel covering the slope (Fig. 40.5a). Although benthic animals were rarely found on the slope, dense sponge colonies were found in the area where dense turbid water covered the seafloor (Fig. 40.5b).

Weak shimmering of clear warm fluid (up to 23 °C) was found on the southwestern slope near the summit at a depth of 1,510–1,540 m in an area covered with red-brown sediment. Many finger-like chimneys consisting of the red-brown sediment were observed in this area (Fig. 40.5c, d), which was named the "Fox site" (Makita et al., in prep.). The shimmering fluid was sampled.

40.4 Fluid, Rock, and Sediment Chemistry

Turbid water, shimmering fluid, rocks, and red-brown sediments were sampled during dive studies and subjected to chemical analyses. The results of the analyses are summarized in Tables 40.1 and 40.2. Analysis of the turbid water showed that the concentrations of major cations (sodium, magnesium, calcium, and potassium) and anions (chloride and sulfate) were similar to those in ambient seawater, but the methane concentration in the turbid water was one or two orders of magnitude higher than that of the ambient seawater (Table 40.1). These observations suggest that the turbid water may be from a hydrothermal plume. The shimmering fluid showed high concentrations of silica, ammonium, and alkalinity relative to seawater, whereas concentrations of magnesium, sodium, and potassium were slightly lower than those of the ambient seawater. Although the data are insufficient for accurate hydrothermal endmember estimation, the estimated endmember concentration of silica reached around 11 mM. The endmember silica concentration corresponds to a reservoir temperature of 260 °C based on the silica geothermometer, assuming equilibrium with quartz (Fournier 1977). The chemical signature enriched in ammonium, methane, and alkalinity suggests interaction with sedimentary organic matter during hydrothermal circulation, similar to other hydrothermal fluids in the Okinawa Trough (Ishibashi and Urabe 1995). The decreased levels of major cations in the fluid may suggest phase separation or segregation in the subseafloor. Hydrogen sulfide was not detected in the fluid.

Most sampled rocks seemed to be pumice and lava fragments based on their visual texture and whitish color (Fig. 40.6). Bulk chemical composition of one lava fragment sample collected during *HyperDolphin* dive #1109 (Table 40.2) showed a high silica content (>75 %) suggestive of rhyolitic magma activity.

The red-brown sediment was rich in iron oxide and was composed mainly of ferrihydrite or possibly microcrystalline goethite (Makita et al., in prep.).

40.5 Biological Observation

Some animal samples were collected during the dive studies, and details were reported by Yamanaka et al. (Chap. 10). Although typical vent endemic species, such as vesicomyid clams, mytilid mussels, and vestimentiferan tubeworms, were not found during the dive studies, one liparid snailfish specimen (Fig. 40.7) obtained during *HyperDolphin* dive #1322 contained remains of undigested *Alvinocaris* shrimp and shell of *Provanna* snail in its gut. These shrimp and snail species are endemic to hydrothermal vents and methane seeps (e.g., Fujikura et al. 2012) and represent feed of snailfish in hydrothermal vent areas (Takemura et al. 2010). The migrating ability of liparid snailfish is not known, and the possible habitat area may be less than several kilometers square. Isotopic signatures obtained from the sponges had significantly low $\delta^{34}S$ values (about +2.5 to +5.0 ‰), indicating that they rely on thioautotrophic products (e.g., sulfur-oxidizing bacteria) that utilize reduced sulfur

Table 40.1 Results of chemical analyses of seawater and shimmering fluid obtained from Tarama Knoll

Date	HPD Dive No.	ID[a]	Mg (mM)	Ca (mM)	Na (mM)	K	SO_4 (mM)	Cl (mM)	Fe (μM)	Si (μM)	NH_4 (μM)	pH	alk. (mM)	CH_4 (nM)	$\delta^{13}C$-CH_4 (‰)	δD-CH_4 (‰)	Note
2009.7.20	1032	N1	53.1	10.3	472.5	9.1	27.4	539.3	na.	124.0	3.0	7.72	2.56	30.3	−35.4	na.	Turbid water
		N2	53.8	10.4	471.6	10.0	27.7	540.4	na.	124.0	2.0	7.81	2.34	16.4	−34.9	na.	Turbid water
2009.7.21	1033	N1	52.2	10.3	474.1	10.3	27.3	540.4	na.	123.0	nd.	7.72	2.50	2.07	−43.1	na.	Ambient seawater
		N2	52.0	10.3	465.5	10.0	27.4	535.9	na.	123.0	1.0	7.64	2.35	45.2	−33.4	na.	Turbid water
2009.7.22	1034	N1	52.5	10.3	472.4	10.2	27.4	539.3	na.	126.5	6.9	7.75	2.37	654	−39.1	−105	Turbid water
		N2	53.8	8.4	480.2	10.3	29.0	538.2	na.	123.7	8.0	7.77	2.42	52.7	−36.5	−132	Turbid water
		V	48.5	9.7	435.0	9.5	na.	na.	na.	na.	na.	na.	na.	2,320	−35.9	−143	Shimmering fluid
		B	50.0	10.0	452.0	9.6	27.7	538.2	na.	128.4	10.8	7.80	2.51	na.	na.	na.	Shimmering fluid
		M	52.0	10.7	474.9	9.0	30.8	539.3	52.9	314.5	38.8	7.57	3.15	na.	na.	na.	Shimmering fluid
2010.4.9	1107	N	53.0	10.5	471.3	10.1	28.3	522.9	na.	131.2	1.2	na.	na.	na.	na.	na.	Turbid water
		M	53.4	10.5	474.5	10.2	28.9	531.4	na.	131.3	1.8	na.	na.	na.	na.	na.	Shimmering fluid
2010.4.10	1108	N1	53.1	10.5	472.3	10.1	21.7	433.4	na	123.0	1.8	na.	na.	na.	na.	na.	Turbid water
		N2	53.3	10.5	473.1	10.1	28.5	526.4	na.	124.2	1.8	na.	na.	na.	na.	na.	Turbid water
		BW1	47.9	10.5	439.9	10.3	27.0	526.5	na.	562.9	78.8	na.	na.	na.	na.	na.	Shimmering fluid
2010.4.11	1109	N1	53.6	10.6	477.2	10.2	29.1	533.8	na.	121.3	0.5	na.	na.	na.	na.	na.	Turbid water
		N2	53.5	10.6	476.6	10.2	28.8	529.9	na.	121.5	1.0	na.	na.	na.	na.	na.	Turbid water
		N3	53.6	10.6	476.6	10.2	28.6	527.9	na.	122.0	1.2	na.	na.	na.	na.	na.	Turbid water
		W1	48.6	12.1	463.5	11.6	na.	na.	na.	na.	na.	na.	na.	na.	na.	na.	Shimmering fluid
		W2	50.0	11.1	461.1	10.8	25.8	523.9	0.078	662.9	59.5	na.	na.	na.	na.	na.	Shimmering fluid
		W3	50.7	12.6	483.0	12.1	na.	na.	na.	na.	na.	na.	na.	na.	na.	na.	Shimmering fluid
		W4	48.8	12.0	463.7	11.6	25.6	523.2	0.14	1,030	98.2	na.	na.	na.	na.	na.	Shimmering fluid
		B	48.2	11.6	454.5	11.2	25.6	522.4	na.	891.7	88.2	na.	na.	na.	na.	na.	Shimmering fluid
		EW1	49.4	12.0	467.6	11.6	26.5	522.1	0.109	948.8	95.8	na.	na.	na.	na.	na.	Shimmering fluid
		EW2	50.0	12.1	473.1	11.7	25.1	519.1	0.082	891.7	93.2	na.	na.	na.	na.	na.	Shimmering fluid
2011.9.15	1322	W1	45.8	11.7	465.1	11.8	26.4	539.6	na.	1,045	94.3	6.39	6.84	na.	na.	na.	Shimmering fluid
		W2	na.	na.	na.	na.	na.	na.	na.	na.	na.	na.	na.	5,170	na.	na.	Shimmering fluid
		W3	51.2	9.5	462.9	10.1	27.7	556.0	na.	198.5	10.1	6.94	2.69	na.	na.	na.	Shimmering fluid
		W4	na.	na.	na.	na.	na.	na.	na.	na.	na.	na.	na.	2,750	na.	na.	Shimmering fluid
		CW2	50.8	9.9	468.2	10.4	27.7	546.5	na.	204.3	12.1	6.80	2.78	11,800	na.	na.	Shimmering fluid
		B	na.	na.	na.	na.	na.	na.	na.	na.	na.	6.92	na.	na.	na.	na.	Shimmering fluid
		N1	51.5	9.8	469.3	10.4	27.8	544.9	na.	113.0	3.2	7.69	2.40	na.	na.	na.	Turbid water
		N2	51.5	10.4	468.4	10.3	28.0	547.3	na.	110.7	2.4	7.65	2.42	na.	na.	na.	Turbid water

[a]Alphabets indicate sampler type, *N* Niskin bottole, *V* Vacumed metal bottle, *B* Plastic bag, *M* M-type sediment sampler, *W, BE, CW and EW* WHATS fluid sampler

na. not analysis

nd. not detected

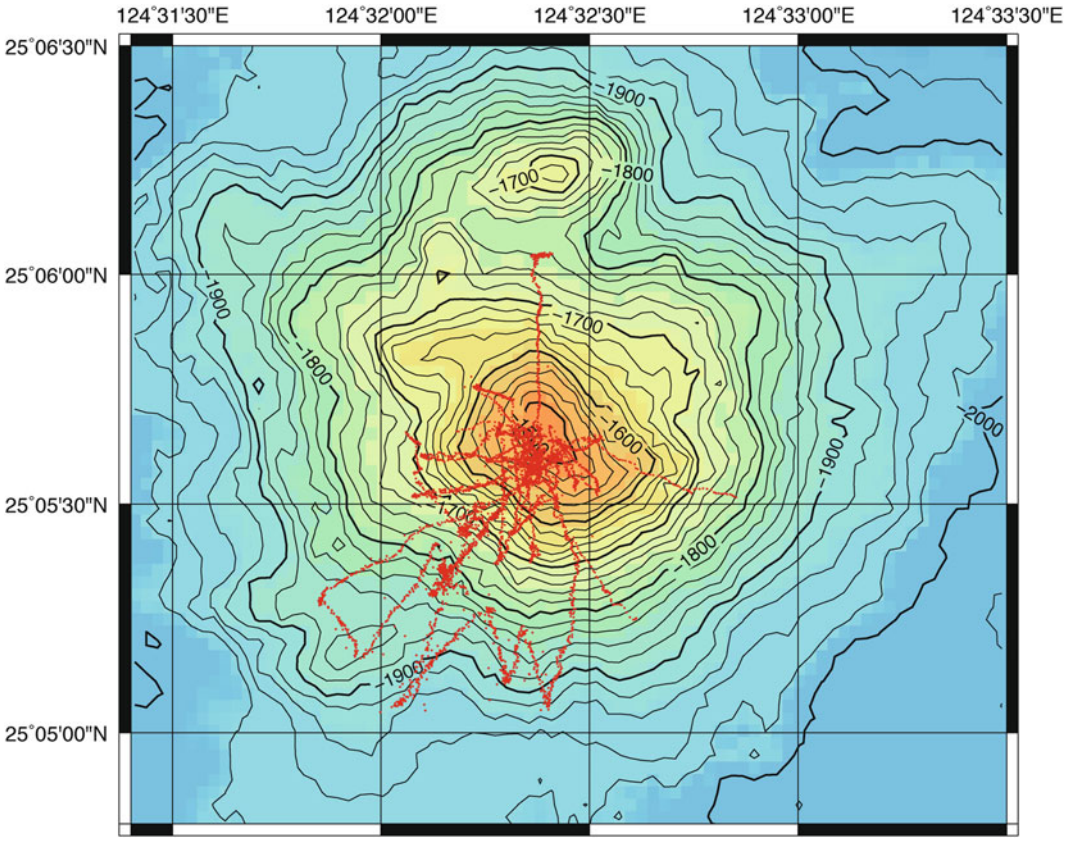

Fig. 40.4 Dive tracks of ROV/*HyperDolphin* surveys of this area are shown as red dotted lines. Seven dives (Dive Nos. 1032–1034, 1107–1108, 1132) were done

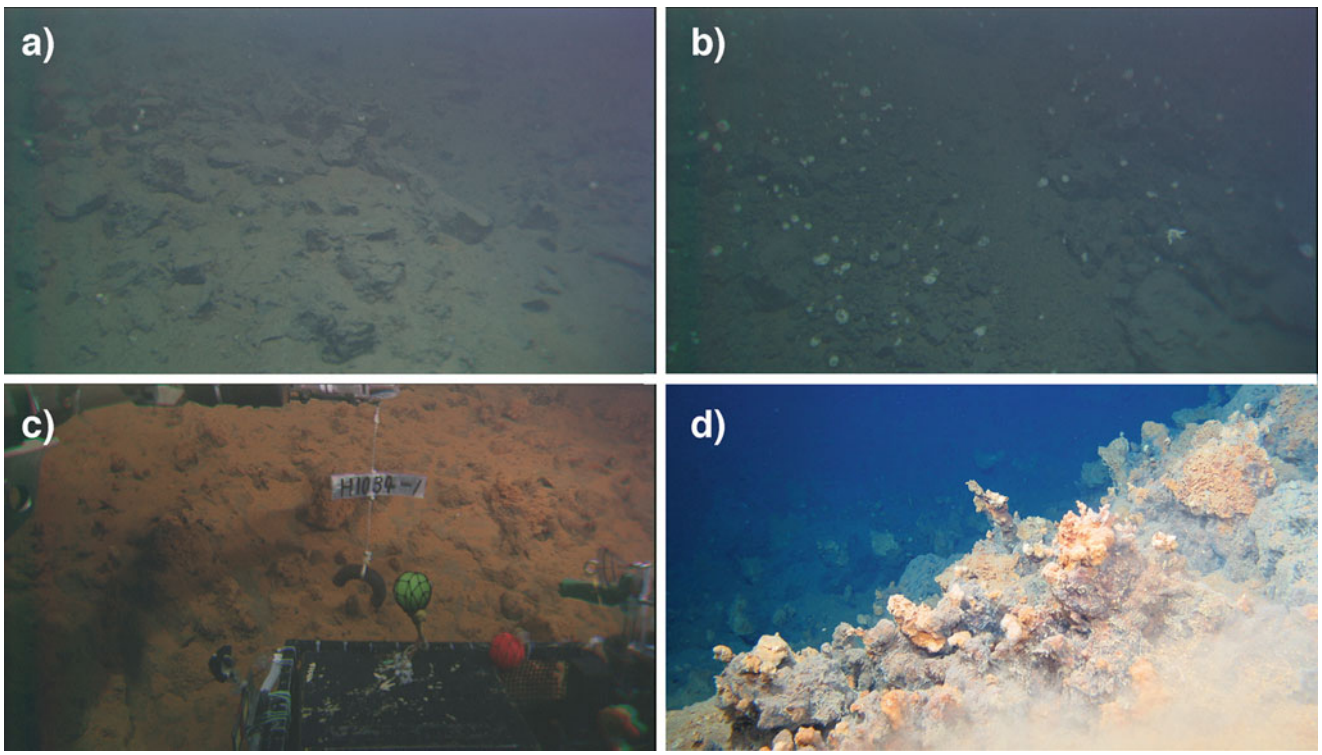

Fig. 40.5 Photographs of the seafloor on the slope of Tarama Knoll. (**a**) Rubble and angular gravel covered the slope. (**b**) Dense sponge colonies were observed in some areas on the slope. (**c**) Red-brown sediment widely covered the southwestern slope near the summit. (**d**) Many "finger" chimneys were found

Table 40.2 Bulk chemical composition of a rock sample obtained from Tarama Knoll

	Sampling point														
Sample No.	Latitude	Longitude	Depth (m)	SiO_2 (%)	Al_2O_3 (%)	Fe_2O_3(T) (%)	MnO (%)	MgO (%)	CaO (%)	Na_2O (%)	K_2O (%)	TiO_2 (%)	P_2O_5 (%)	LOI (%)	Total (%)
HPD1109R01	25°05.581′N	124°32.363′E	1,536	75.25	12.44	3.17	0.102	0.12	2.2	4.61	1.04	0.164	0.02	0.98	100.1

All elements were analyzed using fusion-inductively coupled plasma (FUS-ICP). Detection limit was less than 0.01 %

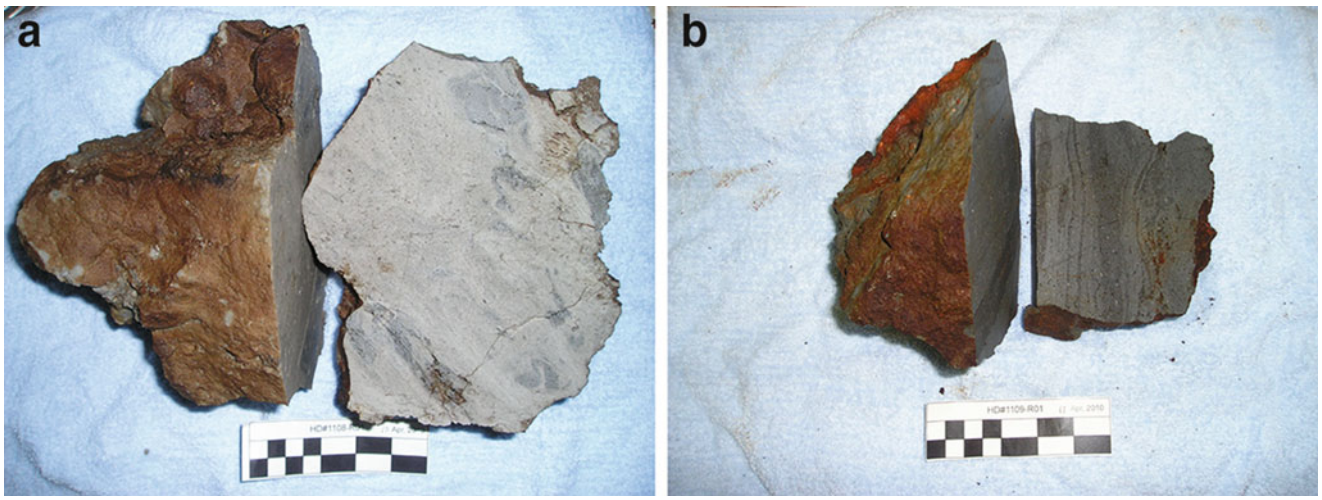

Fig. 40.6 Photographs of rock samples. (**a**) Pumice-like porous and whitish rock. (**b**) Lava fragment

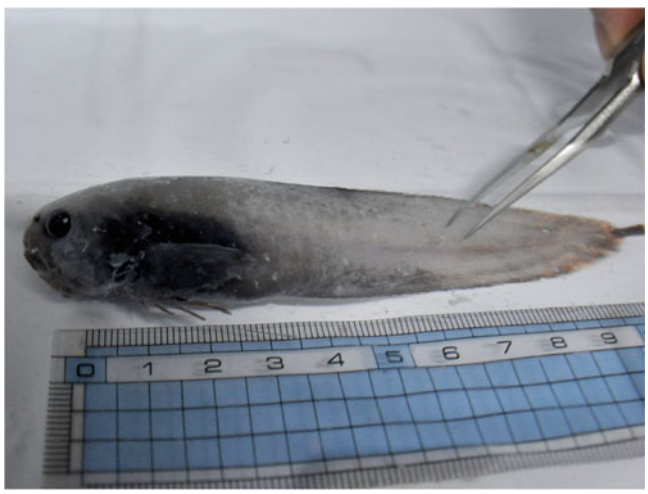

Fig. 40.7 Photograph of liparid snailfish specimen that contained *Alvinocaris* shrimp and shell of *Provanna* snail in its gut. The specimen was sampled during *HyperDolphin* dive #1322 in 2011. This photograph was provided by Mr. M. Miyazaki

compounds (e.g., hydrogen sulfide), possibly of hydrothermal origin, as energy sources (Yamanaka et al., Chap. 10).

Microbial communities in turbid water (plume) were investigated and documented by Sunamura and Yanagawa (Chap. 3). The microbial community structures based on 16S rRNA genes revealed that potential thiotrophic and methanotrophic microbial phylotypes were predominant in the plume. The results were comparable to the microbial communities associated with the active hydrothermal areas in the Okinawa Trough.

The observed dense turbid water (possibly hydrothermal plume water) and biological studies suggest that active hydrothermal venting is occurring in this area, and the venting fluid is expected to contain hydrogen sulfide and venting as a black smoker.

Acknowledgements All of the fluid, water, sediment, and biological samples were obtained through cooperative efforts of the operation team of the ROV/*HyperDolphin*, and the captain and crew of the support ship R/V *Natsushima*, to whom we extend our heartfelt thanks. This research was supported by the Ministry of Education, Culture, Sports, Science and Technology of Japan through a Special Coordination Fund 'TAIGA' project (Grant-in-Aid for Scientific Research on Innovative Areas, No. 20109005).

References

Fournier RO (1977) Chemical geothermometers and mixing models for geothermal systems. Geothermics 5:41–50

Fujikura K, Okutani T, Maruyama T (2012) Deep-sea life: biological observations using research submersibles, 2nd edn. Toukai University Press, Tokyo (in Japanese with English captions)

Ishibashi J, Urabe T (1995) Hydrothermal activity related to arc–backarc magmatism in the western Pacific. In: Taylor B (ed) Backarc basins: tectonics and magmatism. Plenum, New York, pp 451–495

Letouzey J, Kimura M (1986) The Okinawa Trough: genesis of a back-arc basin developing along a continental margin. Tectonophysics 125:209–230

Miyake Y, Shiga N, Nakashima K, Kimura S (2009) Dense colony of Appendicularia (*Oikopleura sp*.) observed in hydrothermal plum of Okinawa Trough, Abstract of Annual joint meeting of The Benthos Society and The Plankton Society of Japan. Sendai, Japan, Oct. 16th to 18th (in Japanese)

Otani Y, Tsuchide M, Shibata A, Kato S, Iwabuchi Y (2004) The list of volcanoes and their activities records in the adjacent seas of Japan, 3rd edition. Rep Hydrogr Oceanogr Res 40:1–61 (in Japanese with English abstract and captions)

Takemura A, Tamotsu S, Miwa T, Yamamoto H (2010) Preliminary results on the reporoduction of a deep-sea snailfish *Careproctus rhodomelas* around the active hydrothermal vent on the Hatoma Knoll, Okinawa, Japan. J Fish Biol 77:1709–1715. doi:10.1111/j.1095-8649.2010.02789.x

Part VI

Appendix II: Drilling Reports

41 Petrography and Geochemistry of Basement Rocks Drilled from Snail, Yamanaka, Archaean, and Pika Hydrothermal Vent Sites at the Southern Mariana Trough by Benthic Multi-Coring System (BMS)

Kentaro Nakamura, Hiroshi Sato, Patricia Fryer, and Tetsuro Urabe, TAIGA 10M Shipboard Scientific Party

Abstract

Petrographic and geochemical characteristics of drill core and surface rock samples from the four hydrothermal vent sites of the Yamanaka, Snail, Archaean, and Pika sites at the Southern Mariana Trough (SMT) are described in order to clarify the geological background of hydrothermal activities. The core samples were drilled by the Benthic Multi-coring System (BMS), penetrating up to ~8 m below seafloor. The recovered samples included both basement rocks and sulfide ores. The basement rocks are further subdivided into basaltic andesite and andesite, most of which are recovered from on-axis and off-axis regions of the SMT, respectively. All of the rocks are characterized by relative enrichment of large-ion lithophile elements with noticeable depletion of Nb and Ta, suggestive of

The online version of this chapter (doi:10.1007/978-4-431-54865-2_41) contains supplementary material, which is available to authorized users.

K. Nakamura (✉)
Precambrian Ecosystem Laboratory (PEL), Japan Agency for Marine-Earth Science and Technology (JAMSTEC), 2-15 Natsushima, Yokosuka, Kanagawa 237-0061, Japan

Submarine Hydrothermal System Research Group, Japan Agency for Marine-Earth Science and Technology (JAMSTEC), 2-15 Natsushima, Yokosuka, Kanagawa 237-0061, Japan

Department of Systems Innovation, School of Engineering, The University of Tokyo, 7-3-1 Hongo, Bunkyo-ku, Tokyo 113-8656, Japan
e-mail: kentaron@sys.t.u-tokyo.ac.jp

H. Sato
School of Business Administration, Senshu University, 2-1-1 Higashimita, Tama-ku, Kawasaki-shi, Kanagawa 214-8580, Japan

P. Fryer
School of Ocean and Earth Science and Technology (SOEST), University of Hawai'i, 1680 East West Rd, Honolulu, HI 96822, USA

T. Urabe
Department of Earth and Planetary Sciences, The University of Tokyo, 7-3-1 Hongo, Bunkyo-ku, Tokyo 113-0033, Japan

TAIGA10M Shipboard Scientific Party (excluding Kentaro Nakamura, Patricia Fryer, and Tetsuro Urabe);
Shin Toyoda, Faculty of Science, Okayama University of Science, 1-1 Ridai, Okayama 700-0005, Japan

Junichi Miyazaki, Institute of Biogeosciences, Japan Agency for Marine-Earth Science and Technology (JAMSTEC), 2-15 Natsushima, Yokosuka, Kanagawa 237-0061, Japan

Nobutatsu Mochizuki, Priority Organization for Innovation and Excellence, Kumamoto University, 2-39-1 Kurokami, Kumamoto 860-8555, Japan

Shingo Kato, Department of Molecular Biology, Tokyo University of Pharmacy and Life Science, 1432-1 Horinouchi, Hachioji, Tokyo 192-0392, Japan

Teruhiko Kashiwabara, Graduate school of Science, Hiroshima University, 1-3-1 Kagamiyama, Higashi-hiroshima, Hiroshima 739-8526, Japan

Fumihiro Sato, Okayama University of Science, 1-1 Ridai, Okayama 700-0005, Japan

Sakiko Kikuchi, Graduate school of Science, Hiroshima University, 1-3-1 Kagamiyama, Higashi-hiroshima, Hiroshima 739-8526, Japan

Shigeshi Fuchida, Graduate School of Science, Osaka City University, 3-3-138, Sugimoto, Sumiyoshi, Osaka 558-8585, Japan

Takahito Nishiuchi, Graduate School of Natural Science and Technology, Okayama University, 3-1-1 Tsushima-naka, Okayama 700-8530, Japan

Jun Kawai, Graduate School of Engineering, Yokohama National University, 79-5 Tokiwadai, Hodogaya, Yokohama, Kanagawa 240-8501, Japan

Motoshige Date, Date City Institute of Funkawan Calture, 21-5 Tateyama, Date, Hokkaido 052-0031, Japan

J.-i. Ishibashi et al. (eds.), *Subseafloor Biosphere Linked to Hydrothermal Systems: TAIGA Concept*,
DOI 10.1007/978-4-431-54865-2_41,

significant influence of subducted slab-derived components into the basement rocks both at the on- and off-axis hydrothermal vent sites. Major and trace element variations of the samples suggest that the Yamanaka, Snail, and Archaean rocks can be explained by a sequence of fractionation of an on-axis magma, whereas only the Pika rocks may be influenced by a different magma component, i.e., off-axis magmatism.

Keywords
Benthic Multi-coring System (BMS) • Geochemistry • Hydrothermal vent sites • Petrography • Southern Mariana Trough

41.1 Introduction

Chemical compositions of seafloor hydrothermal vent fluids have a significant impact on ocean chemistry, hydrothermal vent biological communities, and seafloor mineral deposits. For example, seafloor hydrothermal systems are long known to play a major role in elemental exchange between ocean and oceanic crust, affecting the composition of many elements in seawater (e.g., Edmond et al. 1979; Elderfield and Schultz 1996). Several chemical elements contained in hydrothermal fluids (e.g., H_2S, H_2, and CH_4) also known to support a variety of biological communities sustained by primary production of chemolithoautotrophic microorganisms (e.g., Hessler and Kaharl 1995), which are essentially different from terrestrial ecosystems sustained by photosynthetic primary production. In recent years, furthermore, seafloor mineralization at hydrothermal vents, where metal sulfides precipitated from hydrothermal fluids are accumulated to form sulfide deposits, has attracted particular attention (e.g., Tivey 2007).

The chemical compositions of hydrothermal vent fluids are, in turn, influenced by composition of basement rocks, because hydrothermal fluids are developed by chemical reactions between penetrating seawater and basement rocks (e.g., Seyfried et al. 1991; Shock 1992). Understanding petrological and geochemical characteristics of the basement rocks is, therefore, important to elucidating chemical features of seafloor hydrothermal vent fluids. Here, we report petrographical and geochemical characteristics of basement rock samples drilled at/near the four hydrothermal vent sites (Snail, Yamanaka, Archaean, and Pika sites) located at the Southern Mariana Trough by using Benthic Multi-coring System (BMS).

41.2 Geological Background

The Mariana convergent margin system is located at the eastern boundary of the Philippine Sea region in the Western Pacific (Fig. 41.1). Subduction of the Pacific Plate beneath the Philippine Sea Plate began in the Eocene prior to ~50 Ma (e.g., Seno and Maruyama 1984). By the Middle Oligocene (~30 Ma), volcanism in response to subduction had built a volcanic arc that became localized along a relatively narrow chain, parallel to what would become the Izu-Ogasawara-Mariana trench system (Kobayashi and Nakada 1979). From ~30 to 20 Ma, a series of episodic arc building and rifting events occurred from west to east, and the Kyushu-Palau Ridge, Parece Vela Basin, and West Mariana Ridge were formed during this period. Since 10 Ma, extension has concentrated in the eastern basin of the system, the Mariana Trough.

The area of interest for this study includes hydrothermal systems both at spreading center and off-axis seamounts of the Southern Mariana Trough (SMT), approximately 110 km southwest of the island of Guam (Fig. 41.1). Within the Mariana Trough, this part of the spreading center is unusual in having morphology similar to fast-spreading mid-ocean ridges, despite the fact that the spreading rate in this part of the Mariana Trough is relatively low (45–65 mm/year full rate) (Martinez et al. 2000; Becker et al. 2010). It can be considered that arc magma is more readily available to this part of the spreading center region, because of the short distance between the back-arc spreading center and the arc volcanic front. The influence of the arc magma on the volcanisms at the spreading axis is likely the cause of the unusual ridge morphology. Indeed, Pearce et al. (2005) presented a systematic geochemical mapping for the whole area of the Mariana arc and trough system, showing that volcanic glasses from the middle to northern segments (14–15°, 17°, and 19.5°N) of the Mariana Trough have true mid-ocean ridge basalt (MORB) compositions without any subduction components, whereas those from southern part of the Mariana Trough are apparently affected by the shallow subduction component.

Recent exploration in this region with submersible vehicles has discovered four active hydrothermal vent sites of the Yamanaka, Snail, Arhcean, and Pika sites (Urabe et al. 2004). Two of them (Yamanaka and Snail sites) are situated on the spreading axis, whereas the other two (Archaean and Pika sites) are located on off-axis seamounts, which are on the southeast of the spreading center region (Fig. 41.1).

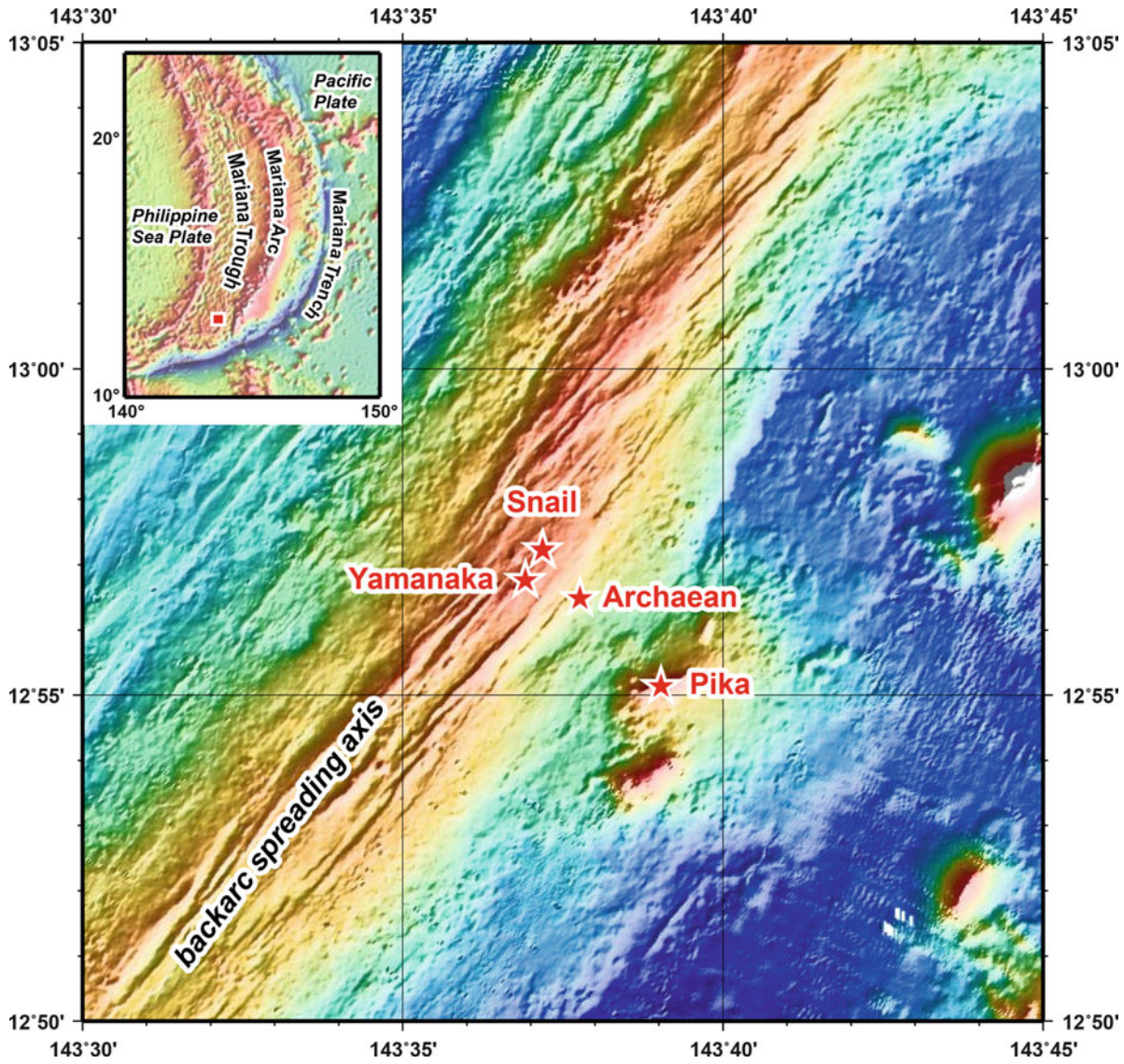

Fig. 41.1 Bathymetric map showing the locations of the four hydrothermal vent sites (the Snail, Yamanaka, Archaean, and Pika sites) at the Southern Mariana Trough

41.3 Site Description

From 14 June to 23 June 2010, we conducted TAIGA10M cruise by R/V *Hakurei-Maru No.2* at the SMT. During the cruise, we performed seafloor drilling with 12 holes at the four hydrothermal vent sites (Yamanaka, Snail, Archaean, and Pika sites) using the Benthic Multi-coring System (BMS); one hole at the Snail site (BMS-01), one hole at the Yamanaka site (BMS-04), seven holes at the Archaean site (BMS-02, 03, 06A, B, C, D, 07), and three holes at the Pika site (BMS-05, 08, 09) (Fig. 41.2). Summary of the BMS sampling during TAIGA10M cruise is given in Table 41.1.

Site BMS-01 This site is located at the Snail hydrothermal site. The target of this drilling was to collect sulfides and basement rocks. We installed BMS right on the axis near the Marker 24 site, where pillow lava was extensively exposed without sediment cover. Drilling was smooth and the drilling speed was constant. After the drilling, fluid venting was observed from the borehole.

Site BMS-02 This site is located at the Archaean hydrothermal site. At this site, we originally planned to recover volcanic rocks beneath the hydrothermal site. The drilling site was sedimented with talus of sulfide blocks, from upslope, covered with about 7 cm of red-colored, soft

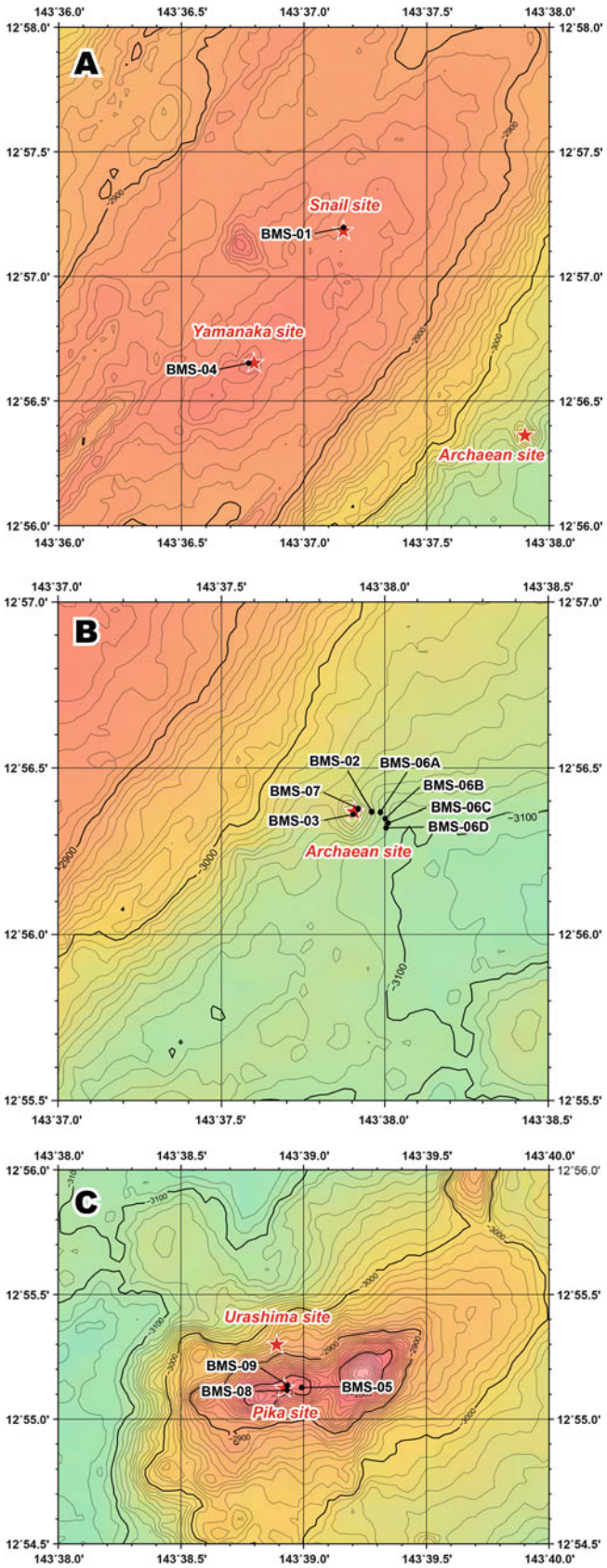

Fig. 41.2 Positions of the BMS drilling at and near the (**a**) Snail, Yamanaka, (**b**) Archaean, and (**c**) Pika hydrothermal sites. Note that newly discovered the Urashima hydrothermal site (Nakamura et al. 2013) located at northern part of the Pika site is also shown in (**c**)

sediment. Because the bit was clogged at depth of 167 cm, we quit drilling at that depth.

Site BMS-03 This site is also located at the Archaean hydrothermal site. We spent a long time searching for basement volcanic rocks, but the seamount hosting the Archaean site is entirely covered by talus of sulfide blocks here as well,. The area where we installed the BMS is similar to that of BMS-02 with 20 cm of red-colored soft sediments covering the sulfide blocks.

Site BMS-04 This site is located at the Yamanaka hydrothermal site. At this site, we planned to sample fresh basement rocks. As at the Snail site, pillow lava was extensively exposed without sediment cover. After the drilling, we noticed that hydrothermal fluid was shimmering from the borehole.

Site BMS-05 This site is located at the Pika hydrothermal site. Targets of this drilling were materials from an inactive sulfide mound and underlying basement rocks. We drilled at the top of the sulfide mound. It has a diameter of more than 5 m and is topped by many small dead chimneys of about 50 cm in height.

Sites BMS-06A to D These sites are located around the Archaean hydrothermal site. In a series of drill holes from 06A to 06D, we intended to recover fresh basement rocks from the site for the first time. At the top of seamount hosting Archaean site, sulfide chimneys and mounds are extensively exposed, whereas pillow and sheet flow lavas, covered by reddish brown sediments, lie at the base of the seamount. Drilling was quite successful and we recovered fresh sulfide blocks (06A), pillow lava (06B, C) and sheet flow lava (06D).

Site BMS-07 This site is also located at the Archaean hydrothermal site. The target of this drilling was to recover fresh sulfide ores. The BMS was installed on top of a hill that is entirely covered by sulfide chimneys or their broken equivalents. There were also a few dead chimneys around the drilling site.

Site BMS-08 This site is located at the Pika hydrothermal site. The purpose of the drilling was to recover high temperature fluid and fresh sulfide ore. The BMS was set on the top of a small mound that turned out to be not a sulfide mound, but a pillow lava mound. After drilling, however, weak fluid venting was observed from the borehole.

Site BMS-09 This site is also located at the Pika hydrothermal site. The target of this drilling was high-temperature hydrothermal fluid. The BMS was installed near a clear smoker chimney. Drilling was done on the edge of a sulfide mound where we observed many slender chimneys (some of them were still active). Unfortunately, however, no fluid venting (not even a low-temperature one) was observed after the drilling.

Table 41.1 Summary of core sampling operations during TAIGA10M cuirse

Drilling site	Date	Device	Position[a]		Water depth[b] (m)	Drilled depth (cm)	Core length (cm)	Core recovery (%)	Casing pipe
			Latitude	Longitude					
Snail site									
TAIGA10-BMS-01	6/15/2010	BMS	12°57.1957′N	143°37.1616′E	2,878.7	477	458	96	Yes
Yamanaka site									
TAIGA10-BMS-04	6/17/2010	BMS	12°56.6515′N	143°36.7749′E	2,843.1	709	435	61	No
Archaean site									
TAIGA10-BMS-02	6/16/2010	BMS	12°56.3696′N	143°37.9599′E	3,073.5	167	92	55	No
TAIGA10-BMS-03	6/16/2010	BMS	12°56.3627′N	143°37.9036′E	3,021.7	330	252	76	No
TAIGA10-BMS-06A	6/19/2010	BMS	12°56.3678′N	143°37.9867′E	3,101.4	112	53	47	No
TAIGA10-BMS-06B	6/19/2010	BMS	12°56.3494′N	143°38.0008′E	3,107.0	243	108	44	No
TAIGA10-BMS-06C	6/19/2010	BMS	12°56.3358′N	143°38.0094′E	3,107.7	138	77	56	No
TAIGA10-BMS-06D	6/19/2010	BMS	12°56.3223′N	143°38.0043′E	3,114.2	205	75	37	No
TAIGA10-BMS-07	6/20/2010	BMS	12°56.3783′N	143°37.9187′E	3,007.6	362	173	48	No
Pika site									
TAIGA10-BMS-05	6/18/2010	BMS	12°55.1271′N	143°38.9919′E	2,820.7	776	356	46	Yes
TAIGA10-BMS-08	6/21/2010	BMS	12°55.1153′N	143°38.9329′E	2,806.1	263	195	74	Yes
TAIGA10-BMS-09	6/21/2010	BMS	12°55.1369′N	143°38.9334′E	2,804.3	425	292	69	No

[a]Position of the drilling site was determined based on GPS data of the ship
[b]Water depth of the drilling site was determined based on MBES data

41.4 Core Description

Descriptions of the 12 cores drilled from the four hydrothermal vent sites are summarized in Fig. 41.3. In this section, we describe petrological characteristics of the 38 core sections from the 12 holes.

41.4.1 Site BMS-01

Core BMS-01-01 section A Basalt to basaltic andesite pillow fragments were recovered in this core section. They are aphyric, angular and have alteration coatings on fracture surfaces. The core pieces have a vitric groundmass and contain vesicles that are elongate and medium to large in size. In the lower part of the core, a second pillow was penetrated. This is also aphyric, with mainly very small vesicles that define trails, suggesting direction of movement of the lava. Larger vesicles are lined with alteration rims of dark reddish brown.

Core BMS-01-01 section B Basalt to basaltic andesite pillow interiors (no glass margins in this section) were recovered. The rock in this section is also aphyric, with very small vesicles, similar to the previous section. There are many vesicle trails throughout the section. In the upper part of this section, fracture surfaces are coated with yellow and gray alteration products (maybe clay minerals). In the lower part, the alteration on fracture surfaces is mainly gray and/or yellowish, but also contains streaks of orange/red/brown.

Core BMS-01-02 section A Basalt to basaltic andesite pillow lava pieces were recovered. The rock is aphyric, with very small vesicles, similar to the previous section. Many vesicle trails are also observed throughout the section. Larger vesicles have a thin lining of a gray alteration product, and the fracture surface has a yellow/orange alteration coating.

Core BMS-01-02 section B Basalt to basaltic andesite pillow interior was recovered. The rock is aphyric, with very small vesicles, similar to the previous section, but occasional large vesicles also occur. In the upper part of this section, there is a yellow and gray alteration coating on fracture surfaces with some brown alteration. In the lower part of this section, fracture surfaces have gray alteration with some streaks of brown and some scattered patches of yellow.

Core BMS-01-02 section C Basalt to basaltic andesite pillow interior was recovered. The rock is aphyric, with very small vesicles, similar to the previous section, but has occasional large vesicles, which increase in number downsection. Some pieces in the middle part of the section are likely the glassy margin of a large pillow. Vesicle trails lie at a high angle to the core. Fracture surfaces are coated with yellow and gray alteration products.

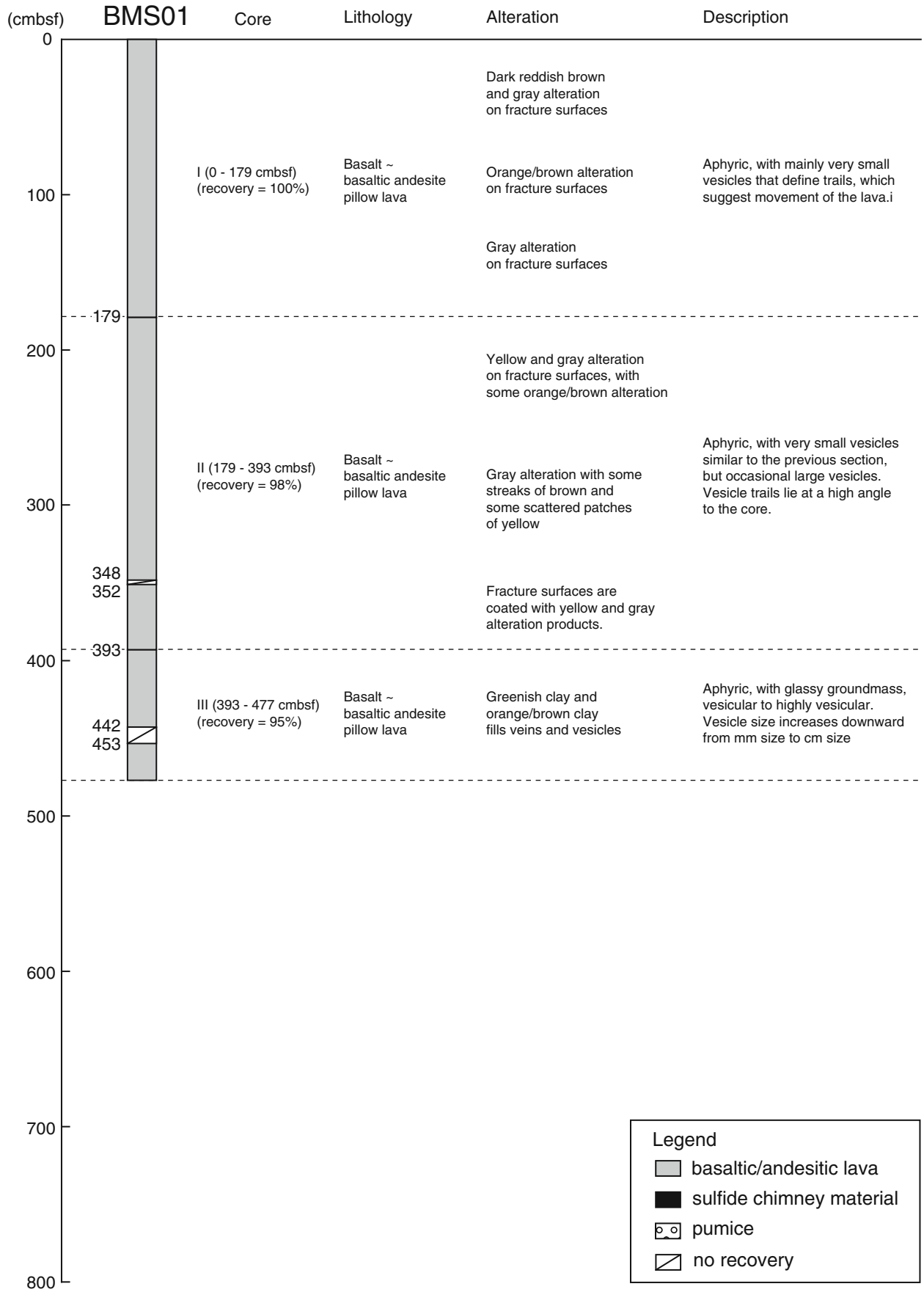

Fig. 41.3 Visual core description for BMS cores drilled from 12 sites at the Snail, Yamanaka, Archaean, and Pika hydrothermal vent sites

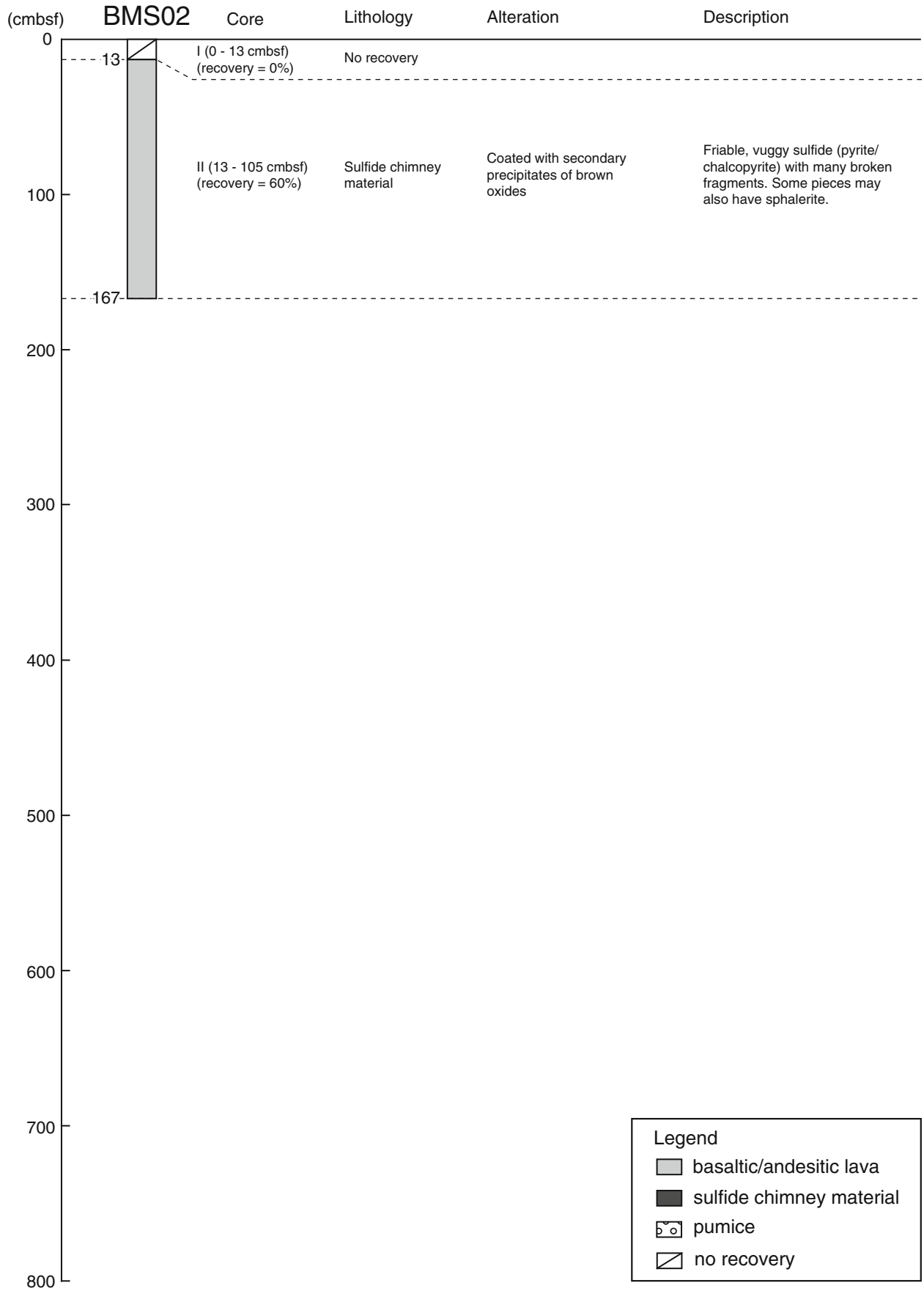

Fig. 41.3 (continued)

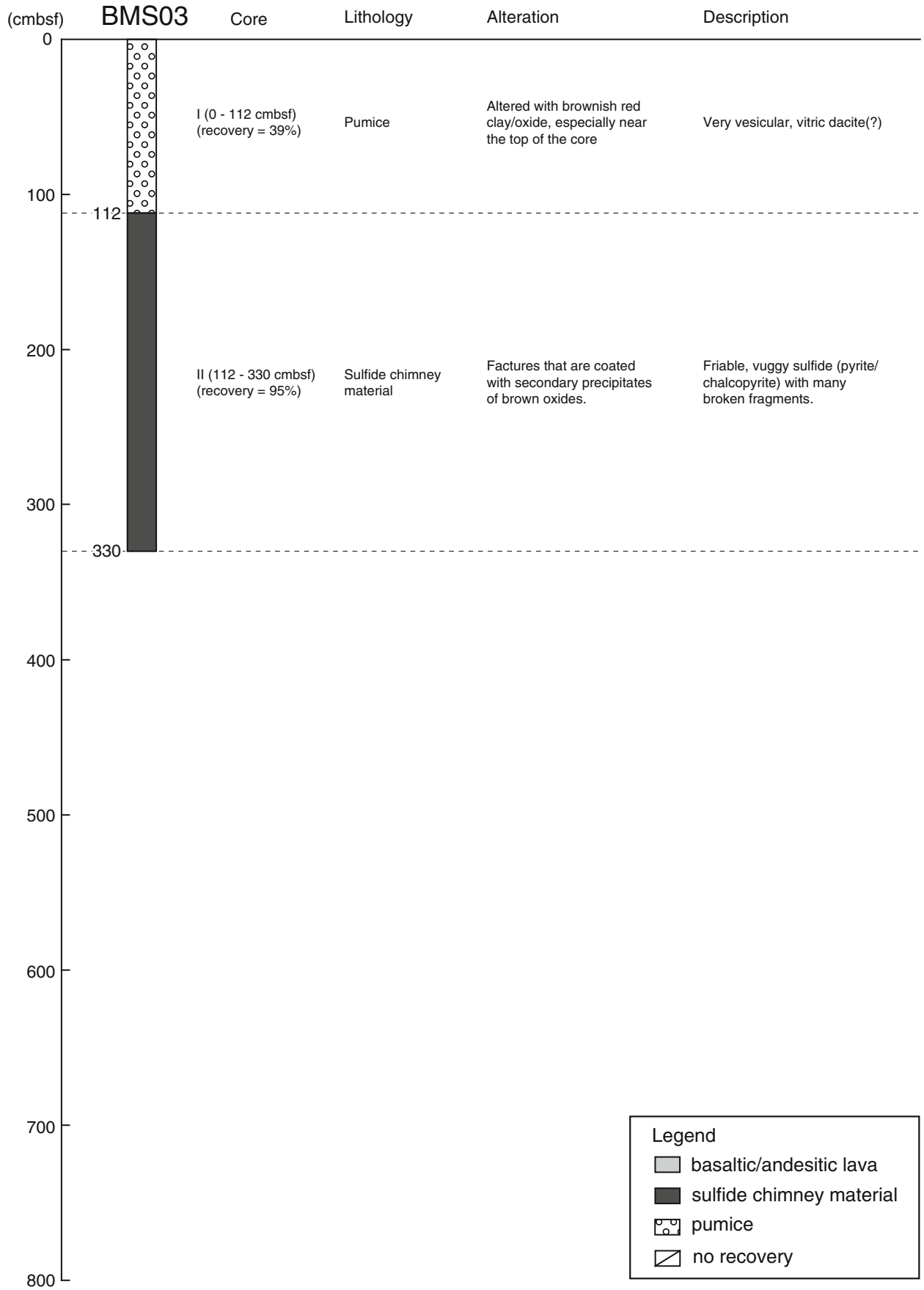

Fig. 41.3 (continued)

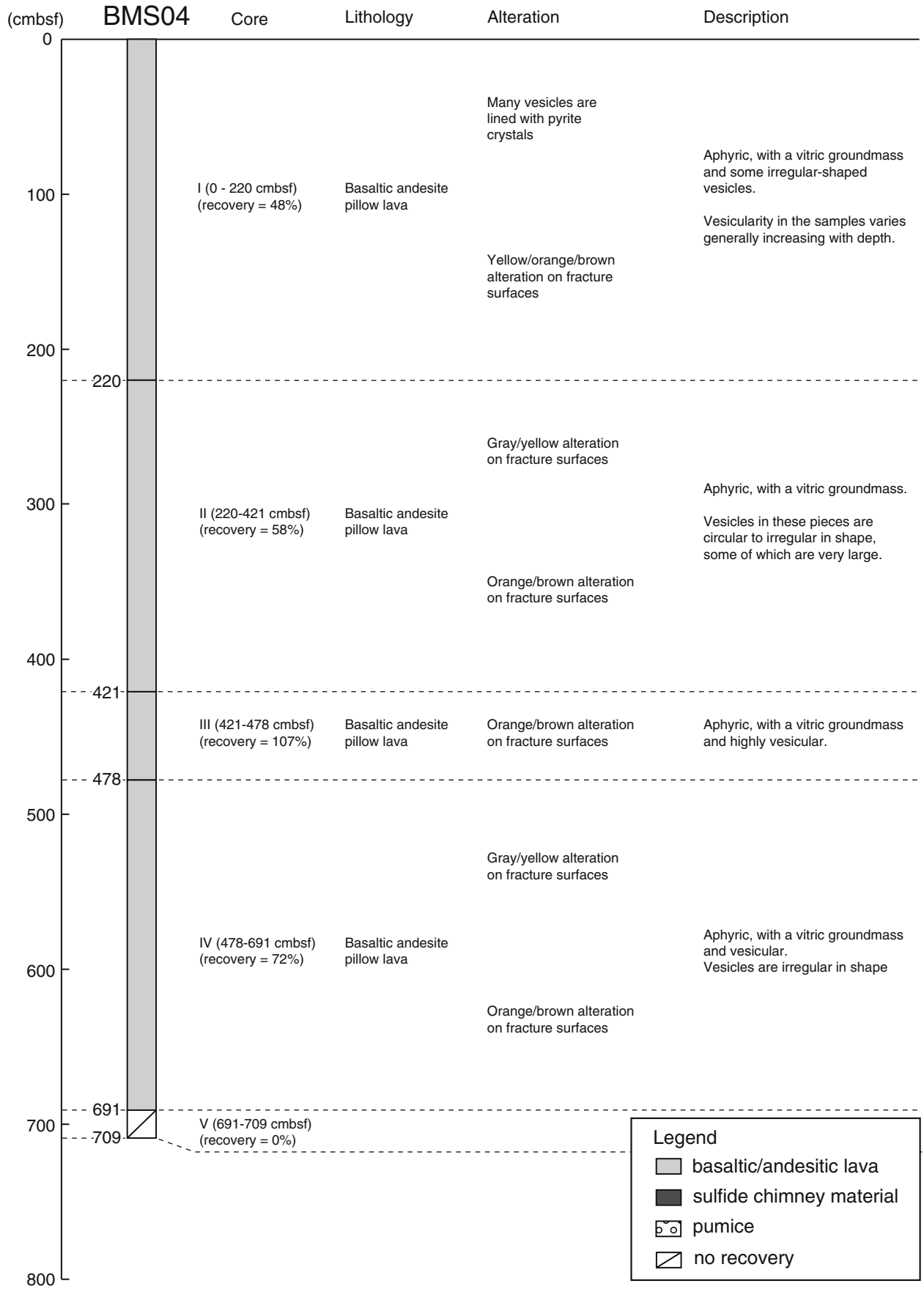

Fig. 41.3 (continued)

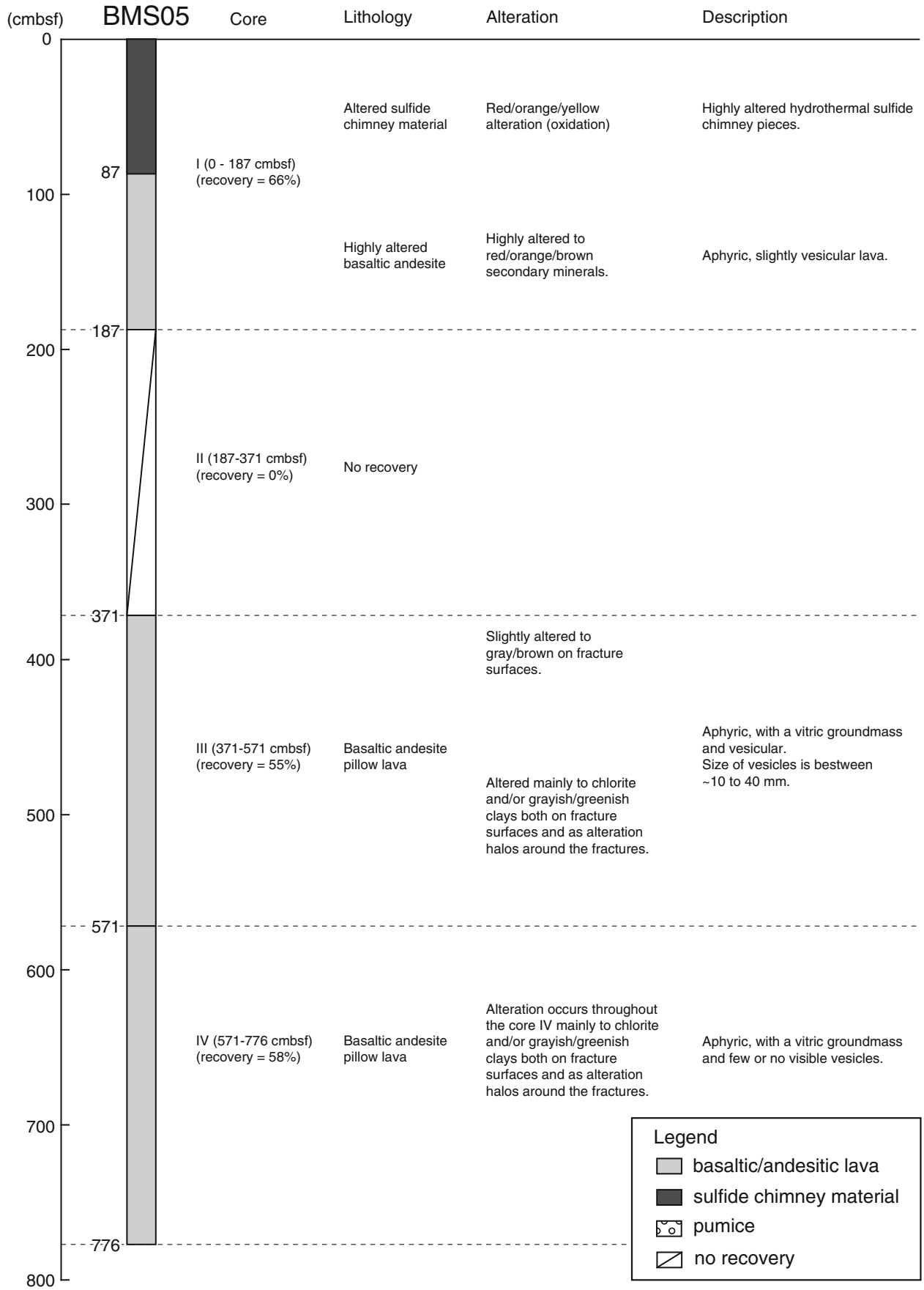

Fig. 41.3 (continued)

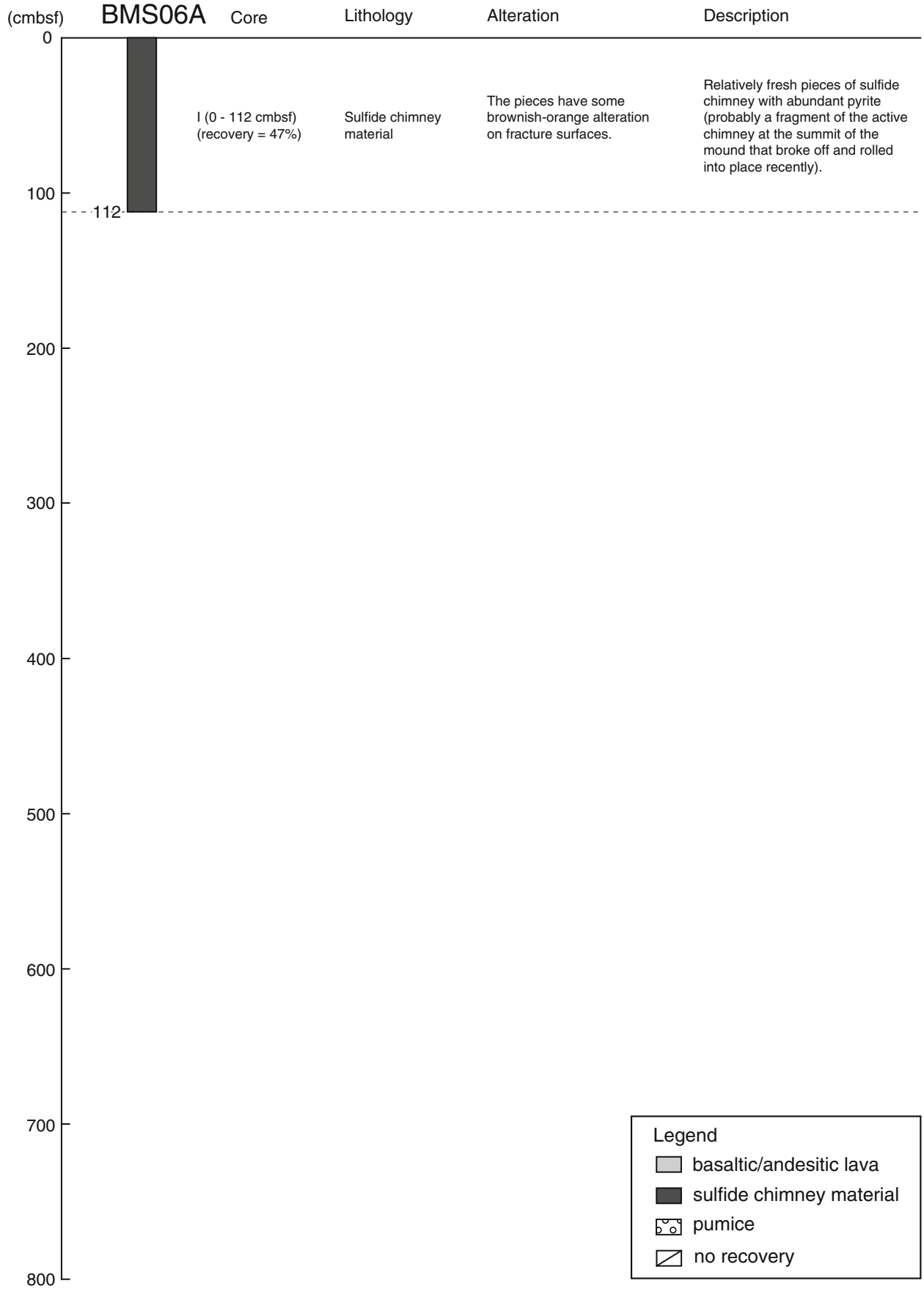

Fig. 41.3 (continued)

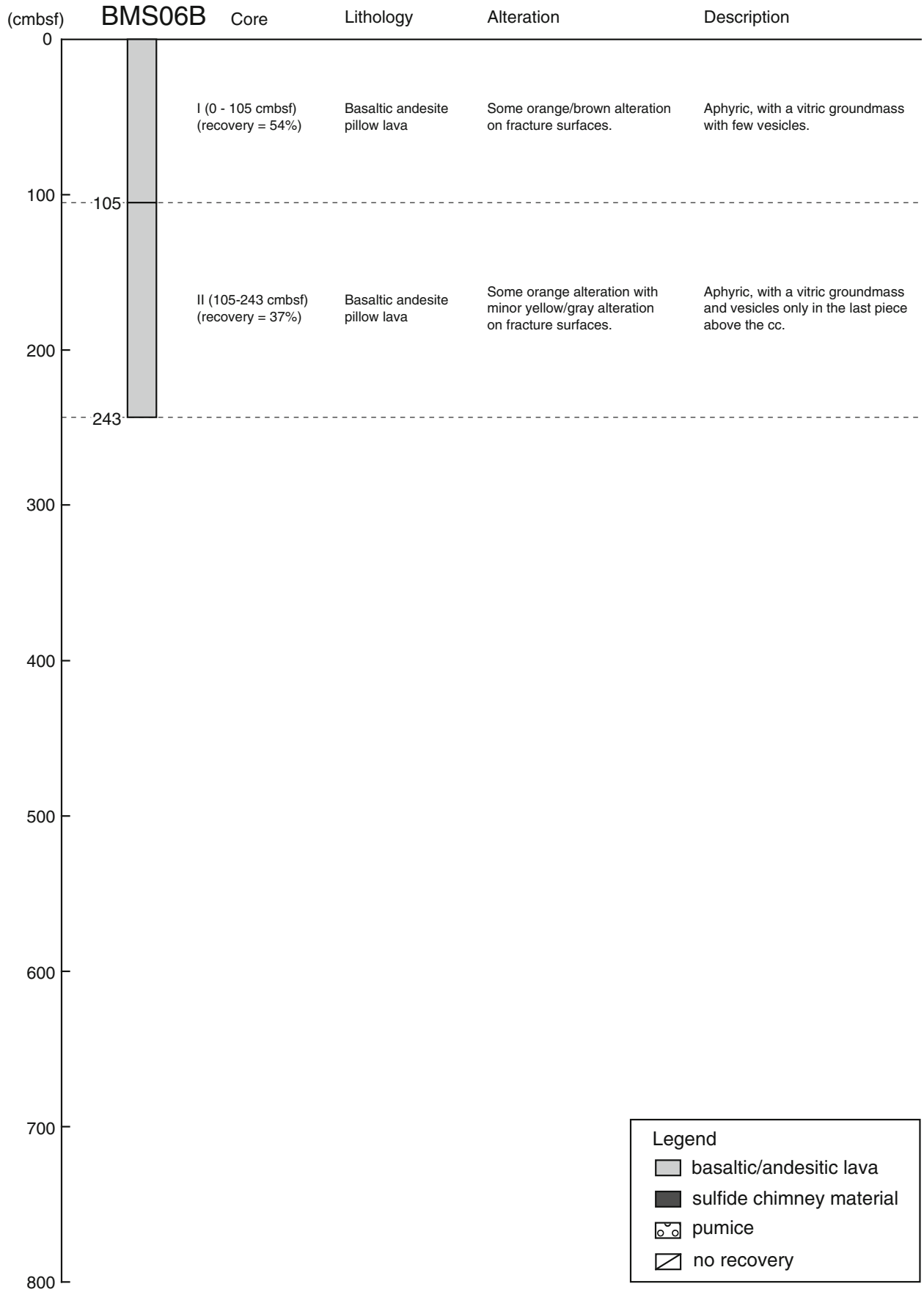

Fig. 41.3 (continued)

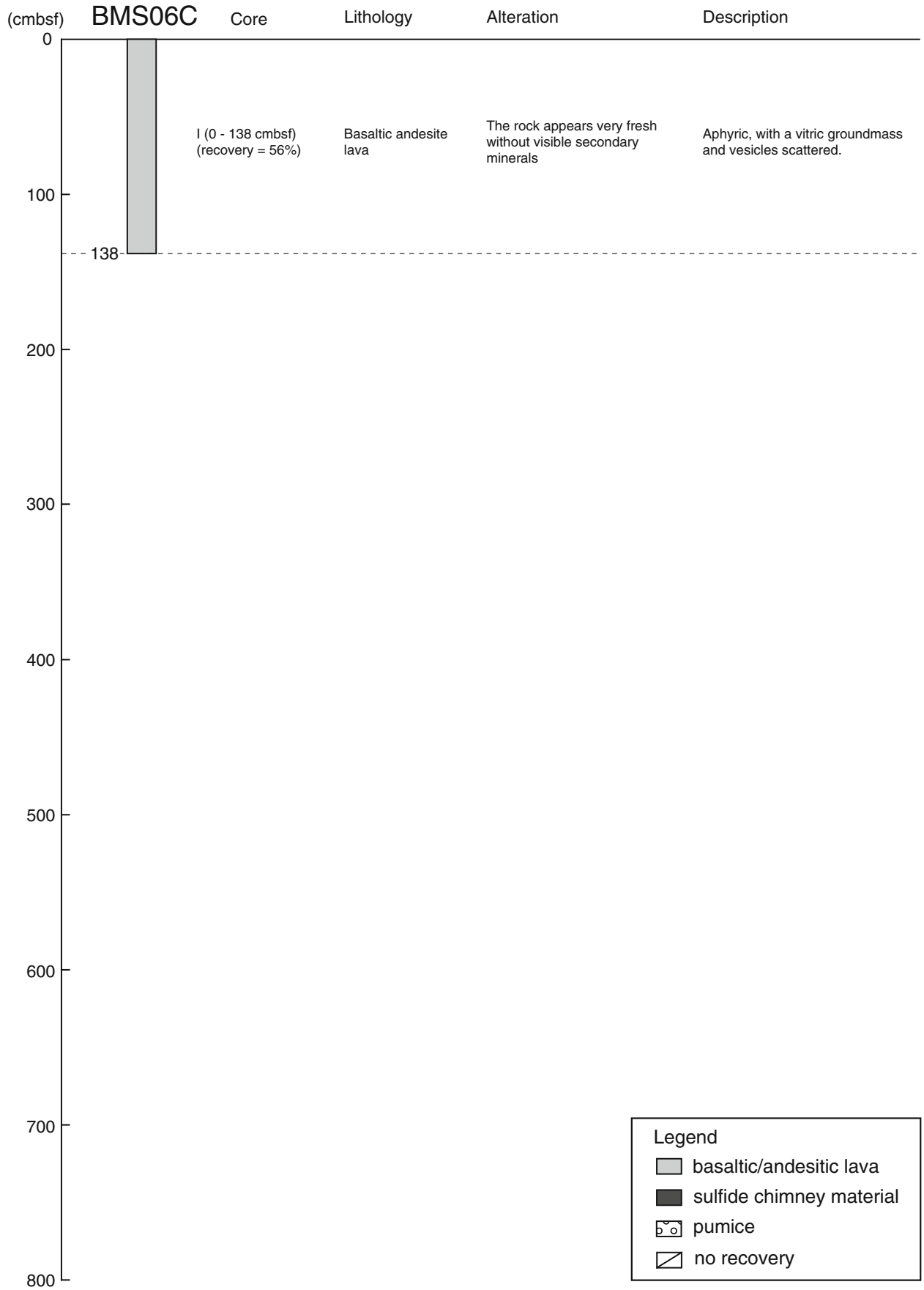

Fig. 41.3 (continued)

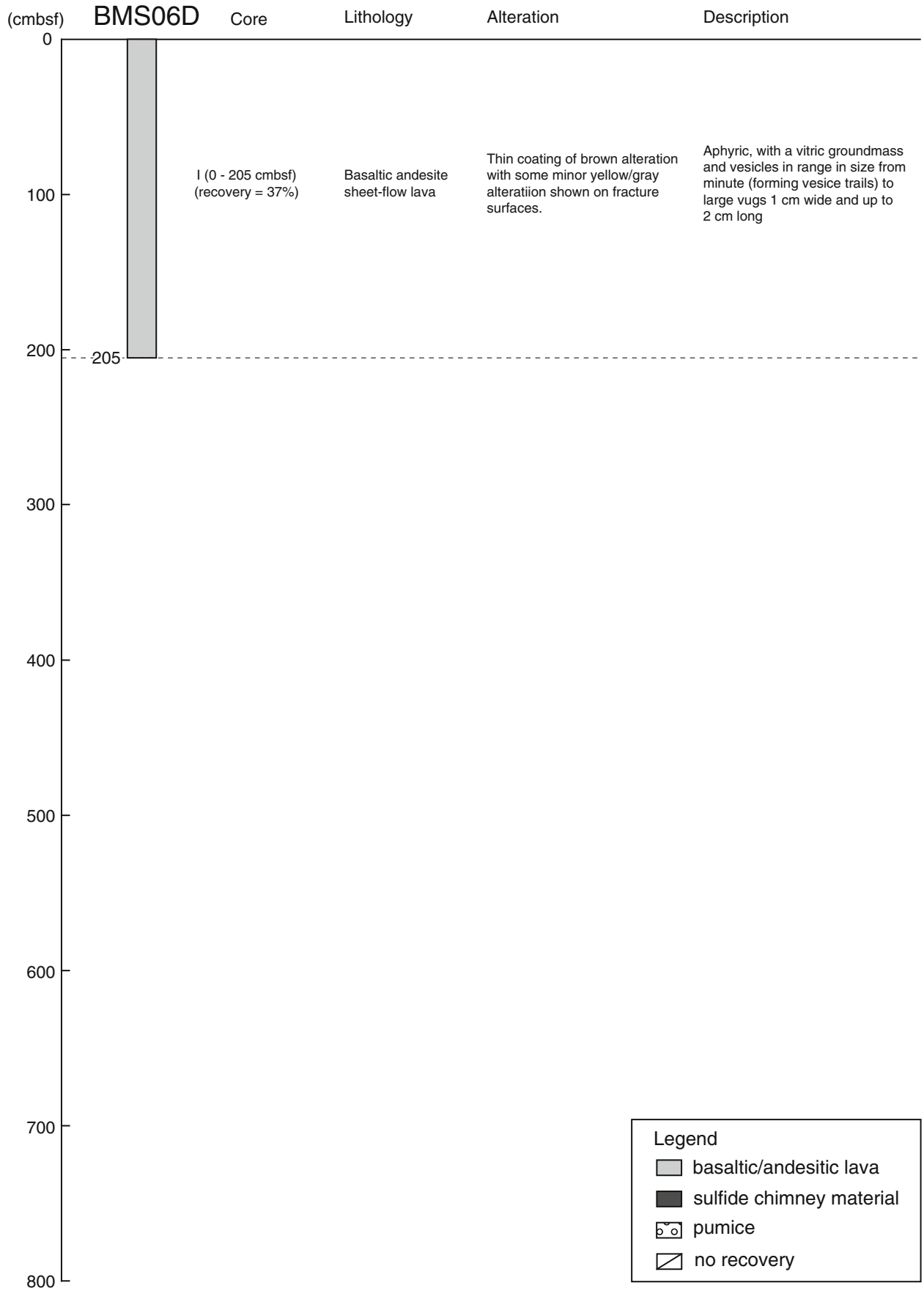

Fig. 41.3 (continued)

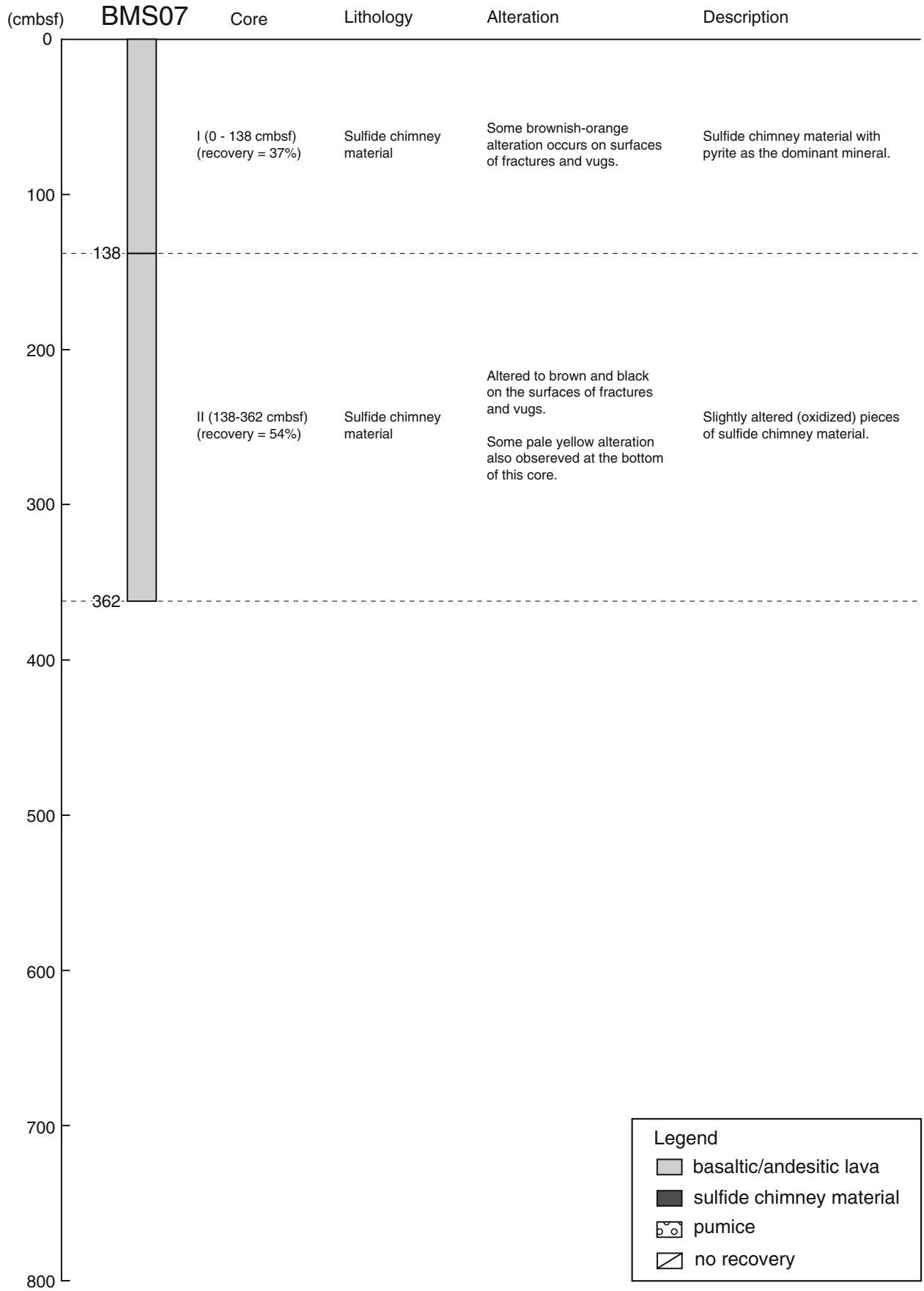

Fig. 41.3 (continued)

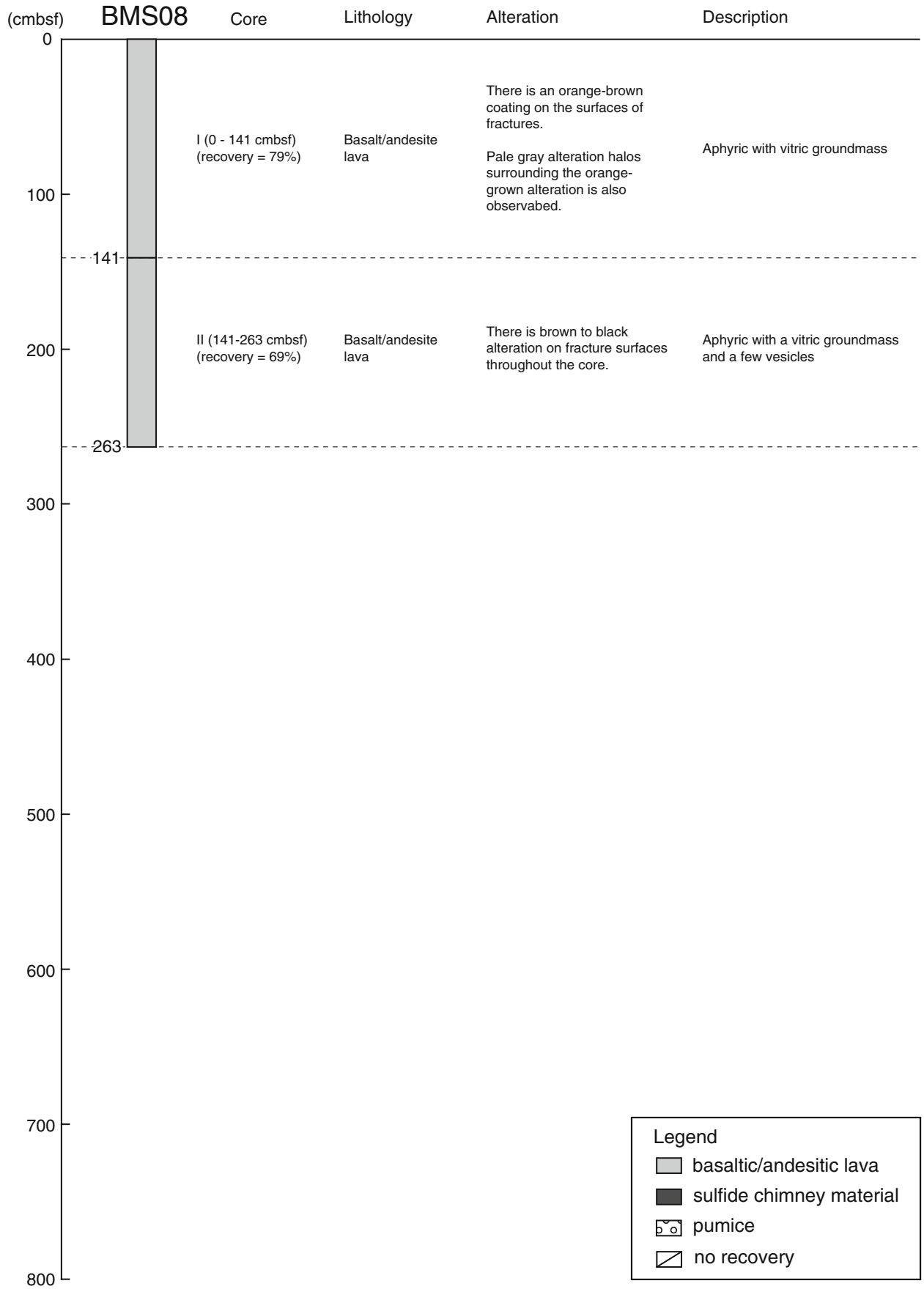

Fig. 41.3 (continued)

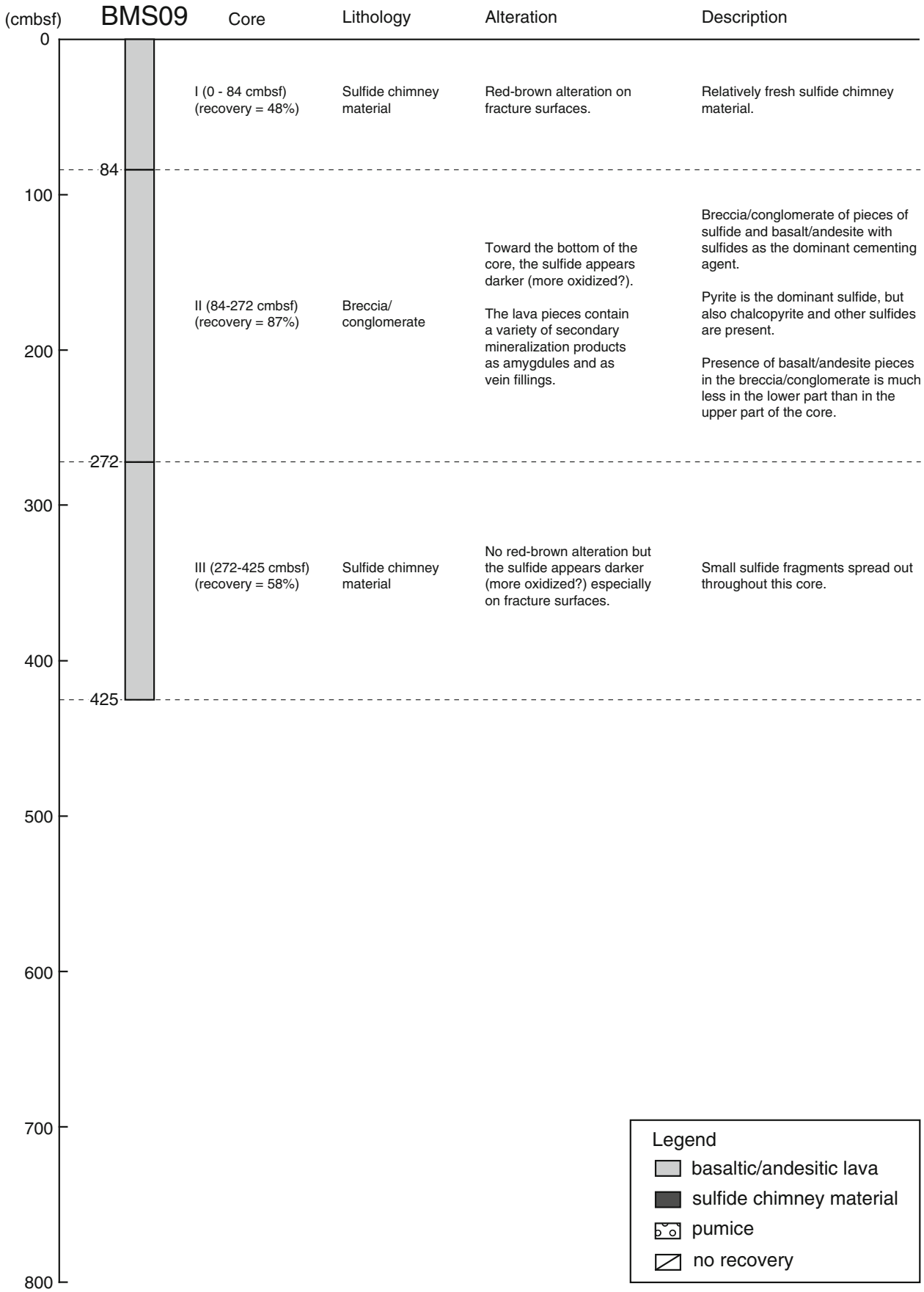

Fig. 41.3 (continued)

Core BMS-01-03 section A Basalt to basaltic andesite pillow lava pieces were recovered. The rock is aphyric, with glassy groundmass and is vesicular. Vesicle size increases downward from mm-size to cm-size. The vesicles are lined with yellowish and orange-brown clay (?) minerals with/without goethite, and greenish clay and/or orange-brown clay fill veins.

41.4.2 Site BMS-02

Core BMS-02-01 No sample was recovered in this core.

Core BMS-02-02 This core comprises sulfide chimney material, a friable and vuggy sulfide precipitate mass (pyrite/chalcopyrite) with many broken fragments. Some pieces in the core were recovered intact, but most have fractures that are coated with secondary precipitates of brown clays (?) or oxides. In the lower part of the section, some pieces may have sphalerite in addition to pyrite/chalcopyrite.

41.4.3 Site BMS-03

Core BMS-03-01 Several pieces of pumice were recovered. The rocks are very vesicular with vitric groundmass, and are likely dacitic in composition and altered (especially near the top of the core) with brownish red clay/oxide.

Core BMS-03-02 section A Only a few small fragments of sulfide chimney material were recovered. Those are friable and vuggy, composed mainly of pyrite and chalcopyrite.

Core BMS-03-02 section B Sulfide chimney material, which is friable, vuggy and composed mainly of pyrite/chalcopyrite, was recovered. Some pieces are very long (up to ~35 cm long), but also there are many broken fragments in the core. Several pieces in core that were recovered intact also have fractures that are coated with secondary precipitates of brown clays(?) or oxides.

Core BMS-03-02 section C Sulfide chimney material similar to that recovered in the previous section was recovered in this section. Some fragments are broken. Fracture surfaces on the core do have some alteration products.

41.4.4 Site BMS-04

Core BMS-04-01 Basalt to andesite pillow lava pieces were recovered in this section. The rocks are aphyric with a vitric groundmass, containing vesicles that have linings that contain tiny pyrite crystals. The rocks are particularly glassy at the top of the section. The vesicularity in the samples varies with depth in the section, larger round vesicles occur at the middle part and irregular vesicles occur at the lower part of the section. Alteration varies in color down-section. There is a gray lining to a vesicle and a fracture coating of yellow to brown in the upper part of the section. At the lower part, the coatings are orange/brown. A yellow to orange/brown alteration occurs at the bottom of the section.

Core BMS-04-02 section A Basalt to andesite pillow lava was recovered. The rock is aphyric, with a vitric groundmass and is vesicular throughout. Vesicles in these pieces are circular to irregular in shape and some of them are very large. Glassy pieces occur in the rubble at the top of the section. Alteration on fracture surfaces is gray/yellow.

Core BMS-04-02 section B Basalt to andesite pillow lava pieces were recovered. The rocks are aphyric, with a vitric groundmass. Vesicles are sparse at the upper and middle parts of the section, whereas at the lower part the rock is much more vesicular. This vesicularity change suggests two pillows were penetrated. Fracture surfaces at the upper and middle part of the section are altered to gray/brown, whereas those in the lower part have generally orange/brown alteration coating.

Core BMS-04-03 This core comprises basalt to andesite pillow lava, which is aphyric with a vitric groundmass and highly vesicular. The small pieces at the top of the section are glassy and probably represent the margin of a pillow. Alteration on fracture surfaces is mainly orange, and vesicles show yellow/orange or gray/yellow alteration.

Core BMS-04-04 section A Basalt to andesite pillow lava was recovered. The rock is aphyric, with a vitric groundmass, and is vesicular. Vesicles in these pieces are irregular in shape. There is glass in the rubble at the top of the section. Alteration on fracture surfaces is gray/yellow or orange.

Core BMS-04-04 section B Basalt to andesite pillow lava was recovered. The rock is aphyric, with a vitric groundmass and vesicles that are scattered and increase in number down-section. Compared to the upper part of the section, there are more vesicles and they are more irregular in shape in the lower part, suggesting that two pillows were penetrated. Glass margins are observed on some pieces. In the upper part, alteration is orange or orange/brown. On the other hand, in the lower part, fracture surfaces have a brown or gray coating.

41.4.5 Site BMS-05

Core BMS-05-01 section A Sulfide chimney material, which was highly altered to black/brown oxide, was recovered.

Core BMS-05-01 section B Highly oxidized sulfide chimney material and basalt to andesite pillow were recovered. The chimney material is highly altered with red/orange/yellow/black contorted precipitates. In addition to the strong oxidation, this may also have undergone silicification. In the lower part of the core, there are two pieces of highly altered (oxidized) basalt to andesite pillow lava. The rock is aphyric, slightly vesicular lava that has been altered to red/orange/brown alteration products.

Core BMS-05-02 No sample was recovered in this core.

Core BMS-05-03 section A Basalt to andesite pillow lava, which is aphyric with a vitric groundmass and vesicular, was recovered. There is a glass margin on the top pieces of this section. Also some red/brown fragments (likely from the section above) occur among the top few pieces of the section. In contrast to the above sections, only some alteration to gray-brown on fracture surfaces is observed in this section.

Core BMS-05-03 section B Basalt to andesite pillow lava was recovered. The rock is aphyric, with a vitric groundmass and has few vesicles at the upper part of the section. Alteration occurs throughout the section, mainly to chlorite and/or greenish clays, both on fracture surfaces and as alteration halos around the fractures. A coating of chlorite is observed in some pieces.

Core BMS-05-04 section A Basalt to andesite pillow lava was recovered. The rock is aphyric, with a vitric groundmass and few vesicles. Alteration similar to the previous section occurs throughout the section. Some pieces have thick alteration halos (~1 cm thick) extending from the fracture surface.

Core BMS-05-04 section B Basalt to andesite pillow lava that is aphyric, with a vitric groundmass and few or no visible vesicles, was recovered. Vesicules occurs only at the lowermost part of the section. A glass margin occurs at the upper part of the section and there are a few small glass fragments in the lower part. The glass intervals suggest two to three pillows were penetrated. Alteration occurs throughout the section mainly to chlorite and/or greenish clays, both on fracture faces and as alteration halos around the fractures.

41.4.6 Site BMS-06A

Core BMS-06A Relatively fresh pieces of sulfide chimney with abundant pyrite (probably a fragment of the active chimney at the summit of the mound that broke off and rolled into place recently) were recovered. The pieces have vugs of various sizes. Some brownish-orange alteration coatings are observed on fracture surfaces.

41.4.7 Site BMS-06B

Core BMS-06B-01 Basaltic andesite pillow lava was recovered. The rock is aphyric, with a vitric groundmass and few vesicles. Some orange/brown alteration occurs especially at the middle part of the section.

Core BMS-06B-02 Basaltic andesite pillow lava, which is aphyric, with a vitric groundmass and vesicles, was recovered. There are glass fragments in the top part of the section and a ~1 cm thick glass margin on top of the top piece of this section. There is some orange alteration coatings (with some minor yellow and gray) on fracture surfaces of the pieces only at the lower part of the section.

41.4.8 Site BMS-06C

Core BMS-06C Basaltic andesite pillow lava was recovered. The rock is aphyric, with a vitric groundmass. A rubble of small fragmets from the top of the section is very glassy. Vesicles are scattered, but are especially common in the middle part of the section. This more vesicular rock contains vertical trails of tiny vesicles. The rock appears very fresh, containing no visible secondary minerals.

41.4.9 Site BMS-06D

Core BMS-06D Basaltic andesite sheet-flow lava was recovered. The rock is aphyric, with a vitric groundmass and vesicles that range in size from minute (forming vesicle trails) to large vugs, 1 cm wide and up to 2 cm long. Some pieces from middle and bottom part of the section have vesicle trails at a high angle to the core and some elongate vesicles on the same trend. There is some minor yellow and gray alteration on the pieces from middle part, and the bottom piece has a thin coating of brown alteration.

41.4.10 Site BMS-07

Core BMS-07-01 Sulfide chimney material with pyrite as the dominant mineral was recovered. The samples are relatively fresh, although most of the pieces appear somewhat oxidized. Vugs occur throughout and some brownish-orange alteration occurs on the upper surface of the last piece in the section.

Core BMS-07-02 section A Altered (oxidized) pieces of sulfide chimney material were recovered. Alterations to brown and black on the upper surface of the first piece and to brown/orange on the upper surface of the second piece were observed.

Core BMS-07-02 section B Altered (oxidized) pieces of sulfide chimney material, similar to those in the previous section, were recovered. There is a brown alteration surface on of some of the small pieces at the top of the section and black/orange coating on the bottom surface of the piece at middle part of the section. An orange alteration surface occurs on the pieces from lower part of the section.

41.4.11 Site BMS-08

Core BMS-08-01 Basalt to andesite lava, which is aphyric with vitric groundmass, was recovered. Alteration to orange-brown mineralization is observed throughout the section.

Core BMS-08-02 Basalt to andesite lava was recovered. The rock is aphyric with a vitric groundmass. A few vesicles occur at the upper part of the section. Much larger vesicles occur in the piece from middle to lower part. Alteration to brown mineralization affects the top two pieces in the section. There is also an orange-brown coating on the surface of the piece from the lower part of the section and a brown alteration coating on the top and bottom of the last piece in the section. Pale gray alteration halos surrounding the brown alteration were also observed on this last piece.

Core BMS-08-03 Basalt to andesite lava was recovered. The rock is aphyric with a vitric groundmass and a few vesicles especially in the middle part of the section. There is brown to black alteration on pieces throughout the section. There is also orange-brown mineralization that occurs in distinct layers in the last piece in the section.

41.4.12 Site BMS-09

Core BMS-09-01 Sulfide chimney material was recovered. Red-brown alteration on fracture surfaces is observed especially on the last three large pieces in the section.

Core BMS-09-02 section A Breccia/conglomerate of pieces of sulfide mixed with basalt/andesite were recovered . Sulfides form the dominant cementing agent. The lava pieces, cemented by sulfide, contain a variety of secondary mineralization products as amygdules and as vein fillings. Pyrite is the dominant sulfide, but chalcopyrite and other sulfides are also present.

Core BMS-09-02 section B Sulfide chimney material and breccia/conglomerate of pieces of sulfide chimney material with much less basalt/andesite in them were recovered. As in the previous section, the dominant sulfide is pyrite. Toward the bottom of the section, the sulfide appears darker, suggestive of more oxidizing.

Core BMS-09-03 Small fragments of sulfide chimney materials were recovered. The pieces are similar to the previous section.

41.5 Bulk-Rock Geochemistry

41.5.1 Analytical Procedures

A total of 28 samples (17 BMS core samples and 11 surface samples) from the Snail, Yamanaka, Archaean, and Pika hydrothermal sites were analyzed. Sampling positions of the surface samples are summarized in Table 41.2. Major element analyses for all the samples were carried out by X-ray fluorescence techniques (XRF) at Senshu University in Japan or by inductively coupled plasma mass spectrometry with alkali fusion digestion (FS-ICPMS) at Actilabs in Canada. Trace elements were analyzed for 11 BMS samples by FS-ICPMS at Actilabs in Canada. For XRF analysis, compositions were determined using glass beads fused in a gold-platinum crucible at 1,150 °C. The glass beads were made from ignited sample powders mixed well with $Li_2B_4O_7$ flux in a 1:5 proportion following the method described by Sato (2010).

41.5.2 Major and Trace Element Characteristics of the Rock Samples

Bulk-rock major and trace element data for the drill core samples recovered by BMS, together with the surface samples collected using the manned submersible *SHINKAI6500* and ROV *ROPOS*, are given in Suppl. 41.1. In this section, we focus on chemical characteristics of basement rocks rather than sulfide ores. Petrological and geochemical features of the sulfide ore samples

Table 41.2 List of surface rock samples used in this study

Sample ID	Date	Position		Water depth
		Latitude	Longitude	
Snail site				
6K1227R02	9/13/2010	12°57.1089′N	143°37.0889′E	2,848
6K904R3[a]	8/2/2005	12°57.1980′N	143°37.0980′E	2,852
Yamanaka site				
6K1227R06	9/13/2010	12°56.7686′N	143°36.6955′E	2,849
R774-0004[b]	3/20/2004	12°57.021′N	143°37.059′E	2,861
R774-0006[b]	3/25/2004	12°53.6376′N	143°36.7962′E	2,828
R779-0002[b]	3/25/2004	12°56.660′N	143°36.789′E	2,827
Archaean site				
6K1221R02	9/5/2010	12°56.2201′N	143°37.8993′E	3,082
6K1223R01	9/7/2010	12°56.3575′N	143°37.7758′E	3,050
6K1224R01	9/9/2010	12°56.4677′N	143°38.0250′E	3,059
Pika site				
6K1222R04-01	9/6/2010	12°55.2007′N	143°38.7425′E	2,876
6K1226R01	9/12/2010	12°55.2962′N	143°39.0282′E	2,917

[a]Samples were collected by SHINKAI6500 during YK05-09 cruise conducted in September, 2005 by Yokosuka
[b]Samples were collected by ROV ROPOS during TN167A cruise conducted in March, 2004 by R/V Thomas G. Thompson
Other samples were collected by SHINKAI6500 during YK10-11 cruise conducted in September, 2010 by Yokosuka

recovered by BMS are described in elsewhere in this book (Ishibashi et al., Chap. 23).

On the total alkalis vs. silica diagram (Fig. 41.4a), most of the on-axis samples from the Snail and Yamanaka sites plot within the basaltic andesite field, whereas all off-axis samples from the Archaean, and Pika sites have higher silica abundances, falling within the field of andesite. In the silica vs. K_2O diagram (Fig. 41.4b), all the samples lie between the low-K tholeiite field and medium-K calc-alkaline field, showing that these samples are relatively depleted in alkali elements.

Multi-element diagrams normalized to N-MORB display noticeable enrichment of fluid-mobile elements such as Cs, Rb, Ba, U, and K with remarkable negative Nb and Ta anomaly (Fig. 41.5). This clearly suggests significant introduction of a subduction component into their parent magmas, which is consistent with the results of Pearce et al. (2005). Elemental abundances are relatively high in off-axis samples, compared with on-axis samples. This reflects the more evolved features (high concentrations of Si and alkali elements) of off-axis samples shown in major element compositions (Fig. 41.4a). In chondrite-normalized REE patterns, off-axis samples exhibit relatively higher REE abundances with minor negative Eu anomalies, compared with on-axis samples (Fig. 41.6). This also suggests that the off-axis lavas are more evolved with crystal fractionation of plagioclase.

In Fig. 41.7, major element versus MgO variation diagrams are shown for the drill core and surface samples, together with volcanic rocks sampled from the other regions of SMT (Masuda and Fryer, Chap. 21). Most of the elements show positive or negative correlation with MgO contents, which can be related to general fractionation trends of volcanic rocks in the SMT (Fig. 41.7). More precisely, the on-axis samples (Snail and Yamanaka) and the Archaean samples seem to lie on a straight line. On the other hand, the Pika samples clearly show departure from the line (Fig. 41.8). The trace element data also show essentially the same tendency (Fig. 41.9), although the number of samples plotted in the minor element versus MgO variation diagrams is significantly smaller than those in the major element diagrams (Figs. 41.7 and 41.8). This result suggests the difference in magmatism between the Pika site and the other three sites. This leads us to consider that the basement rocks of the Archaean hydrothermal site are a differentiated product of on-axis magma, whereas those of the Pika hydrothermal site are not directly related to the on-axis magma (might be related to off-axis magmatism). This interpretation of rock chemistry is generally consistent with geographical features of the two off-axis hydrothermal vent sites; the Archaean site hosted by small seamounts at the foot of the spreading axis whereas the Pika site situated on a relatively large off-axis seamount (Fig. 41.2).

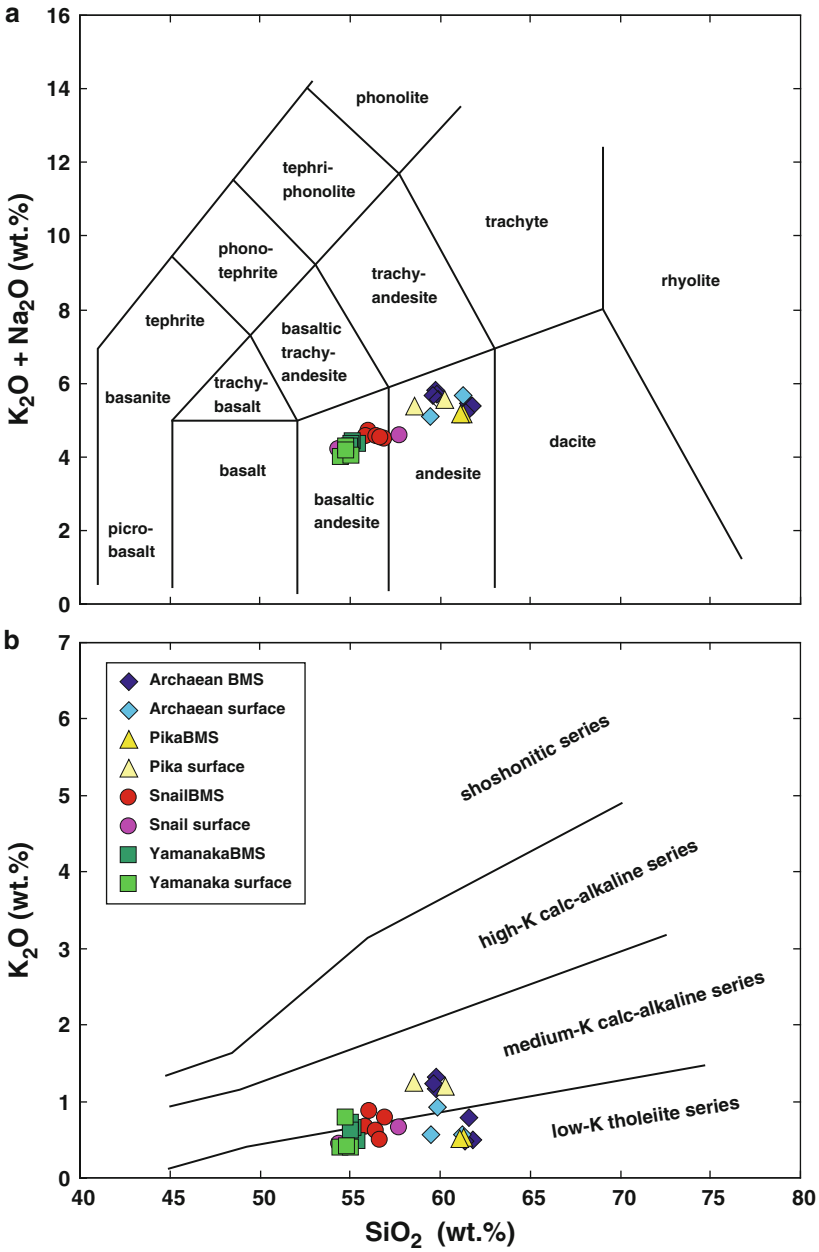

Fig. 41.4 Silica versus (**a**) total alkali and (**b**) K_2O diagrams with fields after Le Maitre et al. (1989) and Rickwood (1989), respectively, illustrating the major element composition of BMS core and surface samples from the Snail, Yamanaka, Archaean, and Pika hydrothermal vent sites

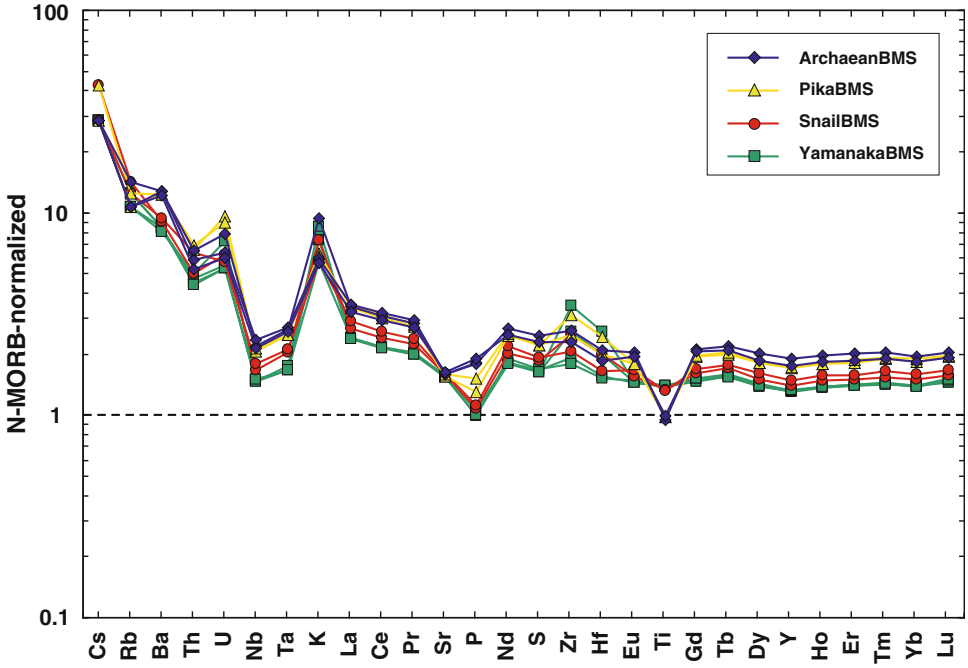

Fig. 41.5 N-MORB-normalized trace element patterns for BMS core samples from the Snail, Yamanaka, Archaean, and Pika hydrothermal vent sites. Normalizing values are after Sun and McDonough (1989)

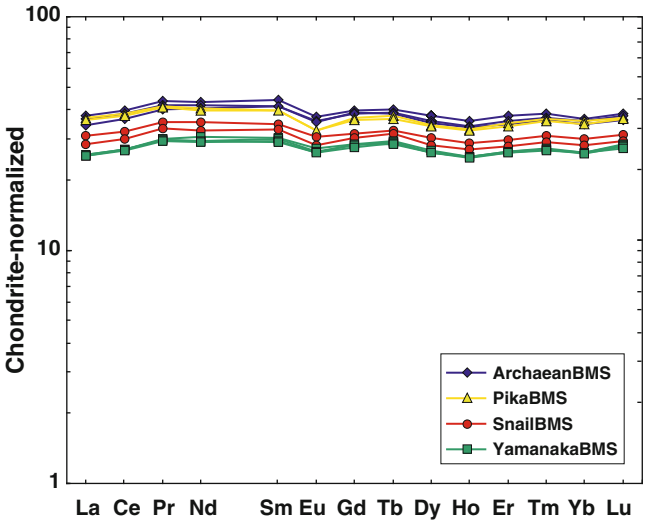

Fig. 41.6 Chondrite-normalized rare-earth element patterns for BMS core samples from the Snail, Yamanaka, Archaean, and Pika hydrothermal vent sites. Normalizing chondrite values are after Anders and Grevesse (1989)

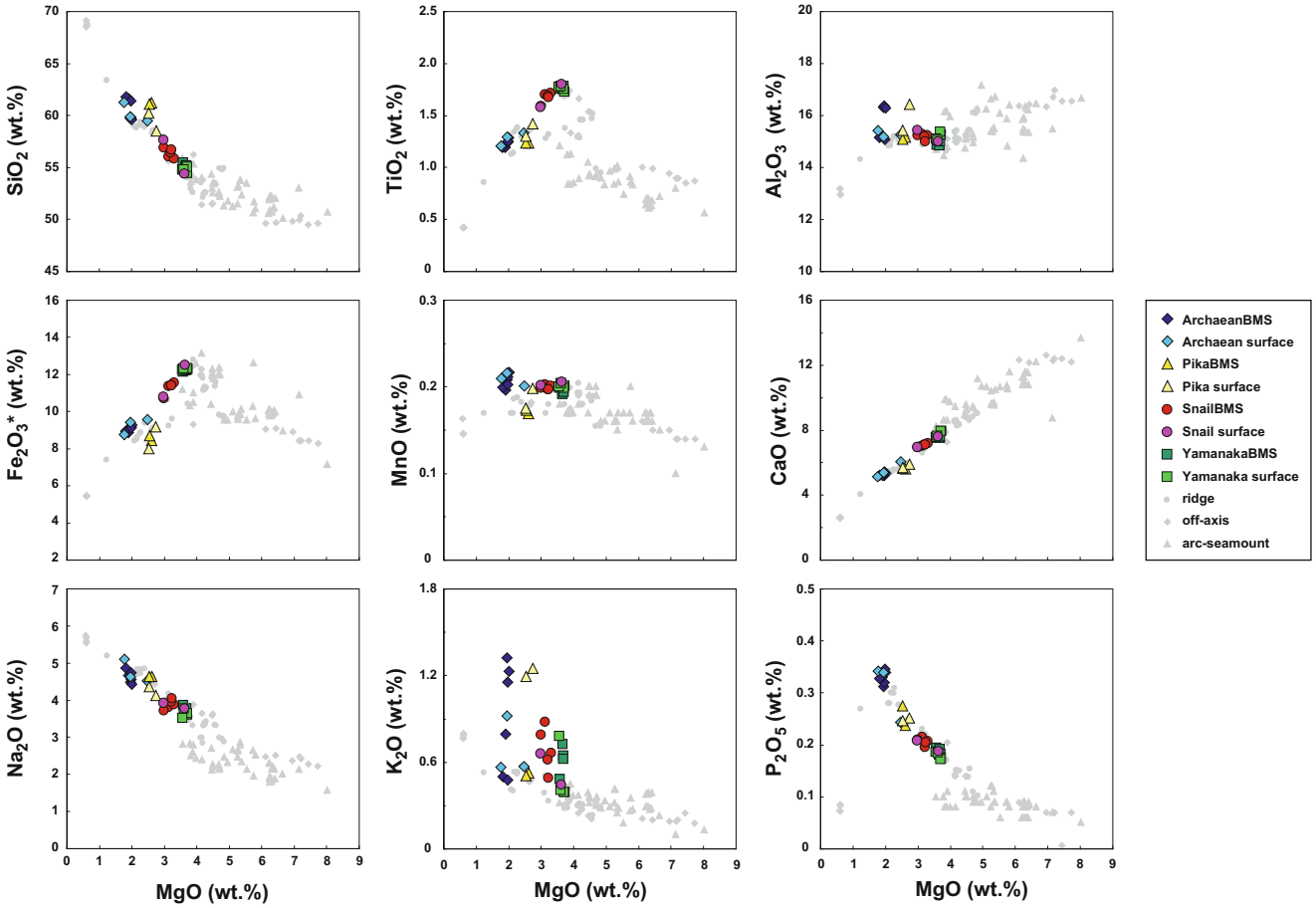

Fig. 41.7 Variation diagrams of major elements vs MgO for BMS core and surface samples from the Snail, Yamanaka, Archaean, and Pika hydrothermal vent sites. Surface samples from ridge axis, off-axis region, and arc-seamounts reported in Masuda and Fryer, Chap. 21 are also shown for comparison

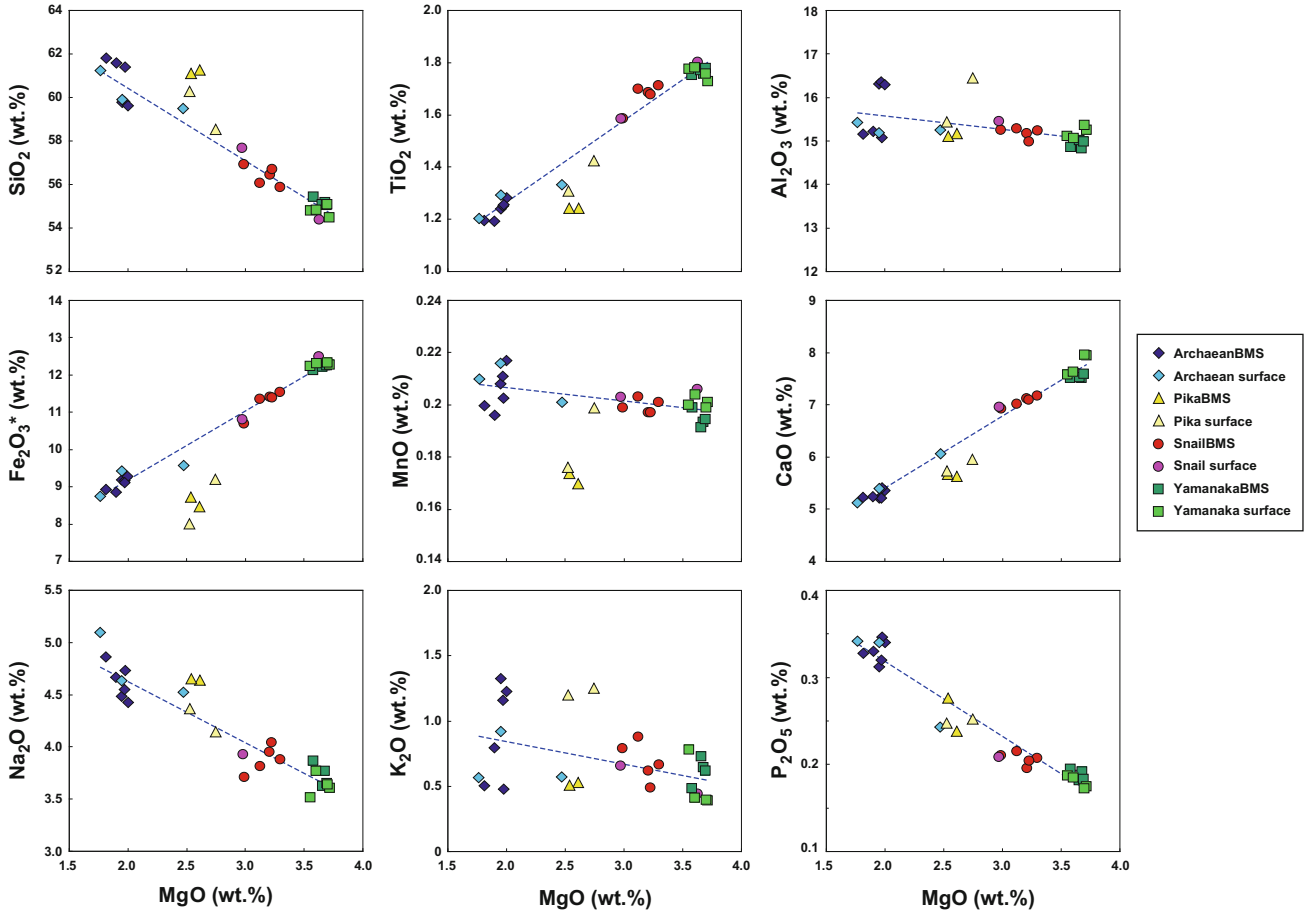

Fig. 41.8 Variation diagrams of major elements vs MgO for BMS core and surface samples from the Snail, Yamanaka, Archaean, and Pika hydrothermal vent sites. *Dotted lines* represent regression lines for Archaean, Snail, and Yamanaka data

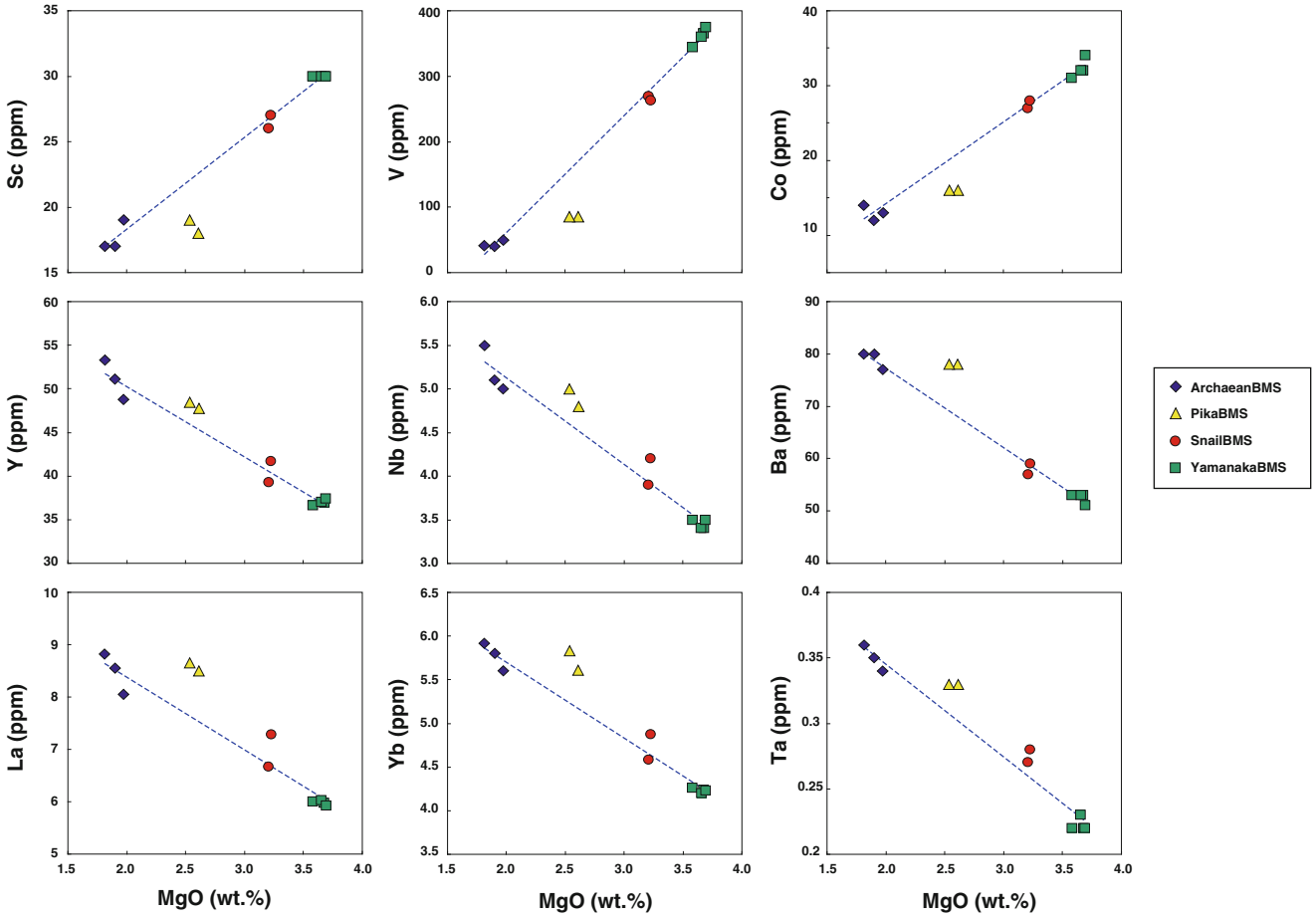

Fig. 41.9 Variation diagrams of minor elements vs MgO for BMS core samples from the Snail, Yamanaka, Archaean, and Pika hydrothermal vent sites. *Dotted lines* represent regression lines for Archaean, Snail, and Yamanaka data

Acknowledgments We thank the BMS operation team led by Mr. Tokuro Kobayashi for the perfect and marvelous operation of BMS and Captain Morio Endo and the crew of the R/V Hakurei-Maru No.2 for their skillful support during the TAIGA10M cruise. Thanks are also due to Ms. Keiko Komiyama for preparation of XRF samples. The constructive and helpful review by an anonymous reviewer is gratefully acknowledged. This research was financially supported by the Ministry of Education, Culture, Science, and Technology (MEXT) of Japan, through a special coordination fund (Project TAIGA: Trans-crustal Advection and In situ biogeochemical processes of Global subseafloor Aquifer).

References

Anders E, Grevesse N (1989) Abundance of the elements: meteoritic and solar. Geochim Cosmochim Acta 53:197–214

Becker NC, Fryer P, Moore GF (2010) Malaguana-Gadao ridge: identification and implications of a magma chamber reflector in the southern Mariana Trough. Geochem Geophys Geosyst 11: Q04X13. doi:10.1029/2009GC002719

Edmond JM, Measure CI, McDuff RE, Chan LH, Collier R, Grant B, Gordon LI, Corliss JB (1979) Ridge crest hydrothermal activity and the balances of the major and minor elements in the ocean: the Galapagos data. Earth Planet Sci Lett 46:1–18

Elderfield H, Schultz A (1996) Mid-ocean ridge hydrothermal fluxes and the chemical composition of the ocean. Annu Rev Earth Planet Sci 24:191–224

Hessler RR, Kaharl VA (1995) The deep-sea hydrothermal vent community: an overview. In: Humphris SE, Zierenberg RA, Mullineaux LS, Thomson RE (eds) Seafloor hydrothermal systems: physical, chemical, biological, and geological interactions, vol 91, Geophysical monograph series. AGU, Washington, pp 72–84

Kobayashi K, Nakada M (1979) Magnetic anomalies and tectonic evolution of the Shikoku inter-arc basin. In: Uyeda S, Murphy R, Kobayashi K (eds) Geodynamics of the western pacific, vol 6, Advances in earth sciences. Japan Scientific Society, Tokyo, pp 391–402

Le Maitre RW, Bateman P, Dudek A, Keller J, Lameyre J, Le Bas KJ, Sabine PA, Schmid R, Sorensen H, Streckeisen A, Woolley AR, Zanettin B (1989) A classification of igneous rocks and glossary of terms: recommendations of the international union of geological sciences, subcommission on the systematics of igneous rocks. Blackwell, Oxford, p 193

Martinez F, Fryer P, Becker NC (2000) Geophysical characteristics of the southern Mariana Trough, 11°50′N-13°40′N. J Geophys Res 105:16591–16607

Nakamura K, Toki T, Mochizuki N, Asada M, Ishibashi J-I, Nogi Y, Yoshikawa S, Miyazaki J-I, Okino K (2013) Discovery of a new hydrothermal vent based on an underwater, high-resolution geophysical survey. Deep Sea Res I 174:2–10

Pearce JA, Stern RJ, Bloomer SH, Fryer P (2005) Geochemical mapping of the Mariana arc-basin system: implications for the nature and distribution of subduction components. Geochem Geophys Geosyst 6:Q07006. doi:10.1029/2004GC000895

Rickwood PC (1989) Boundary lines within petrological diagrams which use oxides of major and minor elements. Lithos 22:247–263

Sato H (2010) Quantitative analyses with X-ray fluorescence analyzer of major elements for rock samples. Bull Inst Nat Sci Senshu Univ 41:15–23 (in Japanese)

Seno T, Maruyama S (1984) Paleogeographic reconstruction and origin of the Philippine Sea. Tectonophys 102:53–84

Seyfried WE Jr, Ding K, Berndt ME (1991) Phase equilibria constraints on the chemistry of hot spring fluids at mid-ocean ridges. Geochim Cosmochim Acta 55:3559–3580

Shock EL (1992) Chemical environments of submarine hydrothermal systems. Orig Life Evol Biosph 22:67–107

Sun S.-S, WF. McDonough (1989) Chemical and isotopic systematics of oceanic basalts: implications for mantle composition and processes. In: Saunders AD, Norry MJ (eds) Magmatism in the ocean basins. Geological Society London, vol 42. Special Publication, pp 313–345

Tivey MK (2007) Generation of seafloor hydrothermal vent fluids and associated mineral deposits. Oceanography 20:50–65

Urabe T, J. Ishibashi, A. Maruyama, K. Marumo, N. Seama, and M. Utsumi (2004) Discovery and drilling of on- and off-axis hydrothermal sites in back-arc spreading center of southern Mariana Trough, western Pacific. Eos Trans AGU 85(47), Suppl, Abstract V44A-03, Dec 2004

Pore Fluid Chemistry Beneath Active Hydrothermal Fields in the Mid-Okinawa Trough: Results of Shallow Drillings by BMS During TAIGA11 Cruise

42

Jun-ichiro Ishibashi, Youko Miyoshi, Kazuya Tanaka, Eriko Omori, Yoshio Takahashi, Yoshiko Furuzawa, Toshiro Yamanaka, Shinsuke Kawagucci, Junichi Miyazaki, Uta Konno, Shota Watanabe, Katsunori Yanagawa, Ryoto Yoshizumi, and Tetsuro Urabe

Abstract

TAIGA11 cruise of R/V Hakurei-maru No.2 was conducted in June, 2011 to study subseafloor geochemical environment below active hydrothermal fields using a shallow drilling system BMS (Benthic Multi-coring System). Three active hydrothermal fields were selected as target fields; the Iheya North Knoll field (27°47′ N, 126°54′ E), the Jade field in the Izena Hole (27°16′ N, 127°05′E), and the Hakurei field in the Izena Hole (27°15′ N, 127°04′ E). In this chapter, we will report chemical composition and isotope ratios of pore fluids extracted from collected sediments. At the Hakurei field in the Izena Hole, BMS drilling attained to 610 cmbsf (cm below the seafloor) in the vicinity of a large massive sulfide mound. The obtained core showed evidence for sulfide and sulfate mineralization below 223 cmbsf. Pore fluid from the corresponding depth showed enrichment in Si, K and Ca, which could be attributed to influence of formation of alteration minerals rather than to involvement of the hydrothermal component. At the Jade field in the Izena Hole, BMS drilling attained to 529 cmbsf at about 300 m apart from the area where high temperature fluid venting congregate. The obtained core comprised grayish white hydrothermal altered mud below 370 cmbsf, although pore fluid showed seawater like composition. At the Iheya North Knoll field, BMS drilling attained to 453 cmbsf at about 200 m apart from the central mound area. The obtained core consisted almost entirely of grayish white hydrothermally altered mud. Pore fluid below 180 cmbsf showed substantial enrichment in major cations (Na, K, Ca and Mg) and Cl, which would be explained as a result of hydration during hydrothermal alteration.

The online version of this chapter (doi:10.1007/978-4-431-54865-2_42) contains supplementary material, which is available to authorized users.

J.-i. Ishibashi (✉)
Faculty of Sciences, Kyushu University, Fukuoka, Japan
e-mail: ishibashi.junichiro.779@m.kyushu-u.ac.jp

Y. Miyoshi
Graduate School of Sciences, Kyushu University, Fukuoka, Japan

Institute for Geo-Resources and Environment, AIST, Tsukuba, Japan

K. Tanaka
Institute for Sustainable Sciences and Development, Hiroshima University, Higashihiroshima, Japan

E. Omori • Y. Takahashi
Graduate School of Science, Hiroshima University, Higashihiroshima, Japan

Y. Furuzawa • T. Yamanaka
Graduate School of Natural Science, Okayama University, Okayama, Japan

S. Kawagucci • J. Miyazaki • U. Konno
Department of Subsurface Geobiological Analysis and Research (D-SUGAR), Research and Development (R&D) Center for Submarine Resources, Japan Agency for Marine-Earth Science and Technology (JAMSTEC), Yokosuka, Japan

S. Watanabe
Graduate School of Life and Environmental Sciences, University of Tsukuba, Tsukuba, Japan

K. Yanagawa • R. Yoshizumi • T. Urabe
Graduate School of Science, the University of Tokyo, Tokyo, Japan

J.-i. Ishibashi et al. (eds.), *Subseafloor Biosphere Linked to Hydrothermal Systems: TAIGA Concept*,
DOI 10.1007/978-4-431-54865-2_42,

Keywords
Clay minerals • Hydration • Hydrothermal alteration • Hydrothermal component • Sulfate reduction

42.1 Introduction

Many of active seafloor hydrothermal systems in the Okinawa Trough are considered to develop within sediment layers basically consist of volcanic and terrigenous material (Ishibashi et al., Chap. 27). Previous studies reported piles of tubular pumiceous sediment on volcanic knolls in the Okinawa Trough (e.g. Kato 1987). Porous volcanic sediment would stimulate subseafloor fluid flow within sediment layers that bears a hydrothermal system. Seafloor drilling during IODP (Integrated Ocean Drilling Program) Expedition 331 demonstrated existence of a hydrothermal fluid reservoir of laterally extensive in a kilometer scale in the volcanic sediment layers on the Iheya North Knoll in the Okinawa Trough (Takai et al. 2012). Significant fluid-mineral interactions are expected to occur within a hydrothermal system at such geological environment.

Hydrothermal activities in the Okinawa Trough are recognized as "TAIGA of methane", since their geochemical characteristics are represented by enrichment in organic-derived species such as CH_4, NH_3 and H_2 (Kawagucci, Chap. 30). These species are considered to be derived from microbiological and thermal decomposition of organic material within the sediment layer during fluid circulation in the recharge and discharge regions (Kawagucci et al. 2013). In addition to them, significant input of magmatic volatiles such as CO_2 and H_2S into the hydrothermal fluid has been commonly recognized among hydrothermal systems in the Okinawa Trough (e.g. Ishibashi and Urabe 1995). Involvement of these volatile and/or organic-derived species into pore fluid would substantially control pH of the fluid.

A Benthic Multi-coring System (BMS) is a powerful tool to directly access the subseafloor environment (e.g. Marumo et al. 2008). Although it may be difficult to penetrate the fluid reservoir even with the maximum capacity, drilling by the BMS is accessible to a region where various interactions are expected to be induced by mixing between the hydrothermal component and entrained seawater. We conducted BMS drilling in the Okinawa Trough from May 31 to June 9 in 2011, during TAIGA11 cruise of R/V Hakurei-Maru No.2. Purpose of the BMS drilling is to reveal evidence for various hydrothermal interactions within sediment layers based on geochemical, mineralogical, microbiological analysis of the obtained core samples. In this chapter, we will describe records of the BMS operations and report visual core descriptions (VCD) of the obtained core samples and geochemistry of pore fluids extracted from them. Mineralogical studies on the core samples will be reported in other chapters in this volume (Miyoshi et al., Chap. 44; Yoshizumi et al., Chap. 43).

42.2 Methodology

42.2.1 Core Sampling Device

A Benthic Multi-coring System (BMS) is a remotely operated seafloor coring system connected via armored umbilical cable to a control console on the support ship R/V Hakurei-Maru No.2 (Fig. 42.1a). This system has 5.5 m in height, 4.4 m in length, 3.6 m in width and 3.9 ton in weight. Figure 42.1b illustrates configuration of the BMS. The BMS has a rotating storage magazine for the drilling equipment (core barrels, drilling rods, and casing pipes) that enables it to core to depths of up to 20 m in 2.2 m intervals. The core barrel (modified version of the NC core barrel) is a double-tube, thin-kerf diamond-bit core barrel that allows for recovery of 49 mm diameter core in consolidated soft and/or hard rock formations. The BMS is equipped with five TV cameras to help search for appropriate drilling sites and to monitor working tools during the drilling operation. The drill bit is usually cooled with seawater. During TAIGA11 cruise, a large-volume, multi-step filtration system was installed on the intake side of the bit cooling system to achieve aseptic drilling. Measurements of temperature within boreholes (up to 300 °C) were conducted using a fully mechanical system embedded in the core barrel. Titanium tubing was prepared for casing some of the drilled holes.

Other than the BMS, a gravity corer (called as LC corer in this cruise) was employed for coring when the sea condition was not good enough for BMS operation. The LC corer is equipped with a 4 m long core barrel and 0.3 m extension installed core catchers.

42.2.2 Core Sampling Operations

Target study fields of the TAIGA11 cruise were selected from active hydrothermal fields in the mid-Okinawa Trough (Fig. 42.2a). Table 42.1 summarizes coring operations during the TAIGA11 cruise conducted in June, 2011. In total, eight BMS operations and two LC core (gravity core) samplings were conducted. Operation hours of the BMS

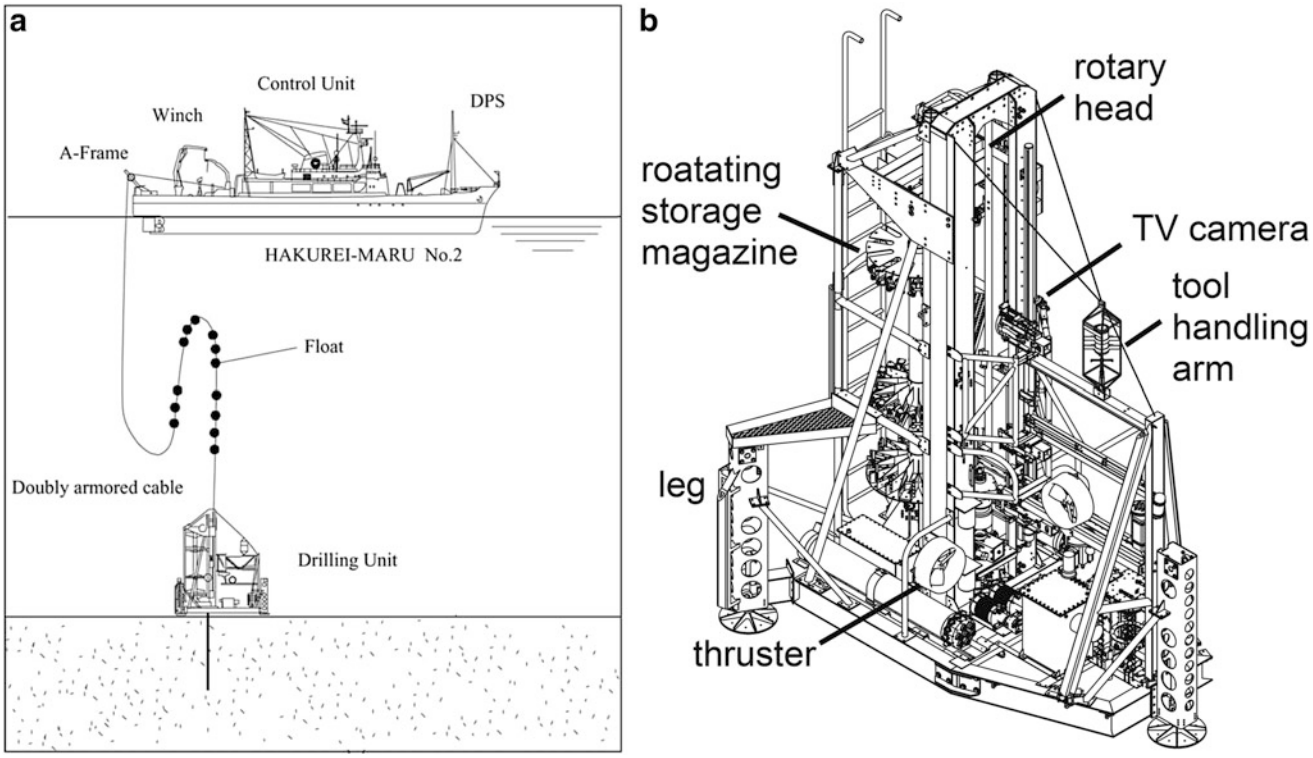

Fig. 42.1 (**a**) Operation scheme of BMS (Benthic Multicoring System). (**b**) Illustrated configuration of BMS (modified after Marumo et al. 2008)

were sometimes restricted by bad sea condition and by approach of fishing boats.

In the Hakurei field in the Izena Hole, three BMS operations were conducted in Stations BMS-H-1, BMS-H-6A and BMS-H-6B (Fig. 42.2b). Station BMS-H-1 was located at about 100 m west from a large sulfide mound which was recognized as the most prominent hydrothermal mound in the northern part of the Hakurei field. This area has been explored intensively by JOGMEC (Japan Oil, Gas and MEetals National Corporation) under a framework of the ocean energy and mineral resources development program. With visual observation by the monitoring camera, seafloor was recognized as covered with sediment including gravels of a few cm diameters, associated with white patches. Drilling at Station BMS-H-1 successfully attained to 610 cmbsf (centimeters below the seafloor). Station BMS-H-6 was located at about 150 m northeast from the large sulfide mound. Drilling at Station BMS-H-6 was ceased due to a trouble in a rotary jaw when drilled to 33 cmbsf (BMS-H-6A). Drilling was re-started after the repair at the same station (BMS-H-6B). However, due to limited time for operation, the drilling attained only to 341 cmbsf and its core recovery was not good.

In the Jade field in the Izena Hole, four BMS operations were conducted at Stations BMS-J-2, BMS-J-3A, BMS-J-3B and BMS-J-5 (Fig. 42.2c). Station BMS-J-2 was located near the Biwako vent site where consolidated sediment with native sulfur was observed. With visual observation by the monitoring camera, seafloor was recognized as covered with large size of consolidated sediment blocks. After the drilling attained to 529 cmbsf, this hole was cased using two casing pipes. Station BMS-J-3 was located in the central area of the Jade field where high temperature fluid venting congregate around the TBS chimney. In this area, gravels of native sulfur were recovered by surface coring (Yokoyama et al., Chap. 31). Due to steep slope topography, the coring operation was limited to pushing the bit without rotation. The first trial attained to 151 cmbsf (BMS-J-3A) and the second trial attained to 164 cmbsf by rotating the bit slowly (BMS-J-3B). During the drillings, emanation of black-colored slime-like fluid from the seafloor about one meter apart from the drilled hole was observed. This hole was cased after the drilling. Station BMS-J-5 was located near the site of liquid CO_2 bubble emanation, which was reported by Sakai et al. (1990). Several trials were required to deploy the BMS on the seafloor in stable condition. Only a short core (30–40 cm) was recovered due to plugging of the bit. In addition to the BMS operations, one LC core sampling was conducted at Station LC-J-2 located in the vicinity of the BMS-J-2.

In the Iheya North Knoll field, one BMS operation at Station BMS-I-4 and one LC core sampling at Station LC-I-1 were conducted (Fig. 42.2d). Station BMS-I-4 was located between IODP Sites C0013 and C0014 (Takai et al. 2012). With visual observation by the monitoring camera, seafloor was recognized as covered with sediment associated with

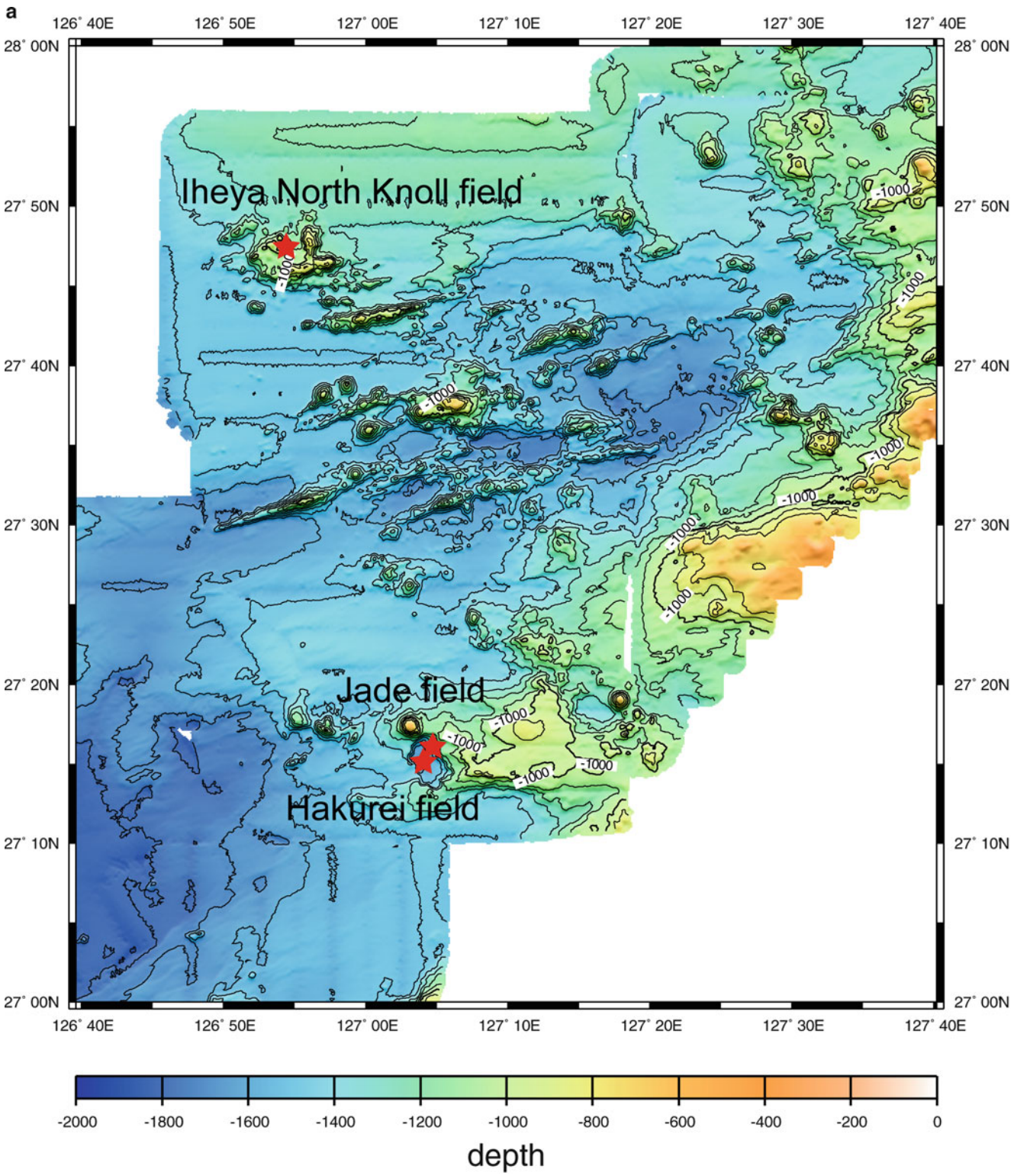

Fig. 42.2 Bathymetric maps of studied hydrothermal fields. Coring stations were superimposed on the maps. (**a**) Locality of the studied hydrothermal fields in the mid-Okinawa Trough. (**b**) Hakurei field in the Izena Hole. (**c**) Jade field in the Izena Hole. (**d**) Iheya North Knoll field

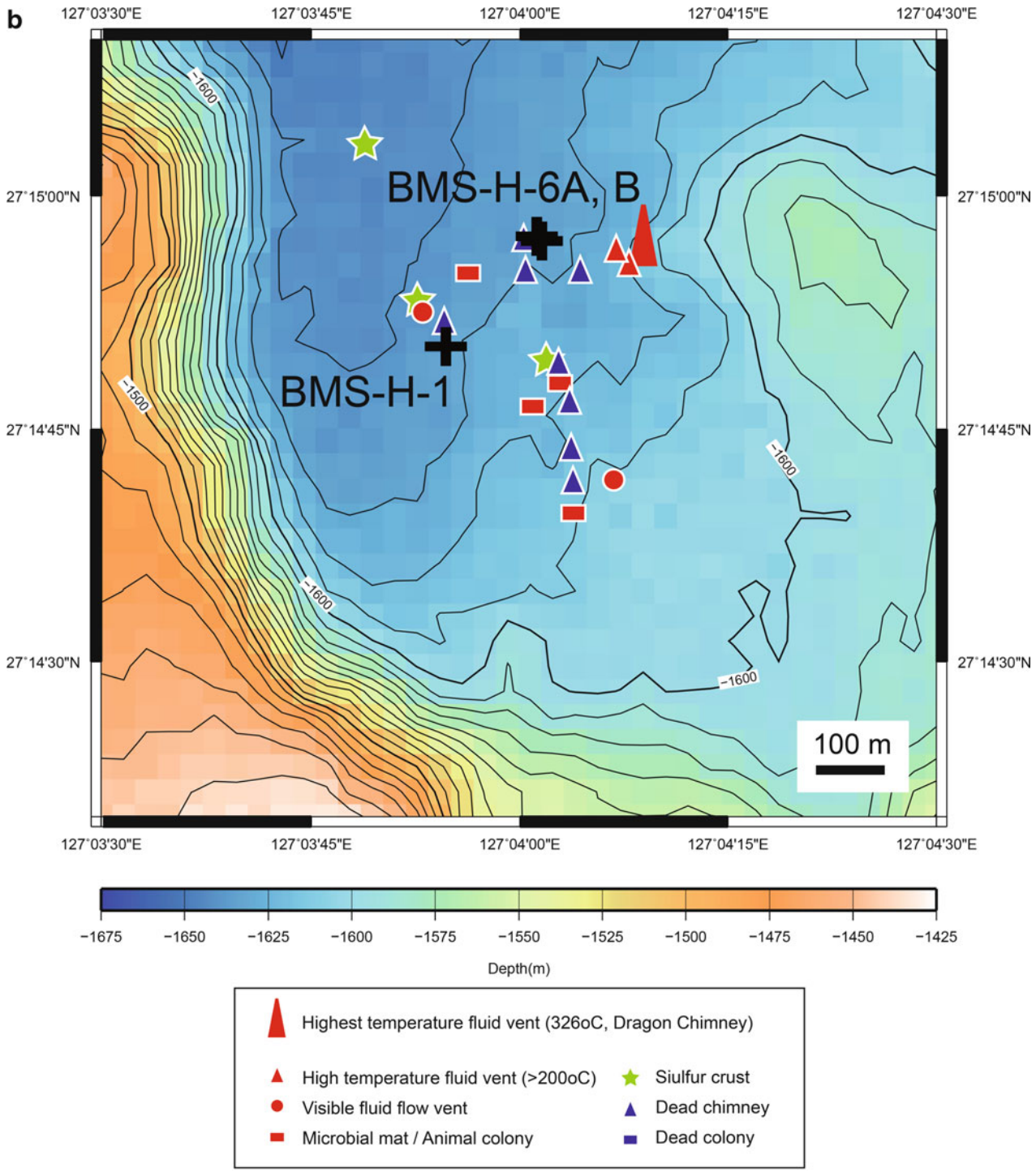

Fig. 42.2 (continued)

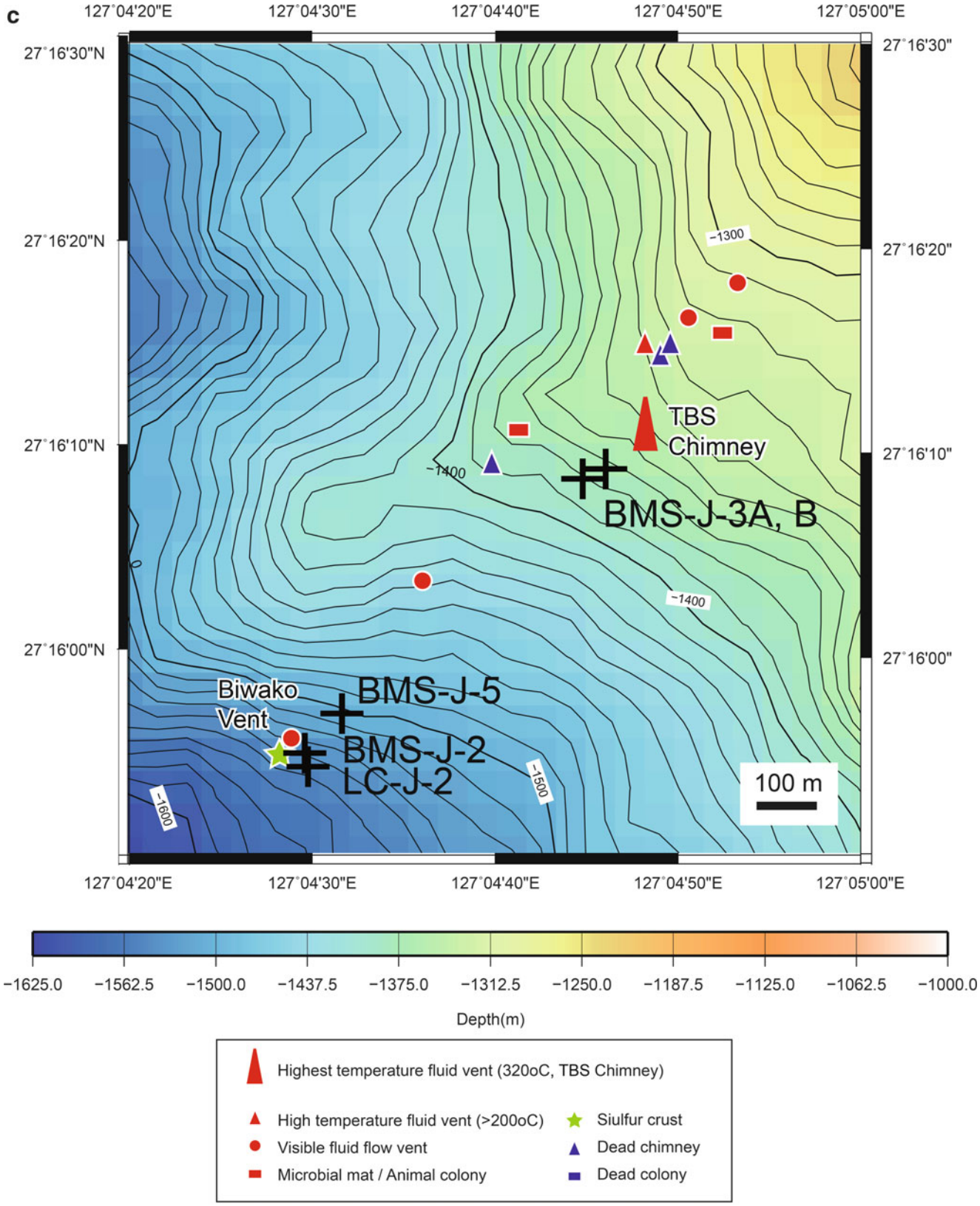

Fig. 42.2 (continued)

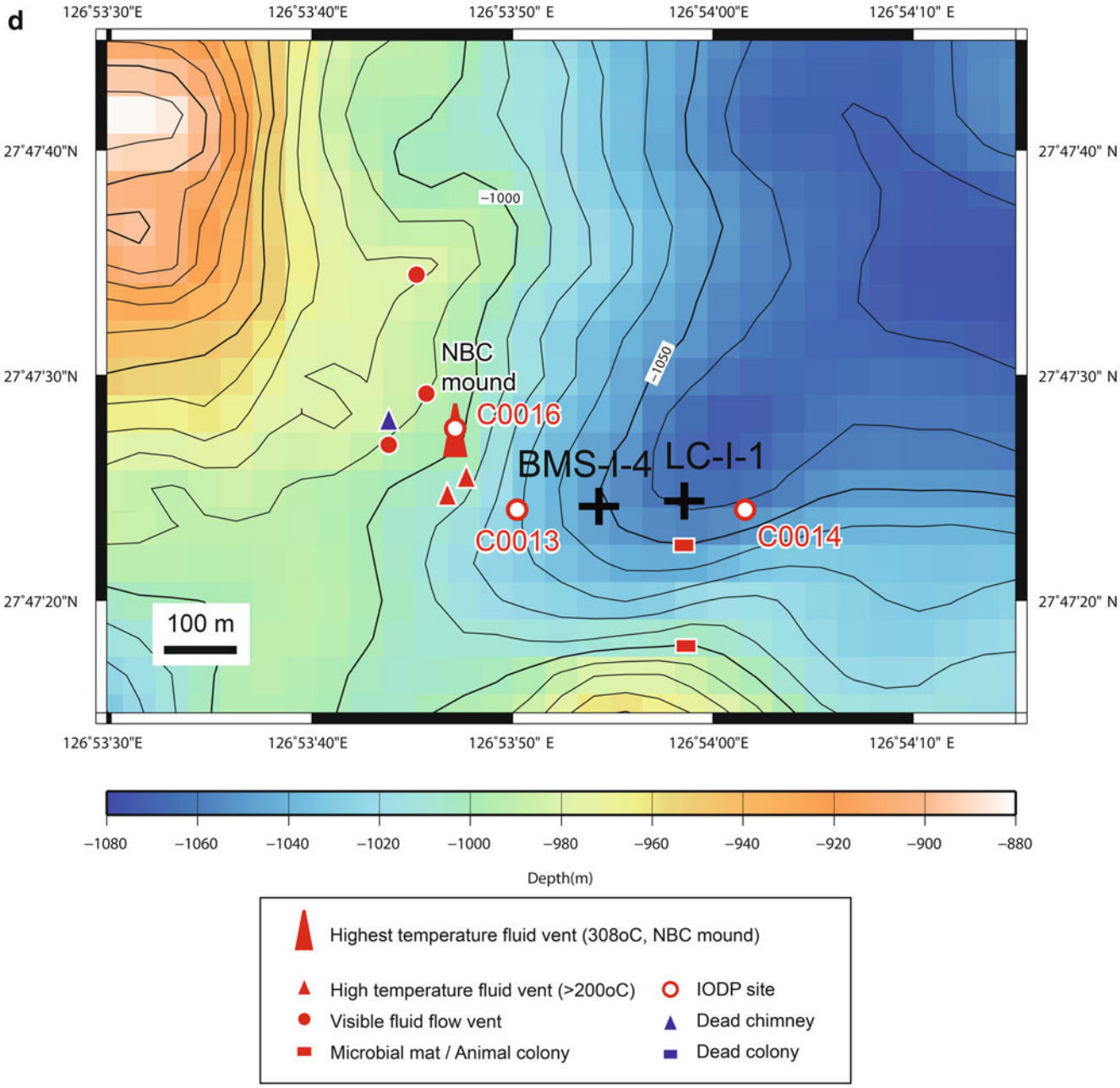

Fig. 42.2 (continued)

bacterial mat and clam shells. During the drilling below 17 cmbsf, emanation of white-colored slime-like fluid from the seafloor around the drilled hole was observed. During the drilling from 80 to 144 cmbsf, substantially less resistance was monitored and the slime-like fluid emanation was ceased. Emanation of slime-like fluid started again when the drilling below 170 cmbsf started, and more dense white-colored slime was observed when the drilling attained to 336 cmbsf. The drilling operation was stopped at 453 cmbsf where high resistance was monitored. After the drilling, borehole temperature measurement was conducted and followed by casing. Emanation of liquid bubbles every a few seconds from the top of the casing pipe was observed when the BMS left the seafloor. Station LC-I-1 was located between Station BMS-I-4 and Site C0014 (Fig. 42.2d).

42.2.3 Handling of Core Samples

As soon as the BMS was returned to onboard, core barrels were removed from the rotating storage magazine. After a core catcher was removed, core inside the core barrel was pushed out slowly using hydrostatic pressure, which was applied by pumping filtered seawater into the other end.

Table 42.1 Summary of core sampling operations during TAIGA11 cruise

Drilling site	Date	Device	Position[a]		Water depth[b] (m)	Drilled depth (cm)	Core length (cm)	Core recovery (%)	Casing pipe
			Latitude	Longitude					
HAKUREI field, Izena Hole									
TAIGA11-BMS-H-1	6/1/2011	BMS	27°14.837′N	127°03.911′E	1,661	610.4	389.0	63.7	No
TAIGA11-BMS-H-6A	6/8/2011	BMS	27°14.950′N	127°04.025′E	1,661	32.9	21.0	63.8	No
TAIGA11-BMS-H-6B	6/8/2011	BMS	27°14.955′N	127°04.019′E	1,660	341.1	109.0	32.0	No
JADE field, Izena Hole									
TAIGA11-BMS-J-2	6/2/2011	BMS	27°15.913′N	127°04.495′E	1,520	529.1	366.7	69.3	Yes
TAIGA11-BMS-J-3A	6/3/2011	BMS	27°16.146′N	127°04.746′E	1,396	151.7	103.0	67.9	No
TAIGA11-BMS-J-3B	6/3/2011	BMS	27°16.154′N	127°04.767′E	1,383	164.6	44.0	26.7	Yes
TAIGA11-BMS-J-5	6/6/2011	BMS	27°15.956′N	127°04.526′E	1,543	75.6	27.0	35.7	No
TAIGA11-LC-J-2	6/6/2011	LC	27°15.924′N	127°04.492′E	1,570	330.0	310.0	93.9	–
Iheya North Knoll field									
TAIGA-BMS-I-4	6/4/2011	BMS	27°47.404′N	126°53.906′E	1,048	453.4	157.0	34.6	Yes
TAIGA11-LC-I-1	6/5/2011	LC	27°47.408′N	126°53.977′E	1,048	230.0	230.0	100.0	–

[a]Position of the drilling site was determined based on GPS data of the ship
[b]Water depth of the drilling site was determined based on MBES data

Then, the core was delivered on an acrylic tubing of a half cylinder shape which was sterilized with alcohol beforehand. Since length of the acrylic tubing was shorter than that of the core barrel, the core was sometimes divided into a few sequentially numbered sections.

As soon as the LC corer returned to onboard, an acrylic inner tubing that had been inserted into a gravity corer was drawn out. Then, the core was divided into two half cylinders using a cutter and gut.

In either case, core samples were laid on a table in the main laboratory of R/V Hakurei-Maru No.2 and photographed. Sampling of sub-samples for each specific study was conducted in parallel to description of the core by visual observation. After all the sub-sampling and description works completed, remained cores were divided by every 10–30 cm length and packed in plastic bags for storage.

42.2.4 Chemical Analysis of Pore Fluid

Pore fluid was extracted from the sediment sub-samples onboard employing two techniques. One is the standard ODP (Ocean Drilling Project) method using a hydraulic sediment press (Manheim and Sayles 1974). The other is an easy-to-use technique using a plastic syringe and small vice (Nakaseama et al. 2008). The latter technique has an advantage of quick handling but a disadvantage of limitation of sample volume (about 30 cm^3 of sediment). In either case, the extraction of pore fluid was conducted within 48 h after the sample recovery.

Chemical analysis of pore fluids for some unstable species was conducted onboard, basically following the protocol adopted by ODP (Ocean Drilling Project) expeditions (Gieskes et al. 1991). Measurement of pH was conducted onboard using a pH electrode at room temperature. Titration alkalinity was determined onboard following the Gran's method. Conventional colorimetric techniques were employed for analysis of Si by the molybdenum blue method, of NH_4 by indophenol method, and of H_2S by methylene blue method. Analytical precision was estimated to be within 3 % relative error for Si and NH_4 based on repeated analysis of artificial seawater. Analytical precision was worse for H_2S due to the volatile and unstable property, and ~10 % discripancy was sometimes recognized for duplicate analysis of the same sample.

Other major chemical species were analyzed on-shore laboratories in Kyushu University and Okayama University. Concentration of Cl was determined by $AgNO_3$ titration following the Mohr method. Concentration of SO_4 was determined by an ion chromatograph (Dionex, DX-100) after 300 times dilution. Concentration of K was analyzed by an atomic absorption spectrophotometer (Perkin Elmer, AAnalyst 100) after 200 times dilution of the acidified subsamples with addition of Cs. Concentrations of Mg and Ca were determined by ICP-AES (Seiko Instruments, SPS1200AR) after 200 times dilution of the acidified subsamples. Concentration of Na was calculated from the charge balance between these major cations and anions. Discrepancy between the calculated Na concentration and determined Na concentration by ICP-AES was less than 5 % for most of samples. Analytical precision for each chemical analysis was estimated to be within ±3 % relative error from replicate analysis.

Head space gas analysis was conducted only for the BMS-I-4 core. For this purpose, appropriate volume (~2 cm^3) of sediment was subsampled into an 8 ml glass vial capped by a butyl-rubber septum under the atmosphere after addition of 0.2 ml $HgCl_2$-saturated solution for

sterilization. After three months storage at −20 °C, concentrations of CH_4 and H_2 in head space of the vial were determined with a gas chromatograph equipped with a helium ionization detector. Together with a result of weighing sediment in the vial, gas content in the sediment was calculated. Detection limit was about 5 ppmv of headspace for both gas species, which roughly corresponds to about 1 nmol/g sediment. Overall analytical error was estimated to be about 20 %.

Hydrogen and oxygen isotope ratios of H_2O were determined by a wavelength scanned cavity ring down spectroscopy analyzer (Liquid Water Isotope Analyzer, Los Gatos Research, Inc.). Analytical precision was estimated to be within ±1.0 ‰ for δD value and ±0.5 ‰ for $\delta^{18}O$ value. Sulfur isotope ratios of dissolved SO_4 were determined by EA/irMS (IsoPrime) following the precedure described in Yamanaka et al. (2008).

42.2.5 Post-drilling Observation

Two months after the BMS drilling during TAIGA11 cruise, a dive expedition of ROV *Hyper-Dolphin* was conducted during NT11-15 cruise. This cruise provided us a desirable opportunity to observe post-drilling feature of the drilled sites. During Dive 1310 of ROV *Hyper-Dolphin* in the Jade field, the top of the casing pipe at Station BMS-J-2 was witnessed. However fluid emanation was not observed. A locality of the drilled hole was confirmed as 27°15.919′ N, 127°04.489′E, which is close to the position determined based on ship GPS data during the drilling. During Dive 1311 of ROV *Hyper-Dolphin* in the Iheya North Knoll field, more than one hour was occupied for exploration around the envisonal locality of Station BMS-I-4, however any signature of the drilled hole was not witnessed. We had no opportunity to observe post-drilling feature for Station BMS-J-3.

42.3 Results and Discussion

42.3.1 Visual Core Description

For the core samples obtained by the BMS, depths were determined in following way. At first, depths of the core tops were determined based on drilled length of the BMS that was monitored onboard. Then, depth intervals were assigned starting from the depth below seafloor at which coring started. Short cores due to incomplete recovery were all assumed to start from the initial depth determined as above way. For the core samples obtained by the LC, the core top was assumed as the seafloor depth and depth intervals were assigned. In either case, material recovered from the core catcher was placed at the bottom of the lowermost section of the recovered core.

Figure 42.3 summarizes a revised version of visual core descriptions (VCD) of the obtained cores. The VCD was originally noted onboard in parallel to sub-sampling procedure. The identified minerals onboard were confirmed or revised based on results of mineralogical analysis conducted after return to the laboratory (Miyoshi et al., Chap. 44). In followings, characteristic lithology for each core is summarized.

In the BMS-H-1 core, sulfide minerals were abundantly identified in several layers. Massive sulfides occupied from 0 to 20 cmbsf. Sulfidic grits were found below 223 cmbsf, underlain by barite and sphalerite mixed layer. Sphalerite was dominant among sulfide minerals in the layer from 339 to 370 cmbsf, whereas chalcopyrite was dominant from 370 to 417 cmbsf. Below 417 cmbsf to the core catcher depth (530 cmbsf), barite was dominant again. The BMS-H-6B core mainly consisted of unaltered sediment including woody pumice.

Most part of the BMS-J-2 core (shallower than 381 cmbsf) was characterized by pumiceous sediment, and spotty white colored grains were noted in some layers. Below 381 cmbsf, the core consisted of hydrothermal mud including abundant clay minerals, which was continuous to the core catcher depth (423 cmbsf). In this layer, occurrence of pyrite and native sulfur was recognized. The BMS-J-3A core was characterized by sediment consisted of pumice, silt, sand and white-colored clay minerals and the BMS-J-3B core showed similar signature. In the BMS-J-5 core, gravels of native sulfur were observed, which plugged the bottom of the corer. In the LC-J-2 core, hydrothermally altered pumice was recognized occasionally in olive brown colored silt and clay sediment. Plant debris was notable in the layer from 100 to 200 cmbsf. Below 300 cmbsf, the core consisted of grayish white colored hydrothermal mud, which was continuous to the core catcher depth (320 cmbsf). During sub-sampling onboard, gas bubbling from the sediment was observed.

In the BMS-I-4 core, evidence for hydrothermal alteration was notable in most entire part. Core of only 30 cm length was recovered during the first coring, and pyrite and clay minerals were found in it. Below 170 cmbsf, the obtained core was dominated by grayish white colored mud mostly consisted of kaolinite, which was continuous to the core catcher depth (370 cmbsf). Together with the observation of white-colored slime-like fluid during the drilling operation, this intensely altered sediment layer was considered to have at least 2 m thickness. During sub-sampling onboard, gas bubbling from the sediment was observed, as well as detection of H_2S smell. The LC-I-1 core was characterized by silt and clay sediment which often included pumiceous material. Below 184 cmbsf,

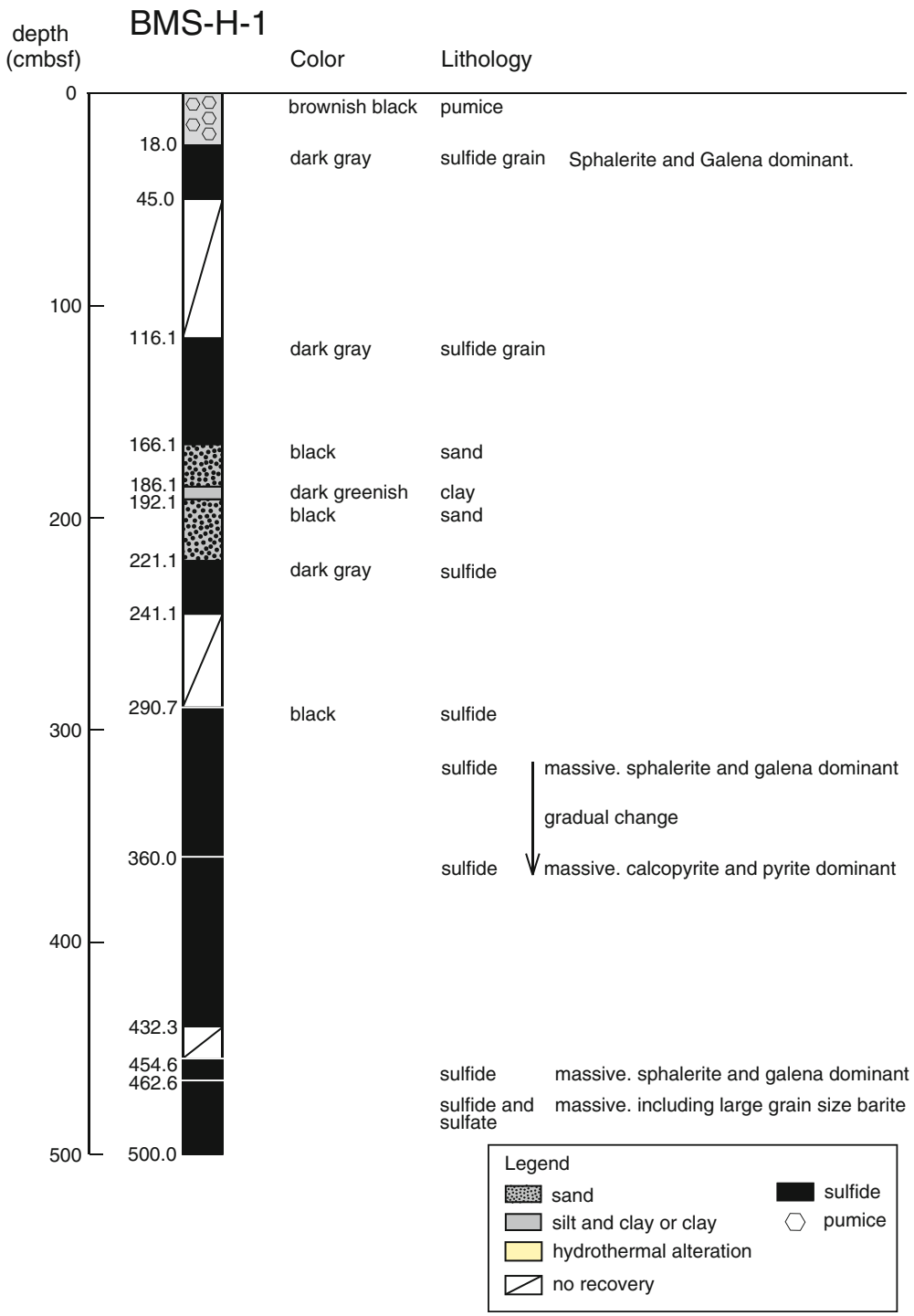

Fig. 42.3 Visual core descriptions (VCDs) of the obtained core samples. The identified minerals were confirmed and/or revised based on results of an onshore mineralogical study (Miyoshi et al., Chap. 44)

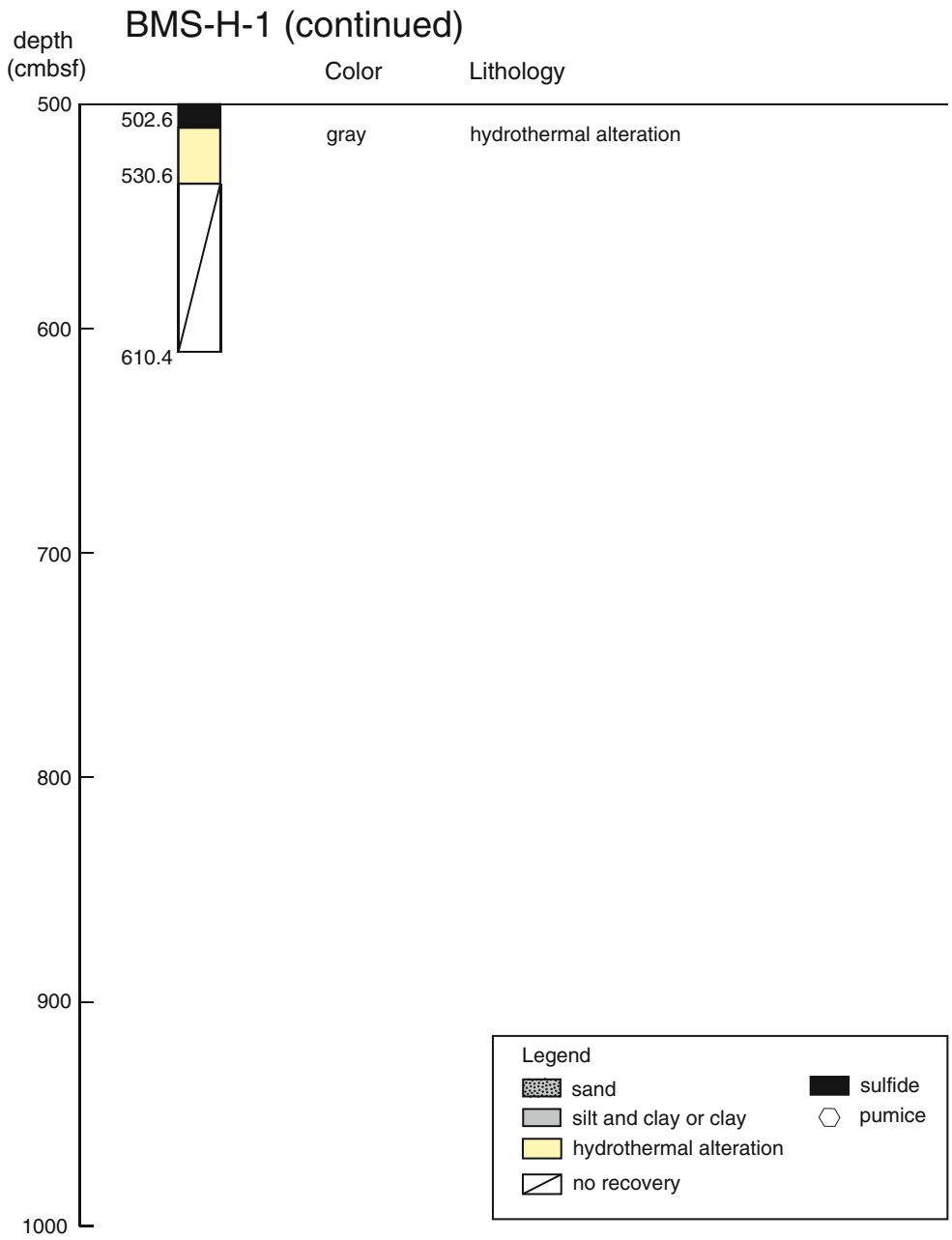

Fig. 42.3 (continued)

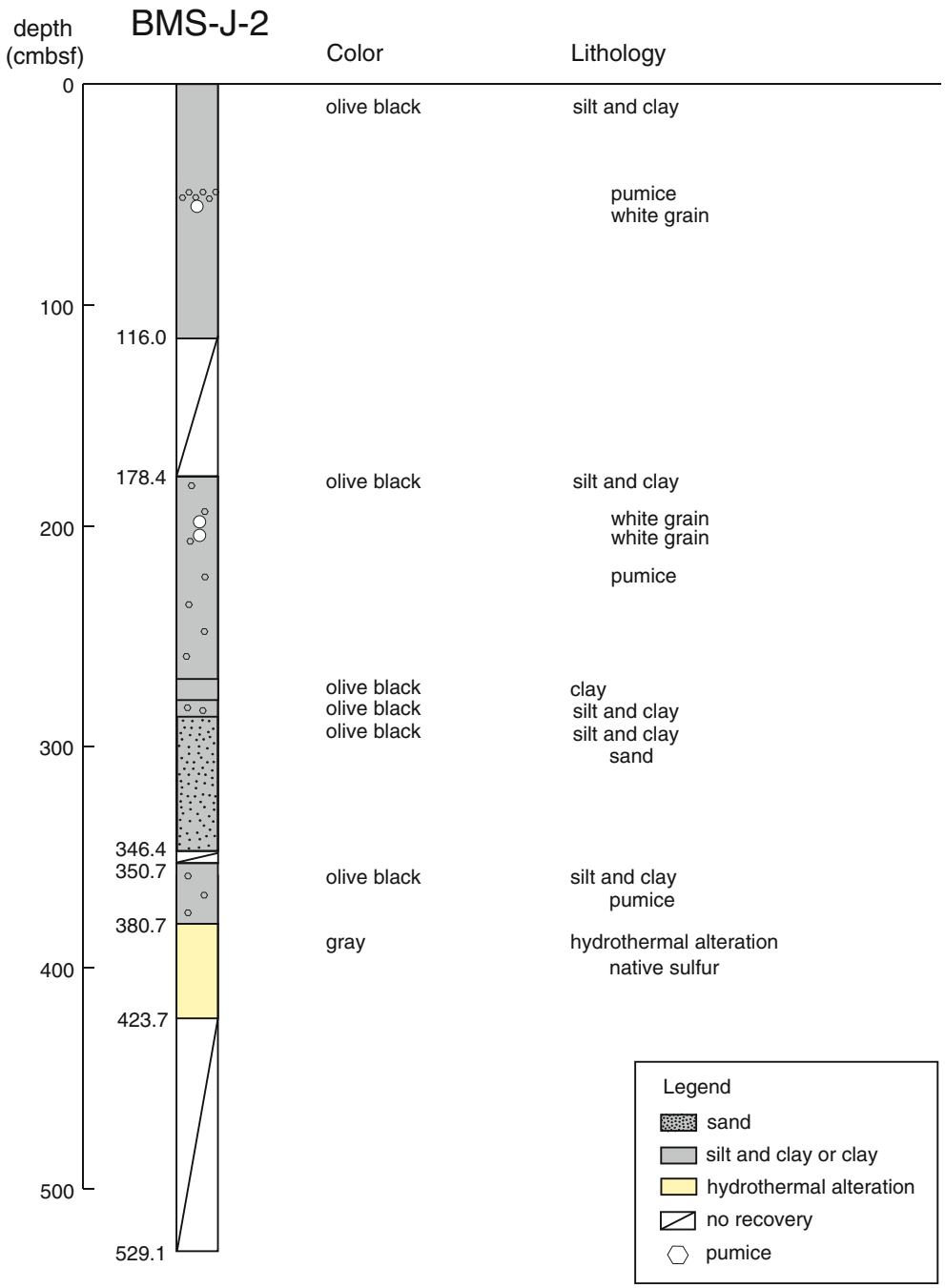

Fig. 42.3 (continued)

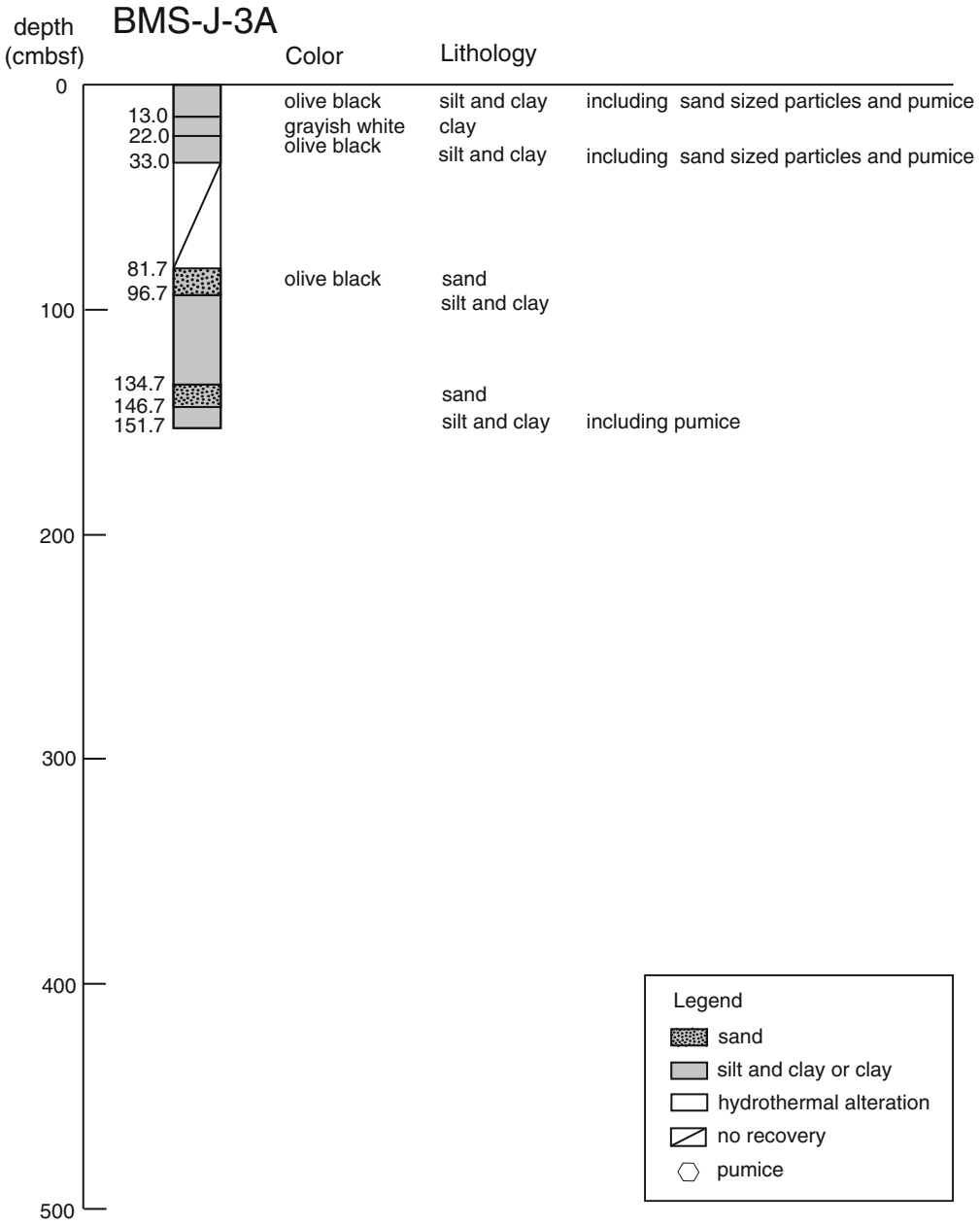

Fig. 42.3 (continued)

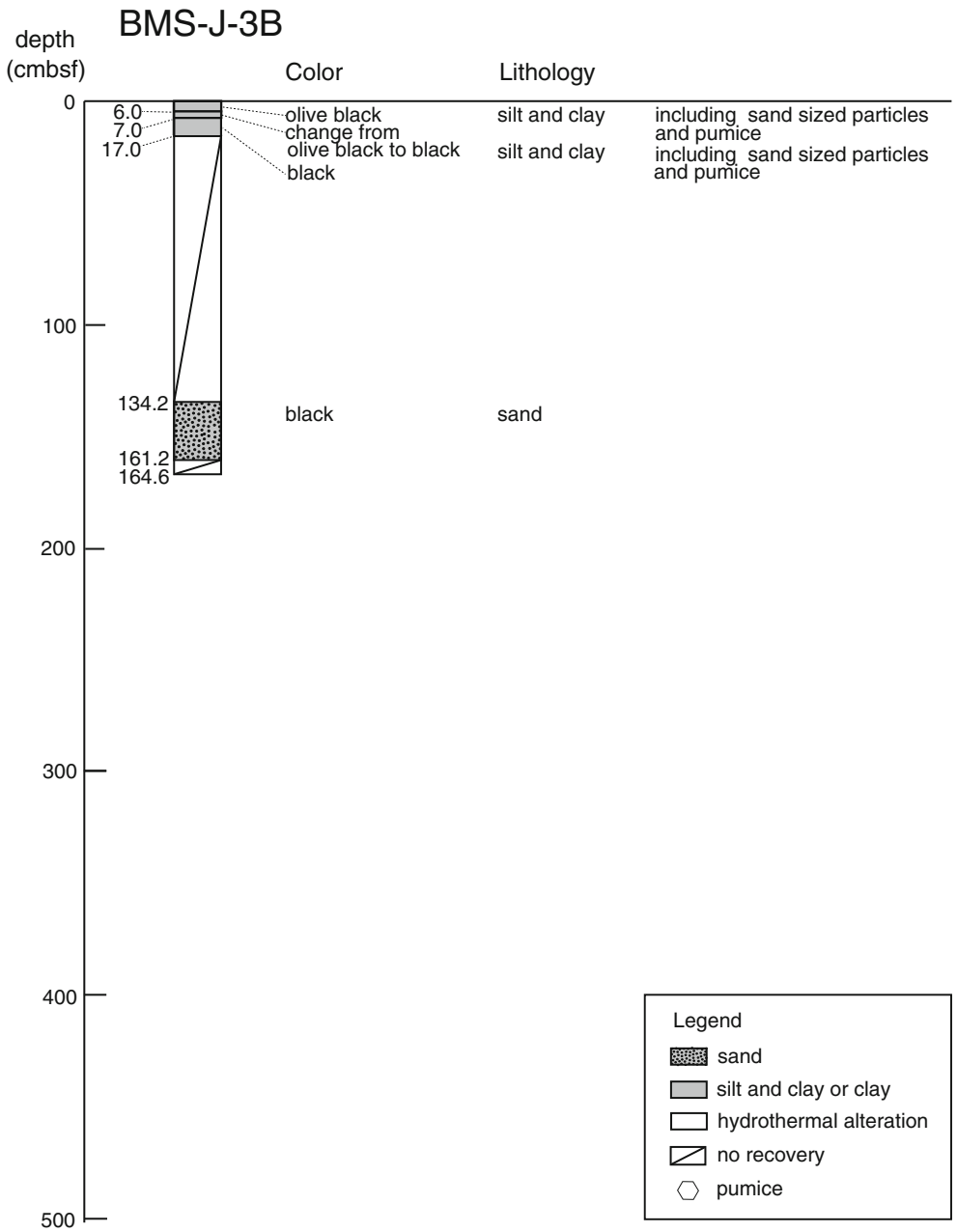

Fig. 42.3 (continued)

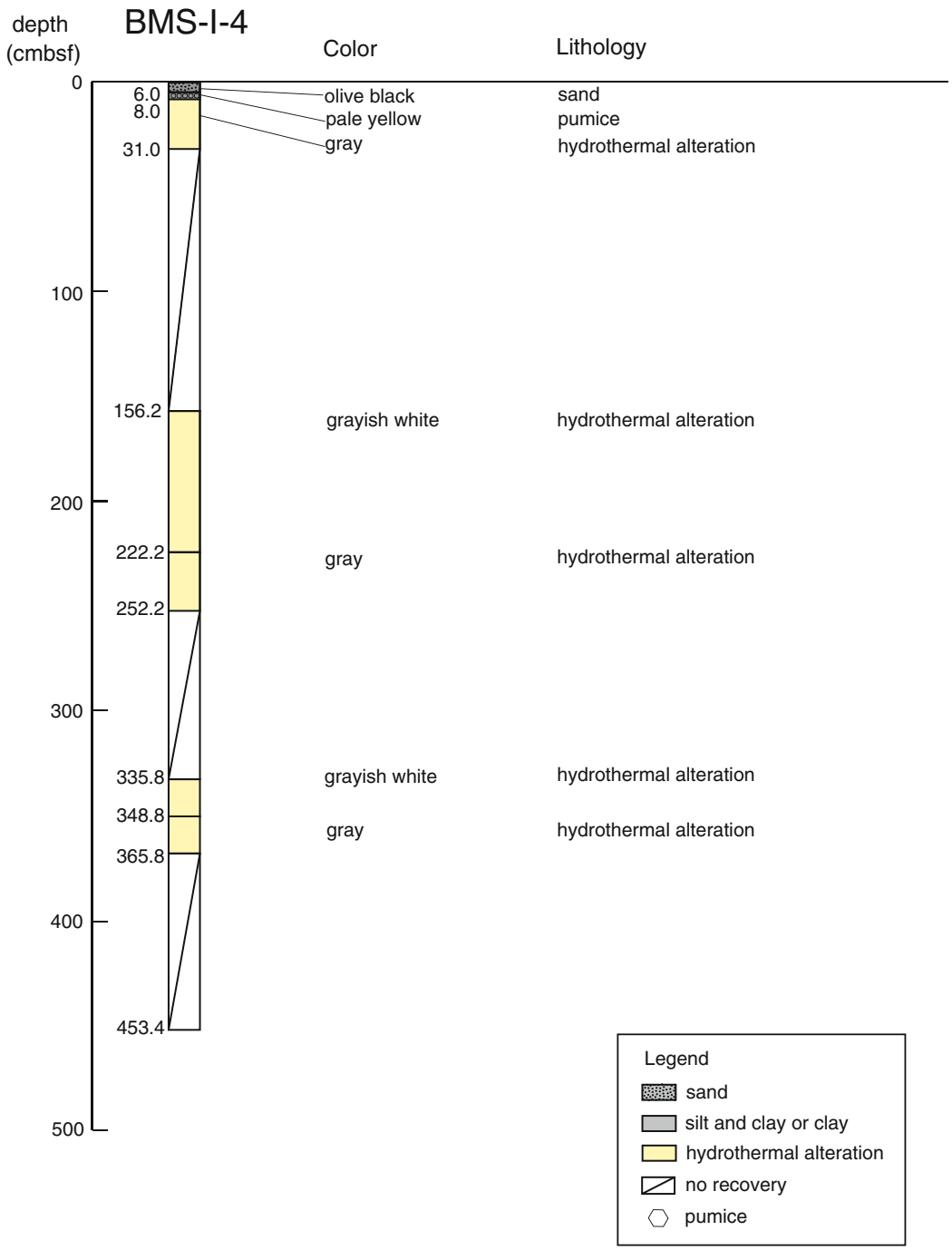

Fig. 42.3 (continued)

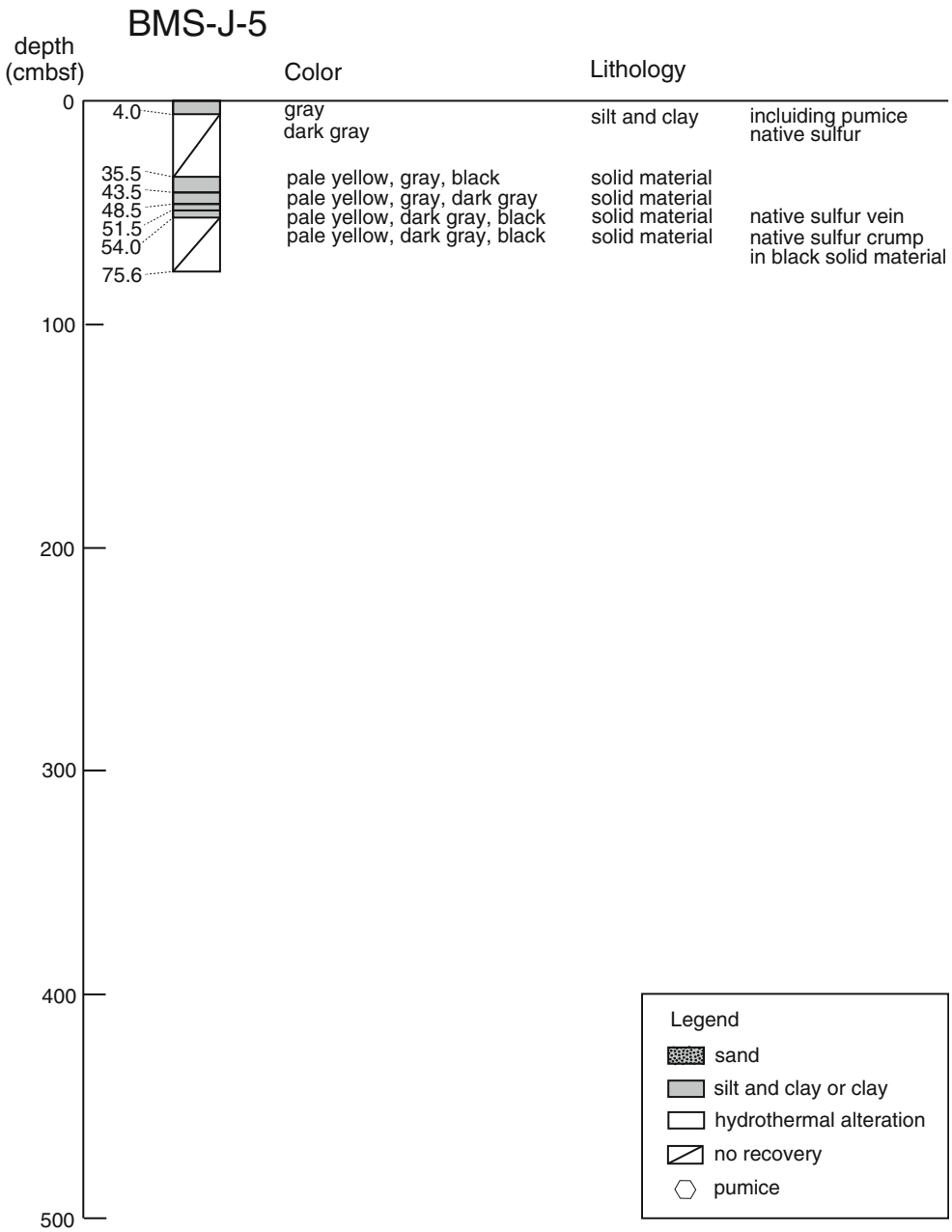

Fig. 42.3 (continued)

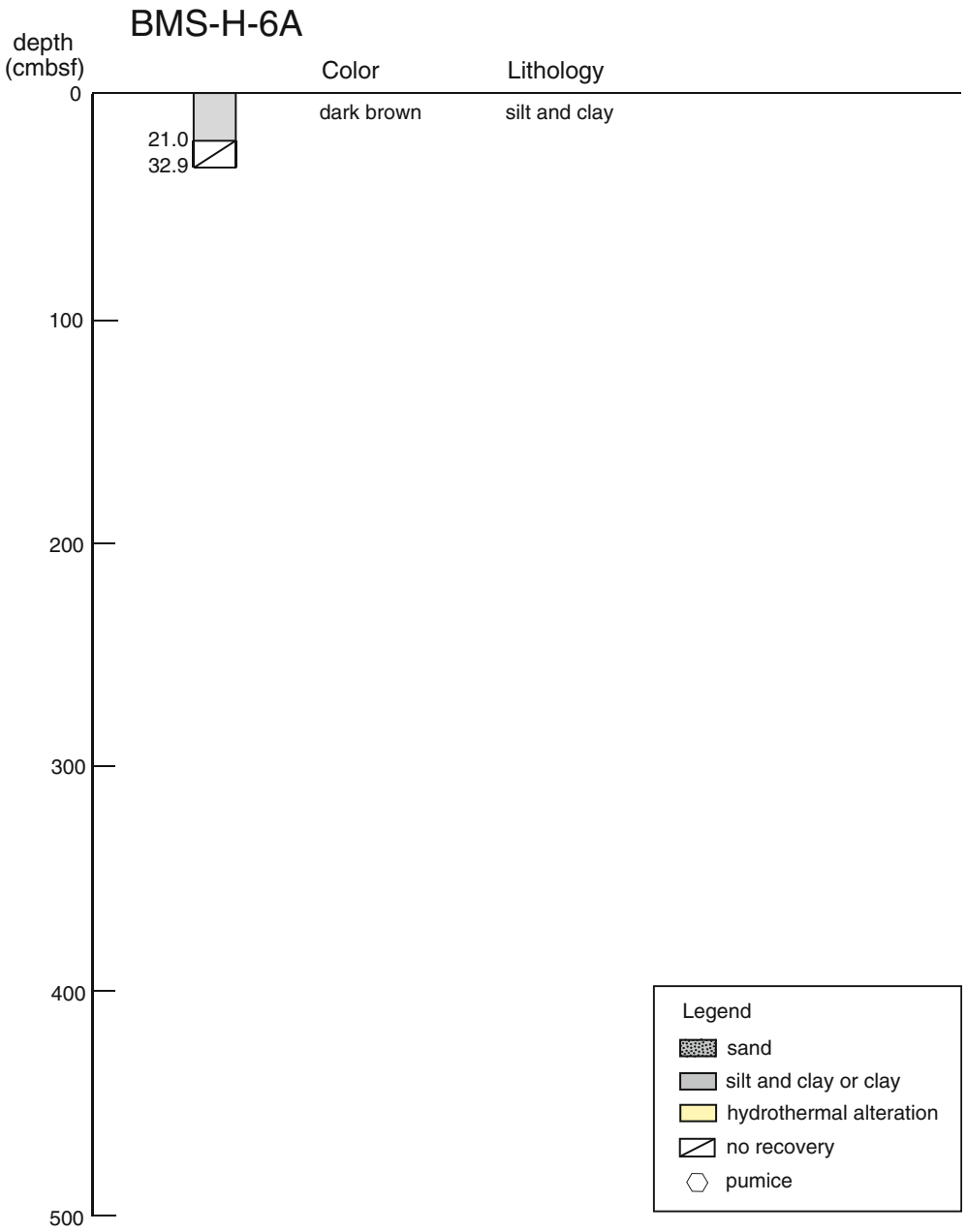

Fig. 42.3 (continued)

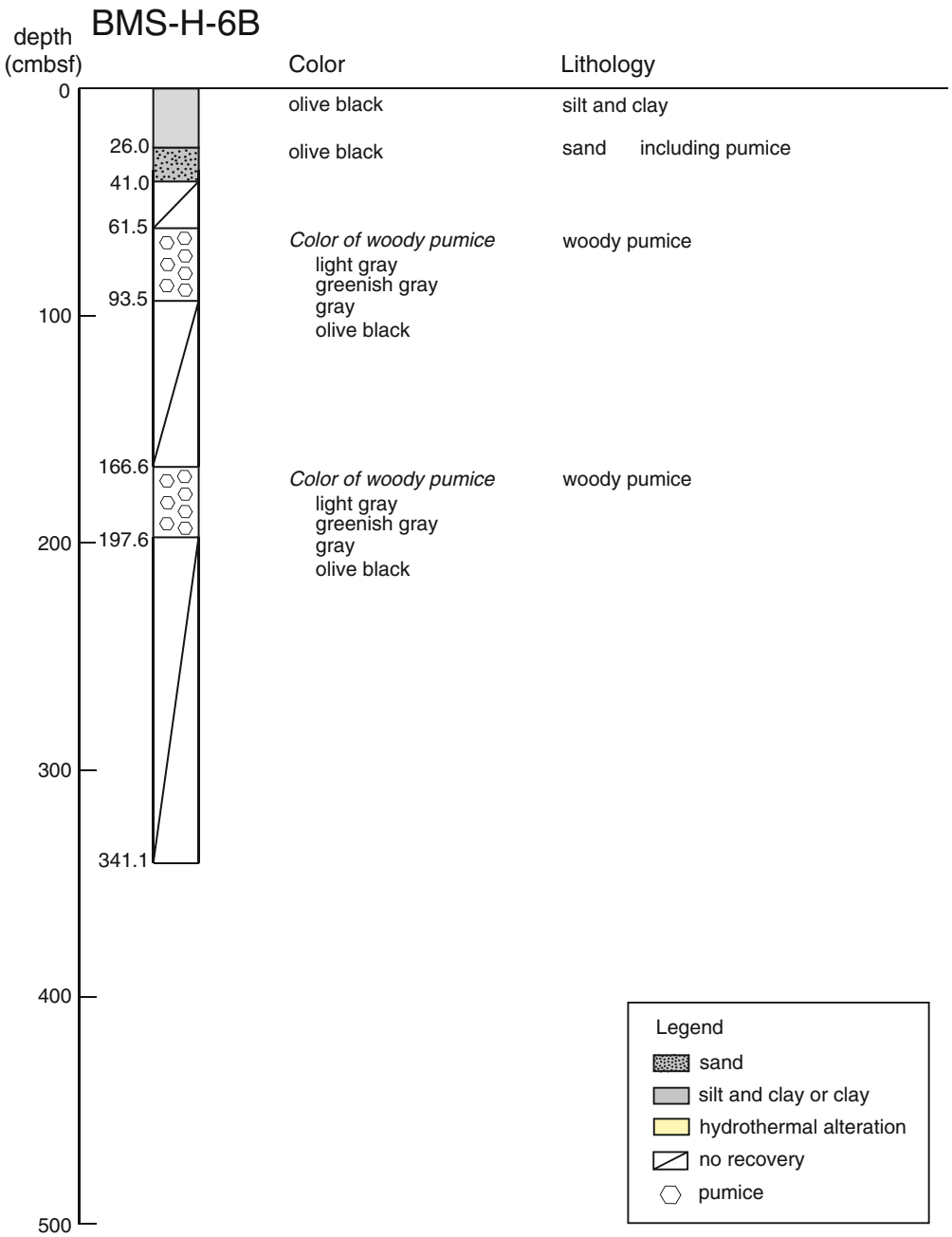

Fig. 42.3 (continued)

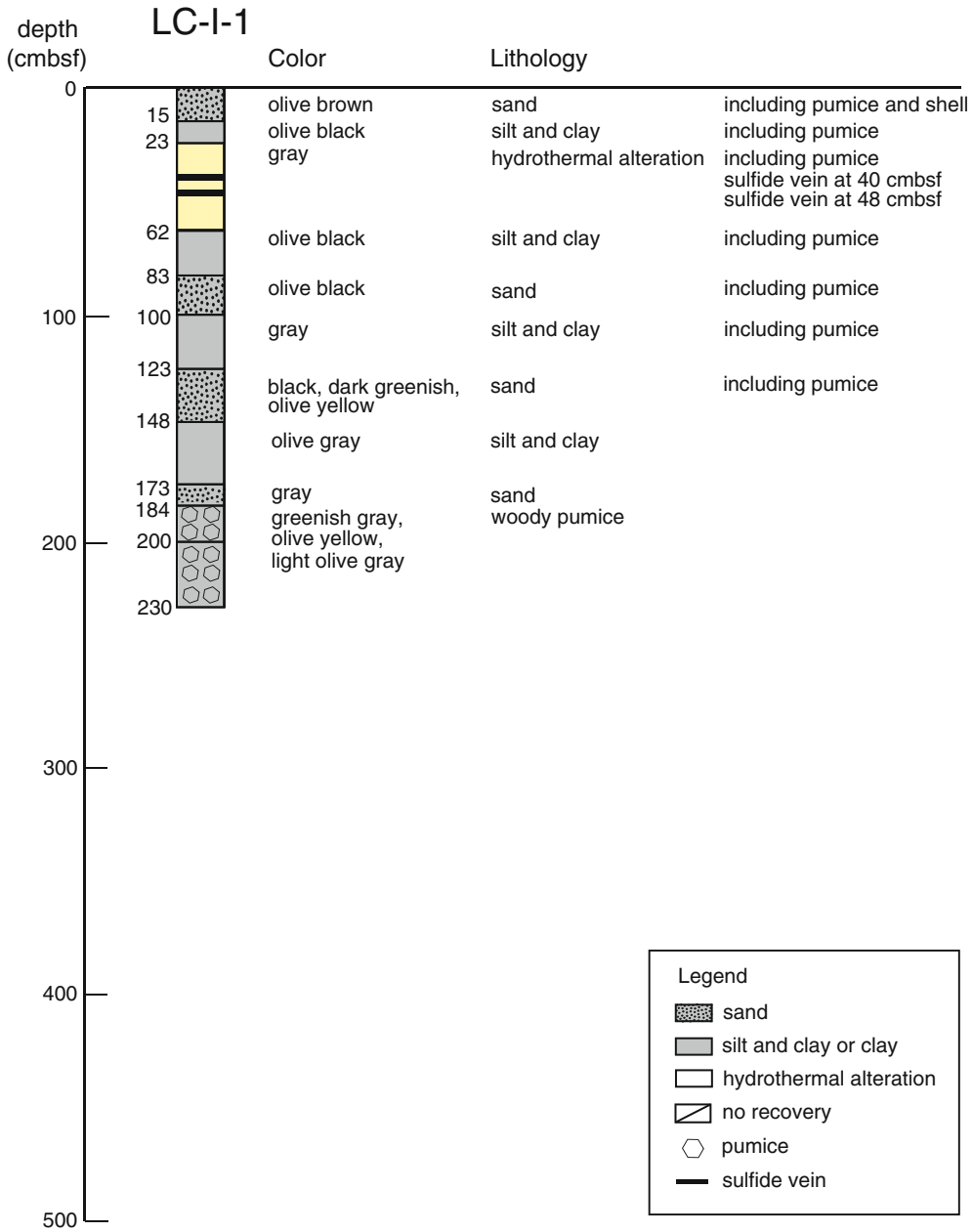

Fig. 42.3 (continued)

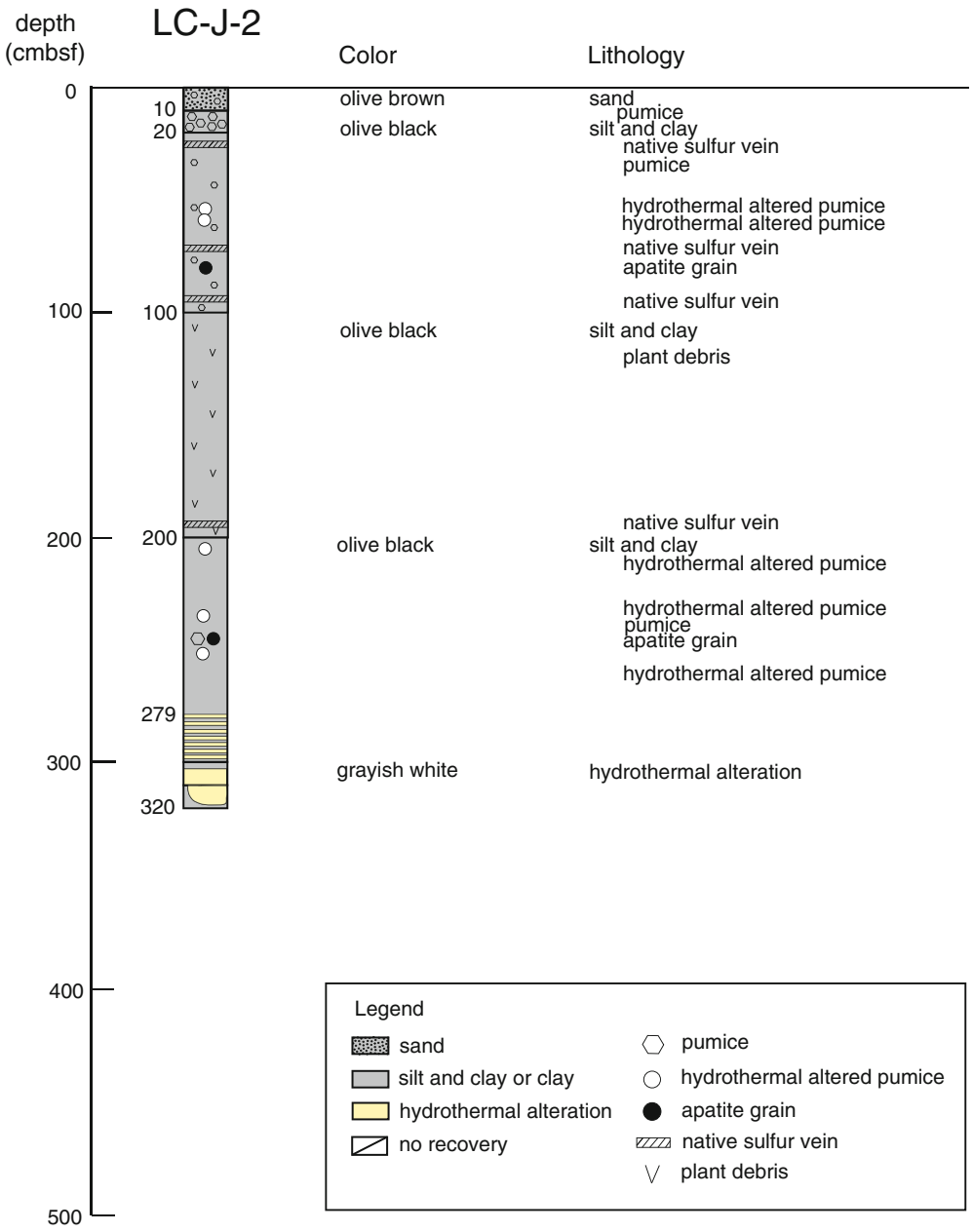

Fig. 42.3 (continued)

large size woody pumices were abundant. It is notable to recognize hydrothermally altered mud dominated from 23 to 62 cmbsf, which included sulfide veins at 40 and 48 cmbsf.

42.3.2 Pore Fluid Chemistry

Results of chemical analysis of pore fluid samples are summarized in Table S1 in the supplementary file. In this table, δD and $\delta^{18}O$ values are expressed in per mill with SMOW and $\delta^{34}S$ values are expressed in per mill with CDT.

42.3.2.1 Pore Fluid in the Hakurei Field

Vertical profiles of pore fluid chemistry collected from the Hakurei field in the Izena Hole are illustrated in Fig. 42.4, and two components diagrams for some major species are illustrated in Fig. 42.5. Due to somehow poor core recovery, profiles from Station BMS-H-1 are rather discontinuous. In spite of the discontinuity, increase in concentration toward deep could be recognized in some major species such as K, Na, Cl and Si. As discussed in the later subsection based on the pore fluid chemistry in the Iheya North Knoll field, this signature could be explained by hydration during hydrothermal alteration in the deeper layer. Observed shift in δD

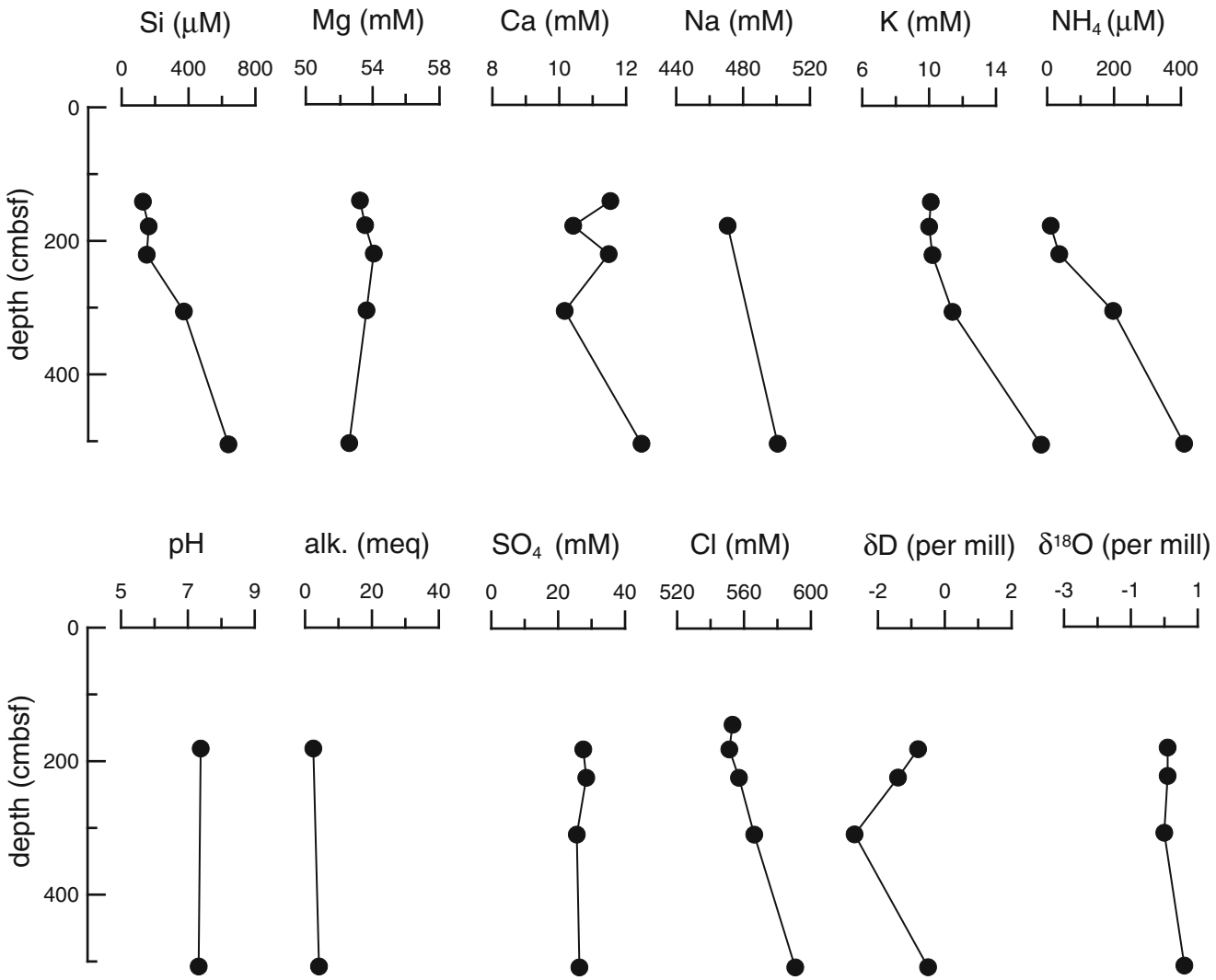

Fig. 42.4 Vertical profiles of pore fluid chemistry in the Hakurei field in the Izena Hole; *closed circles* represent Station BMS-H-1. Units in the figure are abbreviated as follows; *cmbsf* cm below the seafloor, *mM* mmol/L, *meq* meq/L, *μM* μmol/L

values is likely to be in accordance with this idea, since it could be attributed to formation of hydroxide-bearing clay minerals. However, it is difficult to confirm this interpretation because clay mineralogy of the BMS-H-1 core has not been studied. If the above interpretation is the case, limited decrease in concentrations of Mg and SO_4 might be considered as evidence for contribution of the hydrothermal component. While uptake of H_2O by the hydration would cause proportional increase in concnetrations of all the major species, involvement of the hydrothermal component which is completely depleted in Mg and SO_4 would balance this effect. Based on significant sulfide and sulfate mineralization noticed during the visual core observation, it would be reasonable to expect that pore fluid chemistry is affected by contribution of the hydrothermal component. However, only ambiguous evidence was recognized in the present pore fluid.

42.3.2.2 Pore Fluid in the Jade Field

Vertical profiles of pore fluid chemistry collected from the Jade field in the Izena Hole are illustrated in Fig. 42.6, and two components diagrams for some major species are illustrated in Fig. 42.7. At Station BMS-J-2, slight shift in concentration of major species toward deep might be recognized; increase in Mg, Ca and Si coupled with depletion in K (closed triangles in Figs. 42.6 and 42.7). However, even below 381 cmbsf where hydrothermal alteration minerals were obvious, these shifts are too slight. It is difficult to discuss which type of fluid interaction affects pore fluid chemistry. Also at Station BMS-J-3, pore fluid chemistry showed only slight shifts in concentration of major species (reversed triangles in Fig. 42.7).

Contrary to these, pore fluid collected from the LC-J-2 core showed large shift in concentration of several chemical species (open triangles in Fig. 42.6). Decrease in SO_4

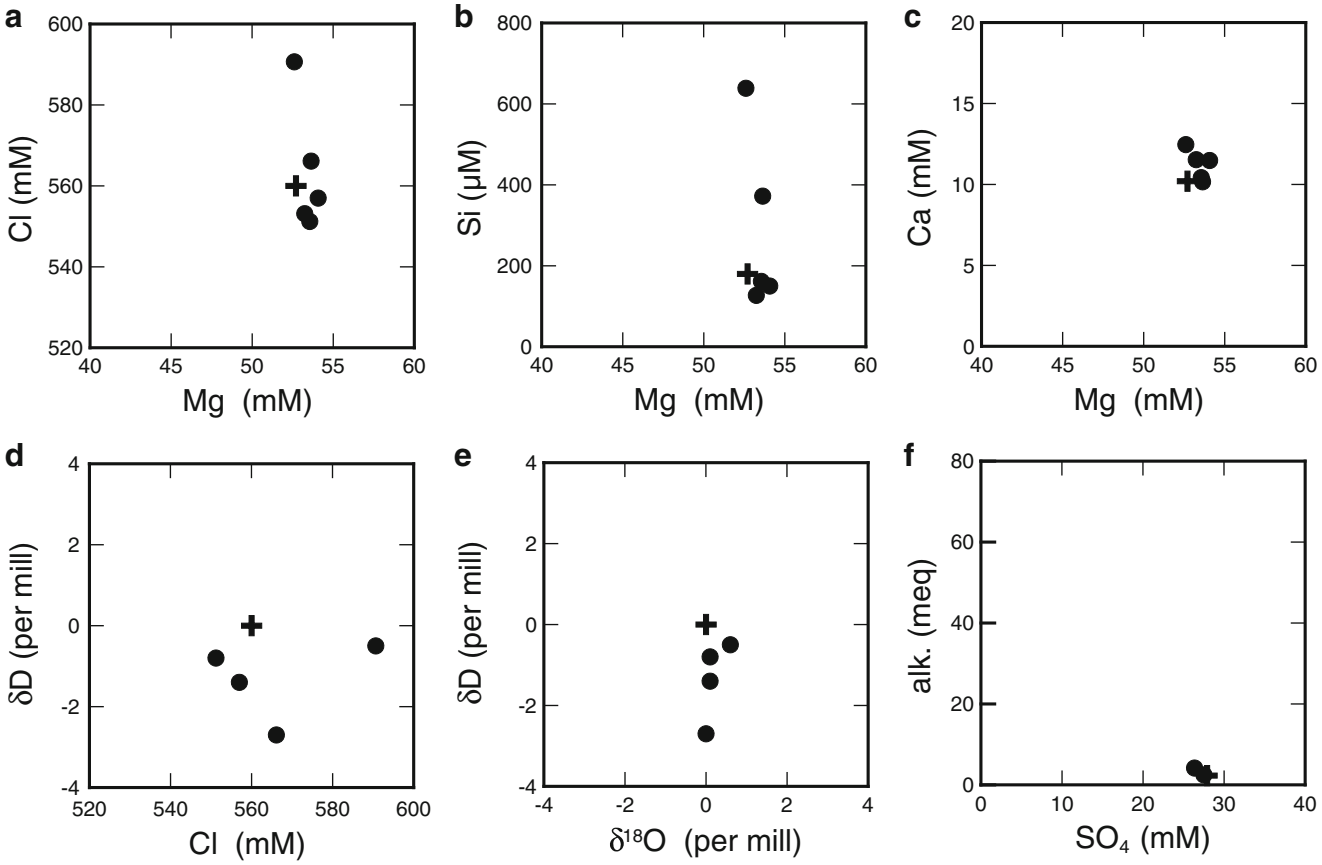

Fig. 42.5 Two components diagrams for the pore fluid samples collected from the Hakurei field: (**a**) Cl vs Mg, (**b**) Si vs Mg, (**c**) Ca vs Mg, (**d**) δD vs Cl, (**e**) δD vs $\delta^{18}O$, and (**f**) alkalinity vs SO_4. Symbols and unit abbreviations are same as in Fig. 42.4

coupled with increase in alkalinity suggests significant sulfate reduction reaction within the sediment. Sulfur isotopic composition of SO_4 showed ^{34}S-eiriched signature up to +50 ‰ (Table S1), which supports the sulfate reduction reaction. Molar ratio between the sulfate decrease to the alkalinity increase is estimated as 2 or higher (Fig. 42.7f), which suggests the sulfate reduction utilizes organic matter as reductant. This interpretation is in accordance with that the maximum of these shifts are recognized around the depths from 100 to 200 cmbsf where abundant plant debris was found during the visual observation. Occurrence of pyrite and native sulfur was identified by the mineralogical study (Miyoshi et al., Chap. 44), which implies these sulfur species are product of the sulfate reduction. On the other hand, profiles for other species are recognized as basically monotonous linear trend, which were characterized as increase toward deep in Mg and Ca concentrations, and as decrease in Na and K concentrations. Similar linear trends are also recognized in δD and $\delta^{18}O$ values, which suggests that pore fluid chemistry at Station LC-J-2 was controlled by mixing process between two components due to elemental diffusion. This interpretation would be in accordance with the result of the visual observation, which discriminated intense grayish white colored hydrothermally altered mud below 300 cmbsf and spotty evidence for hydrothermal alteration in the shallower sediment. If this is the case, the endmember in the deeper layer would be characterized as significant enrichment in Mg and Ca, and depletion in K. This signature cannot be explained by a result of involvement of the hydrothermal component, but could be attributed to formation and/or dissolution of alteration minerals. The mineralogical study revealed occurrence of dolomite and magnesite in the layer from 280 to 320 cmbsf (Miyoshi et al., Chap. 44). Significant increase in Mg, Ca and also excess alkalinity would be explained by dissolution of these carbonate minerals, although it is unknown what triggered the dissolution. The mineralogical study also identified euhedral crystals of K-feldspar in the layer from 300 to 320 cmbsf (Miyoshi et al., Chap. 44). If substantial amount of K-feldspar forms, it would explain depletion in K in the pore fluid.

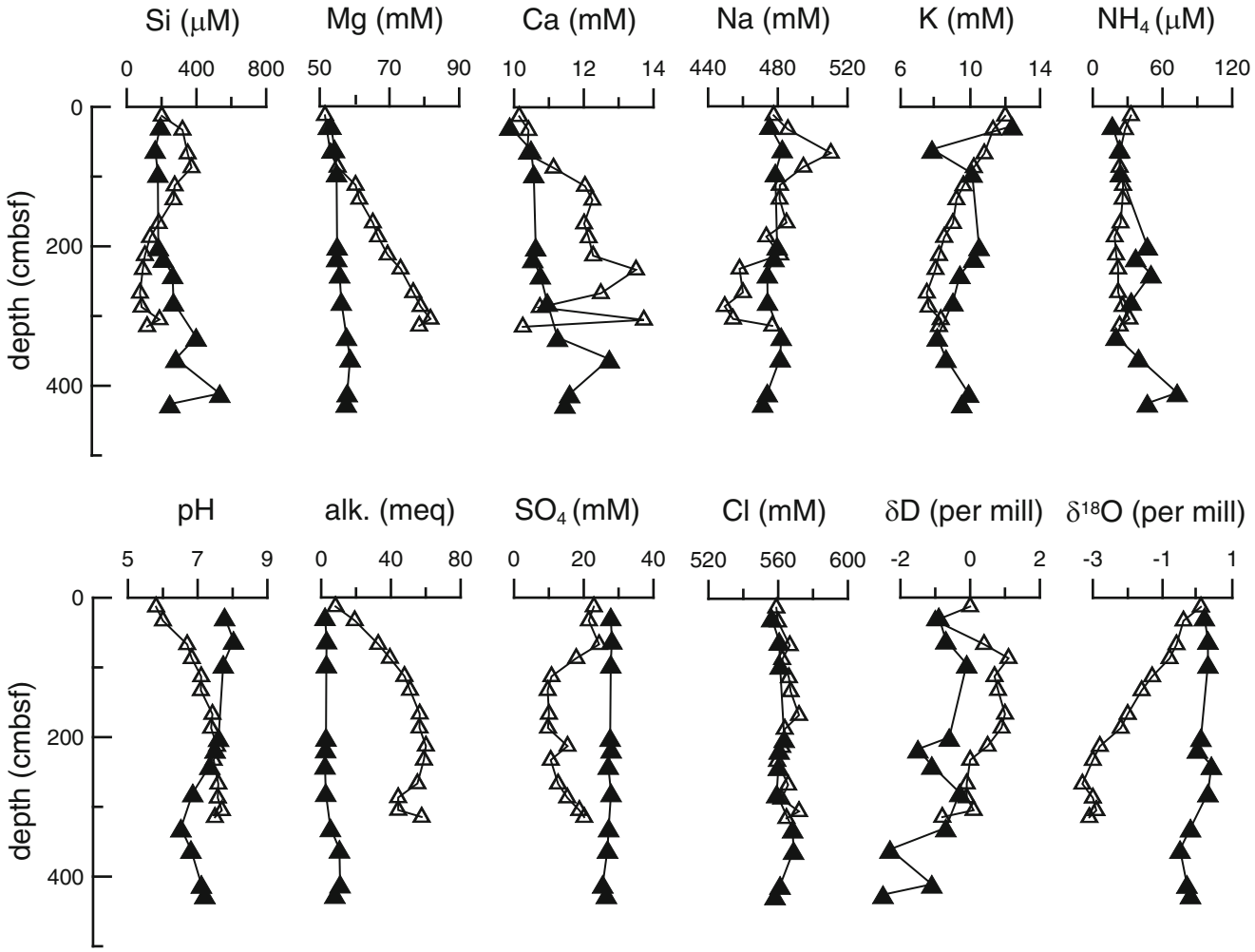

Fig. 42.6 Vertical profiles of pore fluid chemistry in the Jade field in the Izena Hole; *closed triangles* represent Station BMS-J-2, *open triangles* represent Station LC-J-2, and *reverse closed triangles* represent Station BMS-J-3. Units in the figure are abbreviated as follows; *cmbsf* cm below the seafloor, *mM* mmol/L, *meq* meq/L, *μM* μmol/L

42.3.2.3 Pore Fluid Chemistry in the Iheya North Knoll Field

Vertical profiles of pore fluid chemistry collected from the Iheya North Knoll field are illustrated in Fig. 42.8, and two components diagrams for some major species are illustrated in Fig. 42.9. Results of head space gas analysis which was conducted only for the BMS-I-4 core are shown in Table S2 in the supplementary file. Gas contents in sediment were determined for CH_4 and H_2, but H_2 contents in the head space were lower than the detection limit (~1 nmol/g sediment) for all the analyzed samples. At Station BMS-I-4, borehole temperature measurement was conducted and its result is shown in Table S3 in the supplementary file. The measurement was conducted at four different depths, and averaged, minimum and maximum values for 2 min measurement at each depth are listed in this table. These data are illustrated as vertical profiles in Fig. 42.10.

One of notable characteristic of the pore fluid chemistry from Station BMS-I-4 is increase in concentration of major ions below 180 cmbsf (closed diamonds in Fig. 42.8). The coincident increase would be best explained by hydration of the counterpart solid phase during hydrothermal alteration. The mineralogical study revealed occurrence of abundant kaolinite in the BMS-I-4 core (Miyoshi et al., Chap. 44), and hydrothermal alteration to form kaolinite requires hydration. Previous experimental study for isotope fractionation between kaolinite and water reported negative value for a temperature range of 0–300 °C (Gilg and Sheppard 1996), which indicates preferential uptake of δD-depleted hydrogen during the hydration. Therefore, the positive δD values of the pore fluid correlated with high Cl concentrations are

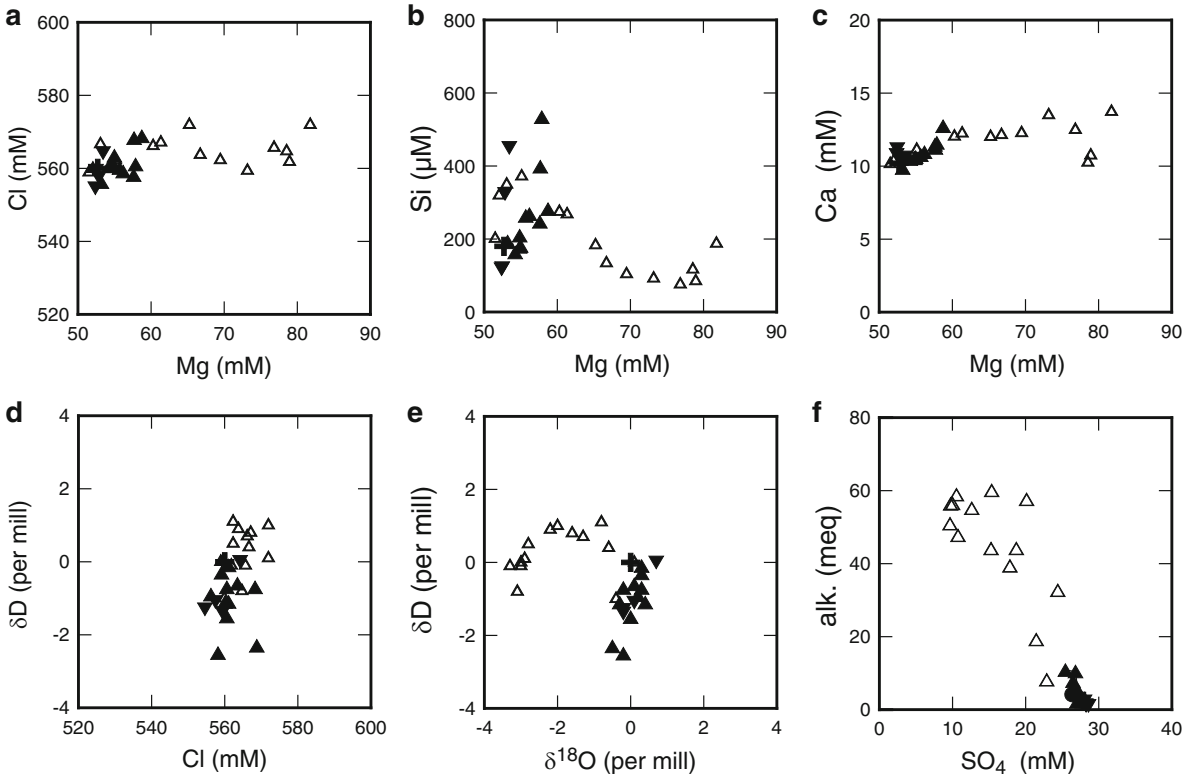

Fig. 42.7 Two components diagrams for pore fluid samples collected from the Jade field: (**a**) Cl vs Mg, (**b**) Si vs Mg, (**c**) Ca vs Mg, (**d**) δD vs Cl, (**e**) δD vs $\delta^{18}O$, and (**f**) alkalinity vs SO_4. Symbols and unit abbreviations are same as in Fig. 42.6

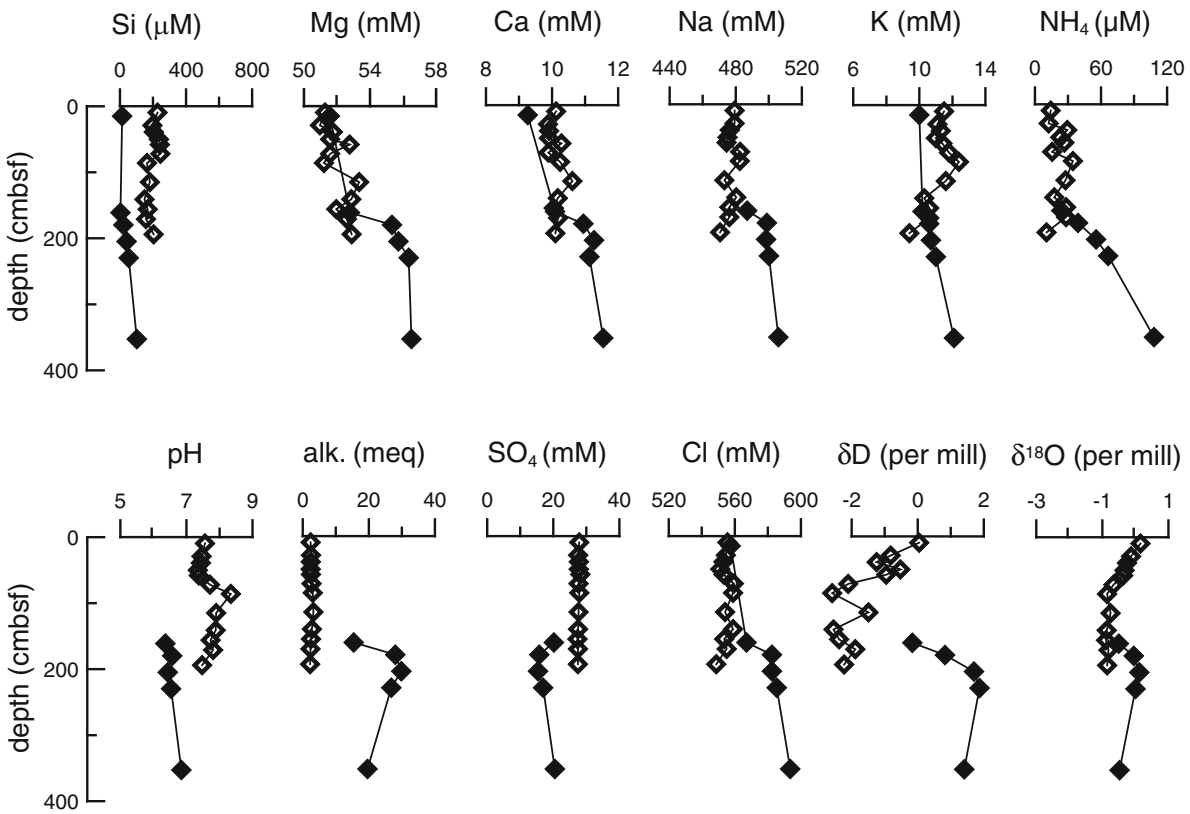

Fig. 42.8 Vertical profiles of pore fluid chemistry in the Iheya North Knoll field; *closed diamonds* represent Station BMS-I-4 and *open diamonds* represent Station LC-I-1. Units in the figure are abbreviated as follows; *cmbsf* cm below the seafloor, *mM* mmol/L, *meq* meq/L, *μM* μmol/L

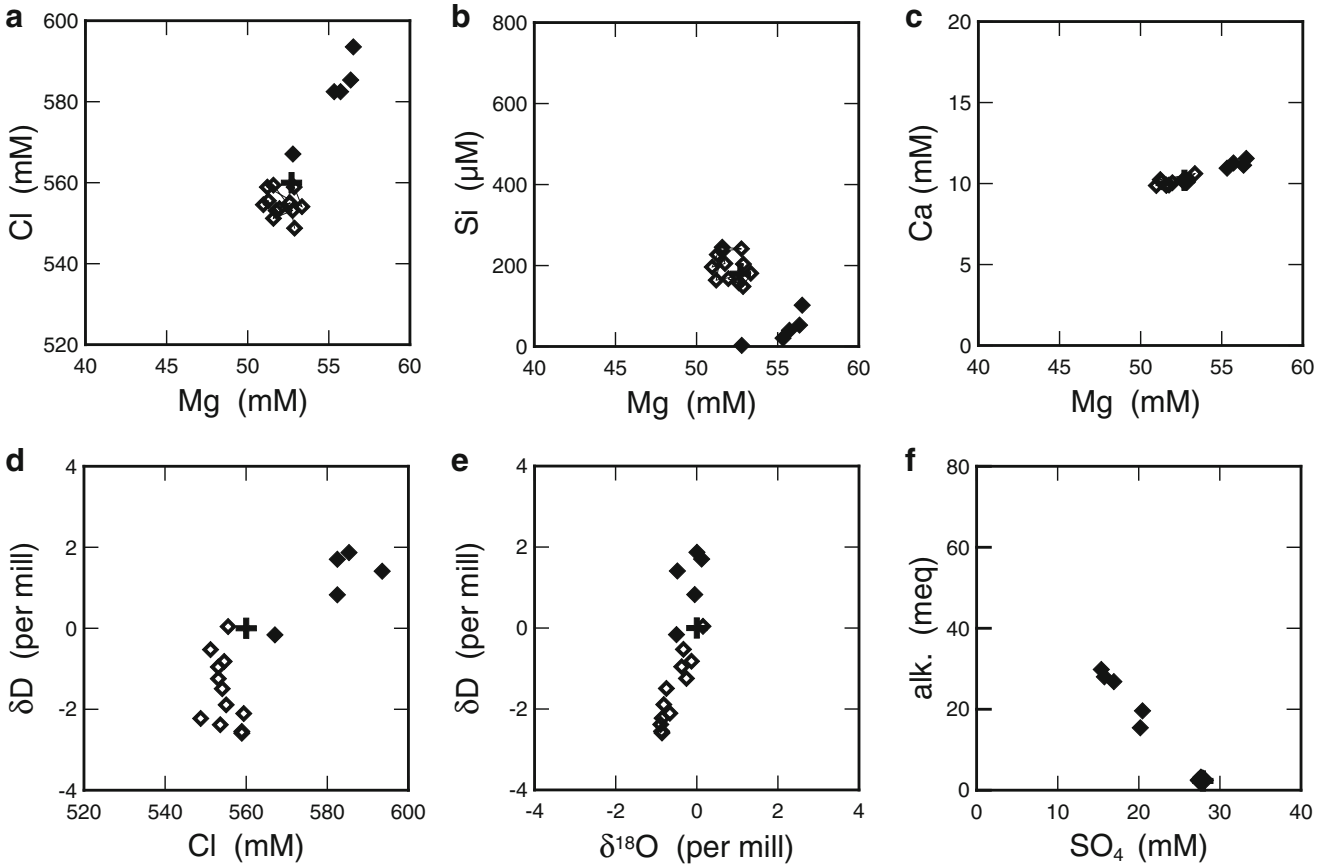

Fig. 42.9 Two components diagram for pore fluid samples in the Iheya North Knoll field: (**a**) Cl vs Mg, (**b**) Si vs Mg, (**c**) Ca vs Mg, (**d**) δD vs Cl, (**e**) δD vs $\delta^{18}O$, (**f**) alkalinity vs SO_4. Symbols and unit abbreviations are same as in Fig. 42.8

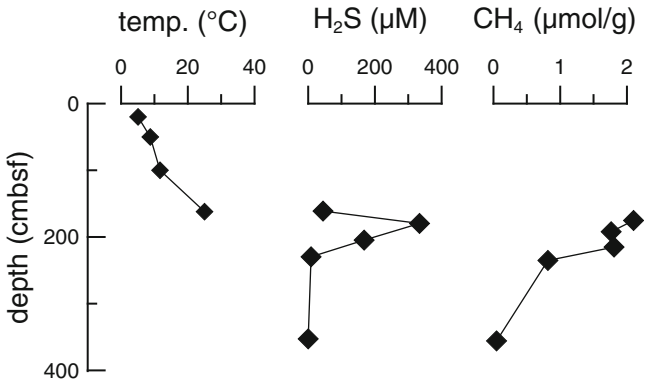

Fig. 42.10 Vertical profiles of borehole temperature, H_2S concentration in pore fluid, and CH_4 content in sediment, at Station BMS-I-4 in the Iheya North Knoll field. Units in the figure are abbreviated as follows; *cmbsf* cm below the seafloor, *μM* μmol/L. The unit of μmol/g for head space gas (CH_4) indicates 1 μmol of gas specie was extracted from 1 g of sediment in wet base

consistent with a result of the hydration reaction (Fig. 42.9). As another characteristic of the pore fluid, rather high contents of CH_4 and H_2S were detected at depths from 170 to 220 cmbsf, which is basically in accordance with observation of gas bubbling from the core samples after recovery. Enrichment in these gas species might be related to high gas concentrations in the hydrothermal fluid of the Iheya North Knoll field (Kawagucci et al. 2011). However, no evidence for input of the hydrothermal component was recognized among the major species (Fig. 42.9). Moreover, results of the borehole measurement suggested that in situ temperature in the corresponding depths is likely to be not so high but around a range from 30 to 60 °C (Fig. 42.10). On the other hand, slight decrease in SO_4 concentration coupled with increase in alkalinity is recognized at depths from 170 to 220 cmbsf, which suggests sulfate reduction reaction. Enrichment in H_2S in the pore fluid would be explained better as a result of production of the sulfate reduction. Since the slope between alkalinity increases to SO_4 decrease is estimated as 2, the enriched CH_4 in the corresponding layer is unlikely to act as the reductant.

Pore fluid chemistry at Station LC-I-1 showed basically no significant deviation from that of seawater (open diamonds in Fig. 42.8). On the other hand, correlated shift between δD and

$\delta^{18}O$ values is clearly recognized (Fig. 42.9). It is difficult to discuss which type of fluid interactions affects pore fluid chemistry based on this data set.

42.4 Summary

Shallow drilling provided us an opportunity to study geochemical environment just below the seafloor of an active hydrothermal field using core samples. Evidence for intense hydrothermal alteration was recognized obviously in three cores; collected from the BMS-I-4 in the Iheya North Knoll field, collected from the LC-J-2 and BMS-J-2 in the Jade field. Evidence for sulfide and sulfate mineralization was obvious in one core, collected from the BMS-H-1 in the Hakurei field. Pore fluid chemistry at Station BMS-I-4 showed coincident increase in many major species. This signature is attributed to hydration reaction during hydrothermal alteration to form kaolinite. Pore fluid chemistry at Station LC-J-2 showed monotonous linear profiles in many major species. This signature is attributed to as a result of dissolution of carbonate minerals in the hydrothermal alteration layer. Contrary to them, pore fluid chemistry at BMS-J-2 did not show substantial shifts in the vertical profile. Pore fluid chemistry at BMS-H-1 showed only slight shifts in the vertical profile which could not well correlated to hydrothermal alteration interactions. Moreover, evidence for involvement of the hydrothermal component into pore fluid was not clearly recognized in all the cores examined in this study.

Acknowledgements We are grateful to Captain Morio Endo and crew of R/V Hakurei-Maru No.2, also to the team leader Tadashi Sato and members of the BMS operation team for their professional skill and careful consideration for collecting core samples. This study was supported by the "TAIGA project," which was funded by a Grant-in-Aid for Scientific Research on Innovative Areas (#20109001-20109006) from the Ministry of Education, Culture, Sports, Science and Technology (MEXT), Japan.

References

Gieskes JM, Gamo T, Brumsack H (1991) Chemical methods for interstitial water analysis aboard JOIDES Resolution. ODP Tech Note, p 15

Gilg HA, Sheppard MF (1996) Hydrogen isotope fractionation between kaolinite and water revisited. Geochim Cosmochim Acta 60:529–533

Ishibashi J, Urabe T (1995) Hydrothermal activity related to arc-backarc magmatism in the Western Pacific. In: Taylor B (ed) Back-arc basin: tectonics and magmatism. Plenum, New York, pp 451–495

Kato Y (1987) Woody pumice generated with submarine eruption. J Geol Soc Jpn 98:11–20

Kawagucci S, Chiba H, Ishibashi J, Yamanaka T, Toki T, Muramatsu Y, Ueno Y, Makabe A, Inoue K, Yoshida N, Nakagawa S, Nunoura T, Takai K, Takahata N, Sano Y, Narita T, Teranishi G, Obata H, Gamo T (2011) Hydrothermal fluid geochemistry at the Iheya North field in the mid-Okinawa Trough: implication for origin of methane in subseafloor fluid circulation systems. Geochem J 45:109–124

Kawagucci S, Ueno Y, Takai K, Toki T, Ito M, Inoue K, Makabe A, Yoshida N, Muramatsu Y, Takahata N, Sano Y, Narita T, Teranishi G, Obata H, Nakagawa S, Nunoura T, Gamo T (2013) Geochemical origin of hydrothermal fluid methane in sediment-associated fields and its relevance to the geographical distribution of whole hydrothermal circulation. Chem Geol 339:213–225

Marumo K, Urabe T, Goto A, Takano Y, Nakaseama M (2008) Mineralogy and isotope geochemistry of active submarine hydrothermal field at Suiyo Seamount, Izu-Bonin Arc, West Pacific Ocean. Res Geol 58:220–248. doi:10.1111/j.1751-3928.2008.00059.x

Manheim FT, Sayles FL (1974) Composition and origin of interstitial waters of marine sediments, based on deep sea drill cores. In: Goldberg ED (ed) The sea, vol 5, Marine chemistry: the sedimentary cycle. Wiley, New York, pp 527–568

Nakaseama M, Ishibashi J-I, Ogawa K, Hamasaki H, Fujino K, Yamanaka T (2008) Fluid-sediment interaction in a marine shallow-water hydrothermal system in the Wakamiko submarine crater, south Kyushu, Japan. Res Geol 58:289–300. doi:10.1111/j.1751-3928.2008.00062.x

Sakai H, Gamo T, Kim E-S, Tsutsumi M, Tanaka T, Ishibashi J, Wakita H, Yamano M, Oomori T (1990) Venting of caron dioxide-rich fluid and hydrate formation in mid-Okinawa Trough Backarc Basin. Science 248:1093–1096

Takai K, Mottl MJ, Nielsen SH, The IODP Expedition 331 Scientists (2012) IODP Expedition 331: strong and expansive subseafloor hydrothermal activities in the Okinawa Trough. Sci Drill 13:19–27. doi:10.2204/iodp.sd.13.03.2011

Yamanaka T, Mizota C, Matsuyama-Serisawa K, Kakegawa T, Miyazaki J, Mampuku M, Tsutsumi H, Fujiwara Y (2008) Stable isotopic characterization of carbon, nitrogen and sulfur uptake of Acharax japonica from central Japan. Plankton Benthos Res 3:36–41

The Characteristics of the Seafloor Massive Sulfide Deposits at the Hakurei Site in the Izena Hole, the Middle Okinawa Trough

43

Ryoto Yoshizumi, Youko Miyoshi, and Jun-ichiro Ishibashi

Abstract

The seafloor massive sulfide (SMS) deposits, which were found in the Izena Hole, the middle Okinawa Trough, show two modes of occurrence, namely, large sulfide mounds on the seafloor and massive sulfide bodies beneath sediments. A 610-cm long sequence of alternating beds of sediment and ore layers was drilled to investigate the lower ore body, at high rates of core recovery (average 64 %), at the northern part of the Hakurei Site in the Izena Hole, the middle Okinawa Trough. Observation on polished sections of the core samples under reflection microscope indicates that the ores (18–166 cmbsf (cm below seafloor)) above the sediment layer (166–221 cmbsf) are porous and contain acicular barite and globular sphalerite with small barite inclusions. These textures are considered to have formed as a result of rapid cooling. On the other hand, ores (221–510 cmbsf) below the sediment layer (166–221 cmbsf) had a massive layer of sphalerite and galena on top (black ore), a middle layer of pyrite and chalcopyrite-rich layer (yellow ore) and a bottom layer of sphalerite and large barite.

Keywords

Hydrothermal activity • Okinawa Trough • Seafloor Massive Sulfide deposit • Sedimented rift

43.1 Introduction

Submarine hydrothermal activity in the middle Okinawa Trough was first discovered at the JADE site in the Izena Hole (Halbach et al. 1989). Although the numbers of seafloor massive sulfide (SMS) deposits found in arc-backarc systems are less numerous than those found in mid-ocean ridge systems, arc-backarc systems are associated with larger SMS deposits with higher concentrations of elements those are often enriched in epithermal environment associated with arc magmas (e.g., Au, Ag, Pb, As, Sb) (Ishibashi and Urabe 1995; Herzig and Hannington 1995, 2000; Urabe et al. 2009). SMS deposits in arc-backarc systems are generally considered as modern analogue for volcanogenic massive sulfide (VMS) deposits of arc-affinity which are represented by Kuroko type deposits (Halbach et al. 1989).

Most of SMS deposits around Japan are distributed along Okinawa Trough basin and Izu-Ogasawara Arc. SMS deposits in the Okinawa Trough contain, on average, high concentrations of Pb, Zn, Sb, As and Ag (Glasby and Notsu 2003). Deep-sea hydrothermal fields in the Okinawa Trough are unique among other back-arc basins in western and southwest Pacific because of the sedimented nature of the rifted basin. Recently, seafloor drilling during Integrated Ocean Drilling Program Expedition 331 revealed sulfide

R. Yoshizumi (✉)
Department of Earth and Planetary Science, Graduate School of Science, The University of Tokyo, 7-3-1 Hongo, Bunkyo-ku, Tokyo 113-0033, Japan
e-mail: yoshizumi@eps.s.u-tokyo.ac.jp

Y. Miyoshi • J.-i. Ishibashi
Department of Earth and Planetary Sciences, Graduate School of Science, Kyushu University, 6-10-1 Hakozaki, Higashi-ku, Fukuoka 812-8581, Japan

J.-i. Ishibashi et al. (eds.), *Subseafloor Biosphere Linked to Hydrothermal Systems: TAIGA Concept*,
DOI 10.1007/978-4-431-54865-2_43,

mineralization associated with hydrothermally altered sediment at two drilled sites, 100 and 450 m east of a hydrothermal mound at the Iheya-North hydrothermal filed in the Mid-Okinawa Trough (Takai et al. 2011; Yeats et al. 2012; Ishibashi et al. 2013; Yeats and Hollis 2013). As the existence of sulfide ores beneath the seafloor has been reported by METI (2011) at the Hakurei Site in the Izena Hole, we conducted drilling at the rim of a sulfide mound to obtain core material composed of sulfide ores between sediment layers.

43.2 Geological Setting

The Okinawa Trough, which is located in the west side of the Ryukyu arc, is back-arc basin that extends ~1,200 km from Kyushu to Taiwan island (Fig. 43.1a). According to Kimura (1990) and Sibuet et al. (1987), the Okinawa Trough has been formed by subduction of the Philippine Sea plate under the Eurasian continent since early Pleistocene (2–1.5 Ma).

The Izena Hole in the middle Okinawa Trough is located at about 110 km northwest from Okinawa Island (Figs. 43.1a, b). The water depth of the basin floor of the Izena Hole is ~1,600 m (Fig. 43.1b). Mud and pumice have been deposited in the Izena Hole since middle Pleistocene (0.9–0.4 Ma), based on biostratigraphic data from calcareous nannofossil in unconsolidated mud (Kato et al. 1989).

The central abyssal hill of the Izena Hole is formed from dacite, and it is known that heat flow at the bottom of the Izena Hole is high (Kato et al. 1989; Halbach et al. 1989). At the center of the Izena Hole (Hakurei Site), the SMS deposits have been found at the Hakurei Site. The Hakurei Site is divided into the north, center and south parts (METI 2011). The target field of this study is located in the north part of the Hakurei Site.

43.3 Material and Methods

43.3.1 Sampling

Drilling was conducted using the exploration vessel *Hakurei-Maru No.2* from May 31 to June 9, 2011 (Ishibashi et al., Chap. 42). According to METI (2011), the SMS deposits have been found in the north mound and underlying subseafloor. These ore deposits are separated by silt and pumice-rich sedimentary layer with a thickness of a few meters. As the shallow subseafloor deposits have been

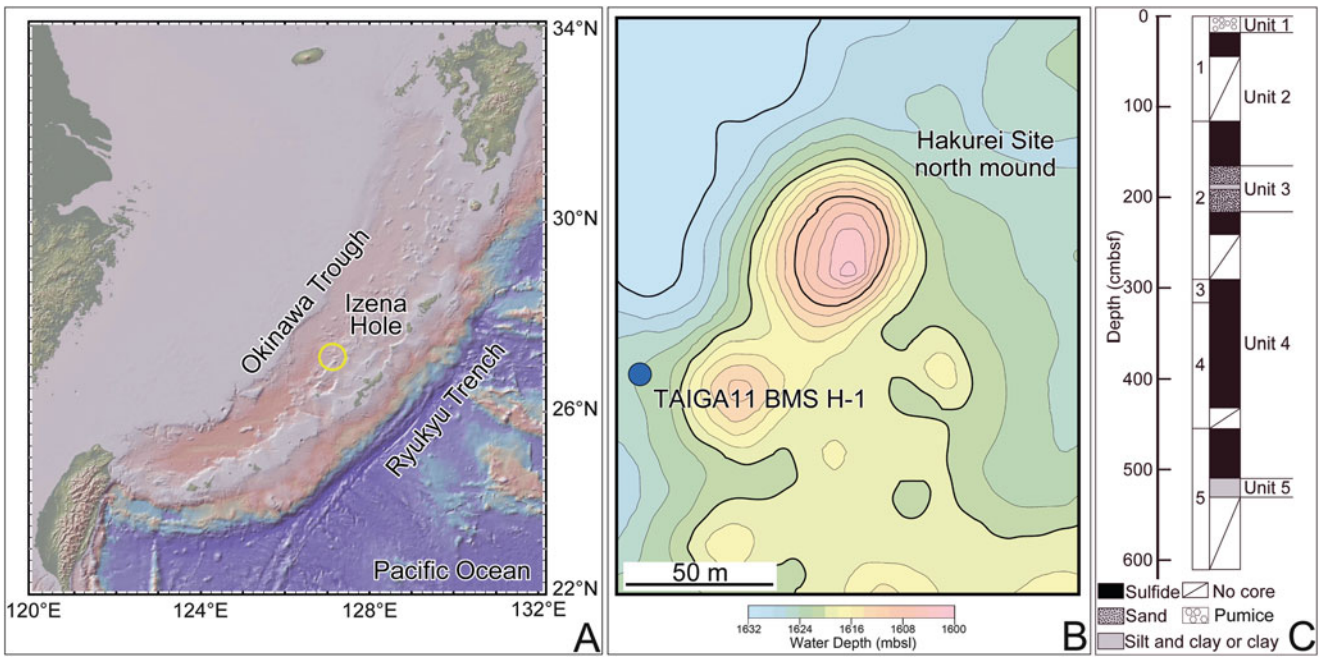

Fig. 43.1 Bathymetric maps of the drilling site and summary of drilled cores. (**a**) Location of the Izena Hole (*yellow circle*) in the Okinawa Trough in the northwest Pacific. (**b**) Bathymetric map of North mound of the Hakurei Site in the Izena Hole. The *blue circle* shows the location of the Hole TAIGA11 BMS H-1. (**c**) The core descriptions of TAIGA11 BMS H-1. *Numbers* of the left side of the column show the order of barrels used for drilling

poorly studied, we drilled at the rim of the mound (TAIGA11 BMS H-1) for researching the subseafloor deposits by Benthic Multi-coring System (BMS) with five core barrels with a length of 2 m. Each barrel was consecutively used to drill to obtain a 10-m long rock sequence. However, several core barrels were retrieved before full penetration. The depth of recovered core is estimated by the penetration depth of each core barrel. If the core length is shorter than the penetrated depth, the core depth was assigned by assuming that the recovered cores filled the core barrel from the top without any void space. The cores were cut into pieces and stored in plastic bags at room temperature after visual description on board.

43.3.2 Sample Preparation and Analytical Methods

For observations of mineral assemblages and textures, polished sections were prepared by embedding in epoxy resin and polishing with corundum powder and diamond paste. The images of the polished sections were obtained by an optical microscope (Nikon ECLIPSE E600POL E6TP-M61) and a CCD camera (Zeiss AxioCam MRc 5). The scanning electron microscope with energy-dispersive spectroscopy (Hitachi S4500) was used to analyze chemical compositions of mineral grains. An accelerating voltage of 15 kV was used for carbon-coated thin sections.

43.4 Results and Discussion

43.4.1 Brief Description of Core Materials

The drilling depth and recovery rate at the hole TAIGA11 BMS H-1 was 610 cm and about 64 %, respectively (Fig. 43.1c). The core column is divided into Unit 1–5 from those characteristics of sediments and ores (Fig. 43.1c). Unit 1 (0–18 cmbsf) was a 18-cm thick layer of dark brown pumice. Unit 2 (18–166 cmbsf) was composed of porous dark ores with metallic luster. Unit 3 (166–221 cmbsf) was a clayish sediment layer including sand-granule with a thickness of 55 cm. Unit 4 (221–510 cmbsf) was composed of massive ores, which color were changed from black to yellow and the black ore including white platy crystals. Unit 5 (510–520 cmbsf) was a 10-cm layer of gray clayish sediment.

43.4.2 Mineral Assemblages and Textures

Polished sections of cored ore sequences of Unit 2 (18–166 cmbsf) and Unit 4 (221–510 cmbsf) were observed every ~10 cm interval using a reflection microscope, according to Matsukuma (1989) for mineral identification. In addition, SEM observations coupled to EDS analysis were conducted to verify the mineral identification.

As for Unit 2 (18–166 cmbsf), pyrite/marcasite (cream color; FeS_2) and sphalerite (gray color; ZnS) were abundant and found to be porous as indicated by black epoxy area (Fig. 43.2a). There were the aggregation of small grains of barite (dark gray; $BaSO_4$) in sphalerite crystals (Fig. 43.2b). In addition, dendritic textures of tetrahedrite/tennatite (greenish gray; $Cu_{10}(Fe,Zn)_2(As,Sb)_4S_{13}$) were observed in sphalerite (Fig. 43.2c). As dendritic texture is generally known to form at low temperatures or under rapid cooling in sulfide chimneys (Ramdohr 1969; Ueno et al. 2003), dendritic tetrahedrite/tennatite might have formed under rapid cooling at the seafloor. As shown in Fig. 43.2d, the ore in bottom of Unit (116–166 cmbsf) was associated with pyrite/marcasite and acicular barite crystals.

On the other hand, as for Unit 4 (221–510 cmbsf), Fig. 43.2e–g shows sphalerite and galena (white; PbS) with the minor occurrence of chalcopyrite (yellow; $CuFeS_2$) and pyrite/marcasite in top of Unit4 (221-about 350 cmbsf), indicating that these ores were continuous. In addition, the minor occurrence of dendritic tetrahedrite/tennatite in sphalerite was found (Fig. 43.2g). Furthermore, sulfide ores of Unit 4 (221–510 cmbsf) were different from Unit 2 (18–166 cmbsf) in terms of low porosity and large grains of metal sulfides. From the middle of Unit 4 (about 350–454 cmbsf), colloform pyrite/marcasite became predominant (Fig. 43.2h). Toward the bottom, mineral assemblages were shifted to pyrite/marcasite and chalcopyrite rich ores relatively (Fig. 43.2i). The arrows in Fig. 43.2j pointed out the co-occurrence of colloform chalcopyrite and pyrite. Sulfide ores in bottom of Unit4 (454–510 cmbsf) were also massive, and large euhedral cystals of barite were observed to be different from barite crystals in Unit 2 (18–166 cmbsf) (Fig. 43.2k). From these peterologic characteristics, five units were assigned and shown in Fig. 43.1c.

The transition of mineral assemblage along depth from black to yellow ores, which was found in the investigated core, is one of main characteristics of the Kuroko type deposits in northeast Japan formed by submarine hydrothermal activity between 17 and 11 Ma (Ohmoto 1996). The cause of the spatial segregation of black to yellow ores in Kuroko type deposits remains to be poorly understood, because various geological processes including burial metamorphism and denudation might have significantly alter the original peteolorogic and geochemical signatures. It is therefore important to investigate the SMS deposits at the Hakurei Site as a modern analogue of Kuroko type deposits.

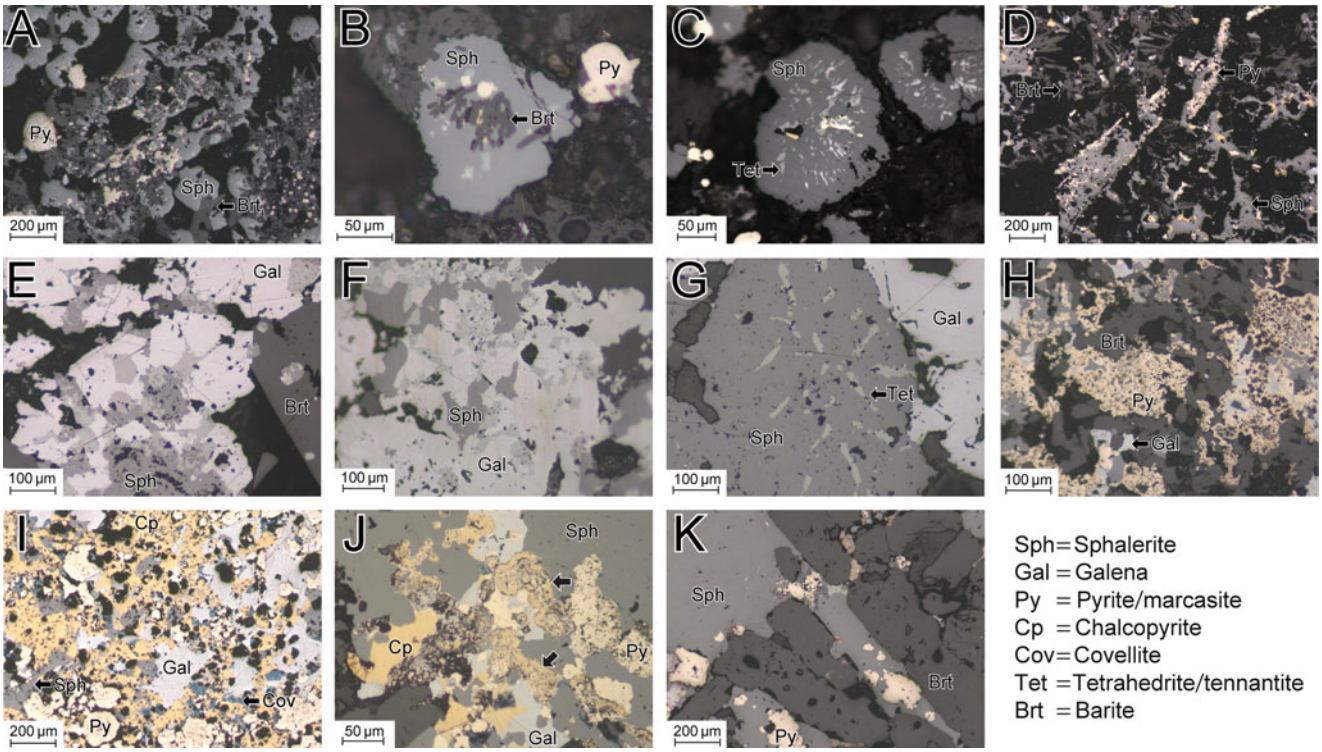

Fig. 43.2 Reflection microscopic images of TAIGA11 BMS H-1 cores. (**a**), (**b**) and (**c**) at 20 cmbsf, (**d**) at 147 cmbsf, (**e**) at 225 cmbsf, (**f**) at 324 cm, (**g**) at 352 cm, (**h**) at 369 cmbsf, (**i**) at 391 cmbsf, (**j**) at 400 cmbsf, and (**k**) at 496 cmbsf

Acknowledgment We are grateful to Captain Morio Endo and crew of R/V Hakurei-Maru No.2, also to the team leader Tadashi Sato and members of the BMS operation team for their professional skill and careful consideration for collecting core samples during TAIGA11 cruise. Earlier version of the manuscript was significantly improved by constructive comments from a reviewer, Prof. Yohey Suzuki. We appreciate his great effort and encouragement. This study constitutes a part of the master thesis of the first author (R. Y.). R. Y. expresses sincerely gratitude to Prof. Tetsuro Urabe who supervised R. Y.'s master course study. This study was partially supported by TAIGA project as a Scientific Research on Innovative Areas by grants-in-aid for scientific research from Ministry of Education, Culture, Sports, Science and Technology of Japan (no. 20109006).

References

Glasby G, Notsu K (2003) Submarine hydrothermal mineralization in the Okinawa Trough, SW of Japan: an overview. Ore Geol Rev 23 (3):299–339. doi:10.1016/j.oregeorev.2003.07.001

Halbach P, Nakamura K, Wahsner M, Lange J, Sakai H, Käselitz L, Hansen R-D, Yamano M, Post J, Prause B (1989) Probable modern analogue of Kuroko-type massive sulphide deposits in the Okinawa Trough back-arc basin. Nature 338(6215):496–499. doi:10.1038/338496a0

Herzig PM, Hannington MD (1995) Polymetallic massive sulfides at the modern seafloor: a review. Ore Geol Rev 10(2):95–115

Herzig PM, Hannington MD (2000) Polymetallic massive sulfides and gold mineralization at mid-ocean ridges and in subduction-related environments. Handbook of marine mineral deposits, pp 347–368

Ishibashi J, Urabe T (1995) Hydrothermal activity related to arc-backarc magmatism in the western Pacific. In: Backarc basins: tectonics and magmatism, pp 451–495

Ishibashi J, Miyoshi Y, Inoue H, Yeats C, Hollis SP, Corona JC, Bowden S, Yang SY, Southam G, Masaki Y, Hartnett H, IODP Expedition 331 Scientists (2013) Subseafloor structure of a submarine hydrothermal system within volcaniclastic sediments: a modern analogue for 'Kuroko-type' VMS deposits. In: Proceedings of the 12th Biennial SGA Meeting, 12–15 August 2013, Uppsala, Sweden, ISBN 978-91-7403-207-9, pp 542–544

Kato Y, Nakamura K, Iwabuchi Y, Hashimoto J, Kaneko Y (1989) Geology and topography in the Izena Hole of the Middle Okinawa Trough—the results of diving surveys in 1987 and 1988. JAMSTECTR Deep Sea Res 5:163–182

Kimura M (1990) Genesis and formation of the Okinawa Trough, Japan. Mem Geol Soc Jpn 34:77–88

Matsukuma T (1989) Ore microscopy of the Kuroko ores in Japan. Institute of Mining Geology, Akita University, 88 p

Ohmoto H (1996) Formation of volcanogenic massive sulfide deposits: the Kuroko perspective. Ore Geol Rev 10(3–6):135–177. doi:10.1016/0169-1368(95)00021-6

Ramdohr P (1969) The ore minerals and their intergrowths, 3rd edn. Pergamon, Oxford, English translation

Sibuet JC, Letouzey J, Barbier F, Charvet J, Foucher JP, Hilde TW, Kimura M, Chiao LY, Marsset B, Muller C (1987) Back arc extension in the, Okinawa Trough. J Geophys Res Solid Earth 92 (B13):14041–14063. doi:10.1029/JB092iB13p14041

Takai K, MJ. Mottl, SH. Nielsen, The Expedition 331 Scientists (2011) Proceedings of IODP, 331: Tokyo (Integrated Ocean Drilling Program Management International, Inc.). doi:10.2204/iodp.proc.331.2011

The Ministry of Economy, Trade and Industry (METI) (2011) Midterm report of the activity during the first stage of development program for seafloor hydrothermal deposits (in Japanese)

Ueno H, Hamasaki H, Murakawa Y, Kitazono S, Takeda T (2003) Ore and gangue minerals of sulfide chimneys from the North Knoll, Iheya Ridge, Okinawa Trough, Japan. JAMSTEC J Deep Sea Res 22:49–62

Urabe T, Iizasa K, Ishibashi J (2009) The latest frontiers of earth science and its application to mineral exploration (part 1) submarine hydrothermal deposits as modern analogy. Shigen Chishitsu 59(1):43–72 (in Japanese with English abstract)

Yeats C, Hollis SP (2013) Actively forming Kuroko-style massive sulfide mineralisation and hydrothermal alteration at Iheya North, Okinawa Trough. Goldschmidt 2013, Florence, Italy, 25th–30th August

Yeats C, Hollis S, Corona JC, Expedition 331 Shipboard Scientific Party (2012) Actively forming Kuroko-style massive sulfide mineralization and hydrothermal alteration at Iheya North, Okinawa Trough—key petrological results of IODP Expedition 331. Abstract, 34th International Geological Congress, Brisbane, August 5–10, 2012

Occurrence of Hydrothermal Alteration Minerals at the Jade Hydrothermal Field, in the Izena Hole, Mid-Okinawa Trough

44

Youko Miyoshi, Jun-ichiro Ishibashi, Kazuhiko Shimada, Mitsuhiro Ooki, Seiichiro Uehara, Ryoto Yoshizumi, Shota Watanabe, and Tetsuro Urabe

Abstract

Mineralogical and geochemical features of hydrothermal alteration minerals in the sediment cores from the Jade hydrothermal field in the Izena Hole, mid-Okinawa Trough, were studied by XRD, EPMA and TEM-EDS analyses. A core sample 1186MBL collected from the surface sediment near the sulfide chimney venting high temperature fluid up to 320 °C was characterized by occurrence of kaolinite, with sulfide minerals such as sphalerite and galena. The kaolinite would be related to be formed under acidic condition caused by oxidation and dissolution of the sulfide minerals by penetrating seawater. Core samples (1188MB, 1193MB) were collected from the surface sediment in the vicinity of clear hydrothermal fluid venting of ~100 °C, which is located in 400 m distant from the sulfide chimney. In these cores, occurrence of chlorite and smectite was identified. The chlorite in the core 1188MB had chemical composition close to Al-rich chlorite which is classified as sudoite, although chlorite found in other hydrothermal fields in the Okinawa Trough is characterized as significantly Mg-rich chlorite. Core samples of up to 4–6 m length were also collected near the low temperature fluid venting to study alteration in deep layers. One of two long core samples (BMS-J-2) was characterized by chlorite and illite assemblage below 380 cmbsf, while the other (LC-J-2) was characterized by abundant occurrence of K-feldspar below 300 cmbsf. Occurrence of euhedral crystals of K-feldspar in size up to several tens μm suggests the formation by precipitation from high temperature fluid.

Keywords

Clay mineral • Electron probe micro-analyzer (EPMA) • Okinawa Trough • Transmission electron microscope (TEM-EDS) • X-ray diffraction (XRD)

The online version of this chapter (doi:10.1007/978-4-431-54865-2_44) contains supplementary material, which is available to authorized users.

Y. Miyoshi (✉)
Graduate School of Sciences, Kyushu University, 6-10-1 Hakozaki, Higashi-ku, Fukuoka 812-8581, Japan

Present address: Institute for Geo-Resources and Environment, National institute of Advanced Industrial Science and Technology (AIST), Central-7, 1-1-1 Higashi, Tsukuba, Ibaraki 305-8567, Japan
e-mail: youko-miyoshi@aist.go.jp

J.-i. Ishibashi • K. Shimada • M. Ooki • S. Uehara
Graduate School of Sciences, Kyushu University, 6-10-1 Hakozaki, Higashi-ku, Fukuoka 812-8581, Japan

R. Yoshizumi • T. Urabe
Graduate School of Science, The University of Tokyo, 7-3-1 Hongo, Bunkyo-ku, Tokyo 113-0033, Japan

S. Watanabe
Graduate School of Life and Environmental Sciences, University of Tsukuba, 1-1-1 Ten-noudai, Tsukuba, Ibaraki 305-8572, Japan

J.-i. Ishibashi et al. (eds.), *Subseafloor Biosphere Linked to Hydrothermal Systems: TAIGA Concept*,
DOI 10.1007/978-4-431-54865-2_44,

44.1 Introduction

Most of active hydrothermal fields in the Okinawa Trough are located in sediment-rich environment (Ishibashi et al., Chap. 29), where extensive hydrothermal alteration is expected to occur as a result of subseafloor fluid-sediment interactions. Marumo and Hattori (1999) documented occurrence of diverse hydrothermal alteration minerals in sediment collected from the Jade field in the mid-Okinawa Trough. Miyoshi (2013) studied geochemical and mineralogical features of hydrothermal alteration minerals in sediment cores obtained by drilling during IODP (Integrated Ocean Drilling Program) Expedition 331 at the Iheya North Knoll field in the mid-Okinawa Trough (Takai et al., 2011). Results of this study suggested layered structure of distinctive alteration zones consisted of various clay minerals.

In this chapter, we report results of mineralogical and geochemical analyses of hydrothermal alteration minerals in sediment collected from the Jade field of the Izena Hole, in the mid-Okinawa Trough (Fig. 44.1a). Recent dive studies documented two different types of hydrothermal fluid venting in the Jade field (Ishibashi et al., 2014). While vigorous venting of high temperature fluid up to 320 °C from sulfide chimneys is observed at water depth of ~1,350 m, diffusive venting of clear hydrothermal fluid of ~100 °C is located at water depth of ~1,550 m. A geochemical study revealed distinctive fluid chemistry between the high temperature fluid and low temperature fluid (Ishibashi et al., 2014). Since mineralogy of hydrothermal alteration minerals reflects physical and chemical conditions of their formation, different types of hydrothermal mineralogy is expected to be identified in sediment collected from the seafloor around these two vent sites. And comparison of their mineralogy would provide important clues to discuss chemical environment within sediment near active vent sites.

44.2 Geological Background

The Jade field is located on a slope of a north-eastern wall of the Izena Hole (Fig. 44.1a). Hydrothermal activity was recognized in an area of 500 m × 300 m at water depth between 1,300 and 1,550 m (Fig. 44.1b). At water depth of ~1,350 m, vigorous venting of high temperature fluid from sulfide chimneys and spires was recognized (Sakai et al., 1990a). A tall sulfide chimney venting the highest temperature fluid in Jade site (=320 °C) was named as Black Smoker Chimney (or TBS Chimney). Active and inactive chimneys are likely to align along NE–SW direction on the slope. At ~150 m northeast from the Black Smoker Chimney, an active sulfide chimney venting clear fluid of 60–70 °C is recognized at water depth of ~1,320 m, which was called as Red Star Chimney. At extension of the alignment in the southwest direction at water depth of ~1,500 m, diffusive venting of clear hydrothermal fluid from a small depression on the seafloor was located, which was called as Biwako Vent (Ishibashi et al., 2014). Temperature of the Biwako Vent fluid was 90 ~ 104 °C. Around the Biwako Vent, emanation of liquid CO_2 bubble was observed in several sites, one of which was reported in Sakai et al. (1990b). Extensive distribution of consolidated sediment containing amorphous silica and native sulfur was recognized also in the vicinity of the Biwako Vent, which was called as Sulfur Reef site.

A previous study documented distinctive fluid chemistry between these venting fluids (Ishibashi et al., 2014). High temperature fluid venting from the Black Smoker Chimney showed slightly higher Cl concentration than that of seawater. And fluid temperature of 320 °C is close to the boiling point at the seafloor depth. Based on the physical and chemical property, the Black Smoker Chimney fluid is considered the mainstream of focused upflow that has undergone slight loss of the vapor phase after the subseafloor phase separation (Ishibashi et al., 2014). Chemical composition of low temperature fluid obtained from the Red Star Chimney was explained by mixing between the hydrothermal component shared with the Black Smoker Chimney fluid and seawater, prior to venting from the seafloor. On the other hand, low temperature fluid venting from the Biwako Vent showed significantly low Cl concentration that is about one thirds of seawater level. Together with notably high H_2S concentration, fluid chemistry of the Biwako Vent is attributed to be originated from the vapor phase segregated during subseafloor phase separation.

Different features between these two areas are notable not only in fluid chemistry but also in appearance of the seafloor surrounding the vent sites (Ishibashi et al., 2014). Abundant sulfide breccia and particles likely formed by collapse of inactive chimneys are recognized on the seafloor around the Black Smoker Chimney and the Red Star Chimney. Contrarily, white patches in sediment implying hydrothermal alteration are notable as well as consolidated sediment crusts on the seafloor in the area around the Biwako Vent. Other than hydrothermal active areas, most part of the seafloor in the Jade field is covered with tuff breccia and woody pumice.

44.3 Materials and Method

44.3.1 Sample Collection

Sediment cores were collected by an acrylic push corer (MBARI-type corer) attached to remotely operated vehicle (ROV) Hyper-Dolphin, which aimed to collect surface sediment up to ~30 cmbsf (centimeters below the seafloor)

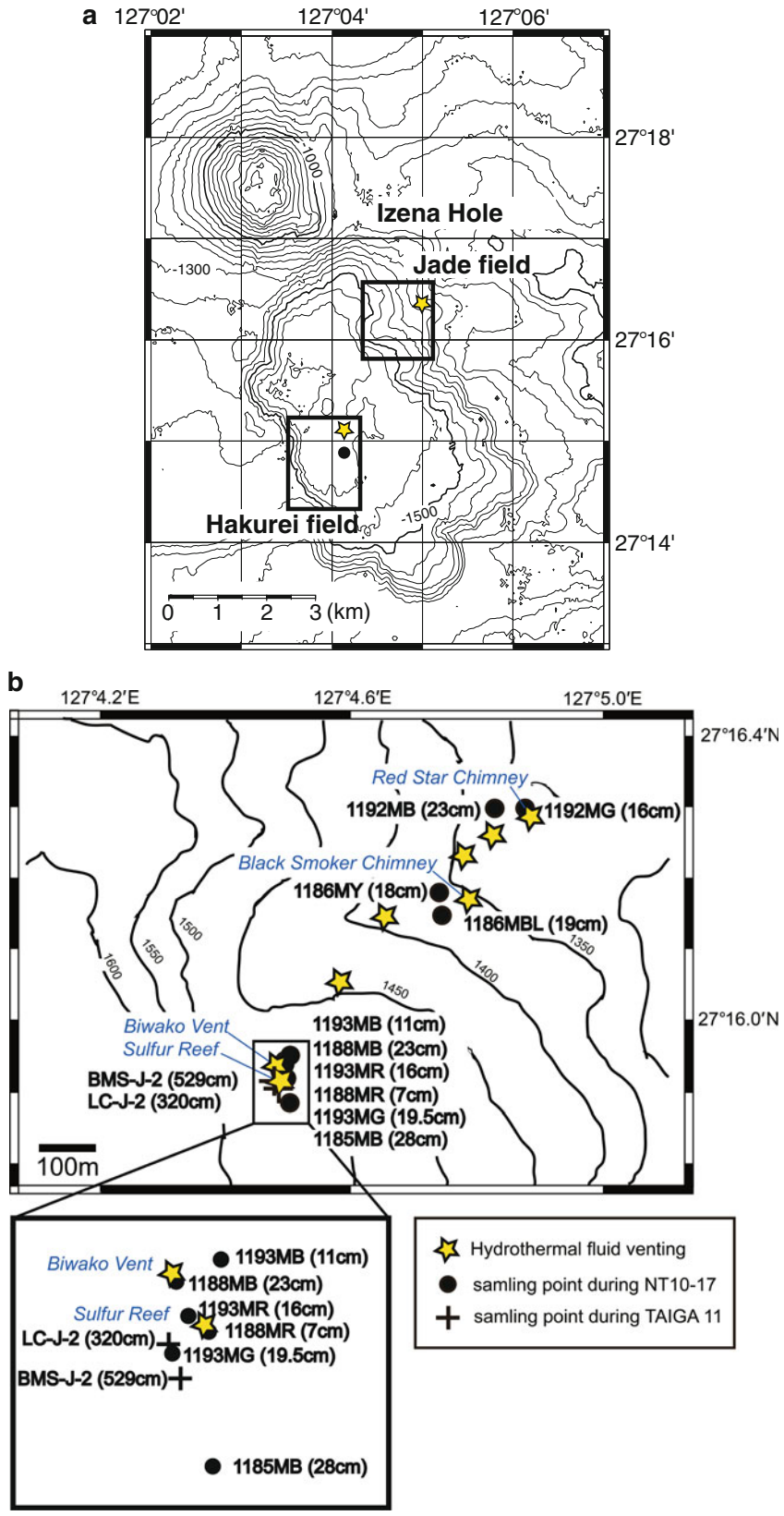

Fig. 44.1 Bathymetric map of (**a**) the Izena Hole and (**b**) Jade field. The upper *box* in (**a**) indicates area shown in (**b**). The *yellow star marks* represent active hydrothermal vent. The *closed circles* and *cross marks* represent the localities of short cores during the NT10-17 cruise, and of long cores during the TAIGA11 cruise

Table 44.1 List of sediment core samples for this study, collected during the NT10-17 cruise and TAIGA11 cruise

Core ID	Latitude	Longitude	Depth (m)	Sampling location
NT10-17				
1185MB	27° 15.885′ N	127° 4.503′ E	1,554	~50 m south of the Sulfur Reef site
1186MY	27° 16.182′ N	127° 4.741′ E	1,357	~50 m west of the Black Smoker Chimney
1186MBL[a]	27° 16.150′ N	127° 4.745′ E	1,376	~50 m southwest of the Black Smoker Chimney
1187MB	27° 14.928′ N	127° 4.148′ E	1,603	~30 m south of the Dragon Chimney in the Hakurei field
1188MR	27° 15.928′ N	127° 4.502′ E	1,523	At the Sulfur Reef
1188MB[a]	27° 15.944′ N	127° 4.494′ E	1,520	Adjacent to the Biwako Vent
1192MB	27° 16.299′ N	127° 4.829′ E	1,312	~50 m west of the Red Star Chimney
1192MG	27° 16.299′ N	127° 4.877′ E	1,306	A few meters distant from the Red Star Chimney (1)
1193MG	27° 15.921′ N	127° 4.493′ E	1,543	At the Sulfur Reef (2)
1193MR	27° 15.933′ N	127° 4.497′ E	1,537	At the Sulfur Reef (3)
1193MB[a]	27° 15.951′ N	127° 4.505′ E	1,521	Adjacent to the CO_2 bubbling site (4)
TAIGA11				
BMS-J-2[a]	27° 15.913′ N	127° 4.495′ E	1,520	~80 m south of the Biwako Vent
LC-J-2[a]	27° 15.924′ N	127° 4.492′ E	1,570	Near the Biwako Vent (5)

[a]These cores were examined in detail by this study, because hydrothermally altered mud was observed in these cores
(1) Native sulfur filling fissures in the sediment was observed
(2) Core sampling was attempted to collect consolidated sediment, but only overlaying sediment was collected
(3) Core sampling was attempted after the consolidated sediment crust was broken by a manupilator
(4) When the corer pulled out, liquid CO_2 bubble was emanated from the seafloor
(5) The sampling locality was determined by navigation of the surface ship

without any disturbance. Hereafter, this type of core is called as a short core. Short core sampling was conducted during the NT10-17 cruise of R/V Natsushima (Japan Agency for Marine-Earth Science and Technology (JAMSTEC)) in September 2010. In total 11 short cores were collected during the cruise, as summarized in Table 44.1. Sampling localities are shown with bathymetric maps in Fig. 44.1b. Two short cores (1186MBL and 1186MY) were collected near the Black Smoker Chimney, two short cores (1192MB and 1192MG) near the Red Star Chimney, six short cores (1185MB, 1188MR, 1188MB, 1193MR, 1193MG and 1193MB) around the Sulfur Reef and Biwako Vent. One additional short core (1187MB) was collected from the seafloor near the Dragon Chimney in the Hakurei field, which is located at ~3 km southwest of the Jade filed and on the basin seafloor of the Izena Hole (Fig. 44.1a).

Another type of coring operation was conducted using a Benthic Multi-coring System (BMS) and a large-diameter gravity corer (LC). As described in Ishibashi et al. (Chap. 31), these coring apparatus enabled us to collect sediment from the surface to 4–6 mbsf (meters below the seafloor), although the sampling sometimes suffered from poor recovery. Hereafter, this type of core is called as a long core. Coring operations with a BMS and LC were conducted during the TAIGA11 cruise of the R/V Hakurei-Maru No. 2 (Japan Oil, Gas and Metals National Corporation (JOGMEC)) in May to June 2011 (Ishibashi et al., Chap. 31). In the Jade field, coring was attempted at four stations (BMS-J-2, BMS-J-3A, BMS-J-3B, and LC-J-2). In this study, the core samples from BMS-J-2 and LC-J-2 were studied because of their good recovery.

44.3.2 Sample Analysis

Sediment subsamples were collected from the obtained cores at 5 to 10 cm intervals. During the expeditions, they were refrigerated. After return to the laboratory, some of the sediment samples were disaggregated in distilled water. After they settled out, they were disaggregated in new distilled water again. The work was repeated several times to remove dissolved salts. Clay fractions (<2 μm) were collected from suspending particles in the distilled water after leaving 5 hours according to the Stokes' law.

Minerals in the sediment samples obtained by NT10-17 expedition were identified by X-ray diffraction (XRD), Rigaku RAD II A, at the Department of Earth and Planetary Sciences, Kyushu University. The XRD was conducted at 30 kV and 15 mA using Ni-filtered Cu-Kα ($\lambda = 1.5418$ Å) radiation. Step scan XRD data (2–64° 2θ, 0.05° 2θ step width, 1.0 s/step) were collected for bulk sediment samples. Step-scan XRD data (2–32° 2θ, 0.05° 2θ step width, 1.0 s/step) were collected for clay fraction samples, under air-dried, ethylene glycol-saturated and HCl treated conditions. Minerals in the sediment samples obtained by TAIGA 11 expedition were identified by X-ray diffraction (XRD), M18XHF22-SRA, MXP18 (BRUKER axs), at the Department of Earth and Planetary Sciences, Kyushu University. The XRD was conducted at 40 kV and 100 or 50 mA using Ni-filtered Cu-Kα ($\lambda = 1.54056$ Å) radiation. Step scan XRD data (2–64° 2θ, 0.05° 2θ step width, 0.5 or 1.0 s/step) were collected for bulk sediment samples. Step-scan XRD data (2–32° 2θ, 0.05° 2θ step width, 0.5 or

Table 44.2 Visual core descriptions of the short core samples, (a) 1186MBL, (b) 1188MB, and (c) 1193MB

Core ID	Core length (cm)	Depth (cmbsf)	Visual description of the core
(a)			
1186MBL	19	0–2	
		2–4	Pumice
		4–9	Sulfur grains, sulfide grains, pumice
		9–15	Sulfur grains, pumice
		15–17	
		17–19	Sulfur lump of pipe-like shape
(b)			
1188MB	23	0–2	Upper layer: unaltered sand sediment Lower layer: white gray colored hydrothermal altered mud
		2–23	White gray colored hydrothermal altered mud
(c)			
1193MB	11	0–4	
		4–7	Pumice
		7–9	Whitish mud, sulfur grains
		9–11	Whitish mud, sulfur grains

1.0 s/step) were collected for clay fraction samples, under air-dried and ethylene glycol-saturated conditions.

Morphology and chemical composition of clay mineral particles were determined using a transmission electron microscope (TEM) equipped with an energy dispersive spectrometer (EDS), JEOL JEM-2010FEF, in the Research Laboratory for High Voltage Electron Microscopy (HVEM), Kyushu University. The TEM (JEOL JEM-2010FEF) was operated at an accelerating voltage of 200 kV. Samples for TEM-EDS analysis were prepared by settling on a carbon-coated copper grid after ultrasonic dispersion of powdered clay fractions in alcohol. To analyze chemical composition, clay mineral particles without overlapping were selected under the TEM observation.

Sediment samples were observed and analyzed using an electron probe micro-analyzer (EPMA), JEOL JXA-8530F, at the Department of Earth and Planetary Sciences, Kyushu University. Determination of chemical composition of minerals in the samples was done by a wavelength dispersive spectrometer (WDS) attached to the EPMA. For this measurement, the samples were fixed with resin onto a thin section and polished.

44.4 Results and Discussion

44.4.1 Lithology and Mineralogy of the Sediment Cores

Three short core samples were selected for detailed mineralogical and geochemical analysis, because hydrothermal alteration minerals were dominantly identified by preliminary XRD analysis. Lithological features for the selected three cores (1186MBL, 1188MB, and 1193MB) are given in Table 44.2. Lithological features for other cores are reported in Supplementary file (Suppl. 44.1). Mineral assemblages of the selected three cores determined by XRD analysis are given in Tables 44.3, 44.4, and 44.5, and illustrated in Fig. 44.2. Results of the preliminary XRD analysis for other cores are reported in Supplementary file (Suppl. 44.2).

Mineral assemblages determined by XRD analysis for the two long cores (BMS-J-2 and LC-J-2) are given in Tables 44.6 and 44.7, and illustrated together with visual core description in Figs. 44.3 and 44.4. Sediment core BMS-J-2 can be divided into two units according to the lithology (Fig. 44.3). Unit I (0–380 cmbsf) was silt and clay-sized and olive black colored sediment and contained small-sized pumice (1–10 mm) occasionally. Unit II (380–424 cmbsf) was gray colored sediment which was hydrothermally altered mud and contained granular size of native sulfur crystals occasionally. Sediment core LC-J-2 core can be divided into two units according to the lithology (Fig. 44.4). Unit I (0–300 cmbsf) was silt and clay-sized and olive black colored sediments and contained small-sized pumice (1–10 mm) occasionally. Terrigenous plant debris was observed occasionally between 100–200 cmbsf. Hydrothermally altered pumice was observed at 53, 58, 80, 200, 230, 248 and 250 cmbsf, and native sulfur vein was observed in 25.5, 71.5, 92 and 97 cmbsf. Unit II (300–320 cmbsf) was grayish white colored sediments which was hydrothermal altered mud.

44.4.2 Occurrence of Hydrothermal Alteration Minerals in the Surface Sediment Near the High Temperature Fluid Venting Site

The 1186MBL core was collected from the seafloor 50 m distant from the Black Smoker Chimney. The sediment core of 19 cm in length was mostly composed of hydrothermally altered mud. Sulfide minerals and native sulfur grains were commonly observed in 0–17 cmbsf, and a native

Table 44.3 Mineral assemblage of the short core samples: 1186MBL

		Bulk mineralogy							Clay mineralogy		
Core ID	Depth (cmbsf)	Q	Pl	Py	Ba	Ga	Sp	S	Sm	Kao	I
1186MBL	2–4	XX		XX	XX	XX	XX		n.a.	n.a.	n.a.
	4–6	XX		XX	XX	XX	XX		XX	XXX	XX
	6–9	XX						XX	n.a.	n.a.	n.a.
	11–13	XX		XX				XX	n.a.	n.a.	n.a.
	15–17	XX		XX				XX	XX	XXX	XXX
	17–19	XX		XX				XX	n.a.	n.a.	n.a.
Sulfur lump collected from 17–19 cmbsf	#1 (black)	XX	XX					XXX	n.a.	n.a.	n.a.
	#2 (gray)							XXX	n.a.	n.a.	n.a.
	#3 (gray)							XXX	n.a.	n.a.	n.a.
	#4 (gray)							XXX	n.a.	n.a.	n.a.
	#5 (gray)							XXX	n.a.	n.a.	n.a.
	#6 (yellow)							XXX	n.a.	n.a.	n.a.

A sulfur lump found in the core at 17–19 cmbsf was divided into six pieces, from #1 (outside) to #6 (inside), and they are provided for XRD analysis
XXX: abundant, XX: common, X: minor
Q quartz, *Pl* plagioclase, *Py* pyrite, *Ba* barite, *Ga* galena, *Sp* sphalerite, *S* native sulfur, *Sm* smectite, *Kao* kaolinite, *I* illite
n.a. not analyzed

Table 44.4 Mineral assemblage of the short core samples: 1188MB

		Bulk mineralogy		Clay mineralogy		
Core ID	Depth (cmbsf)	Q	S	Sm	Chl	I
1188MB	2–4	XXX	XX	n.a.	n.a.	n.a.
	6–8	XXX	XXX	n.a.	n.a.	n.a.
	11–14	XXX	XXX	XX	XXX	XX
	17–20	XXX	XXX	n.a.	n.a.	n.a.

XXX: abundant, XX: common, X: minor
Q quartz, *S* native sulfur, *Sm* smectite, *Chl* chlorite, *I* illite
n.a. not analyzed

Table 44.5 Mineral assemblage of the short core samples: 1193MB

		Bulk mineralogy					Clay mineralogy		
Core ID	Depth (cmbsf)	Q	Pl	Py	Ba	S	Sm	Chl	I
1193MB	3–5	XXX	X	XX	XX	XX	n.a.	n.a.	n.a.
	7–9	XXX	X	XX	XX	XX	XXX	XX	XX

XXX: abundant, XX: common, X: minor
Q quartz, *Pl* plagioclase, *Py* pyrite, *Ba* barite, *S* native sulfur, *Sm* smectite, *Chl* chlorite, *I* illite
n.a. not analyzed

sulfur lump of pipe-like shape was found in 17–19 cmbsf. Kaolinite, smectite and illite were identified in the hydrothermally altered mud by XRD analysis (Fig. 44.5a). Quartz, sphalerite, galena, barite and pyrite were identified in 0–6 cmbsf, and quartz, native sulfur and pyrite was identified in 6–17 cmbsf.

Kaolinite is not a common alteration mineral found ubiquitously in seafloor hydrothermal fields. Formation of kaolinite requires acidic environment, but pH buffer potential of seawater would inhibit such environment in the surface sediment. Marumo and Hattori (1999) documented occurrence of kaolinite in the Jade field, and proposed that the surface sediment was associated with acid pore fluids related to oxidation of hydrothermal H_2S to H_2SO_4. Indeed, pore fluid of the 1186MBL core showed characteristic low pH (pH = 4.2–4.9) below 6 cmbsf, while the pore fluid above that layer showed pH of seawater level (pH = 7.0–7.6) (Yokoyama et al., Chap. 36). Yokoyama et al. (Chap. 36) proposed that this acidity is related to oxidization and dissolution of sulfide chimney fragments by penetrating seawater rather than oxidation of dissolved H_2S. This idea would be supported by observation that the drastic decrease of pore fluid pH below 6 cmbsf corresponds to disappearance of sphalerite and galena both are dominant minerals of sulfide chimneys.

44.4.3 Occurrence of Hydrothermal Alteration Minerals in the Surface Sediment Around the Low Temperature Vapor-Rich Fluid Venting Site

The 1188MB core was collected in adjacent to the Biwako Vent. The sediment core of 23 cm in length was mostly composed of white gray colored hydrothermally altered mud. Quartz and native sulfur were identified by XRD analysis of bulk samples, and chlorite, smectite, and illite were identified in the clay fraction (Fig. 44.5b). The 1193MB core was collected from the seafloor where emanation of liquid CO_2 bubbling was observed in the vicinity of the Biwako Vent. During ROV return to the sea surface, vigorous bubbling from the corer inside was monitored, which is attributed to decomposition of CO_2 hydrate in the sediment as reported by Sakai et al. (1990b). In the sediment core of 11 cm in length, hydrothermally altered mud of

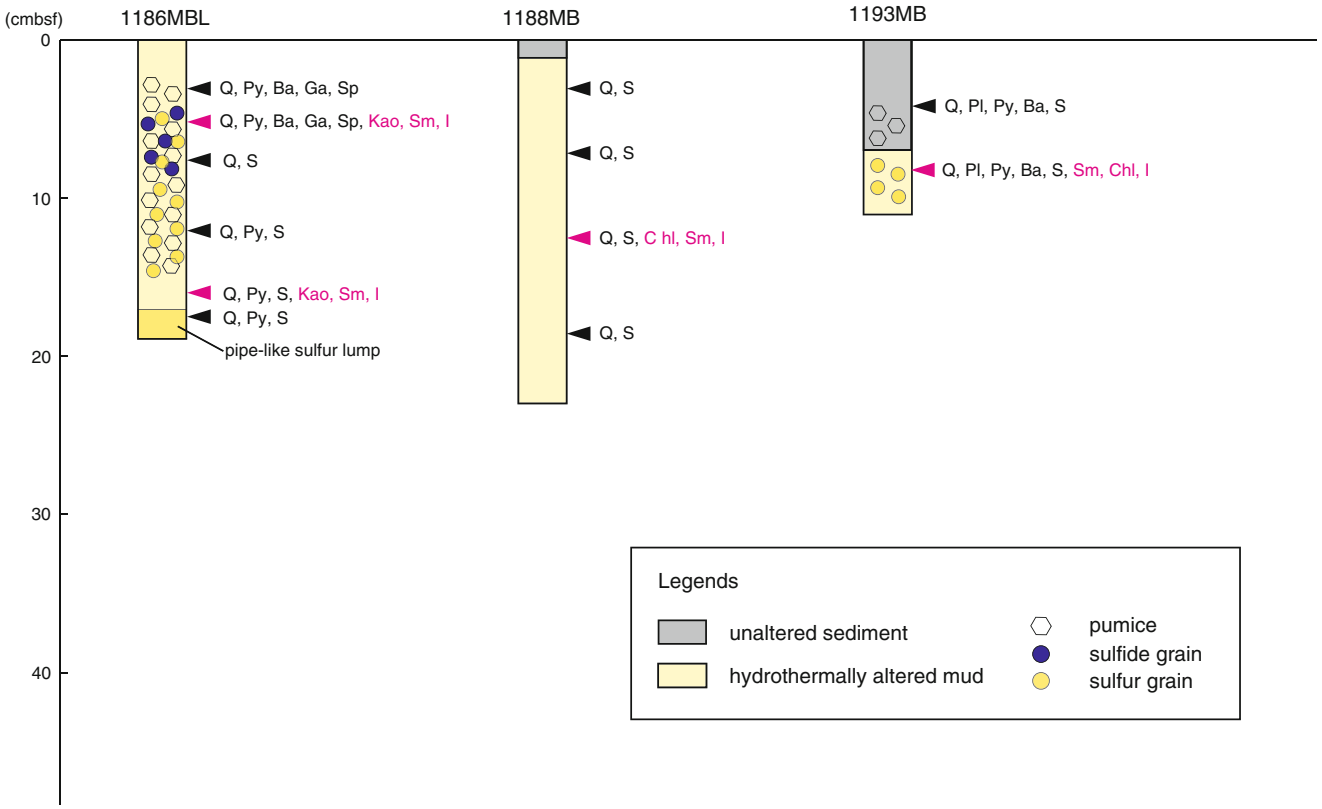

Fig. 44.2 Visual core description and mineral assemblage of the short cores 1186MBL, 1188MB and 1193MB. Abbreviations for minerals are *Q* quartz, *Pl* plagioclase, *Py* pyrite, *Ba* barite, *Ga* galena, *Sp* sphalerite, *S* native sulfur, *Kao* kaolinite, *Sm* smectite, *I* illite, *Chl* chlorite (Clay minerals are highlighted by *red color text*)

Table 44.6 Mineral assemblage of the BMS-J-2 core

	Bulk mineralogy					Clay mineralogy		
Depth (cmbsf)	Q	Cr	Pl	Py	S	Sm	Chl	I
78	XXX	X	X			n.a.	n.a.	n.a.
193.4	XXX		X			n.a.	n.a.	n.a.
203.9	XXX					n.a.	n.a.	n.a.
221.9	XXX			XX		n.a.	n.a.	n.a.
239.9	XXX		X	X		n.a.	n.a.	n.a.
306.5	XXX	X	X			n.a.	n.a.	n.a.
353.7	XXX					n.a.	n.a.	n.a.
363.7	XXX	X	X	X		XXX	XX	XX
380.7	XXX			X		X	XXX	XX
382.7	XXX							
385.7	XXX					X	XXX	XX
390.7	XXX			X				
401.7	XXX			XX		X	XXX	XX
404.7	XXX			XX				
416.7	XXX				XX		XXX	XX

XXX: abundant, XX: common, X: minor
Q quartz, *Cr* cristobalite, *Pl* plagioclase, *Py* pyrite, *S* native sulfur, *Sm* smectite, *Chl* chlorote, *I* illite
n.a. not analyzed

whitish color was recognized in 7–9 cmbsf. The hydrothermally altered mud was whitish mud including native sulfur grains. Barite, native sulfur, pyrite, quartz and plagioclase were identified by XRD analysis of bulk samples, and smectite, chlorite and illite were identified in the clay fraction (Fig. 44.5c).

Chemical composition of clay mineral particles from the 1188MB and 1193MB cores was studied by TEM-EDS analysis. Clay mineral particles from the core 1188MR were analyzed together, since a XRD pattern suggesting dominant occurrence of chlorite was recognized during the preliminary analysis. Sampling localities of these three cores were located in close distance less than of 50 m. The TEM-EDS results are presented as a ternary diagram where Al_2O_3, MgO and Fe_2O_3 ratio is plotted (Fig. 44.6a). Data plots scattered in the region of Al_2O_3-rich indicates that Al-rich clay minerals are dominant in these sediment cores. Thus, smectite in these cores is classified as montmorillonite. To examine chemical signature of chlorite in these cores, structural formulae was calculated from the major element chemical composition (Table 44.8a, b). Relative

Table 44.7 Mineral assemblage of the LC-J-2 core

		Bulk mineralogy								Clay mineralogy		
Depth (cmbsf)	Description of sample	Q	Cr	Pl	Py	Do	Mag	K	Ap	Sm	Chl	I
40	Sediment	XXX			X					n.a.	n.a.	n.a.
45	Pumice	XX	XX	XXX	XX					n.a.	n.a.	n.a.
50	Pumice		XX	XXX	XX					n.a.	n.a.	n.a.
80	Hydrothermal altered pumice	XXX							XXX	n.a.	n.a.	n.a.
140	Sediment	XXX			X					n.a.	n.a.	n.a.
210	Sediment	XXX			X					n.a.	n.a.	n.a.
248	Hydrothermal altered pumice	XXX							XXX	n.a.	n.a.	n.a.
260	Sediment	XXX			X					n.a.	n.a.	n.a.
280	Sediment	XX				XX	XXX			n.a.	n.a.	n.a.
290	Sediment	XXX			X		X			XX	XX	XX
CC (upper part)	Grayish white sediment							XXX		XX	XX	X
CC (upper part)	Olive black sediment	XXX					XX					
CC (lower part)	Grayish white sediment							XXX		XX	XX	X
CC (lower part)	Olive black sediment	XXX					XX					

XXX: abundant, XX: common, X: minor
Q quartz, *Cr* cristobalite, *Pl* plagioclase, *Py* pyrite, *Do* dolomite, *Mag* magnesite, *K* K-feldspar, *Ap* apatite, *Sm* smectite, *Chl* chlorote, *I* illite
n.a. not analyzed

atomic ratio among Al, Mg and Fe for the chlorite is presented as a ternary diagram (Fig. 44.6b). Chlorite from the 1188B core is Al-rich, while hydrothermal chlorite found in other hydrothermal fields in the Okinawa Trough is characterized as significantly Mg-rich chlorite (Marumo and Hattori (1999) for the Jade field and Miyoshi (2013) for the Iheya North Knoll field). Chemical composition of the chlorite in the 1188MB is close to Al-rich chlorite which is classified as sudoite. Occurrence of sudoite has been reported for only a few examples, where chlorite was associated with other Al-rich clay minerals such as pyrophyllite, kaolinite and diaspora in the outer part of an alteration zone surrounding kuroko-type massive sulfide ore deposit (Inoue and Utada, 1989, Hayashi and Oimura, 1964). Similar zoning of hydrothermal alteration minerals might have developed within the sediment layer in the Jade field.

44.4.4 Occurrence of Hydrothermal Alteration Minerals in the Sediment Below the Seafloor Around Active Venting Fluid Sites

The drilled hole for the BMS-J-2 coring operation was confirmed by a ROV dive conducted 3 months after the drilling operation (Ishibashi et al., Chap. 31), which was located ~50 m south of the Biwako Vent. Somehow different mineral assemblages were recognized between in Unit I and II (Table 44.6 and Fig. 44.3). Quartz was dominantly found through Units I to II. Cristobalite and plagioclase were found occasionally in Unit I, but were not found in Unit II. Pyrite was found occasionally in Units I and II. Clay mineralogy of sediments from 364 cmbsf (Unit I) and 381–417 cmbsf (Unit II) was examined by XRD analysis. Smectite, chlorite and illite were identified in 364 cmbsf (Unit I) (Fig. 44.7a). Chlorite and illite were mainly identified in 381–417 cmbsf (Unit II) (Fig. 44.7b, c).

A locality of the LC-J-2 coring site is estimated as very close to the Biwako vent, although it could not be determined accurately because the coring operation was conducted during a surface ship cruise. Intense hydrothermal alteration was recognized only in Unit II (Table 44.7 and Fig. 44.4). Quartz was dominantly found in Unit I. Pyrite was found in Unit I occasionally. In the lower depth (280–300 cmbsf) of Unit I, carbonate minerals, dolomite and magnesite, were recognized. Quartz, cristobalite, plagioclase and pyrite were dominantly identified in pumice grains at 45 and 50 cmbsf in Unit I. A large broad peak around $2\theta = 20–30°$ in the XRD patterns of the grains was also recognized indicating presence of large amounts of volcanic glass. Apatite and quartz were identified in grains of hydrothermal altered pumice at 80 and 248 cmbsf in Unit I (Fig. 44.8a). Abundant K-feldspar was identified in grayish white sediment samples in Unit II (Fig. 44.8b). Quartz and magnesite were found in olive black sediment samples in Unit II. Clay mineralogy was examined for sediments from 290 cmbsf (Unit I) and 300–330 cmbsf (Unit II). Smectite, chlorite and illite were identified at 290 cmbsf (Unit I). Smectite, chlorite and illite were found at 300–330 cmbsf (Unit II) (Fig. 44.8 c).

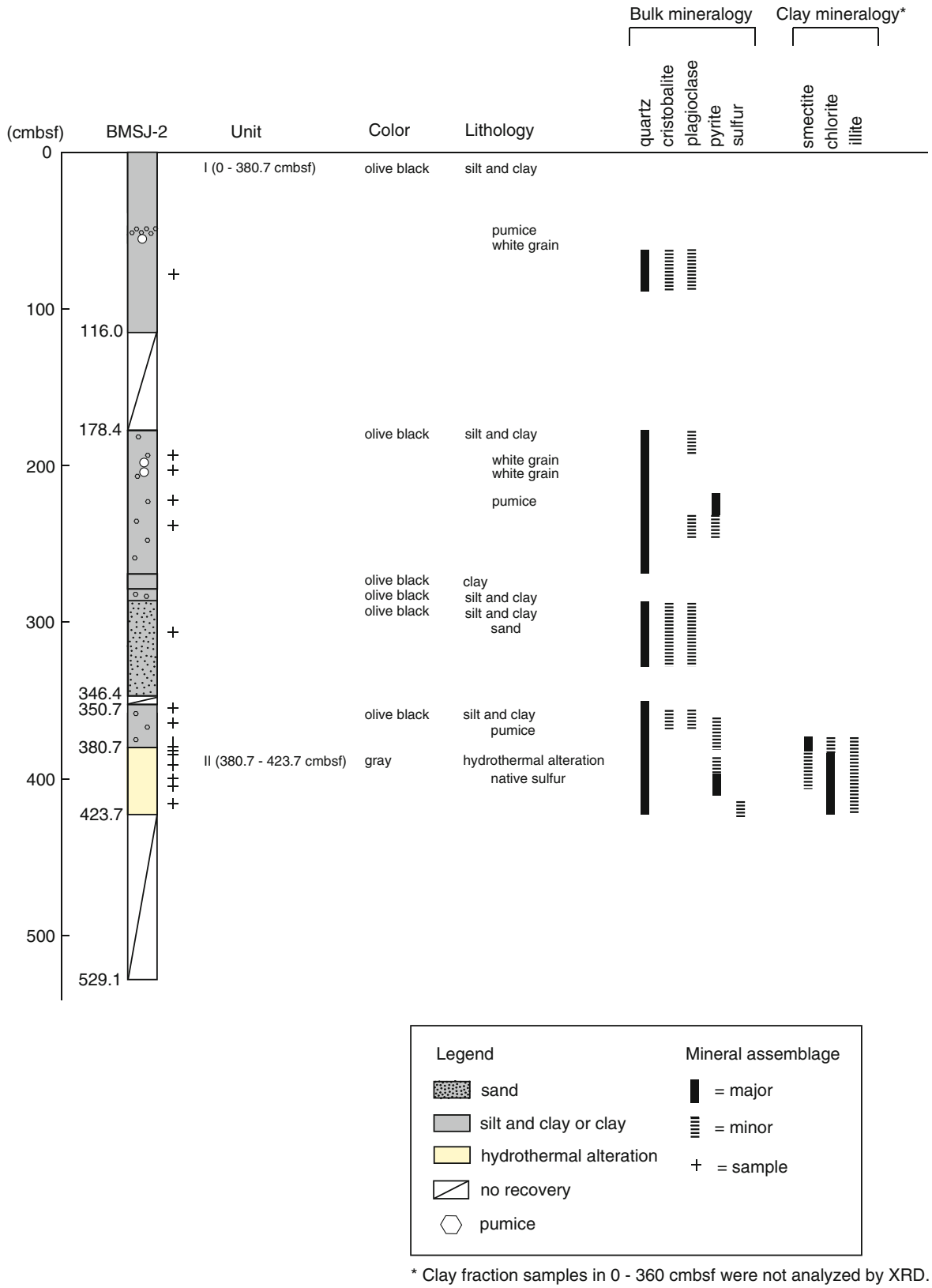

Fig. 44.3 Visual core description and mineral assemblage of the BMS-J-2 core; cmbsf is abbreviation for centimeters below seafloor. The *cross marks* indicate the depths of the samples analyzed in this study. The *bold* and *dashed lines* indicate distribution of main and minor minerals. *Clay fraction samples in 0–360 cmbsf were not analyzed by XRD

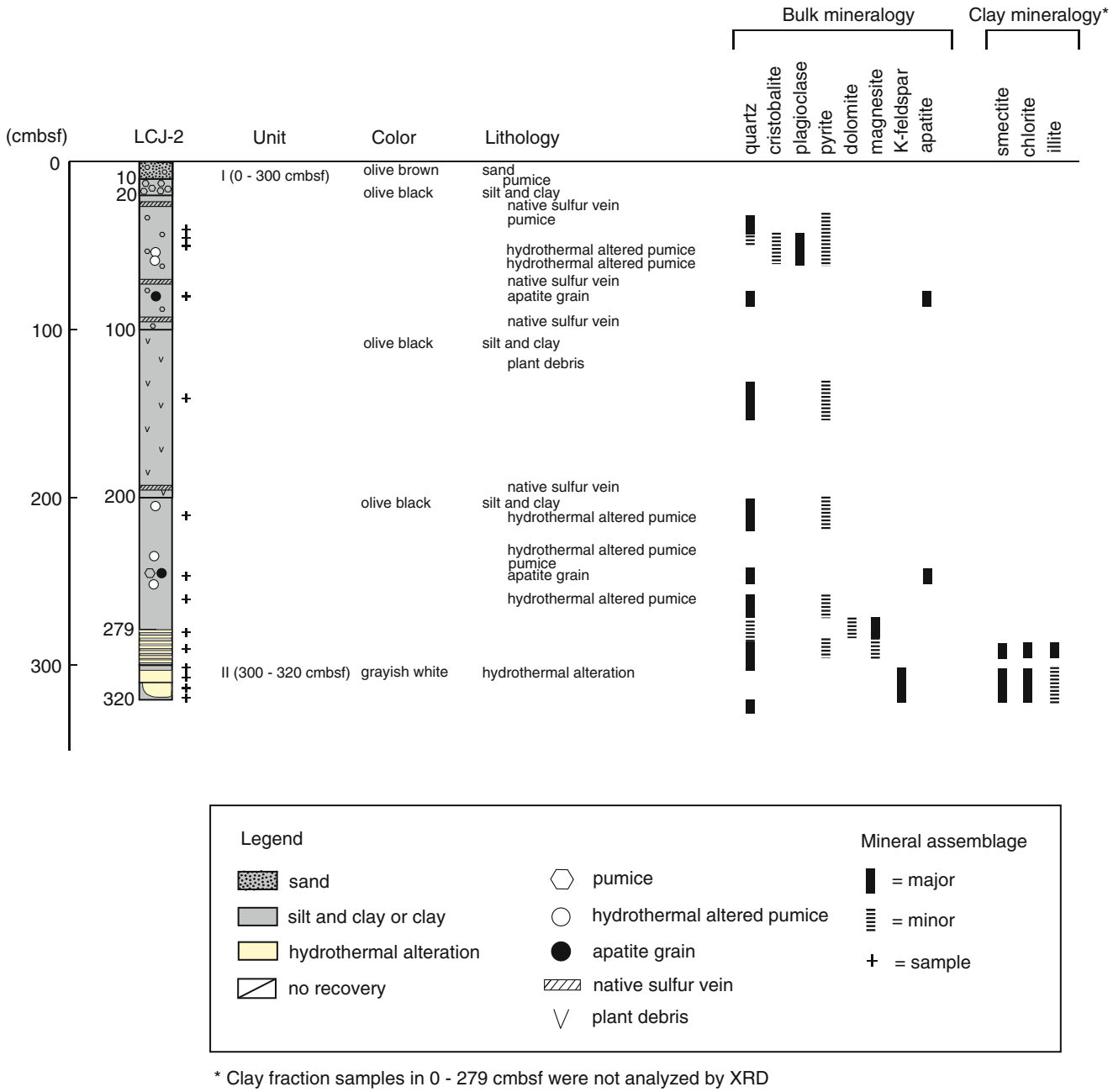

Fig. 44.4 Visual core description and mineral assemblage of the LC-J-2 core; cmbsf is abbreviation for centimeters below seafloor. The *crosses* indicate the depths of the samples analyzed in this study. The *bold* and *dashed lines* indicate distribution of main and minor minerals. *Clay fraction samples in 0–279 cmbsf were not analyzed by XRD

Detailed chemical analysis using EPMA was conducted for specific minerals such as apatite and K-feldspar identified in the LC-J-2 core. Back-scattered electron (BSE) images of the hydrothermal altered pumice where apatite was identified (at 80 cmbsf and 248 cmbsf, Unit I) are shown in Fig. 44.9. Apatite was observed as associated with clay minerals and pyrite (Fig. 44.9a, b). In addition to apatite, monazite was identified as bright white crystals (Fig. 44.9c), which was associated with rutile, pyrite and clay minerals. Determined chemical compositions of the apatite and monazite are given in Table 44.9. The apatite contained minor amounts of REEs (Rare earth elements) and fluorine, and the monazite was more enriched in REE. BSE images of the grayish white sediment where K-feldspar was identified (300–330 cmbsf, Unit II) are shown in Fig. 44.10. Euhedral crystals of K-feldspar in size up to several tens μm

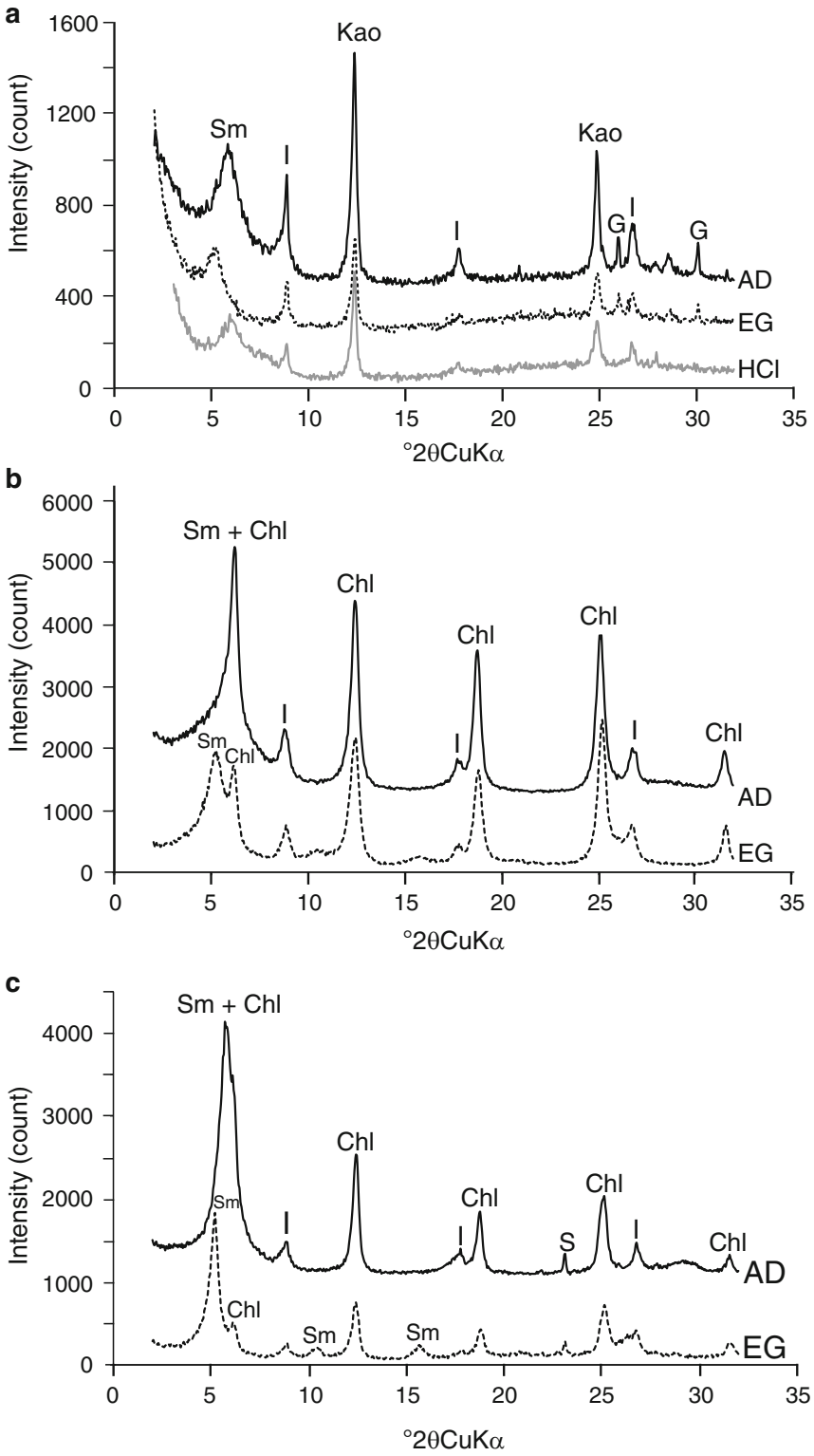

Fig. 44.5 XRD patterns of clay fractions seprated from the samples (**a**) 1186MBL 4–6 cmbsf, (**b**) 1188MB 11–14 cmbsf, and (**c**) 1193MB 7–9 cmbsf. Abbreviations for minerals are *Kao* kaolinite, *Sm* smectite, *Chl* chlorite, *I* illite, *G* galena, *S* native sulfur. The *solid line* (AD), the *dashed line* (EG), and the *gray line* (HCl) indicated XRD patterns of air-dried sample, of ethylene glycol saturated sample, and of HCl treated sample, respectively

were recognized among clay minerals. Off-white portion of the K-feldspar crystals (analytical points #2, #3 and #7 in Fig. 44.10) showed slightly high BaO concentration (BaO = 1.1–2.5 wt%, Table 44.10). Based on the EPMA analysis, clay minerals of feather-like morphology (analytical point #4 in Fig. 44.10) contains Mg, while clay minerals of layer stack morphology (analytical points #6 and #9 in Fig. 44.10) lacks Mg and composed of only Al and Si.

K-feldspar is known as formed by high temperature hydrothermal alteration (Yoshimura, 2001). The observed

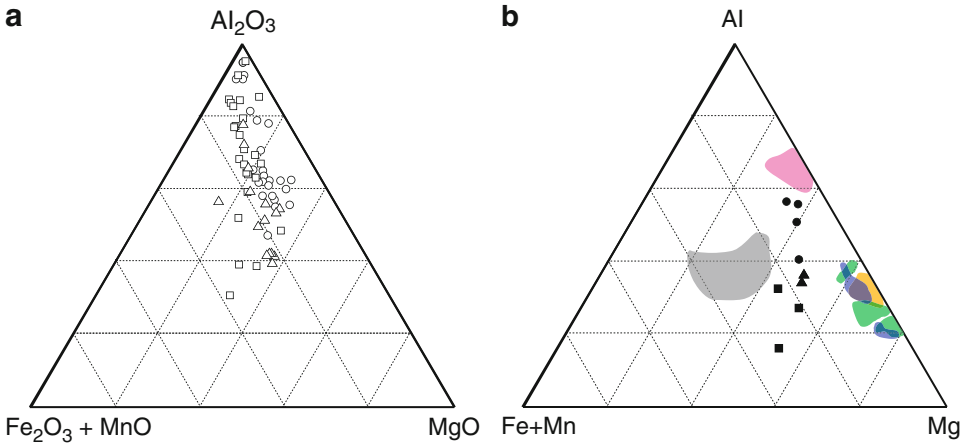

Fig. 44.6 Chemical composition of clay minerals in three short cores collected from near the Biwako Vent. (**a**) Al_2O_3, MgO and Fe_2O_3 ratio of the clay fraction samples, 1188MB 11–14 cmbsf (*open circle*), 1193MB 7–9 cmbsf (*open square*), and 1188MR 4–6 cmbsf (*open triangle*). (**b**) Al, Mg and Fe atomic ratio of chlorite in clay fraction samples, 1188MB 11–14 cmbsf (*solid circle*), 1193MB 7–9 cmbsf (*solid square*), and 1188MR 4–6 cmbsf (*solid triangle*). The *color shaded areas* represent range of chemical composition of chlorite recognized in alteration zones in seafloor hydrothermal fields and around kuroko-type ore deposit. *Orange*: hydrothermal chlorite from the Jade field (Marumo and Hattori, 1999). *Gray*: detrital chlorite from the Izena Hole (Marumo and Hattori, 1999). *Green*: chlorite and chlorite-smectite mixed-layer mineral from the Iheya North Knoll field in the Okinawa Trough (Miyoshi, 2013). *Pink*: sudoite (Al-rich chlorite) from Kamikita mine, Aomori Prefecture, Japan (Inoue and Utada, 1989). *Blue*: Mg-rich chlorite and chlorite-smectite mixed-layer mineral from Furutobe and Hanaoka mines, Akita Prefecture, and Wanibuchi and Iwami mines, Shimane Prefecture, Japan (Shirozu et al., 1975)

Table 44.8 Results of TEM-EDS analysis for chlorite particles separated from cores collected from in the vicinity of the Biwako Vent

Core ID	1188MB	1188MB	1188MB	1188MB	1193MB	1193MB	1193MB	1188MR	1188MR
Depth (cmbsf)	11–14	11–14	11–14	11–14	7–9	7–9	7–9	4–6	4–6
Mineral	Chl	Chl	Chl	Chl	Chl	Chl	Chl	Chl	Chl
(a) Major element composition of chlorite									
Element (wt%)									
SiO_2	43.8	46.4	45.0	42.4	40.1	35.9	31.5	44.0	42.0
TiO_2	n.d.	n.d.	n.d.	n.d.	n.d.	n.d.	n.d.	n.d.	n.d.
Al_2O_3	32.0	32.6	34.0	27.2	23.4	24.7	20.8	23.5	24.2
Fe_2O_3	7.81	7.11	5.49	11.7	18.7	17.5	25.8	12.4	13.5
MgO	16.4	13.9	15.4	18.8	17.9	22.0	22.0	20.1	20.4
MnO	n.d.	n.d.	n.d.	n.d.	n.d.	n.d.	n.d.	n.d.	n.d.
CaO	n.d.	n.d.	n.d.	n.d.	n.d.	n.d.	n.d.	n.d.	n.d.
Na_2O	n.d.	n.d.	n.d.	n.d.	n.d.	n.d.	n.d.	n.d.	n.d.
K_2O	n.d.	n.d.	n.d.	n.d.	n.d.	n.d.	n.d.	n.d.	n.d.
Total	100	100	100	100	100	100	100	100	100
(b) Calculated structural formulae of chlorite: on the basis of $O_{10}(OH)_8$									
Tetrahedral									
Si	3.46	3.63	3.51	3.41	3.32	2.99	2.73	3.55	3.41
Al	0.54	0.37	0.49	0.59	0.68	1.01	1.27	0.45	0.59
Sum	4.00	4.00	4.00	4.00	4.00	4.00	4.00	4.00	4.00
Octahedral									
Al	2.43	2.63	2.64	1.99	1.60	1.42	0.85	1.78	1.73
Fe(3+)	0.46	0.42	0.32	0.71	1.16	1.10	1.68	0.75	0.82
Mg	1.93	1.61	1.79	2.25	2.20	2.73	2.84	2.42	2.47
Total	4.82	4.66	4.76	4.95	4.96	5.25	5.37	4.95	5.02

Chl chlorite
n.d. not detected
Total Fe was expressed as Fe_2O_3

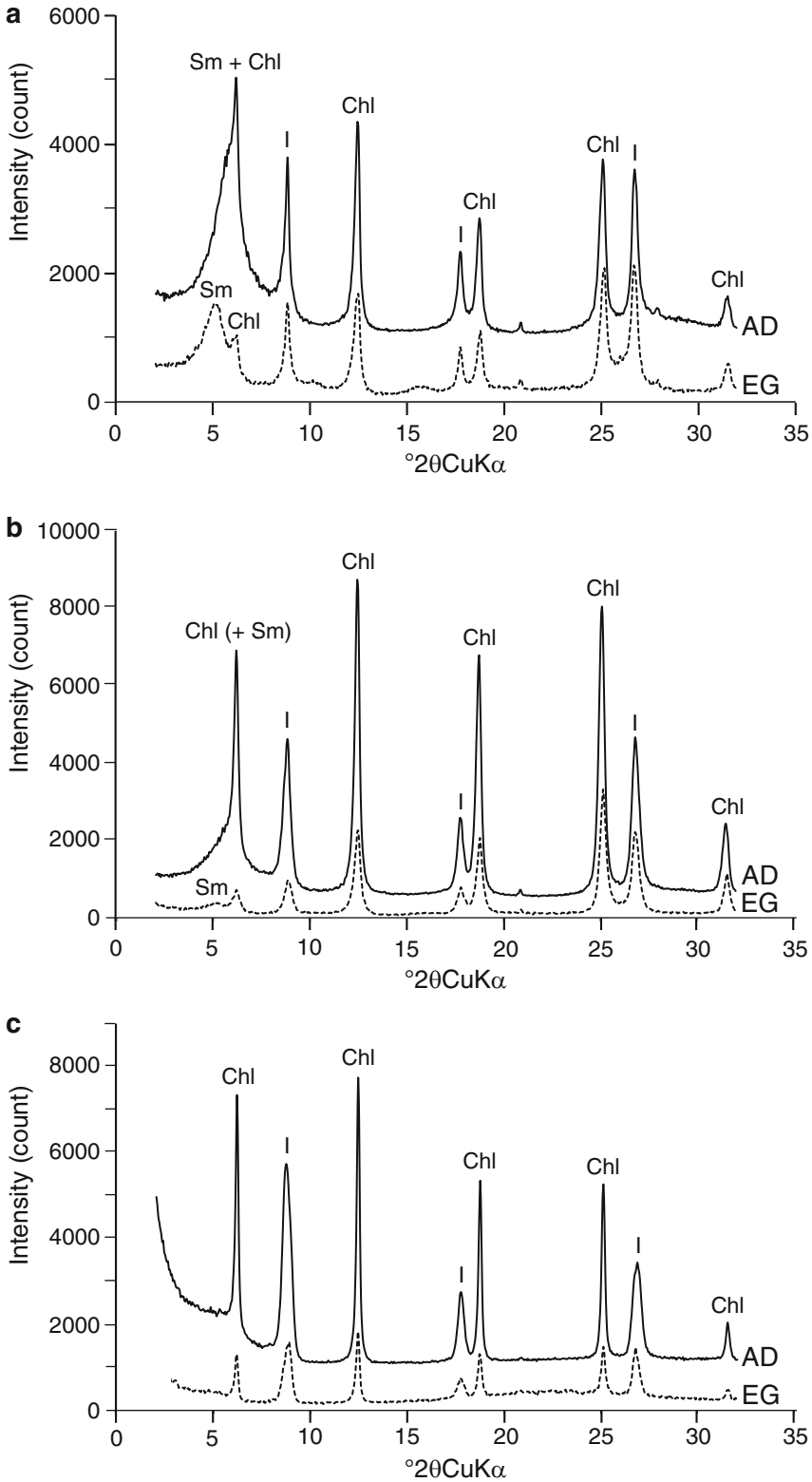

Fig. 44.7 XRD patterns of clay fractions seprated from the BMS-J-2 core at (**a**) 363.7 cmbsf, (**b**) 380.7 cmbsf and (**c**) 416.7 cmbsf. Abbreviations for minerals are *Sm* smectite, *Chl* chlorite, *I* illite. The *solid line* (AD) and *dashed line* (EG) indicate XRD patterns of air-dried samples and ethylene glycol saturated samples

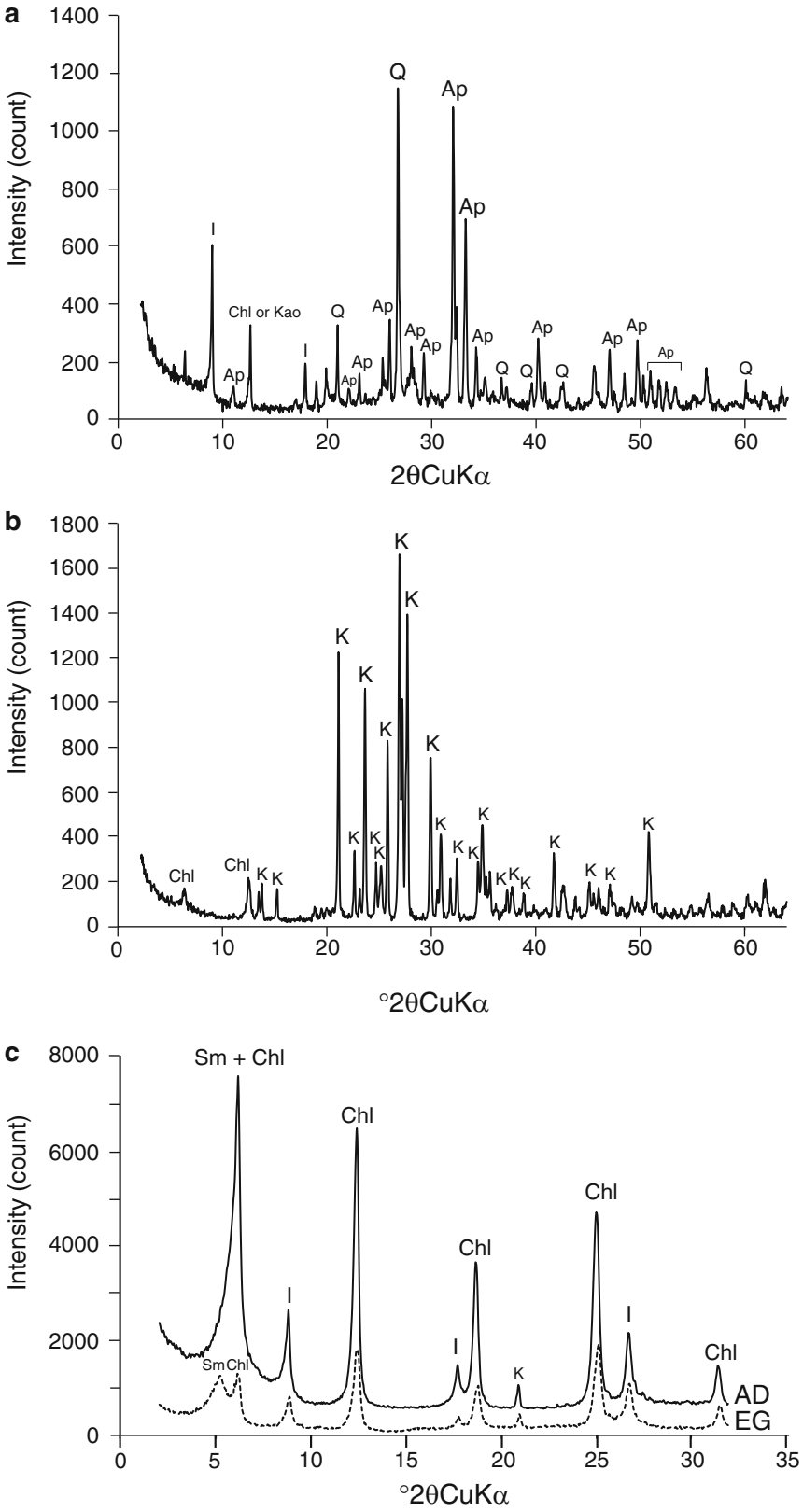

Fig. 44.8 XRD patterns of sediment from the LC-J-2 core, (**a**) hydrothermal altered pumice at 248 cmbsf, (**b**) grayish white sediment from CC (lower part), (**c**) clay fraction of the same sediment as (**b**). Abbreviations for minerals are *Q* quartz, *Ap* apatite, *I* illite, *Chl* chlorite, *Kao* kaolinite, *K* F-feldspar, *Sm* smectite. The *solid line* (AD) and *dashed line* (EG) indicate XRD patterns of air-dried samples and ethylene glycol saturated samples

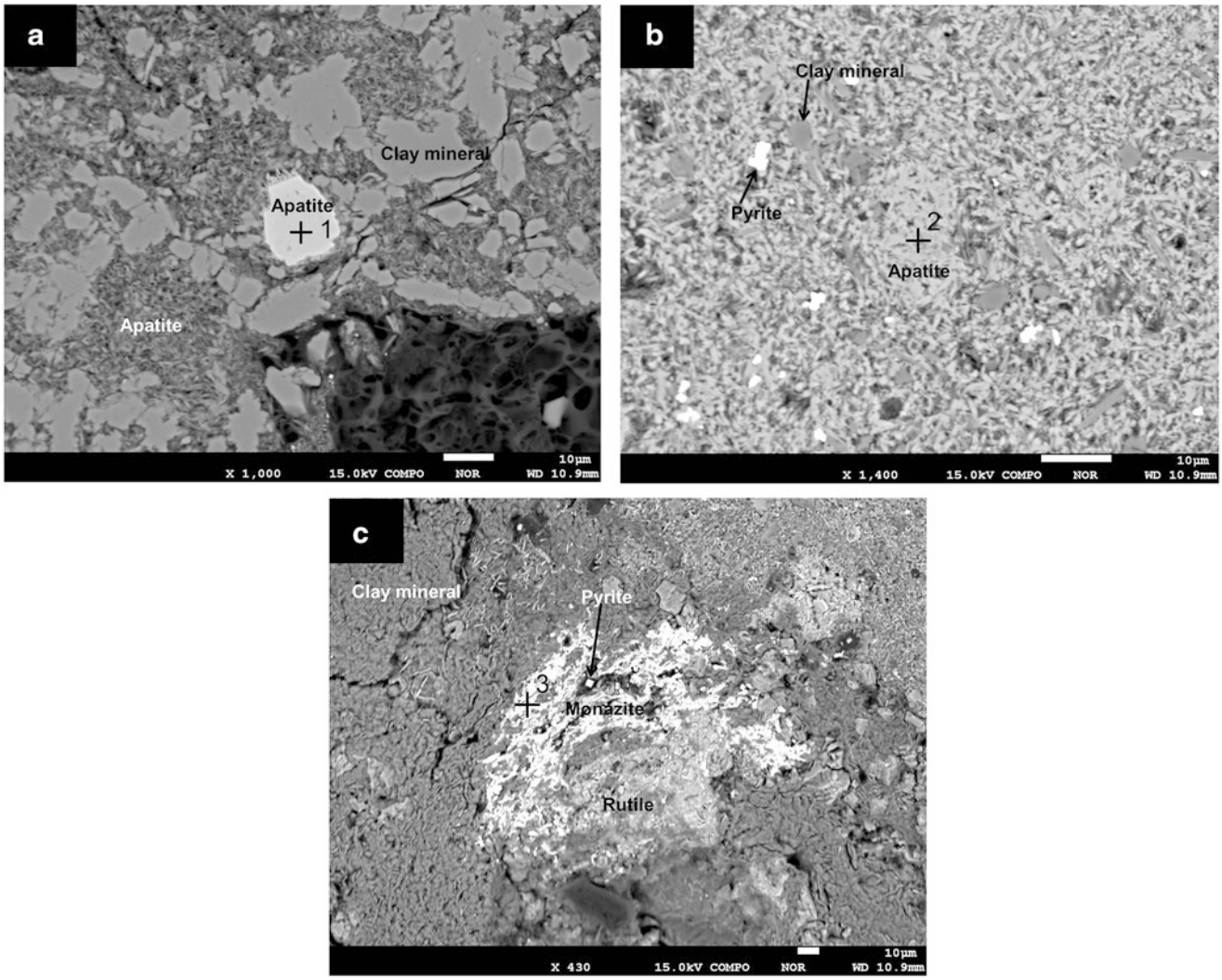

Fig. 44.9 Back-scattered electron (BSE) images obtained by EPMA analysis of hydrothermal altered pumice found in the LC-J-2 core at (**a**) 80 cmbsf, (**b**) 248 cmbsf, and (**c**) 248 cmbsf. The *cross marks* indicate points for determination of chemical composition, which results are listed in Table 44.9

Table 44.9 Results of EPMA analysis for specific minerals in the hydrothermal altered pumice at 80 and 240 cmbsf in the LC-J-2 core

Analyzed point[a]	1	2	3
Mineral	Apatite	Apatite	Monazite
Element (wt%)			
CaO	54.4	48.1	5.30
Y_2O_3	0.24	0.03	0.64
La_2O_3	n.d.	0.03	8.16
Ce_2O_3	0.14	0.18	23.0
Pr_2O_3	0.22	0.01	4.55
Nd_2O_3	0.33	n.d.	9.02
Sm_2O_3	0.07	n.d.	1.42
Gd_2O_3	0.13	0.08	2.83
ThO_2	0.08	n.d.	0.22
UO_2	0.07	0.02	0.01
P_2O_5	43.4	34.3	21.7
F	3.88	4.57	0.53
Total	101	85.4	77.2
ΣREE	1.13	0.33	49.6
ΣLREE	0.76	0.22	46.2
ΣHREE	0.13	0.08	2.83

[a]Numbers of analyzed points correspond to those of cross points in Fig. 44.9
n.d. not detected

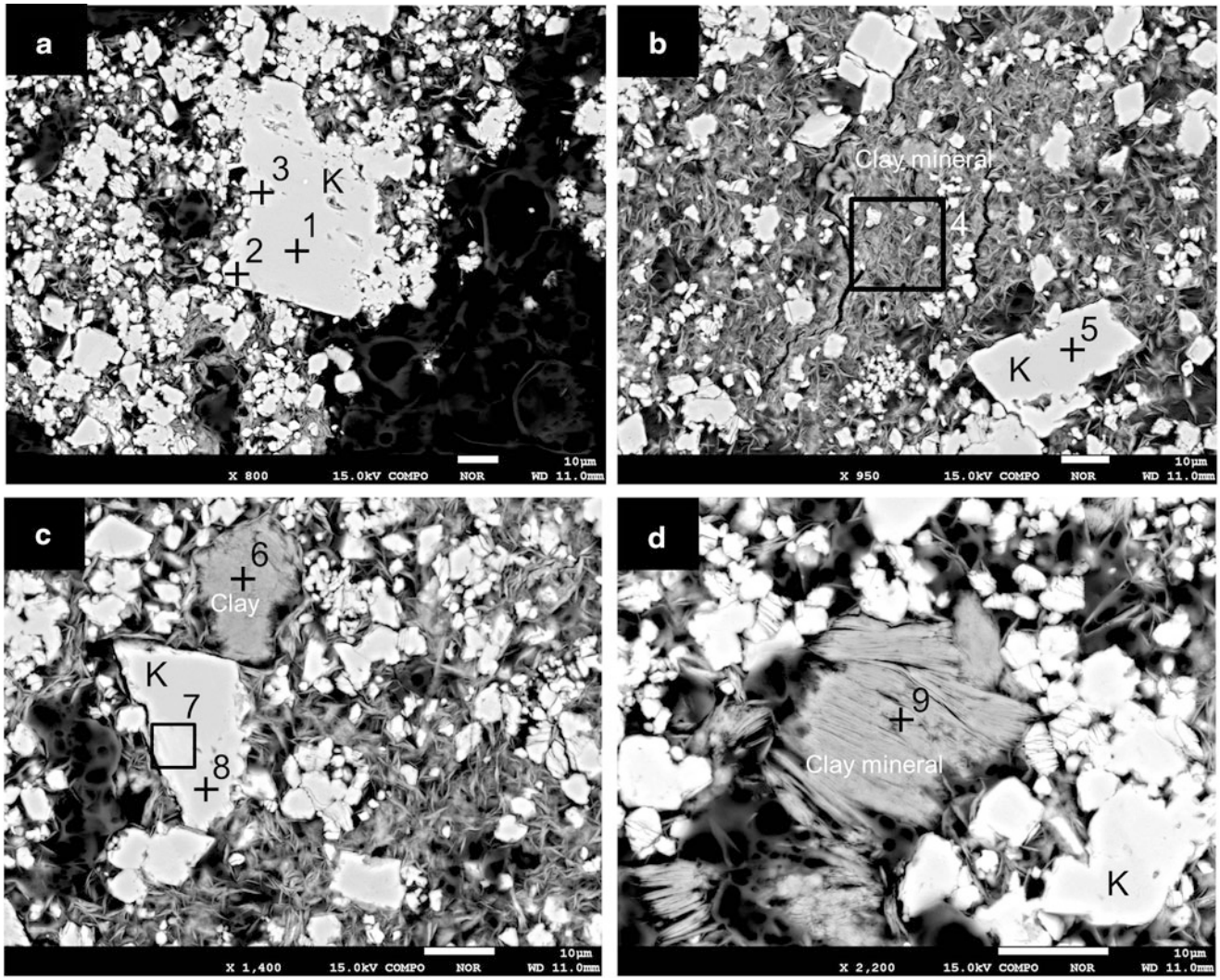

Fig. 44.10 Back-scattered electron (BSE) images obtained by EPMA analysis of the grayish white sediment found in CC (core catcher) of the LC-J-2 core. The *cross marks* indicate points for determination of chemical composition, which results are listed in Table 44.10

Table 44.10 Results of EPMA analysis for specific minerals in the grayish white sediment at CC (core catcher) in the LC-J-2 core

Analyzed point[a]	1	2	3	4	5	6	7	8	9
Mineral	K-feldspar	K-feldspar (Ba-rich)	K-feldspar (Ba-rich)	Feather-like clay	K-feldspar	Layer stack clay	K-feldspar (Ba-rich)	K-feldspar	Layer stack clay
Element (wt%)									
SiO_2	66.3	63.4	63.8	29.9	66.2	46.4	64.8	64.3	47.0
TiO_2	n.d.	0.68	0.57	0.32	n.d.	0.02	0.43	0.01	0.04
Al_2O_3	17.9	18.5	18.7	16.8	17.5	37.0	18.3	17.7	38.1
FeO	n.d.	0.01	n.d.	1.64	n.d.	0.01	n.d.	0.07	0.13
MnO	0.01	n.d.	n.d.	0.13	0.05	0.04	n.d.	0.07	n.d.
MgO	n.d.	0.10	n.d.	16.8	0.03	0.37	n.d.	0.06	0.59
CaO	n.d.	0.05	0.03	0.50	n.d.	0.11	n.d.	n.d.	0.21
Na_2O	0.32	0.30	0.25	0.10	0.11	0.08	0.24	0.21	0.04
K_2O	16.1	15.5	15.6	0.25	14.7	1.76	14.1	15.8	0.10
BaO	0.16	1.09	2.36	n.d.	n.d.	0.31	2.48	n.d.	n.d.
SrO	0.35	0.35	0.45	0.13	0.18	0.55	0.37	0.54	0.20
SO_3	n.d.	n.d.	n.d.	0.18	n.d.	0.16	n.d.	n.d.	n.d.
Total	101	100	102	66.8	98.8	86.7	101	98.8	86.5

[a]Numbers of analyzed points correspond to those of cross points and square areas in Fig. 44.10
n.d. not detected

occurrence as euhedral crystal grown up to larger than 10 μm suggests formation by precipitation from high temperature fluid. Alteration mineral assemblages included K-feldspar were reported for the core obtained by ODP (ocean drilling project) seafloor drilling in the Pacmanus hydrothermal field, the Manus Basin (Paulick and Bach, 2006). They documented chlorite-illite-K-feldspar assemblages accompanied by quartz, smectite, and pyrite in the core below 25 mbsf obtained by drilling immediately adjacent to a high-temperature vent. They suggested that the high temperature alteration is related to sulfide mineralization in a stockwork zone. The alteration mineral assemblage recognized in the Unit II of LC-J-2 core is similar to that found in the Pacmanus hydrothermal field, although the sediment was obtained only 3 mbsf. The hydrothermal mineral assemblage found in this study implies sulfide mineralization below the seafloor around the Biwako Vent, in spite of no evidence on the seafloor.

Acknowledgement We are grateful to the team members of ROV Hyper-Dolphin, crew of R/V Natsushima and onboard scientists during NT10-17 cruise. We are grateful to the team members of the Benthic Multi-coring System (BMS), the crew of the R/V Hakurei-maru No. 2, and onboard scientists during TAIGA11 cruise. We thank the Research Laboratory for High Voltage Electron Microscopy at Kyushu University for their support for TEM analysis. We are grateful to Associate Professor Kyoko Okino of the University of Tokyo, who hosted the first author (Y. M.)'s stay in the Atmosphere and Ocean Research Institute by T-MORE program (TAIGA Mentorship On Research and Education). This article is a part of the doctoral thesis of the first author (Y. M.). We thank Professor Tasuku Akagi of Kyushu University and Professor Harue Masuda of Osaka City University for their insightful advice. This study was supported by a Scholarship for Ph.D. candidates of the Faculty of Sciences, Kyushu University (to the first author (Y. M.)). This study was also partly supported by the "TAIGA project" which was funded by a Grant-in-Aid for Scientific Research on Innovative Areas (#20109004) from the Ministry of Education, Culture, Sports, Science and Technology (MEXT), Japan.

References

Hayashi H, Oimura K (1964) Aluminian chlorite from Kamikita mine, Japan. Clay Sci 2(1):22–30

Inoue A, Utada M (1989) Mineralogy and genesis of hydrothermal aluminous clays containing sudoite, tosudite, and rectorite in a drillhole near the Kamikita Kuroko ore deposit, northern Honshu, Japan. Clay Sci 7:193–217

Ishibashi J, Noguchi T, Toki T, Miyabe S, Yamagami S, Onishi Y, Yamanaka T, Yokoyama Y, Omori E, Takahashi Y, Hatada K, Nakaguchi Y, Yoshizaki M, Konno U, Shibuya T, Takai K, Inagaki F, Kawagucci S (2014) Diversity of fluid geochemistry affected by processes during fluid upwelling in active hydrothermal fields in the Izena Hole, the middle Okinawa Trough back-arc basin. Geochem J 48(3):357–369

Marumo K, Hattori K (1999) Seafloor hydrothermal clay alteration at Jade in the back-arc Okinawa Trough: mineralogy, geochemistry and isotope characteristics. Geochim Cosmochim Acta 63 (18):2785–2804

Miyoshi Y (2013) Mineralogical and geochemical studies of hydrothermal clay minerals below the seafloor at active hydrothermal fields in the island arc and back-arc setting, doctoral thesis in Kyushu University, Japan

Paulick H, Bach W (2006) Phyllosilicate alteration mineral assemblages in the active subsea-floor Pacmanus hydrothermal system, Papua New Guinea, ODP Leg 193. Econ Geol 101:633–650

Sakai H, Gamo T, Kim E-S, Shitashima K, Yanagisawa F, Tsutsumi M, Ishibashi J, Sano Y, Wakita H, Tanaka T, Matsumoto T, Naganuma T, Mitsuzawa K (1990a) Unique chemistry of the hydrothermal solution in the mid-Okinawa Trough backarc basin. Geophys Res Lett 17(12):2133–2136

Sakai H, Gamo T, Kim ES, Tsutsumi M, Tanaka T, Ishibahi J, Wakita H, Yamano M, Oomori T (1990b) Venting of carbon dioxide-rich fluid and hydrate formation in mid-Okinawa Trough Backarc Basin. Science 248:1093–1096

Shirozu H, Sakasegawa T, Katsumoto N (1975) Mg-chlorite and interstratified Mg-chlorite/saponite associated with Kuroko deposits. Clay Sci 4:305–321

Takai K, Mottl MJ, Nielsen SH, The IODP Expedition 331 Scientists (2011) Proceedings of the integrated ocean drilling program, vol 331. Integrated Ocean Drilling Program Management International, Tokyo

Yoshimura (2001) Clay minerals and alterations. The Association for the geological collaboration in Japan (AGCJ), in Japanese

Part VII

Appendix III: Data Reports

Chemical and Isotopic Compositions of Hydrothermal Fluids at Snail, Archaean, Pika, and Urashima Sites in the Southern Mariana Trough

45

Tomohiro Toki, Jun-ichiro Ishibashi, Takuroh Noguchi, Miki Tawata, Urumu Tsunogai, Toshiro Yamanaka, and Kentaro Nakamura

Abstract

Hydrothermal fluids were collected from five hydrothermal fields around the Southern Mariana Trough backarc spreading center for chemical and isotopic analyses. Yamanaka site was interpreted as inactive, so we present results from Snail, Archaean, Pika and Urashima sites. The slightly low pH and negative alkalinity suggests a little bit input of magmatic volatiles, supported by high CO_2 concentrations. Consequently low pH would lead to the hydrothermal fluids rich in Fe compared to the MOR hydrothermal fluids.

Keywords

Backarc spreading center • Geochemistry • Hydrothermal fluid • Iron TAIGA • Magmatic volatile • Southern Mariana

45.1 Introduction

The southern part of the Mariana Trough is an active backarc spreading center that had propagated southward (Fig. 45.1a) (Fryer 1995). Several hydrothermal fields have been mapped around 12°50′N in an alignment perpendicular to the spreading axis (Fig. 45.1b) (Wheat et al. 2003; Ishibashi et al. 2004; Utsumi et al. 2004; Kakegawa et al. 2008; Nakamura et al. 2013). This area is far from continents and large islands, so terrestrial organic matter is absent, and the primary production in surface seawater is poor. On the seafloor, sinking organic matter is very sparse, but flourishing ecosystems are sustained around hydrothermal fields despite high temperatures and pressures (Deming and Baross 1993; Takai and Horikoshi 1999; Kelley et al. 2002). Ecosystems utilizing Fe for energy have been extensively documented, especially around low-temperature hydrothermal vents (e.g., Boyd and Scott 2001; Edwards 2004; Edwards et al. 2003,

The online version of this chapter (doi:10.1007/978-4-431-54865-2_45) contains supplementary material, which is available to authorized users.

T. Toki (✉)
Department of Chemistry, Biology and Marine Science, Faculty of Science, University of the Ryukyus, 1, Senbaru, Nishihara, Okinawa 903-0213, Japan
e-mail: toki@sci.u-ryukyu.ac.jp

J.-i. Ishibashi
Department of Earth and Planetary Sciences, Faculty of Sciences, Kyushu University, 6-10-1, Hakozaki, Fukuoka 812-8581, Japan

T. Noguchi
Marine Technology and Engineering Center (MARITEC), Japan Agency for Marine-Earth Science and Technology (JAMSTEC), 2-15, Natsushima-cho, Yokosuka 237-0061, Japan

M. Tawata
Department of Physics and Earth Sciences, Faculty of Science, University of the Ryukyus, 1, Senbaru, Nishihara, Okinawa 903-0213, Japan

U. Tsunogai
Graduate School of Environmental Studies, Nagoya University, D2-1(510), Furo-cho, Chikusa-ku, Nagoya 464-8601, Japan

T. Yamanaka
Graduate School of Natural Science and Technology, Okayama University, 1-1, Naka 3-chome, Tsushima, Kita-ku, Okayama 700-8530, Japan

K. Nakamura
Precambrian Ecosystem Laboratory (PEL), Japan Agency for Marine-Earth Science and Technology (JAMSTEC), 2-15, Natsushima-cho, Yokosuka 237-0061, Japan

Present address: Department of Systems Innovation, School of Engineering, The University of Tokyo, 7-3-1 Hongo, Bunkyo-ku, Tokyo 113-8656, Japan

J.-i. Ishibashi et al. (eds.), *Subseafloor Biosphere Linked to Hydrothermal Systems: TAIGA Concept*,
DOI 10.1007/978-4-431-54865-2_45,

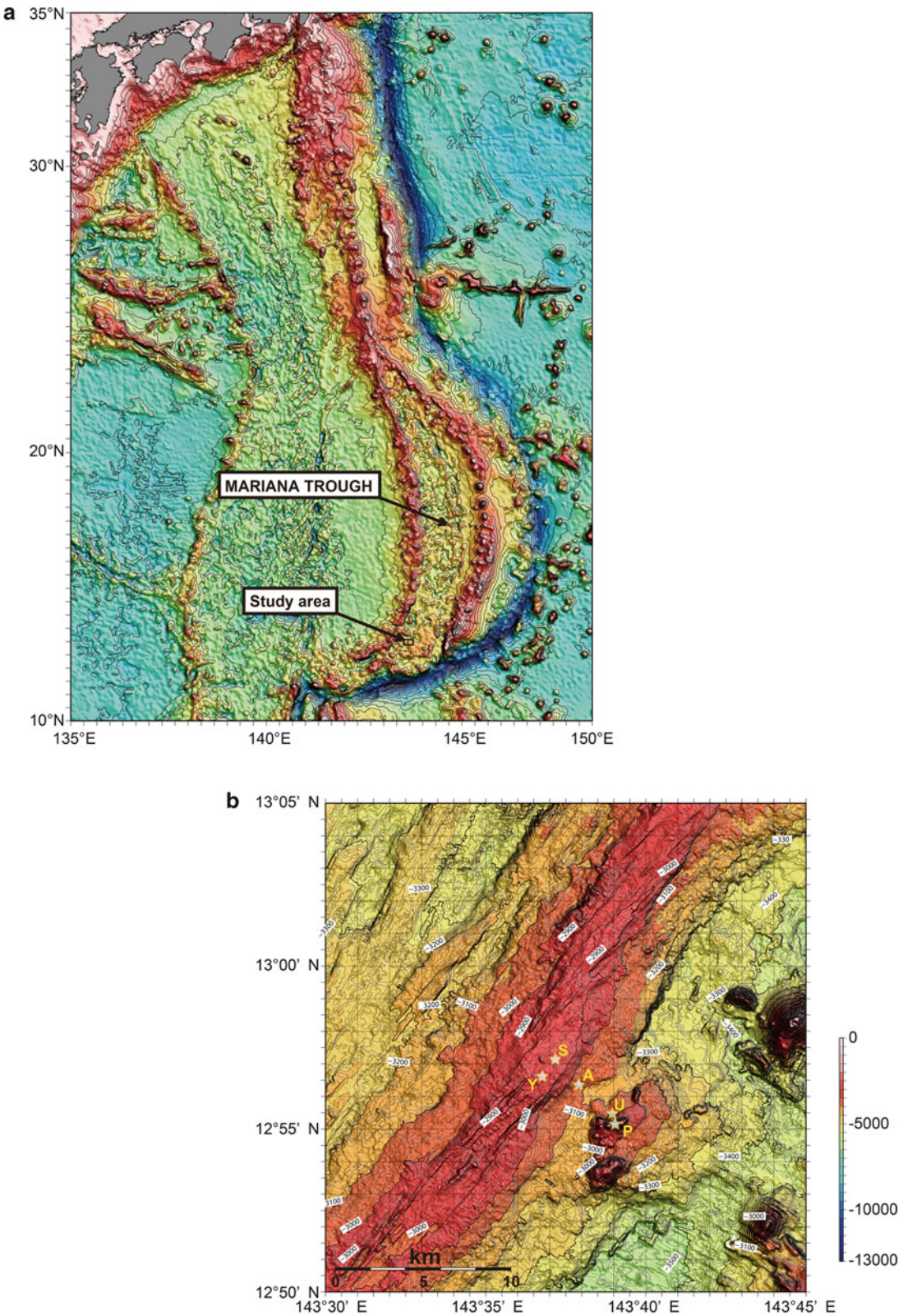

Fig. 45.1 (**a**) A topographic map showing the Izu-Bonin-Mariana trench/arc/back-arc system on the eastern edge of the Philippine Sea plate. A *box* denotes the area of Fig. 45.1b. (**b**) A topographic map around 12°50′N. The *stars* represent the positions of hydrothermal fields in this study. *S*, *Y*, *A*, *P*, and *U* denote the initial letter of Snail, Yamanaka, Archaean, Pika, and Urashima sites, respectively

2011; Little et al. 2004; Kato et al. 2009; Langley et al. 2009; Toner et al. 2009). Ecosystems based on metabolism of inorganic materials are of interest for their potential insight into the origins of life (e.g., Alt 1988; Juniper and Fouquet 1988; Duhig et al. 1992; Juniper and Tebo 1995; Hofmann and Farmer 2000; Reysenbach and Cady 2001).

In the context of the TAIGA project, hydrothermal activity in the Southern Mariana Trough is recognized as Sulfur TAIGA and Iron TAIGA (Urabe et al. Chap. 1), and the project aims to elucidate what kind of ecosystems are prevalent, what kind of metabolisms they employ, and what kind of chemical environments they live in (Urabe et al. 2009). In this tectonic setting, in which hydrothermal activities are extending southward, how ecosystems propagate may shed light on more general questions about the evolution of life processes. Also, a fundamental question about mass flux at Earth's surface is the influence of subducting materials and magmatic volatiles. Extremely acidic fluids affected by magmatic volatiles raise the solubility of metals and mobilize them from rocks to fluids (Gamo et al. 1997b, 2006; Gena et al. 2001; Yang and Scott 2006). This aspect of the metal supply may have a great influence on Fe-utilizing ecosystems. It was with these topics in mind that we investigated the chemical and isotopic compositions of hydrothermal fluids in the Southern Mariana Trough.

45.2 Geological Setting

In the Mariana Trough, the Pacific plate subducts beneath the Philippine Sea plate, and the shape of the trough is convex to the east as a result of backarc spreading (Fig. 45.1a). Spreading activity started between 5 and 10 Ma (Hussong and Uyeda 1981; Karig 1971; Bibee et al. 1980; Eguchi 1984; Yamazaki and Stern 1997), and the northern part of the Mariana Trough represents the early stage of rifting of a backarc basin (Yamazaki et al. 1993). The central part of the Mariana Trough, from 16° to 20°N, represents the early stage of backarc basin spreading, and the volcanic arc and backarc are clearly distinguishable (e.g., Hart et al. 1972; Hawkins 1977; Fryer et al. 1981; Natland and Tarney 1981). The backarc is very close to the volcanic arc south of 16°N, and the spreading center of the backarc is ambiguous south of 12.5°N (Hawkins 1977; Smoot 1990). The hydrothermal fields in this study are located around 13°N. Five hydrothermal systems have been discovered around 13°N, which are aligned perpendicular to the axis (Fig. 45.1b). The Snail and Yamanaka sites are on the spreading axis, and the Archaean, Urashima, and Pika sites are off the axis. Around the area, hydrothermal activities have been documented in the TOTO caldera (Gamo et al. 2004), Forecast vent field (Johnson et al. 1993), and Alice Springs field (Craig et al. 1987; Gamo 1993; Gamo et al. 1997a). Descriptions of these hydrothermal systems are found in the InterRidge Vents Database (Beaulieu 2013).

45.2.1 Snail Site

Snail site is on the spreading axis (12°57.214′N, 143°37.147′E, depth: 2,860 m) (Fig. 45.1b), where hydrothermal fluids as hot as 248 °C were observed in 2003 (Wheat et al. 2003). However, most of the seafloor around the site is covered by snails exposed to low-temperature fluid around 100 °C, and covered by a yellow microbial mat and shimmering fluid below 100 °C (Wheat et al. 2003). The microbial mat may be composed of iron hydroxide and associated with Fe-oxidizing bacteria (Kato et al. 2010). In 2004 and 2010, the Benthic Multicoring System (BMS) penetrated several meters below the seafloor, and basalt was recovered (Urabe et al. 2004). In 2012, an ROV investigation found that hydrothermal fluid of 45 °C was discharging from the casing pipe that was placed in the BMS drilling hole in 2004 (NT12-24 Cruise Report).

45.2.2 Yamanaka Site

Yamanaka site is on a mound about 30 m high on the spreading axis (12°57.6′N, 143°36.7′E, depth: 2,830 m), 1 km northwest of Snail (Fig. 45.1b). Observations have documented many sea anemones and dead chimneys as well as shimmering fluid below 20 °C seeping from the rocky seafloor (Kakegawa et al. 2008). Magnetic mapping in 2009 showed strong magnetization here, suggesting that hydrothermal alteration is weak (Fujii et al. 2013). Based on these facts, Yamanaka has been considered to be past its peak of hydrothermal activity (Yoshikawa et al. 2012).

45.2.3 Archaean Site

Archaean site is on a sulfide mound ~100 m high that is 2 km from the spreading axis (12°56.35′N, 143°38.0′E, depth: 2,990 m) (Fig. 45.1b). The ROV *ROPOS*, during cruise TN167A in 2004, documented black smokers venting fluid at temperatures up to 343 °C (Ishibashi et al. 2004). The BMS drilling campaign in 2010 recovered basalt and andesite from the base of the mound (Nakamura et al., Appendix 3-A1).

45.2.4 Pika Site

Pika site is on a 75 m-high knoll, with two peaks 5 km from the spreading axis (12°55.1′N, 143°38.9′E, depth: 2,830 m) (Fig. 45.1b). The manned submersible *Shinkai 6500*, during

cruise YK03-09 in 2003, documented a black smoker venting high-temperature fluid up to 330 °C at the top of the western peak of the knoll and no hydrothermal activity on the eastern peak (Utsumi et al. 2004). In 2004 the BMS campaign recovered andesite from borehole APM03 (Kakegawa et al. 2008), which means drilling site No.3 of Archaean Park Project in Mariana (Urabe et al. 2001).

45.2.5 Urashima Site

Urashima site is on a mound several meters high 500 m north of Pika (12°55.30′N, 143°38.89′E, depth 2,922 m) (Fig. 45.1b), and several gray smokers venting hydrothermal fluids as hot as 280 °C were documented by *Shinkai 6500* during cruise YK10-10 in 2010 (Nakamura et al. 2013). A strong negative magnetic anomaly was observed by the autonomous underwater vehicle (AUV) *Urashima* in 2009 (Seama et al. Chap. 17), suggesting demagnetization by hydrothermal alteration (Rona 1978; Tivey and Johnson 2002). The site includes black dead chimneys, red-brown shimmering chimneys, and areas of yellow microbial mat exposed to low-temperature hydrothermal fluids. The microbial mat is probably composed of iron hydroxide like that at Snail.

45.3 Materials and Methods

45.3.1 Sampling Methods

Hydrothermal fluids were collected during YK03-09 (October, 2009), TN167A (March, 2004), YK05-09 (July, 2005), YK10-10 (August, 2010), YK10-13 (October, 2010), and NT12-24 (September, 2012) (Suppl. 45.1a and 45.1b) using the ROCS and the WHATS (Tsunogai et al. 2003; Saegusa et al. 2006). The WHATS is multi-bottle gastight sampling system, which avoids degassing and contamination by tightly closing the valves of sample bottles in situ. During sampling, the bottle inlet was held as close as possible to the hydrothermal vent, but in typical operation the inlet sometimes drops off the vent and draws in seawater. With allowance for a small degree of seawater admixture, the sample represents the average composition of hydrothermal fluid during the sampling period. The fluid temperature was recorded during sampling. The samples were collected with two bottles at each vent, one for gas analyses and the other for fluid analyses.

The sample for fluid analyses was first subsampled into two 5-mL vials for measurement of pH, alkalinity, and H_2S concentration. The remaining fluid was then filtered using a 0.45-μm pore-size disk filter attached to a plastic syringe and distributed into 15- and 30-mL plastic bottles. The 15-mL subsample was measured for NH_4^+ and Si concentrations on board, and Cl^- and SO_4^{2-} concentrations on land. The 30-mL subsample was combined with 300 μL of 3N HNO_3 on board the tender ship and then measured for major and minor elements on shore.

The sample bottle for gas analyses was processed as soon as possible (Konno et al. 2006); the fluid in the bottle was transferred to a 300-mL evacuated glass container, then acidified with amidosulfuric acid to convert all dissolved carbonate species to CO_2 in the headspace of the container. The fluid was treated with sufficient $HgCl_2$ to thoroughly convert H_2S to HgS in the vacuum line. The gas phase was transferred to a 50-mL evacuated stainless steel container for gas analyses on shore, and then the residual fluid in the container was filtered for measurement of major elements on shore.

45.3.2 Analysis

The pH was measured by electrode with a precision of ±0.02 (Gieskes et al. 1991). The calibration was done using buffers of pH 4.01 and pH 6.86 once a day before the measurements. Alkalinity was measured by HCl titration, which endpoint was determined by the Gran's plot, with a precision of ±2 % (Gieskes et al. 1991). The concentration of H_2S was measured by colorimetry using methylene blue with a precision of ±10 %. Ammonia concentration was measured by colorimetry using phenol blue with a precision of ±8 %. The Si concentration was determined by colorimetry using molybdate blue with a precision of ±1 %. Chlorinity was analyzed by the Mohr method with a precision of ±1 %. The SO_4^{2-} concentration was determined by ion chromatography with a precision of ±4 %. Major and minor elements (Na, Ca, Mg, Sr, Ba, Mn, Fe, Si, B, and Li) were analyzed by inductively coupled plasma atomic emission spectroscopy (ICP-AES). The K concentration was analyzed by atomic absorption spectrometry. The Na concentration was also calculated independently on the basis of charge balance.

Gas concentrations of O_2, N_2, CO_2, H_2, and He were measured by using gas chromatography with a thermal conductivity detector. CH_4 concentration and its stable carbon isotope ratio were determined with a continuous-flow isotope ratio mass spectrometer (CF-irMS) (Tsunogai et al. 2000). The hydrogen isotope ratio (D/H) of CH_4 was analyzed by using a CF-irMS with a precision of ±10 ‰. The hydrogen isotope ratio of H_2 was analyzed by using a CF-irMS with a precision of ±4 ‰ (Komatsu et al. 2011). Helium isotope ratios ($^3He/^4He$) were measured by using noble gas mass spectrometry with a precision of ±2 % (Sano et al. 2006). The ratio of ^4He to ^{20}Ne was determined by using quadrupole mass spectrometry with a precision of ±10 % (Sano et al. 2006). Dissolved organic matter was measured with a Shimadzu TOC-5000 total organic carbon analyzer with a high-temperature catalytic method.

45.4 Results

The analytical results for hydrothermal fluids from the five sites are shown in Suppl. 45.1a for fluid chemistry and Suppl. 45.1b for gas chemistry, together with the maximum and average temperatures recorded during sampling.

45.4.1 Calculation of End-Member Compositions

Graphs of the concentrations of each chemical component relative to Mg concentration are shown in Fig. 45.2. Under the assumption that pure hydrothermal fluid is free of Mg, its chemical composition was calculated as the y-axis intercept of linear relationship among data plots (Von Damm 1995). The Yamanaka site yielded only low-temperature hydrothermal fluids with compositions that could not be distinguished from that of seawater, and this site is not discussed further. End-member concentrations of the hydrothermal fluids in the remaining four sites are listed in Table 45.1 for aqueous components and Table 45.2 for volatile components, and discussed below.

The end-member carbon isotopic composition of methane, $\delta^{13}C(CH_4)$, was estimated as the intercept of the y-axis on a graph of $\delta^{13}C(CH_4)$ against the reciprocal of CH_4 concentration, as shown in Fig. 45.3 (Keeling 1961). Estimates of this type are based on the assumption that the background concentration is negligible. In the case of methane, background CH_4 in seawater is several nM, whereas CH_4 in hydrothermal fluid is several hundred μM, a difference of five orders of magnitude.

However, because the background CO_2 concentration is substantial in seawater (2 mM) compared to hydrothermal fluid (several tens mM), we relied on a method used in atmospheric chemistry to evaluate end-member $\delta^{13}C(CO_2)$ (Miller and Tans 2003). As illustrated in Fig. 45.4, a product that CO_2 concentration multiplies $\delta^{13}C(CO_2)$ is plotted to CO_2 concentration, when the slope can be taken as $\delta^{13}C(CO_2)$ of the source.

Helium in hydrothermal gases is a mixture of mantle, crust, and seawater contributions. Because ^{20}Ne is negligible in rock, helium isotope ratios can be corrected for seawater admixture using $^4He/^{20}Ne$ ratios, as shown in Fig. 45.5 (Craig et al. 1978).

45.4.2 End-Member Concentrations of Dissolved Constituents

Maximum fluid temperatures were as follows: Snail, 116 °C; Archaean, 343 °C; Pika, 330 °C; Urashima, 280 °C (Table 45.1).

The lowest pH ranged from 2.8 to 3.5, and only at Snail was it greater than 3. Except for Snail, these values are lower than that of hydrothermal fluids in mid-ocean ridges ranging about 3–3.5 on average (Von Damm 1995).

The end-members for all sites have negative alkalinity; −0.94 for Snail, −1.41 for Archaean, −1.14 for Pika, and −1.44 for Urashima. These data suggests that these hydrothermal fluids have substantial strong acidity compared with hydrothermal fluid in the mid-ocean ridge setting, where the fluid is rather neutralized during high temperature fluid-rock interactions. This view is supported by relatively low pH in Southern Mariana Trough hydrothermal fluids.

The Si concentrations were measured by colorimetry on board and by ICP-AES on land, and both end-member concentrations were consistent with each other. Values lay in a narrow range between 16.4 and 17.0 mM except for Snail, where the Si concentration was greater than 18 mM.

The end-member Cl^- concentrations deviated from that of seawater (550 mM) at all sites. At Archaean, the Cl^- end-member in 2004 (466 mM) had a higher concentration than those in 2005 and 2010 (407 mM). At Pika, high-Cl^- fluids (603 mM) were consistently reported after its discovery in 2003, but a low-Cl^- fluid (460 mM) was recovered in 2010 (Table 45.1). Such Cl^- deviations from that of seawater have been reported in many hydrothermal systems in the world, which are thought to be due to phase separation beneath the seafloor (Von Damm 1995). Especially, higher-Cl^- and lower-Cl^- fluids than that of seawater have been sampled, like those at Pika, suggesting that active phase separation beneath the seafloor has occurred there, as mentioned in many hydrothermal systems in the world (Von Damm 1995). A positive Cl^- deviation from that of seawater, like those at Urashima, can be due to input of HCl derived from magmatic volatiles, as mentioned at DESMOS hydrothermal field in Manus Basin (Gamo et al. 1997b). In that case, the hydrothermal fluids also have extremely low pH and an excess of SO_4^{2-} (Gamo et al. 1997b), and we found that hydrothermal fluids from Urashima site have an end-member pH slightly lower than 3 as mentioned above (Table 45.1).

The Na concentration was independently calculated by charge balance as well as measured by ICP-AES. The calculated values were more clearly linear relative to Mg concentrations than the measured values. Although the errors of the calculated concentrations are larger than those of the measured concentrations, we took the calculated values as those of the preferred end-members. The end-member value for Snail was close to that of seawater (460 mM). The end-member Na concentration for Archaean (345 mM) was lower than that of seawater. At Pika, the end-member value in 2003 and 2005 was higher than that of seawater, although sample D1219 W-4, taken in 2010, had a lower value than seawater (Table 45.1). For Urashima, the

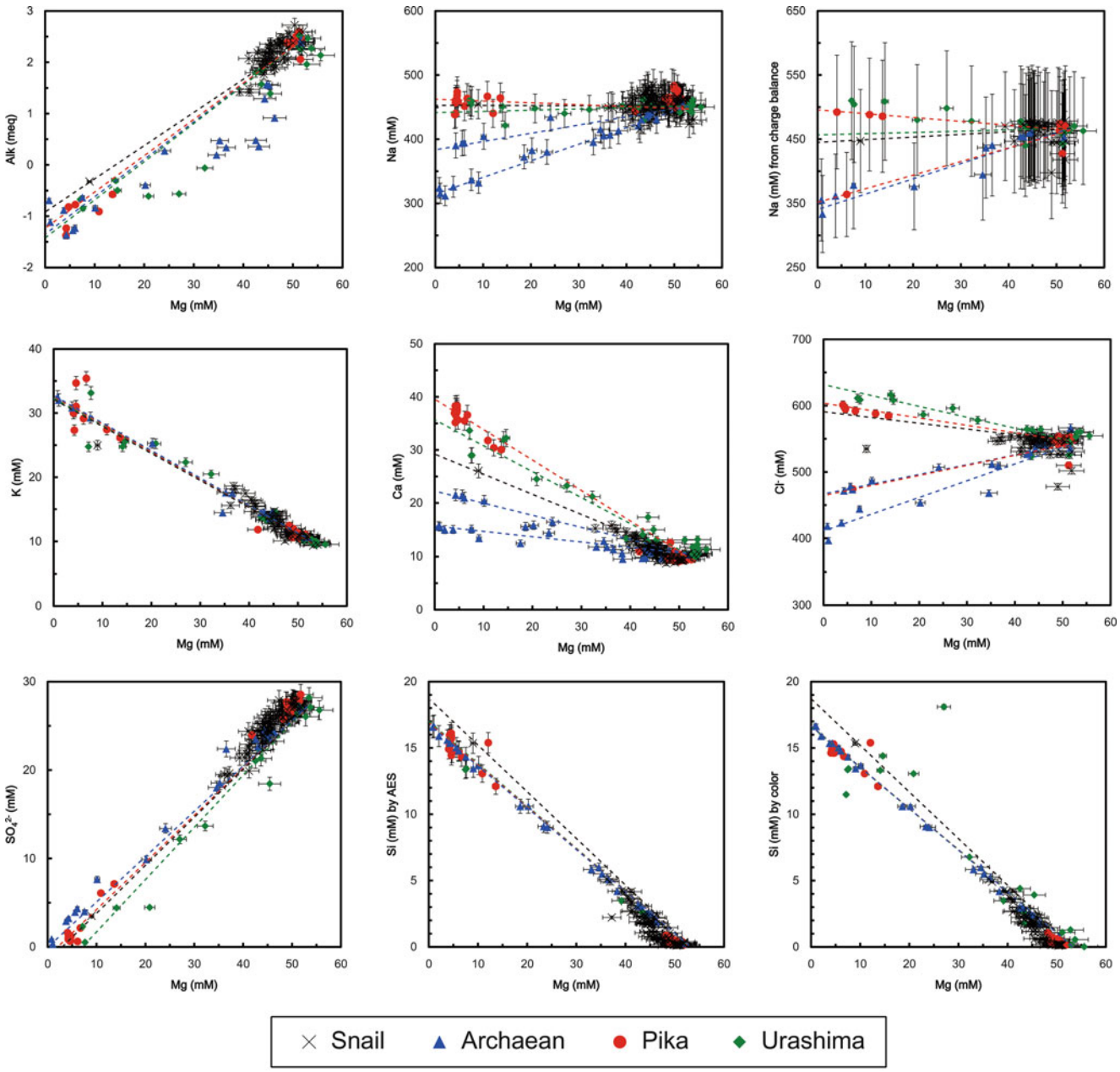

Fig. 45.2 A plot of each chemical component vs. Mg concentration in the hydrothermal fluid for each site in the Southern Mariana Trough in this study

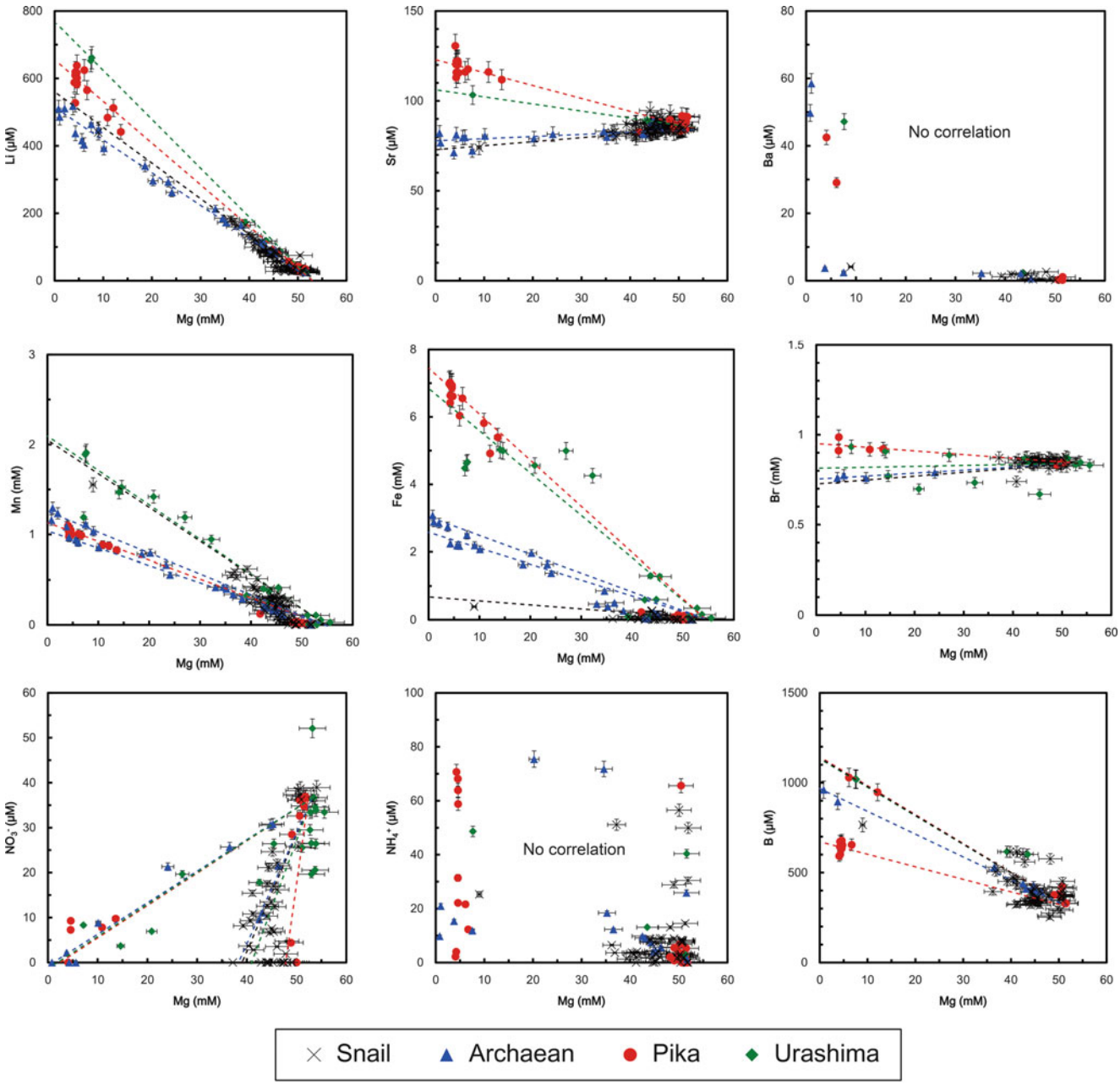

Fig. 45.2 (continued)

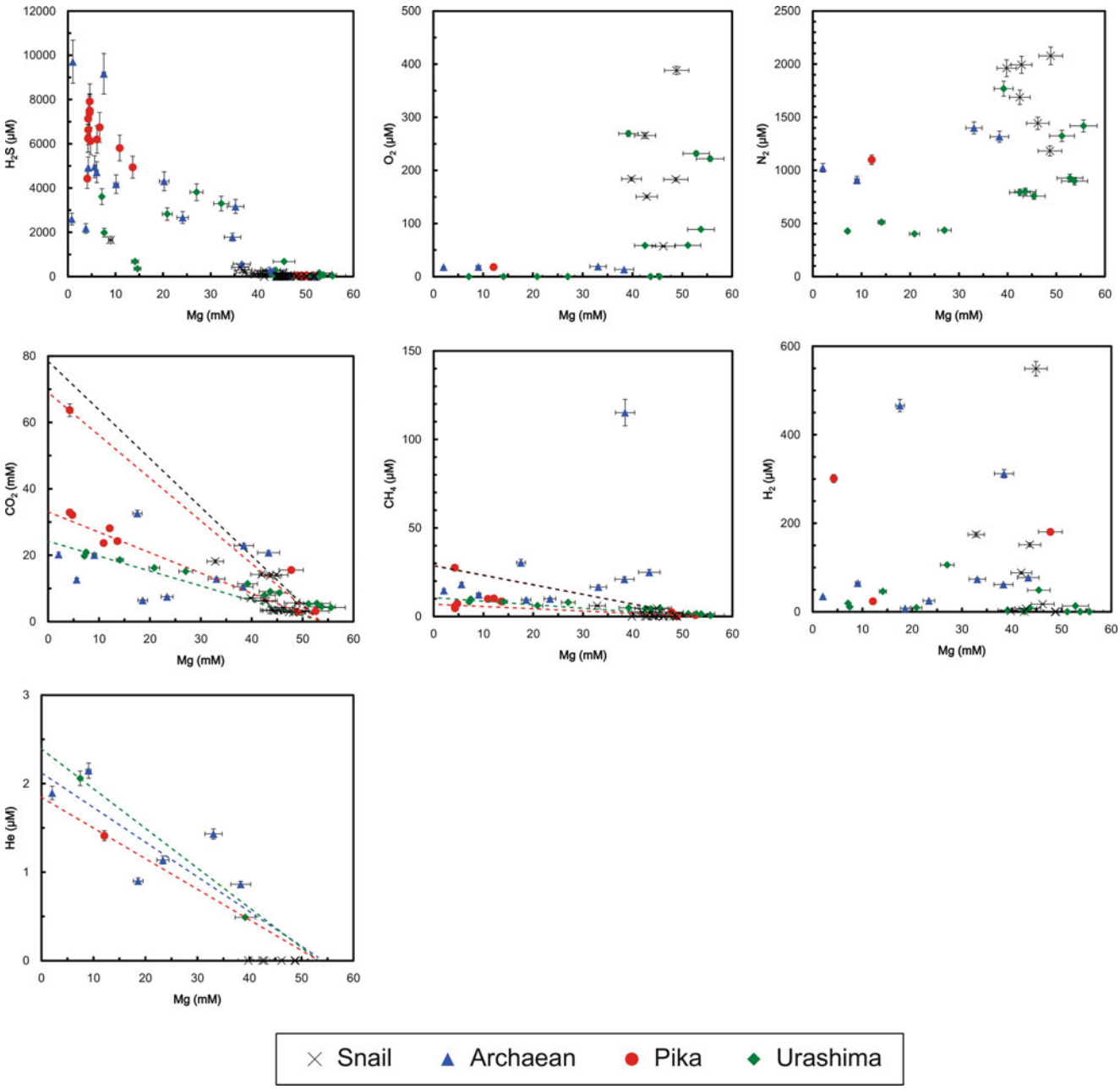

Fig. 45.2 (continued)

end-member Na concentration (515 mM) was higher than that of seawater.

For Ca concentrations, the end-members for all four sites had higher values than that of seawater (10 mM). At Archaean, the end-member Ca concentration for 2004 was higher than the one for 2005 and 2010, which is similar to our finding for Cl^- concentrations.

For K concentrations, end-member values for all sites fell into a narrow range (31.3–32.8 mM), and the values for Pika and Archaean were significantly higher than those for Snail and Urashima.

For Fe concentrations, the end-members for all four sites had higher concentrations than that of seawater (<1 nM). The end-member value was 0.64 mM for Snail, 2.55 mM for Archaean in 2003–2005, 3.00 mM for Archaean in 2010, 7.38 mM for Pika, and 6.37 mM for Urashima (Table 45.1). The end-member Fe concentration at Snail site is as low or lower when compared to those in the

hydrothermal fluids in EPR21°N (0.2–2.4 mM; Von Damm et al. 2002), but otherwise those in the Southern Mariana Trough appear higher as compared with those in EPR21°N. Fe leaches from rocks at low pH attributed to an input of magmatic volatiles (Mottl et al. 1979; Hajash and Chandler 1982; Seyfried and Janecky 1985; Seewald and Seyfried 1990). The cause of Fe enrichment in Pika, Urashima, and Archaean sites would be low pH coming from an input of magmatic volatiles.

The end-members of major elements had two concentrations for both Pika and Archaean and unique values for both Snail and Urashima (Table 45.1).

45.4.3 Distribution of Gas Components

Dissolved oxygen concentrations showed nonlinear relationships to Mg concentrations, so end-member concentrations were not computed (Fig. 45.2). We just explain the concentration for each Mg concentration (Suppl. 45.1b and Fig. 45.2). At Snail, samples contained Mg concentrations higher than 40 mM and had oxygen concentrations higher than that of seawater, ranging around 100–200 μM. At Archaean, samples had Mg concentrations lower than 40 mM and oxygen concentrations lower than 20 μM. The single sample from Pika contained 12 mM Mg and an oxygen concentration of 18 μM. Urashima yielded samples containing from 7 to 54 mM Mg, and oxygen was not detected in samples with less than 40 mM Mg.

Dissolved nitrogen was detected in all samples, but its concentrations showed nonlinear relationships to Mg concentrations (Fig. 45.2). At Snail, all samples contained Mg concentrations above 40 mM, and nitrogen concentrations were higher than that of seawater (500–1,000 μM). At Archaean, two samples had Mg concentrations around 10 and 30 mM, and the N_2 concentration of the latter was higher than that of the former. The single sample from Pika had a Mg concentration of 12 mM and a N_2 concentration of about 1 mM.

End-member dissolved CO_2 concentrations were calculated for each site from their relation to Mg concentrations (data for Archaean did not fit a linear relation). The end-member values were all higher than that of seawater (2.4 mM). At Snail, although the majority of samples had values close to that of seawater, the end-member value, 78.8 mM, was highest among our sites. Although we did not calculate an end-member concentration for Archaean, the range of CO_2 concentrations there was 6.4–32.6 mM. For Pika, samples taken in 2005 had an especially high value (69.1 mM); whereas the end-member concentration for 2003, 2004, and 2010 samples was much lower (33.7 mM). For Urashima, the end-member value was 23.2 mM. The reported range of CO_2 concentrations in hydrothermal fluids from EPR are lower than 10 mM (Von Damm et al. 2002), and so the observed CO_2 concentrations in hydrothermal fluids in the Southern Mariana Trough in this study are relatively higher than those in EPR. Such CO_2 enrichments could be influenced by a little input of magmatic volatiles, as mentioned in hydrothermal systems related to arc systems (Sakai et al. 1990; Gamo 1993; Tsunogai et al. 1994; Gamo et al. 2006; Lupton et al. 2008).

The end-member value of CH_4 for Snail was 29.6 μM, although the error was large because values for most samples were close to seawater values. For Archaean, the data were too scattered to calculate an end-member concentration, but sample D903 W-3, from a clear smoker vent with a maximum temperature of 117 °C, had the highest concentration of CH_4 in this study, 115 μM. For Pika, the 2005 end-member concentration (29.9 μM) was higher than the end-member concentration for the other years (7.2 μM). The end-member value for Urashima was 10.8 μM.

Hydrogen concentrations were not linearly related to Mg concentrations, and we did not calculate H_2 end-member concentrations. The maximum H_2 concentrations were 549 μM at Snail, 466 μM at Archaean, 301 μM at Pika and 105 μM at Urashima.

Helium was not detected in Snail samples. For Archaean, the relation of He to Mg concentrations was not clearly linear, but the end-member concentration was calculated to be 2.1 μM. Although we have only one sample from Pika, the end-member value was 1.8 μM. For Urashima, given the helium concentration in seawater (2 nM), the relationship between He and Mg concentrations was smoothly linear, and the end-member value was 2.4 μM.

45.4.4 Isotopic Compositions of End-Members

The end-member $\delta^{13}C(CO_2)$ ranged from −2.3 to +0.1 ‰ (all values are relative to VPDB): −1.3 ‰ for Snail, −2.0 ‰ for Archaean, +0.1 ‰ for Pika, and −2.4 ‰ for Urashima (Table 45.2), which was the only value higher than that of seawater (0 ‰).

The $\delta^{13}C(CH_4)$ values showed a nonlinear relationship to $1/CH_4$. For Snail, the $\delta^{13}C(CH_4)$ values in CH_4-rich samples were around −5 ‰ and −25 ‰ for Snail, −10 ‰ and −50 ‰ for Archaean, around −5 ‰ for Pika, and −5 ‰ and −0 ‰ for Urashima.

The helium isotope ratios in source fluids, corrected for seawater admixture, were $8.1R_A$ for Snail, $8.4R_A$ for Archaean, $8.3R_A$ for Pika, and $8.0R_A$ for Urashima.

Table 45.1 End-member concentrations of aqueous components in the hydrothermal fluids for all the sites in the Southern Mariana Trough in this study

							CB									
Site	T_{max}	pH_{min}	Alk. (meq)	ΔAlk (meq)	Na (mM)	ΔNa (mM)	Na (mM)	ΔNa (mM)	K (mM)	ΔK (mM)	Li (μM)	ΔLi (μM)	Ca (mM)	ΔCa (mM)	Sr (μM)	ΔSr (μM)	Ba (μM)
Snail	116	3.52	−0.94	±0.04	454	±21	466	±91	31.3	±0.7	555	±22	29.9	±1.1	71.9	±4.0	N.D.
Archaean	343	2.94	−1.41	±0.03					32.8	±0.5	500	±8			76.6	±1.5	N.D.
2004					388	±11							20.6	±0.5			
2005–2010					315	±7	345	±33					15.7	±0.3			
Pika	330	2.86	−1.14	±0.02					32.6	±0.3	644	±9	39.4	±0.5	122.8	±1.7	N.D.
2003–2005					461	±7	495	±63									
2010					436	±15	351	±75									
Urashima	280	2.85	−1.44	±0.03	447	±11	515	±56	31.7	±0.5	764	±28	35.2	±0.8	106.2	±6.3	N.D.

CB means the Na concentrations are calculated by charge balance
AES and Color means the Si concentration are measured by ICP-AES and colorimetry, respectively

Table 45.2 End-member compositions of volatile components in the hydrothermal fluids for all the sites in the Southern Mariana Trough in this study

Site	T_{max}	H_2S (μM)	ΔH_2S (μM)	O_2 (μM)	N_2 (μM)	CO_2 (mM)	ΔCO_2 (mM)	CH_4 (μM)	ΔCH_4 (μM)	H_2 (μM)
Snail	116			N.D.	N.D.	78.8	±12.4	29.6	±5.1	N.D.
Archaean	343			N.D.	N.D.	N.D.	N.D.	N.D.	N.D.	N.D.
2004										
2005–2010										
Pika	330			N.D.	N.D.	33.7	±0.6	7.2	±0.2	N.D.
2005						69.1	±2.1	29.9	±2.0	
Urashima	280	883	±43	N.D.	N.D.	23.2	±0.4	10.8	±0.3	N.D.

N.D. not determined

													AES		Color			
Mn (mM)	ΔMn (mM)	Fe (mM)	ΔFe (mM)	Cl (mM)	ΔCl (mM)	SO_4 (mM)	ΔSO_4 (mM)	Br (mM)	ΔBr (mM)	NO_3 (μM)	ΔNO_3 (μM)	NH_4 (μM)	Si (mM)	ΔSi (mM)	Si (mM)	ΔSi (mM)	B (μM)	ΔB (μM)
2.08	±0.08	0.64	±0.02	588	±6	−1.71	±0.37	0.72	±0.10	−269	±53	N.D.	18.6	±0.8	18.7	±0.3	1,112	±37
						0.01	±0.03	0.75	±0.02			N.D.	16.7	±0.3	16.7	±0.1	959	±34
1.06	±0.02	2.55	±0.06	466	±3					−0.82	±0.04							
1.2	±0.02	3.00	±0.06	407	±2					−372	±5,609							
1.13	±0.01	7.38	±0.10			−1.57	±0.06	0.95	±0.02			N.D.	16.9	±0.2	16.4	±0.1		
				603	±3					−992	±3,483						1,130	±43
				460	±5					−1.5	±0.2						673	±10
2.22	±0.08	6.37	±0.13	629	±4	−3.02	±0.20	0.81	±0.02	−0.9	±0.3	N.D.	17.0	±0.4	16.5	±0.1	1,109	±45

He (μM)	ΔHe (μM)	$\delta^{13}C(CO_2)$ (‰VPDB)	$\Delta\delta^{13}C(CO_2)$ (‰VPDB)	$\delta^{13}C(CH_4)$ (‰VPDB)	$\delta D(H_2)$ (‰VSMOW)	$\delta D(CH_4)$ (‰VSMOW)	$^3He/^4He$ (R_A)	$\Delta^3He/^4He$ (R_A)
N.D.	N.D.	−1.33	±0.10	N.D.	N.D.	N.D.	8.15	±0.09
2.10		−2.00	±0.61	N.D.	N.D.	N.D.	8.37	±0.03
1.83	±0.08	0.14	±0.06	N.D.	N.D.	N.D.	8.27	±0.10
2.40	±0.1	−2.36	±0.17	N.D.	N.D.	N.D.	8.09	±0.19

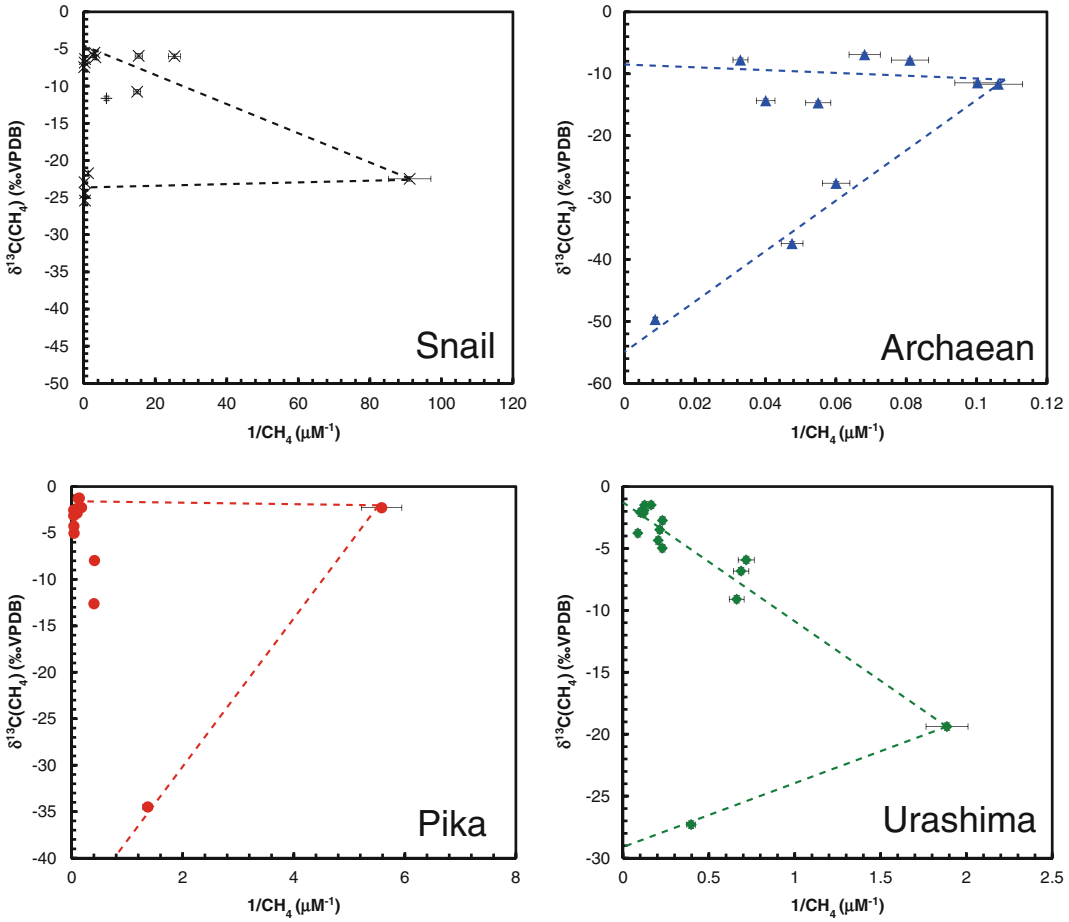

Fig. 45.3 Plots of $\delta^{13}C$ vs. 1/(CH_4 concentration) in the hydrothermal fluids for all the sites in the Southern Mariana Trough in this study

45.5 Summary

Hydrothermal fluids were sampled from several hydrothermal activities around the Southern Mariana backarc spreading center, and analyzed for chemical and isotopic compositions. The fluid chemistry around the Southern Mariana Trough would be influenced by a little input of magmatic volatiles, leading to low pH and high CO_2 concentrations, consequently the hydrothermal fluids are characterized by rich in Fe alongside of the MOR hydrothermal fluids.

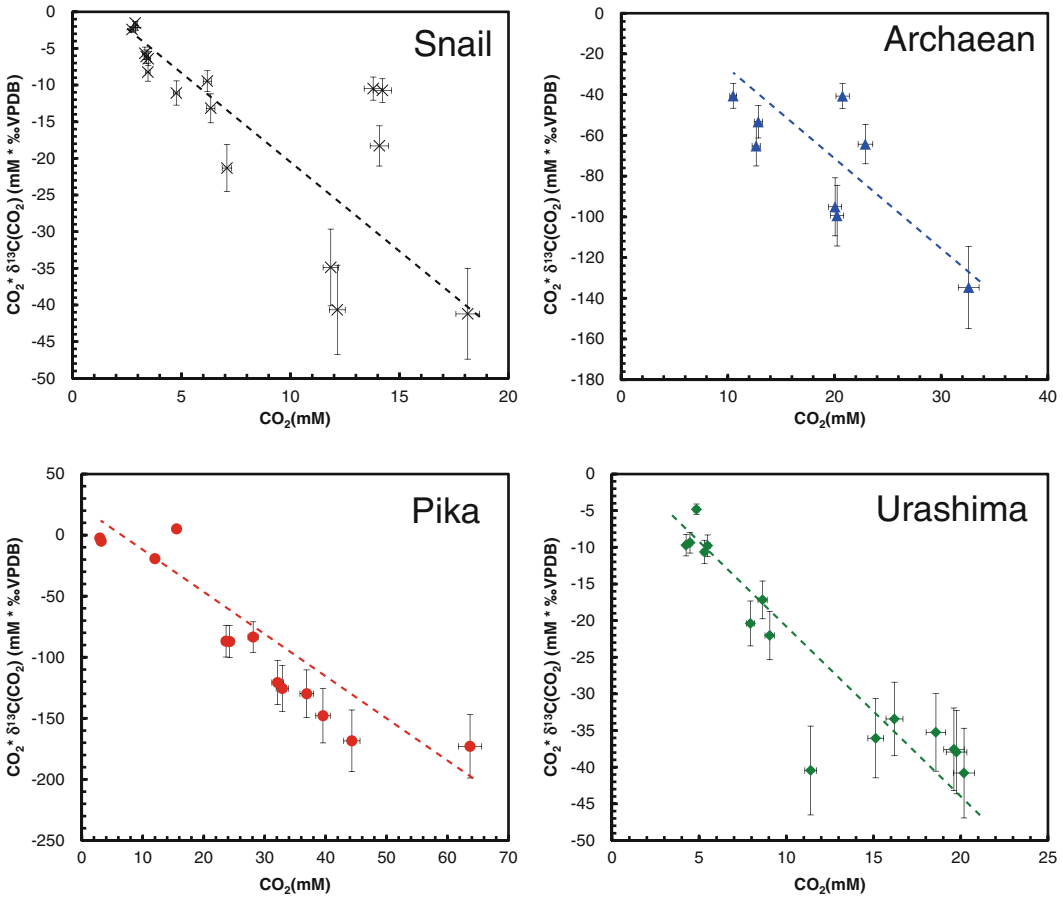

Fig. 45.4 Relationship between CO_2 concentrations and isotopic index from all the sites in the Southern Mariana Trough in this study are plotted, where the index are calculated by multiplying $\delta^{13}C(CO_2)$ by CO_2 concentrations

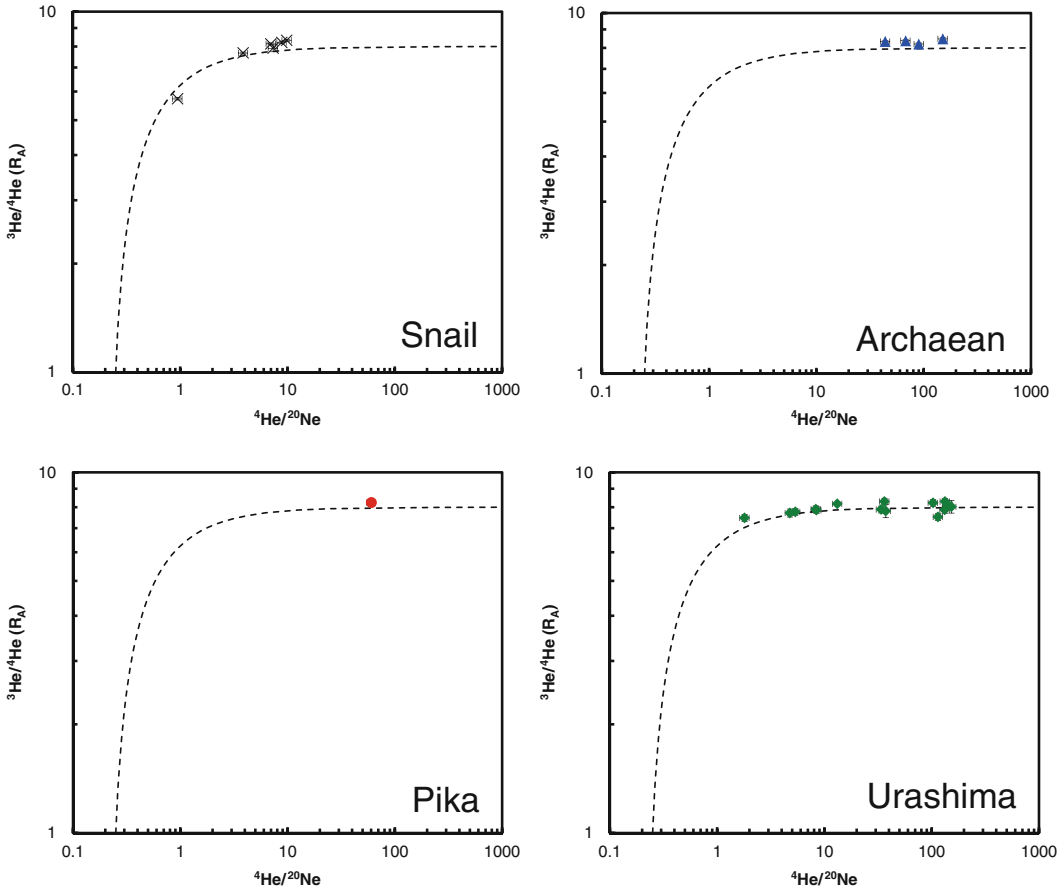

Fig. 45.5 Relationship between $^4He/^{20}Ne$ and $^3He/^4He$ in the hydrothermal fluids for all the sites in the Southern Mariana Trough in this study, together with the mixing line between mantle and seawater

Acknowledgments We thank the captains and crews of the *Yokosuka* and *Natsushima* and the commanders and operation teams of the *Shinkai 6500* and Hyper-Dolphin for sampling. Constructive and helpful reviews by Dr. Shinsuke Kawagucci and Dr. Takezo Shibuya are gratefully acknowledged. This study was supported by the Grant-in-Aid for Scientific Research on Innovative Areas of the Ministry of Education, Culture, Science and Technology (MEXT) "TAIGA project (Trans-crustal Advection and In situ biogeochemical processes of Global sub-seafloor Aquifer)," and partly by International Research Hub Project for Climate Change and Coral Reef/Island Dynamics from the University of the Ryukyus.

References

Alt JC (1988) Hydrothermal oxide and nontronite deposits on seamounts in the eastern Pacific. Mar Geol 81(1–4):227–239

Beaulieu SE (2013) InterRidge global database of active submarine hydrothermal vent fields, InterRidge

Bibee LD, Shor GG Jr, Lu RS (1980) Inter-arc spreading in the Mariana Trough. Mar Geol 35(1–3):183–197

Boyd TD, Scott SD (2001) Microbial and hydrothermal aspects of ferric oxyhydroxides and ferrosic hydroxides: the example of Franklin Seamount, Western Woodlark Basin, Papua New Guinea. Geochem Trans 2:45

Craig H, Lupton JE, Horibe Y (1978) A mantle helium component in circum-pacific volcanic gases: Hakone, the Marianas, and Mt. Lassen. In: Alexander EC, Ozima M (eds) Terrestrial rare gases. Japan Science Society Press, Tokyo, pp 3–16

Craig H, Horibe Y, Farley KA (1987) Hydrothermal vents in the Mariana Trough: results of the first Alvin dives. Eos Trans AGU 68(44):1531

Deming JW, Baross JA (1993) Deep-sea smokers: windows to a subsurface biosphere? Geochim Cosmochim Acta 57(14):3219–3230

Duhig NC, Davidson GJ, Stolz J (1992) Microbial involvement in the formation of Cambrian sea-floor silica-iron oxide deposits, Australia. Geology 20(6):511–514

Edwards KJ (2004) Formation and degradation of seafloor hydrothermal sulfide deposits. Geolog Soc Am Spec Paper 379:83–96

Edwards KJ, McCollom TM, Konishi H, Buseck PR (2003) Seafloor bioalteration of sulfide minerals: results from in situ incubation studies. Geochim Cosmochim Acta 67(15):2843–2856

Edwards KJ et al (2011) Ultra-diffuse hydrothermal venting supports Fe-oxidizing bacteria and massive umber deposition at 5000 m off Hawaii. ISME J 5(11):1748–1758

Eguchi T (1984) Seismotectonics around the Mariana trough. Tectonophysics 102(1–4):33–52

Fryer P (1995) Geology of the Mariana Trough. In: Taylor B (ed) Backarc basins tectonics and magmatism. Plenum, New York, pp 237–279

Fryer P, Sinton JM, Philpotts JA (1981) Basaltic glasses from the Mariana Trough. In: Hussong DM, Uyeda S, Knapp R, Ellis H, Kling S, Natland J (eds) Initial reports of the deep sea drilling project. U.S. Government Printing Office, Washington DC, pp 601–610

Fujii M, Okino K, Honsho C, Dyment J, Florent S, Mochizuki N (2013) Developing near-bottom magnetic measurements using a 3D forward modeling technique: application to hydrothermal vent fields, paper presented at Underwater Technology Symposium (UT), 2013 IEEE International, pp 5–8 March 2013

Gamo T (1993) Revisits to the mid-Mariana Trough hydrothermal site and discovery of new venting in the southern Mariana region by the Japanese submersible Shinkai 6500. InterRidge News 2:11–14

Gamo T, Tsunogai U, Ishibashi J, Masuda H, Chiba H (1997a) Chemical characteristics of hydrothermal fluids from the Mariana Trough. JAMSTEC J Deep Sea Res 69–74 (Special volume, Deep Sea Research in subduction zones, spreading centers and backarc basins, JAMSTEC)

Gamo T, Okamura K, Charlou J-L, Urabe T, Auzende J-M, Ishibashi J, Shitashima K, Chiba H, Shipboard Scientific Party of the Manus Flux Cruise (1997b) Acidic and sulfate-rich hydrothermal fluids from the Manus back-arc basin, Papua New Guinea. Geology 25 (2):139–142

Gamo T et al (2004) Discovery of a new hydrothermal venting site in the southernmost Mariana Arc: Al-rich hydrothermal plumes and white smoker activity associated with biogenic methane. Geochem J 38(6):527–534

Gamo T, Ishibashi J, Tsunogai U, Okamura K, Chiba H (2006) Unique geochemistry of submarine hydrothermal fluids from arc-back-arc settings of the western Pacific. In: Ridge 2000-InterRidge Theoretical Institute "interactions among physical, chemical, biological, and geological processes in backarc spreading systems". American Geophysical Union, Washington DC, pp. 147–161

Gena K, Mizuta T, Ishiyama D, Urabe T (2001) Acid-sulphate type alteration and mineralization in the Desmos caldera, Manus back-arc basin, Papua New Guinea. Resour Geol 51(1):31–44

Gieskes JM, Gamo T, Brumsack H (1991) Chemical methods for interstitial water analysis aboard JOIDES Resolution. Ocean Drill Prog Texas A&M Univ Tech Note 15:1–60

Hajash A, Chandler G (1982) An experimental investigation of high-temperature interactions between seawater and rhyolite, andesite, basalt and peridotite. Contr Mineral Petrol 78(3):240–254

Hart SR, Glassley WE, Karig DE (1972) Basalts and sea floor spreading behind the Mariana Island arc. Earth Planet Sci Lett 15(1):12–18

Hawkins JW Jr (1977) Petrologic and geochemical characteristics of marginal basin basalts. In: Hayes DE (ed) Island arcs, deep sea trenches and backarc basins. AGU, Washington DC, pp 355–365

Hofmann BA, Farmer JD (2000) Filamentous fabrics in low-temperature mineral assemblages: are they fossil biomarkers? Implications for the search for a subsurface fossil record on the early Earth and Mars. Planet Space Sci 48(11):1077–1086

Hussong DM, Uyeda S (1981) Tectonic processes and the history of the Mariana Arc, a synthesis of the results of deep sea drilling project Leg 60. In: Hussong DM, Uyeda S, Knapp R, Ellis H, Kling S, Natland J (eds) Initial reports of the deep sea drilling project. U.S. Government Printing Office, Washington DC, pp 909–929

Ishibashi J et al (2004) Geochemistry of hydrothermal fluids in south Mariana backarc spreading center, paper presented at AGU Fall Meeting 2004. American Geophysical Union, San Francisco, V44A-05

Johnson LE, Fryer P, Masuda H, Ishii T, Gamo T (1993) Hydrothermal deposits and two magma sources for volcanoes near 13°20′N in the Mariana backarc: a view from Shinkai 6500. EOS Trans AGU Fall Meet Suppl 74(43):681

Juniper SK, Fouquet Y (1988) Filamentous iron-silica deposits from modern and ancient hydrothermal sites. Can Mineral 26(3):859–869

Juniper SK, Tebo BM (1995) Microbe-metal interactions and mineral deposition at hydrothermal vents. In: Karl DM (ed) The microbiology of deep-sea hydrothermal vents. CRC Press, Boca Raton, pp 219–253

Kakegawa T, Utsumi M, Marumo K (2008) Geochemistry of sulfide chimneys and basement pillow lavas at the Southern Mariana Trough (12.55°N–12.58°N). Resour Geol 58(3):249–266

Karig DE (1971) Structural history of the Mariana island arc system. Geol Soc Am Bull 82(2):323–344

Kato S, Kobayashi C, Kakegawa T, Yamagishi A (2009) Microbial communities in iron-silica-rich microbial mats at deep-sea hydrothermal fields of the Southern Mariana Trough. Environ Microbiol 11(8):2094–2111

Kato S et al (2010) Biogeography and biodiversity in sulfide structures of active and inactive vents at deep-sea hydrothermal fields of the Southern Mariana Trough. Appl Environ Microbiol 76 (9):2968–2979

Keeling CD (1961) The concentration and isotopic abundances of carbon dioxide in rural and marine air. Geochim Cosmochim Acta 24(3–4):277–298

Kelley DS, Baross JA, Delaney JR (2002) Volcanoes, fluids, and life at mid-ocean ridge spreading centers. Annu Rev Earth Planet Sci 30:385–491

Komatsu DD, Tsunogai U, Kamimura K, Konno U, Ishimura T, Nakagawa F (2011) Stable hydrogen isotopic analysis of nanomolar molecular hydrogen by automatic multi-step gas chromatographic separation. Rapid Commun Mass Spectrom 25(21):3351–3359

Konno U, Tsunogai U, Nakagawa F, Nakaseama M, Ishibashi J, Nunoura T, Nakamura K (2006) Liquid CO_2 venting on seafloor: Yonaguni IV Knoll hydrothermal system, Okinawa Trough. Geophys Res Lett 33, L16607

Langley S, Igric P, Takahashi Y, Sakai Y, Fortin D, Hannington MD, Schwarz-Schampera U (2009) Preliminary characterization and biological reduction of putative biogenic iron oxides (BIOS) from the Tonga-Kermadec Arc, southwest Pacific Ocean. Geobiology 7 (1):35–49

Little CTS, Glynn SEJ, Mills RA (2004) Four-hundred-and-ninety-million-year record of bacteriogenic iron oxide precipitation at sea-floor hydrothermal vents. Geomicrobiol J 21(6):415–429

Lupton J, Lilley M, Butterfield D, Evans L, Embley R, Massoth G, Christenson B, Nakamura K, Schmidt M (2008) Venting of a separate CO_2-rich gas phase from submarine arc volcanoes: examples from the Mariana and Tonga-Kermadec arcs. J Geophys Res Solid Earth 113(B8):B08S12

Miller JB, Tans PP (2003) Calculating isotopic fractionation from atmospheric measurements at various scales. Tellus B 55(2):207–214

Mottl MJ, Holland HD, Corr RF (1979) Chemical exchange during hydrothermal alteration of basalt by seawater—II. Experimental results for Fe, Mn, and sulfur species. Geochim Cosmochim Acta 43(6):869–884

Nakamura K, Toki T, Mochizuki N, Asada M, Ishibashi J, Nogi Y, Yoshikawa S, Miyazaki J, Okino K (2013) Discovery of a new hydrothermal vent based on an underwater, high-resolution geophysical survey. Deep Sea Res I 74:1–10

Natland JH, Tarney J (1981) Petrologic evolution of the Mariana arc and backarc basin system – a synthesis of drilling results in the south Philippine Sea. In: Hussong DM, Uyeda S et al (eds) Initial reports of the deep sea drilling project. U.S. Government Printing Office, Washington DC, pp 877–907

Reysenbach A-L, Cady SL (2001) Microbiology of ancient and modern hydrothermal systems. Trends Microbiol 9(2):79–86

Rona PA (1978) Magnetic signatures of hydrothermal alteration and volcanogenic mineral deposits in oceanic crust. J Volcanol Geotherm Res 3(1–2):219–225

Saegusa S, Tsunogai U, Nakagawa F, Kaneko S (2006) Development of a multibottle gas-tight fluid sampler WHATS II for Japanese submersibles/ROVs. Geofluids 6(3):234–240

Sakai H, Gamo T, Kim ES, Tsutsumi M, Tanaka T, Ishibashi J, Wakita H, Yamano M, Oomori T (1990) Venting of carbon dioxide-rich fluid and hydrate formation in mid-Okinawa Trough backarc basin. Science 248(4959):1093–1096

Sano Y, Takahata N, Seno T (2006) Geographical distribution of $^{3}He/^{4}He$ ratios in the Chugoku district, southwestern Japan. Pure Appl Geophys 163(4):745–757

Seewald JS, Seyfried WE Jr (1990) The effect of temperature on metal mobility in subseafloor hydrothermal systems: constraints from basalt alteration experiments. Earth Planet Sci Lett 101(2–4):388–403

Seyfried WE Jr, Janecky DR (1985) Heavy metal and sulfur transport during subcritical and supercritical hydrothermal alteration of basalt: Influence of fluid pressure and basalt composition and crystallinity. Geochim Cosmochim Acta 49(12):2545–2560

Smoot NC (1990) Mariana Trough by multi-beam sonar. Geo-Mar Lett 10(3):137–144

Takai K, Horikoshi K (1999) Genetic diversity of archaea in deep-sea hydrothermal vent environments. Genetics 152(4):1285–1297

Tivey MA, Johnson HP (2002) Crustal magnetization reveals subsurface structure of Juan de Fuca Ridge hydrothermal vent fields. Geology 30(11):979–982

Toner BM, Santelli CM, Marcus MA, Wirth R, Chan CS, McCollom T, Bach W, Edwards KJ (2009) Biogenic iron oxyhydroxide formation at mid-ocean ridge hydrothermal vents: Juan de Fuca Ridge. Geochim Cosmochim Acta 73(2):388–403

Tsunogai U, Ishibashi J, Wakita H, Gamo T, Watanabe K, Kajimura T, Kanayama S, Sakai H (1994) Peculiar features of Suiyo Seamount hydrothermal fluids, Izu-Bonin Arc: differences from subaerial volcanism. Earth Planet Sci Lett 126(4):289–301

Tsunogai U, Yoshida N, Ishibashi J, Gamo T (2000) Carbon isotopic distribution of methane in deep-sea hydrothermal plume, Myojin Knoll Caldera, Izu-Bonin arc: implications for microbial methane oxidation in the oceans and applications to heat flux estimation. Geochim Cosmochim Acta 64(14):2439–2452

Tsunogai U, Toki T, Nakayama N, Gamo T, Kato H, Kaneko S (2003) WHATS: a new multi-bottle gas-tight sampler for sea-floor vent fluids (in Japanese with English abstract). Chikyukagaku (Geochem) 37(3):101–109

Urabe T, Maruyama A, Marumo K, Seama N, Ishibashi J (2001) The Archaean park project update. InterRidge News 10(1):23–25

Urabe T, Ishibashi J, Maruyama A, Marumo K, Seama N, Utsumi M (2004) Discovery and drilling of on- and off-axis hydrothermal sites in backarc spreading center of southern Mariana Trough, Western Pacific, paper presented at AGU Fall Meeting. American Geophysical Union V44A-03

Urabe T, Okino S, Sunamura M, Ishibashi J, Takai K, Suzuki K (2009) Trans-crustal advections and in-situ biogeochemical processes of global sub-seafloor aquifer: the sub-seafloor "TAIGA" (in Japanese with English abstract). J Geogr (Chigaku Zasshi) 118 (6):1027–1036

Utsumi M, Tsunogai U, Ishibashi J (2004) Direct measurement of microbial methane oxidation at hydrothermal vent ecosystems, paper presented at AGU 2004 Fall Meeting. American Geophysical Union, V41B-1373, San Francisco

Von Damm KL (1995) Controls on the chemistry and temporal variability of seafloor hydrothermal fluids. In: Humphris SE, Zierenberg RA, Mullineaux LS, Thomson RE (eds) Seafloor hydrothermal systems: physical, chemical, biological, andgeological interactions. American Geophysical Union, Washington DC, pp 222–247

Von Damm KL, Parker CM, Gallant RM, Loveless JP, The AdVenture 9 Science Party (2002) Chemical evolution of hydrothermal fluids from EPR 21° N: 23 years later in a phase separating world. EOS Trans AGU Fall Meet Suppl 83(47) Abstract V61B-1365

Wheat CG, Fryer P, Hulme SM, Becker NC, Curtis A, Moyer C (2003) Hydrothermal venting in the southern most portion of the Mariana backarc spreading centerat 12.57 degrees N, paper presented at AGU Fall Meeting. American Geophysical Union T32A-09020, San Francisco

Yamazaki T, Stern RJ (1997) Topography and magnetic vector anomalies in the Mariana Trough. JAMSTEC J Deep Sea Res 13:31–45

Yamazaki T, Murakami F, Saito E (1993) Mode of seafloor spreading in the northern Mariana Trough. Tectonophysics 221 (2):207–222

Yang K, Scott SD (2006) Magmatic fluids as a source of metals in seafloor hydrothermal systems. In: Back-arc spreading systems: geological, biological, chemical, and physical interactions. AGU, Washington DC, pp 163–184

Yoshikawa S, Okino K, Asada M (2012) Geomorphological variations at hydrothermal sites in the southern Mariana Trough: relationship between hydrothermal activity and topographic characteristics. Mar Geol 303–306:172–182

Gamma Ray Doses in Water Around Sea Floor Hydrothermal Area in the Southern Mariana Trough

46

Shin Toyoda, Debabrata Banerjee, Hidenori Kumagai, Junichi Miyazaki, Jun-ichiro Ishibashi, Nobutatsu Mochizuki, and Shigeaki Kojima

Abstract

The dose rates in sea water in the Southern Mariana Trough sea floor hydrothermal area were investigated. The dose rate in sea water was less than detection limit (about 0.1 mGy/year) near the sea surface while it was around 2 mGy/year at the sea floor of hydrothermal area, where those levels of dose rates will be negligible for ESR (electron spin resonance) dating of barite of sulfide deposits. During the dive by a submarine vehicle, there were three locations at which the level of dose rate increases more than ten times as much as the usual level. One was very close to a hydrothermal vent, but no hydrothermal activities were found near the other locations.

Keywords

Gamma ray • Hydrothermal water • NaI spectrometer

46.1 Introduction

Radioactivity in sea water at sea floor hydrothermal area is one of the important factors for trapped electron dating methods such as by electron spin resonance (ESR) (e.g., Takamasa et al. 2013), as it possibly gives doses, hence additional trapped electrons, to the minerals for which analysis is made to obtain ages. Radioactivity in sea water would also be an indicator of hydrothermal activities as the source in sea water of hydrothermal area is dissolved radioactive radium and radon emanated from hydrothermal vents (Kumagai et al. 2012).

Commercial gamma ray spectrometers are not suitable for such studies as they are neither water nor pressure proof. A NaI gamma ray spectrometer was specially designed for deep sea radioactivity (Hattori et al. 2000) and it was used extensively for studies to map the radiation intensities at the sea floor (Hattori and Okano 2001, 2002). In this Chapter, this NaI spectrometer was used to investigate the radioactivity in the sea water at the sea floor around hydrothermal active area. After making calibration for the spectrometer and examining the shielding by the water, the level of radioactivity of the sea water in the South Mariana Trough hydrothermal area was measured. The radioactivity was also continuously monitored during the dives to see the correlation of the radioactivity with the hydrothermal activity.

46.2 Calibration of the NaI Spectrometer

An NaI gamma ray spectrometer was used in the present study, which is designed for deep sea radioactive research. The detector and the preamplifier are enclosed in

S. Toyoda (✉)
Okayama University of Science, Okayama, Japan
e-mail: toyoda@dap.ous.ac.jp

D. Banerjee
Physical Research Laboratory, Ahmedabad, India

H. Kumagai • J. Miyazaki
JAMSTEC, Yokosuka, Japan

J.-i. Ishibashi
Kyushu University, Fukuoka, Japan

N. Mochizuki
Kumamoto University, Kumamoto, Japan

S. Kojima
Graduate School of Frontier Sciences, The University of Tokyo, Chiba, Japan

J.-i. Ishibashi et al. (eds.), *Subseafloor Biosphere Linked to Hydrothermal Systems: TAIGA Concept*,
DOI 10.1007/978-4-431-54865-2_46,

a high-pressure-proof tube of 12 cm in diameter and 60 cm in length. It is wired to the submersible vehicle, SHINKAI6500, to supply the electricity and to output the spectrum data. A special program for this NaI spectrometer installed in a PC in the vehicle records the spectrum every minute.

The background dose at the building No.1 of Okayama University of Science was measured by this NaI spectrometer (Shinkai-type) and by Aloka, JSM-102, for 1 h. The averaged doses were, 69.3 nGy/h, corresponding to 0.697 mGy/year, by Shinkai-type spectrometer and 0.761 mGy/year by Aloka, JSM-102, using G(E) function method. It was found that the dose rate values obtained by Shinkai-type spectrometer have to be multiplied by the correction factor of 1.09.

46.3 Gamma Ray Attenuation by Sea Water

Gamma rays are attenuated by materials with the following equation,

$$\mathrm{I} = I_0 e^{-\mu x} \tag{46.1}$$

where I is the gamma ray intensity, I_0 gamma ray intensity at $x = 0$, x the distance from the source, μ the attenuation coefficient.

Actual gamma ray measurements were performed at the sea floor to examine the attenuation of gamma ray by sea water in the SHINKAI6500 Dive 1228 during cruise YK10-11 operated by JAMSTEC in 2010 at the Southern Mariana Trough. A gamma ray spectrum was obtained for 3 min attaching the end of the spectrometer tube to basalt with the tube vertical to the rock surface at the sea floor. Then the measurements were repeated at a distance, 15 cm, from the rock surface and at 25 cm. After using the program, the dose rate values were obtained being multiplied by the correction factor, as a function of distance as shown in Fig. 46.1. A curve best fit to equation (1) was obtained by the least square method as shown in the figure. The obtained attenuation coefficient, μ, is 0.100 cm^{-1}, being consistent with the literature value of 0.0971 cm^{-1} (Firestone et al. 1999).

46.4 Comparison with OSL Dosimeters

OSL (optically stimulated luminescence) dosimeters made of Al_2O_3:C manufactured by Nagase Landauer, Ltd. were kept in a titanium tube. Two titanium tubes were placed on sulfide deposit at Archaean Site, the South Mariana Trough, during the cruise YK11-10 operated by JAMSTEC in 2011. They were left there for 29 days and were recovered during YK11-11.

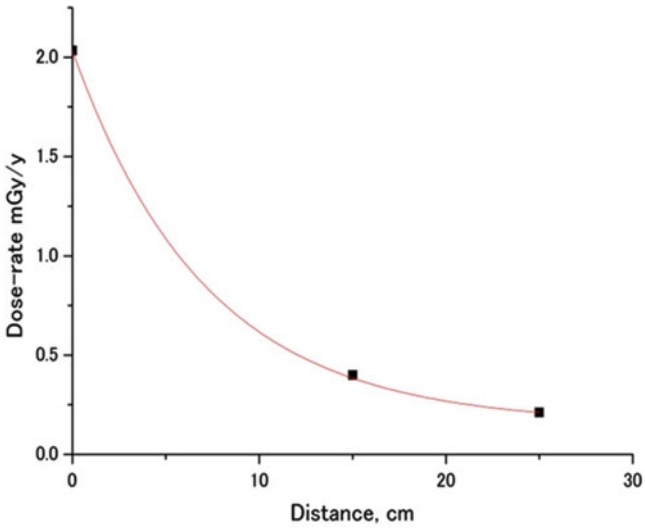

Fig. 46.1 The dose rate observed in water with distance from a basalt surface. The attenuation coefficient was obtained to be 0.100 cm^{-1}

The OSL doses were obtained as the averages of each five specimen. The obtained doses were converted to the dose rates per year to be 1.26 ± 0.20 and 0.86 ± 0.07 mGy/year for the two tubes located 10 cm apart from each other. As the attenuation factor of gamma rays in water is 0.100 cm^{-1} as obtained above, the contribution of the gamma rays in water is drastically reduced beyond 10 cm. The difference in the dose rates, from the two locations 10 cm apart from each other, would probably be due to the heterogeneity of the doses at the sea floor. The actual gamma ray dose was measured during SHINKAI6500 Dive 1221 by the Shinkai-type NaI spectrometer with 12 cm in diameter, at the place same as the titanium tubes were placed with OSL dosimeters inside. The obtained value of 0.92 mGy/year is consistent with the averaged value by the OSL dosimeters of 1.05 mGy/year within the measurement error.

As results of these calibrating studies, it was shown that this Shinkai-type NaI spectrometer can be used for dosimetry of sea water quantitatively.

46.5 Survey of Radioactivity in Sea Water at Hydrothermal Area of the South Mariana Trough

The Shinkai-type NaI spectrometer was placed between the two supports of the submersible vehicle, Shinkai-6500, during the dives, and radioactivity of sea water was continuously monitored. As the position of the spectrometer was at about 80 cm from the sea floor when the vehicle lands at the floor, the measured doses are of the sea water. The dives, 1223 and 1224 were performed at Archaean site, and 1226 at

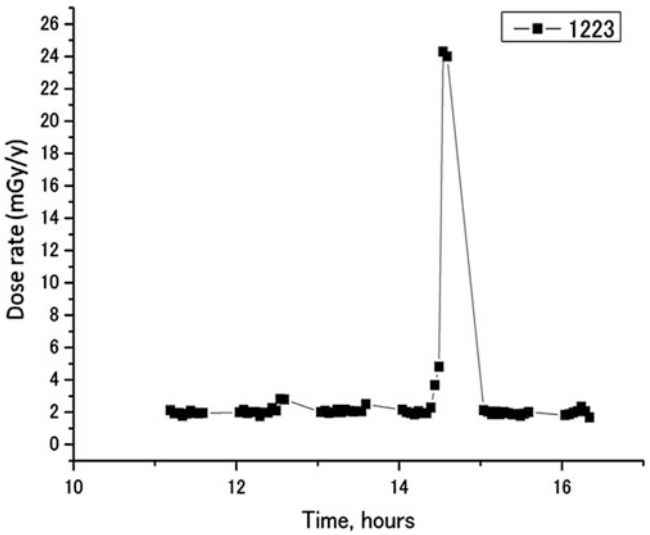

Fig. 46.2 The temporal change of the water radioactivity during the Dive 1223 at Archaean Site. One peak of radioactivity was observed, for which the reason was not found. The horizontal axis denotes the time of the day, while the vertical axis the dose rate in mGy/year

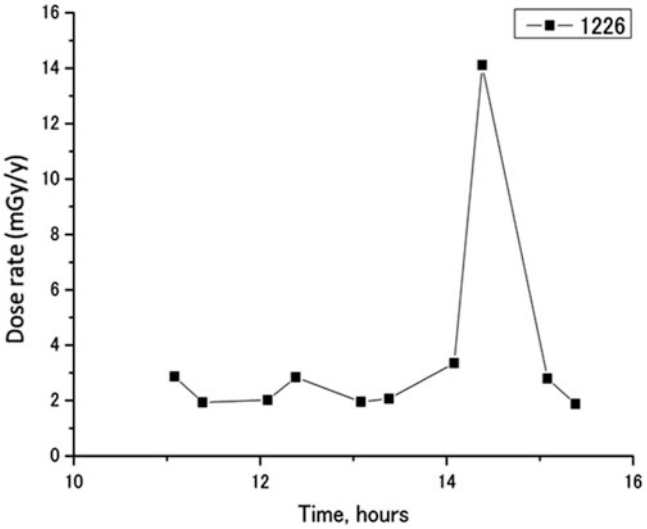

Fig. 46.4 The temporal change of the water radioactivity during the Dive 1226 at Pika Site. One peak of radioactivity was observed, for which the reason was not found. The horizontal axis denotes the time of the day, while the vertical axis the dose rate in mGy/year

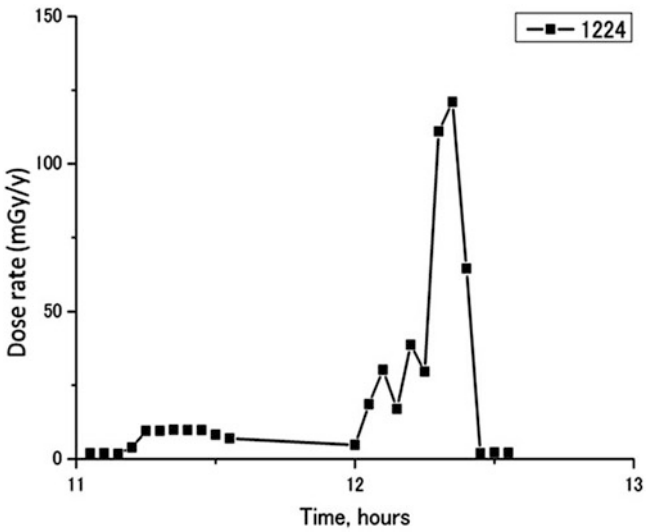

Fig. 46.3 The temporal change of the water radioactivity during the Dive 1224 at Archaean Site. The peaks of radioactivity correspond to the currently active hydrothermal vents. The horizontal axis denotes the time of the day, while the vertical axis the dose rate in mGy/year

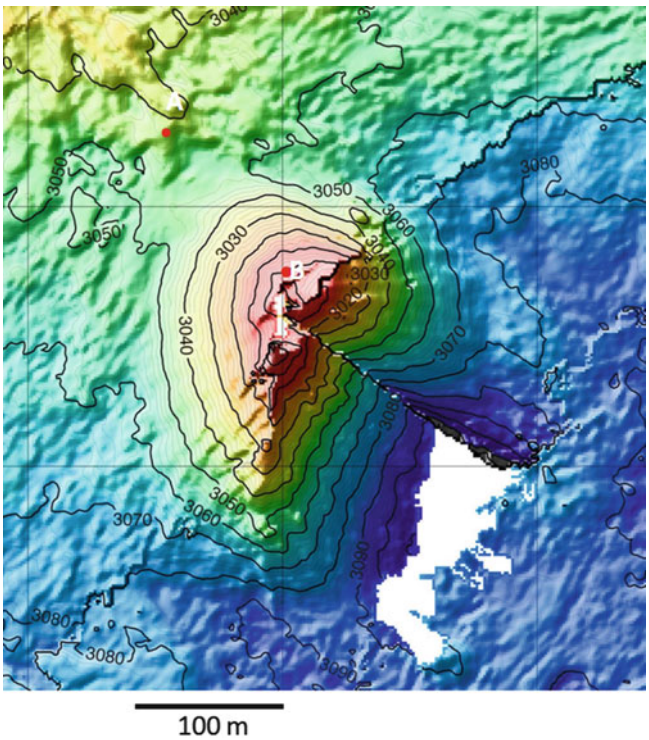

Fig. 46.5 Map of Archaean Site with places where high radioactive water was observed. The location at the top of the rise corresponds to currently active vents (Fig. 46.3), but the reason for higher activity at north–west point (Fig. 46.2) is unknown

Pika site, the Southern Mariana Trough, during the research cruise YK10-11.

The changes of water dose rate were obtained as shown in Figs. 46.2, 46.3, and 46.4. The horizontal axis denotes the time during the day and the vertical axis the dose rate averaged for 5 min in mGy/year. The dose rate was below detection limit of the spectrometer (about 0.1 mGy/year) just after the dive starts at the sea surface (Fig. 46.3). The dose rate increased to about 2 mGy/year when the vehicle arrived at the bottom of hydrothermal area, and stayed constant during the dive. However, one peak at each dive was observed as shown in Figs. 46.2, 46.3, and 46.4 at locations shown in Figs. 46.5 and 46.6. The peak observed during Dive 1224 (Fig. 46.3) was very high up to 120 mGy/year

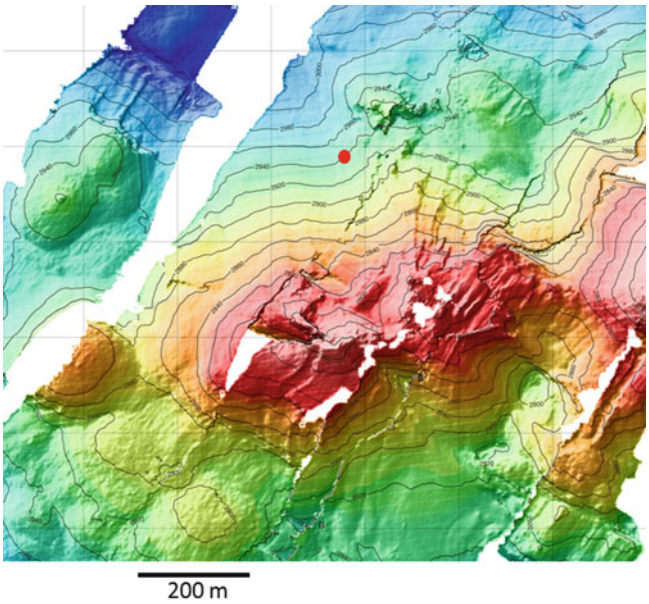

Fig. 46.6 Map of Pika Site with a place where high radioactive water was observed. The reason for this higher activity (Fig. 46.4) is unknown

at the top of the Archaean site (Point B, Fig. 46.5). This was observed when the vehicle stayed at currently active hydrothermal area within about 50 m in distance. However, the other two peaks (Point A, Figs. 46.5 and 46.6) were observed at the foot of the rise where no currently active hydrothermal activities were found. It was observed within 10 min (Point A, Fig. 46.5) and 5 min (Fig. 46.6) corresponding to about 20–10 m in distance. It is possible that these peaks correspond to some unknown currently active hydrothermal vents. If it is the case, another venting can be found by the guide of radioactivity measurements.

The "usual" dose rate of about 2 mGy/year in sea water observed in these sea floor hydrothermal areas is negligible for the dose rate for ESR (electron spin resonance) dating of many barite samples extracted hydrothermal deposits (Fujiwara et al. Chap. 29) as the present dose rate to barite is in the order of several 10 mGy/year.

On the other hand, when the sample is exposed to active hydrothermal vents, the dose rate can be in the order of 100 mGy/year as observed at the three locations in the present study, the sea water dose might have given significant contribution. In this sense, it is recommended to examine the distribution of the dose within the deposit samples. If the dose is higher at the outer part, it is possible that the sample was give high dose rate from the sea water.

46.6 Summary

Radioactivity in the sea water in the hydrothermal area in the South Mariana Trough was investigated using a NaI spectrometer designed for use with submersible vehicle. The radioactivity of the surface sea water was below detection limit while the value of the water in hydrothermal area without currently active vents was about 2 mGy/year, which is most probably mixture of water from active vents with high radioactivity and usual sea water. High water radioactivity was found in water close to currently active vents, but also two places without such vents. The dose from water will not affect dating results unless the sample is continuously exposed to active hydrothermal vents.

Acknowledgements The work was supported by TAIGA project, Grant-in-Aid for Scientific Research on innovative Areas (20109004) funded by the Ministry of Education, Culture, Sports, Science and Technology (MEXT). The authors thank Nagase Landauer, Ltd. for providing and for measuring the OSL dosimeters.

References

Firestone RB, Shirley VS, Baglin CM, Chu SYF, Zipkin J (1999) Table of isotopes, 8th edn. Willey, USA

Hattori M, Okano M, Togawa O (2000) Sea bottom gamma ray measurement by NaI(Tl) Scintillation spectrometers installed on manned submersibles, ROV and sea bottom long term observatory. In: Proceedings 2000 International Symposium on Underwater Technology. IEEE Catalog Number 00EX418, pp 212–217

Hattori M, Okano M (2001) New results of sea bottom radioactivity measurement. JAMSTEC J Deep Sea Res 18:1–13 (in Japanese English abstract)

Hattori M, Okano M (2002) Sea bottom gamma ray measurement - results of study and modeling of sea bottom radioactive environment. JAMSTEC J Deep Sea Res 20:37–52 (In Japanese w/English abstract)

Kumagai H, Iwase R, Kinoshita M, Machiyama H, Hattori M, and Okano M (2012) Environmental gamma-ray observation in deep sea. In: Feriz Adrovic (eds) Gamma radiation. InTECH, Rijeka, Croatia, ISBN 978-953-51-0316-5, pp 55–74

Takamasa A, Nakai S, Sato F, Toyoda S, Banerjee D, Ishibashi J (2013) U-Th radioactive disequilibrium and ESR dating of a barite-containing sulfide crust from South Mariana Trough. Quater Geochronol 15:38–46

^{226}Ra-^{210}Pb and ^{228}Ra-^{228}Th Dating of Barite in Submarine Hydrothermal Sulfide Deposits Collected at the Okinawa Trough and the Southern Mariana Trough

47

Ai Uchida, Shin Toyoda, Jun-ichiro Ishibashi, and Shun'ichi Nakai

Abstract

The ^{226}Ra-^{210}Pb and ^{228}Ra-^{228}Th ages were obtained for barite crystals in hydrothermal sulfide deposits taken at the Okinawa Trough and the Southern Mariana Trough. After calibrating the measurement systems with standard samples with pitchblende, it was confirmed that the U and Th concentrations obtained for GSJ samples are consistent with literature values. It was shown that radon does not escape from barite crystals extracted from hydrothermal sulfide deposits, which indicates that ^{226}Ra-^{210}Pb dating method works for these barite crystals. Most of the ^{226}Ra-^{210}Pb and ^{228}Ra-^{228}Th ages are younger than ESR and U-Th ages, where this inconsistency would be explained by the mixture of the barite crystals with younger and older ages, formed by several hydrothermal events.

Keywords

^{226}Ra-^{210}Pb and ^{228}Ra-^{228}Th ages • Barite crystals • Okinawa Trough • Southern Mariana Trough

47.1 Introduction

Determining the mineralization ages of the hydrothermal deposit will greatly contribute to the studies of temporal variation of submarine hydrothermal activities, as the ages are the essential factors to discuss ore formation process and the surrounded ecosystem sustained by the chemical species supplied by hydrothermal activities. Several dating procedures using disequilibrium of radioisotopes are available for this purpose, such as ^{238}U-^{230}Th method for sulfide minerals (Lalou et al. 1993), ^{226}Ra-^{210}Pb, and ^{228}Ra-^{228}Th methods for barite ($BaSO_4$). Noguchi et al. (2004, 2011) successfully obtained ^{226}Ra-^{210}Pb and ^{228}Ra-^{228}Th ages for barite crystals extracted from mixture of sulfide and sulfate minerals collected from the Okinawa Trough and the Southern Mariana Trough. Noguchi et al. (2011) reported the precipitation ages of hydrothermal chimneys from Izena Hole (Hakurei site) and Yaeyama Graben, by ^{226}Ra-^{210}Pb method, which range from 25 to 74 and from 14 to 53 years, respectively. Even in one chimney structure, precipitation ages are varied, which may mean the growth history of chimney structure. The ^{226}Ra-^{210}Pb ages of samples from the Southern Mariana Trough range from 30 to 35 years.

White and Rood (2001) reported that 3–20 % of ^{222}Rn is lost from the barite crystals, which are used for casing in mining. If this is the case for our barite crystals, the obtained ages will be in error. In this chapter, it is investigated if the barite crystals extracted from the sea-floor hydrothermal sulfide deposits consist of a closed system in the aspect of possible Rn loss, after confirming that the U and Th concentrations obtained for GSJ samples are consistent with literature values.

Secondly, we conducted ^{226}Ra-^{210}Pb and ^{228}Ra-^{228}Th measurements of several hydrothermal deposits collected from the Okinawa Trough and the Southern Mariana Trough.

A. Uchida • S. Toyoda (✉)
Okayama University of Science, Okayama, Japan
e-mail: toyoda@dap.ous.ac.jp

J.-i. Ishibashi
Kyushu University, Fukuoka, Japan

S. Nakai
Earthquake Research Institute, University of Tokyo, Tokyo, Japan

J.-i. Ishibashi et al. (eds.), *Subseafloor Biosphere Linked to Hydrothermal Systems: TAIGA Concept*,
DOI 10.1007/978-4-431-54865-2_47,

47.2 Experimental Procedures

47.2.1 Instruments

We used three low background gamma-ray spectrometers, which are GC1520 (CANBERRA) and EGP-100-10R (INTERTECHNIQUE) in Okayama University of Science and System 8000 (Princeton Gamma-Tech Instruments Inc.) in Kochi University. These three instruments were covered with more than 100 mm thickness of lead block to prevent the environmental gamma-ray, together with 10 mm thickness of copper plate and 5 mm thickness of acrylic plate to decrease the characteristic X-rays and/or bremsstrahlung radiations.

47.2.2 Information of Nuclides

The activities of the following radioactive nuclides were measured in the present study: ^{214}Pb (295 and 352 keV) and ^{214}Bi (610, 1,120, and 1,765 keV) which are daughter nuclides of ^{238}U, hence of ^{226}Ra, and ^{212}Pb (239 and 300 keV), ^{228}Ac (338, 911, and 969 keV),^{208}Tl (583 and 2,614 keV), and ^{212}Bi (727 keV) which are daughter nuclides of ^{232}Th, hence of ^{228}Ra.

47.2.3 Samples

47.2.3.1 GSJ Reference Materials

About 20 g of mixed standard samples (pitchblende standards) for uranium concentrations were prepared by the dilution of Proterozoic age uraninite (UO_2) from Shinkolobwe Mine in Congo, which reaches radioactive equilibrium, with NaCl or quartz (SiO_2) powder in the following contents; 51.32, 83.60, 185.83 ppm in NaCl and 46.84, 109.98, 179.45 ppm in SiO_2, respectively. The concentration of uranium in the uraninite was obtained to be 59.30 % by isotope dilution analysis using an MC-ICP-MS (Micromass, IsoProbe) (Takamasa et al. 2013). JG-3, one of GSJ (Geological Survey of Japan) reference samples (Imai et al. 1995), with Th concentration of 8.28 ppm was used as a Th standard.

Four other GSJ samples (JG-1a, JR-1, JA-2, JB-3) were measured by GC1520 based on one of the pitchblende standard in order to check if the obtained U and Th concentrations are consistent with the literature values. JG-3 was also used for this purpose for uranium concentration. All standard and GSJ samples in powder were compressed and sealed in a plastic container with a diameter of 52 mm and height of 10 mm. They were left for 14 days or more after sealing to attain radioactive equilibrium for radon. Each sample was measured for 7 days to obtain a gamma ray spectrum. Assuming radioactive equilibrium, the concentration of U was calculated from the peak intensities of ^{214}Pb (295 and 352 keV) and ^{214}Bi (610, 1,120, and 1,765 keV), and that of Th was from ^{212}Pb (239 and 300 keV), ^{228}Ac (338, 911, and 969 keV),^{208}Tl (583 and 2,614 keV),and ^{212}Bi (727.2 keV), after subtracting background, in comparison with those peaks of the standard sample.

47.2.3.2 Sulfide Deposit Samples from the Okinawa Trough and from the Southern Mariana Trough

Sulfide breccias, as shown in Table 47.1, were collected from Hatoma Knoll, Yoron Hole, and Izena Hole (Hakurei site) in the Okinawa Trough using Remote Operation Vehicle (ROV) Hyper-Dolphine of Japan Agency for Marine-Earth Science and Technology (JAMSTEC) during the

Table 47.1 Sampling locations

Sample No	Cruise	Latitude	Longitude	Depth (m)
Okinawa Trough				
Yoron Hole				
HPD#1333G06	NT11-20	27°29′383 N	127°32′001 E	591
HPD#1333G05	NT11-20	27°29′383 N	127°32′001 E	591
HPD#1333G03	NT11-20	27°29′328 N	127°32′123 E	580
HPD#1333G07	NT11-20	27°29′383 N	127°32′001 E	591
HPD#1333G08	NT11-20	27°29′383 N	127°32′001 E	591
HPD#1333G11	NT11-20	27°29′425 N	127°32′995 E	566
Hatoma Knoll				
HPD#1331G01	NT11-20	24°51′451 N	123°50′478 E	1,499
HPD#1331G07	NT11-20	24°51′520 N	123°50′559 E	1,490
Hakurei Site of Izena Hole				
HPD#1313G05	NT11-20	27°14′858 N	127°3′962 E	1,613
Southern Mariana Trough				
Archaean				
903R7-2	YK05-09	12°56′3625 N	143°37′9000 E	2,974

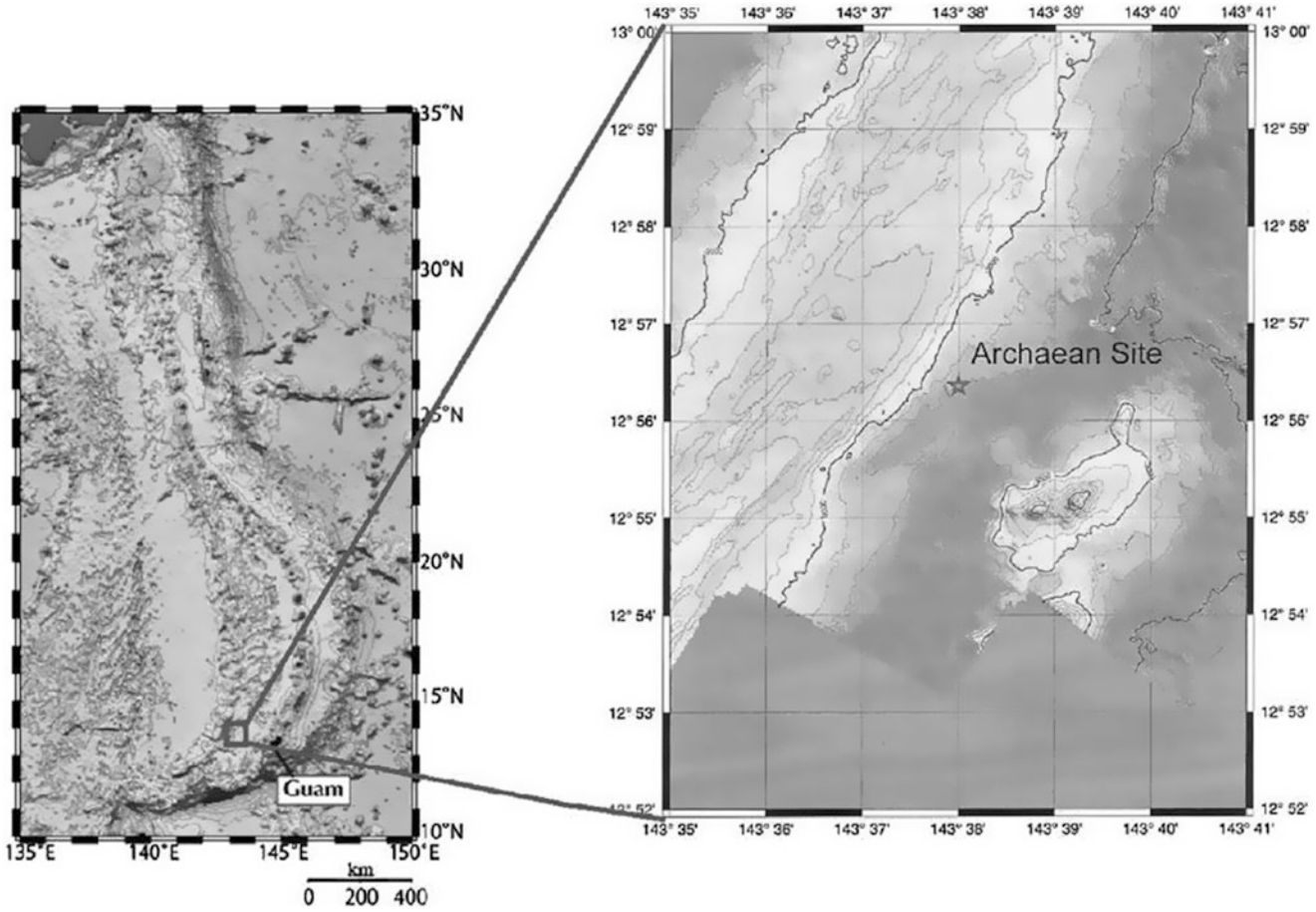

Fig. 47.1 Bathymetric chart of the Archaean site in the the Southern Mariana Trough showing the sampling site of the sulfide crust used for this study (Takamasa et al. 2013)

NT11-20 cruise in 2011 (see details in (Fujiwara et al. Chap. 29)). A sulfide chimney sample was also collected from the Archaean site in the Southern Mariana Trough by manned submersible SHINKAI6500 (JAMSTEC) during the YK05-09 cruise in 2005, the location of which is shown in Fig. 47.1.

Blocks of sulfide breccias were cut into pieces as shown in Fig. 29.3 of (Fujiwara et al. Chap. 29). Barite crystals were chemically extracted from the sulfide deposits as described in (Fujiwara et al. Chap. 29).

47.2.4 Experiments for Rn Loss

The barite crystals extracted from sample 903R7-2, dried and left for about 1 year after extraction, were packed in a columnar shape stainless container with a diameter of 100 mm, a height of 10 mm, a wall thickness of 20 mm, and a cover thickness of 1.5 mm, being sealed by two O rings between the container body and the two covers, to prevent from Rn loss. Gamma ray spectra were obtained for the crystals in the above container by EGP 800-10-R. The measurement was started immediately after sealing the container for 10 days where the spectrum was stored on each day. The ^{222}Rn activity was calculated using both ^{214}Pb (295 keV) and ^{214}Bi (610 keV) peaks. ^{214}Pb (half-life: 26.8 min) and ^{214}Bi (half-life: 19.9 min) are the daughter nuclides of ^{222}Rn (half-life: 3.82 day), therefore, these daughter nuclides are equilibrated with ^{222}Rn within 2 h.

47.2.5 ^{228}Ra-^{228}Th and ^{226}Ra-^{210}Pb Dating

For ^{228}Ra-^{228}Th dating, the bulk samples were gently crushed by agate mortar and about 20 g was sealed in a plastic container with a diameter of 52 mm and height of 10 mm. The barite crystals extracted from samples, 1333G03a and 1313G05l, were ground and about 0.3 g of them were mixed with about 20 g NaCl, then packed into a plastic container with a diameter of 52 and 10 mm in height.

The samples were measured by GC1520 for 10–24 h. JG-3 was used as the equilibrated standard. The gamma

ray peak intensities of ^{228}Ac (911 keV) and ^{212}Bi (727 keV) were obtained. As ^{228}Ac is a daughter nucleus next to ^{228}Ra with a half-life of 6.15 h much shorter than that of parent nucleus of 5.75 years, the activity of ^{228}Ac is considered to be that of ^{228}Ra. As ^{212}Bi is a daughter nucleus of ^{228}Th and the half-lives of the nuclide between these two and that of ^{212}Bi (60.6 min) are much shorter than that of ^{228}Th, 1.91 years, the activity of ^{212}Bi is considered to be that of ^{228}Th.

Activities of ^{226}Ra and ^{210}Pb were measured using IGW14023-16. The gamma-ray spectrometer was calibrated with 4.93 mg of uraninite mixed with 3.009 g of NaCl powder, whose U content is 972.6 ppm. Standard and purified barite minerals, which are diluted with powdered NaCl, are packed into a plastic tube (φ17mm and 58 mm height). The durations of measurement were 8 to 15 h for barite samples and 5 h for the standard. The peak intensities of ^{210}Pb (46.5 keV) and ^{214}Bi (610 keV) were obtained for barite samples and for the standard. Assuming radioactive equilibrium in the standard, the activity ratios of ^{210}Pb to ^{214}Bi were calculated for the barite samples. As ^{214}Bi is a nuclide after ^{226}Ra where the longest half-life of the nuclides between these two is 3.82 days of ^{222}Rn, much shorter than 1,600 years of ^{226}Ra, the activity of ^{214}Bi is considered to be that of ^{226}Ra when no Rn is lost.

47.2.6 Age Calculation

As barite crystals do not accommodate lead but radium at the time of crystallization, ^{210}Pb is accumulated, being simultaneously decaying, as time passes due to the decay of ^{226}Ra. The changes with time of the numbers of these nuclides are expressed by the differential equations,

$$\frac{dN_1}{dt} = \lambda_1 N_1 \tag{47.1}$$

$$\frac{dN_2}{dt} = -\lambda_2 N_2 + \lambda_1 N_1 \tag{47.2}$$

where
N_1: number of ^{226}Ra
N_2: number of ^{210}Pb
λ_1: decay constant ^{226}Ra, 4.33×10^{-4} year^{-1}
λ_2: decay constant of ^{210}Pb, 3.11×10^{-2} year^{-1}.

In the time scale of several 10 years, the decay of ^{226}Ra with the half-life of 1,600 years can be neglected, i.e. the number of ^{226}Ra is constant. Then, N_2 is expressed by

$$N_2 = \frac{\lambda_1}{\lambda_2} N_{10}\left(1 - e^{-\lambda_2 t}\right) \tag{47.3}$$

assuming that initial N_2 is zero.

The activity ratio, r_{Pb}, is therefore written as

$$r_{Pb} = \frac{\lambda_2 N_2}{\lambda_1 N_1} = 1 - e^{-\lambda_2 t}. \tag{47.4}$$

The age, t, is deduced to

$$t = -\frac{1}{\lambda_2} ln(1 - r_{Pb}) \tag{47.5}$$

Similarly, barite crystals do not accommodate Th but Ra at the time of crystallization. ^{228}Th is accumulated, being simultaneously decaying, as time passes due to the decay of ^{228}Ra. The changes with time of the numbers of these nuclide are expressed by the differential equations,

$$\frac{dN_1}{dt} = \lambda_1 N_1 \tag{47.6}$$

$$\frac{dN_2}{dt} = -\lambda_2 N_2 + \lambda_1 N_1 \tag{47.7}$$

where
N_1: number of ^{228}Ra
N_2: number of ^{228}Th
λ_1: decay constant ^{228}Ra, 1.21×10^{-1} year^{-1}
λ_2: decay constant of ^{228}Th, 3.62×10^{-1} year^{-1}.

The solution of these differential equations is

$$N_1 = N_{10} e^{-\lambda_1 t} \tag{47.8}$$

$$N_2 = \frac{\lambda_1}{\lambda_2 - \lambda_1} N_{10}\left(e^{-\lambda_1 t} - e^{-\lambda_2 t}\right). \tag{47.9}$$

where initial N_2 is assumed to be zero and N_{10} is the initial number of ^{228}Ra.

The activity ratio, r_{Th}, is therefore,

$$r_{Th} = \frac{\lambda_2 N_2}{\lambda_1 N_1} = \frac{\lambda_2}{\lambda_2 - \lambda_1}\left(1 - e^{(\lambda_1 - \lambda_2)t}\right) \tag{47.10}$$

The age, t, is then deduced to

$$t = \frac{1}{\lambda_1 - \lambda_2} ln\left(1 - \frac{\lambda_2 - \lambda_1}{\lambda_2} r_{Th}\right) \tag{47.11}$$

47.3 Results and Discussions

47.3.1 Matrix Effect for Pitchblende Standards

Figure 47.2 shows the obtained calibration line of ^{214}Bi (1,120 keV) using the pitchblende standards with matrices of NaCl and SiO_2. The points for both matrices are on a same line indicating no matrix effect on the count rates depending

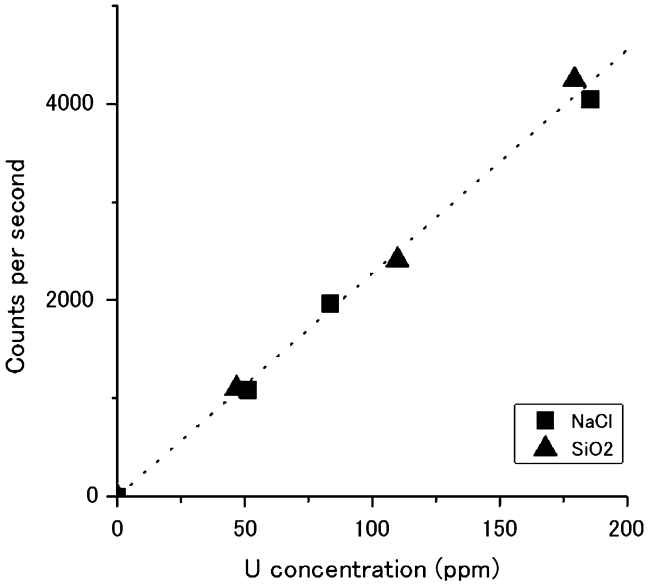

Fig. 47.2 The obtained counts for ^{214}Bi (1,120 keV) as a function of uranium concentrations in pitchblende standard samples

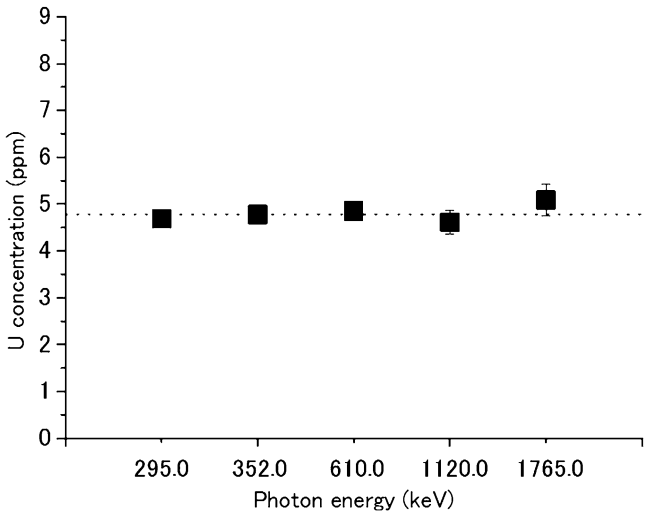

Fig. 47.3 U concentrations as a function of the gamma ray peaks. The uranium concentration was obtained as the weighted mean of these concentrations for the peaks (JG-1a)

on the matrices. One of these pitchblende standard samples, $SiO_2$110, 110 ppm of U in SiO_2, was used as the U standard for the following measurements for GSJ reference samples because the point is closest to the best-fit line.

47.3.2 GSJ Reference Materials

Each examined gamma ray peak gives the concentrations of U or Th as an example shown in Fig. 47.3. The U or Th concentration was obtained as the weighted mean of the U or Th concentrations obtained for those peaks.

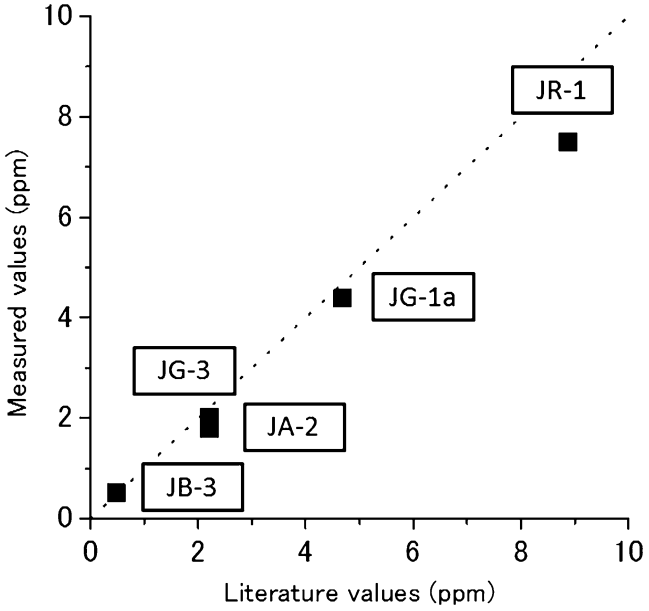

Fig. 47.4 Results of U concentration measurements for GSJ samples

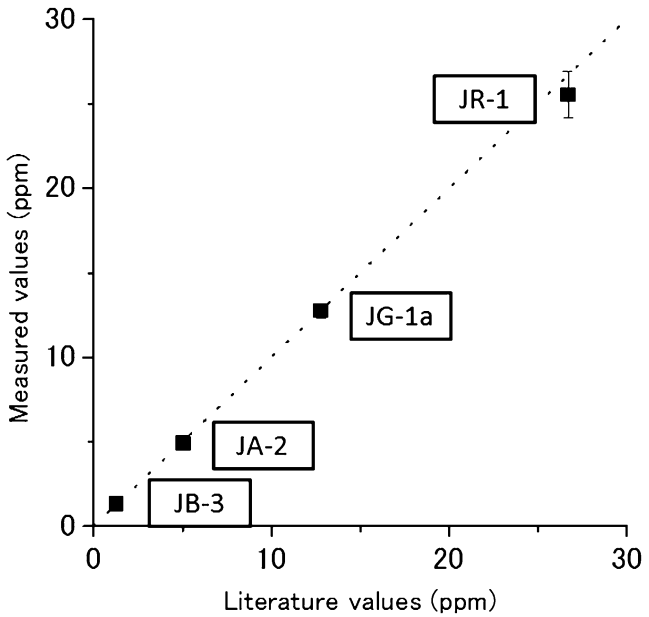

Fig. 47.5 Results of Th concentration measurements for GSJ samples

The U and Th concentrations of GSJ samples were obtained as shown in Figs. 47.4 and 47.5 plotted against the reported value (Imai et al. 1995). The broken lines indicate the one to one correlation. As for U concentrations (Fig. 47.4), the obtained values are consistent with the literature values except for JR-1. The obtained Th concentrations (Fig. 47.5) are all consistent with the literature values.

The present results show that our current system of Ge gamma ray spectrometer works well for GSJ sample assuming radioactive equilibrium except for JR-1.

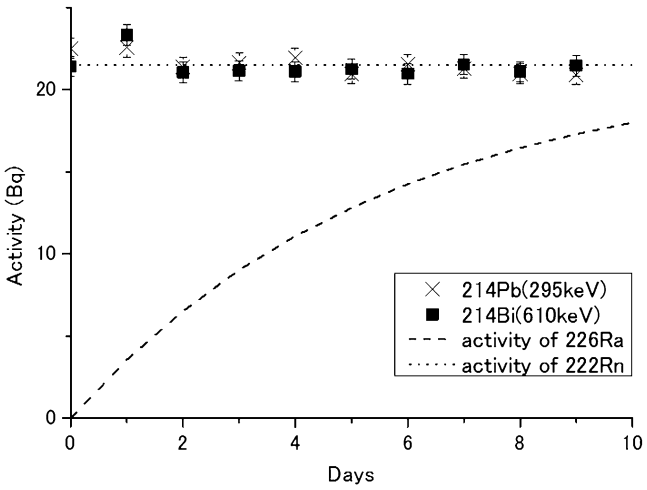

Fig. 47.6 The temporal change of the peak intensities of ^{214}Pb (295 keV) and ^{214}Bi (610 keV) observed in barite crystals after packing them in a stainless container, together with the theoretical temporal change of the activities of ^{226}Ra and ^{222}Rn. ^{226}Ra is constant in this time scale while ^{222}Rn is being accumulated as shown when 100 % is lost before packing

47.3.3 Rn Loss from Barite

Figure 47.6 shows the temporal variation of ^{214}Pb (295 keV) and ^{214}Bi (610 keV) activities of 903R7-2. If the ^{222}Rn is lost from ^{226}Ra in barite, the activities of daughter nuclides of ^{222}Rn are accumulated with time according to the following equation;

$$\frac{dN_2}{dt} = -\lambda_2 N_2 + \lambda_1 N_1 \qquad (47.12)$$

where
N_1: number of ^{226}Ra
N_2: number of ^{222}Rn
λ_1: decay constant ^{226}Ra, 4.33×10^{-4} year^{-1}
λ_2: decay constant of ^{222}Rn, 66.2 year^{-1}

The Eq. (47.12) is deduced to

$$\lambda_2 N_2 = \lambda_1 N_1 \left(1 - e^{-\lambda_2 t}\right) \qquad (47.13)$$

when initial number of N_2, ^{222}Rn, is zero, and N_1 is constant, which is an appropriate assumption as the time scale being considered is in days while the half-life of ^{222}Ra is 1,600 years.

The hypothetical ^{222}Rn accumulation with Eq. (47.13) is shown in Fig. 47.6 by the broken curves. The activities of daughter nuclides of ^{222}Rn were stable during 10 days, therefore, we conclude that there is little ^{222}Rn loss during the chemical treatment.

47.3.4 ^{226}Ra-^{210}Pb and ^{228}Ra-^{228}Th ages

^{226}Ra-^{210}Pb and ^{228}Ra-^{228}Th ages were obtained for the present samples as shown in Table 47.2.

47.3.4.1 Yoron Hole

The ^{226}Ra-^{210}Pb ages of HPD#1333G06 range $22.6^{+1.5}_{-1.4}$ to $26.7^{+1.8}_{-1.7}$ years, being more uniform than ESR ages of 70^{+10}_{-9} to 150^{+30}_{-23} years, but ^{228}Ra-^{228}Th ages are younger than those. The same order of ages with different dating methods were observed also in HPD#1333G07, HPD#1333G08, and HPD#1333G11, where the ^{228}Ra-^{228}Th ages are the youngest, then the ^{226}Ra-^{210}Pb ages, and the ESR ages are the oldest.

The ^{226}Ra-^{210}Pb ages of HPD#1333G05 are consistent within the error, from $71.4^{+11}_{-8.2}$ to 77.0^{+15}_{-10} years. The ESR ages for these samples are 200^{+30}_{-24} to 400^{+66}_{-51} years again much older. It is reasonable that, in this old sample, neither ^{228}Ra nor ^{228}Th was detected.

The ^{228}Ra-^{228}Th ages of HPD#1333G03 $4.4^{+0.81}_{-0.67}$ to $5.2^{+0.99}_{-0.80}$ years are consistent with ESR ages of $4.1^{+0.27}_{-0.26}$ to $5.2^{+0.31}_{-0.30}$ years while ^{226}Ra-^{210}Pb ages are younger to be $2.3^{+1.1}_{-1.0}$ to $3.5^{+1.1}_{-1.1}$ years. The ^{228}Ra-^{228}Th age obtained for extracted barite of HPD#1333G03a is consistent with that of the bulk measurement, indicating that extraction of barite is not necessary for ^{228}Ra-^{228}Th dating.

47.3.4.2 Hatoma Knoll

Neither ^{226}Ra-^{210}Pb nor ^{228}Ra-^{228}Th ages were obtained for HPD#1331G01 due to radioactive equilibrium, for which ESR ages are $2{,}500^{+380}_{-340}$ to $3{,}300^{+710}_{-600}$ years. The ^{228}Ra-^{228}Th age of HPD#133G07 was obtained to be $5.3^{+1.1}_{-0.85}$ years, for which ESR ages was to be $23^{+1.6}_{-1.5}$ years.

47.3.4.3 Izena Hole

As for HPD#1313G05, again, ^{228}Ra-^{228}Th ages is the youngest, then ^{226}Ra-^{210}Pb ages, and ESR age is the oldest. The ^{228}Ra-^{228}Th and ESR ages are respectively consistent within the sample (g to m) while ^{226}Ra-^{210}Pb ages are also consistent except for m. The ^{228}Ra-^{228}Th age obtained for extracted barite of HPD#1333G03l is again consistent with that of the bulk measurement.

47.3.4.4 Archaean Site of the Southern Mariana Trough

The ^{226}Ra-^{210}Pb ages of 903R7-2-08, 09, from the Southern Mariana Trough, are 99.7^{+33}_{-16} and $75.1^{+10}_{-7.7}$ years, respectively, much younger than ESR ages and U-Th ages on sulfide minerals. It is also reasonable that, in older age piece, 903R7-2-3, ^{210}Pb is in radioactive equilibrium with ^{226}Ra.

Table 47.2 Results of ^{226}Ra-^{210}Pb, ^{228}Ra-^{228}Th, ESR and U/Th dating

	^{210}Pb (Bq/g)	^{226}Ra (Bq/g)	Activity ratio of ^{210}Pb to ^{226} Ra	^{226} Ra- Pbage (years) ^{210}	^{228} Th (Bq/g)	^{228} Ra (Bq/g)	Activity ratio of ^{228} Th to ^{228} Ra	^{228} Ra- ^{228} Th age (years)	ESR age[a] (years)	U-Th age (years)
Okinawa Trough										
Yoron Hole										
HPD#1333G06b	11.5 ± 0.47	21.3 ± 0.23	0.54 ± 0.02	$24.9^{+1.7}_{-1.6}$	5.39 ± 0.43	3.90 ± 0.16	1.38 ± 0.12	$10.5^{+}_{-3.0}$\infty	70^{+10}_{-9}	
d	11.0 ± 0.48	21.9 ± 0.24	0.50 ± 0.02	$22.6^{+1.5}_{-1.4}$	3.91 ± 0.32	2.82 ± 0.12	1.39 ± 0.13	$10.8^{+}_{-3.2}$\infty	150^{+30}_{-23}	
f	12.3 ± 0.49	21.9 ± 0.24	0.56 ± 0.02	$26.7^{+1.8}_{-1.7}$	1.49 ± 0.13	1.07 ± 0.05	1.39 ± 0.14	$11.0^{+}_{-3.4}$\infty	120^{+21}_{-17}	
HPD#1333G05a	19.5 ± 0.66	21.9 ± 0.27	0.89 ± 0.03	$71.4^{+11}_{-8.2}$			nd.		330^{+60}_{-45}	
b	15.0 ± 0.53	16.7 ± 0.22	0.90 ± 0.03	$74.2^{+13}_{-9.4}$			nd.		400^{+66}_{-51}	
d	16.1 ± 0.57	17.8 ± 0.23	0.91 ± 0.03	77.0^{+15}_{-10}			nd.		200^{+30}_{-24}	
HPD#1333G03a	2.34 ± 1.05	34.2 ± 0.45	0.07 ± 0.03	$2.3^{+1.1}_{-1.0}$	65.0 ± 5.01	65.4 ± 2.60	0.99 ± 0.09	$4.5^{+0.77}_{-0.65}$	$4.6^{+0.29}_{-0.27}$	
a [b]			nm.		63.1 ± 5.07	64.0 ± 2.94	0.98 ± 0.09	$4.4^{+0.81}_{-0.67}$	$4.1^{+0.27}_{-0.26}$	
b	3.67 ± 1.07	35.2 ± 0.46	0.10 ± 0.03	3.5 ± 1.1	56.1 ± 4.30	53.9 ± 2.12	1.04 ± 0.09	$4.9^{+0.90}_{-0.74}$	$5.2^{+0.31}_{-0.30}$	
c	3.05 ± 1.05	36.3 ± 0.46	0.08 ± 0.03	2.8 ± 1.0	57.8 ± 4.41	54.1 ± 2.13	1.06 ± 0.09	$5.2^{+0.99}_{-0.80}$	$50^{+1.6}_{-1.6}$	
HPD#1333G07a	22.1 ± 0.83	34.0 ± 0.40	0.65 ± 0.03	$33.7^{+2.4}_{-2.3}$	0.78 ± 0.08	0.57 ± 0.03	1.36 ± 0.17	$9.9^{+}_{-3.3}$\infty	$52^{+1.7}_{-1.6}$	
b	20.6 ± 0.82	33.8 ± 0.40	0.61 ± 0.03	$30.2^{+2.1}_{-2.3}$	0.82 ± 0.08	0.65 ± 0.04	1.26 ± 0.15	$7.6^{+3.9}_{-2.0}$	$56^{+1.8}_{-1.7}$	
c	19.0 ± 0.78	32.5 ± 0.39	0.58 ± 0.02	$28.2^{+2.0}_{-1.9}$	0.65 ± 0.06	0.52 ± 0.03	1.26 ± 0.15	$7.6^{+3.9}_{-2.0}$	$28^{+1.2}_{-1.2}$	
d	14.7 ± 0.83	33.7 ± 0.41	0.44 ± 0.03	$18.5^{+1.5}_{-1.4}$	10.2 ± 0.79	9.15 ± 0.37	1.11 ± 0.10	$5.6^{+1.2}_{-0.93}$	$39^{+1.4}_{-1.4}$	
HPD#1333G08a	20.1 ± 0.85	36.0 ± 0.42	0.56 ± 0.02	$26.4^{+1.8}_{-1.7}$	3.00 ± 0.26	2.58 ± 0.11	1.16 ± 0.11	$6.2^{+1.6}_{-1.2}$	$35^{+1.4}_{-1.3}$	
b	15.5 ± 0.77	32.0 ± 0.39	0.49 ± 0.02	$21.4^{+1.6}_{-1.5}$	4.37 ± 0.35	3.74 ± 0.15	1.17 ± 0.11	$6.2^{+1.6}_{-1.2}$	$27^{+1.2}_{-1.2}$	
c	13.8 ± 0.77	30.8 ± 0.38	0.45 ± 0.03	19.1 ± 1.5	12.5 ± 1.04	13.1 ± 0.52	0.96 ± 0.09	$4.2^{+0.7}_{-0.62}$	$9^{+0.51}_{-0.49}$	
HPD#1333G11a	7.34 ± 1.04	36.6 ± 0.48	0.20 ± 0.03	$7.2^{+1.2}_{-1.1}$	47.3 ± 1.64	42.0 ± 1.67	1.13 ± 0.06	$5.8^{+0.71}_{-0.61}$		
Hatoma Knoll										
HPD#1331G01b	1.37 ± 0.23	1.09 ± 0.08	1.25 ± 0.23	–			nd.		3300^{+710}_{-600}	
d	1.23 ± 0.25	1.20 ± 0.08	1.02 ± 0.22	–			nd.		2400^{+300}_{-280}	
f	1.90 ± 0.31	1.85 ± 0.10	1.02 ± 0.18	–			nd.		2500^{+380}_{-340}	
HPD#1331G07			nm.		15.7 ± 1.25	14.6 ± 0.58	1.08 ± 0.10	$5.3^{+1.1}_{-0.85}$	$23^{+1.6}_{-1.5}$	

(*continued*)

Table 47.2 (continued)

	^{210}Pb (Bq/g)	^{226}Ra (Bq/g)	Activity ratio of ^{210}Pb to ^{226} Ra	^{226} Ra- Pbage (years) ^{210}	^{228} Th (Bq/g)	^{228} Ra (Bq/g)	Activity ratio of ^{228} Th to ^{228} Ra	^{228} Ra- ^{228} Th age (years)	ESR age[a] (years)	U-Th age (years)
Hakurei Site of Izena Hole										
HPD#1313G05g	3.35 ± 0.75	18.3 ± 0.31	0.18 ± 0.04	$6.5^{+1.7}_{-1.6}$	20.5 ± 1.61	15.3 ± 0.62	1.34 ± 0.12	$9.3^{+5.7}_{-2.3}$	$14^{+1.9}_{-1.5}$	
i	2.65 ± 0.73	17.3 ± 0.30	0.15 ± 0.04	5.3 ± 1.6	24.0 ± 1.85	19.1 ± 0.77	1.26 ± 0.11	$7.6^{+2.5}_{-1.6}$	$12^{+1.8}_{-1.4}$	
j	2.67 ± 0.72	18.1 ± 0.30	0.15 ± 0.04	5.1 ± 1.5	21.6 ± 1.67	16.6 ± 0.67	1.30 ± 0.11	$8.3^{+3.4}_{-1.8}$	$16^{+2.6}_{-2.0}$	
k	3.34 ± 0.71	18.0 ± 0.29	0.19 ± 0.04	$6.6^{+1.6}_{-1.5}$	17.3 ± 0.60	12.4 ± 0.51	1.40 ± 0.07	$11.1^{+5.5}_{-2.3}$	$15^{+1.8}_{-1.4}$	
l	3.39 ± 0.73	17.7 ± 0.30	0.19 ± 0.04	$6.8^{+1.7}_{-1.6}$	17.6 ± 1.40	13.2 ± 0.54	1.34 ± 0.12	$9.2^{+5.4}_{-2.3}$	$13^{+1.5}_{-1.3}$	
l[b]			nm.		22.3 ± 2.08	16.5 ± 0.83	1.35 ± 0.14	$9.6^{+15}_{-2.8}$	$14^{+1.8}_{-1.5}$	
m	4.68 ± 0.68	19.1 ± 0.29	0.24 ± 0.04	$9^{+1.6}_{-1.5}$	17.0 ± 1.41	12.4 ± 0.50	1.37 ± 0.13	$10.1^{+17}_{-2.8}$		
Southern Mariana Trough										
Archaean										
903R7-2 3	31.8 ± 0.87	30.4 ± 0.33	1.04 ± 0.03	–			nd.		1650^{+340c}_{-280}	
8	27.5 ± 0.78	28.8 ± 0.31	0.95 ± 0.03	99.7^{+33}_{-16}			nd.		780^{+90c}_{-80}	440 ± 15[c]
9	30.8 ± 0.84	34.1 ± 0.35	0.90 ± 0.03	$75.1^{+10}_{-7.7}$			nd.		370^{+50c}_{-50}	318 ± 7[c]

[a]ESR ages were obtained by (Fujiwara et al. Chap. 29)
[b]Extracted barite crystals were powdered and mixed with NaCl
[c]U-Th and ESR ages were obtained by Takamasa et al. (2013)
–: ^{226}Ra-^{210}Pb ages were not obtained due to radioactive equilibrium
nm not measured

Noguchi et al. (2011) obtained an age of 31 years by ^{226}Ra-^{210}Pb method, which is different from our results. This sample is very large about 1 m in total length as shown in Takamasa et al. (2013). The part of the sample analyzed in the present paper is different from the part analyzed by Noguchi et al. (2011). Being a different interpretation from Takamasa et al. (2013), it may be because the formation ages are different for different parts.

47.3.4.5 Comparison of the Ages Obtained by the Three Dating Methods

If the samples were formed by one single hydrothermal event, the ages obtained from ^{226}Ra-^{210}Pb, ^{228}Ra-^{228}Th, and ESR methods should coincide. However, except for HPD#1333G03, the ESR ages are older than ^{226}Ra-^{210}Pb and ^{228}Ra-^{228}Th ages. On the other hand, it is interesting the order of the ages is consistent, i.e., samples with younger ^{226}Ra-^{210}Pb or ^{228}Ra-^{228}Th ages show younger ESR ages and samples with older ^{226}Ra-^{210}Pb or ^{228}Ra-^{228}Th ages show older ESR ages. The problem in calibration of ESR ages would be one possible explanation for this. For example, if the alpha effectiveness they adopt, which is 0.043 (Toyoda et al. 2012), is different, the absolute values of ages become proportionally different. However, the ratio of the ages are not constant for the present study.

Another explanation is that the barite crystals were formed by two or more hydrothermal events and were mixed together. While the ESR method gives the averaged ages, ^{226}Ra-^{210}Pb and ^{228}Ra-^{228}Th methods give that of the last event if the parent nuclide in the crystal formed by the previous event had decayed out, as discussed by Takamasa et al. (2013). This will explain the consistency of ages of several samples, and is consistent with non-uniformity of the age ratios, i.e., HPD#1333G03 was formed by one single event about 5 years ago, while the ^{228}Ra-^{228}Th ages are those of last events and the ESR ages are the averaged ones in the cases of HPD#1333G07 and 08. This will also explain the consistency in the order of ages. When the last event is younger, the averaged age will also become younger and when the last event is older, the averaged age will also become older. For HPD#1313G05 and HPD#1333G11, such discussion may be difficult because the "averaged" (ESR) ages are not old enough for remaining ^{228}Ra to have decayed out. The similar difficulty is for HPD#1333G05 and G06 in which parent ^{226}Ra nuclide do not decay out in several hundred years. The results for HPD#1331G01 would tell that the averaged age is 2,500–3,300 years while the age of the last event is older than 150 years, above which ^{210}Pb is equilibrated with ^{226}Ra.

47.4 Conclusion

^{226}Ra-^{210}Pb and ^{228}Ra-^{228}Th ages were obtained for barite in submarine hydrothermal sulfide deposits taken at the Okinawa and the Southern Mariana Trough. Most of the ages are younger than ESR and U-Th ages, which would be explained by the mixture of young and old crystals, in the latter of which radium nuclide have decayed out. This implies that combination of ^{226}Ra-^{210}Pb, ^{228}Ra-^{228}Th and ESR or U-Th methods will more precisely tell the history of formation of sulfide deposits, i.e., the former gives the ages of younger events while the latter gives the average ages.

Acknowledgements The work was supported by TAIGA project, Grant-in-Aid for Scientific Research on innovative Areas (20109004) funded by the Ministry of Education, Culture, Sports, Science and Technology (MEXT), partly by MEXT-Supported Program for the Strategic Research Foundation at Private Universities (2011–2015, S1101036), and by the cooperative research program of Center for Advanced Marine Core Research (CMCR), Kochi University (12B039, 13A038, 13B032)

References

Imai N, Terashima S, Itoh S, Ando A (1995) 1994 Compilation of analytical data for minor and trace elements in seventeen GSJ Geochemical reference samples, "Igneous rock series". Geostand Newslett 19:135–213

Lalou C, Reyss JL, Brichet E (1993) Actinide-series disequilibrium as a tool to establish the chronology of deep-sea hydrothermal activity. Geochim Cosmochim Acta 57:1221–1231

Noguchi T, Arasaki H, Oomori T, Takada J (2004) Age determination of submarine hydrothermal barite deposits by the ^{210}Pb/^{226}Ra method. Bunseki Kagaku 53:1009–1013 (in Japanese with English abstract)

Noguchi T, Shinjo R, Ito M, Takada J, Oomori T (2011) Barite geochemistry from hydrothermal chimneys of the Okinawa Trough: insight into chimney formation and fluid/sediment interaction. J Mineral Petrol Sci 106:26–35

Takamasa A, Nakai S, Sato F, Toyoda S, Banerjee D, Ishibashi J (2013) U-Th radioactive disequilibrium and ESR dating of a barite-containing sulfide crust from South Mariana Trough. Quater Geochronol 15:38–46

Toyoda S, Sato F, Nishido H, Kayama M, Ishibashi J (2012) The alpha effectiveness of the dating ESR signal in barite. Radiat Meas 47:900–902

White GJ, Rood AS (2001) Radon emanation from NORM-contaminated pipe scale and soil at petroleum industry sites. J Environ Radioact 54:401–413

OSL Dating of Sea Floor Sediments at the Okinawa Trough

48

Vaidehi Varma, Shin Toyoda, Yusuke Isono, Ai Uchida, Debabrata Banerjee, Ashok Kumar Singhvi, and Jun-ichiro Ishibashi

Abstract

In estimating the ages of sea floor hydrothermal deposits, the age of the sediments overlying it would give the youngest limit if the sedimentation age is correct. The OSL (optically stimulated luminescence) method was applied to two sediment cores taken by an acrylic corer from the seafloor in the Okinawa Trough. The ages, obtained by the polymineral fine grain method, did not correlate with the stratigraphic sequence within the core, implying either insufficient bleaching of the sediments at the time of the deposition or mixing of sediments of different ages. The polymineral fine grain OSL dating method did not work to date the present sediment samples at the sea floor in the Okinawa Trough.

Keywords

OSL dating • Polymineral fine grain • Sea floor sediment

48.1 Introduction

The ages of hydrothermal deposits are important to investigate the evolution of the hydrothermal systems. Various dating techniques have been employed, such as U-Th method on sulfide minerals (Takamasa et al. 2013), ESR method on barite (Takamasa et al. 2013; Fujiwara et al. (2014), Chap. 34), and ^{226}Ra-^{210}Pb, ^{228}Ra-^{228}Th method on barite (Noguchi et al. 2004; Uchida et al. (2014), Chap. 41) to provide clues to discuss the evolution of the hydrothermal activities. In the present data report, optically stimulated luminescence (OSL) dating technique was applied to the sediments from the Okinawa Trough.

OSL dating techniques have been widely applied for dating the sedimentary deposits and gave the age of last sun exposure or the age of burial, using naturally occurring minerals, for instance, like feldspar or quartz, present in the sediments. At the time of transportation of sediments, exposure to the sun would completely bleach and reset the OSL signal in them. After their deposition, the natural radioactivity of uranium (U), thorium (Th) and potassium (K) would deposit dose cumulatively over time which would be measured in laboratory as the equivalent dose (D_e) in Gray (Gy). The given radiation dose per year is measured as a dose rate in Gy/year. The ratio of D_e to dose rate gives the age in year of the sediment (Aitken 1998).

The sections of samples collected at Okinawa Trough showed the signature of sulfide deposits. At the sea floor, as time passes, previously formed sulfide deposits by hydrothermal activities, are covered with sediments. If ages of the sediments are obtained by OSL, the ages would give the youngest age limit of the deposits beneath them. This is a pilot study to apply the OSL dating technique to date the sea floor sediments in the aspect of dating of deposits formed by hydrothermal activities.

V. Varma (✉) •
D. Banerjee • A.K. Singhvi
Physical Research Laboratory, Ahmedabad, India
e-mail: vaidehi_varma@yahoo.in

S. Toyoda • Y. Isono • A. Uchida
Okayama University of Science, Okayama, Japan

J.-i. Ishibashi
Kyushu University, Fukuoka, Japan

J.-i. Ishibashi et al. (eds.), *Subseafloor Biosphere Linked to Hydrothermal Systems: TAIGA Concept*,
DOI 10.1007/978-4-431-54865-2_48,

48.2 Samples and Sites of Collection

Two sediment cores were taken by an acrylic (MBARI type) push corer and examined in the present study. One core, HPD1330M1, was taken at Irabu Knoll, the Okinawa Trough (25°14.378′N, 124°52.863′E, depth 1,978 m), during the NT11-20 cruise operated by JAMSTEC in 2011 while the other, HPD1357MB, was at Iheya North Knoll (27°47.301′N, 126°54.538′E, depth 1,109 m) during NT12-06 cruise in 2012. A transparent acrylic tube, 10 cm in diameter and 30 cm in length, was inserted in the sediment by a manipulator of ROV Hyper Dolphin, and the core was retrieved to the submarine vehicle. The core samples were wrapped by Al foils and kept frozen as soon as possible after sample retrieving onboard. The frozen cores were cut in a dark room to separate three sections, top, middle, and bottom (Table 48.1). The part of the surface facing to the tube of each section was trimmed out and used for the measurements of water content and dose rate. The rest inside part of the tube was used for OSL measurements. The water contents were obtained by the weights of the sections before and after drying. After measuring the water contents, the dried section samples were used for gamma ray spectrometry to obtain U, Th, and K concentrations.

48.3 Sample Preparation and Experiments

The sediment samples used to estimate the equivalent doses (D_e) using OSL technique consisted dominantly finer fraction (<11 μm). Thus, the D_e's were measured using the polymineral fine grain (4–11 μm) technique (Zimmerman 1971). The preparation of polymineral fine grain sample discs was the following; chemical treatments with 1 N HCl to remove carbonate and with 30 % H_2O_2 to remove organic matter, deflocculation using 0.01 N Sodium Oxalate, and Stokes settling in absolute (80 %) alcohol to obtain desired grain fraction (4–11 μm). The separated grains were then re-suspended in alcohol. Equal volume of this solution was pipetted into sample tubes (10 mm in diameter) with an aluminum disc at the base. The alcohol was evaporated off at 45°C to obtain a thin (≤20 μm thickness) layer of sample on the discs. A set of 24 discs were prepared for each sample.

An automated Risø TL-OSL reader (TL/OSL-DA-20; Bøtter-Jensen et al. 2010) was used for D_e measurements. Fine grain polymineral samples were stimulated using IR diodes (870 ± 40 nm) and detection was made in the violet-blue emission window (395 ± 50 nm) using a filter combination of Schott BG-39 and Corning 7–59. The bulk signal was dominated by the signal from feldspar. Since feldspar can be stimulated by IR (Hütt et al. 1988), IRSL SAR protocol (Murray and Wintle 2000; Blair et al. 2005) was used. The protocol is shown in Table 48.2. This same protocol was used for all the 24 discs of each sample. The final D_e value is the average of these 24 values.

Dose rate was calculated using the concentration of U, Th, and K and the water content in sediments. Radionuclide concentrations were measured using a low background gamma ray spectrometry. Water content was estimated as per Aitken 1985. Cosmic ray dose was not considered as the samples were at sea floor and would be completely attenuated.

Table 48.2 IRSL SAR protocol used for ED measurements

Step	Operation	Comment
1	β dose	For natural, dose = 0
2	Preheat 260 °C, 60 s	Emptying of unstable traps
3	IRSL 50 °C, 100 s	L_X
4	β test dose	
5	Preheat 260 °C, 60 s	Emptying of unstable traps
6	IRSL 50 °C, 100 s	T_X
7	Return to step 1	

Table 48.1 The depths from the surface of the samples in the cores examined in the present study, the radionuclide concentrations, the D_e values, the measured water contents, the a-value, the natural dose rates, the IRSL ages obtained

Sample	Distance from the top (cm)	U (ppm)	Th (ppm)	K_2O (%)	water content (%)	a-value	D_e Gy)	Dose rate[a] (mGy/year)	Age (ky)
HPD1330M1 upper	2–4	22.5 ± 0.5	2.3 ± 0.4	0.96 ± 0.03	88.29	0.04 ± 0.004	51 ± 3	4.5 ± 0.0	11.4 ± 0.7
1330M1 middle	11–13	14.9 ± 0.2	2.7 ± 0.2	0.91 ± 0.04	95.40		46 ± 3	3 ± 0.0	15 ± 0.9
1330M1 bottom	20–22	18.1 ± 0.2	2.4 ± 0.4	0.98 ± 0.03	80.13		18 ± 1	4 ± 0.0	4.5 ± 0.3
HPD1357MB upper	2–4	3.1 ± 0.1	6.4 ± 0.5	1.48 ± 0.04	94.98		41 ± 3	1.5 ± 0.0	27 ± 1.6
1357MB middle	13–15	2.7 ± 0.1	6.8 ± 0.4	1.69 ± 0.04	88.29		25 ± 3	1.6 ± 0.0	15 ± 1.7
1357MB bottom	24–26	1.6 ± 0.1	6.1 ± 0.4	1.52 ± 0.04	93.09		41 ± 2	1.3 ± 0.0	32 ± 1.3

[a]Cosmic ray dose is not considered

48.4 Results and Discussion

The typical shine down curve of one of the samples, HPD1330M1 Upper is shown in Fig. 48.1. The growth curve of the same sample is shown in Fig 48.2. These curves were very typical and all other samples showed the similar nature of curves. All the samples were analyzed using the same protocol and the result is tabulated in Table 48.1.

As seen from the Table 48.1, the ages cannot be correlated with the stratigraphic sequence, for e.g. HPD1330M1 Upper at the depth of 2–4 cm was older than HPD1330M1 Bottom at the depth of 20–22 cm. This indicated that the ages were not sufficient to explain the history of these samples and no understanding about the hydrothermal activities could be inferred. There could be two reasons for such ages- either there were uncertainties in D_e measurements or in dose rate measurements.

For D_e, it is possible that the samples had not been reset or bleached initially due to which the ages did not show consistency. Bleaching problem could be due to insufficient light available at the sea floor to zero the pre-depositional luminescence signal and thus because of the partial bleaching, these ages were inconsistent with the depth of samples collected. Partial bleaching usually induces grain to grain variation of nominal D_e values, which would be checked by single grain OSL measurements. Alternative reason for these ages could be the rework of the sediments after deposition, resulting in the mixed ages. As the sediment grains should have been mixed if this is the case, this will also induce grain to grain variation of nominal D_e values. However, the present samples are dominated by silt and clay, and so the single grain measurement was not possible. In the single aliquot polymineral method, the signal intensity is already averaged for large number of grains and inter-grain variability in D_e cannot be observed.

Inter-aliquot variability of D_e values was observed in the histograms. Figure 48.3 shows for one of the samples, HPD1330M1 Upper. The histogram was closely packed and there was no indication of dispersion in D_e values. Towards D_e estimation using IRSL signals of feldspar, which is prone to anomalous fading (Wintle 1973), a fading correction is required. However, the fading correction was not performed since; the fading correction will systematically increase the age by not more than 10 % for these young samples and the results would be un-altered.

In the case of dose rate calculations, uncertainty was imparted due to water content. The samples contained more than 80 % of water with sufficient uncertainties.

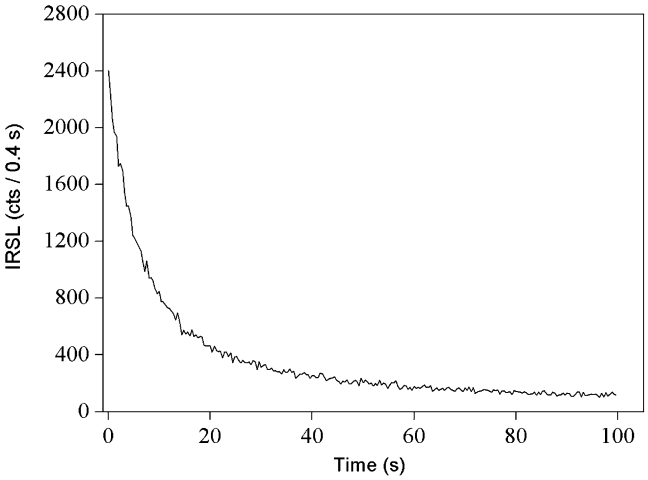

Fig. 48.1 A typical shine down curve observed in HPD1330M1 Upper

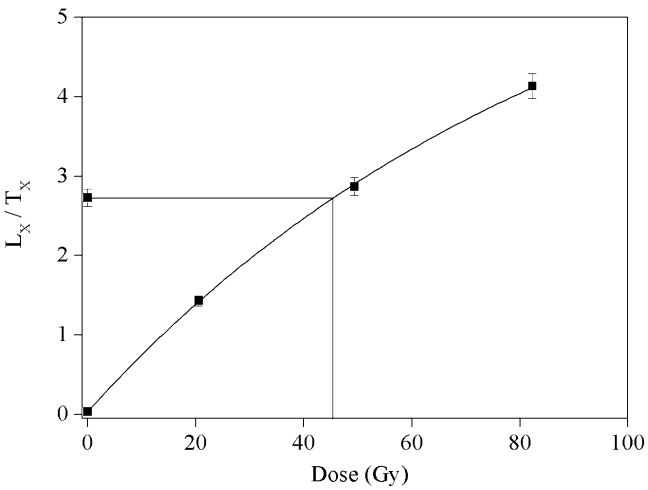

Fig. 48.2 A dose response curve obtained for HPD1330M1 Upper

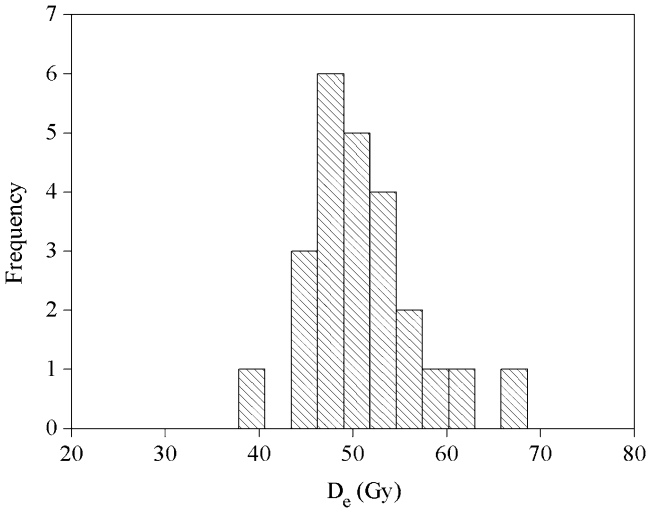

Fig. 48.3 The histogram of D_e values of HPD1330M1 Upper, showing the distribution of D_e values of 24 discs prepared from the sample

Since water attenuates the doses absorbed by sediments, an uncertainty in water estimation can affect the dose rate calculations.

Another important parameter was the alpha efficiency of fine grain. Alpha efficiency was experimentally obtained in the present study for one sample HPD1357MB Bottom (randomly selected) and it was 0.03 ± 0.002. However, we have chosen a general value of 0.04 ± 0.004 for all the present samples, which were obtained by the earlier studies on fine grains by Lai et al. (2008) on Chinese loess and Biswas et al. 2013 on volcanic ashes. The above discussions indicate that applications of OSL dating method for sea floor sediments need further study for better understanding of sea floor deposition and hydrothermal activities.

48.5 Conclusion

Present study uses polymineral fine grain of sea floor sediments to understand the sediments' surrounding hydrothermal activities. The obtained ages are not chronological with the stratigraphic depositional sequence. Thus these ages do not indicate about the pre-depositional history or the hydrothermal activities near the sediment deposits. The two cores came out to be young, around 5–32 ka but these ages are constrained with many uncertainties. Further study is required to have better understanding for sea floor hydrothermal activities.

Acknowledgements The work was supported by Taiga project, Grant-in-Aid for Scientific Research on innovative Areas (20109004) funded by the Ministry of Education, Culture, Sports, Science and Technology (MEXT), and also partly by MEXT-Supported Program for the Strategic Research Foundation at Private Universities (2011–2015, S1101036).

References

Aitken MJ (1985) Thermoluminescence dating. Academic, London

Aitken MJ (1998) Introduction to optical dating. Oxford University Press, Oxford

Biswas RH, Williams MAJ, Raj R, Juyal N, Singhvi AK (2013) Methodological studies on luminescence dating of volcanic ashes. Quater Geochronol 17:14–25

Blair MW, Yukihara EG, McKeever SWS (2005) Experiences with single-aliquot OSL procedures using coarse-grain feldspars. Radiat Meas 39:361–374

Bøtter-Jensen L, Thomsen KJ, Jain M (2010) Review of optically stimulated luminescence (OSL) instrumental developments for retrospective dosimetry. Radiat Meas 45:253–257

Fujiwara T, Toyoda S, Uchida A, Ishibashi J, Nakai S, Takamasa A (2014) ESR dating of barite in sea-floor hydrothermal sulfide deposits taken from Okinawa Trough, Taiga e-book, Chap 34

Hütt G, Jaek I, Tchonka J (1988) Optical dating: K-feldspar optical response stimulation spectra. Quater Sci Rev 7:381–385

Lai ZP, Zöllerb L, Fuchsb M, Brückner H (2008) Alpha efficiency determination for OSL of quartz extracted from Chinese loess. Radiat Meas 43:767–770

Murray AS, Wintle AG (2000) Application of the single-aliquot regenerative-dose protocol to the 375 C quartz TL signal. Radiat Meas 32:579–583

Noguchi T, Arasaki H, Oomori T, Takada J (2004) Age determination of submarine hydrothermal barite deposits by the $^{210}Pb/^{226}Ra$ method. Bunseki Kagaku 53:1009–1013

Takamasa A, Nakai S, Sato F, Toyoda S, Banerjee D, Ishibashi J (2013) U-Th radioactive disequilibrium and ESR dating of a barite-containing sulfide crust from South Mariana Trough. Quater Geochronol 15:38–46

Uchida A, Toyoda S, Ishibashi J, Nakai S (2014) ^{226}Ra-^{210}Pb and ^{228}Ra-^{228}Th dating of barite in submarine hydrothermal sulfide deposits collected at Okinawa Trough and South Mariana Trough, Taiga e-book, Chap. 41

Wintle AG (1973) Anomalous fading of thermoluminescence in mineral samples. Nature 245:143–144

Zimmerman DW (1971) Thermoluminescent dating using fine grains from pottery. Archaeometry 13:29–52

Immediate Change of Radiation Doses from Hydrothermal Deposits

49

Shin Toyoda, Fumihiro Sato, Ai Uchida, and Jun-ichiro Ishibashi

Abstract

The radiation from the sulfide deposits taken at Okinawa Trough was measured on-board by a NaI gamma ray spectrometer immediately after the retrieval of the sample onto the research vessel. Gamma ray peaks were identified as those from daughter nuclei of ^{226}Ra and ^{228}Ra. The slight change with time of the radiation dose from those deposits is probably due to the geometric arrangement in measurements. As results, no change in radiation dose was observed in the time range up to 90 h after retrieval of the samples from the submarine vehicle.

Keywords

Dating • On-board measurement • Radiation • Sulfide

49.1 Introduction

Intense natural radiation is often observed in the sea-floor hydrothermal area due to radium and radon, which are originally produced by decay of uranium and thorium and are dissolved into the hydrothermal fluids. Measurements in the laboratory on land detect only long lived radioactive nuclei, whose half lives are in the order of years or larger, while immediate decrease of radioactivity of hydrothermal sulfide deposits is sometimes observed on the research vessel (Ishibashi, personal communications). The present study aimed to detect possible natural radioactive nuclei of short life time by on-board measurements with a NaI gamma ray spectrometer immediately after retrieving the sulfide deposit samples.

49.2 Samples and Experimental Procedures

Sulfide deposit samples were taken during NT11-20 and NT12-06 cruises with research vessel Natsushima operated by JAMSTEC in September, 2011 and in March, 2012, respectively. Four samples were examined as listed in Table 49.1, which were taken at sea-floor hydrothermal sites shown in Suppl. 49.1, and are shown in Fig. 49.1.

As soon as a sample was retrieved, the sample block of about 15 cm in length was put into a plastic bag. It was then placed in front of the detector of a NaI gamma ray spectrometer having a 3″ detector, Aloka JSM-102, where the full scale of 240 channels are set up to 3,600 keV. The measurements with duration of 30 min were repeated several times successively or with some interval for each sample up to 90 h. After the cruises, the spectrum data were transferred to a PC and were converted to text files. The threshold method (Mercier and Falgueres 2007) was used to obtain the dose rates given by the samples. The counts from the 25th channel to 240th channel were integrated and compared with those obtained for standard calibration concrete blocks (Uchida et al. 2014) in order to obtain the dose rates.

The online version of this chapter (doi:10.1007/978-4-431-54865-2_49) contains supplementary material, which is available to authorized users.

S. Toyoda (✉) • F. Sato • A. Uchida
Okayama University of Science, Okayama, Japan
e-mail: toyoda@dap.ous.ac.jp

J.-i. Ishibashi
Kyushu University, Fukuoka, Japan

Table 49.1 Samples examined in the present study

Sample	Site	Position	Description	Dimension (cm)
HPD#1328G04	Minami Ensei Knoll	28°23.462′N, 127°38.398′E	Sulfide chimney	18 × 18 × 13
HPD#1329G05	Izena (Hakurei)	27°14.815′N, 127°53.736′E	Sulfide chimney	17 × 13 × 8
HPD#1331G05	Hatoma Knoll	24°51.507′N, 123°50.546′E	Kuroko ore	14 × 11 × 10
HPD#1358R02a	Iheya-North	27°47.438′N, 126°53.736′E	Sulfide	20 × 10 × 6

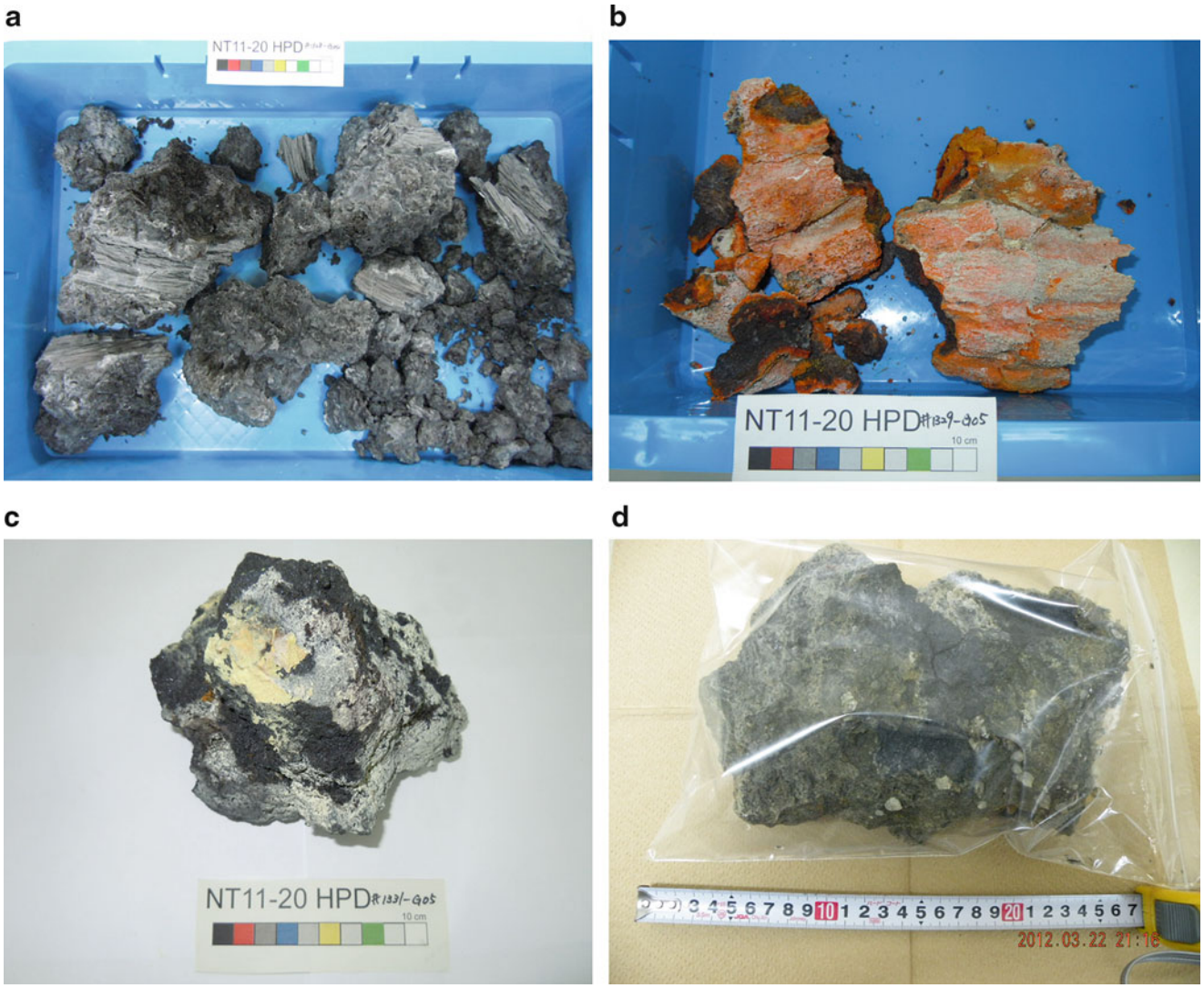

Fig. 49.1 The samples examined in the present study

49.3 Results and Discussions

The spectra observed in the first measurements of the samples are shown in Fig. 49.2. The peaks are identified as those due to ^{214}Bi, ^{228}Ac, ^{40}K, and ^{208}Tl. The spectra observed in the following successive measurements were essentially identical to those in the first measurements. ^{214}Bi is a nucleus of uranium series while ^{228}Ac and ^{208}Tl of thorium series. These are most probably produced by decays of ^{226}Ra and ^{228}Ra contained in the sulfide deposits rather than those of ^{238}U and ^{232}Th as those concentrations in sulfide minerals are in ppm order while those in barite are in ppb order (Toyoda et al., 2014).

The daughter nuclei of ^{226}Ra and ^{228}Ra were observed in HPD#1328G04, HPD#1329G05, and HPD#1331G05, but no daughter nuclei of ^{228}Ra in HPD#1358R02a. This makes the most remarkable difference in the spectra shown in Fig. 49.2. As the half life of ^{228}Ra is 5.75 years, the ages of the former three samples are estimated to be younger than

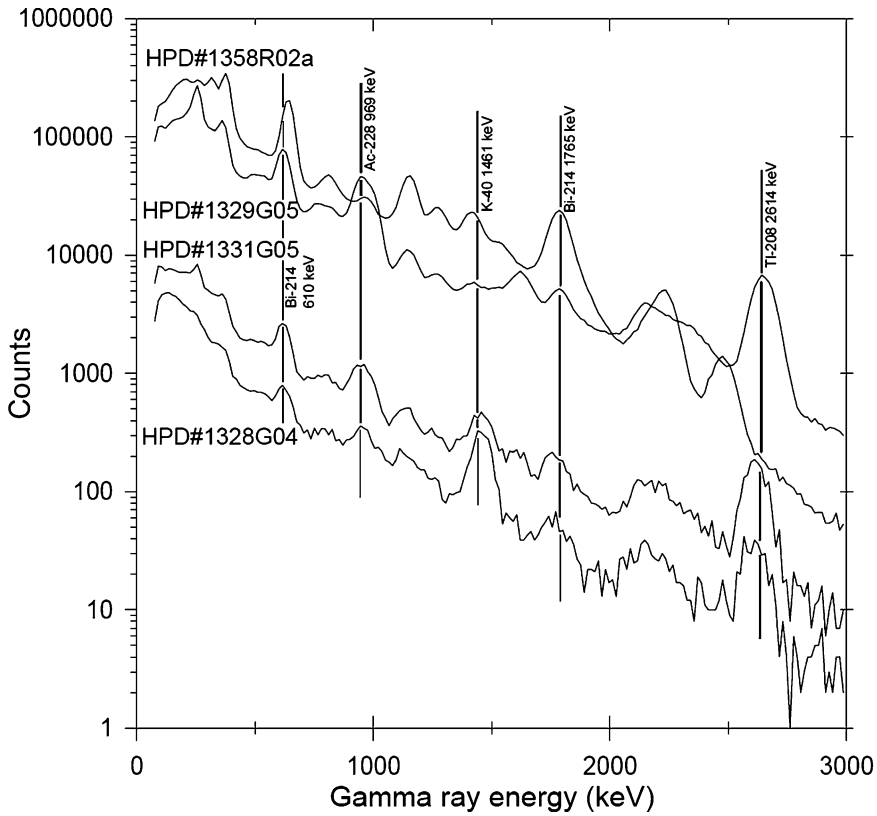

Fig. 49.2 Gamma ray spectra of the samples measured just after the retrieval on the ship by an NaI gamma ray spectrometer

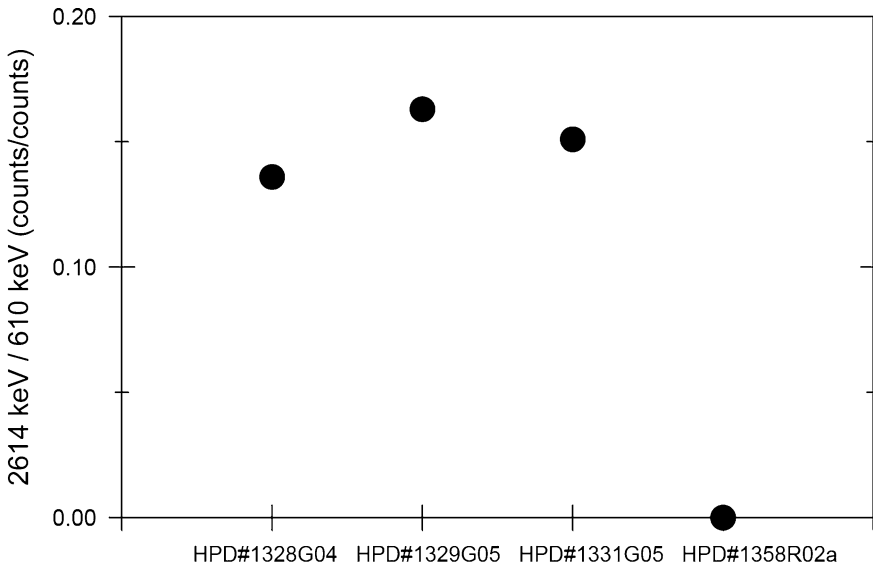

Fig. 49.3 The ratio of the peak of 2,614 keV (^{208}Tl) to 610 keV (^{214}Bi)

several 10 years while the age of the last sample is to be more than several 10 years. The peak due to ^{40}K is observed in HPD#1328G04 and in HPD#1331G05, but not seen in HPD#1329G05. As for the spectrum of HPD#1358R02a, it is not clear whether the peak around 1,461 keV is due to ^{40}K or not. The latter two samples have much higher radioactivity due to daughter nuclei of ^{226}Ra and/or ^{228}Ra relative to that due to ^{40}K than the former two samples probably because of the mineralogy which has not yet been analyzed. The Compton background of those and those daughter nuclei mask the peak of ^{40}K in the former two samples. Except for ^{40}K, the shapes of the gamma ray spectra of HPD#1328G04, HPD#1329G05, and HPD#1331G05 are very similar. The ratio of ^{214}Bi at 610 keV to ^{208}Tl at 2,614 keV is shown in Fig. 49.3, indicating that the relative ratio of ^{226}Ra and ^{228}Ra is the same for these three samples.

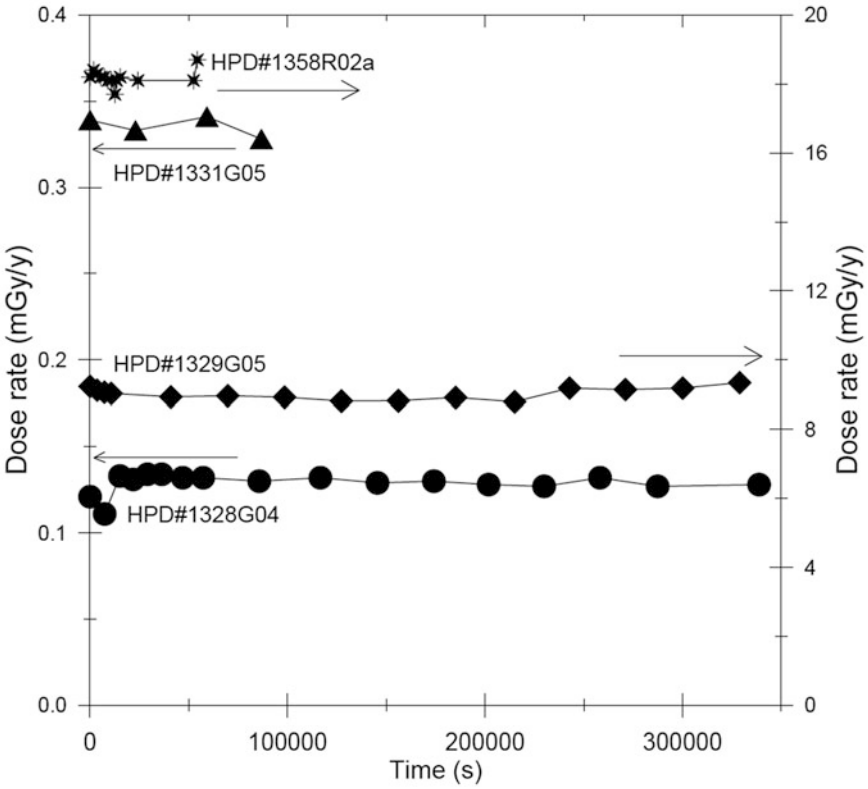

Fig. 49.4 The change in the dose rates from the retrieval of the samples up to 90 h. No change with time was observed

The dose rate given by the samples was calculated from the spectrum by the threshold technique (Mercier and Falgueres 2007) based on the measurements for U, Th, K calibration blocks with known amount of these elements with radioactive equilibrium. Although, therefore, the calculated dose rates should be slightly overestimated due to lack of the consideration for the nuclei between ^{238}U and ^{226}Ra, and ^{232}Th and ^{228}Ra in the measured samples, relative comparison would be meaningful.

The gamma ray spectra obtained by the repeated measurements are almost identical for all present four samples. This leads to the results that the calculated dose rates given by these samples were constant with time as shown in Fig. 49.4. The slight changes with time are shown for HPD#1328R04 and in HPD#1329R05. However, these are probably due to the geometric arrangement in measurement because corresponding similar changes of the intensity of ^{40}K are observed in these samples.

The immediate decrease of radioactivity of the bulk sample, which is sometimes observed on the ship in a time scale of several hours, would possibly be due to the decay of short lived nuclei or loss of radon absorbed on the surface of the sample. However, the reason was not found in the present study.

The present study showed the ability of NaI detector, the resolution of which is much less than the pure Ge gamma ray spectrometer, to detect ^{228}Ra in the samples. As ^{228}Ra in the samples indicates that their ages are young, less than several 10 years, mapping of rough ages of sulfide deposits at the sea floor would be possible when such detection is done during the dives by submarine vehicles.

Acknowledgements The work was supported by Taiga project, Grant-in-Aid for Scientific Research on innovative Areas (20109004) funded by the Ministry of Education, Culture, Sports, Science and Technology (MEXT).

References

Mercier N, Falgueres C (2007) Field gamma dose-rate measurement with a NaI(Tl) detector: re-evaluation of the "threshold" technique. Ancient TL 25:1–4

Toyoda S, Fujiwara T, Uchida A, Ishibashi J, Nakai S, Takamasa A (2014) ESR dating of barite in sulfide deposits formed by the sea floor hydrothermal activities. Radiat Prot Dosimetry 159:203–211

Uchida A, Toyoda S, Tissoux H, Falguères C, Ninagawa K, Miallier D (2014) Dose rate estimation by Aloka NaI scintilation gamma ray spectrometer using the Threshold Technique. Advances in ESR Applications 30:12–15 (in Japanese with English Abstract)

Periodic Behavior of Deep Sea Current in the Hatoma Knoll Hydrothermal System

50

Yasuo Furushima and Hiroyuki Yamamoto

Abstract

Time series physical properties of water column were measured at the Hatoma Knoll hydrothermal field on the Okinawa Trough, using a multi-layered Acoustic Doppler Current Profiler (ADCP). We aimed (1) to provide a deep-sea current data within a small and complicated geographical feature of a caldera and (2) to show the possibility of hydrothermal plume observation by ADCP during the measurement in April 2004 and May 2005 cruises. The deep-sea current data were recovered at the depths between seafloor and 40-m or 60-m-layers above the seafloor. Moreover, acoustic reflection signals were sometimes observed up to 120-m layer above the seafloor due to the trail of hydrothermal plumes. A power spectrum density analysis by fast Fourier transform (FFT) showed the dominant time cycle of the horizontal current velocity, which corresponded to tidal periodicity over an approximate 12-hours period, at each layer. Residual currents, which play an important role in material transport, tended to northwest direction and suggested that most of material might keep retaining within the caldera. The causes of the measurement result of the flow which appeared into a pulse form may indicate fluctuation of the blowout of hydrothermal water. The verification of the fluid mechanism by the numerical model in the local field such as the caldera will be necessary in the future.

Keywords

ADCP • Backscattering • Deep sea current • Hatoma Knoll

50.1 Introduction

Hydrothermal fluids spouting from a deep-sea hydrothermal vent forms hydrothermal plumes by mixing with surrounding seawater. Hydrothermal plume has various physical and chemical signatures, e.g. higher temperatures than surrounding seawater, high chemical components from hydrothermal fluids, and high particle concentration from hydrothermal fluid chemicals. Deep-sea current around the hydrothermal vent field provides a turbulent environment, related to effects such as complex geographical topography and the hydrothermal venting flows. To estimate a heat and chemical flux from a hydrothermal vent, it is necessary to investigate a hydrothermal plume (Baker et al. 2001). Especially for the time series observation, an acoustic

Y. Furushima (✉)
Institute of Biogeosciences, Japan Agency for Marine-Earth Science and Technology (JAMSTEC), 2-15 Natsushima-Cho, Yokosuka, Kanagawa 237-0061, Japan
e-mail: furus@jamstec.go.jp

H. Yamamoto
Institute of Biogeosciences, Japan Agency for Marine-Earth Science and Technology (JAMSTEC), 2-15 Natsushima-Cho, Yokosuka, Kanagawa 237-0061, Japan

Submarine Resource Research Project, Japan Agency for Marine-Earth Science and Technology (JAMSTEC), 2-15 Natsushima-Cho, Yokosuka, Kanagawa 237-0061, Japan

J.-i. Ishibashi et al. (eds.), *Subseafloor Biosphere Linked to Hydrothermal Systems: TAIGA Concept*,
DOI 10.1007/978-4-431-54865-2_50,

instrumentation is useful tool to determine physical environmental factors such as current and water temperature.

It is also important to understand the deep-sea current around the hydrothermal vent, because it gives us to understand how eggs and larvae at the deep sea are distributed and transported among the hydrothermal vent fields. Based on deep-sea current measurements, Thomson et al. (2003) indicated that tidal and wind-generated currents were dominant at the Endeavour segment in the Juan de Fuca ridge, and the hydrothermal plumes tended to stay within the valley. This result suggests that an inhibition of oscillatory currents in the rift valleys of mid-ocean ridges shield larvae from cross-axis dispersion in the deep ocean.

Fujioka et al. (1997) have measured deep-sea currents and water temperature for 1 year using a mooring observatory settled on the TAG hydrothermal mound in the Mid-Atlantic Ridge. They found that 12.42 h cycle corresponded with a lunar semi-diurnal periodicity, known as M2 tidal constituent, was dominated in the TAG site flow, and synchronization of the fluctuation cycle of temperature and pressure with this tidal periodicity. Such a water flow pattern of deep-sea zone strongly influences plume spouting out of hydrothermal vent, larval dispersion and planktonic life.

Mitsuzawa (2003) carried out a towing survey of the deep-sea current using JAMSTEC/Deep Tow system equipped with down-looking ADCP in hydrothermal region in the Southern Mariana Trough. In the Mid Okinawa Trough hydrothermal region, they also carried out the survey of the deep-sea current using the Shinkai 2000 and the ROV Dolphin 3 K equipped with ADCP. Because an acoustic backscatter of ADCP was too weak and heaving effect of the vessel affected the survey in the Mariana Trough, current measurement of deep-sea zone was difficult by conventional method.

Current profile and occasional turbulent is considered as effective factors for chemicals dispersion from the hydrothermal vent, and transportation of eggs and larvae from hydrothermal community. However, few studies have been conducted based on in situ measurements of the physical environmental condition on hydrothermal vent field. In this study, we determined current profiles at the Hatoma Knoll hydrothermal field to characterize the physical environment. The purpose of this study is to reveal the profile of the deep-sea current, and examined an acoustic detection of hydrothermal plume by ADCP.

50.2 Field Observation and Method

50.2.1 Observation Site

Hatoma Knoll has a caldera rim that is open to south, and is located 50 km northwest of Ishigaki Island in Okinawa prefecture, Japan (Ishibashi et al. Chap. 29). Many hydrothermal vents, including some bubbling vents, have been found from the central to the western slope of Hatoma Knoll Caldera. Hatoma Knoll has a height difference of approximately 600 m and most of the hydrothermal vents locate at about 1,500-m in water depth (Fig. 50.1). The total hydrothermal area is estimated to be about 16,800 m^2 (Watanabe 2001). Physical environments were observed for a few weeks using the ADCP at Hatoma Knoll (Fig. 50.1) in April 2004 and May 2005.

50.2.2 Measuring Apparatus

ADCP (Teledyne RD Instruments Workhorse Sentinel, 300 kHz: Fig. 50.1) is an apparatus used to measure multi-layered ocean currents. Using the Doppler effect of ultrasonic wave emitted from four transducers, ADCP provides current direction and velocity, water temperature, depth (pressure) and intensities of reflection signals. The ADCP was placed at almost the same place in the both cruises, located at the west of the caldera apertural area of Hatoma Knoll (Fig. 50.1). Installation and recovery of the ADCP were performed using a remotely operated vehicle HYPER-DOLPHIN (JAMSTEC). Deep-sea current was measured using the ADCP from 16 to 24 April 2004, and from 30 April to 13 May 2005. The ADCP measurement was used the following condition; 10 min interval of sounding, and current profiling range constituted by 60 layers with 2 m-thickness. The deepest layer in water column was located 4 m above ADCP. The current profiling by the ADCP reached to 120 m upper layer from the seafloor.

50.3 Results

50.3.1 In Situ Observation in Hatoma Knoll

Figures 50.2 and 50.3 show the results of current measurement by the ADCP in the apertural area of Hatoma Knoll in April 2004 and May 2005. In both figures, the following are shown: (a) current velocity (mm/s); (b) east–west component current velocity (mm/s); (c) north–south component current velocity (mm/s); (d) vertical component current velocity (mm/s); (e) water temperature (°C, blue line); (f) depth (m, green line). And the red bar graph (g) indicates the number of layers that were measured by the ADCP.

The current velocity was approximately 10 cm/s for the east–west and north–south components, and a periodic fluctuation was observed in synchronization with a shift of water depth. There was a rise and fall in the depth fluctuation twice a day, which was synchronized with the tidal fluctuation. In the measurements in 2004, the water temperature fluctuation exhibited a slight diurnal rise and fall.

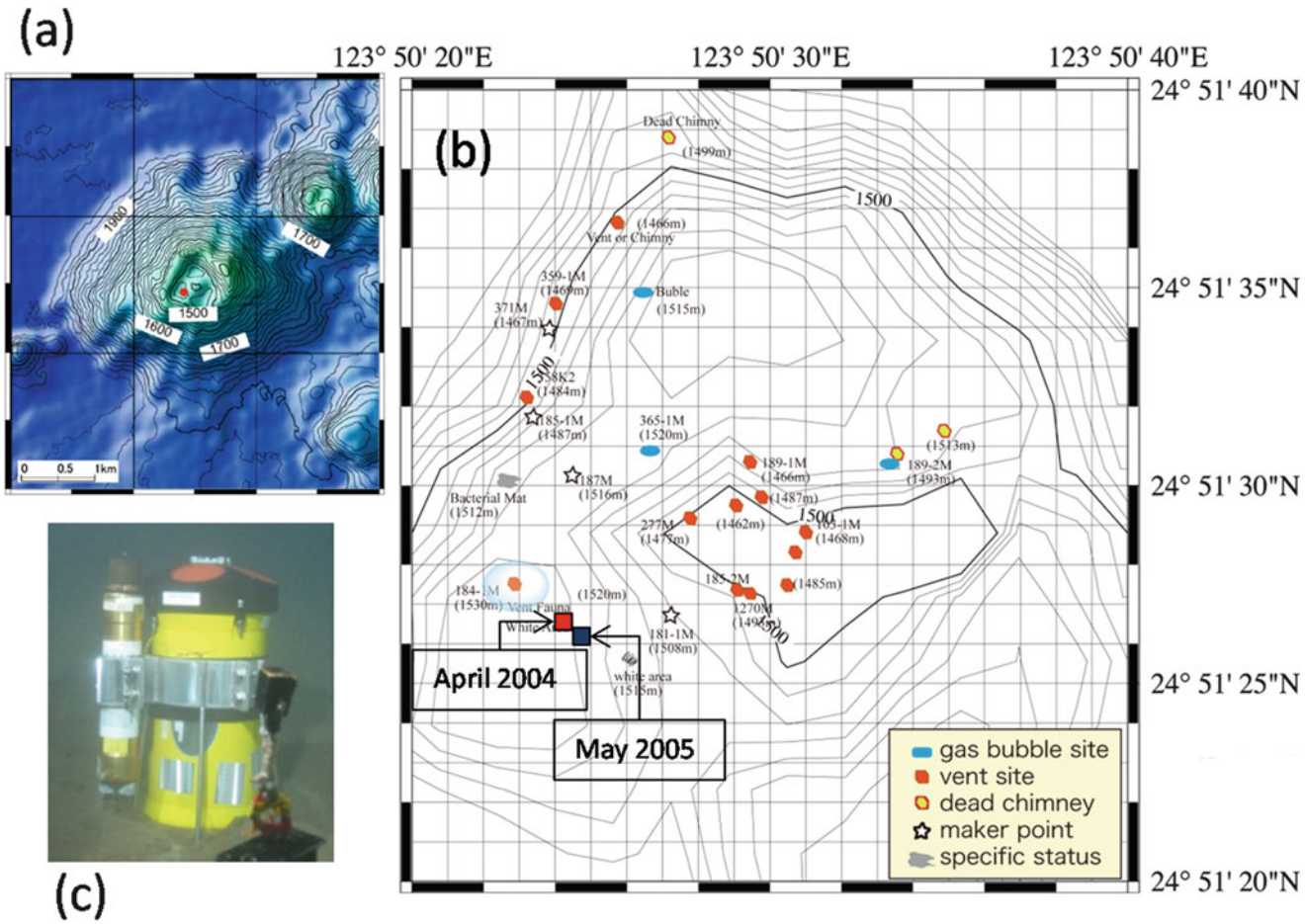

Fig. 50.1 Schematic view of the Hatoma Knoll in Okinawa Trough. (**a**) Bathymetric chart in the Hatoma knoll. (**b**) Locations of ADCP measurements in 2004 (*red square*) and 2005 (*blue square*) cruise and distribution of hydrothermal vents in the Hatoma Knoll Caldera. (**c**) Picture of the ADCP placed on the seafloor in 2004

It is important to stress that the current measurement using the ADCP was not provided in all layers of the area of observation during both years. The measurement result for the consecutive flow was either provided from the bottom to the 20th layer (in 2004 it was provided from the bottom to approximately the 44 m upper layer) or from the bottom to the 30th layer (in 2005 it was provided from the bottom to approximately the 64 m upper layer). However, there was a time zone when it was possible to measure using a pulse form to around the upper layer, in almost all the layers of the area of observation this was possible in a time zone when the tide shifted from ebb tide to high tide, for a time period of approximately 3 h. The depth fluctuation was compared with the possible number of layers included in the measurement (Figs. 50.2 and 50.3, green line and red bar graph).

Variation of the horizontal current velocity of layers 1, 10, 20, 25, and 30 in 2005 is shown in Fig. 50.4. Variation of the vertical flows the layers are shown in Fig. 50.5. The horizontal current (Fig. 50.4) of each layer during high tide showed a direction to a northward. In contrast, during the ebb tide, southward-current was predominant. These fluctuations were similar to the variation in the semidiurnal tidal current in the shallow water region in the Taketomi Submarine Hot Springs of the southern part of Yaeyama Archipelago (http://coral.godac.jp/md/jam_sekisei/4-1a.html). The horizontal current velocity showed slightly faster in the shallower layers below 20-m above the seafloor. We observed the weak and downward current velocities for the vertical axis.

50.3.2 Characteristics of the Dominant Time Cycle at Hatoma Knoll

We analyzed the data set appeared in Fig. 50.4 by a power spectrum in order to examine the dominant time cycle of the horizontal current velocity at each layer (Fig. 50.6). Spectrum density of the current velocity of east–west component

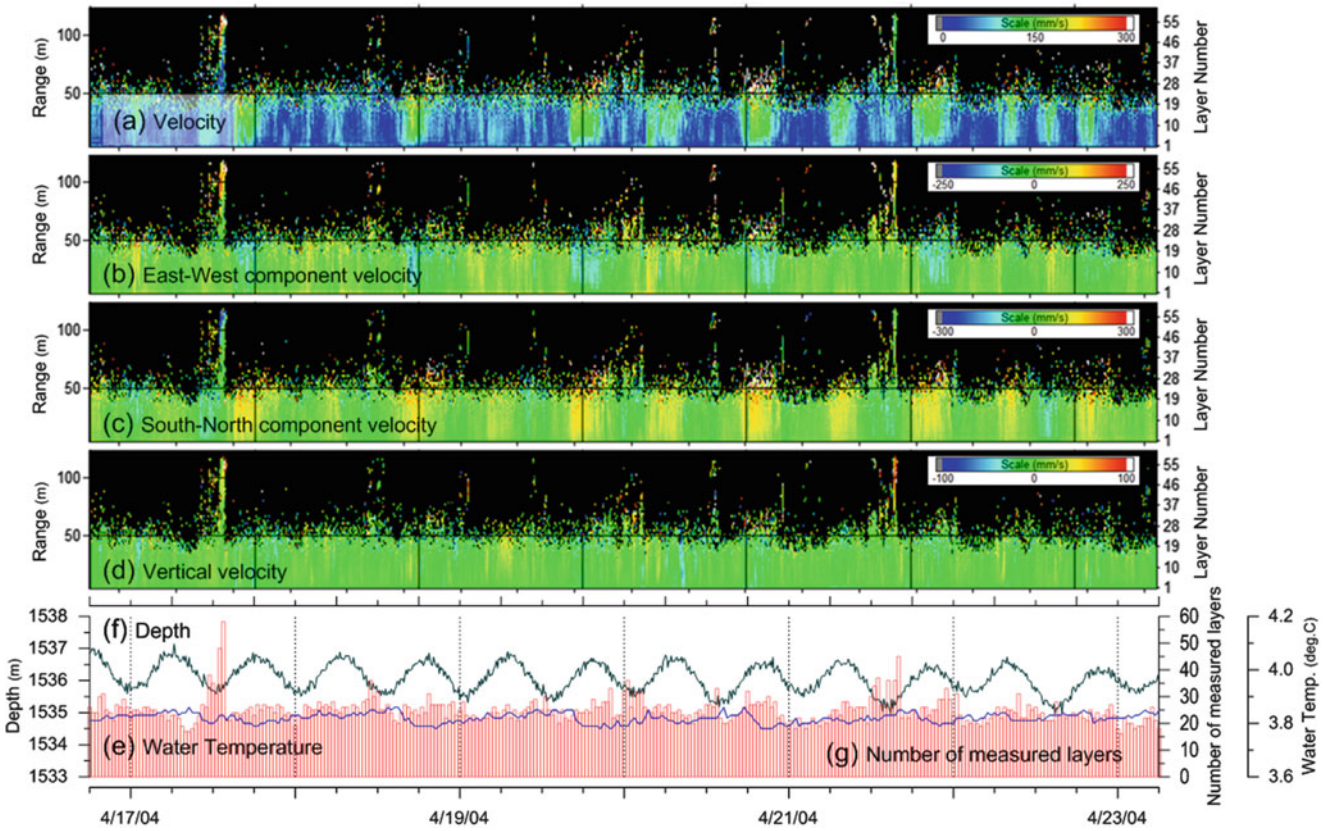

Fig. 50.2 Results of current measurement using the ADCP in April 2004. (**a**) Current velocity (mm/s). (**b**) Current velocity of East–west component (mm/s). (**c**) Current velocity of the north–south component (mm/s). (**d**) Current velocity of the vertical component (mm/s). (**e**) Water temperature (°C): blue line. (**f**) Depth (m): *green line*. (**g**) Number of measured layers: *red bar chart*. The *right axis* shows the layer number. The *left-sided axis* shows the height from the approximate sea bottom. The thickness is set to 2 m, and the flow was measured from the bottom through 60 layers

and north–south component in layers 1 and 20 was calculated using FFT analysis. As a result, we found a dominant time cycle of semidiurnal with approximately 12 h periodicity. The semidiurnal current at deep sea has been observed at the mid Atlantic Ridge (Fujioka and Mitsuzawa 2001) and around the seafloor off the Oahu Island, Hawaii (Aucan et al. 2006).

50.4 Discussion

50.4.1 Tidal Residual Current in the Caldera Structures of Hatoma Knoll

The tidal current in shallow coastal regions is caused by a horizontal repetitive motion of seawater with the rise and fall of the sea's surface due to the tide, and consists of a periodic component in synchrony with the tide (Pond and Pickard 1983). The water particles transported by a tidal current do not return to their original position, due to density stratification and bottom topography, even after completion of an entire period. This current is called the tidal residual current. The tidal residual current (residual current) plays an important role in long-term material transport. In the deep-sea hydrothermal area, the deep-sea residual tidal currents also plays an important role to supply chemical components such as trace minerals originated from hydrothermal fluids and organic materials produced in the plumes (Sunamura and Yanagawa, Chap. 3), as well as to disperse the eggs and larvae of chemosynthetic communities (Vrijenhoek 2010).

Constraint factors for distribution of the hydrothermal plume were buoyancy, chemical composition, the deep-sea current and the seafloor topography. Consequently, the deep-sea current is important for transportation of the plume, chemical compounds, eggs, and larvae of the deep-sea organisms in the hydrothermal vent field. The fluctuation of the residual current at Hatoma Knoll is shown in Fig. 50.7. The residual current was calculated using the 25-h moving average (eliminated in tidal periodicity) of the current measurement results. In the lower layers (from the bottom to the 60 m above the seafloor) of the Hatoma Knoll apertural area, the northward flow was dominant. This indicates that the

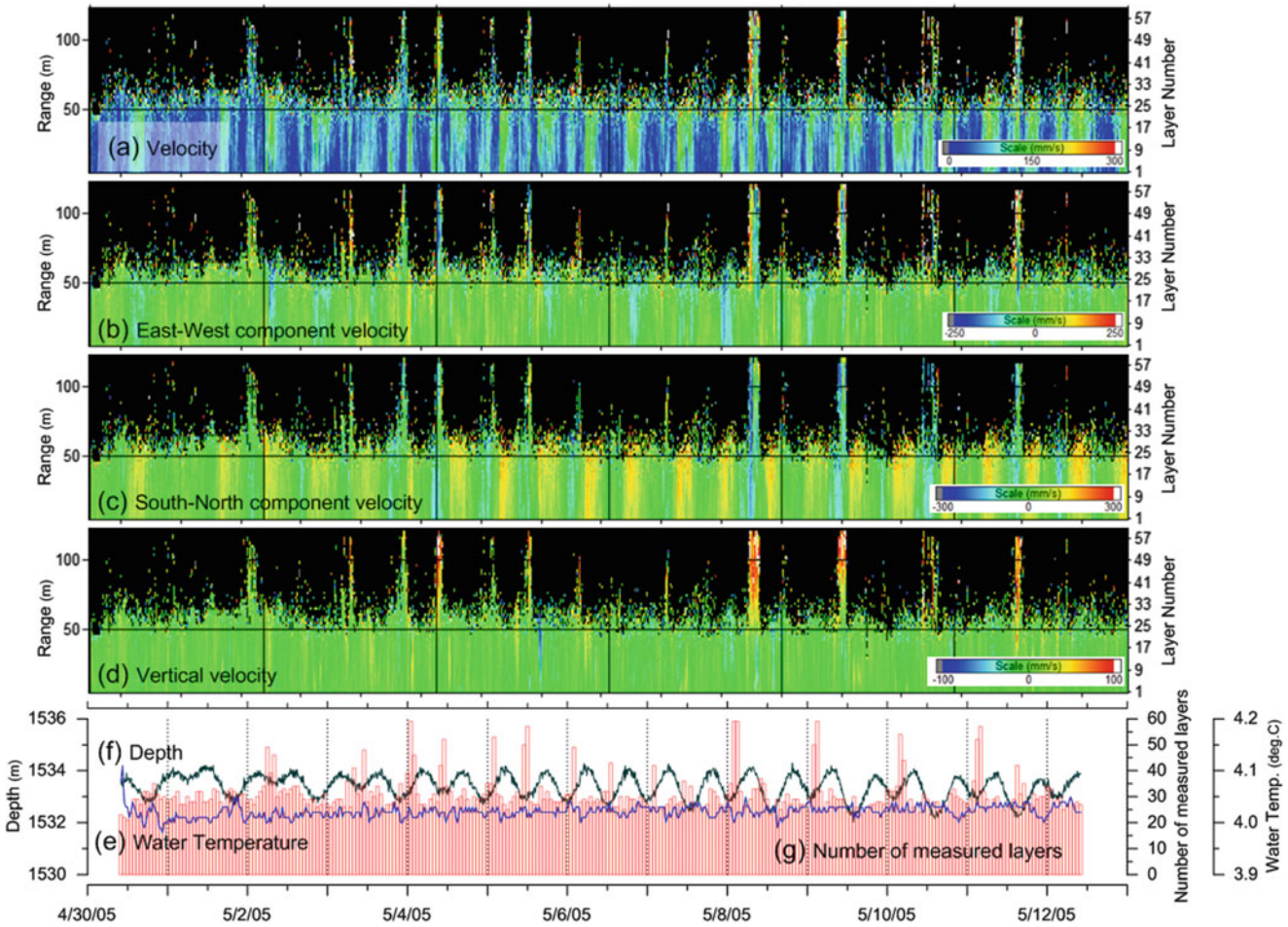

Fig. 50.3 Current measurement results using the ADCP in May 2005. (**a**) Current velocity of East–west component (mm/s). (**b**) Current velocity of the north–south component (mm/s). (**c**) Current velocity of the vertical component (mm/s). (**d**) Current velocity (mm/s). (**e**) Water temperature (°C): blue line. (**f**) Depth (m): *green line*. (**g**) Number of measured layers: *red bar chart*. The right axis shows the layer number. The left-sided axis shows the height from the approximate sea bottom. The thickness was set to 2 m, and the flow was measured from the bottom through 60 layers

material transport from caldera to outside will be weak in the lower layer (approximately 50-m above the seafloor) of the apertural area of the south side in the Hatoma knoll. In other words, outside seawater flows in from apertural area lower layer of the south side in the knoll, and it is considered that the seawater in the caldera flows out other region, such as top of the caldera and the apertural area upper layer. We also calculated the vertical current velocity (Fig. 50.8), and found that the downward flow was prominent in the layers from the sea bottom to the 50 m above the seafloor. Because Hatoma Knoll has a closed topography with the same water-depth of the top of caldera rim, there is a possibility that materials (chemical compounds, eggs and larvae) are resident within the caldera. In addition, a fluctuation period of 2–3 days was found in the fluctuation of the residual current in Fig. 50.7. The reason for such a fluctuation period is not known, but we speculate that a variation in the hydrothermal venting period may be occurring, thereby varying the volume of the hydrothermal water. Therefore a long and continuous measurement of hydrothermal venting fluids and the numerical modeling will be needed to know the main component of the residual current in the Hatoma knoll.

50.4.2 Behavior of the Backscattering

The ADCP measures the current velocity and direction by detection of reflecting sound wave signals. The ADCP transmits high frequency sound waves (300 kHz) from four transducers (Fig. 50.9), and determining the Doppler frequency shift of return-reflected signal from particles in the seawater (Emery and Thomson 2004). Through the ADCP measurements, we can obtain the backscatter signal intensity as well as velocity. Figure 50.10 shows temporal variation of backscatter signal intensity from May 7, 2005 at 18:00 and May 9, 2005 at 18:00, when pulsatile current was observed.

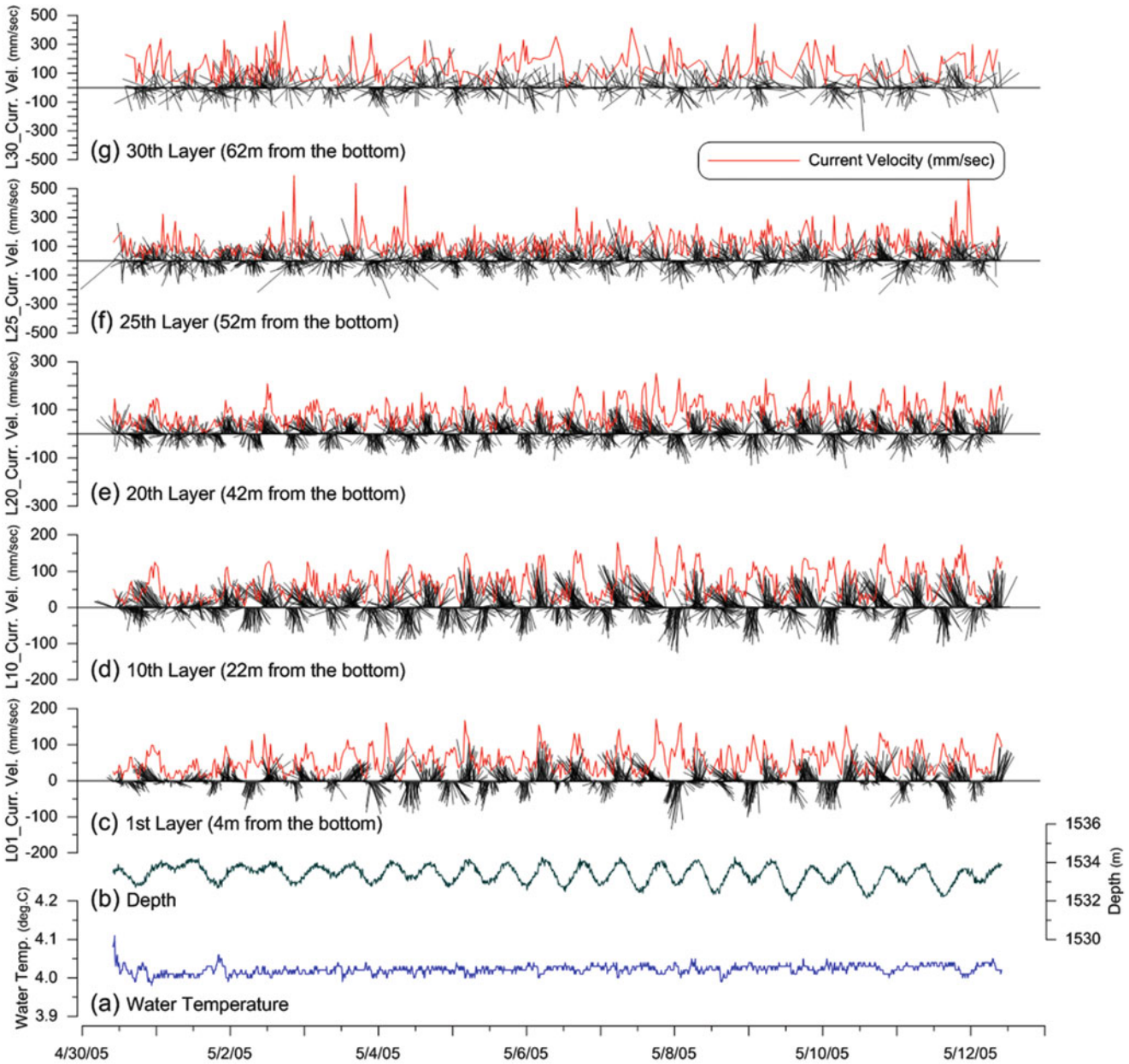

Fig. 50.4 Fluctuation of current velocity, current direction, water temperature, and depth, at the sea bottom. (**a**) Water Temperature (°C). (**b**) Depth (m). (**c**) Fluctuation of the current velocity at layer 1 (4 m from the bottom). (**d**) Fluctuation of the current velocity at layer 10 (22 m from the bottom). (**e**) Fluctuation of the current velocity at layer 20 (42 m from the bottom). (**f**) Fluctuation of the current velocity at layer 25 (52 m from the bottom). (**g**) Fluctuation of the current velocity at layer 30 (62 m from the bottom). Current velocity unit is mm/s. The *red line* in the figure shows current velocity. The *black line* shows the current velocity. The plus value of the current velocity expresses the northward and eastward flow, respectively. In the case of a negative value, the current velocity represents a southward and westward flow

We found sharp and high backscatter intensity signals through the water column from 23:00 on May 7 to 4:00 May 8 and from 23:00 on May 8 to 4:00 on May 9. Four transducers of the ADCP were placed on a circle as shown in Fig. 50.9. In Beam4 at the east side of the apparatus, high backscattering intensity was observed at around 100 m from the bottom at about 0:00 on May 8. The high backscattering was observed at 75 m from sea bottom in Beam2 located in the south side of Beam4 at about 2:00 on May 8. In Beam3, we were not able to identify the distribution of remarkable high backscattering. However, in Beam1, the high backscattering was detected at 50 m from the bottom at about 2:00 on May 8, and at 75 m around 3:00. We consider that the behavior of the high backscattering on ADCP data indicates

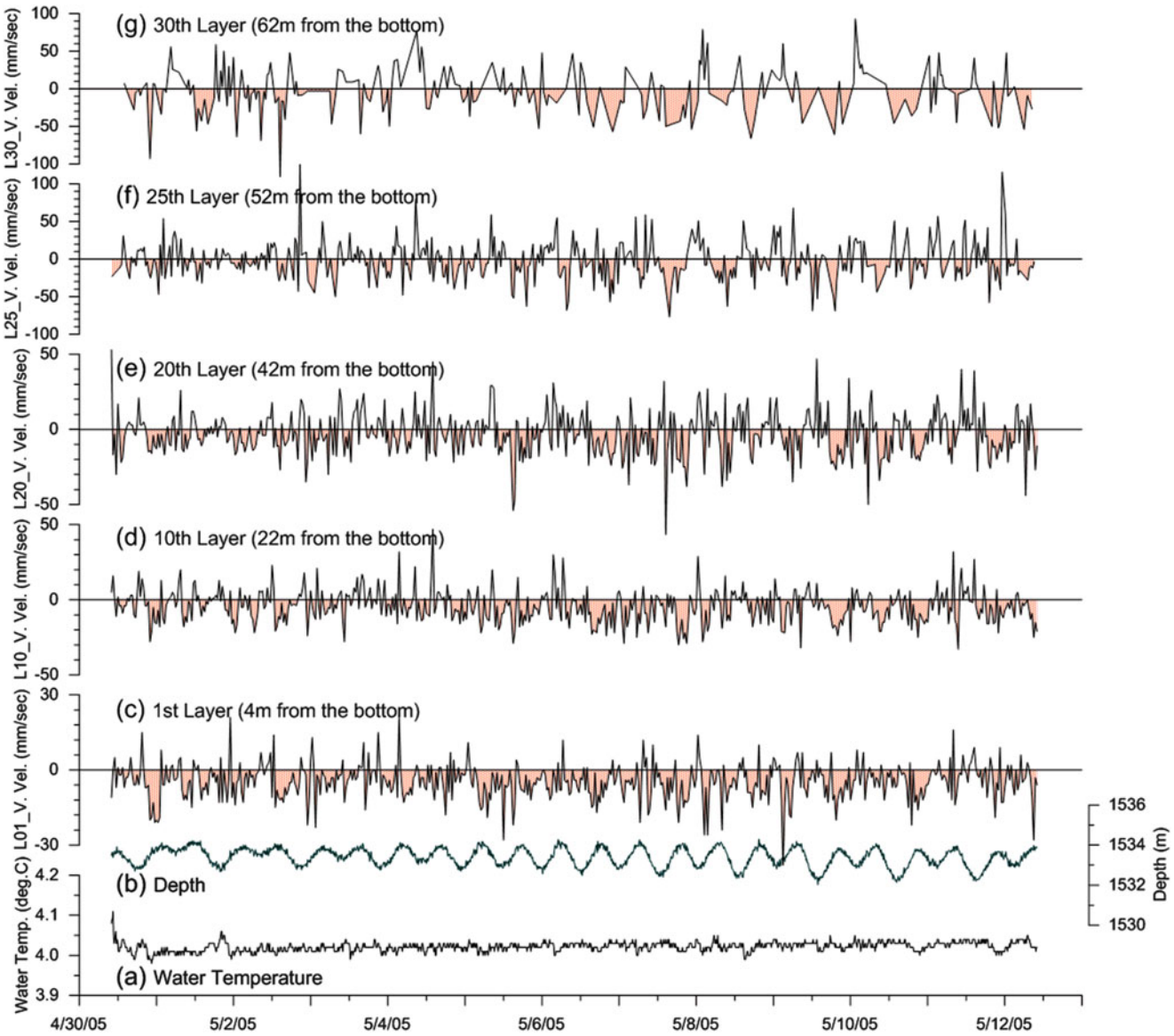

Fig. 50.5 Fluctuation of vertical current velocity, water temperature and depth around the sea bottom. (**a**) Water Temperature (°C). (**b**) Depth (m). (**c**) Fluctuation of the layer 1 (4 m from the bottom). (**d**) Fluctuation of layer 10 (22 m from the bottom). (**e**) Fluctuation of layer 20 (42 m from the bottom). (**f**) Fluctuation of layer 25 (52 m from the bottom). (**g**) Fluctuation of layer 30 (62 m from the bottom). Current velocity unit is mm/s. The *red hatching* in the figure shows the downward current velocity

the movement of the water mass including many particles. Therefore, the distribution of the high backscattering indicates that drifters or marine snow sank down from the upper layer into the lower layer using a clockwise circulation (Figs. 50.9 and 50.10). It is likely that a current measurement would have been impossible because the seawater was extremely clear with low turbidity for 60 m in the upper layer, except during the time zone when the pulsatile current measurement was confirmed. Measurement of ADCP in venting site would be effective to determine the deep-sea current up to 120-m above the seafloor and to observe behavior of hydrothermal plume if behavior of the high backscattering depends on hydrothermal water effect.

The possible reason for the distribution of high backscattering appearing in a pulse form was considered. Furushima et al. (2009) showed that volume of bubble spout from a geyser of 10 m water-depth seafloor on the Taketomi submarine hot spring site where is a shallowest hydrothermal vent in eastern Taketomi Island within the Yaeyama archipelago, Japan, was related to tidal periodicity. Furushima et al. (2009) and Nagao et al. (2011) also indicated that the increased upward flux from the Taketomi geyser shifted to a

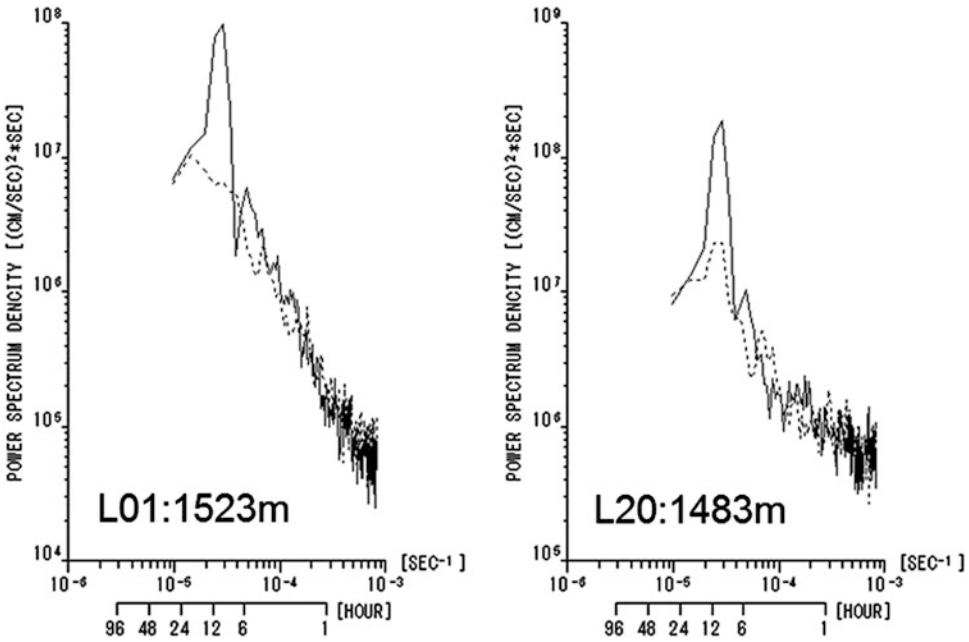

Fig. 50.6 Power spectrum of the East–west (*dashed line*) and the North–south (*solid line*) components of the velocity in layers 1 and 20

flood tide from an ebb tide period. Additionally Oomori (1987) suggested that the Taketomi submarine hot spring originated in the hydrothermal activity underneath the geological structure of Ryukyu archipelago rather than back-arc system. The distribution of high backscattering was found at a time period in the Hatoma Knoll, when shift to a flood tide from an ebb tide (Fig. 50.10). If the hydrothermal system in the Hatoma knoll was affected by the tidal fluctuation same as the Taketomi submarine hot spring, hydrothermal plume upward flux may increase to a flood tide from an ebb tide period. The three-dimensional mapping of the hydrothermal system and verification by the numerical model may be necessary to understand the distribution of high backscattering appearing in a pulse form.

We finally considered the methods to measure the amount of hydrothermal fluids spouting from the many hydrothermal vents in the caldera at Hatoma Knoll. At sites where the bottom topography is flat and hydrothermal water spouts out from the seabed, a current meter emitting an ultrasonic sound horizontally (e.g. DW-Aquadopp, Nortek AS) can be set up on the bottom, and fluctuation of the vertical flow, flux, and variation of fluid flux, can be determined. However, at Hatoma Knoll, hydrothermal fluid vents from a chimney, and some of the chimneys are more than 10 m tall. In addition, the bottom topography of vent filed is very complex, and this makes difficulty of bottom installation-type current measurement. Camilli et al. (2011) showed that in the case of the Deepwater Horizon collapsed at Macondo, three-dimensional imaging method by ADCP and acoustic imaging sonar installed to ROV successfully determined the oil leakage on the wellhead. If this measurement technique could apply to hydrothermal field, it make an quantitative determination method to estimate hydrothermal fluid flux from chimney, and provide the information to investigate the physicochemical influence for the marine ecosystem.

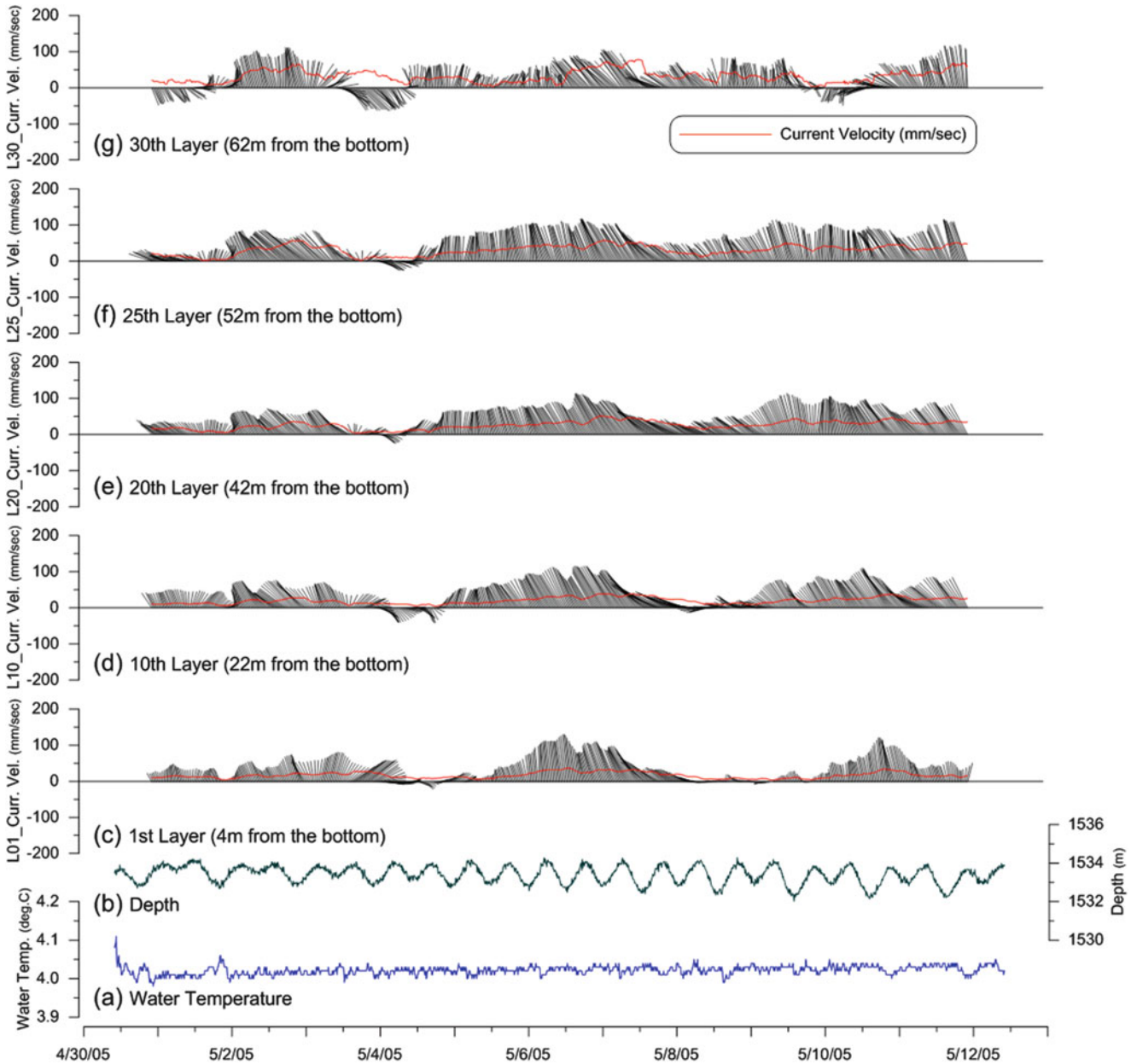

Fig. 50.7 Fluctuation of water temperature and water pressure around the sea bottom. Horizontal current fluctuations with moving average for 25 h calculated in each layer (from the sea bottom to upper layer at 62 m). (**a**) Water Temperature (°C). (**b**) Depth (m): water pressure. (**c**) Fluctuation of the current velocity at layer 1 (4 m from the bottom). (**d**) Fluctuation of the current velocity at layer 10 (22 m from the bottom). (**e**) Fluctuation of the current velocity at layer 20 (42 m from the bottom). (**f**) Fluctuation of the current velocity at layer 25 (52 m from the bottom). (**g**) Fluctuation of the current velocity at layer 30 (62 m from the bottom). The *red line* shows the current velocity. The *black line* shows fluctuation of the current velocity and direction. The plus value of the current velocity expresses the northward and eastward flow, respectively. In the case of a negative value, the current velocity represents a southward and westward flow

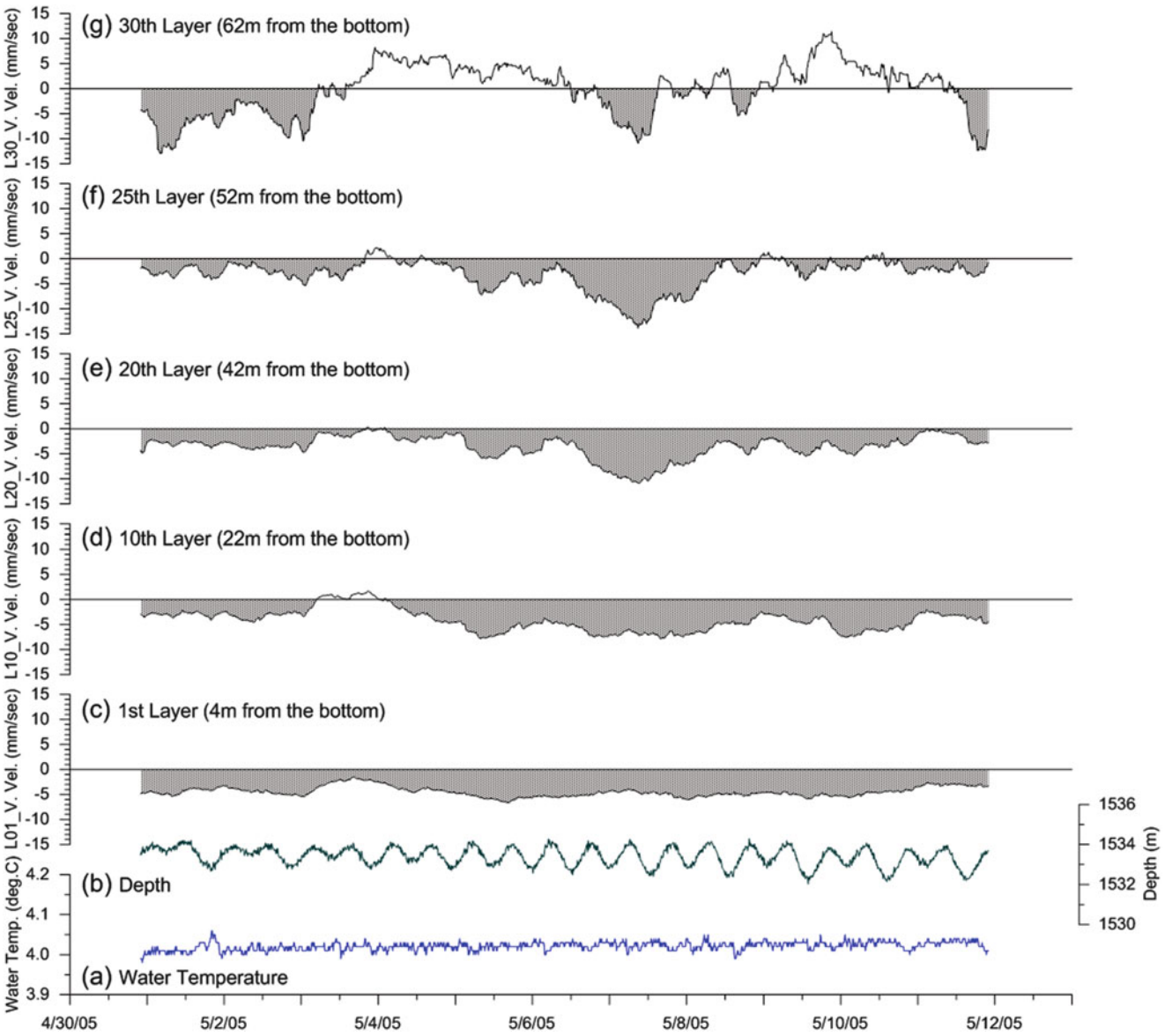

Fig. 50.8 The vertical velocity fluctuation (calculated moving average for 25 h) in each layer; and fluctuation of water temperature and depth. (**a**) Water Temperature (°C). (**b**) Depth (m). (**c**) Fluctuation of the vertical current velocity at layer 1 (4 m from the bottom). (**d**) Fluctuation of the vertical current velocity at layer 10 (22 m from the bottom). (**e**) Fluctuation of the vertical current velocity at layer 20 (42 m from the bottom). (**f**) Fluctuation of the vertical current velocity at layer 25 (52 m from the bottom) (**g**) Fluctuation of the vertical current velocity at layer 30 (62 m from the bottom). The hatching shows the downward current velocity. The *plus value* of the current velocity indicates the upward current velocity, and the *negative value* indicates the downward current velocity

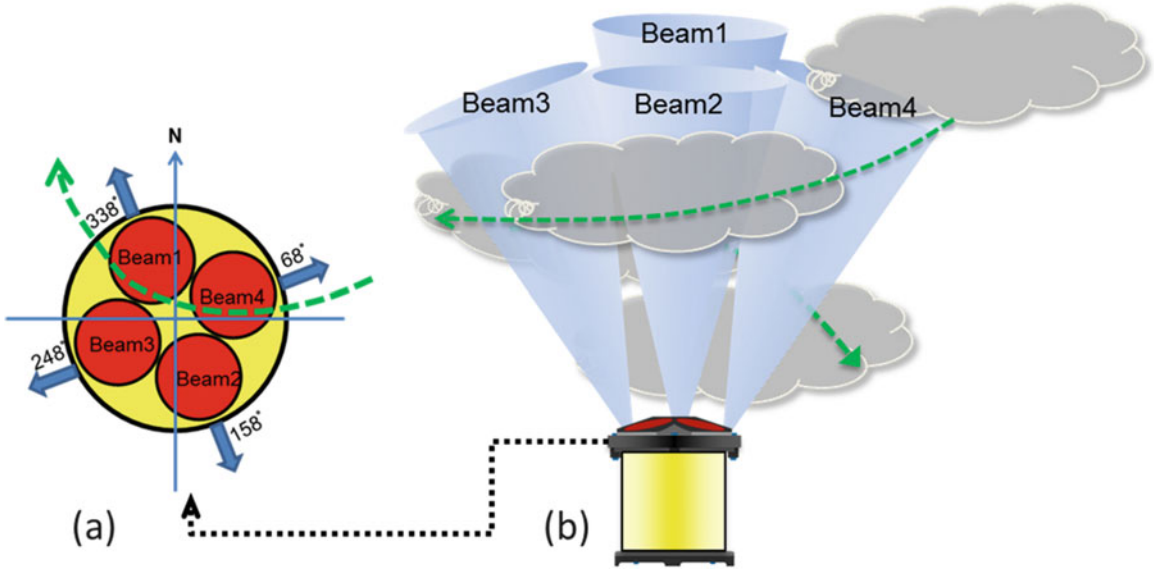

Fig. 50.9 Schematic view of (**a**) the upper ADCP and direction of the transducers, and (**b**) movement of a high backscatter. The *dotted line arrow* indicates that a high backscatter propagates (sink down from the upper layer to lower layer) clockwise

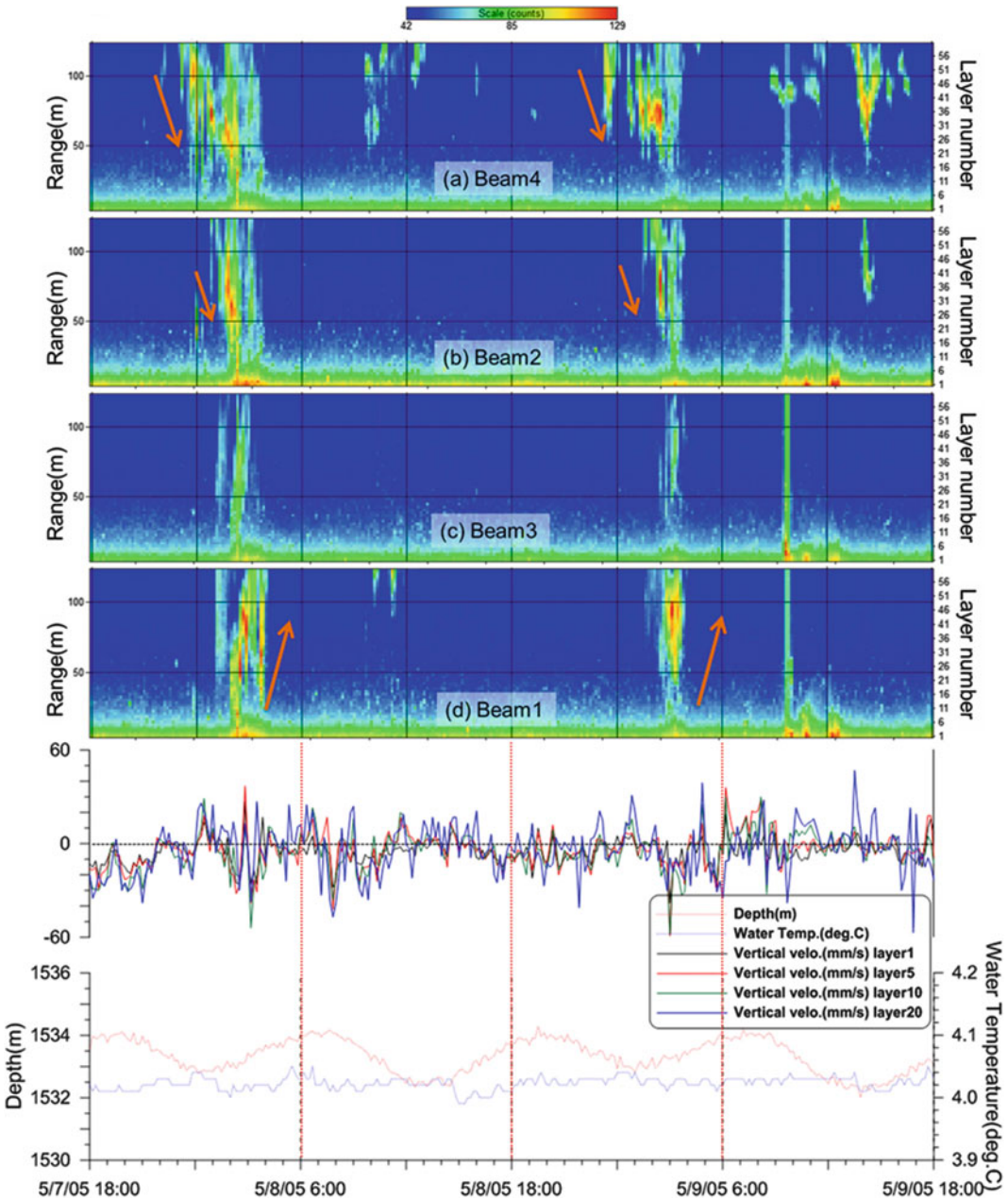

Fig. 50.10 Intensity variation of back scatter signals by ADCP in 2005. The *right axis* shows the layer number. The *left-sided axis* shows the height from the approximate sea bottom. Each thickness was set to a 3 m- resolution and the 50 layers were measured from the seafloor. (**a**) Backscatter signal intensity of Beam 4, (**b**) backscatter signal intensity of Beam 2, (**c**) backscatter signal intensity of Beam 3, (**d**) backscatter signal intensity of Beam 1

Acknowledgements We thank the captain and crew of R/V Natsushima and the deep-sea submersible operation teams of HYPER-DOLPHIN 3000 for supporting the observation and for the installation and recovery of the ADCP. We would like to thank the Ministry of Education, Culture, Sports, Science, and Technology (MEXT), Grant-in-Aid for Scientific Research on Innovative Areas TAIGA (20109003), for its partial support for this research.

References

Aucan J, Merrifield MA, Luther DS, Flament P (2006) Tidal mixing event on the deep flanks of Kaena ridge, Hawaii. J Phys Oceanogr 36:1202–1219

Baker ET, Cormier M-H, Langmuir CH, Zavala K (2001) Hydrothermal plumes along segments of contrasting magmatic influence, 15°20′-18°30′N, East Pacific Rise: influence of axial faulting. Electr J Earth Sci 2:2000GC000165

Camilli R, Di Iorio D, Bowen A, Reddy CM, Techet AH, Yoerger DR, Whitcomb LL, Seewald JS, Sylva SP, Fenwick J (2011) Acoustic measurement of the deepwater horizon Macondo well flow rate. Proc Natl Acad Sci U S A 1100385108:1–5

Emery WJ, Thomson RE (2004) Data analysis methods in physical oceanography, 2nd edn. Elsevier, New York

Fujioka K, Mitsuzawa K (2001) Tide-related variability of hydrothermal activity at the TAG hydrothermal mound, mid-Atlantic Ridge and the East Pacific Rise. J Geodetic Soc Jpn 47(1):434–440

Fujioka K, Kobayashi K, Kato K, Aoki M, Mitsuzawa K, Kinoshita M, Nishizawa A (1997) Tide-related variability of TAG hydrothermal activity observed by deep-sea monitoring system and OBSH. Earth Planet Sci Lett 153:239–250

Furushima Y, Nagao M, Suzuki A, Yamamoto H, Maruyama T (2009) Periodic behavior of the bubble jet (Geyser) in the Taketomi submarine hot springs of the southern part of Yaeyama Archipelago. Jpn Mar Technol Soc J 43:13–22

Mitsuzawa K (2003) The application of ADCP to the measurement of current system at the hydrothermal active areas. In: Proceedings of the IEEE/OES seventh conference on current measurement technology, pp 246–249

Nagao M, Furushima Y, Suzuki A, Yamamoto H, Maruyama T (2011) Relative bubble density and flux discharged from an underwater geyser varying with tide. Ann J Hydra Eng 55:211–216

Oomori T (1987) Chemical composition of submarine hot spring water and associated bottom sediments near taketomi-jima at southern part of the Ryukyu island arc, north-west pacific. J Earth Sci Nagoya Univ 35(2):325–340

Pond S, Pickard GL (1983) Introductory dynamical oceanography, 2nd edn. Pergamon, New York, pp 253–281

Thomson RE, Miha'ly SF, Rabinovich AB, McDuff RE, Veirs SR, Stahr FR (2003) Constrained circulation at Endeavour ridge facilitates colonization by vent larvae. Nature 424:545–549

Vrijenhoek RC (2010) Genetic diversity and connectivity of deep-sea hydrothermal vent metapopulations. Mol Ecol 19:4391–4411

Watanabe K (2001) Mapping the hydrothermal activity area on the Hatoma Knoll in the southern Okinawa Trough. JAMSTEC J Deep Sea Res 19:87–94 (in Japanese with English abstract)

The Gelatinous Macroplankton Community at the Hatoma Knoll Hydrothermal Vent

51

Dhugal Lindsay, Mitsuko Umetsu, Mary Grossmann, Hiroshi Miyake, and Hiroyuki Yamamoto

Abstract

A series of dives around the Hatoma Knoll, Okinawa Trough, have revealed a diverse community of gelatinous midwater animals. Many of these animals are potential predators of the larvae of hydrothermal vent-associated organisms. Due to the lack of published information on the midwater fauna of the Okinawa Trough, this paper endeavours to present a synopsis of the macroplanktonic gelatinous faunal elements present in and around the vent site at all depths where vent larvae may occur—from the surface to the benthopelagic layer. Three pelagic tunicates, eight ctenophores, seven siphonophores, eight hydrozoan medusae and two syphozoan medusae were recognized. Taxonomic treatments and comments on distribution and ecology are provided where such information exists.

Keywords

Gelatinous zooplankton • Taxonomic guide • Vent larvae predators

51.1 Introduction

Limited work has been done on deep-sea benthopelagic fauna, particularly the gelatinous component. In fact, even in the overlying water column, very little work has been published on the gelatinous component of the ocean's midwater zone. Data on the cnidarian community can be gathered using plankton nets but more fragile animals such as ctenophores and appendicularians, for example, are invariably destroyed past recognition. In situ observations on the gelatinous zooplankton community of the midwater zone that include these fragile components are very few and far between, with the notable exception of work done off California (Haddock and Case 1999) and around Japan (e.g. Hunt and Lindsay 1999; Vinogradov and Shushkina 2002; Toyokawa et al. 2003; Lindsay 2005; Lindsay and Hunt 2005; Lindsay and Miyake 2007), and scattered reports from the northern Atlantic (Youngbluth et al. 2008), the south–west Indian Ocean (Lindsay et al. 2000) and the Arctic Ocean (Raskoff et al. 2010). Most of these reports are from areas without active venting. Deep-sea hydrothermal plumes enable high levels of primary production by chemolithoautotrophic microbes and in some cases the amount of organic material produced can be comparable with that of settling particles originating from near the sea surface (Sunamura and Yanagawa, Chap. 3). Such organic material supply should affect the surrounding deep-sea ecosystem, however, very few previous reports exist describing the gelatinous fauna in regions of hydrothermal venting (Vereshchaka and Vinogradov 1999; Burd and Thomson 2000; Skebo et al. 2006). Although Burd and Thomson (2000) reported on the distribution and relative importance of jellyfish at the Endeavour Ridge in the north–east Pacific

D. Lindsay (✉) • H. Yamamoto
Japan Agency for Marine-Earth Science and Technology (JAMSTEC), 2-15 Natsushima-cho, Yokosuka, Kanagawa 237-0061, Japan
e-mail: dhugal@jamstec.go.jp

M. Umetsu • H. Miyake
Kitasato University, 1-15-1 Kitasato, Minami-ku, Sagamihara, Kanagawa 252-0373, Japan

M. Grossmann
Okinawa Institute of Marine Science and Technology (OIST), 1919-1 Tancha, Onna, Okinawa 904-0495, Japan

J.-i. Ishibashi et al. (eds.), *Subseafloor Biosphere Linked to Hydrothermal Systems: TAIGA Concept*,
DOI 10.1007/978-4-431-54865-2_51,

at the species level and found aggregations of the ulmarid scyphomedusa *Stygiomedusa* at the vent plume boundary, there was no information on the ctenophore community due to the net sampling survey method used. Both Vereshchaka and Vinogradov (1999) and Skebo et al. (2006) used in situ visual observations, which should have allowed them to gather information on the fragile ctenophores and larvaceans. However, although the former authors showed that gelatinous animals and radiolarians can dominate plankton biomass throughout the water column, particularly just above and below the main core of the hydrothermal vent plume, at the Broken Spur vent field, mid-Atlantic ridge, and the latter authors also found significant differences in jellyfish abundances between the near-field and far-field areas, the level of taxonomic resolution was only at the Phylum level. The midwater and benthopelagic fauna occurring around deep sea chemosynthetic ecosystems is therefore somewhat of a black box, even though the predation pressure on vent-derived larvae exerted by its inhabitants may be considerable. The taxonomy of these soft-bodied predators is difficult and the information needed to correctly identify many of the species is scattered throughout the literature in a variety of languages. In the present paper we analysed the video record from ten dives of the Remotely Operated Vehicle (ROV) *HyperDolphin* around the Hatoma Knoll hydrothermal vent site (approx. 21°51.45′N 123°50.45′E) and give taxonomic treatments and other information on the gelatinous zooplankton that were observed, in order to stimulate and facilitate further work. As it is not yet known at what depths the larvae of each vent species inhabit during development, we give a synopsis of the gelatinous zooplankton that could eat released eggs and newly-hatched larvae (eg. larvaceans, lobate ctenophores) as well as those that would be expected to prey on larvae nearing their settlement phase (eg. siphonophores and cydippid ctenophores), and their potential predators, in turn. Where a video record existed, it was analyzed from the benthopelagic layers near the vent plumes right up to the near surface layer.

51.2 Materials and Methods

High definition video (1080i) from the ROV *HyperDolphin* SuperHarp high definition video camera (Lindsay 2003) was recorded on HDCAM videotapes without depth or time data superimposed. Standard video (NTSC) was recorded simultaneously on DigiBetaCam tapes with data including depth and local time superimposed as text on the video image. The video record for each dive was reviewed using the original HD-CAM tapes (Sony HDW-500 HDCam recorder, Sony HDTranslation Color Monitor PHM-14M7J) and when organisms that could be identified appeared on the screen, the timecode at which they first appeared and the timecode at which they disappeared from the screen were entered into an Excel worksheet along with the organism's taxon. The DigiBetaCam tapes were then referred to (Sony HDW-M2100 HD Digital MultiPlayer, Sony HDTranslation Color Monitor PHM-20M7J) in order to determine the local time and depth at which each organism occurred through identifying a unique video sequence on each tape as a place marker (e.g. a camera pan to the manipulator followed by a tilt to the sample basket and a jellyfish appearing at left screen) and adding/subtracting timecode values to calculate the approximate location on the DigiBetaCam tape at which the organism should be visible. This allowed the DigiBetaCam tape to be fast-forwarded to the approximate location of the organism in question, which was then searched for by eye and frames synchronized manually using the jog dial on the editing keyboard (Sony BKE-2010). Depth and local time values when the organism first appeared were then entered into the Excel worksheet. Each video sequence was captured (AJA WZZ-KiPro2400) onto a hard disk cartridge at ProRes 4:2:2HQ resolution via HD-SDI and saved in Quicktime format (.mov). Captured files were played back using Quicktime Player 7 version 7.6.6 via Firewire 800, the start and end timecodes of the captured clip noted, and the clip saved to a local hard disk with the filename format incorporating the submersible name (HD = ROV *HyperDolphin*), dive number, start timecode, end timecode, local time, taxon name or organism-specific identification code, taxonomist/person responsible for species ID, and common Japanese name. For example, a clip of the trachymedusa Crossota millsae from timecode 04:49:58;13 to 04:53:58;03 corresponding to local time of first appearance 13:25:20 taken during dive 296 of the ROV *HyperDolphin* and identified by Dhugal Lindsay would be given a filename of HD29604495813to04535803-132520-Crossota_millsae-Dhugal_Lindsay-KUROKURAGENONAKAMA.mov. Still images were extracted from the video files by viewing them at native magnification (Command 1 Actual Size), copying them to the clipboard (Command C Copy), creating a new file in Adobe Photoshop CS5 (version 12.0.4 × 64) with width 1,920 pixels, height 1,080 pixels and resolution 72 pixels/in., and pasting them to the blank canvas (Command P Paste). The still images were then saved as TIFF files with no compression, IBM PC Byte Order and an interleaved pixel order with the frame number incorporated into the file name (e.g. HD296-04502821-Crossota_millsae-Dhugal_Lindsay-KUROKURAGENONAKAMA.tif). These file name formats were picked to act as unique identifiers for video sequences and still images that would allow the files to be linked in a database to both environmental data such as CTD data on depth, temperature and salinity, and to location data for biogeographic studies. Local time was included but not solely used in the filename as resolution would only then be possible in one second intervals, and future progress in automated image

Table 51.1 Dives analyzed during the present study

Dive No.	Date	Surveyed Depth	Time on video	Notes
2K1183	18-May-99	0–1,521	09:42–16:06	Specimens studied
2K1188	28-May-99	0–1,524	09:13–15:57	Specimens studied
HD66	15-Nov-01	1,526–1,527	13:40–15:53	Near bottom only
HD67	18-Nov-01	1,525–1,529	09:45–15:05	Near bottom only
HD225	15-Sept-03	0–1,520	09:25–17:36	Descent at 25 m/min
HD226	16-Sept-03	0–1,532	08:40–17:46	
HD293	16-Apr-04	0–1,530	08:41–16:44	Descent at 25 m/min
HD294	17-Apr-04	0–1,482	17:41–02:14	
HD295	20-Apr-04	0–1,475	11:21–18:43	
HD296	21-Apr-04	0–1,477	08:35–16:32	
HD297	22-Apr-04	0–1,528	08:40–15:27	Descent at 25 m/min
HD708	30-Jun-07	1,472–1,480	14:14–17:18	Near bottom only

2K=Shinkai 2000, HD=ROV HyperDolphin

recognition technologies will need frame level resolution for voucher image libraries. Low resolution video footage of the organisms is archived in the JAMSTEC E-library of Deep-sea Images (J-EDI) and can be accessed through the following URL: http://www.godac.jamstec.go.jp/jedi/public/Sec101.jsf. A "Search by Dive Information" is possible by inputting the Submersible (e.g. HYPER-DOLPHIN) and the Dive No. (e.g. 0294) in the respective fields. Footage of the entire dive has been subdivided into shorter, non-overlapping streaming video clips with unique identifier Video IDs, where the final two numerical values, subdivided by an underbar, are the "in" and "out" timecodes from the original HDCAM-recorded videotapes in the case of ROV *HyperDolphin* Dives 225 or later. The elapsed time window to the right of the sliding bar allows one to move to the video footage of the target organism by subtracting the streaming subclip "in" timecode value from the target filename timecode and typing that elapsed time value into the window. Full resolution video is available from JAMSTEC's Data Management Office (see http://www.godac.jamstec.go.jp/jedi/e/readme.html#readme_img). The video and still data from this analysis is also stored at full resolution on a Buffalo TeraStation hard disk RAID array (TS-QVH8.0TL/R6), accessible by Ethernet, at the Research and Development (R&D) Center for Submarine Resources, JAMSTEC, and is available on request.

A total of ten dives were analyzed (Table 51.1), with four of these dives having been conducted specifically for the purpose of cataloguing the midwater fauna above the Hatoma Knoll hydrothermal vent site (HD226, HD294, HD295, HD296). Dives where the descent speed was approximately 25 m/min (HD225, HD293, HD297) allowed the identification of very few animals, none of which were of a suitable quality to extract still images. The *Shinkai 2000* (2K) video record was in low resolution NTSC format and consequently very few taxa were identifiable to species level, although several species were captured and were examined under a stereo dissecting microscope for the present study. Three ROV *HyperDolphin* dives concentrated on the benthic and benthopelagic layers (HD66, HD67, HD708) with the training dive HD67 having many image sequences of a quality good enough to both identify animals to species level and to extract still images of publication quality. Environmental parameters during the dives were measured with a Seabird SBE19 CTD and SBE13 dissolved oxygen (e.g. Fig. 51.1).

A subset of the observed organisms were collected during the midwater dives using a suction sampler or gate sampler (Lindsay 2003) and photographed alive on board ship in phototanks or planktonkreisels using a digital camera. When organisms were sampled, an identifier as to which cannister or sampler were used (eg. SS1 for Suction Sampler cannister 1) and which sample from the cannister (eg. A, B, etc.) it was, were appended to the Dive Number field in the filename. If the image was a photograph rather than a framegrab then the photo filename was also appended. Terminology for the taxonomic treatments are given in Fig. 51.2.

51.3 Results

51.3.1 General Synopsis

All dives in the vicinity of the Hatoma Knoll in the JAMSTEC video archive were conducted at the hydrothermal vent site and passed through the vent plume. This confounded attempts to compare the number and types of macroplanktonic organisms between vent and non-vent sites and to gauge the possible effects of the vent plume on plankton biomass and community structure.

Large numbers of appendicularian larvaceans were observed within the highly turbid water masses associated with the vent plume but were hardly ever observed at other depths. Almost every individual exhibited the same

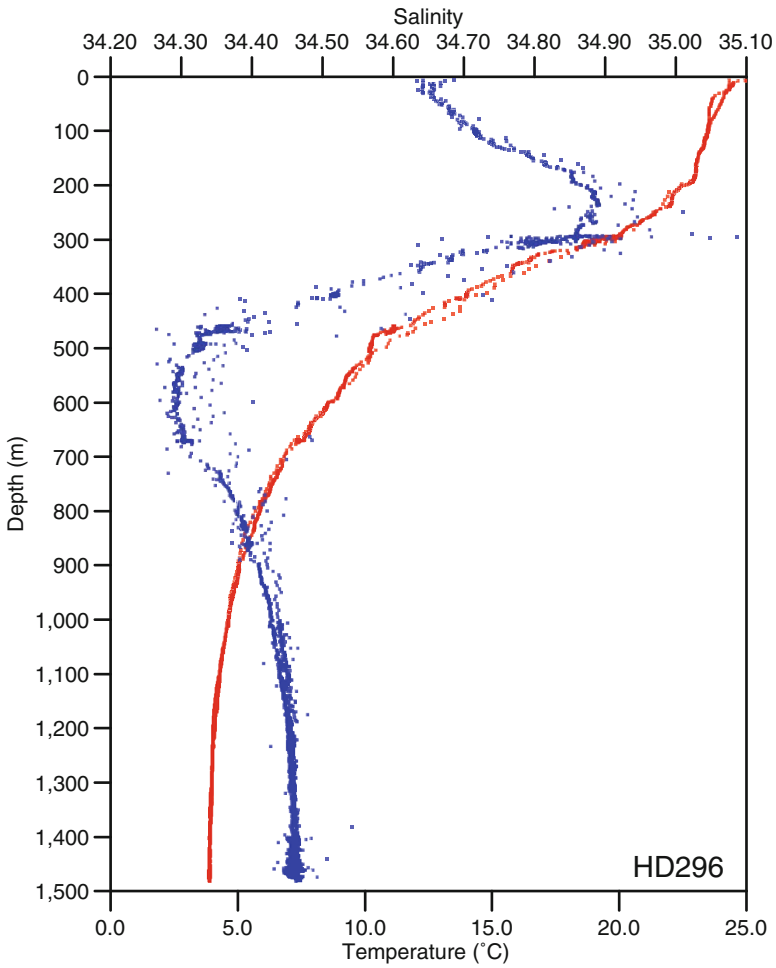

Fig. 51.1 Vertical profiles of temperature (*red*) and salinity (*blue*) vs depth during ROV *HyperDolphin* dive 296

morphology of their filtering houses and the rare behavioural trait of not discarding their house and escaping when caught in the currents produced by the thrusters of the ROV (personal observations). These animals were unable to be collected due to mechanical problems with the ROV, but the house morphology observed on the video record suggests that the vent plume-associated species belongs to the larvacean family Oikopleuridae. These animals could be expected to feed either on bacterial flocs or on the early larval stages of vent animals (see below).

Narcomedusae belonging to the genus *Solmissus* were common below 800 m right up to the vent plume boundary but were not observed in the highly turbid vent plume-affected water masses below 1,350 m. They also occurred, albeit rarely, at shallower depths. *Solmissus* is known to feed exclusively on gelatinous prey but whether this prey includes gelatinous appendicularian larvaceans is not known at this time.

The midwater fauna in the Okinawa Trough over the Hatoma Knoll differed considerably from that off the Sanriku Coast, in Sagami and Suruga Bays, and in the Japan Sea. Most of the siphonophores observed were calycophorans—a result mirroring that of another subtropical oligotrophic area: the south-western Indian Ocean (Lindsay et al. 2000). In particular, clausophyid species were relatively common. Lobate ctenophores belonging to the genera *Bathocyroe* and *Lampocteis* were also observed in relatively large numbers in the deeper layers. The gelatinous macroplankton observed at the site are listed in Table 51.2.

51.3.2 Macroplanktonic Predators Considered Capable of Preying on Vent Larvae

Chordata

Order Copelata

Three species of larvaceans were identified within and around the vent plume. The inner filters of larvacean houses differ in mesh size on a species-specific basis with some species of the genus *Oikopleura* able to feed on particles as

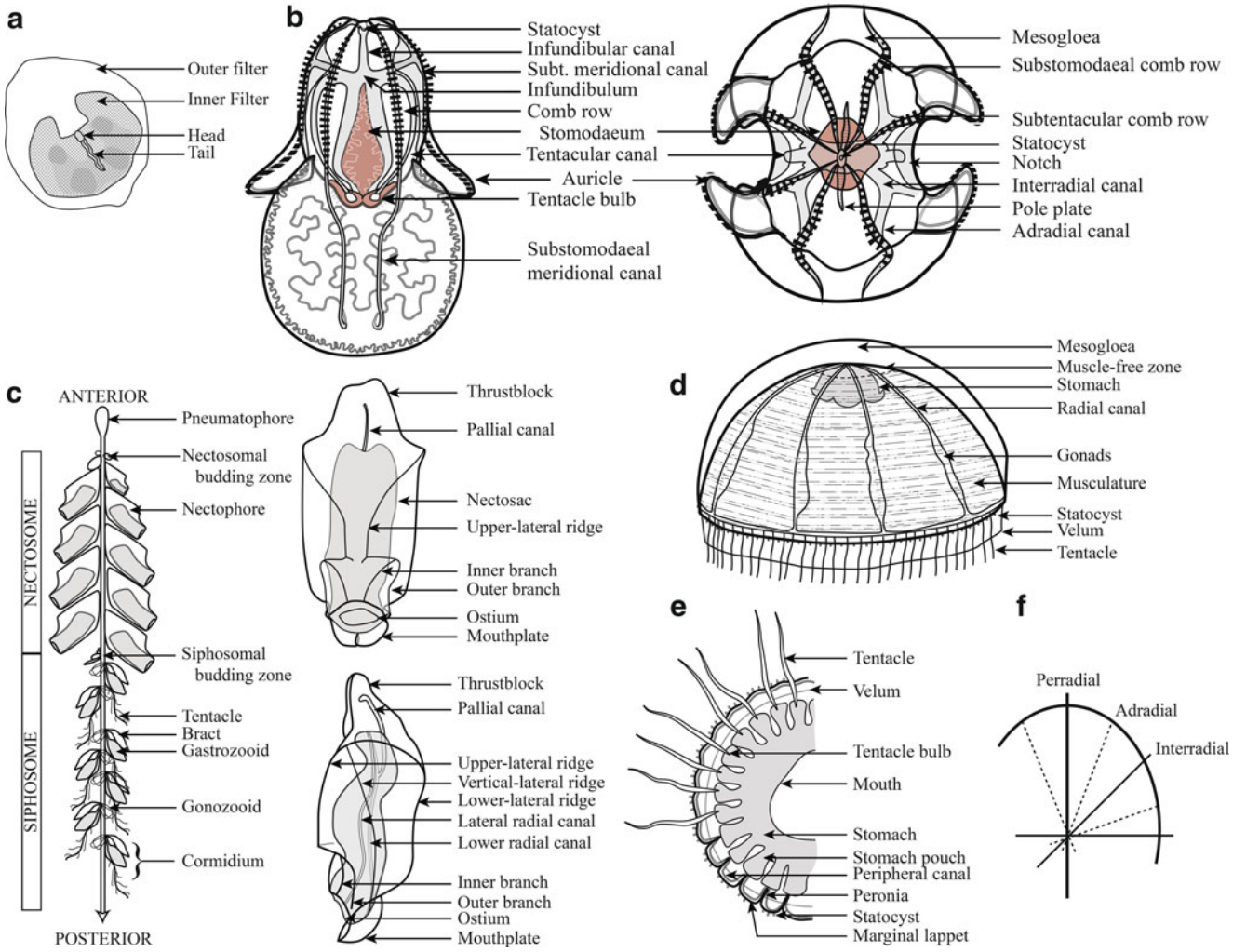

Fig. 51.2 Terminology for (**a**) larvacean appendicularians, (**b**) lobate ctenophores, (**c**) physonect siphonophores, (**d**) trachymedusae, (**e**) narcomedusae, and (**f**) the main axes of radially symmetrical animals

small as 13 μm (Bone 1998), presumably allowing them to feed on the newly-released larvae of some vent species.

Family Oikopleuridae Lohmann, 1915

Subfamily Oikopleurinae Lohmann, 1896

Genus *Oikopleura* Mertens, 1831

Oikopleura sp. A (Fig. 51.3)

This species was identified according to the morphology of its house by Dr. Russell Hopcroft as belonging to the genus *Oikopleura*, with affinities to *O. villafrancae* Fenaux, 1992 (personal communication).

The distribution and abundance of this larvacean species is overlaid on a map of plume-associated turbidity in Fig. 51.4. A direct correlation between turbidity and abundance of larvacean feeding filters was not observed. However, larvacean feeding filters of this morphotype were not observed at depths shallower than 1,400 m, where the physico-chemical signatures indicative of vent plume water were not evident. These larvaceans could conceivably be feeding directly on plume-associated bacterial flocs. However, the few values for bacterial cell density values obtained by Niskin bottle sampling did not show statistically significant correlations with oikopleurid abundances (Sunamura, personal communication). A method of mapping in situ bacterial abundances needs to be developed. If this oikopleurid species can be sampled in forthcoming surveys it is suggested that a PCR analysis of the gut contents as well as a stable isotope analysis of the musculature be attempted in order to determine whether bacteria, vent larvae, or some other organic matter source is being ingested and assimilated.

Subfamily Bathochordaeinae Lohmann, 1915

Genus *Mesochordaeus* Fenaux and Youngbluth, 1990

Mesochordaeus sp. A (Fig. 51.5)

House large, roughly ovoid, to 30 cm in length, almost five times the animal's tail length; inner filter lobed, almost filling external filter; pre-filter absent. This species was observed only at depths shallower than the hydrothermal

Table 51.2 Gelatinous macroplankton identified during the present study

Phylum	Class	Order	Family	Genus	Species	Figure ID	Video voucher filename[a]
Chordata	Appendicularia	Copelata	Oikopleuridae	*Oikopleura*	sp. A	Fig. 51.3	HD67-04215311to04243204-131345-Oikopleura_spA-Dhugal_Lindsay-OTAMABOYANONAKAMA.mov
				Mesochordaeus	sp.A	Fig. 51.5	HD296-02541610to02580712-113020-Mesochordeaeus_spA-Dhugal_Lindsay-OTAMABOYANONAKAMA.mov
				Bathochordaeus	sp.A	Fig. 51.6	HD296-02485503to02524609-112459-Bathochordaeus_spA-Dhugal_Lindsay-OTAMABOYANONAKAMA.mov
Ctenophora	Tentaculata	Lobata	Bathocyroidae	*Bathocyroe*	sp. A	Fig. 51.7	HD295-04323814to04324713-155506-Bathocyroe_spA-Dhugal_Lindsay-CHOUKURAGEMODOKINONAKAMA.mov
			Eurhamphaeidae	*Eurhamphaea*	*vexilligera*	Fig. 51.8a, b	HD294-00402524to00444700-182158-Eurhamphaea_vexilligera-Dhugal_Lindsay-AKADAMAKURAGE.mov
						Fig. 51.8c	HD294-07533005to07533710-013539-Eurhamphaea_vexilligera-Dhugal_Lindsay-AKADAMAKURAGE.mov
			Lampoctenidae	*Lampocteis*	sp. A	Fig. 51.9	HD294-03205911to03254229-210401-Lampocteis_spA-Dhugal_Lindsay-AKAKABUTOKURAGENONAKAMA.mov
			Incertae sedis	Gen.	sp. A	Fig. 51.10	HD294-03321425to03375614-211348-Llyriamodoki-Dhugal_Lindsay-KABUTOKURAGENONAKAMA.mov
		Thalassocalycida	Thalassocalycidae	*Thalassocalyce*	sp. A	Fig. 51.11	HD226-01324712to01350413-101304-Thalassocalyce_spA-Dhugal_Lindsay-KAMENKURAGENONAKAMA.mov
		Cestida	Cestidae	*Cestum*	*veneris*	Fig. 51.12	HD294-00401223to00402502-182133-Cestum_veneris-Dhugal_Lindsay-OBIKURAGE.mov
		Cydippida	Incertae sedis	Gen.	sp. A	Fig. 51.13	HD226-01260709to01273312-100625-Ctenocerosmodoki-Dhugal_Lindsay-KYOURYUUKURAGENONAKAMA.mov
				Gen.	sp. B	Fig. 51.14	HD294-01354502to01422014-191700-CydippidB-Dhugal_Lindsay-FUUSENKURAGENONAKAMA.mov
Cnidaria	Hydrozoa	Siphonophorae	Pyrostephidae	*Bargmannia*	*elongata*	Fig. 51.15	HD296SS2-01281313to01433201-100401-Bargmannia_elongata-Dhugal_Lindsay-NAGAHEBIKURAGE.mov
			Forskaliidae	*Forskalia*	*formosa*	Fig. 51.16	HD294-00222316to00224129-180337-Forskalia_formosa-Dhugal_Lindsay-TSUKUSHIKURAGE.mov
			Incertae sedis	*Marrus*	*orthocanna*	Fig. 51.17	HD226GS1-02573715to03043829-112821-Marrus_orthocanna-Dhugal_Lindsay-HINOOBIKURAGE.mov
				Marrus	sp. A	Fig. 51.18	HD296SS5-02300204to02342229-110605-Marrus_sp-Dhugal_Lindsay-HINOOBIKURAGENONAKAMA.mov

		Prayidae	*Rosacea*	*plicata*	Fig. 51.19	2K1183GS1-SH-08181828to08233308-110330-Rosacea_plicata-Dhugal_Lindsay-NIIAIOIKURAGE.mov
		Clausophyidae	*Kephyes*	sp.(spp.?)	Fig. 51.20	HD296-04380925to04391101-131431-Kephyes_sp-Dhugal_Lindsay-FUTATSUTAINOUKURAGENONAKAMA.mov
			Chuniphyes	*multidentata*	Fig. 51.21	HD67-03365720to03383315-122824-Chuniphyes_multidentata-Dhugal_Lindsay-JUUJITAINOUKURAGE.mov
	Anthoathecata	Bythotiaridae	*Protiaropsis*	*anonyma*	Fig. 51.22a–d	HD226-03255000to03303417-120633-Protiaropsis_anonyma-Dhugal_Lindsay-SUKKIRISUGURIKURAGE.mov
					Fig. 51.22e	2K1188SS3C-SH-08461707to08470016-114159-Protiaropsis_anonyma-Dhugal_Lindsay-SUKKIRISUGURIKURAGE.mov
	Trachymedusae	Halicreatidae	*Halicreas*	*minimum*	Fig. 51.23b	HD294-01575329to01583224-193928-Halicreas_minimum-Dhugal_Lindsay-TENGUKURAGE.mov
			Haliscera	*bigelowi*	Fig. 51.24	2K1188SS2-110000-DSCN0157-Haliscera_bigelowi-Dhugal_Lindsay-HARIUDEKURAGE.JPG
		Rhopalonematidae	*Pantachogon*	*haeckeli*	Fig. 51.25	2K1183SS1A-SH-08340600to08341905-111917-Pantachogon_haeckeli-Dhugal_Lindsay-FUKAMIKURAGE.mov
			Crossota	*millsae*	Fig. 51.26	HD296-04495813to04535803-132520-Crossota_millsae-Dhugal_Lindsay-KUROKURAGENONAKAMA.mov
	Narcomedusae	Cuninidae	*Solmissus*	*incisa*	Fig. 51.27a, b	HD294-02273801to02295812-200911-Solmissus_incisa_32T-Dhugal_Lindsay-KAPPAKURAGENONAKAMA.mov
					Fig. 51.27c, d	HD296-02082815to02113911-104432-Solmissus_incisa_23T-Dhugal_Lindsay-KAPPAKURAGENONAKAMA.mov
		Solmarisidae	*Solmaris*	sp. of Arai et al. 2000	Fig. 51.28	2K1188SS1B-SH-07542623to07543616-104957-Solmaris_sp_Araietal2000-Dhugal_Lindsay-NICHIRINKURAGENONAKAMA.mov
		Aeginidae	*Bathykorus*?	sp. A	Fig. 51.29	HD67-03550811to03570123-124631-Bathykorus?_sp A-Dhugal_Lindsay-HIJIGATATSUZUMIKURAGENONAKAMA.mov
Scyphozoa	Coronatae	Atollidae	*Atolla*	*wyvillei*	Fig. 51.30	2K1188SS2-SH-08101911to08143717-110550-Atolla_wyvillei-Dhugal_Lindsay-MURASAKIKAMURIKURAGE.mov
		Periphyllidae	*Periphylla*	*periphylla*	Fig. 51.31	2K1188SS1A-SH-07343718to07354800-103008-Periphylla_periphylla-Dhugal_Lindsay-KUROKAMURIKURAGE.mov

[a]The video voucher filename can be used to find the original video footage from the JAMSTEC archive

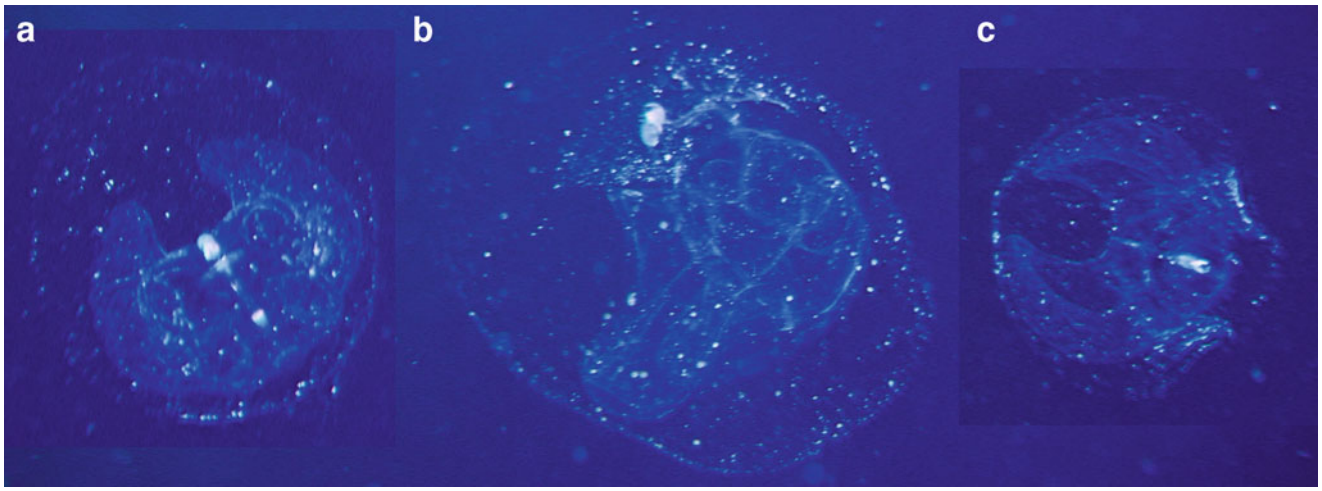

Fig. 51.3 (**a**) Front, (**b**) lateral, and (**c**) top views of the feeding filter "house" of the vent plume-associated larvacean observed at the Hatoma Knoll hydrothermal vent site, possibly *Oikopleura villafrancae*? (ID by Russ Hopcroft)

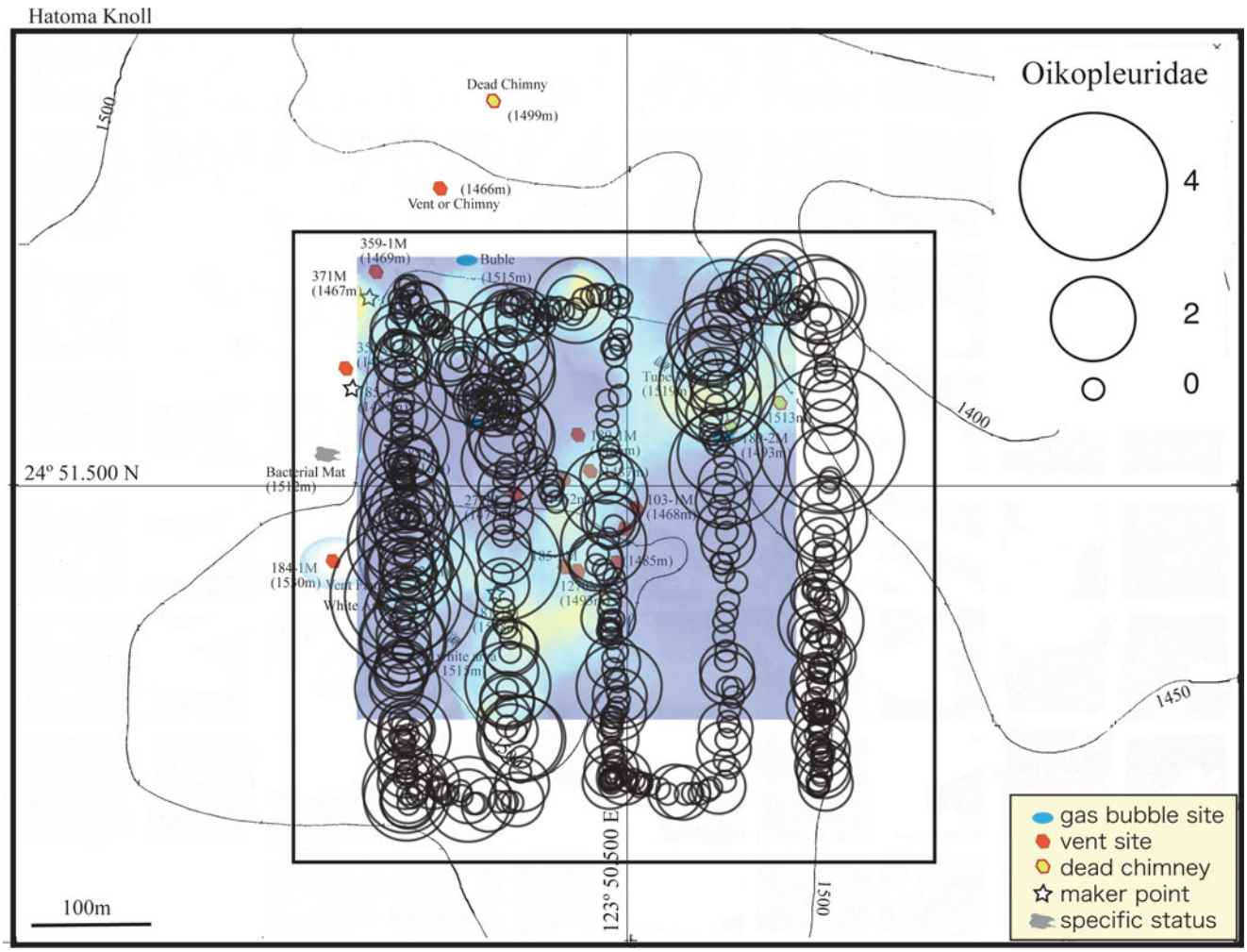

Fig. 51.4 Horizontal distribution of turbidity, a proxy for vent-derived plume water, in the 1,435 m depth layer (40 m altitude) over the Hatoma Knoll hydrothermal vent site in the Nansei Island chain during ROV *HyperDolphin* Dive HD295, April 2004. *Black circles* represent the number of oikopleurid larvacean tunicates observed per minute with the maximum abundance being 12 animals per minute. *Warm colours* indicate areas of highest turbidity

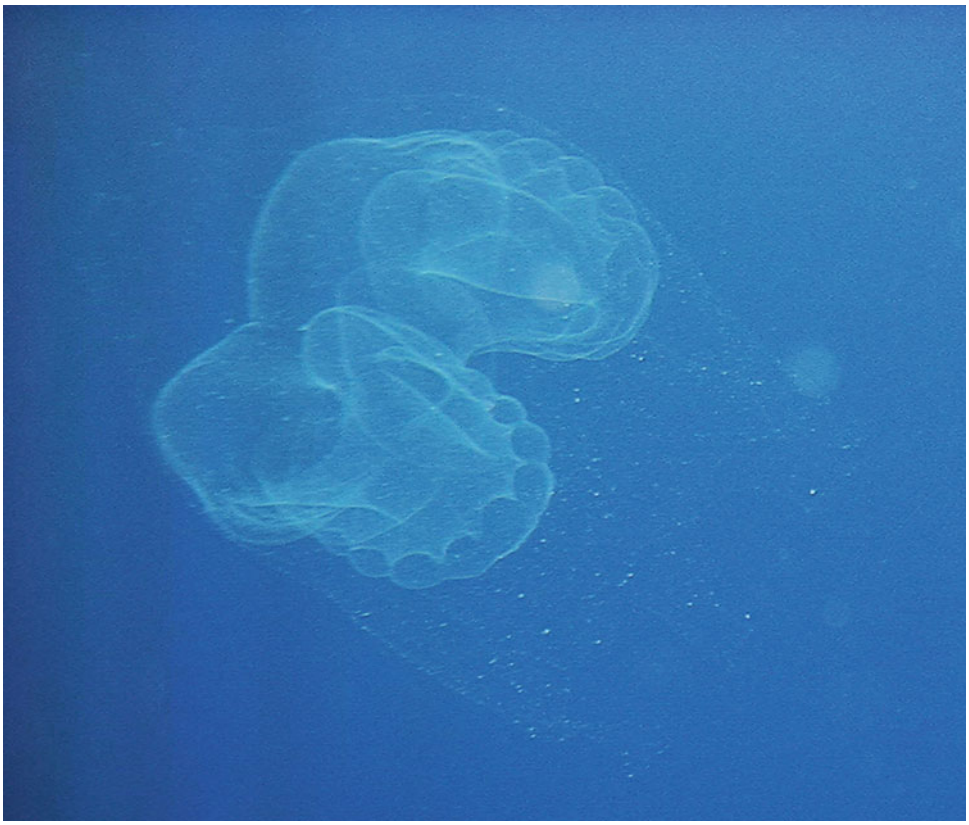

Fig. 51.5 *Mesochordaeus* sp. A observed at 851 m depth during ROV *HyperDolphin* dive 296

vent plume, such as 851 m for the figured animal observed during dive HD296.

Genus *Bathochordaeus* Chun, 1900

Bathochordaeus sp. A (Fig. 51.6)

House large, roughly ovoid, to 2 m length, almost eighty times the animal's tail length; inner filter much smaller than outer filter; pre-filter absent. This species was also only observed only at depths shallower than the hydrothermal vent plume such as 819 m for the figured animal observed during dive HD296. Two species are currently described in this genus.

Ctenophora

Order Lobata Agassiz, 1860

Lobate ctenophores feed by trapping particles on their oral lobes using mucous or sticky colloblast cells, allowing them to feed on a wide range of particle sizes, including extremely small particles such as, presumably, newly-released vent animal larvae.

Family Bathocyroidae Madin and Harbison, 1982

Genus *Bathocyroe* Madin and Harbison, 1982

Bathocyroe sp. A (Fig. 51.7)

Body with a pair of muscular, bowl-like lobes at oral end, body surface smooth, slightly compressed in tentacular plane; with tentacle bulbs positioned near aboral end of stomodaeum, within tentacle sheaths; stomodaeum often darkly pigmented; with four large, elongate, ciliated auricles, positioned well aboral of the mouth; four interradial canals arising from infundibular canal and supplying adradial canals, which connect to meridional canals at their aboral ends; paragastric canals present, with diverticula, branching at mouth before running towards distalmost edge of oral lobes; subtentacular meridional canals united orally to branches of paragastric canals at distalmost edge of oral lobes; substomodaeal meridional canals looping within lobes, connecting orally to adjacent subtentacular meridional canals at distalmost margin of oral lobes.

Comments: At least some species of *Bathocyroe* are capable of vigorous swimming by flapping their oral lobes together in a frogkick motion. The original description of *B. fosteri* Madin and Harbison, 1978 is misleading as to the position of the auricles relative to the stomach, appearing as if they start at the level of the mouth in Fig. 1 (Madin and Harbison 1978a), which they do not. It also states that the subtentacular meridional canals in each oral lobe are connected with each other at the distalmost edge of the oral lobe but the present authors believe a groove may have been mistaken for a canal in the original description as none of the other two described *Bathocyroe* species (*B. paragaster* (Ralph and Kaberry, 1950) and *B. longigula* Horita et al., 2011) or three undescribed species show this character (personal observation). The *Bathocyroe* species observed at the Hatoma Knoll seems most similar

Fig. 51.6 *Bathochordaeus* sp. A observed at 819 m depth during ROV *HyperDolphin* dive 296

Fig. 51.7 *Bathocyroe* sp. A observed at 1,400 m depth during ROV *HyperDolphin* dive 295

morphologically to *B. fosteri*. *Bathocyroe* species have been observed floating with their oral lobes upwards and cupped in a generally conical morphology reminiscent of a sediment trap (personal observations). Such an attitude would be conducive to the collection of sinking marine snow and its associated fauna, as well as to benthic larvae entering the settlement phase.

Family Eurhamphaeidae L. Agassiz, 1860

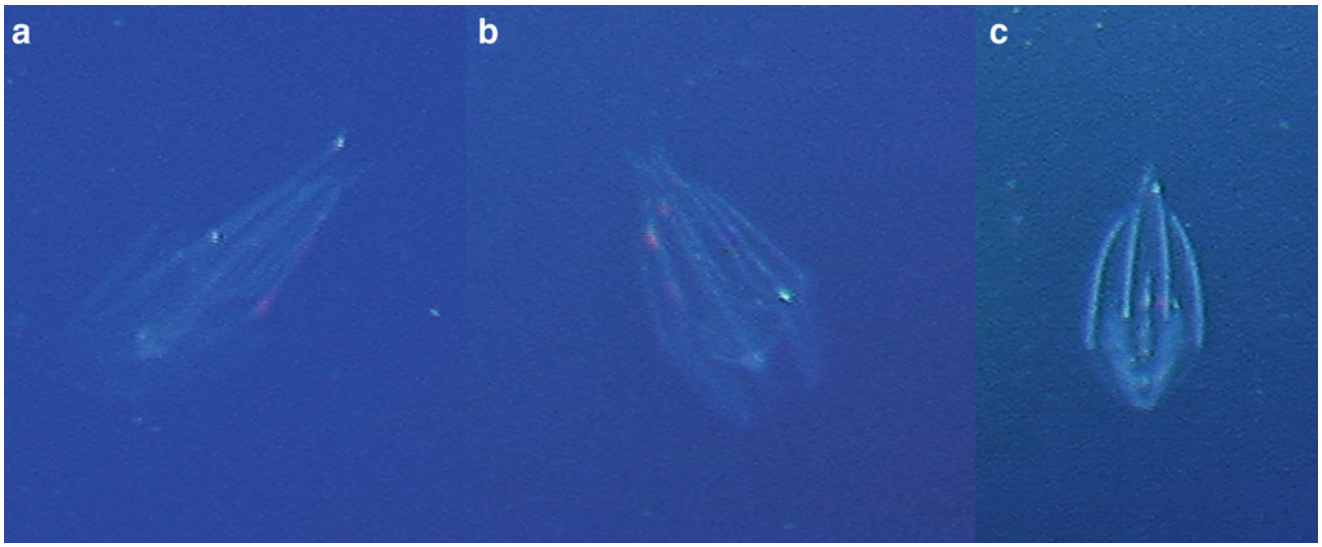

Fig. 51.8 *Eurhamphaea vexilligera* in the (**a**) tentacular and (**b**) stomodaeal planes, with partially opened lobes, observed at 300 m depth during ROV *HyperDolphin* dive 294, and (**c**) in the stomodaeal plane, with closed lobes, observed at 40 m depth during the same dive

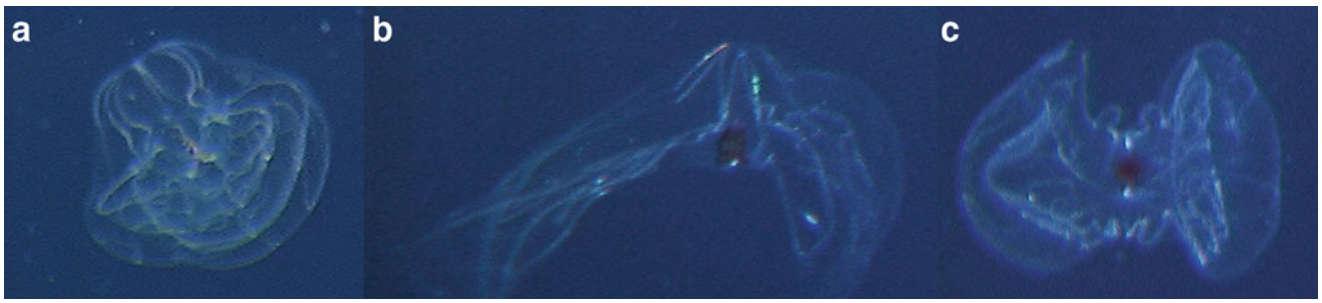

Fig. 51.9 *Lampocteis* sp. A in the (**a**) tentacular, and (**b**) stomodaeal planes, and (**c**) viewed orally, observed at 1,189 m depth during ROV *HyperDolphin* dive 294

Genus *Eurhamphaea* Gegenbaur, 1856

Eurhamphaea vexilligera Gegenbaur, 1856 (Fig. 51.8)

Body with a pair of muscular, bowl-like lobes at oral end, body surface smooth, highly compressed in tentacular plane; auriculo-tentacular sides extended into two subconical processes at aboral end, each with a long filamentous "tail", subtentacular comb rows extending to tips of these aboral processes; substomodaeal comb rows reaching level of bases of aboral processes; small red vesicles, also present in its cydippid larva, interspersed between ctenes of comb rows, extending onto oral lobes along the substomodaeal meridional canals; with four short, broad, ciliated auricles; with small, inconspicuous, unsheathed tentacles, with tentilla, between the lobes; four interradial canals arising from infundibulum, branching into eight adradial canals; substomodaeal adradial canal supplying substomodaeal meridional canal at aboral end of substomodaeal comb row; subtentacular adradial canal supplying subtentacular meridional canal partway along subtentacular comb row slightly aboral of level of deeply sunken statocyst; paragastric canal present.

Comments: vesicles release reddish-brown, luminescent ink when disturbed. Only observed shallower than 300 m depth during the present study.

Family Lampoctenidae Harbison, Matsumoto and Robison, 2001

Genus *Lampocteis* Harbison, Matsumoto and Robison, 2001

Lampocteis sp. A (Fig. 51.9)

Body with a pair of bowl-like lobes at oral end, body surface smooth, slightly compressed in tentacular plane; without deep notch at level of infundibulum between adjacent subtentacular comb rows?; with four short, wide, ciliated auricles, arising from subtentacular comb rows at level of aboral end of stomodaeum; stomodaeum large, strongly pigmented; with small, inconspicuous, unsheathed tentacles between lobes at level of mouth; paragastric canals large, with blindly-ending diverticula; four interradial canals

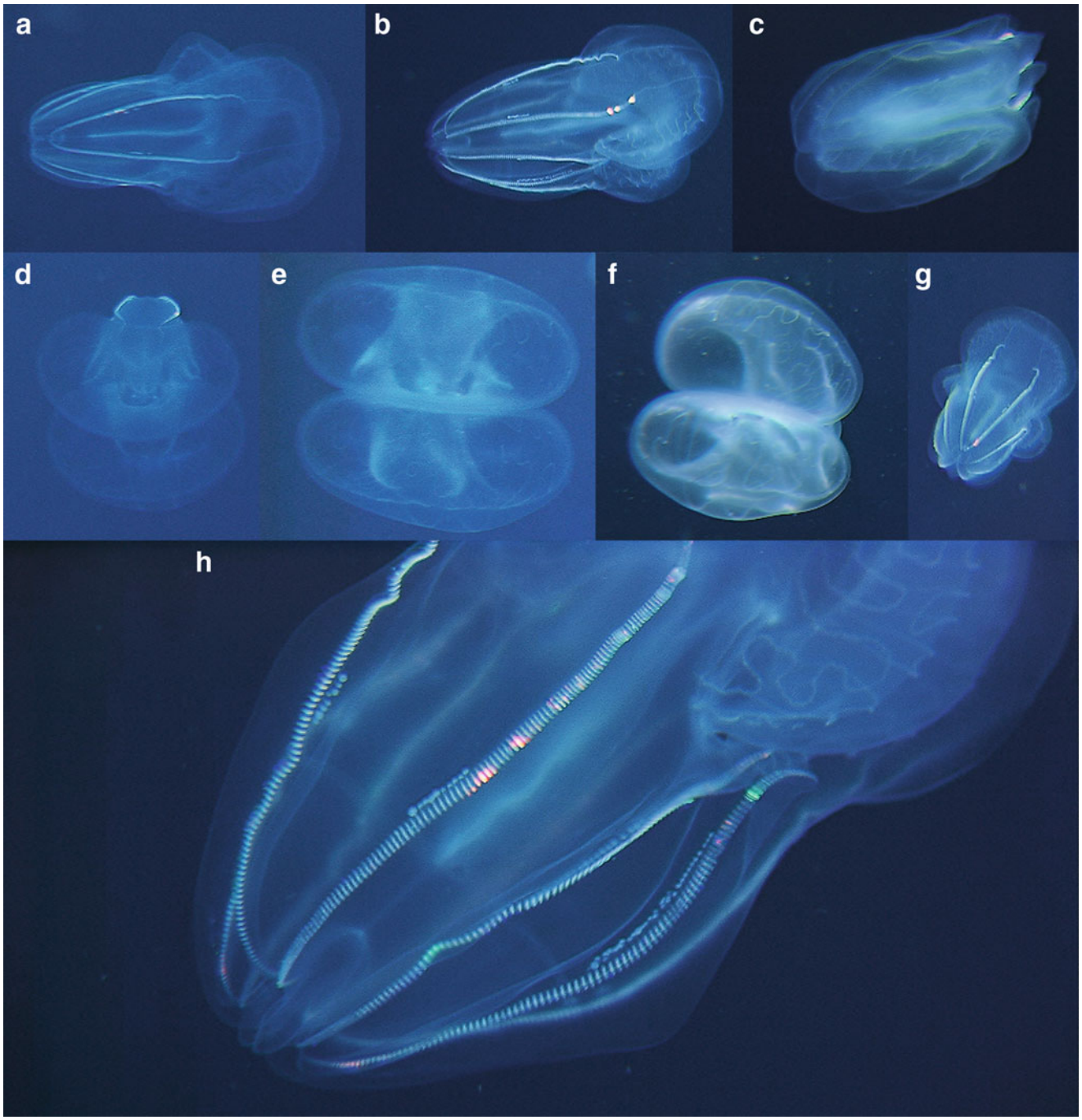

Fig. 51.10 *Lobata* sp. A in the (**a**) tentacular, (**b**) quasi-tentacular, (**c**) oral-stomodaeal, (**d**) oral-tentacular, (**e**) and (**f**) oral, and (**g**) aboral-tentacular planes, with a close-up of the aboral region (**h**) showing the configuration of the adradial canals supplying the meridional canals and auricular stubs. The figured animal was observed at 1,240 m depth during ROV *HyperDolphin* dive 294

arising from funnel and supplying the adradial canals; meridional canals end blindly aborally.

Comments: Apart from the absence of the deep notch at the level of the infundibulum, this species fits perfectly the generic diagnosis of *Lampocteis*. The present authors believe that the diagnosis for the genus *Lampocteis* should be emended by the deletion of this character. The present species seems much softer in consistency than its congener *Lampocteis cruentiventer* Harbison, Matsumoto and Robison, 2001, and is similarly unable to swim using its oral lobes.

Family incertae sedis

Lobata sp. A (Fig. 51.10)

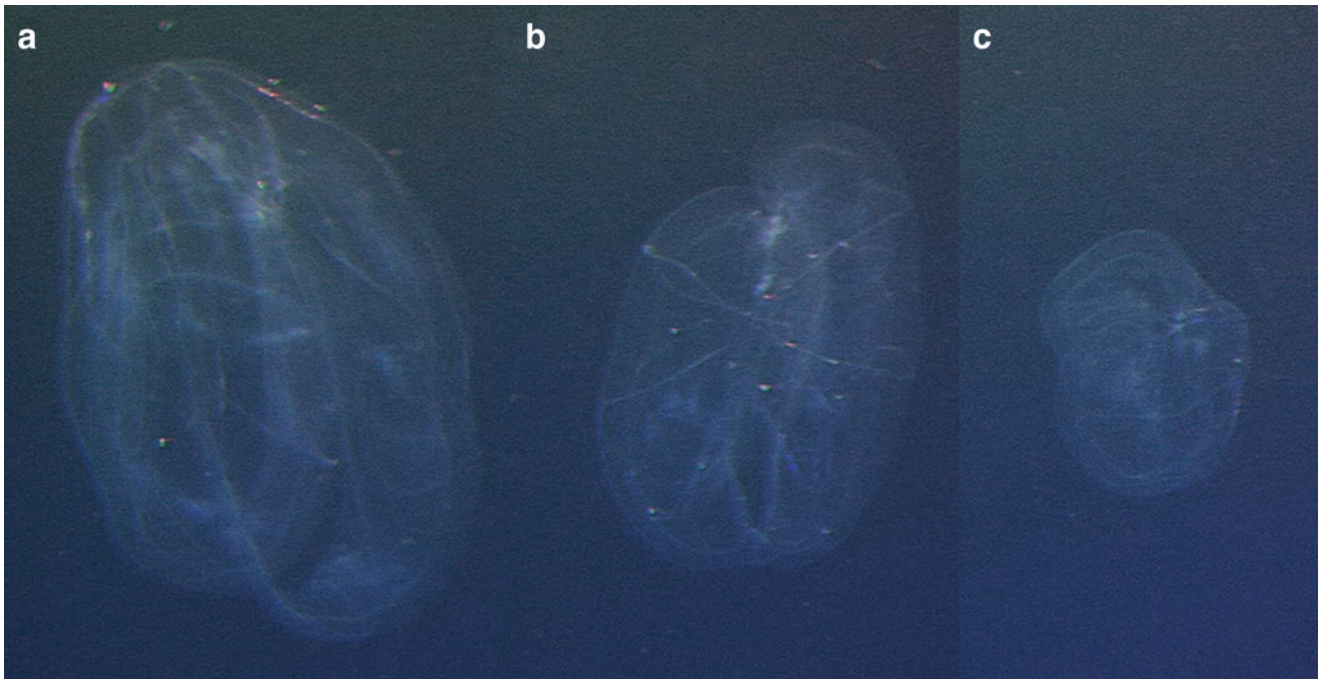

Fig. 51.11 *Thalassocalyce* sp. A in the (**a**) quasi-tentacular, (**b**) aboral, and (**c**) in its medusoid configuration in the quasi-tentacular plane. The figured animal was observed at 895 m depth during ROV *HyperDolphin* dive 226

Body with a pair of muscular, bowl-like lobes at oral end, body surface smooth, slightly compressed in tentacular plane; gelatinous ridges between adjacent comb rows, becoming more pronounced towards aboral end; deeply sunken statocyst, approximately at midpoint between top of stomodaeum and aboral end of gelatinous ridges; without auricles, instead subtentacular comb rows end on stubby protrusions near mouth; with small, inconspicuous tentacle bulbs between the lobes flanking the mouth; stomodaeum long, two-thirds length of substomodaeal comb rows, transparent; infundibular canal short; four interradial canals arising from funnel and supplying the adradial canals; meridional canals end blindly aborally.

Comments: The configuration of the adradial canals supplying the meridional canals partway along their length is the same canal structure as that observed in the Lampoctenidae Harbison et al., 2001, and Lobatolampeidae Horita, 2000. The lack of auricles and the transparent stomodaeum both serve to distinguish it from the Lampoctenidae, while the well-developed lobes, lack of cilia near the distal ends of the subtentacular comb rows, and the substomodaeal comb rows not ending blindly, all serve to distinguish it from the Lobatolampeidae. It seems as if a new family and genus will have to be erected to contain the present species. As in the Lampoctenidae, the lobes are often pursed together when feeding.

Order Thalassocalycida Madin and Harbison, 1978

Family Thalassocalycidae Madin and Harbison, 1978

Genus *Thalassocalyce* Madin and Harbison, 1978

Thalassocalyce sp. A (Fig. 51.11)

Body medusa-like, slightly oval in cross-section with longer axis in tentacular plane, with central conical peduncle bearing gut, mouth and tentacles, lobes and auricles absent; comb rows short; tentacle bulbs situated on sides of central peduncle, halfway down stomodaeum, tentacles with tentilla, without tentacle sheaths; gut wide, flat; mouth slit-like, in stomodaeal plane; medusoid body covered with extensively looping canals arising from meridional canals.

Thalassocalyce inconstans Madin and Harbison, 1978 also has the following feautures: comb rows 25–33 % of total oral-aboral distance, all equal length, around 23 ctene plates each. Statocyst slightly sunken below aboral surface; pole plate extends about halfway to comb rows in stomodaeal plane; paragastric canals run down along flat sides of stomodaeum, turn outward and end blindly at level of mouth. Gut somewhat constricted in center, with upper half expanded into digestive region. Funnel canal broad, extending from digestive region to statocyst. Meridional canals running beneath comb rows end blindly aborally. Two perradial canals arise from gut in tentacular plane, thereafter branching into interradial canals; a tentacular canal branches from one of the two interradial canals in each half of the animal and descends to supply tentacle bulbs; each interradial canal branches into two adradial canals, one adradial canal supplies the substomodaeal

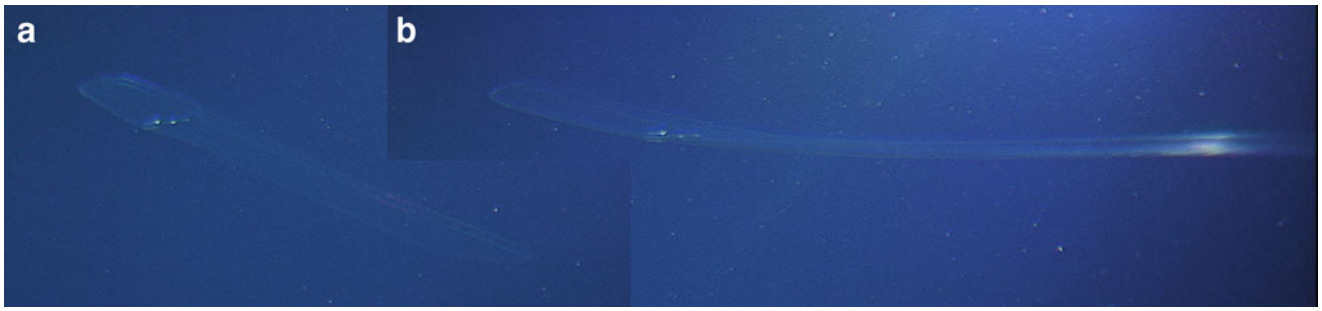

Fig. 51.12 *Cestum veneris* in the (**a**) quasi-tentacular plane, and (**b**) oral view. The figured animal was observed at 299 m depth during ROV *HyperDolphin* dive 294

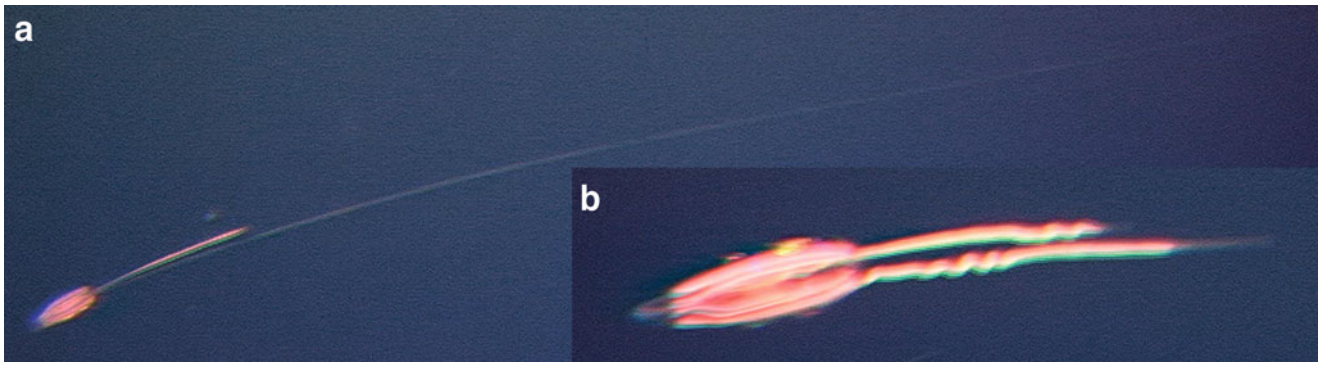

Fig. 51.13 Cydippida sp. A with (**a**) tentacles extended, and (**b**) tentacles partially retracted. The figured animal was observed at 856 m depth during ROV *HyperDolphin* dive 226

meridional canal directly at the oralmost end of the comb row, the other adradial canal (subtentacular) branches off a long, looping canal that runs along the periphery of the bell-like body for one quarter of its circumference before looping back to supply oral end of substomodaeal comb rows at the junction with the other adradial canal; subtentacular adradial canals run straight down to edge of bell before looping back to supply subtentacular comb rows at their oralmost ends; subtentacular canals contain numerous large spherical ova in their descending limbs.

Comments: The form observed at the Hatoma Knoll vent site seemed to be much larger than the maximum size of 15 cm in diameter reported for *T. inconstans* (Madin and Harbison 1978b). Gonads were developed and easily visible in the video record. Although several individuals of *T. inconstans* described by Madin and Harbison (1978b) also had developed gonads at a diameter of only 5 cm, it is possible that the form we observed was just a vastly more mature and developed stage of this species. It is also possible that it could be a larger, undescribed species, so we have refrained from giving a specific epithet for the animals we observed at the Hatoma Knoll until pristine specimens can be sampled, morphological comparisons made, and a molecular analysis undertaken.

Order Cestida Gegenbaur, 1856
Family Cestidae Gegenbaur, 1856
Genus *Cestum* Gegenbaur, 1856
Cestum veneris Lesueur, 1813 (Fig. 51.12)

Body elongate, flattened in tentacular axis, to 1.5 m length, usually <0.8 m; with tentacles arising from deep sheaths, extending along entire oral margin of body, with fine tentilla; substomodaeal comb rows greatly elongated; subtentacular comb rows rudimentary; no lobes or auricles; four interradial canals arising from funnel and supplying adradial canals, subtentacular meridional canals curving upward/orally after supplying the rudimentary comb rows then curve outwards, running along midline of animal to its extreme ends and joining the substomodaeal meridional canals and oral forks of the paragastric canals; gonads continuous under substomodaeal meridional canals.

Comments: body often with yellow or brown pigment spots; escapes by graceful rapid undulating of the body; has a mertensid-like "cydippid" larval stage.

Order Cydippida Lesson, 1843
Family incertae sedis
Cydippida sp. A (Fig. 51.13)

Body elongate, teardrop-shaped with rounded aboral end, compressed slightly in tentacular plane, with grooves

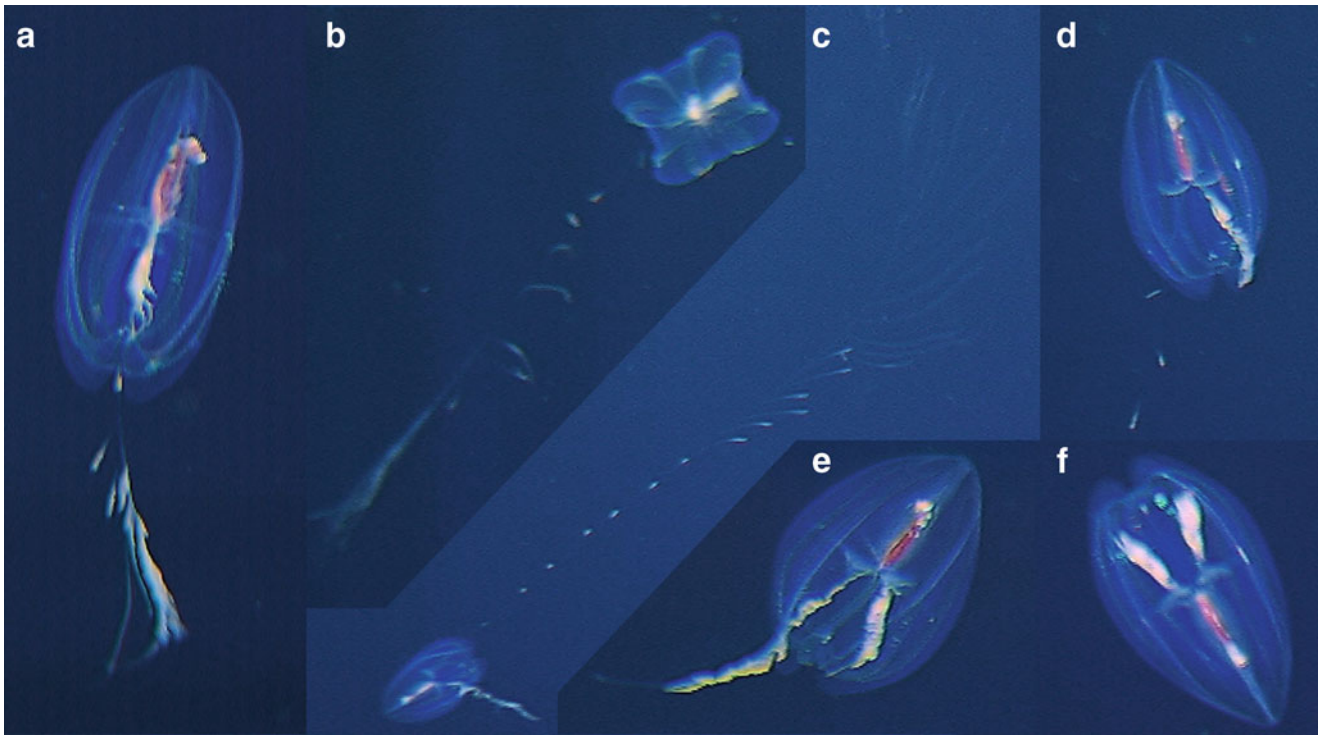

Fig. 51.14 Cydippida sp. B in the (**a**) stomodaeal plane, (**b**) viewed aborally, (**c**) with tentacles extended, (**d**) with one tentacle retracted, (**e**) with both tentacles almost retracted, and (**f**) in the tentacular plane. The figured animal was observed at 534 m depth during ROV *HyperDolphin* dive 294

between comb rows; oral end with four horns/keels, each extending out from between subtentacular and substomodaeal comb rows; comb rows of similar lengths, extending to around two-thirds of body length; meridional canals sink into the mesoglea at oral ends of comb rows and extend to bases of oral horns; stomodaeum large, 70 % of body length; tentacles with tentilla, yellowish, in sheaths, exiting from mid-point of body within deep grooves that extend from the oral to aboral ends of the comb rows; tentacle bulbs parallel, lying close to stomodaeum and extending past its aboral end and the aboral end of the infundibulum, two-fifths to four-ninths of body length, yellow-orange in colour.

Comments: A species resembling the present species has been referred to in several publications as "Ctenoceros" (e.g. Johnsen 2005; Lindsay and Hunt 2005). Individuals observed at the Hatoma Knoll all had orange coloration to the body and meridional canals. Usually they were observed with one tentacle fully extended and the other partially retracted. A new family will need to be erected to contain this undescribed genus and species.

Cydippida B (Fig. 51.14)

Body teardrop-shaped, aboral end with four keels between subtentacular and substomodaeal comb rows, body square in cross-section, with wide grooves between subtentacular comb rows, ridges between subtentacular and substomodaeal comb rows, oral end conical, bluntly tapering; comb rows of similar lengths, covering almost entire body, extending/bending orally over aboral end towards statocyst; stomodaeum large, 50 % of body length; tentacles with filamentous tentillae, whitish, in sheaths exiting from aboral end of body; tentacle bulbs boomerang-shaped, at midpoint of body, flanking infundibulum, perpendicular to oral-aboral axis, one fourth body width in length, whitish.

Comments: Without information on the branching pattern of the interradial and adradial canals it is impossible to tell to which group of the polyphyletic "Cydippida" this species belongs. Tentacle bulbs angled parallel to the oral-aboral axis do not exist in any of the currently described species and we have therefore treated it here as a new genus and species. The stomodaeum may be pigmented along at least half of its length but the video resolution was not high enough to determine if the colour was from an ingested prey item or in the walls of the stomodaeum itself. This species closely resembles the animal on the back cover of Kovacs and Madin (1996).

Phylum Cnidaria

Order Siphonophorae Eschscholtz, 1829

Suborder Physonectae Haeckel, 1888

Family Pyrostephidae Moser, 1925

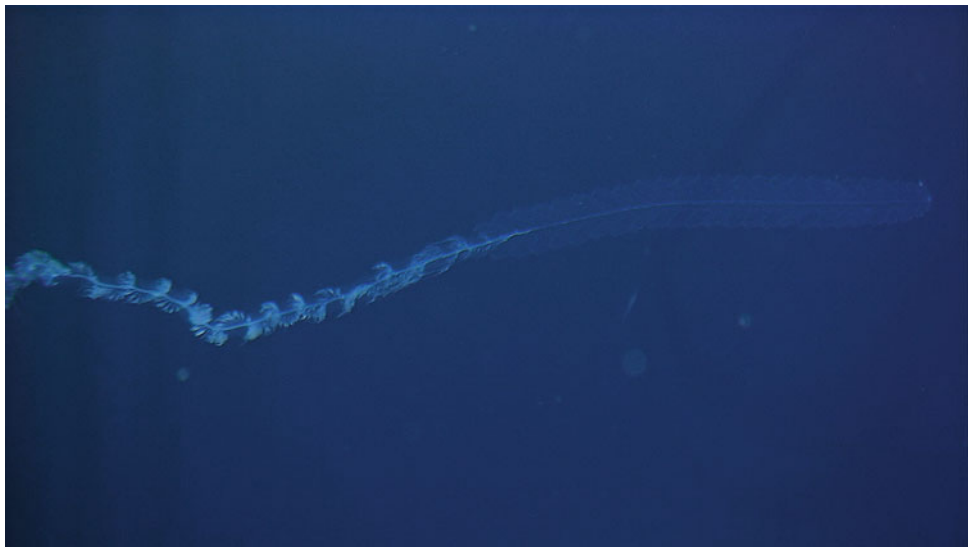

Fig. 51.15 *Bargmannia elongata* captured at 468 m depth during ROV *HyperDolphin* dive 296

Genus *Bargmannia* Totton, 1954

Bargmannia elongata Totton, 1954 (Fig. 51.15)

Pneumatophore: without apical pore.

Nectosome: easily up to 20 pairs of nectophores, insterted on the dorsal side of the stem. Nectophores elongate with a large, triangular thrustblock and mesogleal plug, axial wings vestigial. Nectophore with upper-lateral, lower-lateral, and vertical lateral (meso-lateral) ridges, but no lateral ridge. Upper-lateral ridge extending distally over upper surface of nectophore, passing first diagonally towards upper midline, giving off short ridge, turning abruptly outwards, and then subdividing into inner and outer upper-lateral ridges at 3/10 nectophore length (from ostium); short ridge passing downwards towards upper midline. Outer upper-lateral ridge reaching ostium and without extra branch directed proximally. Mouthplate divided. Nectosac basically cylindrical, with hemispherical muscle-free zone on proximal part. Lateral radial canals straight, arising from the upper radial canal and not forming a junction with the pedicular canal. Upper and lower radial canals straight. Descending branch of pedicular canal absent.

Siphosome: diffuse, with siphosomal tentacles. Devoid of fully-formed dactylozooids. Colonies single-sexed (dioecious). Each cormidium with simple tentacle-like structure attached to stem midway between successive gastrozooids; with single gonodendron; with four bud-like structures (? vestigial dactylozooids) with sexually dimorphic arrangement. Second tentacle and fifth bud occasionally present proximal to a gastrozooid. The full zooid complement of one cormidium comprises one gastrozooid, one siphosomal tentacle (as tentaculozooid), one gonodendron (as gonozooid, either male or female), two gastrozooid-associated bracts, two left lateral bracts, and two right lateral bracts. Tentilla without basal involucrum, straight to slightly twisted cnidoband with large nematocysts, probably stenoteles, and two types of smaller nematocysts, single long terminal filament. Bracts delicate and foliaceous, rounded distally, with patches of ectodermal cells on the upper surface, especially distally, with no semicircular ridge, with or without pair of lateral cusps at midbract.

Comments: An entire individual (HD296SS2), that figured, was captured at 468 m depth during ROV *HyperDolphin* dive 296.

Type Material: Holotype collected in shallow waters at Discovery II station 699 (14.45°N 30.04°W, 0–370 m), west of the Cape Verde islands, in tropical waters. Brit. Mus. (Nat. Hist.) Register No. 1952. 11. 19. 7–25.

Family Forskaliidae Haeckel, 1888

Genus *Forskalia* Kölliker, 1853

Forskalia formosa Keferstein and Ehlers, 1860 (Fig. 51.16)

Nectophores flattened in lateral plane, with large, pointed left axial wing; and shallow, but broad and rounded right wing. Small apical incision between them. Small lateral, but no baso-lateral pockets. No rete mirabile. No sulphur-yellow pigment spot on upper side of ostium of the nectophore. Nectosac extends to just over 40 % nectophore length, radial canals straight. Gastrozooids borne on long peduncles covered with bracts. Four types of adult bract (stem, bolster and two types of knee-shaped); knee-shaped ones without side branch to canal. Gonodendra with female gonophores, in two bunches, attached close to bases of palpacle-bearing gonopalpons; male gonophores borne on long stalk.

Comments: Colonies rotate while swimming. Cylindrical nectosome tapers apically and is narrower than siphosome, which is about three times longer than nectosome in mature, undamaged specimens and also tapered. Pneumatophore not nested within nectophores, clearly extended. Siphosomal stem spiralled, with gastrozooids arranged in four rows. Stomach bases and cnidobands of tentilla orange–red.

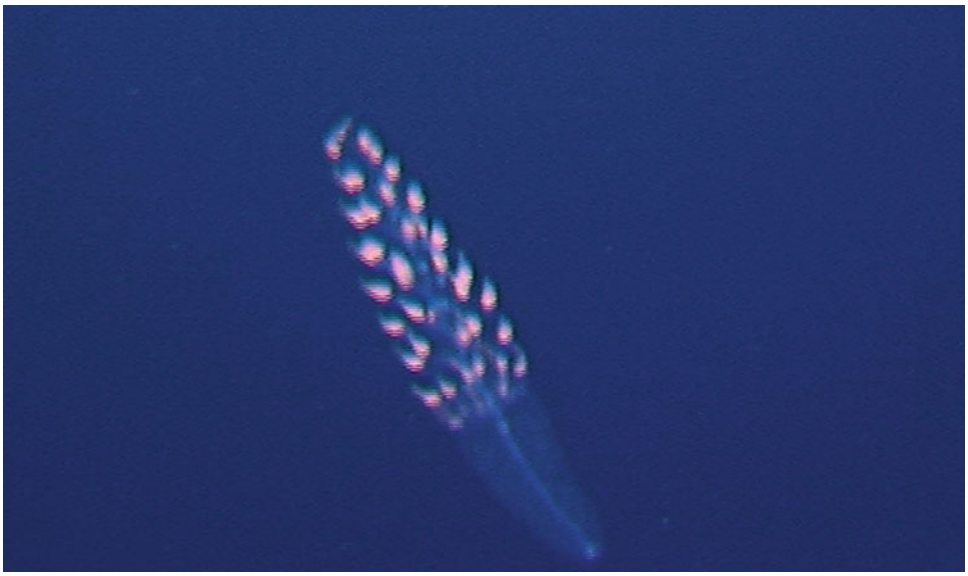

Fig. 51.16 *Forskalia formosa* individual observed at 241 m depth during ROV *HyperDolphin* dive 294

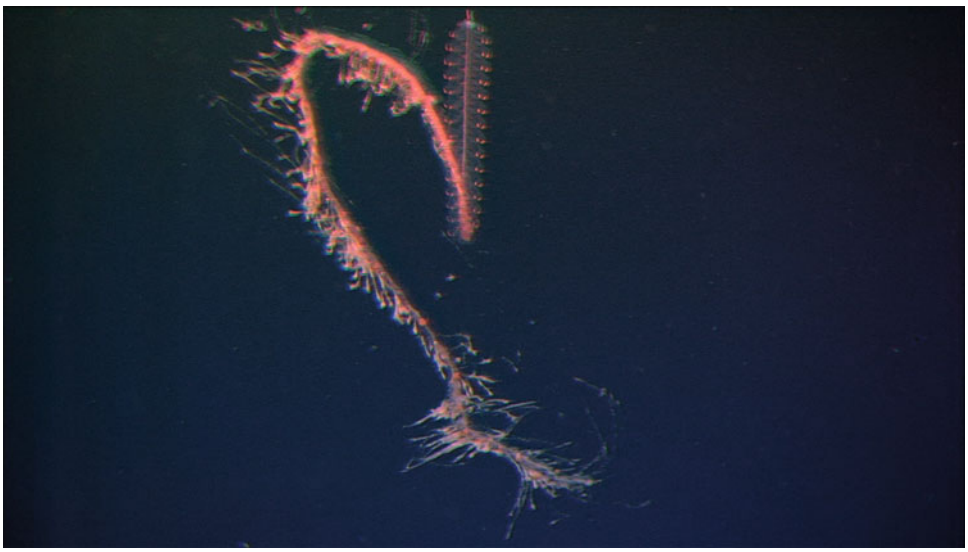

Fig. 51.17 *Marrus orthocanna* individual captured at 1,330 m depth during ROV *HyperDolphin* dive 226

Type Material: Holotype collected from Messina in the Mediterranean Sea in winter 1859–1860 (38.1833N; 15.55E). Paratype collected during Johnson Sea-Link I dive 2943 (position: 35.76N, 3.225W, depth: 590 m, date: 14 April 1991), curated at Natural History Museum, London (reg. no. BMNH 2001.6916).

Family incertae sedis

Marrus orthocanna (Kramp, 1942) (Fig. 51.17)

Nectosome: Nectophores inserted on the dorsal side of the stem, each up to 15 mm high, with a lateral furrow at one-third the nectophore height, with truncate axial wings, broad thrust block and large mesogloeal plug. Upper-lateral ridges bifurcate distally, with bifurcation of nectophoral upper-lateral ridges at same level or proximal to the lateral furrow. No vertical-lateral or lateral ridges. Nectosac with a proximal muscle-free zone. All radial canals of nectosac straight and pigmented deep orange-scarlet. Descending branch of pallial canal absent.

Siphosome: stem pigmented deep orange-scarlet. Distal facet of bracts divided, with median ridge covered in line of nematocysts, bracteal canal divides at distal end into two longitudinal branches that are also overlain with nematocysts. Unicornuate tentacles with no involucrum and straight to loosely-coiled cnidoband. With both male and female gonophores (monoecious), with female gonophores containing a single egg. No palpons on gonodendra or anywhere else.

Comments: An entire individual (HD226GS1) was captured at 1,330 m depth during ROV *HyperDolphin* dive 226.

Type Material: Holotype caught in Baffin Bay (67.7N 60.517W) at *Godthaab* Station 162b in 1928.

Marrus sp. A (Fig. 51.18)

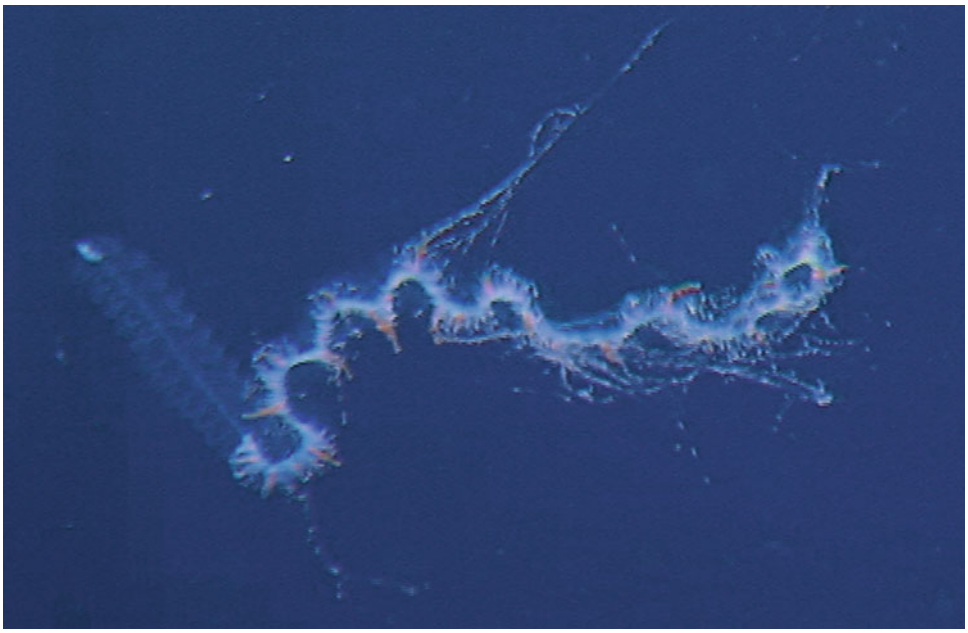

Fig. 51.18 *Marrus* sp. A individual captured at 668 m depth during ROV HyperDolphin dive 296

Nectosome: Nectophores inserted on the dorsal side of the stem; nectosac with a proximal muscle-free zone; radial canals of nectosac all straight. Descending pallial canal absent.

Siphosome: stem white, gastrozooids orange with white mouths; bracts of *Marrus*-type.

Comments: An individual (HD296SS5) was captured at 668 m depth during ROV *HyperDolphin* dive 296, but the specimen was too damaged to determine more than that it was an undescribed species assignable to the genus *Marrus* as it is now defined.

Suborder Calycophorae Leuckart, 1854

Family Prayidae Kölliker, 1853

Subfamily Prayinae Chun, 1897

Genus *Rosacea* Quoy and Gaimard, 1827

Rosacea plicata Bigelow, 1911 (Fig. 51.19)

Polygastric stage—two nectophores. N1 nectophore: up to 24 mm high, rounded and oblong, hydroecium elongate, deep, with a lower sill, ascending surface diverticulum with no anterior swelling and lying close to hydroecial wall, descending surface diverticulum present, nectosac small, lateral radial canals with complex sigmoid shape. N2 nectophore: up to 29 mm high, rounded and oblong, resembling N1, but hydroecium shorter and narrower, with a lower sill, and containing the first cormidia.

Sexual stage—Bract: up to 11 mm wide, smooth, rounded, with three non-apposing lobes (lateral, anterior hydroecial, and posterior hydroecial with a flap on inner surface), six bracteal canals (lateral, anterior and posterior longitudinal canals running parallel to stem, anterior hydroecial, posterior hydroecial, upper) without terminal swellings but with blind branches, anterior hydroecial canal approximately twice length of posterior hydroecial canal, central organ positioned at base of lateral bracteal canal, upper bracteal canal branching from posterior hydroecial canal, distal to posterior longitudinal canal, and reaching upper bracteal margin. Gonophore: with prominent apico-lateral keel, two asymmetric mantle canals, nectosac two-thirds of gonophore height with rounded apex, radial canals straight.

Comments: An individual (2K1183GS1) was sampled at 675 m depth during *Shinkai 2000* dive 1183.

Type Material: Lectotype collected from Bay of Biscay (47.05N, 7.917W) by the H.M.S. *Research* on 25 July 1900 and kept at the Natural History Museum, London, under registration number BMNH1939.6.10.1.

Family Clausophyidae Totton, 1965

Subfamily Kephyinae Mapstone, 2009

Genus *Kephyes* Pugh, 2006 (Fig. 51.20)

Kephyes sp. (spp.?)

Kephyes ovata (Keferstein and Ehlers, 1860).

Polygastric stage: Calycophoran siphonophore with two dissimilar nectophores, with anterior nectophore partially apposed to and partially linearly adjoined to elongate posterior one, nectophores lacking ridges, cusps and mouthplates, laterally compressed, with rounded apices, with somatocysts in both nectophores, somatocyst extending to apex of anterior nectophore; hydroecium in anterior nectophore extensive, greater than 70 % of nectophore height, without median mesogloeal protuberance; nectosac extends to greater than 85 % height of nectophores, looped to slightly looped lateral radial canals, origin of lateral radial canals variable, often arising separately from upper canal, pedicular canal with long descending branch in both nectophores.

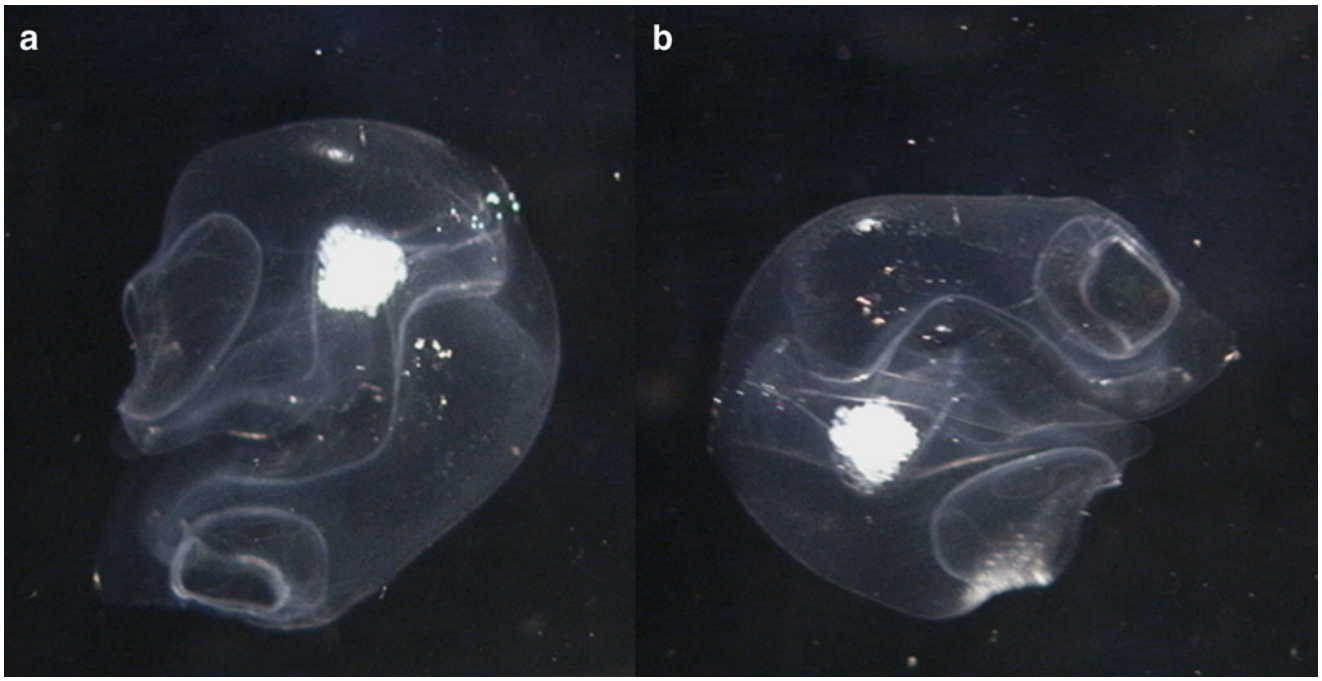

Fig. 51.19 *Rosacea plicata* captured at 675 m depth during *Shinkai 2000* dive 1183 (**a**, **b**)

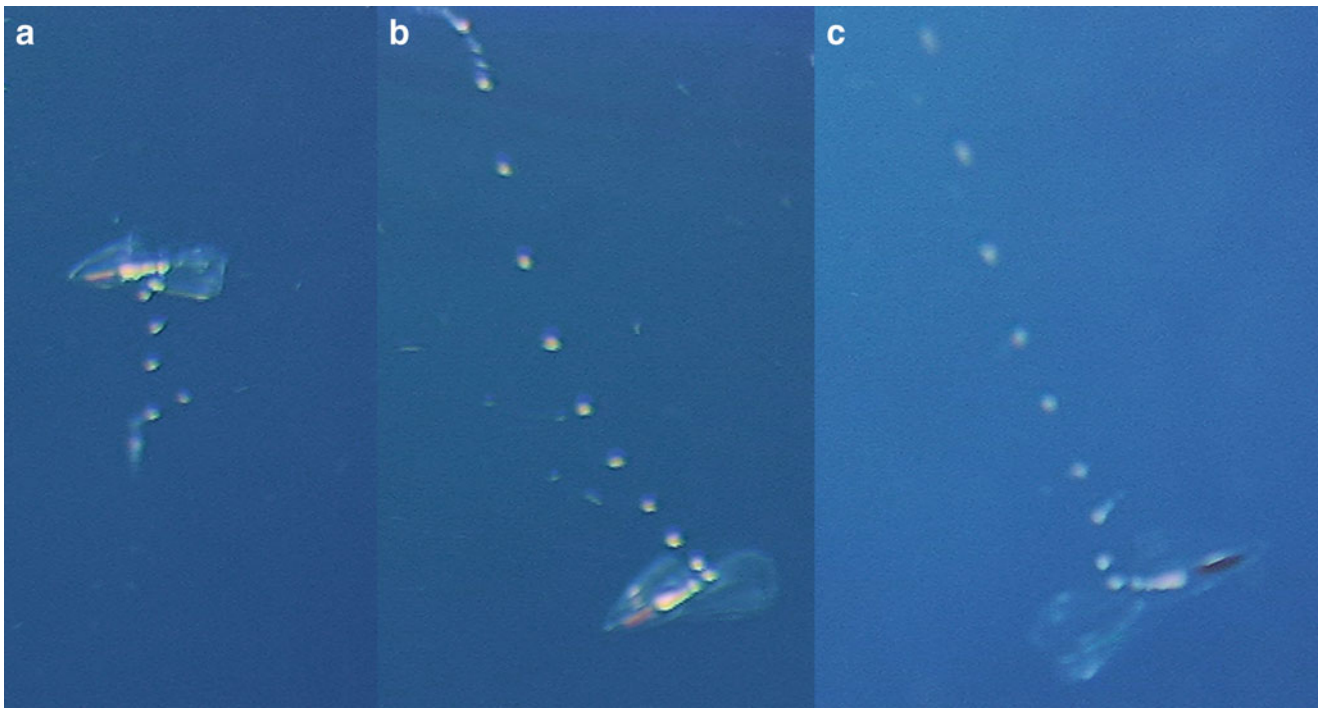

Fig. 51.20 *Kephyes* sp. observed at 1,420 m depth during ROV *HyperDolphin* dive 296 (**a**, **b**, **c**)

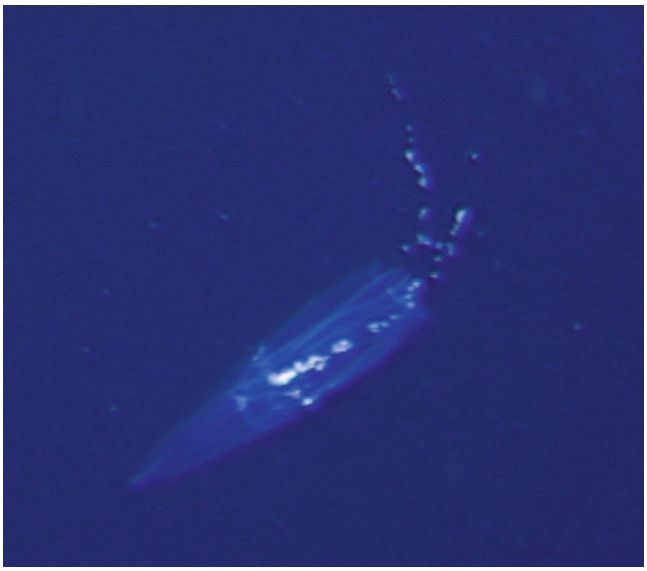

Fig. 51.21 *Chuniphyes multidentata* observed at 1,193 m depth during ROV *HyperDolphin* dive 67

Eudoxid stage: bract headpiece short, with rounded proximal end, bracteal canal system constituted by phyllocyst that almost reaches proximal end of headpiece, two hydroecial canals extending down extensive neck shield, and moderately long longitudinal canal, extending as spurs beyond the origins of the hydroecials; gonophore without distinctive ridges, with large nectosac, with flap on posterior end of right hydroecial wing, pedicular canal divides apically to form two mantle canals.

Comments: At least two species referable to this genus have been identified (personal observation). The quality of the video during the present surveys did not allow accurate identification to species level. Animals identifiable to this genus were observed at 1,078 and 1,096 m depth during ROV *HyperDolphin* dive 67, and 1,420 m during ROV *HyperDolphin* dive 296.

Type Material: Holotype of generic type (*Kephyes ovata*) collected from Messina in the Mediterranean Sea in winter 1859–1860 (38.1833N; 15.55E) described under the name *Diphyes ovata*.

Subfamily Clausophyinae Bigelow, 1913

Genus *Chuniphyes* Lens and van Riemsdijk, 1908

Chuniphyes multidentata Lens and van Riemsdijk, 1908 (Fig. 51.21)

Polygastric stage:

Anterior nectophore: up to 25 mm high. Conical nectophore with 4 ridges at apex, each ridge splitting into two in the nectophore's anterior part. Lower lateral ridges joining lower ridges slightly before posterior margin. All ridges forming small teeth at posterior margin. Hydroecium deep, extending to more than half the nectophore's height and with median mesogleal process. Somatocyst with lateral expansions and distinctly demarcated thin anterior branch extending to nectophore apex. Lateral canals sinuous.

Posterior nectophore: up to 34 mm high. Hydroecial wings well developed, with asymmetric serrated posterior teeth Hydroecial flaps in distal portion of hydroecium. Other ridges with small ostial teeth. Somatocyst thin and elongate, extending to apex of nectophore. Lateral radial canals straight.

Eudoxid stage: indistinguishable from that of *Chuniphyes moserae* Totton, 1954.

Comments: Ridges a pale gold colour. Animals identifiable to species level were observed at 1,193 m depth during ROV *HyperDolphin* dive 67, and 1,364 m during ROV *HyperDolphin* dive 295.

Type Material: Holotype collected from the Molucca Sea, Philippines, at station 141 (1.01S, 127.42E) of the Siboga expedition on 5 August 1899. Catalogue numbers 44F.I and 44F.J (anterior and posterior nectophores).

Order Anthoathecata Cornelius, 1992

Suborder Filifera Kühn, 1913

Family Bythotiaridae Maas, 1905

Genus *Protiaropsis* Stechow 1919

Protiaropsis anonyma (Maas, 1905) (Fig. 51.22)

Exumbrella thick, up to 22 mm high, with deep, rather narrow bell cavity; 4 simple radial canals; no centripetal canals; manubrium barrel-shaped, mouth with four simple lips; "gonads" interradial, on manubrial wall, no transverse folds; 6–12 hollow marginal tentacles, each terminating in a large cnidocyst cluster, no secondary tentacles; no ocelli.

Comments: The genus *Heterotiara* is preoccupied and the correct generic designation for this species is *Protiaropsis* Stechow 1919 (Stechow 1919). Several small individuals have been caught at the Hatoma Knoll (eg. HD294SS4b at 1,416 m depth, 2K1188SS3C at 990 m depth) with bell heights 7–9 mm and with eight tentacles. These were intermediate in morphology with a larger specimen (I050203A-Pa) with a bell height of 20 mm and with 8 tentacles, and with *Kanaka pelagica* Uchida, 1947, the holotype of which is 1.8 mm in bell height. It seems that *K. pelagica* is a junior synonym of *P. anonyma* (Maas, 1905).

Type Material: two syntypes collected during the Siboga Expedition in a vertical haul (0–1,000 m) at Station 148 (0.293S, 129.242E) in the Halmahera Sea, Indonesia, on 10 August 1899.

Order Trachymedusae Haeckel, 1866 (1879)

Family Halicreatidae Fewkes, 1886

Genus *Halicreas* Fewkes, 1882

Halicreas minimum Fewkes, 1882 (Fig. 51.23)

Umbrella thick, disc-like, to 40 mm diameter, with a small, conical apical projection of mesogloea and eight clusters of gelatinous papillae above bell margin; mouth wide, circular, without distinct lips; without peduncle; without centripetal canals; with eight broad, band-like radial canals and a broad ring canal; gonads flattened, extending

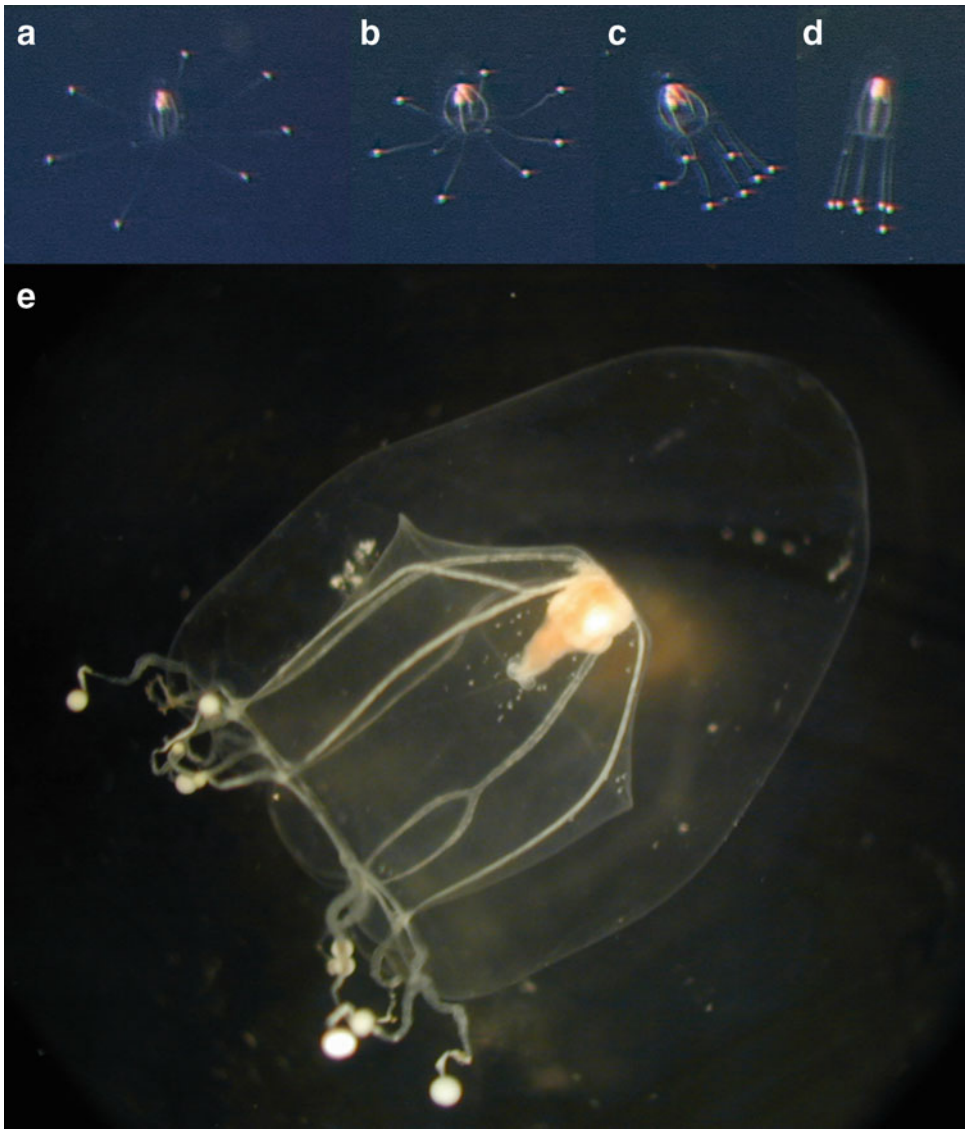

Fig. 51.22 *Protiaropsis anonyma* observed at 1,348 m during ROV *HyperDolphin* dive 226 in (**a**) fishing/feeding position, (**b**, **c**, **d**) during escape, and (**e**) a second individual (height 7 mm) captured at 990 m depth during *Shinkai 2000* dive 1188

along almost entire length of canals; with up to 640 marginal tentacles of different sizes, all structurally alike and arranged in a single series; each marginal tentacle with flexible proximal portion and stiff spine-like distal portion; with 3–4 free ecto-endodermal statocysts per octant.

Comments: An individual was observed at 721 m during ROV *HyperDolphin* dive 294.

Type Material: Holotype collected off the New England Coast.

Genus *Haliscera* Vanhöffen, 1902

Haliscera bigelowi Kramp, 1947 (Fig. 51.24)

Umbrella 15–19 mm wide, 9–10 mm high, almost hemispherical, umbrella with a very thick dome-shaped mesogleal apex comprising about 2/3 of the umbrella height, mesoglea thin at sides and margin; velum very broad; manubrium broad, flat, slightly conical; mouth simple, circular; eight straight, broad radial canals and broad circular canal; in adults, about 12 solid marginal tentacles in each octant, flexible proximally, stiff distally; the base of each tentacle surrounded by a small thickening of marginal cnidocyst tissue; with eight gonads broadly oval, flat, about 2/5 as long as the radial canals, situated slightly nearer the manubrium than to bell margin; three statocysts in each octant.

Comments: One small individual (2K1188SS2) was caught at the Hatoma Knoll during *Shinkai 2000* dive 1188 at 833 m depth.

Type Material: Holotype collected in the Northern Atlantic.

Family Rhopalonematidae Russell, 1953

Genus *Pantachogon* Maas, 1893

Pantachogon haeckeli Maas, 1893 (Fig. 51.25)

Exumbrella to about 15 mm high, sometimes slightly higher than wide, bell-shaped, with thin jelly and without apical thickening or an apical projection when mature;

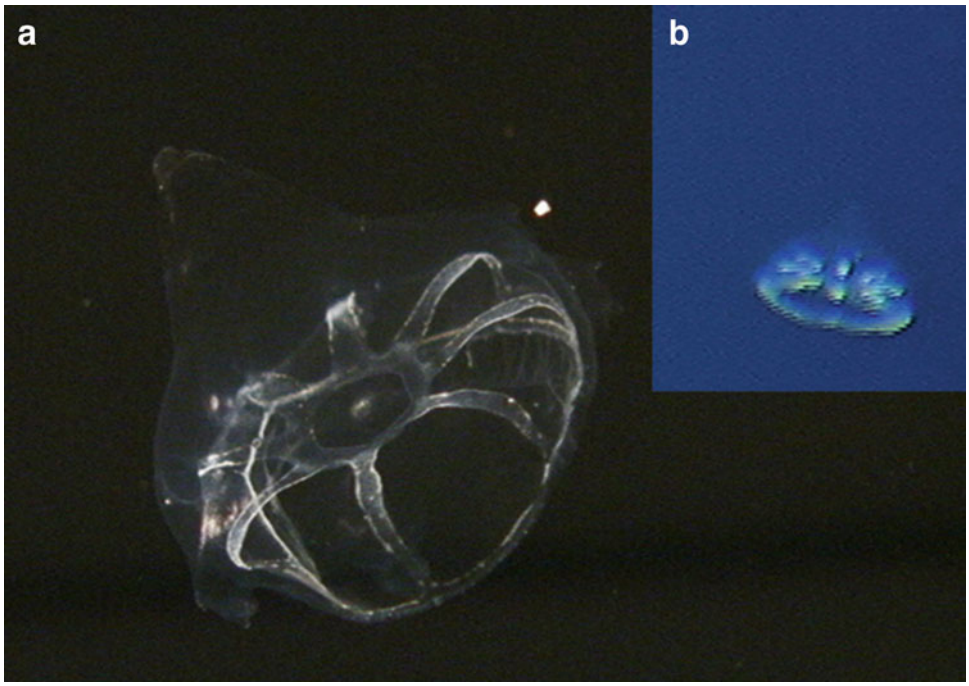

Fig. 51.23 *Halicreas minimum* (**a**) captured at 770 m depth during *Shinkai 2000* dive 1148 at a hydrothermal vent site in the Manus Basin, Papua New Guinea, and (**b**) observed at 721 m during ROV *HyperDolphin* dive 294 at the Hatoma Knoll

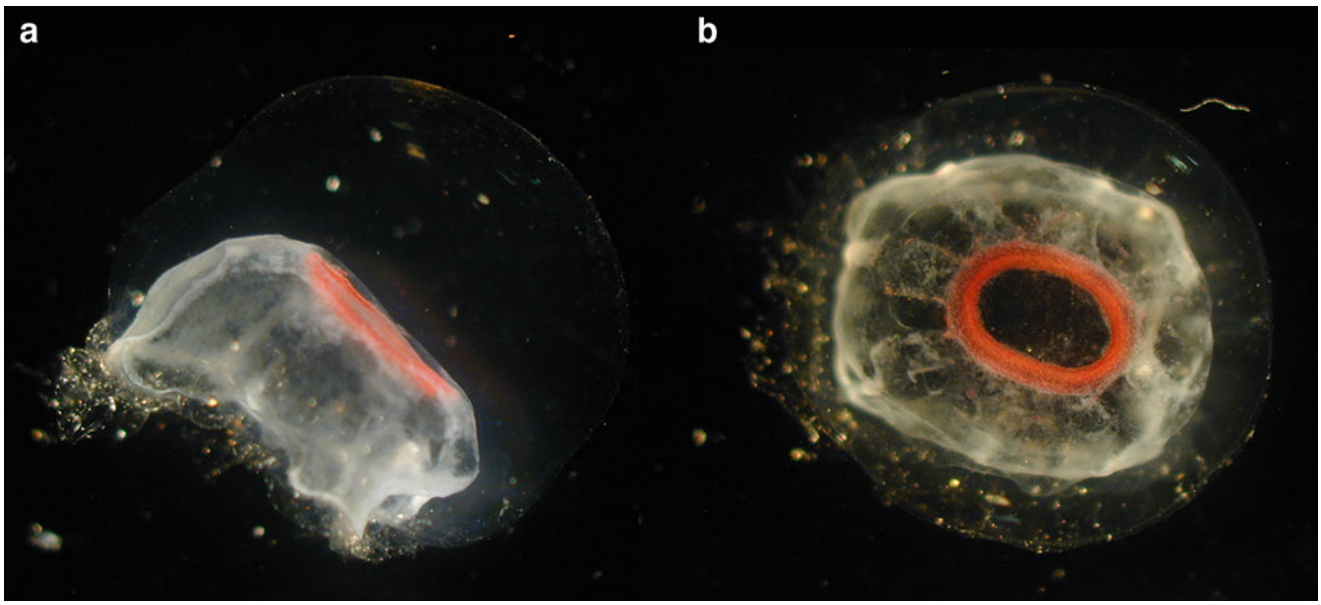

Fig. 51.24 *Haliscera bigelowi* in (**a**) lateral view, and (**b**) apical view, captured during *Shinkai 2000* dive 1188 at 833 m depth

umbrella clear when juvenile, becoming orange to red with maturity; no exumbrellar nematocysts; with very strong and conspicuous musculature and circular, apical muscle-free zone (MFZ); stomach orange to red, narrow, cylindrical, no more than three-quarters of bell height; four small, simple lips; no gastric peduncle; gonads extending along greater portion of the 8 orange, narrow radial canals but not reaching apical MFZ; mature gonads contain large, milky-white eggs along their length and project into subumbrellar cavity; ring canal narrow, with no centripetal canals; 64 solid marginal tentacles all alike and with uniform structure throughout entire length, rarely 56; 64(56) free, club-shaped, marginal statocysts; velum very broad, more than one-third of bell height.

Comments: One individual (2K1183SS1A) was caught at the Hatoma Knoll during *Shinkai 2000* dive 1183 at 753 m depth.

Type Material: Holotype collected southwest of Iceland.

Genus *Crossota* Vanhöffen, 1902

Crossota millsae Thuesen 2003 (Fig. 51.26)

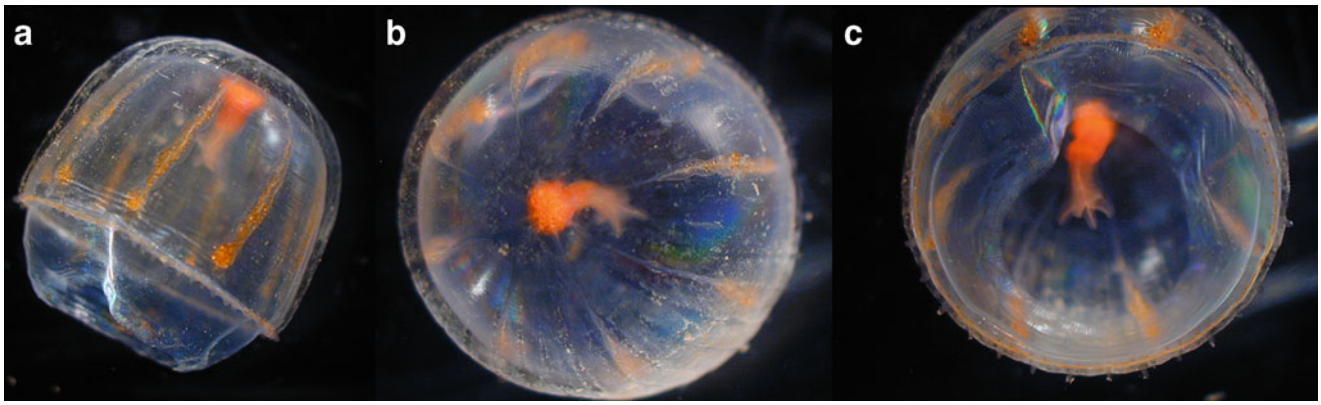

Fig. 51.25 *Pantachogon haeckeli* in (**a**) lateral view, (**b**) apical view, and (**c**) oral view, captured during *Shinkai 2000* dive 1183 at 753 m depth

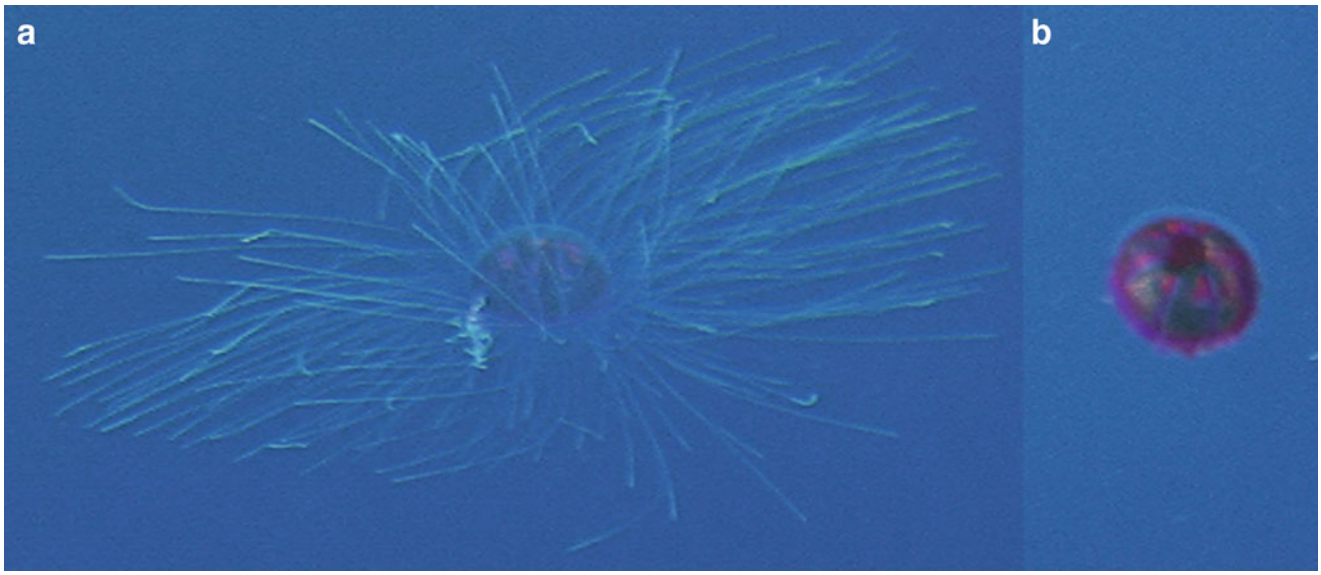

Fig. 51.26 *Crossota millsae* in (**a**) fishing/feeding position in lateral view, and (**b**) in apico-lateral view, observed and captured at 1,440 m during ROV *HyperDolphin* dive 296

Umbrella hemispherical, to 28 mm diameter and 18 mm height, subumbrellar surface burnt-tangerine, mesoglea colorless; without peduncle; numerous meridional exumbrellar furrows; 8 radial canals and a ring canal with no centripetal canals or expansions; "gonads" on radial canals, about 20 % bell height from the manubrium, male gonads pendulous sausage-shaped, female gonads globular with eggs developing into juveniles while attached to the mother; manubrium and gonads bright pink to lavender; up to 220 densely crowded solid marginal tentacles all in one row; 16 free club-shaped ecto-endodermal statocysts.

Comments: this species is bathypelagic and widespread in distribution, having been observed during *Shinkai 6500* dive 547 off the Sanriku coast (Lindsay 2005, Fig. 10, 3,668 m depth, 14:21, 8 Jun 2000), off Hawai'i, California (2,540 m and 3,244 m depth) and in the Sea of Cortez (Thuesen 2003), as well as from depths between 1,614 and 2,093 m in the Chukchi Basin, Arctic Ocean (Raskoff et al. 2010). During the present study it was observed at 1,440 m depth during ROV *HyperDolphin* dive 296.

Type Material: Holotype collected at 2,540 m depth off Monterey, California, on dive 366 of the ROV Tiburon on 2 October 2001 (36.338N, 122.901W) and deposited at the Smithsonian (SBMNH No. 349314).

Order Narcomedusae Haeckel, 1879

Family Cuninidae Bigelow, 1913

Genus *Solmissus* Haeckel, 1879

Solmissus incisa (Fewkes, 1886) (Fig. 51.27)

Umbrella up to 100 mm wide, flat, disk-like, with thin and flexible margin, mesoglea fairly thick but soft and fragile, exumbrella smooth; velum well developed; manubrium large, circular, covering subumbrella surface; 20–40

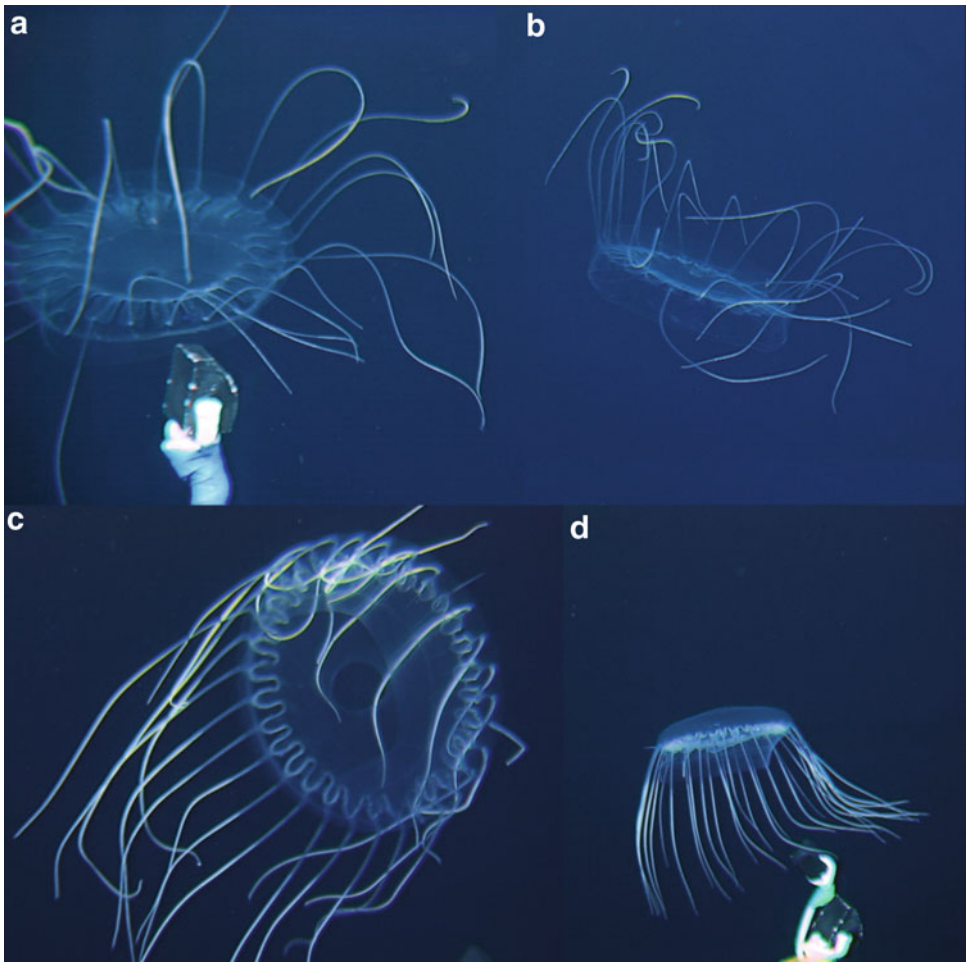

Fig. 51.27 *Solmissus incisa* morphotypes with (**a**, **b**) 23 tentacles captured at 486 m depth during ROV *HyperDolphin* dive 296, and with (**c**, **d**) 32 tentacles captured at 896 m during ROV *HyperDolphin* dive 294

perradial manubrial pouches, oval in outline, usually somewhat longer than wide, septa between them alternating with tentacle roots; 20–40 marginal tentacles, stiff, tapering, up to slightly longer than diameter of umbrella; no peripheral canal system; gonads?; marginal lappets rectangular, about as long as broad, each with 2–5 statocysts, no otoporpae.

Comments: Several different morphotypes of this species were observed. It is likely that several cryptic species are currently being referred to under this species name. Specimens were successfully sampled at 896 m (64 mm diameter, 31 tentacles) during ROV *HyperDolphin* dive 294, and at 486 m depth (23 tentacles) on ROV *HyperDolphin* dive 296, as well as during *Shinkai 2000* dive 1,183 m at 797 m depth (30 mm diameter, 31 tentacles) and dive 1188 at 770 m depth (2K1188GS1: 50 mm diameter, 32 tentacles).

Type Material: The material on which the original description was based was from several broken animals collected at 39°44′30″N 71°04′00″E (Station 2094, 1022 fathoms =1,879 m), 38°48′00″N 72°40′30″E (Station 2104, 991 fathoms =1,666 m), 35°13′10″N 74°57′15″E (Station 2110, surface) by the U.S. Fish Commission steamer *Albatross* in the region of the Gulf Stream in 1883–1884.

Family Solmarisidae Haeckel, 1879

Genus *Solmaris* Haeckel, 1879

Solmaris sp. of Arai, Cavey and Moore, 2000 (Fig. 51.28)

One individual of this species (2K1188SS1B), conforming to the description of Arai et al. (2000) in every respect, was collected during *Shinkai 2000* dive 1188 at 806 m depth. As the bell rim was not intact, and it was not possible to observe the sense organs, at this time it remains impossible to clearly distinguish it from *Solmaris quadrata* Bouillon, Boero and Seghers, 1991. The lack of stomach pouches clearly distinguishes it from *Aegina citrea* and *Aegina rosea*, and the lack of secondary tentacles also distinguishes it from *Bathykorus* species. No traces of a peripheral canal system were observed flanking the peronia, thereby excluding it from the genus *Pegantha*. The taxonomy of the narcomedusae is muddled with at least two families being paraphyletic (Lindsay, personal observation) and it is advised that all specimens be sufficiently described

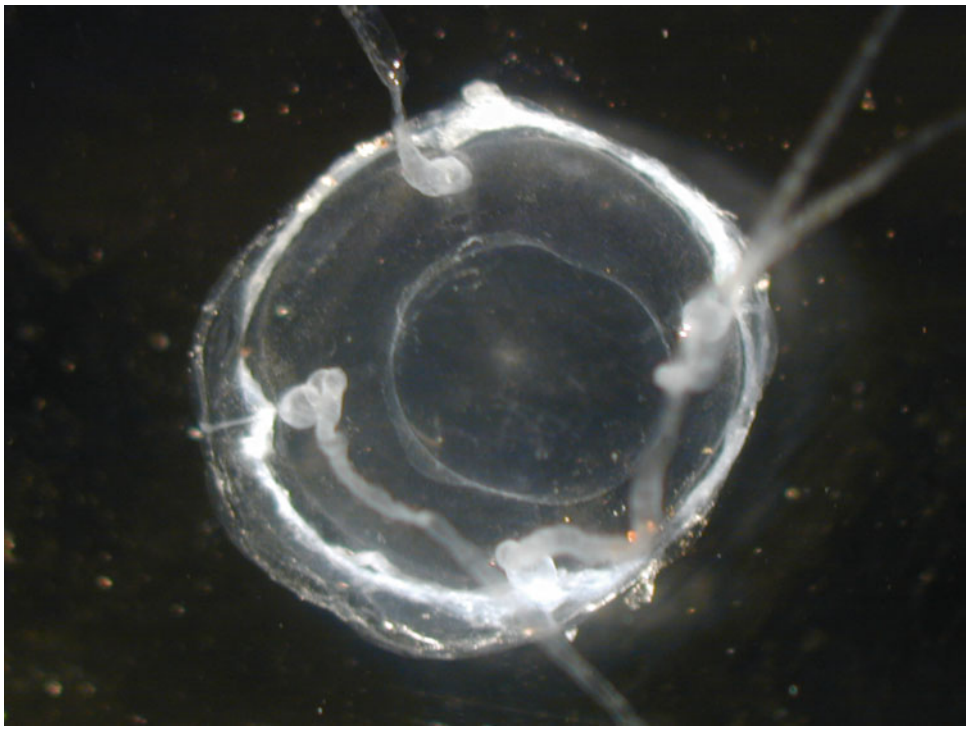

Fig. 51.28 *Solmaris* sp. collected during *Shinkai 2000* dive 1188 at 806 m depth

using the material at hand rather than simply referring them to existing species names, which often encompass multiple cryptic taxa.

Type Material: None, as the species has not yet been formally described. Most of Arai et al.'s specimens were collected off the west coast of Vancouver Island, British Columbia, Canada (Arai et al. 2000).

Family Aeginidae (Gegenbaur, 1857)

Genus *Bathykorus* Raskoff, 2010

Bathykorus? sp. A (Fig. 51.29)

A narcomedusa with four primary tentacles and four secondary tentacles, with its primary tentacles raised flush with the bell until reaching the apex and then curving sharply out at an acute angle in an "elbow" was observed (eg. *HyperDolphin* Dive 67, 1,192 m depth, 12:46, 18 Nov 2001, Fig. 51.29). This swimming behaviour is identical to that of an undescribed *Bathykorus* species that occurs off the Sanriku coast and in the vicinity of Sagami Bay (Hunt and Lindsay 1999, Fig. 5E, as "Narcomedusae sp. B"; Lindsay and Hunt 2005, Table 1, as "Aeginidae the six-tentacled one with elbows and secondary tentacles" and Table 3 as "Narcomedusae sp. A"; Kitamura et al 2008, Fig. 24.15 as "Narcomedusae gen. et sp."; Lindsay and Miyake 2009, as "Aeginidae Genus nov. Species nov."). That species, however, has up to 36 invaginations of the stomach pouches and long secondary tentacles. The sole described species of these genus, *Bathykorus bouilloni* Raskoff, 2010 has only three manubrial pouches and shorter secondary tentacles (Raskoff 2010). The present animal from the Hatoma Knoll has four stomach pouches with no visible invaginations and the secondary tentacles are so small as to be easily missed during video analysis, appearing only as faint whitenings on the bell rim at the midpoint between primary tentacles. The maximum diameter recorded for *B. bouilloni* is 1.5 cm (Raskoff 2010) while that of the undescribed Aeginidae reported by Lindsay and Miyake (2009) was 4 cm. The present observation from the Hatoma Knoll relies on the video record and there is no way to determine the size of the animal, except to say that it "seems smaller than the Sanriku species." It might be possible that these three forms are just ontogenetic stages of the same species with stomach pouch number and secondary tentacle length increasing with growth. However, at present because the distributions of the three forms are discontinuous and the present generic diagnosis for *Bathykorus* states "manubrial pouches 3x tentacle number (rarely more)" (Raskoff 2010) we refer to this animal from Hatoma Knoll as *Bathykorus?* sp.

Order Coronatae Vanhöffen, 1892

Family Atollidae Bigelow, 1913

Atolla Haeckel, 1880

Atolla wyvillei Haeckel, 1880 (Fig. 51.30)

Exumbrella flattened with deep, circular coronal furrow, jelly thickened, lenslike, slightly vaulted, with deep marginal radial furrows, to around 15 cm diameter, pigmented dark brownish red. Tentacles: alternating with marginal sense organs (rhopalia), usually 22 (rarely 17, 19, 20, 21, 29, 32, or 36), one tentacle hypertrophied. Tentacular

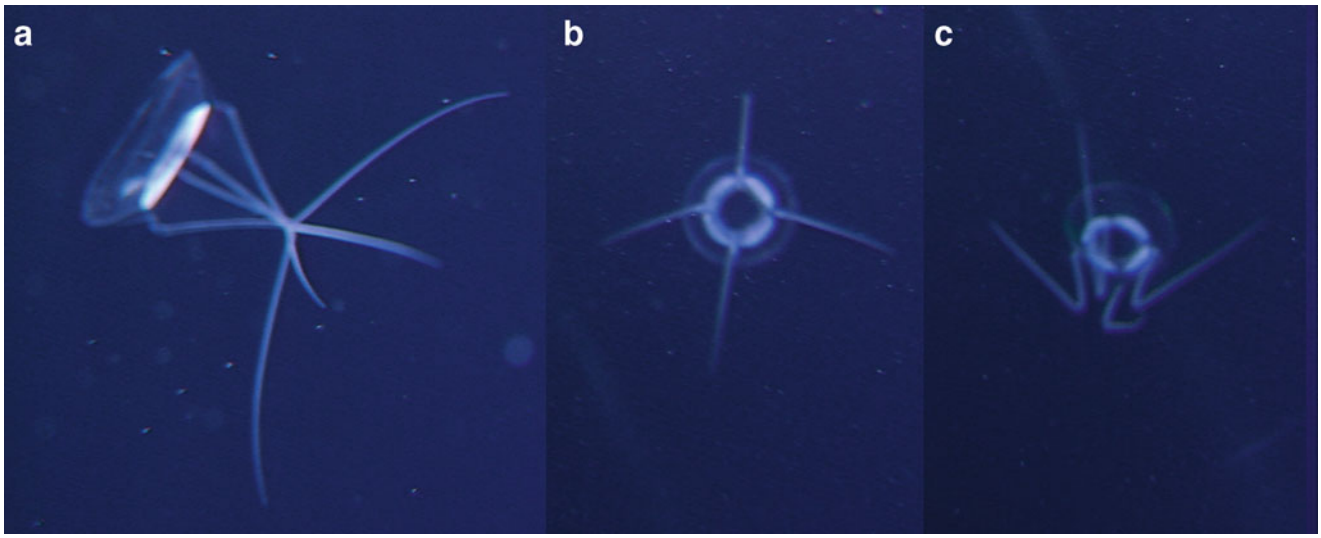

Fig. 51.29 *Bathykorus*? sp. A in (**a**) lateral, (**b**) apical, and (**c**) apico-lateral views, observed during ROV *HyperDolphin* Dive 67 at 1,192 m depth

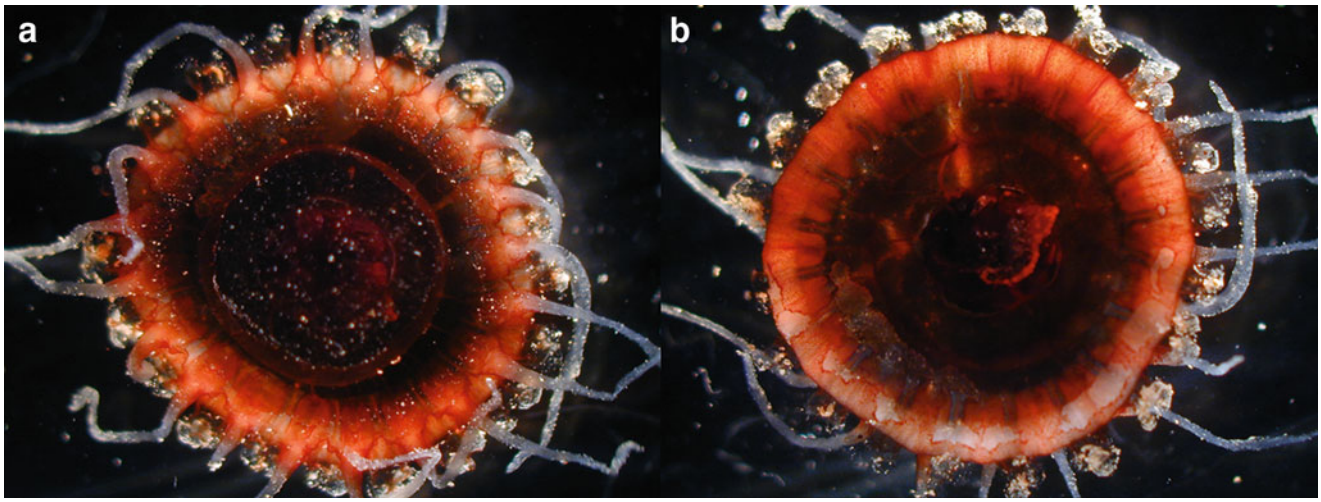

Fig. 51.30 *Atolla wyvillei* in (**a**) apical, and (**b**) oral views, captured at 837 m depth during *Shinkai 2000* dive 1188

pedalia: irregular pentagonal shape, broad base. Rhopaliar pedalia: without linear ridges of warts. Lappets: long, with rounded ends. Coronal muscle: cream-colored, thick, outer portion wavy in appearance owing to radial grooves in tentacular radii. Radial septa: paired, noticeably divergent adaxially, extending beyond margin of coronal muscle. Stomach: projecting downwards from center of bell, pigmented very dark brownish red, margin with four rounded pouches in primroselike contour, no pigment spots between stomach base and gonads. Gonads: eight, adradial; cream-colored with faint orange tint, variable in form; in small specimens (less than 5 cm in diameter) bean-shaped, in mature specimens (greater than 5 cm in diameter) auriform owing to partial abaxial curling of opaque thickened gonadal margin and with central transparent region with thin tissue covering; gonad arrangement variable, with partial contact of 4 gonadal pairs in some specimens; ova: to about 1 mm in diameter, located in center of ovaries.

Comments: An individual (2K1188SS2) was caught at 837 m depth during *Shinkai 2000* dive 1188.

Type Material: H.M.S. Challenger Collection. Five syntypes from 53°55′S, 108°35′E, 3 March 1874, 1950 fathoms, and 42°32′S, 56°27′W, 11 February 1876, 2040 fathoms.

Family Periphyllidae Haeckel, 1880

Periphylla F. Müller, 1861

Periphylla periphylla (Péron and Lesueur, 1810) (Fig. 51.31)

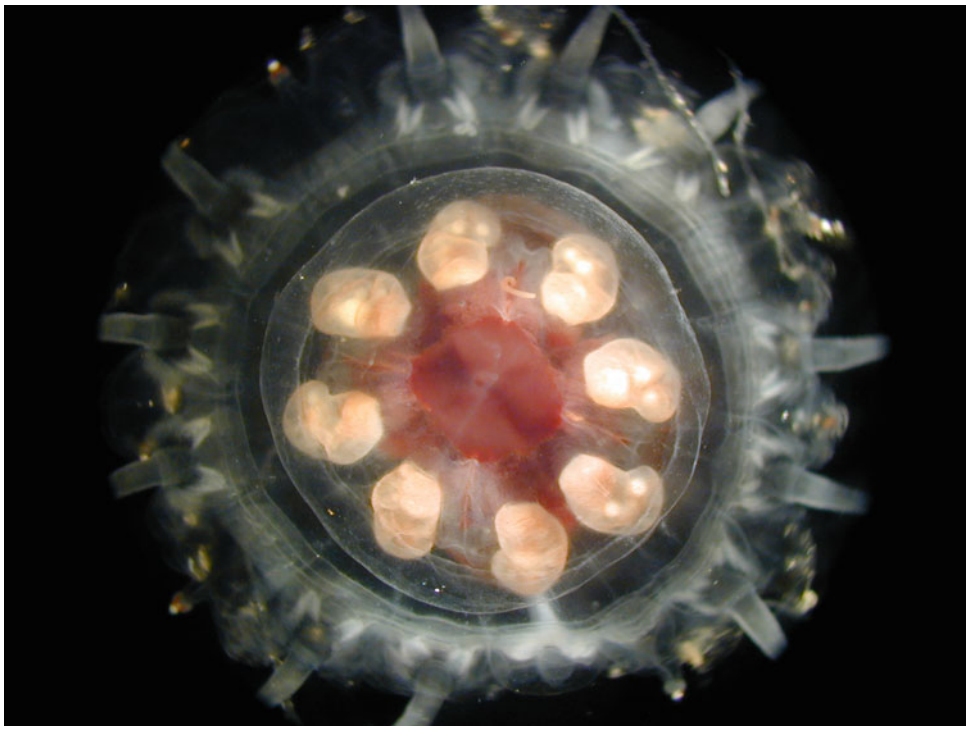

Fig. 51.31 *Periphylla periphylla* collected during *Shinkai 2000* dive 1188 at 751 m depth

Scyphomedusa with pointed or dome-shaped exumbrella, up to 350 mm wide, usually higher than wide, usually transparent, sometimes with a reddish-brown ectodermis, with margin cleft into 16 lappets, with a circular, coronal furrow; four interradial sense organs (rhopalia); 12 (4 × 3) solid marginal tentacles (four perradial and eight adradial) arising from clefts between the lappets; gonads U- or J-shaped, in four pairs, whitish; stomach not extending beyond umbrella margin, with a single mouth opening provided with simple lips, violet or reddish-brown. Pigmentation from a protoporphyrin. Swims with tentacles held forward of the bell. Nematocyst types: holotrichous isorhizas, heterotrichous microbasic euryteles.

Comments: An individual was caught at 751 m depth during *Shinkai 2000* dive 1188.

Type Material: from equatorial Atlantic Ocean, Baudin Expedition.

Acknowledgments This work was partially funded by JSPS grant KAKENHI, (24248032, 23405031), MEXT Grant-in-Aid for Scientific Research on Innovative Areas TAIGA (20109003), and JST grant CREST, the fund for Interdisciplinary Collaborative Research by the AORI, UT.

References

Arai MN, Cavey MJ, Moore BA (2000) Morphology and distribution of a deep-water Narcomedusa (Solmarisidae) from the northeast Pacific. Sci Marina 64(1):55–62

Bone Q (1998) Biology of pelagic tunicates. Oxford University Press, New York, 340

Burd BJ, Thomson RE (2000) Distribution and relative importance of jellyfish in a region of hydrothermal venting. Deep Sea Res I 47:1703–1721

Haddock SHD, Case JF (1999) Bioluminescence spectra of shallow and deep-sea gelatinous zooplankton: ctenophores, medusae and siphonophores. Mar Biol 133:571–582

Hunt JC, Lindsay DJ (1999) Methodology for creating an observational database of midwater fauna using submersibles: results from Sagami Bay, Japan. Plank Biol Ecol 46(1):75–87

Johnsen S (2005) The red and the black: bioluminescence and the color of animals in the deep sea. Integr Comp Biol 45:234–246

Kitamura M, Miyake H, Lindsay DJ (2008) Cnidaria. In: Fujikura K, Okutani T, Maruyama T (eds) Deep-sea life – biological observations using research submersibles. Tokai University Press, Kanagawa, pp 295–320

Kovacs D, Madin K (1996) Beneath Blue Waters: Meetings with Remarkable Deep-sea Creatures. Viking Children's Books, 64 pp

Lindsay DJ (2003) Bioluminescence in the mesopelagic realm, Kaiyo Month Spec Edit 35(9):606–612

Lindsay DJ (2005) Planktonic communities below 2,000 m depth. Bull Plank Soc Jpn 52(2):113–118

Lindsay DJ, Hunt JC (2005) Biodiversity in midwater cnidarians and ctenophores: submersible-based results from deep-water bays in the Japan Sea and North-western Pacific. J Mar Biol Assoc UK 85 (3):503–517

Lindsay DJ, Miyake H (2007) A Novel Benthopelagic Ctenophore from 7,217 m depth in the Ryukyu Trench, Japan, with notes on the taxonomy of deep sea cydippids. Plank Benthos Res 2(2):98–102

Lindsay DJ, Miyake H (2009) A checklist of midwater cnidarians and ctenophores from Japanese waters –species sampled during submersible surveys from 1993–2008 with notes on their taxonomy. Kaiyo Month 41(8):417–438

Lindsay DJ, Hunt JC, Hashimoto J, Fujiwara Y, Fujikura K, Miyake H, Tsuchida S (2000) Submersible observations on the deep-sea fauna of the south-west Indian Ocean: preliminary results for the mesopelagic and near-bottom communities. JAMSTEC J Deep Sea Res 16:23–33

Madin LP, Harbison GR (1978a) *Bathocyroe fosteri* gen. nov., sp. nov.: a mesopelagic ctenophore observed and collected from a submersible. J Mar Biol Assoc UK 58:559–564

Madin LP, Harbison GR (1978b) *Thalassocalyce inconstans*, new genus and species, an enigmatic ctenophore representing a new family and order. Bull Mar Sci 28(4):680–687

Raskoff K (2010) *Bathykorus bouilloni*: a new genus and species of deep-sea jellyfish from the Arctic Ocean (Hydrozoa, Narcomedusae, Aeginidae). Zootaxa 2361:57–67

Raskoff KA, Hopcroft RR, Kosobokova KN, Purcell JE, Youngbluth M (2010) Jellies under ice: ROV observations from the Arctic 2005 hidden ocean expedition. Deep-Sea Res II 57:111–126

Skebo K, Tunnicliffe V, Berdeal IG, Johnson HP (2006) Spatial patterns of zooplankton and nekton in a hydrothermally active axial valley on Juan de Fuca Ridge. Deep-Sea Res I 53:1044–1060

Stechow E (1919) Zur Kenntnis der Hydroidenfauna des Mittelmeeres, Amerikas und anderer Gebiete, nebst Angaben über einige Kirchenpauer'sche Typen von Plumulariden. Zool Jb Syst 42(1)1–172.

Thuesen EV (2003) *Crossota millsae* (Cnidaria: Trachymedusae: Rhopalonematidae), a new species of viviparous hydromedusa from the deep sea off California and Hawaii. Zootaxa 309:1–12

Toyokawa M, Toda T, Kikuchi T, Miyake H, Hashimoto J (2003) Direct observations of a dense occurrence of *Bolinopsis infundibulum* (Ctenophora) near the seafloor under the Oyashio and notes on feeding behavior. Deep-Sea Res I 50:809–813

Vereshchaka AL, Vinogradov GM (1999) Visual observations of the vertical distribution of plankton throughout the water column above the Broken Spur vent field Mid-Atlantic Ridge. Deep-Sea Res I 46:1615–1632

Vinogradov ME, Shushkina EA (2002) Vertical distribution of gelatinous macroplankton in the North Pacific observed by manned submersibles Mir-1 and Mir-2. J Oceanogr 58:295–303

Youngbluth M, Sørnes T, Hosia A, Stemmann L (2008) Vertical distribution and relative abundance of gelatinous zooplankton, in situ observations near the Mid-Atlantic Ridge. Deep-Sea Res II 55:119–125